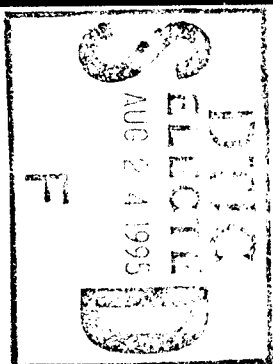


MATERIALS
RESEARCH
SOCIETY
SYMPOSIUM PROCEEDINGS

VOLUME 128

Processing and Characterization of Materials Using Ion Beams



EDITORS

Lynn E. Rehn

Joe Greene

Fred A. Smidt

DISTRIBUTION STATEMENT A

Approved for public release
Distribution Unlimited

MRS

19950822 180

Processing and Characterization of Materials Using Ion Beams

Processing and Characterization of Materials Using Ion Beams

Symposium held November 28-December 2, 1988, Boston,
Massachusetts, U.S.A.

EDITORS:

Lynn E. Rehn

Argonne National Laboratory, Argonne, Illinois, U.S.A.

Joe Greene

University of Illinois, Urbana, Illinois, U.S.A.

Fred A. Smidt

Naval Research Laboratory, Washington, D.C., U.S.A.

Accession For	
NTIS CRA&I	<input checked="" type="checkbox"/>
DTIC TAB	<input type="checkbox"/>
Unannounced	<input type="checkbox"/>
Justification	
By	
Distribution /	
Availability Codes	
Dist	Avail and/or Special
A-1	

DTIC QUALITY INSPECTED 2



MATERIALS RESEARCH SOCIETY
Pittsburgh, Pennsylvania

This work was supported in part by the Office of Naval Research under Grant Number N00014-88-J-1081. The United States Government has a royalty-free license throughout the world in all copyrightable material contained herein.

CODEN: MRSPDH

Copyright 1989 by Materials Research Society.
All rights reserved.

This book has been registered with Copyright Clearance Center, Inc. For further information, please contact the Copyright Clearance Center, Salem, Massachusetts.

Published by:

Materials Research Society
9800 McKnight Road, Suite 327
Pittsburgh, Pennsylvania 15237
Telephone (412) 367-3003

Library of Congress Cataloging in Publication Data

Processing and characterization of materials using ion beams / editors, Lynn E. Rehn, Joe Greene, Fred A. Smidt.

p. cm. — (Materials Research Society symposium proceedings : ISSN 0272-9172 ; v. 128)

Proceedings of a symposium held Nov. 28-30, 1988, Boston, Mass.

Includes index.

ISBN 1-55899-001-1

1. Ion bombardment—Congresses. 2. Ion implantation—Congresses.
3. Surfaces (Physics)—Congresses. I. Rehn, L. E. II. Greene, J. (Joseph)
III. Smidt, F.A. IV. Series. V. Series: Materials Research Society symposium proceedings ; v. 128.

QC702.7.B65P76 1989
620.1'127—dc19

89-3205
CIP

Manufactured in the United States of America

Contents

PREFACE	xv
ACKNOWLEDGMENTS	xvii
MATERIALS RESEARCH SOCIETY SYMPOSIUM PROCEEDINGS	xviii
PART I: ION-BEAM ASSISTED DEPOSITION	
*SOME RECENT RESULTS OF FUNDAMENTAL STUDIES ON BEAM-INDUCED SURFACE PROCESSES Jan Dieleman	3
STRESS MODIFICATION IN TUNGSTEN FILMS DEPOSITED BY ION-ASSISTED EVAPORATION R.A. Roy, R. Petkie, D.S. Yee, J. Karasinski, and A. Boulding	17
CONTROL OF METAL FILM PROPERTIES BY ION ASSISTED DEPOSITION Ronnien A. Roy, Dennis S. Yee, and Jerome J. Cuomo	23
SOFT MAGNETISM AND MORPHOLOGY OF Fe FILMS BY DUAL ION BEAM SPUTTERING M. Nagakubo, T. Yamamoto, and M. Naoe	29
ARGON ION BOMBARDMENT DURING MOLECULAR BEAM EPITAXY OF Ge (001) Eric Chason, K.M. Horn, J.Y. Tsao, and S.T. Picraux	35
EFFECTS OF SPUTTERED PARTICLE ENERGY ON THE PROPERTIES OF SiO ₂ FILMS Yasunori Taga and Takeshi Ohwaki	41
METAL SILICIDES FORMED BY DIRECT ION BEAM DEPOSITION R.A. Zuhr, S.J. Pennycook, T.E. Haynes, and O.W. Holland	47
ION BEAM ASSISTED DEPOSITION OF TITANIUM NITRIDE G.K. Hubler, D. Van Vechten, E.P. Donovan, and R.A. Kant	55
PROPERTIES OF SILICON OXYNITRIDE AND ALUMINUM OXYNITRIDE COATINGS DEPOSITED USING ION ASSISTED DEPOSITION G.A. Al-Jumaily, T.A. Mooney, W.A. Spurgeon, and H.M. Dauplaise	61
PLASMA-ACTIVATED ION BEAM REACTIVE SPUTTERING OF NbN THIN FILMS D.J. Lichtenwalner, Alfredo C. Anderson, and D.A. Rudman	67

*Invited Paper

INVESTIGATION OF TITANIUM NITRIDE SYNTHESIZED BY ION BEAM ENHANCED DEPOSITION	73
Zhou Jiankun, Liu Xianghuai, Chen Youshan, Zheng Zhihong, Huang Wei, Zhou Zuyao, and Zou Shichang	
B _(1-x) N _x ALLOY FILMS PREPARED BY ION BEAM ASSISTED DEPOSITION	79
C.A. Carosella, G.K. Hubler, D. Van Vechten, and E.P. Donovan	
ANALYSIS OF NITROGEN, BORON, AND HYDROGEN OF i-BN FILMS FABRICATED BY THE ION BEAM ASSISTED DEPOSITION	85
J-P. Hirvonen and J.K. Hirvonen	
A NEW APPARATUS FOR DYNAMICAL ION BEAM MIXING	91
M. Jaulin, G. LaPlanche, J. Delafond, and S. Pimbert-Michaux	
*IN SITU PARAMETRIC INVESTIGATION OF THE MECHANISM OF DIAMOND FILM DEPOSITION FROM LOW ENERGY ION BEAMS	101
Y. Lifshitz, S.R. Kasi, and J.W. Rabalais	
ION BEAM DEPOSITION OF DIAMOND-LIKE COATINGS	109
Anton C. Greenwald, James K. Hirvonen, and Narendra K. Jaggi	
*EFFECTS OF IONIZED CLUSTER BEAM BOMBARDMENT ON EPITAXIAL METAL FILM DEPOSITION ON SILICON SUBSTRATES	113
Isao Yamada	
CLUSTER SIZE MEASUREMENTS IN AN IONIZED CLUSTER BEAM SYSTEM	125
D.E. Turner, K.M. Lakin, and H.R. Shanks	
ALUMINUM ATOM SURFACE MOBILITY ON SiO ₂ DURING IONIZED CLUSTER BEAM DEPOSITION	131
Leonard L. Levenson, Amy B. Swartzlander, Hiroaki Usui, Isao Yamada, and Toshinori Takagi	
*ATOMIC-SCALE MODELING OF LOW-ENERGY ION-SOLID PROCESSES	137
Brian W. Dodson	
COLLISION CASCADE DENSIFICATION OF MATERIALS	151
R.H. Bassel, T.D. Andreadis, M. Rosen, G.P. Mueller, and G.K. Hubler	
MOLECULAR DYNAMICS SIMULATIONS OF LOW ENERGY DISPLACEMENT CASCADES IN SILICON	157
A.M. Mazzone	
A THERMAL SPIKE ANALYSIS OF LOW ENERGY ION ACTIVATED SURFACE PROCESSES	163
C.M. Gilmore, A. Haeri, and J.A. Sprague	

*Invited Paper

A MODEL OF A COMBINED FILM DEPOSITION AND ION BOMBARDMENT FOR COATINGS FORMATION Z.A. Iskanderova, T.D. Radjabov, R. Yu. Leiderman, and F.K. Tukfatullin	169
THE INFLUENCE OF DEFECT CONCENTRATIONS ON MIGRATION ENERGIES IN AgZn ALLOYS T.D. Andreadis, M. Rosen, J.M. Eridon, and D.J. Rosen	175
SUPERADDITIVITY IN THE IMPLANTATION OF MOLECULAR IONS G.F. Cerofolini, L. Meda, and C. Volpones	181
PART II: ION-BEAM MIXING	
A COMPARISON BETWEEN HIGH- AND LOW-ENERGY ION MIXING Y.-T. Cheng, E.-H. Cirlin, B.M. Clemens, and A.A. Dow	189
THERMAL SPIKE RELATED NONLINEAR EFFECTS IN ION BEAM MIXING AT LOW TEMPERATURES G-S. Chen, D. Farkas, and M. Rangaswamy	195
DIFFUSION IN IRRADIATED AgZn ALLOYS USING DEFECT-CONCENTRATION DEPENDENT MIGRATION ENERGIES T.D. Andreadis, M. Rosen, and J.M. Eridon	201
A COMPARISON OF THE MIXING RATES FOR Fe-Ti AND Ni-Ti BILAYERS P. Borgesen, D.A. Lilienfeld, R.E. Wistrom, and H.H. Johnson	207
ION-BEAM MIXING IN AMORPHOUS AND CRYSTALLINE Fe-Ti Udo Scheuer, Lynn E. Rehn, and Pete Baldo	213
THE EFFECT OF HYDROGEN CONTENT ON ION BEAM MIXING R.E. Wistrom, P. Borgesen, H.H. Johnson, and D.A. Lilienfeld	219
MAGNETIC ANOMALY AND ICOSAHEDRAL PHASE FORMATION IN Fe-Cu AND Fe-Mo SYSTEMS L.J. Huang, Q.M. Chen, B.X. Liu, Y.D. Fan, and H-D. Li	225
AMORPHOUS AND METASTABLE PHASE FORMATION IN SYSTEMS WITH POSITIVE HEATS OF MIXING USING HIGH-RATE SPUTTER DEPOSITION H.F. Rizzo, A. Echeverria, T.B. Massalski, and H. Baxi	231
MORPHOLOGY OF AMORPHOUS ALLOY FORMED BY ION BEAM BOMBARDMENT Tian Wei, Cai Wei Ping, Li Jun, and Wu Run	237
COMPOSITION- AND TEMPERATURE-DEPENDENCE OF ION MIXING IN AMORPHOUS Si/Ge ARTIFICIAL MULTILAYERS B. Park, F. Spaepen, J.M. Poate, F. Priolo, and D.C. Jacobson	243

ION BEAM INDUCED INTERMIXING OF $\text{WSi}_{0.45}$ ON GaAs S.J. Pearton, K.T. Short, K.S. Jones, A.G. Baca, and C.S. Wu	249
THERMALLY AND ION-INDUCED REACTIONS OF METAL WITH CuO SUBSTRATE Jian Li, S.Q. Wang, and J.W. Mayer	255
ION BEAM MIXING OF HIGH- T_c SUPERCONDUCTOR COMPONENTS P. Børgesen and D.A. Lilienfeld	261
PART III: MICROSTRUCTURAL CHANGES/CHARACTERIZATION	
*ANGLE OF INCIDENCE EFFECTS IN ION BEAM PROCESSING J.M.E. Harper, S.E. Hörnström, P.J. Rudeck, and R.M. Bradley	269
EPITAXIAL GROWTH OF Ni ON Si BY ION BEAM ASSISTED DEPOSITION K.S. Grabowski, R.A. Kant, and S.B. Qadri	279
Ge HETEROEPITAXY ON (100) Si SUBSTRATES BY ION ASSISTED DEPOSITION T.G. Holesinger, D.J. Heim, K.M. Lakin, and H.R. Shanks	285
SILICON HOMOEPITAXY AT LOW TEMPERATURE USING MICROWAVE MULTIPOLAR PLASMA FOR CLEANING AND DEPOSITION R. Burke, M. Guillermet, L. Vallier, and E. Voisin	291
IN SITU HVEM STUDY OF ION IRRADIATION-INDUCED GRAIN GROWTH IN Au THIN FILMS Joyce C. Liu, Jian Li, J.W. Mayer, Charles W. Allen, and Lynn E. Rehn	297
PRECIPITATION OF Ar, Kr AND Xe IN Ni AT ROOM TEMPERATURE A.S. Liu and R.C. Birtcher	303
DEUTERIUM INTERACTIONS WITH ION-IMPLANTED OXYGEN IN Cu AND Au S.M. Myers, W.A. Swansiger, and D.M. Follstaedt	309
THE EFFECTS OF Ar-BOMBARDMENT ON THE DISSOLUTION AND REPRECIPITATION OF CARBONITRIDES IMPLANTED INTO LOW CARBON STEEL Stella M.M. Ramos, L. Amaral, M. Behar, A. Vasquez, and F.C. Zawislak	315
TEMPERATURE AND ORIENTATION EFFECTS IN IRON NITRIDE CRYSTAL FORMATION L.J. Lowder, W. Franzen, and R.J. Culbertson	321
PHASES AND MICROSTRUCTURES OF CARBON-IMPLANTED NIOBIUM J.S. Huang, R.G. Musket, and M.A. Wall	327

*Invited Paper

PHASE STABILITY OF Ni_2Al_3 UNDER ELECTRON IRRADIATION E.A. Kenik and M. Nastasi	333
THE EFFECT OF SIMULTANEOUS ELECTRON AND Kr^+ IRRADIATION ON AMORPHIZATION OF CuTi J. Koike, P.R. Okamoto, L.E. Rehn, and M. Meshii	339
AMORPHIZATION OF Zr_3Al BY HYDROGENATION AND SUBSEQUENT ELECTRON IRRADIATION W.J. Meng, J. Koike, P.R. Okamoto, and L.E. Rehn	345
RADIATION INDUCED AMORPHIZATION IN $\text{YBa}_2\text{Cu}_3\text{O}_7$ AND $\text{GdBa}_2\text{Cu}_3\text{O}_7$ SUPERCONDUCTORS Don M. Parkin and Michael Nastasi	351
STRUCTURAL MODIFICATIONS INDUCED BY THE ELECTRONIC SLOWING DOWN OF SWIFT HEAVY IONS IN MATTER J.C. Jousset, E. Balanzat, S. Bouffard, and M. Toulemonde	357
MICROSTRUCTURAL CHARACTERIZATION OF Al_2O_3 FOLLOWING SIMULTANEOUS TRIPLE ION BOMBARDMENT S.J. Zinkle	363
MICROSTRUCTURES IN SiC AND Si_3N_4 IMPLANTED WITH Ti AND HEAT TREATED R.G. Vardiman	369
ION BEAM ANALYSIS OF O, N, AND B COMPOSITIONS IN MATERIALS USING NON-RUTHERFORD SCATTERING OF PROTONS N.R. Parikh, Z.H. Zhang, M.L. Swanson, N. Yu, and W.K. Chu	375
0.5 MeV SUBMICRON ION PROBE SYSTEM FOR RBS/PIXE K. Inoue, M. Takai, K. Ishibashi, Y. Kawata, N. Suzuki, and S. Namba	381
PART IV: PROPERTIES (TRIBOLOGICAL, OPTICAL, CHEMICAL)	
*TRIBOLOGY OF AMORPHOUS ALLOYS FORMED WITH ION BEAMS D.M. Follstaedt, J.A. Knapp, and L.E. Pope	389
ENHANCED WEAR RESISTANCE BY COMPRESSIVE STRENGTHENING A NOVEL COMBINATION OF LASER AND ION IMPLANTATION TECHNOLOGY H. de Beurs and J. Th. M. De Hosson	403
TRIBOLOGICAL AND MOSSBAUER STUDIES OF ION-IMPLANTED IRON D.L. Williamson, Yi Qu, Ronghua Wei, W.S. Sampath, and P.J. Wilbur	409
THE RELATIONSHIP BETWEEN CRYSTAL STRUCTURE AND HARDNESS OF NITROGEN IMPLANTED IRON SURFACE LAYERS Takanobu Fujihana, Yoshio Okabe, and Masaya Iwaki	415

*Invited Paper

FRICITION CHARACTERISTICS OF B ⁺ - AND N ₂ ⁺ -IMPLANTED Fe-Cr ALLOYS Jun Sasaki and Masaya Iwaki	421
THE CAUSES OF PROPERTY VARIATIONS OF IBAD-TITANIUM NITRIDE R.A. Kant, S.A. Dillich, B.D. Sartwell, and J.A. Sprague	427
CHARACTERIZATION OF TiN FILMS PREPARED BY ION BEAM ASSISTED DEPOSITION Albert L. Chang and R.A. Kant	433
THE FRICTION AND WEAR BEHAVIOR OF ION BEAM ASSISTED NITRIDE COATINGS Thomas G. Tetreault, J.K. Hirvonen, G. Parker, and J.P. Hirvonen	439
MICROSTRUCTURAL STUDIES OF IAD AND PVD Cr COATINGS BY CROSS SECTION TRANSMISSION ELECTRON MICROSCOPY C.C. Cheng, R.A. Erck, and G.R. Fenske	445
UNLUBRICATED SLIDING PROPERTIES OF ION BEAM AND EXCIMER LASER MIXED Fe-Ti-C MULTILAYERED FILMS J-P. Hirvonen, M. Nastasi, T.R. Jervis, J.R. Tesmer, and T.G. Zocco	451
SURFACE MECHANICAL PROPERTIES OF Ti ALLOYS PRODUCED BY EXCIMER LASER MIXING OF Ti ON AISI 304 STAINLESS STEEL T.R. Jervis, J-P. Hirvonen, M. Nastasi, T.G. Zocco, J.A. Martin, G.M. Pharr, and W.C. Oliver	457
COMBINED OXYGEN - NITROGEN ION IMPLANTS INTO Ti6Al4V Anton Greenwald, James Daly, John Meroth, Richard Oliver, Piran Sioshansi, and Clive Clayton	463
GROWTH OF STOICHIOMETRIC BN FILMS BY PULSED LASER EVAPORATION P.T. Murray, M.S. Donley, and N.T. McDevitt	469
EFFECTS OF ION BOMBARDMENT ON THE ENVIRONMENTAL DURABILITY OF SILVER COATINGS G.A. Al-Jumaily, T.A. Mooney, and A. Smajkiewicz	475
A STUDY OF THE ANODIC OXIDATION ON ALUMINIUM BY ION-IMPLANTED Xe IONS MARKER AND RBS ANALYSIS TECHNIQUES Heming Chen, Xinde Bai, Wangpei Li, and Mingjiang Dai	479
*ION BEAM PROCESSING OF OPTICAL MATERIALS F.L. Williams, L.L. Boyer, D.W. Reicher, J.J. McNally, G.A. Al-Jumaily, and J.R. McNeil	483
ION-ASSISTED DEPOSITION OF PROTECTIVE OVERLAYERS FOR MAGNETO-OPTIC ALLOYS Kenneth D. Cornett, Ursula J. Gibson, and Anthony Taylor	495

*Invited Paper

THERMAL ANNEALING INVESTIGATION OF THE OPTICAL PROPERTIES OF $\text{Si}_{1-x}\text{N}_x$ FILMS FABRICATED BY ION BEAM ASSISTED DEPOSITION	501
E.P. Donovan, C.A. Carosella, and D. Van Vechten	
PASSIVATION OF GaAs LASER MIRRORS BY ION-BEAM DEPOSITED Al_2O_3	507
D.J. Webb, H.-P. Dietrich, F. Gfeller, A. Moser, and P. Vettiger	
EVALUATION OF MULTILAYERS FOR SOFT X-RAY FABRICATED BY ION BEAM SPUTTERING	513
I. Kataoka, I. Yamada, K. Eto, and K. Ito	
HIGH DOSE IMPLANTATION OF NITROGEN AND PHOSPHOR INTO SILICA GLASS	519
Takashi Tagami, Keiji Oyoshi, and Shuhei Tanaka	
MICROTOPOGRAPHY OF ION BEAM ETCHED NiP FILMS	525
Kazuhiko Noguchi, Ryuzi Ueda, Yoshitaka Maeyama, Shigeo Sasaki, and Kazumichi Machida	
PART V: ELECTRONIC MATERIALS	
*ION-BEAM-INDUCED EPITAXY AND SOLUTE SEGREGATION AT THE Si CRYSTAL-AMORPHOUS INTERFACE	533
J.M. Poate, D.C. Jacobson, F. Priolo, and Michael O. Thompson	
SEGREGATION OF Ag AND Cu DURING ION BEAM AND THERMALLY INDUCED RECRYSTALLIZATION OF AMORPHOUS Si	545
J.S. Custer, Michael O. Thompson, and J.M. Poate	
STUDY OF ENHANCED SOLID PHASE EPITAXY OF AMORPHOUS SILICON WITH LOW CONCENTRATIONS OF IMPLANTED PHOSPHOROUS	551
Young-Jin Jeon, Won Woo Park, M.F. Becker, and Rodger M. Walser	
INFLUENCE OF PHOSPHORUS DOPANT CONCENTRATION ON RECRYSTALLIZATION OF BURIED AMORPHOUS LAYERS IN $\text{Si}(100)$ PRODUCED BY CHANNELED IMPLANTS	557
R.J. Schreutelkamp, K.T.F. Janssen, F.W. Saris, J.F.M. Westendorp, and R.E. Kaim	
ION-ASSISTED REGROWTH OF DEPOSITED Si LAYERS MECHANISMS AND MORPHOLOGY	563
F. Priolo, C. Spinella, A. La Ferla, A. Battaglia, E. Rimini, G. Ferla, A. Carnera, and A. Gasparotto	
SELF ANNEALING IMPLANTATION OF As^+ IN SILICON	569
M. Berti, A.V. Drigo, R. Lotti, G. Lulli, and P.G. Merli	
ION BEAM SELF ANNEALING IN THIN SILICON FILMS	575
J.D. Rubio, R.P. Vijay, R.R. Hart, and J.D. Pearce	

*Invited Paper

INFLUENCE OF THE IMPLANTED SPECIES ON THE RESIDUAL DAMAGE AFTER HOT IMPLANTS IN SILICON	581
L. Calcagno, C. Spinella, M. Catania, S.U. Campisano, G. Foti, G. Ferla, and E. Rimini	
FURNACE ANNEAL OF a-AXIS SAPPHIRE AMORPHISED BY INDIUM ION IMPLANTATION	587
D.K. Sood and D.X. Cao	
DAMAGE FORMATION IN SEMICONDUCTORS DURING MeV ION IMPLANTATION	593
T.P. Sjoreen, O.W. Holland, M.K. El-Ghor, and C.W. White	
ELECTRICAL ACTIVATION OF HEAVILY DOPED ARSENIC IMPLANTED SILICON	599
J. Said, H. Jaouen, G. Ghibaudo, I. Stoemenos, and P. Zaumseil	
RADIATION DAMAGE OF SiO ₂ /Si BY ENERGETIC NEUTRAL BEAM AND VUV PHOTONS	605
Tatsumi Mizutani, Shigeru Nishimatsu, and Takashi Yunogami	
A COMPARISON OF LOW ENERGY BF ₂ IMPLANTATION IN Si AND Ge PREAMORPHIZED SILICON	611
Gary A. Ruggles, Shin-Nam Hong, Jimmie J. Wortman, Mehmet Ozturk, Edward R. Myers, John J. Hren, and Richard B. Fair	
ION IMPLANTATION DOPING OF SIMOX WITH ³¹ P AND ⁶⁹ Ga	617
K.S. Jones, D. Venables, C.R. Horne, and G. Davis	
LOW-DEFECT, HIGH-QUALITY SIMOX PRODUCED BY MULTIPLE OXYGEN IMPLANTATION WITH SUBSTOICHIOMETRIC TOTAL DOSE	623
F. Namavar, E. Cortesi, and P. Sioshansi	
INFLUENCE OF ION-IMPLANTATION ON CHARACTERISTICS OF PICOSECOND PHOTOCONDUCTIVE SWITCHES	629
John F. Knudsen, Robert C. Bowman, Jr., Duane D. Smith, and Steven C. Moss	
FORMATION OF SHALLOW BORON P ⁺ JUNCTIONS USING Sb AMORPHIZATION	635
E. Ganin, B. Davari, D. Hameiri, G. Scilla, and G.A. Sai-Halasz	
SILICIDED SHALLOW JUNCTION FORMATION USING ION IMPLANTATION AND THERMAL ANNEALING	641
Leonard M. Rubin, N. Herbots, D. Hoffman, and D. Ma	
ON THE STRUCTURE, COMPOSITION, AND I-V CHARACTERISTICS OF Al/Ti:W/a-Si CONTACTS	647
S. Berger and Y. Komem	

SYNTHESIS OF TWO-LAYER TiB_2 - TiSi_2 STRUCTURES BY BORON IMPLANTATION INTO TITANIUM FILM AND RAPID THERMAL ANNEALING	653
V.V. Tokarev, A.I. Demchenko, A.I. Ivanov, V.E. Borisenko, and D.I. Zarovsky	
SYNTHESIS OF TRANSITION METAL EPITAXIAL SILICIDES ON SILICON (100), (111)	659
V.V. Tokarev, V.E. Borisenko, and T.M. Pyatkova	
ATOMIC PROFILES AND ELECTRICAL CHARACTERISTICS OF VERY HIGH ENERGY (8-20 MeV) Si IMPLANTS IN GaAs	665
Phillip E. Thompson, Harry B. Dietrich, James M. Eridon, and Thomas Gresko	
INTERBAND OPTICAL PROPERTIES OF THE MICROCRYSTALLINE COMPONENT WITHIN THE DAMAGE LAYER OF Be^+ -IMPLANTED GaAs	671
G.F. Feng and R. Zallen	
CHARACTERISTICS OF Si-IMPLANTED (211) VERSUS (100) GaAs	677
J. Epp, J.G. Dillard, A. Siochi, R. Zallen, E.D. Cole, S. Sen, A. Vaseashta, and L.C. Burton	
ABOUT SOME PECULIARITIES IN DEFECT APPEARANCE IN ELEMENTAL AND III-V COMPOUND SEMICONDUCTING MATERIALS	683
Maria G. Kalitzova, N.K. Pashov, G. Vitali, and M. Rossi	
ION ENERGY AND DOSE EFFECTS DURING ION-ASSISTED EPITAXIAL GROWTH OF InAs ON Si(100)	689
C.-H. Choi and S.A. Barnett	
ION BOMBARDMENT EFFECTS ON GaAs USING 100eV NITROGEN IONS	695
W.M. Lau	
THIN FILMS OF p-TYPE CdTe GROWN WITH ION-BEAM-ASSISTED DOPING	701
Paul Sharps, Alan L. Fahrenbruch, Adolfo Lopez-Otero, and Richard H. Bube	
ION IMPLANTATION OF BORON IN DIAMOND	707
G.S. Sandhu, M.L. Swanson, and W.K. Chu	
ION IMPLANTATION AND ION BEAM ANALYSIS OF LITHIUM NIOBATE	713
G.W. Arnold	
ION IMPLANTATION OF KNbO_3 AND LiNbO_3 AT ELEVATED TEMPERATURES	719
Ch. Buchal, R. Irmscher, and P. Günter	
EFFECT OF MICROSTRUCTURE ON THE SHEET RESISTANCE OF ION-BEAM DEPOSITED ZnO THIN FILM	725
Saliman A. Isa, P.K. Ghosh, and P.G. Kornreich	

EFFECT OF ION BOMBARDMENT ON THE DOPANT DIFFUSION DURING REACTIVE ION ETCHING (RIE) OF DIELECTRIC FILMS DEPOSITED ON SILICON	731
K. Shenai, N. Lewis, G.A. Smith, and B.J. Baliga	
ELECTRICALLY CONDUCTING THIN FILMS BY ION IMPLANTATION OF PYROLYZED POLYACRYLONITRILE	737
R.A. Basheer	
MICRO-RBS ANALYSIS OF MASKLESSLY FABRICATED STRUCTURES	743
A. Kinomura, M. Takai, T. Matsuo, M. Satou, M. Kiuchi, K. Fujii, and S. Namba	
DEPTH PROFILING OF ION BEAM INDUCED DAMAGE IN SEMICONDUCTOR HETEROSTRUCTURES	749
R. Germann, A. Forchel, G. Hörcher, and G. Weimann	
AUTHOR INDEX	755
SUBJECT INDEX	759

Preface

This volume contains papers presented at the Materials Research Society symposium entitled "Processing and Characterization of Materials Using Ion Beams" which was held in Boston, Massachusetts from November 28 to December 2, 1988. The symposium, which focused on ion-target interactions, was the eleventh in the series of MRS symposia on energetic-beam interactions with solids that has evolved from the original "Laser Annealing" meeting. Clearly, our fundamental understanding of ion-solid interactions has matured considerably during the intervening years. However, as pointed out particularly in the invited presentations, several older questions remain unanswered. The present symposium began with a half-day plenary session, organized jointly with the symposium on "Laser and Particle-Beam Chemical Processes on Surfaces," which was attended by over 500 people. In this opening session, four internationally recognized scientists reviewed recent experimental and theoretical progress in understanding the effects of low-energy ions on surfaces. A second joint session, co-organized with the symposium on "New Materials Approaches to Tribology: Theory and Applications," was held Wednesday morning. Eleven papers on tribological aspects of ion- and laser-modified surfaces were presented and discussed in this session; additional joint papers were presented at the poster session on Thursday evening.

In total, 116 papers were accepted for publication. All papers published in this volume were refereed using the peer review process. The proceedings have been divided according to content into five sections covering the main topics addressed at the meeting: Ion-Beam-Assisted Deposition, Ion-Beam Mixing, Microstructural Changes and Characterization, Properties (Tribological, Optical, Chemical), and Electronic Materials. Please note that although many papers fit appropriately into more than one of these categories, they are for obvious reasons only published in one.

February, 1989

Lynn E. Rehn
Joe Greene
Fred A. Smidt

Acknowledgments

We wish to thank the many participants who contributed to the success of this symposium. In particular we wish to acknowledge the authors and referees, whose efforts made rapid publication of a quality proceedings possible. We also recognize the excellent overviews of currently important topics that were provided by the invited speakers. They are:

J. Dieleman	J.R. McNeil
B. Dodson	J.M. Poate
D.M. Follstaedt	J.W. Rabalais
J.M.E. Harper	J.-E. Sundgren
	I. Yamada

We wish to acknowledge the session chairs, both for insuring that the individual sessions flowed smoothly and for providing direction during the discussion periods. They are:

S.A. Barnett	C. McHargue
J.J. Cuomo	S.T. Picraux
J. Mayer	I. Singer
	H. Wiedersich

It is a sincere pleasure to thank our financial sponsors, the Office of Naval Research (D.E. Polk) and National Electrostatics Corporation.

Finally, we are indebted to D. Livengood at Argonne National Laboratory for invaluable secretarial support.

MATERIALS RESEARCH SOCIETY SYMPOSIUM PROCEEDINGS

ISSN 0272 - 9172

- Volume 1—Laser and Electron-Beam Solid Interactions and Materials Processing, J. F. Gibbons, L. D. Hess, T. W. Sigmon, 1981, ISBN 0-444-00595-1
- Volume 2—Defects in Semiconductors, J. Narayan, T. Y. Tan, 1981, ISBN 0-444-00596-X
- Volume 3—Nuclear and Electron Resonance Spectroscopies Applied to Materials Science, E. N. Kaufmann, G. K. Shenoy, 1981, ISBN 0-444-00597-8
- Volume 4—Laser and Electron-Beam Interactions with Solids, B. R. Appleton, G. K. Celler, 1982, ISBN 0-444-00693-1
- Volume 5—Grain Boundaries in Semiconductors, H. J. Leamy, G. E. Pike, C. H. Seager, 1982, ISBN 0-444-00697-4
- Volume 6—Scientific Basis for Nuclear Waste Management IV, S. V. Topp, 1982, ISBN 0-444-00699-0
- Volume 7—Metastable Materials Formation by Ion Implantation, S. T. Picraux, W. J. Choyke, 1982, ISBN 0-444-00692-3
- Volume 8—Rapidly Solidified Amorphous and Crystalline Alloys, B. H. Kear, B. C. Giessen, M. Cohen, 1982, ISBN 0-444-00698-2
- Volume 9—Materials Processing in the Reduced Gravity Environment of Space, G. E. Rindone, 1982, ISBN 0-444-00691-5
- Volume 10—Thin Films and Interfaces, P. S. Ho, K.-N. Tu, 1982, ISBN 0-444-00774-1
- Volume 11—Scientific Basis for Nuclear Waste Management V, W. Lutze, 1982, ISBN 0-444-00725-3
- Volume 12—In Situ Composites IV, F. D. Lemkey, H. E. Cline, M. McLean, 1982, ISBN 0-444-00726-1
- Volume 13—Laser-Solid Interactions and Transient Thermal Processing of Materials, J. Narayan, W. L. Brown, R. A. Lemons, 1983, ISBN 0-444-00788-1
- Volume 14—Defects in Semiconductors II, S. Mahajan, J. W. Corbett, 1983, ISBN 0-444-00812-8
- Volume 15—Scientific Basis for Nuclear Waste Management VI, D. G. Brookins, 1983, ISBN 0-444-00780-6
- Volume 16—Nuclear Radiation Detector Materials, E. E. Haller, H. W. Kraner, W. A. Higinbotham, 1983, ISBN 0-444-00787-3
- Volume 17—Laser Diagnostics and Photochemical Processing for Semiconductor Devices, R. M. Osgood, S. R. J. Brueck, H. R. Schlossberg, 1983, ISBN 0-444-00782-2
- Volume 18—Interfaces and Contacts, R. Ludeke, K. Rose, 1983, ISBN 0-444-00820-9
- Volume 19—Alloy Phase Diagrams, L. H. Bennett, T. B. Massalski, B. C. Giessen, 1983, ISBN 0-444-00809-8
- Volume 20—Intercalated Graphite, M. S. Dresselhaus, G. Dresselhaus, J. E. Fischer, M. J. Moran, 1983, ISBN 0-444-00781-4
- Volume 21—Phase Transformations in Solids, T. Tsakalakos, 1984, ISBN 0-444-00901-9
- Volume 22—High Pressure in Science and Technology, C. Homan, R. K. MacCrone, E. Whalley, 1984, ISBN 0-444-00932-9 (3 part set)
- Volume 23—Energy Beam-Solid Interactions and Transient Thermal Processing, J. C. C. Fan, N. M. Johnson, 1984, ISBN 0-444-00903-5
- Volume 24—Defect Properties and Processing of High-Technology Nonmetallic Materials, J. H. Crawford, Jr., Y. Chen, W. A. Sibley, 1984, ISBN 0-444-00904-3
- Volume 25—Thin Films and Interfaces II, J. E. E. Baglin, D. R. Campbell, W. K. Chu, 1984, ISBN 0-444-00905-1

MATERIALS RESEARCH SOCIETY SYMPOSIUM PROCEEDINGS

- Volume 26—Scientific Basis for Nuclear Waste Management VII, G. L. McVay, 1984, ISBN 0-444-00906-X
- Volume 27—Ion Implantation and Ion Beam Processing of Materials, G. K. Hubler, O. W. Holland, C. R. Clayton, C. W. White, 1984, ISBN 0-444-00869-1
- Volume 28—Rapidly Solidified Metastable Materials, B. H. Kear, B. C. Giessen, 1984, ISBN 0-444-00935-3
- Volume 29—Laser-Controlled Chemical Processing of Surfaces, A. W. Johnson, D. J. Ehrlich, H. R. Schlossberg, 1984, ISBN 0-444-00894-2
- Volume 30—Plasma Processing and Synthesis of Materials, J. Szekely, D. Apelian, 1984, ISBN 0-444-00895-0
- Volume 31—Electron Microscopy of Materials, W. Krakow, D. A. Smith, L. W. Hobbs, 1984, ISBN 0-444-00898-7
- Volume 32—Better Ceramics Through Chemistry, C. J. Brinker, D. E. Clark, D. R. Ulrich, 1984, ISBN 0-444-00898-5
- Volume 33—Comparison of Thin Film Transistor and SOI Technologies, H. W. Lam, M. J. Thompson, 1984, ISBN 0-444-00899-3
- Volume 34—Physical Metallurgy of Cast Iron, H. Fredriksson, M. Hillerts, 1985, ISBN 0-444-00938-8
- Volume 35—Energy Beam-Solid Interactions and Transient Thermal Processing/1984, D. K. Biegelsen, G. A. Rozgonyi, C. V. Shank, 1985, ISBN 0-931837-00-6
- Volume 36—Impurity Diffusion and Gettering in Silicon, R. B. Fair, C. W. Pearce, J. Washburn, 1985, ISBN 0-931837-01-4
- Volume 37—Layered Structures, Epitaxy, and Interfaces, J. M. Gibson, L. R. Dawson, 1985, ISBN 0-931837-02-2
- Volume 38—Plasma Synthesis and Etching of Electronic Materials, R. P. H. Chang, B. Abeles, 1985, ISBN 0-931837-03-0
- Volume 39—High-Temperature Ordered Intermetallic Alloys, C. C. Koch, C. T. Liu, N. S. Stoloff, 1985, ISBN 0-931837-04-9
- Volume 40—Electronic Packaging Materials Science, E. A. Giess, K.-N. Tu, D. R. Uhlmann, 1985, ISBN 0-931837-05-7
- Volume 41—Advanced Photon and Particle Techniques for the Characterization of Defects in Solids, J. B. Roberto, R. W. Carpenter, M. C. Wittels, 1985, ISBN 0-931837-06-5
- Volume 42—Very High Strength Cement-Based Materials, J. F. Young, 1985, ISBN 0-931837-07-3
- Volume 43—Fly Ash and Coal Conversion By-Products: Characterization, Utilization, and Disposal I, G. J. McCarthy, R. J. Lauf, 1985, ISBN 0-931837-08-1
- Volume 44—Scientific Basis for Nuclear Waste Management VIII, C. M. Jantzen, J. A. Stone, R. C. Ewing, 1985, ISBN 0-931837-09-X
- Volume 45—Ion Beam Processes in Advanced Electronic Materials and Device Technology, B. R. Appleton, F. H. Eisen, T. W. Sigmon, 1985, ISBN 0-931837-10-3
- Volume 46—Microscopic Identification of Electronic Defects in Semiconductors, N. M. Johnson, S. G. Bishop, G. D. Watkins, 1985, ISBN 0-931837-11-1
- Volume 47—Thin Films: The Relationship of Structure to Properties, C. R. Aita, K. S. SreeHarsha, 1985, ISBN 0-931837-12-X
- Volume 48—Applied Materials Characterization, W. Katz, P. Williams, 1985, ISBN 0-931837-13-8
- Volume 49—Materials Issues in Applications of Amorphous Silicon Technology, D. Adler, A. Madan, M. J. Thompson, 1985, ISBN 0-931837-14-6

MATERIALS RESEARCH SOCIETY SYMPOSIUM PROCEEDINGS

- Volume 50—Scientific Basis for Nuclear Waste Management IX, L. O. Werme, 1986, ISBN 0-931837-15-4
- Volume 51—Beam-Solid Interactions and Phase Transformations, H. Kurz, G. L. Olson, J. M. Poate, 1986, ISBN 0-931837-16-2
- Volume 52—Rapid Thermal Processing, T. O. Sedgwick, T. E. Seidel, B.-Y. Tsaur, 1986, ISBN 0-931837-17-0
- Volume 53—Semiconductor-on-Insulator and Thin Film Transistor Technology, A. Chiang, M. W. Geis, L. Pfeiffer, 1986, ISBN 0-931837-18-9
- Volume 54—Thin Films—Interfaces and Phenomena, R. J. Nemanich, P. S. Ho, S. S. Lau, 1986, ISBN 0-931837-19-7
- Volume 55—Biomedical Materials, J. M. Williams, M. F. Nichols, W. Zingg, 1986, ISBN 0-931837-20-0
- Volume 56—Layered Structures and Epitaxy, J. M. Gibson, G. C. Osbourn, R. M. Tromp, 1986, ISBN 0-931837-21-9
- Volume 57—Phase Transitions in Condensed Systems—Experiments and Theory, G. S. Cargill III, F. Spaepen, K.-N. Tu, 1987, ISBN 0-931837-22-7
- Volume 58—Rapidly Solidified Alloys and Their Mechanical and Magnetic Properties, B. C. Giessen, D. E. Polk, A. I. Taub, 1986, ISBN 0-931837-23-5
- Volume 59—Oxygen, Carbon, Hydrogen, and Nitrogen in Crystalline Silicon, J. C. Mikkelsen, Jr., S. J. Pearton, J. W. Corbett, S. J. Pennycook, 1986, ISBN 0-931837-24-3
- Volume 60—Defect Properties and Processing of High-Technology Nonmetallic Materials, Y. Chen, W. D. Kingery, R. J. Stokes, 1986, ISBN 0-931837-25-1
- Volume 61—Defects in Glasses, F. L. Galeener, D. L. Griscom, M. J. Weber, 1986, ISBN 0-931837-26-X
- Volume 62—Materials Problem Solving with the Transmission Electron Microscope, L. W. Hobbs, K. H. Westmacott, D. B. Williams, 1986, ISBN 0-931837-27-8
- Volume 63—Computer-Based Microscopic Description of the Structure and Properties of Materials, J. Broughton, W. Krakow, S. T. Pantelides, 1986, ISBN 0-931837-28-6
- Volume 64—Cement-Based Composites: Strain Rate Effects on Fracture, S. Mindess, S. P. Shah, 1986, ISBN 0-931837-29-4
- Volume 65—Fly Ash and Coal Conversion By-Products: Characterization, Utilization and Disposal II, G. J. McCarthy, F. P. Glasser, D. M. Roy, 1986, ISBN 0-931837-30-8
- Volume 66—Frontiers in Materials Education, L. W. Hobbs, G. L. Liedl, 1986, ISBN 0-931837-31-6
- Volume 67—Heteroepitaxy on Silicon, J. C. C. Fan, J. M. Poate, 1986, ISBN 0-931837-33-2
- Volume 68—Plasma Processing, J. W. Coburn, R. A. Gottscho, D. W. Hess, 1986, ISBN 0-931837-34-0
- Volume 69—Materials Characterization, N. W. Cheung, M.-A. Nicolet, 1986, ISBN 0-931837-35-9
- Volume 70—Materials Issues in Amorphous-Semiconductor Technology, D. Adler, Y. Hamakawa, A. Madan, 1986, ISBN 0-931837-36-7
- Volume 71—Materials Issues in Silicon Integrated Circuit Processing, M. Wittmer, J. Stimmell, M. Strathman, 1986, ISBN 0-931837-37-5
- Volume 72—Electronic Packaging Materials Science II, K. A. Jackson, R. C. Pohanka, D. R. Uhlmann, D. R. Ulrich, 1986, ISBN 0-931837-38-3
- Volume 73—Better Ceramics Through Chemistry II, C. J. Brinker, D. E. Clark, D. R. Ulrich, 1986, ISBN 0-931837-39-1
- Volume 74—Beam-Solid Interactions and Transient Processes, M. O. Thompson, S. T. Picraux, J. S. Williams, 1987, ISBN 0-931837-40-5

MATERIALS RESEARCH SOCIETY SYMPOSIUM PROCEEDINGS

- Volume 75—Photon, Beam and Plasma Stimulated Chemical Processes at Surfaces, V. M. Donnelly, I. P. Herman, M. Hirose, 1987, ISBN 0-931837-41-3
- Volume 76—Science and Technology of Microfabrication, R. E. Howard, E. L. Hu, S. Namba, S. Pang, 1987, ISBN 0-931837-42-1
- Volume 77—Interfaces, Superlattices, and Thin Films, J. D. Dow, I. K. Schuller, 1987, ISBN 0-931837-56-1
- Volume 78—Advances in Structural Ceramics, P. F. Becher, M. V. Swain, S. Sōmiya, 1987, ISBN 0-931837-43-X
- Volume 79—Scattering, Deformation and Fracture in Polymers, G. D. Wignall, B. Crist, T. P. Russell, E. L. Thomas, 1987, ISBN 0-931837-44-8
- Volume 80—Science and Technology of Rapidly Quenched Alloys, M. Tenhover, W. L. Johnson, L. E. Tanner, 1987, ISBN 0-931837-45-6
- Volume 81—High-Temperature Ordered Intermetallic Alloys, II, N. S. Stoloff, C. C. Koch, C. T. Liu, O. Izumi, 1987, ISBN 0-931837-46-4
- Volume 82—Characterization of Defects in Materials, R. W. Siegel, J. R. Weertman, R. Sinclair, 1987, ISBN 0-931837-47-2
- Volume 83—Physical and Chemical Properties of Thin Metal Overlayers and Alloy Surfaces, D. M. Zehner, D. W. Goodman, 1987, ISBN 0-931837-48-0
- Volume 84—Scientific Basis for Nuclear Waste Management X, J. K. Bates, W. B. Seefeldt, 1987, ISBN 0-931837-49-9
- Volume 85—Microstructural Development During the Hydration of Cement, L. Struble, P. Brown, 1987, ISBN 0-931837-50-2
- Volume 86—Fly Ash and Coal Conversion By-Products Characterization, Utilization and Disposal III, G. J. McCarthy, F. P. Glasser, D. M. Roy, S. Diamond, 1987, ISBN 0-931837-51-0
- Volume 87—Materials Processing in the Reduced Gravity Environment of Space, R. H. Doremus, P. C. Nordine, 1987, ISBN 0-931837-52-9
- Volume 88—Optical Fiber Materials and Properties, S. R. Nagel, J. W. Fleming, G. Sigel, D. A. Thompson, 1987, ISBN 0-931837-53-7
- Volume 89—Diluted Magnetic (Semimagnetic) Semiconductors, R. L. Aggarwal, J. K. Furdyna, S. von Molnar, 1987, ISBN 0-931837-54-5
- Volume 90—Materials for Infrared Detectors and Sources, R. F. C. Farrow, J. F. Schetzina, J. T. Cheung, 1987, ISBN 0-931837-55-3
- Volume 91—Heteroepitaxy on Silicon II, J. C. C. Fan, J. M. Phillips, B.-Y. Tsaur, 1987, ISBN 0-931837-58-8
- Volume 92—Rapid Thermal Processing of Electronic Materials, S. R. Wilson, R. A. Powell, D. E. Davies, 1987, ISBN 0-931837-59-6
- Volume 93—Materials Modification and Growth Using Ion Beams, U. Gibson, A. E. White, P. P. Pronko, 1987, ISBN 0-931837-60-X
- Volume 94—Initial Stages of Epitaxial Growth, R. Hull, J. M. Gibson, David A. Smith, 1987, ISBN 0-931837-61-8
- Volume 95—Amorphous Silicon Semiconductors—Pure and Hydrogenated, A. Madan, M. Thompson, D. Adler, Y. Hamakawa, 1987, ISBN 0-931837-62-6
- Volume 96—Permanent Magnet Materials, S. G. Sankar, J. F. Herbst, N. C. Koon, 1987, ISBN 0-931837-63-4
- Volume 97—Novel Refractory Semiconductors, D. Emin, T. Aselage, C. Wood, 1987, ISBN 0-931837-64-2
- Volume 98—Plasma Processing and Synthesis of Materials, D. Apelian, J. Szekely, 1987, ISBN 0-931837-65-0

MATERIALS RESEARCH SOCIETY SYMPOSIUM PROCEEDINGS

- Volume 99—High-Temperature Superconductors, M. B. Brodsky, R. C. Dynes, K. Kitazawa, H. L. Tuller, 1988, ISBN 0-931837-67-7
- Volume 100—Fundamentals of Beam-Solid Interactions and Transient Thermal Processing, M. J. Aziz, L. E. Rehn, B. Stritzker, 1988, ISBN 0-931837-68-5
- Volume 101—Laser and Particle-Beam Chemical Processing for Microelectronics, D.J. Ehrlich, G.S. Higashi, M.M. Oprysko, 1988, ISBN 0-931837-69-3
- Volume 102—Epitaxy of Semiconductor Layered Structures, R. T. Tung, L. R. Dawson, R. L. Gunshor, 1988, ISBN 0-931837-70-7
- Volume 103—Multilayers: Synthesis, Properties, and Nonelectronic Applications, T. W. Barbee Jr., F. Spaepen, L. Greer, 1988, ISBN 0-931837-71-5
- Volume 104—Defects in Electronic Materials, M. Stavola, S. J. Pearton, G. Davies, 1988, ISBN 0-931837-72-3
- Volume 105—SiO₂ and Its Interfaces, G. Lucovsky, S. T. Pantelides, 1988, ISBN 0-931837-73-1
- Volume 106—Polysilicon Films and Interfaces, C.Y. Wong, C.V. Thompson, K-N. Tu, 1988, ISBN 0-931837-74-X
- Volume 107—Silicon-on-Insulator and Buried Metals in Semiconductors, J. C. Sturm, C. K. Chen, L. Pfeiffer, P. L. F. Hemment, 1988, ISBN 0-931837-75-8
- Volume 108—Electronic Packaging Materials Science II, R. C. Sundahl, R. Jaccodine, K. A. Jackson, 1988, ISBN 0-931837-76-6
- Volume 109—Nonlinear Optical Properties of Polymers, A. J. Heeger, J. Orenstein, D. R. Ulrich, 1988, ISBN 0-931837-77-4
- Volume 110—Biomedical Materials and Devices, J. S. Hanker, B. L. Giammara, 1988, ISBN 0-931837-78-2
- Volume 111—Microstructure and Properties of Catalysts, M. M. J. Treacy, J. M. Thomas, J. M. White, 1988, ISBN 0-931837-79-0
- Volume 112—Scientific Basis for Nuclear Waste Management XI, M. J. Apted, R. E. Westerman, 1988, ISBN 0-931837-80-4
- Volume 113—Fly Ash and Coal Conversion By-Products: Characterization, Utilization, and Disposal IV, G. J. McCarthy, D. M. Roy, F. P. Glasser, R. T. Hemmings, 1988, ISBN 0-931837-81-2
- Volume 114—Bonding in Cementitious Composites, S. Mindess, S. P. Shah, 1988, ISBN 0-931837-82-0
- Volume 115—Specimen Preparation for Transmission Electron Microscopy of Materials, J. C. Bravman, R. Anderson, M. L. McDonald, 1988, ISBN 0-931837-83-9
- Volume 116—Heteroepitaxy on Silicon: Fundamentals, Structures, and Devices, H.K. Choi, H. Ishiwara, R. Hull, R.J. Nemanich, 1988, ISBN: 0-931837-86-3
- Volume 117—Process Diagnostics: Materials, Combustion, Fusion, K. Hays, A.C. Eckbreth, G.A. Campbell, 1988, ISBN: 0-931837-87-1
- Volume 118—Amorphous Silicon Technology, A. Madan, M.J. Thompson, P.C. Taylor, P.G. LeComber, Y. Hamakawa, 1988, ISBN: 0-931837-88-X
- Volume 119—Adhesion in Solids, D.M. Mattox, C. Batich, J.E.E. Baglin, R.J. Gottschall, 1988, ISBN: 0-931837-89-8
- Volume 120—High-Temperature/High-Performance Composites, F.D. Lemkey, A.G. Evans, S.G. Fishman, J.R. Strife, 1988, ISBN: 0-931837-90-1
- Volume 121—Better Ceramics Through Chemistry III, C.J. Brinker, D.E. Clark, D.R. Ulrich, 1988, ISBN: 0-931837-91-X
- Volume 122—Interfacial Structure, Properties, and Design, M.H. Yoo, W.A.T. Clark, C.L. Briant, 1988, ISBN: 0-931837-92-8

MATERIALS RESEARCH SOCIETY SYMPOSIUM PROCEEDINGS

- Volume 123—Materials Issues in Art and Archaeology, E.V. Sayre, P. Vandiver, J. Druzik, C. Stevenson, 1988, ISBN: 0-931837-93-6
- Volume 124—Microwave-Processing of Materials, M.H. Brooks, I.J. Chabinsky, W.H. Sutton, 1988, ISBN: 0-931837-94-4
- Volume 125—Materials Stability and Environmental Degradation, A. Barkatt, L.R. Smith, E. Verink, 1988, ISBN: 0-931837-95-2
- Volume 126—Advanced Surface Processes for Optoelectronics, S. Bernasek, T. Venkatesan, H. Temkin, 1988, ISBN: 0-931837-96-0
- Volume 127—Scientific Basis for Nuclear Waste Management XII, W. Lutze, R.C. Ewing, 1989, ISBN: 0-931837-97-9
- Volume 128—Processing and Characterization of Materials Using Ion Beams, L.E. Rehn, J. Greene, F.A. Smidt, 1989, ISBN: 1-55899-001-1
- Volume 129—Laser and Particle-Beam Chemical Processes on Surfaces, G.L. Loper, A.W. Johnson, T.W. Sigmon, 1989, ISBN: 1-55899-002-X
- Volume 130—Thin Films: Stresses and Mechanical Properties, J.C. Bravman, W.D. Nix, D.M. Barnett, D.A. Smith, 1989, ISBN: 0-55899-003-8
- Volume 131—Chemical Perspectives of Microelectronic Materials, M.E. Gross, J. Jasinski, J.T. Yates, Jr., 1989, ISBN: 0-55899-004-6
- Volume 132—Multicomponent Ultrafine Microstructures, L.E. McCandlish, B.H. Kear, D.E. Polk, and R.W. Siegel, 1989, ISBN: 1-55899-005-4
- Volume 133—High Temperature Ordered Intermetallic Alloys III, C.T. Liu, A.I. Taub, N.S. Stoloff, C.C. Koch, 1989, ISBN: 1-55899-006-2
- Volume 134—The Materials Science and Engineering of Rigid-Rod Polymers, W.W. Adams, R.K. Eby, D.E. McLemore, 1989, ISBN: 1-55899-007-0
- Volume 135—Solid State Ionics, G. Nazri, R.A. Huggins, D.F. Shriver, 1989, ISBN: 1-55899-008-9
- Volume 136—Fly Ash and Coal Conversion By-Products: Characterization, Utilization, and Disposal V, R.T. Hemmings, E.E. Berry, G.J. McCarthy, F.P. Glasser, 1989, ISBN: 1-55899-009-7
- Volume 137—Pore Structure and Permeability of Cementitious Materials, L.R. Roberts, J.P. Skalny, 1989, ISBN: 1-55899-010-0
- Volume 138—Characterization of the Structure and Chemistry of Defects in Materials, B.C. Larson, M. Ruhle, D.N. Seidman, 1989, ISBN: 1-55899-011-9
- Volume 139—High Resolution Microscopy of Materials, W. Krakow, F.A. Ponce, D.J. Smith, 1989, ISBN: 1-55899-012-7
- Volume 140—New Materials Approaches to Tribology: Theory and Applications, L.E. Pope, L. Fehrenbacher, W.O. Winer, 1989, ISBN: 1-55899-013-5
- Volume 141—Atomic Scale Calculations in Materials Science, J. Tersoff, D. Vanderbilt, V. Vitek, 1989, ISBN: 1-55899-014-3
- Volume 142—Nondestructive Monitoring of Materials Properties, J. Holbrook, J. Bussiere, 1989, ISBN: 1-55899-015-1
- Volume 143—Synchrotron Radiation in Materials Research, R. Clarke, J.H. Weaver, J. Gland, 1989, ISBN: 1-55899-016-X
- Volume 144—Advances in Materials, Processing and Devices in III-V Compound Semiconductors, D.K. Sadana, L. Eastman, R. Dupuis, 1989, ISBN: 1-55899-017-8

MATERIALS RESEARCH SOCIETY CONFERENCE PROCEEDINGS

Tungsten and Other Refractory Metals for VLSI Applications, R. S. Blewer, 1986;
ISSN 0886-7860; ISBN 0-931837-32-4

Tungsten and Other Refractory Metals for VLSI Applications II, E.K. Broadbent, 1987;
ISSN 0886-7860; ISBN 0-931837-66-9

Ternary and Multinary Compounds, S. Deb, A. Zunger, 1987; ISBN 0-931837-57-x

Tungsten and Other Refractory Metals for VLSI Applications III, Victor A. Wells, 1988;
ISSN 0886-7860; ISBN 0-931837-84-7

Atomic and Molecular Processing of Electronic and Ceramic Materials: Preparation,
Characterization and Properties, Ilhan A. Aksay, Gary L. McVay, Thomas G. Stoebe, 1988;
ISBN 0-931837-85-5

Materials Futures: Strategies and Opportunities, R. Byron Pipes, U.S. Organizing Committee,
Rune Lagneborg, Swedish Organizing Committee, 1988; ISBN 0-55899-000-3

Tungsten and Other Refractory Metals for VLSI Applications IV, Robert S. Blewer, Carol
M. McConica, 1989; ISSN: 0886-7860; ISBN: 0-931837-98-7

PART I

Ion-Beam-Assisted Deposition

SOME RECENT RESULTS OF FUNDAMENTAL STUDIES ON BEAM-INDUCED SURFACE PROCESSES

JAN DIELEMAN

Philips Research Laboratories

5600 JA Eindhoven, The Netherlands

Recent results of studies on the mechanism of processes induced by the interaction of beams of (reactive) particles with surfaces in UHV, often combined with concurrent bombardment of the surface with low-energy ion or excimer laser beams, are reviewed. Angular-resolved mass spectrometry combined with time-of-flight studies on the desorbing products is used as a key diagnostic. A more complete picture is obtained using several other diagnostic tools to characterize the surface before, during or after the interaction. Interactions at Si and Cu surfaces will be emphasized. The review will deal successively with data for interaction with a single beam of Cl_2 , low-energy noble gas ions or excimer laser pulses, followed by data on the concurrent interaction of crossed beams of Cl_2 and low-energy noble gas ions or excimer laser pulses with these surfaces. Some conclusions will be drawn.

1. INTRODUCTION

Growth and etching of thin films, usually via the gas phase, plays a dominating role in the technology of present-day integrated circuits. The ever increasing complexity of these devices has necessitated the development of techniques providing improved quality at reduced substrate temperatures. The reduced substrate temperatures are a necessity because the delicate structures already present in the substrate should not be damaged and the improved quality is essential to get a high yield of well-performing devices. Typically these techniques use dissociation and excitation of gas molecules by plasmas or by photons to enhance surface adsorption and reaction and/or apply surface-localized energy deposition by bombardment of the adsorbate layer and nearby surface region by low-energy electrons, ions, excited neutrals or photons to stimulate surface

reactions and desorption of products. A qualitative and certainly a quantitative understanding of the crucial steps in these important reaction chains is largely lacking. This hampers assessment of basic possibilities and limitations of most of these techniques.

It is the object of this paper to review some recent results of studies on the mechanisms of surface reactions stimulated by low-energy noble gas ion bombardment or by nanosecond excimer laser pulses. These studies have been performed in UHV chambers in which surfaces can be exposed to one beam of particles like chemically active molecules, low-energy noble gas ions or excimer laser photons or concurrently to two beams, one consisting of chemically active molecules and the other of low-energy noble gas ions or excimer laser photons. The discussion will be restricted to the comprehensive studies on the interaction of low-energy noble gas ion beams or excimer laser beams with Si or Cu surfaces in most cases in the presence of chlorine adsorbed on the surfaces from a beam of Cl_2 molecules. For studies on other systems the reader is referred to several recent review papers [1-6]. The main features of the most important diagnostic tool used, viz. mass spectrometry combined with time-of-flight measurements on the neutral "desorption" products, can be found in another recent review [7].

This review paper will deal successively with some data on the interaction of separate Cl_2 beams, low-energy noble gas ion-, or excimer laser-beams with Si and Cu surfaces, the concurrent action of crossed Cl_2 and low-energy noble gas ion beams on Si surfaces, the simultaneous exposure of Si or Cu surfaces to crossed beams of Cl_2 and nanosecond excimer laser pulses and will end with some conclusions. The data on the interaction of only one of these beams with Si or Cu surfaces will be reviewed only for ranges of parameter values also used in the experiments with crossed beams.

2. Cl_2 BEAMS

In the temperature range of 300 to 850 K Cl_2 sticks to Si(111) surfaces with an initial sticking coefficient of about 0.1 until a coverage of about one monolayer is reached. At this saturation coverage the sticking coefficient drops rapidly. Both the initial sticking coefficient and the saturation coverage decrease only slightly with

increasing temperature [8]. At 300 K Si does not react measurably with Cl_2 . At somewhat higher temperatures the main etch product is SiCl_4 , while at temperatures above about 800 K up to 1500 K the main etch product observed is SiCl_2 [9,10]. A comparison of an estimate of the relative contribution of the etch products SiCl_2 and SiCl_4 as a function of temperature from mass spectra alone [10], with an estimate using a combination of mass spectroscopy and time-of-flight [7] clearly shows the very qualitative character of the former estimate. Time-of-flight distributions, using modulation of the product beam, have the form of Maxwell-Boltzmann (MB) distributions at target temperature, suggesting thermal desorption [7]. The desorption of SiCl_2 has been reported to show an activation energy of about 1.75 eV at 1400 K decreasing to about 0.8 eV below 1000 K, with a surface residence time of about 10^{-2} s at 1400 K and accompanied by "unusually" low preexponential (frequency) factors of $3 \times 10^8 \text{ s}^{-1}$ at 1400 K to $8 \times 10^6 \text{ s}^{-1}$ below 1000 K. (which is about 10^5 to 10^6 times lower than "usual"). Calculations have confirmed that chlorine has a high activation energy barrier for diffusion from the surface into the Si [11]. It is difficult to derive from recent literature [12-14] a unified, quantitative picture of the reaction of Cl_2 with Cu surfaces. In the pressure and temperature ranges of interest in the crossed beams experiments to be described later on, i.e. for effective Cl_2 pressures up to about 10^{-4} Torr and temperatures up to about 1000 K, the situation seems to be as follows. At very low pressures (about 10^{-8} Torr) and room temperature the surface coverage increases linearly with dose up to about 2 Langmuir (L) where it saturates at about half of a monolayer. The initial sticking probability is about 0.5 and drops drastically at saturation coverage. The Cl_2 seems to be dissociatively chemisorbed without forming a halide-like overlayer. The overlayer has been reported to contain "free" halogen. This holds even for exposures up to 20 kL in the temperature range 300 to 700 K. However, when the effective pressures are chosen much higher or when Cl_2 at low pressures is condensed on a Cu surface at temperatures of 200 K, thicker Cu halide films are formed. The reaction probability of Cl_2 first decreases with increasing temperature till about 500 K and then increases. This has been explained by a rapidly decreasing sticking probability of Cl_2 on the CuCl surface film and rapid evaporation of Cu-halide, thus exposing "fresh" Cu surface with a high sticking probability, at temperatures above about 500 K. At 300 K thermal etching is immeasurably slow. At temperatures up to about 850 K the dominant etch product is Cu_3Cl_3 , while above 925 K the main desorbing molecule is CuCl .

3. LOW-ENERGY NOBLE GAS ION OR EXCIMER LASER BEAMS

Only a few data are available on physical sputtering of Cu and Si with Ar^+ ion beams of a few keV in UHV [15,16]. At these projectile energies the energy distributions of the main products, sputtered atoms, are described well with a collision cascade (CC) distribution, i.e. the flux of sputtered atoms $\phi(E)$ is proportional to $E / (E+U_0)^3$ where U_0 is the binding energy of the atom. $U_0(\text{Cu}) = 3.5 \text{ eV}$ and $U_0(\text{Si}) = 7.8 \text{ eV}$. For quite a number of elements U_0 is equivalent to the value of the sublimation energy [5], only U_0 of Si is somewhat higher. Sputtering yields at 6 keV are 3.7 atoms/ Ar^+ for Cu and 1.3 atoms / Ar^+ for Si. The values of these yields are consistent with yield formulas (see eq. 6 of ref. 5). Sputtering yields decrease with decreasing projectile energy to values of a few 0.1 atoms/ Ar^+ at 100 eV. With decreasing projectile energy the energy distribution of the sputtered atoms deviates at the high energy end progressively to lower values. This is especially significant for oblique incidence and ejection angles [17,18].

Low-energy noble gas ion bombardment of solids also leads to implantation. The resputtering of these noble gases has been studied for bombardment of Si with Ar^+ [19]. The time-of-flight (TOF) distributions consisted of two contributions, an MB distribution at target temperature which is ascribed to ion bombardment-enhanced diffusion to the surface followed by evaporation (or, below the solidification temperature, sputtering) and a contribution which may be reasonably well simulated with an MB distribution but at a much higher temperature. The latter contribution has tentatively been interpreted as opening of noble gas "bubbles" by ion impact. Recent studies [20], for more noble gases and more solid targets, have shown that the TOF distributions always have a high kinetic energy component and often an MB contribution at target temperature. It also appeared that steady state resputtering is reached already with a fluence of no more than about 10^{15} ions per cm^2 . The latter observation is not easily understood by assuming sputter opening of noble gas bubbles. Hopefully, incidence- and exit angle-dependent studies will shed more light on the mechanism responsible.

The interaction of 308 and 248 nm nanosec laser pulses at laser pulse fluences up to 0.82 and 1.0 Jcm^{-2} respectively with pure Si and Cu surfaces in UHV did not lead to significant etching.

4. CROSSED BEAMS OF LOW-ENERGY NOBLE GAS IONS AND OF Cl_2

By using a combination of TOF studies and mass spectroscopy the composition of the various neutral products desorbing from e.g. a Si surface exposed to crossed beams of low-energy noble gas ions and Cl_2 can be determined [7]. If care is taken to prevent the desorbing products from colliding with each other above the surface [21] also information about the desorption mechanism(s) is obtained. It is much more difficult to make a more quantitative estimate of the relative proportions of the various products. For this quantification one needs to know what the TOF distributions of the various products are to be able to make a $1/v$ correction for the ionization probability in the ionization chamber of the mass spectrometer. Since we have measured these TOF distributions for the products, this correction can be applied. Of course one must take care of collecting the ions produced properly. The important problem remaining is that for most of the molecules encountered in our studies no ionization cross sections are known and it takes a lot of effort to measure them [22]. To get a qualitative impression of the neutral products leaving a Si surface along the surface normal, when exposed to crossed beams of 1 keV Ar^+ ions incident at 60° to the surface normal and of 300 K Cl_2 , the series of experiments illustrated in Fig. 1 have been performed [23].

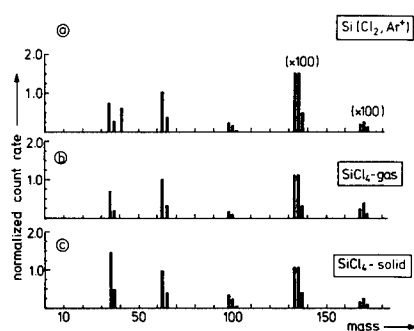


Fig. 1. (a) Mass spectrum of species emitted from silicon under simultaneous exposure to a chlorine-gas beam ($\phi_{\text{Cl}_2} \sim 3 \times 10^{16} \text{ mol cm}^{-2} \text{ s}^{-1}$) and an argon-ion beam ($E_{\text{Ar}} = 1 \text{ keV}$, $\phi_{\text{Ar}} \sim 2 \times 10^{14} \text{ ions cm}^{-2} \text{ s}^{-1}$). The signals for SiCl_3^+ and SiCl_4^+ have been multiplied by a factor of 100. (b) Mass spectrum of room-temperature SiCl_4 gas. (c) Mass spectrum of species sputtered by an argon-ion beam ($E_{\text{Ar}} = 1 \text{ keV}$) from solid SiCl_4 , condensed at liquid air temperature. The mass spectra have been obtained with 10 mA of 70 eV ionizing electrons and are normalized to the SiCl^+ signals.

Using the same settings of the mass spectrometer and a modulation frequency of 10 Hz, the mass spectrum of SiCl_4 gas was measured (b) followed by the mass spectrum of the products sputtered from solid SiCl_4 (c) and then by the crossed beams experiment for a relatively high flux ratio R of Cl_2 to Ar^+ of 150 (a) (Note that in Fig. 1a the SiCl_3^+ and SiCl_4^+ peaks have been multiplied by a factor of 100.) A comparison between the mass spectrum of the gas and the bombarded solid SiCl_4 indicates that part of the SiCl_4 molecules in the solid have been fragmented by the Ar^+ ion impact. TOF measurements on the neutral sputtering products from solid SiCl_4 showed that indeed neutral SiCl molecules are sputtered as such with a CC distribution and a binding energy of only 0.08 eV. A comparison of the results of the crossed beams experiment shown in Fig. 1a with those presented in 1b and 1c proves that SiCl and SiCl_2 are major etch products. A recent repetition of these experiments [24] reproduces these early results very well. This work also shows that the TOF distributions of the more chlorinated products SiCl_3 and SiCl_4 lie at about the same position as those of e.g. SiCl_2 . Even a relatively large difference in ionization cross section of the various neutral products, like for SiF_x neutrals [22], does not change this conclusion. The above conclusion remains valid when R is enhanced to about 500 and when the Ar^+ ion energy is reduced to 250 eV, both measures which cause a relative increase in more halogenated products.

More extensive studies on this system [25,26] have shown that

- a. The main species ejected are Si, Cl, SiCl and SiCl_2 and resputtered Ar
- b. The kinetic energy distributions of these products are composed of two contributions: first a CC distribution comprising more than 80% of the total emission and second an MB distribution at target temperature. The latter contribution is ascribed to ion-bombardment enhanced outdiffusion, followed by evaporation at target temperature. The CC distribution shows that the main removal process is physical sputtering of these molecules. An example of a TOF distribution showing both contributions is given in Fig. 2.

Recently [7] TOF distributions can be measured either by modulation of the ion beam or by chopping the product beam: no significant differences have been found for SiCl^+ . This means that the above-mentioned two contributions are far the most important ones and contributions from higher chlorinated SiCl_x are insignificant. Also long residence times do not seem to play an important role, which is, of course, to be expected for

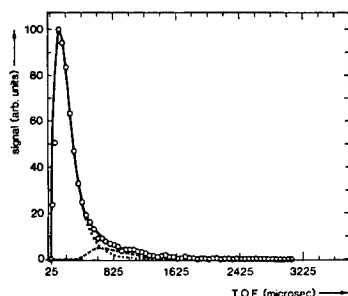


Fig. 2 Time-of-flight distribution of the product SiCl for $\phi_{\text{Cl}}/\phi_{\text{Ar}^+} = 40$. $\theta_{\text{inc}} = 50^\circ$, $\theta_{\text{det}} = 0^\circ$. As demonstrated, a combination of 90% of a collision cascade distribution and of 10% of a Maxwell-Boltzmann distribution at $T = 300$ K fits the data quite well.

physical sputtering processes.

In other recent work [27] a systematic study of the effect of R and of the angle-of-incidence of Ar^+ has confirmed earlier indications [26] that the binding energy of the product SiCl increases from values below 0.2 eV at high values of R and incidence close to the normal to values near 0.6 eV for low R values and high incidence angles. These results have been related to the effective amount of chlorine mixed into the Si by the ion bombardment as measured by Mayer's group [28,29]. The value of U_0 decreases with increasing concentration of chlorine mixed into the Si. As expected the sputtering yield increases in the same way [30].

A most intriguing aspect of this chemically enhanced physical sputtering is that the values of U_0 are so low, i.e. only a few tenths of an eV. As discussed in section 3 there is a one-to-one relation between U_0 and the sublimation energy. If the molecules would have been formed in one Ar^+ impact at the surface and then sputtered from there in a following impact it is difficult to understand why they did not evaporate thermally, except when the frequency factor for this thermal process is exceptionally low. That this could be the case may be derived from the data mentioned in Section 2. If the frequency factor has a value near 10^{13} s^{-1} other explanations have to be found for the high sputtering yields of SiCl (and SiCl_2). Essentially three different explanations have been put forward (except the one with the low frequency factor for desorption). All of them [2,3,26,27] agree about the importance of bond breaking and mixing of chlorine into the Si. Mayer's group [3] assumes subsequent reformation of small molecules and sputtering of the molecules by the tail of the same collision cascade that caused the bond breaking. However, reformation of bonds takes more time than the collision cascade takes. Winters [2] assumes direct formation of molecules during the early bond breaking stage of the collision cascade and sputtering of the molecules thus formed by the tail of the same collision cascade. However, it is difficult to understand why, except for a dissociation correction

[32], a complete collision cascade distribution develops, i.e. with also high-velocity molecules, when only the tail of the collision cascade is used. Finally, Dieleman et al. [26,27] have proposed formation of these molecules in the top film during and after one impact and sputtering of these molecules in a subsequent impact. More research into this interesting and technologically important phenomenon will hopefully lead to a more definitive answer.

Very recently measurements have been extended to Ar^+ ion energies down to 75 eV and to bombardment with Xe^+ ions at higher energies [24]. At the lower energies or for the heavier projectile masses the TOF distribution lose their high velocity part or, differently stated, "shift" to longer flight times. For bombardment with very low ion energies the TOF distributions could be fitted reasonably well with MB distributions at about the same high temperature and an MB distribution at target temperature. These results have been interpreted by assuming evaporation from an ion-induced hot spot. More research will have to be done to decide whether this picture (which holds perhaps also for noble gas resputtering) holds or whether this is simply due to insufficiently developed collision cascades or whether this is equivalent.

For Cu exposed to crossed beams of Cl_2 and low-energy Ar^+ ions the sputtering yield decreases slightly as compared to sputtering with Ar^+ ions alone [13]. Further studies, as described above for Si, will have to be performed to understand this behaviour.

5. CROSSED BEAMS OF EXCIMER LASERS AND Cl_2

The results to be reviewed in this section pertain to the etching of Si and Cu surfaces when exposed to crossed beams of nanosecond excimer laser pulses of mostly 308 nm and a continuous Cl_2 beam (or background pressure) corresponding to an effective pressure at the Si or Cu surface of at most about 10^{-4} Torr. This means that experiments performed at much higher Cl_2 background pressures [32-34] will not be reviewed here.

Recently, some studies on the mechanism of nanosecond excimer laser etching of Si concurrently exposed to Cl_2 at an effective pressure up to about 10^{-4} Torr have been performed [35-38]. At laser pulse fluences up to 0.4 Jcm^{-2} for 308 nm and 1.0 Jcm^{-2} for 248 nm and in the Cl_2 pressure range indicated above Si is easily etched with a maximum etch rate of 30

A per laser pulse. The main products observed are Cl, SiCl and SiCl₂. The TOF distributions can be fitted quite well with MB distributions at temperatures in the range 1400 to 4000 K. The temperature increases with laser pulse fluence and with chlorine pressure up to a pressure of about 10⁻⁴ Torr (at least for a repetition rate of 4 Hz). Each pulse removes all of the chlorine absorbed in the time between two pulses. The most intriguing observation is the increase of the particle temperature with Cl₂ pressure (which is equivalent to surface coverage) until a surface coverage of one monolayer between two laser pulses is reached. Studies on the rovibrational excitation of the product SiCl have shown that these molecules are also internally very hot. This is at least partially consistent with time-resolved reflectivity studies, which indicate that for the higher Cl₂ pressures and laser pulse fluences the laser pulse melts the Si surface. No definitive conclusion has been reached as yet about the desorption mechanism. The most recent studies [38] indicate that, except at the lowest pressures, the desorbing particles interact above the surface. Of course this effect has to be separated from the desorption-induced external and internal energy distributions.

Also for Cu exposed to crossed beams of nanosecond excimer laser pulses at various wavelengths and Cl₂ at effective pressures below 10⁻⁴ Torr relatively little studies have been published [39-42]. In none of these publications attention has been paid to effects of interaction of desorbed particles above the substrate, like described in Ref. 21. This holds almost completely for the work of Osgood et al. [40] and completely for that of Chuang et al. [39]. So it is not possible to draw more definitive conclusions about the mechanisms responsible for the observed high velocities of the desorbed species. In our own work some experimental conditions occurred where this interaction was absent. In addition some data have been collected about the laser-induced modification of Cu surfaces in the presence of a Cl₂ beam. For these reasons the discussion here will be restricted to some of our data.

When Cu containing minute amounts of chlorine is exposed to nanosecond excimer laser pulses at 308 nm in UHV, some Cu₃Cl₃ is desorbed. The kinetic energy distribution of these molecules can be fitted by a Maxwell-Boltzmann distribution at temperatures corresponding very well to those calculated on the basis of the temperature induced in the Cu surface by absorption from the laser pulse. This temperature rises linearly with laser pulse fluence. Of course, this indicates a thermal desorption mechanism. When a clean Cu sample is exposed to crossed beams of nanosecond excimer laser pulses and low pressure Cl₂ beams, the etch

rate at the start of the experiment is no more than about 1% of a monolayer. The TOF distributions of the main products Cu_3Cl_3 and CuCl are fitted quite well with Maxwell-Boltzmann distributions at temperature not very different from those mentioned above. However, the etch rate increases with exposure till a steady state etch rate level is obtained. The TOF distributions of the products remain Maxwell-Boltzmann, but the corresponding temperature rises with exposure till the steady state is reached.

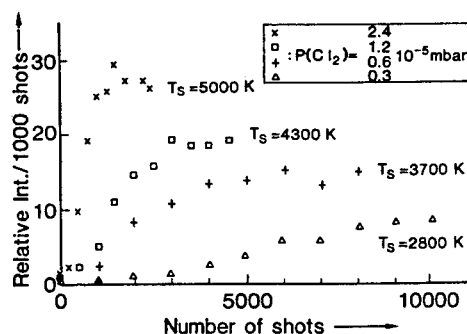


Fig. 3. Evolution of the flux of Cu_3Cl_3 leaving the target as a function of the number of laser shots after the beginning of exposure of a clean Cu surface to Cl_2 for the four values of p_{Cl_2} indicated in the figure. The laser pulse fluence is fixed at 0.45 Jcm^{-2} . The steady-state temperature of the ejected Cu_3Cl_3 is also indicated. $1 \text{ mbar} = 10^2 \text{ Pa}$.

As illustrated in Fig. 3 the steady state level is reached faster the higher the Cl_2 pressure and the steady state "temperature" increases.

Fig. 4 shows that the build-up to the steady state (S) etch rate level is accompanied by a build-up of a rather thick chlorinated Cu surface film. The explanation of these observations is rather straightforward. At the start of the exposure the chlorine adsorbed is only for a small part desorbed from the surface. Because the Cu surface is heated by the laser pulse part of the chlorine remaining will diffuse into the Cu. This process will go on till the chlorinated surface film is so thick that all chlorine sticking to the surface in between laser pulses is removed.

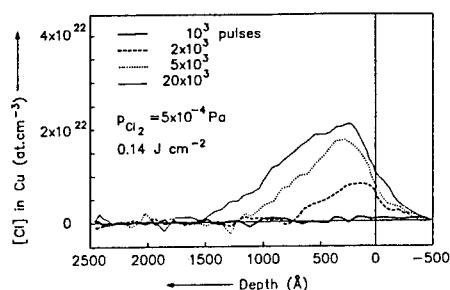


Fig. 4. Cl profiles in etched-single-crystal Cu (100) at various stages of the buildup to S for $F = 0.14 \text{ Jcm}^{-2}$, $p_{\text{Cl}_2} = 5 \times 10^{-4} \text{ Pa}$, and $n = (1, 2, 5, \text{ and } 20) \times 10^3$, respectively. The latter is the S profile. The zero is indicated for ^{35}Cl only. Resolution is 200 Å .

Because the heat conductivity of the CuCl is lower than that of Cu metal also higher temperatures may occur, as observed. But because the TOF distributions will be obscured by interaction between the desorbing species, the temperature corresponding to the MB distribution measured will not be a true measure of the surface temperature.

6. CONCLUSION

The review clearly demonstrates the fascinating and important role chemically active adsorbates play in low-energy ion- and laser-assisted etching. It also shows that much remains to be done to get a better qualitative understanding of the underlying mechanisms.

REFERENCES

1. H.F. Winters, J.W. Coburn and T.J. Chuang, J. Vac. Sci. Technol. B1, 469 (1983)
2. H.F. Winters, J. Vac. Sci. Technol. A6, 1997 (1988)
3. T.M. Mayer, M.S. Ameen and D.J. Vitkavage, in The Chemical Physics of Solid Surfaces and Heterogeneous Catalysis Vol. 5: Surface Properties of Electronic Materials, edited by D.A. King and D.P. Woodruff (Elsevier Science Publishers, New York, 1988), p. 427
4. D.J. Oostra and A.E. de Vries, Nucl. Instr. and Meth. B18, 618 (1987)
5. P.C. Zalm, Vacuum 36, 787 (1986); Surf. Interf. Anal. 11, 1 (1988)
6. A.W. Kolfschoten, Nucl. Instr. and Meth. B19/20, 1001 (1987)
7. J. Dieleman, in Photon, Beam and Plasma Enhanced Processes, edited by A. Golanski, V.T. Nguyen and E.F. Krimmel (European Mat. Res. Soc. Proc. XV, les éditions de physiques, Les Ulis, France), p. 363 (1988):
8. J.V. Florio and W.D. Robertson, Surf. Sci. 18, 398 (1969)
9. R.J. Madix and J.A. Schwarz, Surf. Sci. 24, 264 (1971)
10. F.H.M. Sanders, A.W. Kolfschoten, J. Dieleman, R.A. Haring, A. Haring and A.E. de Vries, J. Vac. Sci. Technol. A2, 481 (1984)

11. M. Seel and P.S. Bagus, Phys. Rev. B28, 2023 (1983)
12. H.F. Winters, J. Vac. Sci. Technol. A3, 786 (1985)
13. S. Park, T.N. Rhodin and L.C. Rathbun, J. Vac. Sci. Technol. A4, 168 (1986)
14. W. Sesselman and T.J. Chuang, Surf. Sci. 176, 32 (1986); 176, 67 (1986)
15. M. Szymonski, Appl. Phys. 23, 89 (1980)
16. J. Dieleman, Le Vide-Les Couches Minces, Suppl. to Vol. 218, 3 (1983)
17. J. Dembovski, H. Oechsner, Y. Yamamura and M. Urbassek, Nucl. Instr. and Meth. B18, 464 (1987)
18. R.A. Brizzolara, C.B. Cooper and T.K. Olson, Nucl. Instr. and Meth. B35, 36 (1988)
19. G.N.A. van Veen, F.H.M. Sanders, J. Dieleman, A. van Veen, D.J. Oostra and A.E. de Vries, Phys. Rev. Lett. 57, 739 (1986)
20. J. van Zwol, S.T. de Zwart, and J. Dieleman, to be published
21. R. Kelly and R.W. Dreyfus, Surf. Sci. 198, 263 (1988)
22. T.R. Hayes, R.C. Wetzel, F.A. Baiocchi and R.S. Freund, J. Chem. Phys. 88, 823 (1988); T.R. Hayes, R.J. Thul, F.A. Baiocchi, R.C. Wetzel and R.S. Freund, ibid. 89, 4035 (1988); R.J. Shul, T.R. Hayes, R.C. Wetzel, F.A. Baiocchi and R.S. Freund, ibid. 89, 4042 (1988)
23. A.W. Kofschoten, R.A. Haring, A. Haring and A.E. de Vries, J. Appl. Phys. 55, 3813 (1984)
24. D.J. Oostra, A. Haring, R.P. van Ingen and A.E. de Vries, J. Appl. Phys. 64, 315 (1988)
25. F.H.M. Sanders, A.W. Kofschoten, J. Dieleman, R.A. Haring, A. Haring and A.E. de Vries, J. Vac. Sci. Technol. A2, 487 (1984)
26. J. Dieleman, F.H.M. Sanders, A.W. Kofschoten, P.C. Zalm, A.E. de Vries and A. Haring, J. Vac. Sci. Technol. B3, 1384 (1985)
27. J. van Zwol, J. van Laar, A.W. Kofschoten and J. Dieleman, J. Vac. Sci. Technol. B5, 1410 (1987)
28. T. Mizutani, C.J. Dale, W.K. Chu and T.M. Mayer, Nucl. Instr. and Meth. B7/8, 825 (1985)
29. E.L. Barish, D.J. Vitkavage and T.M. Mayer, J. Appl. Phys. 57, 1336 (1985)
30. P.C. Zalm, A.W. Kofschoten, F.H.M. Sanders and P. Vischer, Nucl. Instr. and Meth. B18, 625 (1987)
31. R.A. Haring, H.E. Roosendaal and P.C. Zalm, Nucl. Instr. and Meth. B28, 205 (1987)
32. Y. Horiike, N. Hayasaka, M. Sekine, T. Arikado, M. Nakase and H. Okano, Appl. Phys. A44, 313 (1987)

33. R. Kullmer and D. Bäuerle, Appl. Phys. A43, 227 (1987); P. Mogyrosi, K. Piglmayer, R. Kullmer and D. Bäuerle, *ibid.* 45, 293 (1988)
34. J.J. Ritsko, F. Ho and J. Hurst, Appl. Phys. Lett. 53, 78 (1988)
35. T. Baller, D.J. Oostra, A.E. de Vries and G.N.A. van Veen, J. Appl. Phys. 60, 2321 (1986)
36. R. de Jonge, J. Majoor, K. Benoist and D. de Vries, Europhys. Lett. 2, 843 (1986)
37. T. Baller, G.N.A. van Veen and J. Dieleman, in Photon, Beam and Plasma Enhanced Processes, edited by A. Golanski, V.T. Nguyen and E.F. Krimmel (European Mat. Res. Soc. Proc. XV, les éditions de physique, Les Ulis, France), p. 415 (1988)
38. T.S. Baller, J. van Zwol, S.T. de Zwart, H. Feil and J. Dieleman, paper B3.3 this symposium
39. W. Sesselman, E.E. Marinero and T.J. Chuang, Appl. Phys. A41, 209 (1986)
40. L. Chen, V. Liberman, J.A. O'Neill and R.M. Osgood, in Laser and Particle-Beam Chemical Processing for Microelectronics, edited by D.J. Ehrlich, G.S. Higashi and M.M. Oprysko (Mat. Res. Soc. Proc. 101, Pittsburgh, PA 1988) p. 463
41. T.S. Baller, G.N.A. van Veen and J. Dieleman, J. Vac. Sci. Technol. A6, 1409 (1988)
42. G.N.A. van Veen, T.S. Baller and J. Dieleman, Appl. Phys. A47, 183 (1988)

33. R. Kullmer and D. Bäuerle, Appl. Phys. A43, 227 (1987); P. Mogyrosi, K. Piglmayer, R. Kullmer and D. Bäuerle, *ibid.* 45, 293 (1988)
34. J.J. Ritsko, F. Ho and J. Hurst, Appl. Phys. Lett. 53, 78 (1988)
35. T. Baller, D.J. Oostra, A.E. de Vries and G.N.A. van Veen, J. Appl. Phys. 60, 2321 (1986)
36. R. de Jonge, J. Majoor, K. Benoist and D. de Vries, Europhys. Lett. 2, 843 (1986)
37. T. Baller, G.N.A. van Veen and J. Dieleman, in Photon, Beam and Plasma Enhanced Processes, edited by A. Golanski, V.T. Nguyen and E.F. Krimmel (European Mat. Res. Soc. Proc. XV, les éditions de physique, Les Ulis, France), p. 415 (1988)
38. T.S. Baller, J. van Zwol, S.T. de Zwart, H. Feil and J. Dieleman, paper B3.3 this symposium
39. W. Sesselman, E.E. Marinero and T.J. Chuang, Appl. Phys. A41, 209 (1986)
40. L. Chen, V. Liberman, J.A. O'Neill and R.M. Osgood, in Laser and Particle-Beam Chemical Processing for Microelectronics, edited by D.J. Ehrlich, G.S. Higashi and M.M. Oprysko (Mat. Res. Soc. Proc. 101, Pittsburgh, PA 1988) p. 463
41. T.S. Baller, G.N.A. van Veen and J. Dieleman, J. Vac. Sci. Technol. A6, 1409 (1988)
42. G.N.A. van Veen, T.S. Baller and J. Dieleman, Appl. Phys. A47, 183 (1988)

STRESS MODIFICATION IN TUNGSTEN FILMS DEPOSITED BY ION-ASSISTED EVAPORATION

R. A. ROY, R. PETKIE, D. S. YEE, J. KARASINSKI, A. BOULDING, IBM Research Division, T. J. Watson Research Center, Yorktown Heights, NY 10598

ABSTRACT

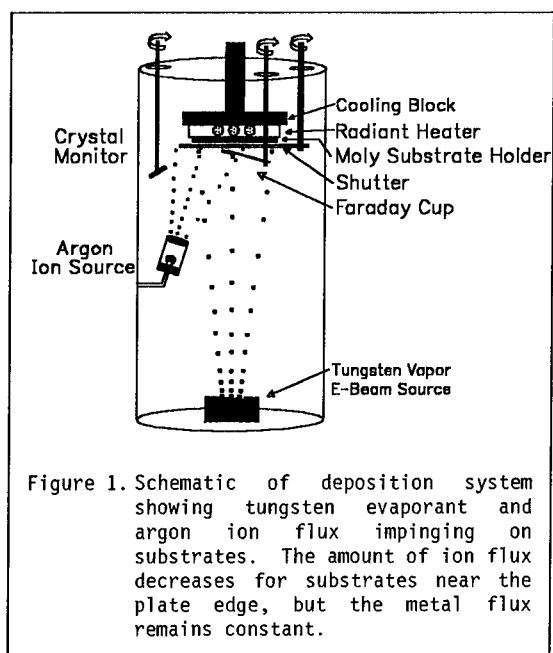
The modification of film stress in evaporated tungsten was studied as a function of deposition environment. Using concurrent ion bombardment of the growing film, the stress was seen to vary systematically with ion energy, ion flux, and substrate temperature. The qualitative behavior fits the model of stress modification developed for niobium films. X-ray diffraction was used to study the structure of the films, and a clear correlation between crystallographic texture and film stress is found. The original structure/impurity model for film stress modification due to ion bombardment has been modified to account for the relationship between film stress and texture.

INTRODUCTION

Modification of film properties by ion bombardment during film growth has long been a recognized phenomenon that can be used to minimize stress in vapor-deposited films (1-10). In refractory metals with bcc crystal structure, we have previously shown that film stress can be modified by a combination of substrate temperature and argon ion bombardment during film growth (7,8). A stress behavior of niobium films attributed to the presence of two ion bombardment mechanisms which had opposite effects on film stress. The first mechanism was impurity removal, which tended to increase tensile stress; the second was termed "structure modification" and was believed to involve changes in the microstructure of the films associated with the trend toward compressive stress at high ion flux. In the current study, we have adopted an experimental methodology similar to the niobium study using tungsten metal. We have expanded the matrix of experimental parameters to include a range of ion flux, ion energy, and substrate temperature to verify whether increasing ion energy has an effect similar to increasing substrate temperature. We have used x-ray diffraction to examine the nature of film structural changes that were believed to occur at high ion flux where film stress became compressive in previous studies of Nb and Cr. We will show that the stress behavior is very similar to niobium, and that changes in stress are closely associated with changes in film texture.

EXPERIMENTS AND ANALYSIS

A schematic diagram of the vacuum system is shown in Fig. 1. The chamber is pumped with a 10 in. diameter cryopump. The base pressure was typically 3×10^{-7} Torr after elevated temperature conditions were attained through use of radiant quartz lamps. The electron beam heated W source and the 6.0 cm. Ar ion source were outgassed and stabilized prior to deposition. During film deposition the chamber pressure resulting from Ar admitted through the ion source was about 1×10^{-4} Torr. The angle of the Ar ion beam incident on the substrate plate was at about 17° from the normal. A 1 cm^2 Faraday cup was used to measure the ion flux as a function of position on the substrate plate. Once the beam stability was established, the W source was stabilized at an evaporation rate of 5 \AA/s



and the samples were exposed to the incident fluxes. After deposition the ion flux was measured again. The ion current density profile of each run was evaluated by averaging and the current density for each sample was determined by interpolation of the flux vs. position curve.

The film stress was evaluated from the change in curvature of the strips after deposition. Film thickness was measured with a profilometer and sheet resistance was measured with a four point probe. The concentration of oxygen was measured on selected samples by electron microprobe. X-ray diffraction of the same selected samples was performed using a Philips goniometer in the normal Bragg-Brentano diffraction

geometry. To determine the type of in-plane film texture, the integrated peak intensities of several of the strongest peaks were compared for each sample.

RESULTS AND DISCUSSION

Film stress as a function of ion flux is shown in Fig. 2a for tungsten films subjected to 400 eV Ar ion bombardment at a series of substrate deposition temperatures. Because the W deposition rate is constant at 5 Å/s, increasing ion flux represents increasing relative arrival rate of argon ions with respect to tungsten atoms at the growing film surface. A flux of 0.1 mA/cm² represents an ion/atom arrival ratio of about 0.2. A maximum in tensile stress of about $10\text{--}15 \times 10^9$ dynes/cm² is observed at all temperatures. The maximum stress due to thermal mismatch is about 2×10^9 dynes/cm² for deposition at 750°C. This means that the majority of the stress measured is intrinsic film stress. The maximum in stress shifts to lower ion flux as the substrate temperature is increased. At higher flux, the films stress decreases and becomes compressive for all films bombarded by 400 eV ions. The trend towards compressive stress at higher ion bombardment is widely observed for vapor-deposited films. The general stress behavior observed is the same for evaporated niobium deposited in the same manner (7). Films were also deposited using a constant substrate temperature and a series of different ion energies. Figure 2b shows the results for a series of films deposited at a constant substrate temperature of 450°C with ion energy varied between 200 and 600 eV. The same tensile stress maximum and trend toward compressive stress is seen as a function of ion flux. The flux at which the maximum stress is reached, as well as that at which stress changes to compressive, shift to lower values as a function of increasing ion energy.

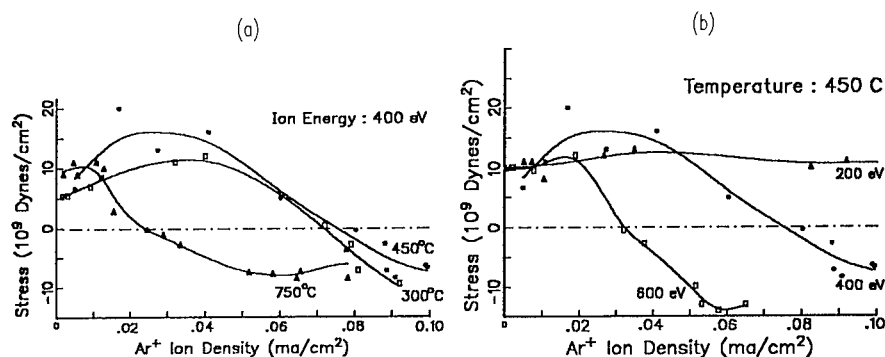


Figure 2. Tungsten film stress as a function of ion flux incident on the growing films. In a) film stress using 400 eV ions at several different substrate temperatures is shown. In b) the substrate temperature is 450°C, and the effect of different ion energies is shown.

At 200 eV the highest ion flux used was not sufficient to induce compressive stress at 450°C. In general, the effect of increasing ion energy seems to mimic that of increasing substrate temperature.

The results of electron probe microanalysis of films deposited using concurrent 400 eV ion bombardment show an initial rapid decrease in oxygen content as a function of increasing ion flux. Figure 3a shows that at 300°C the oxygen content is about 1% without any ion bombardment, but drops to a constant level of about 0.3% at about 0.06 mA. At 750°C (Fig. 3b) the initial oxygen content is lower, about 0.4%, and decreases to a constant value of about 0.1% at about 0.04 mA ion flux. The decrease in oxygen content is in keeping with previous results of evaporated niobium films, where an initial

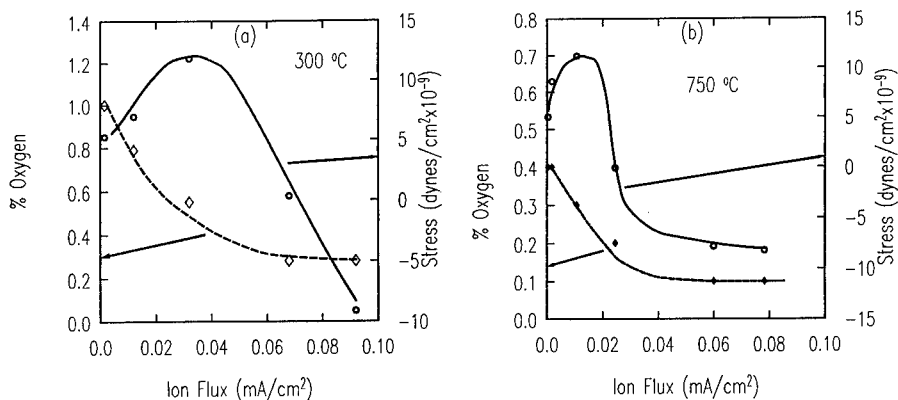


Figure 3. Atomic percent oxygen and film stress shown as a function of Ar ion flux at 400 eV energy. (a) 300°C, (b) 750°C.

decrease at low ion flux was seen. At a flux level corresponding to the same level at which tensile stress reached a maximum, the oxygen content in the films reached a minimum. This coincidence of effects was attributed to the fact that tensile stress obtained a maximum when the films reached a "critical purity" level. At ion flux levels higher than that necessary to reach the critical purity, additional ion bombardment causes structural changes in the growing films which resulted in the observed trend toward compressive stress. In the current study, the initial results cited above suggest that the oxygen content in the films reaches a minimum at ion flux levels somewhat higher than that where the stress maximum occurs, but the trends are the same as that seen in niobium films.

The same series of films shown in figures 2a and 2b were examined by x-ray diffraction to monitor changes in x-ray microstructure, changes which have been previously linked to film property changes in fcc metals (12). For all tungsten films the main peaks observed were from the (110), (211), and (200) reflections. In all films the (110) was the strongest peak, as is the case in randomly oriented polycrystalline tungsten. At low ion flux the relative intensity of the (200) reflection was often significant, but was weak at high flux. The behavior of the (211) peak intensity was complex, but nevertheless showed some interesting parallels to the stress behavior. Figure 4 plots film stress and (211)/(110) ratio as a function of increasing ion flux for various sets of films. In all sets of films the (211)/(110) ratio reaches a maximum at the same ion flux level that the tensile stress reaches a maximum. A decrease in (211)/(110) ratio is universally seen at higher ion flux levels, where the tensile stress decreases. For compressively stressed films the texture does not appear to change significantly with increasing stress; rather the (211)/(110) ratio remains at about 0.05.

It is clear from the maxima in stress and (211)/(110) ratio that more than one mechanism, which have countering effects on film structure and properties, are acting in concert. The evidence that the mechanism predominant at low ion flux is related to impurity removal as suggested previously (7), is supported by the current study in several ways. The first is the systematic shift in the stress maximum to lower ion flux levels as the substrate temperature increases. This is in keeping with the idea that increased substrate temperature and ion flux act in concert to remove oxygen from the growing films by thermal desorption, and selective re-sputtering, respectively. At a sufficiently high substrate temperature, the oxygen content is minimal even in the absence of ion bombardment, so that the stress maximum occurs at zero ion flux, as was seen for niobium films deposited at 400°C. In the current study, at 750°C the stress maximum shifts to near-zero ion flux, about 0.02 ion/atom ratio using 400 eV ion energy. The fact that higher temperature is required for tungsten than niobium to reach the critical purity level may be due to the more refractory nature of tungsten. The shift in the stress maximum to lower flux with increased ion energy suggests that at low relative flux the 600 eV ions are more effective in impurity removal than 200 eV ions, and can be used in lieu of increased substrate temperature.

The above results raise the question as to why the selective removal of oxygen, accomplished by combination of increasing ion flux, ion energy, or substrate temperature, should be associated with increased amount of (211) oriented crystallites. We propose that the presence of oxygen on the growing film surface favors the growth of crystallites with (110) planes parallel to the film surface. It is likely that the incident oxygen molecules behave similar to nitrogen, which has been previously observed to adsorb much more readily on tungsten surfaces other than the (110) (11,12). If this is the case, then long residence time of oxygen will quench the growth of (211) and (111) grains.

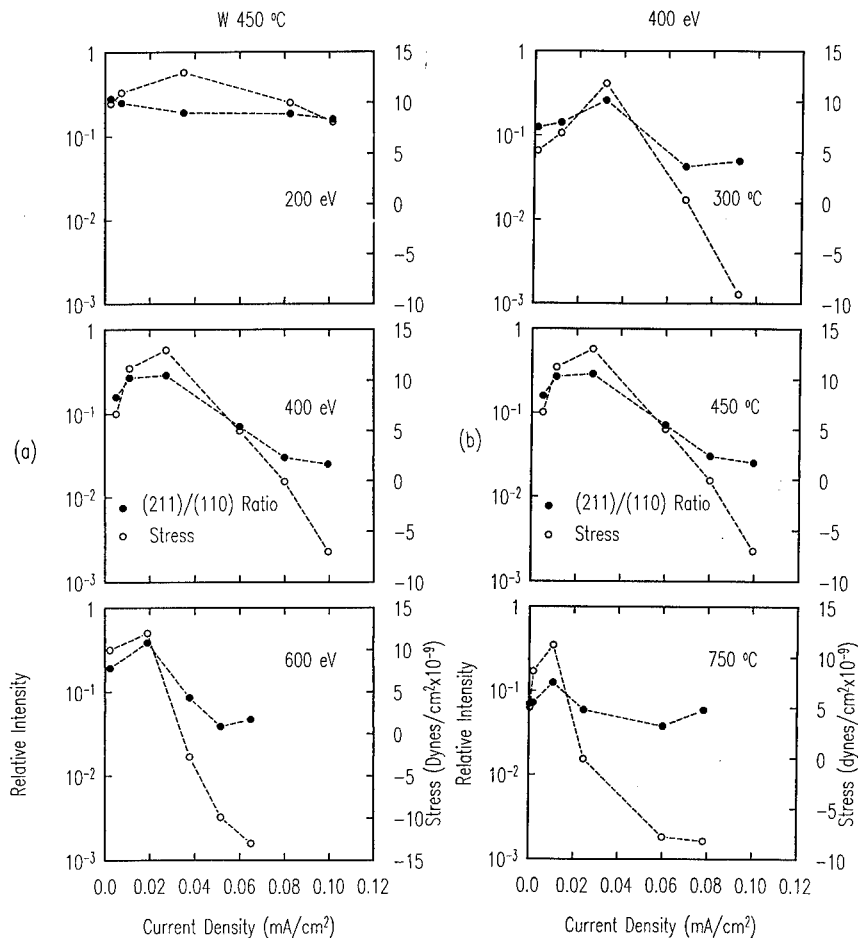


Figure 4. Film stress and (211)/(110) ratio plotted as a function of increasing ion flux: a) 400 eV ion energy is used and results are shown for three different temperatures. b) 450°C substrate temperature is used and three different ion energies are shown.

This is because these orientations present relatively open atomic planes of less than half the (110) area density, more suited for gas adsorption. In the absence of ion bombardment or high temperature, the presence of oxygen will then selectively suppress the growth of crystallite planes other than the (110), which is unlikely to adsorb the oxygen. Under the presence of a small amount of ion bombardment (or with increased temperature) the rapid removal of surface oxygen will allow the growth of non-close-packed planes; these planes otherwise would be covered with adsorbed gas, making growth more difficult. Thus, one initially observes an increase in the relative amount of (211) crystallites as ion bombardment is increased. Significantly, the maximum (211)/(110) ratio observed is about 0.28, which is just above a random texture. This is not unreasonable since the removal of oxygen only removes a barrier to (211) grain

growth but should not suppress the growth of (110) grains, other mechanisms notwithstanding. Thus, the near-random texture observed at the maximum in stress is quite reasonable for growth on amorphous oxide-coated silicon substrates, on which surfaces near-random texture has been seen in evaporated copper (1).

At higher levels of ion flux, the universal trend toward compressive stress seen previously in niobium, chromium, and presently in tungsten films, suggests that momentum transfer processes become dominant. In the present study we have identified a trend toward (110) texture which is coincident with this change in stress. In fact, careful review of figure 4 will show that the (110) (close-packed) texture reaches a maximum (that is, the (211)/(110) reaches a minimum) at the flux level near where the stress changes sign. The increase in close-packed texture for copper films exposed to argon ion bombardment was recently observed by us (1) and has been seen in nickel film growth under high ion bombardment (13). The predominant mechanism which is responsible for this result is believed to be the forward sputtering of film atoms on the film surface (14). In the present study, figure 4 shows that the highest close-packed texture (lowest (211)/(110) ratio) occurs for films subjected to 400 eV ions. At 200 eV the ion bombardment is not sufficient in force to increase the (110) texture substantially, while at 600 eV, a maximum in texture is reached at about 0.1 ion/atom ratio (0.05 mA/cm²), above which the texture begins to degrade.

The above results suggest that what was previously referred to as a dichotomy of impurity control/structure control regimes of ion bombardment, might better be termed : impurity desorption - controlled texture / forward sputter - controlled texture dichotomy. This would denote the fact that crystalline texture is continually being modified as a function of increasing ion flux, whether by impurity desorption, which is important at low temperature, low flux and low ion energy, or by momentum transfer at higher levels. In turn, the texture changes appear to be the key to the stress changes observed. In a forthcoming paper we deal with other features of film structure such as grain size, strain and related properties such as resistivity (15).

REFERENCES

1. R. A. Roy, J. J. Cuomo, and D. S. Yee, J. Vac. Sci. Technol., **A 6** (3) 1621 (1988)
2. D. W. Hoffman and J. A. Thornton, J. Vac. Sci. Technol. **20** (3), 35 (1982)
3. D. W. Hoffman and M. R. Gaerttner, J. Vac. Sci. Technol. **17** (1), 425 (1980)
4. R. S. Berg and G. J. Kominiak, J. Vac. Sci. Technol. **13** (1), 403 (1976)
5. P. Ziemann and E. Kay, J. Vac. Sci. Technol., **A 1** (2) 512 (1983)
6. J. M. E. Harper, J. J. Cuomo, R. J. Gambino, and H. R. Kaufman, in Ion Bombardment Modification of Surfaces: Fundamentals and Applications, O. Auciello and R. Kelley, eds., Elsevier Science Pub. B. V., Amsterdam, 1984
7. J. J. Cuomo, J. M. E. Harper, C. R. Guarnieri, D. S. Yee, L. J. Attanasio, J. Angilello, C. T. Wu, and R. H. Hammond, J. Vac. Sci. Technol., **20** (3), 349 (1982)
8. D. S. Yee, J. Floro, D. J. Mikalsen, J. J. Cuomo, K. Y. Ahn, and D. A. Smith, J. Vac. Sci. Technol., **A 3** (6), 2121 (1985)
9. T. C. Huang, G. Lim, F. Parmigiani, and E. Kay, J. Vac. Sci. Technol., **A 3** (6), 2161 (1985)
10. E. Kay, F. Parmigiani, and W. Parrish, J. Vac. Sci. Technol. **A 5**, 44 (1987)
11. J. P. Hobson, P. A. Redhead, Proc. Fourth Internl. Vac. Conf. (1968) 3, and references therein
12. G. Erlich and F. G. Hudda, J. Chem. Phys., **33**, 1253 (1960)
13. E. Kay, F. Parmigiani, and W. Parrish, J. Vac. Sci. Technol. **A 6** (6), 3074 (1988)
14. K.-H. Muller, Phys. Rev. B, **35** (15), 7906 (1987)
15. R. Petkie, R. A. Roy, D. S. Yee, A. Boulding, K. Kelleher (private commun.)

CONTROL OF METAL FILM PROPERTIES BY ION ASSISTED DEPOSITION

RONNEN A. ROY, DENNIS S. YEE, and JEROME J. CUOMO, IBM Research Division,
Watson Research Center, P.O. Box 218, Yorktown Heights, N.Y., 10598

ABSTRACT

Ion-assisted deposition allows for independent control of ion energy, ion flux, and adatom flux incident on the growing film. We describe herein general trends in property and structure modification of thin film metals using this technique.

INTRODUCTION

Ion bombardment of films during growth has long been recognized as an important tool in modifying resultant film properties. Beginning with bias sputtering and techniques such as ion plating, researchers have sought to control film properties by varying the amount of bombardment (1-4). With the advent of broad beam ion sources the ability to modify and reproducibly control film properties (5-7) has improved due to several factors. A major advantage is that ion energy and ion flux are decoupled, allowing for independent variation of either parameter. Another advantage is that the plasma is contained in the ion source, providing a much simpler deposition environment near the substrate. Thus, one can better quantify the amount and energy of the various species incident on the film/substrate during growth, making the interpretation of data much simpler. In this paper, we focus on the application of ion-assisted deposition (IAD) for property modification of various metal films (6-10). Based on the results of niobium, chromium, copper, and tungsten, we shall highlight the importance of parameter selection, such as ion energy, in controlling property changes. Furthermore, the modifying effects of substrate temperature (T_s) on film properties will be described. A review of film physical property changes, microstructure changes, and their interrelation will be given.

EXPERIMENTS

All of the results described herein are obtained from films deposited by electron beam evaporation with concurrent argon ion bombardment of the growing film using small Kaufman ion sources, described in detail elsewhere (6-10).

RESULTS

Property Modification

Film properties such as stress, microhardness and electrical resistivity, have been modified by concurrent bombardment during deposition. In the case of Cu, the resistivity and microhardness behavior have shown a strong energy dependence (8). At 600 eV ion energy, the resistivity of films rises steeply with ion flux, surpassing $10 \mu\Omega\text{-cm}$ at high flux levels (fig 1). On the other hand films deposited with concurrent 125 and 62 eV Ar ion bombardment (also shown in Fig. 1a) show only a small increase in resistivity from about $2 \mu\Omega\text{-cm}$ at low levels to $2.6 \mu\Omega\text{-cm}$ at high levels. Qualitative differences were also seen in microhardness changes under ion bombardment as the primary

ion energy is lowered. At 600 eV energy microhardness in copper films was found to increase rapidly with increased ion flux, while at 62 eV ion energy decreases in hardness were seen at low to moderate ion flux. Figure 1b shows resistivity vs ion flux from studies of tungsten (10) films evaporated at about 450 °C, with ion energies of 200 and 600 eV. At 200 eV, increased ion flux causes slight resistivity decreases, while at 600 eV, as with copper, the resistivity increases strongly with increased ion flux. Similar behavior is also seen for evaporated Cr (7) and Nb (6).

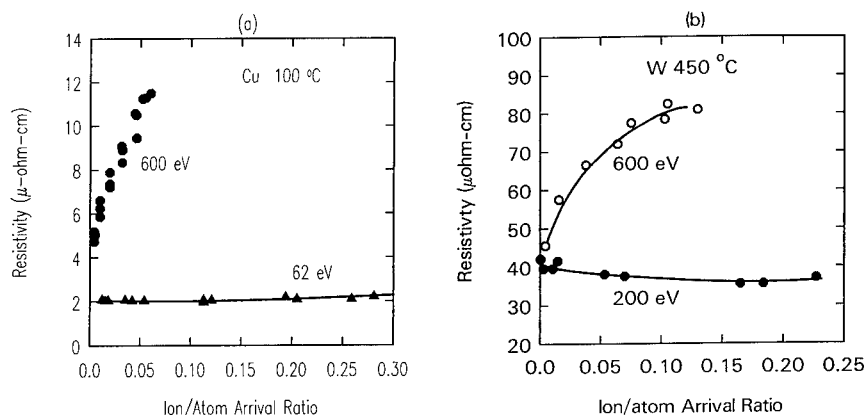


Figure 1: Resistivity as a function of increasing ion flux at different ion energies for a) evaporated copper and b) tungsten films.

Another important film property, stress, has been shown in the case of W and Nb to depend on a combination of substrate temperature and ion bombardment (6,10). Figure 2a shows the stress behavior as a function of ion flux that was observed for niobium films evaporated at various temperatures using 100 eV bombardment. The maximum in tensile stress shifts to higher flux at lower temperatures, reaching approximately the same value before decreasing. Furthermore, the flux at which the maximum stress is reached corresponds to the point at which a minimum oxygen content is reached. Similar stress behavior is also seen in the case of tungsten deposited using 400 eV ion bombardment, as shown in Figure 2b.

Structure Modification

Figure 3 shows crystallite size versus bombardment for Cu films subjected to ion bombardment at different energies. There is a clear dependence of the crystallite size on ion energy in the Cu films, even for the same deposited energy-per-atom (eV/atom). The higher energy ions-particularly at 600 eV-caused a significant reduction in grain size. As a function of increasing energy-per-Cu-atom(or ion flux) the grain size initially diminishes rapidly followed by smaller changes at high flux. On the other hand, at 62 eV no decrease in size with increased ion flux is seen; grain size at high ion flux levels is similar to unbombarded films. Figure 3 also shows grain size changes in Cr films deposited at 360 °C. When subject to 400 eV ion bombardment, high levels of ion flux are seen to decrease grain size, while 100 eV ion bombardment causes a monotonic increase in grain size over the flux range.

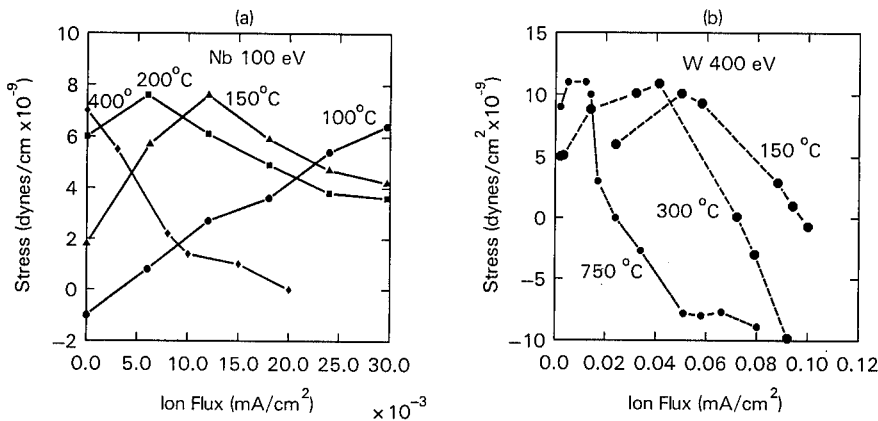


Figure 2: Stress as a function of ion flux in: a) Nb films evaporated with concurrent 100 eV ion bombardment (6); and b) for evaporated W films subjected to 400 eV concurrent ion bombardment shown at a series of substrate temperatures. A tensile stress maximum shifts toward lower ion flux as substrate temperature is raised.

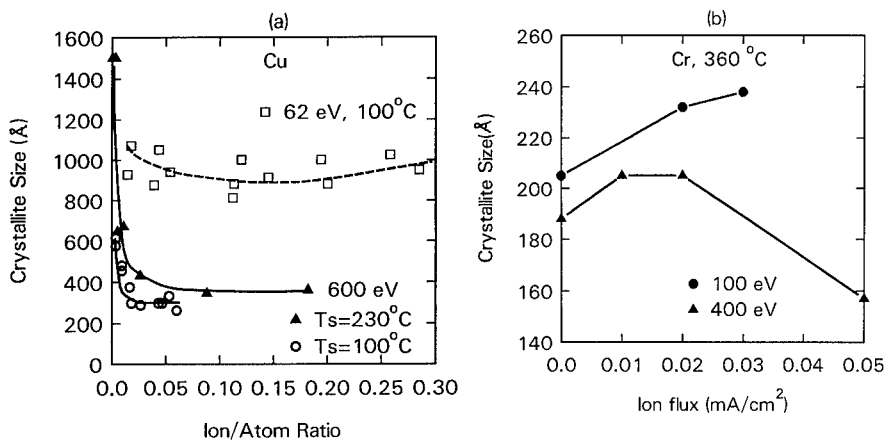


Figure 3: Crystallite size measured by x-ray diffraction for a) evaporated copper films vs ion flux, for 600 and 62 eV ion energy. At 600 eV the size decreases to about 300 Å at high ion flux while at 62 eV it remains above 1000 Å. In b) grain size vs ion flux for evaporated Chromium films deposited at 360°C is shown. At 400 eV a decrease is seen, while at 100 eV an increase occurs.

Changing ion energy has also been found to influence crystallographic orientation in evaporated films, as shown in Fig. 4 for deposition on amorphous silicon oxide substrates. Fig. 4a shows that for copper films deposited with 600 eV ion bombardment a peak in (111) orientation occurs at low ion flux, followed by a decrease in orientation at high ion flux, consistent with results observed by Huang et al. (12) for thin silver films. However, at 125

eV ion energy the degree of (111) orientation increases monotonically over the 0 to 40 eV/atom range studied, showing very strong (111) texture at high flux. At 62 eV, the orientation remains near random over a wide ion flux range. In 4b similar behavior is seen for tungsten films. At 600 eV a maximum in (110) texture as a function of increasing ion flux occurs, above which flux level the (110) texture decreases. By slightly lowering the ion energy to 400 eV, (110) orientation is stronger and continues to increase monotonically up to high levels of ion flux. Lowering the energy further to 200 eV causes the texture to remain near-random over the entire flux range studied.

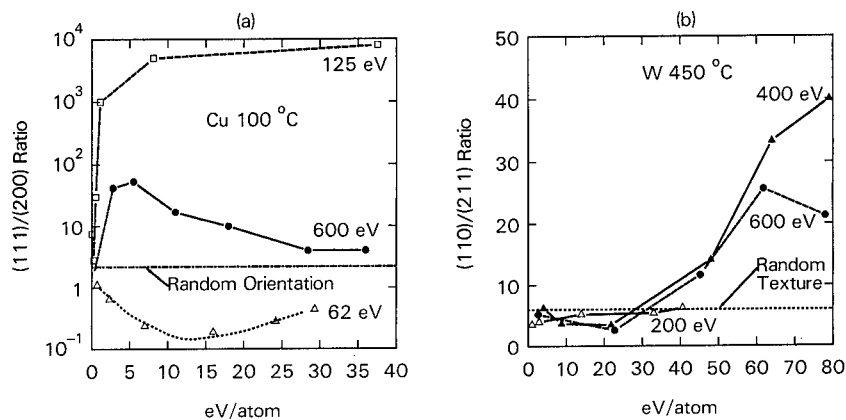


Figure 4: Crystallographic orientation of evaporated a) copper films vs ion flux at different ion energies. Shown is the (111)/(200) ratio obtained using Bragg-Brentano diffractometer geometry. In b is shown the (110)/(211) ratio vs ion flux for three different ion energies for evaporated tungsten.

DISCUSSION

The studies cited above reveal a clear change in the nature of film structure and property behavior under ion bombardment as ion energy is lowered. At 600 eV a large increase in resistance and hardness occurs, which can be directly related to the decrease in grain size caused by increased ion flux (8,13,14). At lower energy the fact that ion bombardment does not strongly decrease the grain size is reflected in the low resistivity and microhardness. In the case of tungsten, niobium, chromium, and copper Fig. 5 shows the inverse relation between resistivity and grain size, which is consistent with work by Parmigiani et al. (15), who found that crystallite size effects dominate other microstructural features in determining resistivity in ion bombarded silver films. The data are plotted as normalized resistance R_{film}/R_{bulk} and fall on roughly two curves, one for Cu and W, and one for Nb and Cr, which approach their bulk resistivity values at relatively small grain size in comparison with copper and tungsten. Nonetheless, the same general trend shows that the resistance is inversely correlated to grain size.

In deposition regimes where grain size changes are not as pronounced, eg. low ion energy in the case of copper or low substrate temperature in the case of tungsten, the effect of crystallographic texture changes on film properties becomes apparent. Properties sensitive to texture, such as stress, hardness, and resistivity, reflect the changes in texture caused by ion bombardment. Figure 6a shows stress vs texture in tungsten films deposited by ion-assisted

evaporation, showing a trend toward compressive stress with increasing (110) texture, and increasing tensile stress with increasing (211)/(110) ratio. Fig 6b shows hardness and resistivity as a function of texture for copper films evaporated with 62 eV concurrent ion bombardment. A minimum in both properties seems to occur for texture near random values with large increases for low (111)/(200) ratios. From the data shown in figure 6 it is clear that, independent of grain size changes, changes in film texture induced by ion bombardment can produce changes in related film properties.

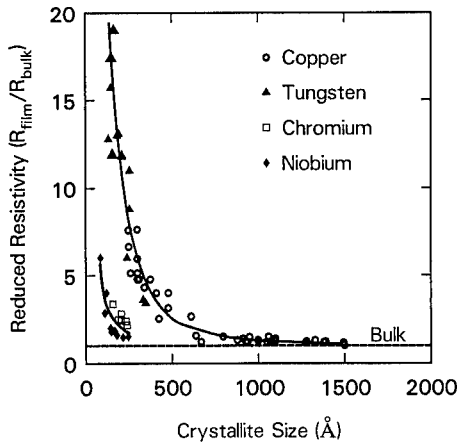


Figure 5: Resistivity vs grain size for various metals with resistivity normalized to the respective bulk values.

Knowledge of the behavior shown above may be important for those concerned with optimizing specific film properties when faced with various empirical constraints typically encountered in more complex deposition environments. For instance, the results of the Nb and W work show that various combinations of temperature, ion flux and ion energy can be used to produce the same property, namely zero-stress. Faced with the constraints on one of these parameters, the other two can be appropriately adjusted to compensate. Other operator-controlled parameters, which indirectly influence film properties can also be varied. In the case of stress changes in refractory metals, these include

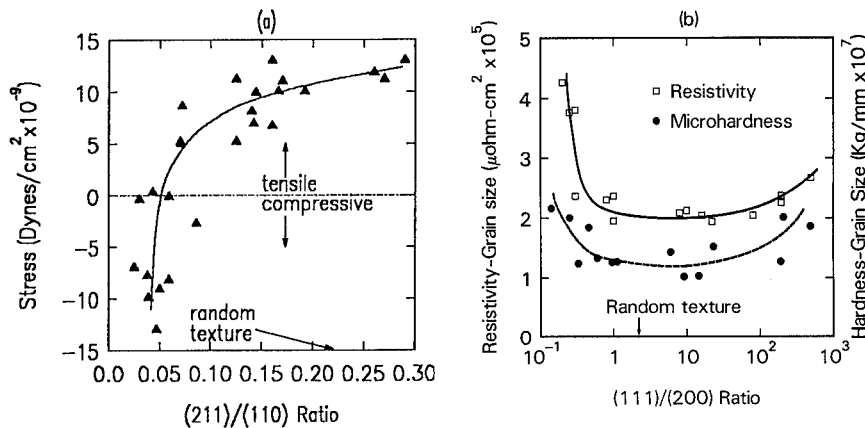


Figure 6. a) shows stress vs (211)/(110) ratio in tungsten films. A correlation is seen between increasing tensile stress and increasing (211)/(110) ratio. b) Resistivity and hardness vs (111)/(200) ratio in copper films subject to 62 eV concurrent Ar ion bombardment showing minima near random texture. Each datum represents the property value for a given film multiplied by its grain size. This is done to eliminate grain size effects (fig. 5).

the metal evaporation rate and the background gas pressure, which effectively determine the metal atom/impurity atom arrival ratio, thus the film oxygen content, and thereby the stress (7). Combinations of properties can be optimized by careful selection of parameter space.

In summary, recent studies of ion assisted metal deposition show common behavior of film properties with changes in ion flux, ion energy, and substrate temperature. These property changes can be directly linked to changes in film microstructure which are sensitive to the same deposition parameters.

REFERENCES

1. D. W. Hoffman and J. A. Thornton, J. Vac. Sci. Technol. 20 (3), 35 (1982)
2. D. W. Hoffman and M. R. Gaerttner, J. Vac. Sci. Technol. 17 (1), 425 (1980)
3. R. S. Berg and G. J. Kominiak, J. Vac. Sci. Technol. 13 (1), 403 (1976)
4. P. Ziemann and E. Kay, J. Vac. Sci. Technol. 21 (3), 828 (1982)
5. J. M. E. Harper, J. J. Cuomo, R. J. Gambino, and H. R. Kaufman, in Ion Bombardment Modification of Surfaces: Fundamentals and Applications, O. Auciello and R. Kelley, eds., Elsevier Science Publishers B. V., Amsterdam, 1984
6. J. J. Cuomo, J. M. E. Harper, C. R. Guarnieri, D. S. Yee, L. J. Attanasio, J. Angilello, C. T. Wu, and R. H. Hammond, J. Vac. Sci. Technol., 20 (3), 349 (1982)
7. D. S. Yee, J. Floro, D. J. Mikalsen, J. J. Cuomo, K. Y. Ahn, and D. A. Smith, J. Vac. Sci. Technol., A 3 (6), 2121 (1985)
8. R. A. Roy, J. J. Cuomo, and D. S. Yee, J. Vac. Sci. Technol. A 6 3, 1621 (1988)
9. R. A. Roy, D. S. Yee, and J. J. Cuomo, (to be published)
10. R. A. Roy, R. Petkie, D. S. Yee, J. Karasinski, A. Boulding, and K. Kelleher, these proceedings
11. J. A. Thornton and D. W. Hoffman, J. Vac. Sci. Technol. 18 (2), 203 (1981)
12. T. C. Huang, G. Lim, F. Parmigiani, and E. Kay, J. Vac. Sci. Technol., A 3 (6), 2161 (1985)
13. E. O. Hall, Proc. Phys. Soc. London B64, 747 (1951)
14. N. J. Petch, J. Iron Steel Inst. 174, 25 (1953)
15. F. Parmigiani, E. Kay, T. C. Huang, J. Perrin, M. Jurich, and J. D. Swalen, Phys. Rev. B, 33 (2), 879 (1986)
16. H. F. Winters and E. Kay, J. Appl. Phys., 38 3928 (1967)
17. A. G. Blachman, Met. Trans. 2, 699 (1971)
18. R. D. Bland, G. J. Kominiak, and D. M. Mattox, J. Vac. Sci. Technol.,
19. B. Window, F. Sharples, and N. Savvides, J. Vac. Sci. Technol. A 6 (4), 2333 (1988)
20. K.-H. Muller, Phys. Rev. B, 35 (15), 7906 (1987)

SOFT MAGNETISM AND MORPHOLOGY OF Fe FILMS BY DUAL ION BEAM SPUTTERING

M. Nagakubo, T. Yamamoto, and M. Naoe

Dept. of Physical Electronics, Tokyo Institute of Technology, 2-12-1,
O-okayama, Meguro-ku, Tokyo 152, Japan.

ABSTRACT

Fe films have been deposited by using dual ion beam sputtering apparatus under various conditions, and the dependence of their magnetic properties and morphology on preparation parameters such as film thickness, δt , and argon gas pressure, P_{Ar} , have been investigated in detail.

The saturation magnetization $4\pi M_s$ of the specimen films did not change remarkably with δt in the range of 50~1000nm. However, with decrease of δt below 50 nm, $4\pi M_s$ decreased to less than 20 kG and coercivity H_c increased to more than 16 Oe. As P_{Ar} increased from 0.5 to 1.6 mTorr without ion bombardment, $4\pi M_s$ decreased to less than 20 kG and H_c increased to about 20 Oe. The SEM micrographs of these films deposited at higher P_{Ar} showed the columnar structure. On the other hand, the films deposited at lower P_{Ar} and ones bombarded by argon ions with proper kinetic energy during deposition did not present any texture and exhibited better soft magnetism. Such a morphology may be attributed to the difference in arrival energy of sputtered Fe particles to film surface and related closely to soft magnetism. It has been found that the dual ion beam sputtering method can control $4\pi M_s$ and H_c with changing P_{Ar} and so prepare Fe films with superior soft magnetism by adjusting the kinetic energy of bombarding argon ions at lower P_{Ar} .

INTRODUCTION

Recently, the ultra-high purity Fe has become of major interest for the revived ferromagnetic materials. Especially, Fe films with soft magnetism may be useful for a thin film type of magnetic head. However, the magnetic properties of Fe films are not always the same as bulk Fe because they are affected by the preparation process and the presence of impurities in films.

Effects of gas addition by ion bombardment of the surface layers of growing films have been already reported.[1] In a previous study, it was verified that the bombardment of argon and hydrogen ions accelerated at a voltage of 500 V and current density of about 20 $\mu A/cm^2$ during deposition improved the soft magnetism of Fe films, resulting from enhancing the microscopic uniformity and atomic ordering in Fe films.

The influence of film thickness δt and working gas pressure, P_{Ar} , on magnetic properties is important from the viewpoint of practical application. Dual ion beam sputtering method is very useful for studying growth uniformity and film morphology because of good controllability of deposition parameters such as P_{Ar} and ion acceleration voltage. In addition, the bombardment of argon ions with proper kinetic energy onto growing surface layer may change the film structure drastically and directly.

In this study, the δt and P_{Ar} dependences on magnetic properties and morphology of Fe films have been investigated, and the effects of ion bombardment to growing surface layer on them have been examined.

EXPERIMENTAL PROCEDURE

Figure 1 shows the schematic diagram of a dual ion beam sputtering apparatus used in this study. Both of the ion sources are Kaufman type. The lower one sputters the target at an incident angle of 60° to its plane. The upper one is the bombarding ion source. Some specimen films were bombarded by argon ions during deposition at an incident angle of 30° to its plane.

The base pressure in chamber was 2×10^{-7} Torr. As a sputtering gas, argon was introduced through the sputtering ion source up to 0.12 mTorr. In case of ion bombardment onto film surface, argon of 0.12 mTorr was added through the bombarding ion source. The total argon pressure in chamber was varied up to 1.6 mTorr by adjusting a gas inlet valve.

The acceleration voltage in the sputtering ion source (V_{mg}) was set at 500V or 1000V. The total current of ions sputtering the target was fixed at about 4mA. For bombarding ion source, the acceleration voltage (V_{sg}) was set at 100V. The current density of bombarding ions on the substrate surface was adjusted at about $20 \mu A/cm^2$, which was measured by ion current monitor. The deposition rates at V_{mg} of 500 and 1000V were 1.3 nm/min and 2.1 nm/min, respectively.

The specimen Fe films were deposited on water-cooled glass slides by sputtering a Fe target of 99.99% purity. The film thickness was varied in the range of about 5~1000 nm. Film morphology was observed by means of scanning electron microscopy (SEM) and crystal structure was analyzed by X-ray diffractometry. Saturation magnetization $4\pi M_s$ and coercivity H_c were determined from M-H hysteresis loops measured by a vibrating sample magnetometer in a maximum field of 10 kOe. Electrical resistivity was measured by means of the four-terminal method.

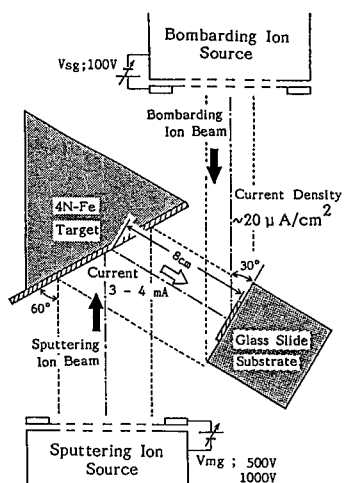


Fig. 1, Schematic diagram of a dual ion beam sputtering apparatus.

RESULTS AND DISCUSSION

Morphology and crystal structure

Figure 2 shows cross sectional SEM micrographs of Fe films deposited under different conditions. All specimen films have the very smooth surface. The cross sections of films deposited at P_{Ar} below 0.3 mTorr did not show an obvious texture at both V_{mg} of 500 and 1000V. Especially, ones at V_{mg} of 1000V showed a dense and columnless structure. However, as P_{Ar} increased above 1 mTorr, the cross sectional morphology of the films at V_{mg} of 500V changed to a columnar structure as seen in Fig. 2 (c). A similar structure was observed in the films at V_{mg} of 1000V. On the other hand, the films bombarded by argon ions at V_{sg} of 100V and a current density of $20 \mu A/cm^2$ did not show such texture even at P_{Ar} of 1.6 mTorr.

In the case of high P_{Ar} , the arrival energy of sputtered atoms decrease through collision process to residual gas atoms, and the mobility of them on film surface is reduced. As a result, the film structure could become columnar. Then, the range of P_{Ar} which may cause the change of film structure can be related to the mean free pass length, λ , of sputtered

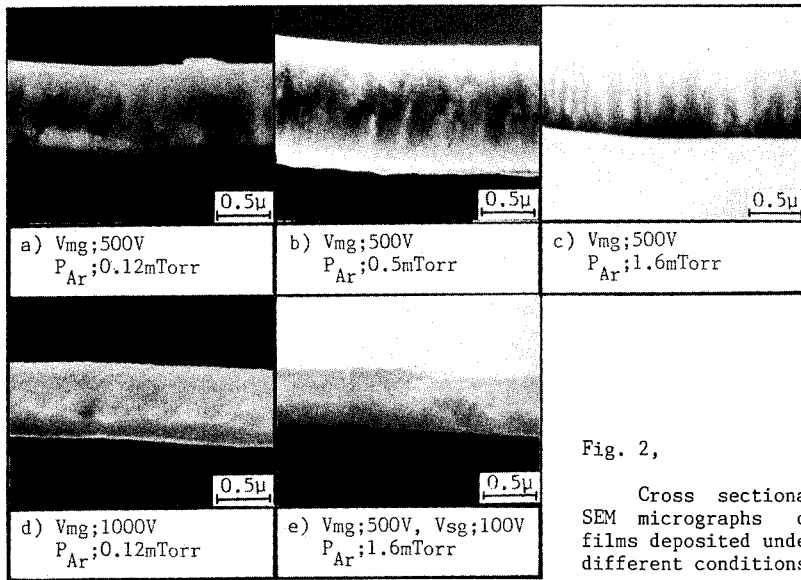


Fig. 2,

Cross sectional SEM micrographs of films deposited under different conditions.

atoms. If the sputtered Fe particles are individual atoms, then λ is calculated from the diameters D_{Fe} , D_{Ar} and weights M_{Fe} , M_{Ar} of Fe and Ar atoms as follows,

$$\lambda = \frac{1}{\pi \left(\frac{D_{Fe} + D_{Ar}}{2} \right)^2 n \sqrt{1 + \frac{M_{Fe}}{M_{Ar}}}} \quad (1)$$

where n is argon density estimated from P_{Ar} . λ based on Eq. (1) is smaller than 8cm at P_{Ar} above 0.8 mTorr. In fact, the distance between target and substrate in the sputtering apparatus used in this study was about 8cm. Therefore, the columnar structure seems to appear in the films deposited at P_{Ar} above 0.8 mTorr. On the other hand, the bombardment of argon ions with proper energy during deposition may increase the mobility of Fe atoms on film surface and eliminate columnar microstructure.

Figure 3 shows the dependence of internal stress σ on P_{Ar} . The films at Vmg of 500V had compressive σ of 3 to 4 $\times 10^9$ dyn/cm² at P_{Ar} below 1 mTorr. In this region of P_{Ar} , the remarkable σ dependences were not observed for the specimen films except for ion-bombarded ones as seen in Fig. 3. But σ of these specimen films decreased in similar way with increase of P_{Ar} above 1 mTorr, especially, σ of the films deposited at Vmg of 500V changed from compressive to tensile at P_{Ar} above 1.6 mTorr.

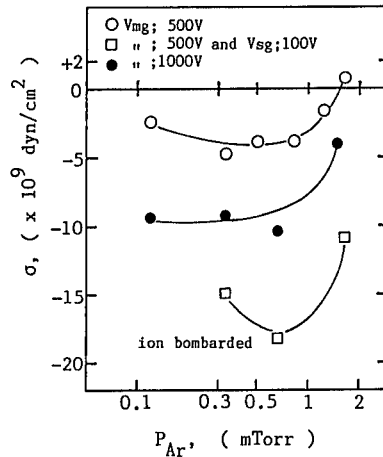


Fig. 3, The dependence of internal stress σ on δt and the effect of ion bombardment.

Generally, it is known that the internal stress, σ , of sputtered films depend on the mobility of random walking atoms and the bombardment of high energy particles onto film surface which may be related closely to morphology.[2][3] The compressive σ of films with columnar structure may be removed by the aid of the tensile stress induced among columns each other due to the atom diffusion. The ion bombardment's "peening effect" could lead to an increase of σ by the formation of defects and inclusion of interstitial argon in the lattice. The high σ in the films bombarded by ions during deposition was probably caused by this effect. Then, the decrease of σ at P_{Ar} above 1 mTorr may be attributed to the bombardment by ions with reduced energy through collision processes with argon atoms and ions raising the packing density of Fe atoms and decreasing the number of vacancies in the films. On the other hand, this interpretation suggest that the increase of σ with increase of V_{mg} from 500 to 1000V may be due to the additional and irregular bombardment by argon atoms recoiled from target plane.

Crystal structure of these films was analyzed by X-ray diffractometry. Figure 4 shows typical X-ray diffraction diagrams of Fe films deposited under various conditions. All films at V_{mg} of 1000V revealed two peaks of (110) and (200) planes of α -Fe crystallites, and the peak of (200) plane became rather dominant at δt below 100 nm. However, the films at V_{mg} of 500V and at P_{Ar} below 0.3 mTorr showed only the peak for the (110) plane. Then, the (200) peak was observed at P_{Ar} above 0.5 mTorr. And the films at V_{mg} of 500V did not reveal any peaks at δt in the range of below 100 nm. On the other hand, as P_{Ar} is above 1 mTorr, the films bombarded by argon ions accelerated at V_{sg} of 100V during deposition did not exhibit clear diffraction peak. This may show that the film has the amorphous-like structure.

Figure 5 shows the dependence of electrical resistivity, ρ , on δt . The resistivity of bulk pure iron is about 10 $\mu\Omega\cdot\text{cm}$. The working argon gas pressure P_{Ar} was kept at 0.12 mTorr. It was impossible to measure ρ of the films with δt below 50nm. The value of ρ was strongly dependent of the film structure. Resistivity at V_{mg} of 500V increased from 25 to 70 $\mu\Omega\cdot\text{cm}$ with a decrease of δt below 300nm, while ρ at V_{mg} of 1000V was constant of the order of 20~30 $\mu\Omega\cdot\text{cm}$ for δt in the same range. Resistivity of these films did not show any remarkable change with an increase of P_{Ar} . The amorphous-like

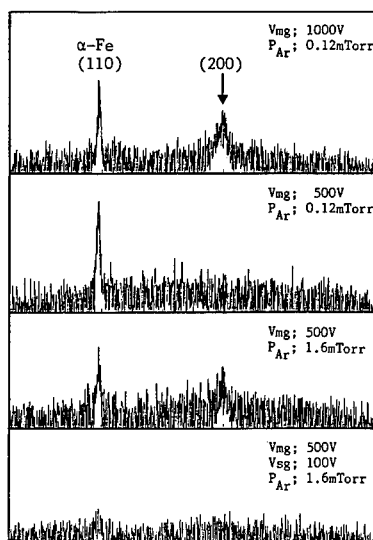


Fig. 4, X-ray diffraction diagrams of Fe films deposited under various conditions.

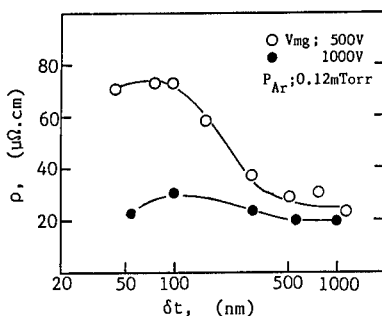


Fig. 5, The dependence of electrical resistivity ρ on film thickness δt .

films had higher ρ than pure bulk Fe. This may be attributed to electron scattering at the boundary of microcrystallites in the films. Taking these results into consideration, the Fe crystallite size and density at V_{mg} of 1000V may be increased over that at V_{mg} of 500V. Such structural difference based on difference of V_{mg} could be caused by bombardment of recoiled argon. The δt dependences of ρ for the films deposited at V_{mg} of 500V may result from the non-uniformity of growth orientation of films.

Magnetic properties

Figure 6 shows the dependence of $4\pi M_s$ and H_c on the film thickness δt . $4\pi M_s$ was about 20 kG for δt above 50 nm at both V_{mg} . But, $4\pi M_s$ of films deposited at V_{mg} of 500 V decreased gradually with decrease of δt in the range below 50 nm, and was about 14.5 kG at δt of 5 nm.

The films deposited at V_{mg} of 500V tended to have lower H_c than the ones deposited at V_{mg} of 1000V and had a minimum H_c of 4 Oe at a δt in the region of 20~150 nm, while the films deposited at δt below 20 nm and above 300 nm had higher H_c . The increase of H_c and the decrease of $4\pi M_s$ observed at δt below 20 nm implies the presence of an initial layer several nanometers thick with semi-hard magnetism. In addition, the oxidization of the surface layer may be noticeable.

The H_c dependences on δt were roughly contrary to those of ρ which were already shown in Fig. 5. The promotion of crystallite growth and grains in films seems to increase the magneto-crystalline anisotropy and to prevent domain wall motion. This may be one of the reasons for a large H_c observed at δt above 300 nm.

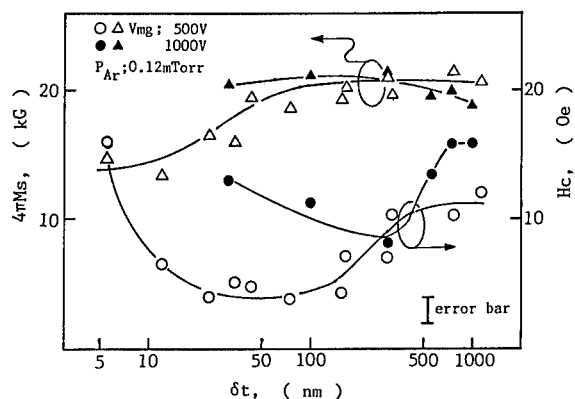


Fig. 6, The dependence of $4\pi M_s$ and H_c on film thickness δt .

Figure 7 shows the dependence of $4\pi M_s$ and H_c on working argon gas pressure, P_{Ar} . P_{Ar} was varied from 0.12 up to 1.6 mTorr at δt in the range of 600 to 1000 nm. For δt in this range, the change of $4\pi M_s$ and H_c is little as seen in Fig. 6. Coercivity tended to increase with increasing P_{Ar} . H_c of the films at V_{mg} of 500V abruptly changed at P_{Ar} above 0.5 mTorr, while that of the films at V_{mg} of 1000V gradually increased to more than 20 Oe at P_{Ar} above 1 mTorr. This result corresponds significantly with X-ray diffraction results as shown in Fig. 4. Namely, the intensity of (200) peak may be closely related to the increase of H_c . The saturation magnetization of these films decreased from about 20 kG with an

increase of P_{Ar} above 1 mTorr at both values of V_{mg} . This indicates that the small $4\pi M_s$ of films with columnar structure may be due to the low packing density of Fe atoms.

On the other hand, when the surface layer of growing films were bombarded by argon ions accelerated at 100V, $4\pi M_s$ and H_c did not change with P_{Ar} in the range of 0.3~1.6 mTorr, and H_c decreased to a low value below 8 Oe. From these results, it has been found that the increase of σ as shown in Fig. 3 is not closely related to the changes in $4\pi M_s$ and H_c , and that bombardment by ions with proper energy improves the uniformity of growth orientation of the films and makes the microstructure dense from the viewpoint of morphology. As a result, the Fe films with excellent soft magnetic properties are obtained by means of the above-mentioned ion bombardment.

CONCLUSION

Fe films with various structure and magnetic properties have been deposited by means of the dual ion beam sputtering method. Film thickness and working gas pressure have been investigated, as have the effects of ion bombardment on the growing surface layer. The summary is as follows;

- 1) The films deposited at lower P_{Ar} revealed dense and columnless structure, which changed to columnar structure at P_{Ar} above 1 mTorr with a decrease in arrival energy of sputtered Fe atoms.
- 2) The films with columnar structure had $4\pi M_s$ below 20 kG with very small compressive internal stress σ .
- 3) The films bombarded by argon ions with proper energy during deposition revealed dense structure even at P_{Ar} of 1.6 mTorr, and had H_c of 8 Oe and $4\pi M_s$ above 20 kG.
- 4) H_c at a V_{mg} of 1000V tended to be higher than that of V_{mg} at 500V. The measurement of electrical resistivity and X-ray diffractometry implied that the higher H_c may be attributed to the crystallite growth of α -Fe due to additional and irregular bombardment of recoiled argon atoms from target.

These results suggest that the dual ion beam sputtering method, which can adjust kinetic energy of bombarding argon ions at lower P_{Ar} , is a very useful technique for preparing Fe films with good soft magnetism.

REFERENCES

1. M. Nagakubo, A. Kawano and N. Naoe, Mat. Res. Soc. Symp. Proc. Vol. 80, 415 (1987).
2. R.D. Bland, G.J. Kominiak and D.M. Mattox, J. Vac. Sci. Technol., 11, 671 (1984).
3. C.T. Wu, Thin Solid Films, 64, 103 (1979).

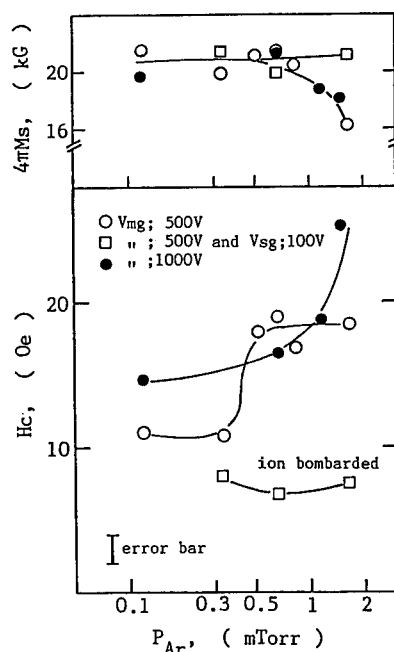


Fig. 7, The dependence of $4\pi M_s$ and H_c of films with δt of 600-1000nm on P_{Ar} and the effect of ion bombardment on soft magnetic properties.

ARGON ION BOMBARDMENT DURING MOLECULAR BEAM EPITAXY OF Ge (001)

ERIC CHASON, K.M. HORN, J.Y. TSAO, AND S.T. PICRAUX
Sandia National Laboratory, Albuquerque, NM 87185

ABSTRACT

Using in situ, real-time reflection high energy electron diffraction (RHEED), we have measured the evolution of Ge (001) surface morphology during simultaneous molecular beam epitaxy and Ar ion beam bombardment. Surprisingly, low-energy Ar ions during growth tend to smoothen the surface. Bombardment by the ion beam without growth roughens the surface, but the surface can be reversibly smoothened by restoring the growth beam. We have measured the effect of such "ion beam growth smoothening" above and below the critical temperature for intrinsic growth roughening. At all measured growth temperatures the surface initially smoothenes, but below the critical roughening temperature the final surface morphology is rough whereas above this temperature the final morphology is smooth.

INTRODUCTION

In MBE growth of single component materials, the crystal grower is generally limited in the number of parameters under his control to substrate preparation (including orientation, miscut and cleanliness), substrate temperature and deposition rate. It has been suggested that low energy ion beams might be used to extend the range for good epitaxy by modifying the growing surface and providing another adjustable parameter to control the growth kinetics[1,2]. Low energy ion beams have already been used as a method of improving non-epitaxial thin film growth by enhancing nucleation and densification of the film, relieving stress, and enhancing thin film adhesion[1]. Atomic cleaning of surfaces by ion beams has been shown to reduce epitaxial growth temperatures[3,4]. Direct ion beam deposition of epitaxial films has been demonstrated[5,6], and the lowest reported temperature for which Si has been grown epitaxially has been by this technique[7].

Recently, we found that low-energy Ar ions during growth of Ge on Ge (001) have a remarkable smoothening effect[8]. This effect is most apparent when surfaces are "extremely" rough, i.e., characterized by spotty, transmission-like RHEED patterns. Such rough surfaces smoothen, during simultaneous ion bombardment and growth, nearly an order of magnitude faster than during growth alone, and are now a routine step in our initial sample preparation sequence.

Although there have been these demonstrations of ion beam-enhanced growth effects, there is little understanding of the effect of the beam on the surface during growth. To understand the mechanism by which ion beams assist surface smoothening during growth, we have systematically measured the effects of ion beams on growth morphology at 300, 400 and 500 C. Whereas previous measurements of ion beam effects have involved post mortem (ex-situ) techniques, the measurements described here were conducted in situ in real-time.

EXPERIMENT

The measurements were performed in an ultra-high vacuum growth chamber of our own design. Base pressure is typically 3×10^{-10} torr rising to 4×10^{-9} torr during deposition. The Ge deposition source is a resistively heated effusion cell with which we achieve growth rates up to 0.10 Å/s. The deposition rate used in these experiments was 0.045 Å/s. The substrates were prepared by sequential pad polishes in Br:methanol and methanol.

The ion source is a PHI sputter gun with a tungsten filament and independent acceleration and focusing electronics. The accessible energy range is 100 eV to 1000 eV; all the measurements described here were made at 500 eV. Typically, the chamber is backfilled with an Ar pressure of 5×10^{-6} torr, resulting in a beam current on the sample of 290 nA.

The technique used for measuring the surface morphology is RHEED. For the measurements described here, a 15 keV electron beam strikes the sample at glancing angle and the diffracted electrons form a pattern on a phosphor screen. The diffraction pattern is acquired by a video camera, then digitized by a frame-grabber and stored on a computer. On-line analysis allows the lineshape, peak width and peak height to be displayed as they are acquired with a data rate of approximately two points per second. The diffraction

condition used is known as the out-of-phase condition [9] where electrons scattered from surfaces separated by one atomic step interfere destructively. This condition gives us the greatest sensitivity to surface roughness; maximum intensity corresponds to a smooth surface while decreasing intensity corresponds to progressively rougher surfaces.

After insertion into the vacuum, the sample is annealed at 700 C for 20 minutes; then a 1000 Å buffer layer is grown at 500 C and the process is repeated. The sample is annealed at 500 C overnight after which the entire growth sequence is repeated. The resulting RHEED pattern is characteristic of a smooth surface, exhibiting a sharp specular beam even in the so-called "out-of-phase" condition which is most sensitive to steps on the surface. After each experiment, a smooth surface can be regenerated from a rough one by a 10 minute anneal at 700 C followed by deposition of 20 Angstroms at 500 C. This treatment was sufficient to restore the surface for all the measurements discussed here. The sample misorientation is typically 0.5 deg as specified by the manufacturer, which is consistent with the observed splitting of the diffracted RHEED beam [10].

RESULTS

RHEED measurements of a Ge (001) surface during ion bombardment and subsequent growth during ion bombardment are shown in figure 1. The measurements were made at 300 C and 500 C. These temperatures were chosen to be above and below the intrinsic growth roughening temperature (375 C)[11]. At 300 C, growth alone roughens the surface; at 500 C growth alone leaves the surface morphology unchanged. The starting surfaces for each measurement were identical according to RHEED. Initially, the ion beam (500 eV Ar, 290 nA) alone was turned on, as indicated in the figures; in both cases the surface gets rougher. After the surface has roughened in each case by approximately the same amount, i.e., the RHEED intensity has decreased by approximately 20%, the Ge source shutter is opened and growth occurs at a rate of 0.045 Å/sec. For both samples, there is an initial improvement in the surface. For the sample at 300 C, the surface subsequently roughens to a steady state value indicating a surface much rougher than the initial surface. For the sample at 500 C, there is a significant improvement in the surface so that the beam stimulated growth surface becomes even smoother than the starting surface.

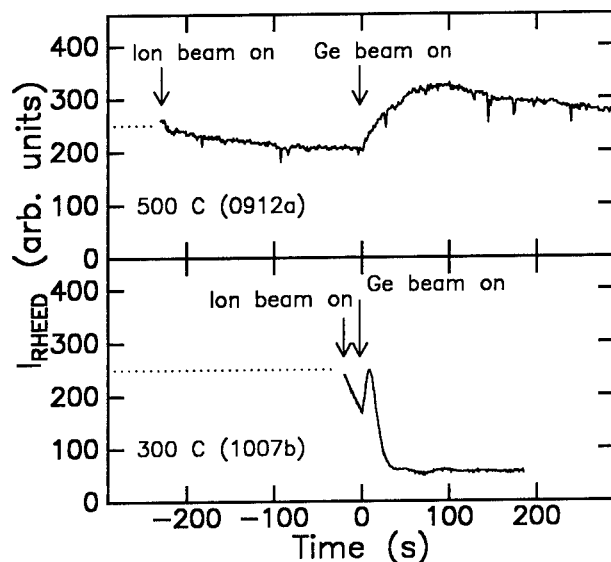


Fig. 1 RHEED intensity during ion beam roughening followed by simultaneous ion bombardment and growth at 500 C and 300 C. The 500 eV Ar is turned on and growth is started as shown in the figure.

A comparison of the improvement of ion beam roughened surfaces at 400 C is shown in figure 2 for simultaneous growth with ion bombardment and growth alone. In both cases there is an initial improvement in the surface. However, in the case of simultaneous ion bombardment and growth, the improvement in the surface persists while for the case of growth alone the improvement decays quickly away. When the growing surface is simultaneously ion bombarded, one achieves a steady state morphology which is much smoother than that for growth alone.

A comparison between roughening achieved by ion beam bombardment and by deposition at 300 C is shown in figure 3. At the times indicated on the figure, the surface is either ion beam roughened or growth roughened. With an ion beam current of approximately 290 nA and a deposition rate of approximately 0.045 Å/sec, the arrival rate of adatoms relative to ions is roughly 8:1. After both surfaces have roughened appreciably, simultaneous ion bombardment and growth is started. In the case of the ion beam roughened surface, the result is similar to that in figure 1; the surface initially smoothenes and then roughens to a steady state value. In the case of the growth roughened surface, turning on the ion beam has no effect on the growth roughening at this low temperature and beam current.

DISCUSSION

Our understanding of surface morphology during MBE is one of a balance between competitive processes on the surface. Processes which roughen the surface include adatom arrival, cluster nucleation and sputtering of atoms from the surface. The roughening processes are balanced by other processes which smoothen the surface, such as migration of adatoms to terrace ledges, the annihilation of adatoms and surface vacancies, and cluster breakup and coalescence. The overall surface morphology can be changed by altering the balance between these processes so that surfaces which may roughen under one set of growth conditions may grow smoothly under a different set of conditions.

The roughening which occurs from ion beam bombardment is expected to be due to the generation of surface defects. Because of the possibility of sputtering surface atoms as well as creating vacancy-interstitial pairs, we expect that the ion roughened surface has a surplus of vacancies over adatoms. In contrast, the roughening which occurs from growth presumably has its origins in the surplus of adatoms and their subsequent clustering. Both of these sources of roughness (adatoms and surface vacancies) should have the same effect of decreasing the RHEED intensity.

As shown in figure 1, the rate of ion-beam roughening decreases at higher temperatures, in a manner qualitatively similar to that of the intrinsic growth roughening[11]. In both cases, we believe the effect can be explained by a change in the balance between smoothening and roughening. At higher temperature, the increase in diffusivity enhances the motion of adatoms and surface vacancies to terrace ledges and other sinks of roughness (e.g. annihilation of adatoms and vacancies).

After ion beam roughening, we expect there to be a surplus of vacancy-like defects on the surface. Initiation of Ge deposition introduces a flux of adatoms onto this surface. We attribute the initial increase in the RHEED intensity to the newly deposited adatoms annihilating with the surface vacancy-like defects and reducing the net surface roughness. This phenomenon is observed at both 300 C, 400 C and 500 C (figures 1 and 2). However, we expect the subsequent evolution of the surface should have a limiting behavior similar to that for intrinsic growth without ions. Indeed, our previous measurements indicate that at 300 C, growth alone will roughen a smooth surface, so the final surface is rough. At 400 C and 500 C, growth alone will not roughen a smooth surface, so the final surface is relatively smooth[11].

A notable feature of Fig. 1 is that the ion-assisted growth at 500 C produces a surface smoother than the initially prepared surface. We are forced to conclude that our standard surface preparation technique is not perfect, and that it leaves surface defects, e.g., metastable clusters. We speculate that ion damage destabilizes such clusters, after which they dissolve into adatoms which migrate to terrace ledges. This smoothening effect of the ion beam is masked by other beam-induced surface damage during ion beam roughening. During simultaneous ion bombardment and growth, the flux of adatoms annihilate with the beam-induced damage but do not form new clusters at 500 C. The resulting surface is thus initially made smoother than the starting surface because of the ion beam assisted breakup of metastable clusters.

This model for surface morphology implies that growth by itself should smoothen an ion-beam roughened surface, and the results shown in figure 2 show this to be true initially. However, the final surface formed by growth alone (after the initial improvement) is

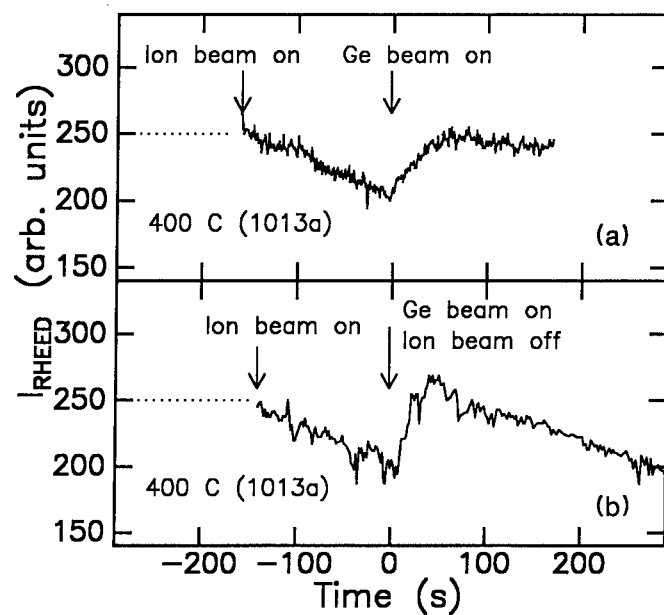


Fig. 2 Comparison of smoothing of ion beam roughened surface by simultaneous ion bombardment and growth with growth alone. Sample temperature is 400 C.

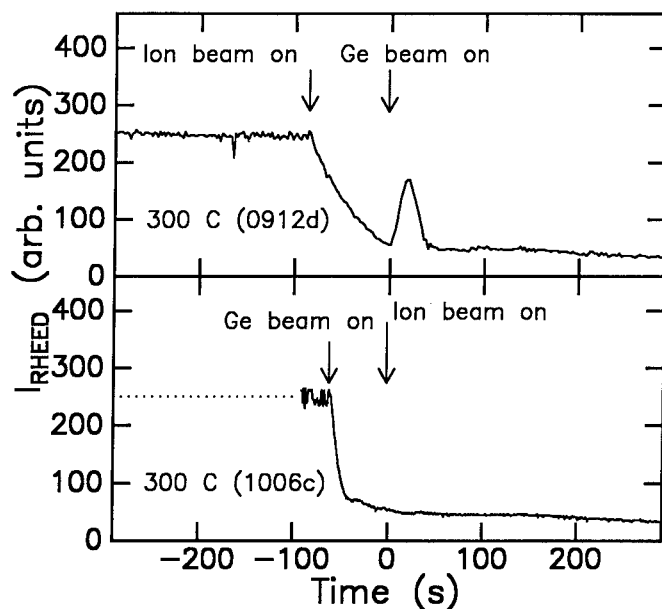


Fig. 3 Comparison of effect of simultaneous ion bombardment and growth on ion beam roughened surface and growth roughened surface at 300 C.

not as smooth as when growth is done in conjunction with ion beam bombardment. A possible explanation is that simultaneous ion beam bombardment during growth does assist in the breakup of clusters and therefore reduces the steady state density of clusters. We have observed that on a surface that was first ion beam roughened and then grown on without the ion beam (as in figure 2b), turning on the ion beam during subsequent growth makes the surface smoother than growth alone. Although the surface does not become as smooth as the original starting surface, it clearly improves. The fact that the surface is rougher by growth alone after ion roughening may indicate that the ion beam has created some other form of surface damage since growth alone does not normally roughen a smooth surface at 400 C. The smoothening effect of the ion beam may be to assist in the removal of this damage during simultaneous growth and bombardment.

The inability of simultaneous growth and ion beam bombardment to improve the growth roughened surface at lower temperatures (figure 3) is also consistent with this interpretation. The roughness caused by growth at 300 C consists of strong adatom clustering which is not annihilated by more growth, with or without ion bombardment. In contrast, the ion beam-induced-roughness consists primarily of vacancy-like defects which can be annihilated by the sudden onset of a flux of adatoms at the start of growth, thereby temporarily smoothening the surface.

CONCLUSION

We have examined the effect of ion beam bombardment on the evolution of surface morphology during MBE growth of Ge (001) in situ and in real time. Simultaneous ion beam bombardment and growth can create a smoother surface than that produced by growth alone at 500 C. Growth alone will temporarily smoothen an ion beam roughened surface, but the steady state surface is degraded to rougher values whereas simultaneous growth and ion bombardment maintains a smoother surface. At 300 C, where both ion beam roughening and intrinsic growth roughening of surfaces is appreciable, simultaneous growth and ion beam bombardment will temporarily smoothen an ion beam roughened surface but the final surface morphology is rough.

We would like to acknowledge the assistance of Dan Buller. This work was performed at Sandia National Laboratories supported by the U.S. Department of Energy under contract DE-ACO4-76DP00789.

REFERENCES

1. J.E. Greene, A. Rockett and J.-E. Sundgren, in *Photon, Beam and Plasma Stimulated Chemical Processes at Surfaces*, edited by V.M. Donnelly, I.P. Herman and M. Hirose (Mater. Res. Soc. Proc. 75, Pittsburgh, PA 1987) pp. 39 - 53.
2. S.B. Ogale, A. Madukhar and M. Thomsen, *Appl. Phys. Lett.* **51** 11 (1987).
3. W.R. Burger and R. Reif, *J. Appl. Phys.* **62**,4255 (1987).
4. T. Ohmi, T. Ichikawa, T. Shibata, K. Matsudo and H. Iwabachi, *Appl. Phys. Lett.* **53** 1 (1988).
5. B.R. Appleton, S.J. Pennycook, R.A. Zuhr, N. Herbots and T.S. Noggle, *Nucl. Instr. and Meth.* **B19/20** 975 (1987).
6. P.C. Zalm and L.J. Beckers, *Appl. Phys. Lett.* **41** 167 (1982).
7. J.P. Biersack and L.G. Haggmark, *Nucl. Instr. and Meth.* **174-257** (1980).
8. E.Chason, K.M. Horn, J. Y. Tsao and S.T. Picraux, manuscript in preparation.
9. J.M. van Hove, P.R. Pukite and P.I. Cohen, *J. Vac. Sci. Tech.* **B3** 563 (1985).
10. P.I. Cohen, P.R. Pukite, J.M. van Hove and C.S. Lent, *J. Vac. Sci. Tech.* **A4** 1251 (1986).
11. E. Chason, J.Y. Tsao, K.M. Horn and S.T. Picraux, *J. Vac. Sci. Tech. B*, submitted.

EFFECTS OF SPUTTERED PARTICLE ENERGY ON THE PROPERTIES OF SiO₂ FILMS

YASUNORI TAGA AND TAKESHI OHWAKI

Toyota Central Research and Development Laboratories, Inc.,
Nagakute-cho, Aichi-gun, Aichi-ken 480-11, Japan

ABSTRACT

The secondary ion energy distributions (SIED) emitted from Si under various conditions of targets (Si, SiO₂) and primary ions (Ar⁺, O⁺) were measured and the thin SiO₂ films were deposited by magnetron sputtering techniques under the corresponding conditions to the SIED experiments. The most probable energies of silicon oxygen cluster ions of Si_mO_n⁺ (m, n=1, 2,...) are equal to those of Al⁺ thermal ions, while those of Si_l⁺ (l=1, 2,...) remain unchanged with the introduction of oxygen in chamber during Ar⁺ ion bombardment. The current-voltage plots of SiO₂ films are also measured and found to be influenced by the deposition conditions.

It is concluded that the differences in current-voltage characteristics of SiO₂ films prepared under various sputtering conditions can be reasonably explained in terms of the changes in the most probable energy of the sputtered particles.

INTRODUCTION

In recent years, significant improvements in thin film quality control have been achieved by sputter deposition or ion-assisted technology [1]-[5]. The key feature of these sophisticated techniques is the use of the ions to sputter deposit material and to add activation energy or chemical activity to the growing film, or combinations of these effects. The ions may be used in a plasma region or high vacuum region (ion beam techniques).

The influence of the kinetic energy of sputtered ions on thin film formation ranges from simple substrate cleaning for enhanced adhesion to morphological changes and the simulation of epitaxial growth [6]. Most work has been concerned with studying the changes in film stress, crystal structure, and composition [7],[8]. These peculiar features of sputtering technology for thin film deposition is generally explained in terms of the energy of sputtered particles.

We have reported the results of the measurements of energy distribution of secondary ions from Si under O₂ and N₂ ion bombardment [4],[9],[10]. A complete understanding of secondary ion emission requires measurements of secondary ion yields as well as their energy distributions. Measurements of secondary ions energy distribution seem to be a particularly suitable technique for characterizing sputtering mechanism. The bombarding energy of the primary ions produced in a plasma region or high vacuum region is usually of the order of KeV or less. Therefore, the values of the most probable energy (E_m) of the SIED may be the most dominant parameter for the characterization of the ejection process by sputtering.

In this paper, we describe the effects of sputtered particle energy on the various properties of SiO₂ films.

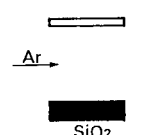
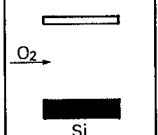
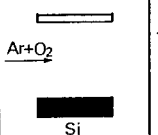
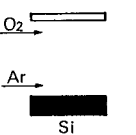
EXPERIMENTAL PROCEDURE

Measurements of the energy distribution of sputtered ions were performed with a UHV-SIMS (Ultra high vacuum - Secondary ion mass spectrometry) apparatus. Details were described previously [4],[11],[12]. The energy and the mass of the secondary ions were analyzed with an electrostatic ion energy analyzer (IEA) and a quadrupole mass analyzer, respectively. The absolute energy of the IEA was about 2.0 eV. The absolute energy of the IEA was calibrated by Al^+ thermal ions. The sample in SIMS study was a mirror-polished B-doped Si(111) with a resistivity of 1-2 Ωcm , which was also used as a substrate for thin film deposition. The sample was cleaned by Ar ion sputtering after being introduced into the chamber.

Radio frequency (RF) magnetron sputtering technique was used for deposition of SiO_x thin films [13]. Hot-pressed SiO_2 and polycrystalline Si targets of 99.9 % purity were bonded to a water-cooled copper backing plate. After evacuation to 1×10^{-6} Torr, sputtering gas was introduced to 5×10^{-3} Torr. SiO_2 films 50 nm thick were thus deposited at the target-to-substrate distance of 150 mm.

Arrangements in deposition chamber for thin film preparation were schematically shown in Table 1. Modes 1, 2 and 3 were normal methods but in Mode 4, the experimental arrangement used was specially designed to isolate the target from oxygen gas, maintaining it in an inert gas atmosphere while introducing an oxygen at the substrate. As a result, experimental apparatus allowing reactive sputter deposition, in which the chemical reaction occurs at the deposition surface, has been developed.

Table 1 Schematic representation of thin film preparation Modes under various conditions.

Mode 1 $\text{Ar}^+ \rightarrow \text{SiO}_2$	Mode 2 $\text{O}^+ \rightarrow \text{Si}$	Mode 3 $\text{Ar}^+ + \text{O}^+ \rightarrow \text{Si}$	Mode 4 $\text{Ar}^+ \rightarrow \text{Si} + \text{O}_2 \text{ gas}$
			

Characterization and evaluation of the film properties thus prepared were carried out in the following manner: Refractive index was measured using ellipsometer used with a He-Ne laser at 633 nm spectrophotometer. Density of the film was determined by the ratio of mass thickness to geometrical thickness; where mass of the films was determined by weighing films deposited on thin glass substrate using a microbalance accurate to 0.1 μg and geometrical thickness by a surface profilometer (Dektak 2A). Stoichiometry of the films thus prepared was also evaluated by Auger electron spectroscopy (AES) and Infrared spectroscopic analysis (IR). A high yield of stable thin film capacitors with high breakdown fields requires continuous, mechanically stable and homogeneous films and suitable electrodes. The current density J (A/cm^2) - the electric field E (MV/cm) characteristics of RF sputtered or RF reactively sputtered SiO_x films on Si substrate were measured with Al electrodes (1000 \AA). The size of electrodes was 0.5 mm in diameter. The J - E plots were all measured at room temperature after annealing the samples in 400°C for 30 min in N_2 atmosphere.

RESULTS AND DISCUSSION

Good agreement in molecular ion intensity is found between our results and Benninghoven's [14]. Similar SIMS spectra were obtained from the following cases of $\text{Ar}^+ \rightarrow \text{SiO}_2$, $\text{O}^+ \rightarrow \text{Si}$, and $\text{Ar} \rightarrow \text{Si}+\text{O}_2$ (gas), in which peaks corresponding to Si^+ , SiO^+ , Si_2^+ , Si_2O^+ , SiO_2^+ and Si_2O_3^+ are included.

Fig. 1 shows the secondary ion energy distribution of Si^+ , SiO^+ , Si_2O^+ and Al^+ thermal ions under oxygen exposure at 4×10^{-7} Torr. Table 2 denotes the most probable energy (E_m) and the average energy (E_a) of secondary ions under different conditions of primary ions (Ar^+ , O^+) and targets (Si , SiO_2). The values of E_m in the case of $\text{O}^+ \rightarrow \text{Si}$ were similar to that of $\text{Ar}^+ \rightarrow \text{SiO}_2$, while those of $\text{Ar}^+ \rightarrow \text{Si}+\text{O}_2$ (gas) do not resemble the above cases, that is, the E_m of Si_mO_n^+ ($m, n=1, 2, \dots$) is almost equal to that of Al^+ thermal ions. It is thought that the formation mechanisms of Si_mO_n^+ in the case of $\text{Ar}^+ \rightarrow \text{Si}+\text{O}_2$ (gas) is different from those of $\text{Ar}^+ \rightarrow \text{SiO}_2$ and $\text{O}^+ \rightarrow \text{Si}$. Thompson [15] reported that the values of E_m are directly associated with surface binding energy

(E_b). The above results indicate the E_b of Si_mO_n^+ is almost equal to that of Al^+ thermal ions. It is thought that these molecular ions are created at the surface really as a result of the interaction between the secondary particles and adsorbed atoms. Molecular ion formation mechanism mentioned above can be interestingly compared to those of chemical sputtering [16], [17].

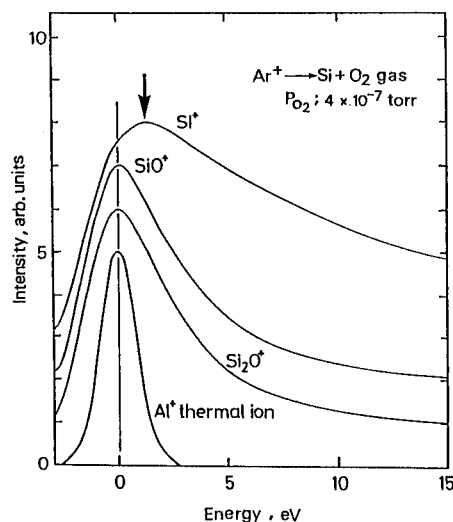


Fig.1 Secondary ion energy distributions of Si^+ , SiO^+ and Si_2O^+ from Si under Ar ion bombardment during O_2 exposure to 4×10^{-7} torr.

Table 2 The most probable energy E_m and the average energy E_a of secondary ions under various conditions. E_a values are shown in parenthesis. * indicates the E_m value equal to Al^+ thermal ions.

	Si^+	Si_2^+	SiO^+	Si_2^+	Si_2O^+	Si_2O_2^+
$\text{Ar}^+ \rightarrow \text{Si}$	1.1(11.0)	0.6(5.2)	—	0.7(7.0)	—	—
$\text{O}^+ \rightarrow \text{Si}$	4.9(16.1)	—	4.2(7.3)	4.6(10.9)	3.0(5.0)	3.3(4.5)
$\text{Ar}^+ \rightarrow \text{SiO}_2$	4.2(17.7)	2.0(10.7)	2.8(8.8)	3.2(12.9)	1.9(5.2)	1.6(3.9)
$\text{Ar}^+ \rightarrow \text{Si}+\text{O}_2$	1.1(14.2)	0.6(7.4)	* (2.4)	0.4(6.3)	* (1.8)	* (1.0)

Almost the same results of the values of E_a were obtained between the cases of $O^+ \rightarrow Si$ and $Ar^+ \rightarrow SiO_2$. However, in the case of $Ar \rightarrow Si+O_2$ (gas), the E_a values are quite different from the above two cases, especially for higher mass molecular ions such as Si_2O^+ and $Si_2O_2^+$.

Sroubek [18] did SIMS experiments in Ni covered with adsorbed atoms and reported that the most probable energy of sputtered adatom ions is relatively low compared with that of bulk atoms. In the present study, the E_m values of $Si_mO_n^+$ as a result of chemical interaction between Si target and O_2 gas molecules were quantitatively determined to be equal to those of Al^+ thermal ions. Therefore, the data by Sroubek agreed qualitatively with the present results. However, a fundamental difference in the physical and chemical meaning is found if the values of E_m are almost equal to those of Al^+ thermal ions or if they shift to lower energies. It can be understood that if the value of E_m is equal to that of Al^+ thermal ions it represents the reaction of Si and O_2 occurring at the surface, but that if the values of E_m shift to lower energy it shows the reaction occurs in the shallow region beneath the surface.

Stuart and Wehner [19] reported that the energy distributions of sputtered atoms are very similar to those of sputtered ions, although the average ejection energies seem to be higher for ions. On the other hand, in practical sputter deposition, most of the sputtered particles are neutral and very small quantities of charged particles are included [20]. Therefore, the difference of E_m and E_a between Si^+ and $Si_mO_n^+$ may play an important role in thin film growth, resulting different properties of SiO_2 films.

Results of characterization and properties of SiO_x films were summarized in Table 3. Quantitative AES analysis [21] shows the non-stoichiometry of the film prepared by Mode 3, that is, the composition of the film was estimated to be $SiO_{1.8}$, although no differences in stoichiometry can be seen among the films by Modes 1, 2 and 4. These results can be explained in terms of insufficient surface oxidation of Si during sputtering in Mode 3. Differences in film density among Modes 1-4 can be reasonably explained by the difference of E_a of sputtered ions shown in Table 1. Modes 1 and 2 may correspond to the situations of the energy distribution experiments of $Ar^+ \rightarrow SiO_2$ and $O^+ \rightarrow Si$, respectively. The values of E_a of the above two cases are high and the corresponding film densities are also high. On the contrary, the low film density prepared by Mode 4 which corresponds to the case of $Ar^+ \rightarrow Si+O_2$ (gas) may be also due to the low value of E_a as shown in Table 1. Consequently, the film density prepared by different preparation mode changes in accordance with the average energy of sputtered particles.

Refractive indexes were almost constant irrespective of the Modes of the film preparation.

Table 3 Characterization and properties of SiO_x films prepared by Mode 1-Mode 4.

	Mode 1	Mode 2	Mode 3	Mode 4
growth rate($\text{\AA}/\text{min}$)	96	22	204	63
density (g/cm^3)	2.00	2.14	1.71	1.90
refractive index	1.43	1.42	1.47	1.43
stoichiometry(AES)	SiO_2	SiO_2	$SiO_{1.8}$	SiO_2
stoichiometry(IR)	SiO_2	SiO_2	SiO_2	SiO_2
$E_b(\text{MV}/\text{cm})$	4.12	9.9	1.32	9.26

It is interesting to note the results of the measurement of breakdown voltage of the film thus prepared in Modes 1-4. The breakdown voltages E_b of the film by Modes 2 and 4 are high and those of Modes 1 and 3 are rather low. In order to elucidate the differences in E_b between the films by Mode 2 and Mode 4, the results of J-E measurements [22],[23] were depicted in Fig. 2, where J-E curve of thermally grown SiO_2 film is shown for comparison. In

the figure, the E_b values of each sample are shown by arrows. Similar E_b values are obtained for Mode 2 and Mode 4, but the changes in J with E are quite different, that is, in the film by Mode 2 begin to increase at $E = 2.5$ MeV/cm, while J in the film by Mode 4 remain unchanged to $E = 5.5$ MeV/cm, then begin to increase gradually. The J-E characteristic of the film of Mode 4 is likely to that of thermally grown SiO_2 films. It can be

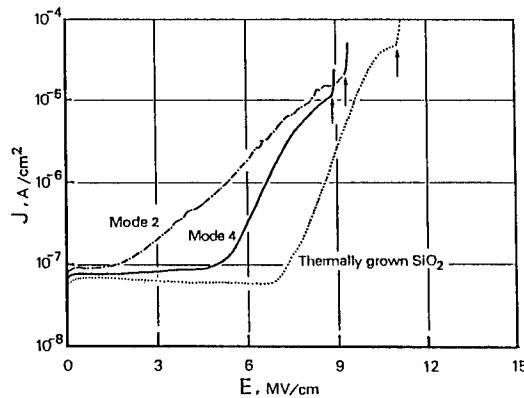


Fig.2 J-E characteristics of Al/SiO₂/Si system for Mode 2 and Mode 4.

explained that the current-transport mechanism in the present cases such as high field and low temperature may be caused as a result of field ionization of trapped electrons into conduction band, which is usually referred to as the Poole-Frenkel effect [22]. Trapped electrons in SiO_2 films prepared by Mode 2 may be induced by high energy bombardment of sputtered particles as indicated in Table 2. On the contrary, the E_a values of sputtered particles in Mode 4 are low in comparison with Mode 2 and the corresponding trapped electrons in SiO_2 films thus prepared will be diminished, resulting in the same J-E characteristic of thermally grown SiO_2 films (in this case, no defect or vacancy was introduced). In conclusion, the differences in J-E plots between the films by Modes 2 and 4 can be reasonably explained in terms of the differences in E_m or E_a of sputtered particles.

It is also of practical interest to note the results of growth rate of SiO_2 films in different thin film preparation Mode. Although the E_b values of the films by Mode 2 and Mode 4 are almost the same, but the growth rate of the film of Mode 4 is three times faster than that of Mode 2. So, the high quality of electrical breakdown properties of SiO_2 film by sputtering technique can be successfully achieved at high growth rate by Mode 4 ($\text{Ar}^+ + \text{Si} + \text{O}_2$ (gas)).

CONCLUSION

The most probable energies of the secondary ion energy distributions of Si_mO_n^+ ($m, n=1, 2, \dots$) are equal to those of Al^+ thermal ions, while those of Si_l^+ ($l=1, 2, \dots$) remain unchanged with the introduction of oxygen in chamber during Ar^+

ion bombardment. The current-voltage plots of SiO_2 films are also measured and found to be influenced by the deposition conditions.

It is concluded that the differences in current-voltage characteristics of SiO_2 films prepared under various sputtering conditions can be reasonably explained in terms of the changes in the most probable energy of the sputtered particles.

REFERENCES

1. P. Sigmund, Phys. Rev. 184, 383 (1969).
2. R. Kelly, Nucl. Instr. and Meth. B18, 398 (1987).
3. M. A. Rudat and G. H. Morrison, Surf. Sci. 82, 549 (1979).
4. T. Ohwaki and Y. Taga, Jap. J. Appl. Phys. 23, 1466 (1984).
5. P. J. Martin, J. Mater. Sci. 21, 1 (1986).
6. C. Weissmantel, K. Bewilogua, D. Dietrich, H. J. Erler, H. J. Hinneberg, S. Klose, W. Nowick, and G. Reisse, Thin Solid Films 72, 19 (1980).
7. T. Takagi, Thin Solid Films 92, 1 (1982).
8. J. J. Cuomo, J. M. E. Harper, C. R. Wu, and R. H. Hammond, J. Vac. Sci. Technol. 20, 349 (1982).
9. T. Ohwaki and Y. Taga, Surf. Sci. 157, L308 (1985).
10. T. Ohwaki and Y. Taga, Nucl. Instr. and Meth. B33, 523 (1988).
11. Y. Taga, in Secondary Ion Mass Spectrometry SIMS V, ed. by A. Benninghoven, R. J. Colton, D. S. Simons, and H. W. Werner (Springer, New York, 1985), p.32.
12. H. Liebl, J. Vac. Sci. Technol. 12, 385 (1975).
13. Y. Sawada and Y. Taga, Thin Solid Films 110, L129 (1983).
14. A. Benninghoven, Surf. Sci. 53, 596 (1975).
15. M. W. Thompson, Philos. Mag. 18, 377 (1968).
16. J. Roth, T. Appl. Phys. 52, 91 (1983).
17. M. Saidoh, H. Gnaser, and W. O. Hofer, Appl. Phys. A40, 197 (1986).
18. Z. Sroubek, Surf. Sci. 44, 47 (1974).
19. R. V. Stuart and G. K. Wehner, J. Appl. Phys. 35, 1819 (1964).
20. Y. Taga, K. Inoue and K. Satta, Surf. Sci. 119, L363 (1982).
21. Y. Taga, A. Isogai and K. Nakajima, Surf. Sci. 86, 591 (1979).
22. S. M. Sze, J. Appl. Phys. 38, 2951 (1967).
23. S. Oh and Y. T. Yeow, Solid-State Electronics 31, 1113 (1988).

METAL SILICIDES FORMED BY DIRECT ION BEAM DEPOSITION*

R. A. ZUHR, S. J. PENNYCOOK, T. E. HAYNES, AND O. W. HOLLAND, Solid State Division, Oak Ridge National Laboratory, Oak Ridge, TN 37831

ABSTRACT

Thin films of transition metal silicides have been produced at low temperatures on Si substrates by direct ion beam deposition (IBD) of the metal ion. Using a mass-analyzed beam of metallic ions rastered over the target at energies on the order of 100 eV and at substrate temperatures near 500°C, stoichiometric silicide films of varying thicknesses up to 300 nm have been formed on both n- and p-type Si. The advantages of this technique over other methods for silicide formation include good control of thickness by current integration, high purity due to the mass analysis, and control of incident ion energy which permits formation of the disilicide phase at low temperatures, thereby minimizing the thermal budget and the associated dopant diffusion in the underlying substrate. Films were characterized by Rutherford backscattering, transmission electron microscopy, and electrical measurements. Co, Fe, Ni, Ti, and W silicides have been formed by this direct deposition process. The effectiveness of the technique has been found to be dependent upon the diffusion characteristics of the particular metal/Si couple involved, with systems in which Si is the dominant diffuser, such as Ti/Si, giving the best results. Stoichiometric TiSi₂ films produced at 550°C by this process show low bulk-like resistivity (15 $\mu\Omega\text{-cm}$) without subsequent high-temperature annealing. All of these characteristics make silicide formation by IBD attractive for integrated circuit fabrication and shallow junction technology.

I. INTRODUCTION

Metal silicides are important as conducting layers or interconnects in the formation of integrated circuits in silicon because of their low resistivity, resistance to electromigration, and thermal stability. Specifically, they have been used to lower the sheet resistance of active areas and gate electrodes in complementary metal-oxide-semiconductor (CMOS) transistors.^{1,2} Physical vapor deposition by either co-sputtering using separate metal and Si targets, or sputtering from a single silicide target, has been used to form stoichiometric silicide films. Silicide films have also been deposited by chemical vapor deposition. Another technique consists of depositing a thin film of the pure metal on a Si substrate and thermally reacting the metal/Si couple. While each of these techniques has its own advantages and disadvantages, they share two common drawbacks. First, the film purity is only as good as the starting material. Any impurities in the sputter-targets or gases will be incorporated directly into the films resulting in a higher intrinsic resistivity. Secondly, as-deposited films must be annealed at high temperatures to lower their resistivity, which is usually much higher than the bulk value. For example, temperatures in excess of 800°C are needed to reduce the resistivity of TiSi₂ films to their lowest value.³ Significant dopant diffusion and therefore degradation and alteration of device performance can occur as a result of such high-temperature cycling.

*Research sponsored by the Division of Materials Sciences, U. S. Department of Energy under contract no. DE-AC05-84OR21400 with Martin Marietta Energy Systems, Inc.

Not only is dopant diffusion in the silicon substrate a problem at these temperatures, but the loss of volatile dopants, such as As, through the silicide film and the lateral diffusion of dopants within the film are also major concerns.^{4,5}

In this work we describe a new technique for producing transition metal silicides that can lead to low resistivity films on Si at temperatures lower than those required by other methods, thereby minimizing many of the problems surveyed above. In particular, by employing the technique of mass-analyzed low-energy ion beam deposition (IBD), stoichiometric thin films of TiSi_2 exhibiting low bulk-like resistivities have been produced at temperatures as low as 550°C.

II. EXPERIMENTAL PROCEDURE

The silicide films made in this study were produced by the direct deposition of low-energy (40–200 eV) metal ions onto cleaned Si substrates.⁶ The metal ion beam is produced at the minimum extraction energy of 35 keV in a commercial ion implantation accelerator (Extrion 200-1000) using a modified Freeman ion source. This 35-keV beam is then magnetically mass analyzed and passed through three stages of liquid-nitrogen trapped differential pumping and a seven degree neutral trap. It then enters the deposition chamber where it is decelerated in a four-element deceleration lens system to the desired final energy. Base pressure in the deposition chamber is in the 1×10^{-10} T range and typically rises to the low 10^{-9} T range during deposition on a heated sample. Energies from 20 to 1000 eV at current densities of 1 to 10 $\mu\text{A}/\text{cm}^2$ are achievable for most elements. The samples are held in a 14 mm diameter Mo holder containing a resistance heater capable of heating the sample surface to 900°C. A Faraday cup is included for positioning and laterally profiling the beam. Surface temperature during deposition was monitored with a calibrated infrared pyrometer. All substrates for the deposition were electronic grade n- or p-type Si doped, respectively, with P or B to resistivities of 5 to 10 $\Omega\text{-cm}$. A few depositions were carried out on heavily doped Si with resistivities of .002 to .005 $\Omega\text{-cm}$. No differences were observed during silicidation of these samples. The samples were cleaned in ethanol, distilled water, and dilute HF prior to mounting in the chamber. In most cases the samples were cleaned *in situ* immediately before deposition by a low-energy beam of Cl ions at a dose of $1 \times 10^{17}/\text{cm}^2$ with the sample at ~550°C. This cleaning procedure is analogous to reactive ion etching and has previously been shown to produce surfaces that foster good epitaxial growth on Si.⁷

After deposition the films were analyzed by Rutherford backscattering (RBS) and ion channeling with 2-MeV He at a scattering angle of 160° to measure film stoichiometry, thickness, and degree of epitaxy. Further information on the microstructure of the films was obtained by transmission electron microscopy (TEM) of cross-sectionally thinned specimens. The electron microscopy was performed with a Philips EM400T transmission electron microscope operating at 100 keV. Sheet resistance measurements were made with a standard four-point probe, and were converted to electrical resistivities using the film thicknesses determined from RBS.

III. RESULTS AND DISCUSSION

Metal silicide films have been formed by IBD of Co, Fe, Ni, Ti, and W onto single-crystal Si substrates at various temperatures and ion energies. These silicide

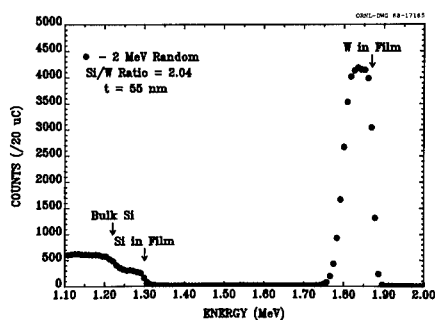


Fig. 1. Random 2 MeV ion scattering spectrum of a 55-nm thick WSi_2 film formed on Si(100) at 500°C and 200 eV by IBD.

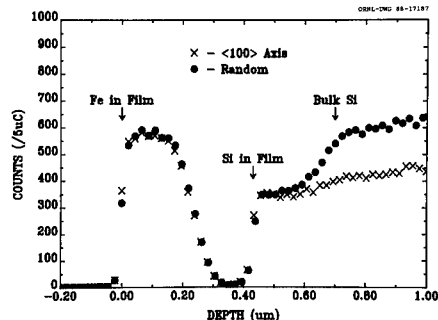


Fig. 2. Channelled (x) and random (•) 2 MeV ion scattering spectra for a 200-nm thick FeSi_2 film formed on Si(100) at 40 eV and 500°C by IBD. No channeling is observed in the spectra.

films can be separated into two categories: those in which the metal is the dominant diffusing atom (Co and Ni) and those in which Si is more mobile (Fe, Ti, and W). The character of the growth process by the IBD technique is expected to be different for these two different cases. Since the range of the metal ions in silicides is less than 2 nm for all the energy/ion combinations reported, movement of the reactants to the active growth site must be by diffusion. This diffusion may be enhanced by the incident ion beam irradiation, however. In the case of the metallic diffusers (Co, Ni) this means that the predominant effect will be the diffusion of metal atoms from the surface region to the bulk Si-silicide interface where the reaction can be driven only by thermal means. For systems in which Si is the dominant diffuser, Si must diffuse from the substrate through the growing silicide film to the near-surface region where it can react with the incident, energetic metal ions. In this case, the energy of the incident ions can be utilized to activate the chemical reaction and promote the growth of high-temperature phases at unusually low temperatures. It is clear then that both thermal and athermal processes should contribute to the formation of these films. The results achieved for the growth of silicides by IBD in each of these two classes will now be examined.

An example of a silicide layer grown by IBD for a system in which Si is the more mobile species, W on Si, is shown in the 2-MeV He ion backscattering spectrum of Fig. 1. This 55-nm thick polycrystalline silicide film was grown at 500°C with an incident ion energy of 200 eV. The uniform height of the scattering from both the W and the Si in the film indicates a constant ratio of Si to W throughout the depth of the overlayer, while the relative heights of the two regions indicate that that ratio is 2 to 1. Thus a uniform stoichiometric 55-nm thick film of WSi_2 has been grown on this Si(100) substrate at 500°C. Because of the large lattice mismatch for this film, no epitaxy was expected or observed in the ion channeling.

Another system for which Si is the dominant diffuser is Fe on Si. Random and aligned backscattering spectra from a 200-nm thick film of FeSi_2 are shown in Fig. 2. This film was grown with a 40-eV Fe ion beam at a substrate temperature of 550°C on Si(100). The yields due to scattering from the Fe and Si in the compound film are again flat, indicating uniform stoichiometry throughout the depth of the film. The ratio of Si to Fe is 2, indicating formation of the disilicide, FeSi_2 . The measured resistivity of this film was $\sim 850 \mu\Omega\text{-cm}$, comparable to the lowest resistivities reported for thin films sintered at temperatures greater than 700°C. The aligned



Fig. 3. Cross-section TEM micrograph of a low-resistivity TiSi_2 film formed on $\text{Si}(100)$ at 100 eV and 550°C by IBD and illustrating the large grain size, sharp interface with the bulk, and lack of inclusions that are typical of TiSi_2 films formed by this technique.

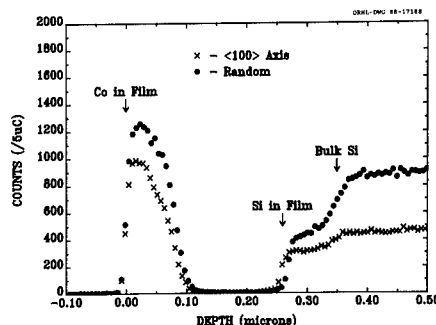


Fig. 4. Random (•) and aligned (x) 2 MeV ion scattering spectra for an 80-nm thick Co silicide film formed on $\text{Si}(100)$ at 40 eV and 500°C by IBD. The film shows some alignment with the bulk and a minimum yield of ~80%.

spectrum shows no appreciable epitaxy with the bulk Si substrate in this case, although other FeSi_2 films have shown some alignment with the surface normal.

In terms of resistivity, the Ti/Si system is particularly useful for semiconductor applications, since the disilicide phase has a low bulk resistivity of 15-20 $\mu\Omega\text{-cm}$. This is another combination in which Si is the more mobile partner, and we have grown stoichiometric TiSi_2 films as thick as 300 nm by the IBD technique at temperatures of 550°C that show low bulk-like resistivity.⁸ This resistivity of 15 $\mu\Omega\text{-cm}$, achieved at a maximum temperature of 550°C, is comparable to the best reported thin-film values that normally require sintering temperatures in excess of 900°C.⁹ This suggests strongly that athermal, beam-induced processes are playing a significant role in the formation of these silicides. A cross-section TEM micrograph of such a film is shown in Fig. 3. This figure illustrates some of the qualities of IBD silicide films that result in low resistivity, such as high purity, good stoichiometry, large polycrystalline grains, smooth interface with the bulk, and absence of oxide, nitride or other inclusions. Lowering the temperature to 400°C results in a uniform, stoichiometric film of TiSi . In both cases the films are formed at temperatures 100 to 200°C lower than they can be formed by purely thermal processes,¹⁰ indicating that the incident ion energy is activating the chemical reaction.

In all metal/Si systems in which Si is known to be the dominant diffuser, uniform films of the low resistivity disilicide phase formed throughout the deposited depth at temperatures near 500°C. This will be contrasted with the silicides described below in which the metal diffuses more readily.

Two silicides in which the metal is the dominant diffuser have been grown by IBD, Co, and Ni. Both of these systems are known to form epitaxial silicides on both $\text{Si}(100)$ and $\text{Si}(111)$.⁹ Co silicides formed by IBD at 500°C on $\text{Si}(100)$ have been shown previously by ion scattering to display varying stoichiometry throughout the film.⁸ Such films are Co rich near the surface, and Si rich near the bulk, indicating an inadequate reaction rate or inadequate transport of material to the growing area. These films also display only marginal alignment with the normal axis of the substrate by ion channeling as indicated by the high minimum yields of the ion scattering spectra of Fig. 4. The Co silicide film in this figure was formed at 40 eV and 500°C on $\text{Si}(100)$ and has a minimum yield on the normal axis of ~80%. This poor

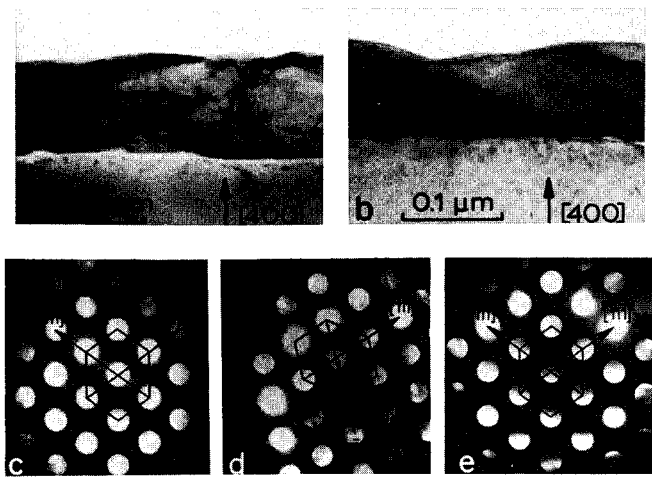


Fig. 5. Cross-section TEM micrographs and convergent beam electron diffraction patterns for a CoSi_2 film grown on $\text{Si}(100)$ at 40 eV and 500°C , showing both epitaxial regions (a,c) and regions twinned on $\{111\}$ planes (b,d) relative to the bulk Si (e).

minimum yield can be explained by looking at the cross-section TEM micrograph and convergent beam electron diffraction (CBED) of this film in Fig. 5, which indicate that a crystalline CoSi_2 film is oriented with respect to the bulk, but consists of both epitaxial regions and regions twinned around the $\{111\}$ planes of the silicide. Region (a) in the figure is epitaxial with the bulk as indicated by the identical CBED patterns generated from the bulk (e) and this region of the film (c). Region (b), on the other hand, shows a diffraction pattern (d) that is inverted about the $\{111\}$ planes relative to the bulk (e). There is a difference in the quality of the interface between the film and the bulk for these two regions. The fully aligned region has a sharp interface, while that of the twinned region is undulating. It is apparent from a comparison of (c) and (d) that twinning about the $\{111\}$ planes in this film results in a misalignment with the $\langle 100 \rangle$ axis of the bulk, thus severely limiting channeling along this normal axis, as observed in the ion channeling of Fig. 4. There is evidence in micrograph (b) of an additional layer on top of the CoSi_2 which could also reduce the ion channeling. This has been studied by electron-induced x-ray fluorescence which shows a factor of 2 decrease in the ratio of Co to Si going from the upper to the lower layer. This points to the formation of two distinct layers, the one nearest the substrate composed of CoSi_2 , and the surface layer composed of CoSi . This is in agreement with the general trend of the backscattering data, although a distinct separation between the two layers has not been observed by ion scattering, probably because of the twinning and small scale surface roughness in the films. It is interesting that the stoichiometries of both the monosilicide and the disilicide appear to be maintained throughout their respective layers.

The Ni/Si system is also one in which the metal is expected to be the dominant diffuser, and one in which epitaxial growth could be expected. A Ni silicide film grown by IBD with 100-eV Ni ions on p-type $\text{Si}(100)$ at a substrate temperature of 560°C is shown in Fig. 6. No appreciable differences were observed between n- and p-type substrates. Aligned $\langle 100 \rangle$ (x) and random (•) ion channeling spectra (a) show a minimum yield of $\sim 60\%$ and a Si to Ni ratio in the near-surface region of

~3:1. This minimum yield is in line with the results observed for Co, but the stoichiometry implied is unexpected. The gradual decrease in the height on the low energy side of the Ni peak indicates either diffusion into the bulk or non-uniform layer thickness. The optical micrograph of Fig. 6b confirms that non-uniform layer thickness is most likely. The surface of this Ni silicide film is seen in the micrograph to be uneven, with small "rods" aligned parallel to the $\langle 100 \rangle$ directions in the plane of the surface. This surface morphology is consistent with the observed shape of the Ni peak and may contribute to the unrealistic Si to Ni ratios measured for this film. Such oriented "rods" have been observed previously for high-temperature, 750°C, growth of Pd silicides.¹¹ The fact that such features are observed on Ni silicide films grown at 560°C is another indication that the energy of the incident ion beam during IBD is producing increased surface mobility and altering the growth processes.

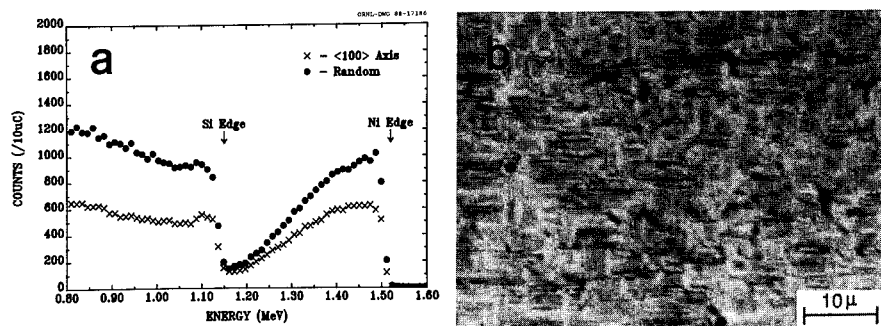


Fig. 6. Random (•) and channelled (x) 2 MeV ion scattering spectra (a), and surface optical micrograph (b), for a Ni silicide film grown on Si(100) at 100 eV and 560°C. The rod-like formations in the micrograph are aligned along $\langle 001 \rangle$ type directions in the surface plane.

IV. CONCLUSION

Low-energy ion beam deposition of the metal ion has been shown to be a viable technique for the formation of silicides on single-crystal Si at low temperatures. Silicides of Co, Fe, Ni, Ti, and W have been formed at temperatures near 500°C. This is a temperature at which diffusion or loss of previously implanted dopants should be insignificant. For the metals in which Si is the dominant diffusing element in the silicide (Fe, Ti, W) the stoichiometric disilicide phase has formed in all cases. For silicides in which the metal is the dominant diffuser, the stoichiometry has varied. These silicides are also the ones in which epitaxial growth might be expected, and epitaxial films have been grown for Co and Ni on Si. Even where epitaxial growth has occurred for these silicides, however, the stoichiometry is not constant and the minimum yields are relatively high. The results support a model in which both thermal and athermal processes are significant and the effectiveness of silicide growth is dependent upon the diffusion characteristics of the particular silicide system. Silicides in which Si is the dominant diffusing atom can be grown most effectively by the IBD technique. As a result, low-resistance films of the disilicide phase, notably TiSi_2 , that exhibit bulk-like resistivities without high-temperature annealing, can be produced at temperatures below 550°C for Si diffusing systems. The characteristics of these films are at least comparable to those

of films produced thermally at significantly higher temperatures. The formation of high-quality, low-resistance silicide films by IBD at low temperatures can lower the thermal budget during semiconductor processing and could find application in several areas of integrated circuit fabrication.

REFERENCES

1. S. P. Murarka, *J. Vac. Sci. Technol.* **17**, 775 (1980).
2. U. Malhotza, T. L. Martin, and J. E. Mahan, *J. Vac. Sci. Technol. B* **2**, 10 (1984).
3. J. Narayan, T. A. Stephenson, T. Brat, D. Fathy, and S. J. Pennycook, *J. Appl. Phys.* **60**, 631 (1986).
4. A. H. van Ommen, H. J. W. van Houtum, and A. M. L. Theunissen, *J. Appl. Phys.* **60**, 627 (1986).
5. D. Fathy, O. W. Holland, B. R. Appleton, and T. S. Stephenson, *J. Mater. Lett.* **5**, 315 (1987).
6. For a complete description of the IBD system, see R. A. Zuhr, B. R. Appleton, N. Herbots, B. C. Larson, T. S. Noggle, and S. J. Pennycook, *J. Vac. Sci. Technol. A* **5**, 2135 (1987).
7. B. R. Appleton, R. A. Zuhr, T. S. Noggle, N. Herbots, and S. J. Pennycook, *Mat. Res. Soc. Symp. Proc.* **74**, 45 (1987).
8. R. A. Zuhr, D. Fathy, and O. W. Holland, p. 119 in *Proc. of the Symposium on Dislocations and Interfaces in Semiconductors*, ed. by K. Rajan, J. Narayan, and D. Ast (The Metallurgical Society, 1988).
9. S. P. Murarka, *Silicides for VLSI Applications* (Academic Press, New York, 1983).
10. S. P. Murarka and D. B. Fraser, *J. Appl. Phys.* **51**, 342 (1980).
11. S. Vaidya and S. P. Murarka, *Appl. Phys. Lett.* **37**, 51 (1980).

ION BEAM ASSISTED DEPOSITION OF TITANIUM NITRIDE

G.K. HUBLER, D. VANVECHTEN*, E.P. DONOVAN and R.A. KANT
 Naval Research Laboratory, Washington, DC, 20375 USA
 *Sachs-Freeman Associate at NRL

ABSTRACT

The composition of titanium nitride films prepared by ion beam assisted deposition was studied as a function of the partial pressure of N_2 gas in the deposition volume, and as a function of the impingement ratio of nitrogen ions (500 eV) to evaporated titanium atoms. The amount of nitrogen incorporated from the ambient gas was derived by subtraction of the fraction introduced by the ion beam. It is shown that the primary effects of ion bombardment are an increase in the sticking coefficient and a reduction in the number of active surface adsorption sites.

INTRODUCTION

Ion beam assisted deposition (IBAD) refers to the process wherein evaporant atoms produced by physical vapor deposition (PVD) are simultaneously struck by a flux of low energy ions¹. The extra energy imparted to the deposited atoms causes bulk atomic displacements and surface atom migration. This can result in improved film properties^{2,3} which include better adhesion and cohesion of the film, modified residual stress, and higher density when compared to similar films prepared by PVD^{4,5}. When the ion beam or the evaporant is a reactive species, compounds such as refractory Si_3N_4 can be synthesized at very low temperatures⁶.

For IBAD compound synthesis the gaseous (beam) atomic species that are incorporated into the film arise from two mechanisms: direct ion implantation and adsorption of ambient gaseous atoms on the growth surface. At typical operating pressures of 10^{-4} Torr, the latter effect can dominate for reactive combinations such as Ti and N.

It is of basic interest to the understanding of IBAD to determine the fraction of beam atoms that are incorporated into the film from each mechanism as a function of the fluxes of evaporant atoms, energetic ions, and ambient gas molecules. The present study focuses on a determination of the composition and thickness of TiN prepared by IBAD as a function of the partial pressure of N_2 gas and the impingement ratio of 500 eV nitrogen ions to evaporated Ti atoms. It extends previous work^{7,8} by including additional data and by introducing a phenomenological model that predicts the amount of gas incorporation.

EXPERIMENTAL PROCEDURE

Typical base pressure of the cryopumped bell-jar deposition chamber is 3×10^{-7} Torr without baking. A constant flow rate of 7 sccm of nitrogen through the ion source raises the pressure to 2×10^{-4} Torr. The electron beam evaporation of Ti with a deposition rate of 9.3 Å/s is controlled with a quartz crystal balance which is shielded from the ion beam. Gettering by the Ti flux on the walls of the chamber causes the pressure to drop

to $\sim 10^{-6}$ Torr. An auxiliary supply of N_2 gas is introduced through a needle valve to control the total pressure in the range $> 10^{-6}$ to 2×10^{-4} Torr. The ion gun discharge, cathode, and extraction currents do not change as the pressure varies within these limits which indicates that the ion beam parameters are constant. An in-situ ion gun alignment system and three Faraday cups arranged in an equilateral triangle surrounding the sample position is used to ensure that the ion beam is centered on the sample. The summed aperture area of the cups totals 0.14 cm^2 . The ion source to sample distance is 26.4 cm and the beam is incident normal to the substrate. The evaporator to sample distance is 29.9 cm and the angle incidence is 20° from the normal to the sample. Most films were deposited onto sputter-cleaned carbon substrates at a temperature of $< 150^\circ \text{ C}$. Composition and the areal density of the films (2000 to 4500 Å in thickness) were measured by means of Rutherford backscattering spectrometry.

The nitrogen ion flux on the sample was calibrated using the silicon-nitrogen system where no ambient N_2 is incorporated into Si films. This is illustrated in Figure 1, where the amount of nitrogen in the silicon nitride films is plotted versus the measured ion current⁸. Although understanding of the overall shape of the curve is straight-forward, interpretation of the specific values and reasons for scatter are discussed elsewhere⁹. The factors taken into account to obtain the calibration include: 1) the output of the ion source includes both atomic and molecular ions, 2) a fraction of the ions are neutralized before reaching the sample and Faraday cups through charge exchange neutralization resonance interactions, 3) the intensity of the beam drops with angle, and 4) some of the incident particles are reflected from the surface.

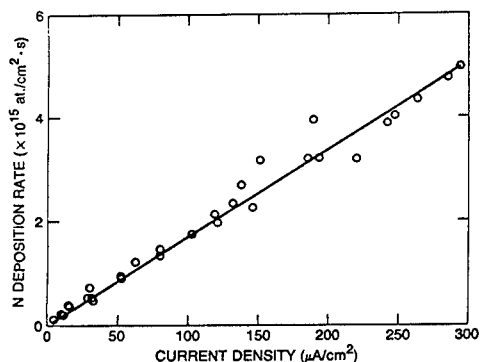


Fig.1 - Deposition rate of nitrogen for 500 eV nitrogen ions incident on a Si film growing at a rate of 10 Å/s versus nitrogen current density. The pressure was 2×10^{-4} Torr.

In the calibration of the ion flux the only parameter not measured was the reflection-coefficient, r . A value of 0.08, computed from the Monte Carlo code Trim¹⁰, was used. A pure silicon surface was assumed for these calculations since the N ions (250 eV/atom) are buried 20-25 Å beneath the surface for both Si and Ti targets. Chemical kinetic studies indicate that nitrogen is physisorbed on Ti surfaces¹¹ at pressures used here. Therefore, a TiN surface was assumed and Monte Carlo calculations predicted $r=0.09$ for 250 eV nitrogen. The same calibration shown in Fig. 1, adjusted for the small difference in r , was used for the amount of N sticking to the Ti films versus ion current. The main assumption to arrive at the amount of gas adsorption is that all unreflected ions stick to the

Fig. 2-N Deposition rate of 500 eV nitrogen ions incident on Ti film growing at 9.3 Å/s vs. ion current (bottom) and N/Ti arrival ratio (top). Pressure = 2×10^{-4} Torr.

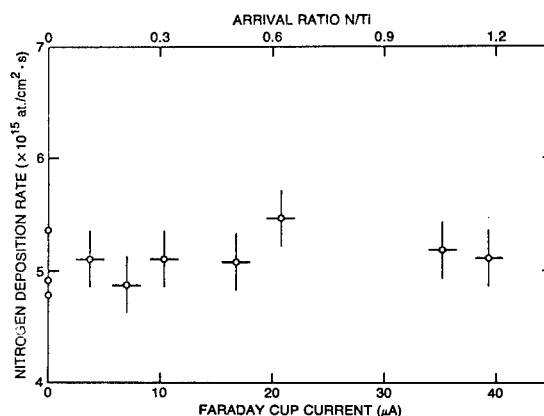
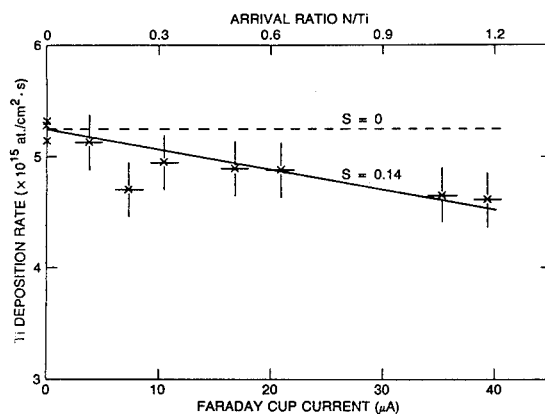


Fig. 3-Deposition rate of Ti vs. ion current (bottom) and the N/Ti arrival ratio (top). Pressure = 2×10^{-4} Torr.



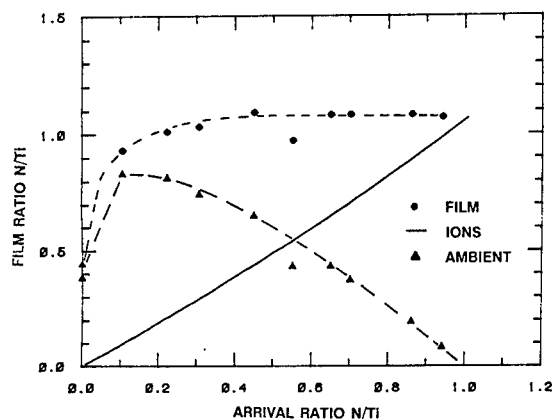
film. It is strictly true for N on Si IBAD. Since the range of 250 eV N in TiN is equal to N in Si (20 Å) and TiN has a large negative heat of formation, we believe the assumption valid.

RESULTS

Figures 2 and 3 show the flux of nitrogen atoms and Ti atoms, respectively, which stick to the film as a function of the measured ion current density and for a pressure of 2×10^{-4} Torr. The calibrated arrival ratio of energetic nitrogen atoms to Ti atoms, defined as R_a , is shown on the scale at the top of each figure. Incorporation of N in the film is independent of arrival ratio. The Ti deposition rate in Fig. 3 undergoes a linear decrease in the growth rate caused by sputtering of Ti. A straight line fit to the data gives the Ti flux (5.3×10^{15} at/cm/s = 9.3 Å/s) at zero current and a sputtering coefficient of 0.14 from the slope. The composition ratio N/Ti in the films versus arrival ratio, R_a , (obtained by dividing the N flux in Fig. 2 by the Ti flux in Fig. 3) is 0.96 for $R_a = 0$.

The composition ratio N/Ti at a constant pressure of 2×10^{-5} is plotted in Fig. 4 versus R_a . The solid line is the calibrated N/Ti ratio assuming the sticking coefficient of beam

Fig. 4-Measured ratio of N/Ti in IBAD films vs. N/Ti arrival ratio (circles); N/Ti from implantation of nitrogen ions (solid line); and N/Ti from N_2 gas incorporation (triangles). Pressure = 2×10^{-5} Torr.



atoms is 1-r and no gaseous atoms adsorbed from the ambient. Subtraction of this line from the data yields the triangle points, which represent the fraction of nitrogen that was incorporated into the film from the ambient. The dashed curves through both the data and the subtracted curve are only guides to the eye.

At this pressure the N/Ti ratio is only 0.4 for $R_a = 0$ and it markedly increases at the lowest R_a measured of 0.1. For $R_a > 0.1$, the amount of nitrogen from the ambient in the film decreases and the amount of nitrogen arising from energetic beam atoms increases. At high R_a nearly all of the nitrogen atoms in the film arise from the ion beam. Three of these films, $R_a = 0.35$, 0.5 and 0.6, were gold in color with the one at $R_a = 0.5$ the most characteristic of stoichiometric TiN.

DISCUSSION

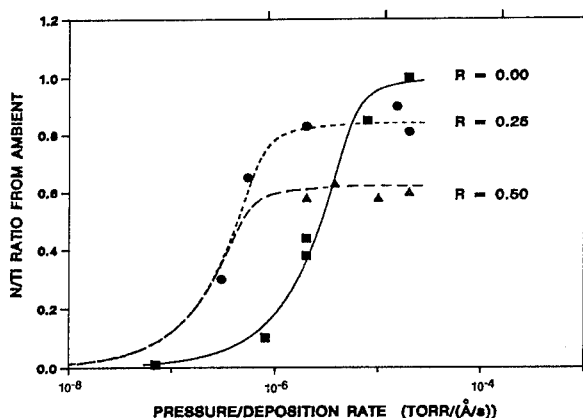
These data can be qualitatively explained by considering the relative arrival rates of the Ti atoms, gas molecules, and energetic ions. For null ion currents, the arrival ratio of N_2 to Ti atoms is 24 at a pressure of 2×10^{-4} Torr. It is therefore not surprising that at the highest pressure, the amount of nitrogen in the film is independent of ion current (Fig. 2). The adsorption sites for N_2 on the surface are saturated by the ambient gas atoms in a shorter time than it takes to deposit the next monolayer of Ti atoms. Since there are two N atoms per absorbed molecule, a ratio $N/Ti = 0.96$ for no bombardment implies one molecular adsorption site per two Ti atoms. Nitrogen is undoubtedly also sputter removed from the surface, but is quickly replaced from the ambient.

At lower pressure (Fig. 4) the arrival ratio of N_2 gas molecules to Ti atoms is smaller and surface chemistry effects are observed. At zero current, the N/Ti ratio is 0.4 and it rises immediately to nearly 1.0 at an arrival ratio of 0.1. This is evidence that the ion beam alters the surface chemistry and changes the effective sticking coefficient.

For Si deposited by magnetron sputtering in controlled partial pressures of oxygen, the incorporation of O_2 has been described by a model which divided the surface adsorbed O_2 into physisorbed and chemisorbed components¹². An activation energy between the physisorbed and more strongly bound chemisorbed state was invoked to explain the dependence of incorporation of

oxygen into the films upon whether the incident O_2 gas was in a ground state or a chemically reactive (plasma activated) state. In the latter case, the sticking coefficient for O_2 increased several orders-of-magnitude so that SiO_2 could be formed at much lower partial pressures of O_2 . Kant¹¹, in a study of the influence of ion bombardment on reactions between titanium and gaseous nitrogen, found that the concentration of surface nitrogen on Ti can be enhanced due to Ti ion bombardment. This effect could be explained if two forms of nitrogen were present. These were presumed to be physisorbed molecular N_2 and reacted nitrogen bonded to Ti to form TiN. It was speculated that the ion bombardment both activated the conversion to the reacted form and sputtered away remaining physisorbed N_2 . The increase in the amount of nitrogen in our films at low arrival ratio could be caused by activation of the energy barrier between the physisorbed (unreacted) and the chemisorbed (reacted) states when extra energy is added to the surface by the ion beam.

Fig. 5 - N/Ti ratio from N_2 gas incorporation in IBAD TiN films versus pressure/deposition rate. $R_a = 0$, boxes; $R_a = 0.25$, circles; $R_a = 0.5$, triangles.



To apply a model to our work, the data for the amount of nitrogen incorporated from the ambient, expressed as N/Ti versus the ratio of pressure/deposition rate, was generated and is plotted in Fig. 5. The boxes are for $R_a = 0$, the circles for $R_a = 0.25$, and the triangles for $R_a = 0.5$. By plotting the data in this way, samples made at different pressures and deposition rates can be included in one figure. For $R_a = 0$, the N/Ti ratio decreases from one to zero with about a one-order-of-magnitude decrease in pressure. Although the data for $R_a = 0.25$ and 0.5 is limited, it shows two interesting aspects of ion bombardment. First, there is a shift of the curve toward lower pressures. Second, the saturation value of N entering from the ambient decreases as R_a increases.

A simple calculation was performed using a dynamic surface coverage model similar to one proposed by Barbie et al.¹². It includes a surface coverage dependent sticking coefficient for physisorption and the concept of dynamic exposure time. The solid line in Fig. 5 is the calculated N/Ti ratio assuming a sticking coefficient of 0.1, a fraction of active surface absorption sites for N_2 of 0.5 monolayers, and a negligibly small thermal desorption rate. The curve is in reasonable agreement with the data for $R_a = 0$. The lines corresponding to

$R_a = 0.25$ (short dashes) and $R_a = 0.5$ (long dashes) are obtained by setting the sticking coefficient to 1.0 and by reducing the surface active fraction of adsorption sites to 0.42 and 0.31, respectively. Thus, it is possible to infer two effects of bombardment: 1) the sticking coefficient for the N_2 increases by a factor of about ten, and 2) the number of active adsorption sites decreases approximately in proportion to R_a . A more complete model would allow for sputtering of surface adsorbed nitrogen which could be part or all of the latter effect.

Attempts to reduce the pressure another order-of-magnitude have been unfruitful because of the poor operating base pressure in our system. This is primarily caused outgassing of internal components and the glass bell jar covering the chamber when the heat load is applied. Under these circumstance control of the N_2 partial pressure is not possible at less than 10^{-5} Torr. Further definition of the dependence of composition of the TiN films on incident atomic fluxes and refinement of the model await installation of a water cooled stainless steel bell jar and will be the subject of future work.

SUMMARY

The absolute amount of N entering from the ambient N_2 gas during production of IBAF TiN films was measured. The technique is based upon accurate calibration of the ion and evaporant fluxes, and RBS measurements of the film composition and thickness. A phenomenological model was found to be in good agreement with the amount of N incorporated from the ambient over a pressure range of 10^{-6} to 2×10^{-4} Torr, R_a between 0.0 and 0.5, and deposition rates between 0.25 and 2.0 nm/s. The method is straightforward and yields absolute values of the sputtering coefficient for Ti, the sticking coefficients of N_2 on the Ti surface with and without ion bombardment, and the number of active surface adsorption sites as a function of the ion to atom impingement ratio.

REFERENCES

1. U.J. Gibson, "Ion-Beam Processing of Optical Thin Films", in Physics of Thin Films, Vol. 13 (Academic Press, 1987) p. 109.
2. D.R. Brighton and G.K. Hubler, Nucl. Instrum. & Meth. in Phys. Res. **B28** (1987) 527.
3. K.-H. Müller, Phys. Rev. B, **35** (1987) 7906.
4. J.J. Cuomo, J.M.E. Harper, C.R. Guarnieri, D.S. Yee, L.J. Attanasio, J. Angilello and C.T. Wu, J. Vac. Sci. & Technol. **20** (1982) 349.
5. R.P. Netterfield, SPIE **678** (1986) 14.
6. C. Weissmantel, Thin Sol. Films **32** (1976) 11.
7. R.A. Kant and B.D. Sartwell, Mater. Sci. Engin. **90**(1987)357.
8. G.K. Hubler, E.P. Donovan, D. Vanvechten and R.A. Kant, "Ion implantation and Plasma Processes for Industrial Applications", (ASM, Metals Park, OH) to be published.
9. D. Van Vechten, G.K. Hubler and E.P. Donovan, J. Vac. Sci. Technol. **A6**, (1988)1934, and unpublished data.
10. J.P. Biersack and L.G. Haggmark, Nucl. Instrum. Methods **174** (1980) 257.
11. R.A. Kant, unpublished data
12. T.W. Barbie, Jr., D.L. Keith, L. Nagel and W.A. Tiller, J. Electrochem. Soc. **131** (1983) 434.

PROPERTIES OF SILICON OXYNITRIDE AND ALUMINUM OXYNITRIDE COATINGS
DEPOSITED USING ION ASSISTED DEPOSITION

G.A. Al-Jumaily*, T.A. Mooney*, W.A. Spurgeon**, and H.M. Dauplaise**

*Barr Associates, 2 Lyberty Way, Westford, MA 01886

**Army Materials Technology Laboratory, Watertown, MA 02172

ABSTRACT

Optical thin films of nitrides, oxynitrides and oxides of aluminum and silicon were deposited using ion assisted deposition. Coatings were deposited by thermal evaporation of AlN and e-beam evaporation of Si with simultaneous bombardment with 300 eV ions of nitrogen, a mixture of nitrogen and oxygen or oxygen. The chemical composition and the index of refraction of the coating was varied by varying the gas mixture in the ion beam. Optical properties of and environmental stability of coatings were examined. Results indicated that coatings are stable even under severe conditions of humidity and temperature.

Introduction

Silicon nitride and oxynitride coatings are becoming increasingly important for optical and microelectronic applications. Optically, silicon nitride has relatively high index of refraction in the visible region of the spectrum. The coatings are hard with exceptional environmental durability. The material has a wide transmission band that extends from the UV to the near IR. Silicon nitride has been deposited by chemical vapor deposition (CVD), rf sputtering, ion implantation, thermal evaporation and ion assisted deposition (IAD). [1,2] The deposition, characterization, and applications of silicon nitride has been reviewed by Morosanu [3]. Deposition of coatings using CVD involves raising the substrate temperature to values as high as 700° C. Thermal evaporation of thin films has the advantage that coatings can be deposited at lower temperatures. However, silicon nitride coatings deposited using conventional thermal evaporation have numerous structural defects which make this method unsuitable for microelectronic applications [3]. Martin et al. [4] used rf sputtering to deposited optical filters using a combination of SiO₂ and Si₃N₄. The filters were found to be stable at extreme conditions of temperature and humidity. Netterfield et al. [1] used IAD to deposit silicon nitride and silicon dioxide coatings by evaporation of silicon (Si) with simultaneous bombardment with low energy nitrogen and oxygen ions respectively.

Aluminum nitride (AlN) and oxynitride have similar properties to silicon nitride and oxynitride. Thermal evaporation of AlN causes the material to dissociate and the resulting films are highly absorbing. Coatings of AlN are deposited by reactive evaporation in 1×10^{-3} Torr of nitrogen backfill in the presence of a glow discharge. Thin films of AlN have also been deposited by reactive sputtering in a planar dc magnetron system [5]. In this paper we examine the optical properties of silicon oxynitrides and aluminum oxynitrides deposited using IAD.

Deposition Arrangement

Coatings were deposited in a 60 cm box coater. Figure 1 is a schematic illustration of the deposition arrangement. The vacuum system is cryogenically pumped to a base pressure of 3×10^{-7} Torr. The backfill pressure for the reactive gases was 1×10^{-4} Torr. The starting materials can be

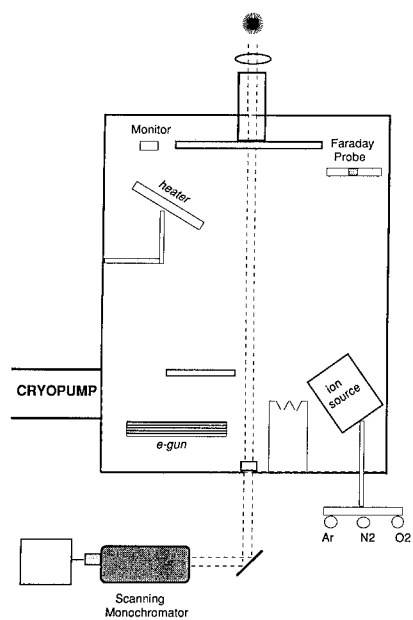


Figure 1. A schematic illustration of the deposition system.

evaporated from a resistively heated boat or an e-beam source. The coating system is equipped with a 3 cm Kaufman ion source, which is used to bombard the sample with low energy ions. Argon, nitrogen, oxygen, or any mixture of these gases can be employed. The relative flow rates of gases are actively controlled using a Siera gas controller which controls the flow rates of either one or two gases. The ion beam flux is characterized using a Faraday probe. The ion source to substrate distance was about 30 cm. The ion source beam current was 15 mA. The substrates are heated to 300° C using quartz lamps. Deposition rate and film thickness are monitored using an optical and a crystal rate monitor. The deposition rate was 0.1 nm/sec. Films were deposited on silicon, fused silica and sapphire substrates. Substrates are cleaned with 300 eV argon ions for three minutes prior to coatings.

Results

Optical properties of coatings were examined using a spectrophotometer, a spectral ellipsometer and an IR spectrophotometer. Results of other testing procedures are presented elsewhere.[6] The index of refraction of the coatings was calculated from spectral transmittance traces. Results are listed in Table I.

Table I

Optical properties of coatings determined from spectral transmittance

Starting Material	Ion	Film	Index	Cut Off Wavelength (nm)
Si	O ₂	SiO ₂	1.42	180
Si	N ₂ +O ₂	SiO _x N _y	1.70	260
Si	N ₂	SiO _x N _y	1.77	350
AlN	N ₂ +O ₂	AlN _x O _y	1.66	240
AlN	N ₂	AlN	2.00	320

The SiO₂ sample was examined using spectral ellipsometry. The index of refraction and the extinction coefficient for the sample were calculated over the spectral range of 300 to 800 nm. Comparing the experimental results to the known properties of the bulk properties of SiO₂ and SiO showed that best fit for the data was obtained by assuming the sample to be made up of 92% SiO₂ and 8% SiO. Calculated values of n and k for the sample as well as bulk values for SiO₂ and SiO are shown in Figures 2 and 3.

The environmental stability of coatings was examined by measuring IR absorption at the water absorption band near 3 μ m.[7] No increase in absorption was observed even after 72 hours of exposure to 95% relative humidity and 65° C.

Discussion

Results presented above illustrate that coatings of the oxynitrides of aluminum and silicon can be deposited with good optical properties using IAD. The coatings have exceptional environmental stability even at extreme conditions of temperature and humidity. Results also indicated that the index of refraction of the coatings can be varied during deposition by

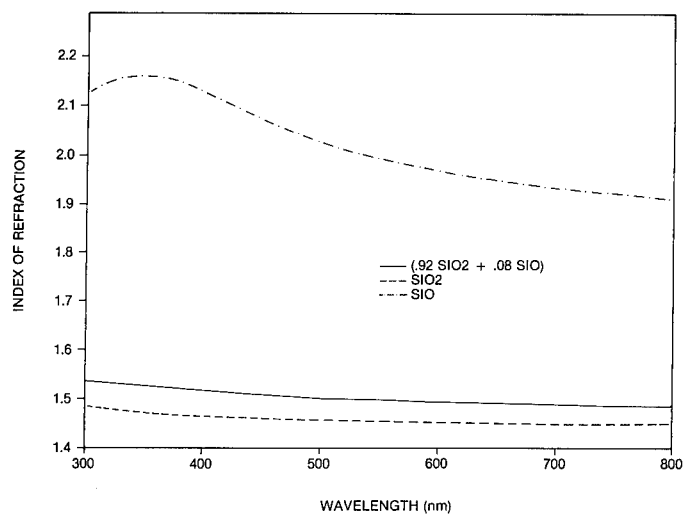


Figure 2. The index of refraction of the silicon oxide sample measured using spectral ellipsometry. Also shown are curves representing the index of refraction of bulk silicon oxide and silicon monoxide.

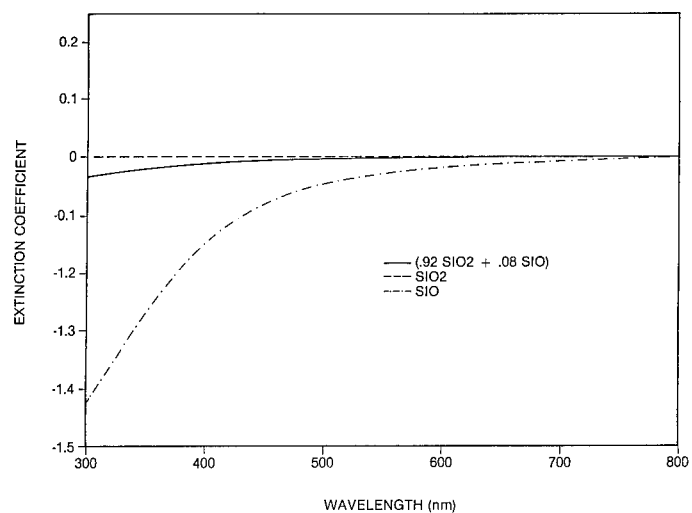


Figure 3. The extinction coefficient of the silicon oxide sample measured using spectral ellipsometry. Also shown are curves representing the extinction coefficient of bulk silicon oxide and silicon monoxide.

varying the gas mixture in the ion beam. The index of refraction of silicon nitride and silicon dioxide are 2.1 and 1.42 respectively. The index of refraction for aluminum nitride and aluminum oxide are 2.2 and 1.65 respectively. This indicates that the index of refraction of coatings can be varied between these limits by varying the gas mixture in the ion beam. This has many practical applications especially for deposition of wideband graded index antireflection coatings and graded index sinusoidal multilayer (rugate) filters. Recently Donovan et al. used a similar procedure to deposit rugate filters for the near IR using IAD of $\text{Si}(1-x)\text{Nx}$. The index of refraction is varied between 3.4 and 2.1 by varying the nitrogen ratio (x). This filter is suitable for the IR only since substoichiometric silicon nitride does not transmit in the visible. Presently, rugate filters are being deposited by co-evaporation of high and low index materials. This process is extremely difficult to implement because it involves the control of two different evaporation sources. Co-evaporation requires that the behavior of the two sources is predictable and consistent throughout the deposition of the entire filter. However, the IAD process discussed above involves only the control of one evaporation source and the gas flow rates into the ion source.

Summary

Coatings of the nitrides, oxynitrides, and oxides of aluminum and silicon were deposited using IAD. Results indicated that coatings are stable under severe conditions of humidity and temperature.

Acknowledgements

The authors acknowledge John Woolam for assistance in spectral ellipsometry measurements and A. Smajkiewicz for valuable discussions. This work was supported by the U.S. Army Materials Technology Laboratory under contract number DAAL04-87-C-0053.

References

- [1]. R.P. Netterfield, P.J. Martin, and W.G. Sainty, *Appl. Opt.* 25, 3808 (1986).
- [2]. E.P. Donovan, D. Van Vechten, A. Khan, C.A. Carosella, and G.K. Hubler, in *Optical Interference Coatings*, 1988 Technical Digest Series, Vol. 6, (Optical Society of America, Washington, D.C. 1988) p. 122.
- [3]. C.E. Morosanu, *Thin Solid Films* 65, 171 (1980).
- [4]. P.M. Martin, W.T. Pawlewicz, D. Coult, and J. Jones, *Appl. Opt.* 23, 2668 (1984).
- [5]. E.V. Gerova, N.A. Ivanov, and K.I. Kirov, *Thin Solid Films*, 81, 201 (1981).
- [6]. G.A. Al-Jumaily, T.A. Mooney, W.A. Spurgeon, and H.M. Dauplaise, to be published in *J. Vac. Technol.* A7, May/June 1989.
- [7]. G.A. Al-Jumaily, T.A. Mooney, L.A. Yazlovitsky, and A. Smajkiewicz, *Appl. Opt.* 26, 3752 (1987).

PLASMA-ACTIVATED ION BEAM REACTIVE SPUTTERING OF NbN THIN FILMS.*

D.J. LICHTENWALNER*,**, ALFREDO C. ANDERSON*, and D.A. RUDMAN**

*MIT Lincoln Laboratory, Lexington MA 02173

**MIT Department of Materials Science and Engineering, Cambridge MA 02139

ABSTRACT

In order to better study and control the processes occurring in a reactive sputtering situation, a unique deposition method has been used in which the Ar-ion-beam sputtering of an elemental Nb target is combined with an auxiliary Ar/N₂ plasma at the substrate. The ion source allows independent control of the sputtering parameters (ion flux, energy). The magnetically enhanced triode plasma provides a source of ionized and excited nitrogen at the film surface, and allows independent control of the substrate plasma parameters. A conductance-limiting enclosure surrounds the substrate, resulting in a pressure differential of nearly an order of magnitude between the substrate and target regions. This enables us to separate the substrate and target reaction regimes at low nitrogen flows. NbN has been investigated because of its technological importance and the fact that it is representative of transition metal nitrides.

With the substrate plasma off and N₂ provided at the substrate, the cubic superconducting NbN (δ phase) is produced even at low N₂ flows, when the target is in the unreacted, metallic state. Upon increasing the N₂ flow, the nitrogen content of the films abruptly increases as the target reaction proceeds. The addition of the substrate plasma results in the nonsuperconducting hexagonal δ' phase, which to our knowledge has not previously been produced as a single-phase thin film. The electrical properties of the δ' phase are reported.

*This work is sponsored by the Office of Naval Research and the Air Force Office of Scientific Research.

INTRODUCTION

Reactive sputtering has proven to be an effective method for producing high superconducting transition temperature (T_c) NbN thin films [1-5], as well as for producing other transition metal nitrides and carbides [6,7]. It is generally accepted that, when using nitrogen flow as the independent parameter, the T_c will have a maximum at a given flow, then slowly decrease at higher flows. The T_c also generally has a maximum for a certain total pressure and sputtering power. Since the noble and reactive gas pressures, current, and voltage are interdependent in typical systems, it is difficult to determine the role of these parameters in the optimization of film properties.

Because the nitrogen pressure at the target and substrate may be nearly equal during film growth and the sticking coefficient of nitrogen on a clean Nb surface is about 0.5 [8], the role each reaction plays in determining final film properties has not yet been clarified. In most studies of reactively sputtered NbN, the highest T_c films were obtained when the target had nitrided (seen by a drop in deposition rate), but it is not clear from those studies if this was a geometrical consequence of target-to-substrate distance or a fundamentally necessary part of the film formation. The deposition system used in this study allows us to separate the target and substrate reactions at low nitrogen flows by means of a pressure differential, so we can

examine the situation of reactive film formation in the absence of any significant target reaction.

In the present study, the effect of adding nitrogen to the substrate region was examined with and without the auxiliary substrate plasma operating. We see that the operation of the plasma causes growth of the δ' phase (which we determine to be non-superconducting above 4.2 K). Without the substrate plasma on, the superconducting δ phase forms even at low nitrogen flows (when the target is not nitrified), although these films are nitrogen deficient and have low T_c 's. In both cases, the nitrogen content of the films increases as the target reaction proceeds, indicating that the reacted target provides a significant flux of reactive nitrogen to the growing film.

EXPERIMENTAL

The deposition system is shown schematically in Figure 1. A Kaufman-type ion source is used to generate an Ar ion beam which sputters an elemental Nb target. Use of the ion source gives independent control of sputtering current and energy. A sputtering voltage of 1200 V and a current of 160 mA have been used in these experiments.

The substrate may be immersed in an auxiliary Ar/N₂ plasma. We use an L.M. Simard triode magnetron source for this application. This plasma is supported between an anode and a hot filament cathode and is magnetically enhanced using a perpendicular magnetic field. The plasma operates in the low millitorr region, which is typical for magnetron sources. A discharge current of 2 A was used for most deposition runs; this gives an ion current density at the substrate of about 25 mA/cm². This was determined using a planar, 0.32-cm-diameter, biased probe (no correction was made for secondary electron effects and sheath area effects). An estimate of the substrate temperature was obtained by bonding a platinum resistor to a substrate using quartz paste; it is nearly 300°C at this plasma current. The temperature reaches about 50°C with the plasma off. The exact plasma-ion energy is not known, but with the substrate floating, the incident ion energies are not expected to be greater than about 30 eV (the maximum voltage drop, anode to substrate, is 50 V).

A conductance limiting enclosure surrounds the substrate region and enables a pressure differential of nearly an order of magnitude to exist between the substrate and target region. During deposition, the chamber pressure is in the mid 10⁻⁴ Torr region while the pressure at the substrate is in the low millitorr range. It is this situation

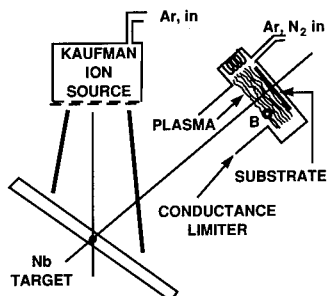


Figure 1. Schematic of ion-beam sputtering system with auxiliary substrate plasma.

which enables us to separate the target reaction from the substrate reaction at low nitrogen flows. However, the conductance limiter also reduces the deposition rate, so a deposition rate of about 0.3 Å/s is obtained at the substrate from the metallic target with the given ion-beam parameters.

The vacuum system is an all metal, bakeable UHV system. It is completely oil free, rough pumped with an oil-free mechanical pump and pumped to high vacuum with a cryopump. Typical background pressures are in the low 10^{-9} Torr range, being mostly He, with all reactive impurities less than 2×10^{-10} Torr after the system has been baked to 200°C.

For most of the films presented here, the nitrogen flow was varied with other parameters fixed, and the substrate plasma was either on or off. The nitrogen was added at the substrate, and argon was always flowing at the substrate even when the plasma was not on, to keep pressures the same in each case. Films were deposited on oxidized Si substrates, with film thicknesses typically 1500 Å. Two films were deposited on single-crystal, cleaved MgO to determine possible epitaxial effects.

Electrical and structural properties of these films have been investigated. The electrical resistivity and critical temperature were determined using a four-point probe, lowered into the vapor of a liquid He dewar for temperature control. A calibrated germanium resistor was used for temperature determination. A 40 µm by 1.27 mm line, patterned with conventional photolithography and etched in a CF_4 plasma, was used for determining resistivity. Film thickness was measured using a Dektak profilometer.

Structural information was obtained using a standard theta/2-theta diffractometer, and a Read thin-film camera. Some films were also analyzed using a Rigaku 300 diffractometer with rotating anode generator, which can operate at a higher power (50 kV, 200 mA) than the normal diffractometer. Auger electron spectroscopy (AES) was used to examine the N/Nb ratios of the films. Absolute ratios were obtained by calibrating against a film analyzed by Rutherford backscattering (RBS). Although the RBS has absolute uncertainties of a few atomic percent, relative N/Nb ratios will be unaffected.

RESULTS

The deposition rate vs nitrogen flow is shown in Figure 2. This deposition rate is that measured outside of the confined substrate region and was unaffected by the operation of the plasma. At a critical flow, the deposition rate drops due to nitride formation at the target, and then levels off as the target saturates.

With the substrate plasma off, films were grown on oxidized Si with nitrogen flows varying from 0.06 sccm to 1.4 sccm. All films were determined to be 100% cubic δ NbN from x-ray diffraction patterns. Figure 2 also shows the N/Nb ratio and the critical temperature of these films as a function of nitrogen flow. The N/Nb ratio appears constant at low flows and is seen to increase at higher nitrogen flows. The T_c varies with N_2 flow in this same way, although the values are quite low. The resistivity of these films is in the low range of those reported for NbN (ranging from 200 to 180 µhm-cm, resistivity ratios of about 0.97). Low resistivities and T_c 's have been observed in other studies of ion beam reactive sputtering of NbN [9,10]. A film grown with N_2 added outside the substrate region (no pressure differential) at a flow of 0.4 sccm was not superconducting above 4.2 K and appeared to be highly distorted Nb from the x-ray diffraction pattern.

Figure 2. N/Nb ratio, T_c , and deposition rate as a function of nitrogen flow. The T_c is for films without the substrate plasma on; the deposition rate is that outside of the substrate region.

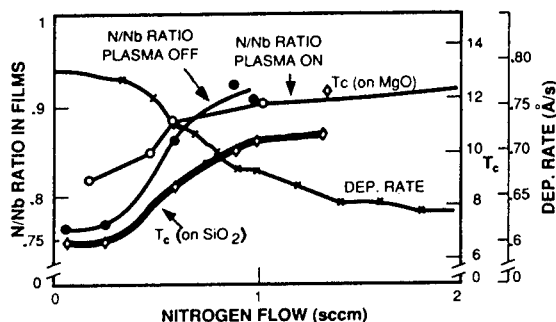
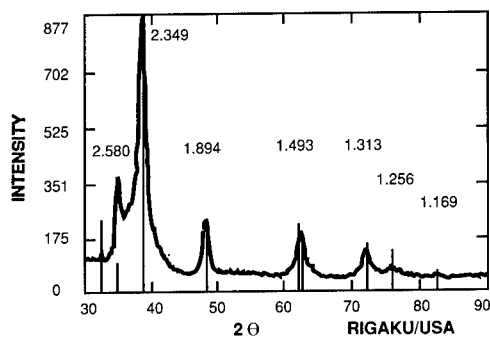


Figure 3. X-ray diffraction profile of hexagonal-phase δ' NbN. Line markers give the peak locations of this phase as listed in the JCPDS file 25-1361.



For films grown with the substrate plasma on, nitrogen flows from 0.18 to 5.55 sccm all produced films which appeared to be 100% δ' hexagonal NbN using each of the mentioned x-ray techniques. A diffraction pattern of a film deposited with 0.6 sccm N_2 and a plasma current of 2 A is shown in Figure 3. Some of these films had superconducting transitions (sharp drops in the resistivity at low temperature), but they did not all go to zero resistance. One film was then grown with a nitrogen flow of 0.6 sccm and a plasma current of 3.5 A, for which the ion bombardment increased to 38 mA/cm² and the substrate temperature was near 400°C. This film also appeared to be 100% δ' NbN and had no T_c onset above 4.2 K. We believe the film to be 100% δ' ; it is metallic with a room temperature resistivity of 171 $\mu\Omega\text{-cm}$ and 20 K resistivity of 156 $\mu\Omega\text{-cm}$. To our knowledge, this is the first report of the electrical properties of the δ' phase. From the AES data, using the same factors as for the cubic NbN, we see a large compositional variation in this set of films, as shown in Figure 2.

To determine if nucleation effects would stabilize the cubic phase, a film was grown on single-crystal MgO. Fully oriented (100) cubic NbN with a pole figure FWHM of 6° was formed with the substrate plasma off. With the plasma on, the film grew as the δ' phase, but it was now oriented, as seen from wide spots in the Read camera. The plane oriented parallel to the substrate was the (100), with a pole figure FWHM of 7.7°. On oxidized Si wafers, the major oriented peak is the (101), and the Read camera gives diffraction rings, indicative of random crystallites. A film was then grown on top of a δ NbN film; a film approximately 200 angstroms thick was grown without the plasma (δ phase), and then the plasma was turned on. The Read camera x-ray showed that this film too grew as δ' NbN.

DISCUSSION

From the deposition rate curve, we see that no significant target reaction occurs below about 0.4 sccm N_2 flow, so substrate reactions would dominate film growth in this region. Although the rate of N_2 impingement on the substrate at 0.3 sccm N_2 flow is 100 times that of Nb arrival, the films grown at these low flows are highly nitrogen deficient. This is observed regardless of whether the substrate plasma is on or off.

Without the substrate plasma on, the amount of substrate reaction appears independent of N_2 flow at low flows, as indicated by the equivalent T_c 's and N/Nb ratios. The incident sputtered Nb and reflected target species may be what determines the amount of substrate reaction. At higher nitrogen flows, the target reaction sets in, and the T_c and N/Nb ratio progressively increase. From the results of Baba et al. [11], the ion bombardment of the target would be expected to cause a nitridization reaction there. It appears that the nitrogen molecule is dissociated at the target much more effectively than it is at the substrate.

As seen in Figure 2, the N/Nb ratio and the T_c of the films grown without the substrate plasma are quite low. NbN is known to be nonstoichiometric; the N/Nb ratio has been reported to vary from about 0.85 to 1.06 [9], and is even lower in some of these films. It has been seen that as this ratio goes to one, the critical temperature maximizes [13], with 17 K being the highest reported [1]. The deficient nitrogen can partly account for the low T_c 's. Also, the energetic reflected particles from the target surface are expected to cause film damage [16,17].

With the substrate plasma on, the nonsuperconducting δ' phase was always obtained. However, the effect of the substrate and target reactions can still be compared. At low flows, before the target had nitrided, the films were still very nitrogen deficient (Figure 2), even though the ionized nitrogen flux to the substrate was much greater than the Nb flux (assuming equal ionization probabilities for Ar and N_2). A slight enhancement of the N/Nb ratio at low flows was seen with the plasma on. However, much more effective nitridization occurred when the target had nitrided, similar to that seen without the substrate plasma on.

Guard et al. [8] have determined that the superconducting phase of NbN (δ NbN, cubic NaCl type, $a=4.38$ Å) is thermodynamically stable only above 1270°C. They also concluded that δ' NbN (hexagonal, $a=2.968$ Å, $c=5.535$ Å) is a metastable phase and is not present on the equilibrium phase diagram. However, they note that at lower temperatures (below 1000°C) the δ' phase may possibly be a stable phase. They observed the δ' phase upon the conversion of cubic δ NbN to ϵ NbN (hexagonal, $a=2.958$ Å, $c=11.272$ Å; N/Nb=0.92-1.0), at temperatures near 1300°C in a nitrogen atmosphere. Terao [19] found that by nitriding thin Nb foils, he obtained a higher nitride, Nb_3N_6 . Upon heating in vacuum, this changed progressively to δ' NbN (1100 - 1200°C), δ NbN (at some higher temperature), and then to lower nitrides. This indicates that during a phase change of δ NbN to a lower-temperature, higher-nitrogen-content phase, δ' NbN would be the first phase to form.

With the substrate plasma on, we believe that the plasma bombardment allowed the atoms to overcome a kinetic barrier and thereby grow as the δ' phase. Based on the ion current at the substrate of 25 mA/cm² and the deposition rate of 0.3 Å/s, the ion/Nb arrival ratio is about 1000. This bombardment density is much higher than that seen in typical sputtering systems. Because for these low-energy ions the sputtering yield and trapping probability is very low [18], the main

effect is expected to be an increased surface mobility. In other systems, such as NbC, TiC, and TiN, the cubic phase is the stable phase. (The addition of carbon to NbN is known to help stabilize the δ phase [2].) Then the annealing effects of bombardment could improve film properties. It is also seen that second phases are present in many NbN films reported [3,4,19]. In our earlier work on dc magnetron reactively sputtered NbN [4], we have seen what we believe is the δ' phase present as a second phase. The x-ray intensity of this second phase increased with sputtering power and was not evident at low power (100 W). We conclude that the increased power resulted in a larger substrate bombardment, similar to the effect of this substrate plasma.

From film growth on single-crystal MgO and δ NbN, we see that nucleation effects that would favor δ phase formation were unable to inhibit the growth of the δ' phase. Nucleation effects were seen to influence film orientation, but growth kinetics control phase formation.

Further studies quantifying the role of ion energy and density at the film surface will be required to determine the range of stability of the δ phase. The role, and mechanisms, of substrate and target reactions also need further study.

REFERENCES

1. K.S. Keskar, T. Yamashita, and Y. Onodera, Jpn. J. Appl. Phys. **10**, 370 (1971).
2. J.R. Gavaler, J. Talvacchio and A.I. Braginski, in Advances in Cryogenic Engineering Materials, ed. by J.P. Clark and R.P. Reed (Plenum, New York, 1985), Vol. 32, p.627.
3. S. Thakoor, J.L. Lamb, A.P. Thakoor, and S.K. Khanna, J. Appl. Phys. **58**, 4643 (1985).
4. A.C. Anderson, D.J. Lichtenwalner and W.T. Brogan, presented at the 1988 Applied Superconductivity Conference, San Francisco, CA 1988 (to be published in the IEEE Trans. Magn.).
5. M. Bhushan, J. Vac. Sci. Technol. A **5**, 2829 (1987)
6. J.-E. Sundgren, B.-O. Johansson and S.-E. Karlsson, Thin Solid Films **80**, 77 (1981).
7. N. Savvides and B. Window, J. Appl. Phys. **64**, 225 (1988).
8. R.A. Pasternak and R. Gibson, Acta Metall. **13**, 1031 (1965).
9. L.-J. Lin, E.K. Track, G.-J. Cui and D.E. Prober, Physica **135B**, 220 (1985).
10. K. Takei and K. Nagai, Jpn. J. Appl. Phys. **20**, 993 (1981).
11. Y. Baba, T.A. Sasaki and I. Takano, J. Vac. Sci. Technol. A **6**, 2945 (1988).
12. G. Brauer and H. Kirner, Z. Anorg. Allg. Chem. **328**, 34 (1964).
13. T. Mitsuoka, T. Yamashita, T. Nakazawa, Y. Onodera, Y. Saito and T. Anayama, J. Appl. Phys. **39**, 4788 (1968).
14. E. Kay, F. Parmigiani and W. Parrish, J. Vac. Sci. Technol. A **5**, 44 (1987).
15. D.J. Lichtenwalner, A.C. Anderson and D.A. Rudman, to be published in J. Vac. Sci. Technol., Jan/Feb (1989).
16. R.W. Guard, J.W. Savage and D.G. Swarthout, Trans. Metall. Soc. AIME **239**, 643 (1967).
17. N. Terao, J. Less Com. Metals **23**, 159 (1971).
18. J.E. Greene and S.A. Barnett, J. Vac. Sci. Technol. **21**, 285 (1982).
19. S.A. Wolf, I.L. Singer, E.J. Cukauskas, T.L. Francavilla and E.F. Skelton, J. Vac. Sci. Technol. **17**, 411 (1980).

INVESTIGATION OF TITANIUM NITRIDE SYNTHESIZED BY ION BEAM ENHANCED DEPOSITION

ZHOU JIANKUN, LIU XIANGHUAI, CHEN YOUSHAN, ZHENG ZHIHONG,
HUANG WEI, ZHOU ZUYAO, ZOU SHICHANG
Ion Beam Laboratory, Shanghai Institute of Metallurgy,
Academia Sinica, Shanghai 200050, China

ABSTRACT

Titanium nitride films have been synthesized at room temperature by alternate deposition of titanium and bombardment by nitrogen ions with an energy of 40KeV. The component depth profiles and the structure of titanium nitride films were investigated by means of RBS, AES, TEM, XPS and X-ray diffraction. The results showed that titanium nitride films formed by ion beam enhanced deposition (IBED) had columnar structure and were mainly composed of TiN crystallites with random orientation. The oxygen contamination in titanium nitride films prepared by IBED was less than that of the deposited film without nitrogen ion bombardment. It was confirmed that a significant intermixed layer exists at the interface. The thickness of this layer was about 40 nm for the film prepared on iron plate. The mechanical properties of the film have been investigated. The films formed by IBED exhibited high hardness, improved wear resistance and low friction.

INTRODUCTION

Titanium nitride film as a coating layer is useful in improving wear and corrosion resistance properties of metals [1] because of its high hardness and good chemical stability. The commonly used methods for preparing such films are still limited in application for reasons, such as high temperature processing, insufficient adhesion of film to substrate etc. The technique of ion beam enhanced deposition (IBED) is one of the newest areas being investigated in respect to modifying surface properties of solids [2-3]. By combining ion implantation with various kinds of deposition, thick, dense and strongly adhesive coating films can be produced. R.A. Kant et al. [4] and B.D. Sartwell [5] have synthesized titanium nitride films by IBED in a chamber backfilled with nitrogen gas. Results showed that the films consisted of TiN crystallites with no preferential grain orientation and the surface was flat and smooth with no indication of porosity. Also the films showed strong adhesion, low friction and wear. The results of M. Kiuchi et al. [6] showed that titanium nitride films formed by IBED had columnar structure with (111) axes preferred orientation. In this paper, we present our work on synthesis of titanium nitride films by alternate Ti-deposition and N⁺-implantation in a processing chamber of higher vacuum. Results on the composition, structure and mechanical properties of the film will be discussed.

EXPERIMENTAL

The growth of titanium nitride films was carried out in an Eaton Z-200 Ion Beam Enhanced Deposition System. The system has

been described in a previous paper [7]. The base pressure in the processing chamber was 10^{-7} Torr, and reached a magnitude of 10^{-6} Torr during processing. Polished sample substrates were made of 40CrNiMo steel, graphite, silicon, rocksalt and iron for different measurements. In order to reduce the oxygen contamination to the film we adopted a titanium deposition rate of 10Å/sec. Because the nitrogen current density which could be obtained in the equipment is only about $40\mu\text{A}/\text{cm}^2$ at 40 KeV, so the process of alternate titanium deposition and nitrogen implantation is arranged to meet the atomic arrival ratio of nitrogen to titanium. The deposited titanium thickness in each cycle is 20 nm. The normal of the substrate was commonly put at 45° to both ion incidence and vapor flux. RBS, AES, TEM, XPS, X-ray diffraction and electron diffraction were used in the investigation of films.

RESULTS AND DISCUSSIONS

Composition control

Samples with graphite substrates were used in RBS analysis. Fig.1 shows the spectrum of a film, with the atomic arrival ratio (N/Ti) of 0.75:1. The concentration ratio of titanium, nitrogen, and oxygen obtained at their maxima in the spectrum is 1:1.1:0.15.

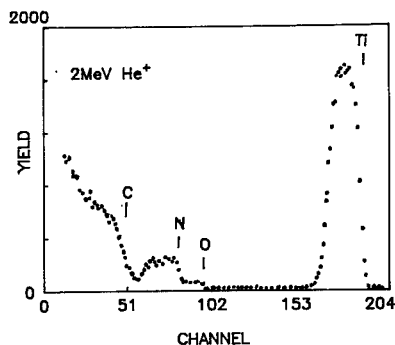


Fig.1 Typical backscattering spectrum of titanium nitride film produced by IBED on graphite substrate.

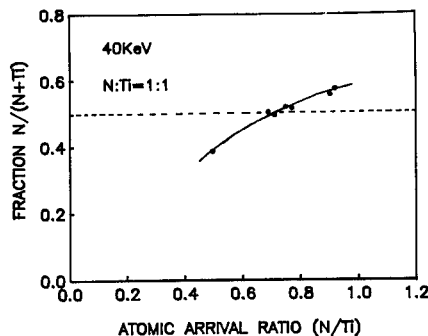


Fig.2 Component ratio $N/(N+Ti)$ in film as a function of atomic arrival ratio N/Ti .

The relationship between the film composition and the atomic arrival ratio (N/Ti) obtained from RBS analysis is shown in Fig.2. The component ratio of nitrogen to titanium of the film is nearly the stoichiometric value when the arrival ratio of nitrogen to titanium is 0.73:1. This situation is mainly related to both nitrogen absorption of the growing film from the residual gas and sputtering of the deposited titanium during ion bombardment.

Component depth profiles

Component depth profiles of the film were obtained using Auger electron spectroscopy combined with argon ion sputtering. Auger peak-to-peak heights for titanium, nitrogen, oxygen, carbon, and iron were obtained as a function of sputtering time. The calculation method of the component ratio of nitrogen to titanium can be seen in article by P.T. Dawson and K.K. Tzatzov [8].

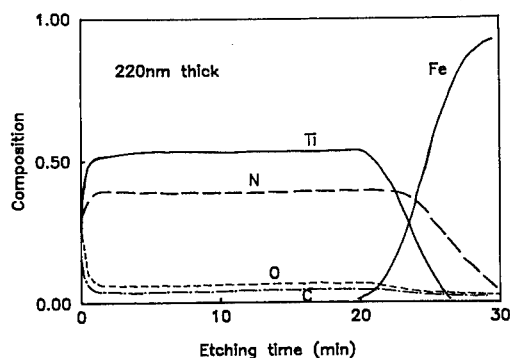


Fig.3 AES depth profiles of a titanium nitride film on iron substrate.

Fig.3 shows the AES measured component depth profiles of a titanium nitride film formed on iron substrate. We can see the contents of titanium and nitrogen increase away from the surface and decrease gradually after passing through a fairly flat maximum and the film composition is of N/Ti=0.75:1. The oxygen and carbon contamination is heavier at the surface, but reduced rapidly to a constant value with increasing depth. The concentration of oxygen in the film is only 6%, less than that in the film deposited without nitrogen ion implantation. There is a transition region from the film to the substrate, and the thickness of the intermixed layer is about 40nm, in agreement with the result obtained from cross-sectional TEM photograph, shown in Fig.7.

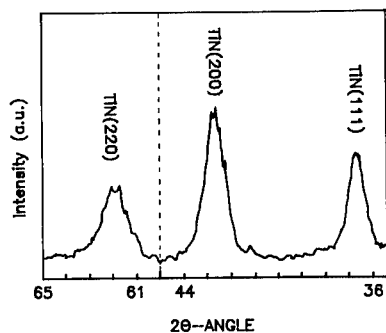


Fig.4 X-ray diffraction of Cu-K α X-rays from a specimen.

Phase and texture

Fig.4 shows the X-ray diffraction spectrum of the film on a (111) silicon wafer. It can be seen that the film is mainly composed of TiN crystallites with random orientation, no phase of Ti_2N is detected. These results also can be obtained from the TEM photograph and the electron diffraction pattern of a film, picked up from a rocksalt substrate, which is shown in Fig.5. It can be estimated that the typical grain size is 30-40nm, similar to the results of R.A. Kant et al. [4].

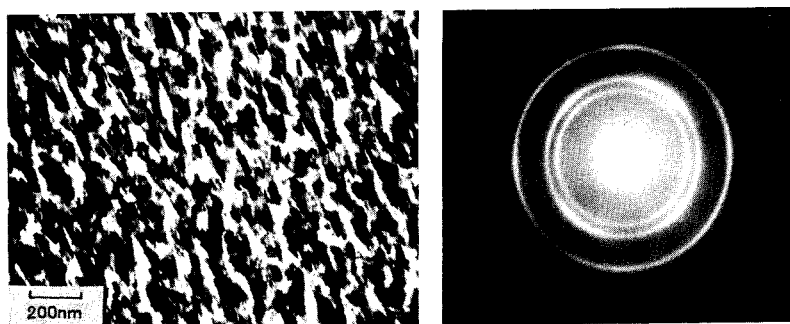


Fig.5 Transmission electron micrograph and corresponding diffraction pattern of a titanium nitride film.

The XPS study was carried out for a specimen with a iron substrate using an ESCA 650, which has a basic vacuum pressure of 3×10^{-9} Torr. In order to detect the inner state of the film, a thin top layer (~ 50 nm) of the film was sputtered off by a 5 KeV argon ion beam impinging at 45° to the substrate normal. Fig.6 shows the spectrum of Ti-2p photoelectrons obtained by $Al-K_\alpha$ irradiation. We can see a peak at 454.9 eV due to Ti-2p ($3/2$) electrons of Ti-N bonding, but no peak at 453.8 eV for metal titanium. We note that there also exists a small peak at 458.5 eV corresponding to the Ti-O bonding. The peak at 461 eV arises from Ti-2p ($1/2$) electrons.

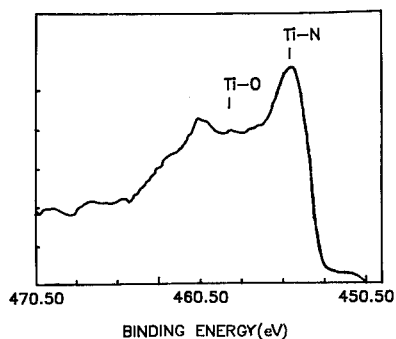


Fig.6 XPS spectrum of Ti-2p photoelectrons after 70 minutes sputtering of the specimen.

From the spectrum of N-1s electrons, a peak at 396.5 eV

can be seen, which corresponds to Ti-N bonding and differs from the 399 eV peak of nitrogen only. These results mean that titanium is mainly bonded to nitrogen, which is consistent with the X-ray diffraction analysis.

Fig.7 is a cross-sectional TEM photograph of an IBED processed silicon sample. We can see, the film seems dense and no porosity at the bottom region of the film. Then, the film grows in a columnar structure with the direction normal to the surface. Under the film there exists an intermixed layer between the titanium nitride film and the silicon substrate, and a nitrogen implanted silicon region. The layered structure of the implanted region might be on the intermittent implantation during film growth.

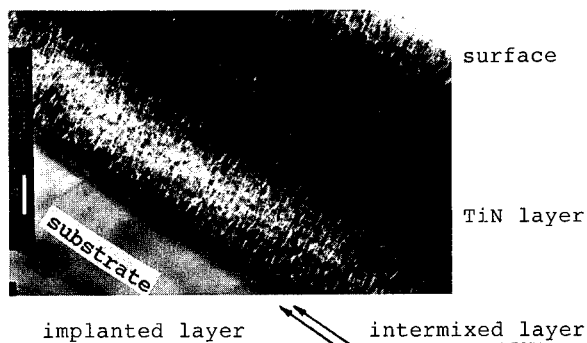


Fig.7 The cross-sectional TEM photograph of a titanium nitride film formed on silicon substrate.

Mechanical properties

40CrNiMo steel samples, coated with titanium nitride film 1 μm thick, were used in measurements of mechanical properties of the film. The values of Knoop hardness of IBED films are shown in table I. It can be seen the Knoop hardness is in a range of 1300-2000Kg/mm² with loads changing from 5g to 25g.

Table I. Knoop hardness (Kg/mm²) of titanium nitride films formed on 40CrNiMo specimens (No.1-3) and of 40CrNiMo substrate only (No.4)

Specimen No.	Load (gf)					
	2	5	10	25	50	100
1	1094	1452	1645	1389	1138	975
2	1138	1976	2017	1462	1156	948
3	1138	1976	1970	1624	1215	948
4	—	—	—	—	—	756

With increase of the load, the Knoop hardness of the film approaches to that of 40CrNiMo substrate.

For the friction and wear test, a GCr15 ball, 1cm in diameter, was pressed against the sample surface with a 349g load and ran along a cycle on the sample disk. The tests were performed under dry sliding conditions and at a sliding rate of 10m/min. For steel substrate only, the coefficient of friction was 0.2 at the beginning, but after 1000 turns the coefficient of friction increased to about 0.6. The titanium nitride film on the 40CrNiMo steel, on the other hand, remained attached to the substrate even after 15000 turns and the friction coefficient in this case was 0.2 throughout the test. The obtained wear resistance is more than ten times of the substrate.

CONCLUSIONS

1. The titanium nitride film has been produced by alternate titanium deposition and nitrogen implantation. The film is mainly composed of TiN crystallites with random orientation and characterized by a columnar texture.

2. The titanium nitride films exhibited high microhardness, strong adhesion, and low friction and wear.

3. The thicker transition region of hundreds angstroms between the film and the substrate, which is formed during IBED process and is composed of a intermixed layer and a nitrogen implanted substrate layer, would be of great benefit to the mutual adhesion and compatibility of both.

REFERENCES

1. W. Alina, A. Erdemir, and R.F. Hochman, in Ion Plating and Implantation, edited by R.F. Hochman (American Society for Metals, 1986) pp.169-172; E.I. Meletis, A. Erdemir, and R.F. Hochman, *ibid.*, pp.173-178.
2. S.M. Rossmagel and J.J. Cuomo, *MRS Bulletin*, **16**, 40 (1987).
3. J.M.E. Harper, J.J. Cuomo, R.J. Gambina and H.R. Kaufman, *Nucl. Instrum. Meth. Phys. Res.* **B7/8**, 886 (1985).
4. R.A. Kant, B.D. Sartwell, I.L. Singer and R.G. Vardiman, *Nucl. Instrum. Meth. Phys. Res.* **B7/8**, 915 (1985).
5. B.D. Sartwell, in Ion Plating and Implantation, edited by R.F. Hochman (American Society for Metals, 1986), pp.81-89.
6. M. Kiuchi, M. Tomita, K. Fujii, M. Satou and R. Shimizu, *Japanese J. Appl. Phys.*, **26**, 98 (1987); M. Satou, Y. Andoh, K. Ogata, Y. Suzuki, K. Matsuda and F. Fujimoto, *ibid.*, **24**, 656 (1985).
7. Liu xianghuai, Xue Bin, Zheng Zhifeng, Zhou Zuyao and Zou Shichang, to be published in *Nucl. Instrum. Meth. Phys. Res. B*.
8. P.T. Dawson and K.K. Tzatzov, *Surface Science*, **149**, 105 (1985).

$B_{(1-x)}N_x$ ALLOY FILMS PREPARED BY ION BEAM ASSISTED DEPOSITION

C.A. CAROSELLA, G.K. HUBLER, D. VAN VEGHTEN* AND E.P. DONOVAN
Naval Research Laboratory, Code 4670, Washington DC 20375-5000

*Sachs Freeman Associates at the Naval Research Laboratory

ABSTRACT

We have produced alloy films of $B_{(1-x)}N_x$ ($x:0$ to 0.5) via ion beam assisted deposition (IBAD). Rutherford backscattering spectroscopy (RBS) measurements show that the stoichiometric films are achieved with a nitrogen to boron atom arrival rate of $N/B = 2.55$. The film N/B ratio for all measured compositions is fit with a model that predicts that the nitrogen sticking coefficient is 0.36 . Measurements of $B_{(1-x)}N_x$ film thicknesses with a profilometer confirm the value of this sticking coefficient. The BN film is transparent and has an refractive index that varies between 1.90 and 1.77 in the range 400 nm to 3100 nm. The refractive index data can be fit with the Sellmeier equation. Films 500 nm thick with N/B less than 0.6 appear metallic; the index decreases linearly with increasing nitrogen content. The films have two broad absorption peaks, centered at 750 cm^{-1} and 1370 cm^{-1} that correspond to BN vibrations. The characteristics of the bands suggest that the films are amorphous or a microcrystalline hexagonal phase. The Knoop microhardness of the films generally decrease with increasing N content. Stoichiometric films have a microhardness of $H_K = 20$ GPa, measured with a 25 gm load.

INTRODUCTION

Boron nitride films have attracted interest in recent years because of their potential applications as optical coatings, low coefficient of friction surfaces and wear resistant coatings. The most common technique for producing the films has been chemical vapor deposition [1]. The films usually contain hydrogen and can be amorphous or poly-crystalline (hexagonal BN phase). Ion assisted techniques have recently been investigated with some evidence of films produced in the cubic form [2]. The crystalline phase so obtained may depend on composition [3].

In this paper we report on the production of $B_{(1-x)}N_x$ films by an IBAD technique, with x varied from 0 to $.5$. E-beam evaporated boron atoms and energetic nitrogen ions (250 eV per atom) are simultaneously deposited on various substrates. The system has been well calibrated in previous work, which permits accurate knowledge of the N/B arrival rates [4]. Film compositions are measured with RBS. Optical properties and microhardness of the films are described.

EXPERIMENTAL

A schematic of the preparation chamber appears elsewhere in these proceedings [5]. A cryopumped vacuum chamber that has a base pressure of about 1×10^{-7} Torr contains a 3 cm Kaufman ion gun and a single-hearth e-beam source. The ion gun is 26 cm below the substrate mounting fixture; the e-beam source is 30 cm below. They have an angular separation of 20 degrees. A water-cooled quartz crystal monitor mounted 4.3 cm from the substrate measures the boron arrival rate and is shielded from the ion beam. Three Faraday cups surround the substrate and measure the ionic portion of the output of the ion gun, which is known to produce 89% N_2^+ and 11% N^+ [4]. The ion currents on the Faraday cups are balanced to ensure uniform deposition. Mass flow of the nitrogen through the ion gun raises the chamber pressure to 2.0×10^{-4} Torr, which for the same mass flow drops to 1.75×10^{-4} Torr during B evaporation. At this pressure, charge exchange

neutralizes 31% of the ions. These factors are accounted for when reporting the ion arrival rates. The substrates were mounted on an uncooled rotating carousel or a water-cooled plug. The uncooled samples heat to a maximum of 230 °C during film deposition; the samples on the plug reach 50 °C. Substrates were sputter-cleaned with the nitrogen ion gun prior to deposition. The boron was e-beam evaporated at 0.4 nm/sec, except for the highest N/B arrival rates where the rate was restricted to 0.3 nm/sec to accommodate the maximum achievable N ion current. Extracted ion beam current ranged from 5 to 40 mA to achieve the desired arrival rate. Computer control of the process was necessary to obtain uniform deposits because the high evaporation temperature of the boron created poor quartz crystal control of the evaporation rate. The ion beam current was adjusted dynamically to keep the arrival rate constant throughout the deposit.

Samples prepared for RBS were deposited on carbon or silicon substrates. The boron deposition thickness ranged from 100 to 400 nm. Backscattering measurements were carried out, at 1.16 MeV to measure stoichiometry in the Rutherford scattering regime, and at 2 MeV to measure film thicknesses where stopping powers are more reliable.

Samples for thickness, optical and microhardness measurements were prepared on silicon or sapphire substrates. Film thicknesses ranged from 400 to 1300 nm. Thicknesses were measured with a profilometer by finding an occasional small flaw on the edge of each sample where the substrate was exposed. Optical measurements were made in the reflectance mode on an ir-visible-uv spectrometer, and in the transmission mode on a Fourier transform infra-red spectrometer (FTIR). Index of refraction was extracted from these measurements with the techniques described by Donovan et al. at this conference [5]. Microhardness measurements are made with a Knoop diamond indenter at 25 grams load. The film thickness is always greater than the indenter penetration depth. The polished (100) silicon substrate had a measured Knoop hardness, $H_K = 9.2$ GPa at 25 gm load.

RESULTS

Figure 1 is an example of RBS data, shown here for a near-stoichiometric BN film, 885 nm thick, deposited on a silicon substrate. Figure 2 shows the RBS determined nitrogen to boron ratio in the films plotted against the N/B arrival rate ratios determined as described above. The N/B film ratios are found by fitting the data with the code RUMP [6].

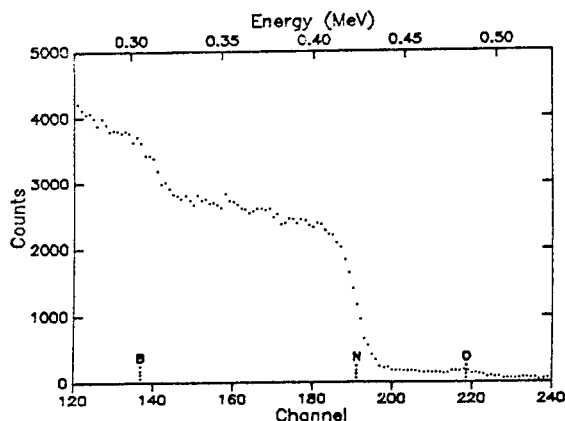


Fig 1. The RBS spectrum for the film N/B = 1.07. This film contains 1.6 at% oxygen and 51 at% nitrogen. The O content is less in all other BN films, and indicates an insufficient vacuum pump-down for this run.

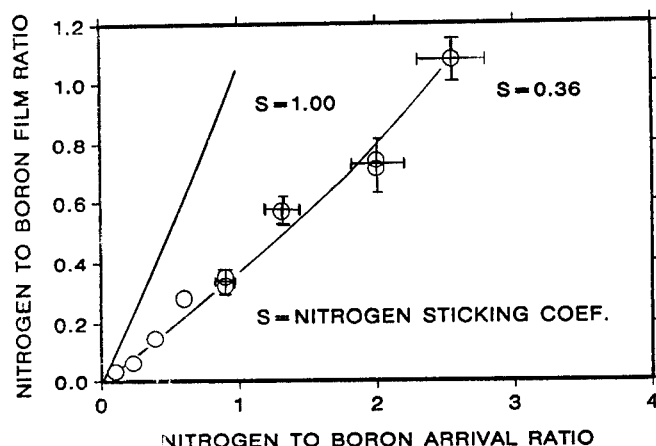


Fig 2. The N/B film ratio derived from RBS data versus the N/B atom arrival ratio. The data is fit with a model that assumes the B sputtering coefficient is 0.04, and predicts that the N sticking coefficient is $s=0.36$. The fit with $s=1.0$ is shown for comparison.

The fits to the data of Figure 2 use a phenomenological model for the IBA process [7]. The model uses 0.04 for the sputtering coefficient of boron by 250 eV N, found from a computer calculation (TRIM) [8]. Assuming that all incident nitrogen atoms stick to the surface then the curve labeled $s=1.00$ results. The slight upward curvature of this line is due to the boron sputtering. $s=0.36$ plus or minus 0.03 fits the RBS data.

The film thickness data are shown in Figure 3. Plotted is the normalized thickness of the film versus the adjusted N/B arrival ratio. (The arrival ratio is adjusted upward to account for B sputtering.) The curve labeled $s=1$ is the predicted thickness of an appropriate mixture of boron (density = 2.34) and BN (density = 2.3). The line through the data is the calculation with the N sticking coefficient $s=0.36$.

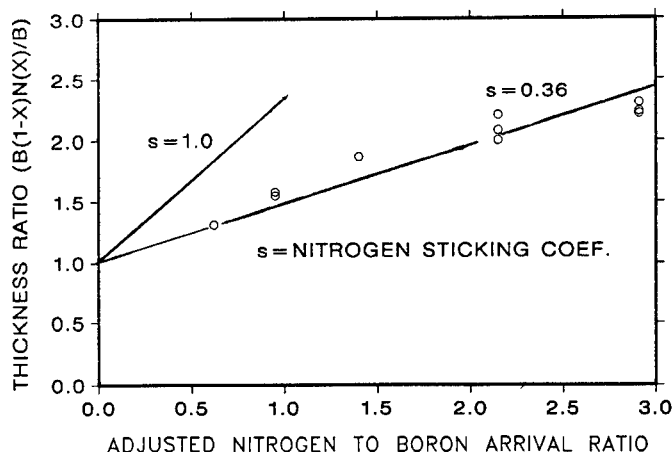


Fig. 3. The measured film thickness ratio of $B(1-x)N_x/B$ versus adjusted N/B arrival rate. The curves are predicted thickness ratios for the nitrogen sticking coefficient $s=1.0$ or $s=0.36$.

Optical data are shown in Figures 4 and 5. The refractive index, n of the films decreases with increasing N content. The data are fit nicely with a straight line. Although not shown here, the films become less absorbing with increasing N content. For a film N/B ratio less than about 0.6 and thickness of about 500 nm the films appear metallic. For films with N/B greater than about 0.8, the films show interference colors on silicon substrates, indicating good transparency. $B_{.5}N_{.5}$ deposited on a transparent sapphire substrate and 1150 nm thick is transparent with a slight tan color. The optical data for this sample confirms low absorption through the visible spectrum. The index of refraction variation with wavelength for the BN film fits the Sellmeier equation

$$n = [(0.682)(3.614 + (1 - \nu^2/1.45 \times 10^9)^{-1})]^{1/2} \quad (1)$$

where ν is the wavenumber in cm^{-1} [9]. n is accurate to 2%, based on either the accuracy of the reflectivity or film thickness measurements.

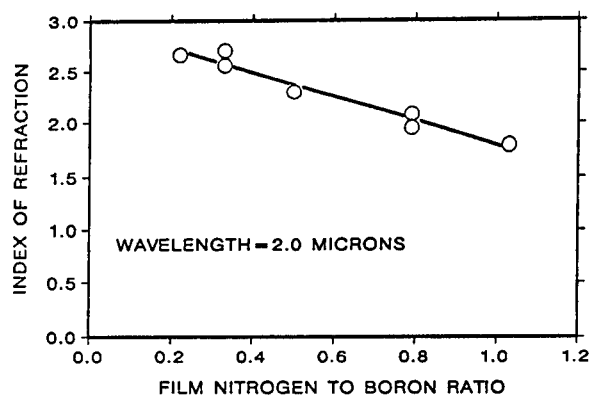


Fig. 4. The index of refraction of the alloy $B_{(1-x)}N_x$ at 2000nm.

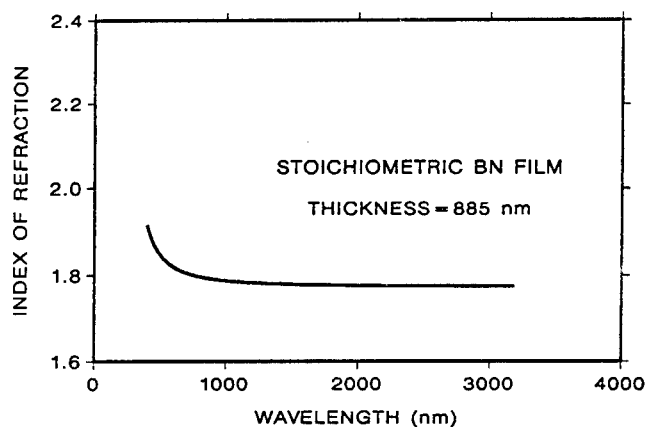


Fig. 5. The index of refraction of $B_{.5}N_{.5}$. The film is 8850 nm thick. The data fit the Sellmeier equation.

The FTIR spectra for an alloy film on Si is shown in Figure 6. There are two prominent absorption peaks due to the film, centered at 750 cm^{-1} and 1370 cm^{-1} . The peaks are attributed to BN vibrations in hexagonal BN [10]. There is no evidence of an absorption peak at 2500 cm^{-1} which would indicate the presence of BH bonds. A boron hydride peak is only observed in films of pure boron that density measurements reveal to be $1/3$ porous.

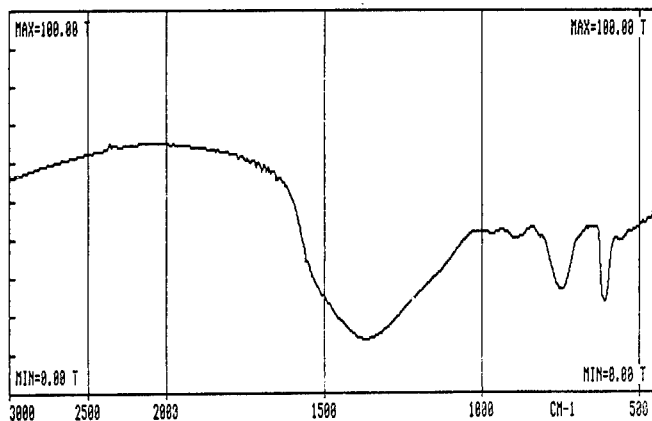


Fig. 6. The FTIR transmission spectrum of a 6600 nm $B_{0.56}N_{0.44}$ film on silicon. The peaks at 750 cm^{-1} and 1380 cm^{-1} are attributed to vibrations of hexagonal BN. The other prominent absorption is due to the silicon substrate. Thin-film interference of the film on the Si is also evident.

The microhardness of the films is shown in Figure 7. The hardness generally decreased with increasing nitrogen content. The microhardness of boron single crystal material is 30 GPa and is shown for comparison [11]. The diamond indents in the thin films are well defined. There is no evidence of microcracking or spallation due to the indents.

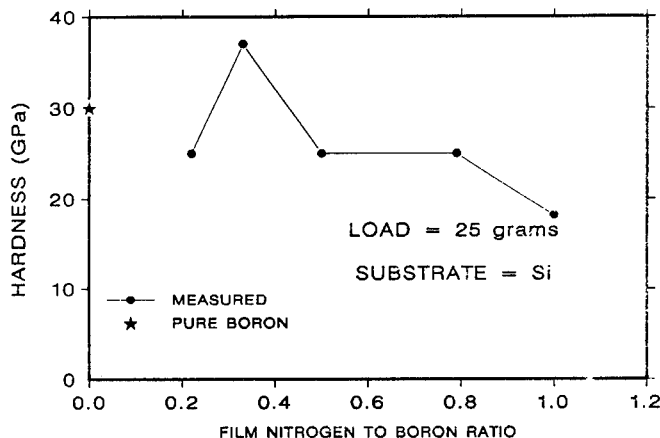


Fig. 7 The Knoop microhardness of the $B_{(1-x)}N_x$ films. The measured films were thicker than the penetration depth of the diamond indenter. The substrate hardness was 9.2 GPa.

DISCUSSION

The IBAD technique can clearly be used to produce stoichiometric BN films. However, the BN IBAD process is quite different from our earlier experiences with the IBAD formation of Si_3N_4 , where data suggest that the sticking coefficient, s of N is 0.9 [7]. s for the BN IBAD process is 0.36. The heat of formation for BN is -60 kcal/mole and for Si_3N_4 is -178 kcal/mole, which gives about the same value per atom of B or Si [12]. Therefore simple thermodynamic arguments cannot account for the differences in observed sticking coefficients. The kinetics of the solid state reactions must differ for the two cases.

The FTIR data suggest that the films are amorphous or perhaps a microcrystalline hexagonal phase. A recent paper by Sainty et al. gives high resolution electron microscopy data that show their IBAD BN films are "...a tangled network of hexagonal ribbons of random orientation." [13]. Data on film properties presented here agree closely with their work. Index of refraction and hardness data are very similar. The density of our material, inferred from thickness measurements, is consistent with that of hexagonal BN (2.3 gm/cm^3). The conclusion is that the BN IBAD-prepared films reported here may be in a microcrystalline hexagonal phase.

REFERENCES

1. K. Nakamura, J. Electrochem. Soc. 33, 1120-1123 (1986).
2. Y. Andoh, K. Ogata, Y. Suzuki, E. Kamiyo, M. Satou and F. Fujimoto Nuclear Instr. and Methods B19/20, 787-790 (1987)
3. M. Satou, K. Yamaguchi, Y. Andoh, Y. Suzuki, K. Matsuda and F. Fujimoto Nuclear Instr. and Methods B7/8, 910-914 (1985).
4. D. Van Vechten, G.K. Hubler and E.P. Donovan, J. Vacuum Sci. and Tech. A6, 1934 (1988).
5. E.P. Donovan, C.A. Carosella and D. Van Vechten, MRS Symposium A (November 1988).
6. L.R. Doolittle, Nucl. Instru. Methods B9, 344 (1983).
7. G.K. Hubler, J. Mat. Science and Engin. (Proceedings of the 1988 SM²IB Conf.) To be published (1989).
8. J.P. Biersack and L.G. Hagmark, Nucl. Instru. Methods 174, 257 (1980).
9. E. Hecht and A. Zajak in Optics, Addison Wesley, Reading, MA (1979).
10. T.H. Yuzuriha and D.W. Hess, Thin Film Solids 40, 199-207 (1986).
11. A.A. Ivan'ko in Handbook of Hardness Data, NTIS, Springfield, VA (1971).
12. C.A. Davies, J.R. Downey, D.J. Frarip, R.A. McDonald and A.N. Syverd J. Phys. Chemical Reference Data 14 Suppl #1, (1985) [JANAS Thermochemical Tables, 3rd Edition].
13. W.G. Sainty, P.J. Martin, R.P. Netterfield, D.R. McKenzie, D.J.H. Cockayne and D.M. Dwyer, J. Appl. Phys. 64(8), 3980-3986 (1988).

ANALYSIS OF NITROGEN, BORON, AND HYDROGEN OF i-BN FILMS FABRICATED BY THE ION BEAM ASSISTED DEPOSITION

J-P. Hirvonen* and J.K. Hirvonen**

*Department of Physics, University of Helsinki, 00170 Helsinki, Finland

**Spire Corporation, Patriots Park, Bedford, MA 01730

ABSTRACT

The concentrations of the main constituents of hard i-BN films produced by the ion beam assisted deposition were measured using the nuclear resonance reactions $^{11}\text{B}(p,\gamma)^{12}\text{C}$ at $E_p = 163$ keV, and $^{15}\text{N}(p,\alpha)^{12}\text{C}$ at $E_p = 429$ keV, respectively. The hydrogen contamination of the samples was investigated using the forward recoil spectroscopy (FRES) technique with a 2 MeV He^+ beam. Some complementary analyses of carbon and oxygen were performed using (d,p) and (d, α) -reactions.

Hyperstoichiometric boron concentration were found in almost all films. The relative concentrations of nitrogen and boron were also slightly dependent on the deposition conditions as well as the deposition temperature. Contrary to this, hydrogen contamination, that was generally at a low level with few exceptions, was more independent of these parameters.

INTRODUCTION

Strong activation involved in many ion beam assisted deposition processes does not only improve the quality and performance of stable compound films, e.g. titanium nitride, but also allows the formation of metastable structures with novel properties. Among these, diamond and diamond-like, as well as hard boron nitride films, are of special interest due to the many superior characteristics.

Deposition of compound films is generally complicated because beside of many other parameters the composition of the film must be controlled with a good accuracy. Ion beam processes, being normally far from the equilibrium conditions, require special attention in this respect. The increased chemical activity of ionized species also attracts many impurities, and contamination with carbon, oxygen, and hydrogen are common in many practical coatings [1].

In this study we have analyzed the boron and nitrogen concentrations in BN films produced by ion beam assisted deposition (i.e. i-BN films). It is assumed that the main properties of the films is determined by the boron to nitrogen ratio. That is why the effect of the process parameters on this ratio is essential to know. In addition, impurities, especially the hydrogen contamination, was examined. Hydrogen is known to possess the active role in hydrogenated i-C films occupying unfilled tetrahedral bondings [2]. On the other hand, in ion-plated hard BN films deposited using NH_3 gas, high concentration of hydrogen has been observed [2]. Moreover, IR spectroscopy has revealed H-B bonding in these films [2]. For this reason, the incorporation of hydrogen could be expected also in the case where hydrogen is available only as a contaminant in the process.

METHODS AND MEASUREMENTS

Hard i-BN films were produced on silicon substrates by ion beam assisted deposition. Boron was evaporated with an electron beam gun simultaneously with nitrogen ion bombardment. The unanalyzed beam contained both N^+ and N_2^+ ions and the acceleration voltage was varied between 600 and 1000 V. Depositions were performed both at ambient and elevated (up to 400 °C) temperatures. A total of nine samples were examined.

The concentrations of boron and nitrogen were measured using the nuclear resonance reactions $^{11}B(p,\gamma)^{12}C$ at $E_p = 163$ keV, and $^{15}N(p,\alpha\gamma)^{12}C$ at $E_p = 429$ keV, respectively. The width of the $^{15}N(p,\alpha\gamma)^{12}C$ resonance at $E_p = 429$ keV is extremely narrow, $\Gamma = 120$ eV [3], allowing precise depth profiling. In this case the depth resolution was determined by the energy resolution of the accelerator used, 400 eV (FWHM) at the energy involved. This corresponds to a depth resolution of 5 nm at the surface of the BN sample. The width of the $^{11}B(p,\gamma)^{12}C$ resonance at $E_p = 163$ keV is, on the contrary, very broad, $\Gamma = 5.7$ keV [6]. In this case the depth resolution was determined by the width of the resonance alone. Consequently, the depth resolution of the boron profiling is only 40 nm at the surface of the BN sample. Because of the low energy of the $^{11}B(p,\gamma)^{12}C$ resonance the molecular beam H_2^+ at the acceleration voltage ≥ 326 kV was used. Both in the nitrogen and boron case the γ -rays were detected using a NaI(Tl) detector 12.7×10.2 cm² in size. The measured γ -ray yields were converted into the absolute concentrations with the help of TiN and TiB₂ calibration samples, respectively.

Hydrogen analysis was performed with the forward recoil spectroscopy (FRES) technique [5] using the He⁺ beam at an energy of 2 MeV. For the determination of the absolute hydrogen incorporation the FRES spectrum from Kapton® was used together with the aid of the computer program RUMP [6]. Complementary analyses of oxygen and carbon were carried out utilizing the deuterium reactions $^{12}C(d,p)^{13}C$, $^{16}O(d,p)^{17}O$, and $^{16}O(d,\alpha)^{14}N$ [7,8] at the energy of $E_d = 925$ keV.

The nitrogen, boron, and hydrogen analyses were performed on all samples, whereas the carbon and oxygen analyses were carried out only on the selected samples.

RESULTS AND DISCUSSION

Shown in Figs. 1 and 2 are examples of nitrogen and boron distributions in two different i-BN films. The sample #1103 can be found to be formed mainly of the main constituents boron and nitrogen with the average ratio $[B]/[N] = 1.5$. In the case of the sample #0626 the nitrogen distribution is very inhomogeneous and the sum of the boron and nitrogen concentrations deviates essentially from 100 %. This indicates the presence of an extra constituent which was verified later with deuterium measurements.

The hydrogen contamination varied strongly. In most cases the contamination was small but detectable, e.g. 0.2-2.0 at.%. The surface contamination, however, was always very pronounced. In Fig. 3 can be seen the FRES spectra from the samples #0626 and #0121. The hydrogen contamination of the former sample was the smallest of the samples examined. The incorporation of hydrogen in the sample #0121 was the highest observed, and the average concentration corresponds to 12 at.%. High hydrogen

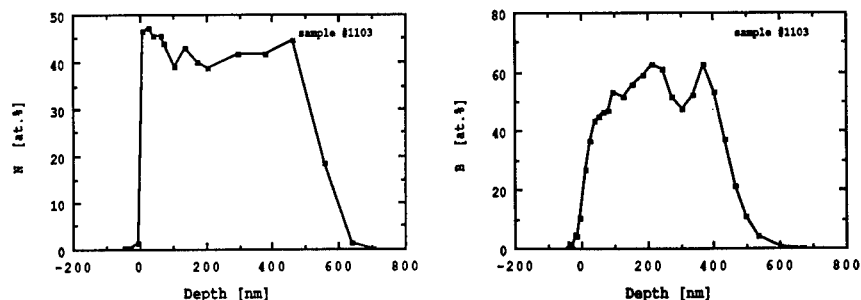


Fig. 1. Nitrogen and boron distributions in the sample #1103.

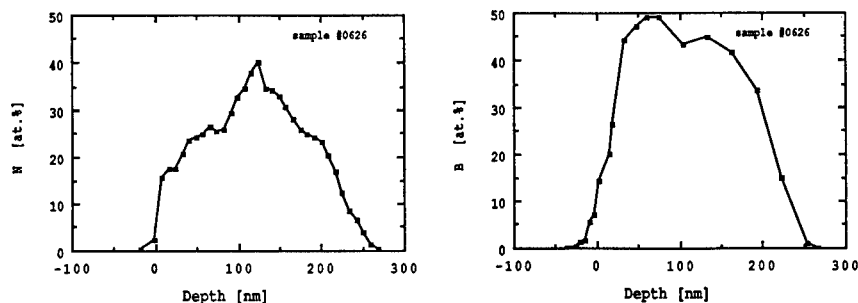


Fig. 2. Nitrogen and boron distributions in the sample #0626.

concentration ($[H] \geq 3.0$ at.%) were measured in three samples, two of which were deposited at the elevated temperature (400 °C).

Deuterium induced particle spectra were also taken from some selected samples. Shown in Fig. 4 are spectra from the samples #0626 and #0121. The signals from different elements are indicated in the figure. The most striking feature in the case of the sample #0626 is the strong signal from the $^{12}\text{C}(d,p)^{13}\text{C}$ reaction. Because the sum of boron and nitrogen in this sample was much less than 100 % (Fig. 2), it can be concluded on the basis of the Fig. 4 that carbon is the third main constituent of this film. This carbon contamination has been traced back to originating from the electron beam inadvertently striking the graphite crucible containing the boron evaporation charge. Because the boron concentration profile in this sample was much more uniform than that of nitrogen, it seems evident that carbon substitute nitrogen in this structure.

The highest level of hydrogen contamination (i.e. 12 at.%) was seen in sample #0121 and is attributed to contamination from residual water vapor and hydrocarbons in the vacuum. In both samples of Fig. 4 detectable amount of oxygen is visible. The oxygen signal was of the same order in all samples. However, in the case of the sample #0121 with the high hydrogen contamination the oxygen signal is slightly stronger indicating that at least part of hydrogen originates in water vapor and that some water is incorporated in the film.

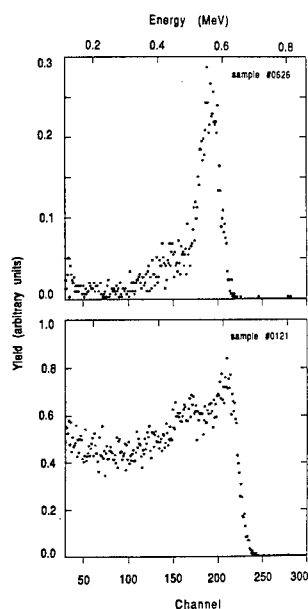


Fig. 3. FRES spectra of the samples #0626 and #0121.

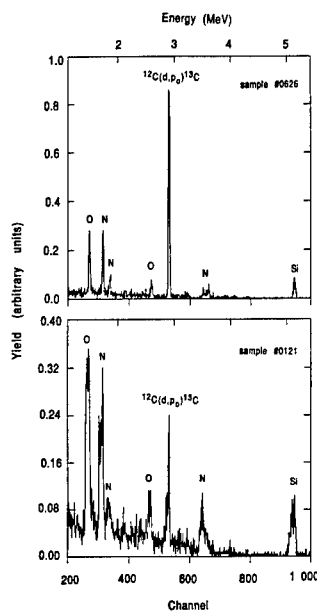


Fig. 4. Deuterium induced particle spectra of the samples #0626 and #0121.

To relate the composition of the samples to the deposition conditions the $[B]/[N]$ ratio was plotted as a function of the quantity R defined as:

$$R = \frac{\text{ion beam current density } (\mu\text{A}/\text{cm}^2)}{\text{arrival rate of evaporant } (\text{\AA}/\text{s})}$$

In Fig. 5 the data for the deposition at room temperature as well as for elevated temperatures are shown. In the room temperature case only the samples with the low contamination level and reliable analysis were involved whereas in the case of the elevated temperature all three samples have been taken into account. The general tendency, as can also be expected, in both cases is the increasing $[B]/[N]$ ratio with the decreasing R . In almost all cases the hyperstoichiometric boron concentration was observed. This is consistent with the observation of Weissmantel et al., who reported the boron concentrations from almost 100 % to 50 % in their i-BN films fabricated with the ion-plating technique [2]. Moreover, as can be seen in Fig. 5 the elevated temperature seems to favor the hyperstoichiometric boron concentrations.

The chemical composition of the i-BN films seems to have good correlation with the mechanical properties. In most cases a high $[B]/[N]$ ratio causes high friction [8], although this behavior is not absolutely unambiguous and depends also on the material of the countersurface in the wear and friction test. A high hydrogen concentration also weakens the mechanical properties, and the sample #0121 with the hydrogen concentration of 12 at. % revealed a brittle fracture type damage in the wear and friction test and also failed in the scratch type adhesion test [8].

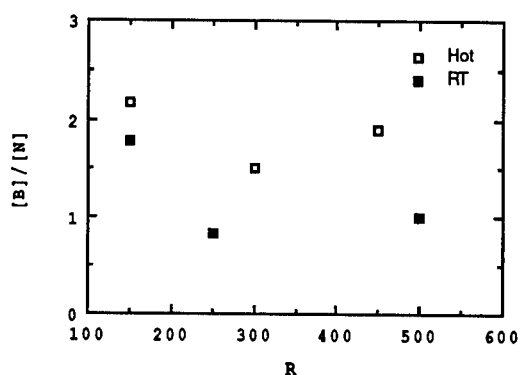


Fig. 5. The dependence of the $[B]/[N]$ ratio on the deposition parameters.

It is interesting to note that the sample with the highest carbon contamination possesses the best tribological properties. This is probably due to the formation of boron carbide. Nitrogen implantation has been shown to improve further the dry sliding properties of boron carbide [9]; the situation that is close to this particular case.

CONCLUSIONS

A comprehensive chemical analysis based on the ion beam methods has been performed on several i-BN films. All films except one had the hyperstoichiometric boron concentration. The ratio $[B]/[N]$ approached the theoretical value at the high current densities of the nitrogen beam in the room temperature depositions.

In three samples high hydrogen contamination was found although the pure nitrogen was used in the ion beam. This impurity level is related to the mechanical behavior of the film. In one case high carbon contamination was observed and correlated with improved mechanical properties.

ACKNOWLEDGEMENTS

The authors wish to thank their ancient forbears for the opportunity to collaborate on this study.

REFERENCES

1. J-P. Hirvonen, R. Lappalainen, A. Anttila, and E. Sirviö, *Proceedings of the 1st International Conference on Plasma-Surface Engineering, Garmisch-Partenkirchen, FRG, in press (1988)*.
2. C. Weismantel in *Thin films from Free Atoms and Particles*, edited by K.J. Klabunde (Academic Press, INC, New York, 1985) p. 153.
3. B. Maurel and G. Amsel, *Nucl. Inst. Meth.* 218, 159 (1983).

4. F. Ajzenberg-Selove, Nucl. Phys. A433, 69 (1985).
5. L.C. Feldman and J.W. Mayer, *Fundamentals of Surface and Thin Film Analysis* (North Holland, 1986) p.31.
6. L.R. Doolittle, Nucl. Inst. Meth. B9, 344 (1985).
7. G. Amsel, J.P. Nadai, E. D'Artemare, D. David, E. Girard, and J. Moulin, Nucl. Inst. Meth. 92, 481 (1971).
8. T.G. Tetreault, J.K. Hirvonen, G. Parker, and J-P. Hirvonen, this symposium.
9. M. Nastasi, R. Kossowsky, J-P. Hirvonen, and N. Elliot, J. Mat. Res., in press (1988).

A NEW APPARATUS FOR DYNAMICAL ION BEAM MIXING

M. JAULIN, G. LAPLANCHE, J. DELAFOND
Laboratoire de Métallurgie Physique (U.A. 131, CNRS)
40, Avenue du Recteur Pineau 86022 POITIERS (France)

S. PIMBERT-MICHAUX, UNIREC
B.P. 50, 42702 FIRMINY (France)

A new apparatus for dynamical ion beam mixing has been developed in our laboratory. The system is based on deposition by ion beam sputtering concurrently with ion beam implantation. It operates under a vacuum of 10^{-5} Pa before deposition and 10^{-3} Pa during deposition.

The ion source, with a cross section area of 45 cm^2 , produces a high current intensity (up to 250 mA) at low energy (a few eV to 2000 eV). It is possible to use either inert or reactive species for the deposition, depending on the required application.

For the ion beam mixing, we use a classical implantor with energies range from 20 to 200 keV.

This technique allows us to synthesize deposits of different materials, either from pure elements or from compounds.

We will apply this technique to develop two types of coatings : titanium carbide and silicon carbide.

Microstructural analysis by Transmission Electron Microscopy (TEM) on $0.1 \text{ }\mu\text{m}$ thick layers have been performed as well as investigations of the tribological behavior of $1 \text{ }\mu\text{m}$ thick coatings on steel substrate (wear tests).

1. INTRODUCTION

Ion implantation is a very useful technique for the modification of surface properties of materials such as wear and corrosion. However, the small thickness of the implanted layer (about $0.1 \text{ }\mu\text{m}$) and sputtering from the surface, which impose a maximum concentration of implanted atoms, are the two major limitations of this process.

To overcome these problems, new techniques which involve ion implantation combined with a simultaneous deposition method are being developed (1,2,3,4,5,6). Now coatings of hard materials, especially refractory carbides, are of increasing interest for industrial applications.

So, in this paper, a new piece of apparatus that synthesizes adherent thin films and uses the low temperature technique of dynamical ion beam mixing (D.I.M.) is presented.

Titanium and silicon carbide films, vapor deposited from bulk materials by sputtering and assisted by a high energy Ar^+ ion beam, are studied. The tribological behavior of these films is characterized by wear tests and their microstructure by Transmission Electron Microscopy experiments.

2. EXPERIMENTAL PROCEDURES

2.1. The sputtering evaporator

It consists of the following points :

- * A vacuum system controlled by a diffusion pump, capable of achieving a residual pressure of $5 \cdot 10^{-5}$ Pa when the ion source is not operating and $5 \cdot 10^{-3}$ Pa during deposition.

- * An ion beam source of Kaufman type (7) (Oxford instrument) originally developed as ion thruster for space propulsion and optimized to obtain the highest ion beam flux for a given gas flow and power input. This ion source is suitable for material processing with well characterized ion beams : the ion current and ion energy are easily measured and independently controlled. The operating gas (inert or molecular species) is ionized inside a discharge chamber containing a tantalum cathode filament and molybdenum anode, producing the ionizing electrons. The resulting primary ions are then accelerated and extracted through two grids to give a well collimated ion beam.

This source can deliver an ion current of 200 mA for a beam diameter of 7.5 cm, for a current density of 4.5 mA/cm^2 . The highest energy of the extracted ions is about 1.5 keV.

- * A water-cooled target holder with four positions, , holding the materials to be sputtered, thus offering the possibility to change targets during the experiment.

- * A water-cooled rotating sample holder to ensure homogeneity of the deposit.

- * A thickness controller utilizing a quartz balance.

This geometry allows a deposition of about 1 Å/s over a diameter of about 10 cm, permitting simultaneous treatment of several substrates of different types.

The evaporation is carried out in a chamber connected to the implanter by a valve so that evaporation can take place independently when ion-assistance is not required.

2.2. The ion implanter

This apparatus is of the type described by Chaumont and al. (8). It consists of the following :

- * A hot cathode source of Bernas-Nier type with an extraction voltage of 30 kV.

- * A mass spectrometer to select the chosen ion.

- * A system of electrostatic scanning permitting an irradiation over an area of $5 \times 7 \text{ cm}^2$.

- * The vacuum in the implanter is ensured by different pumping group (diffusion and cryogenic pumps) allowing a vacuum of about $5 \cdot 10^{-5} \text{ Pa}$ to be obtained in the implantation chamber.

3. EXPERIMENTAL PROCEDURE

3.1. Sample preparation

Stainless steel plates ($2,5 \times 1,75 \text{ cm}$) and discs ($\phi 3 \text{ cm}$) mechanically mirror polished and ultrasonically cleaned were used as substrates for tribological tests.

SiC and TiC coatings were deposited at room temperature up to $1 \mu\text{m}$ in thickness. Ion mixing was performed in both cases with 100 keV Ar^+ ions with an ion/atom arrival rate ratio of 10^{-2} and $3 \cdot 10^{-2}$.

For T.E.M measurements, SiC and TiC coatings were deposited onto freshly cleaved NaCl substrates up to $0,1 \mu\text{m}$ thick.

3.2. Wear tests

Wear tests were performed using a pin-on disc machines without lubrication in normal room air, under an applied, load of 1.7 N, and at a rotational speed of 3 rev.min^{-1} . The pin was a spherical ball 5 mm in diameter made from bearing steel 100 C6 (A.I.S.I. 52100).

The friction force is recorded with a transducer associated with a computer.

Wear can be measured as the volume of removed matter by track length unit (Wear Lineic Density W.L.D.) as $\mu^3\text{m} / \mu\text{m}$.

WLD is measured with a profilometer associated with a X-Y table. A monitor directs the system and simultaneously calculates the WLD.

4. EXPERIMENTAL RESULTS

4.1. Microstructure of coatings (Figure 1)

The synthesized deposits were examined by transmission electron microscopy (JEOL 200 CX, operating at 200 kV).

After evaporation onto NaCl, the salt is dissolved in a water and alcohol bath and then the film is put on to a copper or molybdenum grid

TiC coatings are homogeneous, with very small grains (Fig.1 a) (about 60 Å) at room temperature. The diffraction patterns (Fig.1 b) indicate an ordered f.c.c. crystalline structure of titanium carbide.

The SiC coatings are also homogeneous at room temperature and show an amorphous structure (Fig.1 c and 1 d). An "in situ" anneal was performed : the film remains amorphous up to 1073 K. At this temperature very small crystals began to appear. The diffraction pattern shows characteristic rings of the f.c.c. crystalline structure of β -SiC

4.2. Tribological behavior of coatings

4.2.1. TiC

Thin films of titanium carbide were deposited on a stainless steel substrate (hardness : 180 kg.mm^{-2}) and on a bearing steel A.I.S.I. 52100 (hardness : 700 kg.mm^{-2}) with an ion/atom arrival rate of 10^{-2} .

Figure 2.a shows the evolution of friction during 100 revolutions and 5000 revolutions of the ball disc tribometer for the soft substrate. Up to 100 turns the friction coefficient is nearly constant with small amplitudes of oscillations (12 % around the mean value $\mu = 0.23$). After 100 turns the friction coefficient slowly increases and reaches μ mean value of about $\mu = 0.7$ after 400 turns up to 5000 turns. This value remains constant and the amplitude of oscillations considerably increases up to 50 %. We may consider that after 400 turns the coating is worn through, with some persistence of coating residues within the wear track and wear debris along the track edge as it is shown by scanning electron microscopy (fig.2 b) and by the three-dimensional profiles of wear tracks (fig.2 c).

The same procedure has been used with the hard substrate made from bearing steel A.I.S.I. 52100. The friction coefficient (Fig.3 a) is roughly the same $\mu \approx 0.23$ but this value remains constant up to

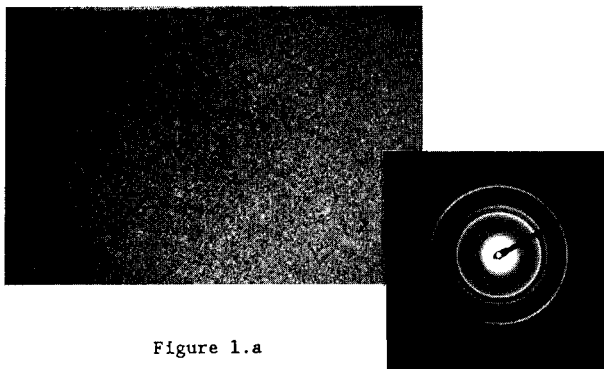


Figure 1.a

Figure 1.b

Figure 1.a : Transmission Electron Microscopy bright field image of a TiC layer vapour deposited on to NaCl with $Q = 10^{-2}$.

Figure 1.b : Transmission Electron Microscopy diffraction pattern corresponding to figure 1.a.

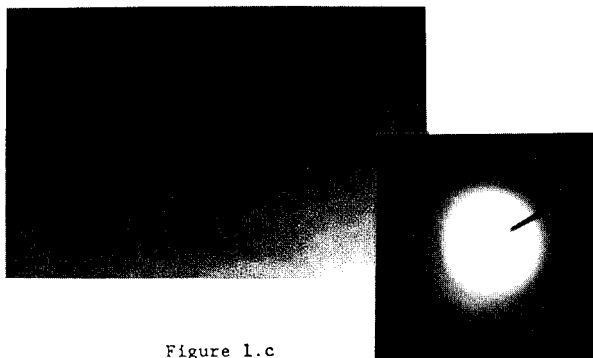


Figure 1.c

Figure 1.d

Figure 1.c : Transmission Electron Microscopy bright field image of a Si₅₀C₅₀ layer vapour deposited onto NaCl with $Q = 4 \cdot 10^{-3}$.

Figure 1.d : Transmission Electron Microscopy diffraction pattern corresponding to figure 1c.

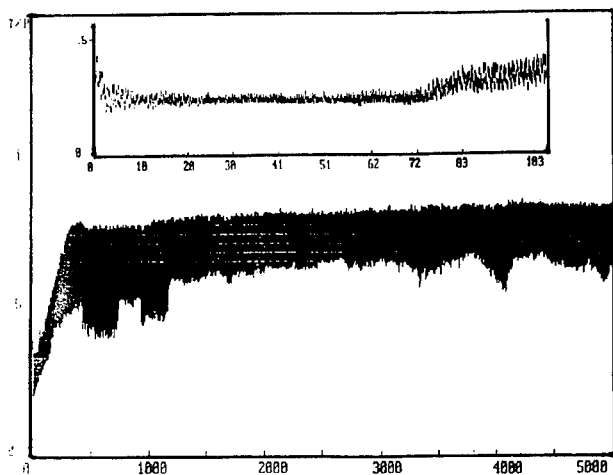


Figure 2.a



Figure 2.b

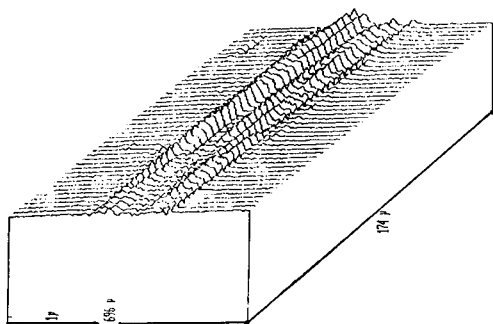


Figure 2.c

- Figure 2.a : Friction coefficient $\mu = T/P$ as a function of the number N_t of turns under an applied load of 1.7 N for TiC coating deposited on stainless steel up to 100 revolutions and up to 5000 revolutions with $Q = 10^{-2}$.
- Figure 2.b : Wear tracks on TiC coated stainless steel after 5000 turns with $Q = 10^{-2}$.
- Figure 2.c : Three dimensional profiles of the wear tracks corresponding to figure 2b.

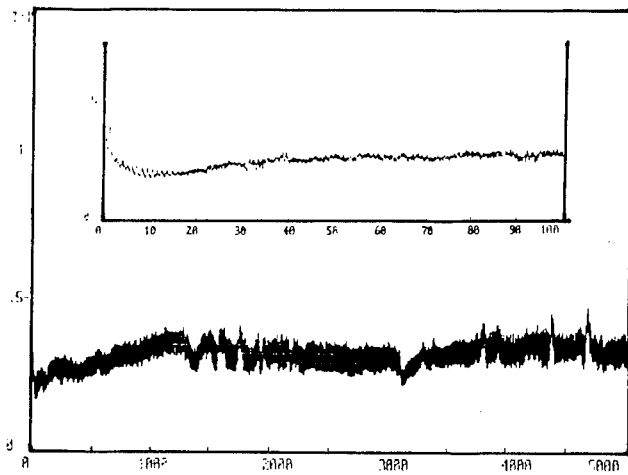


Figure 3.a



Figure 3.b

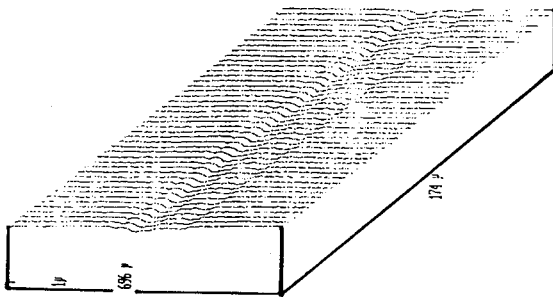


Figure 3.c

Figure 3.a : Same results as on figure 2a for TiC coated bearing-steel.

Figure 3.b : Wear tracks on TiC coated bearing steel.

Figure 3.c : Three dimensional profiles of the wear tracks corresponding to figure 3b.

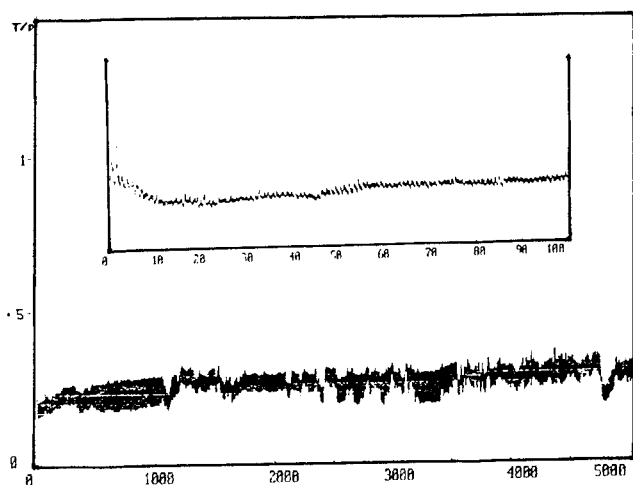


Figure 4

Figure 4 : Same result as on figure 2a with $Q = 3.10^{-2}$.

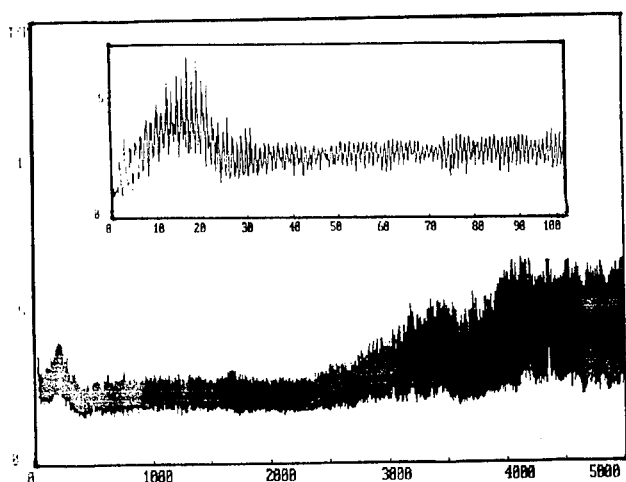


Figure 5

Figure 5 : Same results as on figure 2a for SiC coated stainless steel with $Q = 4.10^{-3}$.

5000 turns, the oscillations being significantly smaller. These tribological properties are more suitable for technical applications. S.E.M. (fig.3 b) and three dimensional profiles (fig.3 c) confirm these results. It is to be noticed that with the two substrates we have an excellent substrate/coating adhesion resulting from dynamical ion mixing.

It is well known that adherence properties strongly depend on ion/atom arrival rate Q . Considering the good results obtained with bearing steel we have tried an higher value of Q ($\approx 3.10^{-2}$). Fig 4 shows the results obtained for the friction coefficient. A slight improvement of the μ value is noticed but this fact is not necessarily significant.

4.2.2. SiC

To make a comparison we have synthesized deposits of SiC on the same soft stainless steel substrate (304) as before with an ion/atom arrival rate of 4×10^{-3} . Fig.5 shows the friction coefficient up to 100 turns and up to 5000 turns. The friction coefficient is nearly constant with small amplitude oscillation (30 %) around the mean value of $\mu \approx 0.23$ up to 2500 turns. After that the μ coefficient slowly increases and reaches a mean value of about 0,45 with a considerably greater oscillation amplitude. The TiC coating on the same substrate is destroyed after 400 turns only, the maximum value of μ being 0.7. So we can say that for similar conditions SiC coating presents better tribological properties.

5.5. CONCLUSION

The dynamical ion mixing technique shows an extremely high potential for surface coating with regard to the number of parameters which can be independently controlled. This allows one to obtain very strongly adherent coatings with compositions difficult to obtain by other methods.

REFERENCES

- [1] H. Kheyrandish, J.J. Colligon and A.E. Hill, Mat. Res. Soc. Symp. Proc. 27 (1984) 513.
- [2] R.A. Kant, B.D. Sartwell, I.L. Singer and R.G. Vardiman. Nucl. Instrum. Methods B7/8 (1985) 915.
- [3] T. Sato, K. Ohata, N. Asahi, Y. Ono, Y. Oka, I. Hashimoto and K. Arimatsu, Nucl. Instrum. Methods B19/20 (1987) 644.

- [4] L. Guzman, F. Giacomozzi, B. Mergesin, L. Calliari, L. Fedrizzi, P.M. Ossi and M. Scotoni, *Mat. Sc. Eng.* 90 (1987) 349.
- [5] P. Moine, O. Popoola, J.P. Villain, N. Junqua, S. Pimbert, J. Delafond, *Surf. Coat. Tech.* 33, (1987) 349).
- [6] N. Junqua, S. Pimbert and J. Delafond, Communication to "Journées Métallurgiques d'Automne" Septembre 1986.
- [7] H.R. Kaufman, J.J. Cuomo and J.M.E. Harper, *J. Vac. Sci. Technol.*, 21 (1982) 725.
- [8] J. Chaumont, F. Lalu, M. Salomé, A.M. Lamoise and H. Bernas, *Nucl. Instrum. Methods*, 189 (1981) 193.

**IN SITU PARAMETRIC INVESTIGATION OF THE MECHANISM
OF DIAMOND FILM DEPOSITION FROM LOW ENERGY ION BEAMS**

Y. LIFSHITZ^{*,**}, S. R. KASI^{*}, AND J. W. RABALAIS^{*}

^{*}University of Houston, Department of Chemistry, Houston,
Texas 77204-5641

^{**}On sabbatical leave from Soreq NRC, Yavne 70600, Israel

ABSTRACT

A general scheme for the analysis of deposition from hyperthermal (10-5000 eV) species is presented. Successful deposition involves consideration of species range, maximum local concentration obtainable, trapping efficiency, radiation damage, and sputtering efficiency. Examples of in situ parametric investigations of carbon deposition performed with a controlled mass selected UHV ion beam facility are presented. A subplantation model for diamond film deposition is discussed. XRD evidence for epitaxial growth of diamond(111) on Si(111) is provided.

INTRODUCTION

Hyperthermal species (energy ~1-5000 eV) are used extensively in film deposition technology in the form of plasma and ion beam techniques for fabrication of different films that include semiconductors, metals, and ceramics [1-6]. The unique advantages of using such species include: (i) epitaxial growth of crystalline films at low substrate temperatures [7-9], (ii) production of metastable (sometimes new) phases [1-6], and (iii) achieving increased film density and hardness [1-6]. Carbon containing hyperthermal species are also widely used [2,3,10,11] for production of films with interesting properties that can vary between those of the two most common carbon allotropes, namely graphite, the stable phase, and diamond, the metastable phase that usually necessitates high pressure and temperature conditions for its formation [12]. Since the work of Aisenberg and Chabot [13], many ion and plasma deposition techniques have been applied for deposition of carbon films. Hard, transparent, insulating carbon films, sometimes including a cubic diamond constituent have been deposited [2,3,10-17].

Most of the practical systems that are used for deposition from hyperthermal species have a complex chemical-physical nature where the different primary deposition parameters have a wide distribution and are difficult to

define and to control [1-6]. The impinging species usually include a mixture of different ions, free radicals, and atoms with a large spread of energy distributions and differing angles of incidence. Most of these systems operate under only high vacuum conditions ($P \geq 10^{-7}$ torr). Some of the processes involve a complex mixture of both hyperthermal and thermal species for deposition. Due to this complexity, the field of deposition from hyperthermal species is characterized by insufficient fundamental understanding. It has been recognized [1-6] that parametric studies by means of controlled, mass selected ion beam deposition (MSIBD), preferably under UHV conditions, combined with in situ diagnostics are essential for the further development of this promising field. The Houston facility [11,17,18] combines all these features. Various in situ surface analysis techniques enable the in situ characterization of layer by layer growth of the evolving film [11,16,17]. The present work deals with the fundamental mechanisms involved in deposition from hyperthermal species. Selected results of parametric investigations of carbon MSIBD conducted in Houston and Soreq NRC Israel are given to demonstrate the power of such an approach in resolving the mechanisms of carbon film deposition. The experimental and theoretical schemes presented here can be adopted for other hyperthermal species as well.

SUBPLANTATION MODEL

The process of deposition from hyperthermal species (suggested name - subplantation) bridges the gap between thermal deposition and ion implantation [19]. Well established notations from the field of ion implantation are helpful for consideration of a specific deposition scheme, depending on parameters such as type and energy of hyperthermal species and type of target. The different aspects of the deposition scheme include: (i) the range and distribution of the projectiles in a specific target, (ii) the maximum local concentration achieved in a hyperthermal deposition scheme, (iii) trapping efficiency or backscattering coefficient, (iv) damage distribution (e.g. number of atomic displacements per impinging species), and (v) sputtering yield. Fig. 1 gives calculated values for all of these quantities for C^+ impinging on C, Si and Au substrates (using TRIM [20], classical trajectory Monte Carlo simulations). Successful deposition of films involves shallow penetration range, high local concentration of deposited material, high

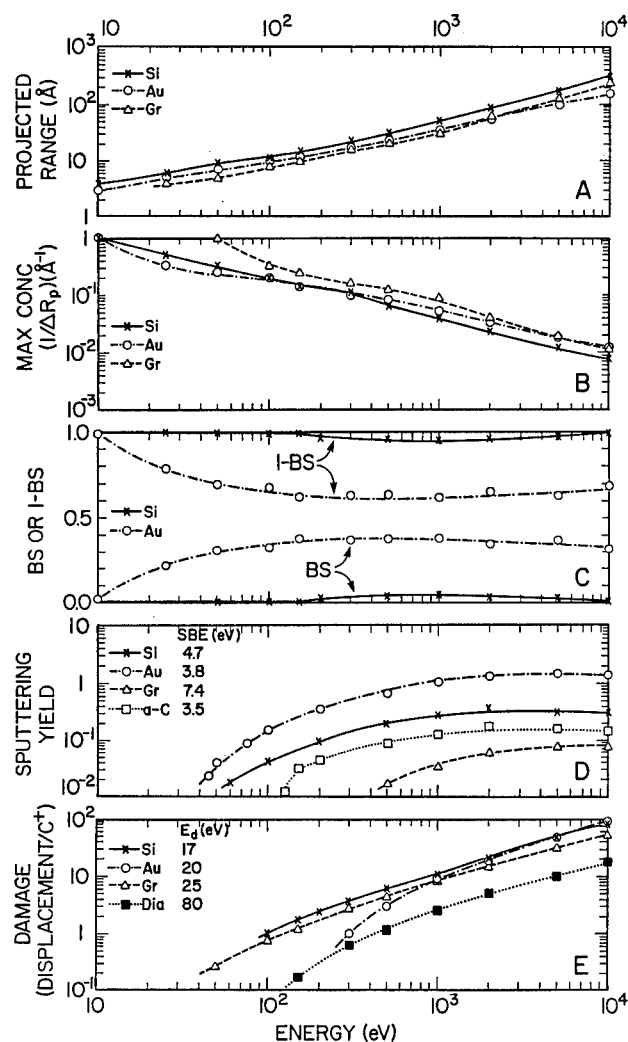


Fig. 1: TRIM [20] calculations of physical phenomena involved in deposition from the hyperthermal species 10 eV-10 keV C^+ ions on C, Si and Au: (A) range, (B) maximum local concentration ($1/(\Delta R_p)$; $\Delta R_p \equiv$ range straggling), (C) backscattering efficiency or trapping efficiency ($1 -$ backscattering efficiency), (D) sputtering yield, (E) damage (number of displacements per impinging C^+ ion). Gr = graphite; a-C = amorphous carbon; Dia = diamond; SBE = surface binding energy; E_d = displacement energy.

trapping efficiency, controlled damage, and low sputtering yield.

The deposition scheme thus necessitates a proper selection of hyperthermal species, target material and energy to meet criteria for film evolution. Other parameters, e.g. target temperature, ambient pressure, and deposition flux, are also important in tuning the properties of the deposited films. The deposition process has two distinct stages: (i) an initial stage that involves hyperthermal species - target interactions until a continuous film of a new matrix is formed (hetero-film growth stage) and (ii) growth of the evolving film by further impingement of hyperthermal species (homo-film growth). The transition from stage (i) to stage (ii) occurs only under specific conditions where the rates of processes such as diffusion and ion mixing are low enough to allow the evolution of a pure film composed of only the impinging hyperthermal species.

APPLICATION TO CARBON DEPOSITION

Three cases of carbon deposition are considered to illustrate the possibilities of initial stage evolution.

(a) 150 eV C^+ impingement on Ni at room temperature exhibits three growth stages illustrated in Fig. 2: (i) carbidic (C-Ni) stage, (ii) graphitic sp^2 (C-C) stage, and (iii) diamond sp^3 stage [16,17,19]. In this deposition scheme the carbon is

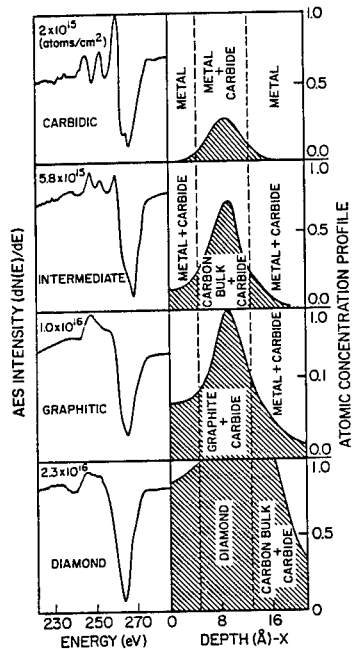


Fig. 2: Stages of diamond evolution on Ni(111) following 150 eV C^+ room temperature bombardment. Left Column - C KLL AES lineshapes for different C^+ fluences. Right Column - subsurface entrapment of energetic carbon and buildup of carbon deposits.

first implanted into the nickel subsurface where it forms a carbide. When the C^+ fluence reaches $\sim 10^{16}$ atoms/cm², a two-dimensional graphitic-like carbon structure is formed. Additional carbon deposition results in enhanced densification to form a diamond sp^3 matrix while the surface Ni atoms are sputtered and diluted so that an sp^3 diamond layer on a Ni substrate evolves.

(b) For 30 eV C^+ impingement on a Li surface, the results show that a Li carbide matrix is formed. This carbide structure does not develop to a graphitic stage even at a carbon dose of 10^{17} C^+ ions/cm² as shown in Fig. 3, i.e. ten times the fluence needed for graphitic evolution of C^+ impinging on Ni. This is due to ion mixing across the Li-C interface and possibly some Li diffusion as well.

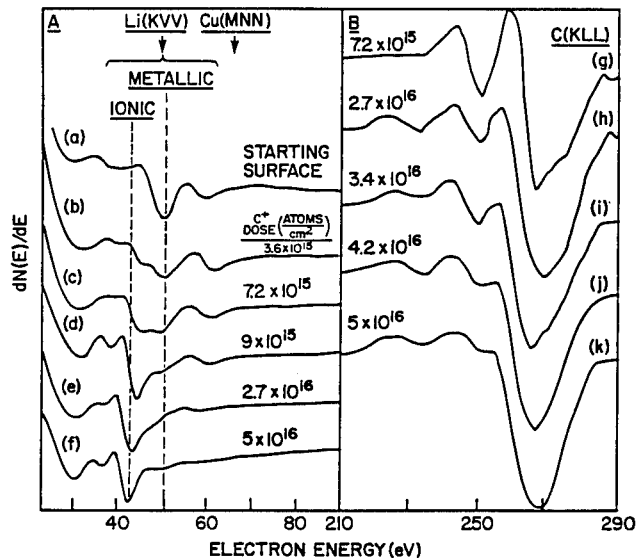


Fig. 3: Stages of film evolution on Li (surface enriched CuLi alloy) following 30 eV C^+ bombardment. Evolution of Li(KVV)(left) and C KLL(right) AES lineshapes indicate formation of Li-C and no graphite or diamond evolution.

(c) For 150 eV C^+ impingement on a Ni substrate maintained at 400°C, rapid diffusion of carbon into the bulk crystal results with no development of an enriched carbon layer on the Ni substrate.

The phase and structure of the evolving film are determined in the second stage of carbon film formation. Room temperature C^+ deposition in the energy range of 60-180 eV results in the growth of a carbon film with an sp^3 short range order [16,17] as shown in Fig. 4. Our recent "subplantation" model [19] describes the evolution of this diamond metastable phase as a combination of two effects: (i) preferential displacement of low displacement energy (LE_d) (graphitic sp^2 type) atoms, leaving the high displacement energy (HE_d) (diamond sp^3 type) atoms in their positions and (ii) the mold effect, i.e. constraints imposed by the host matrix into which the C^+ is implanted.

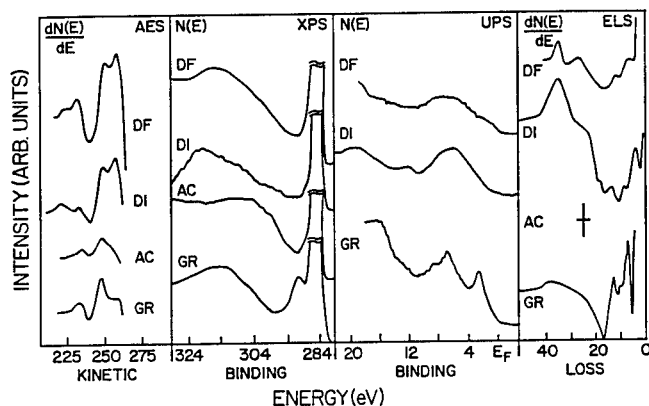


Fig. 4: Evidence for sp^3 (diamond) short range order of films deposited at room temperature by low energy (~60-180 eV) C^+ bombardment. Comparison of surface spectroscopic signatures of carbon in graphite (GR), amorphous carbon (AC), diamond (DI) and diamond films deposited using the Houston facility (DF), measured by AES, XPS, UPS and EELS. No information is presented for the UPS spectrum of AC. The vertical line drawn for AC in EELS indicates the energy loss position of the bulk plasmon peak. The data for GR, AC and DI in AES, and DI in EELS are from [21] while DI in UPS is from [22].

Finally, the possibility of achieving cubic diamond heteroepitaxial growth by carbon MSIBD is also demonstrated. XRD analysis [23] of $\sim 0.7 \mu m$ thick carbon films deposited on Si(111) at room temperature from 120 eV C^+ mass selected ions in Soreq NRC, Israel shows diamond reflections that are very well localized at their predicted positions (Table I) and indicate that (i) the diamond (111) and (220) planes are parallel to the Si(111) and Si(220), respectively, (ii) the diamond rotational spread around its $\langle 111 \rangle$ normal is $\sim 1.7^\circ$, and (iii) the mosaic block size is $\sim 150 \text{ \AA}$.

Table I: XRD evidence for diamond long range order of film deposited from 120 eV C⁺ ions in Soreq NRC, Israel on Si(111); Comparison of selected crystallographic parameters for cubic diamond, hexagonal diamond, and graphite. The measured $\Delta\chi$ (angle between reflection planes) is not exactly 35.3° solely because of a slight misorientation. Evidence for epitaxial growth is presented elsewhere [23].

	Cubic Diamond			Hexagonal Diamond (Lonsdalite)			Graphite			Measured on Deposited Film	
	hkl	2 θ	d	hkl	2 θ	d	hkl	2 θ	d	2 θ	d
2 θ	111	43.9°	2.06	002	43.9°	2.06	101	44.6°	2.03	44.0°	2.06
	220	75.3°	1.26	110	75.3°	1.26	110	77.5°	1.23	75.2°	1.26
$\Delta\chi$	35.3°			90°			80.2°			(35.1°)	

CONCLUSIONS

(1) Deposition from hyperthermal species is a process that involves a trade-off between several physical phenomena including species range, concentration profile, trapping efficiency, damage, and sputtering yield.

(2) A controlled mass selected low energy ion beam facility under UHV with in situ diagnostics is capable of both resolving the (diamond) deposition mechanisms and successfully depositing (diamond) films.

(3) Film deposition from hyperthermal species involves a first stage of substrate-species interaction followed by formation of a pure film whose structure is determined by preferential displacements and by constraints imposed by the host matrix.

(4) The possibility for heteroepitaxial growth of diamond(111) on Si(111) was demonstrated.

ACKNOWLEDGMENT

The authors are grateful to J. L. Robertson and S. C. Moss for the XRD analysis and to G. D. Lempert for deposition of thick films in Soreq NRC, Israel. This material is based upon work supported by the National Science Foundation under Grant No. DMR-8610597.

REFERENCES

1. J.M.E. Harper, et al. in Ion Bombardment Modification of Surfaces, edited by O. Auciello and R. Kelly (Elsevier Science Publishers, New York, 1984), chapter 4.
2. K. J. Klabunde, Ed., Thin Films From Free Atoms and Particles (Academic Press Inc., Orlando, FL 1985).
3. J. Mort, F. Jansen, Eds., Plasma Deposited Thin Films (CRC Press, Boca Raton, FL, 1986).
4. J. E. Greene, et al., J. Crystal Growth 79, 19 (1986).
5. T. Takagi, Thin Solid Films 92 1 (1982).
6. S. M. Rossangel and J. J. Cuomo, Vacuum 38(2), 73 (1988).
7. K. Miyake and T. Tukuyama, Thin Solid Films 92, 123 (1982).
8. P. C. Zalm and L. J. Beckers, Appl. Phys. Lett. 41(2), 167 (1982).
9. B. R. Appleton, R. A. Zuhr, T. S. Noggle, N. Herbots, and S. J. Pennycook, in Beam-Solid Interactions and Transient Processes, edited by M. O. Thompson, S. T. Picraux, J. S. Williams, (Mater. Res. Soc. Proc. 74, Pittsburgh, PA 1987) p. 45.
10. H. Tsai, D. B. Bogi, J. Vac. Sci. Technol. A 5(6), 3287 (1987).
11. Y. Lifshitz, S. R. Kasi, and J. W. Rabalais, Adv. Mater. Manu. Proc. 3(2), 157 (1988).
12. J. E. Field, The Properties of Diamond (Academic Press Inc., London, 1979).
13. S. Aisenberg and R. Chabot, J. Appl. Phys. 42(7), 2953 (1971).
14. E. G. Spencer, P. H. Schmidt, D. C. Joy, and F. J. Sansalone, Appl. Phys. Lett. 29(2), 118 (1976).
15. E. F. Chaikovskii, V. M. Puzikov, and A. V. Semenov, Sov. Phys. Crystallogr. 26(11), 122 (1981).
16. J. W. Rabalais and S. R. Kasi, Science 239, 623 (1988).
17. S. R. Kasi, Y. Lifshitz, J. W. Rabalais, and J. D. Lempert, Angewandte Chemie, Adv. Mater. 100(9), 1245 (1988).
18. H. Kang, S. R. Kasi, J. W. Rabalais, J. Chem. Phys. 88, 5882 (1988).
19. Y. Lifshitz, S. R. Kasi, and J. W. Rabalais, submitted to Phys. Rev. Lett.
20. J. F. Ziegler, J. P. Biersack, and U. Littmark, The Stopping and Ranges of Ions in Matter (Pergamon, Oxford, 1985), Vol. 1.
21. P. G. Lurie, J. M. Wilson, Surface Sci. 65, 476 (1977).
22. B. B. Pate, Surface Sci. 165, 83 (1986).
23. J. L. Robertson, S. C. Moss, Y. Lifshitz, S. R. Kasi, J. W. Rabalais, G. D. Lempert, and E. Rapoport, submitted to Science.

ION BEAM DEPOSITION OF DIAMOND-LIKE COATINGS*

ANTON C. GREENWALD, JAMES K. HIRVONEN and NARENDRA K. JAGGI**

Spire Corporation, Bedford, MA 01730

**Northeastern University, Boston, MA 02115

ABSTRACT

Mass analyzed and non-mass analyzed carbon ion beams were used to deposit coatings on polished silicon wafers. Extremely, hard dense coatings that are structurally similar to i-carbon as determined by Ramon spectroscopy were achieved with high current beams of methane and argon. Residual contaminants of oxygen and nitrogen were minimized.

INTRODUCTION

The objective of this research was to investigate ion beam deposition of carbon as a method to deposit diamond and diamond-like coatings with superior electrical and optical properties.

Ion beam assisted deposition typically introduces compressive stresses into the film [1]. It is believed that this can change the normally observed amorphous structure of carbon films deposited by plasma assisted means into diamond if the hydrogen content can be reduced. Achievement of aligned crystal structure would allow use of the films for electronic devices. Improved transmission in the visible region of the spectrum would allow use of such films for protective coatings on optics.

EXPERIMENTAL RESULTS

Mass analyzed carbon ion films were deposited in a modified end station of a Varian-Extrion 200-1000 ion implanter. An electrostatic lens was used to decrease ion energy to 100 eV to reduce sputtering effects. The deposition rate was very slow, and chemical analysis by ESCA showed that resulting films were heavily contaminated by oxygen and nitrogen. We concluded that the use of a mass analyzed beam to improve the purity of the film is not justified without ultra-high vacuum conditions. For a more practical approach to film deposition, and to reduce the relative background contamination effect, ion beam current density on the substrate had to be increased.

A summary of the different techniques tested to deposit diamond films with non-mass analyzed ion beams are summarized in Table I. They include direct ion beam deposition (IBD) of methane (CH_4^+) as well as IBD of a combined argon and methane beam (Ar^+ plus CH_4^+), and finally Ion Beam Enhanced (assisted) Deposition (IBED) of evaporated carbon films. The purpose of the argon was twofold; to help sustain the ion source as well as to provide nuclear energy loss in the deposition to promote more thermal spikes or displacement collisions thought responsible for creating the local "high-temperature," high-pressure regions necessary to form diamond-like films.

*This research was funded by the U.S. Army Research Office Innovative Research contract number DAAL03-87-C-0028.

TABLE I. ION BEAM DEPOSITION AND ION BEAM ASSISTED DEPOSITIONS
USED TO PRODUCE DIAMOND-LIKE COATINGS ON Si.

Sample No.	Ions	Ion Beam Ratio	Ion Beam Energy eV	J ($\mu\text{A}/\text{cm}^2$)	Carbon Deposition Rate ($\text{\AA}/\text{cm}^2$)	Substrate (Si)	Temp. ($^{\circ}\text{C}$)	Thickness (angstroms)	Knoop Hardness KHN (5 gm)	Optical Refraction Index (n)	Friction: 440C Steel Si_3N_4
1	CH_4, Ar	3:1	400	500	-	(111)	25	-	1150	absorbing film	0.24-0.74 0.2
2	CH_4	-	400	130	-	(111)	25	-	1200	1.52-1.65	0.2 0.18
3	Ar	-	400	100	1-8	(111)	25	-	1000	2.45-2.51	0.23 0.21
4	CH_4, Ar	10:1	400	300	3-5	(111)	25	2000-2900	1400-1700	2.1-2.2	-
5	CH_4, Ar	10:1	400	300	3-6	(111)	25	5200-7200	1300-1900	2.55-2.63	-
6	CH_4, Ar	10:1	400	120	0.5-1.5	(111)	25	1600-2750	1200-1400	2.50-2.65	-
7	CH_4, Ar	10:1	500	350	-	(100)	400	1400	1600	2.30-2.45	0.3 0.19

The system used to produce these films consisted of a high-current, low energy Kaufman type ion source coupled to an electron beam evaporation unit, shown schematically in Figure 1. The ion source was operated in the energy range where previous researchers have seen DLC formation [2] and high enough not to be beam current limited by space charge considerations. The initial deposition (Sample 1) used a 3:1 ratio of CH_4 to Ar pressure into the ion source. This produced too high a sputtering yield with no deposition occurring. Subsequent deposition runs used a methane to argon ratio of 10:1. Operating with pure methane produced other problems including deterioration of the filament (i.e., formation of tungsten carbide) or the buildup of an insulating layer on the source chamber which quenches the plasma before significant deposition can be performed. The evaporation of carbon was carried out with an electron beam evaporator utilizing a graphite block as a charge source and a quartz crystal oscillator to monitor the deposition rate.

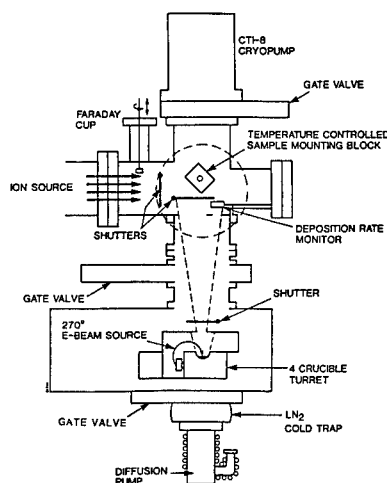


FIGURE 1. SCHEMATIC OF SPIRE'S IBED SYSTEM.

For all cases the measured hardness of the thin DLCs was higher than that of the silicon substrates ($\text{KNH} = 900$ at 5 grams). Only one deposition (Sample 3, Ar^+ onto evaporated carbon) did not involve carbon as a constituent of the ion beam and the coating produced in this manner displayed extremely fast deterioration when exposed to atmosphere as a result of stress and/or chemical activity indicating the importance of incorporating hydrogen onto these for stability.

The variations of the thickness and microhardness are due in part to the falloff of evaporant on the substrate positioned at 45° to both the evaporant flux and ion beam as shown in Figure 1. In addition there are local variations ($\pm 15\%$) within the beam profile affecting sputtering rates and stoichiometry.

A sample film was analyzed for composition and structure. Figure 2 shows the raw ESCA output of the surface of Sample 7 from Table I. The oxygen and nitrogen are significantly reduced from the levels seen for the mass analyzed ion beam deposition. Raman scattering results are shown in Figure 3 indicating that the film is i-carbon with no diamond structure. Analysis of remaining samples in Table I is continuing.

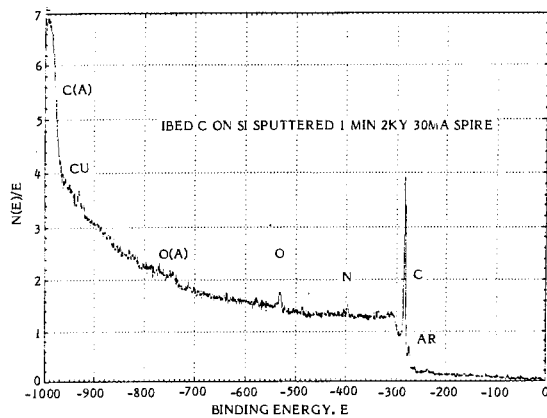


FIGURE 2. ESCA SURVEY OF IBED DIAMOND-LIKE COATING AFTER ONE-MINUTE SPUTTERING.

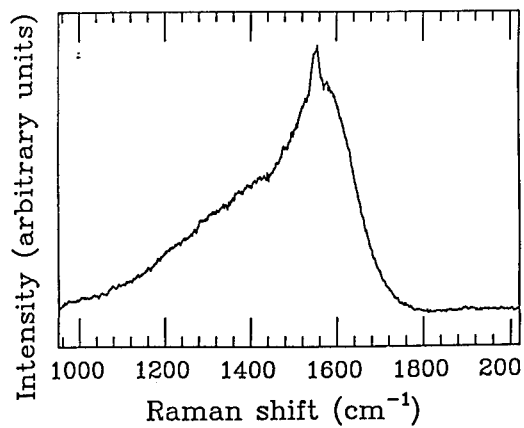


FIGURE 3. RAMAN SIGNAL FROM DIAMOND-LIKE COATING SHOWING I-CARBON SIGNAL AT 1580 AND NO DIAMOND SIGNAL EXPECTED AT 1320.

REFERENCES

1. P.J. Martin, J. Mat. Sci., 21, 1 (1986).
2. H. Tsai and D.B. Bogy, J. Vac. Sci. Technol. A5, 3287 (1987).

EFFECTS OF IONIZED CLUSTER BEAM BOMBARDMENT
ON
EPITAXIAL METAL FILM DEPOSITION ON SILICON SUBSTRATES

Isao Yamada
Ion Beam Engineering Experimental Laboratory,
Kyoto University, Sakyo, Kyoto 606, Japan.

ABSTRACT

The effects of ion beam bombardment during ionized cluster beam (ICB) deposition of metal films on Si(111) and Si(100) substrates have been discussed. In the case of Al deposition, films have been epitaxially deposited on Si(111) and Si(100) substrates at near room temperature. On Si(111) substrates, nearly perfect Al single crystal films could be formed. On Si(100) substrates, Al bicrystals have been grown epitaxially. A remarkable fact concerning these results is that the epitaxial films could be formed at nearly room temperature and on a large lattice mismatch (25%) substrate surface. Atomic resolution TEM analysis suggests that the epitaxy of Al occurs not only on Si surfaces but also at Al/Al grain boundaries. These epitaxial films exhibit extremely high thermal stability and long electromigration life time. To understand the deposition features and film characteristics, the effects of ICB bombardment on the film growth at the initial stage of the deposition and the resultant film structure have been studied. The results show that the role of very low energy ion bombardment is especially important in forming epitaxial metal films. Depositions of Au and Cu on Si substrates have also been made to understand whether ICB deposition may improve the characteristics of other metal films. Preliminary results of these film depositions are also obtained.

INTRODUCTION

Many experiments have been undertaken to prepare various kinds of films by ICB and reactive ICB depositions [1]. These experiments include the deposition of simple metals, such as Au, Cu, Pb, Ag, Al, Sb, Te and others on a range of substrates. More complicated depositions were made of intermetallic or alloy films on such alloys as CuAl, CuNi, MnBi, GdFe, PbTe, ZnPb and FeSi₂. For the case of semiconductors, depositions of Si in a range of crystalline forms from amorphous to single crystal have been made. Films of Ge, GaAs, GaP, ZnS, InSb, CdTe and Cd-Mn-Te, as well as doped semiconductors have also been deposited. Reactive ICB experiments have been performed on a wide range of oxides, nitrides, hydrides and fluorides. Several organic thin films have also been deposited by ICB at lower substrate temperature. In many cases, the films deposited by ICB and RIBC depositions differed markedly from films deposited on the same materials by means of conventional evaporation or sputtering techniques. Among those results, it is especially remarkable that Al films can be epitaxially deposited on Si substrates at near room temperature by using ICB [2].

Since ICB deposition offers the capability of controlling the film structure by applying kinetic energy to the cluster beam during film deposition, the technique has a unique advantage compared to other deposition techniques. The useful kinetic energy an ion beam should have to enhance crystal growth and to promote chemical reaction in the range from above-thermal to a few tens of eV per atom. However, in most of ion beam deposition techniques, individual ions impact on the substrate with a kinetic energy which is too high, producing a significant density of defects, interface diffusion, and inclusion of impurities. Control of the ion beam energy is extremely important for making desirable film properties.

The results of ICB deposition of high quality thermally stable metal films on silicon substrates at near room temperatures [3,4] raised the question of how they are influenced by the deposition method and the deposition conditions. In an earlier paper we have shown that ICB can form epitaxial Al films on both Si(111) and Si(100) substrates [2,3]. This is surprising because the lattice misfit of this material combination is more than 25%. The analysis of Al on Si(111) indicates a single crystalline Al(111) structure, while Al on Si(100) consists of Al(110) bicrystals having unusual rounded grain boundaries [5]. A high thermal stability of ICB-Al/Si structures has been shown by Auger electron spectroscopy (AES) and scanning electron microscopy (SEM). For example, AES spectra of the surface of Al films deposited on Si substrates under various conditions show no Si peak after 30 min annealing at 550 °C in UHV.

In this paper I will first discuss the useful ion beam energy range for film formation. This will be followed by a discussion of ICB bombarding effects on the initial stage of film growth and resultant film structure by taking examples of Al epitaxy on Si(111) and Si(100) substrates. In the Al(100)/Si(100) case, it appears that the epitaxial growth of Al occurs not only at the Si surface but also at Al/Al grain boundaries. The grain boundary formation during the bicrystal formation may be called epitaxial coalescence. Lastly, the results obtained by in-situ RMEED and XPS analyses of Au and Cu film depositions on Si substrates and film material dependencies will be discussed.

USEFUL ION BEAM ENERGY RANGE AND FUNDAMENTAL EFFECTS FOR FILM FORMATION

An important ion beam energy related to the film deposition could be derived in terms of the threshold energy for surface atom displacement. For the low energy ion bombardment, an interaction between ions and substrate atoms can be described by assuming hard sphere collisions. The cross-section for surface atom displacement is expressed by,

$$\sigma_d = \pi R^2 \left\{ 1 - \frac{(M_1 + M_2)^2}{4M_1 M_2} \frac{E_{th}}{E} \right\}$$

where, the hard sphere radius R is determined by the equation,

$$E = \frac{Z_1 Z_2 e^2}{R} \exp\left(\frac{R}{a}\right)$$

In the above equations, E is the kinetic energy of the incident beam, E_{th} is the threshold energy for displacement, a is the electron screening length and M_1 , Z_1 and M_2 , Z_2 are the atomic mass and atomic number of the ion and the surface atom, respectively. Figure 1 shows the calculated cross-section for the displacement of substrate atoms bombarded by different ions. In any ion and substrate material combinations, the displacement cross section increases at energies higher than approximately 50 eV and eventually reaches a maximum value.

The above discussion suggests that an ion beam energy range from approximately above thermal to hundreds of eV is important. Other fundamental phenomena related ion bombardment in this energy ranges are listed as follows;

- 1 enhancement of adatom migration,
- 2 desorption of impurity atoms from the substrate surface and depositing surface,

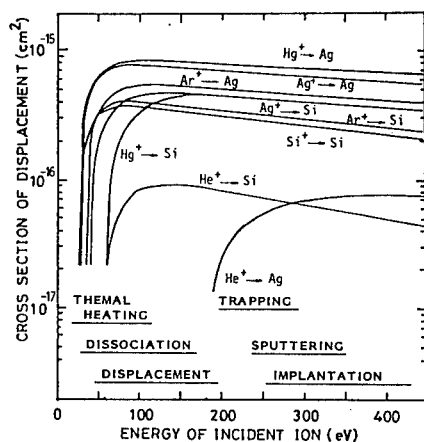


Fig. 1. Cross section of displacement of a lattice atom for various combinations of ion and surface materials.

- 3 displacement of surface atoms,
- 4 formation of nucleation sites,
- 5 trapping or sticking of incident ions,
- 6 sputtering,
- 7 implantation and other inelastic collisions.

These fundamental effects are dependent on incident ion beam energy. However in most of the cases, the energy dependence of each fundamental process overlaps in the range from above-thermal to hundreds of eV. The energy dependence overlap complicates ion beam deposition. Therefore, many experiments are necessary to find the best deposition conditions.

ICB DEPOSITION FEATURES

In ICB deposition clusters of the material to be deposited are formed by adiabatic expansion of the vapor through a nozzle. Theoretical and experimental studies of the cluster formation conditions are reviewed elsewhere [6]. The clusters are then ionized by impact ionization with electrons of an appropriate energy. The cluster size distribution is typically in a range of 100-2000 atoms/cluster.

In ICB deposition, the following processes in the film formation are proposed. When the clusters bombard the substrate surface, both ionized and neutral clusters are broken up into atoms which are then scattered over the surface with high surface diffusion energy. A scattered atom is physically attracted to the substrate surface but it may move over the surface (adatom migration) because of high momentum parallel to the surface derived from the incident kinetic energy. The adatom interacts with other adatoms and/or substrate atoms to form a stable nucleus and finally ceases its movement and becomes a chemically adsorbed atom. Thus, the enhanced adatom migration results in a increased nucleation rate and an increased growth rate of islands.

Using a time-evolution computer simulation, the above mentioned ICB bombardment has been simulated by using the binary collision approximation [7]. Three types of collision events were considered. One was the

collision between two moving particles; the second was the collision between a moving atom and a target atom; and the third was between moving particles and an interstitial. The Moliere potential was used as the interatomic potential. Figure 2 shows the simulated impact of an Al cluster of 500 atoms/cluster with the energy of 5 keV (10 eV/atom) on a Si(111) surface. The results show that many incoming atoms in the cluster are reflected from the surface. The reflected atoms make collision cascades in the cluster. The collisions between virgin atoms in the upper part of cluster and reflected atoms from the dense surface result in the parallel velocity component of Al atoms. These collision events could be the main source of high adatom migration during ICB deposition.

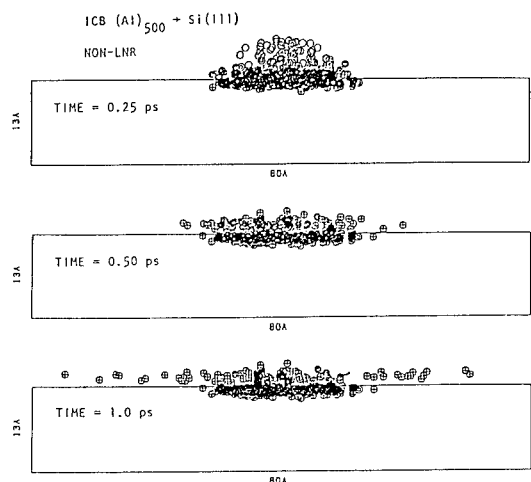


Fig. 2. Simulation of ICB bombardment at $t = 0.25, 0.5$ and 1.0 p sec., where a 5 keV of Al cluster (size 500) is bombarded on Si(111) surface.

CONTROL OF FILM GROWTH PROCESSES BY ICB BOMBARDMENT

Most of deposition procedures in this experiment are as follows. A Poco graphite crucible was heated to 1600 °C by electron bombardment. The crucible hole was 2 mm in diameter and 2mm in length. Si wafers were cleaned by thermal desorption of weak oxide at 850 °C for 15 min. In-situ Auger electron spectroscopy (AES) showed no detectable impurities and 5 keV reflection medium energy electron diffraction (RMEED) exhibited the expected Si reconstructed pattern. Al was deposited from an ICB source at a rate of 10 nm/min in a pressure of $1-2 \times 10^{-9}$ Torr.

The initial stage of the film deposition shows whether or not clusters can break at the substrate. Al ICB depositions on Si substrates were made through a stainless steel mask slit, 50 μ m wide and 1000 μ m long [8]. Figure 3 shows the SEM images of the deposit at the slit and under the slit cover. The substrate temperature was kept at 400 °C. The results show that the surface migration of Al on Si(111) is large. It is clear from the SEM images that the size and the shape of islands formed by the deposits

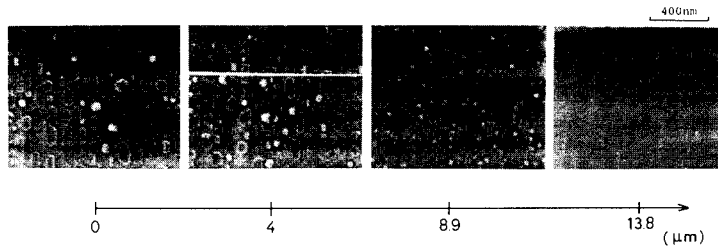


Fig. 3. SEM images of Al crystallites condensed under the mask.

are different at different distances from the mask edge. This suggests that the clusters break up into individual atoms at the substrate. These atoms migrate over the surface and then form islands. If the clusters do not break up, the diameter of the islands should be less than 5 nm if there is no coalescence. The SEM images clearly show that island formation is the result of cluster break up and coalescence influenced by the ion beam bombarding condition. Details of the effects of acceleration voltage and the substrate temperature and surface conditions are reported elsewhere [9].

Surface damage by accelerated Al-ICB on Si(111) and Si(100) substrate surfaces has been measured by Rutherford Backscattering Spectroscopy (RBS) [10]. The experimental results show that the surface disorder produced by ICB bombardment is far lower than that by atomic ion bombardment at the same acceleration voltages. Therefore, the effective cluster bombarding energy is lower due to the break-up of clusters. That is to say, the total cluster kinetic energy is shared, on the average, by many atoms which have individually, relatively low kinetic energy.

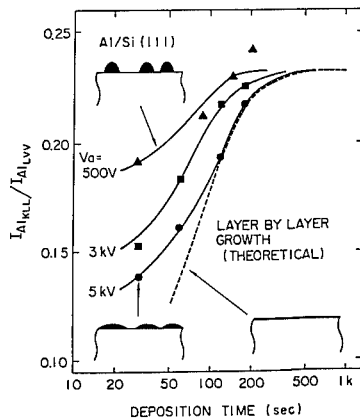


Fig. 4. Peak intensity ratio of Al Auger signals as a function of depositing time.

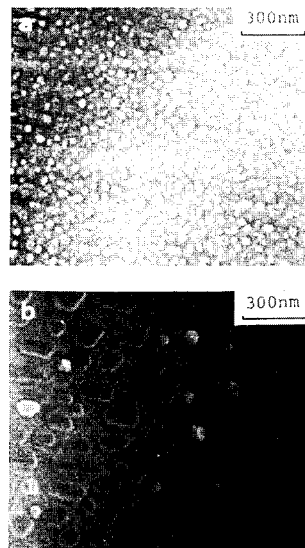


Fig. 5. SEM images of initial stage of depositions at 0 kV (a) and 3 kV (b).

Al film growth processes were observed by in-situ AES and ex-situ SEM observation. Figure 4 shows the ratio of the peak-to-peak intensities of differentiated Auger signals corresponding to the Al_{KLL} (1396 eV) and Al_{LVV} (68 eV) transitions as a function of the deposition time. Since the escape depth of 1396 eV electrons is greater than that of 68 eV electrons, the intensity ratio I_{KLL}/I_{LVV} for films deposited at various acceleration voltages is due to change in the growth morphology of the films. As can be seen in Fig. 4, the aluminum films deposited by the ICB technique at higher acceleration voltages, i.e. 3 and 5 kV, exhibit almost layer-by-layer growth morphology. The transition to the two dimensional growth was also observed by SEM at the initial stage of the film growth. Figure 5 shows SEM images of Al films deposited on 400 °C substrate at the acceleration voltages of 0 and 3 kV. Islands formed on the substrate become flat and larger when the deposition was made at 3 kV [8]. In combination with the AES results described above, these results suggest that a transition from three dimensional to two dimensional growth takes place as the cluster acceleration energy increased to the range of 3 to 5 kV. Usually, film growth features are determined by the substrate and depositing material combination. In ICB deposition of Al films, the growth features could be controlled from three dimensional growth to layer-by-layer growth.

EPITAXIAL DEPOSITION OF AL FILMS ON Si SUBSTRATES

Al epitaxial films can be deposited at room temperature on both Si(111) and Si(100) substrates. Crystal structure and the orientation of deposited films on Si(111) and Si(100) substrates have been examined by 75 keV reflective high energy electron diffraction (RHEED) pattern. Figure 6 shows typical patterns from an Al epitaxial film on Si(111) and their indices. In the case of Si[110] incidence of the electron beam (Fig. 6(a)), the Al(110) reciprocal lattice can be seen, and in the case of Si[211] incidence (Fig. 6(b)) the Al[211] reciprocal lattice can be seen, which indicate the epitaxial relation:

$$Al(111)//Si(111), Al[\bar{1}10]//Si[\bar{1}10]$$

Figure 7 shows the 75-keV RHEED patterns for an Al film on Si(100) and their indices. Figure 7(a) was obtained at Si[011] incidence of the electron beam and Fig. 7(b) was obtained by rotating the sample azimuthally by 35° from the condition of Fig. 7(a). These patterns can be identified from the superposition of two Al patterns with epitaxial relations:

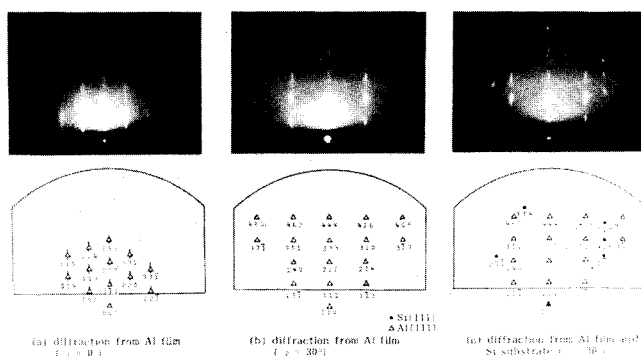


Fig. 6. 75 keV RHEED patterns and their indices from an Al film deposited at 5 kV acceleration voltage on room temperature Si(111) substrate.

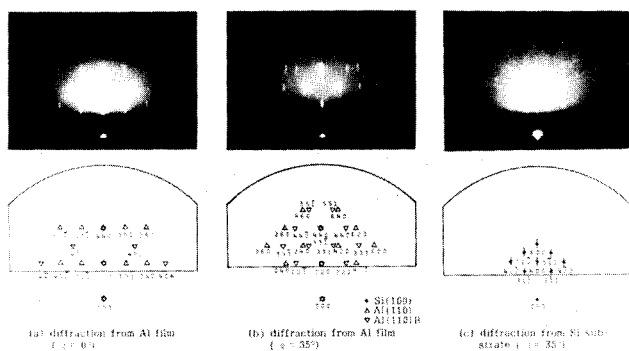


Fig. 7. 75 keV RHEED patterns and their indices from an Al film deposited at 5 kV acceleration voltage on room temperature Si(100) substrate.

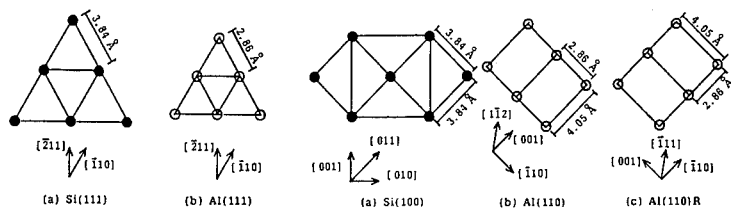


Fig. 8. Schematic relation of crystal orientations of Al films on Si(111) and Si(100) substrates.

Al(110)//Si(100), Al[001]//Si[011] denoted as Al(110),
and
Al(110)//Si(100), Al[110]//Si[011] denoted as Al(110)R.

Epitaxial relations of Al films on Si(111) and Si(100) substrates are illustrated in Fig. 8. It is remarkable that a lattice misfit as large as $(2.86-3.84)/3.84 \times 100 = -25\%$, at least in one direction, permits epitaxial growth of Al on both Si(111) and Si(100) substrates at room temperature.

The deposition process of the Al film was observed by in-situ 5-keV reflective medium energy electron diffraction (RMEED). Figure 9 shows the change of a 5 keV RMEED pattern during the Al deposition on Si(111). A spotty and complex pattern appears at the first stage (Fig. 9. (b)) which corresponds to the three dimensional nucleation of Al with different orientations. After further deposition, this pattern becomes streaky and one orientation becomes dominant (Fig. 9 (c)). After the deposition of more than 10 nm of Al film, only one orientation remains and the RMEED pattern does not change to the end of the deposition of the 360 nm thick Al film (Fig. 9 (d)). The RMEED pattern became streaky at an earlier stage of deposition when the higher acceleration voltage was applied. By further study of the initial deposition process by the diffraction patterns and RBS, the crystalline orientations at the near surface of Si(111) have been determined to be as follows;

Al(100)//Si(111), Al[011]//Si[211], denoted as Al(100),
Al(100)//Si(111), Al[011]//Si[110], denoted as Al(100)',
and
Al(100)//Si(111), Al[011]//Si[121], denoted as Al(100)''.

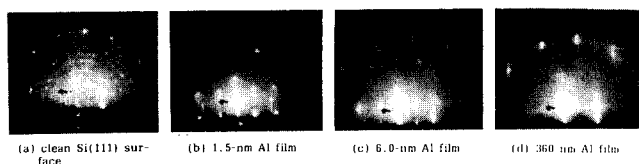


Fig. 9. 5-keV RMEED patterns during Al deposition at 5 kV on room temperature Si(111) substrate.

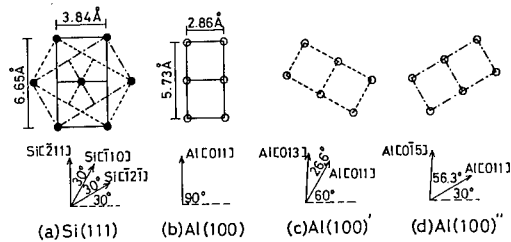


Fig. 10. Schematic illustrations of relative orientation of the Al crystals on Si(111) substrate at the initial stage of deposition.

Figure 10 illustrates the relative orientation between Si substrate and Al film.

By taking into account the above experimental results and discussions, the epitaxial Al film growth process on room temperature Si(111) substrate can be represented as shown in Fig. 11. It is not yet clear that the formation of the very thin accommodation crystalline layer with the large misfit with Si(111) substrate and three different orientations can give the growth of an Al(111) layer on Si(111) substrates with the defined epitaxial relations.

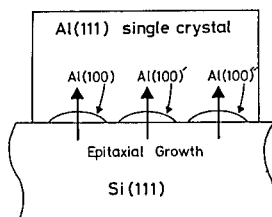


Fig. 11. Schematic representation of Al(111) epitaxial growth on Si(111) substrate.

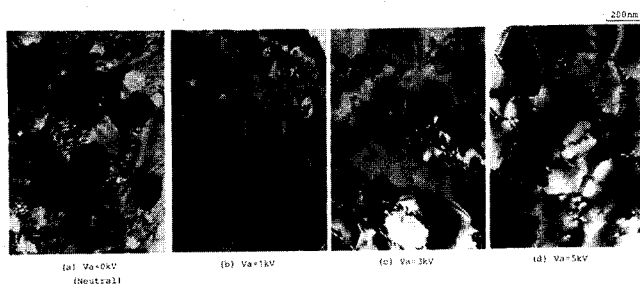


Fig. 12. TEM images of Al films on Si(111) substrates deposited at different acceleration voltages

The effect of acceleration voltage on the crystalline properties has been studied by transmission electron microscopy (TEM). Figure 12 shows the TEM images of Al films on Si(111) substrates at various acceleration voltages. The film deposited at $V_a = 0$ kV shows a high density of Moire patterns. They represent low-angle grain boundaries between neighboring regions which have small misorientation, one to two degrees, with respect to each other. The films deposited at higher acceleration voltages show much cleaner Moire patterns and lower density of the low-angle boundaries than the films deposited at $V_a = 0$ kV.

The Al films were annealed at 400 °C for 60 min in the UHV chamber. Figure 13 shows the transmission electron diffraction (TED) pattern and the TEM images of the film deposited at the acceleration voltage $V_a = 5$ kV after annealing. There were not any non-uniformities in the pattern. After the annealing, both the low-angle grain boundaries and the dislocation loops vanished and the film became almost perfect.

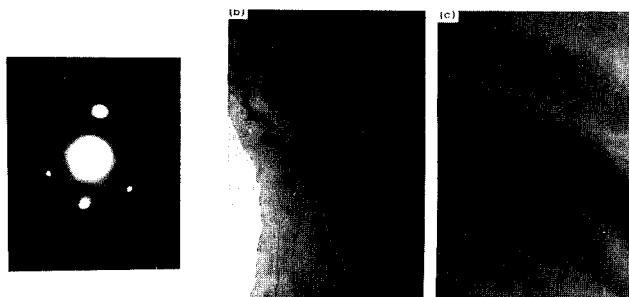


Fig. 13. TED pattern and TEM images of epitaxial film post-annealed at 400 °C.

In contrast to the growth of Al on Si(111), on Si(100) only two Al crystal orientations exist in the entire film from the interface to the film surface. Figure 14 shows a TEM micrograph of the epitaxial Al film. From the TED patterns, the dark and light areas in Fig. 14 represent the orthogonal film structures Al(110) and Al(110)R. The contrast is caused by the difference in electron transmission through the two crystal orientations. Figure 15, taken at Lawrence Berkeley Laboratory by U. Dahmen and K.H. Westmacott, is a high resolution TEM micrograph of a small

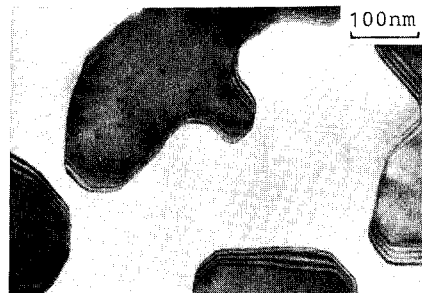


Fig. 14. TEM images of epitaxial Al film on Si(100).

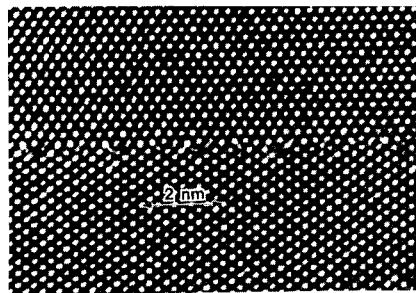


Fig. 15. High resolution micrograph of 90° asymmetrical tilt boundary in Al bicrystal film.

section of a grain boundary in Fig. 14 [11]. It is apparent that only one atomic layer forms the boundary between $\langle 110 \rangle$ asymmetrical grains. Furthermore, it should be noted that the lattice mismatch at the grain boundary is compensated by a presence of vacancies located five or six atom spacings apart along the boundary. One must conclude that grain boundary formation in this case is the result of epitaxial coalescence. Figure 16 is a proposed schematic representation of how the Al(110) bicrystal is formed during ICB deposition. Epitaxial growth of Al(110) and Al(110)R takes place simultaneously at various locations on the Si(100) surface. As the microcrystals grow around nucleation sites, they eventually encounter each other and coalesce epitaxially.

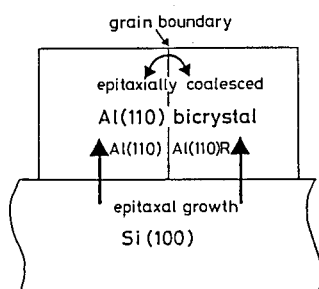


Fig. 16 Schematic representation of Al epitaxial growth on Si(100) substrate.

FILM CHARACTERISTICS

Thermal stability of the epitaxial Al films and the Si interface has been investigated by several evaluation methods including RBS, SEM, AES, and capacitance voltage (C-V) measurements [3,4,5,]. The dependence of the minimum yield obtained by 185 keV H^+ channeling on the annealing temperature does not show any degradation even by annealing at 550 °C. Al films on Si(111) by ICB and conventional vacuum deposition were annealed at 450 °C for 30 min in vacuum. Figure 17 shows the SEM images of the surface and the interface which was revealed by phosphoric acid etching.

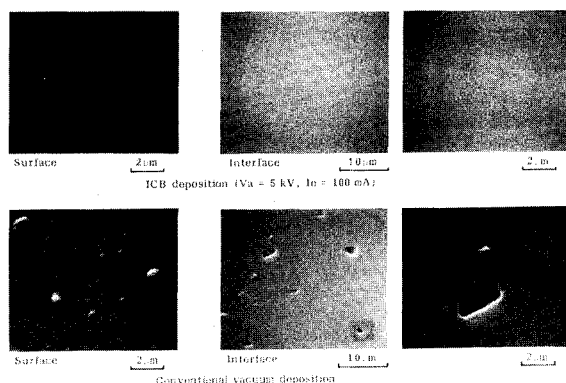


Fig. 17. SEM image of the surface and the interface of Al films on Si(111), post-annealed at 450 °C for 30 min. in vacuum.

On the surface of the film deposited by vacuum deposition, there are annealing hillocks and valleys probably caused by the extended alloy penetration, whereas no irregularity can be seen on the film deposited by ICB. At the interface of the film prepared by vacuum deposition, there are many etch pits caused by alloy penetration, while that by ICB showed a very smooth interface. In addition, AES depth profiling of the samples has shown that the interface of the sample prepared by ICB remained abrupt even after annealing at 550 °C for 30 min. The thermal stability of the interface was measured by forming Schottky barriers of Al/n-Si junctions. The barrier height and ideality factor showed little change after anneals to temperatures up to 550 °C. This behavior is in contrast to that of the junctions prepared by conventional deposition methods, which show changes of more than 0.1 eV in barrier height and 0.1 in ideality factor.

Uniform deposition in a small-size contact hole and along a high step are important for VLSI applications. ICB depositions have been made on various sizes of holes and steps. Figure 18 shows the cross sectional views of the ICB deposited Al films on a Si substrate patterned with BPSG (borophosphosilicate glass) line. A SiN film was deposited on the Al film by CVD to duplicate the Al structure which is easily deformed during the subsequent sample cleaving. For comparison, sputter deposited films and electron beam deposited films were also studied in a similar manner. The excellent step coverage of the ICB deposition could be due to the unidirectional characteristics of ICB. However, the poor coverage by electron beam and sputter depositions suggests that other factors, such as surface migration and creation of nucleation centers, might also be contributing to this result.

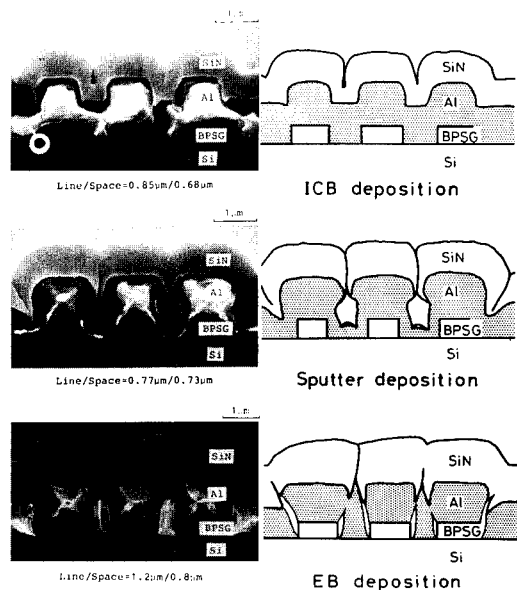


Fig. 18. SEM images of the cross sections of the Al step coverage prepared by ICB, sputtering and electron beam depositions.

COMPARISON WITH OTHER METAL FILMS DEPOSITED BY ICB

Deposition of Au and Cu on Si substrates have also been made to understand whether ICB bombarding effects may depend on different depositing material, because the Au/Si and Cu/Si interfaces have been extensively

studied in the past with a variety of surface analytical techniques [12]. In-situ X-ray photoelectron spectroscopy (XPS) during ICB deposition of Au on Si(111) substrate has been made [13]. The results show that at low coverages, the splitting between the two prominent structures in the Au-5d peaks in the valence band becomes closer to those of pure bulk gold when a film is deposited at high acceleration voltages. In contrast to this an appreciable change of the binding energy of the Si-2p state at low coverage and high acceleration voltage could not be observed. These results suggest that a high density layer is formed and considerable Au-Si interaction is suppressed at the initial stage of film deposition. In the case of Cu/Si(111), however, no appreciable differences were detected between films deposited with the neutral beams and the accelerated ICB [14].

CONCLUSIONS

Fundamental studies of ICB deposition processes suggest that the enhancement of adatom migration and related low energy bombardment are effective to control deposition processes. Especially, change of deposition features from three dimensional to layer-by-layer growth is the unique feature of ICB deposition. These could be the reasons that the epitaxial Al films can be grown on room temperature Si substrates. It is especially interesting to know that Al epitaxy is possible on Si(100) substrates. In the deposition process where Al bicrystals can be grown, it is clear that the epitaxial growth of Al occurs not only Al/Si(100) interface but also at Al/Al grain boundaries of each Al bicrystals during the coalescence. Impurity desorption and high surface migration of adatoms due to ICB bombardment seems to be effective.

REFERENCES

- [1] T.Takagi, Ionized-Cluster Beam Deposition and Epitaxy, (Noyes Publications, New Jersey, 1988).
- [2] I.Yamada, H.Inokawa, and T.Takagi, *J. Appl. Phys.*, **56**, 2746 (1984).
- [3] I.Yamada, C.J.Palmstrom, E.Kennedy, J.W.Mayer, H.Inokawa and T.Takagi in Layered Structures, Epitaxy, and Interfaces, edited by J.M.Gibson and L.R.Dawson (Mater. Res. Soc. Proc., **37**, Pittsburgh, PA 1985) pp.401-406.
- [4] I.Yamada and T.Takagi, *IEEE Trans.*, **ED-34**, 1018 (1987).
- [5] I.Yamada, L.L.Levenson, H.Usui, and T.Takagi in Materials Modification and Growth Using Ion Beams, edited by U.J.Gibson, A.White and P.P.Pronko (Mater. Res. Soc. Proc., **93**, Pittsburgh, PA 1987) pp.253-258.
- [6] I.Yamada, H.Usui, and T.Takagi, *J.Phys. Chem.*, **91**, 2463 (1987).
- [7] Y.Yamamura, I.Yamada and T.Takagi, presented at the 7th Int. Conf. on Ion Implantation Technology, Kyoto 1988. accepted for Nucl. Instr. and Methd.
- [8] L.L.Levenson, M.Asano, T.Tanaka, H.Usui, I.Yamada, and T.Takagi, *J. Vac. Sci. Technol.*, **A6**, 1552 (1988).
- [9] L.L.Levenson, H.Usui, I.Yamada, T.Takagi, and A.B.Swartzlander, presented at 1988 AVS meeting, Atlanta, GA, October 1988. Accepted for publication in *J.Vac. Sci. Technol.*
- [10] I.Yamada, H.Usui, and T.Takagi, *Nuc. Inst. and Methd.*, **B33**, 108 (1988).
- [11] U.Dahmen, C.J.D.Hetherington, J.Douin and K.H.Westmacott, presented at the 1988 MRS Fall Meeting, Boston, Mass., 1988.
- [12] A.Hiraki, *Surface Sci.*, **168**, **74** (1986).
- [13] I.Yamada, H.Usui, H.Harumoto and T.Takagi, in Laser and Particle-Beam Chemical Processing for Microelectronics, edited by D.J.Ehrlich, G.S.Higashi, and M.M.Oprysko (Mater. Res. Soc. Proc., **101**, Pittsburgh, PA 1988) pp.195-200.
- [14] M.Sosnowski and I.Yamada, presented at the 7th Int. Conf. on Ion Implantation Technology, Kyoto 1988. accepted for Nucl. Instr. & Methd.

CLUSTER SIZE MEASUREMENTS IN AN IONIZED CLUSTER BEAM SYSTEM

D.E. TURNER, K.M. LAKIN, AND H.R. SHANKS
Microelectronics Research Center, Iowa State University, Ames,
IA 50011.

ABSTRACT

Ionized Cluster Beam (ICB) deposition has received considerable attention in recent years because of its potential application to low temperature semiconductor and metal film growth. To better understand this deposition process, however, it is necessary to determine the properties of the cluster source and the cluster size distribution obtained. This paper discusses the design of a time-of-flight mass spectrometer with single atom resolution for the measurement of cluster size in a conventional ICB deposition system. Results have been obtained for silver and germanium deposition. In both cases most of the clusters have been found to consist of less than 35 atoms. With the high resolution spectrometer it has been possible to show that certain cluster sizes are more stable than others.

TIME-OF-FLIGHT MASS SPECTROMETER

The time-of-flight mass spectrometer uses a one kilovolt pulse generator to pulse electrons from a tungsten filament across the path of the cluster beam, singly ionizing a narrow band of clusters as shown in figure 1. Under a constant acceleration potential, the large clusters accelerate more slowly than the smaller clusters creating a spatial distribution of the clusters based on size. A faraday cup receives the ionized cluster distribution and creates a signal that is then amplified and filtered. A digital oscilloscope records the arrival of the clusters and averages the signals from 256 individual pulses to produce a time-of-flight distribution. This distribution can then be sent over to a computer for further manipulation, cluster size analysis, mass flux analysis, and storage. Single atom resolution has been achieved for small cluster sizes.

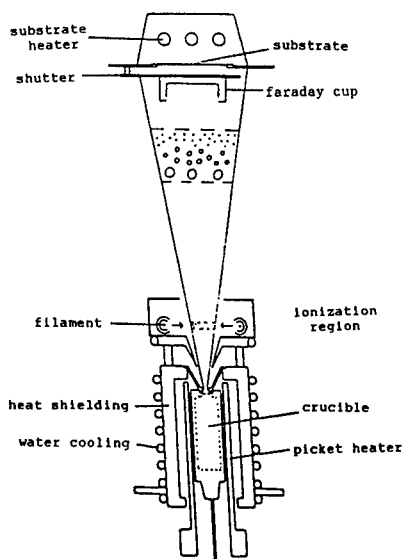


Figure 1 - Illustration of the
Time-of-Flight Mass Spectrometer

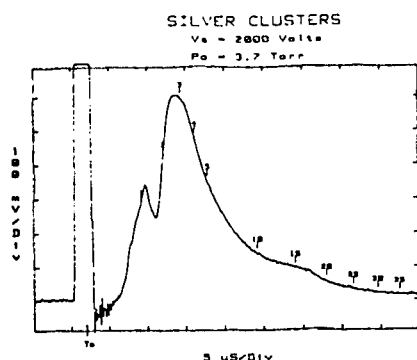


Figure 2 - Silver cluster size distribution

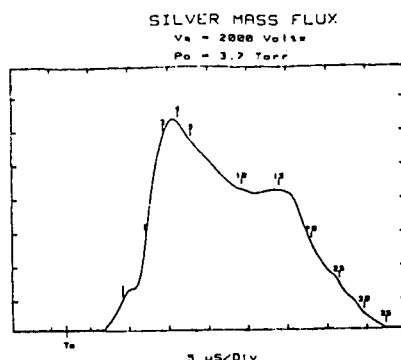


Figure 3 - Silver mass flux distribution

The mass spectrometer was designed so that it doesn't interfere with the normal operation of the source or any of its film growth capabilities. The source and chamber have not been altered except for the addition of a faraday cup mounted on the shutter. A measurement of the cluster distribution can then be taken at the beginning of each film growth after which the faraday cup can simply be swung out of the way. This will in the future allow for direct studies of the film growth characteristics of different cluster distributions.

SILVER

Silver was chosen as a test case for several reasons. First of all, Takagi's group has shown that large clusters of 500-2000 silver atoms can be produced by the ICB technique [1]. Knaur has also used silver as a test case for both his experimental and theoretical investigations into cluster formation [2]. The small cluster distribution by free expansion of silver has also been investigated both theoretically and experimentally [3,4]. Furthermore, silver has a relatively high vapor pressure which provides a wide range of crucible pressures within the limits of our source.

Figure 2 shows a typical time-of-flight distribution for silver in the 1 Torr to 5 Torr crucible pressure range where large cluster formation can occur. A strong monomer peak is present with a shoulder that corresponds to a small number of doubly ionized monomers. The distribution is dominated, however, by a peak at 3 atoms per cluster and then extends clear out to about 35 atoms per cluster with a small bump at 17 to 19 atoms per cluster. A small bump has also been detected at 8 to 9 atoms per cluster but this is more difficult to isolate since it occurs on the side of the dominant N = 3 peak. While the N = 8 to 9 and N = 17 to 19 peaks are very small, they are still significant since the mass flux represented by these is comparable to the main peaks. The mass flux distribution shown in figure 3 corresponds to the cluster size distribution of figure 2 and shows that most of the silver atoms travel to the substrate in the form of clusters of 2 to 20 atoms in size.

The N = 8 to 9 peak and the N = 17 to 19 peak both are not present outside of the 1 Torr to 5 Torr crucible pressure range.

The distribution in this regime is made up of the monomer and trimer peaks only. The ratio between these two peaks remains constant for the full temperature range investigated (up to 1630 C). Only the overall magnitude and the presence of the two peaks at larger cluster sizes changes.

Lower accelerating voltages of 500 volts and below lead to a different distribution that favors smaller clusters. Figure 4 shows the low voltage distribution which exhibits distinct peaks for the doubly ionized monomer, singly ionized monomer, and the dimer.

The trimer peak that is so dominant at normal acceleration levels is not present here while the dimer peak that is usually overshadowed becomes apparent. The low voltage distribution is clearly not an accurate picture of the overall distribution of clusters but it does show that there are a large number of dimers that do not show up as a distinct peak at higher voltages. This also verifies that the shoulder on the monomer peak corresponds to a small number of doubly ionized silver atoms. The distribution is fairly constant for acceleration voltages above this low voltage regime.

These results are very consistent with both the theoretical and experimental evidence available. Calculations by Ghatak and Bennemann [5] show that clusters with an even number of electrons are more stable since all bonds are doubly occupied. Silver has one valence electron so singly ionized clusters with an odd number of atoms have an even number of electrons and thus should be more stable. The dominance of the monomer and trimer peaks support this calculation.

Magic numbers at which clusters are more stable can be calculated from an assumption that the cluster is essentially a structureless spherical potential well as was done by Cohen [6]. This jellium approach is very similar to the calculation of magic numbers for nucleons in a nucleus even though the forces involved are vastly different in nature. This method predicts stable clusters when there are 0, 2, 8, 18, and so forth, valence electrons in the cluster. For singly ionized silver clusters this corresponds to stability at $N = 1, 3, 9,$ and 19 atoms per cluster. This matches the results of the silver distribution extremely well.

Experimental results from Pruett's free expansion experiments [3] also show a strong preference for odd numbered clusters, with the dimer peak being the only even numbered cluster size observed. He likewise sees a trimer peak that is slightly larger than the monomer peak. His distribution for cluster sizes of 5 to 10 atoms per cluster is somewhat different than that observed here primarily because he is using much higher pressures than the less than 40 Torr used here.

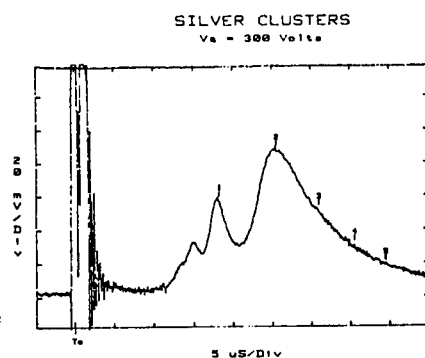


Figure 4 - Silver cluster size distribution for low acceleration

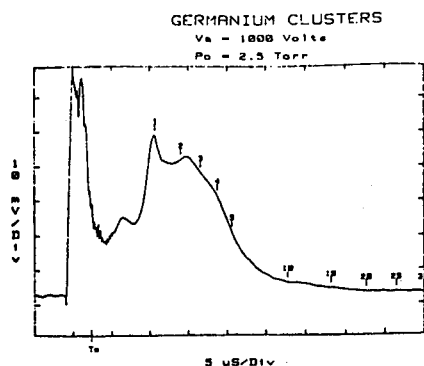


Figure 5 - Germanium cluster size distribution for low temperatures

No large clusters of 500 to 2000 atoms like those reported in the literature have been detected yet. At this time, the resolution of the spectrometer allows us to look at levels down to one thousandth the height of the small cluster peak. This is still a factor of two away from being able to detect a large cluster distribution of the type seen by Takagi (1) in which the large ionized cluster current is approximately a factor of 2000 lower than the small ionized cluster current. The spectrometer is very susceptible to noise due to the small

currents and high amplification involved. Further noise reduction should in the near future provide more insight into whether or not a significant number of large clusters is being produced by our source.

At low crucible temperatures corresponding to crucible pressures below 2.5 Torr, a very sharp monomer peak is observed with a much smaller peak to the left that corresponds to doubly ionized germanium atoms. As seen in figure 5, the main peak is at a maximum at the dimer and has a strong bend at 4 atoms per cluster. The distribution has a tail that extends out to about 17 atoms per cluster.

GERMANIUM

The germanium distribution was also investigated because of our general interest in germanium ICB deposition and the availability of some experimental results for small clusters of germanium. The germanium distribution proved to be much more sensitive to changes in crucible temperature than silver did but produced somewhat similar results otherwise.

At low crucible temperatures corresponding to crucible pressures below 2.5 Torr, a very sharp monomer peak is observed with a much smaller peak to the left that corresponds to doubly ionized germanium atoms. As seen in figure 5, the main peak is at a maximum at the dimer and has a strong bend at 4 atoms per cluster. The distribution has a tail that extends out to about 17 atoms per cluster.

As the crucible temperature is increased, the trimer peak as shown in figure 6 becomes dominant over both the monomer and the dimer peaks. This high temperature distribution is very similar to the silver distribution with a dominant trimer peak and a

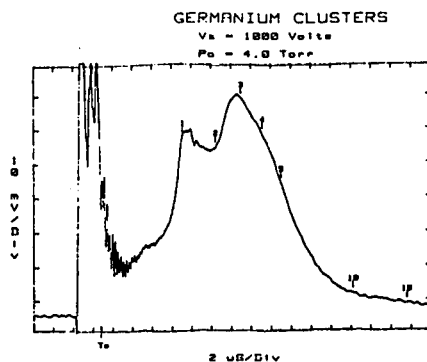


Figure 6 - Germanium cluster size distribution for high temperatures

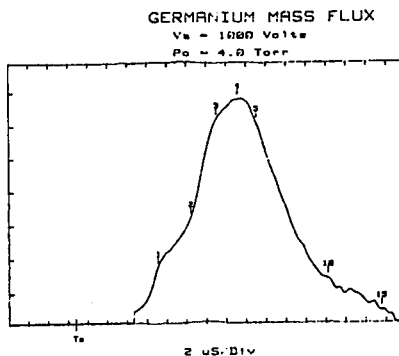


Figure 7 - Germanium mass flux distribution at high temperatures

secondary monomer peak. The germanium mass flux of figure 7, however, shows that most of the mass is being transported to the substrate in clusters of 2 to 8 atoms. This is much different than the 2 to 20 atoms per cluster for silver.

Theoretical analysis of these results are much harder than with silver due to the large number of valence electrons in germanium. Experimental results by Pruett show similarities to the data presented here. He observes a dominant monomer peak with a strong trimer peak and strong peaks at 4 and 6 atoms per cluster as well as evidence of a doubly ionized monomer peak.

No large clusters of germanium have been detected either. Due to the lower vapor pressure of germanium, high rates of mass flux were not attainable within the range of our equipment as they were with silver. The lower mass flux rates, which are acceptable for detection of small clusters, make it even more difficult to provide large enough signals to determine whether a significant number of large clusters of size 500 to 2000 atoms are present. The results for germanium are also therefore inconclusive at this time as to the production of large clusters.

SMALL CLUSTER DISCUSSION

It is clear by both the information presented here and from other literature that even though a significant amount of the mass flux of the ionized cluster beam can be in the form of large clusters, a vast majority of the charge involved is on small clusters. For every singly charged cluster of 1000 atoms, there are on the order of 100 singly charged small clusters of 2 to 20 atoms. Acceleration potentials of up to 8 kilovolts are typically used to give the large clusters added kinetic energies of up to 16 eV per atom. This acceleration also affects the small ionized clusters, however, giving them from 50 eV to 1000 eV per atom for each kilovolt of acceleration. These highly energetic small clusters greatly exceed the 20 eV per atom threshold where defects and other serious damage to film growth can occur. Thus, the majority of the ionized clusters being accelerated toward the substrate are small clusters that are harmful to high quality film growth.

The fact that the ionized cluster beam and the neutral large cluster beam are more collimated than the rest of the supersonic vapor has been demonstrated by Knauer and others. Film growth of germanium on silicon at acceleration potentials of up to several kilovolts has produced films in which the center section is clearly damaged by the impact of the small ionized clusters. The centers of these films look hazy to the naked eye due to the pitting caused by the ionized small cluster beam while the edges where ionized clusters do not impact are very shiny and relatively undamaged.

If large clusters are to be accelerated at high voltages, these small ionized clusters must clearly be removed before the acceleration occurs to avoid film damage due to high energy impacts. This could be done by either setting up a small retarding potential that would only allow large clusters to pass or sweeping the small cluster beam off to one side by use of a small horizontal potential.

CONCLUSIONS

The experimental results for small cluster formation of silver and germanium presented here are in good agreement with all the available experimental and theoretical evidence. A vast majority of the mass flux of the ionized cluster beam detected was in the form of clusters of sizes 2 through 20 for silver and a smaller range of 2 to 8 atoms per cluster for germanium in the temperature ranges investigated.

In most of the literature where large cluster distributions have been detected, no reference is given to the relative number of ionized small clusters involved. In the literature that does make this comparison as well as in the information presented here, it is clear that a majority of the ionized clusters are small even though significant proportion of the mass involved can be in the form of large clusters. These small clusters, when accelerated along with the large clusters, have been found to cause pitting of the films even at the low end of the typical acceleration range.

Future investigations will center around increasing the resolution of the time-of-flight mass spectrometer so that the large cluster distributions can be studied. Incorporation of a field to remove the small ionized clusters is also planned so that a study of film growth in their absence can be made.

REFERENCES

1. H. Usui, A. Ueda, I. Yamada, and T. Takagi, Proc. 9th Symp. on ISIAT 85, 39 (1985).
2. W. Knauer, J. Appl. Phys. 62 (3), 841 (1 August 1987).
3. J.G. Pruett, H. Windischmann, M.L. Nicholas, and P.S. Lampard, J. Appl. Phys. 64 (5), 2271 (1 September 1988).
4. W.A. de Heer, W.D. Knight, M.Y. Chou, and M.L. Cohen, Solid State Physics, Volume 40 (Academic Press, Inc., (1987), p. 137.
5. S.K. Ghatak and K.H. Bennemann, J. Phys. Chem. 91, 2457 (1987).
6. M.L. Cohen, M.Y. Chou, W.D. Knight, and W.A. de Heer, J. Phys. Chem. 91, 3141 (1987).

ALUMINUM ATOM SURFACE MOBILITY ON SiO₂ DURING IONIZED CLUSTER BEAM DEPOSITION

LEONARD L. LEVENSON*, AMY B. SWARTZLANDER**, HIROAKI USUI***,
ISAO YAMADA***, AND TOSHINORI TAKAGI***

*Department of Physics and Energy Science, University of Colorado, Colorado Springs, CO
80933-7150

**Solar Energy Research Institute, 1617 Cole Boulevard, Golden, CO 80401

***Ion Beam Engineering Experimental Laboratory, Kyoto University,
Kyoto 606, Japan

ABSTRACT

An ionized cluster beam (ICB) source was used to deposit Al onto SiO₂ substrates. A 60 μm diameter wire held at the substrate served as a mask. After Al deposition, the wire was removed and the masked area was examined by scanning electron microscopy (SEM) and by scanning Auger microprobe (SAM). The ICB source was operated at 0, 3, and 6 kV acceleration voltages. The substrate was held at 80°, 200°, and 400°C during Al depositions. The Al deposition rate averaged 240 \AA per min. The chamber pressure during deposition was 2×10^{-6} Torr. The diffusion distance of Al under the mask edge was determined from the SEM micrographs and SAM line scans. The maximum diffusion distance for all acceleration voltages occurred at a substrate temperature of 200°C. The maximum diffusion distance at 200°C was 29 μm at 6 kV acceleration voltage. The minimum diffusion distance was 12 μm at 400°C for an acceleration voltage of 6 kV.

INTRODUCTION

The dependence of the microstructure of thin films on deposition conditions has been studied both experimentally and theoretically [1-5]. One primary parameter governing film structure is the substrate temperature ratio T/T_m , where T is the substrate temperature and T_m is the melting point of the film material, both in absolute units. The other primary parameter is the kinetic energy of the impinging atoms, or a quantity which is proportional to the kinetic energy. Both of these factors are related to the surface mobility of surface atoms. However, surface mobility on semiconductor surfaces has not been measured until recently in the case of Ag on Si(111) [6,7] and Al on Si(111) [8,9]. The surface mobility of Al atoms on Si and SiO₂ surfaces is of interest because Al contacts and interconnections are commonly made on Si based integrated circuits. Here, we report on the measurement of the surface mobility of Al atoms deposited from an ionized cluster beam (ICB) source onto SiO₂ surfaces for various substrate temperatures.

EXPERIMENTAL

The construction and operating conditions of ICB sources have been described previously [10]. The source used in this work is similar to that illustrated by Takagi [11]. The graphite crucible was heated to 1500° C by electron bombardment, and the vacuum chamber was shielded by a water cooled thermal radiation shield. The crucible orifice was 2 mm in diameter and 2 mm in length. During Al deposition, the vacuum chamber was held at a pressure of 2×10^{-6} Torr by a liquid nitrogen trapped oil diffusion pump.

The deposition target was a Si bar 6 mm wide, 40 mm long, and 0.3 mm thick. The silicon had been steam oxidized at 900° C so that a SiO_2 film about 1 μm thick covered the polished surface. The unpolished surface had a natural oxide on it. The silicon bar was heated by passing a current through it as illustrated in Fig. 1. The sample temperature was measured by means of a chromel-alumel thermocouple (60 μm diameter wires) attached with a graphite paste. The thermocouple was calibrated with an infrared optical pyrometer. At 80° C, 200° C and 400° C, the estimated errors in temperature were $\pm 5^\circ$, $\pm 10^\circ$, and $\pm 20^\circ$ C respectively. A chromel wire with a nominal diameter of 60 μm was wrapped around the Si bar. This wire served as a simple shadow mask, as shown in Fig. 1.

Before deposition of Al was started, the sample was cleaned by heating to 800° C for two minutes. The sample was then allowed to cool to the temperature desired for deposition before starting deposition from the ICB source which was already in operation. The deposition of Al was started and stopped by means of a simple shutter. The average Al deposition rate was 240 $\text{\AA}/\text{min}$. The electron beam used for ionization of the Al beam was operated with a current of 200 mA at 400 V. The measured ratio of ion current density ($\text{A}/\text{cm}^2\text{-s}$) to Al deposition rate ($\text{atoms}/\text{cm}^2\text{-s}$) showed that 0.13% of the Al beam was ionized for ICB acceleration voltages of 3 and 6 kV. When no acceleration voltage was used (0 kV), the electron beam for ionization was turned off.

After the Al deposition, the wire shadow mask was removed from the sample. Then SEM and Auger electron line scans were used to determine the diffusion distance of Al on SiO_2 for the various substrate temperatures and beam acceleration voltages. In general, the Auger line scans alone are insufficient to measure diffusion distance because for Al film thicknesses greater than a few atomic layers the Auger signal is independent of film thickness. Therefore, the width of the shadowed strip free of Al must be subtracted from the total width of the shadowed strip. Half of this width difference equals the maximum diffusion distance of Al atoms after they hit the surface at the edge of the shadowed zone. This is illustrated schematically in Fig. 2.

An Hitachi model 800 TEM was used in the SEM mode to take micrographs of the shadow zones. The shadow width was between 56 μm and 60 μm . The Al KLL Auger line scans were taken with a Physical Electronics model 600 SAM unit. The primary electron beam for Auger line scans was operated at 15 kV in order to avoid charging of the SiO_2 film. The primary electron beam diameter was approximately 1 μm for the Auger line scans. The estimated error in shadow zone width measurement was $\pm 1 \mu\text{m}$. Therefore, the total estimated error for diffusion distance was $\pm 2 \mu\text{m}$.

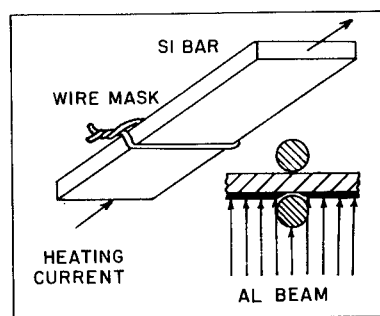


Fig. 1. Schematic of mask arrangement.

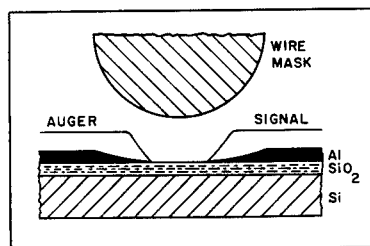


Fig. 2. The relationship between the wire mask, the Al film under the mask, and the Auger line scan signal.

RESULTS AND DISCUSSION

Fig. 3 is a trace of the Auger line scan across the shadow zone of the 0 kV, 80° C Al deposition. The width of the top of this line scan is 56 μm , whereas the width across the bottom of the scan (near-zero Auger signal) is 26 μm . Half of the difference between top and bottom widths is 15 μm . This is taken as the diffusion distance from the edge of the shadow zone. A mechanical trace of the same shadow zone was taken with a Sloan Dektak II profilometer. This trace is shown in Fig. 4. It shows a top width of 56 μm and a bottom width of 47 μm . Thus, while the top widths of both Auger and mechanical scans are equal, the bottom traces are not. This result shows that the spread of Al in the shadow zone is in the form of a film much thinner than the nearly 1,500 Å Al deposit. This film is too thin to be detected by the mechanical profilometer.

Fig. 5 is a SEM micrograph of the 0 kV, 80° C Al deposition shadow zone. The full width of 56 μm measured from this micrograph agrees with the Auger and mechanical scans. Fig. 6 is a micrograph taken at higher magnification at the right edge of the shadow zone. The arrow at the top of this figure indicates where the shadow zone begins. To the left of this arrow, the grain size of the Al deposit becomes smaller until individual grains cannot be resolved beyond 0.75 μm from the shadow edge. The resolution in this micrograph is about 150 Å. A light gray area in this micrograph extends another 0.75 μm beyond the edge of resolved grains. It is probable that this light grey area is due to a rapidly decreasing Al film thickness. Therefore, only the first 1.5 μm of Al diffusion can be discerned in Fig. 6.

The diffusion distances determined from the SEM micrographs and Auger line scans are given in Table I. These results are displayed in Fig. 7.

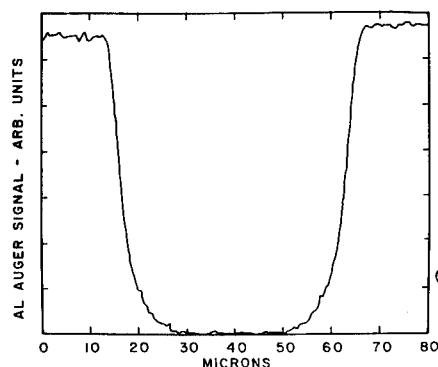


Fig. 3. Al Auger line scan for the 80° C, 0 kV shadow zone after mask removal.

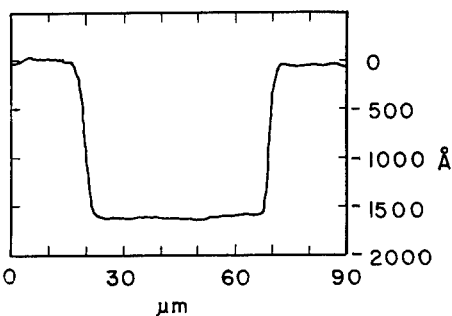


Fig. 4. Profilometer scan of the same shadow zone as in Fig. 3.

It is apparent from Table I and Fig. 7 that the diffusion distance of Al on SiO_2 increases as the acceleration voltage increases at low substrate temperatures. This tendency continues at 200° C, but at 400° C the order is reversed, with higher acceleration voltages producing lower diffusion distances. It is likely that this reversal is caused by an increased evaporation rate at high temperatures. Similar results were found by Hanbucken et al. [6,7] for Ag evaporated onto Si and by Levenson et al. [8,9] for ICB deposition of Al onto Si.

The results presented here are for a limited set of experimental conditions. It is likely that the deposition rate, the ICB source parameters and the partial pressure of gases in the deposition chamber all have some influence on the surface mobility of the impinging atoms. Furthermore, the surface chemistry

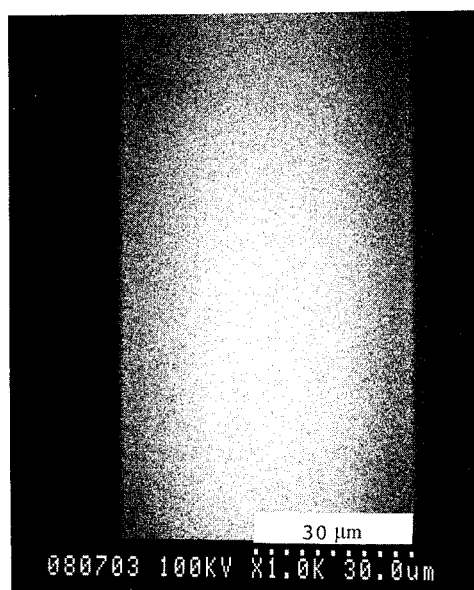


Fig. 5. Micrograph of the 80° C, 0 kV shadow zone.

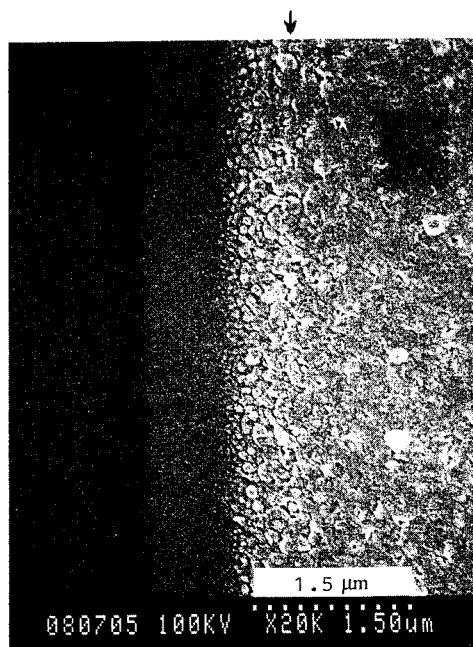


Fig. 6. Higher magnification of right edge of Fig. 5.

TABLE I

ALUMINUM DIFFUSION DISTANCE ON SiO_2
DURING IONIZED CLUSTER BEAM DEPOSITION

SUBSTRATE TEMPERATURE $^{\circ}\text{C}$	ACCELERATION VOLTAGE kV	DIFFUSION DISTANCE μm
80	0	15
70	3	22
80	6	26
200	0	26
200	3	25
200	6	29
400	0	24
400	3	19
400	6	12

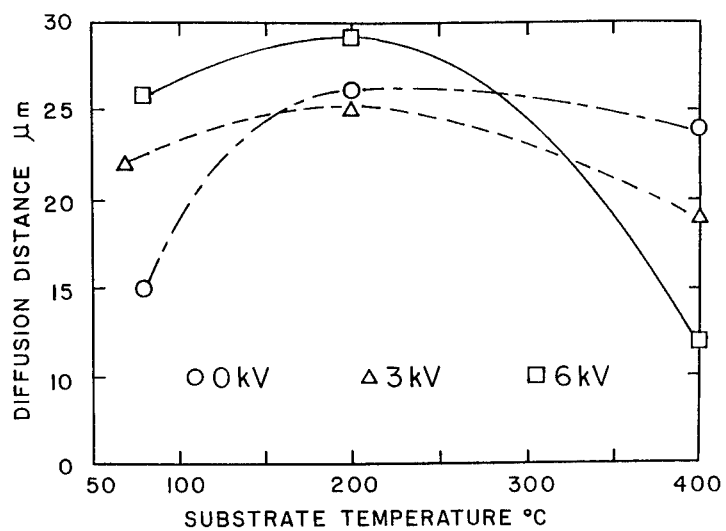


Fig. 7. Surface diffusion distance of Al as a function of acceleration voltage and surface temperature.

and surface structure of the substrate also are expected to influence surface mobility. It is also apparent that in this type of study it is difficult to distinguish between the surface diffusion of Al on Al and the surface diffusion of Al on SiO₂. This because as the Al film becomes thicker, Al atoms must diffuse over aluminum before arriving at the SiO₂ surface. In spite of these limitations, we can conclude that the effective mobility of Al on steam generated SiO₂ is significant.

ACKNOWLEDGEMENT

We wish to thank Mr. Darryl Allman of the NCR Corporation, Colorado Springs, CO, for supplying the steam oxidized Si wafers used in this study.

REFERENCES

1. B.A. Movchan and A.V. Demchishin, Phys. Met. Metallogr. 28, 83 (1969).
2. J.A. Thornton, J. Vac. Sci. Technol. 11, 666 (1974).
3. J.A. Thornton, An. Rev. Mat. Sci. 7, 239 (1977).
4. J.A. Thornton, J. Vac. Sci. Technol. A4, 3059 (1986).
5. P. Messier, A.P. Giri and R.A. Roy, J. Vac. Sci. Technol. A2, 500 (1984).
6. M. Hanbucken, T. Doust, O. Osasona, G. Le Lay, and J.A. Venables, Surf. Sci. 168, 133 (1986).
7. J.A. Venables, J. Vac. Sci. Technol. B4, 870 (1986).
8. L.L. Levenson, M. Asano, T. Tanaka, H. Usui, I. Yamada, and T. Takagi, J. Vac. Sci. Technol. A6, 1552 (1988).
9. L.L. Levenson, H. Usui, I. Yamada, T. Takagi, and A.B. Swartzlander, to appear in J. Vac. Sci. Technol.
10. I. Yamada, H. Takaoka, H. Inokawa, H. Usui, S.C. Cheng, and T. Takagi, Thin Solid Films, 92, 137 (1982).
11. T. Takagi, Z. Phys. D3, 271 (1986).

ATOMIC-SCALE MODELING OF LOW-ENERGY ION-SOLID PROCESSES

BRIAN W. DODSON
Sandia National Laboratories, Albuquerque, NM 87185-5800

ABSTRACT

Various techniques which have been applied to modeling low-energy ($\ll 1$ keV) ion-solid interactions on an atomistic scale are described. In addition to their individual strengths, all such methods also have a number of drawbacks, both fundamental and practical. The range of validity, and the problems encountered external to this range, will be outlined for the different approaches. Finally, examples of molecular dynamics simulations of low-energy ion-solid interactions will be presented.

INTRODUCTION

Growth, surface modification, and doping of artificially structured materials (both metals and semiconductors) using low-energy ($\ll 1$ keV) ion-beams is currently under intense experimental study. The kinetic energy associated with the ion beam can control important effects in near-surface structural kinetics. Such effects include reactive ion cleaning/etching¹, control of surface growth nucleation sites², control over growth morphology³, including relative orientation of epitaxial growth⁴, production of non-equilibrium doping profiles⁵, growth of metastable epitaxial semiconductor alloys⁶, and depth-limited oxidation of semiconductor surfaces.⁷ The growth and fabrication opportunities presented have generated considerable excitement in this field of research.

Rather than pursuing the purely empirical approach of doing every possible experiment, however, it appears more reasonable to establish the behavior of the dominant mechanisms through a carefully chosen subset of experiments, and then develop procedures to predict the behavior of those mechanisms under a wide range of conditions. Such considerations have driven considerable effort on atomic-scale modeling of low-energy ion-solid processes.

This paper reflects an attempt to review the special aspects of modeling low-energy ion beam processes on an atomistic scale. The low-energy regime is defined in physical terms, and the general nature of ion collisions, cascade formation, and healing of the target material is described. The interaction of a low-energy ion with the target is described in detail, because many of the relevant interactions are not important in conventional high-energy beam processes. The three major classes of simulation techniques are then outlined, along with a discussion of the validity of their underlying assumptions in the low-energy regime. Finally, we illustrate the current status of atomic-scale modeling as applied to low-energy ion beam processes through examples of state-of-the-art simulations.

WHAT ARE 'LOW-ENERGY' ION BEAMS?

It is useful to establish physically based limits on the "low-energy" ion beam regime. (Note that we shall call any energetic species impinging on a solid surface an ion, even if it is uncharged.) At the lower end, a reasonable cutoff provides that the kinetic energy of the incoming ions is similar to chemisorption energies for that ionic species on the substrate in question. Note that this energy can, for chemically reactive species, be much higher than typical thermal energies of, e.g., an MBE source. (Thermal energies in an MBE deposition process are typically 0.1-0.2 eV, whereas chemisorption energies for most semiconductors are several eV.) The reason for this choice is that the energy released in forming the chemical bonds is largely dissipated as phonon-like excitations and lattice distortions, which serve to perturb the local environment of the chemisorbed species in a manner similar to the effect of excess kinetic energy supplied by ion beam deposition. A reasonable lower limit for the "low-energy" beam regime in most cases is thus 5-10 eV.

Establishing an upper limit for the "low-energy" regime is not as straightforward. For example, one physically based limit is that the beam velocity should be less than the Fermi velocity of the valence electrons of the target material. This limit generally corresponds to beam energies of several hundred keV, and thus appears much larger than appropriate for our current purposes. A more reasonable limit can be set by determining in what energy range the approximations used in modeling high-energy (>10 keV) ion beam interactions begin to break down. In the high-energy regime, the energetic particles are modeled as "soft-spheres", having monotonically decreasing pairwise repulsive interactions. This is quite reasonable, as rapidly moving atoms do not have time to form chemical bonds (to do so, the residence time Δt of the atoms must be $\gg \hbar/\Delta E$; at typical bonding energies ($\Delta E \approx 1$ eV), Δt is about 1 femtosecond (fsec); in fact, Δt for a 100 keV particle is about 0.1 fsec). In addition, the bonds between substrate atoms do not contribute significant inelastic losses, again because of the disparity in energy scales. At the same time, the pairwise interaction approximation is also appropriate because the dominant interactions take place at small interatomic radii. As a result, the "soft-sphere" approximation is quite reasonable in the high-energy regime.

When does this "soft-sphere" pairwise interaction approximation break down? Discussion of this multifaceted question will take up a significant part of this review. However, various approaches to this question suggest that the high-energy interaction approximation breaks down noticeably at beam energies of a few hundred eV. In addition, the 'breakeven' energy for substrate sputtering (where the beam flux equals the sputtering rate) is on the order of 1000 eV for many systems. For this review, then, the low-energy regime encompasses beam energies of roughly 10-1000 eV. This criterion also agrees with the requirement, in ion-beam deposition, that sputtering processes are limited enough that a positive net flux to the surface is retained.

ATOMIC-SCALE SIMULATION OF LOW-ENERGY ION-SOLID PROCESSES

The overall process of interaction of an energetic ion with a solid can be broken down into three major regimes, each occurring on a different timescale. The first is the collisional regime, in which the incoming ion transfers its kinetic energy to the solid. This can take place either through direct nuclear collisions with the atoms of the solid, or by inducing transitions in the electrons of the solid. The nonequilibrium structure of displaced and/or highly energetic atoms formed within the solid in this period is usually called the collision cascade. The underlying crystal structure of

the solid is often completely disrupted in the cascade, with an accumulation of vacancies in the central region of the cascade and a corresponding number of interstitials generated around the periphery by the action of 'dynamic crowdions'.⁸ The characteristic timescale for development of this structure is a few tenths of a picosecond in the low-energy regime.

The second major process is that of thermalization of the cascade region. Energetic atoms will lose their excess kinetic energy through generation of phonons in the surrounding material. The thermalization regime ends when the cascade region has settled to local thermal equilibrium with the surrounding material, so that the temperature is constant across the region. This will generally occur within a few psec for cascades generated by low-energy ion impact.

Following the collisional and thermalization regimes, the cascade region still exhibits a considerable degree of damage. Over the course of time, this damage may be healed by diffusional processes, or by the action of other incoming ions or atoms (e.g., in ion-assisted growth). The rate of further evolution is a strong function of the experimental conditions, but will typically take place on a timescale which is not amenable to direct atomic-scale simulation. As a result, the primary foci for atomistic simulation of ion-beam processes are the collisional and thermalization regimes, where the relevant physics takes place during the first few psec of interaction.

There are three general classes of simulation techniques for study of atomic-scale structure generated by low-energy ion-solid events. The simplest, and most widely used for high-energy ion processes, are the Monte Carlo methods, with the TRIM-based codes⁹ providing the best-known examples. In this approach, a moving particle approaches an initial atom with a randomly chosen impact parameter. The binary collision approximation, which assumes that the collision dynamics is dominated by the interaction of only the closest atom, allows the collision to be treated as a simple binary scattering event. The impact parameter, the particle masses, and the relative velocity of the two particles, when combined with an interaction potential, allow calculation of the scattering integral, which yields the amount of energy transferred to the solid atom. The ion follows a straight line between subsequent collisions. The angle of deviation in the collision, however, is not used (in pure TRIM-type simulations) to evaluate the distance to the next collision. Instead, the solid is assumed to be amorphous, and the distance and impact parameter for the next collision are chosen randomly based on the average properties of the solid lattice. (One common technique is to rotate the lattice to a random orientation, and project the initial ion trajectory until an impact parameter less than a cutoff value is found.) The scattering integral for this binary collision is then evaluated, and the procedure iterated until the kinetic energy of the incoming ion is dissipated.

The previous paragraph describes only the simplest Monte Carlo ion range simulations. For treatment of cascades, the solid atoms to which substantial amounts of kinetic energy have been transferred must also be followed, as they can produce secondary cascades. To obtain the lateral extent of a cascade, more information about the lattice structure and deflection angle of the collisions must be included in the simulation. Evaluation of the extent of permanent damage is accomplished by identifying an average 'displacement energy' for formation of an interstitial-vacancy pair. In all cases, however, Monte Carlo simulations are essentially pragmatically defined stochastic descriptions with limited basis in first-principles. They provide reasonable accuracy for the collisional regime of high-energy ions because the various approximations applied to the collisions apply there and a given ion experiences a large number of collisions. Thus treating each collision as a statistical average is reasonable, and a highly refined empirical fitting process has been developed over several decades. In the low-energy regime,

however, essentially all of the approximations used in development of Monte Carlo techniques break down. As a result, it is not reasonable to blindly apply this class of simulation to low-energy ion-solid processes. In addition, Monte Carlo techniques are incapable of treating the thermalization regime. Despite these limitations, these are the most commonly used procedures at this time.

A significant refinement of the Monte Carlo techniques is sometimes called the binary-collision lattice technique. The best-known code of this type is probably MARLOWE.¹⁰ These techniques follow the Monte Carlo procedures, save for two factors. First, rather than assuming an amorphous lattice, the actual lattice of the solid determines the trajectories of the incoming ions. Second, the angle of deflection is calculated in each binary collision. The trajectory through the lattice is then followed from collision to collision throughout the lattice until the kinetic energy is dissipated. The result is a deterministic calculation of the ion trajectory and the corresponding cascade, fixed by the crystal lattice, interaction potential, and the initial beam trajectory. Much of the stochastic nature which is the downfall of the Monte Carlo techniques is absent in these binary-collision lattice simulations. This procedure is more accurate for range calculations, because lattice effects, such as channeling, are included. It also provides a more natural description of cascade structure, since the lateral evolution of the cascade is included naturally. However, the treatment of lattice damage is still probabilistic in nature (based on an average displacement energy), the collisions are still assumed to be binary in nature, and the moving particle is assumed to travel on straight lines between these binary collisions. All of these assumptions are questionable in the low-energy regime. Again, the thermalization process cannot be properly treated by this class of techniques.

Finally, the molecular dynamics techniques¹¹ provide a description of ion-solid processes as accurate as the description of interactions between the various parts of the system. In this approach, the Newtonian equations of motion of the individual atoms are integrated in time to obtain the actual trajectory of the entire system through phase space. (For beam energies above 10 eV, the deBroglie wavelength of an ion is several orders of magnitude less than interatomic spacings. The classical trajectory approximation is therefore justified.) This is a wholly deterministic procedure, and naturally includes lattice damage, collective effects of the solid, and simultaneous interactions amongst several particles. In principle, then, the molecular dynamics techniques are the ideal approach toward low-energy ion-solid process simulation, including both the collisional and thermalization phases. The difficulty is that these techniques are orders of magnitude more difficult to carry out from a computational viewpoint. As a result, only a handful of such simulations have been performed at this time.

In this section, three general classes of ion-solid simulations were outlined. Application of these techniques requires various approximations which are perhaps reasonable (at least on average) in the high-energy regime, but which appear likely to fail at low ion energies. The amorphous solid approximation does not even include particle channeling, which is a common effect in the high-energy regime. The binary collision approximation is likely to break down at low energies, where the distance of closest approach is not dramatically smaller than interatomic distances on average. In addition, inelastic interaction with collective modes of the solid can become a dominant influence at low beam energies. The approximation that trajectories are straight between collisions is seriously wrong when the kinetic energy is within an order of magnitude of binding energies in the solid. The statistical approach toward generation of lattice damage is questionable when an ion interacts with only a small number of atoms before thermalizing. Most of the above approximations can be avoided in molecular dynamics simulations.

However, choice of appropriate interactions between the atoms of the solid, and between those atoms and the incoming ion, will always represent a significant approximation. The description of these interatomic interactions defines the fundamental physics controlling the ion-solid processes. Various approximations used to describe these interactions are described in the following section.

ENERGETICS OF LOW-ENERGY ION-SOLID INTERACTIONS

The overall interaction of an energetic ion with a solid results from a complex combination of electronic and nuclear (collisional) interactions. Contributions from electronic interactions include the classical Bohr stopping power, in which kinetic energy is lost to the work required to displace a stationary electron gas, particle-hole creation, excitation of plasmons, charge transfer reactions, and related effects. A classical image charge interaction with the surface may also be present. The nuclear interactions, which are usually treated as interatomic potentials, include the ion-solid interaction potential as well as the solid-solid atomic interaction potential.

Fully accurate treatment of all these interactions poses an extremely difficult problem. Fortunately, in any given energy region, some factors of the overall interaction dominate. In the high-energy regime, for example, the usual approximation is that the ion-solid interaction potential is a sum of purely repulsive pairwise screened Coulomb potentials between the cores of the interacting particles, combined with exchange and correlation energies based on a simple density-functional model and superposition of static charge densities. (An example is the widely used "universal" nuclear interaction potential developed by Ziegler, Biersack, and Littmark.¹²) The electronic interaction is often treated by invoking an electron-density and velocity-dependent "frictional force", which is primarily due to the Bohr stopping power. Factors which are generally ignored in this limit are the image potential, the interaction between the atoms of the solid, and the various localized electronic excitations.

The interactions appropriate for the low-energy regime differ considerably. At low energies, the Bohr electronic stopping power is very small, and can usually be ignored; however, the image potential, charge exchange reactions, and the localized electronic excitations can be quite important. The repulsive nuclear ion-solid interaction used in the high-energy regime is also inappropriate for low-energy interactions, because there can be time for atomic polarization and chemical bonding effects to provide significant attractive interactions. It is also necessary to include solid-state bonding in the target, as the ion trajectories and rate of energy transfer to collective excitations of the solid lattice can also be significant for low-energy ion-solid processes.

In order to model low-energy ion-solid interactions with any of the atomic-scale simulation techniques, tractable approximations for the dominant scattering mechanisms are necessary. The primary difficulty is presented by the ion-solid nuclear and image potentials. In both cases, the high-energy formalism assumes that the ion-atom interaction time is short enough (or equivalently, the ion approaches the surface quickly enough) that redistribution of the valence electrons does not take place. As a result, at sufficiently high beam energies screened Coulomb potentials provide an adequate description of the ion-atom interaction, and there is little or no image potential.

If the ion is moving slowly enough, however, the high-energy formalism breaks down. In the limit of very slow motion, both the ion-solid and the image charge interactions should be treated as adiabatic processes using the

Born-Oppenheimer approximation. In adiabatic interactions, the electrons are always in stationary eigenstates of the current nuclear configuration. As a result, chemical bonding interactions will form, and methods developed for treatment of chemical and solid-state bonding are appropriate for obtaining the ion-solid potential energy surface describing the collision dynamics. Similarly, the polarization of the valence electrons which is responsible for the image potential also has time to develop, and the conventional description in terms of the dielectric constant of the solid is appropriate in this limit. Note that in both high-energy and extremely low-energy processes these effects depend only on the instantaneous positions of the interacting atoms.

NONADIABATIC EFFECTS IN LOW-ENERGY ION-BEAM PROCESSES

In the low-energy regime, the system may not have time during the residence period to fully attain the adiabatic limit. Some degree of electronic redistribution, which may perhaps be described as formation of nascent chemical bonds (which we may term 'protobonds' or 'protobonding interactions'), should occur during the interaction, but the adiabatic (or equilibrium) bonding configurations may not have time to form. (Equivalent statements apply for the image potential.) In this situation, the nature and strength of the ion-atom nuclear interaction will depend not only on the present positions of the particles, but also on the relative velocity and past trajectories of the ion-atom pair. In this intermediate energy range, then, the ion-atom interaction must be treated using a velocity and history-dependent description.¹³

The crossover energy between the high-energy and adiabatic beam energy regimes can be estimated by comparing the timescale for development of bonding interactions with the ion-atom residence period. A typical residence period for low-energy ions is several femtoseconds. It is very difficult, however, to calculate the timescale for formation of protobonds within a time-dependent quantum-mechanical framework. Because of this, several relevant semiclassical estimates are considered, which together establish a qualitative lower limit on the timescale for formation of significant bonding interactions. The uncertainty principle can be used to determine if there is sufficient residence time for bonding interactions to be physically meaningful. From the energy-time uncertainty relation, the residence time required to make bonding interactions physically meaningful is about 0.5 fsec. Protobond formation during low-energy ion-atom encounters is thus meaningful within a quantum-mechanical framework.

Formation of protobonds within the residence period also requires that the electrons move fast enough to redistribute within the residence period, and that the force on the electrons from the forces driving the formations of the protobonds be large enough to drive the redistribution on the same timescale. The first condition requires that the ion be moving much slower than the Fermi velocity, which for metals and semiconductors is generally about two orders of magnitude higher than low-energy ion velocities. The second condition requires that the bonding force on the valence electrons be large enough to cause the electrons to drift on the order of 1 Å during the residence period. This force is on the order of $\Delta E/\Delta x$, or about 1 eV/Å. Upon integration, the time required for an electron distribution to drift 1 Å in a field of this magnitude is about 0.3 fsec, again very small compared to the residence timescale.

These independent semiclassical estimates agree in that the timescale for redistribution of valence electrons, and hence formation of bonding interactions, is potentially sub-femtosecond. (Note again that formation of adiabatic bonding configurations may take a considerably longer period. Only

the initial stages of redistribution of the valence electrons in the dynamically modified nuclear potential are considered here.) Since the residence period for low-energy beam particles in a lattice is generally several femtoseconds, it appears possible that there is an important regime (probably below a few hundred eV) in which non-adiabatic (and hence velocity and history-dependent) bonding interactions can influence beam-solid interactions.

It seems clear that non-adiabatic nuclear interactions may result from dynamic redistribution of the valence electrons during low-energy beam-solid processes. It is not immediately clear, however, that these effects will have a significant influence on the overall nature of the beam-substrate interaction. This question has recently been examined by the present author using molecular dynamics simulations of beam-solid interactions in the two extreme limits (non-bonding versus adiabatic bonding).¹³

A neutral Si beam normally incident on a (2x1) reconstructed Si(100) substrate was chosen for study. Beam energies of 12.5 eV, 50 eV, and 200 eV were considered to study the effect of bonding interactions over a range of velocities. A random distribution of impact positions was chosen so that the effect of uncharacteristic initial conditions could be eliminated. The interaction between the substrate

atoms was treated in both limits using an empirical many-body potential¹⁴, which provides a natural description of cascade processes, vibrational excitation, and other effects due to the incoming beam particles. The non-bonding ion-solid interaction was modeled using the Ziegler, Biersack, and Littmark "universal" nuclear interaction potential. The adiabatic ion-solid interaction is described using the same semiempirical many-body potential as used to describe the solid-solid atomic interactions.

These simulations revealed very significant differences between the bonding and non-bonding ions. For example, the average penetration depth of the 12.5 eV non-bonding ions is 10.5 Å, compared to 2.8 Å for the case of adiabatic bonding. At beam energies of 12.5 and 50 eV, energy loss is substantially more rapid for the bonding ions than for the non-bonding ions. At 200 eV, however, the energy loss is similar for the two cases. This is because the beam energy in this case is much larger than the characteristic bonding energies.

Figure 1 shows examples of collision cascades resulting from identical initial configurations for non-bonding and bonding ions at 12.5 and 50 eV. Major differences appear as the simulation conditions are varied. First, the trajectory of the non-bonding ions is only slightly deflected by interaction with the substrate atoms, whereas the bonding ions follow a strongly curved path through the substrate. This is a simple consequence of the strongly directional covalent bonding active in the latter case. For the same reason, the cascade resulting from the non-bonding ion extends far into the substrate, but has moderate lateral extent and density, whereas the bonding ion produces a cascade restricted to a region near the surface, but having a larger lateral extent and density of displaced atoms (this is best seen in the 50 eV simulations). Another interesting feature of the bonding ions is that the number of displaced atoms is a strong function of the beam energy, with only 3 atoms displaced at 12.5 eV, but 16 atoms displaced in the 50 eV event, despite the fact that the total energy deposition is similar in both cases. (The kinetic energy lost by the 50 eV non-bonding ion during penetration of the substrate lattice is 11.3 eV in this example.) As a result, the beam energy should affect low-energy ion-solid processes not only by varying the available energy, but also by controlling the ion-substrate coupling. As a result, beam energy could take on a new importance in optimization of very-low-energy ion-beam processing.

The simulations presented above establish that the effect of an ion beam on a surface depends strongly on the nature of the interaction of a rapidly moving ion with the substrate atoms. The nature of the interaction should

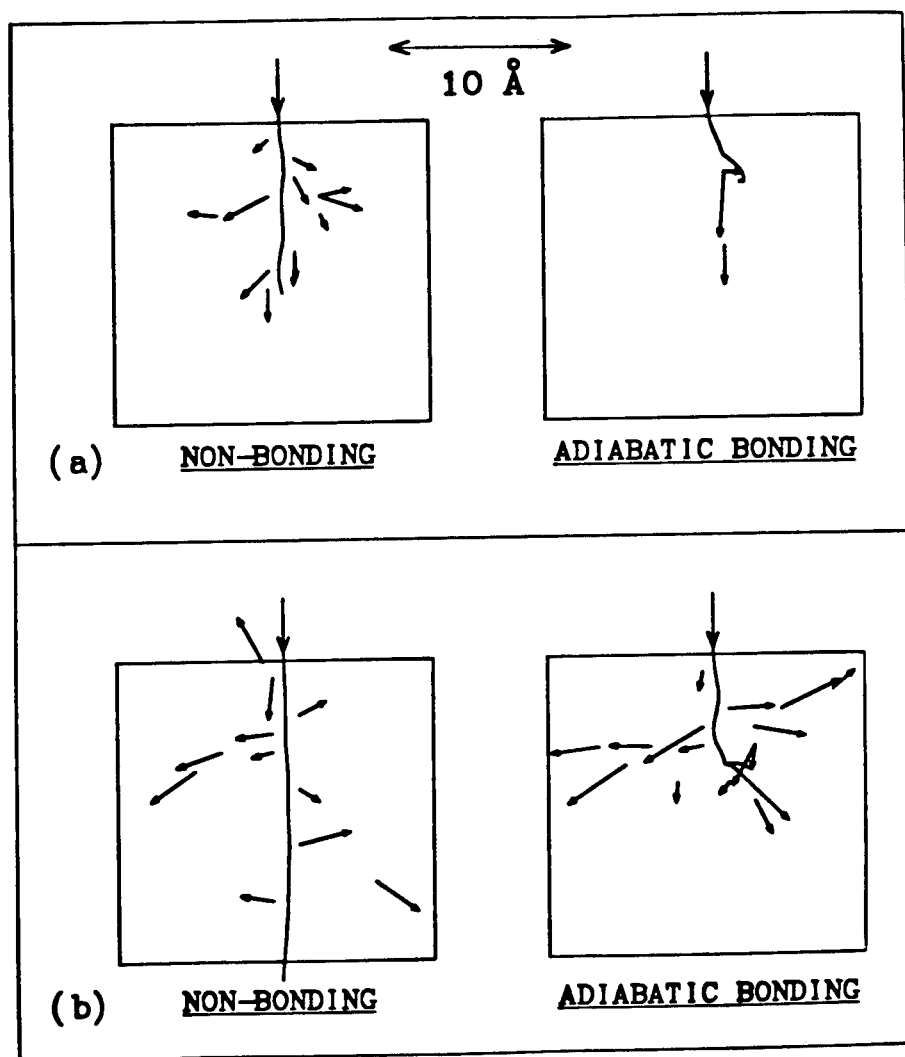


Figure 1. Collision cascades produced in a Si(100) substrate by a very-low energy neutral Si ion at normal incidence. The impact location is the same for all examples shown. The beam energy is 12.5 eV in (a), and 50 eV in (b). The cascades marked "non-bonding" result from use of the universal nuclear potential of Ziegler et. al.¹² to describe ion-atom interactions, whereas those marked "adiabatic bonding" use an empirical many-body potential¹⁴ for ion-atom interactions. In all cases, the substrate atoms interact via this many-body potential to accurately include the effect of lattice vibrations. The distinction between the non-bonding and adiabatic bonding ion-atom interactions is clearly seen.

change with relative velocity of the interacting particles, from nearly adiabatic bonding at the low end of the low-energy regime to repulsive screened Coulomb potentials at the high end. As always, the intermediate regime is the most difficult to treat. Preliminary efforts have been made by various groups toward a time-dependent quantum description of ion-atom interactions in the non-adiabatic energy regime.¹⁵ Although this area of research is progressing rapidly, simulations complex enough to treat the non-adiabatic interactions described in the present paper are apparently beyond the current state-of-the-art.

EXAMPLES OF LOW-ENERGY MOLECULAR DYNAMICS SIMULATIONS

In this section, some low-energy beam-solid simulations which are representative of the current status of the molecular dynamics technique are presented. There are two main areas being studied at this time, concentrating either on ion-beam processes which are not amenable to experimental study or on the problem of identifying appropriate interaction potentials by comparison with relevant experimental studies. Both types of efforts have produced encouraging results.

Many studies have been made of processes which are difficult or impossible to study experimentally. An obvious problem of this type is ion-beam deposition, in which the relevant physics takes place primarily on a psec-nsec timescale. The ion-beam deposition of Lennard-Jones atoms on a two-dimensional substrate over a range of incident kinetic energies has been simulated by Muller.^{16,17} He found that, whereas thermal deposition processes carried out at very low substrate temperatures yielded a spongy, porous microstructure, beam energies equivalent to a few eV were sufficient to drive formation of a nearly perfect epilayer (Figure 2). Similarly, in the case of ion-assisted deposition (ion bombardment simultaneous with thermal deposition), small beam energies were found adequate to greatly improve the epilayer microstructure. It is certainly possible that, in this particular system, the porous microstructure of the thermally deposited epilayer may be an artifact of the extremely short timescales available for structural relaxation in molecular dynamics simulations. The qualitative effect of the incident kinetic energy of the impinging atoms, however, is probably valid for general systems.

More commonly, the initial stages of the low-energy ion-solid interaction are studied using molecular dynamics techniques. Simulations of the interaction of low-energy (<50 eV) neutral Si beams with a (111) silicon substrate have recently been carried out by the present author.^{18,19} The interactions amongst the substrate atoms and between the ion and the substrate atoms are treated using an empirical many-body potential¹⁴ which captures the essence of the covalent solid-state bonding. (The tacit assumption of fully adiabatic bonding was made here. This is probably reasonable in this very-low energy regime.) In the case of near-normal incidence, both the range of the ions and the extent of lattice damage were found to be greater than expected from the conventional Monte Carlo or binary-collision lattice models. The extended range is caused by interactions which efficiently steer the ions into lattice channeling directions, allowing deeper penetration than expected. The increase in lattice damage has at least two sources. First, the range of the potential combined with the collective response of the lattice produces a near-surface region in which the cage effect of the surrounding atoms is less than expected by the simple displacement energy description. Second, the highly directional nature of covalent bonding produces more effective coupling between the kinetic energy of the ion and a given substrate atom. The overall

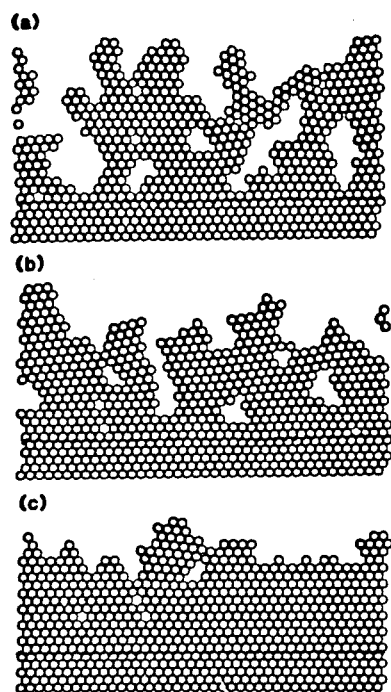


Figure 2. Molecular dynamics simulation of growth of two-dimensional Lennard-Jones crystals. The kinetic energy of the beam atoms is a) 0.05ϵ , b) 0.3ϵ , and c) 1.5ϵ , where ϵ sets the scale of the binding energy. [Roughly, a) corresponds to thermal deposition, and b) to ≈ 10 eV beam deposition.] The influence of added kinetic energy is clearly shown, with beam deposition resulting in growth of material having nearly the ideal crystal density.

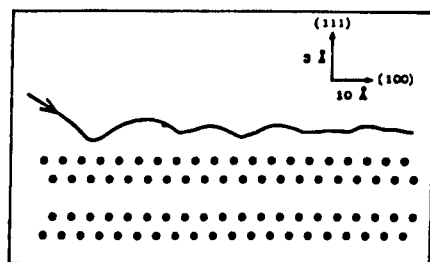


Figure 3. The surface channeling trajectory of a 40 eV silicon atom incident at an angle of 10° on the Si(111) surface. The perpendicular momentum of the beam atom is lost by inelastic generation of collective substrate excitations, causing the beam atom to be trapped at the surface. The resulting trajectory is nearly parallel to, and about 2 Å above, the surface of the substrate.

picture resulting from this study is very different from that suggested by the stochastic simulation techniques.

Grazing incidence trajectories were also studied.¹⁹ In these, incoming neutral Si ions were directed at grazing (3-30°) angles of incidence along the (110) rows of atoms on the substrate surface. Again, all interactions were described by the empirical many-body potential. At larger angles of incidence, the ions were found either to scatter off the surface or stick near the impact site. As the incidence angle is reduced, however, the vertical momentum is absorbed by phonon-mediated inelastic interaction with the substrate, and the ion is steered into a trajectory parallel to and above the substrate, where it is trapped by the chemical bonding between the ion and the substrate atoms (Figure 3). Ions following these 'surface channeling' trajectories experience very little energy loss, and can travel large distances (hundreds of Å) from the point of impact. A closely related effect was recently observed experimentally for low-energy K ions incident on a Si substrate.²⁰

A problem of considerable importance to the plasma/wall interactions which limit the performance of some types of fusion research devices is that of low-energy hydrogen reflection from metal surfaces. Experimental study of this phenomenon is extremely difficult at energies below 100 eV, which is perhaps the most important regime for the applications of interest. In response to this need, Baskes²¹ has studied reflection of neutral H ions from a (100) nickel surface for ion energies from 0.1 to 100 eV. The Ni-Ni and the H-Ni interactions are treated within the framework of the embedded atom method, which is a semiempirical many-body potential with an excellent record of success in treating fcc metals. In the absence of chemical interactions, one expects that the reflection coefficient will go to unity at very low energies. In contrast, the EAM simulations predict that the reflection coefficient goes to zero, consistent with a finite chemical binding energy. The effect of the many-body surface bonding effects begins to appear at ion energies of about 10 eV in this system (Figure 4).

Another interesting study has recently been performed by Garrison and coworkers^{22,23}, who studied the use of the embedded atom method in calculating sputtering from metal surfaces, in particular Rh and Cu sputtering driven by 5 keV Ar ion bombardment. (Although the beam energy is considerably above the low-energy regime, the atomic interactions within the substrate which lead to sputtering generally occur at much lower energies.) The primary result of including the many-body interactions is to approximately double the energy of the peak of the energy distribution, and to increase the size of the high-energy tail (Figure 5). They find that the energy and angular distributions predicted by molecular dynamics simulations are in agreement with the relevant experimental data, although the form of the EAM interactions had to be adjusted to obtain this result. This provides a clear example of the need to include many-body interactions to accurately model low-energy ion-solid processes.

SUMMARY

In this review, we have attempted to establish that there is a physically defined low-energy regime for ion-solid processes. This regime is distinguished from thermal adsorption processes by having incident kinetic energy greater than typical chemisorption energies, and from the high-energy ion-solid regime by the breakdown of the 'soft-sphere' and binary collision approximations. These considerations establish a low-energy regime from about 10-1000 eV, in which collective excitations of the crystal lattice, many-body effects, and ion-solid bonding interactions cannot be safely ignored. The primary atomic-scale simulation techniques applied to high-energy ion-solid

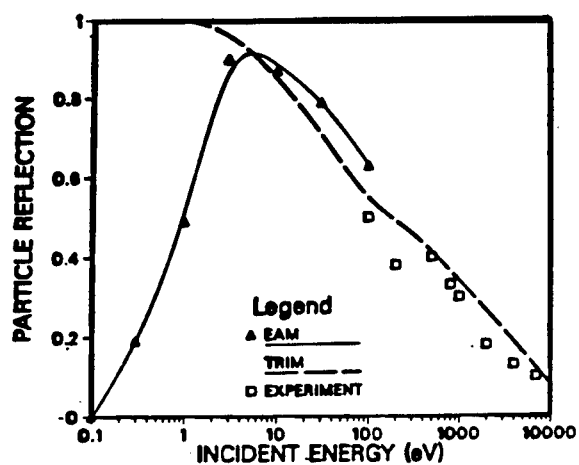


Figure 4. Probability of hydrogen reflection off a Ni(100) surface as a function of incident energy. The solid line represents a many-body treatment, whereas the dashed line is the result of a TRIM-type Monte Carlo code. Below an incident energy of about 10 eV, major differences in reflection coefficient appear.

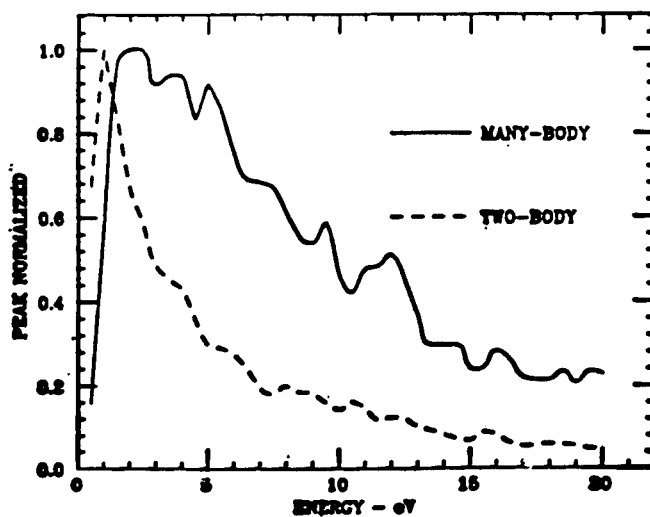


Figure 5. Energy distribution of sputtered atoms from a Cu(111) surface bombarded with 5 keV Ar ions. The two-body interaction is a Moliere core combined with a chemical Morse potential, whereas the many-body interaction is based on the embedded-atom method. When many-body interactions are included, the peak in the distribution shifts to higher energies, and the high-energy tail is much larger than for pairwise interactions.

processes were described, and their shortcomings for the low-energy regime were outlined. Even though the best founded technique is clearly molecular dynamics, there remain fundamental problems concerning appropriate potentials for this non-adiabatic regime. The many-body and non-adiabatic effects are not yet well understood. As a result, atomic-scale simulations of low-energy ion-solid interactions should not yet be regarded as routine tools, but rather as active objects of research in themselves.

REFERENCES

1. N. Herbots, B.R. Appleton, T.S. Noggle, R.A. Zuhr, and S.J. Pennycook, Nucl. Instr. Methods B13, 250 (1986).
2. See, e.g., J.E. Greene, CRC Critical Reviews of Solid State and Materials Science 11, 47 (1983).
3. T.C. Huang, G. Lim, F. Parmigiani, and E. Kay, J. Vac. Sci. Tech. A3, 2161 (1985).
4. L.S. Yu, J.M.E. Harper, J.J. Cuomo, and D.A. Smith, J. Vac. Sci. Tech. A4, 443 (1986).
5. H. Jorke, H.-J. Herzog, and H. Kibbel, Appl. Phys. Lett. 47, 511 (1985).
6. J.E. Greene, J. Vac. Sci. Tech. 1, 229 (1983).
7. N. Herbots, P. Cullen, S.J. Pennycook, B.R. Appleton, T.S. Noggle, and R.A. Zuhr, Nucl. Instr. and Meth. B (in press).
8. A. Seeger, Proc. 2nd UN Int. Conf. on Peaceful Uses of Atomic Energy, vol 6. (IAED, Vienna, 1958) p. 250.
9. J.P. Biersack and L.G. Haggmark, Nucl. Instr. Meth. 174, 257 (1980).
10. M.T. Robinson and I.M. Torrens, Phys. Rev. B9, 5008 (1974).
11. J.B. Gibson, A.N. Goland, M.M. Milgram, and G.H. Vineyard, Phys. Rev. 120, 1229 (1960).
12. J.F. Ziegler, J.R. Biersack, and U. Littmark, The Stopping and Range of Ions in Solids, (Pergamon, New York, 1985).
13. B.W. Dodson, Phys. Rev. Lett. (in press).
14. B.W. Dodson, Phys. Rev. B35, 2795 (1987).
15. e.g., B.M. Deb and P.K. Chattaraj, Chem. Phys. Lett. 148, 550 (1988).
16. K-H. Muller, Surf. Sci. 184, L375 (1987).
17. K-H. Muller, Phys. Rev B
18. B.W. Dodson, Phys. Rev. B36, 1068 (1987).
19. B.W. Dodson, Appl. Surf. Sci. 29, 334 (1987).
20. K.J. Snowdon, D.J. O'Conner, and R.J. MacDonald, Phys. Rev. Lett. 61, 1760 (1988).
21. M.I. Baskes, J. Nuc. Mat. 128-129, 676 (1984).
22. B.J. Garrison, N. Winograd, D.M. Deaven, C.T. Reimann, D.Y. Lo, T.A. Tombrello, D.E. Harrison, and M.H. Shapiro, Phys. Rev. B37, 7197 (1988).
23. D.Y. Lo, T.A. Tombrello, M.H. Shapiro, B.J. Garrison, N. Winograd, and D.E. Harrison, J. Vac. Sci. Tech. A6, 708 (1988).

COLLISION CASCADE DENSIFICATION OF MATERIALS

R.H. BASSEL, T.D. ANDREADIS, M. ROSEN, G.P. MUELLER, AND G.K. HUBLER
Naval Research Laboratory, Washington, D.C. 20375-5000

ABSTRACT

Computer simulations of the collision cascade process were used to investigate surface densification during ion beam assisted deposition (IBAD). The objective of the investigation was to see if densification resulted directly from the cascade, without any contribution from diffusion enhancement brought on by the bombardment. Calculations, using the computer code MARLOWE, were carried out for Ar bombardment of a crystalline Ge target, containing a void, using ion beam energies of 0.065, 0.5 and 1 keV. These results were used as data for a differential equation that describes the effect on void size of the simultaneous Ge atom deposition and Ar ion bombardment of a substrate containing voids. The present attempt examined the effects of irradiations on voids of 17 and 35 vacancies.

INTRODUCTION

In the process of ion beam assisted deposition (IBAD), a beam of low energy ions impinges on the substrate simultaneously with atoms from a vapor source[1]. The energy deposited in the surface by the ions produces near bulk density films as compared to physically vapor deposited (PVD) films, which frequently contain a significant fraction of voids[2]. The increased density of IBAD films is primarily responsible for improved film properties, which include stability of the refractive index[3], reduced film stress[1,4], high adhesion[4], and resistance to chemical attack. These properties, and the low substrate temperature during deposition, make the IBAD technique attractive for applications in thin-film optics and for making coatings that protect against corrosion, wear and oxidation[5].

Yehoda et al.[2] have shown that about a 10% void fraction in PVD Ge films was completely eliminated by simultaneous bombardment with 65 to 300 eV Ar ions. The value of the arrival ratio R of Ar ions to Ge atoms that was required for complete densification agreed well with earlier experiments by Hirsch and Varga[4]. In that work, a critical arrival ratio R_c was required to prevent spontaneous delamination of the films. The energy dependence of R_c was

$$R_c = k E^{-3/2}, \quad (1)$$

where k is a proportionality constant. These two measurements strongly suggest that the reduced stress in the film is a result of the elimination of voids. Brighton and Hubler[6] analyzed the results of Hirsch and Varga by means of simulations of collision cascades and showed that the energy dependence of R_c could be predicted with the assumption that densification is complete when every atom in the deposited film, on the average, is involved in a collision cascade (equivalent to 1 displacement per atom). This result suggested that the densification of the films is caused by atomic rearrangements within the total volume of the collision cascades and not by thermal spikes or enhanced surface migration of adatoms.

It is desirable to develop a detailed understanding of the densification phenomenon, which would aid in the optimization of the IBAD method. For example, in most IBAD films, the amount of incorporated Ar in the film is proportional to R . Therefore, if R_c is known, Ar incorporation is minimized by operating at R_c . The purpose of this work was to extend the calculation of Brighton and Hubler by examination of the details of the atomic rearrangement within the cascades, using three-dimensional collision-cascade simulation methods. Voids were placed in a Germanium lattice and all atomic rearrangements were followed during a collision cascade. In this way, we tested whether or not collision cascades lead to the collapse of voids and, therefore, densification.

Closely related calculations have been reported by K.-H. Muller using molecular dynamics (MD)[7,8]. These important papers demonstrated the densification effects produced by ion bombardment. The MD simulations were useful for showing overall trends of the energy and flux dependence of densification, but may not accurately predict the absolute value of R_c because only two dimensional crystals were used. Another purpose of this work is to extend the investigations of Muller to three dimensions using collision cascade simulations.

In the present study, calculations were made using the collision cascade simulation code MARLOWE[9] (version 12) to find the rate at which vacancies were removed from a void by the cascade as a function of the depth of the void in the target for 65 eV, 500 eV, and 1 keV Ar ion bombardment of Ge. We are only interested in the reduction of the void size by the cascades or

by recombinations of vacancies and interstitials immediately after being generated, not in post-irradiation annealing. Obtaining the rate of shrinkage enabled us to calculate the value of R needed to reduce the void volume to zero before the void was buried beyond the range of the incident beam by the deposition. The effect of void size on the rate of the depletion of vacancies from a void was accounted for in the calculation of R_c . MARLOWE was not used to simulate the deposition, but only to examine the effect of the ion bombardment on existing voids.

COLLISION CASCADE VOID REDUCTION MODEL

A number of simplifying assumptions were made in order to carry out the calculations. Ge is deposited in an amorphous form, but the use of the MARLOWE code restricted us to a crystalline target, because in its amorphous calculation mode the code is not able to keep track of the positions of the void vacancies in a convenient fashion. The density gradient of the Ge was not included in the collision cascade calculation. The surface binding energy, the displacement energy and the energy below which atoms were not tracked were all set equal to 3.5 eV. The ion beam impinged with near normal incidence (to avoid channeling effects) at randomly selected points on the target surface.

The MARLOWE calculation used a semi-infinite Ge target (diamond structure with a lattice length of 5.86 Å) with a test column of area $A=4 \times 4$ lattice lengths. A void of 35 (or 17) vacancies was centered in the column at a given depth at the beginning of the MARLOWE calculation. The effect of an ion bombardment on the void was then observed by examining the MARLOWE results. By repeating the calculation for various depths we were able to mimic the fact that the vapor deposition gradually buries a given void. Thus we obtained results for the effect of the ion beam as a function of depth. The reason for examining two initial voids sizes was to determine the change in vacancy removal rate with change in void size.

It was also assumed that the reduction in the size of the void represented the local density increase directly, i.e., vacancies created by the ion beam that did not recombine immediately were assumed to either combine with the highly mobile interstitials that also remained or to diffuse to the surface. Diffusion of single vacancies and interstitials may be greatly aided by the local high temperatures created by the cascade. In addition, we assumed that a uniform void size is deposited at the surface.

Vacancy and interstitial positions from the MARLOWE calculation were examined to see if recombination with void vacancies occurred. Recombination between a vacancy-interstitial pair took place if the two were closest to each other in comparison with other vacancies and interstitials and if they were within a recombination distance of 2 lattice lengths. The recombination distance selected was based on the separation distance at which instantaneous recombination takes place in an fcc crystal; it does not include diffusion of the species. Molecular dynamics calculations we have made for fcc materials [10] indicate that this is a reasonable value for the recombination distance.

Figure 1 shows the average number of vacancies lost from the void per incident beam atom as a function of void depth for the two void sizes. These values were obtained with 250 to 1000 ion beam histories per calculation, so that the statistical error is less than 5% for the significant portions of the results, and less than 10% for all of the results. As expected, both the depth over which vacancy reduction takes place and the rate of vacancy removal rise with increasing beam energy. Generally the smaller voids lose fewer vacancies per incident ion than the larger voids, because the larger voids have more surface area interacting with the cascade. Values at the surface of the target were obtained by extrapolation. This approximation is adequate in light of other approximations of the model. At present we can not draw any conclusions from the differences of the two sets of curves at the surface.

Because of the weak dependence of the rate of vacancy removal on the void size, it is clear that further MARLOWE runs need to be made using larger values of N . These initial results do not justify any particular cutoff on the initial size of voids.

CALCULATION OF R_c

Let $F(z,N)$ be the number of vacancies removed from a void of size N and a depth z by a single impinging ion of energy E . (The curves in fig. 1 are essentially the functions $F(z,17)$ and $F(z,35)$ plotted as a function of z for the three energies of interest. Depletion of vacancies from a void takes place at the rate governed by the equation

$$dN/dt = - I F(z,N), \quad (2)$$

where

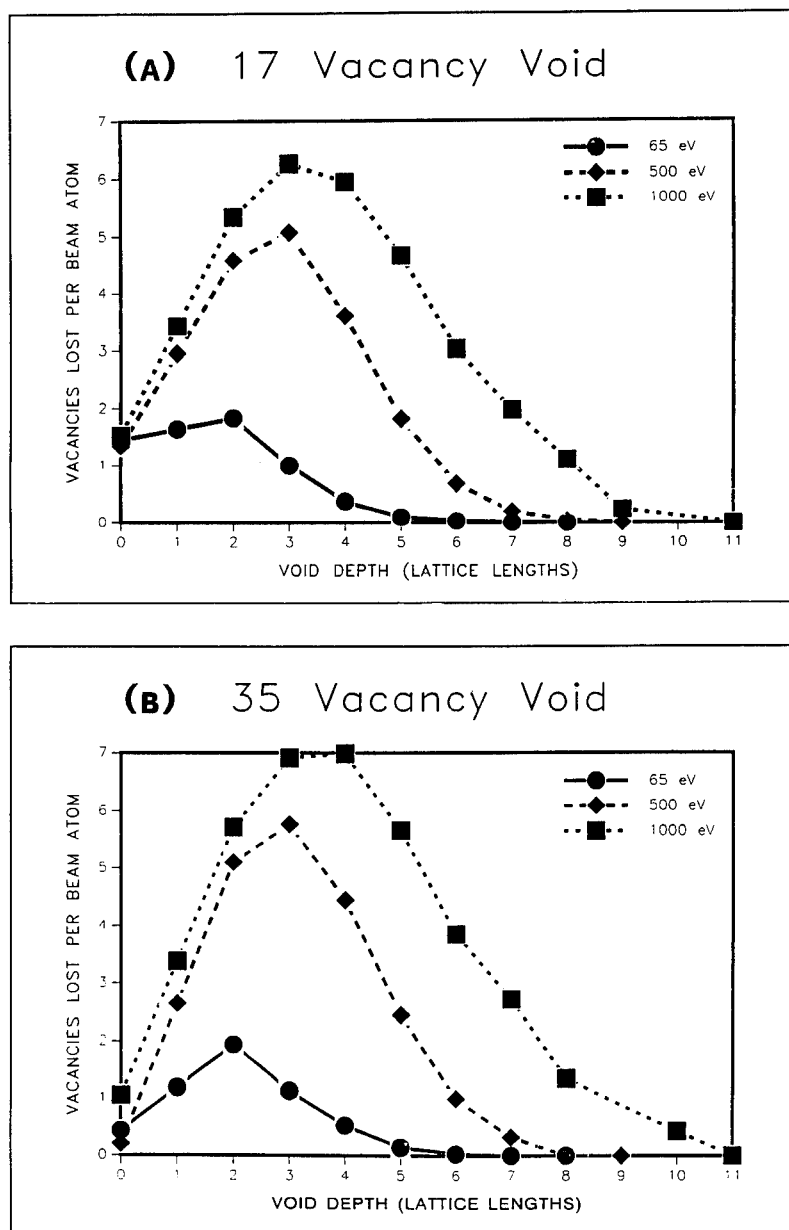


Fig. 1 -- Vacancy removal rates for voids of initial sizes (a) 17 and (b) 35 vacancies.

N = number of vacancies in the void at time t ,
 N_0 = initial number of vacancies in the void,
 t = bombardment time,
 z = depth of the center of the void,
 I = number of beam ions striking the surface (A) per second.

The surface of the material is steadily built up by the vapor deposition, moderated by the sputtering of the surface by the beam ions. The rate at which the surface builds up is given by

$$z = t V = t (D - IS) / C, \quad (3)$$

where

$C = \rho A$ (ρ is the bulk atomic number density),
 D = number of atoms deposited per second, and
 S = sputtering yield.

This last expression allows us to rewrite Eq. (2) as

$$V \, dN/dz = -I F(z, N). \quad (4)$$

The parameter I/V is simply

$$I / V = C R / (1 - RS) \quad (5)$$

where R is the arrival ratio I/D .

APPROXIMATE SOLUTION OF THE DIFFERENTIAL EQUATION

If we approximate $F(z, N)$ with the first two Taylor expansion terms we have

$$\begin{aligned}
 F(z, N) &\approx F(z, N_0) + F'(z, N_0) (N - N_0) \\
 F'(z, N_0) &= dF(z, N)/dN, N=N_0.
 \end{aligned} \quad (6)$$

The quantity $F'(z, N_0)$ can be evaluated from the curves in Fig. 1.

With this approximation the solution of Eq. (4) is

$$N(z) = \exp[-M(z)] \left[N_0 - [CR/(1 - RS)] \int_0^z dZ h(Z) \exp[M(Z)] \right], \quad (7)$$

where

$$M(z) = C R / (1 - R S) \int_0^z dZ F'(Z, N_0), \quad (8)$$

$$h(z) = [F(z, N_0) - N_0 F'(z, N_0)]. \quad (9)$$

(That this is the solution can be checked by substituting into Eq. (4).)

There is no compelling reason to choose a particular N_0 as typical for such irradiation-depositions. In fact, it is clear that we need to include the effects of initial void or more than 35 vacancies. As a preliminary test of our approach, we solve Eq. (7) using the data represented in Fig. 1 and the parameters listed in Table I. We obtained the values of the arrival ratio R such that no void of size 35 vacancies or smaller survived the irradiation process. To find these values of R , z was selected so as to be past the depth where F drops to zero and the value of R giving $N(z)=0$ was obtained through a trial and error process. Integration was carried out using Simpson's 1/3 rule. The values of R obtained are 0.054, 0.016, and 0.0088 for the energies 65 eV, 500 eV, and 1 keV, respectively.

TABLE I
Parameters used in the calculations

S(65 eV)	0.12 atoms/beam ion
S(500 eV)	1.0 atoms/beam ion
S(1 keV)	1.6 atoms/beam ion
C	128 atoms/lattice length
Ge Lattice Length	5.86 Å
N ₀	35 vacancies

DISCUSSION

We are encouraged by these preliminary efforts that this approach will eventually yield a good estimate of the critical ratio for Ge. The calculations reported here are not an attempt to evaluate the critical ratio. To accomplish that we need two sets of data:

- a) more MARLOWE runs, so as to estimate the vacancy removal rate produced by the beam ions as a function of a larger range of void size, and
- b) some estimate from experiment of the distribution of voids sizes that occurs in the absence of any irradiation.

With this data, the methods outlined will allow the calculation of the critical ratio for Ge and, in the process, will serve as a test of the use of MARLOWE to estimate vacancy removal rates. We plan to report these results in the near future.

REFERENCES

- [1] J.W. Cuomo, J.M.E. Harper, C.R. Guarnieri, D.S. Yee, L.J. Attanasio, J. Angilello and C.T. Yu, J. Vac. Sci. Technol. **20**, 39 (1982).
- [2] J.E. Yehoda, B. Yang, K. Vedam and R. Messier, J. Vac. Sci. Technol. **A6**, 1631 (1988).
- [3] P.J. Martin, J. Mater. Sci. **21**, 1 (1986); P.J. Martin, R.P. Welterfield and W.G. Sainty, J. Appl. Phys. **55**, 235 (1984).
- [4] E.H. Hirsch and I.K. Varga, Thin Solid Films **62**, 99 (1980).
- [5] G.K. Hubler, J. Mat. Sci. & Engin., to be published; proceedings of Surface Modification of Metals by Ion Beams, Riva del Garda, Italy, Sept. 12-16, 1988.
- [6] D.R. Brighton and G.K. Hubler, Nucl. Instr. & Meth. in Phys Res. **B28**, 527 (1987).
- [7] See, e.g., K-H. Muller, J. Appl. Phys. **62**, 1796 (1987).
- [8] K-H. Muller, Phys. Rev. **B35**, 7906 (1987).
- [9] M. T. Robinson and I.M. Torrens, Phys. Rev. **B9**, 5008 (1974).
- [10] T.D. Andreadis, et al, "The Influence of Defect Concentrations on Migration Energies in AgZn Alloys," these proceedings.

MOLECULAR DYNAMICS SIMULATIONS OF LOW ENERGY DISPLACEMENT CASCADES IN SILICON.

A.M. MAZZONE

CNR - Istituto LAMEL, Via de'Castagnoli 1 - I 40126 Bologna.

ABSTRACT

Displacement cascades formed in a silicon crystal by As^+ and Si^+ ions with energy in the range 50-500 eV are constructed with a molecular dynamics and a Monte Carlo simulation method. Conspicuous spike effects are observed with the molecular dynamics simulation.

INTRODUCTION

It is known that the evolution of a displacement cascade proceeds through a collisional phase, dominated by two-body collisions and a relaxation phase, during which the deposited energy is radiated by the excited phonons outside the volume of the damaged region.

In a silicon target many-body interactions (spike effects) occurring on the wake of projectiles forming dense cascades are thought to be responsible for an anomalous disordering well above the one produced during the collisional phase [1]. However the form and the extent of such interactions are uncertain and the subject hotly contended.

In this work a molecular dynamics simulation method is used to illustrate the excitation of the silicon lattice atoms resulting from the passage of a silicon and an arsenic ion with energy in the range 50-500 eV. The comparison with the cascade structure obtained with a Monte Carlo simulation method, which is the standard way of treating damage events, indicates the formation of a more diffused disorder sustained by the electrostatic coupling between the lattice atoms.

MOLECULAR DYNAMICS AND MONTE CARLO SIMULATION METHODS

The simulation method is the one described in [2]. In such calculations, after a cycle of lattice equilibration, an ion, endowed with the wanted energy and direction of motion, is ejected from a lattice location. The evolution of the atom assembly is then determined by integrating the classical equations of motion.

Owing to the primary energies considered in this work the cascade is formed by atoms with very different properties. The most energetic recoils have velocities well above the thermal range and are unlikely to share the structural properties of the silicon target. Their energy losses are determined by hard collisions at distances shorter than the normal solid state separation. For such collisions screened coulomb potentials are generally used in Monte Carlo and molecular dynamics simulations [3]. Cascade atoms with energy in the range 1 eV or below are likely to have the characteristics of excited phonons and maintain the structural properties of the silicon target. There has been considerable recent interest in an atomistic simulation of the structural properties of tetrago-

nal semiconductors and classical three-body potentials have been developed which can stabilize the silicon lattice. Generally these potentials have the disadvantage of a greater computational complexity with respect to a simple central potential. A computational advantageous interatomic potential which can also stabilize a silicon lattice was introduced in [4] and recently used in molecular dynamics simulations in [2]. Whereas the range of three-body potentials is limited to a nearest neighbour distance, in [4] a long-range interaction is assumed and the potential extends over two spheres of neighbours. In the first sphere the interaction is described by a simple central Morse potential. A harmonic potential is added in the second sphere of neighbours. This second term guarantees the stability of the lattice against bond rotation and provides for the conservation of all long range orders. Furthermore a plausible radial distribution function is obtained in conditions of high atomic excitation [4].

The results in the following paragraph resume a series of calculations routinely testing all the potentials above, that is i) a three-body potential in the form [5]. Such calculations, however, have been limited to short times and small crystallites, ii) the long-range, Morse-type potential [4], and iii) a mixed form where hard collisions at high energy are provided by a screened coulombic interaction (a universal potential in the form [6] was used) and the structural properties by [4]. As in [2] where this mixed form was firstly adopted, the threshold between the two potentials was set to 1 eV. No critical dependence of the cascade structure on this threshold was found. For the hetero-polar Si-As⁺ interaction only the screened coulombic term [6] was used.

The results below refer to crystallites containing approximately 6000 atoms. If during the evolution of the cascade an energetic atom escapes from the boundaries of the crystallite it is assumed to be lost in the target and never return to the damage core. Consequently only states of the lower kinetics energy are described by the simulation.

The Monte Carlo simulation method is the one reported in [7]. In such calculations, according to the assumption (iii) above which sets the threshold of structural and bonding effects at 1 eV, the localization energy is assumed to be 1 eV and the paths of the displaced atoms are terminated when the energy falls below this threshold. Furthermore the universal potential [6] is used for the evaluation of nuclear losses. Electronic losses are ignored in both Monte Carlo and molecular dynamics simulation.

RESULTS AND CONCLUSIONS

Typical cascade structures in a crystalline silicon target, as obtained from the Monte Carlo calculations, are reported in table 1 (note that in such table range indicates the vector range joining the initial and final location of the moving particle).

It is seen the recoil paths are, on average, short. Only the PKAs range (the Primary Knocked-on Atoms are the atoms directly displaced by the primary particle. Usually they have the higher energies among the cascade atoms) is comparable to the ion range. The PKAs, however, represent only a few percents of the cascade atoms. This range distribution suggests

a tree-shaped form of the cascade with short branches protruding from a main track formed by the path of the primary particle or by the one of the more energetic recoils. The spatial spread, however, appears to be modest. In addition to this limited spread, it is also seen that the ratio between the number of recoils and the number of atoms contained in the cascade volume (indicated as N_c in the table) is low. This feature is however vitiated by the uncertain evaluation of the cascade volume for which only representative estimates can be offered. This fact is indicated in table 1 by the large margins of uncertainty on N_c . N_c is evaluated as $N_c = \rho \cdot dV_c$, ρ being the atomic density of the silicon target atoms and dV_c the cascade volume. If use is made of the range of the ion and of the one of PKAs to define a representative cylinder $dV_c = R_p \cdot R_{pka}^2$, N_c falls in the range some thousands. If the average recoil range R_{rec} is used instead of R_{pka} , N_c is reduced of almost an order of magnitude. Owing to these uncertainties we can only conclude, in a somewhat qualitative manner, that the displacements by impact collisions, localized near the ion path, involve the disordering a few percent of the atoms in the cascade volume, this figure possibly increasing to some tens percent at 500 eV.

The results of the molecular dynamics simulations are reported in the tables 2 and 3. The tables refer, respectively, to an initial state of low (table 2) and high (table 3) kinetics energy indicated in the following as 'cold' and 'warm' lattice. In these simulations the cascade evolution is followed for a time of approximately 0.8 ps when the maximum kinetics energy in the crystallite is generally below the Morse well.

Two phases are observed in the time evolution of the cascade. The first phase is prevailing collisional and energetic recoils with energy well above 1 eV are formed through primary collisions events. However also an increase of the number of atoms with energies in the range 10-100 meV (cold crystal) and 100 meV-1 eV (warm lattice) begins to be seen. During the second part of the transient the continuous loss of energy, via lattice coupling and low-energy secondary collisions, of the atoms with $E > 1$ eV leads to a remarkable increase of the kinetics energy of the average target atom.

Tables 2 and 3 report i) the maximum number of displaced atoms with $E > 1$ eV formed during the collisional phase and ii) the more relevant properties of the energy distribution in the final stages of the simulation (the bracketed values represent the fraction of atoms in the given energy interval in the undamaged crystal). It is seen that the number of displaced atoms with $E > 1$ eV is almost one order of magnitude lower than in the Monte Carlo simulations. The effect is attributed to the movements of the colliding partners during their interaction. The mutual repulsion pushes them aside and prevents energy transfers as large and as frequent as in a Monte Carlo simulation where one of the colliding partner remains immobile during the passage of the other. A second important divergency from the Monte Carlo results is the excitation of large fractions of atoms to states of higher kinetics energy (according to the size of the computational crystallite the fractions in the tables indicate many hundreds-few thousands atoms). The result is, at least in a qualitative form, independent on the detailed form of the interaction potential though there is an obvious dependence of the characteristic

Table 1. Monte Carlo simulation of displacement cascades in a silicon target.

Ion Energy	Ion Range R_p	Number of atoms in the cascade volume N_c	Number of recoils	Recoils average range R_{rec}	PKAs average range R_{pka}	Recoils average energy
[eV]	[Å]			[Å]	[Å]	[eV]
Silicon ion						
500.	14.	700-8000	280	2.2	5.8	7.0
50.	7.3	600-2000	29.0	2.1	3.8	4.0
Arsenic ion						
500.	18.	1600-12000	276	2.1	5.1	6.8
50.	9.2	800-2000	29.0	2.1	3.3	4.3

Table 2. Molecular dynamics simulations. Displacement cascades in a cold lattice

Properties of the undamaged silicon crystal: average kinetics energy per atom = 5.4 meV r.m.s of the atomic displacement distribution from the 0°K location \approx 0.03 Å				
Ion energy	atoms with energy > 1eV	average kinetics energy [meV]	atoms with energy between 10-100 meV [fraction]	atoms with energy between 100 meV-1 eV [fraction]
Silicon ion				
500.	40	80.	0.28	0.23
50.	10	12.	0.78 (0.14)	0.09 (0)
Arsenic ion				
500.	\approx 30	\approx 72.	0.28	0.21
50.	\approx 8	\approx 10.	0.76	0.08

Table 3. Molecular dynamics simulation. Displacement cascades in a warm lattice

Properties of the undamaged crystal: r.m.s of the atomic displacement distribution from the 0°K location = 0.07 Å average kinetics energy per atom = 50 meV				
Ion energy	atoms with energy > 1eV	average kinetics energy [meV]	atoms with energy between 10-100 meV [fraction]	atoms with energy between 100 meV-1 eV [fraction]
Silicon ion				
500.	50	140.	0.54	0.37
50.	10	71.	0.62 (0.7)	0.29 (0.10)

times and of the recoil generation on such parameter. The calculations indicate that the figures in the table, even if actually referring to the combined [4] and [6] potentials, are also representative of the other forms of interaction.

The effects of atomic excitation are attenuated in the warm lattice where the thermal agitation reduces the electrostatic coupling among lattice atoms (Table 2). It is also seen (Tables 2 and 3) a sublinear dependence of the average kinetics energy on the primary energy, the effect being particularly evident in the warm lattice. It is thought that in such cases the more branched form of the cascade, visible from the increased number of displacements with $E > 1$ eV, leads to its effective cooling. However the calculations indicate that an effective cooling is operated by the escape of the energetic recoils from the boundaries of the crystallite. The effect, even if not necessarily unphysical, may represent an artifact of the simulation.

In the cold crystal the increase of the average kinetics energy is slightly lower for As^+ than for Si^+ . In the first case, in fact, the ratio between the mass of projectile and the mass of the target is less favourable to a large energy exchange. The number of high energy recoils is reduced and this, in turn, results into a lower excitation of the crystallite. The result, however, requires some caution. In fact, even if the kinetics energies generated by the passage of the Si^+ ion were found to be constantly higher than the ones due to the As^+ ion, large statistical fluctuations (with a maximum of approximately 10%) were found in the ratio between the two.

In conclusion, the molecular dynamics simulation suggests the formation of a lattice disorder with the characteristics of a diffuse thermal excitation. However, as already mentioned in [2], two cautions must be observed. In the first place the times of the simulations are short in comparison with the typical phonon frequencies in silicon. This casts many doubts on the evolution and stability of such forms of disorder. In the second place, as shown by table 1, the size of the computational crystallite might be comparable (or even smaller) to the cascade volume. A cooling action exerted by the undamaged regions of the crystal in the short times of the cascade formation might have been missed.

REFERENCES

- [1] D. A. Thompson, A. Golansky, K. H. Haughen, D. V. Stefanovich, G. Carter and C.E.Christodoulidis, *Rad. Effects* **52**, 69 (1980).
- [2] A.M.Mazzone, *Nucl.Instr. and Meth. in Phys. Research* **B33**, 776 (1988).
- [3] D.Y.Lo, M.H.Shapiro, T.A.Tombrello, B.J.Garrison and N.Winograd in Computer-Based Microscopic Description of the Structure and Properties of Materials, edited by J. Broughton, W. Krakow and S.T. Pantelides (Mat. Res. Soc. Proc. **63**, 1986) 449.
- [4] Yu.N.Knyzhnikov, *Rad.Effects* **25**, 41 (1975).
- [5] B.W.Dodson, *Phys.Rev.B* **35**, 2795 (1987).
- [6] J.F.Ziegler, J.P.Biersack and U.Littmark, The Stopping and Range of Ions in Solids, edited by J.F.Ziegler (Pergamon Press, New York, 1985), p.
- [7] A.M.Mazzone, *Phil.Mag.Letters* **57**, 741 (1987).

A THERMAL SPIKE ANALYSIS OF LOW ENERGY ION ACTIVATED SURFACE PROCESSES

C.M. GILMORE*, A. HAERI* AND J.A. SPRAGUE**

*School of Engineering and Applied Science, The George Washington University

Washington, DC 20052

**Condensed Matter and Radiation Sciences Division, U.S. Naval Research Laboratory, Washington, DC 20375-5000

ABSTRACT

A thermal spike analysis was utilized to predict the time evolution of energy propagation through a solid resulting from energetic particle impact. An analytical solution was developed that can predict the number of surface excitations such as desorption, diffusion or chemical reaction activated by an energetic particle. The analytical solution is limited to substrates at zero Kelvin and to materials with constant thermal diffusivities. These limitations were removed by developing a computer numerical integration of the propagation of the thermal spike through the solid and the subsequent activation of surface processes.

Introduction

There recently has been considerable interest in the effect of energetic particles during deposition on the processes of thin film nucleation and growth with a number of papers reporting interesting experimental observations [1,2,3]. The importance of the thermal spike in explaining ion beam mixing (the displacement of substrate atoms from their original positions in bulk specimens) has recently been discussed by Averback with the conclusion that ion beam mixing at low temperature is dominated by diffusion during the thermal spike [4]. Therefore, it is reasonable to expect that displacement processes on the surface also will be significantly affected by surface diffusion during the thermal spike. It was the intent of this research to study the effect of the thermal spike caused by an energetic particle on the subsequent activation of surface processes such as desorption and diffusion.

Seitz and Koehler were the first authors to provide an analysis of thermal spikes and to calculate the spike effects on thermally activated processes [5]. In their thermal spike analysis it was assumed that after a characteristic time (t) such as 10^{-13} seconds the energy (Q_p) of the incoming particle that had not been lost to producing permanent structural change in the crystal was transformed into a thermal spike. It was assumed that the temperature of the crystal within the thermal spike was given by the classical heat transfer equations. Seitz and Koehler assumed a thermally activated process and calculated the number of times the process would occur. In Seitz and Koehler's analysis a constant temperature was assumed over a radius at the core of the thermal spike; also it was assumed that the substrate lattice was at absolute zero of temperature.

Vineyard analyzed the thermal activation resulting from a point source inside an infinite solid and from a line source through an infinite solid [6]. Vineyard allowed the specific heat per unit volume (C_v) and the thermal conductivity (K_c) to be dependent upon temperature (T) by a power law relationship of the form:

$$K_c = K_{c0} T^{n-1}; C_v = C_{v0} T^{n-1} \quad 1.$$

where C_{v0} and K_{c0} would be constants and n was any positive number. Since the ratio K_c/C_v is the thermal diffusivity, the assumption that thermal diffusivity is constant and independent of temperature still holds for

Vineyard's analysis. The form of the temperature distribution for a point source was found to be:

$$T(r,t) = \left[\frac{nQ_p C_{vo}^{1/2}}{(4\pi K_{co} t)^{3/2}} \right]^{1/n} \exp \left[- \frac{C_{vo} r^2}{4n K_{co} t} \right] \quad 2.$$

Analysis

In the present analysis of ion beam affected nucleation and growth, it was assumed that ions strike a surface creating a point source of energy at the surface of the semi-infinite half space; values of x from zero to infinity are solid and values from 0 to minus infinity are vacuum. The temperature derived in equation 2 was for a point source of energy Q_p located infinitely deep within a solid. If we consider passing a plane through the origin removing half of the space and also removing half of the point source, the same temperature distribution will result in the remaining solid if the remaining source of energy ($Q_p/2$) is present.

The number surface atoms activated by the thermal spike (N_{AI}) could be evaluated from the integral

$$N_{AI} = \int_{r=0}^{\infty} \int_{t=0}^{\infty} N_1 2\pi r dr v \exp \left[- \frac{E_A}{KT(r,t)} \right] dr dt \quad 3.$$

where E_A is the activation energy for the process being investigated such as desorption or diffusion, N_1 is the number of single adatoms, and v is the vibrational frequency. Utilizing similar substitutions and integration methods as Vineyard the solution is

$$N_{AI} = \frac{vn^{7/3} G(4n/3) Q_p^{4/3} N_1}{8\pi K_{co} C_{vo}^{1/3} (E_A/K) 4n^{2/3}} \quad 4.$$

where G is the gamma function. The analytical solution in Equation 4 for N_{AI} , the number of thermally activated events in the thermal spike region per ion, assumed that the thermal diffusivity was a constant independent of temperature, and that the substrate initial temperature was zero. Equation (4) was analyzed for the example of gold onto NaCl because this combination has been extensively investigated by numerous authors. Recent work by Robins and coworkers indicates that the activation energy for desorption of gold atoms on NaCl is 0.485 eV and the activation energy for diffusion of gold atoms on NaCl is 0.155 eV [7]. Values for specific heat per unit volume and thermal conductivity were taken from data in Toulukian [8]. The adatom density was assumed to be 10^{-7} atoms/ \AA^2 . This is a typical value of the saturation adatom density from the simulations of Zinsmeister [9]. Substitution of appropriate values into Equation 4 shows that the thermal spike produces insignificant activation events; 0.9×10^{-15} atoms are desorbed per incident 100 eV ion, and 2.5×10^{-13} diffusion jumps occur. Another approach to utilizing Equation 4 is to assume that both C_v and K_c are independent of temperature ($n=1$). In this calculation we utilized C_v and K_c values typical of 300 K (1.13×10^{-5} eV/ \AA^3 K and 3.744×10^9 eV/ \AA sec. K respectively). With this input and the remaining input as before the number of atoms desorbed increased to 4.1×10^{-6} ; and the number of surface adatoms diffusing would be 1.9×10^{-5} . Thus the theoretical calculation still indicated an insignificant contribution to surface processes due to the incident ion energy. A trapezoidal numerical integration of Equation 3, however, contributed considerable insight into the reasons for the low number of surface processes activated. Also in the numerical integration several limitations of the theoretical derivation

were circumvented, non-zero substrate temperatures were treated, and a temperature dependent thermal conductivity was incorporated.

In the numerical integration of Equation 3, the temperature $T(r,t)$ was expressed as:

$$T(r,t) = T_0 + \frac{Q_p}{4C_v(\pi K_d t)^{3/2}} \exp - \left[\frac{r^2}{4K_d t} \right] \quad 5.$$

and where K_d (thermal diffusivity) was no longer a constant, rather it was assumed to be a function of temperature given by

$$K_d(T) = A + B T^m \quad 6.$$

where there were no limitations on the values of A, B, and m; except that at temperatures above 1000 K, K_d was assumed constant. For the numerical integration equation 3 was expressed in the differential form:

$$\Delta N_{AI} = 2\pi r \Delta r \Delta t v N_1 \exp - \left[\frac{E_A}{KT(r,t)} \right] \quad 7.$$

The integration was begun for times as short as 10^{-15} sec and continued for times as long as 10^{-12} sec. Radii were taken from 0.25 \AA to 64 \AA .

One test of the numerical integration was to duplicate the computation based upon Equation 4 discussed above, again thermal properties appropriate to 300 K were utilized. The numerical integration result for the number of adatoms desorbed and diffusing was 4.6×10^{-6} and 2.4×10^{-5} respectively in comparison to 4.1×10^{-6} and 1.9×10^{-5} for the calculation with Equation 4. The reason for these low numbers can be seen by analyzing the numerical integration results.

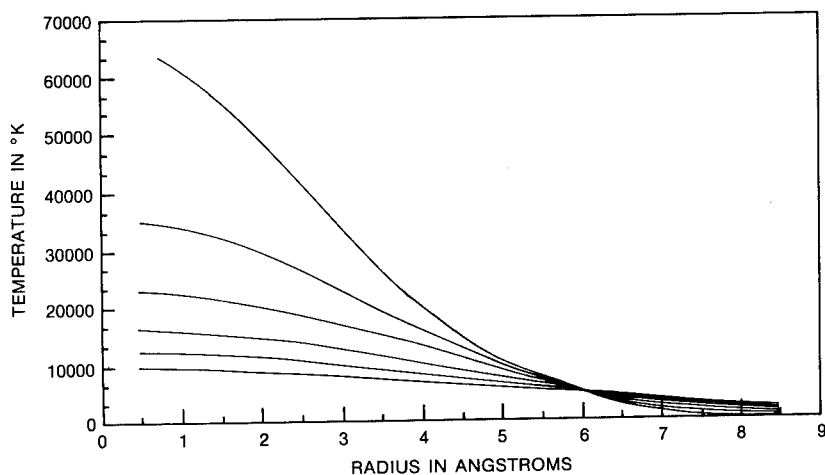


Figure 1 - Calculated temperature distribution from 100 eV particles onto NaCl assuming a substrate temperature of 0°K but utilizing constant thermal properties appropriate to 300°K . The top curve is at 10^{-14} seconds and each lower curve is for a time increment of 0.5×10^{-14} seconds.

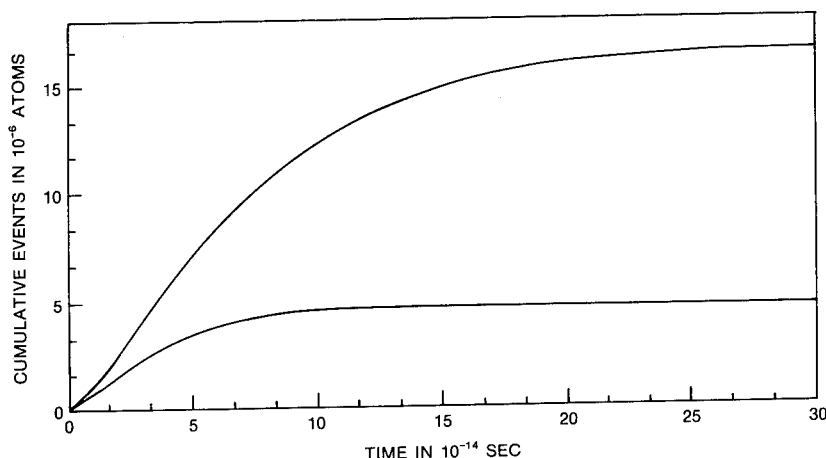


Figure 2 - Cumulative surface activation events for the same conditions as in Figure 1. The upper curve is for surface diffusion and the lower curve is for desorption of Au adatoms on NaCl.

The most important reason that the integral is small is shown in Figure 1 where the temperatures at various times are plotted as a function of radius. It is noted that at very short times and for small radii the temperature is very high. However, for all times the temperature is considerably lower for radii greater than 10 \AA ; thus the adatom spacing on the surface ($\sim 3.1 \times 10^3 \text{ \AA}$) is much larger than the radius from the ion impact site where temperatures are significantly increased. Thus to obtain any significant effects from a thermal spike analysis on surface processes it appears to be necessary to consider the activation of highly concentrated species such as clusters on the surface.

Another reason that the integral in equation 3 is so small is that the pulse is dissipated in a very short time. Figure 2 shows the accumulated activation events as a function of time and it is obvious that most of the activation events occur within 3×10^{-13} seconds, and after that time the thermal pulse is dissipated. The observation that the pulse was dissipated within 3×10^{-13} seconds raises the question of the validity of assuming that the pulse energy equilibrates with the crystal atoms and that Maxwell-Boltzmann statistics can be utilized. A more extensive version of this paper is in press [10].

Conclusions

1. An equation for the number of surface activated events resulting from a thermal spike was derived for the conditions of a zero Kelvin substrate temperature, a constant thermal diffusivity, and a power law temperature dependence for the specific heat per unit volume and for the thermal conductivity.
2. A numerical integration of the activation of surface processes by a thermal spike was developed that allows for a non zero substrate temperature and for a temperature dependent thermal diffusivity. Temperature profiles were derived as a function of time and position and activation probabilities were calculated utilizing a Maxwell Boltzmann probability distribution.
3. The theoretical calculation and the numerical integration were found to predict similar activation probabilities. The number of activated

surface processes was very low for typical steady state concentrations of surface adatoms. A significant contribution from thermal spikes to surface activated processes will only occur for species with high surface concentration because of the small spatial distribution of the energy in the thermal spike.

4. Low energy (~ 100 eV) ions or atoms incident upon a surface will produce a very short lifetime ($\sim 3 \times 10^{-13}$ sec) energy pulse. With pulses this short in duration it is questionable that any sort of local thermal equilibrium is established that would allow the use of Maxwell-Boltzman statistics.

Acknowledgement

C.M. Gilmore thanks the U.S. Naval Research Laboratory and the ONR-ASEE Summer Faculty Program for financial support. A. Haeri developed the numerical integration presented as part of an undergraduate honors research program at the George Washington University.

References

1. M. Marinov, Thin Solid Films, 46, 1977, 267-274.
2. G.E. Lane and J.C. Anderson, Thin Solid Films, 26, 1975, 5-23.
3. G.E. Lane and J.C. Anderson, Thin Solid Films, 57, 1979, 277-283.
4. R.S. Averback, Nuclear Instruments and Methods in Physics Research, B15, 1986, 675-687.
5. F. Seitz and J.S. Koehler, Solid State Physics, Adv. in Research and Applications, 2, 1956, Ed. F. Seitz and D. Turnbull, Academic Press, NY, 307-442.
6. G.H. Vineyard, Radiation Effects, 29, 1976, 245-248.
7. J.L. Robins, J.V.S.T., A5(4), July/Aug. 1987 1742.
8. Y.C. Toulukian, Thermophysical Properties of Matter, Plenum Press, NY, 1970.
9. G. Zinsmeister, Thin Solid Films, 2, 1968, 497-507.
10. C.M. Gilmore, A. Haeri, and J.A. Sprague, to be published in Thin Solid Films.

A MODEL OF A COMBINED FILM DEPOSITION AND ION BOMBARDMENT FOR COATINGS FORMATION

Z.A.ISKANDEROVA, T.D.RADJABOV, R.Yu. LEIDERMAN AND
F.K.TUKFATULLIN
Institute of Electronics, Uzbek Academy of Sciences,
Academgorodok, 700143, Tashkent, USSR

ABSTRACT

The mathematical model of a combined film deposition and high dose ion implantation for coating formation has been developed. Calculations of concentration profiles of implanted element in the film and substrate depending on different parameters of the model have been carried out.

INTRODUCTION

The combined deposition and ion irradiation method for improved films and coatings has recently found a wide application. Preliminary ion-beam treatment of the substrate, simultaneous or alternating film deposition and ion bombardment from a source or at glow discharge, ion implantation at a (specific) intermediate of final stage of multi-layer structure formation, and also various combinations of the above techniques are used [1-8]. This often achieves composition and structure controlled coatings with improved adhesion and better mechanical and physico-chemical characteristics [1,3,5,7,9]. In many cases, the effect is determined by not only an altered film structure but production of film-substrate interfaces and new phases or compounds in the coating proper as well, resulting from ion implantation, especially to high fluences. Here, the concentration level and distribution of an impurity to be implanted play a decisive role and this is the subject of this paper.

A MATHEMATICAL MODEL

The simplest mathematical model of a combined deposition and bombardment process is based on the first order equation [10-12]

$$\frac{\partial n(x,t)}{\partial t} + V(t) \frac{\partial n(x,t)}{\partial x} = I(t)F(x). \quad (1)$$

Here $n(x,t)$ is the density of an impurity to be implanted (atom cm^{-3}); $V(t) = u(t) - v(t)$, where $-u(t)$ is the rate of the deposition-induced move of the surface; $v(t)$ is the surface sputtering rate; $I(t)$ is the ion flux density (ion $\text{cm}^{-2}\text{s}^{-1}$); $F(x)$ is the function of ion range distribution.

With the initial condition $n(x,0) = 0$ and $V(t) \geq 0$, the solution of eq. (1) is

$$n(x,t) = \int_0^t ds_1 I(s_1) \theta(x - \int_{s_1}^t ds_2 V(s_2)) F(x - \int_{s_1}^t ds_2 V(s_2)), \quad (2)$$

where $\theta(x) = 1$ if $x > 0$, $\theta(x) = 0$, if $x < 0$. Equation (2) is valid (neglecting diffusion and ion mixing) provided $n(x,t)/N_0 \ll 1$, where N_0 is the atomic density of the film substance. To estimate the implanted particle concentration for high irradiation doses, we shall proceed from a more general equation

$$\frac{\partial}{\partial t} n(x,t) + (V(t) + I(t)\Omega \int_0^x dy F(y)) \frac{\partial}{\partial x} n(x,t) = I(t) F(x) (1 - \Omega n(x,t)) \quad (3)$$

where Ω is the effective atomic volume of implanted species, the $\Omega \int_0^x dy F(y)$ integral known to be the function of the layer "swelling" at the expense of the ions-at-rest trapped by the film [13-15]. Strictly speaking, both $V(t)$ and $F(x)$ are the functionals of $n(x,t)$: $V(t) = V(t; n(x,t))$, $F(x) = F(x; n(x,t))$. In the examples below, however, the values of $\Omega n(x,t)$ is small enough (or rigorously equal to zero) that the $V(t)$ dependence on $n(x,t)$ can be neglected. To obtain solutions in an analytical and fairly simple form, we shall consider $F(x)$ to be invariable throughout the process. (Situations where this approximation is legitimate are discussed in ref [14]).

Since, for the arbitrary $I = I(t)$ and $V = V(t)$ dependences the solution of eq. (3) is complicated, we shall deal with two most typical cases.

SIMULTANEOUS FILM DEPOSITION WITH A CONSTANT RATE AND ION BOMBARDMENT

The process is described by eq. (3) at $V(t) = V = \text{const}$, $I(t) = I = \text{const}$. Let us introduce dimensionless variables

$$\xi = x/r, \quad \tau = Vt/r, \quad \lambda = I(1-R)\Omega/V, \quad f(\xi) = rF(x)/(1-R), \quad C(\xi, \tau) = \Omega n(x,t) \quad (4)$$

Here R is the reflection coefficient and r (cm) parameter, depending on a particular form of the $F(x)$ is equal to the mean ion range (R_p) or straggling (ΔR_p). Then

$$\frac{\partial}{\partial \tau} C(\xi, \tau) + (1 + \lambda \int_0^\xi dz f(z)) \frac{\partial}{\partial \xi} C(\xi, \tau) = \lambda f(\xi) (1 - C(\xi, \tau)) \quad (5)$$

The solution of this equation at $C(\xi, 0) = 0$ is

$$(1 + \lambda \int_0^\xi dz f(z)) C(\xi, \tau) = \begin{cases} \lambda \int_0^\xi dz f(z), & 0 < \xi < \xi(\tau), \\ \lambda \int_{\chi(\xi, \tau)}^\xi dz f(z), & \xi(\tau) < \xi < \infty, \end{cases} \quad (6)$$

where $\chi(\xi, \tau)$ and $\xi(\tau)$ are the roots of the equations

$$\int_{\chi(\xi, \tau)}^\xi dz (1 + \lambda \int_0^z d\zeta f(\zeta))^{-1} = \tau, \quad \int_0^{\xi(\tau)} dz (1 + \lambda \int_0^z d\zeta f(\zeta))^{-1} = \tau. \quad (7)$$

The $\xi(\tau)$ function for all $\lambda > 0$ ($V = u - v > 0$) lies within the limits $\tau < \xi(\tau) < (1 + \lambda)\tau$, thus, the values of $r \cdot \xi(\tau)$ is always smaller than the film thickness taking into account "swelling"; but larger than that by the "elementary" theory. For large $\xi(\tau)$ and $1 \ll \xi < \xi(\tau)$

$$C(\xi, \tau) \simeq \lambda / (1 + \lambda) \equiv \bar{\Phi} (1 - R) \Omega / (ut - vt + \bar{\Phi} (1 - R) \Omega), \quad (8)$$

where $\bar{\Phi} = I t$. As it should have been expected, the maximum possible impurity concentration in a film is determined by the ratio of the irradiation dose to the resultant film thickness (taking into account "swelling").

ALTERNATING ION BOMBARDMENT AND FILM DEPOSITION

Following ref. /12/, approximate the ion flux and deposition rate by rectangular pulse sequences supposing $I(t)=I = \text{const}$, if $0 < t < T_1$, $I(t)=0$, if $T_1 < t < T_1 + T_2$, $I(t)=I$, if $T_1 + T_2 < t < 2T_1 + T_2 \dots$; $u(t)=0$, if $0 < t < T_1$, $u(t)=u = \text{const}$, if $T_1 < t < T_1 + T_2$ etc. We suppose the process to complete with irradiation at a time $t = T_1 + m(T_1 + T_2)$, where m is the total number of cycles. Let

$$C_m(\xi) = \Omega R(x, t = T_1 + m(T_1 + T_2)), \quad \mu = I(1-R)\Omega/\psi, \quad \tau_1 = \psi T_1/r, \quad \tau_2 = u T_2/r, \quad (9)$$

where $\psi = \text{const}$ is the sputtering rate corresponding to the amplitude value of the flux.

As a result of simple calculations, we find

$$C_m(\xi) = 1 - \prod_{k=0}^m (1 - \theta(\chi_k) C_0(\chi_k)), \quad (10)$$

where

$$\chi_0 = \xi, \quad \chi_k = Y(\chi_{k-1}, \tau_1) - \tau_2 \quad (k \geq 1), \quad (11)$$

$$(1 - \mu \int_0^\xi dz f(z)) C_0(\xi) = \int_\xi^{Y(\xi, \tau_1)} dz f(z), \quad (12)$$

$Y(\xi, \tau_1)$ is the root of the equation

$$\int_\xi^{Y(\xi, \tau_1)} dz (1 - \mu \int_0^z dz f(z))^{-1} = \tau_1, \quad (13)$$

Additionally, the following parameters are convenient to be introduced for further treatment:

$$a = \tau_2 - \tau_1(1 - \mu) \equiv (u T_2 - \psi T_1 + I(1-R)\Omega T_1)/r, \quad (14)$$

which is the resultant film thickness per one cycle in r units and

$$\varphi = \int_0^\infty d\xi C_0(\xi) \equiv (\Omega/r) \int_0^\infty dx n(x, T_1), \quad (15)$$

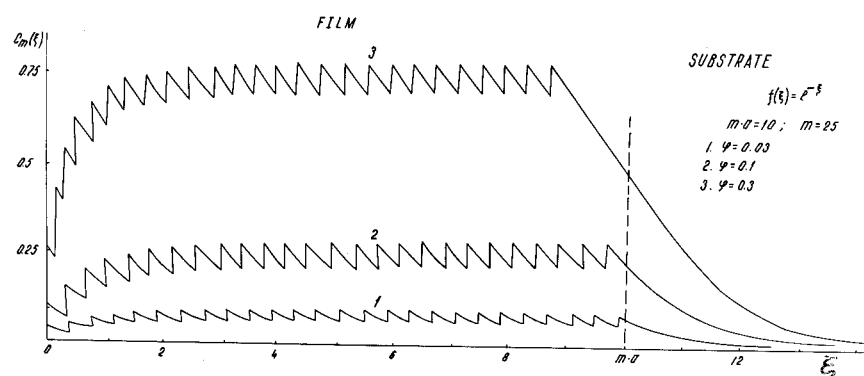
which is the "retained" dose per one cycle in r/Ω units.

The total "retained" dose can be shown to be $(r/\Omega) \int_0^\infty d\xi C_m(\xi) = (r/\Omega)(m+1)\varphi$. Note that at $u T_2 > \psi T_1$ we always have $\varphi < a$.

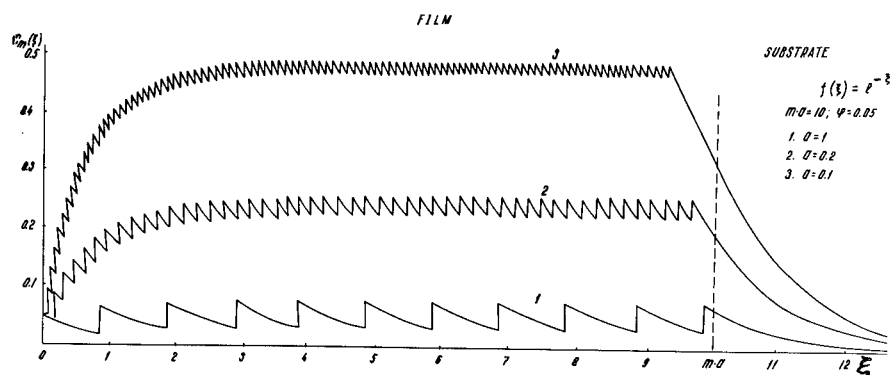
Ignoring the presence of sawtooth oscillations (see fig. 1), one can admit that the $C_m(\xi)$ behaviour is on the whole similar to the $C(\xi, \tau)$ in the previous section. The oscillations occur through the functions $\theta(\chi_k)$. It is clear that at any $m \geq 1$ there is an ξ_m leading to $\chi_m(\xi_m) = 0$; if $\xi > \xi_m$, then all $\theta(\chi_k) = 1$ and the oscillations vanish. The quantities ξ_m and $\chi_m(\xi)$ are similar to the $\xi(\tau)$ and $\chi(\xi, \tau)$ (see eq. (7)).

In particular, we always have $\xi_m < m a$, where $m a$ is the total film thickness in r units. It can be shown that the oscillation amplitude, as a function of φ at a fixed a , is non-monotonic, whereas the ξ_m monotonically decreases with φ increasing and goes to zero at $\varphi = a$.

The solution becomes very simple if $f(\xi) = e^{-\xi/r}$, $r \equiv R_p$ (this is a convenient approximation for the ion range distribution at low energies). In this case



a



b

Fig. 1.
Dimensionless concentration profile for varied
model parameters: a) depending on the φ value;
b) depending on the a value (at prescribed ma).

$$\begin{aligned}
e^{X_*} &= e^{\xi - \kappa a} + (e^\varphi - 1)(1 - e^{-\kappa a})/(e^a - 1), \\
c_0(X_*) &= (e^\varphi - 1)e^{-X_*}/(1 + (e^\varphi - 1)e^{-X_*}), \\
\varphi &= \ln \left(1 + \frac{\mu}{1-\mu} e^{-(1-\mu)\tau_1} \right) \quad (16)
\end{aligned}$$

with $c_m(\xi)$ depending only upon four universal variables: ξ , φ , a and m .

"CONTINUOUS" APPROXIMATION

Equations (10) to (13) provide a ready check on whether the functions $c_{m+1}(\xi)$ and $c_m(\xi)$ are in a recurrent relationship

$$c_{m+1}(\xi) = c_0(\xi) + (1 - c_0(\xi))\theta(\xi - a(\xi))c_m(\xi - a(\xi)), \quad (17)$$

where

$$a(\xi) = a - \varphi + \int_0^\xi dz c_0(z). \quad (18)$$

If $a(\xi)$ and $c_0(\xi)$ are small enough and m is large, then (17) can be replaced by a differential equation similar to (5). Expanding $\theta(\xi - a(\xi))c_m(\xi - a(\xi))$ in terms of $a(\xi)$, within linear terms, substituting the derivative $(\partial/\partial m)c_m(\xi)$ for $c_{m+1}(\xi) - c_m(\xi)$, neglecting the term $c_0(\xi)a(\xi)$ and introducing the notations

$$c(\xi, \tau^*) = c_m(\xi), \quad f^*(\xi) = c_0(\xi)/\varphi, \quad \tau^* = m(a - \varphi), \quad \lambda^* = \varphi/(a - \varphi), \quad (19)$$

we have

$$\frac{\partial}{\partial \tau^*} c(\xi, \tau^*) + (1 + \lambda^* \int_0^\xi dz f^*(z)) \frac{\partial}{\partial \xi} c(\xi, \tau^*) = \lambda^* f^*(\xi) (1 - c(\xi, \tau^*)) \quad (20)$$

The solution of (20) is an "averaged" smooth profile. The more accurate formula below, its derivation we omit for the moment, also includes minor corrections fluctuating within the $0 < \xi < \xi_m$ range:

$$c_m(\xi) \simeq \begin{cases} 1 - \frac{a(0)}{A(\xi)} \left(1 - \frac{1}{2} c_0(0) \eta \left(\int_0^\xi \frac{dz}{A(z)} \right) \right), & 0 < \xi < \xi_m, \\ 1 - \frac{A(\xi_m)}{A(\xi)} (1 - c_0(\xi_m)), & \xi_m < \xi < \infty. \end{cases} \quad (21)$$

Here $A(z) = a(z)(1 + (1/2)c_0(z))$, $\eta(z) = 1 + 2[z] - 2z$, $[z]$ is the integral part of z , $\xi_m = X_m(\xi)$ and ξ_m are the roots of the equations

$$\int_{X_m}^\xi \frac{dz}{A(z)} = m, \quad \int_0^{\xi_m} \frac{dz}{A(z)} = m. \quad (22)$$

Neglecting $c_0(z)$ compared to unity in (21) and (22), we obtain a solution to (20) for the initial condition $c(\xi, 0) = 0$. If ξ_m is large, then (cf. eq. (8))

$$c_m(\xi) \simeq \frac{\varphi}{a} + \frac{1}{2} c_0(0) \left(1 - \frac{\varphi}{a} \right) \eta \left(\int_0^\xi \frac{dz}{A(z)} \right), \quad 1 \ll \xi < \xi_m. \quad (23)$$

For $\varphi/a \ll 1$, the latter estimation coincides with that obtained in ref. /12/. To estimate $c_0(\xi)$ and φ , it is natural, thanks to the assumed small $c_0(\xi)$ (not the $c_m(\xi)$!), to apply the "elementary" (low fluence) theory. Thus, for the Gaussian ion range distribution the "average" level in the film is expressed by

$$\frac{\varphi}{a} \approx \frac{\Omega \Phi \Delta R_p}{\Omega T_1} \frac{i' \operatorname{erfc}(-R_p/\sqrt{2} \Delta R_p) - i' \operatorname{erfc}(-(R_p - \Omega T_1)/\sqrt{2} \Delta R_p)}{u T_2 - \Omega T_1 + (1/2) \Omega \Phi \operatorname{erfc}(-R_p/\sqrt{2} \Delta R_p)}, \quad (24)$$

where $\Phi = I T_1$, putting $1-R = \int_0^\infty dx F(x)$.

FINAL REMARKS

Strictly speaking, our calculations apply to a case where the film and substrate materials are identical. The model used in the present work also allows to treat a more general situation, i.e. different materials, preliminary substrate irradiation, etc. and a number of other practical problems including pulsed irradiation at film deposition with a constant rate. It is noteworthy that recurrent relation (17) can be modified, if necessary so that a change in the target stopping power with accumulating dose would be considered step by step (cf. ref. /13/). A detailed account of these results is the subject of another communication.

References

- /1/ Ch.Weissmantel, Thin Solid Films 58, 101 (1979).
- /2/ Z.A.Iskanderova, L.F.Lifanova and T.D.Radjabov, Vacuum 32, 269 (1982).
- /3/ J.M.E.Harper, T.T.Cuomo, R.J.Gambino and H.K.Kaufman, Nucl.Instr.Meth. B7/8, 886 (1985).
- /4/ S.Schiller, U.Heisig and K.Goedicke, J.Vac.SciTechnol. 1 2, 858 (1975).
- /5/ R.A.Kant, B.D.Sartwell, I.L.Singer and R.G.Vardiman, Nucl. Instr.Meth. B 7/8, 915 (1985).
- /6/ J.S.Colligon, A.E.Hill and H.K.Kheyrandisch, Patent No 04673836 EP (8 January 1986).
- /7/ P.J.Martin, J.Mater.Sci. 21, 1 (1986).
- /8/ D.Fink, J.P.Biersack, M.Stadele, K.Tjan and V.K.Cheng, Nucl.Instr.Meth. 218, 171 (1983).
- /9/ L.F.Lifanova, Z.A.Iskanderova, Surface, No 4, 101 (1988) (in Russian).
- /10/ T.D.Radjabov, Z.A.Iskanderova, Journal of Technical Physics, 48, 1957 (1978) (in Russian).
- /11/ L.I.Pranyavichus, Yu.I.Dudonis, Modification of Properties of Solids by Ion Beams (Vilnius, "Mokslas", 1980) (in Russian).
- /12/ Z.A.Iskanderova, T.D.Radjabov, R.Yu.Leiderman and F.K.Tukfatullin, In Physical Research, v. 8, Energy Pulse and Particle Beam Modification of Materials, Edited by K.Hennig (Dresden, GDR, 1988), pp. 372-374.
- /13/ H.Krautle, Nucl.Instr.Meth. 134, 167 (1976).
- /14/ V.V.Titov, Journal of Technical Physics, 49, 844 (1979). (in Russian).
- /15/ R.Collins, T.March and J.J.Jimenez-Rodriguez, Nucl.Instr. Meth. 209/210, 147 (1983).

THE INFLUENCE OF DEFECT CONCENTRATIONS ON MIGRATION ENERGIES IN AgZn ALLOYS

T.D. Andreadis, M. Rosen, J.M. Eridon, D. J. Rosen
Naval Research Laboratory, Washington, DC 20375-5000.

ABSTRACT

Migration energies in Ag of vacancies, interstitials, Zn impurity atoms, interstitial-impurity complexes, and vacancy-impurity complexes were calculated using Embedded Atom Method (EAM) potentials in Molecular Statics calculations. A new Zn EAM potential was determined and used in these calculations. The dependence of the migration energies on local defect concentrations was determined in a linear approximation. Binding and formation energies of defects are also presented. A new model for the migration energy appropriate for defect reactions is introduced.

INTRODUCTION

Diffusion in an irradiated solid is influenced by the production and interaction of defects in the target. Interstitials and vacancies diffuse and react with each other and with impurities to form complexes. Diffusion and rate coefficients have the general form:

$$R = R_0 \exp[-H_m/kT],$$

where R_0 = a pre-exponential factor,
 H_m = migration energy,
 k = Boltzmann's constant,
 T = absolute temperature.

The value of these coefficients can depend sensitively on the migration energy, since it occurs in the exponent. Few measurements of migration energies are available and still fewer in which concentration dependence is measured.

In this study we calculate migration energies for AgZn alloys as a function of the local defect environment. Credible results require credible potentials. We used Embedded Atom Method (EAM) potentials in Molecular Statics calculations to calculate the migration energies of vacancies, interstitial, Zn impurity atoms, interstitial impurity complexes, and vacancy impurity complexes. Binding and formation energies of defects are also presented.

THE EAM POTENTIALS

The Ag EAM potential was obtained from the work of Daw and Baskes [1], however a Zn potential was newly developed for this study. Zinc is difficult since it has a non-ideal hcp structure (c/a ratio of 1.856). The Zn potential that was developed, however, reasonably reproduced a selected set of bulk properties of Zn and also the heat of solution of Zn in Ag. This potential is adequate for dilute solutions of Zn in Ag.

An EAM potential for silver already exists [1]. It is difficult to create a set of embedding functions for zinc, however. Although other zinc potentials have been reported recently [2,3], we believed that it was important to use a potential derived in a manner similar to that of silver. To this end, the electron density was computed using Roothan-Hartree-Fock

calculations[4], and the pair potential was computed using the same parametrization found in the reference [1].

It was not possible to match all five elastic constants using this parametrization, but as we were examining a dilute solution of zinc in silver this was not deemed important. We were able to provide a reasonable match to two of the elastic constants, C_{11} and C_{33} .

The embedding function was derived using the Rose relation as in reference [1]. We remedied a fairly common[5] problem with the short range behavior of the pair potential by modifying the behavior at less than first neighbor distance of zinc.

Within the EAM formulation, the actual magnitude of the electron density is arbitrary for a pure material. The only adjustable parameter for an alloy is the ratio of the magnitude of the electron density for the pure materials. This was adjusted to match the experimental value of the heat of solution of zinc in silver, which is 0.122 eV [6]. Using these potentials, the binding energy of a vacancy to a zinc impurity in silver was calculated to be 0.093 eV, compared to an experimental value of 0.08 eV [7].

CALCULATION OF THE MIGRATION AND BINDING ENERGIES

The migration energy of a defect is the minimum amount of energy required to move from one equilibrium point in the lattice to another. To calculate the migration energy we used the computer program DYNAMO in molecular statics mode. We fixed the crystal lattice at two points and then mapped the potential energy surface by moving the defect quasi-statically, allowing the crystal to relax about each new position, and then calculating the total crystal energy for each new position. The energy needed for defect motion to the new point is the difference from that at the initial equilibrium position. Typical calculations included crystals with 257 to 500 atoms. Contour plots of the potential energy surface were made and the saddle point energy between equilibrium positions determined. Figure 1 shows the contour plot for interstitial migration energy.

There may be a number of final equilibrium positions to which the defect can migrate, each separated by a saddle point from the initial position. To obtain the average migration energy, these saddle point energies were averaged using a Boltzmann weight factor of $\exp(-E/kT)$.

The concentration dependence entails a more involved calculation. In order to calculate the influence of the presence of other defects it is necessary to average over the migration energies resulting from various defect configurations. To obtain the average migration energy of specie A we first determined the distance, L , over which a second specie B would affect the migration energy of A. A series of calculations were then carried out with one atom of a specie B occupying different lattice locations within the volume around A defined by the distance L . The concentration for this case is defined as

$$C = 1/N_L$$

where N_L the total number of atoms in the volume defined by L . Migration energies for each calculation were obtained as described in the preceding paragraph. A simple average was then taken over the values obtained from the specie B sites in a given shell around the defect. The final migration energy was obtained by averaging over all the shells using as the weight the fraction of the total lattice locations, within the volume defined by L , that are contained in a shell. The two values of the migration energy, one for zero concentration of the defect and the other for C were used to obtain the slope of migration energy as a function of the concentration of specie B.

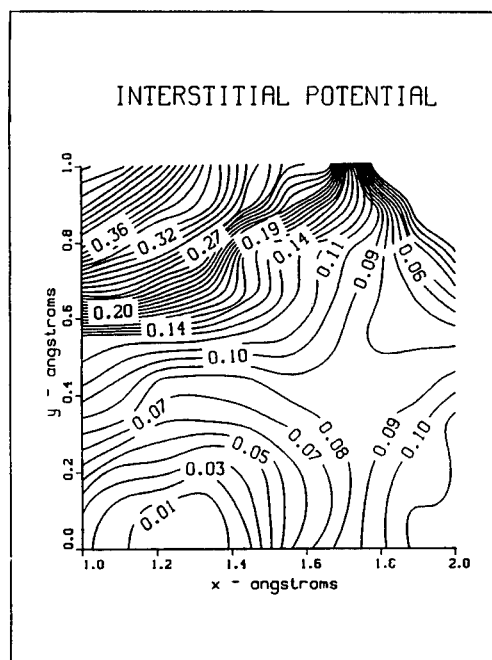


Figure 1. Potential energy surface contours for the case of interstitial migration.

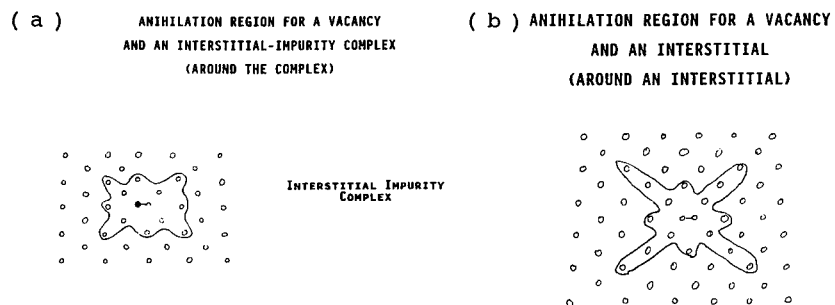


Figure 2. Immediate anihilation regions for (a) a vacancy and interstitial-impurity complex and (b) a vacancy and an interstitial.

Calculations of the migration energy change with defect concentration were simplified for the pairs of reacting species which annihilated when brought sufficiently close. The inverse of the number of lattice locations around a defect A which on being occupied by B lead to annihilation gave the concentration for which the migration energy went to zero.

Binding energies were also calculated using DYNAMO in the molecular statics mode. The binding energy was equal to the difference between crystal energies when the constituents are far apart and when they are combined into a complex. We did not determine the concentration dependence of binding energies.

Table 1 shows the calculated migration energies, the rate of change of the migration energy with increase in defect concentration, and binding energies. Experimentally measured values are shown in parentheses.

TABLE I

DIFFUSION PARAMETERS OF AgZn
CALCULATED USING EAM POTENTIALS

PARAMETER	DILUTE CASE (eV)	CONCENTRATION DEPENDENCE SLOPES DUE TO:		
		VACANCIES	IMPURITIES	INTERSTITIALS
		(eV/concentration change)		
MIGRATION ENERGIES:				
INTERSTITIALS	.095	-3.1	- .17	
INTERSTITIAL-IMP. -A	.78	-7.4	- .80	
VACANCY	.78 (.84 [8])	-5.4	-2.90	-25.
VACANCY IMPURITY	.69	-1.5	- .83	-30.
BINDING ENERGIES:				
INTERSTITIAL-IMP. -A	.70			
INTERSTITIAL-IMP. -B	.70			
VACANCY-IMPURITY	.09 (.09 [9])			
FORMATION ENERGY:				
VACANCY	.97 (1.0 [10])			
CRITICAL CONCENTRATIONS FOR RATE COEFFICIENTS:				
INTERSTITIAL/VACANCY	.008			
VACANCY/IMPURITY	.08			

REACTION MIGRATION ENERGY

It is common practice to use the dilute concentration migration energy in the exponential factor of the rate coefficient. However, in order for two defects to form a complex, for example, they must be near each other, and hence alter the migration energy; i.e. a minimum critical concentration of the opposing species must need exist. This has a severe effect that should be taken into account. The critical concentration is taken as the inverse of the total number of lattice locations where a defect may jump and interact with the second defect. To distinguish the activation energy in

the rate coefficient from the dilute migration energy, we term it the reaction migration energy. Values of the critical concentrations calculated are listed in Table 1. For concentrations less than the critical value, the reaction migration energy is constant.

DEFECT INTERACTIONS

In using DYNAMO to calculate migration energies it was necessary to investigate a number of defect interactions. We will briefly describe some of our observations.

We have calculated annihilation interaction volumes for interstitials reacting with vacancies and for interstitial-impurity complexes reacting with vacancies. The interaction volumes are shown in Fig 2. The interstitial/vacancy interaction volume is exactly as reported in ref [11], but the interstitial-impurity/vacancy interaction volume is quite different. We also find that the configuration for the interstitial-impurity complex may be not only a dumbbell interstitial, as reported in the literature, but that the impurity may also settle in the octahedral position.

In the calculation of the migration energies it is necessary to obtain stable positions that could be reached through migration, i.e. a stable position obtained by crossing a particular saddle region. We find that the migration mechanism is quite different from that described by Johnson and Lam[12] and Dederichs [13]. They describe a jump process which includes orthogonal jumps to near neighbor sites. We found that for the mixed interstitial, the near neighbor position was not stable; an interstitial placed at the nearest neighbor position to an impurity decayed to a mixed dumbbell. The second nearest neighbor position was stable but the jumps were not all orthogonal. In addition some jumps resulted in atomic rearrangements so that the initial configuration was established but with different atoms.

SUMMARY

Defect migration and reaction energies are calculated for a dilute solution of Zn in Ag using semi-empirical EAM potentials. The affect of local defect concentrations on these energies are determined in a linear approximation. We describe a reaction migration energy model which accounts for the affect of interacting species.

The availability of new potentials permits the testing of many assumptions of the defect jumping process as well as the testing of the potential itself by comparisons with observed properties. We find that the Ag - Zn potentials reproduces a number of measurable properties but indicate that a different defect migration scheme exists for the mixed dumbbell.

REFERENCES

1. M.S. Daw and M.I. Baskes, Phys. Rev. B29 6443 (1984).
2. D.J. Oh and R.A. Johnson, Journal of Mat. Res. 3 471 (1988).
3. M. Igaarashi, V. Vitek, paper presented at the World Materials Congress, Chicago, Illinois, Sept., 1988.
4. E. Clementi and C. Roetti, At. Data Nucl. Data Tables 14 177 (1974).
5. G.J. Ackland and R. Thetford, Philosophical Magazine A, 56 15 (1987).

6. R. Hultgren, P.D. Desai, D.T. Hawkins, M. Gleiser, and K.K. Kelley, eds., Selected Values of Thermodynamic Properties of Binary Alloys (American Soc. for Metals, Metals Park, Ohio).
7. H.J. Rockosh, Ph.D. dissertation, Univ. of Munster, 1983.
8. K. Herchbach Phys. Rev. 130 554 (1963).
9. R. Benedek, J. Phys. F: Met. Phys. 17 569. (1987).
10. H. Mehrer and A. Seeger, Phys Status Solidi, 39 647 (1970).
11. M.W. Thompson, Defects and Radiation Damage in Metals (cambridge University Press, Cambridge, 1969), p.45
12. R.A. Johnson and N.Q. Lam, Phys. Rev. B13 4364 (1976).
13. P.H. Dederichs, C. Lehmann, H.R. Schober, A. Scholz, and R. Zeller, J. Nucl. Mat. 69/70 176 (1978).

SUPERADDITIVITY IN THE IMPLANTATION OF MOLECULAR IONS

G. F. Cerofolini*, L. Meda** and C. Volpones**

* EniChem, via Medici del Vascello 26, 20138 Milano MI, Italy

** ST Microelectronics, 20041 Agrate MI, Italy

ABSTRACT

This paper deals with the implantation of molecular ions in silicon. The 'molecular' effect, i.e. the increase of the displacement yield compared with the sum of the atomic yields, is weak for light molecules (e.g., H_2) and for heavy diatomic molecules (e.g., Sb_2 and Bi_2), but, for instance, it is strong for C_6H_6 at energy per atomic mass of the order of 1 keV/amu. Binary collision calculations are used to give a pictorial view of the phenomena occurring along the ion path, and to predict superadditivity and damage columnarity. The increase of pressure and temperature to extreme conditions by implantation of molecular ions is discussed.

INTRODUCTION

Ion implantation into Si is thought of as responsible for two kinds of damage: vacancy-interstitial (v-i) pairs and amorphous islands [1]. V-i pairs are associated with recoil events with low transferred energy E_t (say, in the range 0.05 – 1 keV) while the amorphous phase is the remnant of a kind of collective thermal phenomenon (*hot cloud*) originated either by a recoil with E_t higher than a threshold energy E' ($E' \simeq 5$ keV), or by a lot of nuclear collisions transferring to the crystal more than 500 keV/ μm [2]. The second mechanism is preferred by heavy ions, while the first mechanism is unique for light ions. If the E_t is in the intermediate range, 1 – 5 keV, the temperature of the cloud is insufficient (lower than the energy excess u_0 of the amorphous phase, $u_0 = 0.13$ eV/atom [3]) to produce amorphization; in this case we speak of *warm clouds*. Warm clouds may become responsible for amorphization in two situations: when the additional heating due to the involvement of v-i pairs increases the local temperature above u_0 (this is responsible for superlinearities [2]), or when two warm clouds simultaneously superimpose on one another and originate a hot cloud.

Considerations on the order of magnitude show that, for usual beam instantaneous current densities (of the order of 1 – 10 mA/cm²), two warm clouds (with radius λ of approximately 30 Å [2] and lifetime of the order of 10^{-11} s [4]) generated by two different ions have a negligible probability of being superimposed. If, however, a molecular ion is implanted, the atoms originally forming the molecule travel across the same space region at approximately the same time, irrespective of whether the molecule is or is not broken during the collision at the surface. Hence the possibility that a superimposition exists. Consider a molecular ion AB^+ formed by two light atoms A and B, and imagine that at a depth x ($\pm \lambda$) A releases in a single nuclear collision an energy $E_t^A (< E')$ and B an energy $E_t^B (< E')$; suppose moreover that $E_t^A + E_t^B > E'$. When all these conditions are satisfied, at the depth x A and B cannot separately amorphize, while AB can produce amorphization. If the superimposition of two warm clouds originates a hot cloud, then the amorphization yields must satisfy the condition $y^{AB} > y^A + y^B$. On defining the superadditivity factor η as follows $\eta = y^{AB}/(y^A + y^B)$, the condition for superadditivity is $\eta > 1$. Actually, the amorphization yields y^A , y^B and y^{AB} depend not only on target nuclear properties, but also on target temperature T and impinging power density [3].

The technological relevance of the implantation of molecular ions is essentially related to the BF_3^+ implantation into single crystal Si [5–7], because it allows thin layers to be obtained even implanting at moderately high energy E : assuming the fragmentation of the molecular ion at the surface, B enters the silicon with energy $\frac{11}{48}E$ (because of the atomic mass-to-molecular-mass ratio), and the F amorphization reduces B channeling.

In the following we shall discuss data of y observed in the implantation of other molecular ions. These data refer to experiments carried out *at constant atomic fluence and with energies so chosen that the species enter the target with the same impinging velocity*. The displacement yield was determined by the random and aligned Rutherford backscattering (RBS) spectra by

applying a linear dechanneling correction.

Light ions Mitchell et al. [8] observed that the implantations of atomic and molecular deuterium into (111) Si (8° tilt) at 40 K produce the same damage. No superadditive effect was observed.

Heavy ions Mitchell et al. [8] considered also the implantation of heavy species both in Si and Ge. In particular, for the implantation into (111) Si in random condition (8° tilt) at room temperature, they obtained a yield of 1300 (As^+ , 25 keV), 2450 (Sb^+ , 25 keV), 2000 (Te^+ , 20 keV), and 2500 (Bi^+ , 15 keV); and η equal to 1.7 (As_2^+), 1.7 (Sb_2^+), 1.4 (Te_2^+), and 1.6 (Bi_2^+). A somewhat smaller effect was observed by Thompson et al. [9] for the implantation into randomly oriented (111) Si at 40 K; they analyzed the samples by *in situ* RBS, took into account the damage produced by the alphas during the analysis, and obtained a yield of 1900 (As^+ , 24 keV), and 3100 (Sb^+ , 15 keV) and η equal to 1.1 (As_2^+), and 1.2 (Sb_2^+). This smaller effect may be explained in terms of target temperature, as η increases with T [10].

Middle-weight ions Quite different is the situation for middle-weight ions: when their atomic energies are high enough, η remains of the order of unity; at low atomic energies it assumes values as high as 10 (the energy at which this effect appears is higher the lighter the ion; quantitatively it decreases from approximately 20 keV for B to 5 keV for Si [2]).

Grob et al. [11] implanted BF_n^+ ($1 \leq n \leq 3$) and PF_n^+ ($1 \leq n \leq 5$) into randomly oriented (7° tilt) (100) Si at 77 K. For PF_n^+ molecules was found to range from 1180 (F^+ , 20 keV) and 1880 (P^+ , 33 keV) to 14000 (PF_5^+ , 133 keV), while η was found to vary from 1.1 (PF^+) to 1.8 (PF_5^+). Implantations carried out with SiF_n^+ ($n = 1, 2$) at approximately the same energy per atomic mass, but at room temperature, show: a lower y , a somewhat higher η , and the persistence of superadditivity in the region where superlinearity is present too (table 1). SiF_n^+ ions were implanted into (100) Si at a tilt of 7° , at room temperature with current densities of the order of 1 mA/cm² in a Eaton NOVA commercial ion implanter.

A dramatic increase of y and η with n was observed by Davies et al. [12], who investigated room-temperature implantations of carbon-containing polyatomic ions into (111) Si. In table 2 we have assumed: a negligible displacement yield for H and $y = 12$ for O, obtained by scaling the displacement yield for C times the ratio of the atomic energies.

Table 1: Amorphization yields by Si^+ , F^+ , SiF^+ , and SiF_2^+

ion	E/keV	Φ/cm^{-2}	y
Si^+	34	10^{14}	510
F^+	23	10^{14}	250
$\text{Si}^+ + \text{F}^+$	34 & 23	$10^{14} + 10^{14}$	780
SiF^+	56	10^{14}	1250
$\text{Si}^+ + 2 \text{F}^+$	34 & 23	$10^{14} + 2 \cdot 10^{14}$	1400
SiF_2^+	56	10^{14}	1980

Table 2: Displacement yields by relatively light polyatomic ions

ion	E/keV	y	η
C^+	8.8	9	
O^+	11.7	12	
CO^+	20.5	68	3.2
CO_2^+	32.2	258	7.8
C_6H_6^+	57.0	842	15.6

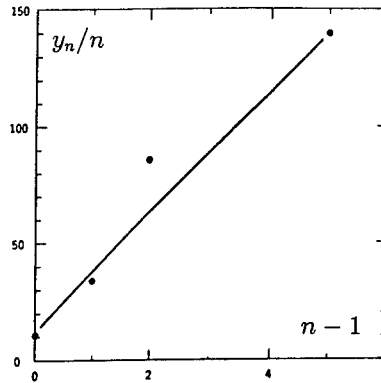


Fig. 1: Graph of y_n/n vs $n-1$. This behavior supports the idea that amorphization is due to the superimposition of two warm clouds.

SUPERIMPOSITION OF WARM CLOUDS

Consider now a molecule formed by the same atomic species (e.g., As₂, Sb₂ and also hydrocarbons, because H is irrelevant for the production of hot and even warm clouds). In the absence of superlinear effects, if warm clouds superimpose on one another only in pairs, the molecular amorphization yield y_n is expected to be given by

$$y_n = y n + \frac{1}{2} Y n(n-1), \quad (1)$$

where: y is the amorphization yield due to hot clouds produced by atoms and Y is the amorphization yield due to the superimposition of two warm clouds, and the factor $n(n-1)$ takes into account the fact that the warm clouds produced by each of the n atoms can superimpose on the ones produced by the remaining $n-1$ atoms. The above equation predicts that y_n/n increases linearly with $n-1$, in agreement with the data of Davies et al. [12] (fig. 1). A log-log plot (not shown) confirms that the power law relating y_n/n to $n-1$ is linear. The fair agreement of experimental data with (1) suggests that amorphization is due to the superimposition of *two* warm clouds. A similar conclusion can be drawn for PF_n⁺ too [11].

How does this superimposition take place? How does an n -tuple of atoms impinging the surface as a molecule move inside the target? Does the molecule dissociate immediately at the surface or do the atoms move for a certain time as a molecule? To give an answer to such questions, consider, for instance, an organic molecule impinging on a Si target with energy in the range 1–2 keV/amu. The following considerations, however, apply to most other molecules and targets. Each C atom loses in electronic collisions an energy of approximately 10² eV per lattice constant. This energy is much higher than the binding energy of the atom in the molecule; this suggests that the molecule is broken immediately after having impinged on the surface. However, these collisions do not produce remarkable changes of lateral momentum, and, because of the Fano factor [13], they are only responsible for a small dispersion in the projected momentum. Hence, *the atoms move synchronously, maintaining approximately the same relative positions as in the molecule, until one or more of them has a collision with high transferred momentum.* The recoils generated by a molecular ion can therefore be calculated from the recoils due to single atoms impinging on the target at the same velocities as the molecule — *recoil events are additive.* The effects of such recoils (i.e., warm and hot clouds) survive for a time ($\approx 10^{-11}$ s) longer than the free travel time ($\approx 10^{-13}$ s) of the impinging atoms [4], so that these effects are simultaneous and can superimpose on one another, provided that they take place at the same positions — *the effects of primary recoils can be superadditive* [1].

For a biatomic molecule formed by middle-weight ions (say, with atomic number Z lower than 10) at relatively low atomic energy (say, lower than 15 keV) η can be evaluated simply. Indeed, these atoms move correlated along an approximately rectilinear path until they have a low impact-parameter collision; this collision, which destroys the molecular correlation, can reasonably be assumed to transfer an energy (higher than E_w) sufficient to form a warm cloud. Since middle-weight ions at relatively low energy have *at most* one of these collisions, the number of superimposing warm cloud is given by $(Y_w 2\lambda/\Lambda_w)^2$, where Y_w is the yield for the events with energy higher than E_w and Λ_w is the maximum depth at which the atom can release an energy higher than E_w . Of course, two superimposing warm clouds can amorphize only when have a sufficient energy, say when $2E_w > E'$. The number of atoms which in this case remain displaced is therefore given by $r_w(Y_w 2\lambda/\Lambda_w)^2$, where r_w is the quenching yield [2] of two superimposing warm clouds, and the superadditivity factor is given by $\eta = [2r_h Y_h + r_w(Y_w 2\lambda/\Lambda_w)^2]/2r_h Y_h = 1 + 2(r_w/r_h)(\lambda/\Lambda_w)^2 Y_w^2/Y_h$, where Y_h and r_h are the yield and quenching efficiency of hot clouds. The parameters r_h and r_w may *a priori* be different because of the different local temperatures and shapes (\Rightarrow quenching efficiency) of hot clouds originated by a single recoil event or by the superimposition of two warm clouds; this difference might account for the dependence of η on T . Consider first the case of E sufficient to produce hot clouds. Taking: $r_h \simeq r_w$, $Y_h/Y_w \simeq \frac{1}{2}$ (this conclusion following from the behavior of the integral cross section as determined by MARLOWE simulation [14] and from having assumed a threshold energy of 5 keV for hot clouds and of 2.5 keV for warm clouds), $\lambda \simeq 30$ Å, $\Lambda_w = 100-1000$ Å, and $Y_w \approx 1$, we have $\eta = 1 + o(1)$. However, if the energy per atom is below or close to the threshold value allowing for direct amorphization, then $Y_h \simeq 0$, and η can assume very large values. Since

in the experiments of Davies et al. [12] the energy was not high enough to allow for direct amorphization, the above considerations explain the high value of η for C_6H_6 as well as the low η for C^+ [15].

AMORPHIZATION BY HEAVY IONS

Consider now monoatomic ions. For any given ion velocity, the yield in primary recoils able to amorphize increases with Z , and the hot clouds they produce remain generally separated from one another even for the heaviest ions. If we consider, however, not only hot clouds but also warm clouds, several of them superimpose to form hot *columns* along the path. Fig. 2 shows a pictorial view of the damage released by Sb^+ implantation. The problem of describing the columnar amorphization has therefore been reduced to the problems of determining the distribution of sufficiently energetic primary recoils (solvable by binary collision codes) and the superimposition of their effects (solvable with the pictorial method shown in fig. 2). The condition for columnar amorphization is $2\lambda Y_w \approx R_p$, where R_p is the projected range of the implanted ion. The damage columnarity χ can be defined as the ratio $\chi = 100 \delta / R_p$ where δ is the average diameter of the amorphous zones. Obviously, since quenching efficiency is not unitary, δ is an underestimate of the size of the hot column immediately after its formation. Fig. 3, empty dots (desumed from raw data of refs. [16,17]), shows how χ varies with Z for assigned energy.

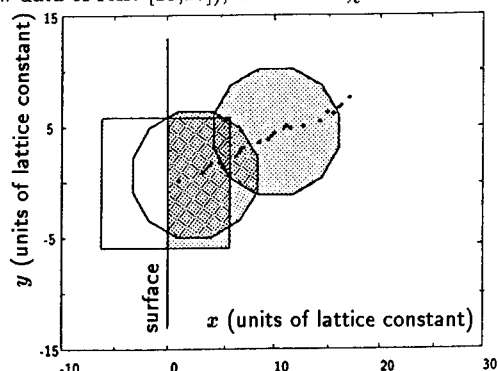


Fig. 2: The projection in a plane perpendicular to the surface (x is the depth and y is the coordinate along the surface) of the ion path (obtained by recording the distribution of primary recoils with E_t higher than the thermal energy, 25 meV) and of the warm and hot clouds produced by the implantation of Sb^+ at 25 keV into (100) Si 7° tilt (length unit is the lattice constant). A warm cloud (circle with radius λ) is assumed to be formed when $E_t > 1$ keV. A hot cloud (square with edge λ) when $E_t > 5$ keV. The formation of a hot column by superposition of warm clouds is evident.

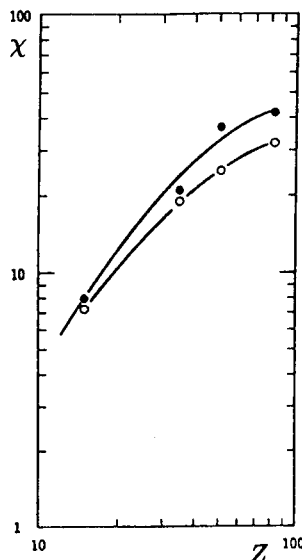


Fig. 3: Damage columnarity vs. atomic number. The graphs show that χ for the atomic ion (empty dots) is the same as for the biatomic molecular (full dots) for $Z < 30$, (when the damage is not columnar). The data for As and Sb are for an energy of 20 keV; the datum for Bi is linearly interpolated from those at 15 keV and 30 keV, while the datum for P is obtained by observing that δ does not vary with E , and increases by about 10% from atom to molecule.

Consider now a biatomic molecule. If the ions have by themselves a high χ , the hot columns generated by the atoms have a probability of the order of unity to be superimposed. Since the two columns involve the same atoms, they produce an *ultrahot column*, which succeeds in releasing heat to the crystal only after its extension, when its temperature is reduced below u_0 . This process leads to $\eta \approx 1$. When the atomic χ is not so high to allow for a single damaged column, the molecular effect increases χ by the mechanism shown in fig. 4. This effect tends to disappear for low Z , because hot clouds have a negligible chance to be superimposed, and for high Z , because the damage is already columnar. Fig. 3 (full dots) confirms these qualitative conclusions. When the damage is fully columnar, the local temperature can be

increased by increasing the number of atoms in the molecule and/or the weight of each atom. In particular, a heavy biatomic molecule can produce a local melting which may lead to new amorphous structures. These amorphous structures are expected to be recoverable only at high temperatures. Indeed, the damage recovery kinetics are slower the higher is χ [16]. The annealing behavior of As, its damage columnarity, the superlinearity it manifests [2], all of these facts suggest that the border between light and heavy ions is somewhere close to $Z = 30$.

PERSPECTIVES

While the increase of the nuclear energy loss with Z is very fast for low Z (from 0.19 keV/ μm for $Z = 1$ to 154 keV/ μm at $Z = 10$ at $E = 100$ keV), it becomes roughly linear for high Z (from 154 keV/ μm for $Z = 10$ to 3000 keV/ μm for $Z = 83$ at the same energy) [18]. This slow increase does not allow the temperature to be increased simply by increasing the mass of the impinging ion.

Completely new perspectives are offered by the implantation of molecular ions. Indeed, if the fractional damage volume [9] is not too far from 1, the nuclear energy losses due to single atoms forming the molecular ion may sum their effects thus originating new effects. These effects are of two kinds:

1) For light ions, such as BF_2^+ , SiF^+ , SiF_2^+ , etc., two warm clouds may superimpose. and originate one cloud sufficiently hot to amorphize. This results in the superadditivity of atomic effects due to single atoms.

2) For heavy and large molecules, the damage is columnar, the superposition of two or more already hot clouds results in more columnar and ultra-hot clouds. The local temperature affects the target according to the following arguments:

Until it remains below about 1500 K ($\approx u_0$) the cloud is able to amorphize. When the temperature becomes of the order of 3000 K, the cloud first melts and then vaporizes. When the cloud vaporizes, the pressure increases to values of the order of $10^8 - 10^9$ Pa. These conditions are similar to the ones existing at a depth of approximately 50 km below the Earth crust, so that molecular ions can become a fundamental tool for the study of matter in such conditions. Possible candidates for getting these conditions are UF_6 , $\text{Mo}(\text{CO})_6$, $\text{W}(\text{CO})_6$, etc.

Suppose now that the molecule is so large to have $\chi \simeq 100$; in this case all hot clouds superimpose to give a unique hot cloud. Assume further that the hot volume is $1000 \times 100 \times 100 \text{ \AA}^3$, thus containing 5×10^5 atoms. In these conditions, all the implantation energy is released to these atoms. If, for instance, $E = 1$ MeV (obtained by implanting a hypothetical molecule formed by 10 equal atoms to each of which the fragmentation at the surface confers an energy of 100 keV), the average energy of the atoms in the hot cloud is only of 2 eV, but the local temperature is huge, of about 2×10^4 K, and so is the pressure, $\approx 10^9$ Pa [19]; these conditions are not too different from the ones existing in the Earth mantle (fig. 5, also ref. [20]). If $E = 1$ GeV, the average energy per atom of the cloud becomes of the order of 1 keV (with temperatures and pressures of the order of 10^7 K and 10^{12} Pa, respectively, typical of the interior of the Sun). The duration of this ultra-hot cloud can be estimated by assuming a quasi-random walk inside the cloud with a mean free path equal to the nearest neighbour distance; this gives a time of the order of 10^{-11} s. These considerations hold true quite independently of target nature, so that molecular ions, formed by molecules with approximately 100 atoms and with a total energy of 1 GeV, can produce in any target hot clouds at temperatures of the order of 10^7 K, with density of the order of 10^{23} cm^{-3} and durations of 10 ps. Possible candidates are very large organic molecules or organometallic compounds involving actinides [21].

At last, we observe that the above considerations hold true quite independently of target nature; in particular, they can be applied to a $\text{Li}^2\text{H}/\text{Li}^3\text{H}$ target. Though the Lawson criterion to get fusion by inertial confinement is not satisfied yet, we realize that we are not far from satisfying it. Hence the suggestion to use molecular ions as a tool for nuclear fusion by inertial confinement. However, any other technique which injects into a target a synchronous shower of ions [22] will be able to produce the same effects.

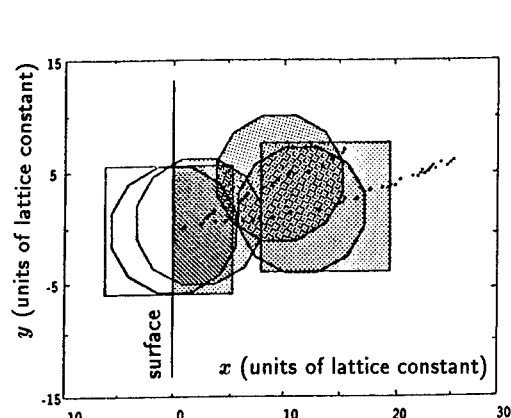


Fig. 4: Projection in a plane perpendicular to the surface of the ion paths and of the warm and hot clouds produced by the implantation of Sb_2 molecule at 50 keV. The formation of hot columns and the increase of columnarity is evident. Symbols are the same as in figure 2.

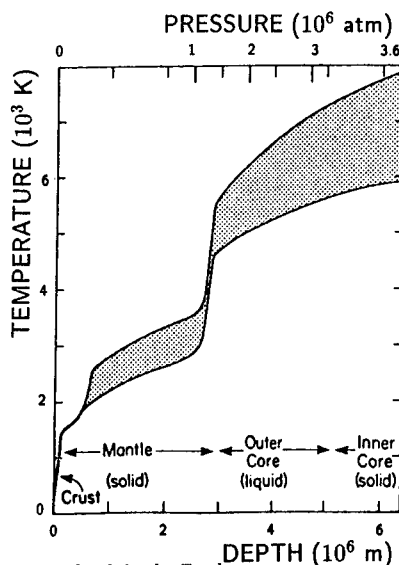


Fig. 5: Estimate of the average temperature and pressure as a function of depth in the Earth.

REFERENCES

1. G.F. Cerofolini and L. Meda, *Phys. Rev. B* **36**, 5131 (1987).
2. G.F. Cerofolini, L. Meda and C. Volpones, *J. Appl. Phys.* **63**, 4911 (1988).
3. E.P. Donovan, F. Spaepen, D. Turnbull, J.M. Poate and D.C. Jacobson, *Appl. Phys. Lett.* **42**, 698 (1983); *J. Appl. Phys.* **57**, 1795 (1985).
4. R.S. Averback, presented at the *Workshop on the Effects of Recoil Spectrum and Nuclear Transmutation on the Evolution of the Microstructure*, Lugano, March 1988.
5. H. Mueller, H. Ryssel and I. Ruge, in: *Proc. 2nd Intl. Conf. Ion Implantation*, I. Ruge and J. Graul eds., Springer-Verlag, Berlin, (1971) p. 85.
6. W. Vandervost, D.C. Houghton, F.R. Shepherd, M.L. Swanson, H.L. Plattner and G.J.C. Carpenter, *Can. J. Phys.* **63**, 863 (1985).
7. S.D. Brotherton, J.P. Gowers, N.D. Young, J.B. Clegg and J.R. Ayres, *J. Appl. Phys.* **60**, 3567 (1986).
8. J.B. Mitchell, J.A. Davies, L.M. Howe, R.S. Walker, K.B. Winterbon, G. Foti and J.A. Moore, in: *Ion Implantation in Semiconductors*, S. Namba ed., Plenum Press, New York, NY (1975) p. 493.
9. D.A. Thompson, A. Golanski, K.H. Haugen, D.V. Stefanovic, G. Carter and C.E. Christoulides, *Radiat. Eff.* **52**, 69 (1980).
10. D.A. Thompson, R.S. Walker and J.A. Davies, *Radiat. Eff.* **32**, 135 (1977).
11. A. Grob, J.J. Grob and A. Golanski, *Nucl. Instrum. Meth. B* **19/20**, 55 (1987).
12. J.A. Davies, G. Foti, L.M. Howe, J.B. Mitchell and K.B. Winterbon, *Phys. Rev. Lett.* **34**, 1441 (1975).
13. U. Fano, *Ann. Rev. Nucl. Sci.* **13**, 1 (1963).
14. M.T. Robinson and I.M. Torrens, *Phys. Rev. B* **9**, 5008 (1974).
15. Assuming, as done in ref. [12], that y observed in the implantation of carbon at 8.8 keV is exclusively due to v-i, allows us to determine the values of binding energy U_b and quit energy E_q required by MARLOWE to describe the formation of the v-i pair. These values are $U_b \approx 40$ eV and $E_q \approx 40$ eV.
16. L.M. Howe, M.H. Rainville, H.K. Haugen and D.A. Thompson, *Nucl. Instrum. Meth.* **170**, 419 (1980).
17. L.M. Howe and M.H. Rainville, *Nucl. Instrum. Meth. B* **19/20**, 61 (1987).
18. J.F. Gibbons, W.S. Johnson and S.W. Mylroie, *Projected Range Statistics*, Dowden, Hutchinson & Ross, Stroudsburg, PA (1975).
19. No latent heat has been considered for this estimate; its existence and value do not modify the following considerations.
20. R. Jeanloz, *Nature* **325**, 303 (1987).
21. F.A. Cotton and G. Wilkinson, *Advanced Inorganic Chemistry*, John Wiley & Sons, New York (1980) p. 1020.
22. G.F. Cerofolini and L. Meda, Italian Patent No. 20321A/87 (April 1987).

PART II

Ion-Beam Mixing

A COMPARISON BETWEEN HIGH- AND LOW-ENERGY ION MIXING

Y.-T. CHENG,* E.-H. CIRLIN,** B. M. CLEMENS,* AND A. A. DOW**

* General Motors Research Laboratories, Warren, MI 48090-9055.

** Hughes Research Laboratories, Malibu, CA 90265.

Diffusion in a thermal spike is shown to be the dominant mechanism for both high- and low-energy ion mixing. The similarity between high- and low-energy ion mixing is the result of the fractal nature of collision cascades.

Recently, high-energy (e.g., several hundred keV) ion mixing has attracted much interest because of its technological importance in surface modification [1]. In contrast, there have been fewer studies of low-energy (e.g., several keV) ion mixing, in spite of its importance to the depth resolution of sputter depth profiling and low-energy ion beam-assisted deposition. One of the basic questions common to both high- and low-energy ion mixing is, of course, the mechanism of the mixing process. In this paper, we provide experimental evidence that diffusion in a thermal spike is the dominant mechanism in both high- and low-energy ion mixing, and we present an interpretation based on the fractal nature of collision cascades.

Over the years, several authors have proposed models of ion mixing. Ion mixing in the absence of radiation-enhanced diffusion has been categorized by two types of ion mixing models. One is based on the transport equations for collision cascades first derived by Lindhard et al. (LSS) [2] and Winterbon et al. (WSS) [3]. This type of model [4-7] takes into account the purely "ballistic" aspects of atomic collisions such as the atomic mass and density, but does not take into account the chemical properties of the solids. This type of model has been called the "ballistic" model of ion mixing. According to the ballistic model, the mixing rate $d(4Dt)/d\phi$, which is the square of the width of the mixed interface per unit ion dose ϕ in bilayer ion mixing experiments, is given by [4,7]

$$\frac{d(4Dt)}{d\phi} = C \frac{\epsilon R_c^2}{\rho E_d}, \quad (1)$$

where ϵ is the energy deposited per unit length due to nuclear collisions, ρ is the atomic density, E_d is the threshold displacement energy, R_c is the range associated with E_d , and C is a function of the atomic mass. The ballistic model was proposed for both high- and low-energy ion mixing. However, eq. (1) has been shown inadequate in describing the magnitude of either high- or low-energy ion mixing [1,8,9].

The second type of model is based on experimental observations from high-energy ion mixing where thermodynamic parameters, such as the heats of mixing ΔH_{mix} and the cohesive energy ΔH_{coh} , strongly influence the ion mixing efficiency [10-14]. It was shown that 600 keV Xe^{++} ion mixing in metallic bilayers consisting of elements with large and negative heats of mixing [15], such as Pt/Ti (-122 kJ/g.at) and Pt/Zr (-151 kJ/g.at), mix more efficiently than bilayers with zero or small negative heats of mixing, such as Pt/Ni (-7 kJ/g.at) or Pt/Mo (-42 kJ/g.at), under identical ion irradiation conditions. A phenomenological model was developed for the observation [10-14]. The model is an extension of the Vineyard's thermal spike model [16] by including Darken's treatment of chemical diffusion [17]. It is shown that [10-14]:

$$\frac{d(4Dt)}{d\phi} = \frac{K_1 \epsilon^2}{\rho^{5/3} \Delta H_{coh}^2} (1 + K_2 \frac{\Delta H_{mix}}{\Delta H_{coh}}), \quad (2)$$

where K_1 and K_2 are two phenomenological constants greater than zero.

Quantitative as well as qualitative agreement between the thermal spike model and high-energy ion mixing has been well documented. Until now, we have more than 21 ion mixing experiments using 600 Xe⁺⁺ ion bombardment of metallic bilayers consisting of 5d/4d or 5d/3d metals that agree quantitatively with the thermal spike model of ion mixing [10-14]. In addition, Westendorp et al. [18] have examined mixing rates of thin Au, Ta and W films sandwiched between Cu layers. The expected chemical trends were observed for irradiations at both 10 and 300 K. Mixing rates for a number of metallic bilayers have been measured by d'Heurle et al. [19], and a strong correlation with the electronegativity difference of the elements involved was found. Since the latter quantities are closely related with the heats of mixing [15], we may regard both correlations as essentially equivalent. Mixing trends in a number of Ni-based bilayers were measured by Bhattacharya et al. [20] and Rai et al. [21], and were found to be in good agreement with the predictions of the phenomenological model. It has also been found that heats of formation or reaction enthalpies provide good guidelines to estimate ion mixing trends in metallic alloy systems or insulating compounds: examples of both kinds include the Ni-Al system [22], Pt mixed with the Ni-based alloy [23], elemental metals mixed with various oxides [24], carbides [25,26], and nitrides [27].

There have also been attempts to further probe the correlation between mixing rate and the cohesive energy ΔH_{coh} . Kim et al. [28] have investigated marker broadening in a large number of metal systems at low temperature. The use of thin markers instead of bilayers is an efficient way to suppress the heat of mixing, since the impurity atoms are rapidly diluted in the matrix during ion mixing. The results show, for fixed ϵ , an order of magnitude increase between marker spreads in Hf and in Au, qualitatively in agreement with the phenomenological model of ion mixing. We now believe that the thermal spike model, rather than the ballistic model, contains the essential features of those ion mixing experiments in which an inert heavy ion, such as Xe or Kr, of a few hundred keV is used to bombard metallic bilayers consisting of elements with atomic numbers greater than 20.

Low-energy ion mixing has been studied mainly in sputter depth profiling. In a typical depth profiling analysis experiment, the chemical composition of the outer surface layer of about 1 nm thick is measured by Auger electron spectroscopy (AES), x-ray photoelectron spectroscopy (XPS), or secondary ion mass spectrometry (SIMS). The composition profile as a function of depth below the surface is obtained by the gradual removal of the surface layer by sputtering with an ion beam of energy between 1 and 5 keV. As the ion beam reaches an interface, the composition profile there is altered as a result of ion mixing. Ion mixing, therefore, limits the depth resolution of sputter depth profiling.

Although the depth resolution of sputter depth profiling can be severely hindered by ion mixing, the sputter depth profiling technique can be conveniently used to study low-energy ion mixing. Recently, we have performed sputter depth profiling of metallic bilayers using XPS or AES and 1 keV Ar⁺ sputtering. The details of the experiment are published in Refs. 29, 30, and 31. Here we focus on the discussion on the mechanism of low-energy ion mixing. We chose to investigate the influence of ion mixing on the depth resolution during sputter depth profiling of metallic bilayers consisting of the same thickness Pt layer on top of a 3d or 4d metal layer: Ti, Ni, Zr, or Mo. The same bilayer systems have been used to demonstrate the influence of thermodynamic parameters on high-energy ion mixing [10-14]. In order to separate the influence of ion mixing from other contributions to the depth resolution, instrumental parameters and sample geometry were kept nearly constant for all bilayer samples and throughout the entire depth profiling experiment. It was then concluded that the variations in the apparent interfacial broadening, Δz , measured by sputter depth profiling, were due primarily to the differences in the extent of ion mixing during sputter depth profiling in the bilayer samples. Table I summarizes these results. We observed that Δz , measured by sputter depth profiling, was greater for bilayers consisting of materials with larger $\Delta H_{mix}/\Delta H_{coh}$. Furthermore, there was a correlation between the

depth resolution, Δz , and the mixing rates, $d(4Dt)/d\phi$, of metallic bilayers irradiated with 600 keV Xe^{++} (see Table I). This experiment suggested that thermodynamic parameters, such as ΔH_{mix} and ΔH_{coh} , influence ion mixing during sputter depth profiling and that the mechanism of ion mixing during sputter depth profiling with ion energies of a few keV is the same as that for ion mixing with ion energies of several hundred keV. The dominant contribution to both high- and low-energy ion mixing is diffusion in thermal spikes.

The similarity between ion mixing with several hundred keV ion irradiation and with a few keV ion bombardment can be understood from the fractal nature of collision cascades. Recently, fractal geometry has been applied to ion-solid interactions [32,33,34]. Using an idealized collision cascade model and the Winterbon-Sigmund-Sanders theory of atomic collisions, it was shown that [32,33]:

- (1) A collision cascade governed by the inverse-power potential $V(r) \propto r^{-1/m}$ ($0 < m \leq 1$) is a fractal with a fractal dimension $D = 1/(2m)$;
- (2) In 3-dimensional space a spike, defined as a "space-filling" collision cascade, occurs only when the dimensionality of the cascade D is greater than 3, or equivalently, $0 < m \leq 1/6$;
- (3) In an actual collision cascade, the fractal dimensionality increases as the cascade evolves, because of the decrease in m as the kinetic energy of the moving atoms decreases;
- (4) A moving atom with a kinetic energy smaller than E_c (the critical kinetic energy at which the potential becomes $V(r) \propto 1/r^6$), but greater than E_d , is capable of generating a local spike.

The values of E_c were calculated in Ref. 33 for collision cascades in single-component systems. It was shown [33] that E_c increases as the atomic number (Z) increases and is smaller than 1 keV for $Z \leq 80$. Together with (4), we obtain:

- (5) In a local spike, the average kinetic energy per moving atom is much smaller than 1 keV.

Let us consider the case where E_0 (the incident ion energy) $\gg E_c \gg E_d$. Such is the case for 100 keV Au^+ implantation into Au. A local spike forms, according to (4), only if the Au atom, which initiates the sub-cascade, has a kinetic energy E with $E_d < E \leq E_c$. For each incident ion of energy E_0 , the average number n of local spikes generated is, from the conservation of energy, on the order of $n = E_0/E_c$. Therefore, the existence of local spikes is determined by E_c , whereas the number of such local spikes is determined by the incident ion energy E_0 . Figure 1 is an illustration of local spike formation.

We can now understand the similarity between high- and low-energy ion mixing, if we assume that the experimentally measured amount of mixing is the sum of ion mixing within individual local spikes. Since the presence of local spikes does not depend on the incident ion energy as it varies from a few keV to several hundred keV, any physically observable process that occurs within a local spike will manifest itself during both high- and low-energy ion bombardment. In particular, if thermodynamics are important in diffusion within local thermal spikes, we must observe the influence of thermodynamics, such as the heat of mixing and cohesive energy, on ion mixing in both high- and low-energy ion mixing experiments.

The assumption that ion mixing is the result of mixing within individual local spikes is supported by the following argument which shows that the probability for spatial overlap of local spikes generated by each incident ion is small when the incident ion energy is on the order of several hundred keV. From the WSS theory [3], we know that the size, R_G ,

Table I Comparison between the depth resolution Δz of sputter depth profiling and the observed mixing rate $d(4Dt)/d\phi_{exp}$ for 5d-3d and 5d-4d metallic bilayers.

System (A-B)	$-\Delta H_m^a$ (kJ/g at)	$-\Delta H_{coh}^b$ (eV/particle)	$d(4Dt)/d\phi_{exp}^c$ (10^5 \AA^4)	Δz^d (sec)
5d-4d metals				
Pt-Zr	151	7.61	1.21	318
Pt-Mo	42	6.77	0.37	146
5d-3d metals				
Pt-Ti	122	6.60	1.28	430
Pt-Ni	7	5.21	0.45	168

- ^a Heat of mixing for $A_{50}B_{50}$, A.R. Miedema, Philips Tech. Rev. **36**, No. 8, 217 (1976).
- ^b Cohesive energy for $A_{50}B_{50}$ calculated from $\Delta H_{coh} = \frac{1}{2}(\Delta H_A^\circ + \Delta H_B^\circ) + \Delta H_m$, where ΔH_A° and ΔH_B° are the cohesive energies of the corresponding solids A and B, obtained from C. Kittel, *Introduction to Solid State Physics*, 5th ed. (Wiley, NY, 1976), and from *Selected Values of the Thermodynamic Properties of the Elements*, edited by R. Hultgren, P. D. Desai, D. T. Hawkins, M. Gleiser, K. K. Kelley, and D. D. Wagman (ASM, Metals Park, Ohio, 1973).
- ^c Experimentally observed mixing rate $d(4Dt)/d\phi$ using 600 keV Xe^{++} irradiation at 77 K. Data from Refs. 10-14.
- ^d Experimentally observed sputter depth resolution Δz . Data from Ref. 29.

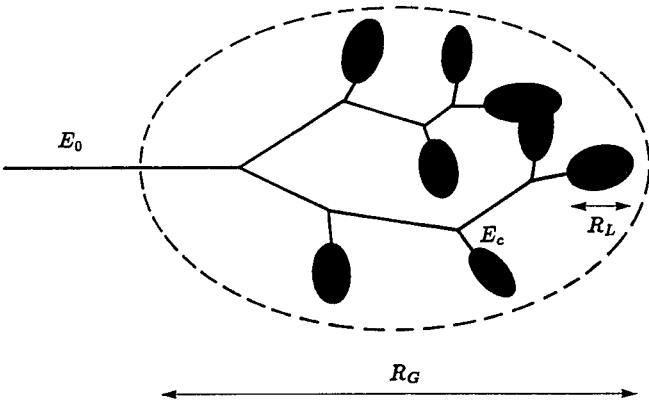


Figure 1. An illustration of a collision cascade and local spikes.

of the overall cascade (see Fig. 1) generated by an ion with incident energy E_0 is given by

$$R_G = \frac{E_0^{2m}}{\rho C_m}, \quad (3)$$

where $m = 1/2$ or $1/3$ for incident ions with energies of a few hundred or a few tens of keV, respectively. C_m is a function of m , the atomic number, and the atomic mass of the solids. The size of each local spike R_L is given by

$$R_L = \frac{E_c^{1/3}}{\rho C_{1/6}}, \quad (4)$$

because a local spike forms when $m = 1/6$.

To the first order approximation, we assume a random distribution of $n = E_0/E_c$ local spikes, each of volume $\frac{4}{3}\pi R_L^3$, in the overall cascade volume $\frac{4}{3}\pi R_G^3$. The fraction p of the volume occupied by the local spikes to that of the overall cascade is given by

$$p = \left(\frac{C_m}{C_{1/6}}\right)^3 E_0^{1-6m} = \begin{cases} \left(\frac{C_{1/2}}{C_{1/6}}\right)^3 E_0^{-2}, & \text{if } m = 1/2; \\ \left(\frac{C_{1/3}}{C_{1/6}}\right)^3 E_0^{-1}, & \text{if } m = 1/3. \end{cases} \quad (5)$$

Therefore, the fraction of the volume occupied by the local spikes decreases as the incident ion energy increases. In other words, the probability for overlapping of local spikes decreases with increasing incident ion energy E_0 . It can be estimated that less than 30% of the overall cascade volume is occupied by local spikes if the incident ion energy is about 10 keV for Ag^+ irradiation into a Ag matrix, and about 30 keV for Au^+ irradiation into a Au matrix. Therefore, the probability of having a global spike, in the sense that most of the overall cascade volume is occupied by overlapping local spikes, is small when the incident ion has an energy greater than a few tens of keV. The breaking up of a cascade into dense subcascades at the energy of a few tens of keV has been observed in computer simulations, using either TRIM [35] or molecular dynamics [36].

In summary, we have provided experimental evidence that the dominant mechanism for both high- and low-energy ion mixing is diffusion in thermal spikes where thermodynamic properties of solids, such as the heat of mixing and cohesive energy, play an important role. The similarity between high- and low-energy ion mixing was discussed based on the fractal nature of collision cascades. This similarity is because local spikes form at low energies and ion mixing occurs mainly within local spikes.

We would like to thank G. B. Fisher, K. J. Greene, M. Van Rossum, and F. T. Wagner for comments and suggestions.

REFERENCES:

- ⁺ Present address: Digital Equipment Co., Northboro, MA 01532.
1. B. M. Paine and R. S. Averbach, Nucl. Instrum. Methods **B7/8**, 666 (1985).
2. J. Lindhard, M. Scharff, and H. E. Schiott, Mat. Fys. Medd. Dan. Vid. Selsk. **33**, 14 (1963).
3. K. B. Winterbon, P. Sigmund, and J. B. Sanders, Mat. Fys. Medd. Dan. Vid. Selsk. **37**, 1 (1970).
4. H. H. Anderson, Appl. Phys. **18**, 131 (1979).
5. U. Littmark and W. O. Hofer, Nucl. Instrum. Methods **168**, 329 (1980).
6. P. Sigmund and A. Gras-Marti, Nucl. Instrum. Methods **182/183**, 25 (1981).
7. S. Matteson, Appl. Phys. Lett. **39**, 288 (1981).

8. Z. L. Wang, J. F. M. Westendorp, and F. W. Saris, Nucl. Instrum. Methods **209/210**, 115 (1983).
9. B. V. King, S. G. Puranik, and R. J. Macdonald, Nucl. Instrum. Methods **B33**, 657 (1988).
10. Y.-T. Cheng, T. W. Workman, M.-A. Nicolet, and W. L. Johnson, Mat. Res. Soc. Symp. Proc. Vol. **74**, 419 (1987).
11. W. L. Johnson, Y.-T. Cheng, M. Van Rossum, and M.-A. Nicolet, Nucl. Instrum. Methods **B 7/8**, 657 (1985).
12. M. Van Rossum and Y.-T. Cheng, Diffusion and Defect Data **57-58**, 1 (1988).
13. Y.-T. Cheng, M. Van Rossum, M.-A. Nicolet, and W. L. Johnson, Appl. Phys. Lett. **45**, 185 (1984).
14. T. W. Workman, Y.-T. Cheng, W. L. Johnson, and M.-A. Nicolet, Appl. Phys. Lett. **50**, 1485 (1987).
15. A. R. Miedema, Philips Tech. Rev. **46**, 217 (1976).
16. G. H. Vineyard, Rad. Effects **19**, 245 (1976).
17. L. S. Darken, Trans. AIME **175**, 184 (1948).
18. J. F. M. Westendorp, F. W. Saris, B. Koek, M. P. A. Vieggers, and I. Fenn-Tye, Nucl. Instrum. Methods **B26**, 539 (1987).
19. F. d'Heurle, J. E. E. Baglin, and G. J. Clark, J. Appl. Phys. **57**, 1427 (1985).
20. R. S. Bhattacharya and A. K. Rai, J. Appl. Phys. **58**, 248 (1985).
21. A. K. Rai, R. S. Bhattacharya, M. H. Rashid, and A. W. McCormick, Mat. Res. Soc. Symp. Proc. **54**, 231 (1986).
22. E. Rimini, M. Nastasi, J. Liu, J. C. Barbour, J.-P. Hirvonen, and J. W. Mayer, Appl. Phys. Lett. **48**, 303 (1986).
23. V. Srinivasan and R. S. Bhattacharya, Surf. Interface Anal. **10**, 131 (1987).
24. G. C. Farlow, B. R. Appleton, L. A. Boatner, C. J. McHargue, C. W. White, G. J. Clark, and J. E. E. Baglin, Mat. Res. Soc. Symp. Proc. **45**, 137 (1985).
25. J. P. Hirvonen, M. Nastasi, and J. W. Mayer, Nucl. Instrum. Methods **B13**, 479 (1986).
26. M. Nastasi, J.-P. Hirvonen, M. Caro, E. Rimini, and J. W. Mayer, Appl. Phys. Lett. **50**, 177 (1987).
27. R. S. Bhattacharya, A. K. Rai, and P. P. Pronko, J. Appl. Phys. **61**, 5263 (1987).
28. S.-J. Kim, M.-A. Nicolet, R. S. Averback, and D. Peak, Phys. Rev. **B 37** 38 (1988).
29. Y.-T. Cheng, A. A. Dow, and B. M. Clemens, Appl. Phys. Lett. **53**, 1346 (1988).
30. Y.-T. Cheng, A. A. Dow, B. M. Clemens, and E.-H. Cirlin, J. Vac. Sci. Tech., in press.
31. E.-H. Cirlin, Y.-T. Cheng, B. M. Clemens, and P. Ireland, J. Vac. Sci. Tech., to be published.
32. Y.-T. Cheng, M.-A. Nicolet, and W. L. Johnson, Phys. Rev. Lett. **58**, 2083 (1988).
33. Y.-T. Cheng, in "NATO Advanced Study Institute Programme, Materials Modification by High-Fluence Ion Beams," edited by R. Kelly and M. da Silva (Cluwer, Dordrecht, 1988), p. 191.
34. K. B. Winterbon, H. M. Urbassek, P. Sigmund, and A. Gras-Marti, Phys. Scripta **36**, 689 (1987).
35. Y.-T. Cheng, unpublished results.
36. R. S. Averback, private communications.

THERMAL SPIKE RELATED NONLINEAR EFFECTS IN ION BEAM MIXING AT LOW TEMPERATURES

G-S. Chen*, D. Farkas and M. Rangaswamy

Department of Materials Engineering, Virginia Polytechnic Institute and State University,
Blacksburg, Virginia 24061, USA

ABSTRACT

A semi-empirical model for ion mixing at low temperatures was developed taking into account collisional mixing and thermal spike effects, as well as the thermal spike shape. The collisional mixing part was accounted for by the Kinchin-Pease model, or, alternatively dynamic Monte Carlo simulation. For the thermal spike, the ion beam mixing parameter Dt/Φ is derived as being proportional to $\chi^{2+\mu}$, where the damage parameter is defined as, $\chi = -F_0/\Delta H_{coh}$, F_0 is the damage energy deposited per unit path length, and μ is a constant dependent on the thermal spike shape and point defect density in the thermal spike regions. The shape of the thermal spike that best fit the experimental results depends on the magnitude of the cascade density. For relatively high density collisional cascades, where thermal spikes start to be important, it was found that a spherical thermal spike model was more consistent with experimental measurements at low temperatures. However, for extremely high density collisional cascade regions, a cylindrical thermal spike gave better results. Finally, three different regions of ion beam induced mixing were recognized according to different density levels of damage energy scaled by the damage parameter χ .

INTRODUCTION

Ion beam induced atomic transport at low temperatures is composed of three different mechanisms which are (i) cascade collisional mixing, (ii) Thermal spike induced short-range diffusion, and (iii) Radiation enhanced diffusion. Extensive theoretical studies have been carried out by Winterbon [1], Andersen [2], and Sigmund [3]. Computer simulation of the process has been developed [4], based on the computer code TRIM [5]. Experimental work has been carried out in different temperature ranges, such as Nb/Si [6] and Cr/Si [7] bilayer systems. It was found that the mixing efficiency is weakly dependent on temperature below certain critical temperature points. Thus, cascade collision mixing was suggested for some time to be the dominating mechanism in the ion beam mixing process. However, most experimental results showed much greater mixing than that predicted by cascade collisional mixing even after using adjusted values of the displacement energy [8,9]. The additional mixing observed can be understood as produced by thermal spike effects.

High density collisional cascades generate displaced atoms in a very localized volume. While these atoms cannot displace other atoms further, they can impart some of their energy to neighboring atoms through a many-body interaction. Thus most of their neighbor atoms are thermalized or energetically equalized in accordance to the Maxwell-Boltzmann distribution, and this results in a liquid-like thermal spike region in which the average characteristic energy of each atom is around 1 eV. This corresponds to an equivalent temperature of the order of 10^4 K. The thermal spike dimension is several tens of angstroms, i.e., approximately ten lattice constants. The thermal spike will quench in about 10^{-11} s [10].

Seitz and Koehler in 1956 [11], and Vineyard in 1976 [12], have developed a quantitative model for the thermal spike concept. They treated the cascade region as the initial conditions for the classical heat transfer equation and used the δ -function approximation to describe it. They assumed that basically the number of thermally activated jumps per unit volume per unit time follows an Arrhenius behavior. This model, however, does not consider the fact that a large number of point defects are created directly by the collision cascade processes. These defects may play an essential role in the subsequent thermal spike induced atomic migration process. This is seen for example in the work of Rubia et.al. [13] who used molecular-dynamics computer simulation to generate the atomic rearrangement picture of the thermal spike. We present here a model for the thermal spike that includes

* Present address: Department of Materials Science and Engineering, University of Illinois at Urbana-Champaign, Urbana, Illinois 61801, USA.

the effects of thermal spike shape as well as the point defects generated by the ion beam. The model allows for different damage regions, according to the energetic density of the cascade. The model is for low temperature regions where radiation enhanced diffusion is not important. After comparing the predictions of the model presented here with experimental results it is possible to establish an ion beam mixing picture with three different regions. For low damage energy densities thermal spikes are not important and cascade collision mixing is dominant. For the high density cascade regions spherical thermal spikes are expected as a consequence of collisional cascades, with the number of generated point defects following the Kinchin-Pease linear dependence [14]. For extremely high density cascade regions the thermal spike shape is expected to be cylindrical.

THEORY

The basic assumption in the present work is that the jumping rate of point defects per unit volume per unit time γ is proportional to the number of defects created in the region, and for each individual point defect, their jumping rate follows the Arrhenius behavior, i.e., $\gamma = \alpha \sigma(x) e^{-Q/RT}$, where α is the jumping rate constant per unit cross section. $\sigma(x)$ is the line-density of point defects at depth x , x being depth below the target surface, and Q is the atomic migration energy scaled by Boltzmann's constant.

The line-density of point defects, $\sigma(x)$, depends on the deposited energy per unit length F_D , which is a function of depth, x . $\sigma(x)$ is obtained by the Kinchin-Pease formula for the binary collision approximation as:

$$\sigma = \frac{0.42 F_D}{E_d} \quad (1)$$

where E_d is the displacement energy of the target atoms.

We consider the different regions of ion beam mixing, according to the line-density levels of the damage energy, defined in the form of the damage parameter χ , which is the damage energy scaled by the cohesive energy of the matrix ΔH_{coh} , i.e., $\chi \equiv -F_D/\Delta H_{coh}$, and associate different thermal spike shapes with different levels of damage energy density.

Spherical Spike In High Density Cascade Regions

We suppose a single isolated cascade with a spherical shape is of dimension λ , with λ a constant. From the Kinchin-Pease formula we obtain the line-density of displaced atoms along the direction of depth, σ_s , in the spherical thermal spike region,

$$\sigma_s = \frac{0.42 E_D}{\lambda E_d} \quad (2)$$

where E_D is the total damage energy deposited by the elastic collision process. Using the heat transfer equation and the initial conditions:

$$T(R, 0_-) = 0 \text{ and } T(R, 0_+) = \frac{E_D}{c} \delta^3(R) \quad (3)$$

where $\delta^3(R)$ is the three dimensional δ -function in spherical coordinates and R is the radial spherical coordinate. The boundary condition is $T(R, t)|_{R \rightarrow \infty} = 0$.

The initial bulk target temperature is simply taken to be zero since at low temperatures radiation enhanced diffusion is suppressed, and the mixing efficiency is only weakly dependent on temperature. Assuming that the heat conduction coefficient κ and specific heat capacity c are temperature-independent constants, for isotropic and chemically homogeneous media the solution to the heat transfer equation is:

$$T(R, t) = \frac{E_D c^{3/2}}{8(\pi \kappa t)^{3/2}} e^{-\frac{cR^2}{4\kappa t}} \quad (4)$$

Considering diffusional jumps in a circular area of radius R parallel to the surface plane and the direction of atomic jumps in this area as perpendicular to this area, the total number

of jumps induced by the thermal spike per unit length of the thermal spike in the spherical model is:

$$\eta_s = \int_0^\infty 2\pi R dR \int_0^\infty \alpha \sigma_s e^{-Q/T(R,t)} dt = \frac{0.42\alpha\lambda^{4/3}}{8\pi c^{1/3} \kappa E_d} \Gamma\left(\frac{4}{3}\right) F_D^{(2+\frac{1}{3})} Q^{-4/3} \quad (5)$$

where Γ is the gamma-function.

The total number of jumps per target atom in the material after being irradiated with dose Φ is then $\eta_s \Phi / \rho$, ρ is the atomic density of the target material. The typical jumping distance r_j can be related to ρ , $\langle r_j^2 \rangle = q_1 \rho^{-2/3}$. Moreover, the migration energy Q may be scaled by the cohesive energy of the matrix, i.e., $Q = -q_2 \Delta H_{coh}$. It is reasonable to assume that the displacement energy of the target E_d can also be scaled by ΔH_{coh} , $E_d = -q_3 \Delta H_{coh}$. Then the ion mixing parameter Dt/Φ is proportional to $\eta_s \langle r_j^2 \rangle / \rho$, or the mixing parameter for the spherical shaped thermal spike can be characterized by the following equation:

$$L_T^s \equiv \frac{D_T^s t}{\Phi} = \frac{B_1}{\rho^{5/3}} \left(-\frac{F_D}{\Delta H_{coh}} \right)^{2+\frac{1}{3}} \quad (6)$$

where B_1 is a constant and is related to c , κ , λ , q_1 , q_2 , and q_3 . Here we use the subscript T to refer to the thermal spike related parameters, and the superscript s to refer to the spherical thermal spike model.

Cylindrical Spike In Extremely High Density Cascade Regions

In this case, the initial condition of the thermal spike is an energetic line described by the damage energy density $F_D \delta^2(r)$, i.e.,

$$T(r, 0_-) = 0 \text{ and } T(r, 0_+) = \frac{F_D}{c} \delta^2(r) \quad (7)$$

where r is the radial distance from the initial energetic line, and $\delta^2(r)$ is the two dimensional delta-function. The boundary condition is $T(r,t)|_{r \rightarrow \infty} = 0$. Similar to that in the case of the spherical thermal spike, the solution to the heat transfer equation is

$$T(r, t) = \frac{F_D}{4\pi\kappa t} e^{-\frac{cr^2}{4\kappa t}} \quad (8)$$

Next, the total number of jumps induced in the thermal spike per unit length can be calculated and is denoted by η_c :

$$\eta_c = \int_0^\infty 2\pi r dr \int_0^\infty \frac{0.42\alpha F_D}{E_d} e^{-Q/T(r,t)} dt = \frac{0.42\alpha F_D^3}{4\pi\kappa Q^2 c E_d} \quad (9)$$

The cylindrical thermal spike induced mixing parameter is

$$L_T^c \equiv \frac{D_T^c t}{\Phi} = \frac{B_2}{\rho^{5/3}} \left(-\frac{F_D}{\Delta H_{coh}} \right)^3 \quad (10)$$

where D_T^c is the effective diffusion coefficient corresponding to thermal spike induced atomic migration, B_2 is a constant and is related to c , κ , λ , q_1 , q_2 , and q_3 . Here we use the superscript c to refer to the cylindrical thermal spike model.

Three Mixing Regions

The cascade collision mixing model occurs in the collision phase of a cascade. It assumes a linear cascade picture, in which two-body interactions are important and the moving atoms collide only with stationary atoms. In this way, the Kinchin-Pease formula is a good approximation in predicting the number of displaced target atoms by knock-on effect. Consequently, the effective diffusion coefficient for cascade collision mixing can be derived by an analytical way, since the collisional atomic mixing process can be considered to be near ideal random mixing. It is appropriate to conceive of the atomic diffusion as occurred

in an elemental cubic volume with isotopic randomness. Thus, the effective diffusion coefficient for cascade collision mixing can be defined [15,16] as $D_b = (1/6) \langle r_b^2 \rangle / P$ where $\langle r_b^2 \rangle$ is the effective mean-square displacement of the knocked-off atoms, P is the displacement frequency of the target atom during the period of irradiation. Using the expression for D_b and the Kinchin-Pease relationship, and scaling $\langle r_b^2 \rangle$ by the atomic density ρ , i.e., $\langle r_b^2 \rangle = q_4 \rho^{-2/3}$, the cascade collision mixing parameter can be written as:

$$L_b = \frac{0.42}{6} B_2 \rho^{-5/3} \left(-\frac{F_D}{\Delta H_{coh}} \right) \quad (11)$$

where B_2 is a constant and is related to q_3 and q_4 .

We now have three mixing regions. The first region denoted as L_b , is the cascade collision region; the second region termed as the Thermal Spike Region I, is related to the thermal spike induced ion mixing in the relatively high cascade regions; the third term is called the Thermal Spike Region II which falls into the extremely high cascade regions. In the second region the thermal spikes are expected to be spherical and in the third one cylindrical.

COMPARISON WITH EXPERIMENTAL DATA

One of the purposes of this work is to attempt to find out how and when the thermal spike induced ion mixing is significant. The systematic experimental data from references [17,18] make it possible to compare the model developed here with the available experimental data. These data are for metallic bilayer samples subjected to the irradiation of 600 keV Xe⁺⁺ at 77 K. It has been realized that the thermal spike induced ion mixing should be much more significant than the cascade collision mixing for these data, since the experiments belong to the energetic heavy ion bombardment ($F_D > 100$ eV/Å). Figure 1 gives the thermal spike induced ion mixing parameter as a function of damage energy deposited in

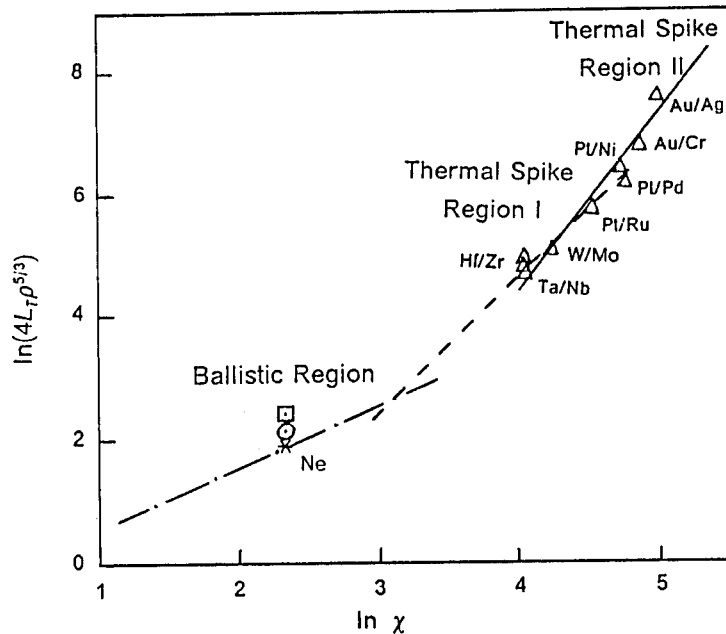


Figure 1. Plot of the ion beam mixing parameter represented by $\ln(4L_T \rho^{5/3})$ as a function of the scaled deposited energy $\ln(-F_D / \Delta H_{coh})$.

the form of a Log-plot with $\ln(4L\rho^{2/3})$ representing the mixing and $\ln \chi$ the damage level. It should be noted that the data for the plot, obtained from refs. [17,18], have negligible chemical effects. In figure 1, the least square fitting in the abscissa range of 4.0 to 4.3 is shown. The slope in this region was found to be 2.24. This compares very well with power factor $(2 + \mu) = 2.33$, which follows from our spherical thermal spike model. On the other hand, for the next region, $\ln \chi \geq 4.3$, a rapid increase in ion mixing parameter obviously deviates from the trend of the region of the spherical thermal spike model. The slope of this region seems much higher than that of the previous region. We attribute the production of defects in this region to the nonlinear cascade effects, i.e., the thermal spike related defects. The slope value in this region appears more consistent with our cylindrical thermal spike model in the extremely high cascade case, i.e., $2 + \mu = 3.0$. Table I lists the power factor of thermal spike models with different shapes. The slope values from the experimental data are also listed, at the relatively high cascade region and the extremely high cascade region. The cascade collision mixing model, in the low cascade regions, is listed with the slope equal to 1.0. For the cascade collision mixing data on ion mixing of metallic layers by Ne from ref. [15] is used (circle symbol). In addition, the cascade collision mixing values calculated from the Anderson Model (square symbol) and the computer simulation code TRALL [4] (star symbol) are also included. For the cascade collision mixing with slope value of 1.0, a straight line could be constructed on the basis of these data. The difference in the slopes of the three regions can be clearly seen the figure.

DISCUSSION AND CONCLUSIONS

Ion mixing at low temperatures can be divided mainly into two phases, as mentioned in the introduction part, i.e., the cascade collision phase and the thermal spike phase. During the cascade collision phase, atoms are displaced from their lattice positions through knock-down events of binary collisions. The elastic energy transferred in each collision must be larger than the displacement energy of the target, E_d . As a result, many Frenkel pair of defects are created at the end of this phase. Low energy many-body collisions are important as the residual energy is partitioned among the atoms in the cascade volume. A significant atomic migration for the Frenkel defects could occur during this phase. The significance of these two phases at different damage levels can be understood within the framework of figure 1. Thus in a semi-empirical fashion, three distinct ion mixing regions at low temperatures dependent on the damage parameter χ can be identified.

For low values of χ ($< 22\text{\AA}^{-1}$): The mixing parameter L essentially has a linear dependence on the damage parameter χ . This is the cascade collision mixing region, where atoms are likely to be displaced from their initial positions via linear collision cascade process, and the residual energy partitioned among the atoms in the cascade volume, may not be able to form a significant thermal spike.

For relatively high values of χ ($22\text{\AA}^{-1} \leq \chi < 75\text{\AA}^{-1}$): Thermal spike enhanced atomic migration starts to be important. The relevant nonlinear effects of ion mixing appear, as opposed to the linear effect of the cascade collision mixing region. Basically, this thermal spike region originates from the first order of nonlinear effects, here it is referred as the Thermal Spike region I. Still, the generation of defects follows the linear cascade behavior in this region, i.e., the Kinchin-Pease formula. However, the cooling phase of the cascade has a substantial influence on the atomic mixing via thermal spikes. The thermal spike in this case possesses a spherical shape and the ion mixing parameter is proportional to $\chi^{2.33}$.

The extremely high value of χ ($\geq 75\text{\AA}^{-1}$): Nonlinear effects of thermal spike induced ion mixing are more significant. In this region, not only the residual energy (thermal spike)

Table 1. The Power Factor $(2 + \mu)$ Obtained in the Different Thermal Spike Models.

	Spherical	Cylindrical
Vineyard's Model	1.67	2.0
Present Model	2.33	3.0
Least Square Fitting	2.24	> 3.0
note: The slope for the cascade collision mixing case = 1.0		

has great nonlinear influence on the atomic migration process, but also the creation of defects may follow nonlinear behavior. In particular, the thermal spike shape in this region is likely to evolve into a cylindrical one and the ion mixing parameter is proportional to χ^3 .

Comparison of our model with experimental data show that, the slope of the experimental data in the extremely high density cascade region appears to be even higher than that predicted by the cylindrical thermal spike model. This is most likely due to the creation of the thermal spike related defects, as reported by Thompson and Walker in the energetic bombardment of semiconductor targets Si and Ge [19].

Heinisch [20] employed a binary collision approximation in his computer simulations of defects production in a cascade volume for the case of FCC metal elements. The cascade pictures tentatively showed that for relatively high density cascades, the cascades are isolated from each other (i.e., the spherical thermal spike case). However, for the case of extremely high density cascades, the cascade tends to become a compact line (i.e., the cylindrical thermal spike case). Thus, in a qualitative fashion the results from our thermal spike model seem consistent with Heinisch's simulation.

ACKNOWLEDGEMENTS

One of the authors (GSC) would like to thank Dr. Y-T. Cheng for providing the published experimental data from the Cal Tech group. Support by the Office of Naval Research under Contract No. N00014-85-K-0110 is acknowledged.

REFERENCES

1. K. B. Winterbon, Ion Implantation Range and Energy Deposition Distributions, Vol. 2 (Plenum, New York, 1975).
2. H. H. Andersen, Appl. Phys. 18, 131 (1979).
3. P. Sigmund and A. Gras-Marti, Nucl. Instr. & Meth. 182/183, 25 (1981).
4. R. Pasianot, Diana Farkas, M. Rangaswamy, and E. J. Savino, to be published.
5. J. P. Biersack and L. G. Haggmark, Nucl. Instr. & Meth. 174, 257 (1980).
6. S. Matteson, J. Roth and M-A. Nicolet, Radiation Effects 42, 217 (1979).
7. S. Wen-Zhi Li, H. Kheyrandish, Z. Al-Tamimi and W. A. Grant, Nucl. Instr. & Meth. B19/20, 723 (1987).
8. R. S. Averback, Nucl. Instr. & Meth. B15, 675 (1986).
9. B. M. Paine and R. S. Averback, Nucl. Instr. & Meth. B7/8, 666 (1985).
10. W. L. Johnson, Y. T. Cheng, M. Van Rossum and M-A. Nicolet, Nucl. Instr. & Meth. B7/8, 657 (1985).
11. F. Seitz and J. S. Koehler, Solid State Physics 2, 251 (1956).
12. G. H. Vineyard, Radiation Effects 29, 245 (1976).
13. T. Diaz de Rubia, R. S. Averback, R. Benedek, and W. E. King, Phys. Rev. Lett. 59 (17), 1930 (1987).
14. J. F. Ziegler, J. P. Biersack and U. Littmark, The Stopping and Range of Ion in Solids, Vol.1, 1985, p.115-116.
15. I. A. Fenn-Tye and A. D. Marwick, Nucl. Instr. & Meth. B18, 236 (1987).
16. J. Bottiger, S. K. Nielsen and P. T. Thorsen, Nucl. Instr. & Meth. B7/8, 707 (1985).
17. M. Van Rossum, Y-T. Cheng, M-A. Nicolet and W. L. Johnson, Appl. Phys. Lett. 46 (6), 610 (1985).
18. T. W. Workman, Y. T. Cheng, W. L. Johnson and M-A. Nicolet, Appl. Phys. Lett. 50 (21), 1485 (1987).
19. D. A. Thompson and R. S. Walker, Rad. Effects 36, 91 (1978).
20. H. L. Heinisch, J. Nucl. Mater. 103/104, 1325 (1981).

DIFFUSION IN IRRADIATED AgZn ALLOYS USING DEFECT-CONCENTRATION DEPENDENT MIGRATION ENERGIES

T.D. Andreadis, M. Rosen, J.M. Eridon
Naval Research Laboratory, Washington, DC 20375-5000.

ABSTRACT

Concentration dependent migration and reaction migration energies, calculated with the molecular dynamics code DYNAMO using Embedded Atom Method Potentials, were inserted into the appropriate diffusion and rate coefficients. The time and space evolution of the concentration of interstitials, vacancies, Zn impurity, interstitial-impurity, and vacancy-impurity complexes was calculated for an irradiated AgZn alloy in the framework of the approach presented in Johnson and Lam. A significant effect on defect segregation and profiles was found.

INTRODUCTION

Johnson and Lam[1] (JL) have presented a segregation model for defect diffusion in an irradiated AgZn alloy. They investigated both spatial and temporal profiles of interstitials, vacancies, and dilute Zn impurities, interstitial-impurity complexes and vacancy-impurity complexes. However the activation energies for migration, or migration energies, which occur in the diffusion and rate coefficients in the diffusion equation, depend on local concentrations of defects. We have determined, within the framework of the JL model, how significant an affect this defect concentration dependence has on the calculated defect profiles using the NRL nonlinear diffusion code, DELOS.

We used the Molecular Dynamics code DYNAMO[2] in its static mode and Embedded Atom Method (EAM) potentials to calculate defect migration energies and their concentration dependence for dilute solutions of Zn in Ag (Table 1). The calculation process will be briefly described here. First, migration energies were calculated for each defect under dilute conditions (a defect in pure Ag). The concentration dependence as a function of the concentration of the other defects was obtained by recalculation of the migration energy with defects present. A linear concentration dependence was assumed and the slopes for the curves of migration energy vs. concentration were obtained. Multiplying the slopes, which are given in Table 1, by the concentration of the corresponding specie gives the change in migration energy from the dilute case. The affects of different species on a migration energy are assumed to be additive. Details of the Molecular Statics calculations are presented elsewhere in these proceedings[3].

REACTION MIGRATION ENERGIES

Diffusion and rate coefficients have the general form:

$$R = R_0 \exp[-H_m/kT],$$

where R_0 = a pre-exponential factor,
 H_m = migration energy,
 k = Boltzmann's constant, and
 T = Absolute temperature .

Rate coefficients for the formation and breakup of complexes of defect species are generally calculated in the literature[1] using a migration energy which is the same as that for diffusion of the individual species. However, even when the concentration of two reactants is extremely dilute, the migration energies of reacting pairs of defects are not equal to the migration energies for diffusion of the separate defects under dilute conditions. For a reaction to occur, even under extremely dilute conditions, a second specie must always be close by (one jump distance). The required proximity of interacting species for a reaction defines a minimum critical concentration of the opposing species and has a severe effect on migration energies at low concentrations. To distinguish the migration energy in the rate coefficient from the migration energy for diffusion, we term it the reaction migration energy.

Values of the minimum critical concentrations calculated relative to the atomic density of the Ag solvent are listed in Table 1. For concentrations less than the critical value, the reaction migration energy is constant while the migration energy for diffusion proceeds linearly to the dilute value as the defect concentration decreases. Above the critical value, the defect concentration dependence of the reaction migration energy is the same as that of the migration energy for diffusion. In the NRL nonlinear diffusion code, DELOS, we have adjusted the migration energy of the rate coefficients to take this into account.

RESULTS

We benchmarked DELOS against the constant migration energy JL calculations using their listed values and obtained their results. A diffusion calculation was carried out for a 1000 Angstrom thick irradiated AgZn target with a constant uniform vacancy-interstitial production rate of 10^{-3} / (atom-sec). The target temperature was 0 degrees Celsius and an initial Zn impurity concentration of 10^{-3} was assumed. Center point values of the defect concentrations for times from 10^{-10} sec to 10^6 seconds matched the JL calculations. Equilibrium depth profiles of the defect concentrations compared well also.

A comparison was made of the results obtained using JL parameters and those using values for migration, formation and binding energies calculated using EAM potentials. The vacancy concentration depth profile at equilibrium dropped by a factor of four and solute concentrations increased by an order of magnitude. Other defect profiles also significantly changed.

Three sets of calculations were made using the data in Table 1. Calculations were made with all the migration energies held constant (at the dilute values obtained with EAM potentials), constant migration energies but with the reaction migration energy model, and then with both the concentration dependent migration energies and the reaction migration energy model. Figure 1 compares the center-of-the-film concentrations of impurities and interstitials as a function of irradiation time for the three cases. The impurity equilibrium concentration ($t > 10^6$) varies by at least an order of magnitude between the first and the latter two cases and the interstitial concentrations exhibit similar differences. Significant differences in the temporal behavior of the curves are also observed.

Figure 2 presents the impurity concentration profiles for the three cases. The surface concentration of the impurity for the case where the migration energy was held constant differs by a factor of 2 from the other

two cases. The bulk of the change at the surface is due to the reaction migration energy model.

Figure 3 contains the vacancy concentration profiles at equilibrium for the three cases. Again we see major differences brought on by the affect of concentration dependent migration and reaction migration energies.

CONCLUSIONS

We find that the diffusion is sensitive to the values used for the migration, formation and binding energies and therefore they should be determined with care. We also find that allowing the migration energies to be dependent on the local concentration of defects affects the results significantly.

TABLE I

DIFFUSION PARAMETERS OF AgZn
CALCULATED USING EAM POTENTIALS

PARAMETER	DILUTE CASE (eV)	CONCENTRATION DEPENDENCE SLOPES DUE TO: VACANCIES IMPURITIES INTERSTITIALS (eV/concentration change)		
MIGRATION ENERGIES:				
INTERSTITIALS	.095	-3.1	- .17	
INTERSTITIAL-IMP. -A	.78	-7.4	- .80	
VACANCY	.78 (.84 [4])	-5.4	-2.90	-25.
VACANCY IMPURITY	.69	-1.5	- .83	-30.
BINDING ENERGIES:				
INTERSTITIAL-IMP. -A	.70			
INTERSTITIAL-IMP. -B	.70			
VACANCY-IMPURITY	.09 (.09 [5])			
FORMATION ENERGY:				
VACANCY	.97 (1.0 [6])			
MINIMUM CRITICAL CONCENTRATIONS:				
INTERSTITIAL/VACANCY	.008			
VACANCY/IMPURITY	.08			

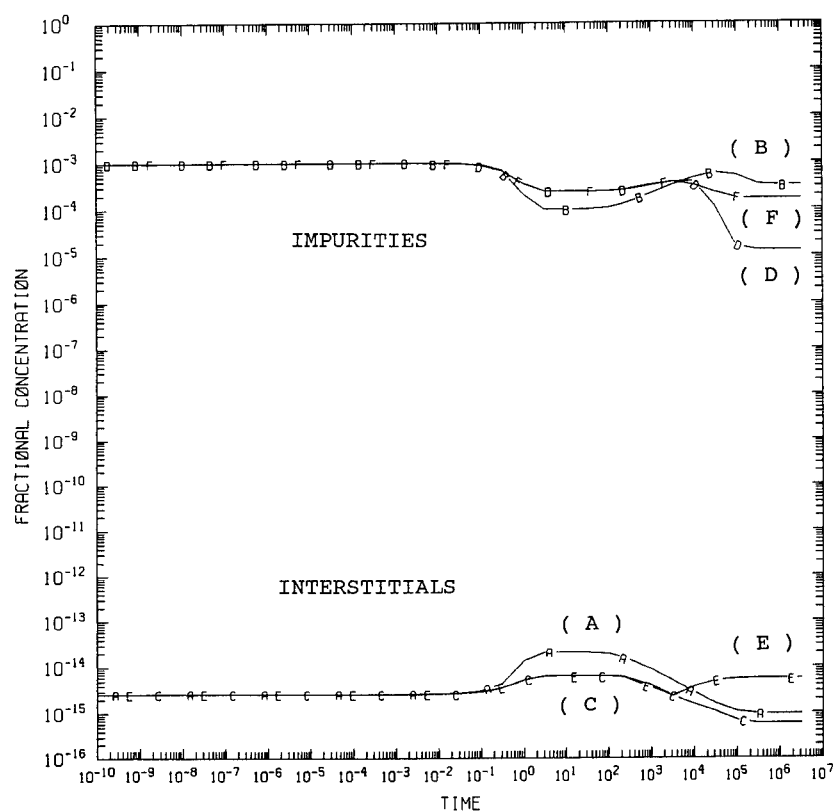


Figure 1. Center point concentrations of interstitials and impurities as a function of irradiation time: (A)(B) constant migration energies, (C)(D) constant migration energies + reaction migration energy model, (E)(F) concentration dependent migration energies and reaction migration energies.

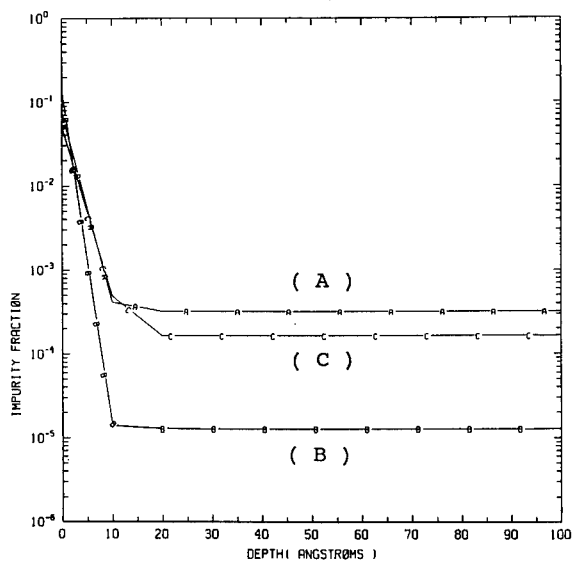


Figure 2. Impurity concentration profiles at equilibrium for: (A) constant migration energies, (B) constant migration energies + reaction migration energy model, (C) concentration dependent migration energies and reaction migration energies.

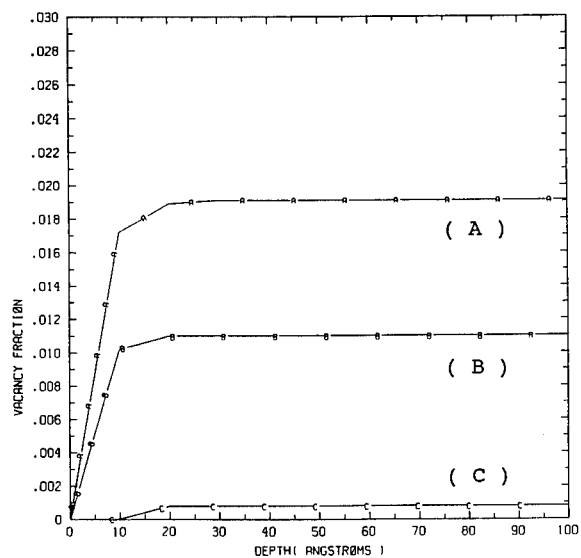


Figure 3. Vacancy concentration profiles at equilibrium for: (A) constant migration energies, (B) constant migration energies + reaction migration energy model, (C) concentration dependent migration energies and reaction migration energies.

REFERENCES

1. R.A. Johnson and N.Q. Lam, Phys Rev B13 4365 (1976).
2. M.S. Daw, M.I. Baskes, and S.M. Foiles (private communication)
3. T.D. Andreadis, et al., "The Influence of Defect Concentrations on Migration Energies In AgZn Alloys", these proceedings.
4. K. Herchbach Phys. Rev. 130 554 (1963).
5. R. Benedek, J. Phys. F: Met. Phys. 17 569. (1987).
6. H. Mehrer and A. Seeger, Phys Status Solidi, 39 647 (1970).

A COMPARISON OF THE MIXING RATES FOR FE-TI AND NI-TI BILAYERS.

P. Børgesen^a, D. A. Lilienfeld^b, R. E. Wistrom^a, and H. H. Johnson^a

a) Dept. of Materials Science and Engineering

b) National Nanofabrication Facility

Cornell University

Ithaca, NY 14853.

USA

ABSTRACT

Previous comparisons of the room temperature mixing of Ni-Ti and Fe-Ti multilayers have shown significant differences in the mixing rates in spite of closely similar heats of mixing as well as ballistic properties. This result suggests contributions from mechanisms other than ballistic and thermal spike effects, or a break-down of present thermal spike models for these materials. In order to identify the mixing mechanisms involved, quantitative measurements were made at various temperatures between 80K and 350K using bilayer samples. Surprisingly, the mixing rates were found to disagree significantly with those estimated for multilayer samples.

INTRODUCTION

The extent of ion beam mixing of a two-component system at an interface is generally expressed as the variance, σ^2 , of the atomic displacement distribution. This quantity usually varies linearly with irradiation fluence, ϕ , and we define the mixing rate as the ratio $\Delta\sigma^2/\Delta\phi$.

Room temperature ion beam mixing of multilayer samples near the 50-50 composition has been seen to be much more efficient in the Ni-Ti than in the Fe-Ti system [1]. In both cases, the intermixed region is known to remain amorphous [2-4]. Since the nuclear masses, and thus the damage energies F_D , in the two systems are very similar, the difference cannot be due to ballistic mixing effects [5,6]. Thermal spike mixing is generally expected to scale in a simple manner with deposited nuclear energy per unit path length, ϵ , and heat of mixing, ΔH_{mix} [7,8]. These parameters are very similar in the two systems [9], which also does not explain the difference.

Recently, the multilayer mixing rates were quantified [9], although with large error bars, and the temperature dependence of the Ni-Ti mixing briefly investigated. Room temperature irradiations with 600 keV Xe-ions were estimated to lead to mixing rates of $\sim 7.5 \times 10^4 \text{ \AA}^4$ and $\sim 1.4 \times 10^4 \text{ \AA}^4$ for Ni-Ti and Fe-Ti multilayers, respectively. However, at 80K the Ni-Ti rate was seen to agree with the Fe-Ti rate to within $\sim 45\%$ (the experimental uncertainty) which would suggest that the difference between the two systems at room temperature is caused primarily by additional contributions from a temperature dependent mechanism, such as radiation enhanced diffusion.

Johnson et al. [8] have proposed the expression

$$2\Delta\sigma^2/\Delta\phi = K_1 \frac{\epsilon^2}{\rho^{5/3}(\Delta H_{coh})^2} (1 + K_2 \frac{\Delta H_{mix}}{\Delta H_{coh}}) \quad (1)$$

for thermal spike mixing of a bilayer sample with large layer thicknesses. ρ is the average atomic density at the depth in question, and ΔH_{coh} is the cohesive energy. In general, we may expect the mixing efficiency to vary with film thickness [8,10], decreasing with increasing thickness for positive ΔH_{mix} (de-mixing during the spike counteracting ballistic mixing effects

[11]), increasing for negative ΔH_{mix} . However, we only expect this to be significant for thicknesses of the order of 5 Å or less [10].

Assuming the experimental values -34 and -31 kJ/mole for the heats of mixing of Ni-Ti and Fe-Ti, respectively, the absolute mixing rates obtained for the multilayers at low temperatures were overestimated by a factor of 2-3.5 by Equation 1 [9]. This discrepancy is unusually large for systems undergoing thermal spike mixing, but an even larger effect has been observed for Ni-Ti bilayers [12]. In the Fe-Ti system the mixing might be significantly reduced due to the unavoidable hydrogen contamination in the as-deposited samples, but measurements on electrolytically charged samples suggest that this effect should be substantially smaller for Ni-Ti [1,9,13].

In the present work we study the mixing of Fe-Ti and Ni-Ti bilayer samples, in an attempt to better quantify and possibly explain the above observations. The magnitude and possible origin of the hydrogen effect is dealt with in a separate contribution [13].

EXPERIMENTAL

Bilayer samples were deposited by electron-beam evaporation onto silicon substrates in an ion pumped system. The pressure was typically $1-2 \times 10^{-7}$ Torr before, and $\sim 5 \times 10^{-7}$ Torr during, deposition. Before and after irradiation samples were analyzed by [14] Rutherford Backscattering Spectrometry (RBS) and [15,16] Forward Recoil Energy Spectrometry (FRES).

Initially, the samples consisted of 4.4×10^{17} atoms/cm² of Fe or 4.7×10^{17} cm⁻² Ni on top of $\sim 2.7 \times 10^{18}$ cm⁻² Ti. RBS analysis showed the samples to contain less than one atomic per cent of impurities [9], except for hydrogen. FRES showed hydrogen concentrations of 10-15 % in the as deposited Ti, apparently a quite typical contamination level for evaporated films. A reduction of the hydrogen contamination would seem to require an anneal of the samples, something which is expected to also influence the subsequent mixing behaviour.

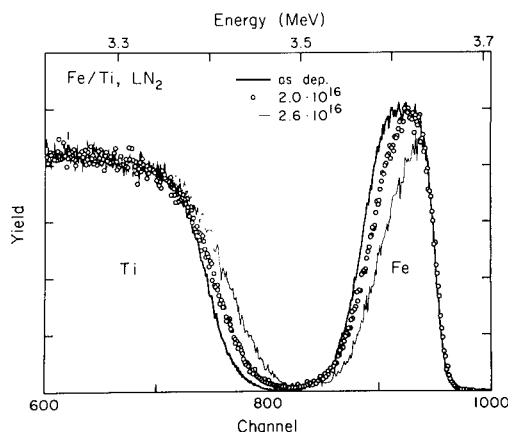


Fig. 1. RBS spectra for 4.88 MeV ⁴He ions incident on a Fe/Ti bilayer sample, at an angle of 70° to the surface normal, before and after irradiation with different fluences of 600 keV Xe-ions at ~80K.

The samples were mounted on an aluminum plate with silver paint and mixed using 600 keV Xe ions. Typical fluxes were $\sim 5 \times 10^{12} \text{ cm}^{-2} \text{ s}^{-1}$. Irradiation fluences were determined directly from the implanted amounts of Xe as measured by RBS.

The progress of mixing with increasing Xe fluence was monitored with RBS. Figure 1 shows examples of the spectra obtained from the Fe/Ti bilayer sample. The irradiation is seen to cause simultaneous mixing and loss of Fe due to sputtering. A similar behaviour was observed for the Ni/Ti samples.

The experimental spectra were simulated using the computer program RUMP [17]. The experimental resolution (including detector, electronics, and effects of geometry and surface roughness) was determined by matching the calculations to the shape of the surface signal. The interface signals generally had the form of complementary error functions, $C \cdot \text{erfc}\{x/\sigma/2\}$, and were fitted with the variance as fit parameter. Figure 2 shows an example of such a fit.

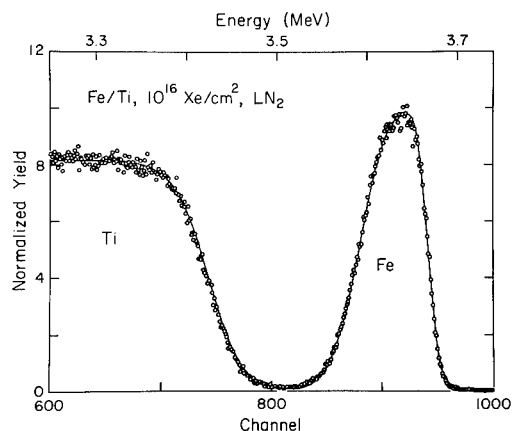


Fig. 2. RBS spectrum for 4.88 MeV ^4He ions incident on a Fe/Ti sample at an angle of 70° , after irradiation with 10^{16} Xe/cm^2 at $\sim 80\text{K}$. Solid line -- simulation [17].

RESULTS

In the course of the present measurements sputtering yields of 3.4 Fe-atoms/Xe-ion and 5.2 Ni/Xe were determined for the top layers. These values are in excellent agreement with extrapolations of experimental values found in the literature [18].

Both for the Fe/Ti and the Ni/Ti samples the variance, σ^2 , is seen to vary linearly with Xe fluence over a substantial range (Figs. 3 and 4). The mixing does not progress much faster with fluence at room temperature than at 80K. In particular, for the Ni-Ti system the temperature dependence is clearly much weaker than the factor of three variation observed for multilayer samples. Conceivably, this dependence could be related to a small difference in effective temperatures between the two sample configurations during "room temperature" irradiations. Perhaps differences in the thermal contact to the sample holder, or the larger number of interfaces, and corresponding thermal mismatch, in the multilayer sample, could result in a greater sensitivity to beam heating of the top layers. To test this hypothesis a few bilayer measurements were performed for a higher irradiation

temperature (77°C), almost certainly raising the surface temperature above that due to any beam heating effect. As seen in Fig. 4, heating the substrate did not lead to more than a 50% effect. We conclude that the measured difference between bilayer and multilayer mixing rates is real.

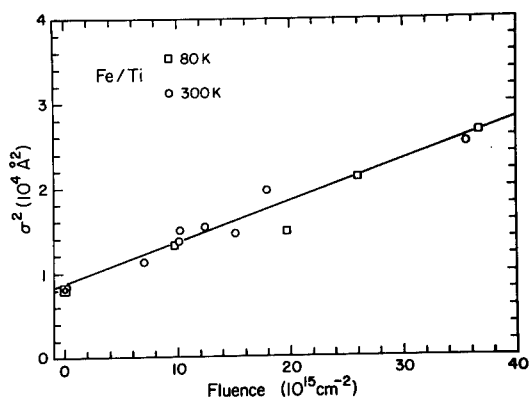


Fig. 3. Variance of the atomic distribution function at the interface of the Fe/Ti sample as a function of irradiation fluence, at various temperatures. Straight line is best fit to 300K points (see text), slope $4.8 \times 10^3 \text{ Å}^4$.

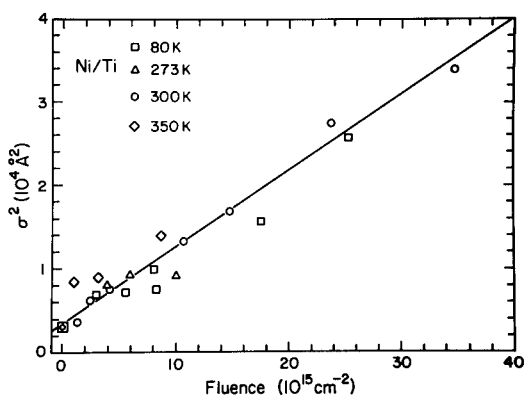


Fig. 4. Variance of the atomic distribution function at the interface of the Ni/Ti sample as a function of irradiation fluence, at various temperatures. Straight line is best fit to 300K points (see text), slope $9.2 \times 10^3 \text{ Å}^4$.

The straight lines in Figures 3 and 4 are least-squares fits to the room temperature results, and correspond to mixing rates $\Delta\sigma^2/\Delta\phi$ of $4.8 \times 10^3 \text{ Å}^4$ and $9.2 \times 10^3 \text{ Å}^4$ for Fe/Ti and Ni/Ti, respectively. The uncertainty in these numbers is estimated as $\pm 25\%$, i.e. the apparent reduction of $\sim 10\%$ in the Ni-Ti mixing at 80K is not necessarily significant.

The difference between the two mixing rates is much larger than predicted by Eq. 1, and it is not believed to be due to errors in the experimental ΔH_{mix} values used [9]. Assuming the ε -dependence of Eq. 1 the Ni-Ti rate agrees to within a few per cent with the room temperature rate reported elsewhere [12,19] for 1 MeV Au-ions. Similar data were not available for Fe-Ti samples.

For the Ni-Ti system the bilayer mixing rate might agree with that determined for the multilayer samples at 80K to within the combined uncertainties [9]. The room temperature results disagree strongly, apparently because of the unexplained temperature dependence of the multilayer mixing (see above). For the Fe-Ti system the bilayer mixing rate is lower than the multilayer value by about a factor of three. This result seems clearly outside the combined errorbars. Since the same computer program (RUMP) was used to evaluate both multilayer and bilayer spectra, the difference in the results is believed to be significant. At present, we cannot offer any explanations as to these differences. The Al-Ti bilayer mixing rate has been found to agree with the previously determined multilayer mixing rate [9] to within 10%. It is not clear whether there is any significance to the observation that the largest differences are found for those mixing rates deviating the most from Eq. 1.

CONCLUSION

The irradiation of bilayer samples with 600 keV Xe ions lead to twice as large a mixing rate in the Ni-Ti as in the Fe-Ti system. This difference is not explained by current ballistic or thermodynamic models. In both systems the mixing rate varied by less than 25% between 80K and 300K. At 350K the Ni-Ti mixing rate may be ~50% larger. This is in strong contrast to a factor of 3-5 increase between 80K and ~300K observed previously for Ni-Ti multilayers [9]. The Fe-Ti mixing rate was a factor of three lower than the corresponding multilayer mixing rate. The reason for this discrepancy will be the subject of future investigations.

ACKNOWLEDGEMENTS

This work was supported by the Division of Materials Research of the National Science Foundation. We acknowledge the Materials Science Center (NSF) at Cornell University for the use of their thin film facilities. The National Nanofabrication Facility is supported by the National Science Foundation under Grant ECS-8619049, Cornell University and industrial affiliates.

REFERENCES

- [1] J.-P. Hirvonen, M. A. Elve, J. W. Mayer, and H. H. Johnson, *Mater. Sci. & Eng.* 90, 13 (1987).
- [2] K. Saito and M. Iwaki, *Nucl. Instrum. Meth.* B7-8, 626 (1985).
- [3] A. K. Rai, R. S. Bhattacharya, P. P. Pronko, and Tai-il-Mah, *Surf. & Interface Anal.* 10, 142 (1987).
- [4] R. Brenier, P. Thevenard, T. Capra, A. Perez, M. Treilleux, L. Romana, J. Dupuy, and M. Brenel, *Nucl. Instrum. Meth.* B19/20, 691 (1987).
- [5] A. Gras-Marti and P. Sigmund, *Nucl. Instrum. Meth.* 180, 211 (1981).
- [6] P. Sigmund and A. Gras-Marti, *Nucl. Instrum. Meth.* 182/183, 25 (1981).
- [7] Y.-T. Cheng, M. Van Rossum, M.-A. Nicolet, and W. L. Johnson, *Appl. Phys. Lett.* 45, 185 (1984).
- [8] W. L. Johnson, Y. T. Cheng, M. Van Rossum, and M.-A. Nicolet, *Nucl.*

Instrum. Meth. B7/8, 657 (1985).

[9] P. Børgesen, R. E. Wistrom, H. H. Johnson, and D. A. Lilienfeld, submitted to J. Mater. Res.

[10] P. Børgesen, D. A. Lilienfeld, and H. H. Johnson, submitted to J. Appl. Phys.

[11] R. S. Averback, D. Peak, and L. J. Thompson, Appl. Phys. A39, 59 (1986).

[12] R. S. Bhattacharya and A. K. Rai, J. Appl. Phys. 58, 248 (1985); see also Erratum, *ibid.* 2798.

[13] R. E. Wistrom, P. Børgesen, D. A. Lilienfeld, and H. H. Johnson, these proceedings.

[14] W.-K. Chu, J. W. Mayer, and M.-A. Nicolet, "Backscattering Spectrometry", Acad. Press, NY, 1978.

[15] J. L'Ecuyer, C. Brassard, C. Cardinal, and B. Terreault, Nucl. Instrum. Meth. 149, 271 (1978).

[16] B. L. Doyle and P. S. Peercy, Appl. Phys. Lett. 34, 811 (1979).

[17] L. R. Doolittle, Nucl. Instrum. Meth. B9, 344 (1985).

[18] O. Almén and G. Bruce, Nucl. Instrum. Meth. 11, 257 and 279 (1961).

[19] A. K. Rai, R. S. Bhattacharya, and M. H. Rashid, Thin Solid Films 137, 305 (1986).

ION-BEAM MIXING IN AMORPHOUS AND CRYSTALLINE Fe-Ti

Udo Scheuer¹, Lynn E. Rehn and Pete Baldo

Materials Science Division, Argonne National Laboratory, 9700 S. Cass Ave,
Argonne, IL 60439

¹now with Institut für Festkörperforschung, KfA Jülich, Postfach 1913, D-5170
Jülich, Fed. Rep. of Germany

ABSTRACT

Crystalline Fe and Fe-10at.%Ti and amorphous Fe-37at.%Ti films with Ag and Hf markers were produced by vapor deposition. Marker spreading during ion-beam mixing between 77 K and 580 K was measured using Rutherford Backscattering (RBS). Marker spreading was also measured between temperatures of 300 K to 700 K after full crystallization of the Fe-37at.%Ti films. Microstructural changes during ion-beam mixing were studied in situ, in a High-Voltage Electron Microscope. Homogeneous nucleation of a metastable bcc phase was observed at high temperatures. The results are discussed in terms of their relevance to "radiation-enhanced" diffusion in amorphous materials.

INTRODUCTION

Atomic diffusion is a well-understood phenomenon in crystalline metals. Diffusion takes place via the motion of point defects, vacancies and interstitial atoms. Using energetic particle irradiation, point defects can be introduced in a controlled manner, and their role in the diffusion process can be evaluated. Under low-temperature irradiation, atomic mixing is observed as a result of recoil mixing, collisional mixing, and thermal spike diffusion. At higher temperatures, defects escape from displacement cascades and migrate long distances, giving rise to "radiation-enhanced diffusion" (RED). Despite that the concept of point defects loses its meaning in amorphous materials, irradiation of amorphous alloys has produced diffusion results remarkably similar to those obtained in crystalline materials. The observed temperature dependence has been interpreted [1],[2] as RED, in analogy to crystalline metals. However, the temperature range accessible for the study of RED in amorphous systems is very narrow. It is limited by cascade mixing at low temperatures and by crystallization at high temperatures. Diffusion in amorphous alloys at or above room temperature is clearly enhanced by irradiation. It is not clear, however, that this enhancement is due to the long-range diffusion of freely-migrating defects. In particular, the onset of the strongly temperature dependent regime between 300 K and 500 K is remarkably low when compared to single-crystalline metals [3]. In order to more closely compare ion-beam mixing and radiation-enhanced diffusion in the amorphous and the crystalline states, we have studied diffusion under irradiation in Fe-Ti alloys. The tracer diffusion coefficients under ion irradiation of Hf and Ag in an amorphous Fe-Ti alloy were measured at temperatures below the crystallization temperature. The Hf tracer diffusion coefficient under irradiation was also determined after crystallization of the films.

EXPERIMENTAL

Amorphous Fe-Ti films were prepared by vapor-deposition of a preformed $\text{Fe}_{25}\text{Ti}_{75}$ alloy onto oxidized $\langle 110 \rangle$ silicon wafer substrates using electron beam heating. The resulting composition of the films changed with deposition time and therefore had to be calibrated. The composition of the films was Fe-37at.%Ti (referred to as a-Fe-37at.%Ti) as confirmed by energy-dispersive (EDS) and electron energy-loss (EELS) spectrometry and RBS, within an accuracy of ± 2 at.%. Hf and Ag markers with a nominal thickness of 1 nm (equivalent to 4×10^{15} atoms/cm²) were deposited by electron beam heating. The thickness of the top and bottom layers of Fe-Ti was 45 nm. Films were also deposited on NaCl substrates for the production of transmission electron microscopy (TEM) samples. The background pressure during evaporation was below 8×10^{-8} Torr. Films were crystallized (referred to as x-Fe-37at.%Ti) by implantation of 2×10^{15} /cm², 1 MeV Krypton ions at a temperature of 823 K. This treatment leads to full crystallization of a bcc-phase with a grain size well above 100 nm. Due to the low dose, marker spreading during crystallization was very small (≤ 1.3 nm). Crystalline alloys with a Ti concentration of 10 at.% (referred to as x-Fe-10at.%Ti) were vapor-deposited from an $\text{Fe}_{55}\text{Ti}_{45}$ alloy. The substrate was heated to 740 K during the deposition, leading to a grain size well above 100 nm.

Irradiations were performed in a target chamber or in situ in the HVEM-Tandem National User Facility at Argonne. 1 MeV Kr ions were used at a flux of about 7×10^{12} Kr ions/cm²s to fluences between 1 and 5×10^{16} Kr ions/cm². For a displacement threshold of 36 eV, this is equivalent to irradiation doses between 19 and 95 dpa at the marker depth [4]. Lower ion doses were used at higher irradiation temperatures. Due to the long range of 1 MeV Kr ions, less than 3 % of the Kr was implanted into the metal film, and no bubble formation was observed. The specimens were heated by attaching them to a copper plate, which in turn was affixed to a light bulb heating stage. The specimen temperature was controlled to an accuracy of ± 3 K using a Chromel-Alumel thermocouple attached to the copper plate.

Backscattering experiments were performed with a 1.7 MeV He beam. The detector was positioned at a scattering angle of 138° , and the sample was tilted 20° from the beam normal, away from the detector. This arrangement yields good depth resolution, with some sacrifice in energy separation between the marker and Fe edges. A computer simulation program [5] was used to evaluate the measured spectra. Diffusion distances, Δx , were extracted by fitting Gaussian distributions to the marker concentration profiles obtained before and after irradiation. All reported results are normalized to an irradiation dose of 1×10^{16} Kr ions/cm², assuming a square root dependence of the marker diffusion on ion dose. The mixing yield was normalized according to $Dt/\phi F_D$, where D is the diffusion coefficient, t is the irradiation time, ϕ is the ion dose, and F_D is the damage energy deposition per unit length. The latter quantity was calculated using the TRIM-Code [4].

The structure and composition of the samples was checked before and after irradiation using conventional TEM, equipped with EDS and EELS. In situ observations were performed in a Kratos/AE1 EM7 High-Voltage Electron Microscope. The sample was tilted 30° so that it was normal to the ion beam. HVEM observations were made at an operating voltage of 300 kV.

RESULTS AND DISCUSSION

The spreading of a Hf marker layer under Kr ion irradiation is shown in figure 1. The square of the diffusion distance is plotted versus the inverse temperature. The amount of mixing at low temperatures (≤ 300 K) is greater in a-Fe-37at.%Ti than in the crystalline alloy of same composition. Mixing in a-Fe-37at.%Ti increases with irradiation temperature above room temperature. After subtraction of a constant value of low-temperature mixing, an apparent activation energy of 0.13 eV is determined. In contrast, the crystalline alloy does not show any increase in mixing up to 700 K within experimental error. Marker spreading is found to be even higher in the iron-rich alloy (x-Fe-10at.%Ti). At low temperatures, similar results are obtained for the Ag marker. In figure 2, the normalized mixing yield at 300 K is plotted versus composition. The mixing yield for Ag in pure iron and iron-rich alloys is found to be approximately $7 \text{ \AA}^2/\text{eV}$, in agreement with literature data [6]. For all compositions, mixing of the large Hf atom is lower by a factor of 2 to 3 relative to mixing of the Ag. A similar dependence of mixing/diffusion on tracer atom size has been found in amorphous alloys in thermal diffusion experiments [7],[8] as well as under irradiation [1]. For Ti concentrations near 37 at.%, mixing is less than 50% of the values for low Ti concentrations, probably due to the more open structure of the latter materials.

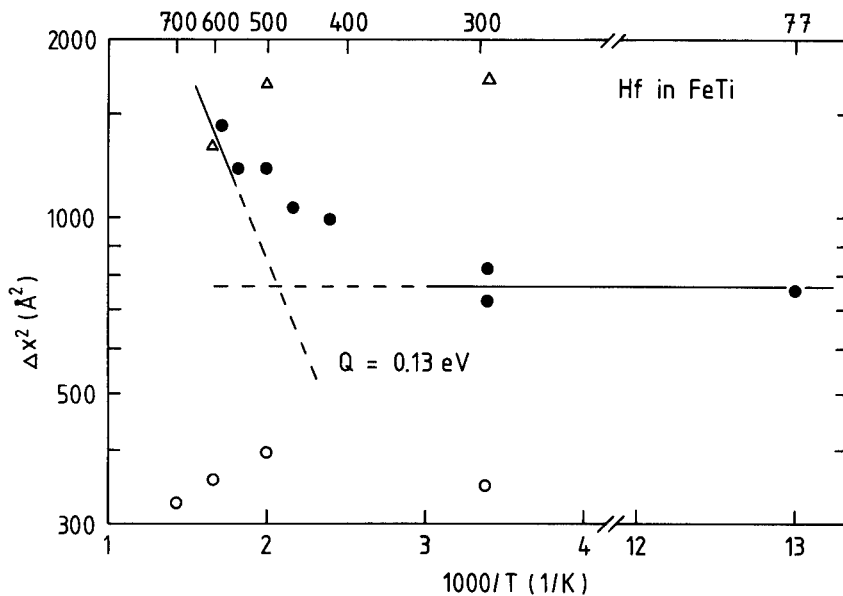


Fig. 1. Arrhenius plot of Hf marker spreading during $1 \times 10^{16}/\text{cm}^2$, 1 MeV Kr ion irradiation at different temperatures in x-Fe-10at.%Ti (Δ), a-Fe-37at.%Ti (\bullet) and x-Fe-37at.%Ti (\circ).

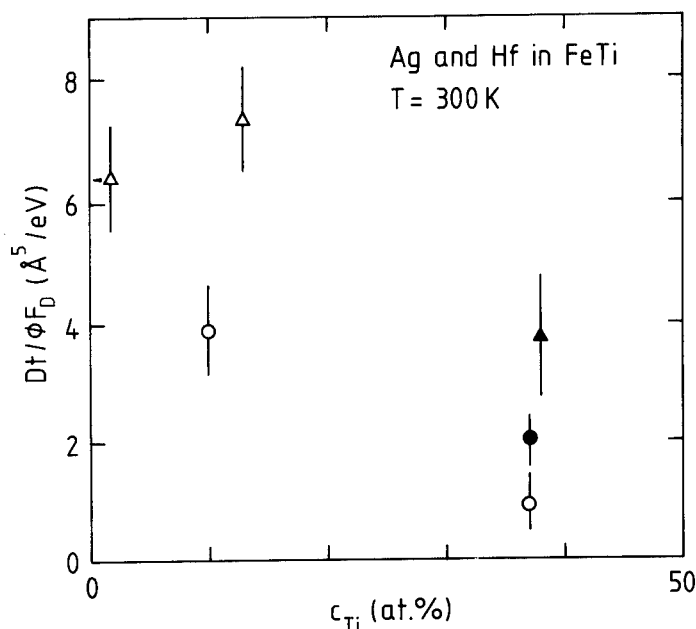


Fig. 2. Spreading of Ag (triangles) and Hf (circles) markers, normalized by ion dose and damage energy, in amorphous (full symbols) and crystalline (open symbols) Fe-Ti alloys and pure Fe for 1 MeV Kr irradiation at 300 K.

The amorphous Fe-Ti alloy under study was found to crystallize after a thermal anneal at 930 K for several minutes. Under Kr ion irradiation, the onset of crystallization, depending on ion dose and irradiation temperature, was observed at temperatures as low as 600 K. The details of ion-bombardment-induced crystallization of Fe-Ti alloys will be published elsewhere [9]. The number of crystallites increases less than linearly with ion dose, indicating nucleation and diffusional growth rather than the result of a single ion event. Mixing of elemental Fe-Ti multilayers [10] as well as irradiation of intermetallic Fe-Ti compounds [11] have shown similar behavior. In the same range of experimental parameters, a mixture of amorphous and crystalline phases was found.

The mixing at low temperatures is probably mainly due to thermal spike diffusion. Purely collisional mixing should be smaller by about a factor of 10, according to the criterion given by Averback [1], and recent Molecular-Dynamics-calculations [12]. It is evident that the contribution of replacement collision sequences (RCS) is small, since RCS cannot propagate in a-Fe-Ti, where the observed mixing is even larger than in x-Fe-Ti. A similar increase of mixing near room temperature has been observed in amorphous systems like Cu-Er [13],

Au:Si [14], Ni/Zr [15] and Au/Zr [15] as well as in crystalline Mo/Al [16], Nb/Si [17] and Ni/Si [18] films. This increase has usually been attributed to radiation-enhanced diffusion. However, the onset temperature is quite low, when compared to single crystal RED experiments in a variety of systems [3], [19]. Furthermore, in several experiments activation energies as low as 0.1 eV [13],[16] have been reported, which is low compared to one-half the vacancy migration enthalpy expected for RED. Only a few dose rate experiments in amorphous systems have been published [2],[14]. The results so far have been controversial [20]. From the present experiments, no unambiguous conclusions may be drawn. It is obvious, however, that in the crystalline samples, no indication of RED up to 700 K has been found. As an alternative explanation for the temperature dependent regime above 300 K, we suggest an intracascade mechanism. That is, the low onset temperature and activation energy are not associated with the free migration of an intrinsic point defect, but rather that thermal-spike-mixing becomes more strongly temperature dependent simply because the underlying thermal processes become strongly temperature dependent. This interpretation has been suggested following recent observations in the Ni/Zr system [21]. In these bilayer experiments, an Arrhenius region similar to the one observed in Fe-Ti was found between 300 and 500 K. Above 500 K, an even stronger temperature-dependence is measured. The authors observed [21] that thermal annealing (i.e. in the absence of irradiation) yields the same two Arrhenius regions. The onset of the high-temperature regime occurs at approximately the same temperature, near 500 K.

Amorphous alloys undergo a structural relaxation upon annealing, leading to high diffusion coefficients during the early stages of annealing, and to a lower stationary diffusion coefficient, characteristic of a well-defined relaxed state, only after long annealing times. Nakamura et al. [22] have observed relaxation of vapor-quenched Fe-Ti alloys in the composition range between 30 and 40 at.% Ti. Since the temperature dependence above 300 K is observed only in the amorphous films, but not in the annealed crystalline ones, it is probably caused by a relaxation effect.

ACKNOWLEDGMENT

The many helps by L.J. Thompson in analyzing the data are gratefully appreciated. This work was supported by the U.S. Department of Energy, BES-Materials Sciences, under contract W-31-109-Eng-38.

REFERENCES

1. H. Hahn, R.S. Averback, F.R. Ding, C. Loxton and J. Baker, *Mater. Sci. Forum* **15-18**, 511 (1987)
2. F.R. Ding, R.S. Averback and H. Hahn, to be published in *J. Appl. Phys.*
3. A. Müller, M.-P. Macht and V. Naundorf, *Proc. 14th. Int. Symp. on Effects of Radiation on Materials*, June 1988, Andover MA, USA, (1989), to be published
4. J.P. Biersack and L.G. Haggmark, *Nucl. Instrum. and Methods* **174**, 257 (1980)

5. Program developed by M. Schalit, R.S. Averbach and L.J. Thompson
6. S.-J. Kim, M.-A. Nicolet, R.S. Averbach and D. Peak, 2nd Workshop on Ion Beam Mixing, Pasadena CA, USA, (1985)
7. J. Horvath, K. Pfahler, W. Ulfert, W. Frank and H. Kronmüller, Mater. Sci. Forum **15-18**, 523 (1987)
8. H. Hahn, R.S. Averbach, K. Hoshino and S.J. Rothman, Proc. 6th Int. Conf. on Rapidly Quenched Metals, August 3 - 7, 1987, Montreal, Canada, (1987)
9. U. Scheuer and L.E. Rehn, to be published
10. J.L. Brimhall, H.E. Kissinger and L.A. Charlot, Rad. Effects **77**, 237 (1983)
11. J.P. Hirvonen, M. Nastasi and J.W. Mayer, J. Appl. Phys. **60**, 980 (1986)
12. T. Diaz De La Rubia, R.S. Averbach, R. Benedek and W.E. King, Phys. Rev. Lett. **59**, 1930 (1987)
13. H. Hahn, R.S. Averbach, T. Diaz De La Rubia and P.R. Okamoto, Mater. Res. Soc. Symp. Proc. **51**, 491 (1986)
14. F. Priolo, J.M. Poate, D.C. Jacobson, J. Linnros, J.L. Batstone and S.U. Campisano, Mater. Res. Soc. Symp. Proc. **100**, 87 (1988)
15. F.R. Ding, P.R. Okamoto and L.E. Rehn, 1987 Fall Meeting of the MRS, Nov. 30 - Dec. 5, 1987, Boston MA, USA, (1987)
16. E. Ma, A.J. Brunner, T.W. Workman, C.W. Nieh, X.-A. Zhao and M.-A. Nicolet, Mat. Res. Soc. Symp. Proc. **100**, 75 (1988)
17. U. Shreter, F.C.T. So, B.M. Paine and M.-A. Nicolet, Mat. Res. Soc. Symp. Proc. **27**, 31 (1984)
18. R.S. Averbach, L.J. Thompson, J. Moyle and M. Schalit, J. Appl. Phys. **53**, 1342 (1982)
19. M.-P. Macht, V. Naundorf and H. Wollenberger, J. Nucl. Mater. **103 + 104**, 1487 (1981), J. Nucl. Mater. **133 + 134**, 420 (1985)
20. L.E. Rehn and P.R. Okamoto, Proc. Int. Conf. on Ion Beam Modification of Materials, June 12 - 17, 1988, Tokyo, Japan, (1988), to be published
21. F.R. Ding, L.E. Rehn and P.R. Okamoto, quoted in [20], to be published
22. Y. Nakamura, K. Sumiyama and H. Ezawa, Hyperfine Interactions **27**, 361 (1986)

THE EFFECT OF HYDROGEN CONTENT ON ION BEAM MIXING

R. E. WISTROM*, P. BØRGESEN*, H. H. JOHNSON*, and D. A. LILIENFELD**

*Department of Materials Science and Engineering, Bard Hall

**National Nanofabrication Facility
Cornell University, Ithaca, NY 14853

ABSTRACT

A qualitative study of ion beam mixing of multilayers has shown that the presence of hydrogen in the sample slows mixing considerably for Fe/Ti, and slightly for Ni/Ti. We have quantified this effect and extended the study to four more systems (Co/Ti, Pd/Ti, Ti/Cu, and Ti/Al) and to lower temperatures. The degree to which H charging reduced the mixing rate varied substantially with multilayer system. H was lost during mixing. H was lost fastest from those films for which the H effect was the smallest. Our data are consistent with a model that relates mixing inhibition to H-vacancy binding energy in the non-Ti component.

INTRODUCTION

Ion beam mixing of multilayer samples effectively produces a wide range of stable and metastable alloys [1,2]. Impurities can influence mixing rates [3-5], but hydrogen contamination is often overlooked since it does not appear in Rutherford backscattering (RBS) spectra. Hirvonen et al. [6] qualitatively compared mixing rates of Ni/Ti and Fe/Ti multilayers, and reported that H charging slightly inhibited mixing of Ni/Ti and strongly inhibited mixing of Fe/Ti. They suggested that H may bind to vacancies to reduce the vacancy mobility, and thus the mixing rate. This would explain why the mixing inhibition was more pronounced for Fe/Ti than for Ni/Ti. We will refer to this mixing inhibition as the "H effect".

The technological importance of alloys containing H getters such as Ti [7-10] makes the H effect of immediate interest. We have quantified mixing results for Fe/Ti, Ni/Ti, Co/Ti, and Pd/Ti multilayers and for Ti/Al and Ti/Cu bilayers. Our mixing rate measurements confirm Hirvonen et al.'s results for Fe/Ti and Ni/Ti. Possible explanations for the effect are discussed.

EXPERIMENT

Multilayer and bilayer samples consisting of Ti and another metal (Ni, Fe, Co, Pd, Cu, or Al) were electron beam deposited in an ion pumped system. Pressures were typically 2×10^{-7} torr before and 5×10^{-7} torr during deposition. To minimize oxidation, Ti was never the top layer. Multilayer compositions and thicknesses are listed in Table I.

Electrochemical charging was performed in deaerated 0.1 N NaOH or 0.001 N H_2SO_4 at about 2 mA/cm^2 for times ranging from 0.5 to 2 hours using a Pt

anode. Hydrogen content was measured by Forward Recoil Energy Spectrometry (FRES) [11]. The H/Ti ratio was approximately one for all charged samples with a wide range of charging times, showing that the H content reached a saturation level.

Cu/Ti and Al/Ti multilayers peeled apart when charged, therefore, bilayer samples of Ti on top of Al or Cu were deposited. For these samples, the H/Ti ratio was less than one after charging, probably due to Ti oxidation. Thin coatings (50Å) of Pd were therefore deposited on top of the Ti to facilitate charging. Control samples showed that these coatings did not significantly influence mixing at the interface [12]. Bilayer compositions and thicknesses are listed in Table II. RBS showed that heavy metal contamination was less than 1%. RBS was performed at resonance energies for C, N, and O. Levels of these elements were less than 2% [13].

Films were mixed at room temperature and 80 K by 600 keV Xe⁺ (5×10^{12} /cm²s) with fluences ranging from 4×10^{15} to 1.8×10^{16} /cm². Exact fluences were measured by RBS. Spectra were simulated by the computer program RUMP [14].

The sample interface RBS signals were relatively abrupt prior to Xe irradiation. The spread of interface signals due to mixing was simulated by a complementary error function ($C \cdot \text{erfc}(x/\sigma\sqrt{2})$) using σ^2 (variance of the atomic displacement distribution due to mixing) as the fit parameter [15]. Degree of mixing was quantified as σ^2 , and mixing rate as σ^2/ϕ (ϕ = fluence). The ability to measure mixing was enhanced by optimizing He²⁺ energies (2.2 to 4.85 MeV) and sample tilt angles (7° to 76°).

RESULTS AND DISCUSSION

Figure 1 shows that the H effect varied dramatically with multilayer composition. Pd/Ti mixed much faster than Fe/Ti, and H charging slowed mixing of Fe/Ti by a factor of seven, but had little influence on Pd/Ti. Mixing rate data of multilayers and bilayers is quantified in Tables I and II which list samples in order of decreasing H effect [13]. The H effect was quantified as the ratio of σ^2/ϕ for the uncharged samples to that for the charged samples. This ratio measures the relative effect of H on σ^2/ϕ , not the absolute effect. Structural analysis of the films was not performed. Mixing amorphizes Ni/Ti, Fe/Ti, Pd/Ti, and Cu/Ti [13].

H content of the charged films decreased during mixing even though FeTi, NiTi, and CoTi alloys form hydrides with H/Ti ≥ 1 [13]. The ratio of H content before and after mixing with $\phi = 8 \times 10^{15}$ /cm² is listed as H loss in Table I. H was lost approximately six times faster from Pd/Ti than from Fe/Ti. Mixing rate appears to correlate directly to H loss rate. In an attempt to identify the cause of the H loss, charged Ni/Ti and Fe/Ti multilayers were mixed with 4×10^{15} Xe/cm² and then H charged again. FRES analysis showed that these samples did not absorb significant amounts of H during the second charging, suggesting that H was lost because of reduced solubilities in the mixed samples. H loss measurements from bilayer samples were difficult to interpret because of the simultaneous intermixing with the Pd coatings [12].

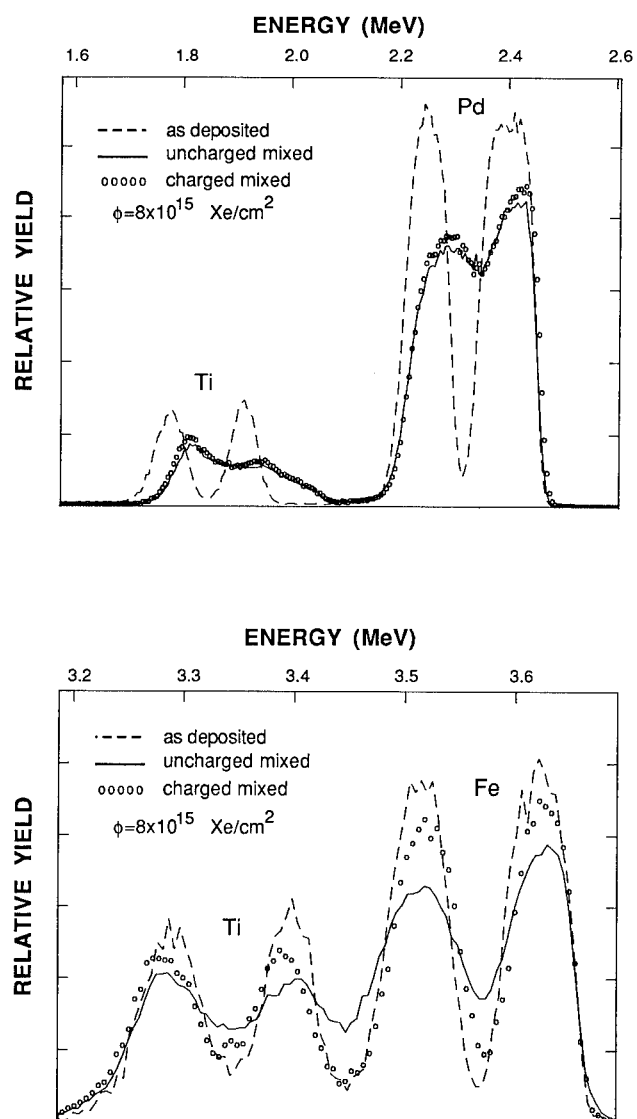


Figure 1: RBS spectra of Pd/Ti multilayers (top) and Fe/Ti multilayers (bottom).

TABLE I

Multilayer Sample Data

Composition	Thickness ($\times 10^{17}$ at./cm ²)				H effect ^a		H loss ^b	H-vac bond ^c
	1st	2nd	3rd	4th	300 K	77K		
Fe/Ti/Fe/Ti	2.20	1.83	2.20	1.83	7 \pm 2		1.3	.53 ev
Co/Ti/Co/Ti	2.00	1.60	2.00	1.60	2.2 \pm 0.7		2.8	
Ni/Ti/Ni/Ti	2.30	1.85	2.30	1.85	2.0 \pm 0.6	3 \pm 0.8	4.4	.43 ev
Pd/Ti/Pd/Ti	2.20	1.83	2.20	1.83	1 - 1.5		8	.23 ev

TABLE II

Bilayer Sample Data

Composition	Thickness ($\times 10^{17}$ at./cm ²)			H effect ^d @300 K	H-vac bond ^c
	Coating	1st	2nd		
Pd/Ti/Al	0.5	4.3	24	2.5 - 5	.52 ev
Pd/Ti/Cu	0.4	5.2	34	1.4 - 2.5	.42 ev

- a. H effect=ratio of σ^2/ϕ for uncharged sample to that for a charged sample both mixed to a fluence of 4×10^{15} Xe/cm² (σ^2 = atomic displacement variance).
b. H loss=ratio of H content before and after mixing to a fluence of 8×10^{15} Xe/cm².
c. Reported by Myers et al. [19].
d. Preliminary data. Same as a. but fluence = 1.8×10^{16} Xe/cm².

A thermal spike mixing model [3] overestimated the room temperature mixing rate of uncharged Fe/Ti and Co/Ti, as well as the 80 K mixing rate of uncharged Ni/Ti by a factor of 2-3.5 [13]. This discrepancy is larger than that usually observed [3,16] and could be due to H contamination (about 10-15 atomic % in the Ti layers for these samples). This contamination effect seems especially likely for Fe/Ti since H charging caused the mixing rate to decrease 7-fold. We were unable to deposit H-free Ti films.

Ion beam mixing of medium and high atomic number materials by heavy ion irradiation is commonly pictured as occurring in three regimes [3,4,17]. During the ballistic regime, the primary ion initiates a series of cascades. As the recoiling atoms lose energy by collisions, nearly all the atoms within a small volume are excited. This volume is often called a thermal spike. After the thermal spike "cools", atoms may rearrange by further transport of radiation induced defects at ambient temperature (radiation enhanced diffusion). Categorizing the mixing inhibition by H as a ballistic regime effect, a thermal spike regime effect, or a radiation enhanced diffusion regime effect, would improve our understanding of the phenomenon.

Due to the low mass of H, it should not strongly influence ballistic mixing.

Since experimental mixing rates were considerably faster than those predicted by binary collision models [13], we conclude that the H effect is not primarily a ballistic regime phenomenon. If the H effect occurs in the radiation enhanced diffusion regime, which is not expected to contribute significantly to mixing at low temperatures [3], then it should be small or absent at 80 K. Since the H effect for Ni/Ti increased at 80 K (Table I), it does not appear to act predominantly in the radiation enhanced diffusion regime.

Thermal spike mixing of the metals studied here is not expected to be strongly influenced by ambient temperature [18]. The mixing rate of Ni/Ti multilayers was reduced by at least a factor of 3 by cooling to 80 K, suggesting that less than one third of the room temperature mixing may be ascribed to a thermal spike mechanism [13,15]. Since the H effect, as we have defined it, is the ratio of two mixing rates, the increase observed upon cooling (Table I) is partially caused by a decrease in radiation enhanced diffusion. This reduction in radiation enhanced diffusion would make the measurement more sensitive to H inhibition of mixing. Considering this and experimental uncertainties, our results do not necessarily require the influence of H on mixing to depend strongly on temperature. H apparently inhibits mixing during the thermal spike and/or during the time between the thermal spike and radiation enhanced diffusion regimes.

Since the samples compared had virtually identical Ti layers, the variation of the H effect for different samples must be due to the properties of the second metal, even though nearly all the H started out in the Ti (due to the low H solubilities of these metals except Pd). During irradiation, one would expect H from the Ti layer to be injected into the second metal and the intermixed region. Differences in heats of mixing between the Me/Ti and Me/Ti/H systems could be responsible for the influence of H, but very specific knowledge of H content as a function of composition would be required to estimate such an effect [13].

Our results agree with Hirvonen et al., who suggested that the H effect is correlated to H-vacancy binding energy in the non-Ti component [6]. Relative mixing rates for the five elements whose H-vacancy binding energies are available in the literature shows that H inhibited mixing to a larger extent for the metals with the higher binding energies. H binding may reduce vacancy mobility. The magnitude of the binding energies suggests that such a mechanism may operate during the last part of the thermal spike regime, or during the time between the thermal spike and radiation enhanced diffusion regimes, when the effective temperature of the spike is low enough so that a significant fraction of the vacancies may be H bonded [13].

One would not expect that the effectiveness of H in inhibiting vacancy transport is determined by H-vacancy binding energy alone. For example, the energy for detrapping of H from vacancies is the sum of H diffusion activation energy (0.07 for Fe and 0.42 for Ni) and H-vacancy binding energy [13]. Therefore, the rate at which H-vacancy complexes dissociate would be higher for Fe than for Ni, even though H-vacancy binding energy is higher for Fe. One would expect H-vacancy complexes to have longer lifetimes in Ni but to form more quickly in Fe [13].

CONCLUSIONS

The presence of H in ion beam mixing samples can dramatically decrease mixing rates depending on which elements are being mixed. Unintentional H

contamination might also significantly decrease mixing rates for some metal pairs. The effect seems to take place during thermal spike mixing or during the cool down after the spike, but before the radiation enhanced diffusion regime. Our data tend to support a model linking the magnitude of the H effect to H-vacancy binding. H loss rate appears to be correlated to the H effect. When the H effect is small, mixing induced H loss tends to be rapid, probably due to a decrease in H solubility.

ACKNOWLEDGEMENT

The division of Materials Research of the National Science Foundation supported this work. We acknowledge the Materials Science Center (NSF) at Cornell University for the use of their thin film facilities. The National Nanofabrication Facility is supported by the National Science Foundation under grant ECS-8619049, Cornell University, and industrial affiliates.

REFERENCES

1. R. J. Gaboriaud and M.-A. Nicolet, *Ann. Phys.* **8**, 563 (1983).
2. D. A. Lilienfeld, J. W. Mayer, and L. S. Hung, *MRS Bulletin* **12** (2), 31 (1987).
3. W. L. Johnson, Y. T. Cheng, M. Van Rossum, and M.-A. Nicolet, *Nucl. Instrum. Meth.* **B7/B8**, 657 (1985).
4. B. M. Paine and R. S. Averback, *Nucl. Instrum. Meth.* **B7/B8**, 666 (1985).
5. J. Böttiger, S. K. Nielsen, H. J. Whitlow, and P. Wriedt, *Nucl. Instrum. Meth.* **218**, 684 (1983).
6. J. -P. Hirvonen, M. A. Elve, J. W. Mayer, and H. H. Johnson, *Mater. Sci. and Eng.* **20**, 13 (1987).
7. J. -P. Hirvonen, J. W. Mayer, M. Nastasi, and D. Stone, *Nucl. Instrum. Meth.* **B23**, 487 (1987).
8. P. Munn, and G. K. Wolf, *Nucl. Instrum. Meth.* **B7/B8**, 205 (1985).
9. D. M. Follstaedt, J. A. Knapp, L. E. Pope, F. G. Yost, and S. T. Picraux, *Appl. Phys. Lett.* **45**, 529 (1984).
10. I. L. Singer and T. M. Barlak, *Appl. Phys. Lett.* **43**, 457 (1983).
11. B. L. Doyle and P. S. Peercy, *Appl. Phys. Lett.* **34**, 811 (1979).
12. P. Børgesen, R. E. Wistrom, T. L. Alford, D. A. Lilienfeld, and H. H. Johnson, to be published.
13. P. Børgesen, R. E. Wistrom, D. A. Lilienfeld, and H. H. Johnson, Submitted to *J. Mater. Res.* (1988).
14. L. R. Doolittle, *Nucl. Instrum. Meth.* **B9**, 344 (1985).
15. P. Børgesen, D. A. Lilienfeld, R. E. Wistrom, and H. H. Johnson, these proceedings.
16. T. W. Workman, Y. T. Cheng, W. L. Johnson, and M.-A. Nicolet, *Appl. Phys. Lett.* **50**, 1485 (1987).
17. D. Peak and R. S. Averback, *Nucl. Instrum. Meth.* **B7/B8**, 561 (1985).
18. R. S. Averback, *Nucl. Instrum. Meth.* **B15**, 675 (1986).
19. S. M. Myers, W. R. Wampler, F. Besenbacher, S. L. Robinson, and N. R. Moody, *Mater. Sci. Eng.* **69**, 397 (1985).

MAGNETIC ANOMALY AND ICOSAHEDRAL PHASE FORMATION IN Fe-Cu AND Fe-Mo SYSTEMS

L.J. Huang, Q.M. Chen, B.X. Liu*, Y.D. Fan and H-D. Li
Department of Materials Science and Engineering, Tsinghua
University, Beijing, 100084, China

*Also at Center of Condensed Matter and Radiation Physics,
CCAST(World Lab), Beijing, China

ABSTRACT

The first observation of a new class of icosahedral phase associated with a magnetic transition in Fe-Cu and Fe-Mo systems are reported. It is found that the icosahedral order can be re-established when the destabilized $\text{Fe}_{60}\text{Cu}_{40}$ icosahedral phase subject to a magnetic transition at high annealing temperature. The $\text{Fe}_{70}\text{Mo}_{30}$ amorphous films obtained by sputtering exhibit a similar behavior at high magnetic transition temperature. A brief discussion of the observed phenomena is addressed.

INTRODUCTION

It has been thought that icosahedral phase can only be formed in alloy systems which have proper off-stoichiometry of the intermetallic compounds or pre-formed icosahedral local order [1] and the reported experimental results are largely from aluminum-based alloy systems. It is therefore of interest to study the possibility of forming icosahedral phase in systems out of the above mentioned empirical rules. Some studies of the magnetic properties of Al-Mn and Al-Mn-Si icosahedral phase revealed that icosahedral structure has some special magnetic features [2-4]. To further unravel the origin of the magnetic anomaly of icosahedral phase and for practical purpose, it is also of interest to bring more experimental evidences on this issue. In this paper, we report our experimental observations of icosahedral phases which formed associated with a magnetic anomaly in Fe-Cu and Fe-Mo systems.

EXPERIMENTAL

The $\text{Fe}_{60}\text{Cu}_{40}$ icosahedral phase was formed by ion mixing the Fe/Cu multilayered samples, which were prepared in a vacuum system, at room temperature using 300 keV inert Xenon ions upto an ion fluence of $1 \times 10^{16} \text{Xe}^+/\text{cm}^2$. The films were then subject to in situ thermal annealing in 200-CX transmission electron microscope (TEM) to study the stability. While the $\text{Fe}_{70}\text{Mo}_{30}$ amorphous films were obtained by co-sputtering the constituent metals onto KCl single crystals by using a planar magnetron sputtering apparatus with complex targets. Annealing of the formed Fe-Mo amorphous film was also carried out in TEM. All the structural characterization was then by analyzing the diffraction patterns obtained by TEM. Magnetic susceptibility was measured by vibrating sample magnetometer (VSM).

9500). The detailed experimentation can be found in our previous publications [5,6].

RESULTS AND DISCUSSIONS

Fe-Cu system

Thermal stability study of the $\text{Fe}_{60}\text{Cu}_{40}$ icosahedral phase formed by ion mixing at room temperature[5] showed that this new metastable phase was easy to destabilize when it was kept at an annealing temperature of 300 °C for more than one hour. When it happened, this new phase decomposed into a mixture of metastable bcc and fcc structures with the lattice constants being 0.281 nm and 0.352 nm, respectively. This result is in agreement with the heat of formation criterion which states that metastable phase formed in systems with large positive heat of formation by ion mixing is usually unstable against thermal annealing. However, upon further heating the obtained mixture upto 800°C corresponding to the magnetic transition temperature in Fe-Cu system, a much denser set of diffraction lines (compared with that of the directed ion mixed one [5]) was observed and all the lines from the pre-annealed metastable bcc and fcc phase disappeared. Figure 1(a) - (d) exhibit these changes both in the micrograph and the diffraction patterns. The measured reciprocal lattice spacings are listed in Table I. These results were then compared with those of the directed ion mixed phase and it was found that several lines were in one-to-one correspondence with those of the ion mixed icosahedral phase. The results were further checked and compared with the calculated reciprocal lattice spacings by using the icosahedral quasicrystal model of Bancel and co-workers[7] and it was showed that the experimental values were in good agreement with the theoretical results. The annealing results therefore explicitly show that an icosahedral order could be established in Fe-Cu system.

The above interesting experimental results are specified by that a magnetic transition in the system may promote the establishment of an icosahedral order. To demonstrate this effect associated with the formation of an icosahedral phase, we measured the change of magnetic states of the films upon increase of ion fluences. Figure 2 presents one of the results. It can be observed in Figure 2 that the coercive force had changed a great deal in the direction of perpendicular and parallel to the film surface. This result is therefore in agreement with the phenomena observed in high temperature annealed samples where the icosahedral order was established only when the annealing temperature was above the magnetic transition temperature of the system. It should be pointed out that previous studies of the magnetic properties of Al-Mn icosahedral phase also found that icosahedral AlMn_{1-x} phases showed strong Curie-Weiss paramagnetism whereas the equilibrium orthorhombic AlMn exhibited only weak paramagnetism and only those manganese atoms which do not have local moments can be substituted by some foreign atoms (e.g. iron) in an icosahedral crystal [2,3]. Moreover, increasing the silicon concentration in the Al-Mn-Si icosahedral crystal would lead to a quasicrystalline to amorphous phase transition with the change

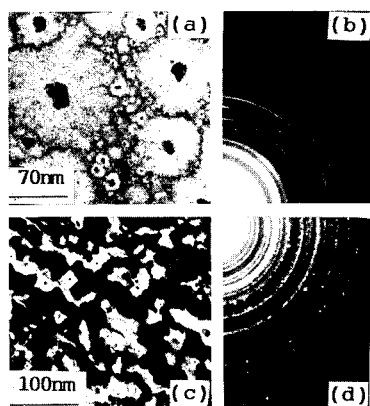


Fig. 1. $\text{Fe}_{60}\text{Cu}_{40}$ icosahedral phase. (a) ion mixed micrograph; (b) diffraction pattern of (a); and (c) micrograph of the same film annealed at 800 °C; (d) the diffraction pattern of (c).

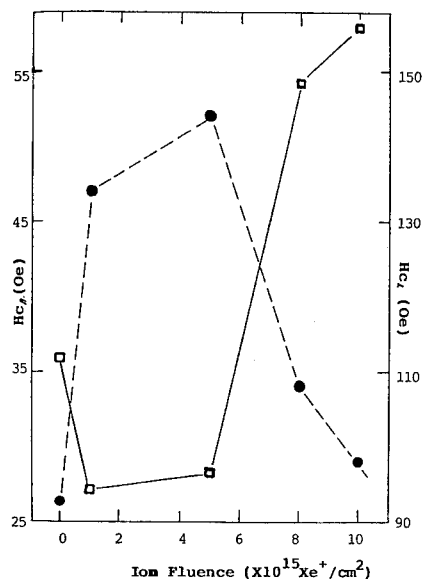


Fig. 2. Change of coercive force with increase of ion fluences.

of the strong paramagnetism to ferromagnetism [4]. These results suggested that the quasicrystals seemed to favor a paramagnetic state. The present observed Fe-Cu high temperature icosahedral phase also underwent a ferromagnetic to paramagnetic transition, but at present this interesting feature is still a mystery.

The observed phenomena in Fe-Cu system are also of interest for the similarities to the spontaneous vitrification (SV) process. A SV process has been thought to achieve when there exists no competing transformation or the equilibrium phase formation requires phase separation, e.g. in miscibility gaps[7]. However, the SV is not accessible at the present observations while an incommensurate order is presented instead. This may come from that the Fe-Cu has a large positive heat of formation and hence a disordered amorphous state is hard to establish. Nevertheless, the trend to change the symmetry is similar.

Fe-Mo system

The interesting phenomena observed in Fe-Cu system leave several issues to explore. The Fe-Cu system is equilibrium immiscible. How can an icosahedral order be established in such a system? The results showed that the phase formation was associated with a magnetic anomaly, i.e. a globe change of the magnetic state of the whole film. To further explain this phenomenon, some similar behaviors should be observed in similar systems. We therefore chose Fe-Mo system as a potential candidate which has a similar magnetic transition temperature

Table I. The measured and calculated reciprocal-lattice spacings and their icosahedral indice at an annealing temperature of $800 \pm 25^\circ\text{C}$.

Index	$\text{Fe}_{70}\text{Mo}_{30}$ (nm^{-1})	$\text{Fe}_{60}\text{Cu}_{40}$ (nm^{-1})	Calculated (nm^{-1})
(43 $\bar{1}$ $\bar{1}$ 22)	10.4		10.1
(2200 $\bar{1}$ 1)	11.9		11.8
(2200 $\bar{1}$ 1)		12.8	12.5
(2430 $\bar{4}$ 0)		16.2	16.5
(110001)	16.8		16.6
(2210 $\bar{2}$ 0)	19.9		20.3
(1110 $\bar{1}$ 0)		20.8	20.3
(3300 $\bar{1}$ 2)	23.9		23.5
(31 $\bar{1}$ $\bar{1}$ 1)		24.0	23.8
(12 $\bar{1}$ 223)		25.2	25.0
(210 $\bar{1}$ 1)	26.9		27.0
(21 $\bar{1}$ 001)		26.9	26.9
(21 $\bar{1}$ 01)		28.4	28.5
(100000)	29.4		29.4
(110000)	31.1		30.9
(100000)		31.3	31.3
(110000)		32.8	32.9
(11 $\bar{2}$ 233)		33.8	33.9
(3200 $\bar{2}$ 2)	34.1		33.9
(220002)		35.1	35.0
(210001)	36.2		36.4
(2300 $\bar{2}$ 2)		36.5	36.1
(2220 $\bar{2}$ 0)	38.0		38.2
(210001)		38.5	38.7
(3200 $\bar{1}$ 1)		39.8	39.4
(220001)	39.9		40.0
(111000)	43.0		42.7
(2210 $\bar{1}$ 0)		43.8	43.7
(111000)		45.3	45.4
(111100)		47.0	46.5
(101000)	49.6		50.0
(210000)	52.6		52.7

as Fe-Cu does. Also, within atomic composition range from 10% to 40% atom molybdenum these two systems share some common features in their respective equilibrium phase diagram.

The sputtered $\text{Fe}_{70}\text{Mo}_{30}$ specimens were checked by both X-ray diffraction and TEM. The analyses showed that the structures of the as-sputtered films were of metastable amorphous phase. These amorphous films were then subject to in situ thermal annealing in TEM with a heating rate of 5 °C/min. The TEM diffraction analyses during annealing showed that the formed metastable amorphous phase was quite stable and no crystallization took place until an annealing temperature of 600°C. Above 600°C, the amorphous phase destabilized and a crystalline bcc phase was observed. However, the amorphous diffraction halo still existed indicating that the amorphous phase did not completely transform into the crystalline bcc phase. When the annealing temperature was further raised to 800°C, corresponding to the magnetic transition temperature of this system (760°C), a new set of diffraction lines appeared. This phenomenon is therefore similar to that observed in Fe-Cu system. The only difference is that here an amorphous phase is extensively presented while in Fe-Cu system are two metastable bcc and fcc phases and the pre-formed bcc Fe-Mo phase did not destabilize. Fig. 3(a) and (b) are the observed micrograph and the corresponding diffraction pattern. The newly observed diffraction lines were also analysed by employing Bancel's six-vector quasicrystal model. The indexing results are listed in Table I, where the diffraction line having the strongest intensity was naturally chosen as the (100000) plane. It should be pointed out, however, that re-indexing the first ten lines could result in a "pseudo-fcc" structure with a lattice constant of 1.05 nm. Nevertheless, this huge fcc lattice is constructed by somewhat unreasonably choosing the biggest reciprocal lattice spacing $Q=10.4 \text{ nm}^{-1}$ as the (111) plane but not the one corresponding to the strongest diffraction intensity. And the similar re-indexing procedure can also be applied to Al-Mn icosahedral quasicrystals in some cases. This huge fcc lattice should be therefore given rise to a new icosahedral phase since the six-vector icosahedral indexing presented a satisfactory agreement between the observed and

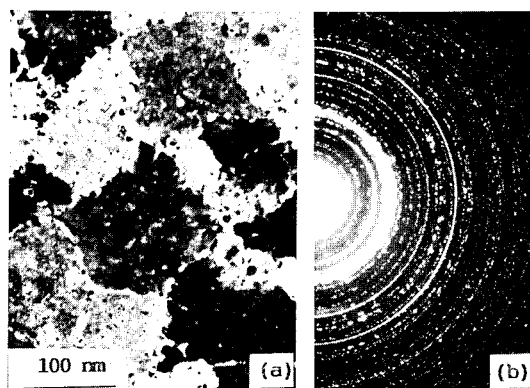


Fig. 3. $\text{Fe}_{70}\text{Mo}_{30}$ icosahedral phase annealed from the amorphous phase at 800 °C. (a) the micrograph and (b) the corresponding diffraction pattern.

calculated values. (see Table I)

TEM analyses also showed that even at high temperature the grain growth or the diffusion was very slow and further growth of the formed new phase in TEM was hard to realise. This phenomenon seems to be common for icosahedral phase formed in solid state as some studies on the stability of the Al-Mn icosahedral phase [9]. It is therefore hard to expect to obtain large icosahedral crystals by employing the present methods of both ion mixing and thermal annealing of the co-sputtered films.

CONCLUDING REMARKS

The experimental observations in this study present that an icosahedral order could also be established in systems without complex intermetallic compounds. The observed magnetic anomaly associated with the new phase formation provided an clue to further unravel the physical origin of the anomalous icosahedral quasicrystalline structures. Detailed studies on this issue are currently underway.

ACKNOWLEDGEMENT

This project is supported by the National Natural Science Foundation of China and part from the International Atomic Energy Agency (Research Contract No. 4731/RB). The staffs of the TEM Laboratory of Beijing University and the Analysis Center of Tsinghua University are acknowledged.

REFERENCE

1. L.A. Bendersky and R.J. Schaefer, *Physica* **140A**, 298(1986).
2. M. Eibschutz et al., *Phys. Rev. Lett.* **59**, 2443(1987).
3. J.J. Hauser, H.S. Chen and J.V. Waszczak, *Phys. Rev. B* **33**, 3577(1986).
4. W.W. Warren, H.S. Chen and G.P. Espinosa, *Phys. Rev. B* **34**, 4902(1986).
5. L.J. Huang et al., *J. Phys.* **F18**, L69(1988).
6. Q.M. Chen, Y.D. Fan and H-D. Li, *Materials Lett.* **6**, 311 (1988).
7. P.A. Bancel et al., *Phys. Rev. Lett.* **54**, 2422(1985).
8. M. von Allmen and A. Blatter, *Appl. Phys. Lett.* **50**, 1873 (1987).
9. J.A. Knapp and D.M. Follstaedt, *Phys. Rev. Lett.*, **55**, 1591 (1985); *ibid.*, **56**, 1827(1986).

AMORPHOUS AND METASTABLE PHASE FORMATION IN SYSTEMS WITH POSITIVE HEATS OF MIXING USING HIGH-RATE SPUTTER DEPOSITION

H.F. RIZZO,* A. ECHEVERRIA,* T.B. MASSALSKI,** AND H. BAXI**

*Lawrence Livermore National Laboratory, Livermore, CA 94550

**Carnegie-Mellon University, Pittsburgh, PA 15213

ABSTRACT

The triode sputtering technique and a "split-target" arrangement were used to produce metastable crystalline and amorphous phases in the Cu-W, Mo-Cu, Ag-Fe, Ag-Cu, Pu-Ta and Pu-V systems. These systems all exhibit liquid and solid immiscibility and have positive heats of mixing and atomic radii that differ by at least 10%. The sputtered coatings, whose thickness varied between 25 and 200 microns, were formed at deposition rates between 35 and 200 Å/s. They were characterized using x-ray diffraction, TEM, microprobe, microhardness, and DSC techniques. The observed amorphous and metastable solid solution phases are discussed in terms of predicated heats of formation for these phases using Miedema's thermodynamic approximations [1] that include chemical, elastic, and structural contributions. Differences in compositional ranges observed by high rate sputter deposition compared to other vapor deposition techniques (e.g., coevaporation) appeared to arise as a result of processes that occur during deposition or immediately following deposition.

INTRODUCTION

Vapor-quenching techniques, such as sputter-deposition or thermal evaporation, are being used increasingly for exploration of alloying behavior, particularly at low temperatures. Under such conditions, non-equilibrium crystalline alloy phases, or amorphous phases, are frequently observed. Sputtering from a split-target makes it possible to produce alloy film deposits that change continuously in composition on a single sample [2]. Work with vapor deposition has demonstrated that single phase regions of primary solid solutions can be greatly extended beyond the regions indicated by equilibrium phase diagrams. These metastable extensions are often followed by wide ranges of amorphous phases. Recent discussions have shown that the compositional extent of the amorphous phases can be correlated with the atomic size differences of elements involved [3] and with the thermodynamic considerations [4-7] related to the relative stability of the competing phases as manifested, for example, by heats of formation (ΔH_f). Superimposed on these factors are of course the usual kinetic considerations that determine the rate of approach to equilibrium [4]. Of particular interest in exploration through sputter-deposited films are alloy systems that show little or no equilibrium miscibility. Such systems are characterized by large and positive heats of mixing and usually involve atomic size differences of more than 10%. Experiments involving solid state amorphization occurring between co-deposited crystalline films [6] and similar explorations [8] involving ion-beam mixing suggested that amorphous phases are to be expected mainly when the ΔH_f is negative. However, amorphous phase formation has also now been reported in several systems with positive ΔH_f [9]. In this work, the triode sputtering technique has been used to produce metastable crystalline and amorphous phases in the systems Cu-W, Mo-Cu, Ag-Fe, Ag-Cu, Pu-Ta, and Pu-V. The phase diagrams for these systems are expected to show a substantial lack of miscibility on alloying. Calculated assessed diagrams for the Cu-W, Mo-Cu, and Fe-Ag systems indicate both solid and liquid immiscibility, as illustrated for the Fe-Ag system in Fig. 1 [10]. This is in agreement with the estimated heats of formation based on the semi-empirical Miedema model [1]. Substantial solid immiscibility is also expected for Pu-Ta and Pu-V. Ag-Cu is a well known eutectic.

EXPERIMENTAL TECHNIQUES

A description of the triode split-target sputtering configuration and procedures is given in earlier papers [2,11]. The compositional range obtained in the coating varied according to the angular distribution of the sputtered components and their respective sputtering yields. The compositions across the free surface of the deposits were determined by x-ray EDS measurements at intervals of 1 to 2 mm. Sections through the thickness of the deposit were made for additional

microprobe measurements and for metallography and microhardness measurements. Coatings were separated from the Al substrate and sectioned into squares of 2–4 mm on a side for TEM, DSC, x-ray diffraction, and x-ray EDS measurements of both the initial and final surfaces.

EXPERIMENTAL RESULTS AND DISCUSSION

The ranges of alloy compositions sputtered and the phases observed for the six systems studied are shown in Fig. 2. Sputtered Ag-Fe alloys between 50 and 58 at.% Ag appeared to be

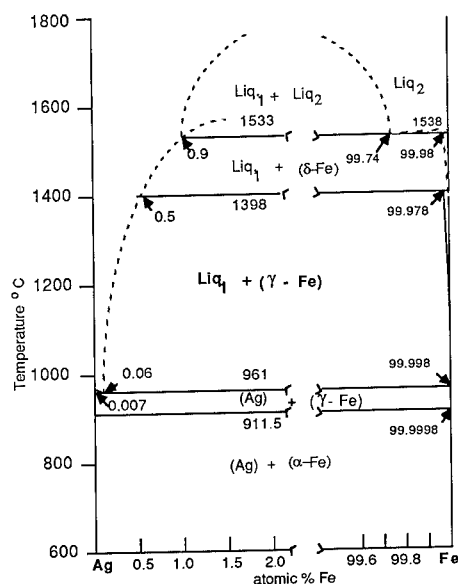


Fig. 1. Ag-Fe binary phase diagram from [10]; it is similar to other systems studied that exhibited liquid and solid immiscibility and positive heats of mixing.

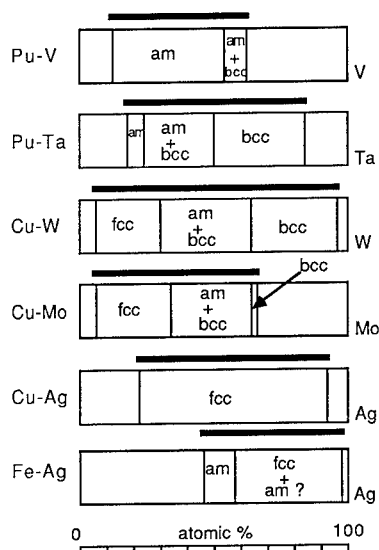


Fig. 2. Non-equilibrium solubility and metastable diagrams of binary alloys sputter-deposited at room temperature in this and previous studies [11,19]. The horizontal line above each diagram corresponds to the compositional range sputtered.

amorphous based on broad x-ray diffraction patterns [2]. In addition, the DSC scans showed broad exotherms for compositions between 50 and 78 at.% Ag, which most likely indicate a broad crystallization range. A DSC trace for Fe-51.5 at.% Ag displayed in Fig. 3 shows a broad exotherm (7.2 kJ/mole) occurring over an extended temperature range (150–450 °C). Thermal stability tests on samples of ~2–3 mg that were heated and held at the peak temperature for 5 minutes and then cooled indicated that decomposition did not start until about 250 °C. X-ray diffraction patterns (XRDs) for 51.5 and 55 at.% Ag compositions after heating to temperatures up to 350 °C are shown in Fig. 4. Lattice parameters calculated for the metastable fcc solid solution range observed between 58 and 97 at.% Ag indicated a large positive deviation from Vegard's law. A plot of nearest neighbor distances (NND) for the metastable fcc phase region is shown in Fig. 5 along with data by Sumiyama et al. [12] for RF-sputtered films produced at room and liquid-nitrogen temperatures. They reported no evidence of amorphous phase formation, which is contrary to Chien and Unruh [13], who reported amorphous films formed by sputtering at liquid-nitrogen temperatures for compositions of 40–60 at.% Ag. They also reported crystallization temperature between 250–300 °C. The large deviation from Vegard's law is not understood. The differences in the propensity to form amorphous films may be related to the deposition rates which were 60, 5, and 0.8 Å/s for this study, for Chien and Unruh, and for Sumiyama, respectively.

Sputtered Ag-Cu alloys of compositions between 22 and 91 at.% Ag did not appear amorphous based on XRDs and DSC measurements. However the measured lattice parameters for compositions between 45 and 70 at.% Ag show a large positive deviation ($\sim 3\%$) from Vegard's

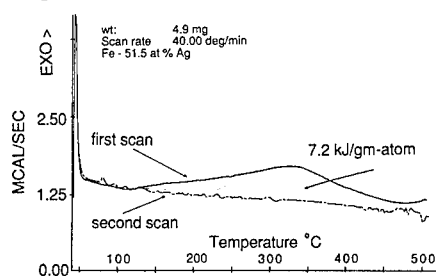


Fig. 3 (above). DSC scans of Fe-51.5 at.% Ag deposit-heated to 500 °C in a Perkin-Elmer calorimeter (DSC-4).

Fig. 4 (right). X-ray diffraction patterns (XRDs) of: (a) Fe-51.5 at.% Ag deposit before and after heating to 350 °C and (b) Fe 55 at.% Ag deposit before and after heating to 200 and 250 °C.

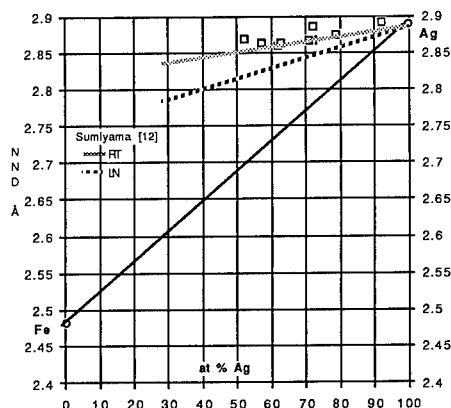
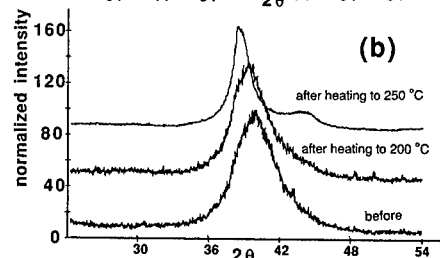
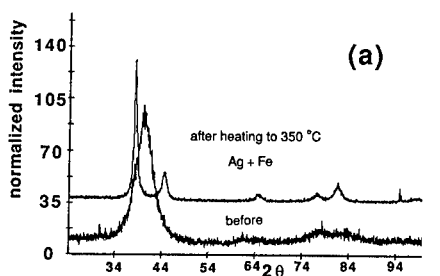


Fig. 5. Calculated nearest-neighbor distances ($NND = .707 a_{fcc}$ or $.866 a_{bcc}$) obtained from metastable fcc phases observed from Fe-Ag deposits sputtered at 20 °C. Data from RF-sputtered deposits at room and liquid-nitrogen temperature by Sumiyama et al. [12] along Vegard's law trend are also shown.

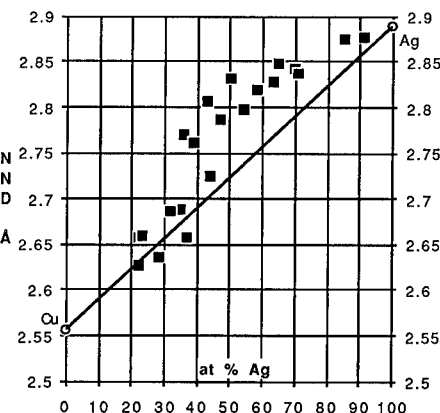


Fig. 6. Calculated NNDs obtained from metastable phases observed in Ag-Cu alloys sputtered at 20 °C.

law (Fig. 6) compared to previous reported data for vapor deposited thin films [14]. DSC measurements for these alloys indicated rather broad low energy exotherms. Thermal stability tests on 37 and 47 at.% Ag samples heated to 200 °C are shown in Fig. 7. The more Ag-rich alloy composition (47 % Ag) appears more stable at 200 °C where the first signs of decomposition are observed. The unexpectedly large lattice parameters for 50 to 60 at.% Ag compositions were previously reported by Stoering and Conrad [15] for liquid-quenched alloys deposited on a Cu cone substrate at -150 °C. They observed that this structure (having expanded lattice parameters that differed from normal solid solution phase observed under other substrate conditions in their study) had a strained modulated microstructure (TEM), which they attributed to clustering of Ag

atoms associated with a spinodal decomposition from the amorphous phase. Another interpretation for this expanded phase is that a highly strained coherent lattice, similar to that observed in metallic multilayers, is formed during the rapid quenching process. Jankowski [16] has reported that multilayer structures with ~ 20 Å periods can increase the elastic energy of the structure by $\sim 20\%$.

Sputtered Cu-Mo alloy compositions between 5 and 65 at.% Mo indicated extended FCC solid solutions up to 35 at.% Mo with the bcc phase extending between 35 and 65 at.% Mo. A mixed amorphous plus bcc phase region was observed between 35 and 60 at.% Mo. The thickness of the amorphous phase was limited (~ 5 μ) before it reverted into a BCC phase. This is similar to what we observed [11] in the W-Cu system, except that amorphous layers as thick as 100 μm could be formed in sputtered Cu-W deposits. The thin amorphous layers in Cu-Mo may be related to the smaller difference in atomic radii. The NND values for the metastable FCC and BCC phases are plotted in Fig. 8 along with other reported data for sputtered [17] and coevaporated [18] films. The low NND values reported for the evaporated films are difficult to understand. However, these values were based only on the 111 diffraction peaks for the fcc and 110 peaks for the bcc structures. Our results are the first reported observation for amorphous phase formation in this system.

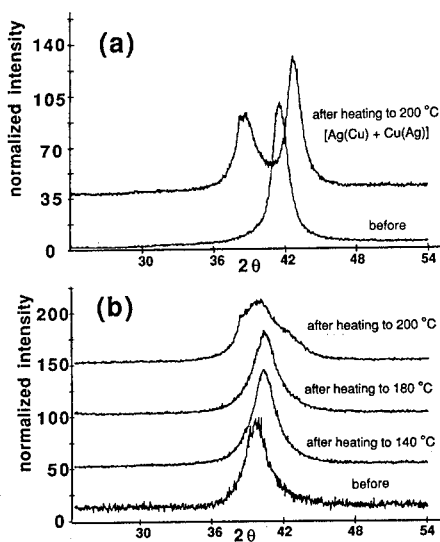


Fig. 7. XRDs of: (a) Cu-37 at.% Ag deposit before and after heating to 200 °C and (b) Cu-47 at.% Ag deposit before and after heating to 140, 180, and 200 °C.

The results for the W-Cu [11], Pu-Ta, and Pu-V systems [19] are similar to those for the Cu-Mo system. Both extended solid solution and amorphous phase regions were observed in these systems. However, for the Pu systems the solid solution phase corresponded to the higher valent ϵ bcc phase rather than the δ fcc Pu phase.

Calculation of enthalpies of formation

Little phase diagram or thermodynamic data are available for systems that exhibit a high degree of immiscibility. Miedema and co-workers [20,21] have developed a semi-empirical model for calculating enthalpies of formation. They have been used recently to model the phase diagrams (i.e., Cu-W [22] and Cu-Mo [23]). Earlier, Nastasi et al. [7] used the Miedema model to compare the stability of phases observed in coevaporated Cu-Ta and Cu-W thin films. More recently, Miedema and Niessen [1] have considered the contribution of elastic effects in the formation of

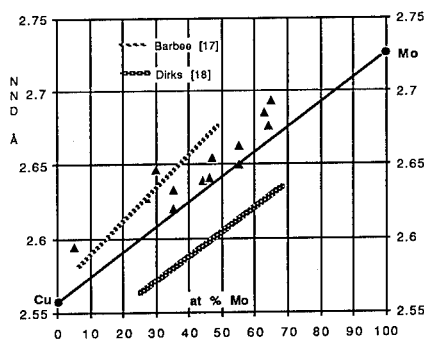


Fig. 8. Calculated NNDs obtained from metastable phases observed in Cu-Mo alloys sputtered at 20 °C.

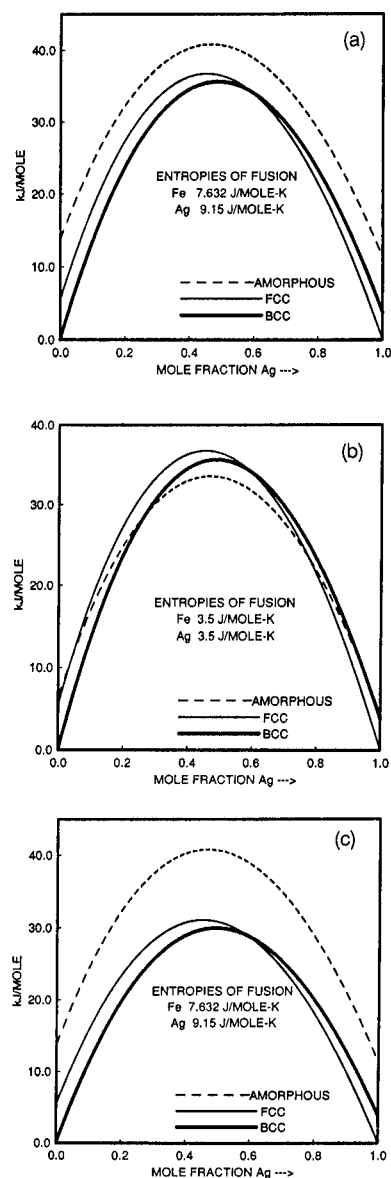


Fig. 9. Calculated enthalpies for Fe-Ag using (a) experimentally-related values for entropy of fusion, (b) Miedema value for entropy of fusion, and (c) same as (a) except neglecting the elastic contribution.

crystalline solid solutions. As a result, the total calculated enthalpy is assumed to involve three terms:

$$\Delta H_{\text{solid solution}}^{\text{for}} = \Delta H_{\text{chemical}}^{\text{for}} + \Delta H_{\text{elastic}}^{\text{for}} + \Delta H_{\text{structure}}^{\text{for}} \quad (1)$$

On the other hand, only two terms are needed for the amorphous phase:

$$\Delta H_{\text{amorphous}}^{\text{for}} = \Delta H_{\text{chemical}}^{\text{for}} + \overline{\Delta H}^{\text{fuse}} \quad (2)$$

The $\overline{\Delta H}^{\text{fuse}}$ term is the weighted average of the enthalpies of fusion of the elements:

$$\overline{\Delta H}^{\text{fuse}} = \overline{T}^{\text{fuse}} \overline{\Delta S}^{\text{fuse}} \quad (3)$$

Miedema and Niessen [1] used a constant best-fit value of $\overline{\Delta S}^{\text{fuse}}$ equal to 3.5 J/mole-K. An alternative way is to accept ΔH^{fuse} values directly from experimental data, which are usually higher than values derived from the fixed value of entropy selected by Miedema and Niessen.

In this work we have calculated the enthalpies of formation (at $T = 0$ K) for the amorphous phase and the crystalline solid solutions in six systems of interest using the most recent Miedema model except that experimental data [24] were used for entropy of fusion and lattice stability parameters [25] used to calculate the $\Delta H_{\text{structure}}^{\text{for}}$.

The differences in considering the elastic effects and choice of entropy of fusion terms on the enthalpies of formation are shown in Fig. 9 for the Fe-Ag system. The use of the best-fit value (Fig. 9b) leads to a significantly different picture as far as the stability of the amorphous phase vis-a-vis the crystalline solid solutions is concerned. As can be seen from Fig. 9b, the amorphous phase has the lowest enthalpy of formation over the range 30–77 at.% Ag, while no such range exists in Fig. 9a. The value of ΔH^{for} obtained by neglecting the elastic effects for the crystalline phases are plotted in Fig. 9c. Ignoring elastic effects leads to a further stabilization of the crystalline solid solutions with respect to the amorphous phase. The calculated values of the enthalpies of formation for the amorphous phase and the crystalline solid solutions for all the systems (at 50 at.%) are as shown in Table I.

Table I. ΔH^{for} at 50 at. % (kJ/mole)

<u>Alloy system</u>	<u>Amorphous</u>	<u>FCC</u>	<u>BCC</u>
Cu-W	51.97	35.07	32.98
Cu-Ag	14.3	7.37	
Cu-Mo	42.99	29.52	27.43
Fe-Ag	40.66	36.45	35.61
Pu-Ta	27.32		8.32
Pu-V	17.2		7.52

The calculations for all the binary systems show no range of compositions where the amorphous structure is metastably favoured over the crystalline solid solutions. This leads us to conclude that the observation of an amorphous phase following sputtering of alloys in these systems is a result of kinetic hindrance to the formation of the crystalline solid solutions.

ACKNOWLEDGMENTS

The authors are grateful to W. Wein and D. Delguidice for DSC, x-ray diffraction, and microprobe analyses. One of us (T.B.M.) gratefully acknowledges partial support from the National Science Foundation (DMR Grant No. 84-12989). Work performed under the auspices of the U.S. Department of Energy by the Lawrence Livermore National Laboratory under Contract W-7405-Eng-48.

REFERENCES

1. A.R. Miedema and A.K. Niessen, presented at the International Symposium on Non-equilibrium Solid Phases and Alloys, Kyoto, Japan, Mar. 1988, to be published.
2. H.F. Rizzo, T.B. Massalski, and E.D. McClanahan, *Metall. Trans.* **19A**, 5 (1988).
3. T. Egami and Y. Waseda, *J. Non-Cryst. Solids* **64**, 113 (1984).
4. T.B. Massalski and H.F. Rizzo, presented at the International Symposium on Non-equilibrium Solid Phases and Alloys, Kyoto, Japan, Mar. 1988, to be published.
5. N. Saunders and A.P. Miodownik, *J. Mater. Sci.* **22**, 629 (1987).
6. W.L. Johnson, *Mater. Sci. Eng.* **97**, 1 (1988).
7. M. Nastasi, F.W. Saris, L.S. Hung, and J.W. Mayer, *J. Appl. Phys.* **58**, 3052 (1985).
8. J.A. Alonso and S. Simozar, *Sol. State Comm.* **48** (9), 765 (1983).
9. B.X. Liu, *Phys. Stat. Sol. A* **94**, 11 (1986).
10. L.G. Swartzendruber, *Bull. Alloy Phase Diagr.* **5**, 560 (1984).
11. H.F. Rizzo, L.E. Tanner, M.A. Wall, E.D. McClanahan, and T.B. Massalski, in *Fundamentals of Beam-Solid Interactions and Transient Thermal Processing*, edited by M.J. Aziz, L.E. Rehn, and B. Stritzker (Mater. Res. Soc. Proc. **100**, Pittsburgh, 1988), pp. 81-85.
12. K. Sumiyama, N. Kataoka, and Y. Nakamura, *Mater. Sci. Eng.* **98**, 343 (1988).
13. C.L. Chien and K.M. Unruh, *Phys. Rev. B* **28** (3), 1214 (1983).
14. W.C. Giessen, *Bull. Alloy Phase Diagr.* **1**, 43 (1980).
15. R. Stoering and H. Conrad, *Acta Metall.* **17**, 933 (1969).
16. A.F. Jankowski, *The Strain Wave Approach to Modulus Enhancement and Stability of Metallic Multilayers*, Lawrence Livermore National Laboratory, Livermore, Calif., UCRL-97446 (1987).
17. T.W. Barbee, Jr. and D.L. Keith, in *Synthesis and Properties of Metastable Phases*, edited by E.S. Machlin and T.J. Rowland (AIME, Pittsburgh, 1980), p. 73.
18. A.G. Dirks and J.J. van der Broek, *J. Vac. Sci. Technol.* **A3** (6), 2618 (1985).
19. H.F. Rizzo, A.W. Echeverria, W. Wein, and T.B. Massalski, *Mater. Sci. Eng.* **98**, 57 (1988).
20. A.R. Miedema, P.F. deChatel, and F.R. deBoer, *Physica* **100B**, 1 (1980).
21. A.K. Niessen, F.R. deBoer, P.F. deChatel, W.C.M. Mattens, and A.R. Miedema, *CALPHAD* **7**, 51 (1983).
22. P.R. Subramanian and D.E. Laughlin, *Bull. Alloy Phase Diagr.*, in press.
23. P.R. Subramanian and D.E. Laughlin, *Bull. Alloy Phase Diagr.*, in press.
24. M.W. Chase, *Bull. Alloy Phase Diagr.* **4**, 124 (1983).
25. L. Kaufman and H. Bernstein, *Computer Calculation of Phase Diagrams* (Academic Press, New York, 1970).

Morphology of Amorphous Alloy Formed By Ion Beam Bombardment

Tian Wei, Cai Wei Ping, Li Jun, Wu Run
Wuhan Iron and Steel University, Wuhan, Hubei, China

Abstract

A study was performed to investigate the morphology of amorphous alloys which were formed on the surface of the samples by means of ion beam bombardment. The specimens of Fe deposited with Cr, Ti, Cr-Ni or Cr-Ni-Cr multilayers were bombarded by high doses of Ar^+ , N^+ or Ti^+ ion beams respectively. TEM and electron diffraction analysis were then used to study the kinetic transformation of amorphous to crystal during heating. The electro-chemical results have showed after that the anodic current density I_c and I_m were reduced remarkably.

Introduction

In the 50's, in the field of material research, wide attention was paid to Klement, Willens and Duwez's research (1) showing that Au-Si amorphous alloy can be made by quenching it in liquified nitrogen. Since then, outstanding progress has been made in the research of making amorphous alloy, as well as the study of its structure and properties (2-3).

Recently developed techniques of ion implantation are used not only in the modification of surface element content, structure and properties including hardness and resistance to wear, friction, oxidation at high temperature and aqueous corrosion (4-7), but also in making surface alloys of different structures (8-9). In this paper, we deal with the formation of amorphous alloys in which the pure iron samples are deposited with Cr or Ti of various thicknesses, Cr-Ni duplex film or Cr-Ni-Cr multilayers bombarded by high doses of Ar^+ , N^+ or Ti^+ ion beams under different conditions. By means of electron diffraction analysis, investigations were made into the amorphous morphology, and the transformation of amorphous alloys to crystals during heating. Also measurements were made of the macroscopic electro chemical properties.

Experiments

1. Preparation of specimens for electrochemical analysis

The specimens of polycrystal pure iron (10×5mm) containing 0.014% C, 0.012% Si, 0.26% Mn, 0.007% P, 0.004% S, 0.001% Al and Fe were polished metallographically and finally, using 1μ diamond paste, finished down to the smoothness of a mirror. After cleaning and drying, they were put into a vacuum evaporator, in which the specimens were deposited with Cr, Ti, Cr-Ni or Cr-Ni-Cr respectively. The vacuum during deposited was 1-2×10⁻⁵ torr, and the thicknesses of the films were evaluated with a microbalance whose error was under 10⁻⁵g.

2. TEM examination

TEM specimens (3×0.1mm) were prepared as mentioned above. Before deposited, the final treatment of the specimens was the reduction of the thickness by jet electro polishing using 10% perchloric acid-alcohol solution. After depositing, this same method was used again on the back side of the specimens in order to further reduce the thickness.

The transimissionelectron microscope, JEM 100CX-II, was used to examine the morphology, local electron diffraction, center-dark-field pattern and the transformation of the structure while kept in a vacuum during heating.

3. Ion beam bombardment

The deposited samples were bombarded with ions in a 400 keV implan-tator made in Holland. The parameters of bombardment are shown in Table-I.

Table-I Parameters of ion beam bombardment

Speci.	film(Å)	target temp. °C	ion	energy keV	dose cm-2
Fe	Cr(400)	-80	Ar ⁺	300	2×10 ¹⁷
Fe	Cr(400)-C(50)	R.T.	Ar ⁺	160	2×10 ¹⁷
Fe	Ti(1400)	R.T.	N ⁺	180	1×10 ¹⁷
Fe	Ti(1400)	R.T.	N ⁺ N ⁺ +	180 50	1×10 ¹⁷ 1×10 ¹⁷
Fe	Ti(1400)	400	N ⁺	180	1×10 ¹⁷
Fe	Cr-Ni(500)	R.T.	Ti ⁺	230	5×10 ¹⁷
Fe	Cr-Ni-Cr(1800)	R.T.	Ar ⁺	180	1×10 ¹⁷

4. The measurement of electrochemical behaviour

For the deposited-pure iron specimens of bombardment or non bombardment, the three sweep potentiodynamic polarization technique was used to examine the passivation behaviour with a Model 351-2 Corrosion Measurement System from Japan. With this technique, the potential scanning speeds were 100mV/min. for the first and second sweep and 50mV/min. for the third sweep. The scanning range was $\pm 1200\text{mV}$ referenced to the saturated Hg electrode potential. The electrolyte is deaerated 1M sodium acetate-acetic acid solution, at 25°C, pH 7.3.

Results

1. TEM examinations

All the amorphous alloys in the surface studied in this work were tested with diffraction pattern plates obtained by electron diffraction.

In this samples of Fe deposited with Cr-C double layers, the C film dropped off very easily before Ar⁺ ion beam mixing. By using SEM, an obvious interface between the Cr film and the C film was observed. The Cr particles were about 0.26-0.5μm in diameter and their distribution was uniformed. After the Ar⁺ ion beam mixing (160keV, 2×10¹⁷Ar⁺cm⁻²), the sample profile could be divided into three fundamental regions;

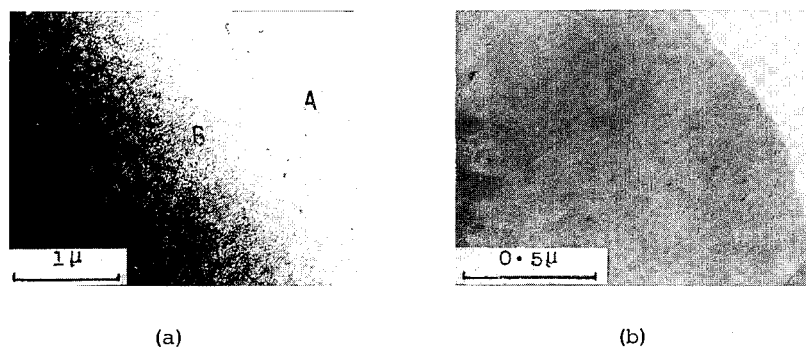


Fig 1 TEM morphology of Cr-C-deposited Fe (160keV , $2 \times 10^{17} \text{Ar}^+ \text{cm}^{-2}$, at room temp.). (a) A: amorphous; B: transition zone and C: Fe substrate. (b) TEM morphology of amorphous alloy for the same sample.

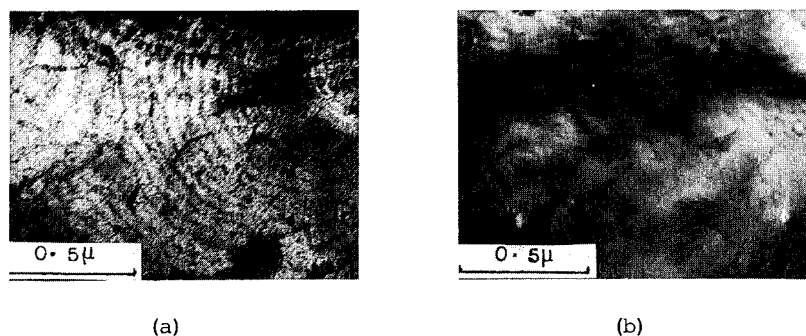


Fig 2 TEM amorphous morphology of Ti-deposited Fe of N^+ ion bombardment at room temp. (a) 180keV and $1 \times 10^{17} \text{N}^+ \text{cm}^{-2}$. (b) 180keV and $1 \times 10^{17} \text{N}^+ \text{cm}^{-2}$ plus 50keV and $1 \times 10^{16} \text{N}^+ \text{cm}^{-2}$.

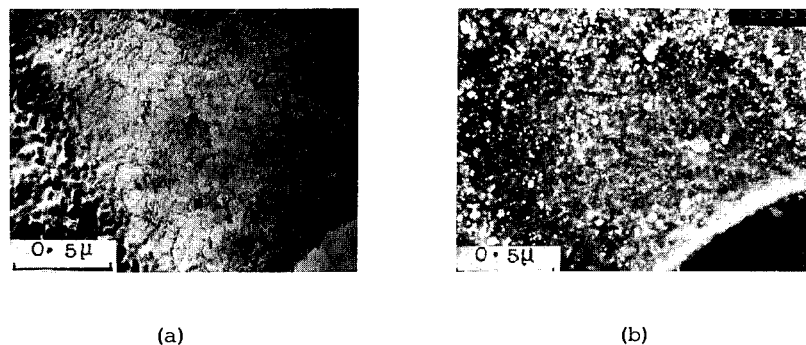


Fig 3 TEM amorphous morphology of Ti-deposited Fe with N^+ ion bombardment. (a) 180keV and $1 \times 10^{17} \text{N}^+ \text{cm}^{-2}$ at 400°C . (b) After heating the amorphous alloy for the same.

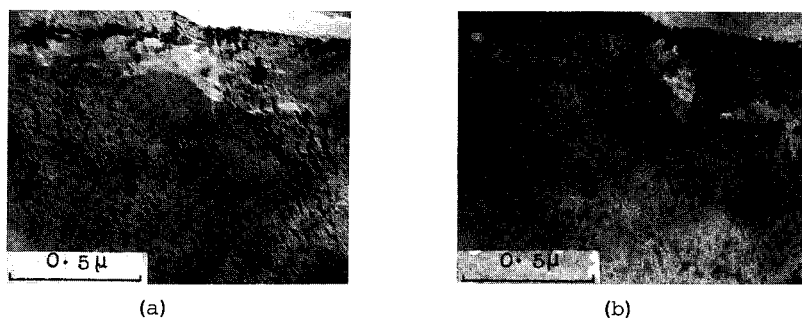


Fig 4 TEM amorphous morphology of Cr-Ni-deposited Fe bombarded with Ti^+ ions. (a) 230keV and $5 \times 10^{15} \text{Ti}^+ \text{cm}^{-2}$. (b) After heating the amorphous alloy for the same sample.

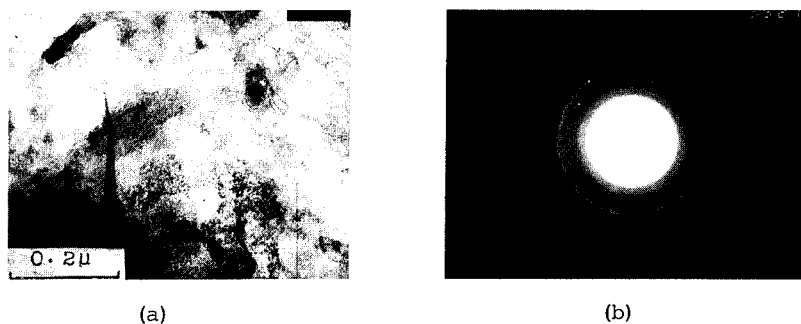


Fig 5 TEM amorphous morphology of Cr-Ni-Cr-deposited Fe mixed with Ar^+ ions. (a) 180keV and $1 \times 10^{17} \text{Ar}^+ \text{cm}^{-2}$. (b) After heating the amorphous alloy for the same sample. The electron-diffraction pattern in excess 100s heating.

the amorphous alloy at the outsurface, polycrystals in the transition region and the Fe substrate (Fig.1a). The transition of the three regions was observed to be gradual without evident interfaces, and layer on the outsurface was typically amorphous and contrast-free. The electron diffraction pattern was distinctly a dispersion crown of typical amorphous characteristics (Fig.1b). In the transition region, it existed the tiny polycrystals and second phase which components of $(\text{Fe}, \text{Cr})_2\text{C}$ and Cr_3C_2 with a dimension of about 400Å.

On the outsurface of the Cr-deposited Fe sample subjected to Ar^+ ion beam mixing (300keV and $2 \times 10^{17} \text{Ar}^+ \text{cm}^{-2}$ at -80°C mixed), there was a perfect amorphous alloy layer on the outsurface. This amorphous layer was contrast-free too, just like the one mentioned in the previous paragraph, see Fig.1b.

The amorphous alloy layer of the Ti-deposited Fe sample (deposited thickness about 1400Å) resulting from bombardment with N^+ ion beam (180keV $1 \times 10^{17} \text{N}^+ \text{cm}^{-2}$) at room temperature showed a finger-print pattern. The amorphous layer appeared imperfect because the N^+ ion was too light to cause a thorough mixing. The amorphous layer was detected by analysis of the electron diffraction pattern. When the bombardment was conducted two times

successively at room temperature with the same sample (where in the first bombardment was carried out at an energy level of 180 keV and adose of $1 \times 10^{17} \text{ N}^+ \text{ cm}^{-2}$ and the second bombardment at 50 keV and $1 \times 10^{16} \text{ N}^+ \text{ cm}^{-2}$) the amorphous substance in outsurface appeared to be contrast-free and ripple-shaped while the amorphous layer looked perfect. Because the peak concentration implanted ions by the second time bombardment moved in front of the peak concentration implanted ions by the first time bombardment, it was beneficial to form the amorphous alloy on the outsurface. See Fig. 2a and Fig. 2b.

The amorphous layer of the Ti-deposited Fe sample (deposited thickness about 1400 Å), after bombardment with N^+ ion beam (180 keV and $1 \times 10^{17} \text{ N}^+ \text{ cm}^{-2}$) at 400 °C, displayed a net-shaped pattern (Fig. 3a). Upon heating the layer with an electronic gun, tiny TiO crystallites immediately precipitated as the second-phase (Fig. 3b).

The stable amorphous alloy layer of Cr-Ni deposited Fe sample (about 500 Å in total) after Ti ion beam mixing, showed a streak-looking pattern under TEM. However, upon heating the layer with electronic gun, it remained amorphous for a long time, as shown in Fig. 4a, 4b.

An amorphous alloy layer of Cr-Ni-Cr deposited Fe sample (total deposited thickness circa 1800 Å) after Ar^+ ion beam (180 keV and $1 \times 10^{17} \text{ Ar}^+ \text{ cm}^{-2}$) mixing, gave high stable and extremely tiny crystallites. They remained stable upon heating at 100 keV and 150 μA with an electronic-gun for 100's, and transformed into polycrystallites in excess of 100 s. See Fig. 5a and 5b.

After Ti^+ or Ar^+ ions bombardment, both samples were dense and uniform amorphous microstructure on the outer surface, and formed the single phase in the near-surface, which upon heating, produced no precipitation of second-phase components, hence high stability. For Fe substrate deposited with Ti film or Cr-C double layer, an amorphous alloy is formed after N^+ or Ar^+ ions bombardment. And, upon heating a second-phase immediately precipitates because this amorphous alloy is unstable and distorted during heating.

It can be concluded that in determining the morphology and stability of an amorphous alloy the following must be considered: the species of chemical activity of ion implanted, characteristics of both the ion and the target, the surface composition formed, the conditions of bombardment involving energy, dosage, current density and the target temperature during implantation etc.

2. Electrochemical results

The deposited films were very tiny and porous. There were potential differences between the film and the substrate in the electrolytic solution. Fe ions in the substrate were dissolved as tiny anodes through the crevice of the layers. So, the activation-passivation were not different in the samples with and without deposited film.

After ion beam bombardment, the passivations of the samples were considerably improved because a compact thin amorphous alloy was formed, the probability of the contact of substrate with electrolyte decreases, and the area and quantity of the tiny anodes both decrease significantly.

Both Ar^+ ion beam mixing and N^+ or Ti^+ ion implantation improved the electrochemical behaviour remarkably. It shows that the critical anodic passivating current density I_c and the minimum anodic passivating current density I_m are more than one order of magnitude lower than the pure Fe or deposited Fe. See Table II.

Table II. Main parameters of electrochemical behaviour

subs.	film A	target temp. °C	ion	energy keV	dose cm	Ic uA/cm	Im uA/cm	E mV	Eop mV
Fe						3300	16.2	1400	-770
Fe	Cr(400)					4500	65	1400	-800
Fe	Cr(400)	R.T.	Ti ⁺	300	5×10^{16}	140	1.6	1430	-755
Fe	Ti(1400)	R.T.	N ⁺	180	1×10^{17}	25	19	1400	-800
Fe	Ti(400)	R.T.	Ar ⁺	300	1×10^{17}	81	31	1450	

Conclusions

1. Amorphous alloy can be formed on the surface of Fe deposited with different films bombarded with high doses of heavy or light ions.
2. The morphology of amorphous alloy is different, depending on the component of surface and the bombardment conditions.
3. The amorphous alloys with different morphologies are different in their electrochemical behaviour.
4. As soon as the amorphous alloy is formed, the corrosion resistance is improved significantly, Ic and Im are decreased by more than one order of magnitude compared with those of metal-deposited Fe or pure Fe.

References

- (1). W.Klement, R.H.Willens & P.Duwez, Nature(London), 187, 869(1960)
- (2). Donald E.Polk Billc. Giessen, American Society for Metals Metallic Glasses. Sept 1976
- (3) H.S.Chen, K.A.Jackson. The influence of alloy composition on glasses formation and properties. Bell lab. Murray Hill, New Jersey
- (4) Dearnaley.G, Thin Solid Films, 107(3), 315-326, 23, Sept. 1983
- (5) Tian wei, Li Jun, Cai Weiping. Nucl. Inst. Meth. in Phys. Research, B21 597-600, 1987
- (6) Santos C.A., Behar M.Baumvol I JR, J. Phys. D. Appl. Phys. 17(3), 556-562, 14 Mar. 1984
- (7) M.A.Nicalet, S.T.Picraux. Ion Mixing and Surface Layer Alloying. Noyes Publications, New Jersey, U.S.A. 1981
- (8) J.W.Mayer, B.Y. Tsaur, S.S.Lan & L-S Hung. Nucl. Inst. and Meth. 1-13, 1981
- (9) B.Y.Tsaur, Z.L.Lian and J.W.Mayer. Appli. Phys. Lett. 36, 823, 1980

COMPOSITION- AND TEMPERATURE-DEPENDENCE OF ION MIXING
IN AMORPHOUS Si/Ge ARTIFICIAL MULTILAYERS

B. Park*, F. Spaepen*, J.M. Poate+, F. Priolo+ and D.C. Jacobson+

* Division of Applied Sciences, Harvard University, Cambridge MA 02138

+ AT&T Bell Laboratories, 600 Mountain Road, Murray Hill, NJ 07974

ABSTRACT

Amorphous Si/Ge artificial multilayers with a repeat length of around 60 Å have been partially mixed with 1.5 MeV Ar⁺ ions at temperatures in the range 77-673K. The change in the intensity of the first X-ray diffraction peak resulting from the composition modulation is used to determine the mixing lengths. The diffusive component of the square of the mixing length, at a given dose, is independent of the dose rate and has an Arrhenius-type temperature dependence, with activation enthalpies between 0.19 and 0.22 eV, depending on the average composition.

INTRODUCTION

In earlier papers [1,2] we demonstrated that the artificial multilayer technique, which has long been known to be the most sensitive method for diffusivity measurements (down to 10⁻²³ cm²/sec) [3,4], can be used for very accurate determinations of ion beam mixing lengths, x , on the order of a few Å. This allows ion beam mixing to be observed and characterized at much lower doses than has been possible by other analysis techniques so far.

The dependence of the degree of ion mixing on the ion dose rate (flux), K , is the object of much study and considerable controversy. Priolo et al. [5,6] studied the ion beam-enhanced diffusion of Au in amorphous Si, and found that the diffusive component of the squared mixing length, $x_D^2 = x^2 - x_0^2$ (x_0 : ballistic mixing length) for a given dose, in the range of 10¹⁷ ions/cm², to be independent of K . For As, In, Sb, Fe and Pt in amorphous Si, they could not observe any ion beam-enhanced diffusion. They attributed this difference in behavior to the respective interstitial or substitutional nature of these solutes in silicon. Müller et al. [7] found that x_D^2 for Ni-isotopes in a Ni single crystal was also independent of K . Averback et al. [8], on the other hand, found that x_D^2 for Cu in amorphous Ni-Zr was proportional to $K^{-1/2}$. Both types of behavior can be described by different regimes in Sizmann's [9] analysis based on rate equations for the formation and annihilation of point defects that govern the diffusion process.

The work presented here on ion mixing of amorphous Si/Ge artificial multilayers is of interest in this context for two reasons. Si and Ge form substitutional alloys at all compositions in the crystalline and amorphous phase. The sensitivity of the multilayer technique allows measurements of ion beam-enhanced diffusion of a substitutional solute in amorphous Si or Ge. It also allows the dose rate-dependence to be tested at much smaller doses.

EXPERIMENTAL PROCEDURE

The artificial multilayers were prepared by ion beam sputtering from alternating elemental targets onto an oxidized Si (100) substrate [10]. The layer repeat lengths, d , were around 60 Å, and were kept constant

within 4%. For each film, d was determined from $\cos(\theta) = n \cdot \cos(\sin^{-1}(N\lambda/2nd))$, where 2θ is the diffraction angle, n is the average index of refraction of the material, N is the order of the reflection, and λ is the X-ray wavelength [11]. The composition of the films was varied, by adjusting the relative layer thicknesses, over the range 25-90 at. % Si. The Ar content was around 1 at. %. The sputtering gas was cleaned in a Ti gettering furnace immediately before use. The films were about 2000 Å thick, and were capped with 150 Å of Si.

The ion mixing experiments were carried out with a swept beam of 1.5 MeV Ar^+ ions at substrate temperatures between 77K and 673K. The irradiated areas were around 1cmx2cm with Ar^+ beam currents in the range 6 to 200 nA with typical beam spot sizes of several mm². The integrated doses were in the range 1×10^{14} to 8×10^{14} ions/cm², and the average dose rates in the range 1.6×10^{10} to 5.5×10^{11} ions/cm²·sec.

The mixing lengths were determined by X-ray diffraction in a θ - 2θ scan on a GE horizontal diffractometer with a rocking stage for precise initial alignment. The mixing length is calculated from $x = [\ln(I_1/I_2)d^2/8\pi^2]^{1/2}$, where I_1 and I_2 are the intensities of the first modulation diffraction peak, respectively before and after irradiation [4].

RESULTS

In the experiments the square of the mixing length was found to vary linearly with dose. This is illustrated in figure 1 for multilayer films of equiatomic average composition. Note that mixing lengths can easily be observed for doses as small as 1×10^{14} ions/cm².

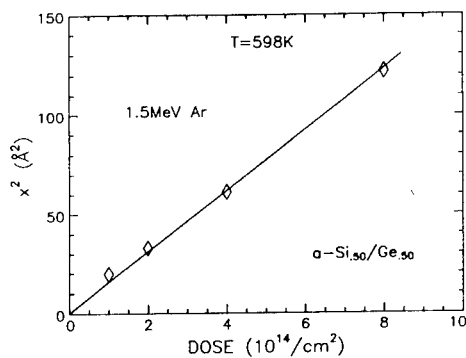


Fig.1. Dependence of the square of the mixing length, x^2 , on dose at 598K from the Si/Ge amorphous multilayer films with 50 at. % Si.

The variation of x^2 with substrate temperature for a given dose is illustrated in figures 2 and 3 for two compositions. In all cases, x^2 is constant at lower temperatures, corresponding to square of the ballistic mixing length, x_0^2 , and increases at higher temperature. The Arrhenius plots of the diffusive part, x_D^2 , (figures 4 and 5) give straight lines with activation enthalpies of 0.22 ± 0.03 eV and 0.19 ± 0.03 eV for the 50 and 75 at. % Si samples, respectively. Parallel measurements of the thermal diffusion lengths, for the same time and temperature, on simultaneously produced control samples showed them to be more than two orders of magnitude smaller than the ion beam-enhanced values, even at the highest temperatures, as illustrated on figure 4 for the 50 at. % Si samples. It should be kept in mind that the thermal components were determined over the total time of the irradiation. Since the beam was swept, the difference between the enhanced and the thermal components is even larger than shown in this figure.

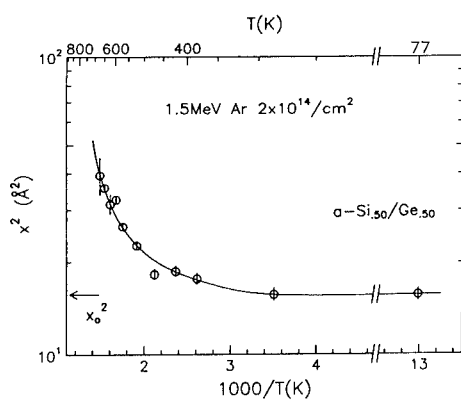


Fig.2. Temperature dependence of the square of the mixing length, x^2 , for the 50 at. % Si films with a dose of 2×10^{14} ions/cm².

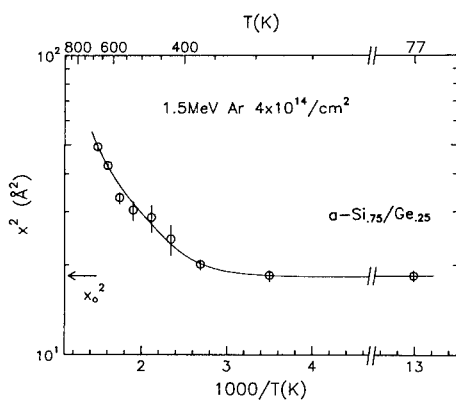


Fig.3. Temperature dependence of x^2 for the 75 at. % Si films with a dose of 4×10^{14} ions/cm².

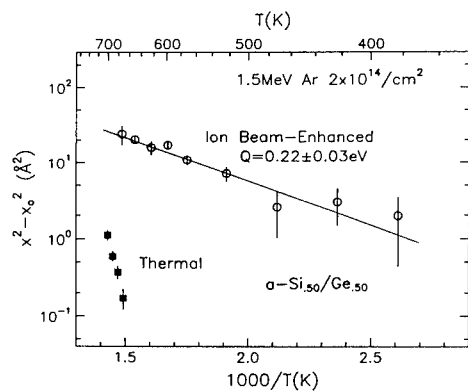


Fig.4. The Arrhenius plot of the diffusive component of x^2 for the 50 at. % Si films. The dose is same as in Figure 2.

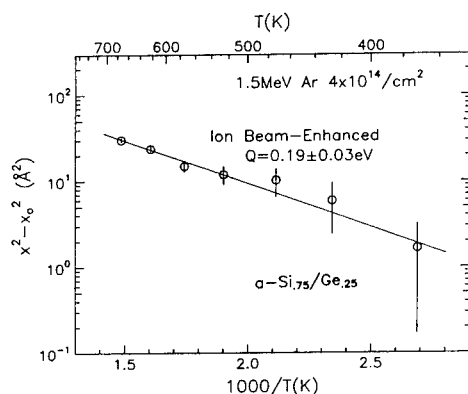


Fig.5. The Arrhenius plot of x_D^2 for the 75 at. % Si films with a dose of 4×10^{14} ions/cm².

In figure 6, x^2 for a given dose is shown as a function of composition for two temperatures. It is worth noting that the ratio of the diffusive and ballistic components of x^2 is fairly constant for the different compositions.

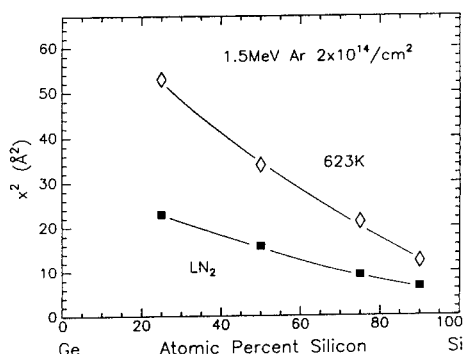


Fig.6. Composition dependence of x^2 for the 25, 50, 75, and 90 at. % Si films at 77K and 623K. The repeat length is around 60Å, and the dose is 2×10^{14} ions/cm².

In all experiments the ion beam enhanced diffusion was found to be independent of dose rate, which was varied by as much as a factor of 35 as shown in figure 7.

DISCUSSION

The ballistic mixing lengths measured in the present experiments are in agreement with the ion mixing studies at higher doses (10^{16} ions/cm²) of Matteson et al. [12] on thin Ge, Sb and Pt markers in amorphous Si if x_0^2 is scaled with the dose and the concentration of the target atom displacements (calculated from the TRIM program [13]). This implies that the results from the artificial multilayer technique can be usefully compared to those from other techniques.

That ion beam-enhanced diffusion can be observed for a substitutional solute in amorphous Si by the present technique suggests that increased sensitivity may be required to detect the phenomenon for the other substitutionals studied by Priolo et al. [6].

Ion beam-enhanced diffusion processes that are independent of dose rate, such as the present ones, can be modeled by the high-temperature

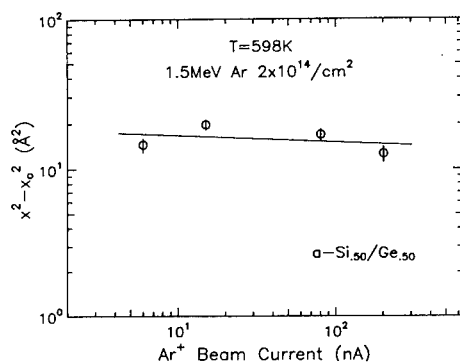


Fig.7. Dependence of the diffusive components of the squared mixing length on Ar^+ beam current at 598K with a given dose of 2×10^{14} ions/cm² for the 50 at. % Si films.

regime of Sizmann's [9] steady state solution of the rate equations for the defect formation and annihilation in ion mixing:

$$x_D^2 = \phi \{ f_v \exp(-Q_v/kT) / k_v + f_i \exp(-Q_i/kT) / k_i \}$$

where $\phi = Kt$ is the dose, v and i are subscripts referring to vacancies and interstitials, f_v and f_i are temperature- and dose rate-independent prefactors, Q_v and Q_i are activation enthalpies of migration, k is Boltzmann's constant, and k_v and k_i are reaction rate constants related to the annihilation of the defects at sinks. The activation enthalpies of these reaction constants are expected to be close to the respective values of Q , since similar atomic motions are involved. A weak temperature dependence of the diffusive mixing length is therefore expected. The small positive activation enthalpy of x_D^2 (a few tenths of an eV) could be accounted for by, for example, a slight temperature dependence of the sink concentration [14], which in turn may depend somewhat on the composition.

CONCLUSION

The artificial multilayer technique can be used effectively to study ion beam-enhanced diffusion at low doses. The diffusive component of the mixing length in amorphous Si/Ge multilayers of different average composition was found to be independent of dose rate, as in the experiments of Priolo et al. [6] on Au in amorphous Si.

An atomistic interpretation of both the weak temperature dependence and the dose rate-independence is provided by one of Sizmann's defect creation and annihilation models [9]. This suggests that in covalent materials, such as Si and Ge, the concepts of vacancies and interstitials can usefully be transferred from the crystalline to the amorphous state. Indeed, it is known from model studies that stable vacancies can be created in continuous random network models of amorphous Si [15]. The dose rate independence of the diffusive component implies that the defect creation and annihilation occur within the collision cascade [16].

ACKNOWLEDGEMENTS

We thank W.L. Brown, M.J. Aziz and E. Nygren for valuable discussions. The work at Harvard has been supported by the National Science Foundation through the Materials Research Laboratory under contract number DMR-86-14003.

REFERENCES

1. B. Park, F. Spaepen, J.M. Poate and D.C. Jacobson, Mater. Res. Soc. Proc. 74, 493 (1987).
2. B. Park, F. Spaepen, J.M. Poate, F. Priolo, D.C. Jacobson, C.S. Pai, A.E. White and K.T. Short, Mater. Res. Soc. Proc. 103, 173 (1988).
3. H.E. Cook and J.E. Hilliard, J. Appl. Phys. 40, 2191 (1969).
4. A.L. Greer and F. Spaepen, in Synthetic Modulated Structures, edited by L.L. Chang and B.C. Giessen (Academic Press, New York, 1985) p.419.
5. F. Priolo, J.M. Poate, D.C. Jacobson, J. Linnros, J.L. Bastone and S.U. Campisano, Appl. Phys. Lett. 52, 1213 (1988).
6. F. Priolo, J.M. Poate, D.C. Jacobson, J.L. Batstone and S.U. Campisano, to be published in the Proceedings of the IBMM (1988).
7. A. Müller, V. Naundorf and M.-P. Macht, J. Appl. Phys. 64, 3445 (1988).
8. R.S. Averback, H. Hahn and Fu-Rong Ding, J. Less-Common Metals 140, 267 (1988).
9. R. Sizmann, J. Nucl. Mater. 69/70, 386 (1978).
10. F. Spaepen, A.L. Greer, K.F. Kelton and J.L. Bell, Rev. Sci. Instr. 56, 1340 (1985).
11. A.M. Kadin and J.E. Keem, Scripta Metall. 20, 440 (1986).
12. S. Matteson, B.M. Paine, M.G. Grimaldi, G. Mezey and M.-A. Nicolet, Nucl. Instr. and Meth. 182/183, 43 (1981).
13. J.F. Ziegler, J.P. Biersack and U. Littmark, The Stopping and Range of Ions in Solids, Pergamon Press, New York (1985).
14. A.D. Marwick, in Surface Modification and Alloying by Laser, Ion, and Electron Beams, edited by J.M. Poate, G. Foti and D.C. Jacobson (Plenum, New York, 1983) p.211.
15. C.H. Bennett, P. Chaudhari, V. Moruzzi and P. Steinhardt, Philos. Mag. A 40, 485 (1979).
16. L.E. Rehn and P.R. Okamoto, to be published in the Proceedings of the IBMM (1988).

ION BEAM INDUCED INTERMIXING OF $\text{WSi}_{0.45}$ on GaAsS. J. PEARTON⁺, K. T. SHORT⁺, K. S. JONES*, A. G. BACA⁺⁺ and C. S. Wu^{**}⁺ AT&T Bell Laboratories, Murray Hill, NJ 07974

* University of Florida, Gainesville, FL 32611

⁺⁺ AT&T Bell Laboratories, Reading, PA 19603^{**} Hughes Aircraft Co., Torrance CA 90509

ABSTRACT

The systematics of ion beam induced intermixing of $\text{WSi}_{0.45}$ on GaAs have been studied after through-implantation of Si or O in the dose range $10^{13} - 5 \times 10^{16} \text{ cm}^{-2}$. SIMS profiling shows significant knock-on of Si and W into the GaAs at the high dose range in accordance with Monte Carlo simulations, but there is virtually no electrical activation ($\leq 0.1\%$) of this Si after normal implant annealing (900°C , 10 sec). This appears to be a result of the high level of disorder near the metal-semiconductor interface, which is not repaired by annealing. This damage consists primarily of dislocation loops extending a few hundred angstroms below the end of range of the implanted ions. Extrapolation of the ion doses used in this work to the usual doses used in GaAs device fabrication would imply that ion-induced intermixing of WSi_x will not be significant in through-implantation processes.

Introduction

One of the biggest problems in GaAs technology is the metallization, both for Schottky and ohmic contacts. In most cases alloyed ohmic contacts are still used - this implies a melting and flowing of the eutectic, limiting downscaling of the contacts, as well as spiking into the GaAs. The metal contacts commonly used in device applications generally exhibit a rather restricted range of Schottky barrier heights, around 0.7-0.8 eV. Recently the use of a thin (15-30Å) Si interface layer between the GaAs and a metal overlayer has been demonstrated to yield contacts with a 1 eV Schottky barrier height [1]. The most common gate metallization for GaAs FET's is WSi_x , which is well established in the self-aligned refractory gate technology. In this case the refractory gate acts as a mask for subsequent n^+ implantation which reduces the resistance between the FET channel and the source and drain [2-5]. The implant must be activated by a high temperature annealing step (850°C - 900°C), and therefore the stability of the WSi_x/GaAs interface has attracted much attention [6-8].

One issue which has not been received as much interest is the effect of ion-beam induced intermixing of the WSi_x and the GaAs during through-implantation of the WSi_x with either Si (for doping of the GaAs) or O (for isolation purposes). A further example in which through-implantation might be used is the use of acceptor implants to create a thin p^+ layer immediately under the Schottky contact to enhance the barrier height [9-12]. The effect of knock-on W and Si in the GaAs substrate is potentially very important - W is a deep acceptor and would be expected to compensate the donors in n-type material, whereas Si is amphoteric but is generally a donor. The latter could lead to uncontrolled doping characteristics in the GaAs after high temperature annealing.

In this paper we explore the stability of $\text{WSi}_{0.45}$ layers on GaAs to high doses of Si or O ions, and the effect of subsequent thermal annealing on interdiffusion characteristics at the metal-semiconductor interface. We also explore the use of $\text{WSi}_{0.45}$ as an overlayer for through-implantation of low doses of Si in order to form n-type regions for FET channels.

Experimental

Deposition of the $\text{WSi}_{0.45}$ films was performed in a standard S-gun sputtering system. The sputtering sequence was fairly standard for this type of deposition-initially the GaAs substrates were sputtered cleaned for a few minutes in a relatively high pressure (low energy) Ar beam. The film deposition was also carried out in Ar using separate W and Si sources. Thicknesses between 300-1000 Å were examined. The choice of sputtering conditions and film stoichiometry were based

on previous calibration experiments which determined the optimum film properties for our particular applications for Schottky contacts [13]. The GaAs substrates were undoped, (100), semi-insulating samples grown by the LEC technique. They were etched for 5 min in 5:1:1 $\text{H}_2\text{SO}_4:\text{H}_2\text{O}_2:\text{H}_2\text{O}$ prior to loading into the sputtering system. The WSi_x/GaAs samples were implanted with O or Si ions at doses between $5 \times 10^{15} - 5 \times 10^{16} \text{ cm}^{-2}$ for study of intermixing effects upon through-implantation or at doses of $10^{13} - 5 \times 10^{13} \text{ cm}^{-2}$ for study of the formation of n-type layers for FET channel formation. The energies of these implants were chosen either to remain mostly in the WSi_x , or to penetrate $\sim 0.2 \mu\text{m}$ into the GaAs, depending on the specific experiment. Annealing was carried out in a Heatpulse 410 system at 900–950°C for 10–300 sec, using the proximity technique. The near-interface region in the samples was examined before and after annealing by ion channelling, secondary ion mass spectrometry and cross-sectional transmission electron microscopy (TEM). In some cases the WSi_x was removed by NF_3 reactive ion etching, and capacitance-voltage (C-V) measurements were made in the GaAs using a Hg-probe as a contact.

Result and Discussion

Our initial task was to determine the uniformity of WSi_x thickness deposited on a 2" ϕ wafer. To do this without the possible problem of interaction of the WSi_x with a GaAs substrate, we did this on a Si wafer. From ion channelling measurements across a wafer diameter, the thickness uniformity was $\leq 10\%$ ($\sim 1000 \pm 100 \text{ \AA}$) for our sputtering conditions. A Monte Carlo simulation using the Transport of Ions in Matter (TRIM) program showed that each 100 \AA of WSi_x requires $\sim 10 \text{ keV}$ of energy for Si ions to penetrate. Therefore, variations in WSi_x layer thickness of order 100 \AA over a 2" ϕ wafer should lead to significant spatial variations in the total dose and resulting charge distribution in any n-type channel region formed by through-Si implantation. We estimate that for through-implantation of Si through 500 \AA of $\text{WSi}_{0.45}$, the thickness uniformity must be better than 3% over the whole wafer area in order to achieve acceptable MESFET threshold voltage uniformity.

We also deposited $\text{WSi}_{0.45}$ on GaAs samples, and annealed them at 950°C for 60 sec. Ion channelling showed a very slight amount of diffusion of W, confined to within 300 \AA of the metal-semiconductor interface. SIMS results showed As and Ga diffusion into the $\text{WSi}_{0.45}$ and W diffusion into the GaAs. This was a small effect compared to the case in which a high-dose, through-implantation preceded the annealing step.

Figure 1 shows ion channelling spectra taken from a 400 \AA $\text{WSi}_{0.45}/\text{GaAs}$ sample, implanted with 50 keV O^+ ions at a dose of $5 \times 10^{16} \text{ cm}^{-2}$. Prior to annealing there is a damage peak visible in the near surface region of the GaAs—this is removed by the standard anneal necessary for implant activation (900°C, 10 sec). There is little evidence for any change in the WSi_x film. Figure 2 shows a collage of TEM cross-sections for two oxygen doses through the WSi_x , both before and after annealing. A comparison of the as implanted samples shows that no amorphous regions have been formed in the GaAs, and that the metal-semiconductor interface appears degraded in the higher dose sample. After annealing a buried band of defects forms in the lower dose-sample this is typical of highly disordered GaAs. A TRIM simulation shows that the mean range of O in this structure is $\sim 550 \text{ \AA}$ (ie. 150 \AA below the $\text{WSi}_{0.45}$ -GaAs interface), with a straggle of $\sim 320 \text{ \AA}$. The buried band of defects obvious in Fig. 2 therefore corresponds to disorder extending from the peak in the damage distribution to the end-of-range. There actually appears to be less damage remaining in the higher dose sample, which shows a variety of rod-like defects and dislocation loops. This might result from beam-induced heating of the sample during the implantation step.

SIMS results showed interdiffusion at the interface upon annealing. Figure 3 shows the atomic profiles of W, O and Ga in a sample implanted with O ($5 \times 10^{16} \text{ cm}^{-2}$, 50 keV), both before and after 900°C, 300 sec annealing. The as-implanted sample appears to show knock-on of W at the 10^{20} cm^{-3} level, whereas after annealing there is diffusion of Ga into the $\text{WSi}_{0.45}$, no apparent motion of the implanted O and more significant diffusion of W into the GaAs within $\sim 500 \text{ \AA}$ of the interface. To get a clearer picture of the amount of W and Si knocked into the GaAs we prepared other samples in which the WSi_x was removed by NF_3 reactive ion etching after the O implantation step. This allows SIMS profiling with improved sensitivity and depth resolution. Figure 4 shows the atomic profiles of W in GaAs after O implantation at 5×10^{15} or $5 \times 10^{16} \text{ cm}^{-2}$. The amount of W scales with O dose, which implies that for the doses of Si or Se used in GaAs device fabrication ($3 - 8 \times 10^{12} \text{ cm}^{-2}$ for channel formation) the amount of W knocked into the GaAs would be $\leq 10^{16} \text{ cm}^{-3}$ to depths $\leq 500 \text{ \AA}$. Since the peak doping levels in the GaAs channel are between $2 - 6 \times 10^{17} \text{ cm}^{-3}$, this implies that ion-induced intermixing is not significant for through-implantation in GaAs device fabrication.

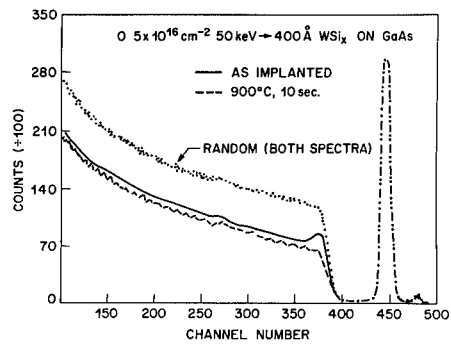


Figure 1. Ion channelling spectra before and after annealing (900°C, 10 sec) from a 400 Å $\text{WSi}_{0.45}$ /GaAs sample implanted with O ($5 \times 10^{16} \text{ cm}^{-2}$, 50 keV).

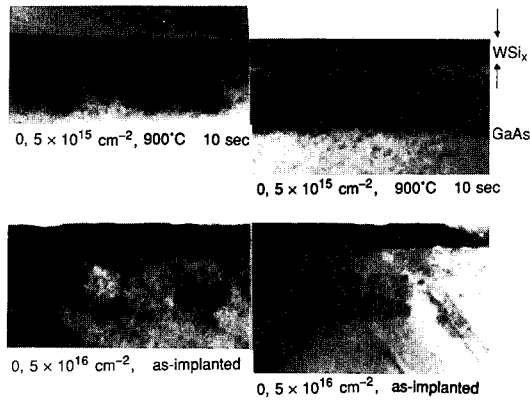


Figure 2. TEM cross-sections from 400 Å $\text{WSi}_{0.45}$ /GaAs samples after implantation with O at $5 \times 10^{15} \text{ cm}^{-2}$ (top left) or $5 \times 10^{16} \text{ cm}^{-2}$ (bottom left), and after subsequent annealing at 900°C for 10 sec (top right and bottom right respectively).

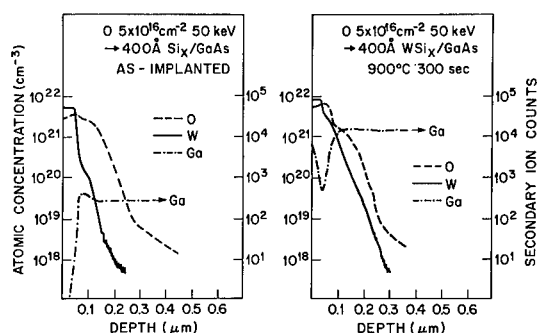


Figure 3. SIMS atomic profiles of O, W and Ga in 400Å $\text{WSi}_{0.45}/\text{GaAs}$ samples implanted with O ($5 \times 10^{16} \text{ cm}^{-2}$, 50 keV), before and after annealing at 900°C for 10 sec.

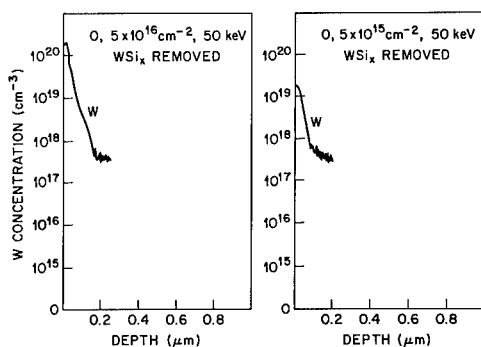


Figure 4. SIMS profiles of W knocked into GaAs by through-implantation of 400Å of $\text{WSi}_{0.45}$ on the GaAs surface by 50 keV O^+ ions at a dose of $5 \times 10^{16} \text{ cm}^{-2}$ (left) or $5 \times 10^{15} \text{ cm}^{-2}$ (right).

Similar results were obtained for Si knock-on under the same conditions. Figure 5 shows SIMS profiles of Si after through-implantation of O at two different doses. Once again there is a significant amount of Si incorporated into the GaAs, even more so than was the case with W because of the much higher mass of Si. Even though the amount expected to be knocked-on for device level doses would now be of the same order as the doping in the channel, the depth of these Si ions places them in the zero-bias region of the carrier profiles. In the case of high dose through-implantation, very little of the knocked-on Si becomes electrically active after annealing. Figure 6 shows the atomic and electrically active Si concentrations after O through-implantation and subsequent annealing at 900°C, 10 sec. Less than 0.1% of the Si becomes active, due presumably to the high level of disorder in the interfacial region after such high-dose implantation. It must be remembered that it is point defects in GaAs that control the degree of electrical activity of implanted ions, but the presence of a high density of visible defects in TEM implies also the presence of a significant point defect concentration.

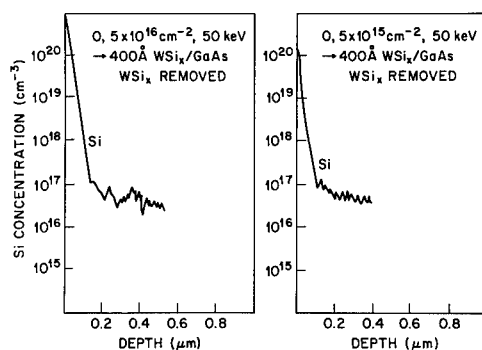


Figure 5. SIMS profiles of Si knocked into GaAs by through-implantation of 400Å of $\text{WSi}_{0.45}$ or the GaAs by 50 keV O^+ ions at a dose of $5 \times 10^{16} \text{ cm}^{-2}$ (left) or $5 \times 10^{15} \text{ cm}^{-2}$ (right).

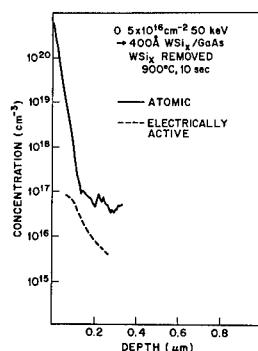


Figure 6. Atomic and electrically active profiles of Si in GaAs after through-implantation of 400Å of $\text{WSi}_{0.45}$ on the GaAs by 50 keV O^+ ions at a dose of $5 \times 10^{16} \text{ cm}^{-2}$, and subsequent annealing (900°C, 10 sec).

It would be expected that lower dose through-implantation would lead to better percentage wise activation. Figure 7 shows the range of carrier profiles obtained over a 2" ϕ semi-insulating GaAs wafer coated with 1000Å of $\text{WSi}_{0.45}$, implanted with Si at a dose of $1 \times 10^{13} \text{ cm}^{-2}$ (180 keV) and annealed at 900°C, 10 sec. The distribution of profiles is relatively tight and the activation is comparable to direct Si implantation under the same conditions. This implies that knock-on of W or Si is not significant under these conditions. The spread in carrier profiles is also comparable to that obtained with direct Si implantation, and emphasises again the feasibility of through-implantation with the WSi_x acting as an encapsulant for the activation anneal.

Conclusions and Summary

Through-implantation of WSi_x by Si for creation of doped regions in GaAs, or by O for isolation has been investigated. Given a sufficiently uniform WSi_x deposition the activation characteristics of Si appear similar to direct implantation into a bare GaAs substrate. For ion doses around $5 \times 10^{16} \text{ cm}^{-2}$ there is significant knock-on of both W and Si into the GaAs, although extrapolation to device level doses would imply that this is not a problem.

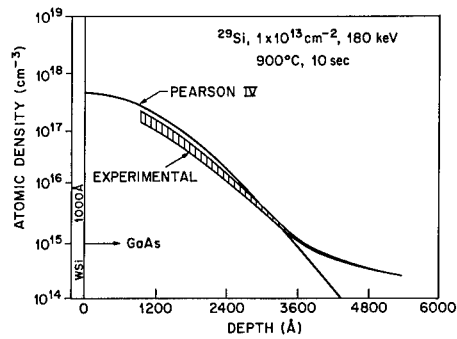


Figure 7. Theoretical and experimental carrier profiles in GaAs after through-implantation of 1000Å of WSi_{0.45} on the GaAs with Si, $1 \times 10^{13} \text{ cm}^{-2}$, 180 keV and subsequent annealing at 900°C, 10 sec. The shaded region represents the range of carrier profiles measured at 12 spots over a 2" ϕ wafer. The Pearson IV distribution is the theoretically predicted ion distribution.

References

1. J. R. Waldrop and R. W. Grant, *Appl. Phys. Lett.* 52, 1794 (1988).
2. N. Yokoyama, T. Ohnishi, K. Odanie, H. Onodera and M. Abe, *IEEE Trans. Electron. Dev.* ED29 1541 (1982).
3. T. N. Jackson and J. F. De Gelormo, *J. Vac. Sci. Technol.* B3 1676 (1988).
4. A. Callegari, G. D. Spiers, J. H. Magerlein and H. C. Guthrie, *J. Appl. Phys.* 61 2054 (1987).
5. M. Kanamori, K. Nagai and T. Nozacki, *J. Vac. Sci. Technol.* B5 1317 (1987).
6. D. A. Allan, *IEEE Proc.* 133 18 (1986).
7. S. Takatani, N. Matsuoka, J. Shigeta, N. Hashimoto and H. Nakashima, *J. Appl. Phys.* 61 220 (1987).
8. K. M. Yu, S. K. Cheung, T. Sands, J. M. Jaklevic, N. W. Cheung and E. E. Haller, *J. Appl. Phys.* 60, 3235 (1986).
9. S. M. Baier, G. Y. Lee, H. K. Chung, B. J. Fure and N. C. Cirillo, *Electronics Lett.* 23 224 (1987).
10. K. L. Priddy, D. R. Kitchen, J. A. Gryzb, C. W. Litton, T. S. Henderson, C.-K. Peng, W. F. Kopp and H. Morkoc, *IEEE Trans. Electron. Dev.* E34 175 (1987).
11. W. E. Stanchina, M. D. Clark, K. V. Vaidyanathan and R. A. Juliens, *J. Electrochem. Soc.* 134 967 (1987).
12. G. Fernholz, R. Westphalen, W. Lange and H. Beneking, *Electronics Lett.* 23 722 (1987).
13. A. G. Lahav and C. S. Wu (to be published).

THERMALLY AND ION-INDUCED REACTIONS OF METAL WITH CuO SUBSTRATE

JIAN LI, S.Q. WANG AND J.W. MAYER

Department of Materials Science and Engineering, Cornell University, Ithaca, NY 14853

ABSTRACT

Thermally and ion-induced reactions of transition metals Zr, Ti, Cr and Ag with CuO substrates have been studied by Rutherford backscattering spectrometry and X-ray diffraction techniques. Reactions resulted in the configuration of $ZrO_2/Cu_2O/CuO$ from Zr/CuO structure and TiO_x/Cu_2O from Ti/CuO structure after thermal annealing and ion irradiation. No significant reaction has been found in Cr/CuO after vacuum annealing at 410°C and 300 Kev Xe ions irradiation at 240°C. Ag atoms balled up on CuO surface after annealing at 610°C. A comparison of the reaction layers has been made in both metal/SiO₂ and metal/CuO systems after thermal annealing and ion irradiation. Both heats of reaction and bond strength in the substrates can influence the chemical reactivity between metal layer and substrate.

I. Introduction

Copper oxide, which plays an important part in high T_c superconductor materials, has some interesting properties. CuO is not stable in vacuum during thermal annealing. CuO thin films on SiO₂ substrates transform to Cu₂O after 750°C annealing in vacuum. A top layer of metal on CuO may enhance or reduce this phase transformation, because this metal layer may act as a sink for oxygen or a cap to prevent oxygen loss. In this study, we have investigated the chemical reaction of metal layers Zr, Ti, Cr and Ag with CuO substrate. We have tried to correlate the reaction products to the heat of reaction in metal/CuO system, and made a comparison with the reaction in metal/SiO₂.

Ion beam mixing in metal/insulator systems has been extensively studied [1,2]. Farlow et.al [3] summarized the ion beam mixing of metal on insulators. The substrate dependence for refractory metals has been found. In this paper, we will study ion beam mixing in metal/CuO and metal/SiO₂ systems. The bond strength of the substrate may influence the interfacial reaction in M/CuO and M/SiO₂ systems for this low temperature ion irradiation processing.

II. Experimental procedure

CuO films (160 nm) were prepared by reactive sputtering Cu in oxygen ambient on SiO₂ substrates. The base pressure in the sputtering chamber was $5-9 \times 10^{-7}$ Torr. The CuO/SiO₂ substrate was then baked at 300°C for 30 minutes before the coatings of metal films. The metals were deposited onto CuO/SiO₂/Si substrates by either e-beam heating (Zr, Ti and Cr) or resistance heating deposition (Ag). For Zr/CuO reaction study, CuO bulk ceramic sample, which was mechanically polished, was also chosen as a substrate material. The film thickness was

measured by Rutherford backscattering spectrometry showing that the film thickness for Zr, Ti, Cr and Ag are 110 nm, 62 nm, 59 nm and 72 nm, respectively.

Thermal annealing was carried out in a vacuum of 2×10^{-7} Torr at temperatures ranging from 410°C to 610°C for a duration of 30 minutes. Each sample was Xe ions irradiated with energy to place the mean range of ions beyond the metal/CuO interface, except for Ag/CuO sample. For Zr/CuO sample, 600 Kev Xe^{++} ions were irradiated; for Ti/CuO and Cr/CuO samples, 300 Xe^{+} ions were irradiated at 240°C. For Ag/CuO sample, room temperature Xe^{+} ions irradiation with energy of 300 Kev was performed. The dose was 1.5×10^{16} Xe/cm^2 for all samples. The current density was 1 $\mu\text{A}/\text{cm}^2$.

Rutherford backscattering spectrometry (RBS) at 2.1–3.0 MeV He^{++} was used as the principal method of analysis, the tilt angle of Zr/CuO, Ti/CuO and Cr/CuO samples was 7°. For Ag/CuO sample, the tilt angle was 20°. Phase identification was performed by X-ray diffraction using both Guinier camera and diffractometer. The morphology of selected samples was also examined by employing a scanning electron microscope (SEM).

III. Results

Significant reactions in Zr/CuO and Ti/CuO systems have been found after either thermal annealing or ion irradiation. The backscattering spectra of Zr film on CuO bulk ceramic substrates (dash line) and after annealing of samples at 550°C for 30 minutes (solid line) and after 600 Kev Xe^{++} ions irradiation to a dose of 1.5×10^{16} Xe/cm^2 (dots) are shown in Fig.1. From these spectra, it is clear that the signal heights of Zr decrease and the signal heights of Cu near high energy edge increase and the signal from a portion of oxygen appears in the Zr film after thermal annealing and ion irradiation. The compositions in different layers are calculated, based on RUMP program [4], to be $\text{Zr}_1\text{O}_{2.1}$ near the surface and $\text{Cu}_{1.9}\text{O}$ near the CuO substrate, indicating that two layers of reacted products have been formed on CuO substrates. The X-ray diffraction data confirm the presence of two compounds ZrO_2 and Cu_2O , showing that the reaction $4\text{CuO} + \text{Zr} \rightarrow 2\text{Cu}_2\text{O} + \text{ZrO}_2$ occurs after thermal annealing and ion irradiation. Figure 2 shows the X-ray diffraction spectrum of an irradiated Zr/CuO sample. It is worthwhile to mention that the thickness of Cu_2O layer is about 500 nm, much larger than the range of ions. This kind of long range migration of oxygen to the surface is possibly due to the beam heating effect, which is more significant to bulk insulator CuO substrate.

Spectra, similar to those for Zr/CuO, are obtained for Ti/CuO sample after thermal annealing at 410°C for 30 minutes (solid line) and 1.5×10^{16} $\text{Xe}^{+}/\text{cm}^2$ irradiation at 240°C (dots) as shown in Fig.3. From these spectra, the CuO phase is totally transformed to Cu_2O due to oxygen out-diffusion. After thermal annealing and irradiation, the measured ratios of the signal heights of Ti, Cu and O in the top Ti oxide layer and Cu oxide near SiO_2 substrate are $\text{Ti}_1\text{O}_{1.6}$ and Cu_2O for annealed sample and $\text{Ti}_1\text{O}_{1.8}$ and Cu_2O for irradiated sample. The phase identification by X-ray diffraction with Guinier camera, indicates that the Cu oxide phase next to SiO_2 is Cu_2O , while

the phase identification of Ti oxide is complicated, because there are many Ti oxide phases. No diffraction lines corresponding to TiO and TiO_2 phases were found.

From Fig.4, backscattering spectra showed that no detectable reaction in Cr/CuO system has been found after thermal annealing at 410°C for 30 minutes and $1.5 \times 10^{16} \text{ Xe/cm}^2$

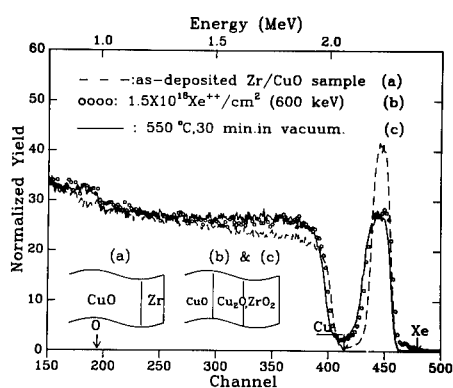


Fig.1. 2.1 MeV backscattering spectra of 110 nm Zr on CuO substrate before and after thermal annealing and ion irradiation. (7° tilt)

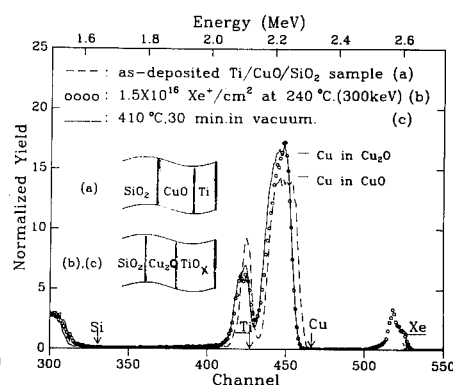


Fig.3. 3.0 MeV backscattering spectra of 62 nm Ti on 160 nm CuO film before and after thermal annealing and ion irradiation at 240°C . (7° tilt)

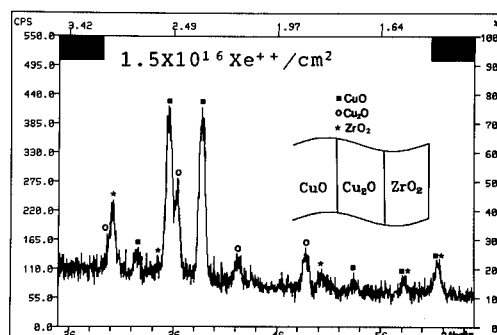


Fig.2. X-ray diffraction lines from diffractometer for Zr/CuO sample after ion irradiation. This shows that Cu_2O and ZrO_2 phases are formed.

irradiation at 240°C . No obvious islanding effect has been found by scanning electron microscope.

For Ag/CuO system, Ag atoms tend to coalesce or to ball up into islands upon high temperature annealing. Secondary electron micrographs (SEM) show that Ag atoms have coalesced

into islands less than $1\text{ }\mu\text{m}$ in diameter after 610°C for 30 minutes annealing in vacuum. From backscattering spectra in Fig. 5., the broadening of Ag and Cu peaks corresponds to the balling of Ag thin film on CuO surface. The RBS simulation result shows that no reaction has taken place between Ag and CuO. Ion beam irradiation to a dose of $1.5 \times 10^{16} \text{Xe}^+/\text{cm}^2$ induces total sputtering of Ag on CuO surface due to the high sputtering yield of Ag. The reaction results are summarized in Table I for the four M/CuO systems.

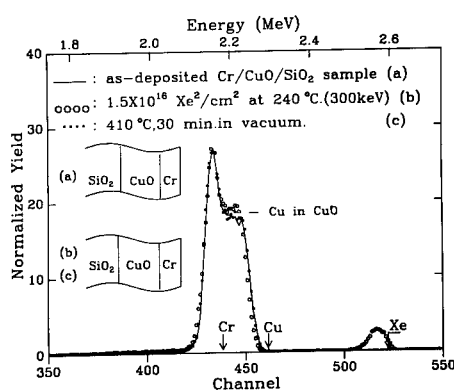


Fig.4. 3.0 MeV backscattering spectra of 59 nm Cr on 160 nm CuO film before and after thermal annealing and ion irradiation at 240°C . (7° tilt)

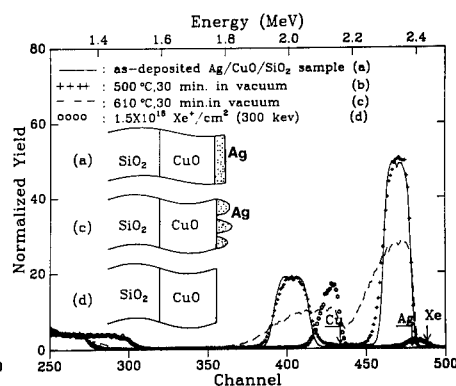


Fig.5. 2.8 MeV backscattering spectra of 72 nm Ag on 160 nm CuO film before and after thermal annealing and ion irradiation. (20° tilt)

Table I: thermally and ion-induced reactions in M/CuO:

reactants	processing	end structures
CuO/Zr	550°C , 30min	$\text{CuO}/\text{Cu}_2\text{O}/\text{ZrO}_2$
	$1.5 \times 10^{16} \text{Xe}^{++}/\text{cm}^2$ at RT	$\text{Cu}_2\text{O}/\text{ZrO}_2$
CuO/Ti	410°C , 30min	$\text{Cu}_2\text{O}/\text{TiO}_x$ ($1 < x < 2$)
	$1.5 \times 10^{16} \text{Xe}^+/\text{cm}^2$ at 240°C	$\text{Cu}_2\text{O}/\text{TiO}_x$ ($1 < x < 2$)
CuO/Cr	410°C , 30min	CuO/Cr
	$1.5 \times 10^{16} \text{Xe}^+/\text{cm}^2$ at 240°C	CuO/Cr
CuO/Ag	610°C , 30min	$\text{CuO}/\text{Ag}(\text{balled up})$
	$1.5 \times 10^{16} \text{Xe}^+/\text{cm}^2$ at RT	CuO (Ag sputtered)

IV. Discussion

Thermodynamic considerations based on the heats of reaction have been applied to explain the reaction in metal/ SiO_2 and metal/ Al_2O_3 systems [5], i.e. a chemical reaction is favorable when the difference between the heats of formation of the reaction products and the reactants is negative. The thermodynamic predictions are consistent with experimental observation in these two systems. In metal/CuO systems, we calculate the heats of reaction at 300 K, assuming that the reaction products are Cu_2O and metal oxides [6,7]. The results of these calculations for all possible combinations of Cu_2O and oxides are plotted in Fig.6. The reaction in both Zr/CuO and

Ti/CuO systems take place, because the corresponding heats of reaction are large negative. Although Cr/CuO reaction is thermodynamically favorable, the ΔH° is approaching zero. No significant reaction occurs after 410°C, 30 minutes annealing. From Fig.6., it is found that Ag/CuO reaction is not thermodynamically favorable, and Ag atoms tend to coalesce on the CuO surface after 610°C for 30 minutes annealing.

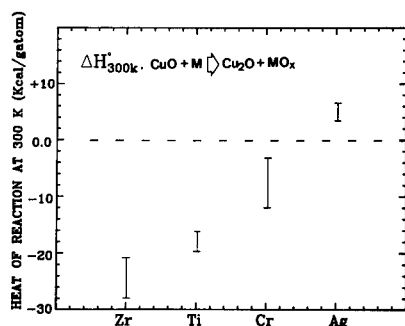


Fig.6. Calculated heats of reaction at 25°C for various metals with CuO.

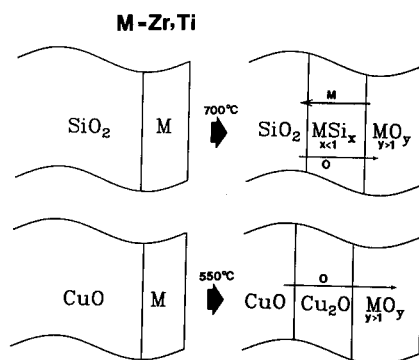


Fig.7. Schematic diagrams showing the different reaction layers in M/SiO₂ and M/CuO after thermal annealing.

It is of interest to compare the reacted layers in both M/SiO₂ and M/CuO systems after thermal annealing. For refractory metals (Zr, Ti and V) on SiO₂ [8], two layer structures, a metal rich silicide and metal oxide layer form after high temperature annealing. Oxygen atoms released from dissociation of SiO₂ diffuse and dissolve into the whole region of the refractory metal films, which act as sinks to the oxygen; meanwhile, the metal atoms next to the SiO₂ react with the free Si to form silicide. For refractory metals (Zr, Ti) on CuO after thermal annealing, phase transformation takes place from CuO to Cu₂O due to oxygen out-diffusion to the sink materials, such as Zr and Ti etc., and top metal layer is oxidized. Cu₂O, instead of pure Cu or Cu alloy, forms near the interface of CuO and MO_x. The sample geometry after thermal annealing for both M/SiO₂ and M/CuO is drawn in Fig.7.

For CuO/SiO₂/Si sample, phase transformation from CuO to Cu₂O occurs in vacuum after 750°C annealing for 30 minutes. In Zr/CuO/SiO₂/Si and Ti/CuO/SiO₂/Si samples, Zr and Ti layers may act as sinks for oxygen. The transformation temperature can be greatly reduced to 400-550°C. In contrast, Ag on CuO substrate can not act as a sink for oxygen, because no interfacial reaction occurs upon thermal annealing. However, Ag can not be chosen as a cap layer on CuO to prevent oxygen loss, because Ag atoms tend to coalesce on CuO substrate after high temperature annealing. It is of interest to examine the behavior of Ag layer on high T_c superconductor film upon 600°C annealing,

since Ag is currently used as a contact material. So far the behavior of Cr on CuO is not clear after high temperature annealing, and further work needs to be done.

In our study, we also performed ion beam mixing study in M/CuO and M/SiO₂ systems. The previous work showed that the collisional, diffusional and chemical processes were involved in the M/oxides ion mixing. Ballistic mixing or no mixing occurs in refractory metal/SiO₂ systems, and the prediction of the reaction enthalpy of the metal and substrate is still in general valid for the interfacial reaction. Unlike Zr/CuO and Ti/CuO systems, no significant reaction has been observed in Zr/SiO₂ and Ti/SiO₂ samples after high dose ion irradiation, meaning that there is strong substrate dependence for ion irradiation induced reaction in M/oxide samples. We propose that the mobility of oxygen in the substrate and the bond strength in the substrate are most likely to influence the interfacial reaction. It is not easy to break the bonding between Si and oxygen, compared with the bonding between Cu and oxygen, because the bond strength for Si-O, (106 kcal/mole) is more than twice that for Cu-O, (44 kcal/mole) [9]. In this sense, bond strength in the substrate materials, besides heats of reaction, can also influence the chemical reactivity between the metal layer and substrate.

In summary, the chemical reactivity between metal layers (Zr, Ti, Cr and Ag) and CuO substrates are different. The interfacial reaction can be determined by the heats of reaction. The bond strength of the substrate may also influence the chemical reactivity between metal and substrate upon ion irradiation.

Acknowledgments

This work was supported in part by DARPA (K.Rhyne). We would like to thank G.Schmidt at the Technical Operations Laboratory for preparing CuO films.

References

- [1] B.R.Appleton, H.Naramoto, C.W.White, O.Holland, C.Mchargue, G.C.Farlow, J.Marayan, J.M.Williams, Nucl.Instrum.Methods, B1 167, (1984).
- [2] J.E.E.Baglin, G.J.Clark, Nucl.Instrum.Methods, B7/8, 881, (1985).
- [3] G.C.Farlow, B.R.Appleton, L.A.Boatner, C.J.Mchargue, C.W.White, G.J.Clark, J.E.E.Baglin, Mater.Res.Soc.Symp.Proc., ed. by P.K.Biegelsen, G.A.Rozgonyi, and C.V.Shank (MRS, Pittsburgh, 1985), V45, 137.
- [4] L.R.Doolittle, Nucl.Instrum.Methods, B9, 344, (1985).
- [5] X.-A.Zhao, E.Kolawa and M.-A.Nicolet, J.Vac.Sci. Technol. A4, 3139, (1986).
- [6] M.-A.Nicolet and S.S.Lau, in VLSI Electronics Microstructure Science, V6, ed. by N.G.Einspruch, (Academic press, 1983), 453.
- [7] The Oxide Hand book (second Edition), edited by G.V.Samsonov, (IFI/Plenum, 1982).
- [8] S.Q.Wang and J.W.Mayer, J.Appl.Phys., 64, 4711, (1988).
- [9] F.P.Fehlner and N.F.Mott, Oxid.Metals, 2, 59, (1970).

ION BEAM MIXING OF HIGH- T_c SUPERCONDUCTOR COMPONENTS.

P. Børgesen* and D. A. Lilienfeld#

*) Department of Materials Science and Engineering

#) National Nanofabrication Facility

Cornell University
Ithaca, NY 14853

ABSTRACT

The design of the necessary multilayer structures for producing superconducting thin films by ion beam mixing methods requires, among others, the knowledge of the individual (binary) mixing rates. In order to measure these, various combinations of Y, Ba, Cu, and Bi were irradiated with 600 keV Xe-ions at 80K and 300K. The systems exhibited a wide range of mixing behaviors which are also of fundamental interest. Ba and Cu readily formed the BaCu phase, and further mixing with Cu progressed only via binary collision mechanisms. At 80K Cu and Y were rapidly mixed in any ratio by thermal spikes, whereas a Cu rich sample rapidly formed the Cu₆Y phase at 300K. Ba could not be mixed into Y or a Y-Cu mixture. Finally, irradiation of polycrystalline layers of Cu and Bi apparently lead to rapid motion of Bi along grainboundaries at both temperatures.

INTRODUCTION

The discovery of high temperature superconductors has motivated an interest in a wealth of new systems for which the fundamental ion-solid interaction parameters are unknown. As part of an ongoing effort to produce high- T_c superconducting thin films by ion beam mixing, as well as an interest in basic ion-solid interactions, the behaviour of the various components during mixing is being investigated.

Until now, the elements studied most thoroughly are those of the Y-Ba-Cu-O system. These materials appear to be quite unfavourable for the production of superconducting films by ion beam mixing. Originally, it was hoped that an appropriately designed multilayer sample would be mixed sufficiently during the implantation of the necessary oxygen, but it appears that substantial pre-mixing, for instance by implantation of Ba, is needed [1]. However, a study of the basic materials properties seems to suggest that the newer compounds, such as Bi-Ca-Sr-Cu-O, might be more suitable for this approach. Least promising would seem to be the mixing of Cu and Bi, which are miscible in the liquid, but immiscible in the solid phase.

Attempts were made to measure basic mixing rates for combinations of the elements Y, Ba, Cu, and Bi. For most of these, the design of samples that will survive transfer to implanter and analysis chamber is a major problem. For instance only relatively thin films of Ba and Y buried in a more stable material (e.g. Cu) could be studied. The measurement of quantitative mixing efficiencies was complicated by the formation and stability of phases such as Cu₆Y and BaCu.

EXPERIMENT

Films were deposited on SiO₂ substrates in an ion pumped system by electron beam evaporation. The base pressure was $\sim 10^{-7}$ Torr. Yttrium and barium films were covered by a Cu film for protection. Even with the Cu protective layer the Y and Ba thicknesses were limited as thicker films would have caused rapid deterioration of the samples upon exposure to air (see below). In spite of these precautions, only limited amounts of mixing were

possible before the samples would no longer survive the transfer to the analysis chamber.

Samples were mounted on aluminum plates with silver or carbon paint and irradiated with 600 keV Xe-ions. Typical fluxes were $\sim 5 \times 10^{12} \text{ cm}^{-2} \text{ s}^{-1}$. Irradiations were performed with substrates at both 300K and $\sim 80\text{K}$.

Before and after irradiation, samples were analysed by Rutherford Backscattering Spectrometry (RBS) at several energies and angles of incidence. Results were evaluated by comparison with spectra simulated by means of the computer program RUMP [2]. Initial sample compositions are listed in Table 1.

TABLE 1: Initial sample compositions. Thicknesses in units of $10^{17} \text{ atoms/cm}^2$.

Sample #	Layer 1		Layer 2		Layer 3		Layer 4	
	Elem.	Thickn.	Elem.	Thickn.	Elem.	Thickn.	Elem.	Thickn.
1	Cu	4.8	Ba	1.29	Cu	7.2		
2	-	5.27	-	5.44				
3	-	4.6	-	0.23	Cu	34		
4	Cu	5.0	Y	2.1	Cu	7.4		
5	-	5.0	-	1.2	-	7.5		
6	-	5.2	-	0.28	-	35		
7	Cu	1.9	Y	2.43	Ba	1.02	Y	3.6
8	Cu	4.7	Bi	10.7				
9	Bi	2.05	Cu	35				

We express the "degree of mixing" as the variance, σ^2 , of the atomic displacement distribution at the interface in question. In the literature [3, 8] distributions are often quantified in terms of $Dt (= \sigma^2/2)$, because of the formal similarities to diffusion experiments. Where applicable, elemental distributions at interfaces were fitted with complementary error functions, $\text{C-erfc}[x/\sigma/2]$, with σ as fit parameter. We define the mixing rate as the slope $\Delta\sigma^2/\Delta\phi$ of the variance versus fluence (ϕ) curve, and the 'mixing efficiency' [3] as $\Delta\sigma^2/2\Delta\phi F_D$. The damage energy per unit track length, F_D , was estimated using the Monte Carlo computer program TRIM [4].

RESULTS

Ba-Cu. These elements are virtually insoluble in the solid state, but soluble in all proportions in the liquid. The phase diagram [5] shows the existence of two distinct phases in this system, the line compounds BaCu and Cu_{13}Ba . Both Ba and the alloys are extremely reactive in air.

An attempt to deposit a 1000 Å thick Ba film between two Cu layers (sample #1) resulted in the formation of a layer of a composition near BaCu (Fig. 1). It is believed that this phase formation is caused primarily by the substrate heating due to the deposition of the first Cu layer, which required considerably more power than the Ba evaporation. The deposition of $\sim 4000 \text{ Å}$ Ba directly on the SiO_2 , followed by a similar amount of Cu (sample #2), did not have such an effect. Instead, the thicker Ba film was found to contain 3-4 O-atoms per Ba-atom (after exposure to air). The top Cu layer was not significantly oxidized at this time, but rapidly degraded even in a desiccator. Since the more gradual deterioration of the samples with the thinner Ba (#1 and #3) was seen to progress from the sample edge we suggest

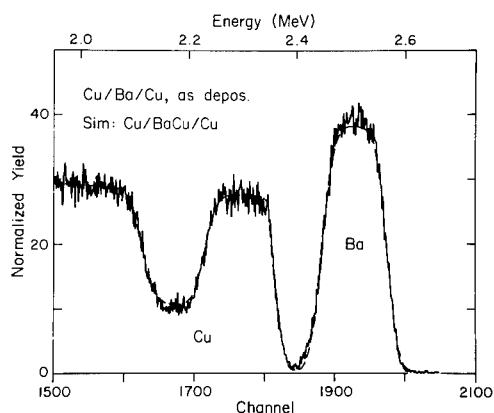


Fig. 1. RBS spectrum for 3.04 MeV ^4He ions incident on Cu/Ba/Cu sample at 70° to surface normal. Broken curve -- simulation [2] assuming 480 Å Cu on top of BaCu layer, all on thick Cu.

that the oxygen enters the Ba film (as O_2 or H_2O [6]) laterally rather than through the top Cu layer. This effect clearly limits the Ba film thicknesses that can be used. Even if we should succeed in depositing unmixed Cu and Ba layers in a multilayer sample, we suggest that it would take only a very small irradiation fluence to produce the BaCu phase. Aiming for the $\text{Y}_1\text{Ba}_2\text{Cu}_3$ compound the question remains whether this may be mixed any further to produce other Ba-Cu ratios. Models for regular solutions [7,8] predict the largest heat of mixing for the 1:1 composition, i.e. in the absence of phase formation thermal spike mixing of a Ba-Cu bilayer sample would be expected to lead to the BaCu composition. Except for the possible formation of the Cu_{13}Ba phase only ballistic effects should therefore drive the mixing past the BaCu phase.

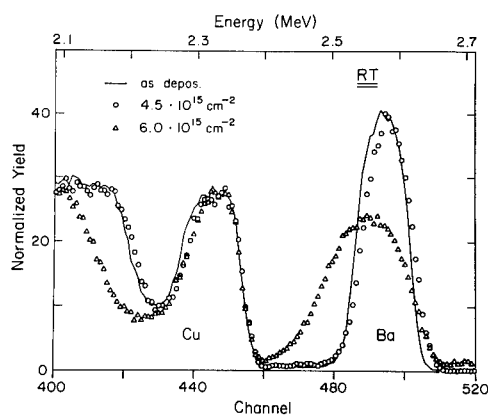


Fig. 2. RBS spectra for 3.07 MeV ^4He ions incident on Cu/BaCu/Cu sample (see text) at 60° , before and after room temperature Xe irradiation. Solid curve -- as deposited; (o) -- after $4.5 \times 10^{15} \text{ cm}^{-2}$; (Δ) -- after $6 \times 10^{15} \text{ cm}^{-2}$ (spectrum also shows O-content, see text).

Irradiation of the Cu/BaCu/Cu samples (#1 and #3) with a limited fluence of Xe ions ($\leq 5 \times 10^{15} \text{ cm}^{-2}$) led to a very small amount of mixing (Fig. 2). The sudden broadening of the Ba signal at slightly larger fluences is caused by the uptake of almost 4 O-atoms per Ba-atom upon exposure to air (compare above). Apparently, the irradiation resulted in a breakdown of the protective Cu surface layer. For still larger fluences (at 80K) the Ba was seen to redistribute in a manner that suggests a sudden accumulation of Ba, in some form, near the surface, rather than further mixing into the Cu. The use of a

very thin Ba film (sample #3) allowed a more sensitive study of the large-fluence behaviour: The initial mixing did not change the shape or width of the narrow Ba (BaCu) layer substantially. However, after room temperature irradiation with 9×10^{15} Xe-ions/cm² almost all of the Ba was suddenly found at the surface, again in a quite narrow distribution (100-200 Å). In contrast, a similar irradiation at 80K suddenly led to a roughly uniform distribution of Ba at all depths. We speculate that the room temperature results indicate a radiation enhanced motion of Ba to the surface along Cu grain boundaries, whereas the low temperature irradiation probably leads to precipitation of the BaCu phase throughout the Cu.

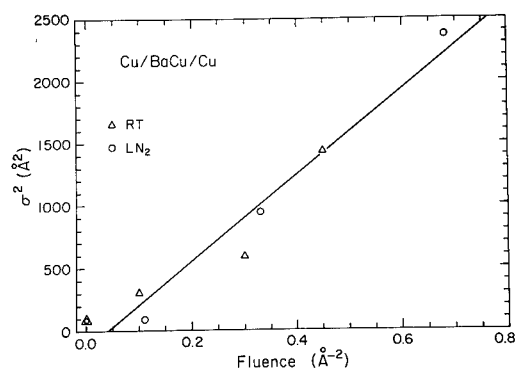


Fig. 3. Variance of atomic distribution at BaCu-Cu interface vs. Xe fluence. (Δ) -- at 300K; (○) -- 80K. Straight line is least squares fit to 300K values, slope corresponds to mixing rate of $2.8 \times 10^3 \text{ Å}^4$.

Figure 3 shows the interface intermixing σ^2 as a function of Xe fluence ϕ , for those samples not containing significant amounts of oxygen. For sample #3 the signal was fitted by a gaussian, and the broadening evaluated in a manner similar to that used in 'marker' experiments [3,9]. The scatter in the data is quite large, but there does not appear to be a significant difference between room temperature and liquid nitrogen temperature results. The small average mixing rate indicated by the straight line corresponds to a mixing efficiency of about $5 \text{ Å}^5/\text{eV}$, in excellent agreement with predictions based on collisional models [10,11]. We conclude that neither thermal spikes [8] nor radiation enhanced diffusion [12] contribute measurably to the mixing.

Cu-Y. The phase diagram [5] for this system shows the existence of a number of phases ranging from CuY to Cu₆Y. Room temperature irradiation of samples #4-6 with Xe fluences as low as 10^{15} cm^{-2} was found [13] to result in the formation of the Cu₆Y phase. None of the compositions corresponding to the less Cu rich phases were observed. The negligible solubility of Cu in Y, and vice versa, seemed to prevent the further dilution of the available yttrium, and the phase remained stable during continued irradiation.

The observed phase formation could be suppressed by cooling the substrate to 80K, and a mixing rate of $\sim 4 \times 10^4 \text{ Å}^4$ was determined. This value exceeds the estimated ballistic mixing rate by more than a factor of 5, and agrees with the thermal spike model of Johnson et al. [8] to within a factor of two [13].

Ba-Y. The heat of mixing for this system is positive and quite large (90 kJ/mole, [7]), so that we might even expect ballistic mixing effects to be counteracted by subsequent de-mixing during the thermal spike [14]. Indeed, irradiation did not result in any measurable intermixing of Ba and Y, neither at 300K nor at 80K. Figure 4 shows that the upper Y layer is mixed with the

Cu (as expected, see above), whereas the Ba distribution remains unchanged. The same was found to be the case at liquid nitrogen temperature.

For the production of the ternary alloy by ion beam mixing of multilayers one might attempt to mix Ba into an already mixed Cu-Y layer. However, the results are again discouraging. Unlike for samples #4-6 the Y was the more abundant element in the present sample, and the spectra corresponding to Xe fluences of $3 \times 10^{15} \text{ cm}^{-2}$ or more are seen (Fig. 4) to agree with the formation of a layer of average composition near CuY, capped by a copper oxide. There was no indication that continued irradiation led to Ba mixing into any of these layers either, until the sample started to deteriorate.

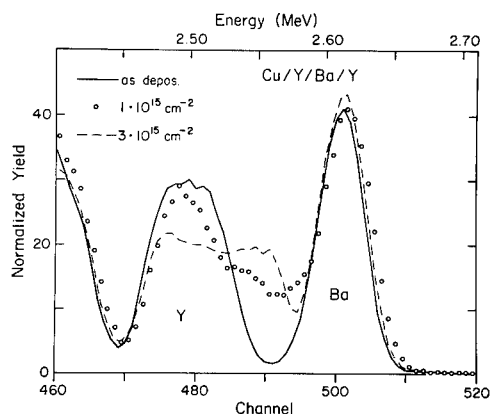


Fig. 4. RBS spectra for 3.07 MeV ^4He ions incident on Cu/Y/Ba/Y sample at 60° , before and after room temperature Xe irradiation. Solid curve -- as deposited; (o) -- after 10^{15} cm^{-2} ; broken curve -- $3 \times 10^{15} \text{ cm}^{-2}$.

Cu-Bi. The solid solubility for this system is negligible, but the liquid is miscible in all proportions [5]. Averbach et al. [15] irradiated epitaxial layers of these elements with 0.5-1 MeV Kr ions and found a mixing efficiency of $95 \text{ \AA}^5/\text{eV}$ at 6K. At room temperature no mixing occurred.

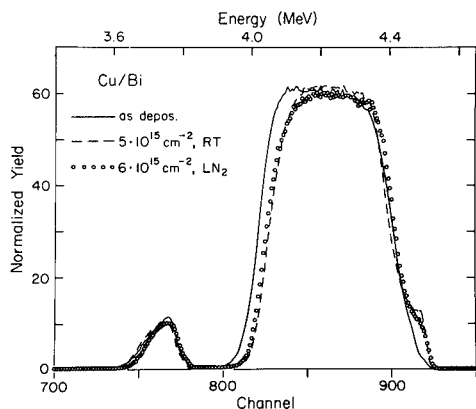


Fig. 5. RBS spectra for 4.87 MeV ^4He ions incident on Cu/Bi sample at 60° before and after Xe irradiation. Solid curve -- as deposited; broken curve -- after $5 \times 10^{15} \text{ cm}^{-2}$ at 300K; (o) -- after $6 \times 10^{15} \text{ cm}^{-2}$ at 80K.

The production of epitaxial layers is not very attractive for most applications. However, for polycrystalline films, Bi might penetrate the Cu along grain boundaries rather than truly mixing into it [15]. Indeed, Xe-irradiation of a 550 \AA Cu film on top of a thick layer of Bi (#8) was seen

to lead to the rapid penetration of a small amount of Bi to the surface (Fig.5). This behaviour was independent of temperature between 80K and 300K. The 'step' in the high energy edge of the Bi signal is characteristic of either phase formation or grain boundary motion, rather than diffusional intermixing. Phase formation, however, would not explain the observed continuous increase in step height with Xe fluence, and TEM of a mixed sample showed no sign of a compound phase.

Room temperature irradiation of a 725 Å Bi film on top of Cu (#9) failed to produce a similar effect, providing yet another argument against phase formation. Instead we observed a very large sputter yield (≥ 60 Bi/Xe), and no measurable intermixing even after irradiation with 8×10^{15} Xe-ions/cm².

For the Y-Ba-Cu system there is not much hope that pre-implantation of oxygen will facilitate the subsequent mixing sufficiently [1]. However, the same is not necessarily the case for the Bi-Ca-Sr-Cu system. Preliminary RBS measurements on the room temperature irradiation of sample #8 with 50 keV O-ions at fluences up to 2.4×10^{17} cm⁻² show a quite different behaviour (gradual penetration of the Bi to the surface, but no 'step' in the Bi signal, compare Fig. 5), probably due to the very different energy deposition. Further studies are in progress.

CONCLUSIONS

The production of superconducting thin films by ion beam mixing of the metals and implantation of the oxygen is not a very promising approach for the Y-Ba-Cu system. Ba could not be mixed effectively into Y or a Y-Cu mixture, and would only form the BaCu phase with Cu.

The method may be more suitable for the Bi-Ca-Sr-Cu system, but polycrystalline layers of Bi and Cu are not readily mixed at practical temperatures.

ACKNOWLEDGEMENTS

This work was supported in part by a contract from DARPA (K. Rhyne). We acknowledge the Materials Science Center (NSF) at Cornell University for the use of their thin film facilities. The National Nanofabrication Facility is supported by the National Science Foundation under Grant ECS-8619049, Cornell University and industrial affiliates.

REFERENCES

- [1] D. A. Lilienfeld and P. Børgesen, presented at the 1988 MRS Fall Meeting, Boston, MA, 1988 (unpublished).
- [2] L. R. Doolittle, Nucl. Instrum. Meth. B9, 344 (1985).
- [3] B. M. Paine and R. S. Averback, Nucl. Instrum. Meth. B7/8, 666 (1985).
- [4] J. P. Biersack and L. G. Hagmark, Nucl. Instrum. Meth. 174, 257 (1980).
- [5] Binary Alloy Phase Diagrams, ed. T. B. Massalski (ASM, 1986).
- [6] Handbook of Chemistry and Physics, CRC Press (1988).
- [7] A. R. Miedema, F. R. de Boer, and R. Boom, CALPHAD 1, 341 (1977).
- [8] W. L. Johnson, Y. T. Cheng, M. Van Rossum, and M.-A. Nicolet, Nucl. Instrum. Meth. B7/8, 657 (1985).
- [9] P. Børgesen, D. A. Lilienfeld, and H. H. Johnson, submitted to J. Appl. Phys.
- [10] A. Gras-Marti and P. Sigmund, Nucl. Instrum. Meth. 180, 211 (1981).
- [11] P. Sigmund and A. Gras-Marti, Nucl. Instrum. Meth. 182/183, 25 (1981).
- [12] R. Sizmann, J. Nucl. Mater. 69/70, 386 (1978).
- [13] P. Børgesen and D. A. Lilienfeld, submitted to J. Appl. Phys.
- [14] R. S. Averback, Nucl. Instrum. Meth. B15, 675 (1986).
- [15] R. S. Averback, D. Peak, and L. J. Thompson, Appl. Phys. A39, 59 (1986).

PART III

Microstructural
Changes/Characterization

ANGLE OF INCIDENCE EFFECTS IN ION BEAM PROCESSING

J.M.E. HARPER*, S.E. HÖRNSTRÖM**, P.J. RUDECK*
and R.M. BRADLEY***

*IBM Thomas J. Watson Research Center, Yorktown Heights NY 10598

**Linköping University, Linköping, Sweden

***Department of Physics, Colorado State University, Fort Collins CO 80523

Abstract

The angle of incidence of ion bombardment is an important processing parameter, which can strongly affect the shape, composition and microstructure of bombarded surfaces. We describe several phenomena directly related to the angle of ion incidence during ion beam etching and ion beam assisted deposition. First, the development of surface ripple topography during ion beam etching is modeled. Surface perturbations are shown to grow under ion bombardment, while surface self-diffusion acts to select a characteristic wavelength. The orientation of these characteristic ripples changes by 90° as the angle of ion incidence is varied from near-normal to near-glancing angle. The second example is the effect of angle of incidence on the etching rate of Ta under mixed Ar- O_2 ion bombardment. For pure Ar bombardment, the sputtering yield of Ta increases with angle of ion incidence slower than $\sec\theta$, producing a maximum etch rate at normal incidence. Above a critical pressure of O_2 , however, the yield increases faster than $\sec\theta$ dependence, producing a maximum etch rate at a non-normal angle of incidence. The third example is the effect of angle of incidence on the preferential sputtering of Al relative to Cu in Al-5%Cu thin films. Films deposited by evaporation with simultaneous Ar ion bombardment at 500 eV show a depletion of Al relative to Cu. This composition change is enhanced by increasing the angle of incidence away from normal, resulting in a higher Cu concentration in a film deposited on a tilted surface. Finally, a mechanism is described for the generation of oriented microstructure in films deposited under simultaneous glancing-angle ion bombardment, demonstrated previously for Nb. Grain orientations are selected which allow channelling of the ion beam. These results show that the shape, composition and microstructure of films deposited under ion bombardment respond to changes in angle of incidence, and that these effects need further study and modeling.

I. Introduction

The effects of ion bombardment on materials at normal incidence have been well studied, and provide a variety of useful mechanisms for materials modification. Less well studied, however, is the influence of angle of incidence of ion bombardment during etching or deposition processes. In this paper, we demonstrate that the angle of ion incidence is an important processing parameter which can strongly affect the shape, composition and microstructure of bombarded surfaces and thin films. The

examples are chosen from recent studies of the effects of angle of incidence on surface ripple formation, etch rates of Ta in Ar/O₂ mixtures, preferential sputtering in Al-5%Cu, and in-plane orientation of the crystallographic microstructure of ion bombarded Nb films.

II. Surface ripple formation

Prolonged ion beam etching has often been observed to produce periodic height modulations (ripples) on the surfaces of both amorphous and polycrystalline materials (1,2). The wavelength of these ripples is typically in the range of hundreds to thousands of angstroms, and their orientation relative to the ion beam changes with angle of incidence (3), as shown in Fig. 1. For near-normal angles of incidence, the wave vector of the modulations is parallel to the component of the ion beam in the plane of the surface. For incidence angles above a critical angle, near grazing incidence, the wave vector is perpendicular to this component of the beam direction. An understanding of ripple formation mechanisms is important in all applications where the shape of ion etched surfaces must be controlled.

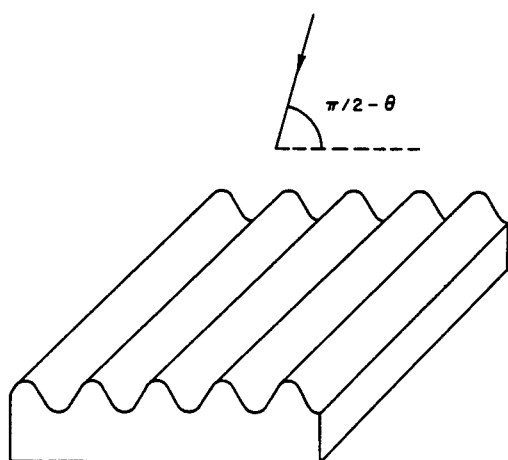
We describe in reference 1 a model of ripple formation which accounts for the change in orientation and approximates the wavelengths reported. To date, there are few quantitative studies with which to compare details. However, the model makes specific predictions for the dependence of wavelength on ion flux and temperature which can be tested. The removal of material from a surface by sputtering is governed by the deposition of energy at the surface from ions impacting nearby. The model of ripple formation is based on Sigmund's description of the distribution of energy deposition, characterized by an average depth, and Gaussian widths parallel and perpendicular to the beam direction (4).

The steady-state shape of a surface depends on the relative etch rates at the troughs and crests of surface perturbations. For normal incidence bombardment, the energy deposited at the bottom of a trough exceeds that deposited at the top of a crest, due to the greater proximity of nearby impacts in the trough (Fig. 2). Thus, troughs etch faster than crests, and surface perturbations of all wavelengths should be unstable under ion bombardment. Countering this instability is the smoothing effect of surface self diffusion, which tends to erase short-wavelength perturbations, and therefore selects a steady state wavelength of ripples.

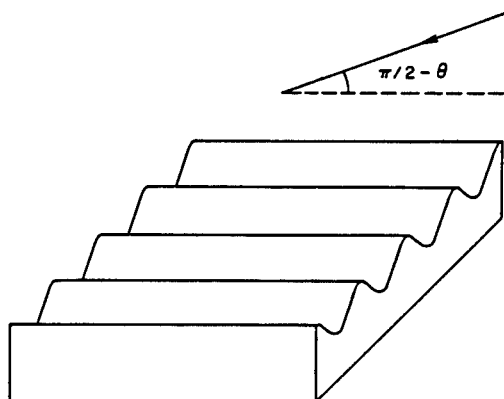
Under conditions of high temperature T and low ion flux f , such that surface self diffusion (characterized by an activation energy ΔE) dominates over ion activated diffusion, the ripple wavelength λ depends on flux and temperature according to (1):

$$\lambda \sim (fT)^{-1/2} \exp(-\Delta E/2k_B T)$$

In addition, the orientation of the ripples is determined by the smaller wavelength of ripple wave vectors either parallel or perpendicular to the in-plane beam direction. The angular dependence of the wavelength is shown in Fig. 3, for which θ is measured from the surface normal. The details of the linear stability analysis and the limits of validity are given in reference 1. The occurrence of ripples in ion beam

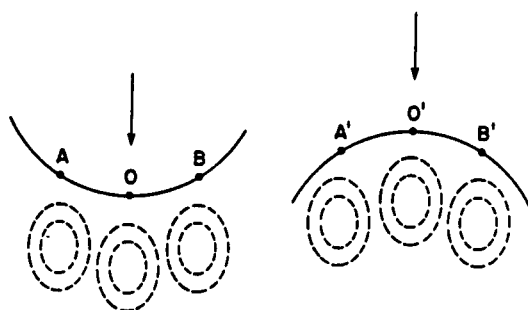


(a)

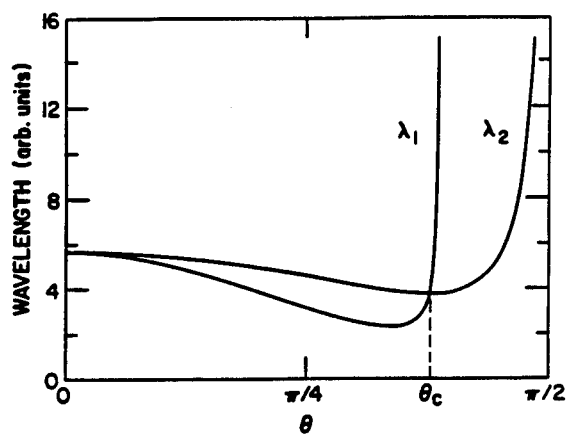


(b)

1. Dependence of ripple orientation on the angle of ion incidence (1).



2. Comparison of energy deposition in a trough and on a crest (1).



3. Wavelengths of ripples as a function of angle of ion incidence. Ripples with wave vector parallel to the in-plane component of the ion beam direction are shown as λ_1 , and the perpendicular orientation is shown as λ_2 (1).

etching is therefore based on the fundamental sputtering process, and the distinct change in direction with angle of incidence underscores the importance of angle as a control parameter.

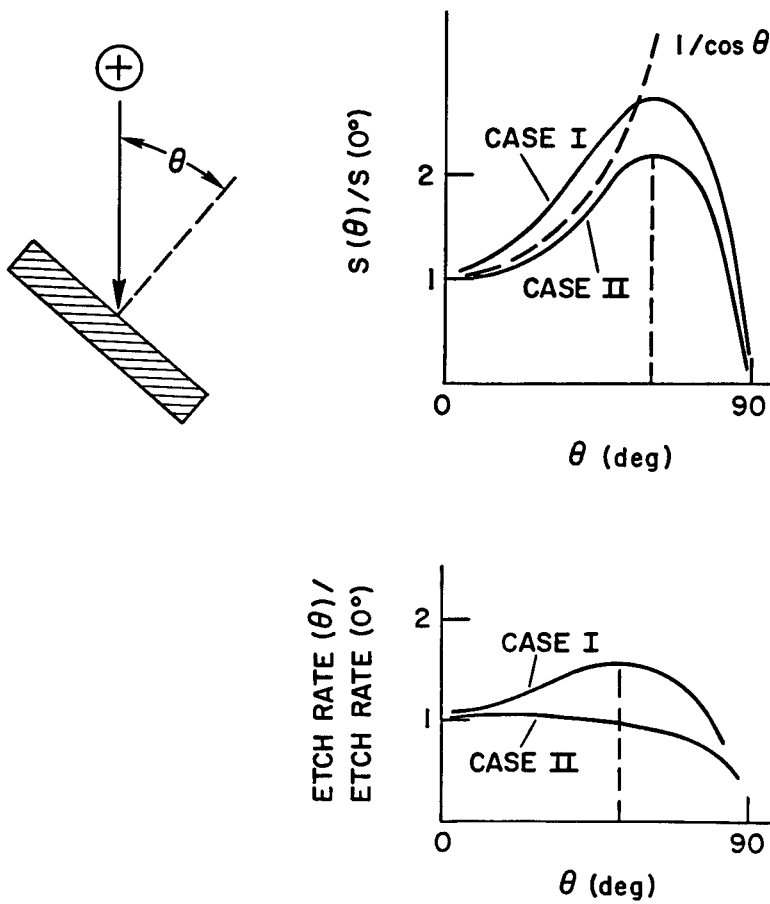
III. Ion beam etching of Ta in Ar/O₂

While the occurrence of ripples on ion etched surfaces has not been extensively modeled, the increase of sputtering yield with angle is a more familiar and well-modeled phenomenon (5). As shown in Fig. 4, the sputtering yield of typical materials increases with angle of incidence, reaches a maximum at an angle in the range 50-80°, then decreases to zero at the angle of total ion reflection, near 90°. The resulting etch rate, measured in thickness per unit time, depends on the product of sputtering yield and ion flux. Therefore, the etch rate may or may not have a maximum at an off-normal angle, according to whether the yield rises faster or slower than $\sec\theta$. Extensive measurements, for example by Oechsner (6), have shown that the angular dependence of sputtering yield depends on ion energy and mass. In studies of reactive ion beam etching, Okano et al. (7) showed a pronounced change in the angular dependence of the sputtering yield of SiO₂ when using C₂F₆ as compared with Ar. The sputtering yield with C₂F₆ showed far less angular dependence than the usual increase found with Ar, while the overall value increased due to the chemical etching component. We have examined the angular dependence of the sputtering yield of Ta under mixed Ar/O₂ etching, for which the etch rate is suppressed under the addition of O₂. This combination provides a complementary result to that of Okano et al. (7). We find that the increase of sputtering yield with angle for Ta is enhanced with the addition of O₂, while the absolute value decreases. The etch rate of Ta as a function of partial pressure of O₂ in Ar is shown in Fig. 5 for an ion energy of 300 eV and ion flux of 0.1 mA/cm². For all angles, the etch rate undergoes a transition to a low value at a critical pressure of O₂. However, the relative magnitudes of etch rates at normal incidence (0°) and off-normal incidence (60°) are reversed by the addition of oxygen. When the same data is shown as sputtering yield relative to the normal incidence value (Fig. 6), it is evident that the yield in pure Ar remains below $\sec\theta$, while the yield in mixed Ar/O₂ rises faster than $\sec\theta$. The practical implication is that in pure Ar, normal incidence surfaces will etch fastest, while above a critical pressure of O₂, sloping surfaces will etch fastest, enhancing the development of a faceted surface after prolonged etching. Here, we see an interplay between angle of incidence and etching gas composition which changes the overall character of etched surface profiles. Further modeling of etching in reactive gas environments is needed to understand these large changes in angular dependence of sputtering yields.

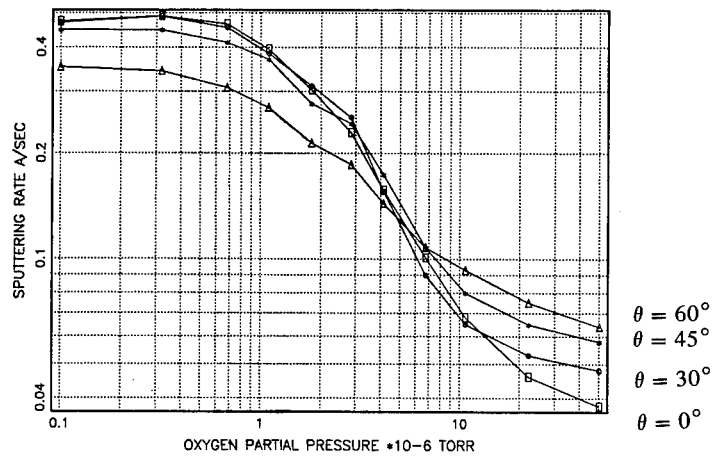
IV. Preferential sputtering in Al/5%Cu thin films

In addition to the above effects on surface shape produced by ion bombardment, there are changes in composition brought about by preferential sputtering of one species relative to another in multicomponent materials. Preferential sputtering by ion bombardment during thin film growth causes a shift in composition relative to that obtained in the absence of ion bombardment (8). We have found that in addition to the usual increase in sputtering yield with angle described above, there is a

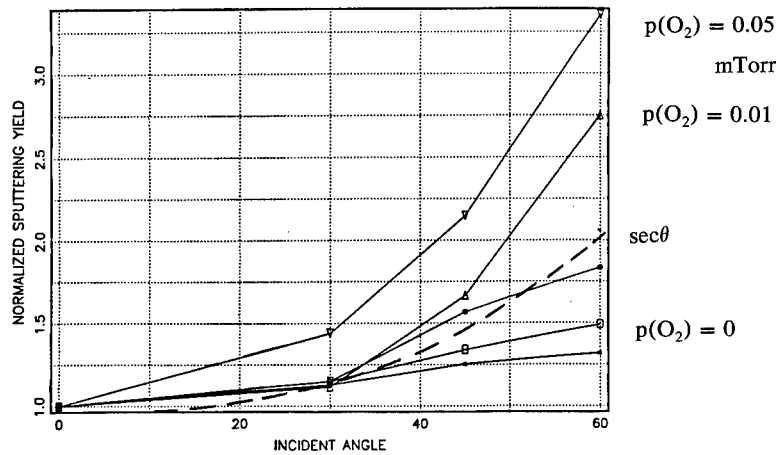
ANGULAR DEPENDENCE OF SPUTTERING YIELD AND ETCH RATE



4. Typical behavior of sputtering yield and etch rate as a function of angle of ion incidence.



5. Etch rate of Ta as a function of partial pressure of O_2 in Ar, for various angles of incidence.



6. Sputtering yield of Ta as a function of angle of incidence for various partial pressures of O_2 , relative to the normal incidence value.

fundamental enhancement of preferential sputtering with increased angle of incidence, which further shifts the film composition away from that obtained under normal incidence.

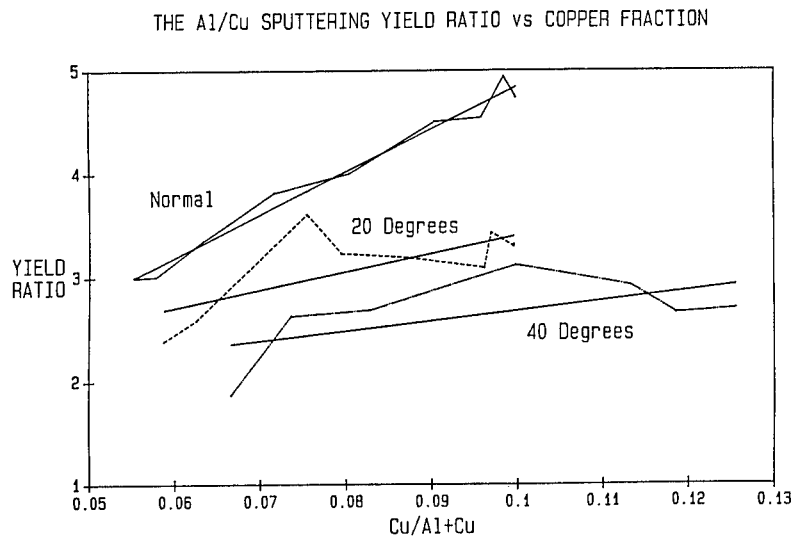
The experimental approach, described in reference 9, was to ion bombard a growing film of Al-5at%Cu with 500 eV Ar ions at various values of flux and angle of incidence. The resulting film compositions, together with the known arrival rates of film atoms and ions, provide values for the sputtering yields of Al and Cu, their incorporation probability, fraction resputtered, and additional information on Ar content. In the case of Al-5%Cu, Al is found to have up to five times the yield of Cu, even though in the pure elements the yield of Al is half that of Cu (Fig. 7). The effect of increasing angle away from normal incidence is to decrease this ratio somewhat. However, when the resulting Cu content is plotted as a function of fraction resputtered (Fig. 8), it shows a roughly linear dependence on the fraction resputtered, in accordance with previous modeling for a two-element material in which one element is a minor constituent (8).

In a growing film, sloping surfaces receive lower arrival rates of atoms than flat surfaces, according to $\cos\theta$, and lower ion flux by the same ratio. Therefore, the ratio of ion to atom arrival rates remains the same on sloping and flat surfaces. What differs significantly, however, is the fraction resputtered, which is proportional to the sputtering yield. On a sloping surface the fraction resputtered therefore exceeds that on the flat surface, up to nearly glancing incidence (see Fig. 4). This fundamental effect enhances the composition shift on a sloping surface, since it experiences a higher fraction resputtered than a flat surface. As an example, based on the results for Al-Cu (9), for an ion bombardment condition which shifts the Cu content from 5% in a non-bombarded film to 7% on the flat, a surface at 40° slope will have 11% Cu in the growing film. Therefore, the effect of angle of incidence on preferential sputtering can greatly modify the film composition on step corners and other sloping features.

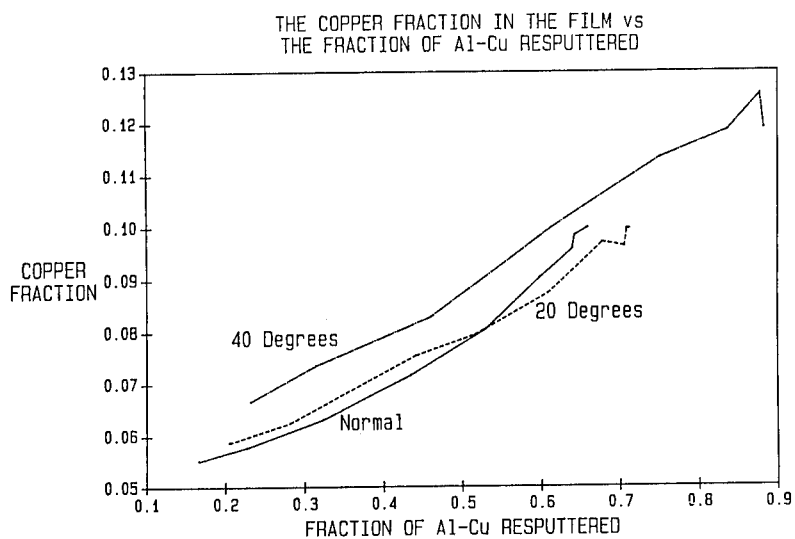
V. Crystallographic alignment in niobium

Ion bombardment has many effects on the microstructure and degree of preferred orientation of thin films (10). Here again the angle of incidence is an additional control parameter which deserves further study. As reported in reference 11, we have demonstrated that off-normal incidence ion bombardment during deposition can induce azimuthal (in-plane) alignment of a thin film. The demonstration of restricted texture in Nb films was achieved using 200 eV Ar ion bombardment at an angle of 70° from normal incidence. Analysis of the grain orientations selected by ion bombardment showed that in addition to the (110) fiber axis induced by the substrate plane, the majority of crystallites were oriented such that a planar channelling direction coincided with the ion beam direction. This selected orientation has a lower than average sputtering yield, and therefore dominates in the resulting grain growth during deposition.

Modeling of this ion-induced orientation process (12) gives a framework for understanding the asymptotic degree of alignment and time constant to reach this level, as a function of the ion/atom arrival rate ratio. Detailed prediction of the degree of alignment requires specific values for the sputtering yield along channelling di-



7. Sputtering yield ratio of Al to Cu as a function of Cu content in the film, for various angles of incidence (9).



8. Copper fraction in ion bombarded films as a function of the fraction of arriving material resputtered (9).

rections, as well as information on the layer-by-layer degree of granular epitaxy, which introduces a temperature dependence. Further modeling and experimentation to establish these relationships will help to establish how effective angle-selected ion bombardment can be in aligning thin film microstructure.

Summary

The examples given here demonstrate that the angle of ion incidence is an important process parameter in ion beam etching and in thin film deposition in the presence of ion bombardment. Angle of incidence can greatly modify the shape, composition and crystallographic microstructure of materials. Several phenomena have been identified which will benefit from further theoretical modeling and experimentation. These include the effects of ion flux, temperature and angle on the generation of surface ripples, behavior of etch rates in reactive gases, origins of preferential sputtering in alloys, and the limits of alignment induced by ion bombardment of polycrystalline thin films.

References

1. R.M. Bradley and J.M.E. Harper, *J. Vac. Sci. Technol.* A6, 2390 (1988).
2. G. Carter, M.J. Nobes, F. Paton, J.S. Williams and J.L. Whitton, *Radiat. Eff.* 33, 65 (1977).
3. F. Vasiliu, I.A. Teodorescu and F. Glodeanu, *J. Mater. Sci.* 10, 399 (1975).
4. P. Sigmund, *J. Mater. Sci.* 8, 1545 (1973).
5. I.H. Wilson, S. Chereckdjian and R.P. Webb, *Nuc. Instr. and Methods in Phys. Research B7/8*, 735 (1985).
6. H. Oechsner, *Appl. Phys.* 8, 185 (1975).
7. H. Okano and Y. Horiike, in "Plasma Processing" R.G. Frieser and C.J. Mogab, eds., p. 199, Electrochemical Society Proceedings Series, Pennington NJ (1981); see also B.A. Heath and T.M. Mayer, p. 365, in *VLSI Electronics*, Vol. 8, Microstructure Science, eds. N.G. Einspruch and D.M. Brown (Academic, New York, 1984).
8. J.M.E. Harper and R.J. Gambino, *J. Vac. Sci. Technol.* 16, 1901 (1979).
9. P.J. Rudeck, J.M.E. Harper and P.M. Fryer, *Appl. Phys. Lett.* 53, 845 (1988).
10. J.M.E. Harper, J.J. Cuomo, R.J. Gambino and H.R. Kaufman, in "Ion Bombardment Modification of Surfaces: Fundamentals and Applications", R. Kelly and O. Auciello, eds. (Elsevier, 1984) p. 127.
11. L.S. Yu, J.M.E. Harper, J.J. Cuomo and D.A. Smith, *Appl. Phys. Lett.* 47, 932 (1985).
12. R.M. Bradley, J.M.E. Harper and D.A. Smith, *J. Appl. Phys.* 60, 4160 (1986).

EPITAXIAL GROWTH OF NI ON SI BY ION BEAM ASSISTED DEPOSITION

K.S. GRABOWSKI, R.A. KANT and S.B. QADRI*

Naval Research Laboratory, Code 4670, Washington, DC 20375

*Sachs/Freeman Associates, Inc., Landover, MD 20785

ABSTRACT

Epitaxial Ni films were grown on Si(111) substrates to a thickness of about 500 nm by ion beam assisted deposition at room temperature. The films were grown using 25-keV-Ni ions and electron-beam evaporation of Ni at a relative arrival ratio of one ion for every 100 Ni vapor atoms. The ion beam and evaporant flux were both incident at 45° to the sample surface. Standard θ - 2θ X-ray diffraction scans revealed the extent of crystallographic texture, while Ni {220} pole figure measurements identified the azimuthal orientation of Ni in the plane of the film. Films grown without the ion beam consisted of nearly randomly oriented fine grains of Ni whereas with bombardment the Ni (111) plane was found parallel to the Si (111) plane. In all the epitaxial cases the Ni [110] direction was perpendicular to the axis of the ion beam, suggesting that the azimuthal orientation of the film was determined by channeling of the ion beam down {110} planar channels in the Ni film. Additional experiments with different ions, energies, and substrates revealed their influence on the degree of epitaxy obtained.

INTRODUCTION

It has been shown that Ni can be grown epitaxially on a number of substrates at temperatures near 200°C ; for example on ZnSe [1], diamond [2], sapphire [3], NaCl [4], and a variety of other substrates tabulated in [5]. Unfortunately, Ni has been shown to react with a Si substrate at these temperatures to form silicides [6,7].

An alternative approach would be to reduce the temperature required for epitaxy by simultaneously bombarding the surface with sub-keV energy ions during Ni deposition. This approach has succeeded for a number of other systems as has been reviewed by Greene [8] and Smidt [9], and since it has been shown to work for Cu on Si [10], may be expected to work for Ni on Si.

While that approach may yet be shown to work, this work describes the rather remarkable formation of epitaxial or perhaps pseudo-epitaxial Ni films on Si at room temperature by using 25-keV-Ni ion bombardment during Ni deposition. Considering the relatively high energy utilized where substantial radiation damage would be expected, such good epitaxy was not anticipated. This result may be related to the observation that grains in as-deposited thin films can reorient under keV-ion bombardment to encourage channeling of the incident ion beam. Such observations have been reviewed by Smidt [9] and Dobrev [11], and shown specifically for Ni films by Wang et al. [12].

EXPERIMENTAL PROCEDURE

Electron beam evaporation was used to deposit 500-nm-thick Ni films on room temperature substrates 1×0.5 cm in size. During growth, the films were typically bombarded with 25-keV Ni^+ ions supplied by an ion implanter. Selected samples were bombarded instead with Ar^+ ions either from an ion implanter at 25 keV, or from a Kaufman ion gun at 500 or 100 eV. The pressure during 25-keV irradiations was 5×10^{-5} Pa but increased during low-energy Ar bombardment to 2×10^{-2} Pa due to Ar from the ion gun. The substrates used were as-received wafer material of Si(111), Si(100),

InSb(100), and GaAs(110) orientations. They were positioned at 45 degrees to both the ion and vapor fluxes which were horizontal and vertical, respectively. Substrate preparation consisted of rinsing with acetone then alcohol, and sputter cleaning by $1 \times 10^{15} \text{ cm}^{-2}$ of 25-keV ions or $1 \times 10^{16} \text{ cm}^{-2}$ of low energy Ar ions, using the same ion beam parameters selected for deposition. Film deposition began at the end of the sputter cleaning process, i.e., without interrupting the ion bombardment. Film thickness was monitored using a quartz crystal thickness monitor and deposition rates ranged from 0.1 to 0.35 nm/s. The process was computer controlled to maintain a constant ratio of ion flux to vapor flux, R , with values of R ranging from 0.005 to 0.03.

X-Ray diffraction scans were obtained using $\text{Cu K}\alpha$ X-rays in a standard horizontal θ - 2θ diffractometer. Power levels between 250 and 900 watts were used with a scan rate of either 0.5 or 0.125 deg/min. A curved graphite monochromator removed the $\text{Cu K}\beta$ X-rays. Integrated intensities were normalized by scaling them to X-ray tube power and scan rate. Pole figure measurements were performed using Ni(220) reflections from $\text{Cu K}\alpha$ X-rays with a Ni filter. A spiral motion of the sample was used, tilting the sample 2.5 degrees out of the plane of diffraction for each sample rotation, ending at a tilt of 80° .

RESULTS

Dramatic changes in Ni grain orientation on Si(111) substrates were produced by 25-keV Ni^+ ion beam assisted deposition (IBAD). Fig. 1 compares diffraction scans from a film deposited with no ion flux ($R=0$) after the initial sputter cleaning step (dashed line) with a similar film deposited with an arrival ratio (R) of 0.01 (solid line). The different background levels reflect different X-ray tube power settings. Note the absence of all the Ni peaks except for (111) and (222) in the IBAD film, and compare this to the $R=0$ film which has all the expected Ni peaks at similar intensities, but has a (111) intensity less than 1% of that for the IBAD film. IBAD under these conditions promotes the closest packed plane orientation of the fcc Ni film, i.e., (111). Lattice parameter determinations for such IBAD films indicates agreement with the bulk Ni value within the measurement accuracy of 0.05%. Preliminary analysis of (111) and (222) peaks from IBAD films indicates their broadening is predominately from nonuniform strain in the film and not from small particle size.

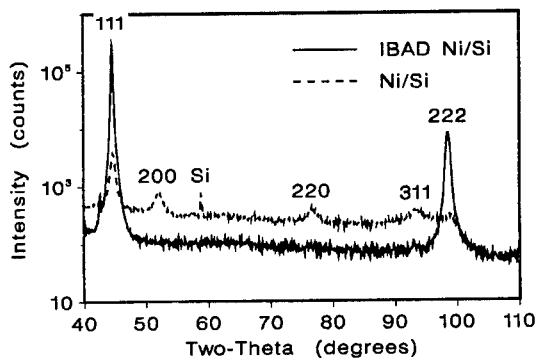


Fig. 1. Diffraction scans from 500-nm-thick Ni films on Si(111) for no ion flux during deposition (dashed) or with 25-keV-Ni ion flux at an arrival rate 1% of that of the Ni vapor atoms (solid).

While Fig. 1 shows that preferential film orientation occurs for the selected deposition conditions, it can not differentiate between strong fiber texture where azimuthal rotation in the plane of the film is permitted, and epitaxy where such rotational freedom is not allowed. However, this determination has been made by $\text{Ni}\{220\}$ pole figure measurements, such as those shown in Fig. 2 for films grown by 25-keV Ni IBAD with $R=0.01$. These figures show that pseudo epitaxy of $\text{Ni}(111)$ on $\text{Si}(111)$ is produced.

In Fig. 2(a), the three-fold symmetry expected for an epitaxial $\text{Ni}(111)$ film is seen, but since the film has twin variants rotated 180° from each other about the $[111]$ axis, the pole figure plot shows six-fold symmetry. The orientation relationship is therefore either $\text{Ni}[\bar{1}10] \parallel \text{Si}[\bar{1}\bar{1}2]$ or $\text{Ni}[\bar{1}\bar{1}0] \parallel \text{Si}[\bar{1}\bar{1}2]$ for the two variants. It is not clear at this time whether the variants arise from twinning within individual grains of Ni or from 180° misorientations between growing islands of Ni. Both variants do exhibit fairly poor epitaxy though, as evidenced by a relatively large azimuthal angular breadth of about 15° for the $\text{Ni}(220)$ poles. For both variants the ion beam was incident approximately orthogonal to the $\text{Ni}[\bar{1}\bar{1}0]$ direction. Since sample orientation was not adequately recorded for this sample, the two ion-beam directions possible are shown in Fig. 2(a).

A different orientation relationship between Ni and the Si substrate is shown in Fig. 2(b) where the Si substrate has been rotated 90° clockwise in the figure, and much less twinning is observed. In this case, $\text{Ni}[\bar{1}\bar{1}0] \parallel \text{Si}[\bar{1}\bar{1}0]$ was predominately observed, again with a relatively large azimuthal angular breadth. The ion beam was again incident approximately orthogonal to the $\text{Ni}[\bar{1}\bar{1}0]$ direction, as shown in the figure. Both Figs. 2a and 2b are consistent with the ion beam being incident along close to the $\text{Ni}(1\bar{1}0)$ planar channeling direction. These two pole figures suggest that the direction of the ion beam on the film is more important to determining the azimuthal orientation of the film than the orientation of the $\text{Si}(111)$ substrate. However, this remains to be confirmed. For this reason, the films should perhaps be considered pseudo-epitaxial.

The ability to produce such well oriented films was studied under a variety of other deposition conditions. A summary of the results found for

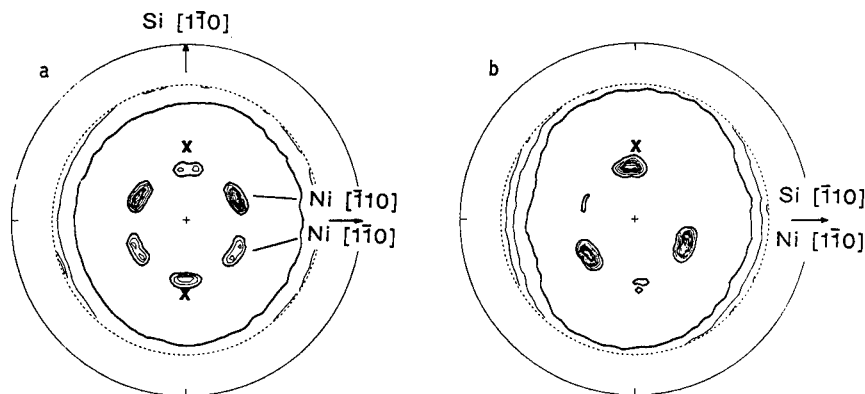


Fig. 2. $\text{Ni}(220)$ pole figures showing oriented $\text{Ni}(111)$ films for 25-keV-Ni IBAD, grown with $R=0.01$ on $\text{Si}(111)$ substrates. In (a) $\text{Si}[\bar{1}\bar{1}2] \parallel \text{Ni}[\bar{1}\bar{1}0]$ or $\text{Ni}[\bar{1}\bar{1}0] \parallel \text{Si}[\bar{1}\bar{1}2]$ but in (b) $\text{Si}[\bar{1}\bar{1}0] \parallel \text{Ni}[\bar{1}\bar{1}0]$. The direction of the incident ion beam is indicated by an x. Only one of the two possible directions shown in (a) is correct.

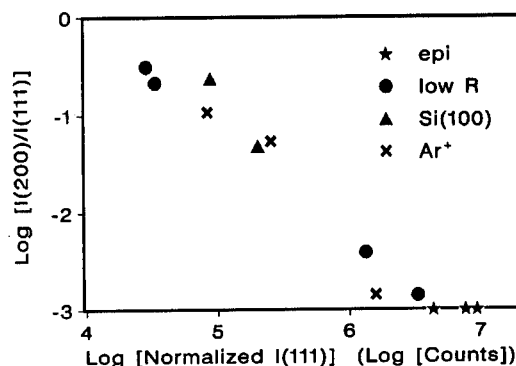


Fig. 3. Degree of preferential orientation of 500-nm-thick films for a variety of deposition conditions. Each symbol represents one sample. Integrated Ni(200) and Ni(111) intensities are represented for films grown: with 25-keV Ni⁺ at R=0.01 on Si(111) substrates (★), or on Si(100) substrates (▲), or at R≤0.005 on Si(111) (●), or with Ar⁺ at R=0.03 on Si(111) (×). The pseudo-epitaxial films (★) actually had no measurable I(200), but are plotted on this scale as a reference for normalized I(111).

500-nm-thick films is shown in Fig. 3, where the ratio of integrated intensity of Ni(200) to Ni(111) diffraction peaks, $I(200)/I(111)$, is correlated with the normalized integrated intensity of Ni(111) diffraction peaks (normalized $I(111)$). Greater preferential orientation of the film results in a smaller ratio $I(200)/I(111)$, and a greater normalized $I(111)$.

Only the pseudo-epitaxial films formed with R=0.01 on Si(111) (★) lacked any measurable contribution of Ni(200) diffraction. When R was dropped to 0.005, a slight amount of Ni(200) diffraction appeared, and the normalized Ni(111) intensity was slightly reduced to 3.3×10^6 . It appears that a critical R value near 0.01 exists. Without any ion flux during deposition (R=0) the two data points in the upper left corner of Fig. 3 were obtained.

To ascertain whether pseudo epitaxy is merely a nucleation effect, films were grown to 25-nm thickness at R=0.01, then the Ni ion beam was turned off. If the deposition also ceased, the films exhibited pseudo-epitaxial behavior, considering their thickness ($I(200)=0$, normalized $I(111)=2.14 \times 10^5$). But, if the deposition continued to a total Ni thickness of 500 nm, some Ni(200) diffraction became evident, although not at the levels seen for the R=0 cases. Furthermore, the Ni(111) intensity (normalized $I(111)=1.33 \times 10^6$) was below that of the pseudo-epitaxial films. This analysis indicates that preferred-orientation growth is encouraged by 25-nm-thick oriented seed material, but that it cannot be sustained without further use of the ion beam.

The contribution of substrate crystallography to preferential orientation of Ni was also examined by using Si(100), InSb(100), and GaAs(110) substrates while maintaining desirable deposition conditions (25-keV Ni ions, R=0.01). Despite the improved matching of lattice parameters in going from Si to InSb (misfit decreases from +12.4 to +8.8%), no pseudo-epitaxial growth was observed for either (100) substrate. Instead, a slight predominance of Ni(111) growth was observed, being slightly stronger for the Si(100) substrate. Similar results were obtained for the GaAs(110) substrate, expected to have a -11.9% misfit for Ni. Taken together, these results indicate that substrate orientation is also important to the formation of the observed pseudo-epitaxial films.

To understand the influence of ion energy on film epitaxy, 500-nm-thick Ni films were grown on Si(111) with Ar ions at 0.1, 0.5, and 25 keV using $R=0.03$. The higher the energy used, the better the epitaxy obtained. However, at 25 keV some contribution of I(200) was observed, in contrast to the Ni-ion case. This can perhaps be attributed to Ar retention in the film causing either stress in the film or acting as dechanneling centers for the incident ion beam. The poorer quality of oriented film growth observed for the lower Ar-ion energies may be related to a decreased damage yield at the lower ion energies, or in other words, too low an ion flux.

Estimating that on average every atom in the film must be displaced approximately once by the ion beam (1 dpa) for complete relaxation of the film to occur during growth, one would desire an arrival ratio, R , such that $1/R$ equals the average number of vacancies produced per incident ion. Calculated values of this critical arrival ratio, R_c , and the projected ion range, R_p , are shown in Table I for each of the ions used. These values were calculated by the TRIM code [13] using a displacement threshold energy of 23 eV. It is interesting to note that for Ni ions R_c matches well the observation that an R greater than 0.005 is needed to entirely eliminate Ni(200) diffraction. Furthermore, at the lower ion energies R_c is substantially greater than the $R=0.03$ used in these experiments. Further evaluation of this concept of critical arrival ratio is certainly needed.

Table I. Critical Arrival Ratio and Range of Incident Ions

<u>Ion</u>	<u>Energy (keV)</u>	<u>R_c</u>	<u>R_p(nm)</u>
Ni	25	.0032	6.4
Ar	25	.0034	9.3
Ar	0.5	.145	0.6
Ar	0.1	.769	0.3

DISCUSSION

The type of films formed in this work could perhaps be best described as being strongly oriented. However, this terminology connotes fiber texture of the film, which is not nearly as accurate a depiction of the films as the terms epitaxial or pseudo epitaxial. Hence, these latter terms have been used throughout.

In contrast, Yu et al. [14] only observed restricted fiber texture (i.e., less than epitaxial quality) for Nb films grown on amorphous silica, using 200-eV Ar ions incident 20° away from grazing incidence. Therefore, the specifics of the deposition conditions are clearly important. More limited experiments have shown that oriented growth of TiN [15], and of a Ni-Fe alloy [16] can occur during ion assisted deposition. In the former case, grains were oriented to promote $\langle 100 \rangle$ axial channeling of the sub-keV N ion beam, whereas in the latter case glancing incidence of the sub-keV Ar ion beam promoted closest packed plane growth (i.e., (111)) for the fcc alloy.

A working hypothesis, therefore, is that inclined incidence of the ion beam can simultaneously promote two preferences in film orientation. The deposited energy encourages a closest packed plane orientation of the film's surface thereby minimizing surface energy, while the azimuthal rotation of the film is selected to allow channeling of the incident ion beam. Other grain orientations are eliminated by virtue of the higher damage deposited by the non-channelled ion beam. With normal incidence of the ion beam these two preferences are in conflict so poorer quality epitaxy is expected. Furthermore, at low energies the channeling width becomes so broad that little preference in azimuthal orientation would be expected.

SUMMARY

Ion beam assisted deposition using 25-keV-Ni ions at room temperature promotes growth of Ni films oriented to have a closest packed plane orientation (i.e., (111) orientation for fcc Ni). This is not just a nucleation effect.

Azimuthal orientation of the film is apparently influenced by channeling of the inclined incidence ion beam.

A critical arrival ratio (R_c) is needed for best epitaxy. This may coincide with ~1 dpa damage level in the film.

Substrate crystallography also influences the orientation of a growing IBAD film.

Trapping of inert gas atoms in the film degrades the epitaxy of the film.

ACKNOWLEDGEMENT

The authors acknowledge the generous assistance of Randy Walker in fabricating these samples and Carl Vold for providing access to the X-ray diffraction equipment.

REFERENCES

1. B.T. Jonker, J.J. Krebs, and G.A. Prinz, J. Appl. Phys. **64**, 5340 (1988).
2. P. Pavlidis, Thin Solid Films **42**, 221 (1977).
3. C.J. Sparks, M. Hasaka, D.S. Easton, S. Baik, T. Habenschuss, and G.E. Ice in Interfaces, Superlattices, and Thin Films, edited by J.D. Dow and I.K. Schuller (Mater. Res. Soc. Proc. **77**, Pittsburgh, PA 1987) pp. 495-502.
4. B. Egert, W. Kirstein, J. Kessler, and F. Thieme, Thin Solid Films **50**, L7 (1978).
5. Enrique Grunbaum in Epitaxial Growth, Part B, edited by J.W. Matthews (Academic Press, New York, 1975) pp. 611-674.
6. K.N. Tu and J.W. Mayer in Thin Films, Interdiffusion and Reactions, edited by J.M. Poate, K.N. Tu, and J.W. Mayer (Wiley, New York, 1978) pp. 359-405.
7. K.N. Tu, E.I. Alessandrini, W.K. Chu, H. Krautle, and J.W. Mayer, Jap. J. Appl. Phys., Suppl. 2 Pt. 1, 669 (1974).
8. J.E. Greene, CRC Critical Reviews in Solid State and Materials Sciences **11**, 47 (1983).
9. F.A. Smidt, presented at the NATO Advanced Study Institute on Structure-Property Relations in Ion-Beam Surface Modified Ceramics Theory and Practice, Il Ciocco, Italy, 1988, (to be published).
10. T. Ohmi, T. Saito, T. Shibata, and T. Nitta, Appl. Phys. Lett. **52**, 2236 (1988).
11. D. Dobrev, Thin Solid Films **92**, 41 (1982).
12. P. Wang, D.A. Thompson, and W.W. Smeltzer, Nucl. Instrum. Meth. **B7/8**, 97 (1985); **B16**, 288 (1986).
13. J.P. Biersack and L.G. Hagmark, Nucl. Instrum. Meth. **174**, 257 (1980).
14. L.S. Yu, J.M.E. Harper, J.J. Cuomo, and D.A. Smith, J. Vac. Sci. Technol. **A4**, 443 (1986); Appl. Phys. Lett. **47**, 932 (1985).
15. Y. Andoh, K. Ogata, H. Yamaki, and S. Sakai, presented at the Ion Beam Modification of Materials Conference, Tokyo, Japan, 1988; M. Kiuchi, K. Fujii, T. Tanaka, M. Satou, and F. Fujimoto, Nucl. Instrum. Meth. **B33**, 649 (1988).
16. Y. Nagai, A. Tago, and T. Toshima, J. Vac. Sci. Technol. **A5**, 61 (1987).

Ge Heteroepitaxy on (100) Si Substrates by Ion Assisted Deposition

T.G. Holesinger, D.J. Heim, K.M. Lakin, and H.R. Shanks
Iowa State University, Microelectronics Research Center
Ames, IA.

Abstract

Ge films have been grown by ion-assisted deposition on Si(100) substrates. Initial studies were conducted to determine the growth and morphology of Ge using a modified crucible arrangement and ionization chamber. It was observed that a narrow substrate temperature range existed for the deposition of smooth Ge films without ion assistance. Ionization and acceleration appear to induce additional damage to the film without improving crystalline quality.

Introduction

The deposition of Ge on Si has received considerable attention in recent years.¹ Ge-Si superlattices hold promise for development of novel devices and Ge has also been proposed for use as a buffer layer between Si and GaAs.^{2,3,4} GaAs and Si have about a 4% lattice mismatch while the lattice constants of Ge and GaAs are nearly identical. However, Ge films are in general characterized by a high dislocation density. This paper describes an ion-assisted growth technique used in an effort to reduce defects and improve the crystalline quality of Ge films.

Procedure

The Ge films were deposited in a UHV ionized-cluster beam system (ICB) with a base pressure of 1×10^{-10} torr. A description of this technique can be found elsewhere.⁵ This system included an insitu ellipsometry system described in an earlier paper.⁶ Ge was evaporated from pyrolytic graphite coated carbon crucibles operated at temperatures up to 1850°C. These crucibles had caps with a 1mm diameter by 1mm thick nozzle. The crucible arrangement along with the ionization and acceleration configuration is shown in Figure 1.

The Si wafers used for substrates were first cleaned in 1,1,1-trichloroethane (TCE), acetone, and methanol to remove organic contaminants. The substrates were subsequently etched in a dilute HF solution and immediately loaded into the system. The wafers were heated to 800°C for 1 hour prior to deposition to desorb the residual oxide. Deposition rates were varied from 0.5 to 5 angstroms per second with film thicknesses ranging from 0.3 to 2 microns. The pressure increased during deposition, due to outgassing of the source, into the range between 1×10^{-8} to 5×10^{-7} torr. The main constituents were nitrogen and hydrogen as monitored by a residual gas analyzer (RGA)

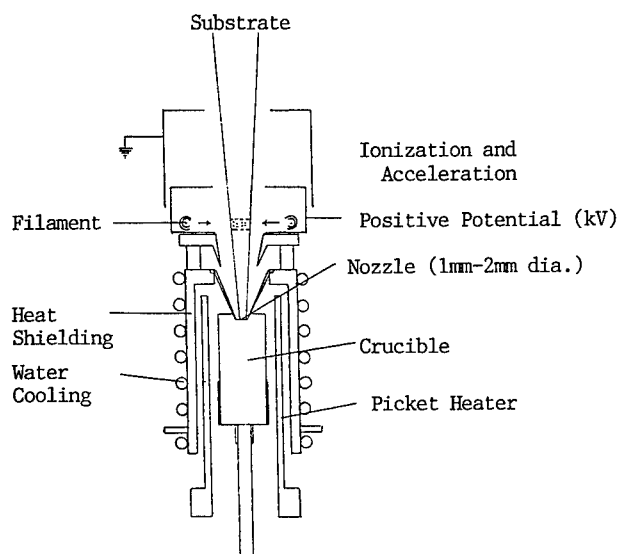


Figure 1) Crucible, ionization, and acceleration apparatus used for ion-assisted deposition of Ge films.

Characterization

The surface morphology was examined using Nomarski and Scanning Electron Microscopes (SEM). Changes in surface morphology and resistivity across the wafer were detected by observing the haze under a high intensity light in conjunction with four-point probe resistivity measurements. These observations were then correlated with ellipsometry and reflection high energy electron diffraction (RHEED) results. X-ray diffraction (XRD) data was taken using a powder diffractometer to determine crystalline characteristics, while etching provided an estimate of the defect density in the film.

Table 1
Sample Substrate Deposition Ion. Accel. Structure Growth

	Temp.	Rate				
Ge #1	250°C	2.2 A/s	--	----	PC	rough
Ge #12	350°C	2.2 A/s	--	----	SC	smooth
Ge #13	400°C	2.1 A/s	--	----	SC	island-type
Ge #22	400°C	4.2 A/s	40 mA	----	SC	island-type
Ge #42	400°C	1.2 A/s	--	----	SC	island-type
Ge #43	400°C	4.0 A/s	30 mA	1.0 kV	SC	island-type
Ge #44	400°C	2.8 A/s	30 mA	3.0 kV	SC	island-type
Ge #49	325°C	1.0 A/s	--	----	SC	smooth

Note: PC = polycrystalline; SC = single crystal

Results

The films as deposited at various temperatures were mirror smooth and visual inspection revealed few or no defects. Damage and defects were observable under a microscope or high intensity light. A listing of sample film deposition parameters is given in Table 1. SEM and Nomarski observations have shown three temperature ranges for the growth of Ge on Si without the use of ionization and acceleration. Below substrate temperatures of 300°C, the films were rough with a high density of pinholes and other defects. XRD showed that most films tended to be polycrystalline or amorphous. At these temperatures, crystalline films could only be deposited at a rate of 0.1 angstroms per second or less. When the substrate was held between 300°C and 350°C, the growth appeared smooth with few pinholes. SEM observations showed no discernable surface features while RHEED showed streaked patterns indicative of a smooth surface. A typical sample is shown in Figure 2. Above 350°C, island-type structures begin to appear in the surface morphology while the streaked pattern in the RHEED photograph was replaced by spots and chevrons indicating a rougher surface. Ellipsometry results also corroborate these observations.[6] The elongation of the islands predominately in one direction is believed to be caused by the orientation of the substrate relative to the Ge flux.

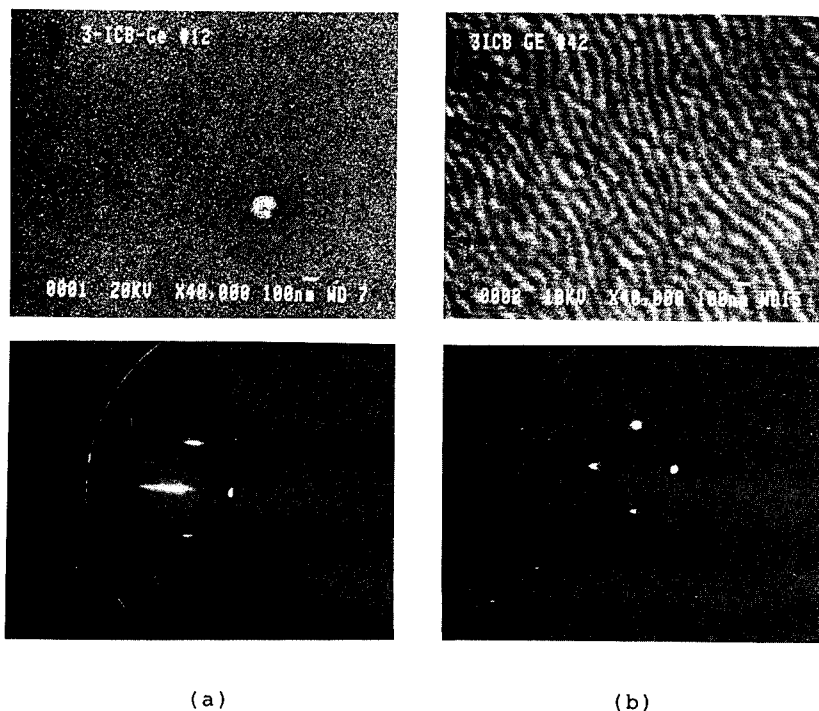


Figure 2) SEM and RHEED micrographs of Ge films
 a) Ge film #12 deposited at 350°C
 b) Ge film #42 deposited at 400°C

The XRD results for several films are shown below in Figure 3. The double peaks correspond to the copper $K\alpha_1$ and $K\alpha_2$ lines. The (400) peaks for both the Ge film and Si substrate are shown. It is evident that the crystalline quality in all the films is degraded when compared to the Si (400) peak. We believe this is caused by carbon incorporation from the crucible during deposition. Auger analysis has shown up to 2% carbon concentration in these films. This is unfortunate since the high temperature demands of the ICB deposition technique severely limit the types of crucible materials that can be used. Also, the crystalline quality is not seen to improve with the addition of ionization and acceleration as seen in Figure 3. Little change was seen in the XRD data between film #13 deposited without ion assistance and film #44 deposited at 30 mA ionization and 3 kV acceleration. Etch pit densities for all the films were around $5 \times 10^{-8} \text{ cm}^{-2}$. Note that peak shifts in the XRD data come from sample centering errors and minor changes in instrument alignment from run to run. The absolute values of the peak positions are probably no more accurate than ± 0.10 degrees.

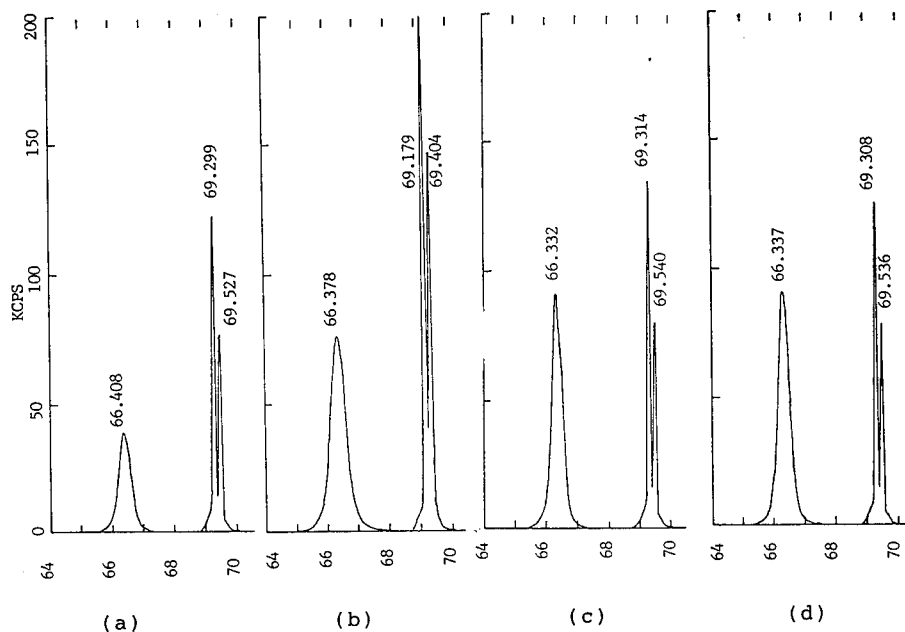


Figure 3) XRD data for Ge films deposited at 400°C for various ionization and acceleration levels.
 a) Ge film #13 deposited without ion-assistance
 b) Ge film #22 deposited with 40mA ionization
 c) Ge film #43 deposited with 30mA ionization and 1 kV acceleration
 d) Ge film #44 deposited with 30mA ionization and 3 kV acceleration

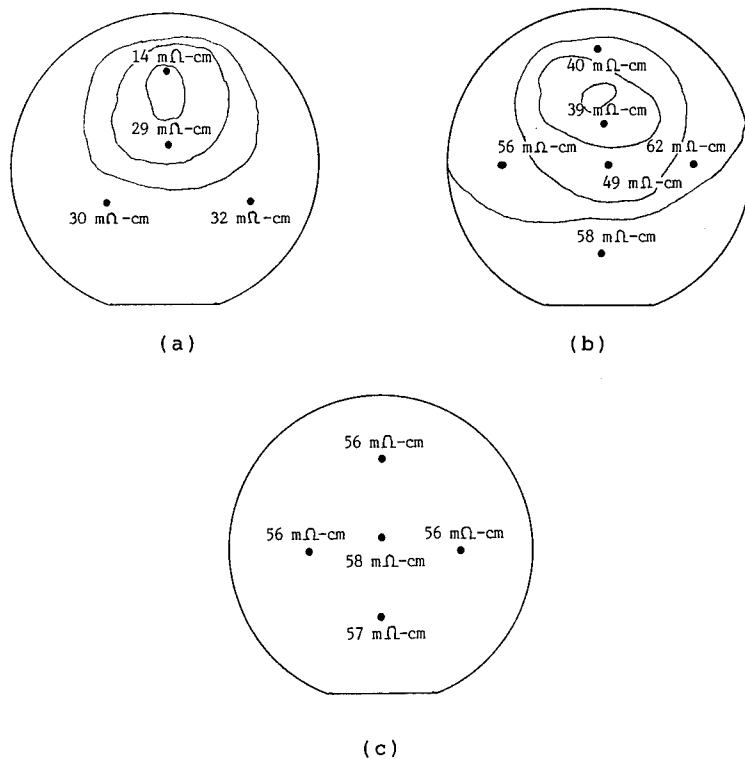


Figure 4) Haze and resistivity sketches of Ge films
 a) Ge film #44 deposited with 30 mA ionization and 3 kV acceleration
 b) Ge film #43 deposited with 30 mA ionization and 1 kV acceleration
 c) Ge film #49 deposited without ion-assistance

The effects of ionization and acceleration have not been fully determined. However, it is clear that damage to the film was caused by the ion beam. In Figure 4a, damage to film #44 from ionization and three kilovolts acceleration was observed in an area centered over the nozzle. The sketch shows the contrast in surface morphology as observed under a high intensity light and the corresponding decrease in the resistivities in the damaged areas. This damage decreases towards the edges with a increase in the resistivity of the film. It has been found that defects in Ge are electrically active and act as acceptors.[1] As the acceleration was decreased, the affected area increased, but the contrast between the damaged and undamaged regions was reduced. There was an overall increase in the resistivity of film #43 as shown in Figure 4b. Figure 4c shows a film deposited without ion-assistance. The surface morphology is uniform as are the resistivity measurements.

There could be several reasons why ion-bombardment caused this damage. One possibility is defects caused by carbon incorporation during film growth were enhanced by the additional energy. Sputtering due to the high acceleration voltages could also have contributed to defects such as vacancies in the lattice and a rougher morphology compared to the undamaged regions. It has been shown that the Ge mass flux for the ICB system is peaked around clusters of 4 to 5 atoms.⁷ This would correspond to energies between 750 and 500 eV per atom for 3 kV acceleration and energies between 250 and 200 eV per atom for 1 kV acceleration. At these energies, some sputtering and shallow implantation would occur that could account for the damage to the film. Additional experiments are being performed at lower energies to determine if ion-assistance can be used to improve film quality.

Summary

We have found three temperature ranges of growth as a function of the substrate temperature at deposition rates of .5 to 5 angstroms per second. The best temperatures for growth were between 300°C and 350°C. When ionization and acceleration were used, damage to the film was shown to occur with a decrease in the film resistivity. Experiments are continuing to determine if there are some deposition conditions under which ionization and acceleration do increase film quality.

Acknowledgements

The authors express their appreciation to the Air Force Office of Scientific Research for funding of this project.

References

1. J.M. Baribeau, T.E. Jackman, D.C. Houghton, P. Maigne, and M.W. Denhoff, *J. Appl. Phys.* **63**, 5738 (1988).
2. J. Bevk, J.P. Mannaerts, L.C. Feldman, B.A. Davidson, and A. Ourmazd, *Appl. Phys. Lett.* **49**, 286 (1986).
3. P. Sheldon, K.M. Jones, R.E. Hayes, B.Y. Tsaur, and J.C.C. Fan, *Appl. Phys. Lett.* **45**, 274 (1984).
4. P. Sheldon, B.G. Yacobi, K.M. Jones, and D.J. Dunlavy, *J. Appl. Phys.* **58**, 4186 (1985).
5. T. Takagi, I. Yamada, M. Kunori, and S. Kobiyama, *Proc. Int. Conf. Ion Sources*, 2nd (1972).
6. D.J. Heim, T.G. Holesinger, K.M. Lakin, and H.R. Shanks, *Materials Research Symposium* **116** 523 (1988).
7. D.E. Turner, K.M. Lakin, and H.R. Shanks, to be published in *Materials Research Symposium on Processing and Characterization of Materials Using Ion Beams* Fall Meeting, 1988.

SILICON HOMOEPITAXY AT LOW TEMPERATURE USING MICROWAVE MULTIPOLAR PLASMA FOR CLEANING AND DEPOSITION

R. BURKE, M. GUILLERMET, L. VALLIER and E. VOISIN
PMI, UJFG & URA D0844 of CNRS ; CNS-CNET, BP 98, 38243 Meylan Cedex, FRANCE

ABSTRACT

The Microwave Multipolar Plasma (MMP) offers unique features for plasma assisted deposition by combining multipolar magnetic confinement and microwave excitation. Independent control of the plasma-surface interaction parameters (neutral flux, ion flux and ion impact energy) has led to low temperature (400-800°C) silicon epitaxial growth in pure or H₂ diluted silane MMPs.

Prior to the epitaxial growth of Si, a plasma cleaning is applied to remove O and C atoms contaminant from the substrate surface. Ar and H₂ were tested on 2 and 4 inch, (100) oriented, silicon wafers loaded "as received" and heated at the deposition temperature. The cleaning is effective in both cases giving a pure Si Auger spectrum. However, a LEED signature is only observed when operating at very low bias of the sample (low energy ions) and the lower the substrate temperature, the lower the energy allowed to obtain a LEED pattern. The cleaning process is also checked and inspected by post-deposition analyses, including TEM, RBS, SIMS and Secco etch.

Various layer thicknesses were grown according to the characterization method. Specular epitaxial films are obtained for a large range of plasma and substrate parameters. The temperature may be as low as 400°C but the best results are obtained in the 600-700°C range. Interestingly, epitaxy is lost when the ion energy is increased. These results show a compromise between ion energy and substrate temperature. One needs to work at low ion energy to enhance the surface reaction while avoiding surface damage, but the temperature has to be sufficiently high to restructure the surface. Preliminary results on intentional doping reveal further potentialities of this low energy controlled interaction for low temperature plasma processing.

INTRODUCTION

Plasma assisted epitaxy is now widely developing for low temperature (< 800°C) silicon epitaxial growth in order to minimize diffusion and auto-doping effects [1,2]. We present results on a new technique using (silane) Microwave Multipolar Plasma which combines both the surface cleaning prior to deposition and a high epi-growth rate. Due to the independant control of plasma production and the electrical bias of the substrate, the user is in control of the energy of the ion impinging the surface from a few 10's eV down to 0 eV ; we will show the unique nature of this low energy controlled interaction to achieve an efficient surface cleaning step or an abrupt doping profile. Therefore Microwave Multipolar Plasma appears to be an efficient and versatile tool in advanced material research.

EXPERIMENT

The results presented in this paper are based on an experiment dedicated to silicon homoeptitaxy using silane microwave plasma. Special care was given to the design of the apparatus which consists of the parts : a load-lock, the deposition reactor and a surface analysis chamber.

The load-lock

Up to 100 mm diameter Si wafer can be loaded in a small stainless steel chamber with turbomolecular pumping which assures an ultimate pressure of 10^{-7} mbar in a few 10's of minutes ; then it is transferred into the plasma reactor. It is pointed out already that there is no laminar flow or clean room environment surrounding the loading operation, which may lead to defect generation during the epi-growth.

The deposition reactor

A 450 mm diameter and 600 mm length stainless steel cylinder contains the two main components of the experiment : the microwave multipolar structure producing the plasma and the heated substrate holder placed in its center . An oil free turbomolecular pumping (1000 l/s) results in a base pressure of 10^{-9} mbar after a gentle bakeout at 200°C of the whole system. This low pressure in the high vacuum range has to be compared to the working pressure during plasma treatment which stays in the low 10^{-3} mbar range.

The concept chosen to produce the plasma is the combination of a multipolar magnetic structure with several local rod applicators fed by 2.45 GHz microwave power ; the electron cyclotron resonance condition is ensured along the rows of the permanent magnets creating the multipolar field, thus efficient plasma production is achieved at low pressure (10^{-3} mbar). This plasma production technique, called Distributed Electron Cyclotron Resonance, is described elsewhere [3] ; it yields large volume of dense and quiescent plasma with a plasma potential close to the ground ; moreover, the user is in control through an electric bias, of the energy of the ion flux impinging on a substrate surface in contact with the plasma. To conclude, this technique is well suited to investigate the effect of low energy ion flux during plasma treatment. Precisely, 8 rows of sealed permanent magnets are placed along the inner cylinder body to form the multipolar magnetic field and they are associated with 6 antennas fed by a 200 W max microwave generator each ; matching impedance networks optimize the plasma generation (at the periphery of the chamber) to give the most dense desired plasma in interaction with the Si surface placed in the middle.

The second important component is the substrate holder ; two types were used according to the heating source. The first one consisted of a cesium heat-pipe heated by a sealed filament and was designed to operate with a 100 mm Si wafer deposited on its top ; despite a good temperature homogeneity, outgassing and thermal inertia plus a max Si surface temperature of 600°C only have led us to use another equipment. The second one was based on a conventional Joule heated stripped filament which faces the back side of the wafer but it is isolated from the plasma with a quartz bell-jar and a differential pumping ; in this later case, only 2" or 3" wafer can be heated up to 850°C with good uniformity, keeping the base pressure at 10^{-8} mbar.

To complete the description of the experimental set-up, the gas supply must be discussed ; VLSI grade silane is used for plasma deposition and is added with arsine or phosphine diluted in hydrogen for doping studies, while argon or hydrogen are used during the plasma cleaning-step. In all cases, mass flow controllers regulate the flow to give a plasma pressure in the 10^{-3} mbar range (baratron monitored).

The analysis chamber

A transfer mechanism brings the Si substrate into an UHV surface analysis chamber equipped with an Auger Electron Spectrometer (CMA type) and a transparent screen for Low Energy Electron Diffraction patterning ; therefore, elemental analysis can be performed just after the plasma process in an almost "in-situ" way, as well as crystallographic studies.

RESULTS

Our main results concern the Si surface cleaning step prior to the epi-growth and the deposition itself, both achieved in plasma condition at low temperature. Here as an example, we will limit ourselves to (100) oriented, N type, commercial unprocessed silicon wafers and we will survey the influence of the plasma parameters on the two processes, especially the ion energy.

Plasma cleaning

Our goal was to prepare an Si surface as clean as possible before starting the epitaxy ; especially C and O contaminants have to be well removed, and the surface has to be crystalline. Classical preparation calls for a high temperature step under UHV conditions, and a gaz containing chlorine, ... whereas plasma treatment allows low temperature processing [4].

H₂ plasma action was first investigated ; standard conditions are a total pressure $P = 0,3$ Pa, an ion density $n^+ = 6.10^9$ cm⁻³ with an electron temperature $T_e = 0,8$ eV for a moderate 600 W microwave power input. The ion current density measured on the DC biased substrate is of the order of 0.5 mA.cm⁻² ; it stays almost constant when the bias changes from the floating potential (3 V) up to - 100 V with respect to the plasma potential (5 V). For a floating silicon wafer, we observe that an efficient cleaning is achieved in a few minutes (no C and O traces on the Auger spectrum) only if the wafer is dipped in diluted HF before loading in the system ; under these conditions a LEED pattern is present, changing from 1×1 to 2×1 for temperature above 700°C ; in that case the HF dip can be avoided. Obviously, atomic hydrogen produced in the plasma is the dominant agent during the cleaning process ; it reduces the native oxide and the carbonated compounds still present at the surface. After this treatment, epitaxial growth with silane plasma was successful down to 400°C which confirms a correct cleaning ; more sensitive analysis like SIMS and TEM, however, reveals that residues are still present at the interface and could generate defects in the epi-layer. A defect density of 10^9 cm⁻² is measured at 500°C which drops to 10^6 cm⁻² at 700°C but it is hard to discern the cleaning part from the growth part in the defect creation as they were performed at the same temperature. However, this change could be simply attributed to the different substrate heater employed, as the heat-pipe used for the low temperature studies (below 600°C) generates higher residual contamination. The results on the H₂ plasma should be compared to the Ar plasma cleaning, which is presented below.

Experimental conditions with Ar are the same, except a lower total pressure $P = 0,1$ Pa with a slightly higher ion density $n^+ = 3.10^{10}$ cm⁻³ and electron temperature $T_e = 2,2$ eV ; correlatively, the ion current density reaches a 0.8 mA.cm⁻² value. The energy of the ions impinging on the surface becomes significant. O and C traces on Auger spectrum can be removed even at ambient temperature with a moderate energy (60 eV) but it leads to Ar incorporation and amorphisation of the surface ; the mechanism looks like a classical sputtering one. Above 600°C, no argon incorporation is observed. Thus a very good cleaning can be achieved, leaving a well defined 2×1 LEED signature above 620°C, but only if the ion impact energy is in the few 10's eV range or lower. Two points have to be noticed : first, the higher the ion energy, the higher the cleaning kinetics ; secondly, the higher the energy, the higher the temperature needed to restore the crystal order modified by the ion impact. For example, a wafer loaded as received (with its native oxide) is fairly well cleaned in 2 minutes at 30 eV ion energy and 700°C, leaving a 2×1 LEED pattern and a virgin Si Auger spectrum, while it takes 7 minutes with a 10 eV energy ; and if the energy is 70 eV, one can never observe a clear 2×1 LEED even though a good chemical cleaning is observed in a few 10's of seconds. Cross sectional TEM and SIMS performed after the epi-growth show a significantly better interface following argon cleaning, compared to an H₂ cleaning at the same temperature.

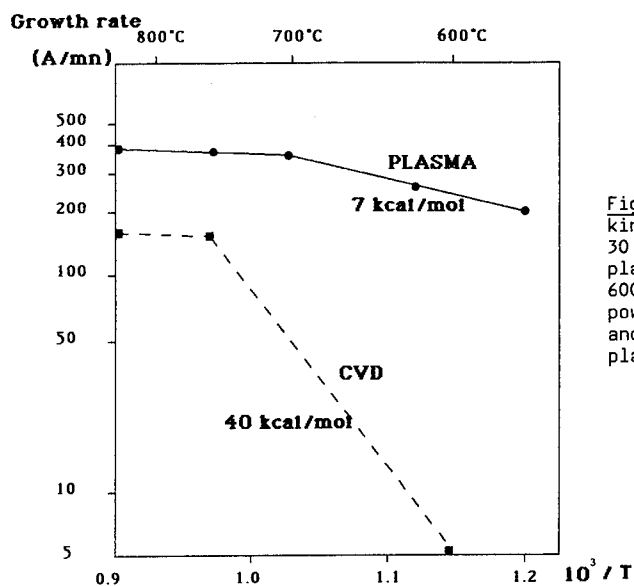
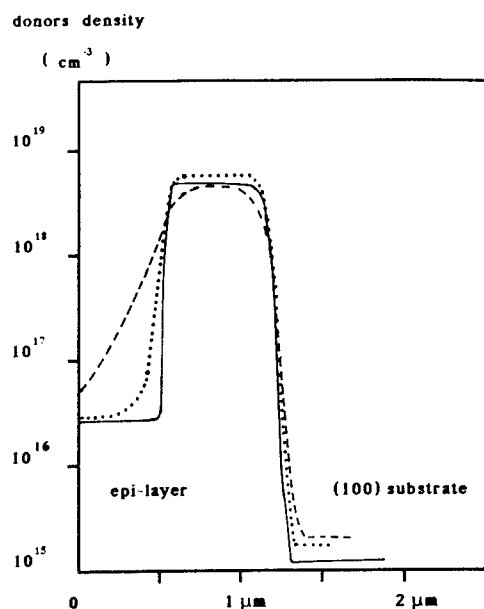


Fig. 1 : Growth rate kinetics at $P = 0.3$ Pa, 30 sccm SiH_4 flow for plasma deposition with 600 Watt microwave power (straight line) and for CVD without plasma (dashed line).

Fig. 2 : Spreading Resistance Probe profiles on step-like intentionally doped epi-layers with As for the same experimental conditions at $T = 720^\circ\text{C}$, except an ion energy of 40 eV (dashed line), 48 eV (dotted line), and 55 eV (straight line).



To summarize we observe that the plasma cleaning technique described in this paper, is able to produce Si surfaces as clean as other conventional techniques ; furthermore, the low energy controlled ion fluxes allowed in the microwave multipolar plasma represents a new approach to low temperature processing by using plasma.

Plasma deposition

Silane is introduced in the reactor just after the cleaning step ; typical values measured for a pure SiH_4 plasma at a total pressure of $P = 0,3 \text{ Pa}$ are an ion density $n^+ = 4.10^{10} \text{ cm}^{-3}$ with an electron temperature $T_e = 0,5 \text{ eV}$, for a 600 W microwave power excitation. Numerous deposits were performed by varying the experimental parameters : Silane flow, substrate temperature, microwave power and ion energy. Fig. 1 reveals the plasma enhancement of the growth rate in comparison with CVD conditions achieved in the same reactor without plasma ; due to the gas phase decomposition, plasma assisted epitaxy offers high growth-rate at low temperature. Moreover, we measure a growth-rate increasing with the microwave power injected in the plasma as it generates more dissociated molecules ; on the contrary, no clear influence of the ion energy on the growth rate was detected. Let us concentrate on the epitaxy results. By diluting SiH_4 in H_2 or Ar, epitaxial growth is obtained down to 450°C but a high density of dislocations, stacking faults and precipitates are present. The ion flux collected on the substrate is still in the $0,5 \text{ mA.cm}^{-2}$ range and the epi-quality is again sensitive to the ion impact energy (LEED monitored) ; under 600°C one needs to work below a 20 eV energy threshold to preserve the 2×1 LEED pattern otherwise the deposited layer becomes polycrystalline. On the other hand no limitation occurs above 700°C for the explored energy range (0 to 80 eV). Good material quality is obtained for temperature above 650°C in pure silane plasma, confirmed by TEM, RBS, SIMS, Seeco etch whilst ERDA indicates a bulk-like hydrogen concentration in the epi-layer. Presently, epi-growth achieved in pure silane plasma at 700°C with an argon cleaning leads to a correct material, though a density of 10^7 defects per cm^2 (dislocations and precipitates) remains due to the poor experimental environment. Hall effect characterization measures an N type residual doping of $5.10^{14} \text{ donors/cm}^3$ with a mobility which is bulk-like within 5 %. Intentional doping was then explored. Arsine or phosphine diluted in H_2 are introduced during the plasma deposition. First, one notices that no change occurs in the epi-growth rate and that very high dopant concentrations are achievable. Secondly, the ion energy has a drastic influence on the doping profiles ; while smooth transition in dopant concentration are observed for low energy impact, well defined abrupt interfaces are obtained above a threshold of 50 eV for our standard epi-growth condition at 700°C ; Fig. 2 illustrates this result. One observes that the control of the energy of all of the ions interacting with the surface offers new facilities in doping control ; one more time it is mentioned that this result is obtained via a low energy process which minimizes the induced defects ; it has to be compared to more sophisticated techniques which give similar results, like partially ionized molecular beam epitaxy [5], but for a higher energy and consequently a higher temperature. Preliminary electric characterization indicates a correct activity of the incorporated dopants. Presently, work is still in progress and will continue with P type doping.

DISCUSSION

Plasma cleaning and plasma assisted epitaxy are achieved at low temperature using microwave multipolar plasma. Among the several experimental parameters, the impact energy of the ions on the treated surface is important. It appears clearly in our results, thanks to the relatively high current density allowed on the substrate ($j \approx 0,5 \text{ mA.cm}^{-2}$) due to an efficient plasma source at low pressure, and to the unique control of the ion energy in a very

low range. Concerning the cleaning, the hydrogen plasma action seems to be an essentially pure chemical process and the ion energy doesn't affect drastically the results, although a more systematic investigation is needed. On the contrary, low energy ions are undoubtedly needed with argon to achieve a low temperature cleaning process. In that case the involved mechanism could be a very soft sputtering enhancing the surface desorption of the native oxide, but the temperature should be high enough both to sustain the surface order during ion bombardment, and to desorb argon atoms. Anyway, our results are coherent with others found in the numerous literature on Si surface cleaning with or without plasma. A complete study remains to be done to give an optimised process. Our goal was simply to check the cleaning facilities of the microwave multipolar plasma, and our results are better than expected.

Numerous results concerning plasma assisted epitaxy are also available. This experiment dedicated to silicon homoepitaxy was designed to test our technique of plasma excitation with microwave in a multipolar magnetic field; the results on plasma deposition presented in this paper indicate a correct operation and growth rate kinetics similar to other plasmas results. High epi-growth rates are available at low temperature; however our material quality has to be improved even though TEM and SIMS give nice results, and work is in progress to lower the dislocation density. Preliminary results indicate we have to work in the 650-750°C range with a standard RCA wet cleaning before loading. Then systematic electric characterization like C(V) and DLTS will indicate the semi-conductor quality of the epi-layers.

The ions created in the silane plasma as well as the neutral species, must be characterised in order to investigate their influence on the epi-quality; that's why we have recently coupled a mass spectrometer to the plasma reactor. Nevertheless, early experiments on As intentionally doped layers reveal a well defined threshold in impact energy leading to a different behaviour of dopant incorporation. This interesting result is presently not understood; but it is argued that it was observed thanks to the microwave multipolar plasma. More experiments and analyses are a necessary to draw conclusions.

REFERENCES

- [1] B.S. Meyerson, E. Ganin, D.A. Smith, and T.N. Nguyen
J. Electrochem. Soc. 133, 1232, (1986)
- [2] T.J. Donahue, and R. Reif
J. Appl. Phys. 57, 2757, (1985)
- [3] M. Pichot, A. Durandet, J. Pelletier, Y. Arnal, and L. Vallier
Rev. Sci. Instrum. 59, 1072, (1988)
- [4] J.M. Comfort, L.M. Garverick, and R. Reif
J. Appl. Phys. 62, 3398, (1987)
- [5] T. Sugiyama and T. Itoh
Appl. Phys. Lett. 52, 883, (1988)

IN SITU HVEM STUDY OF ION IRRADIATION-INDUCED GRAIN GROWTH IN Au THIN FILMS

JOYCE C. LIU, JIAN LI AND J. W. MAYER

Department of Materials Science and Engineering, Cornell University,
Ithaca, NY 14853; CHARLES W. ALLEN AND LYNN E. REHN
Materials Science Division, Argonne National Laboratory, Argonne, IL 60439

ABSTRACT

In situ observations of 1.5 MeV Xe⁺ ion irradiated Au films at room temperature and at 150°C reveal the evolution of grain growth: the average grain size increases by the mechanisms of grain boundary migration and grain coalescence.

INTRODUCTION

Ion irradiation induced grain growth has been observed in several materials, including Ni, Au, Si and Ge [1,2,3,4]. Similar to investigations of thermally induced grain growth, the objective is to establish a relationship between grain size and irradiation time or between grain size and ion dose when the dose rate is constant. Results from Ag⁺ implanted Ni thin films [1,2] show that the average grain diameter is proportional to the ion dose. For Au, Si, and Ge, it is found, however, that the increase of grain size with the dose exhibits a power law dependence [3]. Since previous studies of ion irradiation induced grain growth are all based on observation following irradiations [1,2,3, 4], a direct observation of the ion irradiation induced grain growth is useful for understanding the mechanism, kinetics and driving force of this process. The evolution of grain growth in ion irradiated Au thin films is observed in an electron microscope, and some of the results are discussed in the present paper.

EXPERIMENTAL PROCEDURE

Au films with thickness ~55 nm were prepared by sputter deposition on NaCl substrates. The grain size distribution is uniform and the average size is about 25 nm. Moreover, grains in the as-deposited films were preferentially oriented in <111>. Self-supporting films were then irradiated with 1.5 MeV Xe⁺ ions at a dose rate of 1.7 x 10¹¹/cm².sec to minimize Xe implantation in the films and the effect of beam heating. The experiments were carried out at the HVEM-Tandem User Facility at Argonne National Laboratory [5], where a 2 MeV Tandem accelerator is interfaced to an AEI EM-7 1.2 MV high voltage transmission electron microscope (HVEM). The ion beam is introduced into the HVEM via a 33° ion-beam access tube; i.e., the ion beam is 33° from the electron beam in the microscope. During irradiations at room temperature and 150°C, microstructural changes of the films are examined in situ with the HVEM operated at 500 kV. The evolution of grain growth is followed by recording the images continuously on video tape and sequentially on photographic film.

OBSERVATIONS AND DISCUSSION

Direct observations

Direct observation of the Au films during ion irradiation reveal a dynamic picture of the induced grain growth; i.e., a gradual increase of average grain size is associated with dynamic changes in lattice defect structures. Although individual defects were not resolved due to their high density, the change of defect structure is suggested by the continuous

change of contrast in different areas of a single grain during irradiation. An example of the evolution of a single grain is shown in the dark field images of Fig. 1. The observed defects are presumed to be dislocation loops, since it has been previously reported that high concentration of vacancies in a collision cascade can collapse to form dislocation loops under irradiation at room temperature [6,7]. Such Frank loops can expand by climb or become glissile when converted to prismatic loops by unfaulting. The observed contrast change due to dislocation rearrangement during ion irradiation, therefore, can be attributed to interactions of point defects and dislocations, dislocations with one another, dislocations and grain boundaries and dislocations and the free surfaces. The excess point defect concentration accelerates atom diffusion. Dislocation movement to grain boundaries can in turn cause structure changes in boundaries and thus affect grain boundary migration and grain orientation. The actual role of dislocations in the radiation-induced grain growth process is not clear, however, and certainly warrants further study.

Growth by grain boundary migration

Dark field images of the Au films irradiated with 1.5 MeV Xe^+ at 150°C and room temperature are shown in Fig. 2 and Fig. 3, respectively. The images cover a dose range from 5.4×10^{13} to $5.1 \times 10^{14}/\text{cm}^2$ for the 150°C irradiation, and from 1.7×10^{14} to $5.1 \times 10^{14}/\text{cm}^2$ for the room temperature irradiation. It is noticed that the majority of the grains in the films are larger than the film thickness which is about 55 nm, so that the consecutive images demonstrate the evolution of 2-dimensional growth at both temperatures. Following grain "d" in Fig. 2 very closely, we noticed that after an irradiation of $5.4 \times 10^{13} \text{Xe}^+/\text{cm}^2$ the grain had an irregular shape with diameter approximately equal to 110 nm. As the dose had increased from 5.4×10^{13} to $1.1 \times 10^{14} \text{Xe}^+/\text{cm}^2$, the size of this grain increased about 30% by consuming its surrounding smaller grains. Then, the grain shape became hexagonal by continuous consumption of neighboring grains. At the final stage, after a dose of $5.1 \times 10^{14} \text{Xe}^+/\text{cm}^2$, the grain appears to be a hexagon with sides of almost equal length and angles about 120° at the vertices. Similar development is found in Fig. 3 for grain "D" irradiated at room temperature.

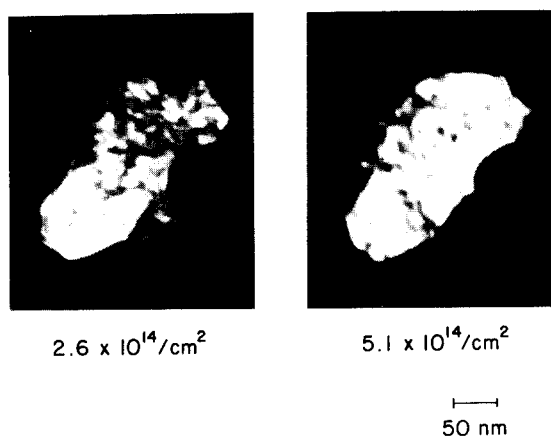


Fig. 1. Dark field images of Au films irradiated by 1.5 MeV Xe^+ at 150°C with doses of 2.6×10^{14} and $5.1 \times 10^{14}/\text{cm}^2$.

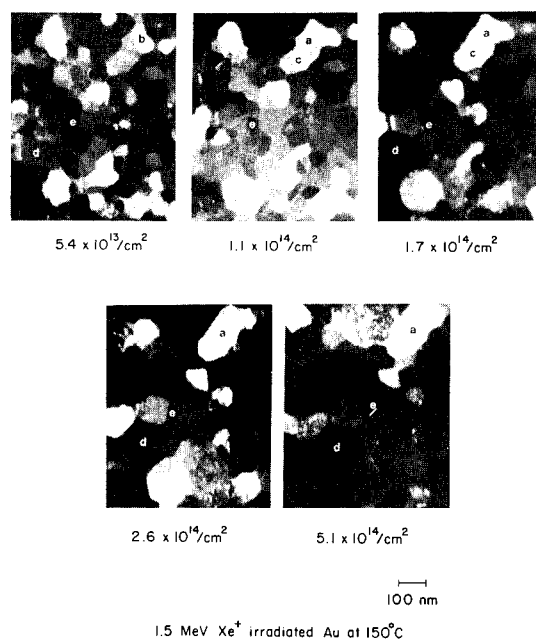


Fig. 2. Dark field images of Au films irradiated by 1.5 MeV Xe⁺ at 150°C with doses from 5.4×10^{13} to 5.1×10^{14} /cm².

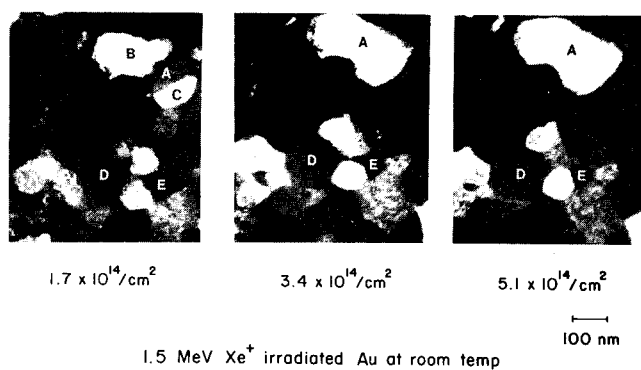


Fig. 3. Dark field images of Au films irradiated by 1.5 MeV Xe⁺ at room temperature with doses from 1.7×10^{14} to 5.1×10^{14} /cm².

The evolution of grains "d" and "D" represents a process of grain enlargement during the ion irradiation. In parallel, a process of grain shrinkage is also revealed. The grain labeled "e" in Fig. 2 had a size of 55 nm after irradiation with $5.4 \times 10^{13} \text{Xe}^+/\text{cm}^2$. Afterward, its dimension did not change significantly with the ion dose until its neighboring grains became relatively larger. According to Fig. 2, the transition took place after an irradiation of approximately $1.7 \times 10^{14} \text{Xe}^+/\text{cm}^2$, when grain "e" with concave boundaries was surrounded by three larger grains. When the dose was further increased to $5.4 \times 10^{14}/\text{cm}^2$, the size of grain "e" was reduced to only 18 nm. Similarly, the shrinkage of grain "E" in Fig. 3 is also observed.

The change of morphology in this irradiated Au film resembles the two-dimensional grain growth described by Hillert [8] in his defect model, where an array of hexagons is defined as perfect structure. If a defect, e.g., a 5-side grain, is introduced into a perfect array, grain boundary migration tends to occur because of the free energy difference caused by the curved boundaries. Therefore, the in situ observations of the evolution of grains, such as the shrinkage of small grains with concave boundaries and the development of stable hexagonal structures, in the irradiated Au films indicates that the main driving force of grain growth during irradiation is reduction of grain boundary energy. Further, the grain growth in these particular areas is accomplished by the gradual migration of grain boundaries towards grains with higher free energy without any formation of nuclei.

Grain coalescence

Besides the observed grain boundary migration, it is also noticed that the contrast between some grains varies during the irradiations. Such evidence can be found in Figs. 2 and 3 of the irradiated Au films. For instance, in Fig. 2 after an irradiation of $5.4 \times 10^{13} \text{Xe}^+/\text{cm}^2$ grain "a" was distinguished from grain "b" by the contrast, and it was separated from grain "c" by a boundary which was decorated with dislocations. As the dose increased to $1.1 \times 10^{14}/\text{cm}^2$, the sharp boundary between the original grains "a" and "b" disappeared, causing a dramatic change of the geometric shape of grain "a". At this point, the boundary between grain "a" and "e" was still present, which was determined not only by the contrast but also by the existing vertices on both ends as a result of balancing the surface tension of relevant boundaries. As the irradiation continues, the boundary between grains "a" and "c" gradually faded away by a dose of $5.1 \times 10^{14}/\text{cm}^2$. The absence of that grain boundary is confirmed by the straightening of the relevant boundaries between the coalesced grain and its neighboring grains. Moreover, the contrast between grains "a" and "c" became less, indicating the two grains merged into the same orientation. It is further displayed from these micrographs that the contrast between this coalesced region relative to its surrounding grains has changed during the irradiation, which could be caused by a relative orientation change between this area and the neighboring grains or between the film and the incident electron beam. The same grain coalescence process is observed at room temperature from the merging of grains "A, B, C" in Fig. 3.

In a previous study of thermal annealing behavior of cold rolled 3% silicon-iron single crystal, Hu [9] observed in an electron microscope that recrystallized nuclei could be formed by coalescence of subgrains in a high dislocation density area. He also noticed that the orientation of the coalesced grain differed from that of the original subgrains from which it was formed. A schematic diagram of this coalescence process is given in Fig. 4 by Li [10]. At the initial stage (Fig. 4(a)), the two grains are misoriented by a small angle. During thermal annealing the low-angle boundary "CH" is eliminated by dislocation climb along this boundary and by a relative rotation of the two grains, which is achieved by short-range

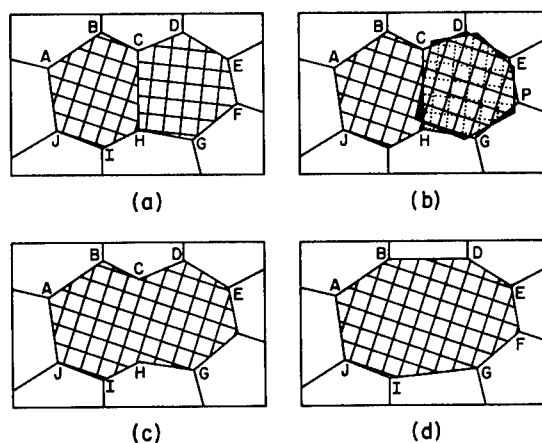


Fig. 4 Schematic representation of subgrain coalescence: (a) original structure; (b) rotation of one grain; (c) coalesced subgrain and (d) rearrangement of affected boundaries. (After Li, Ref. [10])

diffusion of atoms along the boundaries from the shaded to unshaded areas (Fig. 4(b)). Then, the affected boundaries of the coalesced grain are rearranged to remove the unstable angles (Fig. 4(c) and (d)). According to his description, the coalescence of subgrains during thermal annealing is very similar to the merging of some grains in the irradiated films.

Due to the relatively low surface energy, the grains with $\langle 111 \rangle$ normal to the surface of the irradiated Au films are thermodynamically more favored than grains with other orientations. Since the grain coalescence takes place at low-angle grain boundaries, it is suggested that the grain coalescence is significant only in a process of two-dimensional grain growth where a fair number of grains are oriented in $\langle 111 \rangle$ and share low-angle boundaries. Because grain growth by coalescence is not the only mechanism of grain enlargement in the irradiated films, satisfactory kinetic data for this process were not obtained.

SUMMARY

In situ observations of 1.5 MeV Xe^+ ion irradiated Au films at room temperature and at 150°C reveal the evolution of grain growth. In the process of two-dimensional growth, the average grain size increases by the mechanisms of grain boundary migration and grain coalescence.

ACKNOWLEDGMENTS

The Cornell work was supported in part by the National Science Foundation (John Hurt) and the Argonne effort by the U. S. Department of Energy, Basic Energy Sciences--Materials Sciences, under Contract W-31-109-Eng-38. The assistance of Loren Funk and Edward Ryan of Argonne National Laboratory is gratefully acknowledged.

References

- [1] P. Wang, D. A. Thompson and W. W. Smeltzer, Nucl. Instrum. Methods **B7/8**, 97 (1985).
- [2] P. Wang, D. A. Thompson and W. W. Smeltzer, Nucl. Instrum. Methods **B16**, 288 (1986).
- [3] H. A. Atwater, H. I. Smith and C. V. Thompson, in Beam-Solid Interactions and Phase Transformations, edited by H. Hurz, G. L. Olson and J. M. Poate (Materials Research Society, Pittsburgh, PA, 1986), Vol. 51, p. 337.
- [4] H. A. Atwater, C. V. Thompson and H. I. Smith, J. Appl. Phys. **64**, 2337 (1988).
- [5] A. Taylor, C. W. Allen, and E. A. Ryan, Nucl. Instrum. Methods, **B24/25**, 598 (1987).
- [6] W. Jäger, J. Microsc. Spectrosc. Electron. **6**, 437 (1981).
- [7] M. A. Kirk, I. M. Robertson, M. L. Jenkins, C. A. English, T. J. Black, and J. S. Vetrano, J. Nucl. Mater. **149**, 21 (1987).
- [8] M. Hillert, Acta Metall. **13**, 227 (1965).
- [9] H. Hu in Electron Microscopy and Strength of Crystals, edited by G. Thomas and J. Washburn (Interscience, New York, 1963) p. 546.
- [10] J. C. M. Li, J. Appl. Phys. **33**, 2958 (1962).

PRECIPITATION OF Ar, Kr AND Xe IN Ni AT ROOM TEMPERATURE*

A. S. LIU AND R. C. BIRCHER

Materials Science Division, Argonne National Laboratory, Argonne, IL 60439

ABSTRACT

Transmission electron microscopy (TEM) has been used to study the precipitation of inert gases (Ar, Kr and Xe) injected into Ni at room temperature. The nucleation and size distribution of precipitates were found to be insensitive to the type of inert gas atom but dependent on gas concentration (ion fluence). The precipitate density decreases and the sizes increase with increasing gas concentration. In all cases, the inert gases precipitate as solid fcc crystals with their axes aligned with those of the host Ni lattice. For the same inert gas concentration, the lattice parameter is larger for the higher atomic mass in accord with bulk results. The lattice parameter of each type of inert gas precipitate increases with increasing gas concentration owing to the pressure relaxation that accompanies precipitate growth. This results in melting of large precipitates in accord with the behavior of bulk quantities of the gases at low temperatures.

INTRODUCTION

Studies of inert gases injected into metals have shown that the inert gas precipitates into cavities under very high pressures [1,2,3,4]. These pressures are sufficient to solidify the gases at temperatures greatly in excess of their freezing temperatures at 1 atm. In all cases studied, the crystal axis of the solid precipitates aligned with the crystal axis of the host metal. Detailed investigation [3,4] of the precipitation of Kr as a function of implantation fluence reveals that cavity growth leads to a lowering of the cavity pressure to the point that melting of the precipitates occurred. Melting and freezing is also observed during thermal cycling.

Experimental

Thin single-crystal Ni films (70 nm thick) were prepared by evaporation of high purity Ni. Coated NaCl was cleaved into small pieces, and specimens were floated on a water-methanol mixture onto Cu TEM grids. Implantations were performed with 100 keV Ar⁺, 180 keV Kr⁺ or 200 keV Xe⁺ ions at fluxes less than $2 \cdot 10^{16} \text{ m}^{-2} \text{ sec}^{-1}$. During implantation, the TEM grids were clamped at their periphery against a Cu plate. Implantation energies were selected on the basis of results from the TRIM computer code [5] so that the gas-concentrations depth profile within the Ni films peaked near the foil center and decreased to near zero at both foil surfaces. Estimates calculated with the TRIM computer code [5] are given in Table I for ion range, peak gas concentration, damage production and sputtering. Sputtering causes the peak in the inert gas concentration to shift closer to the back specimen surface. Estimates of sputtering given in Table I may be high due to reduced sputtering of the surface oxide. Sputtering results in a more uniform gas concentration through the thickness of the Ni thin film and reduces the maximum gas concentration. In addition, removal of the surface layer allows implanted gas to escape and causes inert gas precipitates to rupture through the surface. The data presented in all figures has been corrected for sputtering.

*Work supported by the U. S. Department of Energy, BES-Materials Sciences, under Contract W-31-109-Eng-38.

TABLE I

	Ar	Kr	Xe
ENERGY(keV)	100	180	200
RANGE (nm)	37	33	27
PEAK CONCENTRATION (at. %/ 10^{20} m^{-2})	2.74	3.14	4.26
DISPLACEMENTS (dpa/ 10^{20} m^{-2})	13	33	44
SPUTTERING YIELD	3.5	7.3	12

Post-implantation TEM observations were made with a JEOL JEM-100-CX at an operating voltage of 100 keV and at magnifications up to 100,000 times. Details within the specimens greater than 1 nm were detectable. The inert gas-filled cavities were imaged in bright field by use of defocus contrast. Selected-area diffraction patterns were produced with the electron beam parallel to the $\langle 100 \rangle$ specimen normal. A traveling, optical microscope was used to determine the positions on the micrograph of intensity maxima due to solid-gas and Ni $\{200\}$ reflections, and the average solid-gas lattice parameter was then calculated. The estimated uncertainty was 0.5 % due to weakness of the solid-gas reflections and the over exposure of the film by the Ni diffraction spots.

RESULTS AND DISCUSSION

Precipitates

TEM images of rare gas precipitates are shown in Fig. 1 for Ni implanted with Ar, Kr or Xe at room temperature. Within experimental resolution, precipitates become visible at the same concentration for the different inert gases in spite of differences in their atomic mass and damage production. For all gases, the small precipitates appear to be spherical.

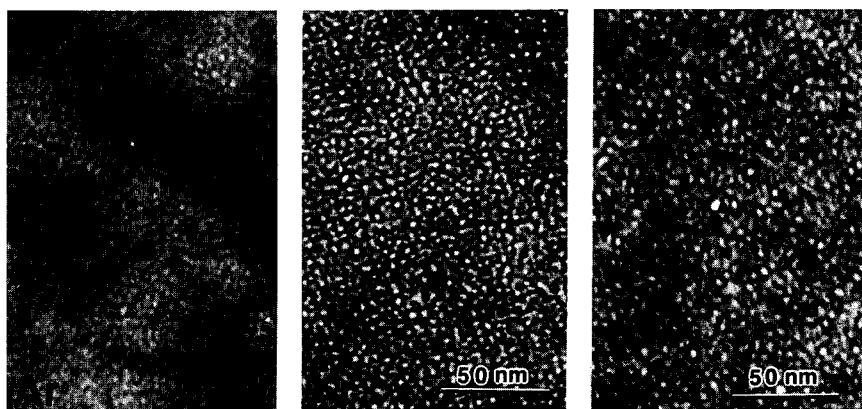


Fig. 1 TEM images of Ni implanted at room temperature with either $2 \cdot 10^{20} \text{ m}^{-2}$ Ar, Kr or Xe.

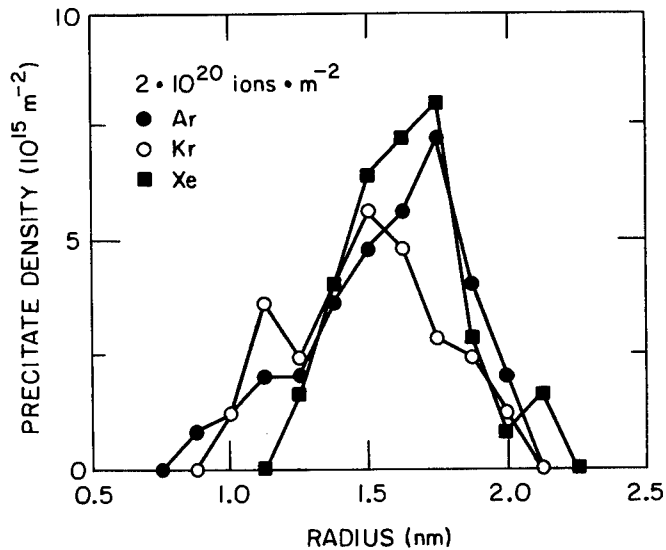


Fig. 2. Variation of rare-gas precipitate density with size for Ni implanted with either of $2 \cdot 10^{20} \text{ m}^{-2}$ Ar, Kr or Xe at room temperature.

With increasing gas concentration, the precipitates increase in size and become somewhat irregular in shape. The precipitate size distributions are shown in Fig. 2 for a fluence of $2 \cdot 10^{20} \text{ ions/m}^2$. The size distributions are similar for each type of inert gases indicating that precipitation kinetics at room temperature depends weakly on the type of inert gas. Modeling with rate theory indicates that this is due to limited gas and precipitate mobility at room temperature [6].

Precipitate Phase

The phase of the inert gas precipitates is revealed by electron diffraction. Examples are shown in Fig. 3 for Ni implanted with $2 \cdot 10^{20} \text{ ions/m}^2$ at room temperature. The patterns for all the rare gases show diffraction spots from both the Ni host lattice and solid gas precipitates. The existence of solid gas precipitates can be demonstrated from images produced from the extra diffraction spots [3,4]. The gases are held in the solid state by the high pressures generated by the walls of the cavities in which they are located. In all cases, the inert gases condense in a fcc lattice aligned with the Ni host lattice. Diffraction from solid precipitates is observed for fluences above about $1 \cdot 10^{20} \text{ ions/m}^2$ or about 3 at. % for all gases studied. The gas lattice parameter is larger, diffraction spots closer to the central spot, for higher atomic mass inert gas. This is consistent with the bulk lattice parameters of the different inert gases at low temperatures. At higher fluences, a diffuse ring appears in the diffraction patterns because the larger, low pressure precipitates are liquid. This is detectable at about $4 \cdot 10^{20} \text{ Ar/m}^2$, between 3 and $4 \cdot 10^{20} \text{ Kr/m}^2$ and about $2 \cdot 10^{20} \text{ Xe/m}^2$.

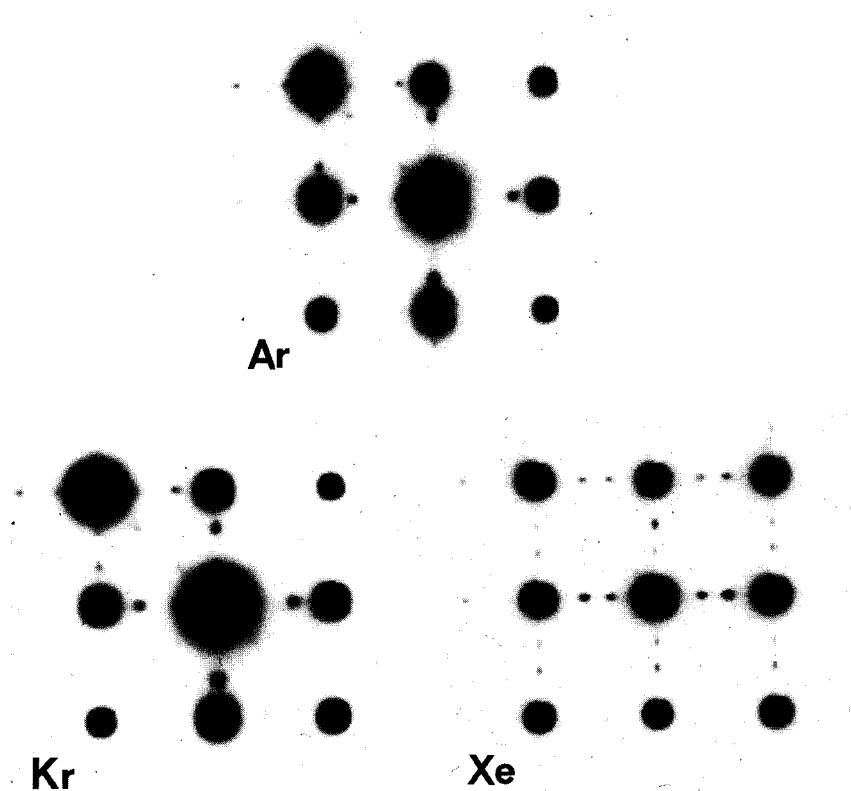


Fig. 3. (100) Electron diffraction patterns from Ni implanted at room temperature with either $2 \cdot 10^{20} \text{ m}^{-2}$ Ar, Kr or Xe.

Precipitate Properties

Average lattice parameters were determined from electron diffraction patterns, and their variations with fluence are shown in Fig. 4. As has been observed for Kr precipitates in Ni and Al, the lattice parameters increase toward asymptotic limits with increasing fluence. The lattice parameter at a given inert gas concentration, is larger for higher atomic mass inert gas. This result is in accord with the behavior of bulk quantities of the inert gases at low temperatures where they are solids at one atmosphere pressure.

Average precipitate pressures can be determined from the gas densities with the use of experimental results for solid Ar expansion at room temperature [7] and theoretical equations of state for Kr and Xe [8]. The pressures are similar for the different inert gases. As the average precipitate increases in size, the average pressure decreases. The average pressures range from about 40 kbar for small precipitates to about 10 kbar for the largest precipitates. The lower average pressure is determined by melting of large precipitates (8 kbar for Kr and 11.5 kbar for Ar at room temperature) and the removal of their contributions to the solid-gas lattice parameter. The pressures seem to be primarily dependent upon precipitate size and not inert gas type.

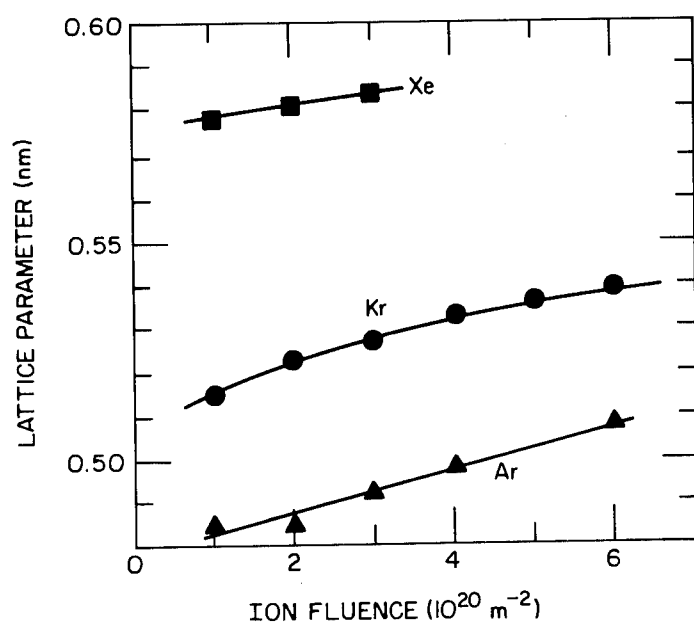


Fig. 4. Lattice parameter of solid rare-gas precipitates in Ni at room temperature as a function of ion fluence.

CONCLUSIONS

The precipitation of inert gases in Ni at room temperature is insensitive to the type of inert gas atom but dependent on gas concentration. Precipitate density decreases and the size increases with increasing gas concentration. In all cases, the gases precipitate as solid fcc crystals with their axes aligned with those of the host Ni lattice. For the same gas concentration, the lattice parameters are larger for higher atomic mass inert gas, and increase toward asymptotic limits with increasing gas concentration owing to pressure relaxation that accompanies precipitate growth. This results in melting of large precipitates and is in accord with the behavior of bulk quantities of inert gases at low temperatures.

References

- [1] A. vom Felde, J. Fink, Th. Möller-Heinzerling, J. Pflüger, B. Scheerer and G. Linker, *Phys. Rev. Lett.* **53**, 922 (1984).
- [2] W. Jäger and J. Roth, *J. Nucl. Mater.* **93&94**, 756 (1980).
- [3] R. C. Birtcher and W. Jäger, *Ultramicroscopy* **22**, 267 (1987).
- [4] R. C. Birtcher and A. S. Liu, in *Fundamentals of Beam-Solid Interactions and Transient Thermal Processing*, edited by M. J. Aziz, L. E. Rehn and B. Stritzker (*Mater. Res. Soc. Proc.* **100**, Boston, MA 1987) pp. 225-230.

- [5] J. Biersack and L. G. Haggmark, Nucl. Instr. and Meth. 174, 257 (1980).
- [6] J. Rest and R. C. Birtcher, submitted to J. Nucl. Mater.
- [7] L. W. Finger, R. M. Hazen, G. Zou, H. K. Mao and P. M. Bell, Appl. Phys. Lett. 39, 892 (1981).
- [8] C. Ronchi, J. Nucl. Mater. 96, 314 (1981).

DEUTERIUM INTERACTIONS WITH ION-IMPLANTED OXYGEN IN Cu AND Au

S. M. MYERS*, W. A. SWANSIGER**, AND D. M. FOLLSTAEDT*

*Sandia National Laboratories, Div. 1112, Albuquerque, NM 87185

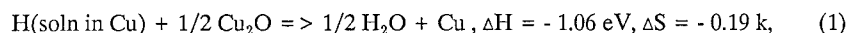
**Sandia National Laboratories, Div. 8343, Livermore, CA 94550

ABSTRACT

The interactions of deuterium (D) with oxygen in Cu and Au were examined using ion implantation, nuclear-reaction analysis, and transmission electron microscopy. In Cu, the reduction of Cu_2O precipitates by D to produce D_2O was shown to occur readily down to room temperature, at a rate limited by the transport of D to the oxides. The reverse process of D_2O dissociation was characterized for the first time below the temperature range of steam blistering. The evolution of the $\text{Cu}(\text{D})\text{-Cu}_2\text{O-D}_2\text{O}$ system was shown to be predicted by a newly extended transport formalism encompassing phase changes, trapping, diffusion, and surface release. In Au, buried O sinks were used to measure the permeability of D at 573 and 373 K, thereby extending the range of measured permeabilities downward by about six orders of magnitude.

INTRODUCTION

Precipitates of low-stability oxides within metals have long been recognized to undergo a reduction reaction with hydrogen leading to the formation of H_2O inclusions. A widely recognized example is the reduction of Cu_2O particles in Cu [1,2]. This strongly exothermic reaction is given by



where k is the Boltzmann constant. The specified net changes in enthalpy, ΔH , and in the nonconfigurational entropy, ΔS , were obtained by combining the known heats and entropies of formation for Cu_2O and H_2O with the published activation enthalpy and prefactor for hydrogen solution in Cu [3,4]. The process of Eq. (1) is responsible for "steam embrittlement", which affects impure coppers when they are heated in hydrogen ambients. This degradation is especially pronounced at temperatures of about 1000 K and above, where high pressures within the H_2O inclusions cause catastrophic rupturing of the Cu matrix.

In the present investigation, the interactions of hydrogen with O in Cu and Au were examined mechanistically using ion implantation and nuclear-reaction analysis. The study had four motivations. First, we wished to determine the kinetics of the solid-state reduction reaction with Cu_2O precipitates in Cu, and further to do this for a range of temperatures extending down to 300 K. Although this reaction had previously been shown to occur readily at temperatures of several hundred °C and above, the rate-determining steps had not been established and quantified so as to provide a predictive capability, and observations were lacking for near-ambient temperatures. A second objective was to characterize the reverse of the reaction of Eq. (1), which had not previously been examined. This process reintroduces hydrogen into solution, thereby permitting its migration to the surface and subsequent release. Thirdly, we used the ion-implanted $\text{Cu}(\text{H})\text{-Cu}_2\text{O-H}_2\text{O}$ system to test a transport formalism which describes hydrogen behavior in materials where phase changes, trapping, diffusion, and surface release are concurrent. Finally, buried O sinks in Au were exploited to extend the temperature range of measured hydrogen permeabilities from 573 to 373 K, thereby demonstrating a sensitivity to permeabilities orders of magnitude smaller than those detectable by conventional methods.

Our experiments on Cu began with O ion implantation and vacuum annealing to produce a dense distribution of oxide precipitates at a selected depth. Deuterium (D) was then introduced by ion implantation or by heating in D_2 gas. Subsequently, specimens were annealed under vacuum to the point of D release. The uptake, internal redistributions, and escape of the D were monitored through profiling with the nuclear reaction $\text{D}({}^3\text{He}, \text{p}){}^4\text{He}$, and at key stages of the evolution the microstructure was examined by transmission

electron microscopy (TEM) in identically processed foils. The resulting data were quantitatively interpreted through comparisons with solutions of the aforementioned transport formalism.

THE REDUCTION REACTION IN Cu

Figure 1 shows the calculated implantation profiles of O and D within a Cu specimen that was used to observe the interaction of D with Cu_2O precipitates. The two peaks are Gaussian with first and second moments taken from the Monte-Carlo range code TRIM [5]. The O and D were separated in depth so that their subsequent reaction could be detected through nuclear-reaction profiling. The O was implanted first, at an energy of 120 keV and to a fluence of 1000 nm^{-2} . This room-temperature treatment was followed by vacuum annealing at 773 K for 30 minutes to produce precipitates of Cu_2O . Transmission electron microscopy of identically treated Cu foils confirmed the expected cubic phase of the oxide particles and showed the average size to be about 50 nm. After being installed in a vacuum chamber used for temperature ramping, the sample was sputtered with Cu ions to clean the surface. The temperature of the specimen was then reduced to below 150 K, and D was implanted at 60 keV to a fluence of 160 nm^{-2} . Finally, the temperature was ramped upward at 2 K/minute.

During temperature ramping, the depth distribution of the D was periodically probed by bombarding with ^3He at 0.4 MeV and counting protons from the reaction $\text{D}(^3\text{He},\text{p})^4\text{He}$. For this ^3He energy, the nuclear cross section was calculated to vary with depth as shown in Fig. 1, based on published cross sections and electronic stopping powers [6,7]. The sensitivity to D is seen to be substantially greater in the O-implanted region than at the depth of D implantation. Consequently, as the D migrated to the oxide precipitates, and as it was later released at the surface, these events were marked by an increase and then a decrease in the measured proton yield from the nuclear reaction.

Data from the above temperature-ramp experiment are given by the circles in Fig. 2. The quantity plotted on the vertical axis is an approximation to the areal density of D that has reacted with the oxide precipitates, and it is obtained from the proton yield by using the nuclear cross section at the center of the O peak in Fig. 1. The release of D from implantation-induced vacancy traps at the initial injection depth, and its migration to and reaction with the oxide precipitates, is seen to occur in a stage starting below 300 K and centered at about 340 K. Subsequently, near 700 K, there is release from the O-implanted region and escape at the nearby surface. Detailed TEM indicated that the loss of D did not involve blistering or other disruptions of the D_2O inclusions. Hence, this loss is ascribed to a thermally activated reversal of the reaction of Eq. (1), with D being reintroduced into

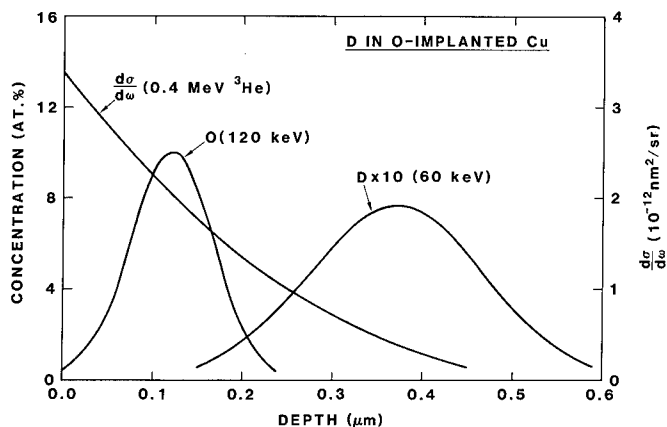


Figure 1. Implantation profiles and nuclear cross section from an experiment used to observe the interaction of D with Cu_2O precipitates in Cu.

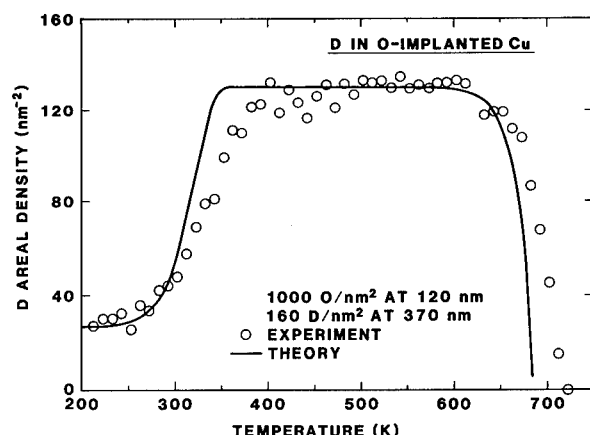


Figure 2. Deuterium areal density at oxide precipitates in Cu during temperature ramping of the specimen of Fig. 1.

solution and then diffusing to the surface. The apparently incomplete reaction of the D, involving 130 D/nm² instead of the implanted fluence of 160 D/nm², is actually an artifact of the simplified data analysis: the D migrating from the initial implantation depth tended to react with the first oxide particles encountered, and these lay at greater depths where the nuclear cross section was smaller than the value assumed in converting from the proton yield.

The occurrence of oxide reduction in the implanted alloys was further evidenced by other experimental results. For example, when the areal density of implanted D was increased to 830 nm⁻² and the areal density of O reduced to 200 nm⁻², the reaction with the oxides saturated at 380 D/nm², close to the value of 400 D/nm² that would correspond to the composition of D₂O. A similar saturation level was observed when the D was introduced by annealing in D₂ gas at 473 K. Moreover, the gas-phase charging was shown by TEM to cause the progressive removal of the Cu₂O phase.

These studies were made possible by at least two features of alloying by ion implantation. In particular, the reaction of Eq. (1) could be followed down to room temperature because the small D diffusivity was compensated by the submicrometer migration distance, and because the low D solubility was bypassed through the athermal injection of the D. Similarly, the highly endothermic reverse reaction occurred at measurable rates below the temperatures of steam blistering because of the microscopic diffusion distance to the surface where D release occurred.

THEORETICAL MODELING

The alloy evolution reflected in Fig. 2 was modeled using a transport formalism already discussed elsewhere [8], but extended here to include phase-change reactions as well as the trapping, diffusion, and surface release treated earlier. For the present experiments the equations can be written

$$(\partial/\partial t)C_s(x,t) = D_s (\partial^2/\partial x^2)C_s - S_T(x,t) - S_R(x,t) \quad (2)$$

$$(\partial/\partial t)C_i(x,t) = S_i(x,t), \quad i = T, R \quad (3)$$

where the source-sink terms S have the form

$$S_T(x,t) = 4\pi R_T D_s N_h [C_s A_T(x) - C_s C_T - z C_T \exp(-Q_T/kT)] \quad (4)$$

for trapping-detrapping processes and

$$S_R(x,t) = 4\pi R_R D_s N_h n_R^{-1} A_R(x) [\gamma(A_R - C_R) C_s - \gamma(C_R) C_{E0} \exp(-Q_R/kT)] \quad (5)$$

for phase change reactions such as that of Eq. (1). Here C_s is the atomic fraction of D in solution in the host matrix, z is the number of solution sites per host atom, C_T is the atomic fraction of D bound to defect traps, C_R is the atomic fraction of D that has reacted with the oxide precipitates, R_T is the effective trap radius and R_R the radius of the precipitates, D_s is the diffusion coefficient for unbound D in Cu, N_h is the atomic density of the host, n_R is the maximum number of D atoms which can react with one precipitate, and the quantities $A(x)$ are the maximum atomic fractions of D which can be bound by the various mechanisms at depth x . The quantities Q are the net enthalpy changes per D atom caused by detrapping or by reversal of the reduction reaction of Eq. (1), and $C_{E0} \exp(-Q_R/kT)$ is the solubility of D in Cu for three-phase equilibrium among Cu, Cu_2O , and D_2O . Finally, the function $\gamma(C)$ is defined as one for positive C and -1 otherwise; in numerical solutions, this function serves to halt the forward and reverse reduction reactions of Eq. (1) when the Cu_2O or D_2O is fully consumed. The boundary condition for D release at the surface is

$$L = K_L N_h [C_s(x \rightarrow 0, t)]^2 \quad (6)$$

where L is the molecular flux expressed as atoms per unit area and time, and K_L is the surface recombination coefficient. This system of equations is readily solved using numerical methods [9].

Equations (2)-(6) were used to model the experiment of Figs. 1 and 2. In these calculations, it was possible to evaluate most of the parameters on the basis of independent information. From previous studies of ion-implanted D in Cu not containing O, the trapping at vacancy defects was assigned a binding enthalpy of $Q_T = 0.42$ eV [10]. The reaction enthalpy and entropy given in Eq. (1) correspond to $Q_R = 1.06$ eV and $C_{E0} = 1.2 \approx 1$, and the stoichiometry specified there relates $A_T(x)$ to the O profile in Fig. 1. Both the D diffusivity D_s and the recombination coefficient K_L were taken from the literature [11,12]. This left undetermined only the concentration profile of the defect traps initially occupied by the implanted D; as a first approximation, the trap profile was equated to the D implantation profile, the justification being that vacancies not attached to D become mobile in Cu below the onset of D detrapping. As a convenient way of compensating for the apparently incomplete reaction of the D, which was in fact an artifact of the simplified data analysis as discussed above, the D concentration profile in Fig. 1 was scaled downward from an areal density of 160 nm^{-2} to 130 nm^{-2} .

The results of the above model calculation are given by the curve in Fig. 2, and the agreement with experiment is seen to be good, given the minimal adjustment of parameters. This illustrates the predictive capabilities of such modeling, and it tends further to support our interpretation of the thermal evolution of the implanted Cu-Cu₂-D system. As one example, the close correspondence between the predicted and observed temperatures of the internal redistribution near 340 K indicates that the reaction of Eq. (1) is limited primarily by the transport of D to the oxides, as assumed in the model calculations.

DEUTERIUM PERMEATION

Sinks formed by O ion implantation were used to measure the permeabilities of D in Cu and Au. These sinks were introduced at greater depths than in Fig. 1 by using an implantation energy of 1.7 MeV, corresponding to calculated O ranges of $1.04 \mu\text{m}$ in Cu and $0.79 \mu\text{m}$ in Au; after O implantation, precipitation annealing was performed at 773 K as discussed above. Calculations using thermodynamic data indicate that the implanted O should immobilize D even more strongly in Au than in Cu, with a binding enthalpy exceeding 2 eV; this is consistent with our observation that D loss from Au occurred only at temperatures above 1000 K, and then through blistering of the D_2O inclusions. The permeability measurements were accomplished by repeatedly heating the specimens in D_2 gas and using nuclear-reaction profiling to monitor the accumulation of D at the sinks after it had migrated through the overlying metal. The permeability, which is the product of

diffusivity and solubility, was then equated to the measured flux of migrating D divided by the migration distance and by the square root of the applied pressure.

Figure 3 shows two measured concentration profiles of D in a specimen of O-implanted Cu which was repeatedly annealed in D_2 gas at 473 K and a pressure of 86 kPa (0.86 atm). These profiles were obtained by measuring the proton yield from the reaction $D(^3\text{He}, p)^4\text{He}$ as a function of incident ^3He energy and then performing a deconvolution as described elsewhere [13]. After 15 minutes of accumulated exposure a relatively small areal density of D had reacted with the tail of the O distribution extending toward the surface, whereas after 165 minutes the reaction approached completion over the entire profile of implanted O. Similar behavior was observed in Au, and in Fig. 4 the progressive permeation of D to O sinks in this metal is shown for gas-phase charging at 373 K. In this particular case, the very small permeability was measured by using the high D_2 pressure of 88 MPa (870 atm) and by employing lengthy exposures. The permeability was obtained directly from the slope of the data as indicated above, yielding the value given on the figure.

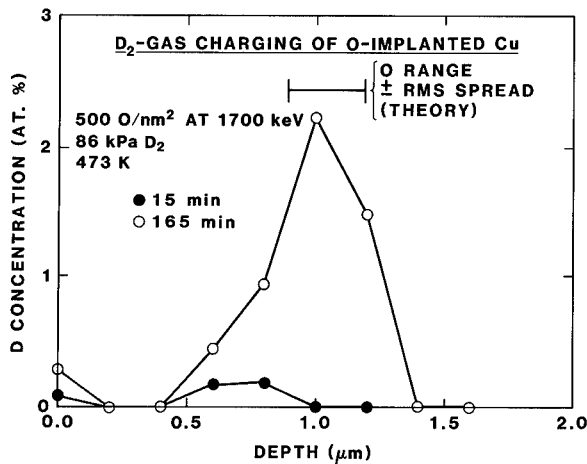


Figure 3. Depth profiles of D in O-implanted Cu after annealing in D_2 gas at 373 K for 15 and 165 minutes.

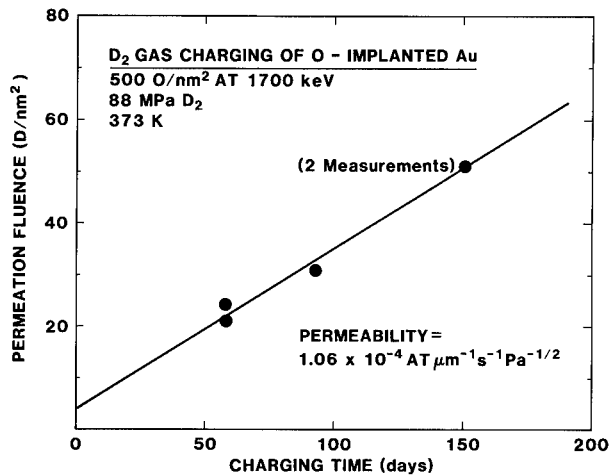


Figure 4. Permeation of D to implanted O in Au during annealing in D_2 gas at 373 K.

A selection of permeabilities obtained by the above approach is given in Table I, and comparison is made with results from conventional foil permeation experiments involving measurements of gas throughput. The agreement between the ion-beam and foil-permeation results is seen to be good where the temperature ranges overlap. In Au, however, the last entry extends the temperature range of available information from 573 to 373 K, corresponding to a reduction of almost six orders of magnitude in the permeability. This measurement was possible because of the submicrometer permeation distance, the compatibility of the method with high-pressure exposure, the extended time of the exposure, and the detectability of permeated fluences much smaller than those measured with gas-flow methods.

Table I. Deuterium permeabilities in Cu and Au from the present ion-beam studies and previous foil permeation experiments.

Host	Temperature (K)	Permeability from ion beams ($\text{AT} \cdot \mu\text{m}^{-1} \text{s}^{-1} \text{Pa}^{-1/2}$)	Permeability from foil perm. ($\text{AT} \cdot \mu\text{m}^{-1} \text{s}^{-1} \text{Pa}^{-1/2}$)
Cu	373	3.6	5.5 (Ref. 2)
Au	573	46	45 (Ref. 14)
Au	373	0.00011	none

CONCLUSION

The kinetics of hydrogen-associated oxidation-reduction reactions in Cu-Cu₂O-H₂O alloys were characterized in experiments utilizing ion implantation in conjunction with nuclear-reaction analysis. The evolution of these alloys was shown to be described quantitatively by a newly extended transport formalism incorporating published thermodynamic information. Buried O sinks formed by ion implantation facilitated measurements of hydrogen permeability in Au at temperatures much lower than those accessible to conventional methods.

REFERENCES

- [1] J. D. Fast, Interaction of Metals and Gases (Academic Press, New York, 1965), pp. 54-57.
- [2] G. R. Caskey, Jr., A. H. Dexter, M. L. Holzworth, M. R. Louthan, Jr., and R. G. Derrick, *Corrosion-NACE* **32**, 370 (1976).
- [3] CRC Handbook of Chemistry and Physics.
- [4] W. R. Wampler, T. Schober, and B. Lengeler, *Phil. Mag.* **34**, 129 (1976).
- [5] J. P. Biersack and L. G. Hagmark, *Nucl. Instrum. Meth.* **174**, 257 (1980).
- [6] W. Moller and F. Besenbacher, *Nucl. Instrum. Meth.* **168**, 111 (1980).
- [7] J. F. Ziegler, Helium Stopping Powers and Ranges in All Elements (Pergamon Press, New York, 1977). The stopping power for ³He at energy E was equated to that reported for ⁴He at (4/3)E.
- [8] S. M. Myers, W. R. Wampler, F. Besenbacher, S. L. Robinson, and N. R. Moody, *Mater. Sci. Eng.* **69**, 397 (1985).
- [9] A. C. Hindmarsh, in Scientific Computing, ed. R. S. Stepleman (North-Holland Publishing, Amsterdam, 1983), pp. 55-64.
- [10] F. Besenbacher, B. Bech Nielsen, and S. M. Myers, *J. Appl. Phys.* **56**, 3384 (1984).
- [11] L. Katz, M. Guinan, and R. L. Borg, *Phys. Rev. B* **4**, 330 (1971).
- [12] K. L. Wilson, R. A. Causey, M. I. Baskes, and J. Kamperschroer, *J. Vac. Sci. Technol. A* **5**, 2319 (1987).
- [13] S. M. Myers, G. R. Caskey, Jr., D. E. Rawl, Jr., and R. D. Sisson, Jr., *Metall. Trans. A* **14**, 2261 (1983).
- [14] D. R. Begeal, *J. Vac. Sci. Technol.* **15**, 1146 (1978).

THE EFFECTS OF Ar-BOMBARDMENT ON THE DISSOLUTION AND REPRECIPITATION OF CARBONITRIDES IMPLANTED INTO LOW CARBON STEEL

STELLA M.M. RAMOS, L. AMARAL, M. BEHAR, A. VASQUEZ AND F.C. ZAWISLAK
Instituto de Física, UFRGS, 91500 Porto Alegre, Brasil

ABSTRACT

The effects of Ar post-bombardment on the dissolution and reprecipitation of carbonitrides present in N_2^+ implanted 1020 low carbon steel are investigated using conversion electron Mössbauer spectroscopy (CEMS). The results are compared with similar experiments where samples of the same steel were post-bombarded with He. The experimental data show that the Ar is more efficient in the dissolution of precipitates and also more efficient in the precipitate retention at 450 °C, for the same peak concentration.

INTRODUCTION

In previous works we have reported results showing the effects of alpha particle post-bombardment on nitrides and carbonitrides produced by N implantation into Fe [1] and into low carbon steel [2] respectively. In both cases the alpha irradiation affected the thermal behaviour of the precipitates by raising the temperature at which they started to dissolve. Besides these results, particular effects have been found for each case. The alpha bombardment produced partial nitride dissolution in the Fe matrix [1] whereas for the low carbon steel complete dissolution and reprecipitation of carbonitrides have been observed at low bombardment fluences [2,3]. As discussed previously [3] the above effects are strongly dependent on the kind of precipitates involved in the process as well as on the type of matrix in which the precipitates are formed.

An extension of this research is to investigate the influence of the type of ions used in the post-bombardment experiments. Therefore, in the present work we report results of Ar post-bombardment effects on carbonitrides produced by N implantation in low carbon 1020 steel samples. The N implanted samples have been annealed, Ar post-bombarded and further thermally treated. The characterization and evolution of the precipitates are followed, at each stage, using ^{57}Fe conversion electron Mössbauer spectroscopy (CEMS). It is shown that the Ar post-irradiation produces carbonitride dissolution and reprecipitation. In addition we show that the thermal behaviour of the precipitates is affected by the presence of the Ar in the N implanted region.

EXPERIMENTAL

Mechanically polished discs of 1020 low carbon steel ($C=0.2$; $Mn=0.9$ wt%) were implanted at the HVEE 400 kV ion implanter of the Institute of Physics, Porto Alegre. The N_2^+ implantation was performed at 150, 80 and 40 keV in order to obtain a plateau from the surface up to around 120 nm. The typical implanted fluence was $6 \times 10^{16} \text{ N}_2/\text{cm}^2$ and the N concentration at the plateau was around 40%. The Ar was implanted at an energy of 150 keV, leaving the Ar particles in the N implanted region. The samples were studied as a function of the Ar fluence in the range from 10^{14} to $1.0 \times 10^{16} \text{ Ar}/\text{cm}^2$. The implantation density current was always lower than $1 \mu\text{A}/\text{cm}^2$, thus during the implantation process the temperature of the sample was maintained around 25 °C.

The various 1020 low carbon steel samples have been exposed to the following treatment: N_2 implantation, annealing at 400 °C, post-bombardment with Ar^+ ions at different fluences and further annealing at 450 and 500 °C. The annealings were made in a vacuum better than 10^{-6} Torr and always for 1 hour.

The carbonitride identification was done using CEMS data obtained in the backscattering geometry. The CEMS technique analyses the near-surface region up to 150 nm from the metal surface. The emitted electrons were detected in a pancake type counter in which a continuous flux of He/Methanol was allowed to flow. Data were taken on a conventional constant acceleration Mössbauer spectrometer. The source was ^{57}Co in a Rh matrix.

RESULTS

The carbonitrides formed in Fe and/or in various kinds of steels have been extensively investigated via Mössbauer spectroscopy, and their characteristic hyperfine parameters (magnetic field H , quadrupole splitting E_Q and isomer shift δ) are well established. Table I shows the parameters used in the analysis of our work, which agree with the data published by several authors [5-7].

TABLE I

^{57}Fe Mössbauer parameters obtained from the least square fit to the present data. H_1 , H_2 , H_3 and H_4 are the sets of characteristic magnetic fields corresponding to Fe, $\epsilon\text{-Fe}_{2+x}(\text{C,N})$, $\epsilon\text{-Fe}_{3.2}(\text{C,N})$ and $\theta\text{-Fe}_3(\text{C,N})$, respectively, and Q_1 and Q_2 are the characteristic quadrupole splitting corresponding to $\epsilon\text{-Fe}_2(\text{C,N})$ and $\epsilon\text{-Fe}_{2+x}(\text{C,N})$. The isomer shift δ is given relative to Fe metal at room temperature

	H (kG)		E_Q (mm/s)	δ (mm/s)
Fe	331 \pm 3	H_1		0.01 \pm 0.02
$\epsilon\text{-Fe}_{2+x}(\text{C,N})$	279 \pm 4	H_2		0.27 \pm 0.05
	218 \pm 4			0.25 \pm 0.02
	133 \pm 5		-0.06 \pm 0.02	0.43 \pm 0.04
		Q_2	0.76 \pm 0.02	0.36 \pm 0.02
$\epsilon\text{-Fe}_{3.2}(\text{C,N})$	238 \pm 3	H_3		0.31 \pm 0.02
	298 \pm 3			0.24 \pm 0.04
$\theta\text{-Fe}_3(\text{C,N})$	198 \pm 5	H_4		0.45 \pm 0.02
$\epsilon\text{-Fe}_2(\text{C,N})$		Q_1	0.32 \pm 0.02	0.40 \pm 0.02

The CEMS spectrum of the N as implanted 1020 sample shows the characteristic quadrupole doublet of the ξ or $\epsilon\text{-Fe}_2(\text{C,N})$ superimposed to the magnetic sextet of the martensitic steel, and a smaller contribution of the $\theta\text{-Fe}_3(\text{C,N})$ phase. As is well described in the literature, [6,8,9] it is not possible to distinguish, via Mössbauer experiments, between ξ - and ϵ -nitrides or carbonitrides. However, results from glancing X-ray diffraction experiments performed on similar systems [5], have shown that carbonitrides are formed whenever a carbon steel is N implanted. Therefore, in what follows, it is assumed that we formed carbonitrides and in this particular case we are in presence of $\epsilon\text{-Fe}_2(\text{C,N})$ precipitates.

As shown in fig. 1.a and table II, the 400 °C annealing of the N implanted sample produces the complete dissolution of the $\epsilon\text{-Fe}_2(\text{C,N})$ precipitates and the subsequent formation of $\epsilon\text{-Fe}_{3.2}(\text{C,N})$ carbonitrides. The $\theta\text{-Fe}_3(\text{C,N})$ compound is slightly affected by the thermal treatment.

Three equal N implanted, 400 °C annealed samples, were Ar post-bombarded. The bombardment with a fluence of 3×10^{14} Ar/cm² (sample 1 in table II) changes

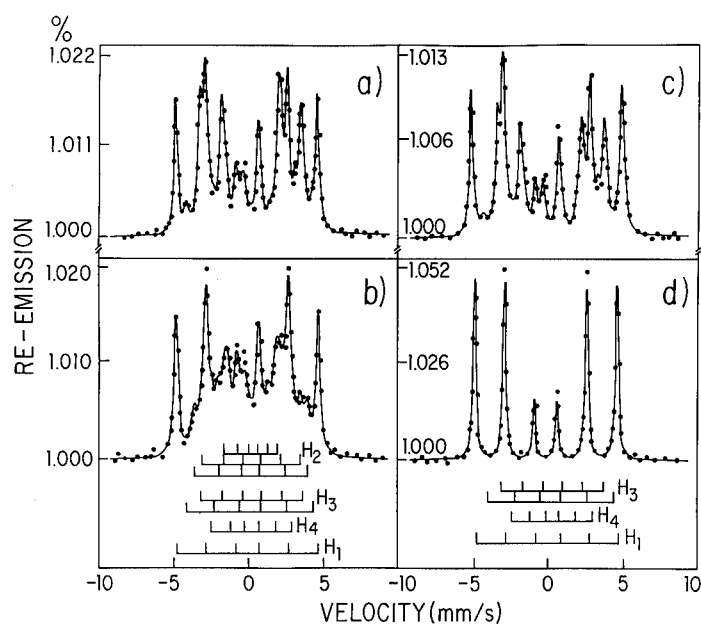


Fig. 1 - ^{57}Fe CEMS spectra measured at RT for sample 2: a) N implanted and 400 °C annealed; b) irradiated with 3×10^{15} Ar/cm 2 ; c) annealed at 450 °C; d) annealed at 500 °C.

Precipitates	Fe Matrix	$\epsilon\text{-Fe}_2(\text{C,N})$	$\epsilon\text{-Fe}_{3.2}(\text{C,N})$	$\epsilon\text{-Fe}_{2+x}(\text{C,N})$	$\theta\text{-Fe}_3(\text{C,N})$
Samples					
1020+N	0.40	0.48	-	-	0.12
400 °C	0.47	-	0.46	-	0.07
Sample 1					
3×10^{14} Ar/cm 2	0.41	-	-	0.53	0.06
450 °C	0.90	-	0.10	-	-
Sample 2					
3×10^{15} Ar/cm 2	0.37	-	-	0.54	0.10
450 °C	0.44	-	0.44	-	0.12
Sample 3					
1.0×10^{16} Ar/cm 2	0.40	-	-	0.50	0.10
450 °C	0.64	-	0.25	-	0.11

TABLE II

Normalized CEMS spectral areas of carbonitride precipitates irradiated with different Ar fluences and annealed. The three samples have been initially N implanted and annealed at 400 °C. Typical errors are 5%.

drastically the carbonitride phases. The $\epsilon\text{-Fe}_{3.2}(\text{C,N})$ precipitate has been completely dissolved and reprecipitated into $\epsilon\text{-Fe}_{2+x}(\text{C,N})$, with $x < 1$. On the other hand, the $\theta\text{-Fe}_3(\text{C,N})$ phase seems to be stable under Ar-irradiation (even at higher fluences) as well as under further annealings.

The data of table II show that increasing the Ar bombarding fluence does not produce further effects in the amount of the reprecipitated $\epsilon\text{-Fe}_{2+x}(\text{C,N})$ carbonitride. However, the results of subsequent annealing of the samples at 450 °C depends on the previous Ar fluence. As is observed in table II, the annealing of sample 1 at 450 °C produces a drastic reduction of the ($\epsilon + \theta$) carbonitrides (from 0.59 to 0.10) showing that a considerable amount of N has out

diffused from the N implanted and CEMS analysed region.

On the other hand, samples 2 and 3 irradiated with higher fluences of Ar behave in different way under annealing. In both cases the annealings at 450 °C produce a complete dissolution of $\epsilon\text{-Fe}_{2+x}(\text{C,N})$ and back transformation into $\epsilon\text{-Fe}_{3.2}(\text{C,N})$ with a retention of carbonitrides much larger than in sample 1. Further annealing of the samples at 500 °C results in the total dissolution of all the carbonitrides present in the CEMS analysed region. Figures 1.b-d show the CEMS spectra for sample 2 irradiated with $3 \times 10^{15} \text{ Ar/cm}^2$ and annealed at 450 and 500 °C respectively.

DISCUSSION

The Ar post-bombardment of the N implanted 1020 low carbon steel produces two main features: i) dissolution and reprecipitation of the carbonitrides; ii) modification of the thermal behaviour of the precipitates. Similar effects have been observed in α -post bombardment experiments [2,3], but there are several features which are specific of the Ar post-bombardment.

Dissolution and Reprecipitation

The lowest irradiation fluence of Ar, $3 \times 10^{14} \text{ Ar/cm}^2$ (see table II) corresponds to 1 dpa. This fluence already produces a complete $\epsilon\text{-Fe}_{3.2}(\text{C,N})$ into $\epsilon\text{-Fe}_{2+x}(\text{C,N})$ transformation. Increasing the fluence to $1.0 \times 10^{16} \text{ Ar/cm}^2$ (30 dpa) there is practically no more effect on the transformation of the carbonitrides. This result is in agreement with the data of ref. [2] where we have shown that the $\epsilon\text{-Fe}_{3.2}(\text{C,N})$ carbonitride is highly unstable under He post-bombardment. At an He fluence corresponding to 0.1 dpa the $\epsilon\text{-Fe}_{3.2}(\text{C,N})$ starts to dissolve and reprecipitate into $\epsilon\text{-Fe}_{2+x}(\text{C,N})$. Therefore it is not surprising that at 1 dpa both the Ar and He post-bombardment produce the complete $\epsilon\text{-Fe}_{3.2}(\text{C,N})$ to $\epsilon\text{-Fe}_{2+x}(\text{C,N})$ transformation.

In the $\epsilon\text{-Fe}_{2+x}(\text{C,N})$ hcp carbonitride structure, the C and N atoms are interstitial n.n. to the Fe atoms. For this phase, the magnetic hyperfine fields corresponding to one, two and three C or N n.n. are $H_1^1 = 279 \text{ kG}$, $H_2^1 = 218 \text{ kG}$ and $H_3^1 = 132 \text{ kG}$ respectively [6] (see table I). Therefore from the resonant areas of each Mössbauer pattern spectrum it is possible to assign the population corresponding to each n.n. configuration.

Concerning the $\epsilon\text{-Fe}_{2+x}$ produced after He or Ar irradiation, there is a different n.n. distribution in the two cases. When α -irradiated, the 1, 2 and 3 n.n. populations are almost equal and of the order of 0.15 [2]. In the case of Ar-irradiation at the same dose of 1 dpa ($\phi = 3 \times 10^{15} \text{ Ar/cm}^2$), the population with 3 n.n. is around 0.24 while the other two are 0.15.

During the last years a considerable amount of work has been done investigating the stability of coherent and semi-coherent precipitate phases under neutron and heavy ion irradiation. However these studies did not lead to a plausible explanation of the processes of dissolution and reprecipitation of the precipitates as a result of irradiation. Nelson et al [10] argue that both processes are due to a competitive effect between radiation enhanced diffusion and cascade dissolution and disordering. On the other hand, Vaidya [11] suggests that the stability of the precipitates, under irradiation, is associated with the modification of the interfacial dislocations.

Presently we do not have a conclusive explanation of our results, and in principle both models can be used to describe them.

Thermal Behaviour

Previous works [5,7] have shown that non irradiated carbonitrides present in Fe and in steel matrices are stable only up to 400 °C. For higher

temperatures the precipitates dissolve as consequence of N out-diffusion from the implanted region.

The results of our work show that the presence of Ar atoms in the N implantation region increases the temperature at which the precipitates remain stable: at 450 °C the samples retain most of the carbonitrides. This behaviour is similar to the N implanted pure Fe and 1020 carbon steel post-bombarded with alpha particles. In the first case the retention of nitrides was effective up to about 550 °C [1] and in the second case [2] up to 450 °C.

This feature of the post-irradiated samples can be understood if we analyse the behaviour of Ar atoms in metals, which is similar to He. In general Ar is not soluble in metals but it can accumulate in large quantities via the formation of Ar-Vacancy complexes (Ar-V). For low implantation fluences at room temperature, usually small Ar-V systems are formed. However, for higher temperatures and larger fluences the Ar-V complexes agglomerate, grow in size, and eventually form Ar bubbles. The above mechanism can be associated with the retention effect observed in the present work. The implanted Ar particles create Ar-V complexes which end up at the grain boundaries of the precipitates. When the samples are annealed, two competitive effects can occur. First the Ar will act as trapping centers for N released from the precipitates. Therefore, the N diffusion would be inhibited and the precipitates will remain stable at higher temperatures. Second, the same annealing process will favour the agglomeration of the Ar-V complexes which will become larger, less disperse and less efficient in the N inhibiting diffusion mechanism.

It is interesting to compare the amount of ϵ -carbonitrides retained at 450 °C for the same peak concentration of He and Ar irradiation. As is evident in table II after an irradiation of 3×10^{15} Ar/cm² (0.5 at% peak concentration) the proportion of retained ϵ -carbonitrides at a temperature of 450 °C is 0.44. The irradiation of a similar sample with the same peak concentration of He (7×10^{15} a/cm²) produces a proportional retention of 0.25 of the ϵ -carbonitrides at 450 °C. This means that for the same peak concentration the Ar is twice more effective than He in the retention of the carbonitrides.

This feature can be tentatively explained as follows. For the same peak concentration (3.5×10^{15} Ar/cm² and 7×10^{15} He/cm²) the alpha irradiation is equivalent to 1 dpa, while Ar produces 10 dpa. The number of Ar-V complexes should be larger than the He-V ones and therefore the N diffusion should be more inhibited in the first case than in the second as is shown by the experiment.

A final feature should be pointed out. The retention effect produced by Ar not only is more effective than the one produced by He but it also extends for a larger concentration. Figure 2 shows the proportion of retained carbonitrides as a function of the Ar and He peak concentration. For the He irradiation the retention effect starts at around 0.35 at% and ceases to be effective at 0.75 at%. Instead, for Ar the lowest concentration is around 0.05%, reaching a maximum of retention around 0.5 at% and slowly decreasing for higher concentrations. This behaviour should be related with the size and number of He-V or Ar-V complexes. For retention purposes they are ineffective when their number is very small (low concentration), and also become less effective when as a consequence of increasing the irradiation fluence, the complexes become larger.

The retention effect can be of potential technological application in metallurgy, where retention of protective carbonitrides at higher temperatures is of major importance.

REFERENCES

1. M.Behar, P.J.Viccaro, M.T.X.Silva, A.Vasquez, C.A.dos Santos and F.C.Zawislak, Nucl. Instr. and Meth. B19/20, 132 (1987).
2. S.M.M.Ramos, L.Amaral, M.Behar, G.Marest, A.Vasquez and F.C.Zawislak, to be published in J. Phys. F: Metal Physics.

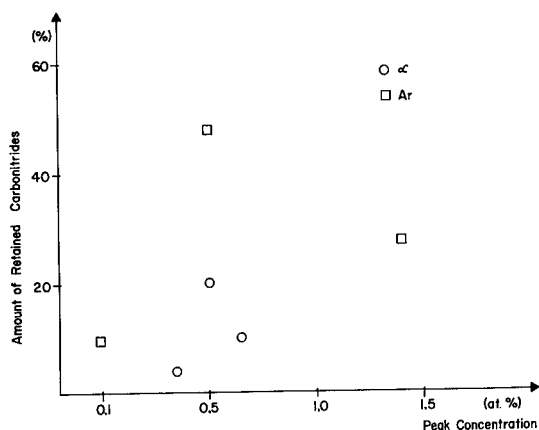


Fig. 2 - The proportion of retained ϵ -carbonitrides after 450 °C annealing as function of the Ar and He peak concentration (in at%).

3. S.M.M.Ramos, L.Amaral, M.Behar, G.Marest, A.Vasquez and F.C.Zawislak, to be published in J. Mat. Science.
4. J.F.Ziegler, J.P.Biersack and U.Littmark, in The Stopping and Range of Ions into Solids, edited by J.F.Ziegler (Pergamon Press, 1985).
5. G.Marest, in Ion Implantation 1988, edited by F.H.Wühlbier (Trans-Tech. Publication, 1988).
6. D.Firrao, M.Rosso, G.Principi and R.Frattini, J.Mat. Sci. 17, 1773 (1982).
7. C.A.dos Santos, M.Behar, J.P.de Souza and I.J.R.Baumvol, Nucl. Instr. and Meth. 209, 907 (1983).
8. C.A.dos Santos, M.Behar and I.J.R.Baumvol, J. Phys. D17, 551 (1984).
9. C.A.dos Santos, Ph.D. Thesis, 1985 (unpublished).
10. R.S.Nelson, J.A.Hudson and D.Y.Mazey, J. of Nucl. Mat. 44, 318 (1972).
11. W.N.Vaidya, J. Nucl. Mat. 83, 223 (1979).

TEMPERATURE AND ORIENTATION EFFECTS IN IRON NITRIDE CRYSTAL FORMATION

L. J. LOWDER, W. FRANZEN, AND R. J. CULBERTSON
Army Materials Technology Laboratory, Watertown, MA 02172-0001

ABSTRACT

Pure rolled iron foils 0.025 mm thick have been implanted at two different angles of incidence and at several different temperatures. The implantation dose in each case was 5×10^{17} atoms/cm². Both implanted and unimplanted foils were analyzed by transmission x-ray diffraction. Foils implanted at $320 \pm 5^\circ\text{C}$ exhibit peaks that correspond to the formation of several different phases of iron-nitride crystals, as observed by other investigators.[1,2] No such formation takes place at an implantation temperature of -20°C . We have evidence that the orientation of the iron nitride crystals is correlated with the orientation of the iron crystals.

INTRODUCTION

The morphology of micro-crystals of iron nitride formed during nitrogen implantation of iron is interesting because of its relation to the change in mechanical properties (hardness, friction, wear) brought about by the implantation. Temperature is an important parameter in this connection because the sample may be heated by the ion beam during implantation or in later use by mechanical working.

Rauschenbach and his collaborators [1,3-7] have carried out an extensive series of studies on the crystal structure of nitrogen-implanted iron as a function of temperature and other parameters. From their work and subsequent work carried out in this laboratory [2] it is known that the growth of the metastable phase $\gamma'-Fe₄N tends to be favored at implantation temperatures above 300°C . Since the first-order maximum that corresponds to diffraction from the (200) planes of $\gamma'-Fe₄N can be clearly resolved from other structures in the diffraction pattern, we decided to investigate the morphology of micro-crystals of this substance formed in iron when implanted with nitrogen at different temperatures, using a transmission x-ray spectrometer as an analytical tool. Other phases of iron nitride are not as well resolved from one another, nor from the carbo-nitrides that have been reported by some investigators [3].$$

EXPERIMENT

The implanted iron was in the form of 0.025 mm thick high-purity Johnson Matthey Foils. The total impurity content of these foils does not exceed 30 ppm, with no single impurity element present at a concentration greater than 5 ppm. Foils were mounted on a temperature-controlled sample holder consisting of a shielded copper plate 1.2 cm thick that could be heated by a 4 kV electron beam from the rear, or cooled by thermal links to a cold reservoir, as shown in Fig. 1. The implanter used is a Zymet Z-100 machine that generated an unanalyzed beam consisting of 60% N₂⁺ and 40% N⁺ ions at 80 keV. The x-ray diffractometer used is a Picker diffractometer set up in transmission using Mo K α radiation ($\lambda=0.7093\text{\AA}$). A feature of the spectrometer is that it allows the orientation of the crystallites formed during implantation to be investigated by changing the foil-tilt angle ω (see Fig. 2). A preliminary experiment had suggested a correlation between ω_{max} and the angle of incidence β of the nitrogen ions, where ω_{max} is the tilt angle for which the (200) peak of $\gamma'-Fe₄N is most intense. Since an analysis of preliminary data suggested the presence of hydrocarbons in the residual gas of the implantation vacuum chamber, as indicated by cementite and carbo-nitride diffraction peaks, an effort was made to reconstruct the high-vacuum pumping system of the implanter in order to eliminate the source of carbon contamination.$

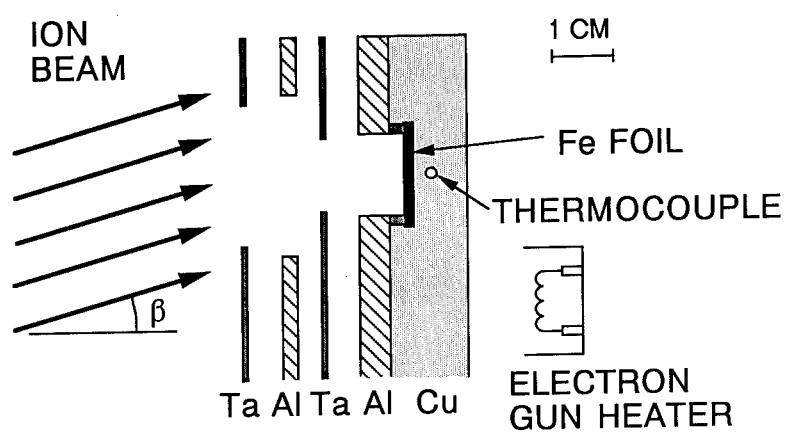


Fig. 1. Diagram of temperature-controlled sample holder (top view).

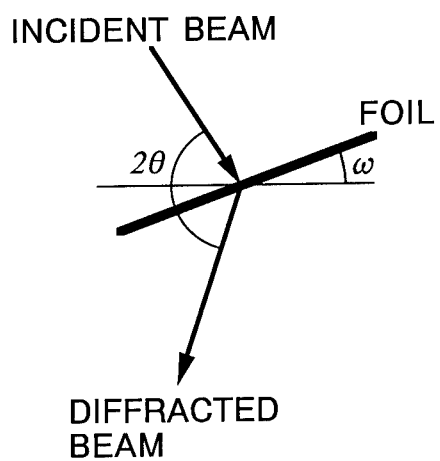


Fig. 2. Diagram illustrating definition of the angles ω and θ in transmission x-ray spectroscopy.

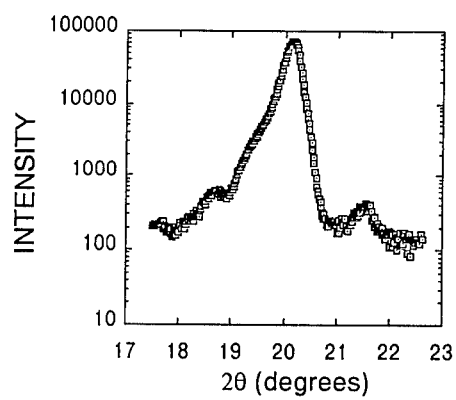


Fig. 3a

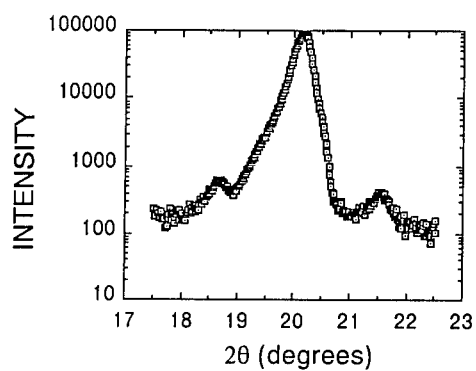


Fig. 3b

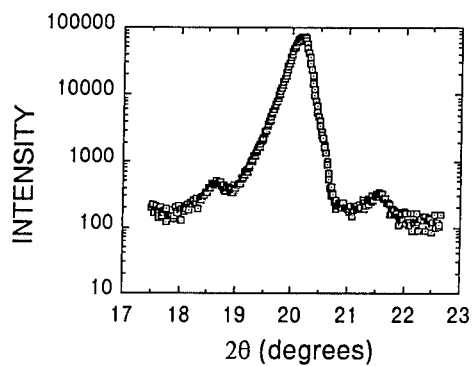


Fig. 3c

Fig. 3. Transmission x-ray patterns for foil implanted at 320 °C: (a) $\omega = 0^\circ$, (b) $\omega = 2.5^\circ$, and (c) $\omega = 5^\circ$.

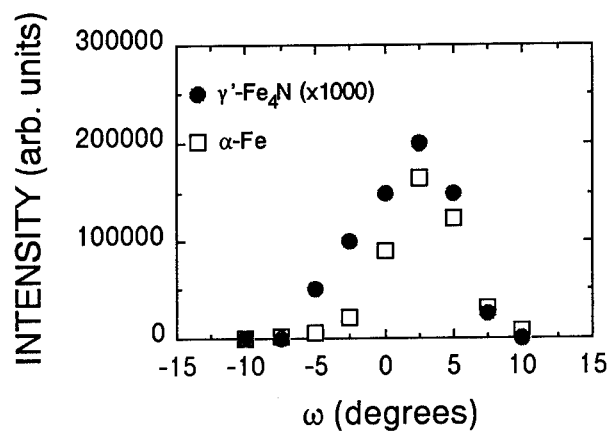


Fig. 4a

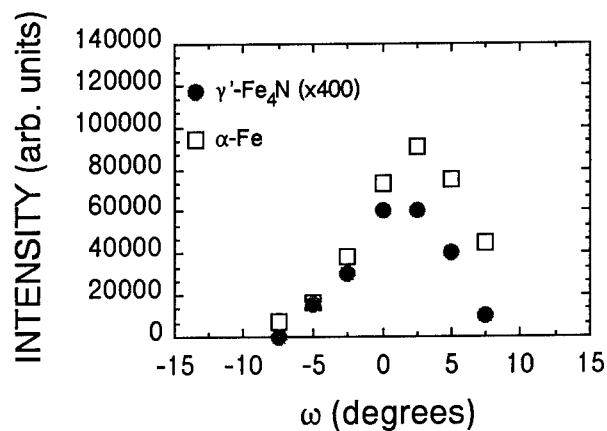


Fig. 4b

Fig. 4. Comparison of the amplitudes of the peaks that correspond to diffraction from the (110) planes of α -Fe and the (111) planes of γ' -Fe₄N: (a) $\beta = -7.5^\circ$ and (b) $\beta = +7.5^\circ$.

The vacuum is now maintained by two Edwards diffusion pumps filled with Dow-Corning 705 silicon oil, and backed by mechanical pumps equipped with activated alumina foreline filters. Mass-spectrometer analysis of the residual gas in the implantation chamber does indeed indicate almost complete absence of hydrocarbons under these conditions.

RESULTS AND DISCUSSION

Typical transmission x-ray spectra recorded with a foil implanted under the improved vacuum conditions are shown in Figs. 3a-3c. Implantation took place at a temperature of $320 \pm 5^\circ\text{C}$ and an energy of 80 keV, with a total dose of 5×10^7 N atoms/cm². The main peak corresponds to first-order diffraction from the (110) plane of α -Fe; the smaller peak at right corresponds to first-order diffraction from the (200) plane of γ' -Fe₄N. The three plots differ only in the value of the tilt angle ω , that is the angle between the bisector of the incident and diffracted beam directions on the one hand, and the plane of the foil, on the other hand, as indicated in Fig. 2.

An analysis of similar data obtained under the same beam conditions but at two different angles of incidence β is shown in Figs. 4a and 4b. It is clear from these results that the γ' -Fe₄N crystallites formed during implantation are aligned parallel to the preferred direction of the α -Fe crystals, and there is no correlation between crystallite orientation and angle of incidence β , contrary to the supposition that we had made on the basis of earlier data obtained in a hydrocarbon-contaminated implantation chamber. It is interesting to observe that the α -Fe crystals are not aligned exactly parallel to the plane of the foils ($\omega=0^\circ$), but at a small angle with respect to this plane.

SUMMARY

The growth of γ -Fe₄N crystals takes place along the direction defined by the crystal structure of the underlying matrix and is not influenced by the line of dislocations and vacancies created by the ion beam as it penetrates the surface of the foil. Foils implanted at both higher temperatures (400°C) and lower temperatures (30°C and 220°C) showed much less prominent γ' -Fe₄N diffraction peaks, in agreement with observations of other investigators. Foils implanted at -20°C show no iron nitride crystal formation.

ACKNOWLEDGEMENTS

We gratefully acknowledge the technical assistance of D. Henderson and helpful discussions with E. A. Johnson and P. L. Sagalyn.

REFERENCES

1. B. Rauschenbach and A. Kolitsch, Phys. Stat. Soc. **a80**, 211(1983).
2. R. J. Arnett *et al.* Proc. Mat. Res. Soc. **23**, 99(1987).
3. B. Rauschenbach and K. Hohmuth, Crystal Res. & Tech. **19** (11), 1425 (1984).
4. B. Rauschenbach, Nucl. Inst. Meth. B **15**, 756(1986).
5. B. Rauschenbach, Nucl. Inst. Meth. B **18**, 34(1986).
6. B. Rauschenbach, K. Hohmuth and G. Kaestner, Nuc. Inst. Meth. B **23**, 316 (1987).
7. B. Rauschenbach, A. Kolitsch and K. Hohmuth, Phys. Stat. Soc. **a80**, 471(1983).
8. S. Fayville, D. Trehenx and C. Esnouf, Nucl. Inst. Meth. B **7/8**, 171 (1985).

PHASES AND MICROSTRUCTURES OF CARBON-IMPLANTED NIOBIUM

J.S. HUANG, R.G. MUSKET, AND M.A. WALL

Lawrence Livermore National Laboratory, Livermore, CA 94550

ABSTRACT

Polycrystalline niobium was implanted with 200, 100, and 50 keV carbon ions to create a uniform distribution of carbon over a thickness of about 0.25 μm . Samples implanted with calculated carbon content of 0.6, 1.9, 5.8, and 16 atomic percent were prepared, and the uniformity of the carbon distribution with depth was confirmed by Auger electron spectroscopy analysis. Glancing-angle X-ray diffraction analysis and transmission electron microscopy were used to characterize the phases and microstructures formed. The results indicated that no detectable second phases were present except on the surfaces where an amorphous phase and many particles were formed from contamination. Despite the low equilibrium solubility limit of carbon in Nb, we have created metastable solid solutions of Nb and C with carbon contents as high as 16 at. %.

INTRODUCTION

High-dose ion implantation is a useful process to modify the mechanical properties of metals. It is known that the implantation of metalloid ions results in improvement of microhardness and increases wear resistance and fatigue life. Ion implantation is a non-equilibrium process and the laws of classical thermodynamics, for instance, the Gibbs phase rule can not always be applied. Although implantations of Fe alloys with C and N metalloids had been studied extensively, little has been done on Nb. The objective of this work was to analyze the phases formed by high-dose implantations of carbon into Nb. The Nb-C system is interesting since it has been shown [1] that the precipitation of niobium carbide, Nb_2C , involved large amounts of plastic deformation at low temperatures, which can suppress the kinetics of the precipitation. It is expected that the limit of solubility of carbon can be extended significantly beyond that predicted by the equilibrium phase diagram.

EXPERIMENTAL DETAILS

The Nb was a commercial grade material of 99.9 wt% purity with the carbon content less than 0.003 wt%. The material was annealed at 1473 K for one hour and mechanically polished to a finish of 0.1 μm before carbon implantation. The as-annealed material had an average grain size of 40 μm . The carbon ion implantations were conducted with, sequentially, 200, 100, and 50 keV C^+ ions near room temperature ($<150^\circ\text{C}$) with fluence ratio of 4.5:2:1, respectively. The maximum total fluence was $3.0 \times 10^{17} \text{ C/cm}^2$, and the typical rastered beam current density was about 4 $\mu\text{A/cm}^2$. The vacuum in the sample chamber was about 10^{-4} Pa during implantation. The three-stage implantation was calculated by TRIM [2] to give a uniform carbon distribution in the implanted region of each sample, which was about 0.25 μm thick, centered about 0.17 μm from the surface. Samples with 0.6, 1.9, 5.8, and 16 at.% carbon were prepared.

The implanted sample was characterized with Auger electron spectroscopy (AES), glancing-angle-incidence Cu X-ray diffraction analysis and transmission electron microscopy (TEM). Both 2-degree and 6-degree incidence angles were used for the X-ray diffraction. We calculated that, for 2-degree incidence, about 70% of the total signal would be from the materials within the implanted region and, for 6-degree incidence, about 33% from the implanted region. Both cross-sectional and plan-view (view from surface) TEM samples were prepared. An ion-milling technique was used in the final stage of thinning to obtain perforated holes and thin areas from mechanically polished slices. The ion-milling was conducted with the sample holder chilled by liquid nitrogen. For the plan-view samples, the thinning was done only from one side (the substrate side) to preserve the implanted materials for examination. The transmission electron microscopy was conducted with a JEOL-200CX STEM which has an UTW (ultra thin window) EDX (energy dispersive X-ray) detector.

EXPERIMENTAL RESULTS AND DISCUSSION

AES sputter profiles were measured to determine the depth distributions of C, O, and Nb. Except for the pre-profiling spectrum, the carbon Auger peak had the sharp and symmetrical shape typical of carbon in metal carbides [3]. Since niobium carbide standards were not available, we determined the sensitivity factors for C and Nb by assuming the concentrations calculated using TRIM for the implanted fluences. This assumption should be valid for such a broad, relatively uniform distribution. The sensitivity factors found for 5-keV electrons were 0.44 for the carbide-shaped carbon KLL peak and 0.27 for the Nb MNN peak. For the oxygen KLL peak, a sensitivity factor of 0.41 was measured using an Al_2O_3 film on aluminum.

The contents of carbon versus depth in the as-implanted samples, analyzed by AES, are shown in Fig. 1. The analysis is not sensitive enough to determine the distribution in the lowest-dose sample. For the other samples, as expected, the concentration of carbon is relatively uniform near the center of the implanted regions. On the surfaces there was slight enrichment of carbon and large enrichment of oxygen. The enrichment of oxygen is about the same for all the samples with concentration between 50 and 70 at.%. This enrichment is presumably due to the adsorption of oxygen on the surfaces during ion-implantation and post-implantation air exposures.

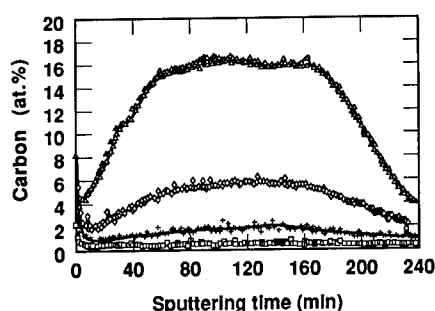


Fig. 1. AES profiles of carbon concentration versus depth in the implanted samples.

The shapes of carbon Auger signals from the surfaces and the implanted regions of all the samples are represented in Figs 2a and 2b. The signal of the surface carbon is like that of graphite, while that of the carbon in the implanted layer was typical of a carbide [3]. As will be discussed later, it is not possible to use this difference to diagnose the presence of carbide precipitates.

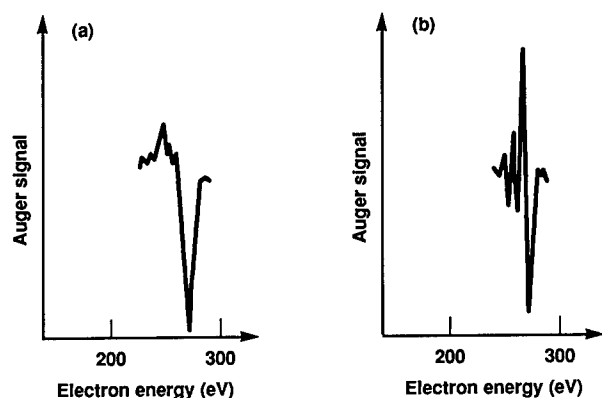


Fig. 2. Typical carbon Auger signal on surfaces (a) and within implanted regions (b) obtained from a 5.8 at.% carbon sample.

The results of X-ray diffraction analysis showed no additional peaks for the 0.6 and 1.9 at.% carbon samples. For the 5.8 and 16 at.% samples we found additional peaks which were located

near the peaks for BCC Nb. Figs. 3a and 3b show examples of X-ray analysis results for diffraction using 6-degree and 2-degree incidence angles, respectively. For analysis using a 6-degree incidence angle, the X-ray signal comes from both the implanted region and the substrate. The additional peaks can be attributed to the diffraction from implanted Nb; the major peaks correspond to the substrate. The additional peaks (see the Table 1 below) have greater d-spacings. This suggested the implanted carbon was incorporated in the Nb lattice as interstitials and dilated the lattice.

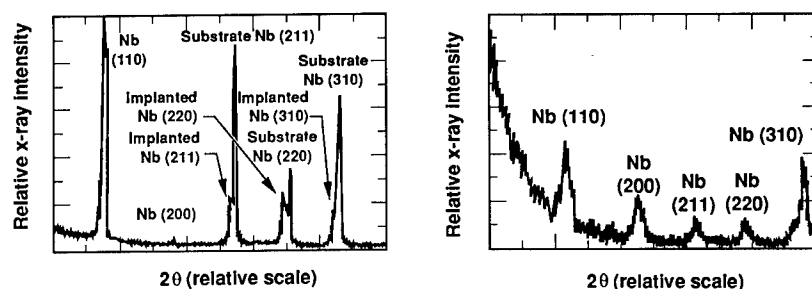


Fig. 3. Typical results of X-ray diffraction analysis from 5.8 at.% carbon sample using glancing incidence angle of (a) 6 degrees and (b) 2 degrees.

For the analysis using 2-degree incidence angle (Fig. 3b), the background X-ray signal is much higher due to a larger fraction of forward-scattered, non-diffracted X-rays. We calculated that 70% of the signal would be from the implanted region for an ideal surface. Therefore, the observed X-ray peaks are mainly from the implanted region. The broad peaks resulted from an overlap of signals from the substrate and the implanted regions. Consequently, we did not observe the additional peaks from the substrate. An indexing of the observed peaks indicated that the implanted region has a BCC Nb lattice. There was no indication of other peaks related to a second phase such as NbC or Nb₂C. Table I compares the tabulated d-spacings for Nb, NbC and Nb₂C phases with those measured with 6-degree X-ray diffraction for all our samples. Due to the minor difference in d-spacing among the samples, we only list the range of values. However in general, the d-spacing increased with the concentration of carbon.

Table I. Comparison of d-spacings (Å) measured for the implanted samples with tabulated values

Measured(*)	2.34 - 2.41	1.65 - 1.70	1.35 - 1.39	1.17 - 1.21	1.05 - 1.07
Nb	2.34(110)	1.65(200)	1.35(211)	1.17(220)	1.05(310)
NbC(**)	2.58(111)	2.23(200)	1.58(220)	1.35(311)	1.29(222)
Nb ₂ C(***)	2.69(10 $\bar{1}$ 0)	2.48(0002)	2.37(10 $\bar{1}$ 1)	1.83(10 $\bar{1}$ 2)	1.56(11 $\bar{2}$ 0)
Nb ₂ C(****)	4.25(111)	3.68(021)	2.36(421)	1.83(422)	1.57(460)
	1.42(043)	1.41(423)	1.33(462)	1.04(843)	

* The lower value is for the 0.6 at.% carbon sample and the upper value is for the 16 at.% carbon sample.

** FCC structure [4]

*** High-temperature phase, HCP structure [4]. A 4.97 Å peak for (0001) plane was also observed in electron diffraction. [4]

**** Low-temperature phase, orthorhombic (slightly distorted HCP). [5]

A cross-sectional TEM image of the sample with 16 at.% C is shown in Fig. 4 along with its diffraction pattern. Except for the small black dot images, which are due to the ion beam damage during sample preparation, there is no evidence of any precipitate formation. The diffraction

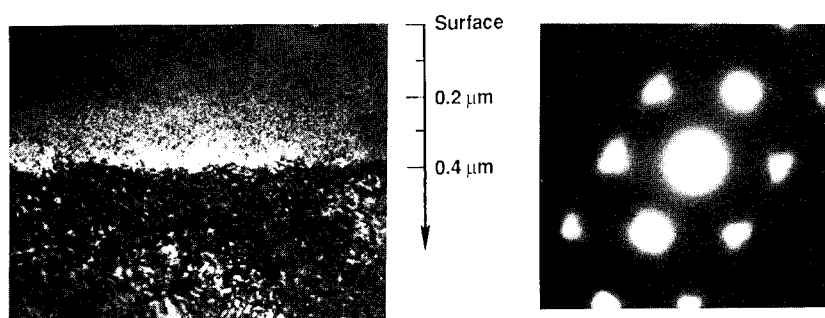


Fig. 4. Cross-sectional TEM bright field image of the sample implanted to 16 at.% carbon. The (111) diffraction pattern shows the implanted region (0–0.4 μm) is a slightly dilated (3%) BCC Nb phase.

pattern shows a six-fold symmetry and can be indexed as either a $\langle 111 \rangle$ BCC pattern for a Nb phase or a $\langle 111 \rangle$ FCC pattern for an equilibrium NbC phase [4], or a $\langle 0001 \rangle$ HCP pattern for an equilibrium Nb₂C phase [4]. If it was a NbC phase, then the first order spots (nearest to the transmitted beam) would have to be indexed as {220} spots which should have a d-spacing of 1.58 Å [4]. If the pattern was indexed as that of the equilibrium Nb₂C phase, then the first order spots would have to be indexed as {10 $\bar{1}$ 0} spots which should have a d-spacing of 2.69 Å [4]. However the d-spacing was calculated as 2.41 (± 0.04 Å), which is about 3 % percent higher than the {110} d-spacing, 2.34 Å, for pure Nb. (The variation of the d spacing is due to the uncertainty of the camera constant of the microscope during the course of this study.). Therefore we concluded that the implanted material has a BCC crystal structure. The increase of d spacing suggested that the implanted carbon atoms existed as interstitials. In addition, there is indication of streaks on the {110} spots, which could be due to an anisotropic distortion of the Nb BCC lattice by the implanted interstitial carbon atoms, or by the lattice strain associated with the defects created by the ion implantation, or by the defects created by the ion milling during the TEM sample preparation. The absence of additional diffraction spots could indicate there is no equilibrium carbide formation, or any carbide formed is too small to be detected, or there are too few carbides. The latter two factors are not very likely. Based upon the Gibbs phase rule, the amount of carbide would be about 37 wt% if Nb₂C, or about 28 wt% if NbC. For such high amount of precipitates, electron diffraction pattern should have extra spots or rings even if the precipitates are as small as 10 Å.

A plan-view TEM bright field image and selected area diffraction patterns were taken from thin and thick areas of the 16 at.% carbon sample. We observed many fine precipitates which had diameters between 40 and 200 Å, in the thinner area. However, there were fewer precipitates in the thicker area. This difference and the fact that we did not observe these particles in the cross-sectional TEM sample suggested that these particles existed only on the surface of the implanted sample. Using energy dispersive X-ray (EDX) analysis, we found that the thinner area was very rich in oxygen and slightly enriched with carbon. This was consistent with the results of Auger analysis. The diffraction pattern from the thinner area showed a broad center ring typical of an amorphous material and three other rings with many spots which were typical of polycrystalline materials with very small grains or fine precipitates. The d-spacings for these spots were calculated as 2.50, 2.21, and 1.57 Å. Using selected area diffraction and dark field imaging techniques, we concluded that the three rings with diffraction spots were diffracted from the precipitates as seen in the bright field image. The d-spacings of these precipitates were close to those of NbN and NbO [6] as well as those of NbC [4]. Therefore, at this moment, we cannot definitely define the composition of these precipitates. In any case, they probably resulted from contamination since they only exist on the surface and Auger analysis showed that the surface was enriched with oxygen and carbon. The thicker area reflected information both from the surface and the sub-surface implanted Nb, therefore the diffraction pattern consisted of the rings from the amorphous phase, and diffraction spots from the precipitates and the implanted Nb.

The results of TEM investigations on the 5.8 at.% carbon sample were similar to those of the 16 at.% sample, i.e., the presence of an oxygen-rich amorphous film, the presence of fine precipitates on surface, and an increased lattice constant of the niobium.

Since TEM and X-ray diffraction studies indicate no carbide is formed and the Auger analysis shows the signal of carbon is similar to that of a carbide, it is not warranted to use the shape of carbon Auger signal to detect the presence of niobium carbide precipitates. The shape of the Auger signal depends mainly on the nearest-neighbor bonding. As long as carbon is bonded mainly to Nb, its Auger peak shape should be somewhat independent of the phase. It has been noted [7] that many carbides, oxides, and nitrides of transition metals exist as interstitial structures with the C, N, and O atoms in the octahedral interstices of the cannonball-type packed metal lattices. Terao [4] reported that, for NbC, carbon atoms are in the octahedral interstices of an FCC Nb lattice and, for Nb₂C, in the octahedral interstices of an HCP Nb lattice. In Nb₂C, the carbon atoms are arranged in an ordered manner such as AX_hBX_iA..., where A and B represent the two atomic positions of HCP lattice and X_h and X_i represent the octahedral interstitial planes which are two-thirds and one-third filled, respectively. Therefore, carbon atoms are always in interstices whether they are in NbC, Nb₂C, or in implanted Nb, and it is difficult to differentiate the phase from the shape of the Auger signal.

A 16 at.% carbon sample was annealed in a TEM microscope using a hot stage. Fig. 5 shows a dark field image of the sample heated up to about 973 K and an associated diffraction pattern. The diffraction pattern indicates the presence of spots with d-spacings as large as 4.98 and 2.77 Å, which roughly match the d-spacings of {0001} and {1010} planes of Nb₂C [4]. This result further suggests that the as-implanted material is a metastable BCC solid solution of Nb and C atoms.

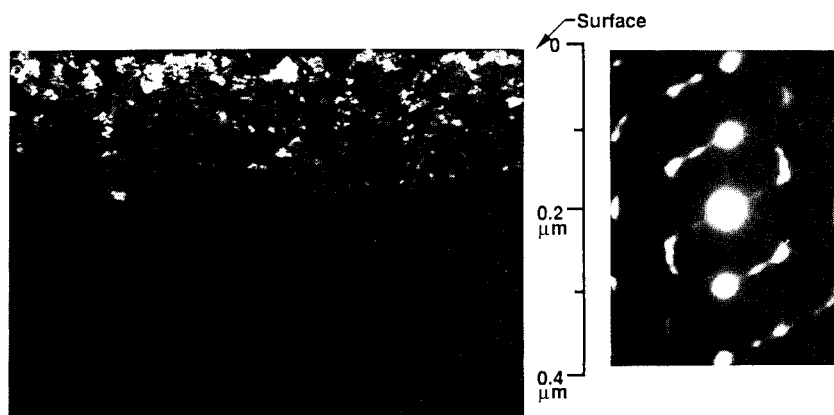


Fig. 5. TEM dark field image and an associated diffraction pattern for a Nb sample implanted to 16 at.% carbon and heated slowly in the TEM to 973 K.

For the compositions studied here, the equilibrium phases are a BCC Nb phase and a orthorhombic (or slightly distorted HCP) Nb₂C phase. Our results indicate that the Nb₂C phase does not form. The precipitation of Nb₂C in Nb involves a significant change of crystal structure. Pedraza and Pedraza [1] analyzed Nb₂C carbide precipitation in Nb. The precipitation was accompanied by a very large volume change, about 18%, which requires a large energy for plastic deformation. It is possible that this required increase of plastic energy more than offsets the chemical driving force for the precipitation; therefore, the nucleation and growth kinetics of the precipitation are very slow. In addition, low diffusivities during implantation near room temperature would limit the precipitation rate. This could explain why the ion implantation creates a metastable Nb solid solution up to 16 at.% C while the solubility limit for carbon in Nb is well less than 1 at.% near room temperature. The TEM image in Fig. 5 appears to support this argument as more and larger carbide particles are present near the surface where the thickness of the sample is smaller and the plastic constraint for the nucleation and growth can be surface-

relieved. Furthermore, the compressive stress applied by the substrate on the implanted regions could also reduce the kinetics of the precipitation and explain the metastability observed. A quantitative analysis is needed to more clearly understand the factors responsible for the metastability in Nb-C alloys processed by high-dose ion implantation and is the subject of our future paper.

SUMMARY

We have studied the phases and microstructure of Nb implanted with carbon to concentrations of up to 16 at.%. The following statements can be made:

- Carbon ion implantation created metastable solid solution of Nb and carbon for all the compositions studied with a lattice constant larger than that of the pure niobium. These results suggested implanted carbon atoms were located in interstices.
- Auger spectroscopy could not differentiate the carbon atoms in niobium carbides from those existing randomly in Nb metal as interstitials.

ACKNOWLEDGMENTS

We appreciate the assistance of R. Patterson in conducting the ion implantations and B. Olsen in the X-ray diffraction measurements and TEM sample preparation. We also appreciate the interesting discussions provided by G.F. Gallegos and E.N. Kaufmann. Work performed under the auspices of the U.S. Department of Energy by the Lawrence Livermore National Laboratory under Contract W-7405-Eng-48.

REFERENCES

1. A.J. Pedraza and D. Pedraza, *Nucl. Instr. Methods Phys. Res.* **B16**, 270 (1986).
2. Z.F. Ziegler, J.P. Biersack, and U. Littmark, *The Stopping and Range of Ions in Solids*, Vol. 1.(Pergamon Press, New York, 1985).
3. L.E. Davis, N.C. MacDonald, P.W. Palmberg, G.E. Riach, and R.E. Weber, *Handbook of Auger Electron Spectroscopy*, 2nd edition.(Physical Electronics Industries, Eden Prairie, 1976).
4. N. Terao, *Jpn. J. Appl. Phys.* **3**, 104 (1965).
5. E. Rudy and C.E. Brukl., *J. Am. Ceram. Soc.* **50**, 265 (1967).
6. E. Becker, *Z. Phys.* **31**, 269 (1925).
7. G. Hagg, *Z. Phys. Chem. B* **11**, 152 (1930); **12**, 413 (1931).

PHASE STABILITY OF Ni_2Al_3 UNDER ELECTRON IRRADIATION

E.A. KENIK* AND M. NASTASI**

*Metals and Ceramics Division, Oak Ridge National Laboratory, Oak Ridge, TN 37831-6376

**Materials Science and Technology Division, Los Alamos National Laboratory, P.O. Box 1663, Los Alamos, NM 87545

ABSTRACT

In-situ electron irradiations at 200, 300, and 1000 keV have been performed on Ni_2Al_3 at 100 and 300 K. At low doses, the Ni_2Al_3 partially disorders to a B2 structure with a lattice parameter of 0.284 nm, close to that extrapolated for β -NiAl at 60 at.% Al, the Ni_2Al_3 composition. The electron dose required to disorder the Ni_2Al_3 decreased with increasing accelerating voltage and possibly with decreasing temperature. At high doses, precipitation of aluminum from the B2 matrix occurs, along with radiation-induced sputtering and radiation-induced segregation. Lattice parameter changes for the B2 structure observed during irradiation are explained in terms of the compositional dependence of the lattice parameter of β -NiAl. The B2 structure remains stable to a dose of 6×10^{28} electrons/m², with no amorphization detected.

INTRODUCTION

Intermetallic compounds exhibit several types of instability under irradiation, including point defect clustering, chemical disordering¹⁻³, dissolution or precipitation of second phases^{3,4} and amorphization⁵⁻⁷. The current electron irradiations of Ni_2Al_3 are part of a continuing study of radiation damage of aluminum-nickel intermetallic compounds⁸⁻¹⁰. Under Xe or Ne ion irradiation at temperatures from 77 to 400 K, Ni_2Al_3 disordered to the B2 structure, with the possibility of some amorphization occurring at the lowest temperatures⁸. On the other hand, NiAl₃ was amorphized by either ion or electron irradiation near 100 K, while showing little or no indication of prior chemical disordering⁹. In the current study, which is a continuation of earlier work¹⁰, the stability of Ni_2Al_3 under electron irradiation is evaluated. From the comparison of the radiation response of these intermetallic compounds, some insight may be gained into the damage mechanisms operative under irradiation and into the factors which determine the stability of intermetallic compounds under irradiation.

EXPERIMENTAL

Thin (~35 nm) multilayered films of alternating aluminum and nickel were electron beam deposited onto a NaCl substrate. The substrate was dissolved in deionized water and the Ni/Al film was mounted on 3 mm molybdenum grids. The films were vacuum annealed for 1 to 2 h at 623 K to allow interdiffusion between the layers. Rutherford backscattering was employed to characterize the film composition and homogeneity. Electron diffraction indicated that the films were fine-grained (~20 nm) Ni_2Al_3 , the prototype for the trigonal D_{5d}^{13} structure, with no appreciable amount of other phases. The specimens were irradiated with 1000 keV electrons in a Hitachi HU-1000B microscope or with 200-300 keV electrons in Philips EM430 and CM30 microscopes. These microscopes are equipped for nominal room temperature or low temperature (~100 K) irradiations. Electron fluxes were measured with a Faraday cup or exposure meters previously calibrated with a Faraday cup. In this paper, all electron doses are given in units of 10^{28} electrons/m² and are indicated as such in the figures. Selected area diffraction (SAD) patterns were used to monitor changes in structure as a function of irradiation dose. Local compositions were measured with the use of energy dispersive x-ray spectroscopy (EDS) at 100 kV in a Philips EM400T-FEG or at 300 kV in Philips EM430 or CM30 instruments. Each analytical electron microscope was equipped with an EDAX detector and either an EDAX 9100 or 9900 analyzer. Measured x-ray intensities were converted to compositions via experimental k-factors based on the unirradiated film. No absorption corrections were made, as the effect on calculated composition at the film thicknesses used (~35 nm) is small. It was shown at 300 kV that radiation-induced segregation or sputtering

did not significantly influence compositions measured via EDS for times a factor of ten greater than those typical for x-ray microanalysis. In some cases, x-ray linescans were taken in the scanning transmission electron microscopy mode to measure elemental redistribution during irradiation.

RESULTS AND DISCUSSION

Figure 1 shows SAD patterns from a 300 keV electron irradiation of a Ni_2Al_3 specimen at ~ 100 K to doses of (a) $0.02 \times$, (b) $0.2 \times$, and (c) 1.2×10^{26} electrons/ m^2 at an electron flux of $\sim 7 \times 10^{22}$ electrons/ m^2s . A gradual decrease in the intensity of some of the Ni_2Al_3 superlattice lines [e.g., the inner three rings in Fig. 1(a)] is observed. After continued irradiation, some of these lines disappeared entirely (e.g., the first, second, fifth, and sixth rings), whereas other lines remained weak but visible (e.g., the third, seventh, and eleventh rings). The resulting diffraction pattern exhibited a characteristic weak-strong-weak-strong sequence of rings which matched a B2 structure with lattice parameter $a_0 = 0.284$ nm (determined with the unirradiated Ni_2Al_3 as an internal standard). The presence of the B2 superlattice lines indicates that irradiation has not completely disordered the Ni_2Al_3 from the B2 structure to the parent bcc lattice which would have random site occupancy. The same effect has been reported for ion irradiation of Ni_2Al_3 ⁸. On the other hand, the low intensity of the B2 superlattice lines indicates that the B2 lattice is not well-ordered. This disorder is associated with 1) the radiation-induced mixing of nickel and aluminum atoms onto the wrong sublattices and 2) the presence of excess aluminum relative to the equiatomic stoichiometry required for perfect B2 ordering.

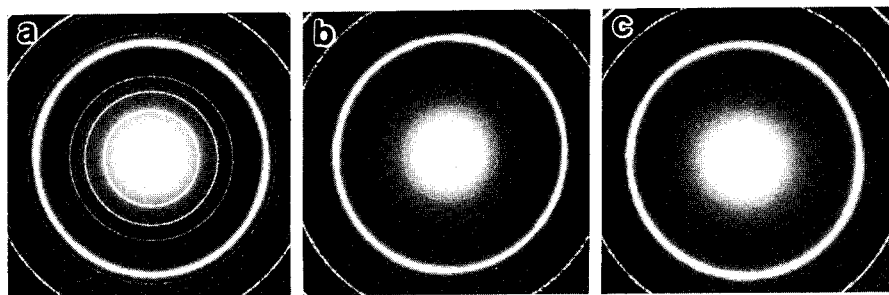


Fig. 1 SAD patterns of Ni_2Al_3 irradiated at 100 K with 300 keV electrons at a flux of 7×10^{22} electrons/ m^2s to doses of (a) 0.02×10^{26} , (b) 0.2×10^{26} , and (c) 1.2×10^{26} electrons/ m^2 , as indicated in figure.

β -NiAl has the B2 structure and would have an extrapolated lattice parameter of 0.2845 nm at 40 at. % Ni, based on published lattice parameter versus composition data¹¹. As was first noted in that work¹¹, the Ni_2Al_3 and NiAl structures are related through the placement of ordered nickel-site vacancies in the B2 structure and an attendant distortion to the trigonal Ni_2Al_3 structure. Thus the transformation from Ni_2Al_3 to NiAl can be described as the disordering of these vacancies. As reported in the earlier work¹⁰, this transformation has been induced by electron irradiations at both 100 and 300 K with 200, 300, and 1000 keV electrons. The electron doses required to disorder Ni_2Al_3 to the B2 structure were determined as a function of temperature and accelerating voltage. A lower dose was required for disordering at 1000 kV relative to 200 or 300 kV, reflecting the higher damage efficiency of higher energy electrons. In part, this higher efficiency may reflect the occurrence of replacement collision sequences at 1000 kV, which produce many disordering events for a single displacement event. A slightly higher electron dose was required for disordering at 300 K relative to that for a 100 K irradiation. This may indicate that thermally induced defect recombination or radiation-enhanced diffusion is aiding the reordering process.

The irradiation-induced B2 structure should be unstable since its composition lies outside the equilibrium range for β -NiAl (45–60 at. % Ni at ≤ 900 K). In order to investigate the stability of the B2 structure with respect to further disordering or amorphization, higher dose irradiations were performed at 300 kV with higher electron fluxes. Figure 2 shows SAD

patterns from a Ni_2Al_3 specimen irradiated with 300 keV electrons at 100 K to doses of 26×10^{26} and 90×10^{26} electrons/ m^2 at a flux of $\sim 1.4 \times 10^{24}$ electrons/ m^2s . In addition to the rings corresponding to the B2 phase, extra rings corresponding to interplanar spacings of 0.231, 0.120, and 0.0918 nm were observed. These spacings are slightly ($\sim 1\%$) less than those of the 111, 113, and 133 planes of aluminum at ~ 300 K. The other aluminum interplanar spacings overlap those of the B2 structure to within 0.5 %. The measurements were made at 100 K, but thermal expansion of aluminum can only account for a 0.35 % difference in lattice parameter. As nickel is an undersized atom relative to aluminum^{11,12}, nickel dissolved in the aluminum should decrease the lattice parameter. Though the equilibrium solubility of nickel in aluminum is very low (~ 0.02 at.%), it has been shown that irradiation will significantly increase that limit¹³. Combined convergent beam electron diffraction and EDS studies confirmed the presence of aluminum-rich, fcc precipitates with $a_0 \approx 0.40$ nm.

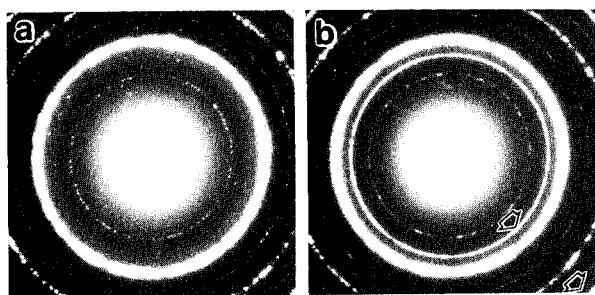


Fig. 2 SAD patterns of Ni_2Al_3 irradiated at 100 K with 300 keV electrons at a flux of 1.4×10^{24} electrons/ m^2s to doses of (a) 26×10^{26} and (b) 90×10^{26} electrons/ m^2 , as is indicated in figure.

The formation of essentially pure aluminum is interesting since aluminum and Ni_2Al_3 are separated by NiAl_3 in the equilibrium phase diagram, but formation of NiAl_3 during the irradiation was not indicated in the SAD patterns. This is consistent with the instability of NiAl_3 under electron irradiation mentioned earlier⁹. A similar phase decomposition has been reported for W-Re alloys (5-25 wt % Re) under neutron irradiation, where the cubic chi phase forms and the intervening sigma phase was not observed¹⁴. Follstaedt and Romig have studied metastable phase formation in nickel implanted aluminum and fit their results to a proposed metastable Ni-Al phase diagram¹⁵. They did not observe the Ni_3Al and Ni_2Al_3 phases and only the Al(Ni) solid solution and β -NiAl phases occur for alloys <50 at.% Ni. Therefore, the precipitation of aluminum from the irradiated β -NiAl observed in the current study is consistent with such a metastable phase diagram. The matrix remains weakly B2-ordered up to doses of $\sim 600 \times 10^{26}$ electrons/ m^2 without any indication of amorphization. This contrasts to the behavior under ion irradiation, where amorphization does occur^{8,15}.

Mass loss was observed in some of the high dose irradiations at 300 kV and is illustrated for irradiation at 100 K in Fig. 3. The intensity of bremsstrahlung X-rays, which is proportional to the local mass thickness, indicated that the center of the irradiated area had decreased to half the mass thickness of the unirradiated film. The data shown in Fig. 3(b) indicate that both aluminum and nickel K x-ray intensities decreased at the center of the irradiated area, indicating loss of both aluminum and nickel. In the composition profile [Fig. 3(c)], the center is enriched in aluminum (>75 at.% Al), indicating that nickel was lost preferentially. Bradley and Zaluzec have analyzed electron-induced sputtering in terms of the mass and sublimation energy of atomic species¹⁶. For Ni-Al alloys, preferential sputtering of aluminum is predicted from the larger kinetic energy transferred to aluminum and its presumably lower sublimation energy in the intermetallic compound. The discrepancy between the predicted and observed behavior probably results from radiation-induced segregation (RIS) driven by fluxes of point defects to sinks¹⁷. At low temperatures, only self-interstitials are mobile and undersized atoms, such as nickel, will be transported via interstitial diffusion to defect sinks. The surfaces of the film would tend to become nickel enriched and sputtering from the electron-exit surface could result in preferential nickel loss as observed. Figure 3(d) is a higher magnification image of the center of the irradiated area underfocussed by $\sim 2.4 \mu\text{m}$. The original grain boundaries appear lighter indicating a local decrease in mass thickness, which may represent a bulk effect (composition or density difference) or a thickness effect (grain boundary grooving). As grain boundaries in the adjacent unirradiated material do not exhibit this behavior, this effect must be associated with either RIS or sputtering. High resolution EDS with an ~ 5 nm probe indicated that the grain boundaries near the center of

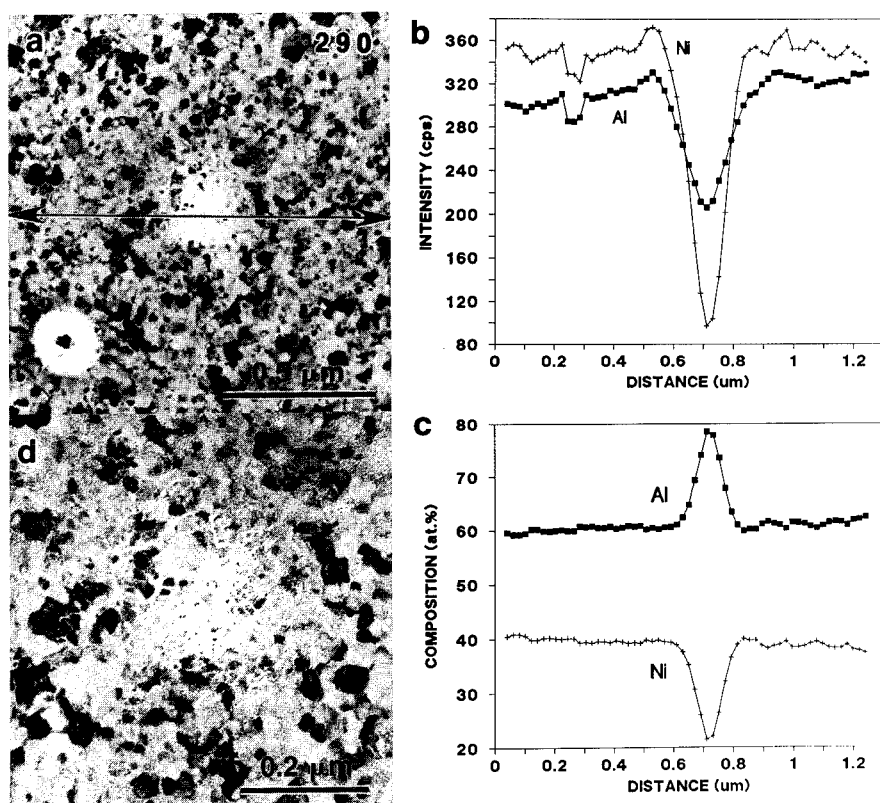


Fig. 3 Mass loss in Ni_3Al . (a) Area irradiated at 100 K with 300 keV electrons at a flux of 8×10^{24} electrons/ m^2s to dose of 290×10^{26} electrons/ m^2 , as indicated in figure. Arrow indicates location of x-ray line scan. (b) K x-ray intensities and (c) composition determined from x-ray linescan. (d) Central area at higher magnification and $2.4 \mu\text{m}$ underfocus showing lower mass thickness at irradiated grain boundaries.

the irradiated area exhibit Al/Ni ratios ~ 1.7 times higher than the adjacent matrix. This indicates that the local decrease in mass thickness apparent in Fig. 3(d) arises at least in part from a composition difference.

Radiation-induced segregation also occurred during the 300 keV irradiations at 300 K¹⁰. In that case, both mass loss at the beam center and mass thickening near the periphery of the beam were observed. Mass transport is required for mass thickening to occur. The thickened regions were enriched in nickel consistent with RIS preferentially transporting nickel with the flux of self-interstitials. Whereas both aluminum and nickel were sputtered from the center of the irradiated area, the zone depleted of aluminum was roughly twice as wide as that depleted of nickel, which resulted in a nickel-enriched region just beyond the nickel-depleted center. The origin of such a profile has been discussed previously in terms of the combined effects of preferential sputtering and RIS away from the high defect region¹⁰. In their work on RIS in Ni-Al alloys at high temperature (~ 1000 K), Okamoto and Lam also found aluminum enrichment in the center of the irradiated area, which they explained with a vacancy RIS model¹⁷. However, at the current irradiation temperatures (≤ 300 K), vacancies are probably not mobile and therefore a self-interstitial RIS mechanism appears to be operative. Unfortunately, the preferential sputtering and RIS complicate the interpretation of the high dose study on the stability of the B2 structure. Therefore, it is not clear if the precipitation of aluminum from

the irradiated β -NiAl is related to the instability of that phase or to precipitation driven by RIS.

The radial redistribution of elements by RIS was found to be sensitive to the electron distribution in the probe. With the use of an aberrated probe, it is possible to form a probe that has a local current density minimum at its center. Irradiation at 100 K with such a probe results in aluminum depletion at the center of the irradiated area and aluminum enrichment at the region of maximum current density. Figure 4 gives the apparent composition and β -NiAl lattice parameter of the central region as a function of irradiation time (300 minutes $\approx 8.6 \times 10^{27}$ electrons/m²). The apparent aluminum composition monotonically decreases with dose. However, while the lattice parameter generally increases with dose, there is a sharp drop between 180 and 240 minutes. At this same time, aluminum starts to precipitate out of solution. On the other hand, for irradiation with a Gaussian probe at similar flux and dose, the apparent composition does not change and the lattice parameter of the B2 phase remains essentially constant, except for a slight increase ($\sim 0.5\%$) associated with the precipitation of aluminum. No significant mass loss was observed in either irradiation, indicating that preferential sputtering effects can be ignored. The observed behavior of lattice parameter in these two irradiations may be associated with the roughly parabolic composition dependence of the lattice parameter of β -NiAl, which exhibits a maxima at ~ 49.5 at.% Ni¹². In the first irradiation, RIS decreases the aluminum content of the B2 phase and increases the lattice parameter towards the maximum near 49.5 at.% Ni. The subsequent aluminum precipitation further decreases the aluminum content, presumably beyond the local maxima. This would result in a decrease in the lattice parameter, as observed. In the second irradiation, the slight increase in lattice parameter observed is consistent with a slight decrease in aluminum content of the B2 phase near 40 at.% Ni when the aluminum precipitates.

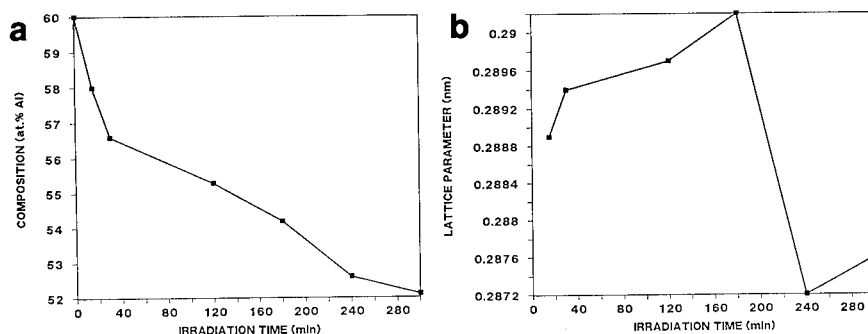


Fig. 4 (a) Apparent composition and (b) lattice parameter as a function of irradiation time with the use of an aberrated probe with a local electron density minimum at center (Irradiation at 100 K with 300 keV electrons at a flux of 4.8×10^{23} electrons/m²s).

SUMMARY

Electron irradiation disorders Ni_2Al_3 to the B2 structure with a lattice parameter of 0.284 nm, which is close to the extrapolated value for β -NiAl at 40 at.% Ni. The B2 structure remains stable to doses of at least 600×10^{26} electrons/m², with no amorphization indicated. The dose required for disordering decreases with increasing electron energy and possibly with decreasing irradiation temperature. High dose irradiation results in precipitation of aluminum metal, changes in mass thickness, and elemental redistribution. Radiation-induced segregation and preferential sputtering complicate the interpretation of the observed instability of the B2 phase. Localized thinning occurs in part by sputtering. However, radiation-induced segregation is required to explain the observed composition changes. Radiation-induced segregation occurs by diffusion of mobile self-interstitials, whereby undersized nickel segregates with the interstitial flux to boundaries, surfaces, and unirradiated areas. The observed lattice parameter changes during irradiation are explained with reference to the compositional dependence of the lattice parameter of β -NiAl.

ACKNOWLEDGEMENTS

The authors wish to thank Drs. K.B. Alexander, P. Angelini, and J. Bentley for useful discussions and review of this manuscript. Research sponsored in part at Oak Ridge National Laboratory by the Division of Materials Sciences, U.S. Department of Energy, under contract DE-AC05-84OR21400 with Martin Marietta Energy Systems, Inc. and at Los Alamos National Laboratory by the U.S. Department of Energy.

REFERENCES

1. J. L. Brimhall, H. E. Kissinger, and L. A. Charlot, *Radiation Effects*, **77**, 273 (1983).
2. L. M. Howe and M. H. Rainville, *J. Nucl. Mater.*, **68**, 215 (1977).
3. P. Wilkes, *J. Nucl. Mater.*, **83**, 166 (1979).
4. R. S. Nelson, J. A. Hudson, and D. J. Mazey, *J. Nucl. Mater.*, **44**, 318 (1972).
5. J.L. Brimhall, E.P. Simonen, *Nucl. Instr. Meth. Phys. Res.*, **B16**, 187 (1986).
6. R. W. Gilbert, M. Griffiths, and G. J. C. Carpenter, *J. Nucl. Mater.*, **135**, 265 (1985).
7. E. H. Lee and E. A. Kenik, *J. Mater. Res.*, **3**, 840 (1988).
8. M. Nastasi, L.S. Hung, H.H. Johnson, and J.W. Mayer, *J. Appl. Phys.* **57**, 1050 (1985).
9. M. Nastasi, J.M. Williams, E.A. Kenik, and J.W. Mayer, *Nucl. Instr. Meth. Phys. Res.* **B19/20**, 543 (1987).
10. E. A. Kenik and M. Nastasi, in *Proc. of 46th Electron Microscopy Society of America Meeting*, edited G.W. Bailey (San Francisco Press, San Francisco, CA 1988) p. 560; *Ultramicroscopy* (In Press).
11. A. J. Bradley and A. Taylor, *Proc. Roy. Soc. London*, **159**, 54 (1937).
12. W. B. Pearson, *Lattice Spacings and Structures of Metals and Alloys* (Pergamon Press, New York, 1958) p. 39.
13. S.T. Picraux, D.M. Follstaedt, J.A. Knapp, W.R. Wampler, and E. Rimini, in *Laser and Electron-Beam Solid Interactions and Materials Processing*, edited by J.F. Gibbons, L.D. Hess, and T.W. Sigmon (*Mater. Res. Soc. Proc. 1*, Pittsburgh, PA 1981) pp. 575-582.
14. R.K. Williams, F.W. Wiffen, J. Bentley, and J.O. Stiegler, *Metall. Trans.*, **14A**, 655 (1983).
15. D.M. Follstaedt and A.D. Romig Jr, in *Microbeam Analysis - 1985*, edited by J.T. Armstrong (San Francisco Press, San Francisco, CA 1985) pp. 173-178.
16. C. R. Bradley and N. J. Zaluzec, in *Analytical Electron Microscopy - 1987*, edited by D.C. Joy (San Francisco Press, San Francisco, 1987) pp. 117-120.
17. P. R. Okamoto and N. Q. Lam, in *Advanced Photon and Particle Techniques for the Characterization of Defects in Solids*, edited by J.B. Roberto, R.W. Carpenter, and M.C. Wittels (*Mater. Res. Soc. Proc. 41*, Pittsburgh, 1985) pp. 241-246.

THE EFFECT OF SIMULTANEOUS ELECTRON AND Kr^+ IRRADIATION ON AMORPHIZATION OF CuTi *

J. Koike (1,2), P. R. Okamoto (1), L. E. Rehn (1), M. Meshii (2)

1. Materials Science Division, Argonne National Laboratory, Argonne, IL 60439
2. Dept. of Materials Science and Engineering, Northwestern University, Evanston, IL 60208

ABSTRACT

CuTi was irradiated with 1-MeV electrons and Kr^+ ions simultaneously at temperatures from 10 to 423 K. Retardation of Kr^+ -induced amorphization was observed with simultaneous electron irradiation at 295 and 423 K. The retardation effect increased with increasing irradiation temperature and relative electron-to- Kr dose rate. In contrast, simultaneous irradiation below 100 K showed an additive effect of electron- and Kr^+ -induced amorphization. The results can be explained by the mobility point defects introduced by electron irradiation interacting with Kr^+ -induced displacement cascades.

INTRODUCTION

A recent study [1] has shown that amorphization of Si during irradiation with 1-MeV Kr^+ ions at 10 K can be strongly retarded by simultaneously irradiating the sample with a 1-MeV electron beam. The retardation effect under simultaneous irradiation was found to occur only when the calculated electron displacement rate (dpa/s) exceeded that for the Kr^+ beam by a factor of about two. Although not yet fully understood, the retarding effect clearly indicates that the primary damage state characteristic of ions which produce dense displacement cascades can be significantly altered by additional Frenkel pair production by electrons. The present paper reports the effect of simultaneous irradiation with 1-MeV electrons and 1-MeV Kr^+ ions on the amorphization behavior of the intermetallic compound, CuTi .

In contrast to Si, which becomes amorphous under Kr^+ irradiation but not under electron irradiation, CuTi can be rendered completely amorphous by both types of charged particles [2]. As suggested in a recent theoretical study [3] of the amorphization kinetics of intermetallic compounds under simultaneous irradiation conditions, the Kr^+ -induced crystalline-to-amorphous transition in CuTi can be suppressed or accelerated by simultaneous electron irradiation depending on the irradiation temperature and on the relative dose rate of the electron and ion beams employed.

EXPERIMENTAL PROCEDURE

The preparation and homogenization treatments of the polycrystalline samples of CuTi have been described previously

*The work is supported by DOE W-31-109-ENG-38 and NSF DMR-8411178.

[4]. Simultaneous irradiations with 1-MeV electrons and Kr^+ ions were carried out in situ in the Argonne National Laboratory High Voltage Electron Microscope interfaced to a 2-MeV tandem accelerator. Kr^+ irradiations were performed using three different current densities of 1.7×10^{10} , 5.1×10^{10} and 3.4×10^{11} ions/cm²/s. The corresponding atomic displacement rates obtained by TRIM calculation [5] using a threshold energy of 21 eV [6] are 5×10^{-5} , 1.5×10^{-4} and 1.0×10^{-3} dpa/s, respectively. Electron irradiations were performed with a fully focused beam. A Faraday cup located above the specimen position was used to measure total beam current (I_T), and a movable Faraday cup located in the viewing chamber was used for beam profiling and for measuring the peak electron flux (I_p). Typical beam profiles employed for this study can be described approximately by a Gaussian distribution, $I(r) = I_p \cdot \exp\{-1/2(r/\sigma)^2\}$ [1]. The parameter σ is the standard deviation of the distribution, and was calculated from the measured electron fluxes using the relationship $\sigma = (I_T/2\pi I_p)^{1/2}$. The beam parameters were chosen to obtain a peak electron flux of 2×10^{19} electrons/cm²/s, corresponding to a calculated peak displacement rate of 1×10^{-3} dpa/s.

RESULTS

Figure 1 shows the temperature dependence of the critical dose required for amorphization of CuTi when irradiated separately with either 1-MeV electrons or Kr^+ . The critical dose for electrons was obtained from the calculated dose at the position where a bend contour of a strongly excited Bragg reflection disappears in the bright field image, while that for Kr^+ was determined by the dose at which crystalline spots completely disappear in the diffraction pattern. There is a critical temperature (T_c) below which CuTi can be rendered completely amorphous; at higher temperatures the specimen remains crystalline. T_c for 1-MeV electrons is about 220 K for a calculated displacement rate of 1×10^{-3} dpa/s. For the same calculated displacement rate, T_c for Kr^+ is substantially higher than that for electrons, and has been found to increase with

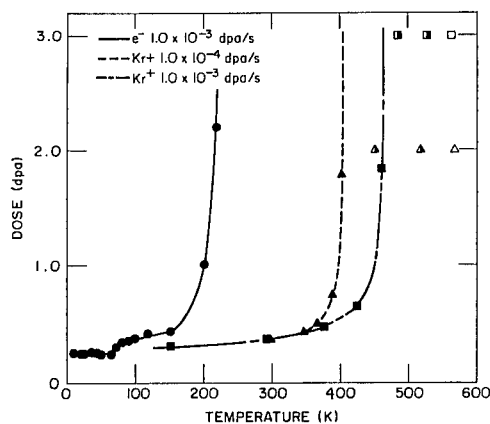


Fig.1
The temperature dependence of the critical dose for amorphization with 1-MeV electrons and Kr^+ at the indicated dose rate. Filled symbols denote complete amorphization; half-filled and open symbols denote partial and no amorphization, respectively.

dose rate as shown in Fig.1 by the two different curves obtained for Kr^+ displacement rates of 1×10^{-4} and 1×10^{-3} dpa/s. Another difference between electrons and Kr^+ is that with electrons CuTi cannot be partially amorphized above T_C , whereas with Kr^+ , partial amorphization (denoted by the half-filled symbols) does occur above T_C up to an upper limiting temperature (T_U) of ~ 523 K. Above T_U no amorphization occurs regardless of the dose rate. Extrapolation of the Kr^+ data to low temperatures indicates that the critical doses for electrons and for Kr^+ ions converge to the same value of ~ 0.25 dpa below ~ 70 K.

Figure 2 shows a result of a simultaneous electron and Kr^+ irradiation carried out at room temperature which, as shown in Fig.1, is above T_C for electrons. The bottom plot shows the radial variation of the calculated dose rate determined from the measured values of I_T and I_p and assuming the Gaussian intensity distribution. The total electron dose scaled on the right-hand side is for an irradiation time of 6000 seconds. The corresponding quantities for the spatially uniform Kr^+ beam are also indicated by a dashed line on the plot. The bright field image of the microstructure printed to the same scale shows that after 6000 seconds of simultaneous irradiation, most of the sample irradiated only by the Kr^+ beam has become amorphous, whereas the central part of the region simultaneously irradiated by the electron beam retains a high degree of crystallinity. This is evidenced by the residual bend contour, and by the electron diffraction patterns taken from inside and outside of this region shown at the top of Fig.2.

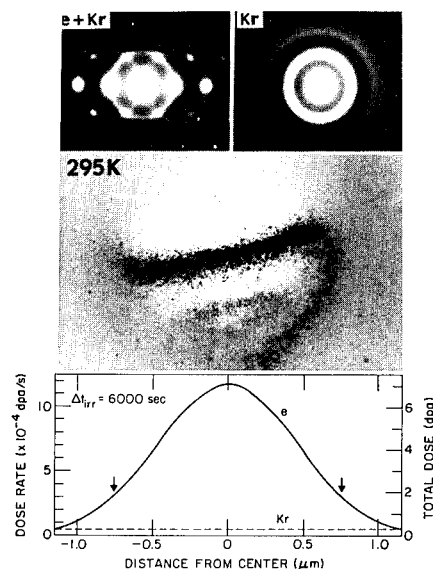


Fig.2
The diffraction pattern and the bright field image after simultaneous electron and Kr^+ irradiation at 295 K for 6000 seconds. A calculated dose rate and the total dose are shown on the bottom.

This result clearly shows that amorphization induced by Kr^+ ions is strongly retarded by the electron beam at room temperature. The two arrows on the dose-rate plot indicating the approximate positions where the bend contour disappears show that the retardation effect occurs only in regions where the calculated electron dose rate is ≥ 6 times that of the Kr^+ beam.

This critical electron-to-Kr⁺ dose rate ratio required to suppress amorphization depends on temperature. This has been demonstrated by maintaining the sample at room temperature and increasing the ion current density to obtain a Kr⁺ dose rate equal to the peak electron dose rate of 1×10^{-3} dpa/s. The previous crystalline region becomes completely amorphous as shown in Fig.3. However, Fig.4 shows that at 423 K a retardation effect still occurs under the same electron and ion beam conditions employed in Fig.3.

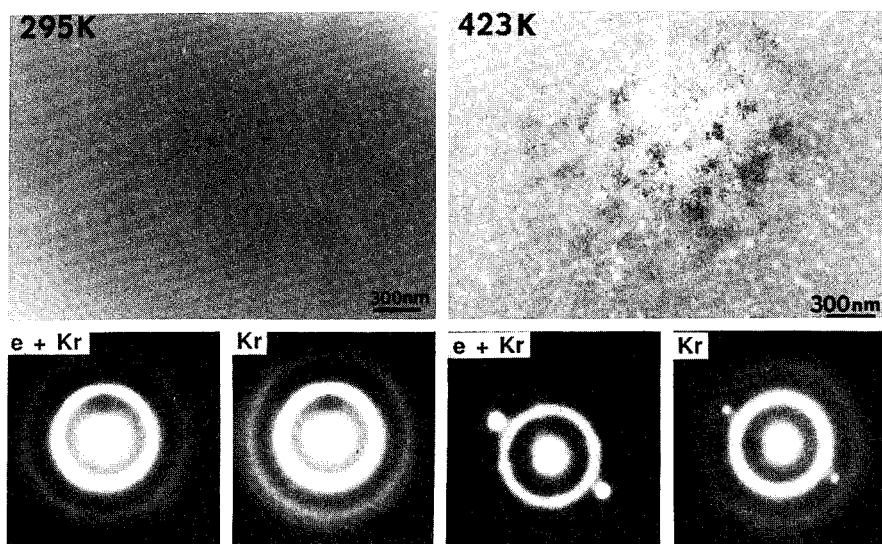


Fig.3 The bright field image and diffraction patterns after the simultaneous irradiation at 295 K for 4000 seconds. The calculated dose rate of Kr⁺ is equal to the peak electron dose rate in Fig. 2.

Fig.4 The bright field image and diffraction patterns after the simultaneous irradiation at 423 K for 4000 seconds. The dose rate is the same as in Fig.3.

The effect of temperature was further investigated by carrying out simultaneous irradiations below T_c for electrons, where CuTi can be completely amorphized by both electrons and Kr⁺. A result at 10 K is shown in Fig. 5; the beam conditions are the same as those employed in Fig.2. In contrast to the retardation observed at room temperature, the central region of the simultaneously irradiated area becomes completely amorphous before regions irradiated only with Kr⁺ ions. This effect is not prominent in the periphery where the amorphization process is dominated by Kr⁺ irradiation. Similar results were observed at 50, 100, and 150 K.

As the break in the bend contour expands outward with increasing irradiation time, the total dose accumulated at a given position can be calculated from the known dose-rate profile by multiplying by the irradiation time. The calculated dose at the positions where the bend contours disappear

(indicated by arrows in the bottom figure) was taken to be the critical dose required for complete amorphization. For quantitative analysis of the critical dose, a peak electron dose of 1.2×10^{-3} dpa/s and a Kr^+ dose rate of 1.5×10^{-4} dpa/s were employed. The calculated critical doses for electrons and Kr^+ ions at 10 K have been plotted in Fig.6 as a function of the distance (r) from the electron beam center. Increasing r is equivalent to decreasing the relative electron to Kr^+ dose rate as shown on the bottom of Fig.5. Hence the critical doses measured at larger distances represent larger Kr^+ doses (denoted by open squares in Fig.6). For increasing r , the critical electron dose (denoted by open circles) is found to decrease, and the sum (denoted by filled circles) of the critical electron and Kr^+ doses remains almost constant at ~ 0.24 dpa. Note that this value is very close to the critical dose for electron irradiation alone. Similar additive effects of electron and Kr^+ were observed at 50 and 100 K.

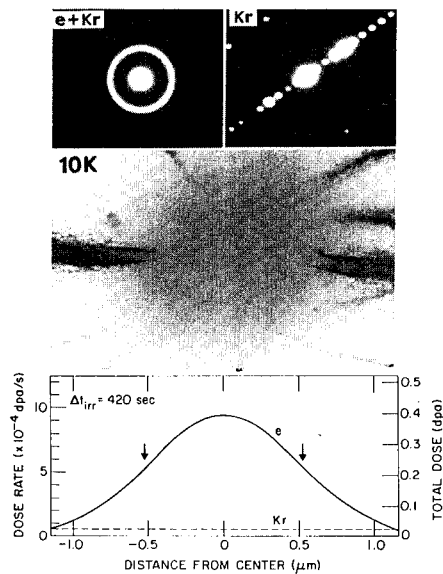


Fig.5
Sample irradiated at 10 K
for 420 sec. The
calculated dose rates for
electrons and Kr^+ are
about the same as in
Fig.2.

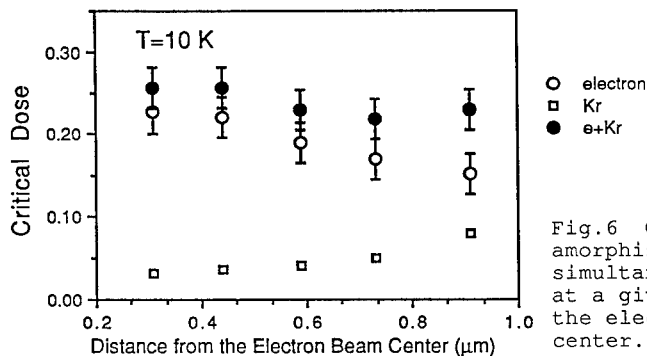


Fig.6 Critical dose for
amorphization under
simultaneous irradiation
at a given position from
the electron beam
center.

DISCUSSION

Significant differences in amorphization behavior under simultaneous irradiation were observed above and below T_C for electrons. In a previous work [4], electron irradiation of CuTi above T_C was reported to produce mobile point defects resulting in defect aggregation and retention of a high degree of chemical order. These point defects are not mobile below T_C as evidenced by chemical disordering preceding amorphization. The correlation in the temperature dependence between point defect mobility and amorphization suggests that the retardation of Kr^+ -induced amorphization above T_C is due to annealing of the displacement cascade damage produced by Kr^+ irradiation by the additional mobile point defects produced by electron irradiation.

Below T_C , electrons and Kr^+ ions were found to contribute additively to amorphization (c.f. see Fig.6). The present work suggests that the crystalline-to-amorphous transition below is controlled by the accumulated displacement density, independent of how the defects are produced. This is consistent with the converging critical dose for electrons and Kr^+ ions at low temperature when the sample is separately irradiated as shown in Fig.1.

CONCLUSION

(1) Above 295 K, amorphization induced with Kr^+ ions was retarded by simultaneous electron irradiation. (2) The retardation effect was greater with increasing irradiation temperature and with increasing electron-to- Kr^+ dose rate. (3) At 10, 50 and 100 K, the effect of simultaneous Kr^+ and electron irradiation was additive.

REFERENCES

1. D. N. Seidman, R. S. Averbach, P. R. Okamoto, and A. C. Baily, Mater. Res. Soc. Proc., **51**, 349 (1986).
2. J. Koike, P. R. Okamoto, L. E. Rehn, M. Meshii, J. Non Cryst. Solids, **106**, 230 (1988).
3. D. F. Pedraza, Phys. Rev., **38**, 4803 (1988).
4. J. Koike, P. R. Okamoto and M. Meshii, Mater. Res. Soc. Proc., **74**, 425 (1987).
5. J. P. Biersack and L.G. Hagmark, Nucl. Inst. and Methods, **174**, 257 (1970).
6. D. E. Luzzi, H. Mori, H. Fujita and M. Meshii, Acta Met., **34**, 629 (1986).

AMORPHIZATION OF Zr_3Al BY HYDROGENATION AND SUBSEQUENT ELECTRON IRRADIATION

W. J. Meng, J. Koike, P. R. Okamoto, and L. E. Rehn
MATERIALS SCIENCE DIVISION, ARGONNE NATIONAL LABORATORY
ARGONNE, ILLINOIS 60439

ABSTRACT

1-MeV electron irradiation of hydrogenated Zr_3Al ($Zr_3AlH_{0.96}$) at 10K is studied. A more than 20 fold reduction in the critical dose required for complete amorphization is observed for the hydrogenated specimen as compared to the un-hydrogenated Zr_3Al under identical irradiation conditions.

INTRODUCTION

Recent work on the ordered intermetallic compound Zr_3Al ($L1_2$ -type superlattice) has demonstrated a correlation between a critical volume expansion of the crystalline lattice and the onset of amorphization during ion bombardment. The volume expansion results in a dramatic softening of the shear modulus, which is remarkably similar to that seen in simple metals during heating to melting[1]. Although the volume expansion preceding amorphization during ion bombardment is associated with the loss of chemical long-range order (CLRO)[2], a lattice dilation of similar magnitude, e.g., $3(\Delta a/a) \sim 2.5\%$, also occurs prior to the onset of amorphization of Zr_3Al during hydrogenation[3]. In contrast to irradiation, no significant change in CLRO occurs during hydrogenation[3], indicating that the expansion results from hydrogen occupying interstitial sites in the ordered compound. These observations imply that dilatational strain, rather than chemical disordering per se, plays the key role in the onset of amorphization. Moreover, by also reducing the free energy difference between the crystalline and amorphous phases, the presence of hydrogen can be expected to reduce the amount of displacement damage required to completely amorphize an intermetallic compound.

Previous work by Koike et al.[4] on un-hydrogenated Zr_3Al has shown that a critical electron dose in excess of 26 displacements per atom (dpa) is needed to completely amorphize the compound when irradiated at 10K with 1-MeV electrons. This critical dose is anomalously large compared to the typical 1 dpa or less reported in a recent survey of intermetallic compounds which undergo amorphization during electron irradiation[5]. In contrast to these more easily amorphizable materials, point defect aggregation was observed during irradiation of Zr_3Al at 10K, which suggests that the anomalously large critical dose is related to dynamical point-defect recovery processes. As

will be shown, under identical irradiation conditions, the presence of hydrogen causes a more than a 20 fold reduction in the critical dose.

EXPERIMENTAL PROCEDURES

Zr₃Al alloys used in this study were prepared by arc-melting, and subsequently homogenizing at 900°C for 12 days. The homogenized alloy consists predominantly of L1₂-Zr₃Al, with a few percent of the Zr₂Al phase. Details of the hydrogenation procedures have been previously described[3]. TEM samples of hydrogenated specimens were prepared by electropolishing with an acid free solution[6]. Electron irradiations were carried out at 10K in the Argonne HVEM with a 1-MeV electron beam focused to ~ 1 μm in diameter. The peak electron flux was measured by a Faraday cup to be ~ 2.5×10^{19} e/cm²·sec. Using an average total displacement cross section, σ_d , for Zr₃Al of 40 barns[7], this peak electron flux corresponds to a peak displacement rate of ~ 1×10^{-3} dpa/sec. This point will be discussed later.

RESULTS AND DISCUSSION

Details of the hydrogenation of Zr₃Al are described elsewhere[3,8]. The specimen used in this study was hydrogenated at 340°C for 21 hours. The overall hydrogen to metal ratio (H/M) is 0.24 (Zr₃AlH_{0.96}). The initial grain size is around 10 μm. Detailed examination revealed that after hydrogenation an amorphous phase has nucleated homogeneously in certain grains where the amorphous/crystalline interface is no longer sharply defined[8]. In other grains which have remained crystalline up to this point, a high density of planar defects resulted from the hydrogenation treatment.

Fig. 1 shows a series of (130) zone-axis electron diffraction patterns taken at 10K from a grain rendered partially amorphous by hydrogenation prior to electron irradiation. Figs. 1(a), 1(b), and 1(c) correspond to electron doses of 0, 0.12, and 0.6 dpa, respectively. The existence of strong superlattice spots in Fig. 1(a) signifies a high degree of CLRO in the remaining crystalline material of the hydrogenated sample. At 0.12 dpa, Fig. 1(b) shows that the intensity of superlattice spots is greatly reduced with respect to that of fundamental spots, indicating that chemical disordering is taking place. By 0.6 dpa, Fig. 1(c) shows that the irradiated region has been almost completely amorphized. Fig. 2 shows the corresponding transition in bright-field mode. With the irradiated area centered around the center of the bend contour, the detailed bend contour contrast is diminished by 0.12 dpa, and has completely disappeared by 0.6 dpa.

Fig. 3 shows irradiation induced changes in the (100) zone-axis electron diffraction patterns taken at 10K from one of the grains containing a high density of planar defects, i.e., a grain which remained crystalline after hydrogenation. Figs. 3(a), 3(b), and 3(c) correspond to

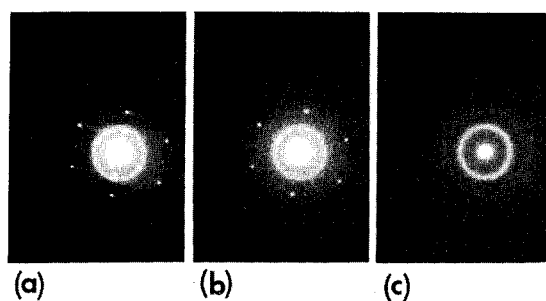


Fig. 1. $L1_2$ - Zr_3Al (130) zone-axis diffraction patterns; (a), (b), and (c) correspond to 0, 0.12, and 0.6 dpa respectively. Irradiation carried out with 1-MeV electrons at 10K.

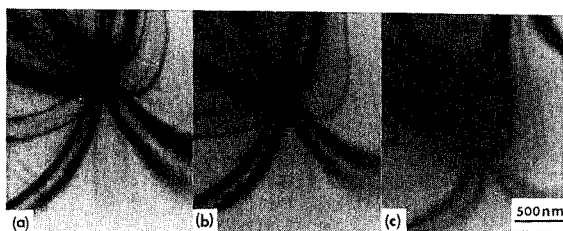


Fig. 2. Bright-field images of the irradiated region in Fig. 1; (a), (b), and (c) correspond to 0, 0.12 and 0.6 dpa.

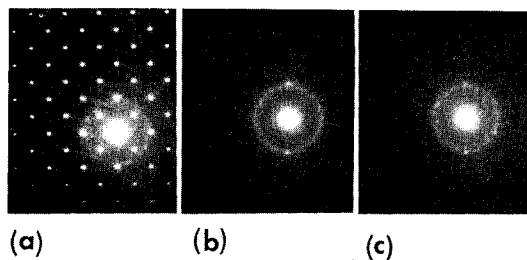


Fig. 3. $L1_2$ - Zr_3Al (100) zone-axis diffraction patterns; (a), (b), and (c) correspond to 0, 1.1, and 1.7 dpa respectively. Irradiation carried out with 1-MeV electrons at 10K.

electron doses of 0, 1.1, and 1.7 dpa respectively. It is evident from Fig. 3(b) that by 1.1 dpa, over 90% of the irradiated area has been rendered amorphous. From 1.1 to 1.7 dpa, no further changes occur in the electron diffraction patterns. However, some remnant Bragg spots are still present by 1.7 dpa. Fig. 4 shows a bright-field image of the irradiated area after 1.7 dpa, from which it can be seen that the crystalline matrix has become featureless although residual contrast is still evident from the planar defect region. Thus we conclude that the initially crystalline matrix is rendered amorphous by about 1 dpa, whereas the planar defect region is more resistant to amorphization. Based on these observations, the total electron dose necessary to amorphize $\text{Zr}_3\text{AlH}_{0.96}$ by 1-MeV electrons is at least 20 times less than that required to completely amorphize un-hydrogenated Zr_3Al .

We have used an average total displacement cross section of 40 barns (same as un-hydrogenated Zr_3Al) to convert the total electron dose to dpa. With the addition of hydrogen, secondary displacement events such as displacement of hydrogen by incoming electrons and subsequent displacements of Zr or Al by recoiling hydrogen atoms become possible. In systems with large mass mismatches, such as Pt-C, such secondary displacements can contribute significantly to the



Fig. 4. Bright-Field image of the irradiated region in Fig. 3 after 1.7 dpa.

displacement of heavier atoms[9]. We have estimated the relative importance of hydrogen secondary displacement events of the Zr and Al atoms as follows. First, the primary displacement cross section for 1-MeV electrons incident on hydrogen, assuming a displacement threshold T_d of 4 eV, is 40 barns[7]. This is close to the average total displacement cross section for 1-MeV electrons incident on Zr_3Al , assuming an average displacement threshold T_d of 25 eV[7]. The assumption of $T_d = 4$ eV for hydrogen as compared to the usual assumption of an average T_d for Zr_3Al of 25 eV assumes the possibility of hydrogen being displaced with greater ease. Thus electron induced primary displacement events have roughly equal cross sections for displacing Zr, Al, or hydrogen. The maximum kinetic energy transfer from a 1-MeV electron to hydrogen is 4.4 keV[10]. TRIM[11] calculations for 4.4 keV hydrogen incident on Zr_3Al assuming an average displacement threshold of 25 eV yields ~ 1.8 displacements per hydrogen per angstrom. Taking the target density to be the weighted average of that of pure Zr and Al (i.e., 4.6×10^{22} atom/cm³), and assuming every displaced hydrogen will recoil with the maximum kinetic energy of 4.4 keV, the upper bound on the number of secondary displacement events of Zr and Al due to hydrogen is only $\sim 40\%$ of the primary Zr and Al displacement events. It should also be pointed out that our assumption that every hydrogen will recoil with the maximum kinetic energy possible grossly overestimates the actual frequency of secondary displacement events, since the hydrogen primary recoil spectrum is heavily weighted toward smaller energy transfers[10]. Thus our estimate demonstrates that additional secondary displacement events due to the presence of hydrogen cannot be the cause of the observed 20 fold reduction in the total electron dose required to amorphize $Zr_3AlH_{0.96}$ as compared with un-hydrogenated Zr_3Al . As mentioned before, the addition of hydrogen into the $L1_2$ phase decreases the free energy difference between the $L1_2$ and the amorphous phase. This may account for the greatly reduced electron dose required for amorphization. In addition, point defect aggregation has not been observed during irradiation of the hydrogenated specimen, which is similar to all of the other intermetallic compounds which undergo electron irradiation induced crystal to glass transformation at a dose level of about 1 or 2 dpa[5].

In summary, we have studied the process of combined hydrogenation and subsequent 1-MeV electron irradiation of the ordered intermetallic compound Zr_3Al . Hydrogenation causes a more than 20 fold reduction of the critical dose required for complete amorphization. The combination of different processing techniques, such as hydrogenation and electron irradiation, may prove to be very useful in extending the range of metastable materials which can be synthesized by solid-state techniques.

This work was supported by the U. S. Department of Energy, Basic Energy Sciences-Materials Science, under contract No. W-31-109-Eng-38. We thank R. C. Birtcher and N. Q. Lam for helpful discussions, and B. J. Kestel for technical assistance.

REFERENCES

1. L. E. Rehn, P. R. Okamoto, J. Pearson, R. Bhadra, and M. Grimsditch, *Phys. Rev. Lett.* **59**, 2987 (1987).
2. P. R. Okamoto, L. E. Rehn, J. Pearson, R. Bhadra, and M. Grimsditch, *J. Less-Common Met.* **140**, 231 (1988).
3. W. J. Meng, P. R. Okamoto, L. J. Thompson, B. J. Kestel, and L. E. Rehn, *Appl. Phys. Lett.* **53**, 1820 (1988).
4. J. Koike, P. R. Okamoto, L. E. Rehn, and M. Meshii, submitted to *Met. Trans.* (1988).
5. D. E. Luzzi and M. Meshii, *Res Mechanica* **21**, 207 (1987).
6. B. J. Kestel, *Ultramicroscopy* **19**, 205 (1986).
7. O. S. Oen, *Cross Sections for Atomic Displacements in Solids by Fast Electrons*, ORNL-Rep. No. 4897 (1973).
8. W. J. Meng, P. R. Okamoto, B. J. Kestel, L. J. Thompson, and L. E. Rehn, submitted to *Phys. Rev. B* (1988).
9. P. G. Regnier, N. Q. Lam, and K. H. Westmacott, *J. Nucl. Mater.* **115**, 286 (1983).
10. J. W. Corbett, *Electron Radiation Damage in Semiconductors and Metals* (Academic Press, New York, 1966).
11. J. P. Biersack and L. G. Haggmark, *Nucl. Instrum. Methods* **174**, 257 (1980).

RADIATION INDUCED AMORPHIZATION IN YBa₂Cu₃O₇ AND GdBa₂Cu₃O₇ SUPERCONDUCTORS

DON M. PARKIN* AND MICHAEL NASTASI**

*Center for Materials Science, Los Alamos National Laboratory, Los Alamos, NM 87545.

**Materials Science and Technology Division, Los Alamos National Laboratory, Los Alamos, NM 87545

ABSTRACT

The response of YBa₂Cu₃O₇ and GdBa₂Cu₃O₇ high temperature superconductors to particle irradiation is examined. Both ion and electron irradiations have been shown to first produce an orthorhombic-to-tetragonal transformation at relatively low doses followed by a tetragonal-to-amorphous transformation at doses roughly a factor of 10 higher. Analysis of the displacement stoichiometry that results from 120, 300, and 1000 keV electron irradiations, 400, and 500 keV O irradiations, and 300 keV helium irradiations indicate that the orthorhombic-to-tetragonal transformation is driven by O atom displacements either alone or in the presence of metal atom displacements and that the transformation to the amorphous phase is driven by displacements on the Y, Gd or other rare earth atom site.

INTRODUCTION

Investigations of the response of the ceramic high temperature superconductors have shown them to have a very rich, diverse and complicated interaction with various radiation fields.¹ One specific effect is that after sufficient dose of 300 keV electrons,² 1 MeV electrons,³ 300 keV He ions,⁴ 400 keV O ions,⁵ and 500 keV O ions,⁶ an insulating amorphous phase is formed in YBa₂Cu₃O₇ and after 1 MeV electron irradiation in GdBa₂Cu₃O₇. This observation has technological importance in electronic device applications where it can be used to form devices such as a SQUID.⁶ In a more fundamental context, however, amorphization can be used to study both the crystal stability of these materials as well as how they interact with radiation.

In this paper we present a model of irradiation induced amorphization in YBa₂Cu₃O₇ and GdBa₂Cu₃O₇. It is shown that the amorphization process consists of two transformations. First, displacement produced disorder on the O sublattice transforms the orthorhombic structure to tetragonal. After further irradiation when sufficient numbers of Y or Gd atoms have been displaced, the defected tetragonal phase transforms to the amorphous phase.

CASCADE STOICHIOMETRY

The large mass difference among the O, Cu, Ba, Y, and Gd atoms in the YBa₂Cu₃O₇ and GdBa₂Cu₃O₇ superconductors has a strong effect on how particle irradiation couples to the material and starts the damage process. Mitchell et al.⁷ who irradiated YBa₂Cu₃O₇ and GdBa₂Cu₃O₇ with 120 keV electrons and Kirk et al.⁸ who irradiated YBa₂Cu₃O₇ with 131- and 152- keV electrons, both concluded that the displacement energy E_d was near 20 eV for O atoms. The maximum recoil energies of the metal atoms from direct electron collisions are 6 eV or less. Further, the observation of twin boundary motion^{7,8} is a direct indication of O displacement.

Under low energy electron irradiation, the cascade starts with only O displacements with the reasonable assumption that the metal atom displacement energies are equal to or greater than that for O. This is a situation

in which only one sublattice is involved in the displacement process. As we increase the electron energy, the cascade will start to evolve and include more of the atoms (sublattices). A convenient way to describe this process is to calculate the cascade stoichiometry defined as the relative number of displaced atoms of each atom type. The cascade stoichiometry can be written as $A_w B_x C_y D_z$ in the same manner as that for the material.

The average stoichiometry S per target atom is written as

$$S = \sum_i P_i \int_{T_1}^{T_m} \frac{d\sigma_i}{dT} S_i(T) dT \bigg/ \int_{T_1}^{T_m} \frac{d\sigma_i}{dT} dT, \quad (1)$$

where i is summed over the recoil atoms, in this case O, Cu, Ba, Y or Gd. P_i is the relative probability of producing a recoil of type i , $d\sigma_i/dT$ the differential scattering cross section, and $S_i(T)$ is the recoil energy dependent stoichiometry. Results for O recoils in $YBa_2Cu_3O_7$ and $GdBa_2Cu_3O_7$ from TRIM Monte Carlo simulations^{3,9} for recoil energies appropriate for 1 MeV electron irradiations are shown in Fig. 1. The data are presented for $E_d = 20$ eV and $E_d = 40$ eV for all atoms, respectively. The values of $S(T)$ are given by setting the value for Cu equal to 3. It can be clearly seen that in O cascades, the Cu and Ba displacements evolve in the same way in $YBa_2Cu_3O_7$ and $GdBa_2Cu_3O_7$, whereas, Y and Gd displacements are quite different. This is principally a kinematic effect due to their different masses. Calculated cascade stoichiometries for several irradiation conditions with $E_d = 20$ eV are given in Table I.

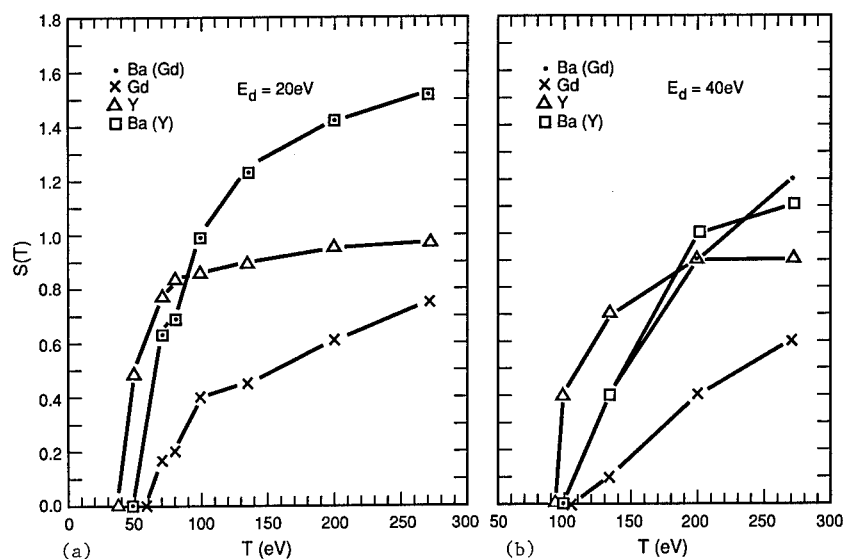


Fig. 1 Cascade stoichiometry for O recoils in $YBa_2Cu_3O_7$ and $GdBa_2Cu_3O_7$ based on TRIM calculations for energies appropriate for 1 MeV electrons. The data are for (a) $E_d = 20$ eV and (b) $E_d = 40$ eV for all atoms with $S(T)$ being determined by setting the value for Cu equal to 3.

Table I. Calculated Cascade Stoichiometry*

Particle	Energy	YBa ₂ Cu ₃ O ₇	GdBa ₂ Cu ₃ O ₇
electron	120 keV	Y ₀ Ba ₀ Cu ₀ O	GdBa ₀ Cu ₀ O
electron	300 keV	Y _{0.3} Ba _{0.1} Cu ₃ O ₇	Gd _{0.01} Ba _{0.1} Cu ₃ O ₇
electron	1 MeV	Y _{0.4} Ba _{0.3} Cu ₃ O ₇	Gd _{0.1} Ba _{0.3} Cu ₃ O ₇
helium	300 keV	YBa ₂ Cu ₃ O ₅	-
oxygen	400 keV	YB ₂ Cu ₃ O ₆	-
oxygen	500 keV	YB ₂ Cu ₃ O ₆	-

* $E_d = 20$ eV for all atoms

AMORPHIZATION MODEL

Mitchell et al.⁷ have shown that the loss of the twin structure under 120 keV electron irradiation at 90 K in YBa₂Cu₃O₇ and GdBa₂Cu₃O₇ is due to irradiation disordering of the O anions. This disordering produces an orthorhombic-to-tetragonal transformation. The "untwinning" process occurs extremely rapidly indicating that the transformation takes place when a critical amount of disorder is reached. The tetragonal structure forms displacively without long-range diffusion. Electron micrographs of 1 MeV electron irradiation of a grain boundary region in GdBa₂Cu₃O₇ after Nastasi et al.³ are shown in Fig. 2. In Fig. 2(a) the unirradiated grain boundary and twin structure are shown. In Fig. 2(b) the same region is shown after a dose of 2.5×10^{21} e/cm² (0.10 dpa) where the twins have faded, indicating the orthorhombic-to-tetragonal transformation. A similar transformation was observed by Egner et al.⁴ in YBa₂Cu₃O₇ after 300 keV He irradiation at a dose of 0.01 dpa.

The orthorhombic-to-tetragonal transformation is seen under 120 keV electron irradiation where only O atoms are displaced. It is also observed under 1 MeV electron irradiation where all atoms are displaced. The very heavy Y, Ba, and Gd atoms have cascade stoichiometry values of 0.4, 0.3, and 0.1 respectively (see Table I). These values are lower than the compositional ones which are 1, 2, and 1. The transformation is also seen under

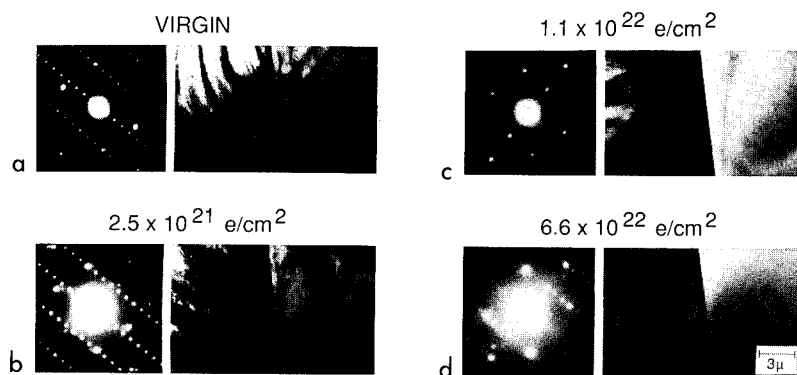


Fig. 2 Electron diffraction patterns and micrographs from a GdBa₂Cu₃O₇ grain boundary region (a) before electron irradiation, and (b) after an exposure to 2.5×10^{21} e/cm², (c) 1.1×10^{22} e/cm², and (d) 6.6×10^{22} e/cm².

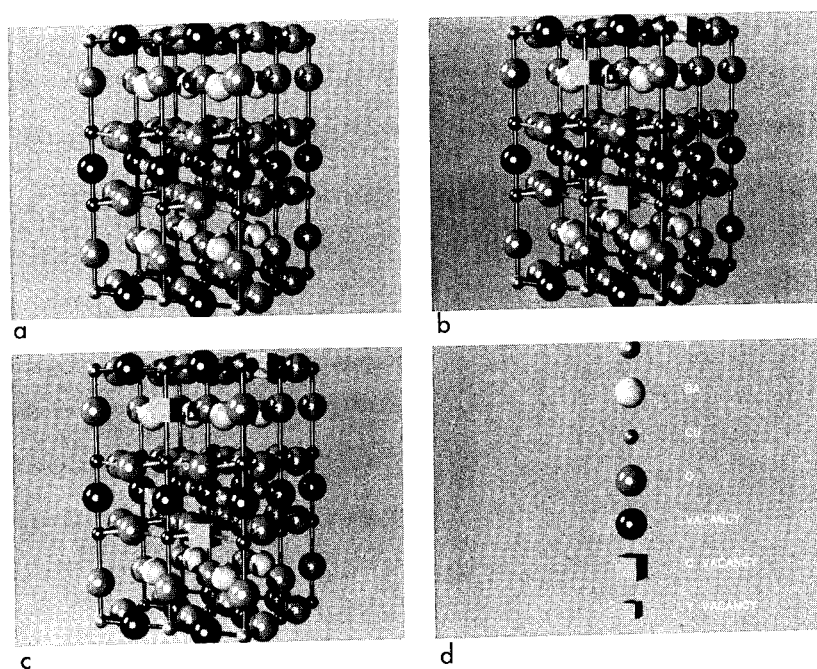


Fig. 3 Crystal structure of YBa₂Cu₃O₇. In (a) is the perfect structure, (b) illustrates O vacancies, (c) O vacancies and a Y vacancy, and in (d) is shown the legend identifying each atom or vacancy type.

300 keV He ion irradiation where the cascade stoichiometry is quite close to that of the material. These data show that O displacements alone are sufficient to drive the orthorhombic-to-tetragonal transformation. Under conditions where O and other atoms as well are displaced, the transformation also occurs and is likely driven primarily by the O displacements. This conclusion is illustrated in Fig. 3. In Fig. 3(a), we see the crystal structure of unirradiated YBa₂Cu₃O₇ with ordered O atoms and O vacancies. The sufficient condition for the orthorhombic-to-tetragonal transformation by producing O vacancies at normally occupied O sites is shown in Fig. 3(b) where O vacancies are indicated by the boxes.

Upon further irradiation the tetragonal phase transforms to an amorphous phase. This is illustrated in Figs. 2(c) and (d) for GdBa₂Cu₃O₇. At a dose of 1.1×10^{22} e/cm² (0.46 dpa) the material remains crystalline but is increasingly losing contrast. At a dose of 6.6×10^{22} e/cm² (2.77 dpa) the material becomes amorphous as indicated by the loss of contrast and the broad diffuse diffracted ring in Fig. 2(c). Observed amorphization doses for YBa₂Cu₃O₇ are ~ 0.1 dpa for 300 keV He ions,⁴ 500 keV O ions⁶ and 2 MeV He ions,¹⁰ and near 1 dpa for 1 MeV electrons.³ Amorphization occurs at a dose roughly 10 times that for the orthorhombic-to-tetragonal transformation.

Nastasi et al.³ compared in detail the amorphization of YBa₂Cu₃O₇ and GdBa₂Cu₃O₇ with 1 MeV electrons. In grain boundary regions they found the amorphization dose in YBa₂Cu₃O₇ to be between 1.7 - and 2.3×10^{22} e/cm² and in GdBa₂Cu₃O₇ to be between 4.1 - and 6.6×10^{22} e/cm². For large single grains the amorphization dose for YBa₂Cu₃O₇ was between 2.5 - and 3.1×10^{22} e/cm² and at a dose of 1.5×10^{23} e/cm² amorphization was not yet observed in GdBa₂Cu₃O₇. The amorphization doses for GdBa₂Cu₃O₇ are roughly between 3

and 5 times higher than those for $\text{YBa}_2\text{Cu}_3\text{O}_7$. As is shown in Table I, this factor of 3 to 5 is in good agreement with the difference between the cascade stoichiometry values for Y and Gd. All other values for Ba, Cu, and O are the same. They concluded that amorphous phase formation is dependent on displacement cascade stoichiometry and/or the number of displacements that occur at Y and Gd lattice sites.

We propose that displacements of the Y, Gd or other rare earth atom are a necessary condition for amorphization. This condition is illustrated in Fig. 3(c) where O vacancies (displacements) are shown along with a vacant (displaced) Y site. Displacements of the other metal atoms, Ba and Cu, also occur but they are not sufficient for amorphization. Amorphization then proceeds by a sequence of two sublattice specific displacement processes. First an orthorhombic-to-tetragonal transformation is driven by O atom displacements either alone or in the presence of metal atom displacements. At some higher dose, roughly an order of magnitude after the first transformation, the tetragonal phase transforms to an amorphous phase driven by the presence of displacements on the Y, Gd or other rare earth atom site.

We gratefully acknowledge the assistance of Melvin Prueitt (Los Alamos National Laboratory) for supplying the computer generated crystal structures. This work performed under the auspices of the U. S. Department of Energy.

References

1. For a review see D. M. Parkin, *Met. Trans.*, to be published.
2. G. J. Clark, A. D. Marwick, F. K. LeGoues, R. B. Laibowitz, R. Koch, and P. Madakson, *Nucl. Instrum. Methods B* **32**, 405 (1988).
3. M. Nastasi, D. M. Parkin, T. G. Zocco, J. Koike, and P. R. Okamoto, *Appl. Phys. Lett.* **53**, 1326 (1988).
4. B. Egner, J. Geerk, H. C. Li, G. Linker, O. Meyer, and B. Strehlau, *Jpn. J. Appl. Phys.* **26**, (Supp. 26-3), 2141 (1987).
5. K. Murakami, O. Eryer, K. Takita, and K. Masuda, *Jpn. J. Appl. Phys.* **26**, L1731 (1987).
6. G. J. Clark, F. K. LeGoues, A. D. Marwick, R. B. Laibowitz, and R. Koch, *Appl. Phys. Lett.* **51**, 1462 (1987).
7. T. E. Mitchell, T. Roy, R. B. Schwarz, J. F. Smith, and D. Wohlleben, *J. Electron Microsc. Tech.* **8**, 317 (1988).
8. M. A. Kirk, M. C. Baker, J. Z. Liu, D. J. Lam, and H. W. Weber, in High Temperature Superconductors, edited by M. B. Brodsky, R. C. Dynes, K. Kitazawa, and H. L. Tuller (Materials Research Society Proceedings **99**, Pittsburgh, PA 1988) pp. 209.
9. J. F. Ziegler, J. P. Biersack, and U. Littmark, The Stopping and Range of Ions in Solids, Vol. 1 of The Stopping and Ranges of Ions in Matter, edited by J. F. Zeigler (Permagon, New York, 1985).
10. G. C. Xiong, F. Weschenfelder, O. Meyer, G. Linker, H. C. Li, and J. Geerk, HTSCM²S-Interlaken, in press.

STRUCTURAL MODIFICATIONS INDUCED BY THE ELECTRONIC SLOWING DOWN OF SWIFT HEAVY IONS IN MATTER*

J.C. JOUSSET, E. BALANZAT, S. BOUFFARD and M. TOULEMONDE
Centre Interdisciplinaire de Recherches avec les Ions lourds, (CIRIL) (CEA-CNRS)
B.P. 5133, rue Claude Bloch, 14040 Caen Cédex, France

* Experiments performed at GANIL National Laboratory, Caen, France

In the last five years, the use of GeV heavy ions, such as those accelerated at GANIL, has lead to a breakthrough in the knowledge of the effects induced by the huge energy deposition which occurs during the slowing down of a swift heavy ion in matter.

The specific interest of GeV heavy ions comes from the fact that during ~ 0.9 of their large range ($\sim 100 \mu\text{m}$) the electronic stopping power dominates the elastic stopping power by a factor of 2.10^3 whatever the ion or the target. Moreover, the electronic stopping power is very large : a few $\text{keV}/\text{\AA}$. If we consider now how this energy spreads radially around the ion path, it can be assumed, as an order of magnitude, that a few tens of eV/atom are transmitted to the target electrons during 10^{-15}s in a cylindrical volume containing some tens of atomic units (1-4). This situation is quite unusual, compared to the case either of the displacement cascades, where the energy is transmitted by elastic events to the target atoms, or of the short powerful laser pulses irradiations where the energy transmitted to the target electrons is lower. This unusual situation constitutes the very interest of swift heavy ions irradiation experiments.

As previously discussed [5], it has to be underlined that the duration of the electronic interactions is much shorter, by two or three orders of magnitude, compared to the target atomic vibration period. The main questions to be answered are : how is this high energy transmitted to the target electrons, either by direct ionization or excitation, relaxed in the atomic (or molecular) structure of the irradiated solid ? Or, more precisely, how can the high density electronic excitation created in the wake of the ion-projectile be converted in atomic motion leading to induced stable lattice defects or phase modifications ? None of the models which have been so far proposed are really able to account for the whole of the observed effects. To give only one example : the well known Coulombian explosion spike model [6] which may account for the latent tracks induced by heavy ions in some insulators is completely unable to explain any of the effects of atomic mobility induced by electronic stopping power in bulk metallic materials [7-11].

Numerous experimental results have been obtained at GANIL for many different types of target : magnetic oxides, polymers, ionic crystals, semi-conductors, organic conductors, metallic conductors and high Tc superconductors. We shall present hereafter only two typical results for i) an insulator : a magnetic oxide, the yttrium iron garnet, ii) a metallic conductor, the amorphous $\text{Fe}_{85}\text{B}_{15}$ alloy.

IRRADIATION FACILITY

The experiments are performed in the IRABAT facility set up by CIRIL at Caen. The main characteristics of IRABAT are :

- i) the ion beam is swept uniformly on surfaces of $30 \times 30 \text{ mm}^2$, the fluence is continuously measured all along the irradiation and known at better than 10% .
- ii) the irradiation temperature is controlled from 6 K up to 600 K for ion fluxes around $10^9 \text{ i/cm}^2\text{s}$ without any warming up superior to a few degrees.
- iii) measurements of parameters like electrical resistivity, magnetic hysteresis loops, [12] Hall effect [13] can be performed in situ at low temperature all along the irradiation.

RESULTS AND DISCUSSION

Insulators

Only the typical case of the magnetic oxide yttrium iron garnet $\text{Y}_3\text{Fe}_5\text{O}_{12}$ will be presented here. The study of such a material is particularly convenient for our purpose since this oxide is completely insensitive to individual electronic excitation (electron or γ irradiation for

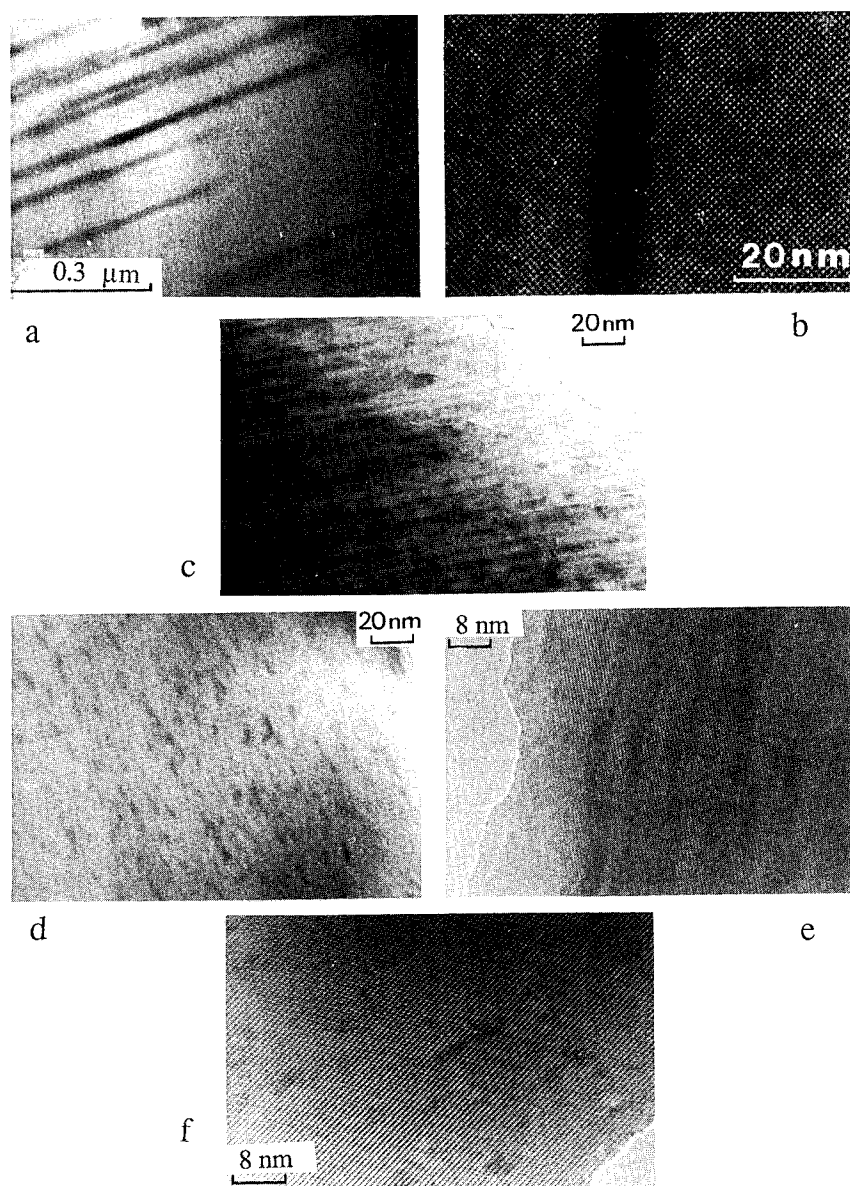


Figure 1 - (By courtesy of F. STUDER [19] and C. HOUPERT [21]). TEM observations of the relationship between the value of dE/dx and the morphology of induced latent defects.

Domain (see text)	dE/dx MeV/ μm	Figure	Morphology
①	25	a, b	continuous cylinder
②	11	c	discontinuous
	8.5	d, e	cylinder
③	6.6	f	spheroidal

example). As a contrary, the first experiments have evidenced an important effect of the high density electronic excitations [14-17]. This effect consists of a disorder observable by a decrease in the saturation magnetization and clearly related to the electronic stopping power dE/dx and not to the atomic elastic displacements [17]. Mössbauer spectrometry experiments have verified [18] that a paramagnetic phase is induced and permitted to measure the variation of the fraction F of this disordered phase with dE/dx .

Two observations have been made : i) the disordered phase appears above a threshold value for dE/dx , ii) two rates are observable in the variation of F vs dE/dx . The detailed analysis of many Mössbauer spectra has clearly shown that the hyperfine magnetic field becomes parallel to the induced latent tracks for the high values of the electronic stopping power dE/dx .

As a contrary for lower values of dE/dx the isotropic orientation of the hyperfine magnetic field of a sintered sample is kept while the anisotropic orientation of the hyperfine magnetic field of a single crystal is lost [18]. These observations suggest that by decreasing dE/dx , the shape of the defects goes from a cylindrical symmetry to a spherical one. These observations have been verified by medium and high resolution electronic microscopy in order to study systematically the defect morphology [19-21] (Figure 1).

The results are the following : three domains in the values of dE/dx can be distinguished.

① *high values, namely $> 17 \text{ MeV}/\mu\text{m}$* . - Figure 1a and 1b -

The latent ion track is made of a continuous damage cylinder whose radius can be easily measured and compared with Mössbauer results as well as Rutherford backscattering measurements [19]. The radius increases with dE/dx . This continuous cylinder induces a crystalline stressed shell around the amorphous track [19, 20] where the hyperfine magnetic field becomes aligned with the direction of the track as it is observed by Mössbauer spectrometry.

② *intermediate values, $8 \text{ MeV}/\mu\text{m} - 17 \text{ MeV}/\mu\text{m}$* - Figure 1c, 1d and 1e -

The latent track is made of discontinuous cylinders [20]. The hyperfine magnetic field remains parallel to the track.

③ *low values $< 8 \text{ MeV}/\mu\text{m}$* - Figure 1f -

Then the latent track is made of isolated extended defects with a spheroidal shape. The hyperfine magnetic field becomes isotropic since the stressed shell around the defect has a spheroidal shape. It is not known below which value of dE/dx the effects induced by the elastic collisions become predominant [15].

The doses which have to be deposited in a sample in order to induce a paramagnetic fraction of 50 % are very different in each of the three domains ①, ② and ③. They are 12 MGy, 21 MGy, 120 MGy and 1 000 MGy for $42 \text{ MeV}/\mu\text{m}$ (domain ①), $17 \text{ MeV}/\mu\text{m}$ ①, $8 \text{ MeV}/\mu\text{m}$ ② and $4 \text{ MeV}/\mu\text{m}$ ③ respectively.

This description of the ion induced latent tracks in garnet, over a large range of dE/dx , can be compared to previous data obtained in mica. The present results are in good agreement with the damage description of DARTYGE [22,23] for the domain ② and ③ as well as with the continuous cylindrical track description of ALBRECHT [24,25] for the domain ①.

Metallic conductor - amorphous $\text{Fe}_{85}\text{B}_{15}$

Among the recently observed effects induced in metallic conductors by electronic energy losses such as annealing of pre-existing lattice defects [9] [10], the effects on amorphous metallic alloys are certainly the most striking .

Since the pioneer experiments of D. LESUEUR [7]. It is known, that electronic energy losses induce important structural modifications in amorphous metallic alloys. KLAUMUNZER has clearly demonstrated that a large anisotropic deformation [26], presumably without volume change [27], is created by high energy heavy ions irradiation : the sample dimensions perpendicular to the ion beam increase while the dimension parallel to it shrinks.

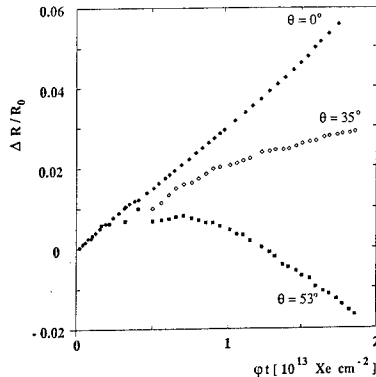
This *growth phenomenon* has been observed for numerous amorphous metallic alloys as well as oxide glasses [28].

Making use of the experimental features of the IRABAT facility, it is possible to follow, all along the irradiation experiment, the induced variations of the electrical resistance. This parameter is, in this case, particularly convenient since it allows observation of both the electrical resistivity (i.e. intrinsic modifications of the alloys structure) and the shape factor (i.e. the growth phenomenon itself) with high accuracy. Indeed, as the anisotropy of the effect is related to the beam direction, by varying the angle of incidence of the beam with respect to the sample, we can separate the resistivity and the shape factor effects. The samples are ribbons (20 mm long, 1 mm wide, 21 μm thick) prepared by melt spinning. The electrical resistance is measured along the length. In these experimental conditions, one has a very simple relation :

$$\frac{\Delta R}{R} = \Delta\rho/\rho + 2\Delta_{\perp}(1 - 3\sin^2\theta) \quad (1) \quad \text{with } \Delta_{\perp} = \frac{\Delta L}{L} \text{ (for } \theta = 0)$$

where R is the electrical resistance, ρ the electrical resistivity, θ the angle between the incident ion beam and the normal to the sample following its length L .

The results obtained [11] [29,30] with this method have shown i) a clear effect of the angle θ at high fluences (Figure 2) which confirms the growth description model of KLAUMUNZER, ii) more surprisingly, at low fluences, no effect of θ . Following the relation (1) it is clear that, at low fluences such an effect is related to a variation of the electrical resistivity. The initial slope of $\Delta\rho/\rho$ vs ϕt represents consequently the variation of $\Delta\rho/\rho$ with ϕt .



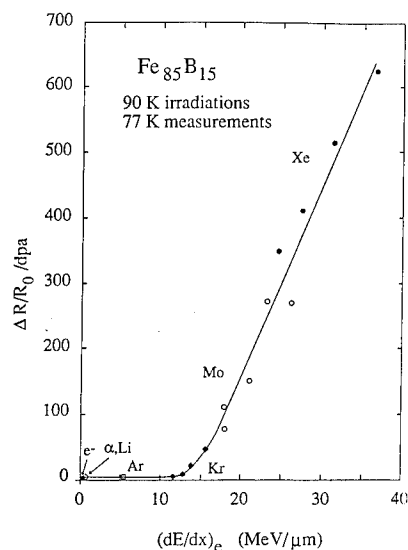
To distinguish the effects induced by elastic collisions between the ion and the target atoms from those induced by the electronic energy losses, the following plot has been

made : on y-axis, the initial slope of $\frac{\Delta R}{R}$ vs ϕt divided by the calculated number of displaced atoms by elastic collisions (dpa) ; on x axis, the value of the electronic energy losses for various different ions from Ar to Xe. If the $\Delta\rho/\rho$ induced effect is only due to elastic collisions events, the curve must be an horizontal line.

Figure 2 - Variation of the relative increase of electrical resistance of irradiated $\text{Fe}_{85}\text{B}_{15}$ amorphous alloy for three angles of incidence of the ion beam.

Figure 3 clearly shows a non linear behaviour. Above a threshold value of 13 $\text{MeV}/\mu\text{m}$ the electrical resistivity relative variation increases sharply. At 40 $\text{MeV}/\mu\text{m}$ the electronic energy losses induce, in this metallic alloy, an effect which is by two orders of magnitude higher than the effects due to elastic collisions.

This effect on the electrical resistivity has been interpreted [11] as due to the creation of defects by the electronic energy losses. Since the experiments of AUDOUARD [31 - 33] it is indeed assumed that defects (in the short range order of the amorphous alloy) can be created by electrons or light ions irradiations - i.e. elastic collisions, in amorphous metallic alloys, defects which behave like Frenkel pairs in crystalline metals. The observed increase of $\Delta\rho/\rho$, related to the creation of these defects saturates at around 2 to 6 % as in the heavy ions experiments [29]. The annealing behaviour of the irradiation sample is also similar after electron or heavy ion experiments [29].



The elementary processes which induce such atomic displacements are, so far, not yet understood. It is clear anyhow that any interpretation must take into account : i) the existence of a huge collective excitation in the wake of the incoming ion ii) the experimental fact that this effect (as well as the growth effect) has been observed only with amorphous state i.e. in materials where, due to the presence of free volume, many different atomic configurations are possible for the defects.

Figure 3 -Variation of the initial slope of $\Delta R/R_0$ per dpa (i.e. initial increase of $\Delta \rho/\rho$) vs the electronic stopping power. α, Li are ^{10}B fission fragments.

CONCLUSION

In materials which are not sensitive to single localized electronic excitations, it is demonstrated that above a threshold value of the electronic stopping power an important damage is induced

In insulating magnetic oxides, a highly disordered paramagnetic phase is created along the ion path. Different damage yields have been put in evidence which correspond to changes in the morphology of the induced defects.

In amorphous metallic alloys, above a threshold value, the electronic energy losses induce a damage two orders of magnitude higher than the elastic collisions. A two step process is observed in the damage production : at low fluences defects in the short range order are created while at high fluences, sample growth appears.

REFERENCES

- [1] E.J. KOBETICH and R. KATZ
Phys. Rev. 170 (1968) 391
- [2] J. FAIN, M. MONIN and M. MONTRET
Radiat. Res. 57 (1974) 379
- [3] R.N. HAMM, J.E. TURNER, R.H. RICHTIE and H.A. WRIGHT
Radiat. Res. 104 (1985) S-20
- [4] M.P.R. WALIGORSKI, R.N. HAMM and R. KATZ
Nucl. Tracks Radiat. Meas. 11 (1986) 309
- [5] E. BALANZAT, J.C. JOUSSET and M. TOULEMONDE
Nucl. Inst. and Meth. B 32 (1988) 368
(Proceedings of 4th REI Conference Lyon 1987)
- [6] R.L. FLEISCHER
Prog. Mat. Sci. X (1981) 97[7]
- [7] D. LESUEUR
Rad. Effects 24 (1975) 201
- [8] S. KLAUMUNZER, MING-DONG HOU, G. SCHUMACHER and LI CHANG-LIN
Mat. Res. Soc. Symp. Proc 93, (1987) 21
(Proc. MRS Spring meeting Los Angeles, USA, 1987)

- [9] A. DUNLOP, D. LESUEUR, G. JASKIEROWICZ and J. SCHILDKNECHT
Submitted to Nucl. Inst. and Meth. B
- [10] A. IWASE, S. SAGAKI, I. IWATA and T. NIHIRA
Phys. Rev. Lett. 28 (1987) 2450
- [11] A. AUDOUARD, E. BALANZAT, G. FUCHS, J.C. JOUSSET, D. LESUEUR and L. THOME
Europhysics Lett. 3 (1987) 327
- [12] R. STEPHAN, J. PROVOST, A. MAIGNAN, J. DURAL, D. GROULT, J.C. JOUSSET and B. RAVEAU
Rev. Phys. Appl. 23 (1988) 873
- [13] J. FAVRE, C. BLANCHARD and M. TOULEMONDE
Private communication
- [14] D. GROULT, M. HERVIEU, N. NGUYEN, B. RAVEAU, G. FUCHS and E. BALANZAT
Rad. Eff. 90 (1985) 19
- [15] P. HANSEN, H. HEITMAN and P.M. SMIT
Phys. Rev. B 26 (1982) 3539
- [16] G. FUCHS, F. STUDER, E. BALANZAT, D. GROULT, J.C. JOUSSET and B. RAVEAU
Nucl. Inst. Meth. B 12, (1985) 471
- [17] G. FUCHS, F. STUDER, E. BALANZAT, D. GROULT, M. TOULEMONDE and J.C. JOUSSET
Europhysics Lett. 3 (1987) 3
- [18] M. TOULEMONDE, G. FUCHS, N. NGUYEN, F. STUDER and D. GROULT
Phys. Rev. B 35 (1987) 6560
- [19] M. TOULEMONDE and F. STUDER
Phil. Mag. to be published
- [20] D. GROULT, M. HERVIEU, N. NGUYEN and B. RAVEAU
J. of Sol. Stat. Chem. to be published
- [21] C. HOUPERT
to be published in Nucl. Inst. Meth. B (1988)
proceedings of the IBMM Conference Tokyo 1988
- [22] E. DARTYGE, M. LAMBERT and M. MAURETTE
J. de Phys. 37 (1976) 939
- [23] E. DARTYGE, J.P. DURAUD, Y. LANGEVIN and M. MAURETTE
Phys. Rev. B 23 (1981) 5213
- [24] D. ALBRECHT, P. ARMBRUSTER, R. SPOHR, M. ROTH, K. SCHAUPERT, H. STUHRMANN
Appl. Phys. A 37, (1985) 37
- [25] D. ALBRECHT, E. BALANZAT and K. SCHAUPERT
Nucl. Track Radiat. Meas. 11 (1986) 93
- [26] S. KLAUMUNZER and G. SCHUMACHER
Phys. Rev. Lett. 51 (1983) 1987
- [27] S. KLAUMUNZER, MING-DONG HOU and G. SCHUMACHER
Phys. Rev. Lett. 57 (1986) 850
- [28] S. KLAUMUNZER, CHANG-LIN LI and G. SCHUMACHER
Appl. Phys. Lett. 51 (1987) 97
- [29] A. AUDOUARD, E. BALANZAT, G. FUCHS, J.C. JOUSSET, D. LESUEUR and L. THOME
Eur. Phys. Lett. 5 (1988) 241
- [30] A. AUDOUARD, E. BALANZAT, G. FUCHS, J.C. JOUSSET, D. LESUEUR and L. THOME
Accepted for publication in Nucl. Inst. and Meth. B (1988)
- [31] A. AUDOUARD, J. BALOGH, J. DURAL and J.C. JOUSSET
J. Non Cryst. Sol. 50 (1982) 71 and
Radiat. Eff. 62 (1982) 161
- [32] A. AUDOUARD and J.C. JOUSSET
J. Phys. (Paris) Colloq. 9 (1982) 423
- [33] A. AUDOUARD, A. BENYAGOUR, L. THOME and J. CHAUMONT
J. Phys. F 15 (1985) 1237

MICROSTRUCTURAL CHARACTERIZATION OF Al_2O_3 FOLLOWING SIMULTANEOUS TRIPLE ION BOMBARDMENT

S. J. ZINKLE*

*Oak Ridge National Laboratory, P.O. Box 2008, Oak Ridge, TN 37831-6376 USA

ABSTRACT

The through-range microstructure of polycrystalline alumina has been examined by cross-section TEM following simultaneous implantation of 2.0 MeV Al^+ , 1.44 MeV O^+ , and 0.2 to 0.4 MeV He^+ ions at room temperature to a dose of 3.1 keV/atom. The specimen remained crystalline following the irradiation, and four distinct radiation-induced defect features were observed: Network dislocations, dislocation loops, small cavities, and oblong clusters that may be aluminum colloids. The microstructure near the implanted ion region was qualitatively similar to that observed in irradiated regions far from the implanted zone.

INTRODUCTION

Ion implantation of ceramics such as Al_2O_3 has received a considerable amount of attention in recent years [1-3]. Ion implantation is being studied as a means for improving properties such as wear resistance and fracture toughness near the surface of ceramics, and is also convenient for fusion reactor radiation effects studies. Most of the emphasis has been directed toward determining conditions that produce amorphization. The specimen temperature and chemical species of the implanted ion are recognized to be important experimental parameters for producing the amorphous state. Implantations conducted near or above room temperature often do not cause Al_2O_3 to become amorphous, whereas implantation at liquid nitrogen temperatures can produce amorphous alumina for damage energies of less than 1 keV/atom [1,3]. It has been reported that alumina implanted at room temperature can be amorphized by Zr ions for damage levels >5 keV/atom, whereas implantation to similar doses with any of 13 other ions did not produce the amorphous state [1]. On the other hand, some studies suggest that alumina may be amorphized at room temperature by several different ion species for damage levels of about 5 keV/atom [2,4].

The microstructure of alumina irradiated at room temperature is examined in this study in an attempt to gain some understanding of the microstructural changes induced by implantation. Ion irradiation studies in metals have established that injected ions can have a large influence on the resultant microstructure [5]. Therefore, cross-sectional analysis techniques were used to examine the depth dependence of the irradiated region. High energy ions were employed so that the implanted ion region could be distinctly separated from regions where only displacement damage occurred. The chemical effects associated with the implanted ions were minimized by simultaneous implantation of Al^+ and O^+ ions in a nearly stoichiometric ratio. Helium was also injected during the irradiation in order to study the effects of gas on microstructural development.

EXPERIMENTAL PROCEDURE

Polycrystalline alumina specimens (grain size = 30 μm) were irradiated as mechanically polished transmission electron microscope disks in a 9-specimen array. The irradiations were performed at room temperature using the Van de Graaff accelerator facility at Oak Ridge National Laboratory,

which was recently modified to allow simultaneous irradiation with three different ion beams [6]. The specimens were irradiated with simultaneous beams of 2.0 MeV Al^+ , 1.44 MeV O^+ , and 0.2 to 0.4 MeV He^+ ions. The energies of the Al^+ and O^+ ions were chosen so that the calculated implantation depth for both species in Al_2O_3 was 1200 nm. The fluences for the Al^+ and O^+ beams were about 6.9×10^{20} and $8.3 \times 10^{20}/\text{m}^2$, respectively, which produced an excess of Al^+ ions relative to the stoichiometric ratio. The irradiation produced a calculated damage energy density of 3.1 keV/atom in the peak damage region (1100 nm depth). The energy of the helium ion beam was continuously ramped between 0.2 and 0.4 MeV during the irradiation in order to produce a uniform concentration (1100 appm) of He from the near-surface region to a depth of 1000 nm. The displacement damage associated with the He implantation was $\ll 0.1$ keV/atom.

The microstructure of the irradiated region was examined in cross-section using standard specimen preparation techniques that involved dimpling and ion milling of glued specimens. The depth dependence of the radiation damage was investigated by comparing the microstructure in regions centered around a depth of 700 nm from the original implanted surface ("midrange") with the microstructure observed at depths of 1000 to 1500 nm ("peak").

RESULTS

The ion irradiation produced small defect clusters and dislocations. All regions of the specimen were observed to remain crystalline following the irradiation. The general depth-dependent microstructure is shown in Fig. 1. A dark band centered at the mean implantation depth of the Al^+ and O^+ ions (1200 nm) is evident. However, the defect microstructures observed in the midrange and peak damage regions were found to be qualitatively identical. The dark band was most prominent under strong two-beam conditions where transmission of the electron beam in the undamaged crystal was maximized. This suggests that the band is associated with lattice strain effects from the high concentration of implanted ions.

Comparisons between the midrange and peak damage microstructures to date have failed to detect any significant difference between these regions. The figures shown in the remainder of this paper are all taken from the peak damage region, where the most extensive analysis has been performed. The various microstructural features identified in the peak damage region have also been observed in the midrange region. However, a detailed quantitative comparison between these regions has not yet been completed.

The dominant microstructural feature associated with the irradiation was the formation of a high density of dislocations, as shown in Fig. 2. These dislocations were most easily viewed under strong- or weak-beam dark field conditions. A Burgers vector analysis revealed that there were a mixture of dislocation types. Figure 3 shows part of a series of

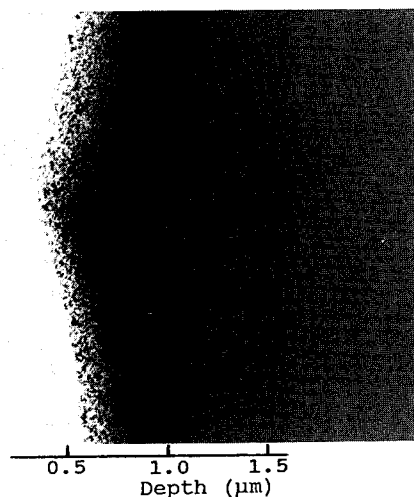


Fig. 1. Depth-dependent microstructure of irradiated alumina.

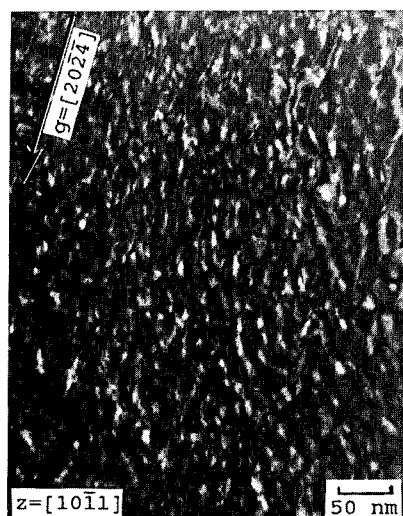


Fig. 2. Weak beam ($g,3g$) microstructure of irradiated alumina showing network dislocations.

different diffraction contrast conditions that were used to analyze the dislocations. The array of dislocations that are visible in the left panel of Fig. 3 (nearly aligned along the diffraction vector) are out of contrast in the center panel, where $g = [12\bar{1}0]$. These dislocations were visible in the right panel, where $g = [0\bar{2}22]$. This indicates that the Burgers vector of these dislocations is along $[0001]$ and suggests that they are perfect dislocations with $b = 1/3[0001]$. Other dislocations (such as those visible in the center panel of Fig. 3) were identified to have Burgers vectors in $\langle 10\bar{1}1 \rangle$ directions. Previous studies of alumina irradiated at elevated temperatures [7,8] have identified network dislocations with Burgers vectors of $b = 1/3\langle 10\bar{1}1 \rangle$ and $b = 1/3\langle 11\bar{2}0 \rangle$. The development of the network dislocations is the result of interactions between unfaulted loops, $b = 1/3\langle 10\bar{1}1 \rangle$, lying on either the basal or prism habit planes [7,8]. Lee et al. [8] also suggested that a small fraction of the dislocation network observed in ion-irradiated

alumina had $b = 1/3[0001]$. However, they did not observe any network dislocation formation for irradiation temperatures below 600°C .

In the present case, it appears that the dominant component of the dislocation network has $b = 1/3[0001]$. This suggests that the mechanism for the formation of the dislocation network in alumina irradiated at room temperature is different from the high temperature mechanism outlined in the literature.

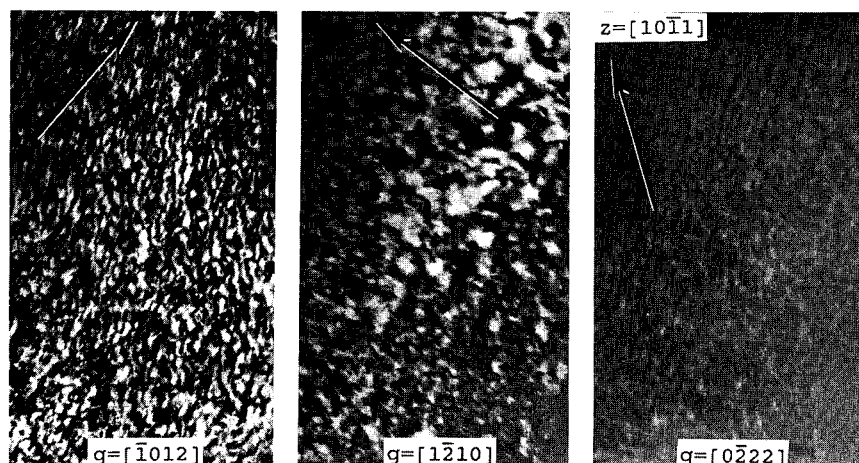


Fig. 3. Part of a series of micrographs used to determine the Burgers vectors of network dislocations in alumina. Centered dark field images.

A second structural feature associated with the ion implantation was the presence of small cavities, as shown in Fig. 4. It is likely that the development of these cavities is assisted by the coimplantation of helium during the irradiation. The mean cavity diameter was about 2 nm.

A low density of defect clusters that exhibited contrast expected for dislocation loops was observed under certain diffraction conditions. Figure 5 shows the weak beam microstructure where some of the suspected loops are visible. The size of these defect clusters ranged up to 20 nm in diameter. Tilting experiments suggested that the clusters resided on (0001) and $\{10\bar{1}0\}$ habit planes, which is in agreement with loop observations from previous studies [7,8].

Some aligned streaks were observed in the microstructure under a variety of diffracting conditions, with the direction of the streaks generally coinciding with the diffraction vector. Figure 6 shows an example of this streaking that was observed for various diffraction vectors near the [0001] zone axis. A closer inspection of the microstructure revealed that the individual streaks were invariably associated with a defect cluster that exhibited weak contrast under most imaging conditions. These clusters did not exhibit the contrast expected for voids or gas bubbles (i.e., their visibility remained poor even for underfocused kinematical conditions). Furthermore, the contrast did not agree with that expected for loops. The size of these clusters ranged from 10 to 30 nm.

Figure 7 shows an example of these clusters taken with imaging conditions where they appear dark-diffracting in the bright field image. It is possible that these clusters are aluminum colloids which have been identified in studies of alumina irradiated at elevated temperatures [9,10]. The formation of aluminum colloids in the peak damage region is plausible since the Al^{+}/O^{+}

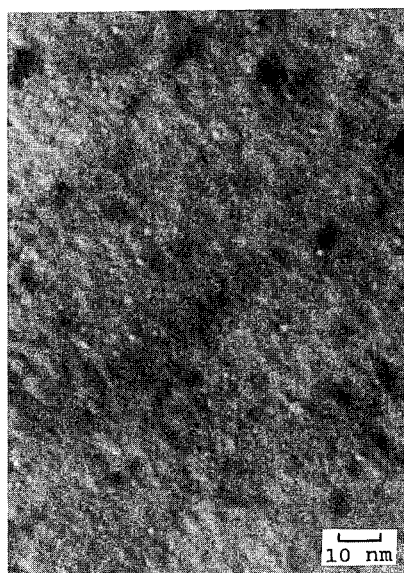


Fig. 4. Cavity formation in irradiated alumina.

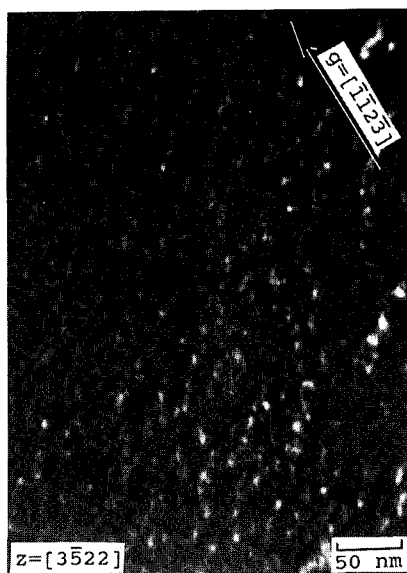


Fig. 5. Weak beam (g,2g) microstructure showing the presence of small loops on different habit planes.

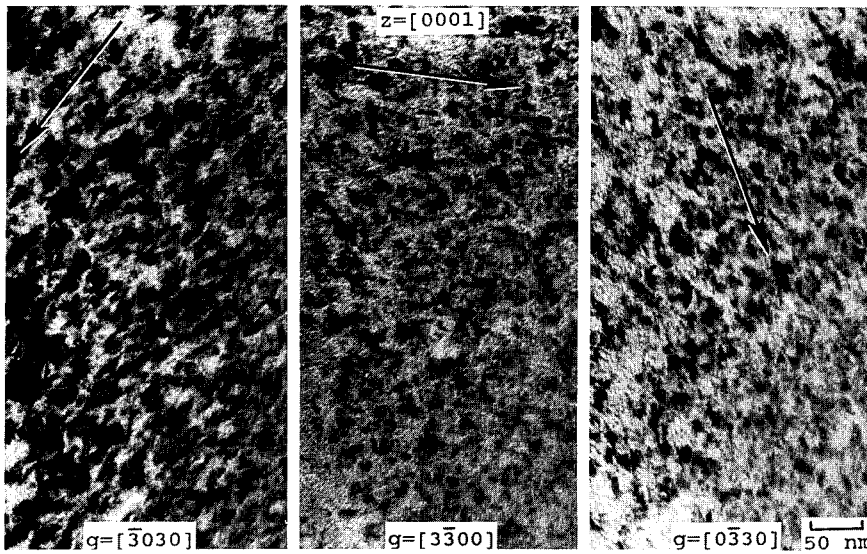


Fig. 6. Bright field images showing the tendency for contrast observed in the foil to be aligned in the direction of the diffraction vector.

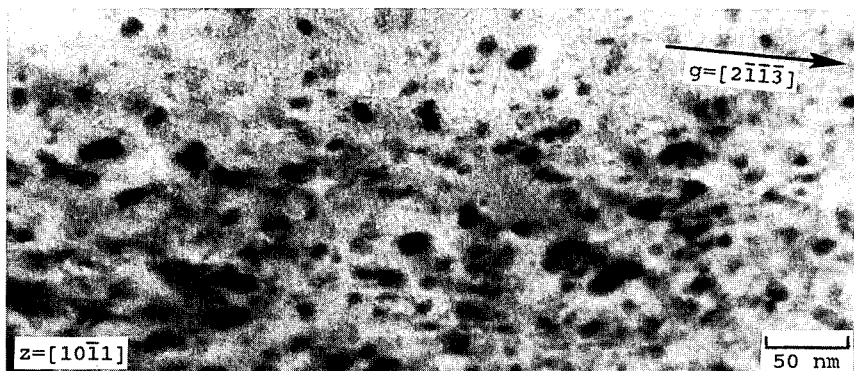


Fig. 7. Unidentified defect clusters observed near the peak damage region in irradiated alumina.

implantation ratio of 0.83 produced an excess of Al^+ ions relative to the stoichiometric ratio. These defect clusters are visible when imaging is performed with $g = [0006]$ near the zone axis of $[1\bar{1}00]$, which is consistent with the observations of Shikama and Pells [9]. However, the contrast associated with these clusters is generally much weaker than that observed for colloids formed by high temperature irradiation.

DISCUSSION

The microstructural features observed in the midrange and peak damage regions were qualitatively similar. This indicates that the Al^{+} and O^{+} ions implanted at room temperature have a small effect on the resultant microstructure of alumina. Specimens irradiated at 923 K showed a similar weak depth dependence [11].

The dislocation network observed in this study suggests an explanation for the resistance of alumina to amorphization during room temperature implantation. The low density of dislocation loops and high network dislocation density suggest that loops formed in alumina during room temperature irradiation are somehow able to interact with one another to form a dislocation network. Point defects produced by the irradiation may then be absorbed at these dislocations, which act as unsaturable sinks through a process of dislocation climb [7]. This prevents the buildup of residual displacement damage defects to the critical level needed for amorphization to occur. It may be speculated that amorphization will occur under conditions where the dislocation climb mechanism is inoperative. Irradiation at low temperatures reduces the point defect mobility so that dislocation loop growth and interaction may be impeded. Implantation of ions which react chemically with alumina may similarly restrict the mobility of point defects and dislocation loops. There is evidence that amorphization of alumina by Zr^{+} ions occurs only when the matrix Zr concentration exceeds a certain level [12].

SUMMARY

Ion implantation of alumina at room temperature with simultaneous beams of Al^{+} , O^{+} , and He^{+} did not produce amorphization for doses up to 3.1 keV/atom. Network dislocations with Burgers vectors along [0001] were identified. A low density of dislocation loops lying on (0001) and {1010} planes were observed, along with cavities and unidentified defect clusters that may be aluminum colloids.

This research was sponsored by the Office of Fusion Energy, U.S. Department of Energy, under contract DE-AC05-84OR21400 with the Martin Marietta Energy Systems, Inc.

REFERENCES

1. C.J. McHargue et al., *J. Materials for Energy Systems*, **8**, 255 (1986).
2. P.J. Burnett and T.F. Page, *Rad. Effects* **97**, 123 (1986).
3. S. Kobayashi, T. Hioki and O. Kamigaito, *Proc. XIth Int. Cong. on Electron Microscopy* (Kyoto, 1986), p. 1303.
4. T. Hioki et al., *Nucl. Instrum. Methods B* **7/8**, 521 (1985).
5. F.A. Garner, *J. Nucl. Mater.* **117**, 177 (1983).
6. M.B. Lewis et al., submitted to *Nucl. Instrum. Methods B* (1988).
7. F.W. Clinard, Jr., G.F. Hurley, and L.W. Hobbs, *J. Nucl. Mater.* **108&109**, 655 (1982).
8. W.E. Lee, M.L. Jenkins and G.P. Pells, *Phil. Mag. A* **51**, 639 (1985).
9. T. Shikama and G.P. Pells, *Phil. Mag. A* **47**, 369 (1983).
10. Y. Katano, H. Ohno and H. Katsuta, *J. Nucl. Mater.* **155-157**, 366 (1988).
11. S.J. Zinkle, *NATO-Adv. Study Inst. on Structure-Property Relationships in Surface Modified Ceramics*, edited by C.J. McHargue et al. (Kluwer Academic Publishers, 1988).
12. P. Angelini, P.S. Sklad, C.J. McHargue, M.B. Lewis, and G.C. Farlow, these Proceedings.

MICROSTRUCTURES IN SiC AND Si₃N₄ IMPLANTED WITH Ti AND HEAT TREATED

R. G. Vardiman
Naval Research Laboratory
Washington, DC 20375-5000 USA

ABSTRACT

Bulk SiC and Si₃N₄ have been implanted with Ti at room temperature, and subsequently vacuum heat treated between 800° and 1100°C. All specimens were backthinned by ion milling and examined in TEM. SiC becomes amorphous on implantation, and develops a fine dispersion of TiC precipitates up to 800°C. At 900°C recrystallization has begun, possibly nucleated by the TiC particles. Si₃N₄ shows fine TiN particles in an amorphous matrix even as implanted. This structure is retained up to 900°C. At 1000°C, regrowth of the Si₃N₄ apparently from the substrate begins, and the TiN particles also grow as large as 200nm.

INTRODUCTION

Considerable interest has developed in recent years in the use of silicon carbide and silicon nitride as structural materials, particularly for high temperature applications. Although these materials possess many attractive properties, it has been felt desirable to improve their friction and wear behavior, as well as their propensity for surface cracking. To this end a number of studies [1-15] have explored the effect of ion implantation on the microstructure and mechanical properties of Si and Si₃N₄.

Much more extensive work has been done on SiC than on Si₃N₄. It has been found that SiC is made amorphous by relatively low ion doses [1-10]. This effect appears to depend on the buildup of damage in the implanted layer [3,8], and is not strongly dependent on the type of ion (aside from the varying efficiency of different ions in creating damage). Si₃N₄ is expected to be comparably easy to amorphize. Surface mechanical properties are distinctly altered in the implanted amorphized material [4,6,11-14].

A number of studies have looked at the recrystallization behavior of ion amorphized SiC [1,5,10,15], with no good agreement found on the recrystallization temperature, which varied from 750°C to 1500°C or higher. In most cases Rutherford backscattering-channelling (RBS-C) was used to determine the occurrence of recrystallization, with some use of Raman scattering and transmission electron microscopy (TEM). Recrystallization temperatures determined by different techniques in the same study were found to differ substantially [10]. No work on recrystallization of ion amorphized Si₃N₄ has been found in the literature.

The present study was primarily undertaken with the hope of developing a unique surface microstructure—a dispersion of TiN or TiC precipitates in an amorphous matrix. This has indeed been found. Determination has also been made of the approximate recrystallization temperature for both materials.

EXPERIMENTAL METHODS

The silicon carbide used here was sintered high density α -phase, the so-called 6H hexagonal polytype. The silicon nitride was hot pressed NC132 α -Si₃N₄, also with a hexagonal crystal structure, with about 1% impurities, principally MgO. Both materials had no observable porosity. Initial grain size was approximately 10 μ m for the SiC and 1 μ m for the Si₃N₄.

All implants were for a dose of 2×10^{17} at/cm² at an energy of 175 keV. The range of titanium ions in both materials is approximately 100 nm and the theoretical maximum concentration is nearly 26 at pct. Implanted surfaces were polished with 0.5 μ m alumina, and beam current was adjusted to keep the specimen temperature during implantation to approximately 50°C.

3 mm discs about 100 μ m thick were used for implantation, and subsequently dimpled on the unimplanted side, masked on the implanted side with a silicone compound, and ion milled to perforation.

Heat treatments were performed for one hour in vacuum, with the vacuum typically in the range of 4 to 8×10^{-7} torr. Both already thinned and unthinned specimens were used for the heat treatments, with no difference found in the resulting microstructures.

RESULTS

SiC

As implanted, SiC specimens showed only an amorphous surface layer. Crystalline substrate could be found in the thicker sections; it was not possible to discern any damage in this substrate material.

Heat treatments at 700 and 800°C did not produce any recrystallization of the SiC. However, at both temperatures a fine dispersion of precipitates (0.04 to 0.08 nm) with a face centered cubic crystal structure was observed, as shown in

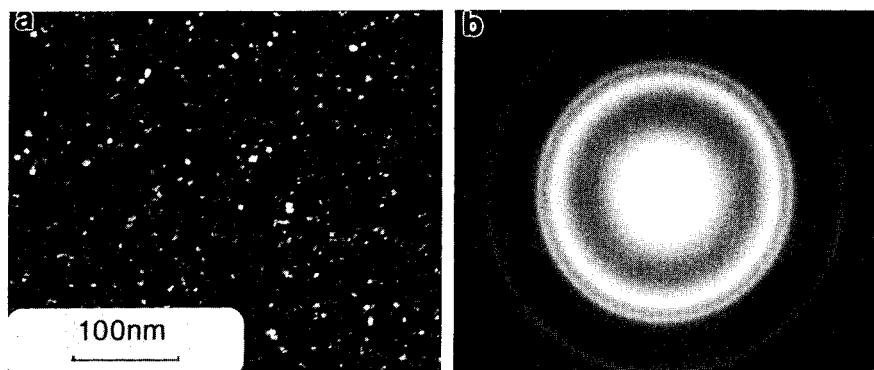


Fig. 1. Titanium implanted SiC, heated 1 hr. at 800°C in vacuum: (a) dark field ((111) and (200) reflections); (b) selected area diffraction pattern.

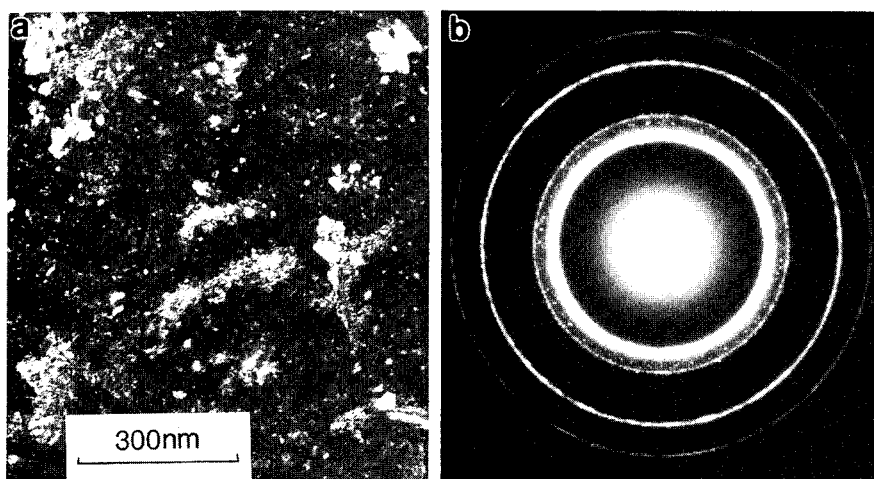


Fig. 2. Titanium implanted SiC, heated 1 hr. at 1000°C in vacuum: (a) dark field ((111) and (200) TiC, (101), (006), (103), and (104) SiC); (b) selected area diffraction pattern.

Fig. 1. The electron diffraction pattern cannot clearly distinguish between TiC and the cubic form of SiC, which not only have the same crystal structure but also nearly identical lattice parameters (0.436nm for SiC, 0.433nm for TiC).

Heating to 900°C or above gave clear evidence of recrystallization. Hexagonal SiC rings appear in the diffraction pattern, and while small precipitates are still present, a larger, more irregular phase is now visible (Fig. 2). Increasing the temperature from 900 to 1100°C causes only an increase in the amount of recrystallized material. TiC precipitates grow very little throughout this temperature range.

Si₃N₄

The as implanted Si₃N₄ surface is not solely amorphous as was the SiC. A fine dispersion of a face centered cubic phase is clearly present. In this case since Si₃N₄ has no cubic polytype, the precipitate may be unambiguously identified as TiN. On heating up to 900°C, this microstructure is little changed (Fig. 3).

Heating at 1000°C or above produces a reappearance of the Si₃N₄ phase (Fig. 4). This phase does not occur as strain free recrystallized grains, but as apparently highly strained irregular coherent patches (Fig. 4b). The thinnest foil areas (material nearest the surface) do not show the Si₃N₄ phase, but only the TiN diffraction rings (Fig. 4c). The TiN itself shows considerable grain growth at 1000°C or above, developing a bipolar size distribution. The largest grains are now up to 200nm, while many grains remain 10nm or smaller (Fig. 5). Little change can be seen in this microstructure between 1000 and 1100°C.

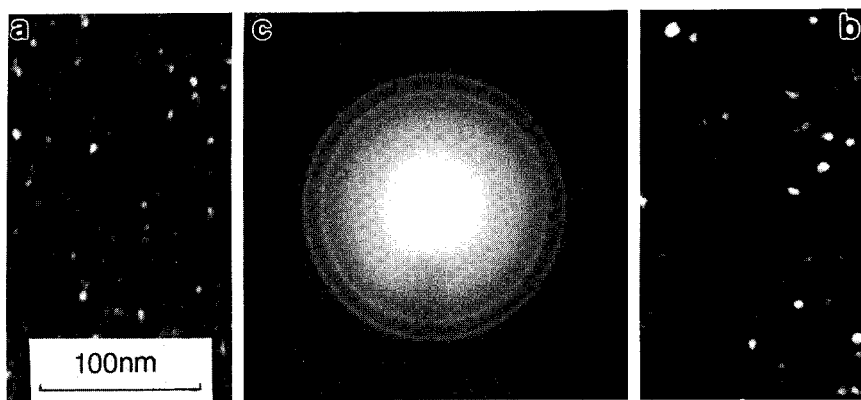


Fig. 3. Titanium implanted Si_3N_4 : (a) dark field, as implanted; (b) dark field ((111) and (200) reflections), 1 hr. at 900°C ; (c) selected area diffraction pattern for (b).

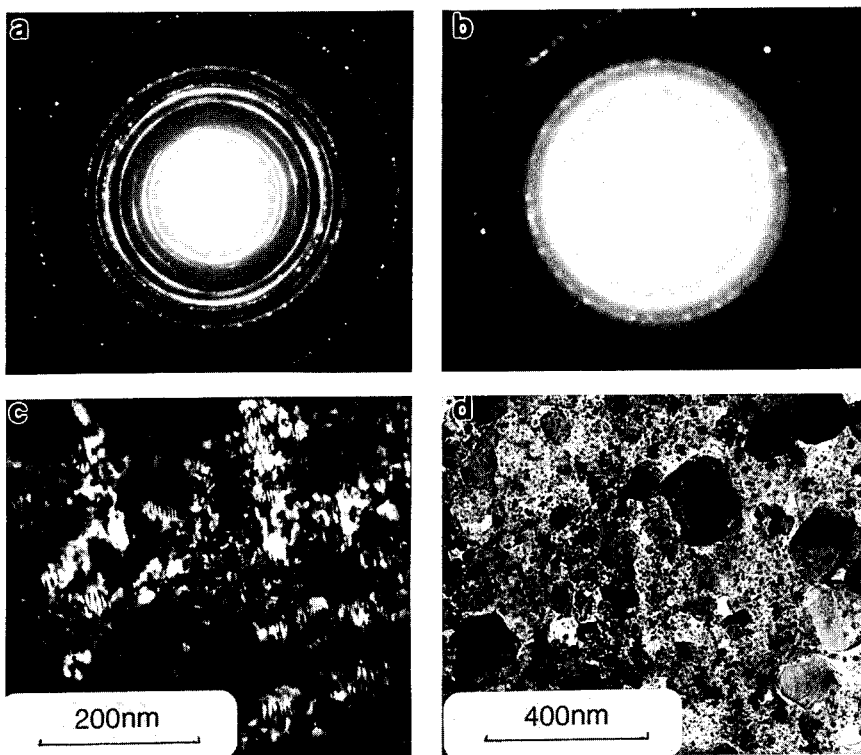


Fig. 4. Titanium implanted Si_3N_4 , heated 1 hr. at 1000°C in vacuum: (a) typical selected area diffraction pattern; (b) very thin area (near surface) selected area diffraction pattern; (c) dark field ((101), (110), and (200) Si_3N_4 reflections); (d) bright field showing bipolar TiN precipitate size distribution.

DISCUSSION

It would seem much more reasonable to identify the precipitates found at the lower temperatures in implanted SiC as TiC rather than cubic SiC. Titanium has a well known affinity for carbon, and the appearance of the hexagonal SiC phase at 900°C indicates that the SiC has no inclination toward its cubic form. Recrystallization in this material occurs with strain-free grains showing no preferred orientation, thus unlikely to be developing as regrowth of the substrate. The recrystallization temperature found here, between 800° and 900°C, lies toward the lower end of the broad range found in the literature. There is some question in the interpretation of data from RBS-C and Raman scattering [10]. The only other TEM study [5] reported some epitaxial regrowth from the substrate at 900°C. One difference in the present study is the presence of TiC precipitates closely matched to the SiC lattice, which may serve as nucleation centers for recrystallization thus lowering the temperature at which it begins.

A difference in diffusion rates of nitrogen and carbon and titanium may be the reason for the presence of precipitates in as implanted Si₃N₄ but not in SiC. This could also account for the rapid growth of some TiN grains (Ostwald ripening) at 1000°C, a growth not observed for the TiC precipitates even at 1100°C.

The recrystallization pattern for Si₃N₄ indicates a regrowth from the substrate. Because of the dissimilarity in crystal structures, the TiN precipitates are less likely to serve as nucleation centers in Si₃N₄ than are the TiC precipitates in SiC where the close packed planes match nearly identically. Regrowth from a moderately damaged crystalline layer adjacent to the amorphous region may explain the range of orientations and irregular pattern of growth seen in Fig. 4. These grains may also have a high defect density, as has been observed in epitaxially regrowing SiC [5].

No evidence has been found in these materials for silicon or silicide phases. These could be missed in small quantities, but it is unclear at this point whether titanium simply displaces silicon, and if so where the excess silicon is located. TiC and TiN may of course exist in strongly carbon or nitrogen deficient compositions. Further surface analysis is intended to clarify this point.

Singer [14] has found mixed results in the surface mechanical properties of titanium implanted (to twice the present dose) SiC and Si₃N₄, with hardness decreased (as expected for an amorphous layer) and toughness unchanged or decreased. The microstructure of TiC or TiN precipitates in an amorphous matrix achieved in the present work by heat treatment may prove quite interesting in this respect, and further experiments are planned to investigate this.

ACKNOWLEDGMENTS

I am indebted to Dr. C. C. Wu for supplying the material used here, and to Dr. B. D. Sartwell and his implantation group for doing the implantations. I also thank Dr. I. L. Singer for his advice and suggestions.

REFERENCES

1. A. A. Hart, H. L. Dunlap, and O. J. Marsh, Rad. Eff. 9, 261 (1971).
2. A. B. Wright and D. M. Gruen, Rad. Eff. 33, 133 (1977).
3. J. M. Williams, C. J. McHargue, and B. R. Appleton, Nucl. Inst. Meth. 209/210, 317 (1983).
4. C. J. McHargue, G. C. Farlow, C. W. White, J. M. Williams, B. R. Appleton, and H. Naramoto, Mat. Sci. Eng. Eng. 69, 123 (1985).
5. P. S. Sklad, P. Angelini, C. J. McHargue, and J. M. Williams, Proc. 42nd Ann. Meet. Electron Microscope Soc. of America (San Francisco Press, 1984) p. 416.
6. C. J. McHargue and C. S. Yust, Jour. Am. Cer. Soc. 67, 117 (1984).
7. B. R. Appleton, H. Naramoto, C. W. White, O. W. Holland, C. J. McHargue, G. Farlow, J. Narayan, and J. M. Williams, Nucl. Inst. Meth. B1, 167 (1984).
8. J. A. Spitznagel, S. Wood, W. J. Choyke, N. J. Doyle, J. Bradshaw, and S. G. Fishman, Nucl. Inst. Meth. B16, 237 (1986).
9. C. J. McHargue, G. C. Farlow, G. M. Begun, J. M. Williams, C. W. White, B. R. Appleton, P. S. Sklad, and P. Angelini, *ibid*, p. 212.
10. H. G. Bohn, J. M. Williams, C. J. McHargue, and G. M. Begun, J. Mater. Res. 2, 107 (1987).
11. S. G. Roberts and T. T. Page in Ion Implantation into Metals, eds. V. Ashworth, W. A. Grant, and R. P. M. Proctor (Pergamon Press, 1982) p. 135.
12. C. J. McHargue and J. M. Williams in Metastable Materials Formation by Ion Implantation, eds. S. T. Picraux and W. J. Choyke (Elsevier, New York, 1982) p. 303.
13. P. J. Burnett and T. T. Page, Proc. Brit. Cer. Soc. 34, 65 (1984).
14. I. L. Singer, Surf. Coat. Tech. 33, 487 (1987).
15. A. B. Campbell, J. Shewchun, D. A. Thompson, J. A. Davies, and J. B. Mitchell in Ion Implantation in Semiconductors, ed. S. Namba (Plenum Press, N.Y., 1975) p. 291.

ION BEAM ANALYSIS OF O, N, AND B COMPOSITIONS IN MATERIALS USING NON-RUTHERFORD SCATTERING OF PROTONS

N. R. PARIKH, Z. H. ZHANG, M. L. SWANSON, N. YU, AND W. K. CHU
Department of Physics and Astronomy, University of North Carolina,
Chapel Hill, NC 27599-3255, USA

ABSTRACT

Elastic scattering of protons with energies from 1.5 MeV to 2 MeV was used to determine the concentration of oxygen in Y-Ba-Cu-O compound, nitrogen in GaN films, and boron in B-Si glass and other materials. Proton scattering from light elements in this energy range exhibits non-Rutherford scattering cross section, which are enhanced by a factor of 3 to 6 or more relative to the Rutherford scattering cross sections. Thus the sensitivity for the light element detection is considerably larger than that obtained by He ion scattering.

Quantitative analysis by proton scattering is discussed and compared with other methods.

INTRODUCTION

Within the low MeV energy range, there are mainly five ion beam techniques for materials analysis, namely, Rutherford Backscattering Spectrometry (RBS), Ion Channeling, Elastic Recoil Detection, Nuclear Reaction Analysis (NRA), and Particle Induced X-rays Emission (PIXE) [1-2]. Among these, RBS is probably so far the most commonly used technique. Over the past years, He ions of few MeV energy have been almost exclusively used as probe ions in the RBS technique. However, He ion RBS is not sensitive to light elements in a heavy element matrix. On the other hand, proton beams of few MeV, which have not often been used in conventional RBS analysis, are much more sensitive to light elements as compared with He ions, as protons have non-Rutherford scattering cross sections usually up to 1-2 orders of magnitude larger than the Rutherford cross section. There are several difficulties associated with using proton non-Rutherford scattering as an analysis tool. One of the main difficulties is that the interpretation of the proton scattering spectrum usually is not as straightforward as that of a He ion RBS spectrum, because the proton elastic scattering cross sections normally have resonance peaks while the He ion Rutherford cross section has a monotonic dependence on energy. This difficulty can be overcome, if the absolute cross section data are known; computer simulation then can be used to interpret the proton scattering spectrum since the proton stopping powers in most materials are known [3]. Rauhalu et. al., have used this technique to analyze the oxygen distribution in Y-Ba-Cu-O compounds [4]. Proton elastic scattering cross sections had been measured mostly in the 50's and 60's. [5-8]. There are discrepancies among the data published by different authors. Besides, the data were mostly published in curve form instead of tabulated form. There are some tabulated data available [9,10], but most of them are for the proton energy higher than 2.5 MeV; therefore, these data are not very useful for light element detection since various nuclear processes other than elastic scattering will come into the picture when the energy is higher than 2.5 MeV, which might make the interpretation of the proton spectrum more complicated. Recently, the Helsinki group has accurately measured the proton elastic scattering cross sections for light elements C, N, O, and Si [11] and published these data either in tabulated form or in numerical fitting form, which greatly facilitates the application of protons as a probe ions for detection of light elements.

This paper will present some examples to illustrate the composition analysis of materials containing light elements. The composition of nitrogen in a GaN film and oxygen in a Y-Ba-Cu-O compound were analyzed. In

addition, the detection of boron in different substrates has been investigated.

RESULTS AND DISCUSSIONS

The measurements were carried out in a conventional RBS chamber with proton and He ions from a 2.5 MeV van de Graaff accelerator in the University of North Carolina at Chapel Hill. A surface barrier Si detector with sensitive area of 100 mm² and FWHM = 15 keV was used. The detector - target distance was 10.5 cm. To define the solid angle, the detector was covered by a slit which has a width of 3 mm.

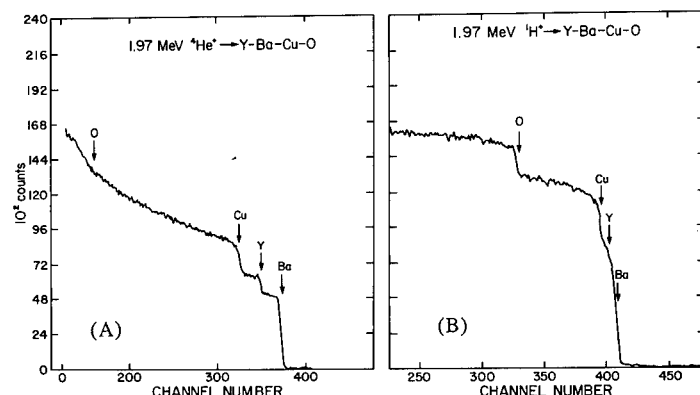


Fig.1, 1.97 MeV He RBS spectrum(A) and 1.97 MeV proton scattering spectrum (B) for Y-Ba-Cu-O compound. The arrows shows the scattering from surface atoms.

Figure 1 shows the 1.97 MeV He ion RBS spectrum (Fig.1A) and 1.97 MeV proton elastic scattering spectrum (Fig.1B) of a Y-Ba-Cu-O compound. In the He ion RBS spectrum, the signals from Y, Ba, and Cu are clear and well separated, however, the signals from oxygen can hardly be seen. This is because the Rutherford scattering cross section (σ_R) is proportional to the square of the atomic number of the elements, so that lighter elements have lower yields. Furthermore, the He ion kinematic factor for oxygen is so small ($K = 0.3708$ at 160°) that the oxygen signal only appears in the low energy portion of the spectrum, where the spectrum usually has high background. However, by using a proton beam, due to the nuclear potential scattering, the elastic scattering for oxygen is enhanced 5.5 times above σ_R at $E_p = 2$ MeV and $\theta_{Lab} = 170^\circ$. Also, because the kinematic factor for protons ($K = 0.7829$ at 160°) is larger than that for He ions, the oxygen signal in the proton spectrum appears in the high energy region. These effects result in a clear oxygen signal step in the proton elastic scattering spectrum (Fig.1B).

By combining the He RBS spectrum and proton elastic scattering spectrum the composition analysis is straightforward. The ratio N_{Ba}/N_Y and N_{Cu}/N_Y can be calculated from He ion RBS spectrum (Fig.1A)[1]. It turns out that $N_Y : N_{Ba} : N_{Cu} = 1 : 2 : 3$. The oxygen composition fraction can be calculated by comparing the spectrum surface height of oxygen with that of other elements in the proton scattering (Fig. 1B), which gives the ratio N_O/N_Y . The results are $N_O/N_Y = 6.1$, which is smaller than that of normal superconducting 1-2-3 phase compound. Since this sample was annealed in a sealed quartz tube, the large oxygen deficiency is not surprising. In the calculation, both the proton and He ion scattering from Y, Ba, and Cu were assumed to follow the Rutherford cross section. For Cu, this assumption is a good approximation when the proton incident energy is below 2.6 MeV [12]. Care has to be taken when the sample

contains medium heavy elements, eg. Ti, since the deviation of their proton elastic scattering cross sections from Rutherford cross sections might not be negligible in the low MeV range. No effort was made to correct for the screening effect, which can be taken into account by using the information from Ref. 12.

Detection sensitivity depends on the experimental condition, including the sample condition, and the criteria of the sensitivity. Considering the case of light element(A) in a thick heavy target(B), the light element signals will superimpose on the background which is composed of heavy element signals and pulse pile-up. The sensitivity is mainly affected by the statistical fluctuation of the background. Then the sensitivity might be defined as the minimum amount of light element which generates the signal counts equaling to twice the statistical fluctuation of the background. Taking $\text{Cu}_{1-x}\text{O}_x$ as an example, for copper signal counts $H_{\text{Cu}}=10000$, the oxygen detection sensitivity will be 7%. If H_{Cu} increases to 90000, then the sensitivity will be improved to 2.3%. It is obvious that the heavier the matrix element(B), the lower the sensitivity for light element(A). If the sample is a thin film (compound) deposited on a substrate(C) which is lighter than element A and the film is thin enough, then the signals from light element A, heavy matrix element B and substrate C will be well separated from each other. Since in a such case the sensitivity is mainly affected by the pulse pile-up, which can be minimized by reducing the beam current and using fast electronics, the sensitivity for a thin film can be few times higher than that for a thick target. The same argument about the sensitivity given here for oxygen can be applied for the detection of nitrogen and boron, which will be discussed below.

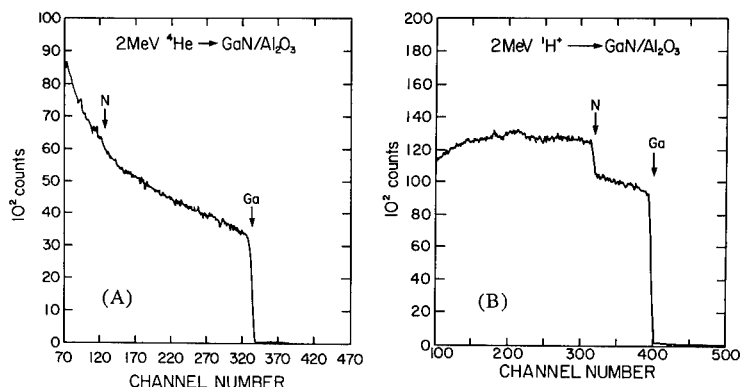


Fig. 2, Energy spectra for 2 MeV He ions (A) and 2 MeV protons(B) incident on GaN film. Scattering from surface atoms are indicated by arrows.

The example for nitrogen analysis is given using a GaN thick film. In the energy range of $E_p = 1.77$ MeV to 2.3 MeV, the proton- ^{14}N elastic scattering cross section varies quite smoothly and it increases with the scattering angle. In the present measurements, the proton energy was set at 2 MeV and the scattering angle was 165° . The 2 MeV He RBS spectrum is shown in Figure 2A. Due to the low kinematic factor ($K = 0.3194$ for 160°) and the small atomic number of nitrogen, the 2 MeV He ion can not resolve the nitrogen spectrum from the high background. However, the proton ($K = 0.7561$ for 160°) elastic scattering enhanced the nitrogen signal yields (Fig. 2B) and moved the nitrogen surface signal from Channel 120 in the He RBS spectrum (Fig. 2A) to channel 310 in the proton scattering spectrum (Fig. 2B), so that the nitrogen yields became measurable. Calculation using the surface height of Ga and N signals shows that the surface composition of this GaN film is Ga : N = 0.99 : 1.

The composition profile can be obtained if computer simulation is used.

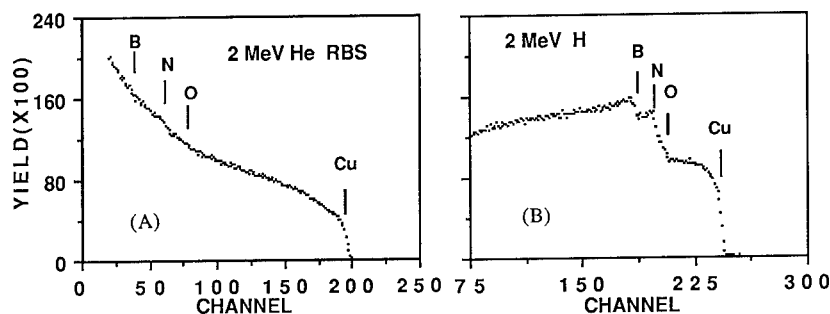


Fig. 3, (A) 2 MeV He ion RBS spectrum and (B) 2 MeV proton scattering spectrum. The surface positions corresponding to respective elements are indicated.

In the boron case, the proton elastic scattering cross section in the energy range from 0.8 MeV to 2.0 MeV has values 2 to 7 times larger than Rutherford cross section [7,8]. Below 2 MeV, tabulated proton elastic scattering cross section data for ^{11}B is so far only available at two angles, $\theta_{\text{C.M.}} = 152^\circ 36'$ and $\theta_{\text{C.M.}} = 90^\circ$ [9], and for ^{10}B is only available at one angle $\theta_{\text{C.M.}} = 90^\circ$. For better mass resolution, $\theta_{\text{C.M.}} = 152^\circ 36'$ was chosen in the experiment. The incident energy for both He ions and protons was 2 MeV. At this energy, proton scattering has a cross section enhancement $R = 7.5$ (for ^{11}B). The sample is a mixture of BN powder and CuO powder (pressed into a pellet), which has an atomic ratio, $\text{Cu} : \text{B} : \text{N} : \text{O} = 1 : 1 : 1 : 1$. Figure 3B shows the 2 MeV proton scattering spectrum. The oxygen, nitrogen, and boron steps on the spectrum are clearly resolved and the calculation of the composition is feasible if the relevant cross sections are known. However, in the He ions RBS spectrum (Fig. 3A), these steps are almost swamped by the statistical fluctuations of the high background. The spectrum steps corresponding to Cu and oxygen are not sharp. This is because the mixing of BN powder and CuO powder is not uniform and the surface of the sample is not quite smooth.

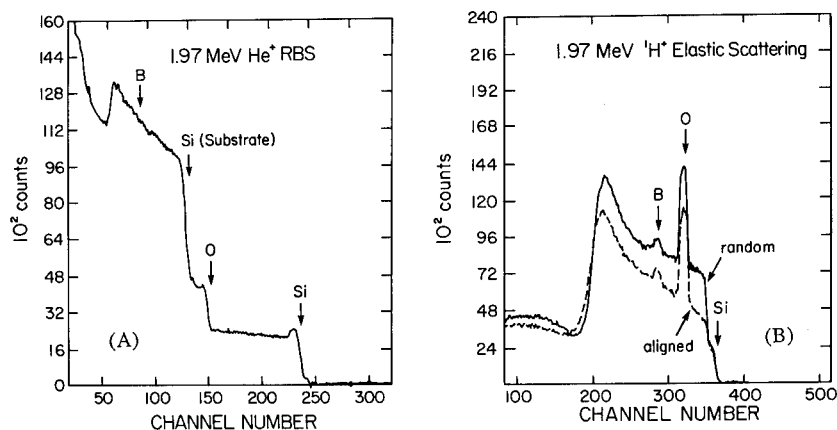


Fig. 4, (A) 1.97 MeV He ion RBS spectrum and (B) 1.97 MeV proton scattering spectrum. Sample under investigation is B-Si glass deposited on Si substrate. In (B) both aligned and random spectra are shown.

Another example is the detection of boron in B-Si glass (borosilicate), which is conventionally used in Si industry for passivation. The sample is a B-Si glass film deposited on Si. This sample had been measured by using nuclear reaction $^{10}\text{B}(n, ^4\text{He})^7\text{Li}$, which shows that the ^{10}B concentration is $1 \times 10^{17}/\text{cm}^2$ [14]. Figure 4A and Figure 4B are the He ion RBS spectrum and proton scattering spectrum respectively. The spectrum steps which are corresponding to the surface of the Si, oxygen, and boron in the B-Si glass as well as the surface of the Si substrate are indicated by arrows on the spectrum (Fig. 4). In the He ion RBS spectrum (Fig. 4A), the signals corresponding to the surface boron should appear around channel 90, however, the He scattering is not able to resolve it. On the other hand, in the proton scattering spectrum (Fig. 4B), the boron signal is a clear measurable peak superimposed on Si signals. Natural boron consists of about 80% ^{11}B and 20% ^{10}B . Proton elastic scattering of ^{11}B and ^{10}B both have cross sections a few times larger than the Rutherford cross sections. But, no tabulated proton elastic scattering cross section data for B^{10} at the scattering angle chosen in this experiment ($\theta_{\text{C.M.}} = 152.036^\circ$) are available. In fact, a literature search by the authors indicated that below 2.5 MeV, the proton elastic scattering cross section data for ^{10}B and ^{11}B are insufficient for a quantitative measurement. Because of this reason, no effort was made to estimate the boron concentration in the BN-CuO mixture and in B-Si glass. Nevertheless, the fact that the sensitivity of proton elastic scattering to boron is much higher than that of He ion RBS is clearly demonstrated in these examples.

The third B sample tested is a thin Si foil ($1.4 \mu\text{m}$) which contains thermally diffused boron. No measurable boron signals could be seen in the 2 MeV proton scattering spectrum (not shown). The Si foil was fabricated by conventional chemical etching processes using an EDP etching solution [15]. The thermally diffused boron acts as an etching stopper. When the etching solution reaches the Si layer within which the boron concentration is above 7×10^{19} B atoms/ cm^3 , the etching will stop. The boron solubility in Si is about 10^{20} B atoms/ cm^3 . That means that our preliminary experiment had indicated that the amount of boron which is detectable for proton elastic scattering is above $10^{16}/\text{cm}^2$, i.e., at least one order of magnitude higher than that of Nuclear Reaction Analysis (NRA) [16-18]. The same Si foil sample had been measured by the coincidence technique, using a collimated thermal neutron beam from the nuclear reactor at the National Bureau of Standard [19]. The two particles from the $^{10}\text{B}(n, ^4\text{He})^7\text{Li}$ nuclear reaction were recorded in coincidence. A clear measurable boron signal peak was obtained in the coincidence energy spectrum (not shown), which indicated that the neutron nuclear reaction coincidence has better sensitivity for boron detection than proton elastic scattering. The advantage of the proton elastic scattering technique is that it can detect several elements in one measurement, as can be seen in Fig. 3B.

SUMMARY

The examples shown here demonstrated that the low energy ($E_p < 2.5$ MeV) proton elastic scattering (PES) is a useful technique for detection of light elements such as O, N, and B in materials.

PES retains most of the advantages of He ion RBS, such as speed, simplicity and capability of depth profiling. But PES is much more sensitive to light elements than He ion RBS. As compared to He ions, protons have a larger accessible depth [1] and create less radiation damage. The latter factor might be important for certain materials such as diamond. However, the mass resolution and depth resolution of protons is lower than that of He ions [1]. Besides, care has to be taken in interpreting the proton scattering spectrum, not letting the proton inelastic scattering confuse the interpretation.

Oxygen and nitrogen have often been analyzed by using charged particle nuclear reactions [20,21]. The commonly used reactions are $^{16}\text{O}(d, p)^{17}\text{O}$

with $E_d = 0.9$ MeV, for which the cross section is < 5 mb/sr, and $^{14}\text{N} (d, ^4\text{He}) ^{12}\text{C}$ with $E_d = 1.2$ MeV, for which the cross section is < 1.4 mb/sr [2]. Both reaction cross sections are much less than that of PES, which is about 80 - 90 mb/sr for oxygen with $E_p = 2 - 2.5$ MeV [2], and 81 - 106 mb/sr ($E_p = 1.9 - 2.3$ MeV) for nitrogen [11].

In the case of boron, as demonstrated in this report, the PES technique is less sensitive than NRA using the $^{11}\text{B} (p, ^4\text{He}) ^8\text{Be}$ and $^{10}\text{B} (n, ^4\text{He}) ^7\text{Li}$ reactions. But PES usually gives more information than NRA, since PES can detect elements other than boron in just one measurement.

REFERENCES

- [1]. Wei-Kan Chu, J. W. Mayer and M-A. Nicolet, "Backscattering Spectrometry" (Academic Press, New York, 1977).
- [2]. J. W. Mayer and E. Rimini, eds., "Ion Beam Handbook For Material Analysis" (Academic Press, New York, 1977).
- [3]. H. H. Andersen and J. F. Ziegler, "Hydrogen Stopping Power and Ranges in All Elements" (Pergamon Press, New York, 1977).
- [4]. E. Rauhala, J. Keinonen and R. Jarvinen, Appl. Phys. Lett., 52, 1520 (1988)
- [5]. F. K. McGowan, W. T. Milner, H. J. Kim, and Wanda Hyatt, Nuclear Data, A2 No. 1-2, 1 (1969).
- [6]. A. J. Ferguson, R. L. Clarke, H. E. Gove, and J. T. Sample, Chalk River Project Report PD-261, 1956 (Unpublished).
- [7]. G. W. Taftfert and S. Rubin, Phys. Rev., 103, 196 (1956).
- [8]. J. C. Vorley and W. Whaling, Phys. Rev., 128, 315 (1962).
- [9]. H. J. Kim, W. T. Milner and F. K. McGowan, Nuclear Data, A3, No. 2, 123 (1967)
- [10]. H. J. Kim, W. T. Milner and F. K. McGowan, Nuclear Data, A1, No. 3-4, 203 (1966).
- [11]. E. Rauhala, Nucl. Instr. & Meth., B12, 447 (1985); M. Luomajarvi, E. Rauhala, and M. Hautala, Nucl. Instr. & Meth. B9, 255 (1985).
- [12]. V. Y. Golovnya, A. P. Klyucharev, B. A. Shilyaev and N. A. Shlyakhov, Soviet J. Nucl. Phys. Vol. 4, 547 (1967)
- [13]. M. Hautala and M. Luomajarvi, Rad. Effects, 45, 159 (1980)
- [14]. N. R. Parikh and T. Hossain, Private communication.
- [15]. N. W. Cheung, Rev. Sci. Instrum. 51, 1212 (1980)
- [16]. E. Ligeon and A. Bontemps, J. Radioanal. Chem. 12, 335 (1972)
- [17]. J. U. Andersen, E. Lagsgaard and L. C. Feldman, Rad. Effects, 12, 219 (1972)
- [18]. J. F. Ziegler, B. L. Crowder, G. W. Coole, J. E. E. Baglin and B. J. Masters, Appl. Phys. Letters, 21, 16 (1972)
- [19]. N. R. Parikh et al., To be published.
- [20]. G. Amsel, J. P. Nadel, E. Dartemare, D. David, E. Girard and J. Moulin, Nucl. Instr. & Meth. 92, 481 (1971).
- [21]. B. Sundqvist, L. Goezi, I. Koersner, R. Bergman and U. Lindh, in "Ion Beam Surface Layer Analysis", Vol. 2, P. 945 (Plenum Press, New York and London, 1975).

0.5 MeV SUBMICRON ION PROBE SYSTEM FOR RBS/PIXE.

K. INOUE*, M. TAKAI, K. ISHIBASHI*, Y. KAWATA*, N. SUZUKI*
AND S. NAMBA

Faculty of Engineering Science and Research Center for Extreme
Materials, Osaka University, Toyonaka, Osaka 560, Japan.

* Electronics Technology Center, Kobe Steel Ltd., Nishi-ku, Kobe 673-02,
Japan

ABSTRACT

A nuclear microprobe-forming system for the microscopic RBS/PIXE measurement of micro devices has been developed and installed at the Research Center for Extreme Materials, Osaka University. The use of precision quadrupole magnets and an objective collimator ensures a final spot size of less than 1 μ m.

INTRODUCTION

MeV ion beams with a typical beam size of 0.5-1 mm for RBS and channeling effect measurements have been successfully used to study ion-implanted semiconductors [1-3]. At the same time, however, the feature sizes of semiconductor processing have been reduced to the submicron range. Maskless processes using focused ion or laser beams, for example, are being developed. Furthermore, fabrication of multilayered wirings or interconnections of metals between gates is being studied for ULSI's.

In such situations, a nondestructive three-dimensional micro-analyzing method with a lateral resolution in the micron-to-submicron range becomes indispensable to realize future devices. It is, in particular, important to get information on three dimensional structures, crystallinity, atomic composition and distribution.

In conventional microscopic analysis, such as Auger electron spectroscopy (AES), a sample surface layer must be sputtered by Ar ions to analyze the subsurface layers. This repeated pre-treatment makes such analysis time-consuming and results in inexact readings of depth.

Use of a microbeamline for MeV ions with a beam-spot diameter of less than 3 μ m is one way to deal with the above problem. Several groups have developed such systems [4-10]. The first such system in Japan was constructed and is already in operation by a group including several of the present authors at the Government Industrial Research Institute Osaka (GIRIO) [10-12].

This study reported on a new microbeamline with 0.5 MeV helium ions developed at the Research Center for Extreme Materials at Osaka University. Each of the components and the adjusting mechanism of the system were carefully designed to attain a submicron spot size, building on the experiences gained from the research on the GIRIO system. This paper includes full descriptions of the quadrupole magnet and objective collimator.

BEAMLINE

Table 1 and Fig. 1 show the specifications and the schematic diagram of the beamlines, respectively. The Disktron-type accelerator supplies the probe-forming system with helium ions or protons with an energy of 0.5 MeV. Typically it provides a current of over ten

Table 1
Specification of the microbeamline at Osaka University

(Ion source system)	
Accelerator	disktron
Ion source	duoplasmatron
Momentum analyzer	bending magnet
(Beam characteristics)	
Ion	H^+, He^+, He^{++}
Acceleration voltage	500 kV (maximum)
Energy spread (estimated)	0.02 %
Divergence θ, ϕ (estimated)	1.2 mrad
Typical current for 500 keV H^+, He^+	10 μA ($< 2 \text{ mm } \phi$)
Beam level	1450 mm
(Microbeam system parameters)	
Objective distance (slit - Qmag.)	1634.5 mm
Image distance (Qmag.- target)	188 mm
Pole length	40 mm
Gap between adjacent Q-poles	40 mm
Q-magnet: Bore radius	2.5 mm
Coil turn	130 turn
Inner radius of beam duct	1.5 mm

Ion source

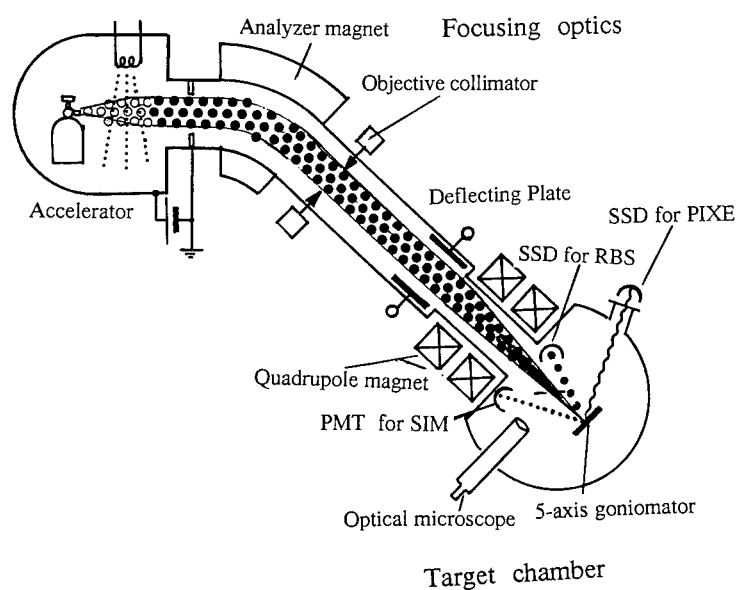


Fig.1 A schematic diagram of the microbeamline.

μA . The accelerator also has a Freeman-type ion source, which provides heavy ions for implantation. An ion probe is formed by the demagnification beam-optics consisting of objective slits and strong focusing magnetic lenses. Ions passed through the objective aperture are focused onto the target surface by the lens with horizontal and vertical demagnification factors of 1/3.5 and 1/14, respectively. The target chamber is equipped with an optical microscope and three detectors: a photomultiplier-tube coupled with a scintillator for secondary electrons, a surface-barrier type Silicon Solid-State Detector for RBS, and a Si(Li) SSD for PIXE. A 5-axis goniometer originally designed for micro-channeling measurements is also included. The chamber is evacuated down to 10^{-8} Torr by turbo-molecular and cryogenic pumps. In front of the lenses, two pairs of beam deflecting plates with a length of 32 mm are inserted and applied with a maximum voltage of ± 140 V.

Computer-controlled beam scanning and signal processing can be used to reconstruct varieties of RBS/PIXE mapping images. Raster scanning with a narrow energy window, corresponding to specific elements or layers, gives an areal mapping image representing the distribution of arbitrary elements on a sample surface layer [11]. Line scanning and event-by-event energy analyzing of RBS ions produce a tomographic image representing the concentration of an arbitrary element as a function of lateral location and depth.

Quadrupole lens

When a cylindrical-type magnet is used to focus MeV ion beams, its magnetic field must be stronger by several hundred times than that of an ordinary electron microscope, the value of which is too large for normal conducting magnets. Therefore, it was decided to employ quadrupole magnets with a small bore radius of 2.5 mm. However, in such magnets, parasitic aberrations, induced by the imperfect fabrication of a pole piece, are significantly enlarged. Therefore a conventional circular-type pole piece, as shown in Fig. 2 (a), was found to be inadequate in forming a micron probe.

To minimize lens aberrations, each pole piece was cut to a hyperbolic surface, as shown in Fig. 2 (b), with an accuracy of within a few microns, by wire discharge milling. With a larger cut-off angle of the hyperbolic curve, a more accurate field is obtained. However, the saturation of the magnetic permeability of the pole pieces occurs and degrades the resulting magnetic field. The cut-off angle is optimized to be 37° , the value of which ensures a quadrupole field with an accuracy of less than 10^{-4} over 80% of the bore radius area, by a numerical analysis code called ELF-MAGIC. Details of the analysis will be published elsewhere [13].

Objective Collimator

The energy loss resulting from the edge scattering of the ion beam at the collimator is too serious a problem to ignore, because it gives rise to the degradation of the energy resolution in RBS measurement and leads to the enlargement of the probe size because of a chromatic aberration. To minimize the number of forward-scattering ions, it was decided to employ a new cylindrical type of slit-edge made of molybdenum, with a diameter of 10 mm (cf. Fig. 3), instead of the conventional wedge-shape [5]. As the former can also be fabricated with greater precision than the latter, a small aperture can be defined more exactly. The roughness of the edge surface was, in this

study, found to be about 150 nm.

An objective aperture is formed by two pairs of edges horizontally and vertically. Each of edges is driven by stepping motors, respectively, with a resolution of 1 μ m per step. However, two motors of each pair are not individually controlled, but synchronized each other by setting of two parameters: a width and a center position of the aperture. Such control system is very useful for a beam alignment and a tuning. Special care is taken to reduce heating of the edges mounted on the holder made of insulators: additional skirts made of stainless steel were placed in front of the edges to get rid of most of the diverging beams. Without the skirts, the thermal expansion of the edges causes erratic change in the aperture size.

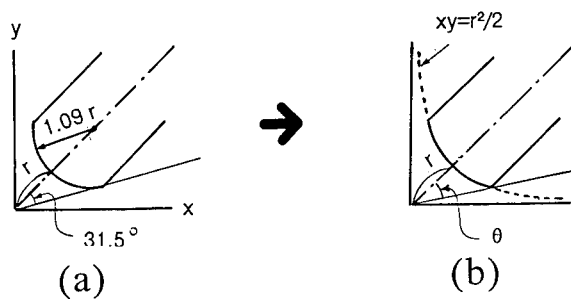


Fig.2 A cross-sectional view of the pole piece of the quadrupole magnet.
a) Conventional circular type, b) Hyperbolic type

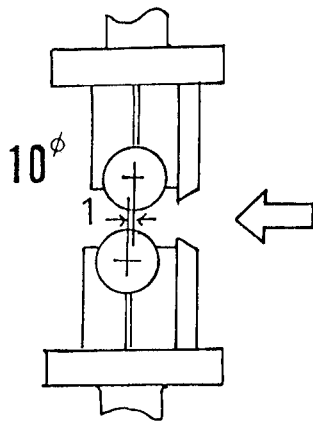


Fig.3 A cross-sectional view of the objective collimator edges.

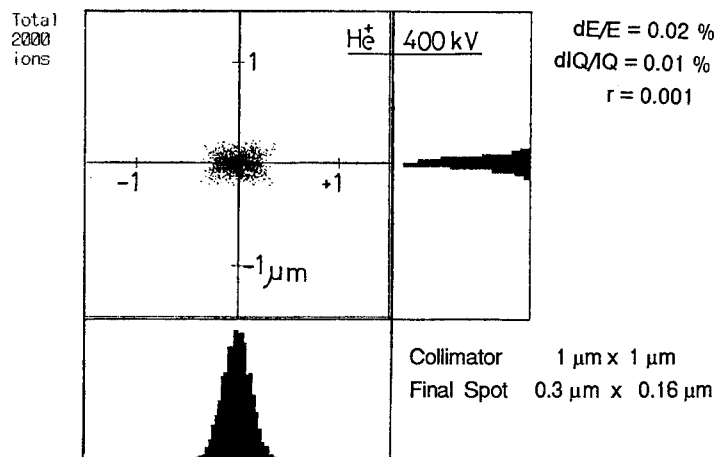


Fig.4 Monte Carlo simulation of the beam spot image and intensity at a target surface.

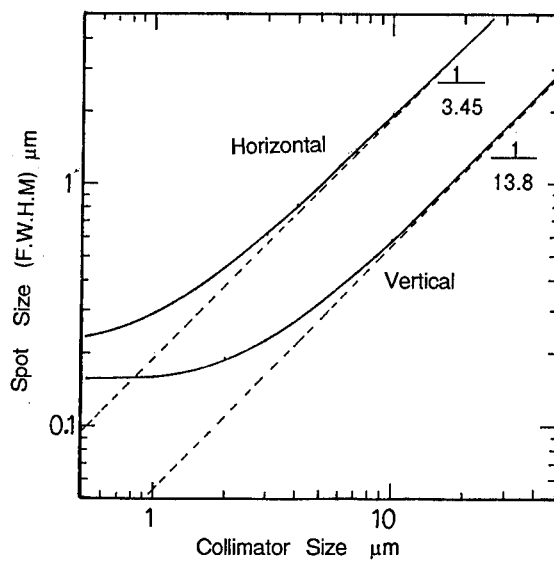


Fig.5 Beam spot size as a function of objective collimator width. Broken lines stand for demagnification factors of Q-magnets.

SIMULATION

To estimate the minimum attainable probe size, which is the main object of the project, a computer simulation of the trajectories of a number of ions was carried out by the Monte Carlo method using transfer matrix formalism, as described elsewhere [10]. Fig. 4 shows the simulated beam spot image at the target under the assumed conditions of an energy spread of 0.02%, instability of magnet excitation of 0.01% and a rotational misalignment between adjacent Q-magnets of 0.001. Fig. 5 shows the simulated beam spot size as a function of collimator width. A linear decrease in probe size along broken lines, which stand for the demagnification factors of the Q-magnets, saturates with a collimator width of less than $2\sim 3\text{ }\mu\text{m}$. The minimum probe size with optimum current density is found to be larger than $0.5\text{ }\mu\text{m}$ square.

CONCLUSION

A nuclear ion probe system for micro-RBS/PIXE measurements has been developed at Osaka University.

The use of precision quadrupole magnets and an objective collimator ensures the achievement of a fine spot size of less than $1\text{ }\mu\text{m}$.

This work was partially supported by the System of Joint Research with Industry in 1987 (Kobe Steel Ltd., and the Ministry of Education and Culture, Japan).

REFERENCES

1. M. Takai, K. Gamo, K. Masuda and S. Namba: Japan. J. Appl. Phys. 12, 1926 (1973)
2. M. Takai, K. Gamo, K. Masuda and S. Namba: Japan. J. Appl. Phys. 14, 1935 (1975)
3. Backscattering Spectroscopy, edited by W. K. Chu, J. W. Mayer and M. A. Nicolet (Academic Press, New York, 1978)
4. G. J. F. Legge: Nucl. Instrum. and Methods. 197, 243 (1982)
5. R. Nobiling: Nucl. Instrum. and Methods. 212, 197 (1983)
6. P. Bayerl and P. Eichinger: Nucl. Instrum. and Methods. 149, 243 (1982)
7. H. Kneis, B. Martin, R. Nobiling, B. Povh and K. Traxel: Nucl. Instrum. and Methods. 197, 79 (1982)
8. M. Takai, K. Matsunaga, K. Inoue, M. Izumi, K. Gamo, M. Satou, and S. Namba: Japan. J. Appl. Phys. 26, L550 (1987)
9. M. Takai, A. Kinomura, K. Inoue, K. Matsunaga, M. Izumi, K. Gamo, S. Namba and M. Satou: Nucl. Instrum. and Methods. B30, 260 (1988)
10. K. Inoue, M. Takai, K. Matsunaga, M. Izumi, K. Gamo, S. Namba, and M. Satou: Nucl. Instrum. and Methods. B30, 580 (1988)
11. A. Kinomura, M. Takai, K. Inoue, K. Matsunaga, M. Izumi, T. Matsuo, K. Gamo, S. Namba and M. Satou: Nucl. Instrum. and Methods. B33, 862 (1988)
12. M. Takai, A. Kinomura, M. Izumi, K. Matsunaga, K. Inoue, K. Gamo, M. Satou, and S. Namba: Mat. Res. Soc. Symp. Proc. 108, 51 (1988)
13. K. Ishibashi, K. Inoue, Y. Kawata, M. Takai, and S. Namba, in preparation.

PART IV

Properties (Tribological,
Optical, Chemical)

TRIBOLOGY OF AMORPHOUS ALLOYS FORMED WITH ION BEAMS

D. M. FOLLSTAEDT, J. A. KNAPP AND L. E. POPE
Sandia National Laboratories, Albuquerque, NM 87185-5800

ABSTRACT

The changes in friction and wear properties (i.e., tribology) of steels due to thin surface alloys formed by ion beams are surveyed, and considered in light of their microstructures. Amorphous alloys containing both Ti and C are found to give superior performance in comparison to alloys with N, B, C, P or Ti. All the amorphous layers reduce friction, but the duration of benefits and wear resistance at high loads vary with composition. By examining similar amorphous alloys with Ti alone or C alone, the critical roles played by each in resisting wear are demonstrated. Amorphous alloys with Ti and C appear to be quite hard.

INTRODUCTION

Ion implantation has been developed during the last two decades as a method to modify the near-surface region ($< 1 \mu\text{m}$) of metals to alter their chemical [1] and mechanical [2] surface-related properties. Despite the thinness of the implanted layer, significant benefits are readily achieved. The treatment can reduce friction coefficients and wear rates of an unlubricated sliding wear couple when the proper elements are implanted into one member [3]. An example of the significant reductions obtainable is shown in Fig. 1 with 304 stainless steel (SS), where the friction coefficient is reduced by implantation from 0.7 to 0.3, and the wear depth from $1 \mu\text{m}$ to $0.2 \mu\text{m}$. The electron micrographs show that these reductions are accompanied by a change from an adhesive wear mode, in which material is torn out of the wear track, to an abrasive wear mode for which only sliding grooves are seen.

Improvements in mechanical properties have been obtained for a number of metals [2], but here we examine work done on steels and some supporting results from Ni and Co alloys. The unlubricated sliding friction and wear results for several implanted species and other ion-beam alloying methods will be surveyed to identify the most promising treatments, and used with characterizations of microstructure to elucidate important aspects of the tribology of implanted steels. This will lead us to focus on amorphous surface alloys, especially those produced by implanting Ti and C together.

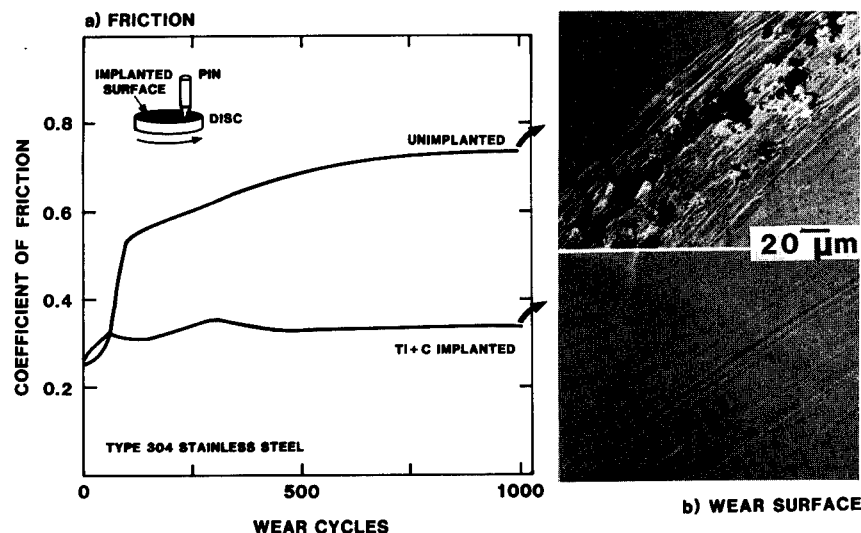


Figure 1. a) Friction traces for 440C pin with 12 g load on 304 disks, unimplanted and implanted with 2×10^{17} Ti/cm², 180-90 keV, plus 2×10^{17} C/cm², 50 keV. b) Scanning electron micrographs of the corresponding wear tracks.

General Features of Ion-Implanted Metals

Ion implantation has several advantages over other surface treatments, as well as some disadvantages. A major advantage is that any element can be introduced into any material, often to high concentrations (10's of atomic percent), independently of usual thermodynamic alloying constraints; thus metastable concentrations and phases are often achieved. In several aspects, implantation is superior to coatings for tribological improvements: 1) it can be done at room temperature, thus avoiding unwanted microstructural changes in the substrate which might occur with heating, such as during carburizing; 2) no significant dimensional changes occur in the component; and 3) there is no interface between the treated layer and substrate. The ions are accelerated to 10's or 100's of keV and penetrate the surface to produce a gaussian-like composition profile within the material. Thus adhesion of the modified layer is not a problem.

However, ion implantation has two serious disadvantages: 1) high cost, and 2) shallow treated depth, $\leq 1 \mu\text{m}$, and often only $\sim 0.1 \mu\text{m}$. For these reasons, applications are limited to critical components (expensive to make or replace) and to relatively mild wear regimes. Among components being commercially treated are cutting tools, dies [4], refrigeration pistons [5], ball bearings [6], and knee and hip-joint prostheses [5].

Another possible limitation is that incident ions sputter atoms from the material, which limits the maximum implanted atom fraction to about $1/S$, if S atoms are sputtered per incident ion, assuming $S > 1$ [7]. The concentrations needed to improve mechanical properties are generally 10's of atomic percent; these are readily achievable for light metalloids like B, C, or N in steels (up to 70 at.% C in Fe), but require high implanted fluences ($> 10^{17}$ atoms/cm²). However, heavier species like Ti give increased sputtering; at high fluences the surface concentration rises and the atomic fraction from the surface to the ion range approaches $1/S$. Such a profile is shown in Fig. 2a) for 4.2×10^{17} Ti/cm² implanted into 304 SS at 180 keV [8]. The concentration appears to be nearly sputter-limited at 40 at.% Ti, in fair agreement with $S = 2$ as evaluated for Ti implantation into 52100 steel [9].

Commonly Used Treatments

The element most often implanted to modify mechanical properties of steels is N [4,10], which reduces wear on a wide variety of steels, including low alloy steels and some stainless steels. This treatment has been applied to cutting tools and dies, and is commonly used commercially in preference to other species because intense beams can easily be obtained with the pure gas; for this reason, less expensive implantation methods which do not use magnetic isotope separation of the accelerated beam have been developed for nitrogen [11]. However, reduced friction is not usually reported for N implantation. In our tests on 304 and 15-5 PH SS, significantly lower friction was not observed [12]. Furthermore, wear was not significantly reduced for the hard bearing steels 52100 [13], 440C [14] and 100Cr6 [15]. Thus the benefits of N implantation are limited to wear reduction on softer steels.

The surface alloys formed on Fe and steels after N implantation have been examined with transmission electron microscopy (TEM) and found to be crystalline [12,16-18]. At the high fluences and concentrations often used to reduce wear (e.g., 4×10^{17} N/cm² at 50 keV, ~ 45 at.% N [12]), hexagonal Fe₂N [18] or mixed (Fe,Cr)₂N [12] was found in the implanted alloy. The formation of such interstitial phases in implanted metals has been explained by considering the atomic sizes of the metal and metalloid atoms [19]; i.e., the N atom is small enough to occupy interstitial sites in the close-packed metal sublattice.

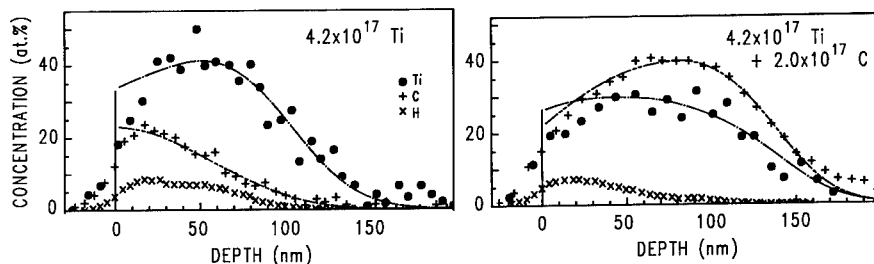


Figure 2. a) Composition profiles for 304 SS implanted with a) Ti alone, and b) Ti + C. The Ti and C concentrations were determined with 6 MeV He backscattering, while the H concentration was obtained with elastic recoil detection using 24 MeV Si [8]. H is an unimportant contaminant found at high Ti fluences.

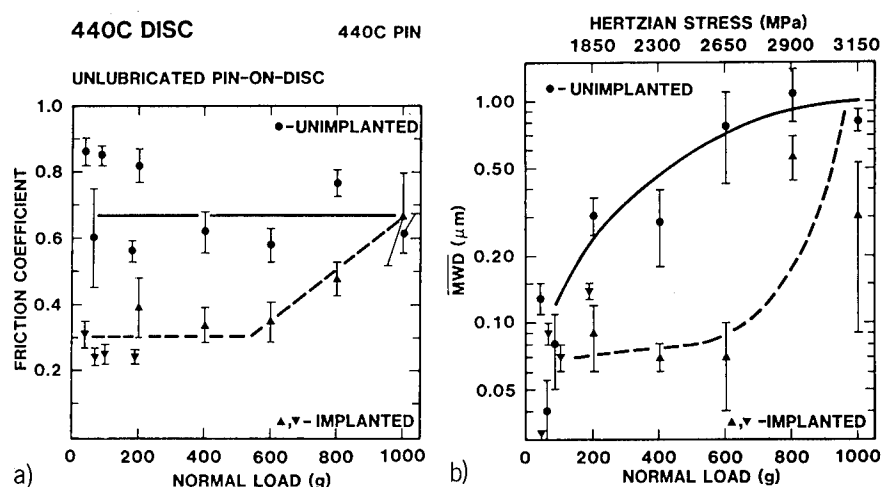


Figure 3. a) MWD and b) friction coefficient for 440C pins sliding on unimplanted and Ti + C-implanted 440C disks plotted versus pin load.

A second implantation treatment has emerged in the last decade: the dual implantation of Ti and C (Ti + C). This process gives benefits which N implantation does not: it reduces friction as well as wear, and provides these reductions for hard bearing steels [13,14,20]. This treatment produces an amorphous surface alloy, which has been found intact across wear tracks [21,22] and is thus closely associated with the benefits of Ti + C implantation. Figure 3 illustrates the reductions in friction coefficient and wear depth which we obtained for 440C (discussed below). The friction coefficients are reduced by ~ 50% and wear depths by up to ~ 90% in comparison to unimplanted values. Reduced friction and wear have been found with Ti + C implantation for all steels examined [23].

The disadvantages of ion implantation are more pronounced with the Ti + C treatment. It is more costly compared to N implantation because two species must be implanted, and Ti is more difficult to implant. Titanium ions must be generated either by plasma sputtering Ti metal, or by dissociation and ionization of TiCl_4 vapor, which results in corrosive Cl in the vacuum system. Furthermore, the resulting currents of Ti^+ are lower than those of a gaseous species. Nonetheless, Ti + C is the treatment of choice when reduced friction is needed or when bearing steels must be treated, and is being evaluated for use on the 440C ball bearings in the liquid oxygen turbopump of the U.S. Space Shuttle main rocket engine [6].

Overview

In this paper, we first summarize the tribological results and current understanding of near-surface alloys on steels implanted with Ti + C. We then review findings for other amorphous alloys formed by ion beam methods, which include implanting one of the metalloids B, C or P, as well as a newer technique: ion beam mixing of alternating layers of Fe and Ti. The Fe/Ti alloys have also been implanted with metalloids to determine if further benefits result. These results are compared to those with Ti + C for two reasons. First, we want to search for other species which give the benefits of Ti + C, but are easier to apply. Second, by examining amorphous alloys with different compositions, the separate roles played by microstructure and composition in reducing friction and wear are clarified. Detailed comparisons are possible using published results and our data on newly discovered amorphous alloys formed when 304 and 440C SS are implanted with C alone [24]. Related studies with Ni- and Co-based alloys provide supporting evidence for the conclusions drawn.

Implantation of Ti + C will be seen to be superior to other species providing reduced friction in that its benefits persist in more severe wear regimes. Thus if implantation meets the performance and economic demands of the component, then Ti + C appears to be the treatment of choice, although other elements may be useful for very mild wear applications. However, if ion beam mixing can meet the requirements, including adequate adhesion to the substrate, then a mixed Fe/Ti layer implanted with C or N may be a better choice. Ion beam mixing and a related treatment, Ion Beam Enhanced Deposition (IBED) [25], may offer similar benefits to

implantation but at lower cost; however, their application to components has not been investigated to the extent that ion implantation has.

The second aspect of our survey indicates that reduced friction is associated with the amorphous structure, since it is observed to some extent with all such alloys. In a related study summarized near the end of this paper, we have shown that oxidation during wear of the amorphous surface alloy is also a key factor in achieving the reduced friction observed in unlubricated air testing [26,27]. Thus reduced friction appears to result from oxidation of the amorphous structure in an as yet undetermined way. On the other hand, the composition of the amorphous alloy determines its wear resistance and thus the duration of reduced friction as well. Significant concentrations of both Ti and either C or N are essential to sustaining the benefits during extended wear under heavy contact stresses.

STEELS IMPLANTED WITH Ti + C

Ion implantation of Ti + C has been shown to reduce friction and wear for all steels tested to date, which cover a wide range of hardnesses and compositions, including stainless and non-stainless steels [23]. Furthermore, the steels include different phases: ferritic (bcc), austenitic (fcc) and martensitic (bct). Similar results have been observed by a number of investigators [3,13,20,28] and are thus widely accepted.

Friction and Wear of Stainless Steels

At Sandia National Laboratories, we have investigated four stainless steels implanted with Ti + C: 440C, Nitronic 60, 15-5 PH and 304, with Knoop hardnesses from 789 to 180, in that order. An unlubricated pin-on-disk configuration [3] was used to test implanted steels in laboratory air with a nominal relative humidity of 35%. The disks were mechanically polished to a surface roughness of less than $0.05\text{ }\mu\text{m}$. The 8.28 mm long pins were hardened 440C unless otherwise noted, and were similarly polished to a 0.79 mm radius. The disks were rotated at 54 rpm with the pins positioned to make tracks with diameters of 3-5 mm. The loads applied to the pins varied from 12.5 to 1000 g. Tests with a given load were run for 1000 cycles. The frictional force on the pin was measured continuously with a load cell and normalized to the applied load to obtain the coefficient of friction (see Fig. 1). During the first ~ 100 cycles, the coefficient increases from an initial low value to one believed characteristic of the two wear surfaces after extended sliding contact. To summarize friction results, values at the end of 1000 cycles are plotted versus load, as in Fig. 3a). Wear is quantified by measuring the greatest depth of the wear track at four positions with a profilometer and averaging to obtain the mean Maximum Wear Depth (MWD).

Figure 3 shows a) friction coefficients and b) MWD as a function of applied load for unimplanted 440C disks and disks implanted with $2 \times 10^{17}\text{ Ti/cm}^2$ (180-90 keV) followed by $2 \times 10^{17}\text{ C/cm}^2$ (50 keV) [14]. At loads $\leq 600\text{ g}$, both friction and wear are significantly lower for disks implanted with Ti + C than for unimplanted disks; the friction coefficient is reduced by $\sim 50\%$ to 0.3, and the MWD by up to $\sim 90\%$ to $< 0.1\text{ }\mu\text{m}$. The wear tracks on 440C show a change from adhesive to abrasive wear with implantation, like that seen in Fig. 1 for 304. The calculated Hertzian stresses of the loaded pin on the disk are also indicated in Fig. 3. Benefits persist through 1000 cycles for loads up to 600 g, where the Hertzian stress (2650 MPa) is 40% greater than the yield stress of bulk 440C at maximum hardness (1840 MPa). Obtaining benefits at such high stresses is important because ball bearings operate near their yield stress. Note that the loss of reduced friction correlates with the increase in wear depth to $\sim 1\text{ }\mu\text{m}$, which is typical of unimplanted steel and greatly exceeds the implanted layer thickness. Furthermore, compositional analysis indicates that the Ti is gone from the center of such tracks [14,21]. Thus the loss of benefits corresponds to wearing through the amorphous layer.

Similar benefits which disappear with increasing applied load were observed for the other stainless steels, and even for pure Fe [3]. Shown in Fig. 4 are MWD values for 304. Although the loads are lighter, friction and wear are found to be reduced for Hertzian stresses up to 1100 MPa, which is 3.5 times the yield stress and indicates significant durability of the implanted layer. The amorphous layer has been observed intact across wear tracks [21] and indentations [29], which indicates that it is ductile and able to conform to undulations produced when the soft 304 substrate is deformed under high contact stresses.

Microstructure Analysis

The surface alloy produced by implanting Ti + C into Fe alloys is a ternary amorphous phase requiring both Ti and C, $\text{Fe}(\text{Ti},\text{C})$. Its composition limits have been determined in pure Fe [30]; e.g., for 20 at.% Ti, $> 4\text{ at.}\%$ C is required. The implantation treatment discussed for 440C gives $\sim 20\text{ at.}\%$ Ti and $\sim 20\text{ at.}\%$ C, and all the steels so implanted have been found to be

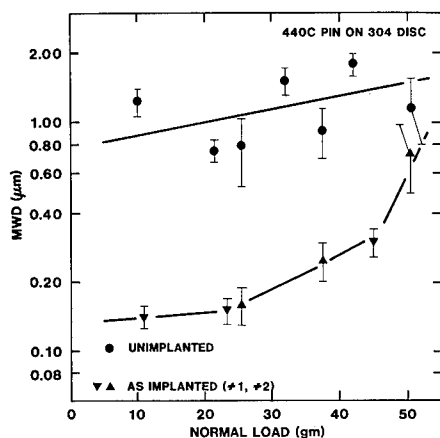


Figure 4. (left) MWD for 440C pins sliding on unimplanted and Ti + C-implanted 304 disks.

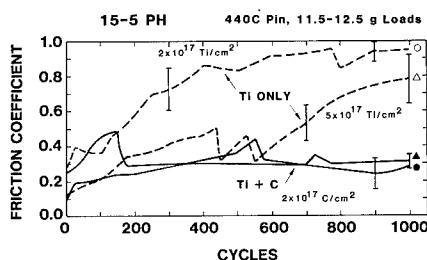


Figure 5. (above) Friction traces for 440C pins with 12.5 g load on 15-5 PH for two Ti fluences, each with and without subsequent C implantation.

amorphous [22]. Although higher Ti concentrations can be obtained (see Fig. 2), ion implantation has not achieved the 50 at.% Ti apparently needed to produce the binary amorphous Fe-Ti phase [31]. Thus both Ti and C are required to form the amorphous phase in ion-implanted alloys. This requirement can be understood in light of Auger electron spectroscopy [20] and electron energy loss spectroscopy (in TEM mode) [32] studies of atomic bonding. Examinations of signal shapes from both Ti and C indicate that the two elements are binding to each other in the amorphous phase; such bonded atoms, perhaps paired as "TiC molecules", apparently destabilize the bcc lattice and produce the amorphous structure.

It is important to note that implantation of Ti into Fe and steels also incorporates some C into the implanted alloy at the surface [13,33,34], even for relatively high vacuums of $\leq 2 \times 10^{-6}$ torr. Such C can be seen in Fig. 2a) for 304 SS implanted with only Ti. The source of the C has been shown to be residual carbonaceous molecules in the implantation vacuum, as demonstrated with experiments using CO_2 labeled with ^{13}C [35]. This incorporated C accounts for the reductions in friction and wear achieved with the implantation of Ti alone [13,20]. However, the benefits are of more limited duration, since the incorporated C extends only through about the first half of the Ti profile. Furthermore, friction testing indicates that once the surface C layer is worn through, the deeper "uncarburized" metal with implanted Ti adheres more strongly to the pin [20]. Thus in Ti-implanted steels, the presence of C is critical to obtaining the amorphous layer and tribological benefits.

To demonstrate the effects of implanting additional C, we did two studies. First, Ti was implanted at 180 keV into pure Fe, and the thickness of the amorphous layer was determined by ion channeling to be 58 nm [30]. After implanting additional C at 50 keV, the thickness increased to 103 nm; depth-profiling showed that most of the Ti was then included in the amorphous layer. The amorphous layers were imaged in isolation from the substrate with TEM, which also indicated that the thickness increased with C implantation. Second, samples of 15-5 PH were implanted with Ti alone, and with the same implantations of Ti followed by C [36]. Identical tests were done on both sets of samples so that one-to-one comparisons could be made between results obtained with and without implanted C. In nine out of ten such comparisons, samples with additional implanted C showed low friction for a greater number of cycles than when only Ti was implanted; two pairs of the friction traces demonstrating this extension of benefits are shown in Fig. 5.

The importance of having both Ti and C present at the same depths led us to develop methods to depth profile both species in steel substrates with heavier Fe, Cr and Ni atoms [8,30]. Using 6 MeV He backscattering, depth profiles of implanted species can be obtained with ~ 10 nm resolution. Figure 2b) shows that 180 keV Ti implantation followed by 50 keV C implantation gives overlapping profiles as required for maximum duration of benefits. We have recently found that the amorphous phase can also be formed by implanting C before Ti into stainless steels [8]; this is consistent with our discovery that such steels are amorphized after C implantation alone (discussed below) [24]. Implanting Ti after C gives higher Ti contents since less of it is removed by sputtering [8]; however, the C energy should apparently be increased from 50 keV to 70 or 80 keV to give overlapping profiles.

We have found that high fluences of Ti ($3.4\text{--}5 \times 10^{17}$ Ti/cm 2 , 180 keV) in 304 and 15-5 PH SS produce TiC precipitates embedded in the amorphous layer [8]. Such precipitates were not observed in 52100 steel [20] with only 1.5 at.% Cr, and the higher Cr content (18 at.%) of

the stainless steels is believed to have induced the precipitation. The TiC lattice constant suggests that Cr is incorporated into the precipitates. A remaining question is whether high Ti fluences and the associated carbides further enhance the benefits beyond those of lower fluences adequate to form the amorphous phase. The work with 15-5 PH [36] (see Fig. 5) suggests that higher fluences do extend the benefits, but additional testing is needed to confirm this.

Co and Ni Alloys

The implantation of Ti + C has been shown to form amorphous layers and provide benefits in other alloys based on Co and Ni. A commercial Co alloy, Stoody 3 (Co-31Cr-12.5W-2.2C, in wt.%), which consists of several carbide structures in a (metastable) fcc matrix [37], was implanted with 5×10^{17} Ti/cm² at 190 keV. The Ti implantation produced a vacuum-carburized surface layer as on steels [38], and the matrix was found to be amorphized by the Ti and C [37]. This treatment reduced the friction coefficient from 0.6 to 0.2 during unlubricated sliding against a 52100 steel ball [39], and the wear scar was significantly reduced. In addition, the resistance to cavitation erosion was improved [40]. The implantation of Ti + C amorphizes chemical-vapor-deposited Ni as well [41]. The results with Fe and Co alloys suggest that this treatment will reduce friction and wear in Ni alloys also.

ION BEAM MIXING

Another method to form metastable surface alloys with ion beams has emerged in the last decade, and has recently been used to improve tribological properties. Ion beam mixing intermixes two elements deposited in alternating layers by ion irradiating them to form a homogeneous binary alloy [42]. This method offers two advantages over ion implantation. First, the concentration is determined by the relative thicknesses of the elemental layers, and is not limited by sputtering. Second, lower ion beam doses are required, which reduces the cost of treatment. The irradiation can also intermix the alloy layer with the substrate to increase its adherence. However, ion beam mixing of components has been studied less than ion implantation. Like implantation, ion beam mixing displaces many atoms and forms metastable phases; thus we can compare the properties of similar alloys formed by the two methods. The comparison of results with Fe/Ti alloys, along with subsequent C implantation of the layer, offers new insight into how implantation of Ti + C reduces the friction and wear of steels.

Ion Beam Mixing of Fe/Ti

Hirvonen and coworkers have investigated the ion beam mixing of Fe/Ti layers with varying concentrations of Ti [31,43-46]. Typically, five layers each of Fe and Ti were deposited in a vacuum of 2×10^{-7} torr for total thickness of 100 nm; the outermost layer was Fe [43]. The layers were irradiated with 600 keV Xe⁺⁺ to a fluence of 8×10^{15} Xe/cm² in a vacuum of 5×10^{-7} torr. This energy is sufficient for the inert Xe to pass through the surface layers and intermix them with the substrate, which increases their adhesion. In microstructure studies [31], a supersaturated solid solution of Ti in bcc Fe was found for up to 30 at.% Ti. At 50 at.% Ti, an amorphous phase formed. A binary metallic amorphous alloy is expected based on the observed amorphization of crystalline FeTi (B2, like CsCl) during ion irradiation [47]. Thus at this high Ti concentration, which has not been attained with implantation, C is no longer necessary to stabilize the amorphous phase.

Similar Fe/Ti layers were ion beam mixed on 304 SS, and the friction of 3.13 mm diameter balls sliding on them was monitored. Friction was highest for Ti-rich layers, lower for < 50 at.% Ti, and lowest near 50 at.% Ti when tested with hardened Cr balls [44,46]. When layers with 48 at.% Ti were tested using ceramic balls with a load of 16.8 g, the coefficient was reduced from the unimplanted value of 0.7 to 0.3 for ~ 200 cycles [43], as seen in Fig. 6. Increasing the load to 33.5 or 50.3 g reduced the duration of low friction. The wear tracks on the ion mixed layer consisted of smooth grooves instead of the adhesive wear surface of untreated 304. The Hertzian stresses in these tests (estimated to be 520-830 MPa for 16.8 g) are like those for which benefits are found for 304 implanted with Ti + C (Fig. 4); however with implantation, benefits persist for more than 1000 cycles (Fig. 1) [22,48].

C Implantation of Fe/Ti

The effects of metalloid implantation on the properties of the ion mixed layer with 48 at.% Ti were also examined [43,45]. After implantation of 3×10^{17} C/cm² at 50 keV, the friction coefficient with the ceramic ball is seen in Fig. 7 to be reduced to ~ 0.3 for 1000 cycles for 16.8, 33.1 and 50.3 g loads, with stresses as high as those used for 304 in Fig. 4. Wear tracks again indicated much less adhesion than those on untreated 304. The microstructure of the

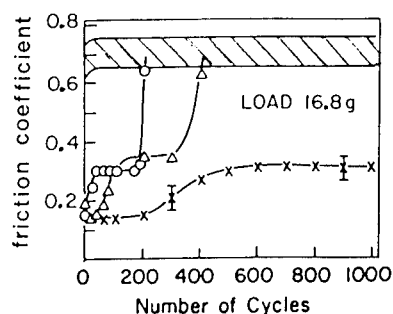


Figure 6. (left) Friction coefficient versus cycles for ceramic balls and Fe/Ti layers on 304: (o)-mixed with 600 keV Xe, (Δ)-mixed and implanted with 1.7×10^{17} N/cm², 50 keV, and (x)-mixed and implanted with 3×10^{17} N/cm², 50 keV [43]. Dashed band represents values for untreated 304.

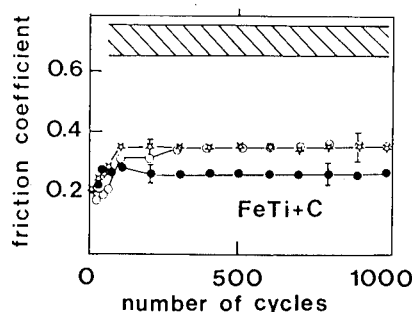


Figure 7. (right) Friction coefficient versus cycles for ion beam mixed Fe/Ti layers implanted with 3×10^{17} C/cm², 50 keV, for pin loads of (o)-16.8 g, (x)-33.5 g, and (●)-50.3 g [45]. Dashed band represents values for untreated 304.

C-implanted Fe/Ti has been examined with TEM and found to consist of fine carbides in an amorphous matrix [49]; thus the comparison of results with and without implanted C is between two amorphous alloys. It is clear that the C content of the amorphous layer plays a significant role in its ability to resist being abraded away. Since Ti is very reactive and was not deposited nor irradiated under UHV conditions, some C may have been incorporated during deposition and mixing. Nonetheless, the dramatic increase in duration of benefits clearly indicates that C is an important component of low-friction, wear-resistant, amorphous Fe(Ti,C) surface alloys. While C is necessary to stabilize the amorphous phase in implanted alloys, we infer that it plays a key role in the mechanical properties as well.

N IMPLANTATION OF BINARY ALLOYS WITH Ti

In this section, we show that another metalloid, N, can be used in place of C in alloys with Ti to reduce friction and wear and to extend the duration of benefits. Some alloys with Ti and N are amorphous like those observed with C, while others are crystalline and thought to exhibit reduced friction because of a large volume fraction of TiN, which is known to give low friction as a deposited surface layer [25].

Fe-Ti

The amorphous Fe/Ti alloys formed by ion beam mixing were also implanted with 3×10^{17} N/cm² at 50 keV [43,45], and the duration of reduced friction and wear was again extended beyond that for Fe/Ti alone, as clearly demonstrated in Fig. 6. However, the duration with N was not always for as long as achieved with C; for instance, with a 50.3 g load, benefits persisted for 500 cycles with N, but for > 1000 cycles with C. In addition, alloys implanted with 1.7×10^{17} at/cm² of both N and C gave results similar to the alloys implanted with 3×10^{17} C/cm². Thus N can apparently be substituted for C in this alloy to give similarly extended benefits. The extended low friction with N implantation contrasts with results obtained with 15-5 PH SS implanted with Ti and N, for which wear was reduced, but not friction [32]. However, there are some key differences in composition and microstructure between these two alloys, which may explain the differing results.

In the implantation study [32], pure Fe was implanted with Ti followed by N to produce peak concentrations of ~ 20 at.% Ti and 27 at.% N. While a thin amorphous alloy with some incorporated C was found just below the surface, the microstructure at depths of the peak Ti and N concentrations consisted of fine (5-10 nm) TiN precipitates in the bcc Fe matrix. This microstructure is like that of 304 SS which was first amorphized by implanting Ti + C, and then devitrified by annealing 15 min. at 650°C: fine TiC particles in a matrix of metallic bcc and fcc Fe-based alloys [48]. Assuming that the bcc 15-5 PH steel implanted with Ti and N also had fine TiN precipitates, its friction and wear results are consistent with our hypothesis that

the bcc and fcc phases must be amorphized to reduce friction. Although single-phase TiN surfaces also give low friction [25], the dominant constituent (by volume fraction) in the surface alloy on 15-5 PH is the bcc phase, which adheres to the pin and gives high friction. The hard TiN particles in 15-5 PH and the TiC particles in the devitrified alloy on 304 are presumably responsible for the reduced wear observed in these alloys.

In contrast, the Ti concentration of the ion beam mixed alloy was much higher before N implantation [43,45]: 50 versus 20 at.%. The mixed Fe/Ti alloy was also amorphous, instead of crystalline bcc as for Ti-implanted Fe, and this initially amorphous structure may have caused the alloy to remain amorphous after N implantation. The possibility of an amorphous Fe(Ti,N) phase is supported by the finding of a similar amorphous structure when the phase NiTi is implanted with N (below) [50], and by the fact that both Fe and Ni-based alloys are similarly amorphized by Ti + C implantation, as discussed above. The N implantation may have induced some TiN precipitation, but even then the matrix might still be amorphous, as in the cases of C-implanted Fe/Ti [49] and TiC precipitation in stainless steels implanted with high concentrations of Ti [8,14,27]. An amorphous Fe(Ti,N) alloy with embedded TiN precipitates is expected to reduce friction and wear by analogy to Fe(Ti,C).

If TiN precipitation destabilized the amorphous structure and formed a two-phase alloy of TiN + bcc Fe, the high concentrations of Ti and N would produce a large volume fraction of TiN in the layer, which could give a low-friction wear surface [25]. The mixed and implanted Fe(Ti,N) alloy had nearly equal atomic fractions of Fe, Ti and N, which would result in a greater volume fraction of TiN ($> 1/2$) than found in the Fe or 15-5 PH implanted with Ti and N. Such a crystalline microstructure was found for PdTi and PtTi alloys deposited on 304 SS and implanted with N [51,52]. Although N extended the benefits found with the binary amorphous, as-deposited PdTi and PtTi alloys, it also crystallized them into TiN and fcc Pd or Pt. A high fraction of TiN presumably accounts for the low friction of these surface alloys.

Ni-Ti

Moine et al. [50] have investigated the unlubricated friction and wear of NiTi alloys before and after N implantation. The same trends were observed for alloys with the B2 structure as well as the martensitic structure (distorted B19) for near-equiatomic compositions. These phases, like FeTi (B2), become amorphous after low dose irradiation with any species [47,53]. The friction coefficient for a spherical bearing steel ball on untreated alloys rose to ~ 1 after about 10 cycles, with a large "stick-slip" amplitude (± 0.4). Significant improvements were found with 160 keV N⁺ implantation and increased with fluence: friction was reduced to < 0.2 and remained low for 500 cycles (10^{16} N/cm²), 1500 cycles (10^{17} N/cm²) and $> 10,000$ (3×10^{17} N/cm²). The stick-slip variations were also greatly reduced. Thus the system behaves like Fe-Ti by performing better with increasing N fluence, and supports the important role identified for metalloids. All the implanted alloys were confirmed to be amorphous.

Two other results from this study are noteworthy. First, Ne implantation did not give any improvement even though the alloy was amorphous. While this result differs with that for ion beam mixed Fe/Ti, it dismisses the possibility of the benefits being artifacts of ion implantation, and confirms the importance of N. Second, when an alloy with 10^{17} N/cm² was annealed at 550°C to crystallize it, the benefits of implantation were lost: the period of low friction dropped from 1500 to 70 cycles. The higher energy and lower fluence relative to that for N-implanted Fe/Ti (above) give a much lower peak concentration of ~ 16 at.% N. This results in a lower volume fraction of TiN, more like that for Fe implanted with Ti and N, thus accounting for the increased friction after crystallization. All the findings together indicate that a Ni-based amorphous phase with both Ti and N gives low friction and increasingly resists being worn away with greater N concentrations.

IMPLANTATION OF METALLOIDS

In this section we examine the friction and wear of steels and Ni after implantation with C, B or P; results with N were summarized above. Boron and P are known to form amorphous phases in Fe alloys, and we report below our discovery that C implantation amorphizes 304 and 440C SS, instead of forming carbides as for pure Fe. The C-implanted steels offer a direct comparison to alloys implanted with both Ti and C: the low friction found with C alone does not persist for as long as with Ti + C, indicating that the amorphous layers without Ti are more readily worn away. Amorphous alloys with P and P + C are also more readily worn away. Implanting B into 440C gives significant benefits, but not to the extent observed for Ti + C. All the results together suggest that reduced friction is associated with the amorphous structure, but wear resistance is determined by composition.

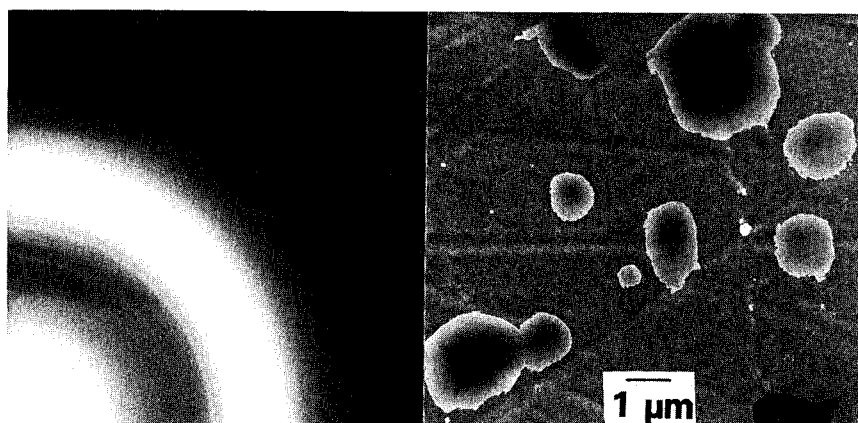


Figure 8. a) Electron diffraction pattern from the surface layer on 440C implanted with 2×10^{17} C/cm², 30 keV: diffuse rings - amorphous metal, sharp rings - surface Fe₃O₄, and isolated spots - M₂₃C₆ carbides. b) Bright-field TEM image of the amorphous layer with amorphized carbides (light areas) and thick carbides (dark areas) suspended on it.

C Implantation

Shown in Fig. 8a) is an electron diffraction pattern from a free-standing amorphous surface layer on 440C SS implanted with 2×10^{17} C/cm² at 30 keV. The radii of the diffuse rings are essentially the same as for amorphous Fe alloys with both Ti and C [20]. The bright-field micrograph in Fig. 8b) shows the free-standing amorphous surface layer; large M₂₃C₆ carbide precipitates in the original 440C structure were not readily removed by electropolishing, and some remain suspended on the layer (dark areas). We have also found amorphous layers on 304 SS implanted with C. This amorphous structure is quite obviously different from the crystalline Fe₂C (hexagonal) observed when pure Fe is implanted with up to 49 at.% C [44]. An amorphous phase was even less expected since N forms the analogous crystalline compound Fe₂N when implanted into pure Fe [22], 304 [12] or 15-5 PH SS [16]. The additional elements in the stainless steels apparently stabilize the amorphous phase; in particular, Cr (~ 18 at.%) may bind to C just as Ti does. We are currently examining the microstructures of Fe(Cr) alloys implanted with C to check this hypothesis.

The friction and wear properties of C-implanted 440C were examined for three fluences: 1.2, 2.0 and 3.0×10^{17} C/cm², at 30 keV. Depth profiles for these treatments are shown in Fig. 9, with corresponding peak concentrations of 27, 37 and 51 at.% C. The plateau beyond 150 nm is due to the 4 at.% C present in bulk 440C SS. For the intermediate-fluence alloy, shown to be amorphous in Fig. 8, reduced friction (≤ 0.3) persisted for 1000 cycles in two of the four tests with a 25 g load, as shown in Fig. 10. Tests with 12.5 g loads gave low friction for 1000 cycles, while 50 g loads gave reductions only for ~ 250 cycles. Higher loads did not show clear evidence of reduced friction. Thus 25 g is believed to characterize the load-carrying ability of this implanted alloy. The low-fluence alloy showed no benefits. The high-fluence alloy showed a lesser but consistent reduction in friction from 0.8 (unimplanted) to 0.4-0.5 for loads up to 50 g. The lesser reduction with the high-C alloy is not yet understood.

The wear tracks on the intermediate-fluence alloy were examined with depth profilometry. For the tests which exhibited reduced friction for the entire 1000 cycles with 12.5 and 25 g loads, the MWD's were ≤ 0.03 μm. These tracks showed no indication that the C-implanted layer (~ 0.09 μm thick) was worn through. The wear topography was very different at higher loads and for the two tests exhibiting high friction with 25 g loads after 1000 cycles. Profilometry showed a significant buildup of material in the tracks which apparently was transferred from the pins to the disk; the pins from such tests were indeed found to be more worn. In some areas of the high-friction tracks, wear depths greater than the implanted depth were found. We infer that in these tests the amorphous surface layer was worn through, allowing pin material to adhere to the substrate and collect in the wear track.

While benefits can be clearly established for the implantation of C alone, the maximum applied load is much less than that for Ti + C: 25 g versus 600 g, with corresponding maximum Hertzian stresses of 900 MPa versus 2700 MPa. The two surface alloys on 440C had very

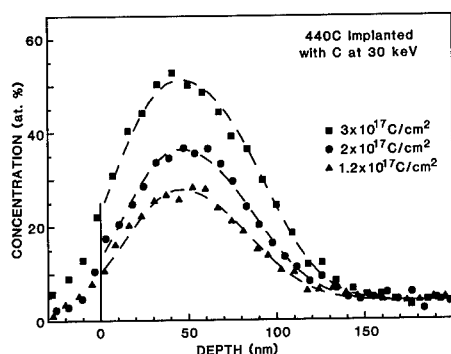


Figure 9. (left) Depth profiles for C-implanted 440C.

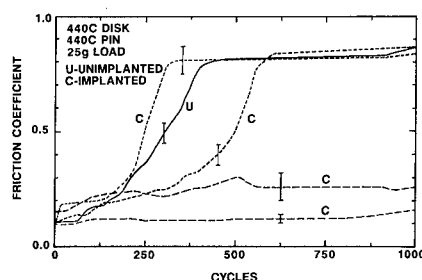


Figure 10. (right) Friction traces for 440C disks implanted with $2 \times 10^{17} \text{ C/cm}^2$ at 30 keV, obtained with 440C pins and 25 g load (dashed). The reference trace (solid) from an unimplanted disk is denoted with U.

similar implanted depths, 90 nm for C (Fig. 9) and ~ 100 nm for Ti + C [55], so that direct comparison indicates differences in mechanical properties of the implanted layers, and not thickness. These results and those on ion mixed and implanted layers indicate that the mechanical properties of amorphous Fe(Ti,C) phases are superior to amorphous Fe phases with either Ti alone or C alone, and that Ti and C are of comparable importance in producing the tribological benefits of the ternary amorphous phase.

Pure Ni has also been implanted with C and the friction and wear of the surface alloy characterized by Nastasi et al. [56]. A fluence of $4.2 \times 10^{17} \text{ C/cm}^2$ implanted with 35 keV C^+ at room temperature was found to reduce the friction coefficient from 0.6 to 0.5 in testing against hardened Cr steel balls 3.13 mm in diameter with a 16.8 g load. The phase of the room-temperature implanted alloy was metastable hexagonal Ni_3C . It is notable that implanting at 77 K instead formed an amorphous alloy with the same C fluence, and that friction was further reduced to 0.4. Thus while friction was somewhat reduced with the crystalline microstructure, the amorphous structure is preferred.

P and P + C Implantation

We have previously investigated the friction and wear properties of 304 and 15-5 PH SS implanted with P and P + C [57]. The P was implanted to $1.4 \times 10^{17} \text{ P/cm}^2$ at 100 keV to produce a surface layer ~ 150 nm deep with up to ~ 22 at.% P. Examination with TEM showed that 304 implanted with P had only a partially amorphous surface layer. The steels were also implanted with this dose of P followed by $1 \times 10^{17} \text{ C/cm}^2$ at 40 keV to produce overlapping P and C profiles with a total metalloid content of ~ 30 at.%; this treatment produced fully amorphous surface alloys on both steels.

Although both treatments reduced friction for the two steels during some tests, the benefits were of short duration and limited to light loads. Figure 11 shows several friction traces obtained for 15-5 PH. Implantation of P reduced friction for < 500 cycles at the light load of 12.5 g; P + C increased the duration, but not always to 1000 cycles. Benefits could not be identified at higher loads. For both steels, the results with either treatment were judged to be inferior to the Ti + C treatment. For example, in Fig. 5 reduced friction with Ti + C is shown to persist for 1000 cycles with the same test conditions, and such benefits are also observed at higher loads. The MWD values (in μm) are also given in Fig. 11; note in a) that wear depths $> 1 \mu\text{m}$ are found for the traces not showing reduced friction at the end of 1000 cycles, while the test with sustained low friction also has an MWD ($0.24 \mu\text{m}$) comparable to the implanted thickness. This correlation is consistent with associating reduced friction with the presence of an amorphous layer, and its loss with the layer being worn through. The P and P + C layers are then inferred to wear away faster than the Ti + C layer.

B Implantation

Hirano and Miyake [58,59] have examined the friction and wear of 440C implanted with $1.8 \times 10^{17} \text{ B/cm}^2$ at 40 keV. The unlubricated tests used a 440C ball of diameter 6.35 mm. The friction coefficient was reduced from 1.0 to 0.2, but the reduced value persisted for only

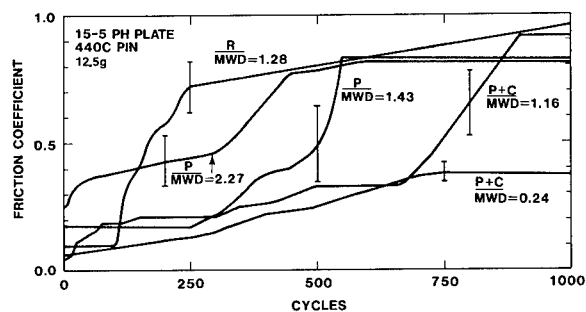


Figure 11.
Friction traces obtained with 440C pins and 12.5 g load on 15-5 PH disks: R-unimplanted reference, P and P + C-implanted.

~ 200 cycles for the ~ 100 nm implanted layer with < 10 at.% B. The wear scar was also reduced. We calculate a Hertzian stress of 980 MPa for this test. Thus the B-implanted layer also appears to wear away more quickly than Ti + C layers, which sustain higher contact stresses (2650 MPa). However, the implanted concentration, ~ 10 at.% B, is relatively low for a fully amorphous layer, and the benefits of B implantation might be enhanced with higher doses.

The microstructure and hardness of B-implanted Fe have been examined for a higher fluence, 4.55×10^{17} B/cm², implanted at 90 keV. However, this study [60] used a high beam current (100 μ A/cm²) and input power to the sample (9 W/cm²). For implantation at 40 and 300°C, x-ray diffraction showed that crystalline Fe₂B formed, but for implantation at -20°C, the reflections were broadened, indicating greater disorder. The B-implanted Fe was found to be harder than pure Fe, with the greatest increase (~ 10x) for -20°C. Other work examining Fe implanted with B at lower power (0.2 W/cm²) found an amorphous surface layer [19,61]. The friction and wear studies discussed above were done with 0.5 W/cm², for which an amorphous phase is expected to form. The hardness study then implies that the reduced friction of B-implanted 440C SS resulted from a hard amorphous phase.

Boron-implanted Ni has also been found to have a somewhat reduced friction coefficient (< 0.4) relative to that of unimplanted Ni (0.5) [62]. Based on other work, an amorphous surface alloy is again expected to have been formed [19].

FURTHER PROPERTIES OF AMORPHOUS Fe(Ti,C)

Oxidation During Wear

With the optimum microstructures and compositions identified, we turn to understanding how friction and wear are reduced. The benefits obtained in air are closely related to oxidation during sliding contact [26,27]. Friction coefficients obtained on 304 SS implanted with Ti + C are lower when tests are run in air or a partial pressure of O₂ (2.1×10^{-5} Pa, or 1.6×10^{-7} torr) than in ultra-high vacuum ($< 4 \times 10^{-7}$ Pa) or pure N₂; the reductions in wear depth show the same trend. The wear tracks made in air or O₂ had increased oxygen, and TEM indicated that the phase was hexagonal (Cr,Fe)₂O₃. The friction remained low until the end of the O₂ test, which implies that this oxidized surface was responsible for low friction.

Similar oxidation effects have been found by Hirano and Miyake for B-implanted 440C [59] and Fe [63]. During unlubricated sliding in air, B-implanted specimens had a high electrical contact resistance with the pin during the initial low-friction part of the test. With continued wear, the friction increased, and the contact resistance dropped. Low electrical resistance was also found for unimplanted specimens. A high friction coefficient (1.2) was observed for B-implanted Fe tested in high vacuum (5×10^{-4} Pa), which decreased after introducing O₂ (5×10^{-1} Pa). These authors conclude that B implantation gives benefits by promoting an insulating Fe₂O₃ wear surface which does not readily spall off the hardened B-implanted ferrous materials. Thus oxidation appears to play similar roles in the tribology of amorphous surface alloys implanted with B or Ti + C. Additional investigation is needed to determine how such oxidized surfaces reduce friction and wear.

Hardness

We believe another feature of amorphous Fe(Ti,C) is also important for its improved tribological performance: increased hardness. This increase can be inferred from the improved benefits found during sliding abrasive wear of implanted steels, but is more directly indicated

by other studies. The microhardness in the near-surface of 52100 steel was investigated using an indenter capable of resolving hardness changes within implanted layers [64]. When 2×10^{17} C/cm² was implanted at 40 keV followed by 5×10^{17} Ti/cm² at 190 keV, an ~ 50% increase in hardness relative to that of 52100 bearing steel was found at a depth of ~ 40 nm. Since indentation is influenced by the softer substrate, the amorphous layer may in fact be even harder. Implanted surfaces with lower Ti fluences or with only implanted Ti did not show increased hardness, presumably because the amorphous layer did not have optimum composition, or was too thin to be detected. Increased hardness is also indicated by abrasive wear tests using diamond-particle polishing. The wear resistance was found to be increased by 6x for 52100 implanted with 4.6×10^{17} Ti/cm² at 190 keV, and by 10x for 304 [66]. In such tests on unimplanted steels, wear resistance increased with hardness, which implies that the reduced wear of Ti-implanted 52100 reflects a harder amorphous surface layer.

Another indication of the hardness of amorphous Fe(Ti,C) comes from studies of melt-quenched amorphous Fe_{70-x}M_xMo₁₂C₁₈ alloys [67]. When a carbide-forming element (M) replaced Fe, the hardness increased roughly linearly with x. Titanium was especially effective, and produced a significant increase (from $H_V = 920$ to 1030 DPN) for only 2 at.% Ti. Amorphous C-implanted steel can thereby be inferred to increase in hardness when Ti is also implanted, which would improve performance just as we observe. We suggest that implanting C into amorphous Fe/Ti layers increases their hardness also.

Recent analyses by Singer [68] and by Hubler [2] have examined the load-carrying capability of implanted materials. Using reported stress levels obtained by finite-element analysis of ductile metals during cyclical sliding of a pin, they developed an expression for the maximum applied load L_{max} which can slide on a plate with friction coefficient μ and hardness H without permanent deformation:

$$L_{max} = (1-\mu)^3 F(H), \quad (1)$$

where the function F increases with H . The expression indicates that higher loads can be carried when μ is smaller; decreasing μ from 0.7 to 0.3 increases the prefactor on F by more than 10x. It has been argued [2] that this change in μ accounts for the wear reduction observed at high loads on 440C implanted with Ti + C (Fig. 3). However, by comparing the results with amorphous Fe/Ti layers, C-implanted 440C, and amorphous layers with both Ti and C, the hardness function is seen to play a significant role in increasing the maximum load at which benefits of the layers persist, since this load varies greatly among these alloys, even though μ is essentially the same (0.2-0.3). It is notable that amorphous Fe(Ti,C) wears longer and is apparently harder than amorphous Fe(P,C), since Fe₈₀P₁₃C₇ and Fe₇₂Cr₈P₁₃C₇ are among the strongest metallic glasses [69].

Extensions to Other Alloys

Several extensions of the above ion beam treatments can be identified. The benefits of amorphous phases with metal-metalloid combinations are not limited to Fe(Ti,C). Other carbide formers, including Zr, Nb, Hf, and Ta, are expected to work in place of Ti; benefits have been reported with Ta [70,71]. These heavier elements are less favorable because of shallower implanted depths and increased sputtering, but may be useful because of additional benefits such as reduced corrosion [29,71]. Amorphous phases with Ti + C have been found in Co and Ni alloys; we speculate that the phase and its benefits may also be found in other metals nearby in the periodic table, such as Cu. The combination of B + Ti has been examined to a limited extent and found to give benefits in Fe but not Ni [62].

CONCLUDING REMARKS

The major findings of the above survey are: 1) amorphous surface layers give reduced friction, 2) wear resistance changes with composition of the surface alloy, and 3) the longest duration of benefits is obtained with both Ti and either C or N. These findings were well established for Fe-based steels, and found to hold in a more limited number of studies on Ni and Co alloys as well. Substituting N for C in alloys with high Ti content produces nearly equivalent performance; however the resulting microstructure may then consist of large fractions of TiN. While all amorphous alloys were found to give reduced friction, its duration varied significantly with implanted species. Alloys with Ti and either C or N showed benefits at higher loads and increased wear cycles than found with metalloids alone, or with Ti alone. It is clear that both Ti and either C or N are needed for optimum mechanical properties.

New techniques are being investigated to extend the use of surface modification treatments, in particular, to form thicker layers at reduced the cost. Treatments combining deposition with irradiation (IBED, ion beam mixing) are attractive because they overcome these

two disadvantages but retain the ability of ion beams to form adherent layers and produce metastable phases. A recent technique simultaneously applies deposition and irradiation to ball bearings [72]. A new type of implantation using a plasma discharge offers new abilities to implant irregularly shaped surfaces and to treat at lower cost [73].

Finally, new applications for ion beam treatments need to be identified. If Ti + C implantation is chosen for regular use on ball bearings in the Space Shuttle, it may encourage similar applications, like jet engine bearings. Although friction is lower in air or O₂ than in ultra-high vacuum, we have nonetheless found reductions with Ti + C in vacuum relative to unimplanted disks during testing in a newly-developed in-situ tribometer [26,27]. This finding suggests the treatment may be useful in vacuum systems for semiconductor manufacturing or in space. The implantation of cutting tools with N may have new applications; for instance, tools used to machine hazardous metals in closed environments are difficult to change, and even modest improvements in lifetime are appealing [74].

REFERENCES

1. C. R. Clayton, in Surface Alloying by Ion, Electron and Laser Beams, eds. L. E. Rehn, S. T. Picraux and H. Wiedersich (ASM, Metals Park, Ohio, 1987), p. 325.
2. G. K. Hubler, in Surface Alloying by Ion, Electron and Laser Beams, eds. L. E. Rehn, S. T. Picraux and H. Wiedersich (ASM, Metals Park, Ohio, 1987), p. 287.
3. L. E. Pope, F. G. Yost, D. M. Follstaedt, J. A. Knapp and S. T. Picraux, in Wear of Materials 1983, ed. K. C. Ludema (ASME, New York, 1983) p. 280.
4. J. K. Hirvonen, Mat. Res. Soc. Symp. Proc. **27**, 621 (1984).
5. P. Sioshansi, Mat. Sci. Eng. **90**, 373 (1987).
6. L. Ng and Y. Naerheim, 1987 Ball Bearing Technical Symposium, Orlando FL, 1987.
7. Z. L. Liao and J. W. Mayer, J. Vac. Sci. Tech. **15**, 1629 (1978).
8. D. M. Follstaedt, J. A. Knapp and L. E. Pope, submitted to Nucl. Inst. Meth. B.
9. D. Farkas, I. L. Singer and M. Rangaswamy, Mat. Res. Soc. Symp. Proc. **27**, 609 (1984).
10. S. T. Picraux, Ann. Rev. Mat. Sci. **14**, 335 (1984).
11. A. Armini, in Industrial Heating, January 1986, p. 17.
12. F. G. Yost, L. E. Pope, D. M. Follstaedt, J. A. Knapp and S. T. Picraux, Thin Solid Films **107**, 287 (1983).
13. C.A. Carosella, I.L. Singer, R.C. Bowers, and C.R. Gossett, in Ion Implantation Metallurgy, eds. C.M. Preece and J.K. Hirvonen (TMS-AIME, Warrendale, PA, 1980) p. 103.
14. L. E. Pope, F. G. Yost, D. M. Follstaedt, S. T. Picraux and J. A. Knapp, Mat. Res. Soc. Symp. Proc. **27**, 661 (1984).
15. A. Kluge, K. Langguth, R. Ochsner, K. Kobs and H. Ryssel, Proc. IBMM88, Tokyo, Japan, June 1988, to appear in Nuclear Instruments and Methods (preprint).
16. B. L. Doyle, F. G. Yost, S. T. Picraux, D. M. Follstaedt, L. E. Pope and J. A. Knapp, Nucl. Inst. Meth. **B7/8**, 38 (1985).
17. R. G. Vardiman and I. L. Singer, Mat. Lett. **2**, 150 (1983).
18. B. Rauschenbach and A. Kolitsch, Phys. Stat. Sol. (a) **80**, 211 (1983).
19. K. Hohmuth, B. Rauschenbach, A. Kolitsch and E. Richter, Nucl. Inst. Meth. **209/210**, 249 (1983).
20. I. L. Singer, C. A. Carosella and J. R. Reed, Nucl. Inst. Meth. **182/183**, 923 (1981).
21. D. M. Follstaedt, F. G. Yost, L. E. Pope, S. T. Picraux and J. A. Knapp, Appl. Phys. Lett. **43**, 358 (1983).
22. D. M. Follstaedt, F. G. Yost and L. E. Pope, Mat. Res. Soc. Symp. Proc. **27**, 655 (1984).
23. D. M. Follstaedt, Nucl. Inst. Meth. **B10/11**, 549 (1985).
24. D. M. Follstaedt, L. E. Pope and J. A. Knapp, to be published.
25. R.A.Kant, B.D.Sartwell, I.L.Singer and R.G.Vardiman, Nucl. Inst. Meth. **B7/8**, 915 (1985).
26. L. E. Pope, D. M. Follstaedt, J. A. Knapp and J. C. Barbour, Mat. Res. Soc. Symp. Proc. **100**, 175 (MRS, Pittsburgh, 1988).
27. L. E. Pope, J. A. Knapp and D. M. Follstaedt, Thin Solid Films, to be published.
28. T. E. Fischer, M. J. Luton, J. M. Williams, C. W. White and B. R. Appleton, ASLE Trans. **26**, 466 (1983).
29. G.K.Hubler, P.Trzaskoma, E.McCafferty and I.L.Singer, in Ion Implantation into Metals, eds. V.Ashworth, W.A.Grant and R.P.M.Proctor, (Pergamon, New York, 1982), p. 24.
30. J. A. Knapp, D. M. Follstaedt and B. L. Doyle, Nucl. Inst. Meth. **B7/8**, 38 (1985).
31. J-P. Hirvonen, M. Nastasi and J. W. Mayer, J. Appl. Phys. **60**, 980 (1986).
32. D.M.Follstaedt, J.A.Knapp, L.E.Pope and S.T.Picraux, Nucl. Inst. Meth. **B12**, 359 (1985).
33. J. A. Knapp, D. M. Follstaedt and S. T. Picraux, in Ion Implantation Metallurgy, ed. C. M. Preece and J. K. Hirvonen (TMS-AIME, Warrendale, PA, 1980) p. 152.
34. D. M. Follstaedt, J. A. Knapp and S. T. Picraux, Appl. Phys. Lett. **37**, 330 (1980).
35. I. L. Singer and T. M. Barlak, Appl. Phys. Lett. **43**, 457 (1983).

36. D. M. Follstaedt, J. A. Knapp, L. E. Pope, F. G. Yost and S. T. Picraux, *Appl. Phys. Lett.* **45**, 529 (1984); erratum, **46**, 207 (1985).
37. S. A. Dillich and R. R. Biederman, *Mat. Sci. Eng.* **90**, 91 (1987).
38. S. A. Dillich and I. L. Singer, *Thin Solid Films* **73**, 219 (1981).
39. S. A. Dillich, R. N. Bolster and I. L. Singer, *Mat. Res. Soc. Symp. Proc.* **27**, 637 (1984).
40. N. V. H. Gately and S. A. Dillich, *Mat. Sci. Eng.* **90**, 333 (1987).
41. A. W. Mullendore, L. E. Pope, A. K. Hays, G. C. Nelson, C. R. Hills and B. G. LeFevre, submitted to *Thin Solid Films*.
42. J. W. Mayer, B. Y. Tsaur, S. S. Lau and L.-S. Hung, *Nucl. Inst. Meth.* **182/183**, 1 (1981).
43. J.-P. Hirvonen, M. Nastasi and J. W. Mayer, *Appl. Phys. Lett.* **51**, 232 (1987).
44. J.-P. Hirvonen, M. Nastasi and J. W. Mayer, *Appl. Phys. Lett.* **49**, 1345 (1986).
45. J.-P. Hirvonen, M. Nastasi and J. W. Mayer, *Mat. Res. Soc. Symp. Proc.* **93**, 335 (1987).
46. J.-P. Hirvonen, M. Nastasi, J. R. Phillips and J. W. Mayer, *J. Vac. Sci. Tech.* **A4**, 2997 (1986).
47. J. L. Brimhall, H. E. Kissinger and L. A. Charlot, *Rad. Eff.* **77**, 237 (1983).
48. D. M. Follstaedt, L. E. Pope, J. A. Knapp, S. T. Picraux and F. G. Yost, *Thin Solid Films*, **107**, 259 (1983).
49. M. Nastasi and J.-P. Hirvonen, unpublished results.
50. P. Moine, O. Popoola and J. P. Villain, *Scripta Met.* **20**, 305 (1986).
51. L. R. Zheng, L. S. Hung and J. W. Mayer, accepted by *J. Appl. Phys.*
52. L. R. Zheng, L. S. Hung and J. W. Mayer, accepted by *Mat. Lett.*
53. P. Moine, J. P. Riviere, N. Junqua and J. Delafond, *Mat. Res. Soc. Symp. Proc.* **7**, 243 (1982).
54. D. M. Follstaedt and J. A. Knapp, *Mat. Res. Soc. Symp. Proc.* **51**, 473 (1986).
55. D. M. Follstaedt, J. A. Knapp and P. S. Peercy, *J. Non-Cryst. Sol.* **61&62**, 451 (1984).
56. M. Nastasi, J.-P. Hirvonen, T. R. Jervis, G. M. Pharr and W. C. Oliver, *J. Mat. Res.* **3**, 226 (1988).
57. L. E. Pope, S. T. Picraux, D. M. Follstaedt, J. A. Knapp and F. G. Yost, *J. Mat. Energy Sys.* **7**, 27 (1985).
58. M. Hirano and S. Miyake, in *Proceedings of the Japan Society of Lubrication Engineers International Tribology Conference, Tokyo, 1985* (Elsevier, Amsterdam, 1985), p. 245.
59. M. Hirano and S. Miyake, *J. Tribology, Trans. ASME* **107**, 467 (1985).
60. M. Hirano and S. Miyake, *Appl. Phys. Lett.* **52**, 1469 (1988).
61. A. Ali, W. A. Grant and P. J. Grundy, *Phil. Mag.* **B37**, 353 (1978).
62. I. L. Singer and K. J. Hafterson, Naval Research Laboratory Memorandum Report 5512, January 30, 1985, Washington, D.C.
63. M. Hirano and S. Miyake, *Intl. Conf. on Ion Beam Modification of Materials*, June, 1988, Tokyo, Japan; to be published in *Nuclear Instruments and Methods* (preprint).
64. W. C. Oliver, R. Hutchings, J. B. Pethica, I. L. Singer and G. K. Hubler, *Mat. Res. Soc. Symp. Proc.* **27**, 603 (1984).
65. I. L. Singer, R. N. Bolster and C. A. Carosella, *Thin Solid Films* **73**, 283 (1980).
66. R. N. Bolster and I. L. Singer, *ASLE Trans.* **24**, 526 (1981).
67. A. Inoue, T. Iwadachi, T. Minemura and T. Matsumoto, *Trans. Jap. Inst. Met.* **22**, 197 (1981).
68. I. L. Singer, *Mat. Res. Soc. Symp. Proc.* **27**, 585 (1984).
69. T. Matsumoto and R. Maddin, *Met. Sci. Engr.* **19**, 1 (1975).
70. I. L. Singer, *Appl. Surf. Sci.* **18**, 28 (1984).
71. G. K. Hubler, I. L. Singer and C. R. Clayton, *Mat. Sci. Eng.* **69**, 203 (1985).
72. P. Sioshansi, 6th *Intl. Conf. on Ion Beam Modification of Materials*, 6/88, Tokyo, Japan.
73. J. R. Conrad, *J. Appl. Phys.* **62**, 777 (1987); J. R. Conrad, J. L. Radtke, R. A. Dodd, F. J. Worzala and Ngoc C. Tran, *J. Appl. Phys.* **62**, 4591 (1987).
74. B. Barton, private communication.

ENHANCED WEAR RESISTANCE BY COMPRESSIVE STRENGTHENING A NOVEL COMBINATION OF LASER AND ION IMPLANTATION TECHNOLOGY

H. DE BEURS AND J. Th. M. DE HOSSON

Department of Applied Physics, Materials Science Centre, University of Groningen,
Nijenborgh 18, NL-9747 AG Groningen, The Netherlands

ABSTRACT

Despite the advantages of laser processing for the production of wear resistant materials, laser surface melting results in tensile stresses because the melted layer shrinks during resolidification. These tensile stresses may lead to severe cracking of the material and to deleterious effects on the wear behaviour. Our basic idea presented in this paper is to convert the high tensile stresses in the laser melted surface into a compressive state after implantation. In general, neon implantation is not very effective in the reduction of wear rates. However, neon implantation into laser melted steel turns out to reduce the wear rate substantially.

INTRODUCTION

Many successful wear resistant materials consist of particles of a hard phase dispersed in a more ductile matrix. Such dispersions can be prepared by powder metallurgical techniques or by solidification of an eutectic structure from a melt. However, in the former technique the coatings produced by spray processes remain separated from the substrate by a sharp interface which is always a potential source of weakness. In the latter type of technique materials are prepared from the melt and the proportion of hard phases is controlled by equilibrium thermodynamics. A different approach, as presented in this paper, is to modify the surface layer by using a 1.5 kWatt CW CO₂ laser beam. Among the available laser applications, laser surface melting turns out to be a powerful technique for the production of wear resistant layers since it combines the advantages of local hardening, the possibility of surface alloying and the use of high quench rates. The latter may result in new metastable phases with novel wear properties. Indeed, not only the hardness, but also the ductility and internal stresses play an important role in the wear process. These phenomena are also affected by a laser surface treatment.

Despite the advantages of laser processing for the production of wear resistant materials, laser surface melting results in tensile stresses because the melted layer shrinks during resolidification. As a result high tensile stresses in the surface layer are generated which may lead to severe cracking of the material. Tensile stresses in the order of several hundreds MPa are possible, which detrimentally influence the wear behaviour. Our basic idea is to convert these tensile stresses produced by laser melting into compressive ones by ion implantation. When pressurized bubbles of implanted ions are nucleated in the surface layer, one can imagine that the corresponding compressive stress field could annihilate the tensile stress field of the laser melted material. Furthermore, the surface layer might also be strengthened during wear, due to the interaction between moving dislocations and the bubbles.

The material under investigation is RCC-steel (2.05 wt% C, 11.05 wt% Cr, 0.62 wt% W and bal. Fe). It has been chosen because it shows a constant hardness profile after laser melting. Furthermore, this material does not have a martensitic phase after laser melting, and compression due to martensite is not expected.

EXPERIMENT

In this study a transverse flow Spectra Physics 820 CO₂ laser system has been used. The parameters of the treatment are: a measured power on the surface of 1350 W, a focal length of 127 mm, a focus point at 15 mm above the surface, resulting in a melted track of 2 mm. Tracks are made adjacent to each other at a distance of 1 mm apart under a protective argon atmosphere. After laser melting the microstructure consists of a dendritic structure of retained austenite, which is surrounded by M₃C carbides. The measured dislocation density is 10^{13} - $10^{14}/\text{m}^2$. A high vacancy concentration is to be expected due to the high quenching rate during laser melting. As a matter of course, the ion implantation process produces point defects as well. The surface roughness created by laser melting is smoothened by grinding with SiC paper and finally polished using diamond paste.

Wear performance is tested on a conventional pin-on-disk wear tester¹. A ruby crystal ball with a diameter of 5 mm is pressed upon a rotating sample. The ball does not show any significant damage during the experiments. Before each test the ball is rotated or replaced to have a well defined starting condition. A constant speed of 5.0 cm/sec or 0.5 cm/sec and a constant load of 2.3 N have been chosen. According to Hertzian stress analysis it can be shown that in the present situation no plastic yielding due to the ball pressure occurs. The normalized force F of this configuration is about 0.03-0.06^{2,3}. The effect of humidity is reduced by applying absolute ethanol. In addition the experiments are carried out under a dry nitrogen atmosphere. The profile of the wear track is determined with an interference microscope. Measurements with a standard profilometer failed because of the small resolution in depth. Hardness measurements are carried out with a Leitz Vickers hardness tester. The load applied is 25 gr.

Implantations are carried out using an Extrion 200 kV implanter with doses of 3×10^{16} , 1×10^{17} and 3×10^{17} ions/cm² at an energy of 50 keV per Ne⁺-ion. Stereo-transmission electron microscopy⁴ for depth profile analysis is done using a JEM 200 CX operating at 200 keV.

OBSERVATIONS AND ANALYSES

Ne bubble nucleation

Figure 1 shows a TEM picture of a laser melted-Ne implanted layer. Bubbles with a radius up to 34 nm are observed. Coalesced bubbles are found with the same appearance as found by Johnson, Mazey and Evans⁵. To determine the implantation depth the back side thinning method has a disadvantage since there is no guarantee that the front surface near the polished hole will not be affected by the polishing solution. Therefore thin foils have been implanted as well. Figure 2 shows a stereo TEM-picture of an implanted foil exhibiting the depth distribution of the bubbles throughout an austenitic cell. The bubble density is 5.7×10^{20} bubbles/m³. A distribution of bubble radii is shown in figure 3. The mean bubble radius is 20 nm and the mean volume is $4.5 \times 10^4 \text{ nm}^3$.

Wear behaviour and hardness measurements

The wear performance is depicted in Figure 4. The measured wear rate and running-in parameters are listed in table - I. The wear rate decreases with increasing Ne dose. At a dose of 3×10^{16} Ne⁺ ions/cm² the wear rate increases after 6000 turns. The depth of the wear track is then about 160 nm, which is two times the calculated implantation depth.

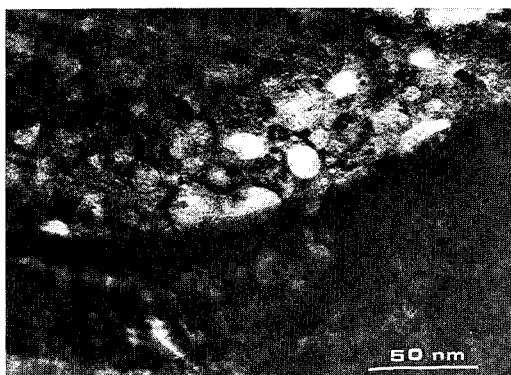


Fig. 1 Coalescence of bubbles after implantation with $3 \times 10^{17} \text{ Ne}^+$ ions/cm² into laser melted steel. Preparation according to the back side thinning method.

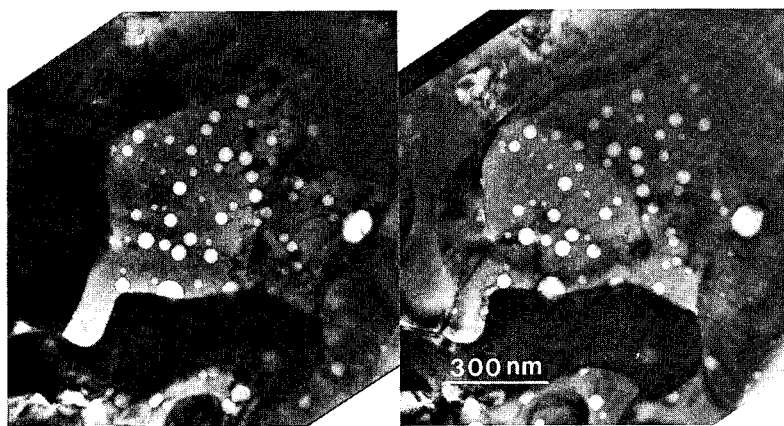


Fig. 2 Stereo TEM picture of neon bubbles in an austenite cell. Implanted dose is $3 \times 10^{17} \text{ Ne}^+$ ions/cm². Stereo angle between pictures is 20°.

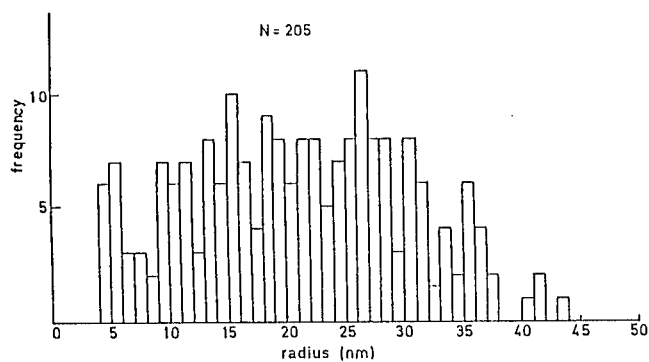


Fig. 3 Bubble size distribution after implantation of $3 \times 10^{17} \text{ Ne}^+$ ions/cm² into laser melted steel.

Hereafter the wear rate increases strongly, which is due to the interfacial layer causing both compressive and tensile stresses to be present in the wear track. Such a transition is also found with the highest dose implantation. Extended measurements done at lower loads show, after 15000 turns, when the depth of the wear track is about the same as compared to the lowest dose implantation, an increase in wear rate. The wear rate increases gradually to a value of the not implanted laser melted steel.

TABLE I

Ions	Dose ($\times 10^{17}/\text{cm}^2$)	Temp. ($^{\circ}\text{C}$)	Wear rate ($\times 10^{-15}\text{m}^3/\text{m}$)	Running in wear ($\times 10^{-12}\text{m}^3/\text{m}$)
No implantation		-	1.0	5.4
Ne ⁺	0.3	90	0.7	4.5
Ne ⁺	1	90	0.7	9.6
Ne ⁺	3	90	0.2	4.9

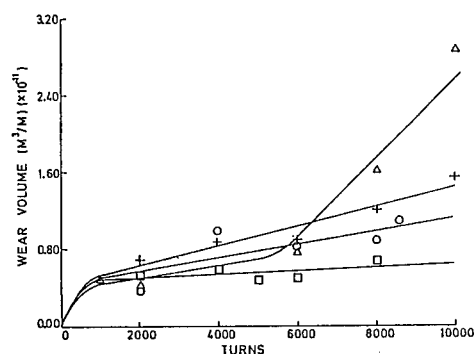


Fig. 4 Measured wear volume of neon implanted laser melted steel.

+ not implanted,
 Δ 3×10^{16} ions/ cm^2 ,
 \circ 1×10^{17} ions/ cm^2 ,
 \square 3×10^{17} ions/ cm^2 .

Vicker's hardness measurements across the laser melted tracks are depicted in fig. 5. The measured profiles show a hardness varying from 650 HV up to 950 HV. This means an extra hardening due to Ne of 350 HV. It has to be emphasized that the real hardness of the implanted layer is very difficult to measure, because the Vicker's hardness indenter penetrates the layer. We only conclude that there is a significant hardening which is at least up to 900 HV and probably higher. This extra increase in hardness might be due to the compressive stress which increases the yield stress. Further hardening is to be expected from bubbles which impede dislocation movements.

Clearly the stress fields of the Ne bubbles interact with the stress field of moving dislocations during wear and plastic deformation. Dislocations may bypass the bubbles either by pure glide (Orowan process) and cross slip or by shearing the bubbles. The stress field around a bubble determines whether a dislocation will reach the bubble and penetrate or will bypass by bowing around the bubble. Usually in aged-hardened alloys the contribution of modulus hardening to the shearing force, required to cut a particle by glide dislocations, is small. The modulus hardening arises from the differences between the elastic moduli of matrix and particle. Since the elastic energy of a dislocation is a function of the shear modulus, a change in energy and hence a force will be associated with a dislocation interacting with a particle whose shear modulus differs from that of the matrix.

The extreme case is the interaction with a void or a bubble, in which the elastic energy is reduced to zero and the system can be described with image forces. So, the modulus hardening in this case of Ne bubbles is a crucial contribution to the hardening since the dislocations experience in the neighbourhood of the Ne bubbles always an attractive force component towards the bubbles. In addition, dislocations may bow around a bubble. The latter is experimentally observed pointing at the Orowan mechanism (Fig. 6a) as well as dislocations pinned by bubbles (Fig. 6b).

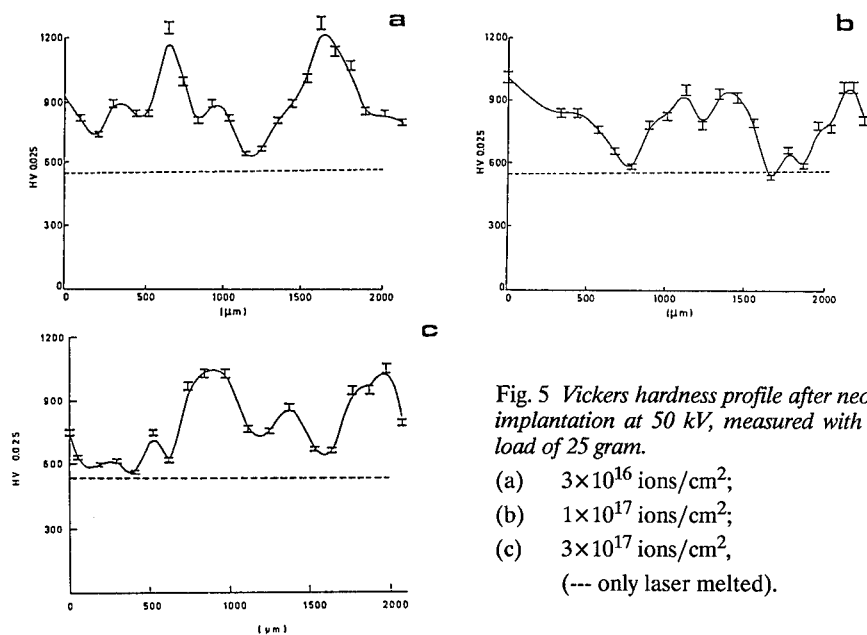


Fig. 5 Vickers hardness profile after neon implantation at 50 kV, measured with a load of 25 gram.

- (a) 3×10^{16} ions/cm²;
 - (b) 1×10^{17} ions/cm²;
 - (c) 3×10^{17} ions/cm²,
- (--- only laser melted).

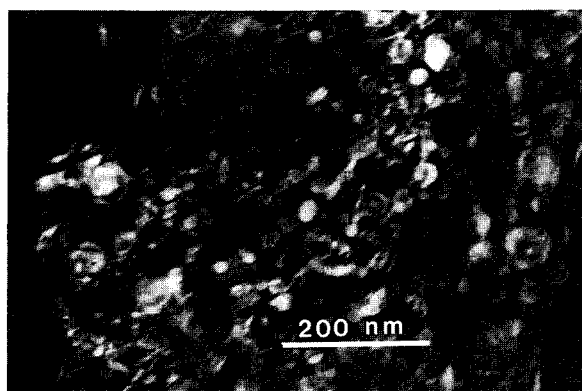


Fig. 6 (a) Dislocations interacting with bubbles after straining a thin foil.

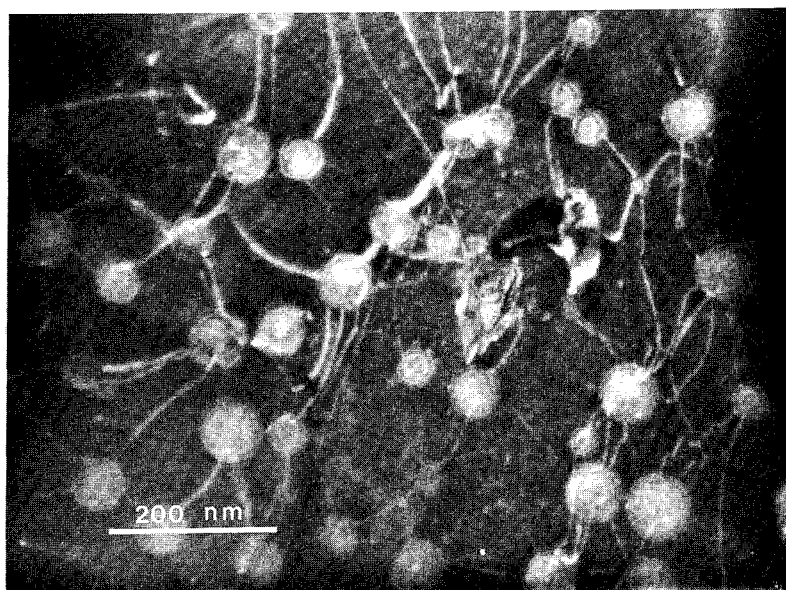


Fig. 6 (b) *Neon bubbles nucleated at dislocations after implantations.*

More details regarding the pressure field around the bubbles, the dislocation-bubble interaction and a comparison with N^+ -implantation will be published elsewhere ^{6,7,8}.

CONCLUSION

Neon implantation contributes to compressive strengthening by the formation of bubbles. The volume of the bubbles is high enough to compensate for the tensile stress state after laser melting and the bubbles contribute to a further hardening of the austenitic cells. Orowan looping has been observed by in situ TEM deformation experiments, but more dominant is the pinning of dislocations at bubbles by image forces, a mechanism which in aged hardened alloys is known as modulus hardening. Wear measurements after neon implantations even show a strong improvement in wear which cannot be ascribed simply to an increase in hardness, but is more likely caused by a conversion of the tensile stress state into a compressive stress state.

REFERENCES

1. W. C. Oliver, R. Hutchings, J. B. Pethica, *Met. Trans. A* **15**, 2221 (1984).
2. H. Czichos, *Tribology*, Elsevier Sci. Publ. Comp. Amsterdam (1978).
3. S. C. Lim, M. F. Ashby, *Acta Metall.* **35**, 1 (1987).
4. G. Boom, M. Sikkens, J. Th. M. De Hosson, *Ultramicroscopy* **19**, 83 (1986).
5. P. B. Johnson, D. J. Mazey, J. H. Evans, *Rad. Eff.* **78**, 147 (1983).
6. H. de Beurs, J. Th. M. De Hosson, *Appl. Phys. Letters* **53**, 663 (1988).
7. H. de Beurs, J. Hovius, J. Th. M. De Hosson, *Acta Metall.* **36**, No. 12, 1988.
8. H. de Beurs, J. Th. M. De Hosson, submitted to *Acta Metall.*

TRIBOLOGICAL AND MÖSSBAUER STUDIES OF ION-IMPLANTED IRON

D.L. WILLIAMSON*, YI QU*, RONGHUA WEI**, W.S. SAMPATH**, AND P.J. WILBUR**

*Department of Physics, Colorado School of Mines, Golden, CO 80401

**Department of Mechanical Engineering, Colorado State University,
Fort Collins, CO 80523

ABSTRACT

A modified pin-on-disc wear test technique and conversion electron Mössbauer spectroscopy (CEMS) have been used to characterize the tribological and microstructural properties, respectively, of pure Fe implanted with N and Ar ions at high current densities. CEMS measurements were made before and after wear testing. For the lubricated, mild adhesive wear conditions used here, no evidence was found for iron-nitride dissolution or N atom migration. Disorder of $\gamma'-Fe₄N did occur as a result of the wear process. All N-implanted surfaces were tribologically superior to the Ar-implanted surface and an extremely wear-resistant surface layer about 30-50 nm thick was produced with a dose of 8×10^{16} N atoms/cm², at a dose rate of 100 μ A/cm². However, once this layer was worn away the wear rate returned sharply to that of unimplanted pure Fe. A high retained N dose has been observed even for a dose rate of 750 μ A/cm² during which the sample reached 280°C.$

INTRODUCTION

Tribological improvements induced by ion implantation of engineering materials are well documented [1-3]. However, the mechanisms by which such improvements are realized remain poorly understood, in part due to the complexity of the surface modification produced by this highly non-equilibrium process and in part due to the inherent complexity of the substrate materials typically selected for study. In addition, the relatively shallow depth of the modified layer (~100 nm) leads to special problems in both microstructural analysis and tribological testing. The lack of durability of such a shallow layer and the long processing time are often-cited disadvantages of ion implantation.

Based on the above considerations we have implemented a systematic program of research with the following major aspects: (1) use of metallurgically simpler substrates (pure Fe here); (2) use of the non-destructive, near-surface-sensitive, microstructural probe known as conversion electron Mössbauer spectroscopy (CEMS) applied to both the as-implanted and worn surface; (3) development of a modified pin-on-disc wear test that generates a large worn area for the Mössbauer studies; (4) and use of a unique, high current density, broad beam ion implantation system based on ion-rocket technology. This paper describes some effects of high current density N and Ar implantation into pure Fe on the near surface microstructure as determined by CEMS. Results of tribological testing of some of these surfaces are also presented together with CEMS results after various stages of wear.

EXPERIMENTAL METHODS

Ion Implantation

The ion implanter used in this work has been designed specifically for the high dose level that is required for mechanically active surfaces. Details of the system have been described elsewhere [4,5]. The beam is not mass separated and in the case of nitrogen implantation consists of about 70% N_2^+ and 30% N^+ . The substrates studied here were 99.9985 % pure Fe (≈ 0.5 mm grain size) in the form of either a wear disc, WD, 4.6 cm in diameter by 2 mm thick or a $6.25 \text{ cm}^2 \times 2$ mm square plate, SQ (not wear tested). The samples were polished to a finish with ± 15 nm mean vertical fluctuations.

Numerous samples have been implanted under a variety of conditions. A subset of samples has been selected here to illustrate the experimental methods and several of the important results obtained to date. Implantation conditions for this subset are summarized in Table I. The thermal contact between the sample and the Cu fixture was simply metal-to-metal for samples WD1 and WD2 and was improved with colloidal graphite for the remaining samples listed. The atom dose is calculated from the ion dose assuming 70% N_2^+ , 30% N^+ , and 100% Ar^+ . The $750 \mu\text{A}/\text{cm}^2$ dose rate used for sample SQ led to the total dose of 6.8×10^{17} atoms/ cm^2 in only 85 seconds of implantation.

Wear Testing

A pin-on-rotating disc apparatus has been modified to generate a large worn area suitable for Mössbauer analysis after a wear test. The pin (99.9985% pure Fe), which has a 3.2 mm hemispherical radius at the contact point when wear testing begins, oscillates with a constant radial velocity that is a small fraction of the tangential velocity at the contact point. The mean tangential velocity is 13 cm/s. The resulting uniformly worn surface on the disc has a 4.3 cm o.d. and a 2.1 cm i.d. The tests are done in lab air with a circulating lubricant of 10 % oleic acid in kerosene and with a normal load of 4.9 N. These wear test conditions are chosen to produce mild adhesive (plasticity dominated) wear [6-8]. The wear rates of both pin (not implanted) and disc are determined by periodic mass loss measurements. The $\pm 11 \mu\text{g}$ accuracy obtained for the discs corresponds to a ± 1.3 nm accuracy for the change in average thickness of the disc wear zone.

Table I. Samples and implantation conditions. All samples were implanted at 60 keV with N ions except WD4 which was implanted with Ar. T is the peak temperature measured at the back of the 2 mm thick samples during implantation. T was not measured for WD1 and WD2.

Sample	Dose Rate ($\mu\text{A}/\text{cm}^2$)	Ion Dose ($10^{17}/\text{cm}^2$)	Atom Dose ($10^{17}/\text{cm}^2$)	T ($^{\circ}\text{C}$)
WD1	100	0.5	0.85	-
WD2	100	4.0	6.8	-
WD3	100	4.0	6.8	182
WD4(Ar)	100	1.0	1.0	83
SQ	750	4.0	6.8	278

Mössbauer Spectroscopy

The CEMS technique used for this study has been described in an earlier application to Ti-implanted steel [9]. There it was shown that about 80% of the CEMS signal originates from a surface layer of 100 nm. Based on this signal-versus-depth curve [9], the approximate thickness of a near surface compound formed as a result of ion implantation can be obtained from the observed CEMS fraction of that compound.

The ion-implanted or worn sample is mounted in the gas-flow CEMS detector and the gamma-ray beam is collimated to strike a $\sim 2 \text{ cm}^2$ area of the ion-implanted or worn surface for analysis. The Mössbauer spectral parameters obtained from the computer fits (isomer shift, quadrupole splitting, magnetic hyperfine field, and linewidth) are compared with literature values for phase and/or crystallographic site identification. Parameters are available [10] for all known phases in the Fe-N phase diagram [11].

RESULTS AND DISCUSSION

CEMS Analysis of As-Implanted Samples

Figure 1 displays the CEMS data of the five samples listed in Table I and the stick diagrams identify the various Fe-nitrides found. The identification of the orthorhombic(ζ)- Fe_2N was aided by x-ray diffraction since its Mössbauer parameters are almost identical to those of hexagonal(ϵ)- Fe_{2+x}N ($0.02 \leq x \leq 0.22$). The ϵ -phase in WD1 is found to have $x=1$ based on the magnetic field. Sample WD2 shows a large resonance fraction of the ordered fcc(γ')- Fe_4N which is readily identified by its three magnetically inequivalent Fe sites. Significant N migration must occur during implantation for the ordered, stoichiometric ζ and γ' phases to form. The resonance fractions of the Fe nitrides lead to approximate values of the thickness d of a uniform layer of that phase as described above. It was assumed that the layer extends from the surface to the depth d . These thicknesses can then be used to calculate the total atomic N/ cm^2 retained in the form of Fe-nitrides. These bonded N

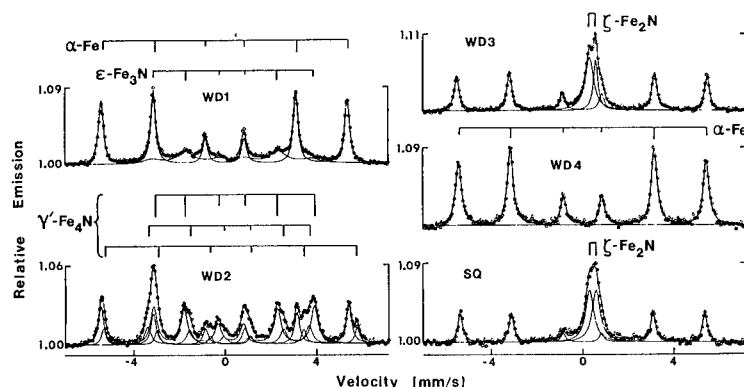


Fig.1 CEMS results from as-implanted samples

Table II. Quantitative estimates of the nitride thicknesses d and the bonded N atomic concentrations (area densities) from CEMS resonance fractions F .

Sample	Nitride	F (%)	d (nm)	Bonded N ($10^{17}/\text{cm}^2$)
WD1	$\epsilon\text{-Fe}_3\text{N}$	27	30	0.7
WD2	$\gamma'\text{-Fe}_4\text{N}$	71	100	1.8
WD3	$\zeta\text{-Fe}_2\text{N}$	44	60	1.9
SQ	$\zeta\text{-Fe}_2\text{N}$	58	80	2.7

concentrations and values of d are listed in Table II. The assumptions used guarantee that these quantitative estimates represent minimum values. Auger depth profiling of sample WD1 shows a Gaussian-shaped N distribution peaked at 50 nm below the surface and with a width at half height of about 60 nm.

The bonded N density is only slightly lower than the implanted N dose for sample WD1 suggesting that essentially all of the N is retained and in the form of $\epsilon\text{-Fe}_3\text{N}$ for this sample. On the other hand, the bonded N density is only about 1/3 of the implanted dose for the other samples, suggesting that the selected implantation dose has exceeded the maximum retained dose as determined by sputtering and/or out-diffusion of N from the surface during implantation. Note that WD2 and WD3, implanted under identical conditions except for the better thermal contacting method for WD3, have nearly the same bonded N concentration but two different nitrides. This can be understood if WD2 reached a significantly higher temperature than WD3 during implantation such that the nitride concentration drops from Fe_2N to Fe_4N concurrent with a thickening of the nitride layer, consistent with the d values in Table II. It is interesting that the $750 \mu\text{A}/\text{cm}^2$ dose rate used for SQ yielded a larger bonded N density than the $100 \mu\text{A}/\text{cm}^2$ rate used for WD2 and WD3.

The Ar implanted sample has CEMS resonance lines that are 25% broader than unimplanted pure Fe. Also, the magnetic hyperfine field and the isomer shift are both slightly larger than those of pure Fe. The increased linewidth can be interpreted as due to a distribution of local Fe environments caused by defects and inhomogeneous strain induced by the Ar implantation. The modified magnetic field and isomer shift are consistent with a slight increase in the average lattice constant in the near-surface region, thereby implying that this region is in a state of residual compressive stress.

Wear Testing and CEMS Analysis of Worn Surfaces

Figure 2 compares mass loss data for three of the implanted wear discs listed in Table I with those from unimplanted pure Fe. The right hand ordinate gives the mean depth of wear obtained by dividing the mass loss by the product of wear area and Fe mass density. Note that the initial wear rate of the pure Fe is about twice that of the steady state rate which is reached after about 10 h. This rather long break-in period is associated with the work-hardening of the relatively large disc wear area produced by the oscillating pin.

Figure 3 shows a series of Mössbauer spectra from WD3 after increasing periods of wear. The $\zeta\text{-Fe}_2\text{N}$ gradually disappears as a result of the wear process without changing to another type of nitride.

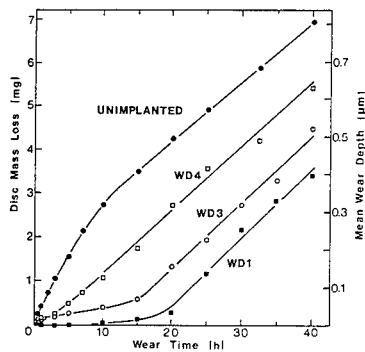


Fig.2 Wear test results

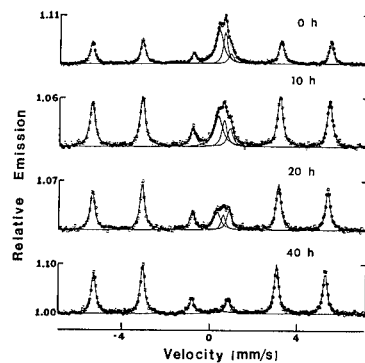


Fig.3 Effect of wear on WD3

Figure 4 compares the spectrum of as-implanted WD2 with those after 7 and 15 h of wear. In this case there is a clear change in the γ' -Fe₄N resonance: the lines have broadened to such a degree that the three magnetic hyperfine fields are no longer resolved and suitable fits are obtained with two six-line patterns, one of which has much broader lines. However, the resonance area fraction of this nitride component does not change from the as-implanted value of 70% as a result of wear testing up to 15 h. The wear data for this sample are not included in Fig. 2 because the sample was implanted over only half of the disc so the mass loss is due primarily to that from the unimplanted half. Profilometer scans of the boundary between an unworn region and the implanted worn region show no evidence for wear (other than an increased surface roughness). This result is consistent with no change in the nitride CEMS fraction. X-ray diffraction from the worn surface shows that the γ' -phase is still present so we interpret the changes in the Mössbauer spectrum of the γ' -phase shown in Fig. 4 as due to a short range disordering of the N atoms as a result of the wear process.

CEMS analysis of WD1 after increasing periods of wear shows behavior similar to WD2 in that the linewidth of the ϵ -phase increases but the resonance fraction remains nearly constant up to about 20 h of wear. The latter is shown in Fig. 5 together with the fractions of ζ -Fe₂N obtained from WD3. Comparison of these data with the mass loss curves in Fig. 2 and the

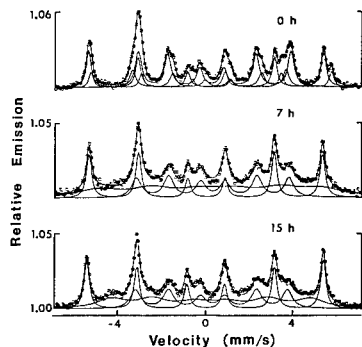


Fig.4 Effect of wear on WD2

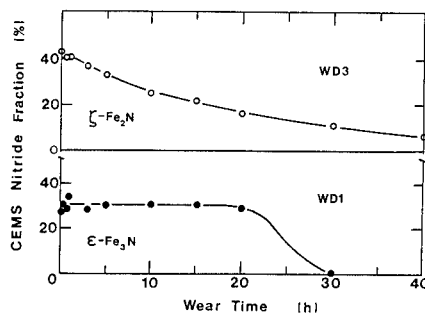


Fig.5 Effect of wear on nitride fractions

values of d in Table II leads to the following observations: (1) there is an obvious change in wear rate that occurs at a mean wear depth that is in good agreement with the estimated Fe-nitride thickness; (2) this increased wear rate is close to that of the unimplanted Fe in the steady-state mode; (3) the wear behavior of the two distinct nitrides (ϵ and ζ in WD1 and WD3, respectively) is different: ϵ showing essentially no loss until a rather abrupt disappearance between 20 and 30 h wear coincident with the sharp increase in wear rate, and ζ exhibiting a gradual decrease with no abrupt change near 15 h at which time the wear rate increases quickly to that of the unimplanted Fe; (4) traces of the ζ -phase remain for WD3 even after a mean wear depth of 500 nm. The last result is in contrast to several reports of improved wear lasting much beyond depths where any N can be detected [1,12,13]. We suggest that our result is due to mechanically transferred material containing ζ -Fe₂N whose presence is not beneficial once the original implantation-modified layer is worn away. We recently demonstrated that a conventional pin-on-disc wear test can give misleading results [5].

The wear improvement for the Ar-implanted sample seen in Fig. 2 is substantial but clearly inferior to those of the N-implanted discs. The improvement is attributed to the defects and residual compressive stress in the near-surface layer suggested by the CEMS analysis. It is interesting that the Ar implantation causes the wear curve to have initially nearly the steady-state wear rate. This suggests that the Ar implantation induces effects similar to those of work-hardening such that this stage of the wear process is bypassed.

The major conclusions that we draw from these results are presented in the Abstract. The support of the National Science Foundation under grants MSM-8617811 and MSM-8704488 is gratefully acknowledged.

References

1. G. Dearnaley, Mater. Sci. Engr. **69**, 139 (1985).
2. I.L. Singer, Applic. Surf. Sci. **18**, 28 (1984).
3. H. Herman, Nucl. Instrum. Meth. **182/183**, 887 (1981).
4. P.J. Wilbur and L.O. Daniels, Vacuum **36**, 5 (1986).
5. P.J. Wilbur, R. Wei, and W.S. Sampath, in Surface Modification of Metals by Ion Beams, Riva del Garda, Italy (1988, in press).
6. S.M. Lim and M.F. Ashby, Acta Metall. **35**, 1 (1987).
7. N.P. Suh, Wear **44**, 1 (1977).
8. S.P. Shepard and N.P. Suh, J. Lubric. Technol. **104**, 29 (1982).
9. D.L. Williamson, F.M. Kustas, D.F. Fobare, and M.S. Misra, J. Appl. Phys. **60**, 1493 (1986).
10. Mössbauer Effect Reference and Data Journal, edited by J.G. Stevens, V.E. Stevens, and W.L. Gettys (Mössbauer Effect Data Center, Asheville 1978-1988).
11. H.A. Wreidt, N.A. Gokcen, and R. H. Nafziger, Bull. Alloy Phase Diagrams **8**, 355 (1987).
12. S. Fayeulle, Wear **107**, 61 (1986).
13. J.T.A. Pollock, R.A. Clissold, P.J. Paterson, and C.J. Veitch, Nucl. Instrum. Meth. Phys. Res. **B19/20**, 263 (1987).

THE RELATIONSHIP BETWEEN CRYSTAL STRUCTURE AND HARDNESS OF NITROGEN IMPLANTED IRON SURFACE LAYERS

Takanobu FUJIIHANA

Advanced Technology Inc., Nase 84, Totsuka, Yokohama, Kanagawa, 245 JAPAN

Yoshio OKABE

Saitama Institute of Technology, Okabe-machi, Ohsato, Saitama, 362-02 JAPAN

Masaya IWAKI

RIKEN (The Institute of Physical and Chemical Research),
Hirosawa 2-1, Wako, Saitama, 351-01 JAPAN

A study has been made of the relationship between crystal structure and hardness of N-implanted Fe-surface layers. The substrates used were polycrystalline Fe-sheets 1 mm thick with a purity of 99.9 %. The ion implantation of $^{14}\text{N}^+$ was performed with doses ranging from 7.5×10^{16} to 1×10^{18} ions/cm² at an energy of 100 keV. The substrate temperatures during implantation were kept at -40, 20, 100 and 200 °C. The crystal structure of N-implanted layers was identified by X-ray diffraction method (XRD). The near surface hardness was measured by a Knoop hardness tester. The XRD patterns revealed that the iron-nitride peculiar to each implantation condition was formed, and the iron-oxide was embedded in the nitrides in case of higher temperature implantation. N-implantation led to hardness increase, whose degree also depended on implantation conditions. The comparison between the structure and hardness of implanted layers indicated that, among the phases of iron-nitrides produced by 20 °C implantation, ϵ -phase is the hardest and the γ -Fe₂O₃ and γ' -Fe₄N formed by 200 °C implantation are harder than the ϵ -phase nitrides. These results are discussed with respect to the surface composition estimated by Rutherford backscattering spectrometry (RBS) using 1.5 MeV $^4\text{He}^+$ -ions.

1. INTRODUCTION

Over the last decade, N-ion implantation into iron and steels has been employed for fundamental studies on these surface layers and its applications. In particular, a great improvement has been made of tribological properties such as wear and hardness [1-3]. In order to research the improvement mechanisms, the composition and structure in N-implanted layers have been investigated by means of Auger electron spectroscopy (AES) [4], conversion electron Mössbauer spectroscopy (CEMS) [5], high voltage electron microscopy (HVEM) [6] and so on, but these mechanisms have not sufficiently been made clear. We previously reported that the surface hardness of the quenched stainless steel (AISI 420) is at its maximum with a dose of 5×10^{17} ions/cm² in case of 75 keV N-implantation at near room temperature [3]. The phenomenon can also be seen for N-implanted pure-iron [7]. Even as regards these results, the relationship between crystal structure and hardness of N-implanted surface layers are not clear yet.

In this report, N-ion implantation into Fe-sheets has been carried out at various substrate temperatures to form iron-nitrides. The composition and crystal structure of implanted layers are evaluated by Rutherford backscattering spectrometry (RBS) and X-ray diffraction (XRD), respectively. The near surface hardness measured by a Knoop hardness tester is discussed with respect to surface composition and structure.

2. EXPERIMENTAL PROCEDURE

The substrates used were polycrystalline Fe-sheets 1 mm thick with a purity of 99.9 %. The nominal composition of the substrate is as follows: C 0.015 %, N 0.015 %, O 0.03 %, Mg 0.01 %, S 0.01 %, Ni 0.001 %, Cd 0.01 % and W 0.001 %. Before ion implantation, the surfaces of all specimens were

mechanically mirror-polished using a buffing wheel with 0.5 μm alumina slurry, and were ultrasonically cleaned in trichloroethylene.

The ion implantation of $^{14}\text{N}^+$ was performed with doses ranging from 7.5×10^{16} to 1×10^{18} ions/cm² at an energy of 100 keV. The ion beam current density of N^+ was approximately 1.0 $\mu\text{A}/\text{cm}^2$. The substrate temperatures during implantation were kept at -40, 20, 100 and 200 °C by cooling the target holders with liquid nitrogen or water, and warming them up at a heater. These temperatures were monitored by using a pair of alumel-chromel thermocouple fixed on target holders. The pressure in the process chamber during implantation was approximately 1.5×10^{-4} Pa.

The composition of N-implanted layers was estimated by means of RBS using 1.5 MeV $^4\text{He}^+$ -ions with fluence of 3 μC . Backscattered particles were detected at an angle of 150 ° and analyzed by a solid state detector and conventional electronics. The pressure in the measurement chamber was below 5×10^{-4} Pa.

The identification of crystal structure produced by implantation was investigated by XRD using 40 kV, 40 mA $\text{CuK}\alpha$ radiation. In XRD measurements with Seeman-Bohlin geometry, the X-ray incident angle was fixed at 5 ° from the rotating specimen surface and the diffracted X-ray was caught by sweeping the detector angle. The structure was identified by referring to JCPDS (Joint Committee on Powder Diffraction Standards) cards.

The near surface hardness was determined by means of the Knoop indentation measurements. The applied load was 2 gf.

3. RESULTS AND DISCUSSION

3-1. Composition in N-implanted layers

Fig. 1 shows the RBS spectra for unimplanted and N-implanted specimens. Ion implantation was performed with a dose of 5×10^{17} ions/cm² at 20 °C. The surface edge of Fe is located at the half yields, and its backscattering energy is 1.15 MeV. The edge of N-atoms is drawn at 0.5 MeV, but the increase of yields induced by implanted N-atoms could hardly be observed near this energy. Comparing the spectrum for unimplanted specimen with that for N-implanted specimen, N-depth profile can be expected from the decrease in yields of the host Fe-atoms owing to the implanted N-atoms. The method for expecting the N-profile is introduced by Anttila et.al. at N-implantation into Ti [8].

Fig. 2 shows the relationship between the tentative N-concentration and backscattering energy as a function of dose in the case of 20 °C implantation. The tentative N-concentrations are indicated by the ratio of decreasing yields ($1 - \text{Fe}_i/\text{Fe}_u$), which are calculated from RBS spectra, e.g. shown in fig. 1. Fe_i and Fe_u are the yields for Fe-atoms at any given energy of the implanted and unimplanted specimens, respectively. The doses for (a), (b), (c) and (d) in the figure are 1×10^{17} , 2.5×10^{17} , 5×10^{17} and 1×10^{18} ions/cm², respectively. The profiles of implanted N-atoms below the dose of 2.5×10^{17} ions/cm² are similar to those predicted by the LSS theory [9]. In case of implantation at the dose of 5×10^{17} ions/cm², although the profile shows a gaussian distribution, the maximum N-concentration in the experiment is slightly lower than the theoretical value. Comparing (c) with (d) in the figure, it seems that the maximum N-concentration at the dose of 1×10^{18} ions/cm² does not exceed one at the dose of 5×10^{17} ions/cm² and implanted N-atoms migrates towards the Fe-surface; the migration of N-atoms causes the N-distribution to change from a gaussian type to an error-functional type according to the increase in N-dose. The saturation of N-concentration in Fe during implantation is obtained by AES measurements in a report of Singer [4]. The saturation phenomena like this are reported in cases of N-implantation into Al [10], Ti [11] and Cr [11], and in each case the maximum N-concentration is approximately 50 at%. These results suggest that the error-functional distribution of N-atoms in this experiment is not caused only due to surface sputtering. The migration of implanted N-atoms may be dependent on the effect of radiation damage and new compounds formation during implantation, and this will be discussed later in relation to the

crystal structure.

Fig. 3 shows the profiles of the tentative N-concentration for N-implanted specimens at a dose of 5×10^{17} ions/cm² as a function of substrate temperature. The substrate temperatures during implantation are indicated in the figure. The gaussian-like distribution is observed in case of the implantation below 100 °C. The profile for 200 °C implantation is quite different from others; it shows an error-functional distribution and its maximum N-concentration is lower than those for lower temperature implantations. The result suggests that the migration of N-atoms, shown in case of implantation with a dose of 1×10^{18} ions/cm² at 20 °C, is enhanced at 200 °C implantation. For the implantation with a dose of 10^{17} ions/cm² at an energy of 40 keV, the surface migration of N-atoms implanted into Fe- and steel-substrates was observed for the specimen annealed after implantation and the one implanted at 200 °C [12,13], but the shapes of the N-profile are different from our results.

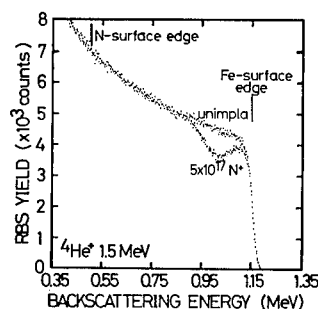


Fig. 1. RBS spectra for unimplanted and N-implanted Fe with a dose of 5×10^{17} ions/cm² at 20 °C.

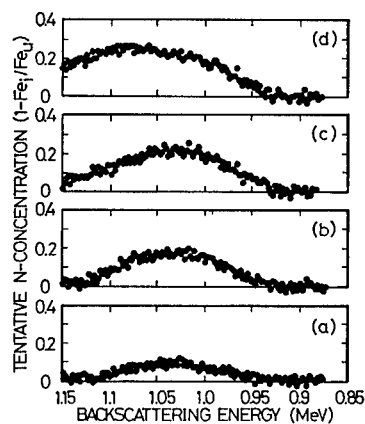


Fig. 2. Profiles of tentative N-concentrations for implanted Fe at 20 °C with various doses; (a) 1×10^{17} , (b) 2.5×10^{17} , (c) 5×10^{17} , (d) 1×10^{18} ions/cm². Fe_i and Fe_u are the yields for Fe-atoms of the implanted and unimplanted specimens, respectively.

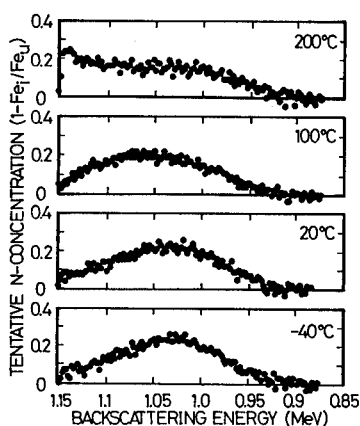


Fig. 3. Profiles of tentative N-concentrations for implanted Fe at a dose of 5×10^{17} ions/cm² with various substrate temperatures. Fe_i and Fe_u are the yields for Fe-atoms of the implanted and unimplanted specimens, respectively.

3-2. Crystal structure

Direct evidence of compounds formed in implanted layers was obtained by XRD studies. Fig. 4 shows the XRD patterns for the specimens implanted at 20 °C as a function of dose. The doses for (a), (b), (c), (d) and (e) in the figure are 7.5×10^{16} , 1×10^{17} , 2.5×10^{17} , 5×10^{17} and 1×10^{18} ions/cm², respectively. As shown in the figure, all of the XRD patterns show the formation of iron-nitrides in addition to those from Fe-substrate (α -Fe). The diffraction peaks at a dose of 7.5×10^{16} ions/cm² indicate the formation of Fe₄N and Fe₃N. At a dose of 1×10^{17} ions/cm², the diffraction peak corresponding to Fe₂N_{1-x} is observed instead of the peak from Fe₄N. At a dose of 2.5×10^{17} ions/cm², the diffraction peaks show the formation of Fe₃N and Fe₂N, and for further N-implantations, those corresponding to only Fe₂N are observed. The Fe₄N observed at the lowest dose implantation has a γ' -phase with the f.c.c. cell, and Fe₃N and Fe₂N_{1-x} has an ϵ -phase with the hexagonal cell lacking N-atoms. The Fe₂N observed at higher dose implantation has a ζ -phase with the orthorhombic cell, produced by the distortion of ϵ -phase: the ϵ -phase nitride is transformed into ζ -phase one by occupation of N-atoms in orderly positions. The phenomena like these transformations of nitride structures induced by N-implantation are reported by Fayeulle et.al. and Raushenbach et.al. using a CEMS [5] and HVES [6], respectively.

From the results of the composition and structure analyses, the formation of iron-nitrides in this experiment would be explained as follows. For N-implantation at a dose of 7.5×10^{16} ions/cm², implanted N-atoms combine with Fe-atoms to exist as Fe₄N and Fe₃N in Fe-metals. With progress of N-dose, the structure of nitrides changes from Fe₄N and Fe₃N to Fe₂N_{1-x} and Fe₂N, and finally the structure becomes Fe₂N; the stoichiometric ratio of Fe₂N may be reached at the depth of maximum N-concentration, when N-ions are implanted at the dose between 2.5×10^{17} and 5×10^{17} ions/cm². Such a high dose N-implantation induces the compressive stress in the implanted layers, as seen in a report of Hutchings [14]. The compressive stress and radiation damage produced by N-implantation may become the driving force for the migration of implanted N-atoms towards the Fe-surface. In addition to stress and damage, new compounds formation may cause the change in the density and the coefficient of thermal diffusion to enhance the migration of N-atoms. As the results, only Fe₂N structure was formed and the N-distribution becomes an error-functional type at the dose of 1×10^{18} ions/cm². These phenomena of crystallization and migration of implanted atoms with a high dose implantation into metals are called self-ion beam induced crystallization (SIBIC) [10].

Fig. 5 shows the XRD patterns for N-implantation at a dose of 5×10^{17} ions/cm² with various substrate temperatures. The substrate temperatures during implantation are indicated in the figure. All implanted specimens show the diffraction patterns from Fe₂N in addition to those from Fe-substrate. At the 100 °C implantation, additional weak diffraction peaks from Fe₂O₃, Fe₄N and Fe₂N_{1-x} are observed as compared with those for 20 °C implantation. The intensity of diffraction peaks from Fe₂O₃ and Fe₄N increases and that from Fe₂N_{1-x} disappears as the substrate temperature increases. This Fe₂O₃ is a γ -phase with the structure of spinel, which has a Fe-vacancy in the structure. The results of both XRD and RBS measurements suggest that Fe₂N changes to Fe₄N according to the increase in substrate temperature. The formation of Fe₂O₃ can be explained as follows; O-atoms impinge in the surface layer by cascade mixing of surface-oxide on Fe, as seen in the case of N-implantation into Al [10], and the iron-oxide may be crystallized by the thermal effect and/or ion bombardment effect during higher temperature implantation.

3-3. Near surface hardness

Fig. 6 shows the relationship between the relative change in Knoop hardness and N-dose at 20 °C implantation. The applied load was 2 gf. The hardness increases up to a dose of 1×10^{17} ions/cm² but decreases beyond this dose. This result is different from that for 150 °C implantation presented by

Pethica et.al. [15]. By comparing the hardness with the structure, it is indicated that the structure of nitrides produced by N-implantation at 20 °C is hardened in the following order : ζ -Fe₂N < ζ -Fe₂N+ ϵ -Fe₃N < ϵ -Fe₃N+ γ' -Fe₄N < ϵ -Fe₂N_{1-x} + ϵ -Fe₃N. From this result a conclusion is drawn that the ϵ -phase is the hardest among those of iron-nitrides produced by N-implantation at 20 °C, which therefore suggests that the defects in the crystal structure are related to the increase in hardness.

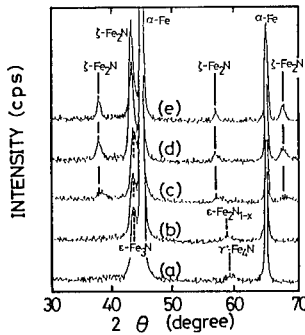


Fig. 4. XRD patterns for N-implanted Fe at 20°C with various doses; (a) 7.5×10^{16} , (b) 1×10^{17} , (c) 2.5×10^{17} , (d) 5×10^{17} , (e) 1×10^{18} ions/cm².

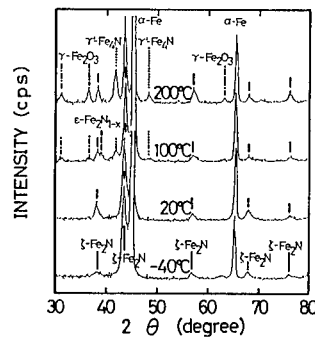


Fig. 5. XRD patterns for N-implanted Fe at a dose of 5×10^{17} ions/cm² with various substrate temperatures.

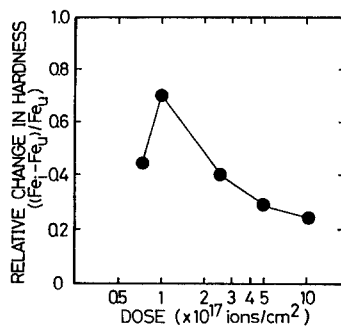


Fig. 6. Relative change in Knoop hardness for N-implanted Fe at 20 °C as a function of dose. F_{ei} and F_{eu} are the hardness of the implanted and unimplanted specimens, respectively. The applied load was 2 gf.

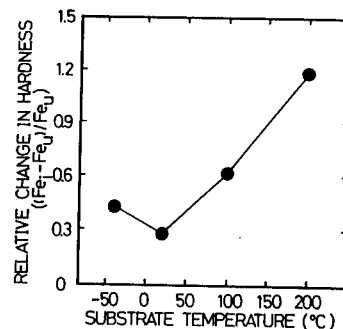


Fig. 7. Relative change in Knoop hardness for N-implanted Fe at a dose of 5×10^{17} ions/cm² as a function of substrate temperature. F_{ei} and F_{eu} are the hardness of the implanted and unimplanted specimens, respectively. The applied load was 2 gf.

Fig. 7 shows the relative change in Knoop hardness for N-implantation with a dose of 5×10^{17} ions/cm² as a function of substrate temperature. The applied load was also 2 gf. Although the phases of nitride revealed by XRD measurements are the same, the hardness for implantation at -40 °C is slightly higher than that for 20 °C implantation. From this result, it is derived that the residual stress produced by -40 °C implantation would be larger

than the one produced by 20 °C implantation. In case of 100 °C implantation, the relative change in hardness is twice as much as that for 20 °C implantation. Comparing fig. 6 with fig. 7, this value approaches the maximum one observed for 20 °C implantation with the dose of 1×10^{17} ions/cm². As regards the crystal structure, this result indicates that the formation of not only ϵ -phase nitrides but also γ -Fe₂O₃ and γ' -Fe₄N produced by higher temperature implantation plays an important role in the increase of Fe-surface hardness. As shown in the figure, the hardness increases greatly for implantation at 200 °C. The results suggest that the uniform formation of these harder compounds, which is an error-functional distribution, is also important for the increase in hardness.

4. SUMMARY

The relationship between crystal structure and hardness of N-implanted Fe-surface layers has been investigated by measuring the Knoop hardness, structure and composition. N-ion implantation was performed with doses ranging from 7.5×10^{16} to 1×10^{18} ions/cm² at 100 keV. The substrate temperatures during implantation were kept at -40, 20, 100 and 200 °C. The composition and structure were estimated by RBS and XRD, respectively, and were compared with the Knoop hardness. The main results are as follows.

(1) In case of the high dose N-implantation, the migration of N-atoms towards Fe-surface occurs at even 20 °C implantation and is enhanced by higher temperature implantation, and consequently, the depth profile of implanted N-atoms has an error-functional distribution.

(2) In case of 20 °C implantation, the comparison between structure and hardness indicates that the ϵ -phase is the hardest among the phases of iron-nitrides.

(3) The γ -Fe₂O₃ and γ' -Fe₄N formed during N-implantation at 200 °C is harder than the ϵ -phase nitrides produced at 20 °C implantation.

Anyway from these results, the substrate temperature higher than room temperature is suitable for obtaining harder Fe-surfaces.

The authors would like to thank Mr. Naoharu Matsuzawa of Saitama Institute of Technology for his co-operation in the experiments.

REFERENCES

1. N.E.W.Hartley, W.E.Swindlehurst, G.Dearnaley and T.F.Turner, *J. Mater. Sci.*, **8**, 900(1973).
2. J.K.Hirvonen, *J. Vac. Sci. Techn.*, **15**, 1662(1978).
3. M.Iwaki, T.Fujihana and K.Okitaka, *Mater. Sci. Eng.*, **69**, 211(1985).
4. I.L.Singer, *J. Vacuum*, **34**, 10/11, 853(1984).
5. S.Fayeulle, G.Marest, N.Moncoffre and J.Tousset, *Appl. Surf. Sci.*, **32**, 141(1988).
6. B.Raushenbach, A.Kolitsch and K.Hohmuth, *Phys. Stat. Sol.*, **80**, 471(1983).
7. D.Newey, H.M.Pollock and M.A.Wilkins, in: *Ion Implantation into Metals*, ed. by V.Ashworth, W.A.Grant and R.P.M.Procter, (Pergamon Press, 1982)p.157.
8. A.Anttila, J.Keininen, M.Uhrmachar and S.Vahvaselka, *J. Appl. Phys.*, **57**, 4, 1423(1985).
9. J.Lindhard, M.Scharff and H.F.Schiott, *K. Dan. Vidensk. Selsk. Mat. Fys. Medd.*, **33**, 14, 1(1963).
10. S.Ohira and M.Iwaki, *Mater. Sci. Eng.*, **90**, 143(1987).
11. T.Fujihana, Y.Okabe and M.Iwaki, to be published in *Proc. of Intl. Conf. on Surface Modification of Metals by Ion Beams*, Riva Del Garda, 1988.
12. T.Barnavon, H.Jaffrezic, G.Marest, N.Moncoffre, J.Tousset and S.Fayeulle, *Mater. Sci. Eng.*, **69**, 531(1985).
13. N.Moncoffre, G.Hollinger, H.Jaffrezic, G.Marest and J.Tousset, *Nucl. Instr. and Meth.*, **B7/8**, 177(1985).
14. R.Hutchings, *Mater. Sci. Eng.*, **69**, 129(1985).
15. J.B.Pechica, R.Hutchings and W.C.Oliver, *Nucl. Instr. and Meth.*, **209/210**, 995(1983).

FRICITION CHARACTERISTICS OF B⁺- AND N₂⁺-IMPLANTED Fe-Cr ALLOYS.

JUN SASAKI* and MASAYA IWAKI**

*Nippon Steel Corp.,

10-1 Fuchinobe 5-chome, Sagamihara-shi, Kanagawa 229, JAPAN

**RIKEN, Wako, Saitama 351-01, JAPAN.

ABSTRACT

A study has been made on friction and hardness of boron and nitrogen ion implanted Fe-Cr alloys. Ion implantation has been carried out with doses ranging from 5 wt% up to 20 wt% at energies of 50, 100 and 150 keV at room temperature. Reciprocal traces for friction coefficient measurements were performed by using a Bowden-Leben tester at a low speed without lubricant. Hardness was measured by using a micro-Vickers tester at a load of 2gf. Hardness of the specimen increases after the implantation with either of ion species. Friction measurements with reciprocal sliding show that a life-time of decreased friction coefficient depends on implanted ion species, Cr concentrations and acceleration energies. For B⁺-implantation, the lower the chromium contents are, the longer a decreased friction coefficient lasts. Meanwhile, the friction reduced by nitrogen implantation lasts longer for higher chromium content substrates. Dependence of friction coefficient on an acceleration energy is discussed for B⁺-implantation.

INTRODUCTION

Tribological properties for nitrogen and boron implanted steels have been reported by several researchers; implantation into 440C [1] and 18W-4Cr-1V steel [2] showed promise for boron ion implantation in tribological applications.

Nitrogen is the most established ion species, showing improvement in the mechanical properties of steel-surface layers. In this study, friction characteristics of N₂⁺- and B⁺-implanted Fe-Cr alloys has been investigated with respect to Cr concentration in the alloys and implantation depth.

EXPERIMENTAL

Substrates used were Fe-Cr alloy plates with four different Cr contents of 5, 10, 15 and 20wt%. They were prepared as-rolled without heat-treatment. Substrates' surfaces were mechanically mirror-polished down to 0.5μm by diamond slurry with particles.

Nitrogen ion implantation has been performed with doses up to 5×10^{16} N₂⁺/cm² at an energy of 50keV. For boron implantation, two series of implantation were performed. One was performed for variation of the total dose from 1×10^{15} up to 2.5×10^{16} with fixed energy at 150keV. The other series provided three different thicknesses of the modified layer with three different

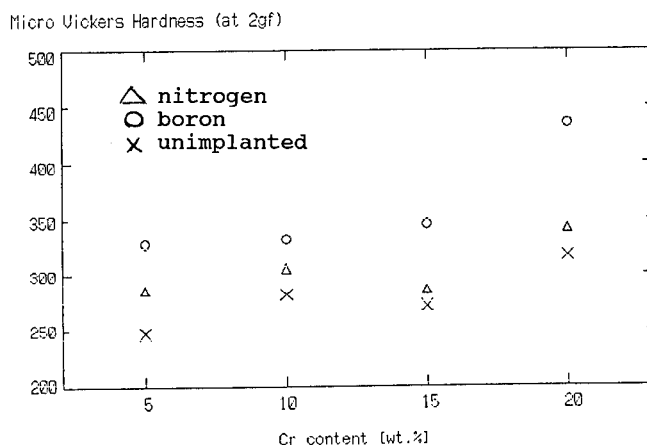


Fig.1 Micro-Vickers hardness at 2gf for unimplanted, B⁺- and N₂⁺-implanted specimens as a function of Cr content of the substrates

acceleration energies at 50, 100 and 150keV. The atomic ratio of the implant to bulk content at the distribution peak would be 1.5 at%. The total dose for each acceleration energy was derived by means of calculation based on LSS theory as 1×10^{16} , 1.55×10^{16} and 1.93×10^{16} B⁺/cm², respectively. A part of a surface of each specimen was masked by aluminum sheets to make an implanted surface and an unimplanted surface on the same specimen. The target chamber was evacuated by a turbomolecular pump for a background pressure of the higher range of 10^{-7} mmHg.

Friction coefficient measurements were carried out by using a Bowden-Leben type friction tester. An unimplanted S45C, equivalent to AISI1045 carbon steel pin with a spherically milled rubbing surface, slides reciprocally without lubricant on the implanted specimen. The sliding was rather low, 0.7 mm/sec, to avoid effects of heating during the rubbing motions. The ambient laboratory air was at the humidity of 40 - 50 %. Applied force was always 0.245N.

The hardness of the specimens was measured with a micro-Vickers indentation hardness tester. Applied load was always 2 gf for a duration of 15 seconds.

Estimation of chemical states in the implanted layers was performed with a X-ray Photoelectron Spectroscopy (XPS) combined with Ar sputtering.

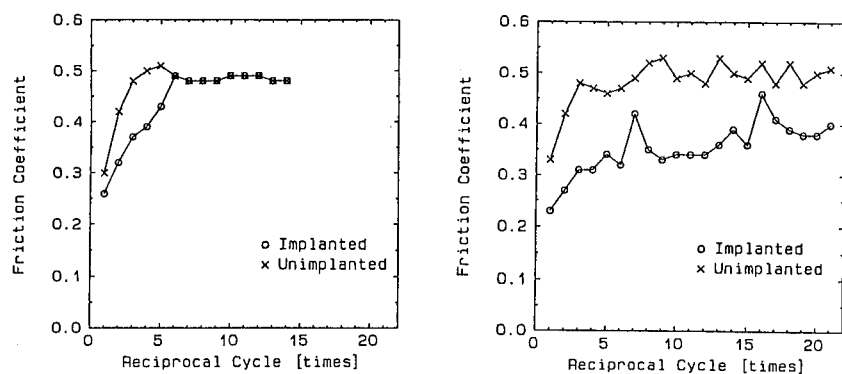


Fig.2 Friction coefficient of (a) 5 wt% Cr and (b) 20 wt% Cr substrate for N_2^+ -implanted and unimplanted, with dependence on the number of sliding reciprocations.

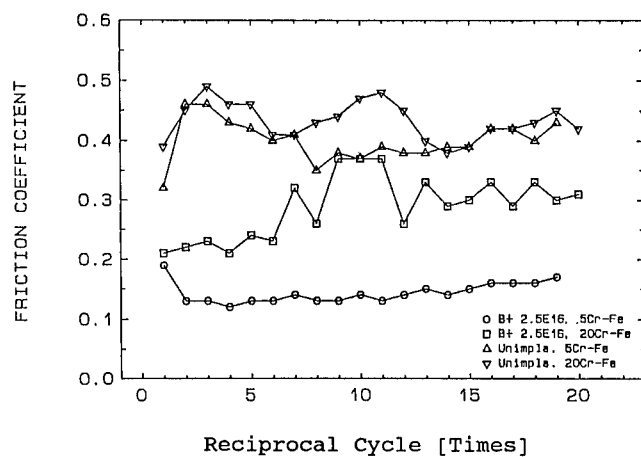


Fig.3 Friction coefficient of B^+ -implanted and unimplanted 5 Cr% and 20 Cr% specimens with dependence on the number of sliding reciprocations.

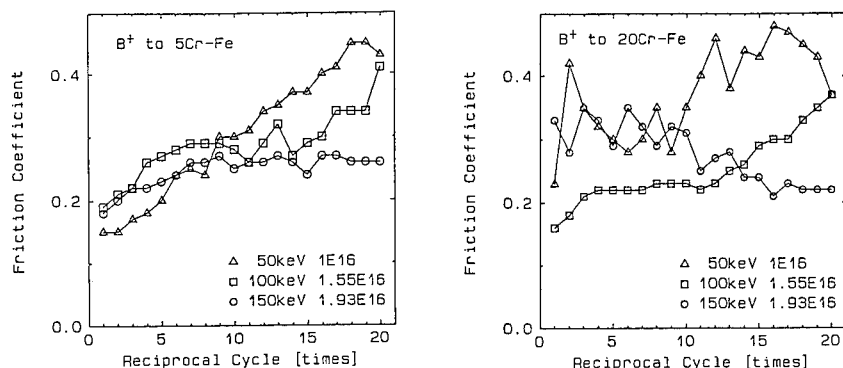


Fig.4 Friction coefficient of coefficient of (a) 5 Cr% and (b) 20 Cr% substrates for B⁺-implanted and unimplanted specimens with dependence on the number of the sliding reciprocation with a variety of implant depth.

RESULTS AND DISCUSSION

Figure 1 shows the micro-Vickers hardness of the B⁺- and N₂⁺- implanted and unimplanted specimens as a function of chromium concentration for Fe-Cr alloy substrates. The increase in micro-Vickers hardness for the implanted surface was observed for both implantations. The hardness of the unimplanted specimens has a tendency to increase as the chromium concentration increases. One of the authors showed the relationship between relative hardness and relative wear volume for nitrogen and boron implanted tool steels in a reference. [5] As the relative hardness increased, the relative wear volume of boron implanted steels decreased more steeply than nitrogen implanted steels.

In the results of Figure 1, hardness of boron implanted specimens are always higher than that of nitrogen implanted specimens. The thickness of the layer modified by B⁺-implantation at 150keV and N₂⁺-implantation at 50keV are about 250 nm and 25 nm, respectively. Vickers hardness is obtained by the indentation of a stylus on a surface of each specimen. Hardness values measured are, thus, not a "true" hardness of the implanted layer itself because of the penetration of the stylus through the modified layers. The values are dependent on thickness of the layers, indented load and indentation time. The thinner a modified layer is, the lower the hardness appears to be. A simple comparison of the increase of hardness caused by each ion species cannot, therefore, be made in Figure 1.

It should be noted that the change in friction of the B⁺-implanted surface was drastic, even at a rather low dose; i.e. the friction coefficient of the implanted surfaces started to decrease at a 5×10^{15} B⁺/cm² dose and leveled at around 0.2, at a 2.5×10^{16} B⁺/cm² dose.

Figures 2 (a) and (b) show the friction coefficient as a function of sliding reciprocation cycle for 5 Cr% and 20 Cr% substrates with the 5×10^{16} N_2^+ /cm² implantation dose. At the initial sliding, the friction coefficient is relatively low for unimplanted specimens due to the influence of the existence of surface oxides. N_2^+ -implantation causes the friction to decrease in the initial stage because of surface hardening, but the life-time of a lower friction coefficient depends on the Cr content. After six sliding reciprocations, the friction coefficient of the nitrogen implanted surface for the 5 Cr% substrate does not show any more difference from the unimplanted surface. On the other hand, the friction coefficient of the implanted 20 Cr% surface is always lower than that of the unimplanted. For a nitrogen implantation, the low friction coefficient lasts longer in the case of higher Cr concentration.

The friction coefficient for B^+ -implanted alloys are shown in Figure 3, as a function of the reciprocating cycle. The B^+ -implanted 5 Cr% surface shows lower friction coefficients than the 20 Cr% substrate. The friction of the B^+ -implanted 5 Cr% specimen seems to be the most stable when compared with any of the nitrogen or boron implanted specimens.

Figures 4 (a) and (b) show friction characteristics of B^+ -implanted 5 % Cr and 20 % Cr substrates in reciprocal friction tests, respectively. The total dose values were selected through the LSS based calculations in such way as to give 1.5 at% of boron content at a depth of the maximum concentration in the distribution; 1×10^{16} , 1.55×10^{16} and 1.93×10^{16} B^+ /cm² for 50, 100 and 150 keV implantation, respectively. In Figure 4 (a), the friction coefficients during the initial traces have almost no difference between each acceleration energy. The phenomena of friction suggest that the higher energy implantation maintains low values for the longer time.

On the other hand, in Figure 4 (b), the friction characteristics of 20 Cr% specimen are somehow different. The 50keV implantation did not cause sufficient decrease of the friction coefficient. For the 100keV implantation, the decreased friction coefficient appears in the initial stage but does not last long time. Friction coefficient for the 150 keV implantation goes down as the sliding reciprocation proceeds. These characteristics may be explained in terms of the different threshold contents of boron to make the friction decrease. If the threshold content of boron for decreasing friction in the 5 Cr% substrate is lower than that of the 20 Cr% substrate and exceeds even at the surface of 5 % Cr substrate but not at the surface of 20% Cr substrate, the different characteristics shown in Figure 4 would be caused by the difference of the boron content at the temporal conditions of the wearing surface during the reciprocal sliding.

In the XPS spectra observed for the nitrogen implanted specimen shown in a reference [6], formation of Cr_2O_3 and almost no metallic Cr was observed at outermost surface layer. Below the oxide layer, there is a mixture of CrN, Cr_2N , Fe_4N and metallic state of Cr and Fe. The friction coefficient in the initial reciprocation can be governed by the surface oxide layers, and the friction coefficient of the implanted layer appears in the following sliding.

In observed XPS spectra of boron implanted specimens with a $2.5 \times 10^{16} \text{ B}^+/\text{cm}^2$ dose, it was difficult to assign the formation of Cr and Fe boride compounds, because of their too slight shift from the metallic states and of the low dose value.

SUMMARY

Hardness and friction characteristics of B^+ - and N_2^+ -implanted Fe-Cr alloys have been studied with variation of alloyed Cr content. N_2^+ - and B^+ -implantations were performed at room temperature with doses of up to 5×10^{16} ions/ cm^2 at 50 keV and 2.5×10^{16} ions/ cm^2 ranging from 50 to 150 keV, respectively. Hardness was measured by using a Micro-Vickers tester for 15 seconds of indentation with 2 gf load. Chemical states in the modified layer was investigated by using XPS. The main results are summarized in the following.

- 1) Increase in Vickers hardness was observed for both N_2^+ - and B^+ -implantation. Because of the difference in thickness of the layer modified by each ion species, however, the change in the hardness could not be simply compared with one another.
- 2) Both N_2^+ - and B^+ -implantation brought a decrease in friction coefficient. Friction coefficient of boron implanted surfaces decreased at lower dose than nitrogen implanted surfaces.
- 3) In the reciprocating friction measurements of the N_2^+ -implanted surfaces, the low friction coefficient of 20 Cr% specimen lasted longer than 5 Cr% specimen. Meanwhile, the low friction coefficient of the B^+ -implanted 5 Cr% specimen lasted longer than that of 20 Cr% specimen.
- 4) The life-time of the low friction coefficient for the boron implanted specimens depended on both thickness of the modified layer and the Cr content in the substrates.

REFERENCES

- 1, M.Hirano and S.Miyake, Trans.ASME, J.Tribology 107, 467 (1985)
- 2, P.B.Madakson, Mater.Sci.Eng. 69, 167 (1985)
- 3, Ion Implantation, G.Dearnaley, J.H.Freeman, R.S.Nelson and J.Stephen (North-Holland, 1973)
- 4, J.K.Hirvonen, J.Vac.Sci.Tech.15, 1662 (1978)
- 5, M.Iwaki, Mater.Sci.Eng. 90, 263 (1987)
- 6, J.Sasaki and M.Iwaki, (to be published)

THE CAUSES OF PROPERTY VARIATIONS OF IBAD-TITANIUM NITRIDE

R. A. KANT*, S. A. DILLICH**, B. D. SARTWELL*, and J. A. SPRAGUE*

*Naval Research Laboratory, Washington, D.C. 20375

**Worcester Polytechnic Institute, Worcester, MA 01609

ABSTRACT

The influence of the growth conditions on the composition, microstructure, and mechanical properties of TiN formed with low energy Ar^+ ion bombardment during reactive physical vapor deposition was studied. The ratios of the incident ion and atom fluxes at the growth surface were varied systematically and were found to have a strong influence on both the composition and the microstructure of the films. These changes correlated well with measured changes in mechanical and optical properties. The films were examined using Auger electron spectroscopy, transmission electron microscopy, and their mechanical properties were studied using hardness, friction, and wear testing.

INTRODUCTION

There are several methods for making thin films of TiN and many employ some form of ion bombardment during deposition to improve film properties. However, there has been only limited understanding of the role of the bombardment and a satisfactory explanation has not been available for many of the observed variations of physical properties. One of the major problems has been that, until recently, the deposition parameters could not be independently controlled nor fully characterized, e. g., ion energy and flux are usually coupled and an unknown fraction of the ions may be multiply charged or neutralized causing difficulties in measuring ion flux. Thus, variations in a single processing parameter could cause other parameters to change in an uncontrollable or unpredictable manner and lead to unpredictable and potentially undesirable property changes. Several years ago Kant et al [1] developed an apparatus which allowed independent control over, and characterization of, each of the deposition parameters. They used that system to ion bombard TiN during reactive deposition at room temperature. The resultant films were consistently and inexplicably different from conventionally prepared TiN. Finding the source of the differences was complicated by the very lack of information about the conventional processes that motivated the work in the first place. In a subsequent study, Kant examined the influence of ion bombardment on surface reactions between Ti and gaseous N [2]. Although that investigation did not involve film deposition, the results indicated that significant quantities of unreacted or excess gas molecules could be present at a growth surface during deposition and that ion bombardment should substantially reduce their levels. The purpose of the work reported here was to investigate the extent to which the presence and incorporation of such excess gases during reactive deposition of TiN affect film properties, and the extent to which ion bombardment induced property changes could be attributed to gas incorporation. TiN films were grown for a matrix of carefully controlled and well characterized ionic and atomic fluxes at the growth surface. The films were examined using hardness, friction, and wear testing and the results were interpreted in terms of analysis using Auger electron spectroscopy (AES) and transmission electron microscopy (TEM).

EXPERIMENTAL METHOD

Titanium nitride films, 500 nm thick, were grown at about 0.1 nm/s on mechanically polished, 12 mm diameter disks of AISI 52100 steel at room temperature in a cryogenically pumped chamber with a base pressure of 5×10^{-5} Pa. Ti was evaporated by electron beam heating in a diffusion pumped chamber beneath the sample chamber and reached the substrate through a small aperture

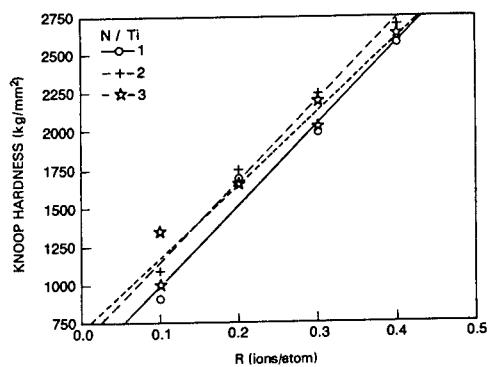


Fig. 1. The influence of the Ar^+/Ti flux ratio on hardness at 5 g load.

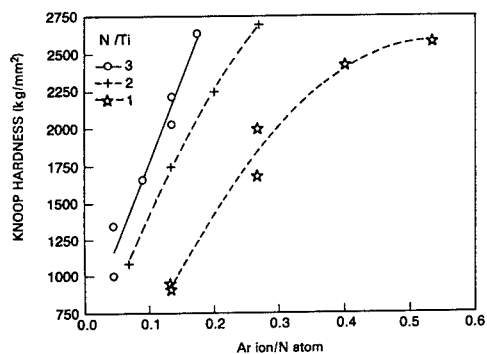


Fig. 2. The influence of the Ar^+/N_2 flux ratio on hardness at 5 g load.

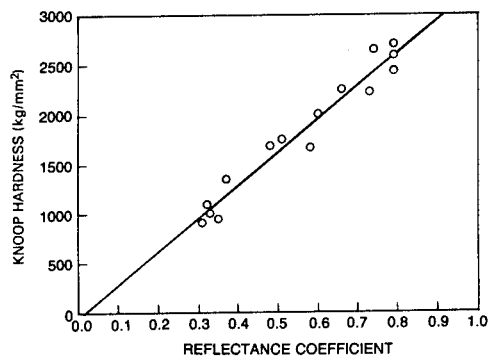


Fig. 3. The correlation between microhardness measured with a 5 g load and reflectance measured at 1 μm .

connecting the two chambers which promoted differential pumping [1]. The growing films were surrounded by a cold wall at 77 K and were deposited in N partial pressures ranging from 2×10^{-4} Pa to 8×10^{-4} Pa. During growth, the films were bombarded with 500 eV Ar^+ ions from a Kaufman style ion gun and excess Ar from that ion gun increased the chamber pressure to 2.7×10^{-2} Pa. The N gas pressure was controlled by a leak valve and was monitored by a residual gas analyzer. The substrates were positioned at 45 degrees to the vapor and ion fluxes which were vertical and horizontal, respectively. Since the magnitude of each incident flux is relevant only when compared to the other fluxes present, we state our process parameters in terms of flux ratios rather than using their magnitudes. Thus, depositions were conducted for Ar^+/Ti flux ratios, R, of 0, .1, .2, .3, and .4, while the ratios of the N_2 gas flux to the Ti vapor flux were 1, 2, and 3 and the Ar^+/N_2 ratios ranged from 0 to 0.6. Because the high background pressure degrades the absolute accuracy of the residual gas analyzer, the flux ratios involving N_2 gas should be understood to be relative values.

RESULTS

Knoop hardness measured at 5 gf increased nearly linearly with increasing ion bombardment rate R (see Fig. 1). The hardness was also found to be sensitive to the other arrival ratios, (ion flux to N_2 flux and N_2 flux to Ti flux). For Fig. 2, the data were divided into three groups each with fixed ratio of N_2 gas flux to Ti vapor flux. Note that within each group, hardness increased as the Ar^+ flux increased relative to the N_2 gas flux. Such an increase in the Ar^+/N_2 flux ratio would be expected to reduce the unreacted N at the growth surface. Since the films were only 500 nm thick and on relatively soft steel substrates (KHN=750), the depth of penetration of the Knoop indenter at 5 gf was still significantly greater than the film thickness and thus the actual hardness values are expected to be somewhat larger than the observed values. In addition, it was found that the color of these films varied with the hardness. This variation was quantified by measuring the optical reflectance at a wave length of 1000 nm, with Fig. 3 illustrating the high correlation between hardness and reflectance. It is important to note that this correlation provides a simple means of estimating the hardness of very thin TiN films which would be difficult to measure by indentation methods.

Friction and wear properties were investigated using a tribometer (ball-on-disk machine) with a 6 mm diameter 52100 steel ball under a load of 5 N,

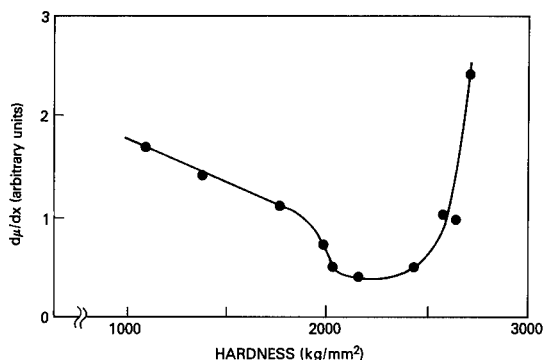


Fig. 4. Rate of change of the coefficient of friction with sliding distance during friction/wear test as a function of film thickness.

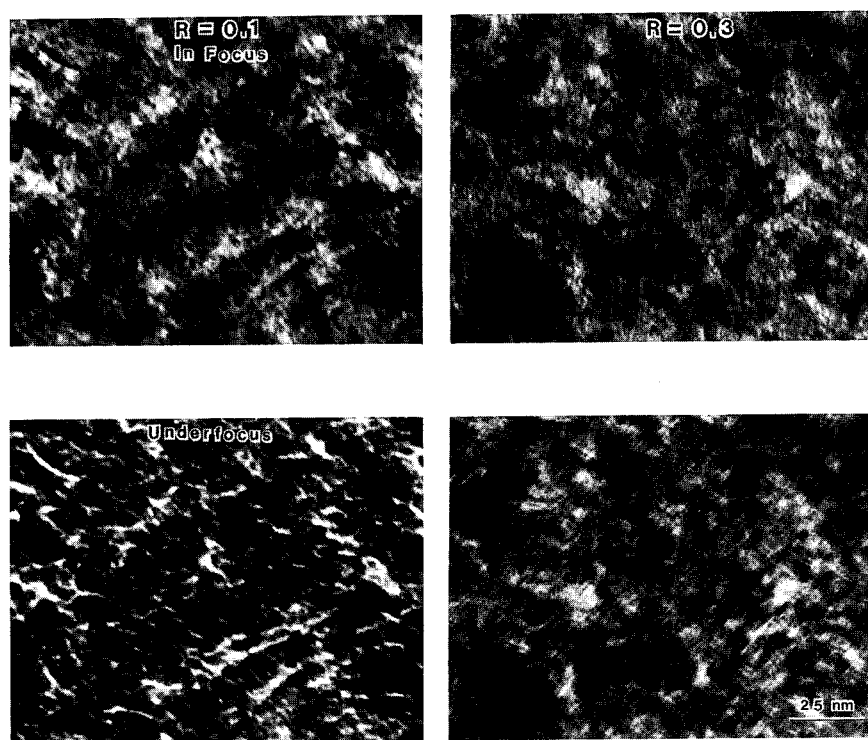


Fig. 5. The influence of the Ar^+/Ti flux ratio on grain-boundary porosity.

creating Hertzian stresses of the same order of magnitude as the yield stress of 52100 steel. Tests were run at a sliding speed of 1 cm/s without lubrication. The friction coefficient, recorded throughout each run, remained low, 0.2, until the onset of film removal. Thereafter it increased and asymptotically approached 0.6 (the value for steel on steel). The rate of increase of the friction coefficient with sliding distance during film removal is plotted as a function of film hardness in Fig. 4 and exhibits a clear minimum for films of intermediate hardness. The three different regions of the curve suggest that a distinctly different wear mechanism is operating in each region. The low hardness films are also ductile and are expected to be readily smeared or plowed resulting in relatively rapid film removal leading to a rapid rise in friction. As the hardness of the film increases, smearing is retarded and the wear rate drops until only the abrasive and adhesive wear modes remain. The rate of change of the friction coefficient increased very rapidly for the hardest films indicating a catastrophic failure mode. This appeared to be due to adhesion between the ball and the film since large amounts of film material were found on the balls after these tests, but there was only localized removal of the film from portions of the wear track.

Composition and microstructure were evaluated using AES and TEM respectively. Films for TEM analysis were deposited on NaCl substrates, removed from the salt by dissolution of the substrate in distilled water, and placed on grids for examination. The microscopy revealed a very small grain size (10 nm) and a fine network of pores, (voids or bubbles) at the grain boundaries. Such structures are identified by the way their contrast varies with changes in focusing conditions. Fig. 5 is an example of such a through-focus series of photos. The size and number per unit area of these features were found to decrease with increasing R.

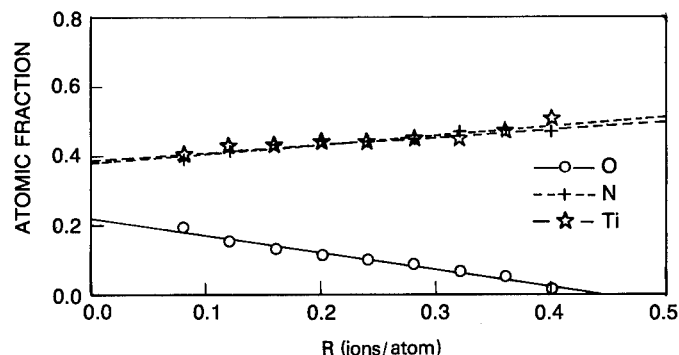


Fig. 6. The influence of Ar^+/Ti flux ratio on film composition.

Fig. 6 is a plot of the AES data which were analyzed by a method described previously [1]. Note that the N/Ti composition ratio in the films was very nearly one for all cases and that the extent of the oxygen contamination decreased linearly with increasing Ar^+/Ti flux ratio, R. In addition, energy dispersive X-ray measurements indicated the films contained small amounts of Ar which increased linearly with R reaching a maximum value of 1.1 atom percent at $R = 0.4$.

DISCUSSION AND CONCLUSIONS

The central questions motivating this study were: what physical processes are responsible for observed variations in physical properties of reactively

deposited TiN with concurrent ion bombardment and how are such processes related to the deposition parameters? The N/Ti composition ratio in the TiN was very close to one for all the cases examined indicating clearly that the property changes are not associated with this ratio. Because of the high correlation between film properties and oxygen content, it is very tempting to attribute the property changes to the incorporated oxygen. However, considerable caution is in order here since previous studies [3] provide examples of soft TiN with low oxygen concentrations. Thus high oxygen content may be sufficient to reduce hardness, but it is not necessary. The results presented above show that the mechanical properties are dominated by the Ar^+/Ti flux ratio during growth, and that the properties are correlated with an irradiation induced porosity reduction. Such pores may contain trapped N_2 and O_2 . Previous work has shown that the ion bombardment of Ti reduces the accumulation of unreacted gases by sputter removal and by activating the formation of TiN. The AES data show clear evidence of reduced oxygen due to bombardment but indicates that the N/Ti in the film is not affected by bombardment. However, Rutherford backscattering (RBS) analysis of similarly prepared TiN [4] has shown evidence of superstoichiometric TiN. These findings can be reconciled by noting that RBS would be sensitive to N_2 trapped in pores, whereas, AES would not. The increase in hardness with increased Ar^+/N_2 flux ratio suggests that the bombardment may be reducing the incorporation of unreacted N_2 . We speculate that the pores and/or the trapped gases within them lead to incomplete bonding between grains. Such weak intergranular bonding together with the small grain size would be expected to cause nanocrystalline behavior [5], i.e., decreased yield strength leading to the soft and ductile behavior observed for films prepared at lower bombardment rates. Similarly, the electrical conductivity between grains would be impaired leading to shorter electron mean free paths and a corresponding reduction in optical reflectance.

REFERENCES

1. R. A. Kant, B. D. Sartwell, I. L. Singer and R. G. Vardiman, Nucl. Instr. and Meth. B7/8 (1985) 915-919.
2. R. A. Kant and B. D. Sartwell, to be published.
3. R. A. Kant and B. D. Sartwell, Mater. Sci. & Engin., 90 (1987) 357.
4. G. K. Hubler, D. Van Vechten, E. P. Donovan and R. A. Kant, "Ion Beam Assisted Deposition of Titanium Nitride", presented at ASM Conference on Ion Implantation and Plasma Assisted Processes for Industrial Applications, May 22-25, 1988, Atlanta, GA.
5. J. Karch, R. Birringer and H. Gleiter, Nature, 330 (1987) 556-558.

CHARACTERIZATION OF TiN FILMS PREPARED BY ION BEAM ASSISTED DEPOSITION

ALBERT L. CHANG* AND R. A. KANT**

*Westinghouse Electric Corp., P. O. Box 185, Boston, MA 02258

**Naval Research Laboratory, Washington, D.C. 20375

ABSTRACT

One of the advantages of the ion beam assisted deposition process is its controllability of the processing parameters such as: ion-to-atom arrival ratio and the ion energy. In this study, the effects of the nitrogen ion energy (from 1 KV to 30KV) on the TiN film morphology and microstructures were systematically investigated as a function of ion-to-atom arrival ratios, using TEM, XTEM, SEM, ESCA and other analytical techniques.

INTRODUCTION

The ion beam assisted deposition (IBAD) process combines the conventional ion implantation with simultaneous vapor deposition (or with simultaneous sputtering) to produce a surface coating with beneficial properties and comparable microstructures offered by the conventional ion implantation process. Unlike conventional ion implantation, the IBAD process is capable of producing films several microns in thickness while a typical 100 KV ion implantator usually produces a modified surface layer with ~100 nm in thickness. Since the stoichiometry and the microstructure of the IBAD coating are independent of those of the substrate material, this process offers the potential of applying protective coatings on a wide variety of engineering materials for various tribological environments so long as the film offers desirable properties and it is highly adherent to the substrate.

Recent work at NRL [1-3] demonstrated that low-friction-highly-adherent ductile TiN films on a 52100 steel substrate can be obtained by the IBAD process using 30 KV nitrogen ions with simultaneous Ti evaporation. Baglin [4] at IBM indicated that the adhesion of the metal-ceramic interface was enhanced dramatically by simultaneous ion bombardment of 500 eV argon ions during vapor deposition of metal films on ceramic substrates. This work suggested that high energy ions (greater than, say, 10 KV) were not necessary to produce highly adherent IBAD films on substrates.

It will be highly desirable if the excellent properties of the IBAD films, prepared by using the higher energy (30 KV) ion beam, can be produced by using the lower energy (1 KV) ion beam, leading to a significant reduction in processing cost. The current study intends to investigate the effects of ion energy (using 30 KV and 1 KV nitrogen ions) and the ion-to-atom arrival ratio on the microstructure and the tribological performance of the IBAD films. This paper summarizes the results of the microstructural characterization of the IBAD films.

EXPERIMENTAL

For the 30 KV nitrogen ion IBAD process, a Varian Implanter was used as the ion source

which was attached to a specimen chamber with an electron-beam evaporator inside. For the 1 KV nitrogen ion IBAD process, a 3 cm diameter Kaufman ion gun was used with the same evaporator. The ion-to-atom arrival ratio (R) was controlled by monitoring the ion current, the evaporation rate and the background gas pressure in a feedback loop. The ion-to-atom arrival ratio studied varied from 0.01 to 0.03 for the 30 KV IBAD process and from 0.01 to 0.3 for the 1 KV IBAD process.

IBAD films used in microstructural characterization were deposited on single crystal NaCl substrates. These films were ~100 nm in thickness. Good thin film TEM specimens were easily obtained by dissolving the NaCl substrate in water. Thick IBAD films (~2.7 microns) used for the cross-section TEM (or XTEM) and SEM fractography were deposited on single crystal silicon wafers. Tribological evaluation IBAD specimens were deposited on AISI M50 steel substrate. Prior to each deposition, the substrate surface was sputtered clean by the ion beam to reduce contamination.

For the XTEM study, where transmission electron microscopy was performed perpendicular to the film thickness direction, the specimen preparation technique used was similar to that of Bravman et al [5]. The objective of the XTEM study was to examine the grain morphology of IBAD films to ascertain whether columnar grains (rather than equiaxed grains) were formed along the thickness direction during the IBAD process. For the current study, substrates were maintained at ambient temperature during the IBAD process.

ESCA analysis of the IBAD films was performed on a Leybold-Heraeus Surface Analysis System. The vacuum of the system during the analysis was maintained at 1×10^{-9} mbar. Comparative rolling-contact-fatigue (RCF) tests were performed on uncoated and IBAD TiN coated AISI M50 steel rods using a Federal Mogul RCF tester with a maximum Hertzian stress of 786 ksi.

RESULTS AND DISCUSSION

Figure 1 shows the effect of ion energy on the morphology of the IBAD microstructure. The SEM fractographs of the 2.7 microns thick films appear to indicate a change in the grain morphology from the columnar grain structure in the PVD (0 KV) condition to a more or less equiaxed grain structure in the 1KV and 30 KV IBAD conditions. The TEM dark-field micrographs taken from the diffracted ring indicate a trend of increasing grain size as the ion energy is increased from PVD (0 KV) to 1 KV to 30 KV. Notice that the diffraction pattern of the PVD condition is similar to that of IBAD conditions.

The effect of ion-to-atom arrival ratio on the microstructure of the IBAD film is shown in Figure 2. As the ratio increased from 0.01 to 0.03 to 0.3, increasing grain size were observed. This observation suggests that the higher-arrival-ratio-lower-energy IBAD process is roughly equivalent to the lower-arrival-ratio-higher-energy IBAD process. In other words, it is the ion energy per arriving atom that seems to control the formation of TiN grains.

Previous NRL work [1-3] and recent ESCA analysis by Dauplaise et al [6] all indicated that significant amounts of oxygen and carbon were incorporated along with the nitrogen during the TiN IBAD process. Furthermore, the ESCA results indicated that the Ti 2p doublet peaked at 459 eV (for the TiO_2 type bonding) instead of peaking at 455 eV (for the Ti-N type bonding). It was also noticed that increasing the ion-to-atom arrival ratio from 0.01 to 0.3 led to an increase in

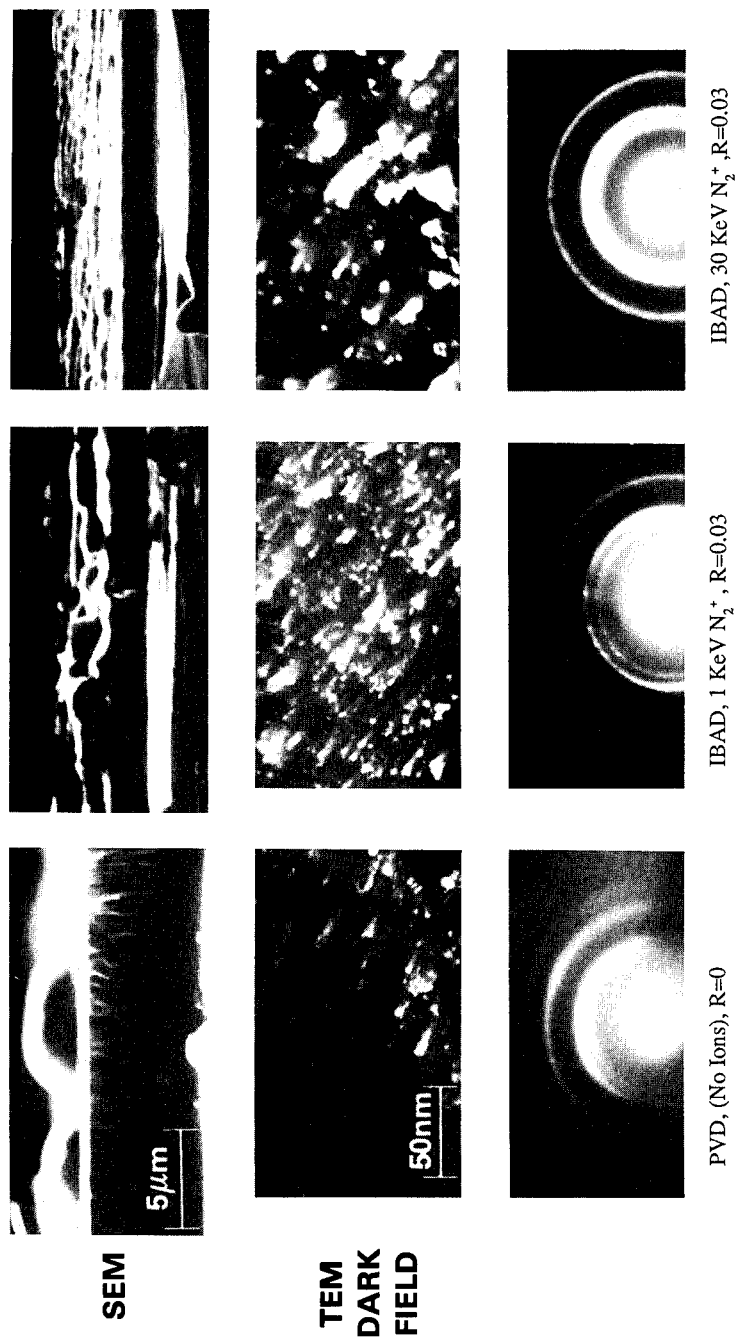


Figure 1. Effects of nitrogen ion energy on the morphology of IBAD films. In SEM fractographs shown on the top, the ~2.5 micron thick films were deposited on Si substrates. Columnar grains were seen on the PVD film while no columnar grains were observed in IBAD films. In TEM dark-field micrographs shown in the middle row, these micrographs were taken from ~100 nm thick films deposited on NaCl substrates. The grain size of TiN appears to increase with increasing ion energy. In the bottom row, all SAD patterns show the same cubic Fm3m NaCl-type structure with lattice parameter of ~0.417 nm. ESCA analysis suggests Ti(O, N, C) substitutional solid solution.

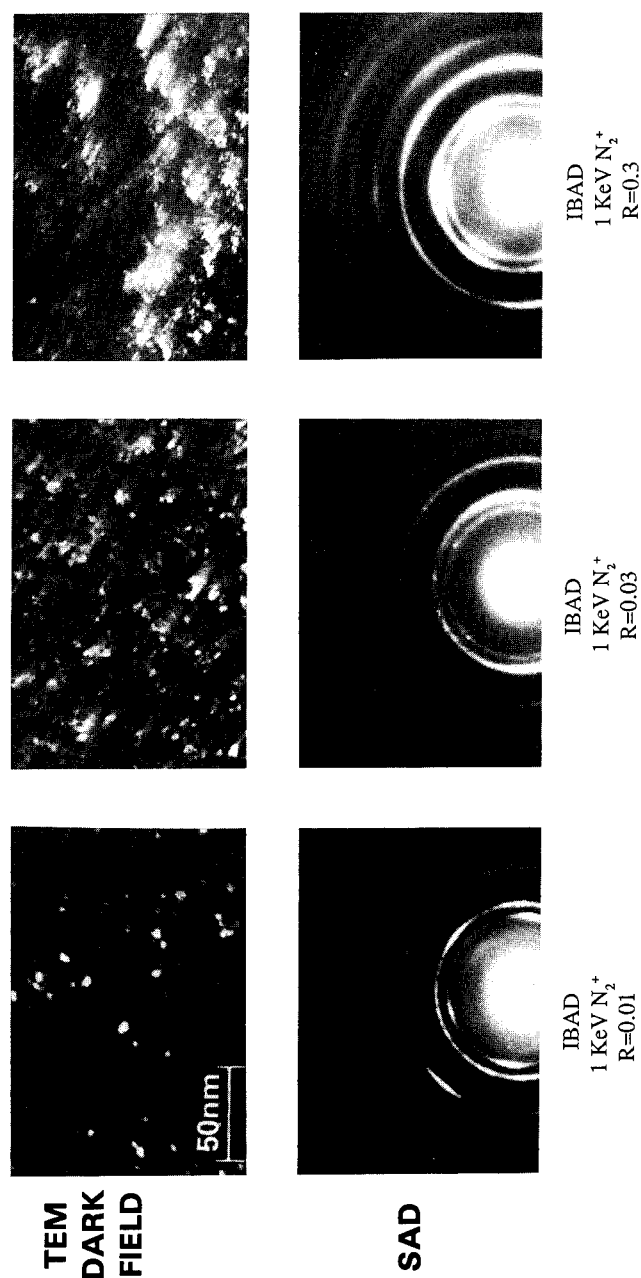


Figure 2. Effects of ion-to-atom arrival ratio (R) on the morphology of IBAD films prepared by using 1 KeV N_2^+ ions. TEM dark-field micrographs were taken from $\sim 100\text{nm}$ thick IBAD films deposited on NaCl substrates. The grain size of TiN appear to increase with increasing ion-to-atom arrival ratio. The SAD patterns indicate an increase of lattice parameter from $\sim 0.417\text{nm}$ for $R=0.01$ and 0.03 to $\sim 0.428\text{nm}$ for $R=0.3$. This increase in lattice parameter with increasing R suggests substitution of nitrogen for oxygen inside the IBAD film at higher R .

the lattice constant of the IBAD film by ~2.5% as measured from the TEM diffraction rings. It should be pointed out that TiO, TiN and TiC all have the same cubic NaCl-type crystal structure with slightly different lattice constants: 0.4177 nm (TiO), 0.424 nm (TiN) and 0.4327 nm (TiC). Since no evidence of TiO, TiN and TiC phase separation was observed in the diffraction patterns, it is reasonable to assume that the current silver-colored "TiN" IBAD films are actually Ti(O,N,C) type substitutional solid solutions with varying amounts of oxygen, nitrogen and carbon. It is therefore suggested that increasing the ion-to-atom arrival ratio tends to substitute more nitrogen for oxygen in the IBAD film, expanding the lattice parameter.

The grain morphology in IBAD films was investigated further by comparing the TEM (along the thickness direction) and the XTEM (normal to the thickness direction) micrographs. As seen from Figure 3, both TEM and XTEM micrographs and their associated diffraction patterns indicate no columnar grains in IBAD films prepared by 1 KV nitrogen ions and with an ion-to-atom arrival ratio of 0.03 at ambient substrate temperature.

Recent tribological evaluation by Kant et al [7] on these silver-colored soft TiN IBAD films prepared by 1 KV nitrogen ions indicated excellent adhesion to the substrate. Similar to the 30 KV IBAD films reported earlier, the 1 KV IBAD films were ductile during wear. Evaluation of the effect on the rolling contact fatigue (RCF) performance of M50 steel rods coated by the IBAD process was conducted by Middleton et al [8]. Results of the on-going RCF test will be reported elsewhere when completed.

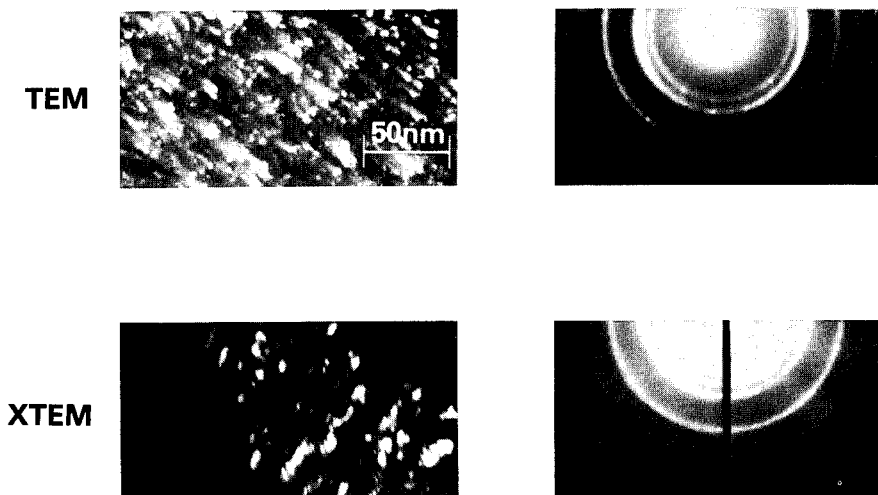


Figure 3. Comparison of TEM and XTEM on IBAD film with 1 KeV N_2^+ , $R=0.03$. No evidence of columnar grains was observed in the IBAD film.

CONCLUSIONS

1. At the ion-to-atom arrival ratio of 0.03, increasing the nitrogen ion energy tends to increase the grain size in the IBAD films.
2. At the constant nitrogen ion energy of 1 KV, increasing the ion-to-atom arrival ratio tends to increase the grain size in the IBAD films.
3. Increasing the ion-to-atom arrival ratio tends to substitute more nitrogen for oxygen in the IBAD films. The IBAD films studied were all silver-colored. They all showed cubic NaCl type crystal structure with varying amounts of oxygen, nitrogen and carbon in the Ti(O,N,C) type substitutional solid solution.

ACKNOWLEDGMENT

This work is supported by U. S. Army Materials Technology Laboratory through Contract DAAL04-88-C-0013. Additional funding was provided by AVSCOM, Ft. Eustis, VA.

REFERENCES

1. B. D. Sartwell, Ion Plating And Implantation: Application to Materials, R. F. Hochman ed., Atlanta, GA, pp. 81-89 (1985)
2. R. N. Bolster, I. L. Singer, R. A. Kant, B. D. Sartwell and C. R. Gossett, presented at International Conference on Metallurgy Coatings, April 11-15, 1988, San Diego, CA
3. G. K. Hubler, D. Van Vechten, E. P. Donovan and R. A. Kant, presented at ASM Conference on Ion Implantation and Plasma Assisted Processes for Industrial Applications, May 22-25, 1988, Atlanta, GA
4. J. E. E. Baglin, MRS Symposium on Thin Films: The Relationship of Structure to Properties, MRS Symposium Proceedings, 47, pp. 3-10 (1985)
5. J. C. Bravman and R. Sinclair, J. Electron Microscopy Technique, 1, pp. 53-61 (1984)
6. H. M. Dauplaise and A. L. Chang, , U. S. Army Materials Technology Laboratory Technical Report (to be published)
7. R. A. Kant, S. A. Dillich, B.D. Sartwell and J. A. Sprague, (presented at this MRS meeting, A3.6/S3.6, Fall 1988)
8. R. Middleton and A. L. Chang, U. S. Army Materials Technology Laboratory Technical Report, (to be published)

THE FRICTION AND WEAR BEHAVIOR OF ION BEAM ASSISTED NITRIDE COATINGS

Thomas G. Tetreault, J.K. Hirvonen, and G. Parker
Spire Corporation, Patriots Park, Bedford, MA 01730
J.P. Hirvonen, University of Helsinki, Helsinki, Finland

ABSTRACT

The method of Ion Beam Enhanced Deposition, (IBED), was used to produce hard films of $i\text{-BN}$, $i\text{-Si}_x\text{N}_y$ and $i\text{-Ti}_x\text{N}_y$. The friction, hardness, adhesion, and wear behavior of these nitride coatings were examined using a ball-on-disc friction/wear tester. The friction and wear results were sensitive to stoichiometry and the presence of impurities (e.g., hydrogen) in the film as well as the choice of ball material (400C stainless steel or silicon nitride).

INTRODUCTION

Because of their high hardness and refractory nature, many nitride compounds are excellent candidates for coatings in a variety of high mechanical and/or thermal stress applications [1]. As is often the case with any coating, and in particular with coatings to be used under conditions of high stress, a key limiting factor to optimum performance is its ability to adhere to the substrate upon which it was deposited.

Recently, the technique of IBED has become an increasingly studied method of applying highly adherent coatings. The IBED process, shown schematically in Figure 1, consists of an electron beam evaporation of a solid phase (viz., boron, silicon, or titanium) onto a substrate and simultaneous bombardment of the growing layer with energetic (100 - 1000 eV) ions (viz., N_2^+ and N^+). Ion beam bombardment results in a mixed zone interface between substrate and coating, and characteristically gives IBED-grown films superior adhesion as well as higher density and lower porosity, compared to similar films by more conventional techniques, due to the reduction of columnar microstructure growth.

EXPERIMENTAL

The IBED facility shown schematically in Figure 2, is a two-chambered, differentially pumped, high vacuum system. The lower evaporation chamber contains the electron beam evaporator and is pumped by a four-inch LN_2 trapped diffusion pump. The upper target chamber contains the sample holder and is pumped by an eight-inch cryopump. The usual working base pressure for the system throughout is 1×10^{-7} torr (1.3×10^{-5} pa) with water being the predominant component as determined by an in-situ residual gas analyzer.

For the coatings in this study, the evaporation rate of the solid phase was set at 2-4 Å/sec and was controlled by a quartz crystal rate monitor while the nitrogen ion flux at the substrate was 150-500 microamps/cm². The ratio of ion flux to evaporant rate was varied per deposition in order to influence the stoichiometry of the resulting coatings. All coatings were deposited on Si (100) wafers.

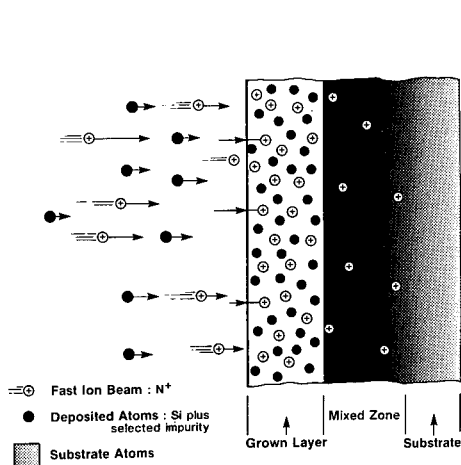


FIGURE 1. SCHEMATIC REPRESENTATION OF THE IBED PROCESS.

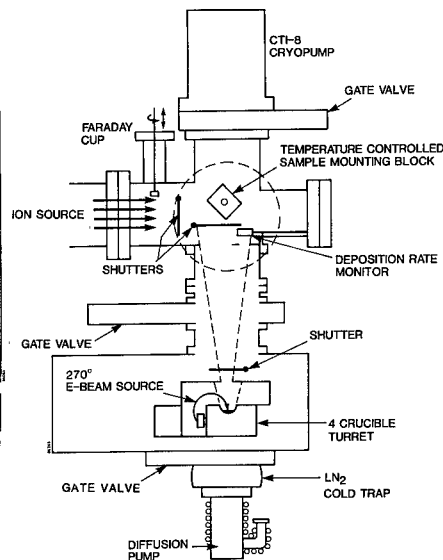


FIGURE 2. SCHEMATIC OF THE IBED FACILITY

The friction and wear behavior of the coatings were investigated using an in-house built ball-on-disc apparatus shown in Figure 3. The test sequence involves a combination of adhesive and abrasive wear. Either continuous circular motion or reciprocating line motion of ball on coating is possible. Ball materials compared were silicon nitride and 440C stainless steel. All tests were run unlubricated in air.

The load on the ball normal to the test sample can be varied by means of adding calibrated mass to the weight pan. During testing, the test stage is moved beneath the stationary loaded ball and the horizontal displacements of the ball/lever arm assembly are recorded on a strip chart recorder from the output of a load cell in the lever arm. Prior to the test, the recorder output is calibrated under a known load/displacement so that under the true test conditions the recorded signal yields the friction force of the ball/coating system. The coefficient of friction, μ , can now be calculated as the ratio of the normal force to the friction force.

The wear for the various systems was evaluated by measuring the depth profile of the wear scar seen on the coating using a Dektak profilometer and comparing it to the size of the wear flat on the ball surface under microscopic inspection. A new ball surface was used for each test. By measuring the diameter of the contact area of the ball, the volume loss of the ball can be calculated in a manner similar to Hartley [2]. A dimensionless wear parameter, K , can be derived for the ball following Archard [3]:

$$K = 3H(\Delta V)/Ns$$

where H , ΔV , N and s are respectively the hardness of the ball, the volume loss of the ball, the load, and the sliding distance. Figure 4 shows a typical wear track profile and associated ball wear flat.

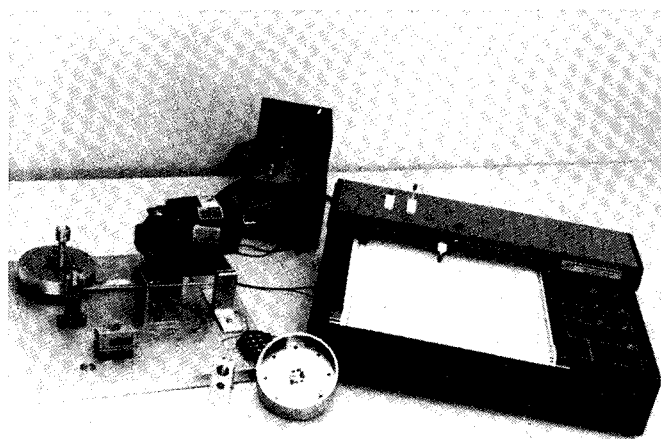


FIGURE 3. FRICTION/WEAR APPARATUS.

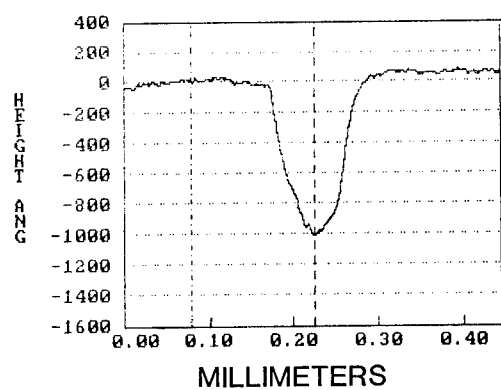


FIGURE 4. REPRESENTATIVE WEAR TRACK PROFILE AND ASSOCIATED BALL WEAR (400X) FOR 440C STAINLESS STEEL BALL ON i-BN SYSTEM.

The Knoop microhardness of each coating was determined using a Tukon hardness tester at a 5 gram load. Adhesion of the coatings was examined qualitatively by means of the traditional "Scotch" tape test in addition to a diamond scratch method. The tape test involves pulling off a piece of Scotch tape which has been firmly pressed onto the coating over the uncoated/coated boundary regions. The scratch technique entails dragging a diamond point under a constant load over a similar boundary region. In each case, the test region is evaluated with optical microscopy for any evidence of delamination or adhesive failure. The scratch method also affords a qualitative determination of ductile or brittle behavior in the coatings.

RESULTS AND DISCUSSION

Table I summarizes the results of the hardness and adhesion testing of the nitride coatings investigated. A coating was said to have passed the tape test if after removal of the tape no coating loss, flaking, or cracking was observed. Similarly, passing the scratch test means that no cracking or spalling of the coating was observed along the scratch. The character was qualitatively termed ductile if the scratch had smooth, plastically deformed edges and brittle if the scratch edge was cracked or rough.

TABLE I. HARDNESS, ADHESION, AND CHARACTER OF IBED NITRIDE COATINGS.

Sample #	Knoop Hardness Kg/mm ² (5 g load)	Adhesion Tape/Scratch	Character
0626 BN	3500	Pass/Pass	Ductile
0721 BN	2200	Pass/Pass	Ductile
0121 BN (Hot)	2500	Pass/Fail	Somewhat brittle
1103 BN (Hot)	3600	Pass/Pass	Ductile
0317 BN	1300	Pass/Pass	Ductile
0927 Ti _x N _y	1100	Pass/Pass	Ductile
0928 Si _x N _y	3900	Pass/Pass	Ductile
Si(100) control	1216		Brittle

The variation in coefficient of friction with sliding distance is summarized in Figures 5 and 6 for the Si₃N₄ ball and the 440C ball respectively. Additionally Figure 5 includes the boron to nitrogen ratio of the i-BN films determined by nuclear reaction resonance analysis as well as a qualitative mention of hydrogen content, [H], from forward recoil spectrometry. [It should be noted that coating #0121 was worn through after about 600 cycles and that data after that point are not representative of the true coefficient for the coating.] Figure 6 includes the wear parameter, K, for the 440C systems investigated.

There appears to be a general increase in friction with increasing B/N ratio in the Si₃N₄ ball system while little difference is seen with the 440C system. Hydrogen content of the film seems to have an effect on the friction in both ball systems, i.e., friction increasing with [H].

In the i-BN system, adhesive transfer of ball material to the coating occurred only with sample #0317. After the 440C ball test, several patches (<1000 Å thick) could be seen on the coating. A more continuous distribution of patches (~1 micron thick) was present after the Si₃N₄ ball test. The occurrence of this phenomena may be related to the lower hardness associated with this coating (see Table I).

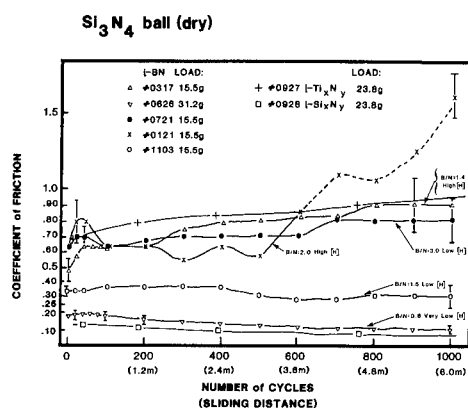


FIGURE 5. COEFFICIENT OF FRICTION VERSUS SLIDING DISTANCE. (Si₃N₄ ball, dry, on IBED nitride coatings.)

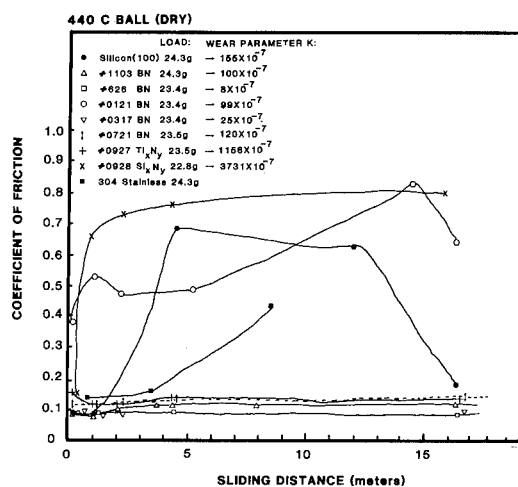


FIGURE 6. COEFFICIENT OF FRICTION VERSUS SLIDING DISTANCE. (440C ball, dry, on IBED nitride coatings.)

Patches of 3000-5000 Å thickness were seen on the i-Ti₃N₂ coating following the Si₃N₄ ball test while patches of ~1 micron thickness were found on the i-Si₃N₄ coating after testing with the 440C ball (see Figure 7).

No evidence of wear whatsoever was found on either ball or coating in the Si₃N₄ ball on i-Si₃N₄ system.



FIGURE 7. PORTION OF WEAR TRACK (SAMPLE #0928 i-Si₃N₄) SHOWING ADHERED MATERIAL FROM 440C BALL (400X).

CONCLUSIONS

Hard nitride coatings of i-BN, i-Si₃N₄, and i-Ti₃N₄ have been deposited by the IBED method and examined for friction and wear using a ball-on-disc tester. Many of the coatings show low friction ($\mu \approx 0.1$) against 440C stainless steel and Si₃N₄ counterfaces. The coatings generally show a ductile behavior with very good adhesion to the substrate [Si(100)]. Friction seems to increase in the i-BN system with increasing B/N ratio and also when hydrogen content is higher.

Clearly, there is a need for further investigation into the role that deposition parameters play in determining the mechanical behavior of IBED nitride coatings. The promising results presented here, however, suggest that we next examine the behavior of these films on an application oriented substrate such as M52 steel.

ACKNOWLEDGMENTS

The authors wish to thank AFWAL and R. McConnell for their support in this research.

REFERENCES

1. H. Holleck, J. Vac. Sci. Technol. A4(6), pp. 2661-2669 Nov./Dec. 1986
2. N.E.W. Hartley, Tribology International, p. 65 April 1975.
3. J.F. Archard, Journal of Applied Physics, Vol. 24, p. 981 (1953).

MICROSTRUCTURAL STUDIES OF IAD AND PVD Cr COATINGS BY CROSS SECTION TRANSMISSION ELECTRON MICROSCOPY

C. C. CHENG, R. A. ERCK, AND G. R. FENSKE

Materials and Components Technology Division, Argonne National Laboratory, 9700 S. Cass Ave, Argonne, IL 60439

ABSTRACT

Cross section transmission electron microscopy was used to study the microstructure and interface structure of Cr films deposited by ion-assisted deposition as a function of the incident ion energy. High-energy ion bombardment (1 keV) was found to enhance the adhesion of the deposited film owing to the formation of an intermixed layer, whereas deposition with low-energy ions (100 eV) was found to reduce or eliminate grain boundary porosity. A tailored Cr film with excellent adhesion and no grain boundary porosity was deposited by combining high- and low-energy ion bombardment.

INTRODUCTION

Coatings are applied to materials for a large and growing number of purposes, including increased wear resistance, reduced friction, corrosion protection, optical requirements, electrical conduction or insulation, or simply for decorative effect. Conventional chemical and physical vapor depositions (CVD and PVD) still play the major roles in fulfilling most of these purposes. However, the use of energetic-ion beams to modify the near-surface region of materials has been increasingly explored in recent years, especially for tribological purposes.

Among ion beam processes, ion-assisted deposition (IAD) is a relatively new technique involving ion bombardment and concurrent PVD to produce controlled films. Many investigators have shown that ion bombardment can be used to increase nucleation rates [1], enhance adatom mobilities [2], promote the adhesion of films [3], increase the film density [4,5], decrease the average grain size [6], inhibit the formation of a columnar structure [7], reduce the internal stress [8], and increase the overall defect density [9].

The tribological and chemical properties of films strongly depend on the structure of the film and in particular, on the grain morphology and the structure of the substrate/coating interface. Studies of the film microstructure are necessary to understand the kinetics of film formation and the resulting in-use performance. Transmission electron microscopy (TEM) is a powerful tool for studying the microstructure of thin films, which often possess small-size grains and many crystalline defects. Observations by TEM are most commonly performed with the electron beam normal to the plane of the film. Because the film microstructure changes during film growth, cross section TEM studies give a more complete picture of the film structure and the film/substrate interface. Thus, it is possible to study the relationship between the film and substrate microstructures. This is especially important for IAD because the grain microstructure and the substrate/film interface are strongly influenced by the energetic ions. Grain and interface structures depend on a number of IAD process parameters, including the incident ion energy, the ion/vapor arrival rate, and the deposition temperature. A series of Cr depositions was therefore performed in this study to investigate the effects of the incident ion energy on the microstructure of the deposited film and on the structure of the substrate/coating interface.

EXPERIMENTAL PROCEDURES

Chromium films were electron beam evaporated onto substrates that were at room temperature. The deposition rate was stabilized by means of a quartz crystal rate monitor positioned above and to the side of the substrate. A movable shutter was used to shield the substrate from the vapor while the evaporation conditions were stabilized. Energetic Ar ions were produced with a Kaufman-type ion source that neutralized the ion beam by means of a heated filament. The current density of the ion beam was measured prior to each deposition with a calorimeter that could be inserted into the path of the beam in front of the specimen. The metal

vapor and the ions were incident on the specimen at angles of $\sim 45^\circ$ and $\sim 55^\circ$ to the surface, respectively. Typical base pressures in the turbopumped system were in the low 10^{-5} Pa range; the Ar pressure during coating was $6 \cdot 10^{-3}$ Pa, with a gas flow of 3 sccm. The depositions were performed at ion/vapor arrival rates of approximately 0.4 and Cr vapor deposition rates of approximately 0.4 nm/s.

The method used to prepare specimens for cross section TEM is described in detail elsewhere [10]. In this study, the ion beam milling was performed with an Ion Technology, Inc. mill with two ion beam sources. The ion sources were operated at a voltage of 6 kV, which gave an ion current of 2 mA. The specimen was first etched at an angle of 20° to the surface for ~ 2 hours. In the final etching stage, the angle was reduced to 15° . Usually, etching of 1-2 hours at 15° was needed to obtain an electron-transparent specimen.

RESULTS AND DISCUSSION

Figure 1 shows a cross section TEM micrograph of a PVD Cr film deposited at a Cr vapor deposition rate of 0.4 nm/s. The film microstructure is columnar and grain boundary porosity is present in the form of long, narrow pores (arrows). It is a structure typical of zone 1 in a Movchan-Demchishin diagram [11]. The columnar structure and grain boundary porosity are thought to be due to low surface mobility and to geometrical shadowing effects [12].

Figures 2, 3, and 4 show cross section TEM micrographs of IAD Cr films deposited with 1-keV, 300-eV, and 100-eV ion bombardment, respectively. Grain boundary porosity can be identified in the IAD films bombarded with 1 keV ions (Figure 2), and 300 eV ions (Figure 3). Figure 4 shows no grain boundary porosity in the specimen that was bombarded with 100 eV ions. However, some narrow pores were observed in regions near the top of the film in this specimen. Therefore, concurrent ion bombardment can be used to reduce or eliminate the grain boundary porosity one normally obtains in PVD films, but the bombarding ions must be of low energy. It should also be noted that the porosity in the 1-keV IAD film (Figure 2) is much coarser than in the PVD film in Figure 1, or in the 300-eV IAD film in Figure 3.

It has been found both experimentally [4] and theoretically [5] that increases in film density can occur during IAD. It is thought [13] that they may occur as a result of collisional events in the first few monolayers. The collision of ions of sufficient energy with atoms in the growing film drives knock-on atoms deeper into the film, filling in porosity. If the collision cascade occurs at or near the surface, the vacancies produced will be filled in by the arriving vapors. Thus there is an optimum ion energy for the reduction of grain boundary porosity such that copious numbers of knock-on atoms are produced and the resulting cascades are sufficiently close to the surface. At higher energies, however, the ion-scattering cross section decreases [5] and vacancies are produced much deeper inside the film thus broadening the porosity of the growing films.

Chromium films deposited by PVD and IAD with 100-eV Ar bombardment, as shown in Figures 1 and 4 respectively, exhibited a gap between the film and the substrate, indicating that adhesion is a problem. In contrast, no gap was observed in the 300-eV and 1-keV IAD films. An Fe-Cr intermixing layer, detected by X-ray energy dispersive spectrometry (XEDS), was observed near the interface region of these 300-eV and 1-keV IAD films. Moreover, the columnar grain morphology of these 300-eV and 1-keV IAD films, especially near the interface, was found to be relatively shorter and smaller than that of PVD and 100-eV IAD films. This suggests that 300-eV ion bombardment can cause an intermixing between the growing film and the substrate at the interface region and also increase the nucleation rate of the growing film at the interface. In the 1-keV IAD samples, a similar intermixing layer was observed, but it cannot be seen in Figure 2 because the layer is out of contrast. Further, many dislocations were observed in the growing film near the interface region, which made the grain morphology of this sample very difficult to resolve.

Good adhesion is considered to be one of the most important necessities for good film performance. Adhesion of films is generally understood to depend on a variety of aspects of the interface region [12], such as its atomic bonding structure and the state of stress. Ion bombardment has been found [5] to have a large influence on the interface structure and thus on the adhesion of films. The mechanism may be an increase in the density of nucleation sites, and/or formation of an intermixing layer at the interface region. The increase in the density of nucleation sites can reduce the amount of agglomeration and void formation that occurs during

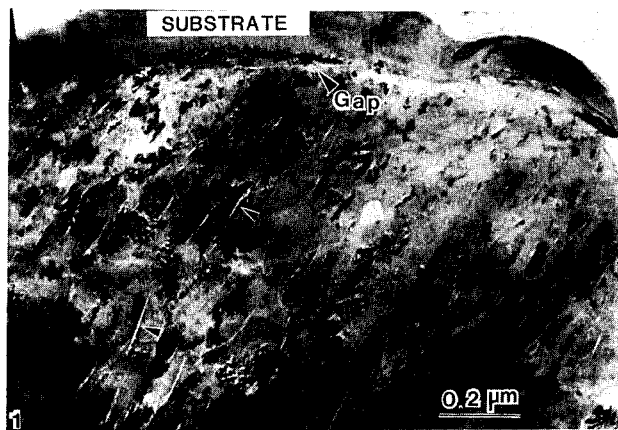


Figure 1. Cross-sectional TEM view of a PVD Cr Film.

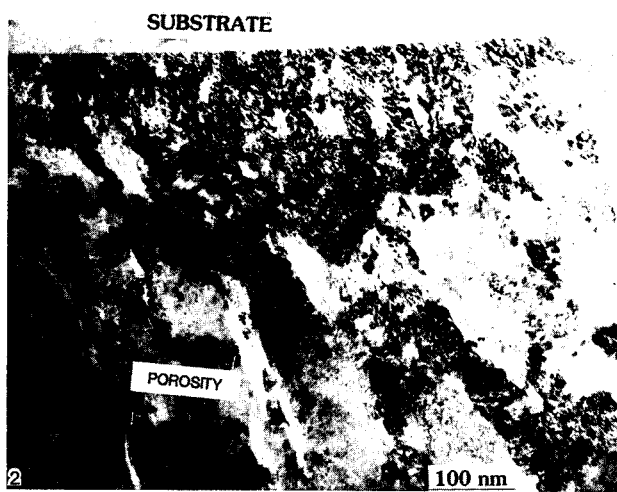


Figure 2. Cross-sectional TEM view of an IAD Cr film deposited with 1-keV Ar ions.

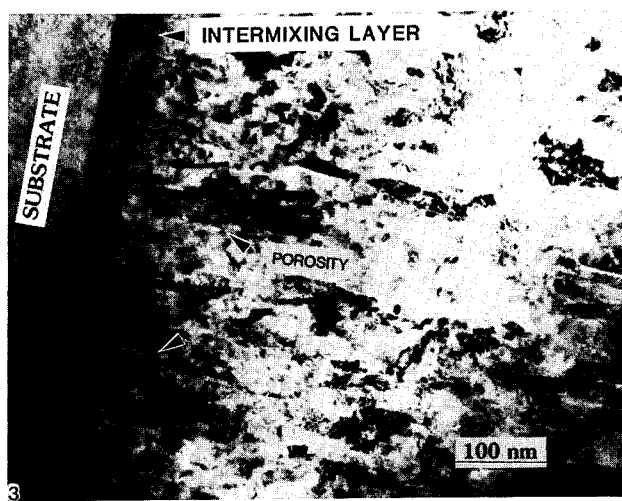


Figure 3. Cross-sectional TEM view of an IAD Cr film deposited with 300-eV Ar ions.

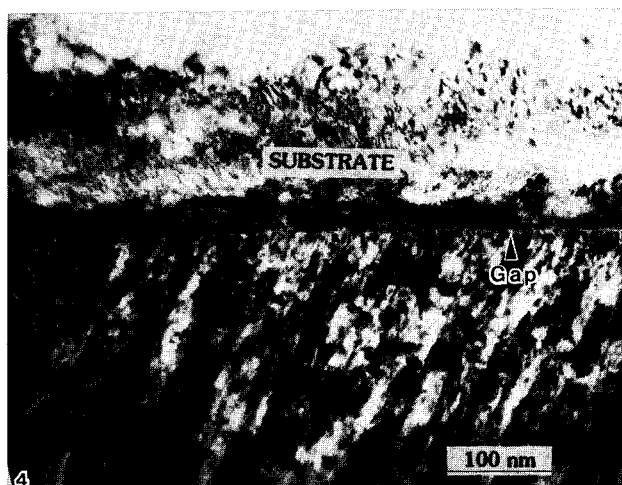


Figure 4. Cross-sectional TEM view of an IAD Cr film deposited with 100-eV Ar ions.

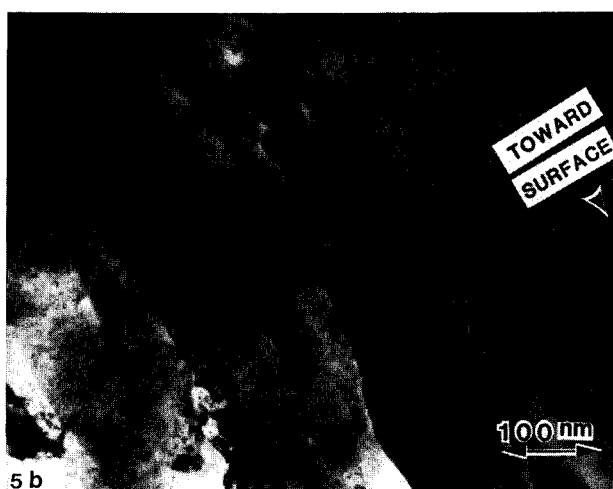


Figure 5. Cross-sectional TEM views of an IAD Cr film deposited with a combination of 1-keV and 150-eV Ar ions. (a) Near the interface region; (b) near the surface region.

the initial island growth [14]. The formation of an intermixing layer can serve as a "glue" between film and substrate [12]. In addition, Rossmagel and Cuomo [8] have shown that ion bombardment can convert a tensile stress, commonly found in a PVD film, to a compressive stress, further enhancing the integrity of deposited films. Coincidentally, they found that the ion energy needed to change the stress from tensile to compressive for an IAD Cr film was between 200 and 300 eV, which correlates well with our observations. In summary, the increase in adhesion of Cr film due to ion bombardment is a combination of effects, i.e., the formation of an intermixing layer, an increase in nucleation rates, and a change of stress at the interface region.

One advantage of IAD is its capability to more easily produce films with tailored properties for varied purposes. In this study, we have shown that film deposition with low-energy ions can produce a dense microstructure with very little grain boundary porosity, but that adhesion may be poor. On the other hand, deposition with high-energy ions seems to produce a more adherent film, but grain boundary porosity becomes a problem. To produce a film with good adhesion and little grain boundary porosity, we used high-energy ions (1 keV) to bombard the sample prior to and during the start of the deposition. As the film became established (~20 nm thick) the energy of the bombarding ions was progressively reduced to 150 eV and kept at 150 eV for the remainder of the deposition. Figures 5a and 5b show cross-sectional views of this tailored film, near the interface and surface regions, respectively. As expected, an intermixing layer at the interface is seen in Figure 5a, evidently due to the initial 1-keV bombardment. No grain boundary porosity was observed in the film even near the surface region, as shown in Figure 5b.

CONCLUSION

Grain boundary porosity and film adhesion are of concern in conventional vapor deposition processes. Ion-assisted deposition can reduce or eliminate the amount of grain boundary porosity by depositing the film with low-energy ion bombardment. The adhesion of deposited films can be increased by depositing the film with initial high-energy ion bombardment that causes the formation of an intermixing layer. In this study, a tailored Cr film that experienced no detachment from the substrate and no grain boundary porosity was deposited by the combination of the high- and low-energy ion bombardments.

ACKNOWLEDGMENT

Work supported by the Tribology Program, Energy Conversion and Utilization Technologies Division, U. S. Department of Energy under Contract W-31-109-ENG-38.

REFERENCES

1. R. P. Netterfield and P. J. Martin, *Appl. Surf. Sci.* **25**, 265 (1986).
2. M. Marinov, *Thin Solid Films* **46**, 267 (1977).
3. J. E. E. Baglin, *Mater. Sci. Eng.* **B1**, 1 (1988).
4. P. J. Martin, R. P. Netterfield, and W. G. Sainty, *J. Appl. Phys.* **55**, 235 (1984).
5. K.-H. Mullen, in *Materials Modification and Growth Using Ion Beams*, edited by U. Gibson, A. E. White, and P. R. Pronko (*Mater. Res. Soc. Proc.* **93**, Pittsburgh, PA, 1987) pp. 275-285.
6. C. Huang, G. Lim, E. Parmigiani and E. Kay, *J. Vac. Sci. Technol.* **A3**, 2161 (1985).
7. B. O. Johansson, J.-E. Sundgren and U. Helmersson, *J. Appl. Phys.* **58**, 3112 (1985).
8. S. M. Rossmagel and J. J. Cuomo, *Vacuum* **38**, 73 (1988).
9. E. Parmigiani, E. Kay, T. C. Huang, J. Perrin, M. Jurich, and J. D. Swalen, *Phys. Rev.* **B33**, 879 (1986).
10. A. Erdemir and C. C. Cheng, *Ultramicroscopy*, accepted for publication, (1989).
11. B. A. Movchan and A. V. Demchishin, *Phys. Metal. Metallogr.* **28**, 83 (1969).
12. D. M. Mattox, in *Deposition Technologies For Films and Coatings*, edited by R. F. Bunshsh et al. (Noyes Publications, Park Ridge, NJ, 1982) p. 66.
13. P. J. Martin, *Vacuum* **36**, 585 (1986).
14. D. M. Mattox, in *Adhesion Measurements of Thin Films, Thick Films and Bulk Coatings*, *ASTM STP 640*, edited by K. L. Mittal (ASTM, Warrendale, PA, 1978) p. 54.

UNLUBRICATED SLIDING PROPERTIES OF ION BEAM AND EXCIMER LASER
MIXED Fe-Ti-C MULTILAYERED FILMS

J-P. Hirvonen, M. Nastasi, T.R. Jervis, J.R. Tesmer,
and T.G. Zocco
Materials Science and Technology Division, Los Alamos National
Laboratory, Los Alamos, New Mexico 87545, USA

ABSTRACT

Multilayered Fe-Ti-C films consisting of eleven sublayers were vacuum deposited onto an AISI 304 stainless steel substrate and subsequently mixed using either 400 keV Xe ions or an excimer laser operating at a wavelength of 308 nm. Ion mixing was accomplished in a two step process: the multilayers were first irradiated with 1×10^{17} Xe/cm² at 520 °C, after which half of the sample was irradiated with 5×10^{15} Xe/cm² at 0 °C. Laser mixing was carried out at both 1.1 and 1.7 J/cm² with the number of pulses varied between 1 and 10. Pin-on-disc studies revealed only slight differences between the two kinds of ion beam mixed samples, whereas the dry sliding properties of laser mixed samples were strongly dependent on the total fluence used. In the optimum conditions, similar friction coefficients were obtained on both kinds of samples.

INTRODUCTION

As an alternative to titanium implantation into steels, ion beam mixing of multilayer Fe-Ti structures [1] or laser mixing of a single titanium layer [2] have been studied. Ion beam mixing is generally a non-equilibrium process and entirely independent of the substrate if multilayered structures of several different elements are used [1]. In this sense ion beam mixing is unique and different e.g. from ion implantation. Laser treatment based on the surface melting and subsequent rapid solidification can also be used with multilayered structures, or to produce mixing between a single surface layer and a substrate. The quench rate of laser melting is, however, slower than that of ion implantation or ion beam mixing and this may restrict the possible available microstructures. The processing time of laser surface treatment is the shortest and no vacuum is required, which is an advantage. Despite the differences among these three methods, they provide novel techniques to tailor surface sensitive properties and are of considerable interest from a tribological point of view.

Ion beam mixing of a multilayer Fe-Ti structure results in an amorphous microstructure around the equal atomic composition [1] whereas the microstructure of laser mixed surfaces depends on the amount of mixing. In the case of laser melted Ti on AISI 304 stainless steel an amorphous microstructure is obtained for some levels of mixing [2]. A crystalline structure returns with increasing mixing. Minor constituents of a substrate as well as the substitution of titanium by iron on a one to one basis is also observed in the modified surface [2,3].

The tribological properties of ion or laser beam induced Ti alloys on AISI 304 stainless steel have been reported elsewhere [4-7]. Ion beam mixing of the multilayered Fe-Ti structure produces a lowered friction, although in a test of 1000 passes

the modified surface layer were partially through [4]. In that work samples with linearly varying concentrations of the constituents in a lateral direction were employed. It was observed that the tribological properties were the best around the composition of 50 at. % of Ti. The most striking feature of the surface mechanical properties of the ion beam mixed Fe-Ti alloy was the apparently improved ductibility [5]. In general these results were parallel to those of Follstaedt et al. [8], who implanted titanium into 15-5 stainless steel. Improvement in the tribological properties was observed with increasing titanium fluence, though this improvement never lasted for the 1000 revolutions of the pin-on-disc test. Presumably the titanium concentration in our previous work [4] was higher than the highest one used in ref. [8] probably giving a slightly longer lasting improvement.

The surface mechanical properties of laser melted Ti alloys on AISI 304 stainless steel are very similar to those of ion beam mixed Fe-Ti or titanium implanted steel explained above [6]. Some special features, however, can be noticed [7]. The optimum tribological behavior was obtained at a certain total fluence and this fluence was dependent on the initial thickness of the single titanium layer on the steel. Moreover, the microhardness measurements performed with a nanoindentation technique revealed that the relative hardness of the laser melted surface was lower than that of the untreated material.

The beneficial effects of carbon on the mechanical properties of the surface in titanium implanted steel are well established [8-10]. Carbon implantation into an ion beam mixed Fe-Ti alloy also significantly improves tribological behavior of AISI 304 stainless steel [11]. Consequently, the natural extension of ion and laser beam mixing of Ti with iron or steel is the mixing of ternary multilayer structures consisting of titanium, iron, and carbon. In this work we report the first results of the tribological measurements of ion or laser beam mixed Fe-Ti-C alloys on 304 stainless steel.

EXPERIMENTAL METHODS AND MEASUREMENTS

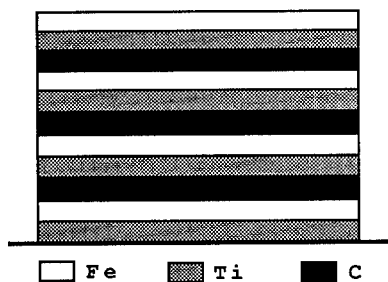


Fig.1. A schematic picture of a multilayered structure.

individual sublayers. Before deposition the substrates were mechanically polished with a diamond paste down to a grade of 0.3 μm and subsequently cleaned in an ultrasonic bath. The total thicknesses of the evaporated iron and titanium layers were

The multilayer structure consisting of eleven sublayers, as illustrated in Fig. 1, was evaporated in vacuum using an e-gun thin film deposition system onto AISI 304 stainless steel substrate of commercial quality. The Vickers hardness of the substrate was 2.21 GPa. The vacuum at the beginning of the deposition was 5×10^{-7} torr and increased to 10^{-6} torr during evaporation. The entire ternary multilayer sample was deposited without breaking vacuum between the evaporation of the

determined as 550 and 600 Å by Rutherford backscattering spectroscopy (RBS). The total carbon concentration after deposition was determined as 5.1×10^{17} C/cm² using the nuclear reaction $^{12}\text{C}(\text{d},\text{p})^{13}\text{C}$ at a deuterium energy of 900 keV.

Ion beam mixing was carried out using Xe^{++} ions at an energy of 400 keV. Based on our earlier studies on ion beam mixing of iron-carbon and titanium-carbon which showed mixing at room temperature to be minimal [12,13], the sample was first bombarded at 520 °C at a fluence of 1×10^{17} Xe/cm². At this temperature the mixing process has been proved to be controlled by radiation enhanced diffusion [13]. Subsequent to the high temperature mixing half of the sample was irradiated at 0 °C with 5×10^{15} Xe/cm². Mixing between different sublayers was found to be complete after this treatment. Because of the high irradiation dose sputtering of the surface layer occurred, and the final thickness was 1000 Å. The corresponding carbon concentration was 3.6×10^{17} C/cm².

Laser mixing of the multilayer structure and alloying with the stainless steel substrate was performed with an excimer laser operated at 308 nm. The treatment was carried out in air at both 1.1 and 1.7 J/cm² with the number of pulses varied between 1 and 10. The repetition rate of pulses was about 1 Hz so that the sample was entirely cooled to the room temperature between the separate pulses. RBS revealed considerable mixing even after the mildest treatment, e.g. 1 pulse at 1.1 J/cm². Mixing in this case occurred presumably between individual sublayers. On the other hand at the highest total fluence deep diffusion of titanium and probably carbon into the substrate was observed. The carbon concentration in the surface layer had decreased to $4.6 - 2.7 \times 10^{17}$ C/cm² depending on the total fluence.

No detectable increase in oxygen concentration was found during either ion beam mixing or laser alloying as determined with the reaction $^{16}\text{O}(\text{d},\alpha)^{14}\text{N}$ at a deuterium energy of 900 keV.

Tribological properties were tested utilizing a pin-on-disc apparatus. Hardened steel pin with a radius of curvature of 3 mm was employed. The friction force was monitored continuously during the measurements. The tests were terminated either after 1000 revolutions or after the increase of the friction indicating the penetration of the pin through the modified surface layer. The load on the pin was 31.2 g. This load produces a Hertzian stress of 440 MPa on the untreated substrate. This is comparable to a yield strength 310 MPa of the base material. The sliding speed was 22 mm/s. Friction and wear measurements were performed in room air without lubrication.

The wear tracks were investigated with the scanning electron microscope (SEM).

RESULTS AND DISCUSSION

The friction coefficients as function of the number of revolutions are shown in Fig. 2 for both types of ion beam mixed samples. As compared to the friction coefficient of the untreated steel ($\mu = 0.9$) the steady state friction of the ion beam mixed surfaces are significantly lower. Within the error bars, which represent the oscillation of the friction during the measurements, the friction coefficients are the same in this regime. After about 2500 revolutions the friction coefficient of both samples begins to rise indicating the surface layer being

worn through. The friction coefficient of the sample bombarded also at 0 °C increases faster than that of the sample bombarded only at 520 °C. This may indicate a slightly better wear resistance of the latter sample. In Fig. 3 the friction coefficients of two laser mixed samples are shown. The corresponding total fluences are 1.1 and 11 J/cm², respectively. The general behavior of these curves differs from those shown in Fig. 2, as no steady state regime can be found. Instead the friction coefficients increase slowly but continuously. In the case of the high total fluence there is also an abrupt change after 2500 revolutions.

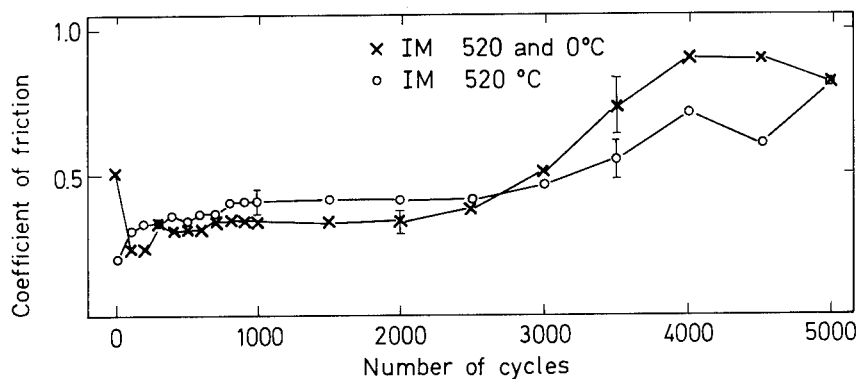


Fig. 2. The friction coefficient of the ion beam mixed samples as the function of a number of revolutions. The mixing temperatures used are shown in the figure. The friction coefficient for untreated steel was 0.9.

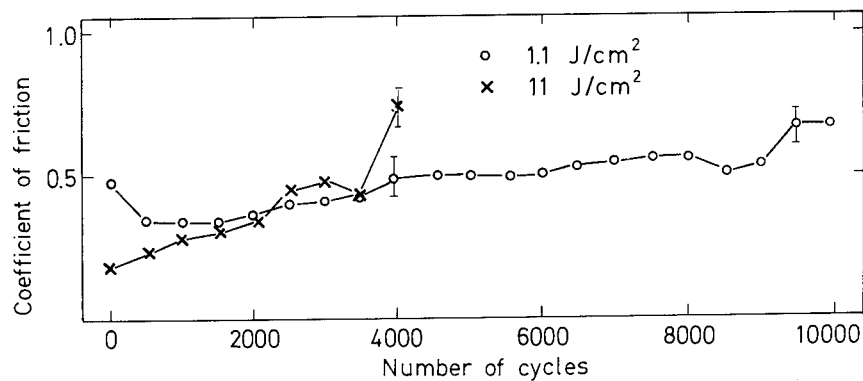


Fig. 3. The friction coefficient of two laser mixed samples as the function of a number of revolutions. The total fluences used are shown in the figure.

Scanning electron microscopy also revealed remarkable differences between the samples. The wear scar of the untreated substrate material exhibited severe damage even after only 1000 revolutions as shown in Fig. 4A. This damage can be characterized as a ductile fracture under the high surface pressure. The wear scars of the ion beam mixed samples after the identical test consist of smooth parallel grooves typical of wear tracks in our previous studies of ion beam mixed materials [5,14]. Comparing further the sample ion beam mixed also at 0 °C (Fig. 4B) to that received the bombarded only at 520 °C (Fig. 4C) shows fewer and shallower grooves on the latter sample. This indicates that the wear resistance was slightly decreased by the 0 °C irradiation.

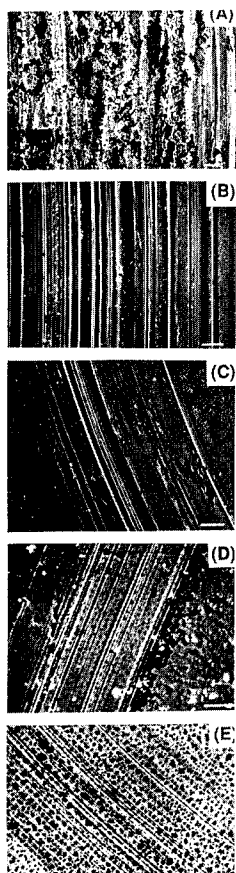


Fig. 4. SEM micrographs of wear scars. A) stainless steel. Ion mixed at B) 520 + 0 °C and C) 520 °C. Laser mixed with D) 11 and E) 1.1 J/cm². Marker length is 10 μm.

This was also confirmed by SEM of the samples after the test of 5000 revolutions. Contrary to the untreated sample the wear tracks on both the ion beam mixed samples exhibited no sign of a ductile fracture after 1000 revolutions. The initiation of fracture type damage on the surface seems to be extremely well inhibited.

The most striking feature of the SEM micrograph of the laser mixed sample is the dispersion of precipitates or inclusions on the surface. This is especially clear in the sample mixed with the low, 1.1 J/cm² total fluence, Fig. 4E. The precise microstructure is not known at this moment. Because this kind of surface was not found on AISI 304 stainless steel mixed only with a single titanium layer [6] the structure must be caused by carbon in the present samples. The morphology of the wear scar on the laser mixed samples also differ from that of the ion beam mixed ones. The grooves or scratches are more finely distributed and no deep grooves can be observed in the case of low total fluence. The wear resistance of this sample was also excellent and a great deal of the original modified surface was still left in the wear track after 10000 revolutions. On the other hand, the wear scar of the sample mixed with the high total fluence, though relatively smooth, has signs of a collapse at the edge of the track. This is probably caused by the softening of the base material during the high fluence treatment.

The wear resistance of the best of laser mixed samples in this work seems to be better than that of ion beam mixed samples. This does not necessarily indicate a real difference. Because of sputtering the ion beam mixed surface layer was significantly thinner than the laser mixed surface. The impractically

high dose of Xe ions required in the ion beam mixing of the present samples is, however, a fact that can be reflected in some tribological properties.

CONCLUSIONS

It is concluded that ion or laser beam mixed multilayered Fe-Ti-C structures on AISI stainless steel exhibited significantly altered tribological properties as compared to those of an untreated substrate material. Except for the sample laser mixed with the highest total fluence all samples possessed a lowered friction and increased wear resistance. In addition, all surface modified samples revealed many characteristics of their own which cannot yet be explained on the basis of the present measurements. A common feature to all was the absence of adhesive interaction between the sliding steel pin and the modified surface and the inhibition of fracture type damage at the surface.

ACKNOWLEDGEMENTS

Ion implantations and RBS analysis were carried out in the Los Alamos Ion Beam Materials Laboratory. This work was supported in part by the United States Department of Energy.

REFERENCES

1. J-P. Hirvonen, M. Nastasi, and J.W. Mayer, *J. Appl. Phys.* **60**, 980 (1986).
2. T.R. Jervis, M. Nastasi, and T.G. Zocco, *Mat. Res. Soc. Proc.* **100**, 621 (1988).
3. T.R. Jervis, M. Nastasi, T.G. Zocco, and J.A. Martin, *Appl. Phys. Lett.* **53**, 75 (1988).
4. J-P. Hirvonen, M. Nastasi, J.R. Phillips, and J.W. Mayer, *J. Vac. Sci. Technol. A* **4**, 2997 (1986).
5. J-P. Hirvonen, M. Nastasi, and J.W. Mayer, *Appl. Phys. Lett.* **49**, 1345 (1986).
6. T.R. Jervis, J-P. Hirvonen, and M. Nastasi, *J. Mat. Res. Nov-Dec.* (1988). In press.
7. T. R. Jervis, J-P. Hirvonen, M. Nastasi, T.G. Zocco, J.A. Martin, G.M. Pharr, and W.C. Oliver, this symposium.
8. D.M. Follstaedt, J.A. Knapp, L.E. Pope, F.G. Yost, and S.T. Picraux, *Appl. Phys. Lett.* **45**, 529 (1984).
9. I.L. Singer and R.A. Jeffries, *Appl. Phys. Lett.* **43**, 925 (1983).
10. J.B. Pethica, R. Hutchins, and W.C. Oliver, *Nucl. Inst. Meth.* **209/210**, 995 (1983).
11. J-P. Hirvonen, M. Nastasi, and J.W. Mayer, *Mat. Res. Soc. Proc.* **93**, 335 (1987).
12. J-P. Hirvonen, M. Nastasi, and J.W. Mayer, *Nucl. Inst. Meth.* **B13**, 479 (1986).
13. M. Nastasi, J.R. Tesmer, and J-P. Hirvonen, *Mat. Res. Soc. Proc.* **93**, 215 (1987).
14. J-P. Hirvonen, J.W. Mayer, M. Nastasi, and D. Stone, *Nucl. Inst. Meth.* **B23**, 487 (1987).

SURFACE MECHANICAL PROPERTIES OF Ti ALLOYS PRODUCED BY EXCIMER LASER MIXING OF Ti ON AISI 304 STAINLESS STEEL

T. R. JERVIS*, J-P. HIRVONEN*, M. NASTASI*, T. G. ZOCCO*, J. A. MARTIN**, G. M. PHARR***, AND W. C. OLIVER****

*Materials Science and Technology Division

**Chemistry and Laser Sciences Division, Los Alamos National Laboratory, Los Alamos, NM 87545

***Department of Materials Science, Rice University, Houston, TX 77251

****Metals and Ceramics Division, Oak Ridge National Laboratory, Oak Ridge, TN 37831

ABSTRACT

We have investigated the properties of surface alloys of Ti formed by excimer laser melting and mixing of Ti overlayers on AISI 304 stainless steel substrates. The thickness of the initial Ti surface layers and the fluence and number of pulses used to mix the surface were varied to investigate a broad range of processing conditions. Samples were uniformly translated at different speeds under repetitive pulses of homogenized laser radiation at 308 nm to vary the number of pulses incident on the sample. We investigated the surface structure and composition, the wear and friction behavior, and the surface hardness of the resulting alloys.

The extent of mixing is observed by Rutherford backscattering spectroscopy to be proportional to the number of pulses incident on the sample. Amorphous surface layers are formed at some mixing levels with a composition which indicates that Ti substitutes for Fe in the stainless steel on a one to one basis. Incorporation of C from surface and interface contamination is observed but at a level much below that found in comparable ion implanted materials.

Friction coefficient measurements indicate that there exists an optimum level of mixing for each layer thickness. Excessive mixing degrades both the coefficient of friction and the wear performance in dry sliding tests.

As with the tribological measurements, the surface hardness showed a dependence on amount of mixing. The surface hardness of the as deposited samples was higher than that of the laser mixed samples, initially decreased with mixing, and finally increased with further mixing.

INTRODUCTION

Surface processing techniques have been shown to alter the surface properties of materials as they relate to a number of applications including tribology. In particular, Ti ion implantation [1] and ion mixing of Ti/Fe multilayers [2] have been shown to dramatically improve the tribological properties of bulk materials which are normally not suitable for tribological applications. These techniques generally form surface layers with excellent adhesion to the substrate material. Melting and mixing of added surface layers using ultraviolet light from an excimer laser can quickly and efficiently process large areas of metal surfaces. The concentration of an added constituent can be chosen arbitrarily to meet the application requirements. Also, because the process itself is very fast, the mixing can be performed in air or in a shield gas environment, eliminating the time required for vacuum system pumpdown.

The use of infrared (IR) lasers (Nd:YAG and CO₂) for surface processing has been investigated at length [3], but the resulting surfaces are generally not sufficiently smooth to be used for tribological applications without further mechanical processing which may alter the mechanical and chemical properties of the surface. While there is substantial industrial experience with IR lasers, excimer lasers offer a dramatic increase in process efficiency for metal processing. In the IR region of the spectrum, metals are generally good mirrors with only a few percent of the photon energy absorbed. This means that most of the incident energy is reflected from the surface, particularly from a polished surface as would be the case in tribological applications. On the other hand, metals absorb rather strongly in the UV, with approximately 50% of the energy being absorbed directly in the metal surface. Further, the energy only affects a layer of the order of 1 micrometer in thickness so that less energy is required for melting and mixing. In terms of photon output, excimer lasers are comparably efficient to CO₂ lasers so that the net effect is an increase in

processing efficiency of approximately 10^3 . Further, since the cooling rate of thinner surface melted layers is quite high, of the order of 10^9 K-sec $^{-1}$, excimer laser processing provides access to metastable phases which have been shown to provide improved tribological performance[4].

The structure and chemical composition which results from excimer laser mixing of Ti layers on 304 stainless steel has been reported elsewhere[5,6]. In brief, we find that mixing can produce a surface layer with approximately equal concentrations of Fe and Ti and with concentrations of the lesser constituents of 304 stainless steel nearly as high as in the parent material. In this case, the surface layer, or a layer near the surface, is amorphous. Further, we find C at a level of approximately 15% of the Ti concentration. This is substantially less than that found in Ti implanted material in which the C concentration is typically 25% of the Ti concentration[7]. In samples which are more thoroughly mixed by increasing the number of pulses, the amorphous phase is not found.

We examined the tribological properties of laser mixed Ti/stainless steel surfaces as well as the surface hardness as measured by the mechanical properties microprobe. In this paper we will discuss the relationships among the tribological properties, the surface hardness, and the processing parameters used.

EXPERIMENT

We used excimer laser radiation to melt and mix Ti surface layers of varying thickness into AISI 304 stainless steel substrates. Prior to laser processing, the sample coupons were polished to a surface finish with surface roughness (R_a) ~ 75 nm and sputter cleaned and coated with Ti in an oil-free cryopumped evaporation chamber. While this reduced the contamination of the surface by hydrocarbon pump oil, it did not eliminate it. Residual C at the Ti/SS interface and on the surface was incorporated into the layers at a concentration of approximately 7% as measured by Auger electron spectroscopy. The samples were kept in a desiccator but no particular effort was made to prevent air exposure either before or after laser processing. Layers of 50 nm, 100 nm, 200 nm, and 500 nm were deposited.

Samples were treated with 308 nm light from an excimer laser. Since the output of excimer lasers is spatially nonuniform, a multi-element beam homogenizer was used. This device produces a square output pattern with a spatial uniformity of better than 95%. The pulse energy used in the results reported here was 100 mJ and 200 mJ with a spot size of 0.10 cm 2 for pulse fluences of 1.0 and 2.0 J-cm $^{-2}$ respectively. Thermal analysis of energy deposition and cooling[8] indicates that the melt depth is of the order of 500 nm and that the melt duration is of the order of 100 ns for the 1.0 J-cm $^{-2}$ case. Cooling is very rapid with the surface temperature returning to ambient in less than 0.1 sec. The samples were translated continuously in front of the laser beam at speeds which correspond to one, two, four, nine, and eighteen pulses in each location. The laser repetition rate was 1.0 Hz so that the sample had ample opportunity to return to ambient temperature between pulses.

Samples were analyzed by Rutherford Backscattering (RBS), using 3.0 MeV He $^+$ ions at the Los Alamos Ion Beam Materials Laboratory. As expected from the thermal analysis mentioned above, the RBS results demonstrate that the extent of mixing is directly proportional to the number of pulses incident on the sample[6,8]. Because the surface layer is initially Ti and there is an effectively infinite supply of Fe in the substrate, the process of mixing has the effect of changing the composition of the surface layer from the Ti to the Fe rich end of the phase diagram. This will of course depend on the thickness of the layer and the overall depth of melt.

Friction measurements were made using a pin-on-disc apparatus. The pin was a hardened Cr-steel ball 6 mm in diameter. The load used was 31.2 gr, which produces a surface stress comparable to the yield strength of the base material. Measurements were carried out in room air without lubrication. Sliding speed was 2.2 cm-sec $^{-1}$ and the tests were terminated after 1000 revolutions. Both the wear track and the slider were analyzed by scanning electron microscopy and energy dispersive spectroscopy. This analysis was used to determine the wear mechanism.

Surface hardness measurements were performed using a nanoindenter, a commercial hardness testing instrument which continuously monitors load and displacement during indentation with nanometer scale resolution[9]. Indents were made with a triangular pyramid diamond indenter, the geometry of which was chosen so that the depth to area ratio is very close to that of the square base pyramid indenter used in the conventional Vickers hardness tester.

Five indents were made on each specimen. Grain boundaries are decorated by laser processing and each array of indents was placed within a single grain. The indents were made at a constant displacement rate of $4 \text{ nm}\cdot\text{sec}^{-1}$ to a depth of 200 nm, after which the indenter was held at maximum load for 10 sec, and then unloaded. In addition to the Ti coated and laser mixed materials, measurements were also made on untreated, thermally annealed (1050 C for 1 hr), and laser melted AISI 304 stainless steel.

Hardness was calculated from the loading portions of the load-displacement data from the relationship:

$$H = P/A,$$

where P is the measured load and A is the projected area of the indent. This area was determined using an empirically established area-depth relation. As discussed by Doerner and Nix[10], the appropriate depth to be used in this calculation is one for which the elastic contribution to the displacement has been removed. This has not been done in the data reported here so that absolute values of the hardness are not meaningful although the elastic contribution is small.

RESULTS AND DISCUSSION

Figure 1 shows the coefficient of friction after 1000 passes obtained on unprocessed samples as a function of Ti layer thickness. The thickness dependence of the friction coefficients on unprocessed samples can be explained as follows. In the case of the 50 nm Ti film, the friction coefficient after 1000 revolutions was almost the same as the untreated substrate. Scanning electron microscopy (SEM) revealed that the film was entirely peeled off and the friction is characterized by the coefficient between the substrate and the pin. At the other extreme, the 500 nm Ti film gives very high friction. This also is understood in terms of the SEM examination. Examination of the 500 nm Ti film after testing revealed large fractures and fragmentation of the surface, leaving a very uneven wear track. The reasons for this fragmentation may include internal stresses in the film as well as the possibility of different structure in the thicker film. In the cases of 100 and 200 nm films, the coefficient of friction was considerably lower even on unprocessed samples than on the base material. Although it is known that the tribological properties of Ti are poor, the Ti films in this case provided a hard coating which was thick enough to carry the load of the pin. The decrease in friction compared to the base material is mainly due to reduced ploughing; the interaction between the pin and the sample being mainly adhesive.

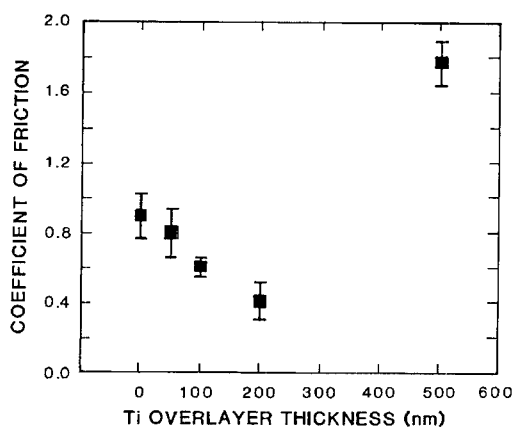


Figure 1. Coefficient of friction measured after 1000 revolutions on thin films of Ti on AISI 304 stainless steel prior to laser processing.

Results of irradiation at 2.0 J-cm^{-2} are not presented as they did not show consistent trends. The results which were obtained were also substantially worse than for the lower fluence case. These surfaces were not as smooth as those treated at the lower fluence and this may be the reason for their degraded performance. The threshold for ablation of the surface is close to 2.0 J-cm^{-2} , and substantial deformation of the surface occurs at this fluence.

Figures 2 and 3 present the results of friction measurements made after 1000 revolutions on the 50 and 100 nm Ti overlayers as a function of number of pulses at 1.0 J-cm^{-2} . The general trend shown in these figures is common. The coefficient drops initially and then increases again with further mixing. In the 200 and 500 nm cases, the coefficient of friction did not show a significant rise at large numbers of pulses but saturated at 0.3 and 0.45 respectively. This is due to the fact that the depth of melt in these cases is not sufficient to cause substantial diffusion of Fe to the surface as discussed in the introduction. In every case however, the laser mixed samples showed a lower coefficient of friction than the unmixed samples. In separate experiments, laser melting of AISI 304 stainless steel did not have any significant effect on the wear and friction properties of the material[11].

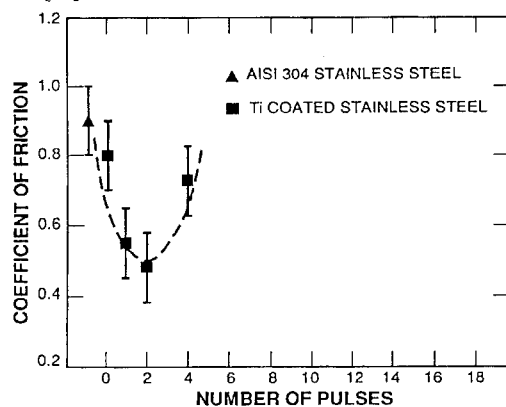


Figure 2. Coefficient of friction measured after 1000 revolutions on laser mixed 50 nm Ti overlayer on AISI 304 stainless steel as a function of number of pulses at 1.0 J-cm^{-2} .

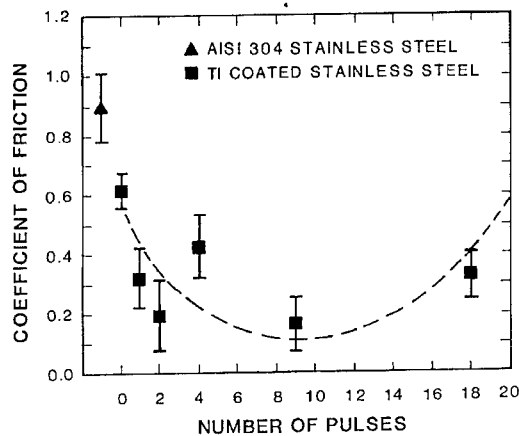


Figure 3. Coefficient of friction measured after 1000 revolutions on laser mixed 100 nm Ti overlayer on AISI 304 stainless steel as a function of number of pulses at 1.0 J-cm^{-2} .

In earlier ion beam mixed Fe/Ti multilayers on AISI 304 stainless steel, mixing initially induced a ductile, low friction surface layer in all but the most Ti rich portion of the sample[2]. This low friction behavior lasted only for a short time, however. After 1000 cycles, low friction persisted only in the Ti₅₀Fe₅₀ composition range. Based on these results, we expect that the friction coefficient in laser mixed samples would decrease and then increase again for increased mixing. In the results presented here, the low friction composition/microstructure is limited as expected. As mixing proceeds, we expect progressively more Fe to diffuse to the surface for the thinner layers, resulting in increased friction. The fact that the minimum in the friction coefficient varies with overlayer thickness indicates simply that the amount of mixing required for optimum friction coefficient is greater for thicker Ti overlayers. As discussed above, we do not see an increase in friction coefficient in the thicker layers because they are not as thoroughly mixed, even after many pulses.

Analysis of the wear tracks of the 100 nm layer in the scanning electron microscope after 1000 passes of the pin sheds light on the wear processes involved[8]. In the as deposited condition, the wear track reveals a strong adhesive interaction between the pin and the surface. This interaction is entirely absent after processing by 9 pulses of radiation. The wear track is slightly scratched indicating only an abrasive wear mechanism. It is of interest to note that a round defect seen in the surface of the laser processed sample does not nucleate damage in the wear track. These defects are common artifacts of laser processing, probably due to microscopic inhomogeneities in the surface or local fluctuations in the beam intensity, but are seen in this case not to affect the wear track.

The improved tribological behavior of the surfaces was confirmed by energy dispersive spectroscopy of the pins. In the case of untreated stainless steel, loose wear debris was found on the pin and identified as originating in the stainless steel. Ti was found on pins from the as deposited samples. After testing on laser processed materials, neither loose debris nor Ti deposits were found on the pins in cases where low friction was obtained. Moreover, in these cases the surface of the pin was undamaged and the original surface structure was observable after the friction testing. This is in contrast to the untreated stainless steel and as deposited samples.

In order to ascertain the effect of laser processing on the surface hardness of the material independent of Ti incorporation, measurements were made of the surface hardness of uncoated AISI 304 stainless steel in the as received-polished form (work hardened), after laser processing with various numbers of pulses and fluences of UV laser radiation, and after conventional thermal annealing (1050 C for 1 hr). In the as polished condition, the surface hardness at a depth of 100 nm was 3.8 ± 0.2 GPa. After laser processing, independent of number of pulses or fluence, the hardness was 2.4 ± 0.2 GPa, as it was after thermal annealing but no laser processing. It is clear that the effect of laser processing is to anneal the material in ways essentially similar to conventional thermal processing.

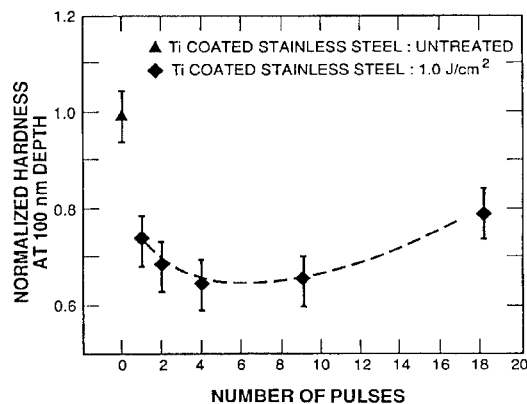


Figure 4. Relative surface hardness measured at a depth of 100 nm in laser mixed 50 nm overlayer of Ti on AISI 304 stainless steel as a function of the number of pulses at $1.0 \text{ J}\cdot\text{cm}^{-2}$.

Figure 4 shows the effect of laser processing on the surface hardness of the sample coated with 50 nm of Ti. As was seen in the friction measurements, the effect is proportional to the amount of mixing; decreasing initially and then increasing again. Ti coated materials are in every case much harder in the as received form than uncoated materials, presumably as a result of a surface oxide. The hardness results on the 50 nm layer indicate that, while the friction coefficient in this case decreases with mixing and then increases sharply, something is happening which causes the hardness to increase more slowly. The surface chemistry of these samples, particularly the thinner ones, is dramatically complicated by the presence of the minor constituents of the stainless steel, not to mention oxygen and carbon. Earlier work in laser melted uncoated 304 stainless steel indicates that multiple pulses change the surface chemistry of the material in significant ways, primarily by increasing the Cr content of the surface oxide [12,13]. It appears that surface hardness may be less sensitive to surface chemistry than is friction coefficient.

CONCLUSIONS

We have examined the effect of excimer laser surface processing parameters on the friction behavior and surface hardness of Ti/stainless steel surface alloys. We find that for a given overlayer thickness, there is an optimum level of mixing for minimum friction coefficient. Comparison with ion beam mixed Fe/Ti multilayers as well as previous work on laser mixed samples suggests that the optimum composition consists of equal parts of Fe and Ti. Analysis of the wear pin indicates that the reduced friction observed is due to a shift from an adhesive to an abrasive wear mechanism. There is no direct correlation with surface hardness, although mixing results in layers which are initially softer than the as deposited case and which harden with further mixing. Other factors being equal, decreased hardness has a detrimental effect on abrasive wear resistance. The change in the sliding mechanism may be due to alloying of minor constituents and/or to the interaction of the modified surface with the environment as well as to the Fe/Ti composition and microstructure.

ACKNOWLEDGEMENTS

We would like to thank T. Archuleta, H. Nutter, and the personnel of the Los Alamos Ion Beam Materials Laboratory for technical assistance. This work was supported by the United States Department of Energy under contracts W-7405-ENG-36 through the Los Alamos Center for Materials Science, DE-AC05-76OR00033 with Oak Ridge Associated Universities, and DE-AC05-84OR21400 with Martin Marietta Energy Systems, Inc.

REFERENCES

1. D. M. Follstaedt, J. A. Knapp, L. E. Pope, F. G. Yost, and S. T. Picraux, *Appl. Phys. Lett.* **45** 529 (1984).
2. J-P. Hirvonen, M. Nastasi, and J. W. Mayer, *Appl. Phys. Lett.* **49** 1345 (1986).
3. C. W. Draper and P. Mazzoldi, eds., *Laser Surface Treatment of Metals* (Martinus Nijhoff, Dordrecht, 1986).
4. J-P Hirvonen, J. W. Mayer, M. Nastasi, and D. Stone, *Nucl. Instrum. B* **23** 487 (1987).
5. T. R. Jervis, M. Nastasi, and T. G. Zocco in *Fundamentals of Beam Solid Interactions and Transient Thermal Processing*, edited by M. J. Aziz, L. E. Rehn and B. Stritzker (Mater. Res. Soc. Proc. **100**, Pittsburgh, PA 1988).
6. T. R. Jervis, M. Nastasi, T. G. Zocco, and J. A. Martin, *Appl. Phys. Lett.* **53** 75 (1988).
7. J. A. Knapp, D. M. Follstaedt, and B. L. Doyle, *Nucl. Instrum. Methods. B* **7** 38 (1985).
8. T. R. Jervis, J-P. Hirvonen, and M. Nastasi, *In Press*, *J. Mater. Res.* Nov-Dec (1988).
9. W. C. Oliver, R. Hutchings, and J. B. Pethica, *ASTM Spec. Tech. Pub.* **889**, 90 (1986).
10. M. F. Doerner and W. D. Nix, *J. Mater. Res.* **1** 601 (1986).
11. S. Fayeulle and I. L. Singer (personal communication).
12. T. R. Jervis, D. J. Frydrych, and D. R. Baer, *Mater. Lett.* **6** 225 (1988).
13. D. R. Baer, D. J. Frydrych, and T. R. Jervis, in *Environmental Degradation of Ion and Laser Beam Treated Surfaces*, edited by G. S. Was and K. Grabowski (The Metallurgical Society, Warrendale, PA 1989).

COMBINED OXYGEN - NITROGEN ION IMPLANTS INTO Ti6Al4V

ANTON GREENWALD, JAMES DALY, JOHN MEROTH, RICHARD OLIVER, PIRAN SIOSHANSI,
and CLIVE CLAYTON*

Spire Corporation, Patriots Park, Bedford, MA 01730

*State University of New York at Stony Brook, NY

ABSTRACT

The alloy preferred for medical prostheses, Ti6Al4V, was ion implanted with oxygen and nitrogen alone and in combination at varying energies, 25 to 120 keV, and varying dose levels, 10^{17} to 10^{18} ions/cm². Measurements were made of microhardness, corrosion resistance, chemical bonding of implanted species, and (with UHMW polyethylene) pin-on-disk wear and friction. The addition of oxygen to nitrogen implants now used in production was found to have little effect on wear or any other parameter.

INTRODUCTION

The objective of this research is to utilize ion implantation to improve the tribomechanical properties of Ti6Al4V, an alloy being used for orthopaedic prostheses. Previous experimentation has shown that ion implantation with nitrogen has substantially improved the wear characteristics of this alloy [1]. It has been reported that oxygen, present as a contaminant in the vacuum system, was incorporated into the surface during nitrogen implantation, and that this oxygen had the effect of reducing friction [2]. It has also been suggested that the nitrogen implants reduced wear by actually stabilizing oxide phases of the alloys which formed on the surface during normal use [3]. Ion implantation of oxygen alone has had a deleterious effect on the wear of this alloy [4]. Experiments reported here were designed to optimize implant conditions and investigate possible benefits of intentionally implanting oxygen along with nitrogen.

RESULTS

Sample Preparation

Samples for testing hardness, friction and corrosion were disks approximately 1 cm diameter by 5 mm thick, cut from an alloy rod 6.1% Al, 4.2% V, 0.17% Fe, less than 0.1% other elements with the balance being Ti. The disks were polished to a mirror finish using 0.05 micron powdered alumina slurry in the last step. All samples were thoroughly cleaned with a final alcohol rinse before implantation. Disks were held on a water cooled plate during ion implantation. Hemispherical pins for pin-on-disk wear measurements were similarly prepared from 0.63 cm diameter stock. The pins were not actively cooled during implantation; instead, the ion beam was defocused so as to cover a large area and the maximum temperature of the pins during the procedure was kept under 100°C.

Hardness and Friction

A large factorial matrix experiment was devised for testing the correlation of four variables (ion energy and dose for each of two ions, oxygen and nitrogen) [5]. Implantation conditions are given in Table I. A total of 16 different conditions were chosen, with four sample conditions duplicated to

TABLE I. FACTORIAL MATRIX SAMPLE CONDITIONS.

Sample Number	O ⁺ Dose (Ions/cm ²)	O ⁺ Energy (keV)	N ⁺ Dose (Ions/cm ²)	N ⁺ Energy (keV)
1	0.0	0	2E+17	25
2	0.0	0	3E+17	120
3	0.0	0	1E+17	120
4	0.0	0	6E+17	25
5	3.0E+17	25	2E+17	25
6	3.0E+17	25	3E+17	120
7	3.0E+17	80	1E+17	120
8	3.0E+17	80	6E+17	25
9	1.5E+17	25	1E+17	66
10	1.5E+17	25	4E+17	25
11	1.5E+17	52	2E+17	25
12	1.5E+17	80	3E+17	120
13	1.5E+17	25	1E+17	120
14	1.5E+17	25	6E+17	25
15	1.5E+17	80	2E+17	25
16	0.0	0	2E+17	66
17	0.0	0	6E+17	25
18	0.0	0	3E+17	120
19	3.0E+17	25	3E+17	120
20	1.5E+17	25	6E+17	25
21,22,23,24	0.0	0	0	0

check variability of the results and four more unimplanted samples included for baseline comparisons.

Sample hardness was measured with a Tukon microhardness tester, which uses the width of an indent made by a diamond under a variable load to determine the hardness. Five measurements at each of four loads (1,2,5 and 10 grams) were taken. In all cases hardness at the maximum load was identical, indicating that at this point the implanted surface was broken through by the measurement. The results shown in Table I and Figure 1 were taken at a 1 gram load. For all possible oxygen implant conditions (including the null set) the sample hardness increased with dose and energy of the nitrogen ion implant. There was no correlation for an increase in hardness with any oxygen implant condition, the nitrogen conditions dominating the data.

Friction of an UHMWPE pin scraping across the surface of these samples with water lubrication was measured under a light load (1.2 Nt). This test does not correspond to wear seen for an artificial knee joint which should use a metal pin on a UHMWPE (ultrahigh molecular weight polyethylene) disk. Friction tests were repeated on a limited number of such samples during wear tests. The results of this experiment are shown in Figure 2 where lower energy oxygen implants gave lower friction.

The chemical composition of the implanted layer for sample number 7, Table II, was investigated by ESCA. The ion implantation parameters were chosen to yield a uniform composition versus depth profile in the near surface region of this sample. After a four minute sputter etch to remove surface contaminants the surface composition profile showed the formation of Ti-N, Ti-O and maybe Ti-O-N bonds (Figure 3). The latter bonds could be responsible for reported stabilization of the oxide layer.

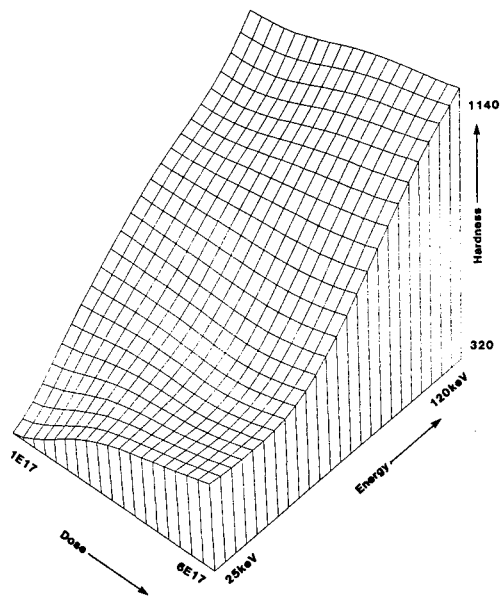


FIGURE 1. HARDNESS VERSUS NITROGEN IMPLANT DOSE AND ENERGY.

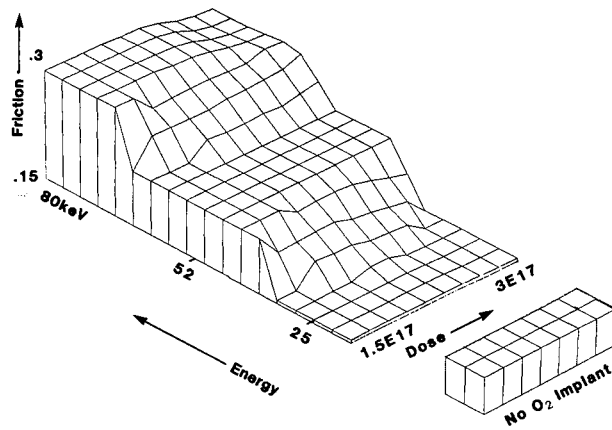


FIGURE 2. FRICTION VERSUS OXYGEN IMPLANT DOSE AND ENERGY.

TABLE II. ION IMPLANT CONDITIONS AND RESULTS FOR WEAR AND CORROSION TESTS.

Implantation Parameters				Electrochemical Data			
Sample Number	Ion	Dose ($10^{17}/\text{cm}^2$)	Energy (keV)	E_{corr} (mV) SCE	Polarization I_{corr} ($\mu\text{A}/\text{cm}^2$)	Resistance* ($k\ \Omega/\text{cm}^2$)	Fric-tion Coef-ficient
1	N_2^+	1	80	-145	0.01	1667	0.04
		2	80				
3	N_2^+	1	80	-130	0.01	2857	0.09
		2	80				
		O^+ 1.5	80				
5	None			-369	.04	558	0.06
7	O^+	1.5	40	N.A.	N.A.	N.A.	N.A.
		3.0	80				
		6.0	160				
	N^+	1.5	40				
		3.0	80				
		6.0	160				

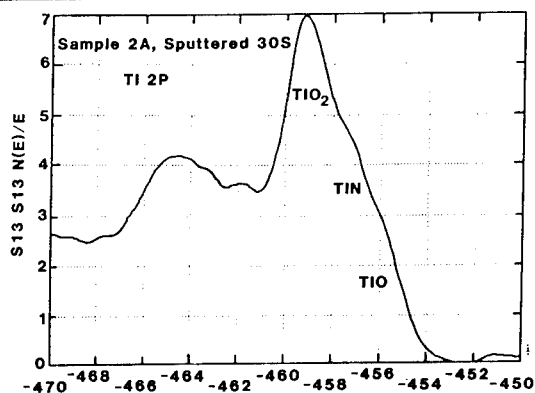
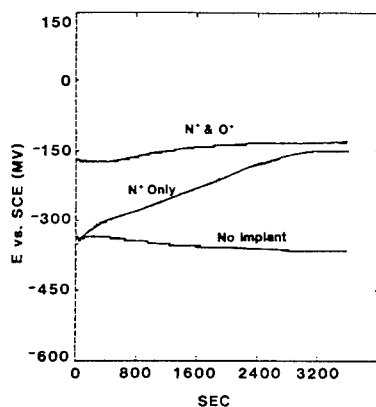


FIGURE 3. ESCA ANALYSIS OF SAMPLE 7, TABLE II.

Corrosion Measurements

Electrochemical corrosion measurements were performed in Ringer's solution at 37°C with only the ion implanted surface exposed to the bath. Ion implant conditions are given in Table II. Without further surface treatment, samples were immersed in the solution for one hour to reach a relatively stable state prior to tracing the potentiodynamic curve. During this period the E_{corr} vs time was recorded (Figure 4). The data implies that there is some initial difference between the nitrogen-only and the nitrogen-plus-oxygen implants which is not stable.

FIGURE 4. CORROSION POTENTIAL (E_{corr}) VERSUS TIME.

Polarization curves for the three samples (Figure 5) were recorded at a scan rate of 1 mV per second. This data indicates that both ion implantation treatments produce very significant improvements in the anodic dissolution behavior of this titanium alloy in the bio-environment. The range of validity for this case is no more than 100 mV above the corrosion potential, a region where the current densities of the implanted samples was two orders of magnitude lower than that of the untreated sample. The test was extended to much higher potentials, where the oxygen and nitrogen implanted sample looked better, but this is outside the valid range.

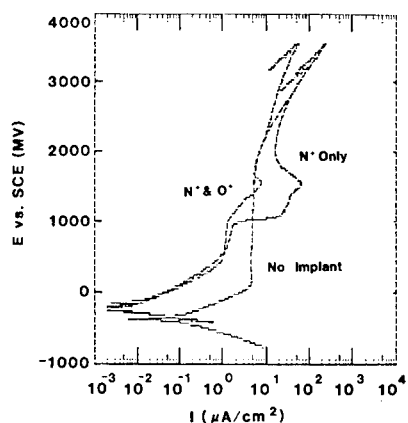


FIGURE 5. POLARIZATION CURVES.

Wear Tests

Pins of titanium alloy were implanted according to the parameters listed in Table II. Pin-on-disk wear tests were performed in Ringer's

solution at 25°C at a sliding speed of 3.4 cm/sec to a total distance of 210 m. The load on the pins, which were 6.4 mm diameter with hemispherical tips, was 1.2 Nt. Friction measurements, which were constant, are given in Table II. Figure 6 shows the wear for either implant condition (a, b) compared to the unimplanted sample. The wear scars on the unimplanted pin have approximately four times as much material removed as the scars on the pin with nitrogen-plus-oxygen implants. The pin implanted with nitrogen alone shows the buildup of debris from the plastic disk on either side of the bearing surface, but wear marks are very shallow and certainly not as deep as polishing marks still visible.

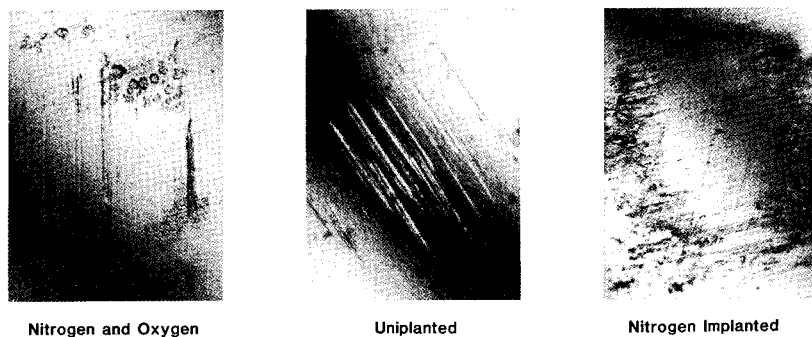


FIGURE 6. WEAR SCARS ON Ti 6Al4V PINS (Table II).

CONCLUSIONS

Deliberate ion implantation of oxygen with nitrogen into titanium alloys does not reduce the wear compared to that seen with the nitrogen implant alone. Both implantation conditions showed improvement compared to unimplanted samples.

ACKNOWLEDGEMENTS

This research was partially supported by the National Science Foundation under grant NSF ISI-8607171.

REFERENCES

1. P. Sioshansi, R. Oliver, F. Matthews, J. Vac. Sci. Technol. A 3, 2670 (1985).
2. R. Hutchings and W.C. Oliver, Wear 92, 143 (1983); R. Hutchings, Mater. Sci. Eng. 69, 129 (1985).
3. F. Pons, J.C. Pivin, G. Farges, J. Mater. Res. 2, 580 (1987).
4. R. Vardiman and R. Kant, J. Appl. Phys. 53, 690 (1982).
5. Expert in a Chip, Inc., RDI Box 3840, Hockessin, DE 19707.

GROWTH OF STOICHIOMETRIC BN FILMS BY PULSED LASER EVAPORATION

P. T. Murray*, M. S. Donley**, and N. T. McDevitt**

* Research Institute, University of Dayton, Dayton, OH 45469

** AFWAL/MLBM, Materials Laboratory, Wright-Patterson AFB, OH 45433-6533

ABSTRACT

The feasibility of growing stoichiometric thin films of BN by pulsed laser evaporation has been investigated. Films grown under high vacuum conditions were N-deficient. This result is consistent with thermodynamic calculations, which indicate that B metal formation, with concomitant N_2 desorption, is energetically favored over BN formation. Stoichiometric films were grown in NH_3 with substrate temperatures of 400, 500, and 1000°C. Analysis of films grown under these conditions by grazing incidence x-ray diffraction indicates the films to be highly oriented, hexagonal BN.

INTRODUCTION

There is a need for solid lubricant films with superior thermal stability and with tribological properties which are not degraded by air exposure. BN is one such candidate material. Thin films of BN have been grown by a variety of techniques, the most common of which entail reacting NH_3 and B_2H_6 at high substrate temperatures [1,2]. Murarka and coworkers [3] found that a substrate temperature of 800°C was required to grow stoichiometric BN films; at lower temperatures, the films were N-deficient. Adams and coworkers [4] investigated the properties of films grown between 250 and 600°C. Their results indicated that the films thus grown had a composition of $B_2NH_{1.5}$. Yamaguchi and Minakata [5] used a two furnace technique and found the films grown above 500°C to be stoichiometric. Despite these advances, there is still a need for improved deposition processes, particularly those which allow growth of stoichiometric BN at even lower substrate temperatures.

The purpose of the work presented here was to determine the feasibility of growing stoichiometric BN films by pulsed laser evaporation (PLE). Among the advantages of PLE are the potential for congruent evaporation, the capability of growing high purity films, and the relative ease with which even refractory materials, such as BN, can be evaporated. An additional advantage, which is particularly pertinent to deposition of BN for high precision tribology applications, is the fact that PLE has the potential of allowing film growth at lower substrate temperatures than conventional processing techniques.

EXPERIMENTAL

The apparatus used for film deposition and subsequent surface analysis has been described in detail previously [6]. The system consists of a deposition chamber which is directly connected to a Perkin-Elmer (PHI) Model 550 XPS/AES surface analysis system. A specimen introduction port and transfer arm allow film growth in the deposition chamber and subsequent

This work was sponsored by the Materials Laboratory, Air Force Wright Aeronautical Laboratories, Aeronautical Systems Division (AFSC), United States Air Force, Wright-Patterson Air Force Base, OH 45433-6533.

XPS/AES analysis of the deposited film without air exposure. The frequency-doubled output ($\lambda = 0.53 \mu\text{m}$) of a Q-switched Nd:YAG laser (15 ns pulse duration) was used to evaporate the BN target. The laser was focused to a 0.9 mm spot at the target and was scanned across the target to produce uniform films. The laser power density was approximately 1.5×10^8 watts/cm² per pulse, and the target-substrate distance was approximately 3 cm. Films were grown on Si(111) substrates, some of which were resistively heated during deposition. The base pressure in the deposition chamber was 2×10^{-8} Torr, which increased to 2×10^{-7} Torr during film growth. A number of films were also grown in 5×10^{-3} Torr of NH_3 . The NH_3 was obtained from Matheson and was used without further purification.

Time-of-flight (TOF) measurements were recorded on the positive ions ejected from a BN target. These measurements were carried out in a separate vacuum chamber and consisted of two different modes. The first entailed recording TOF mass spectra with a reflectron [7] spectrometer. The second entailed recording velocity distributions; these measurements involved using a short drift region followed by a channel electron multiplier. Both types of TOF measurements were recorded with a home-built transient digitizer with 12.5 ns/channel resolution.

RESULTS AND DISCUSSION

Shown in Figure 1(a) is an Auger spectrum of the BN target used in this study. This spectrum was recorded after the target had been mechanically abraded in vacuum in order to remove contaminants originally present on the sample surface. There are B and N peaks present in the spectrum, as well as smaller peaks due to C and O. The N and B peak shapes are in good agreement with a spectrum of bulk, stoichiometric BN previously reported by Hanke and Muller [8]. The appearance of a substantial C peak, as well as a smaller O peak in this spectrum suggests that either mechanical abrasion in vacuum removed only part of the original surface contamination or that both C and O were present in the BN target. Shown in Figure 1(b) is an Auger scan of a film grown under high vacuum conditions, with the substrate at room temperature. This spectrum is different from that of the target in two important aspects. First, this film would appear to have contained relatively less N than did the target. Second, the B peak shape of the film is considerably different than that seen in the target spectrum; in fact, the B peak shape is more characteristic of metallic B. This spectrum suggests that PLE of BN under these conditions produced films which were primarily metallic B, with very little N incorporation.

Films were grown in NH_3 in order to restore the N stoichiometry. Shown in Figures 1(c), (d), and (e) are Auger spectra of films grown in NH_3 at substrate temperatures of 400, 500, and 1000°C, respectively. The B and N peak shapes in all three spectra are similar to that of the BN target. Shown in Table I are the calculated atomic ratios obtained from the Auger data. The N/B ratios in all films grown in NH_3 are consistently near unity, with the film grown at 500°C exhibiting a somewhat larger value of 1.1. It can be concluded that growth of films in NH_3 does indeed restore the N stoichiometry, even at substrate temperatures as low as 400°C. The film grown at 1000°C contained the smallest impurity level of all samples examined in this work, with a C/B ratio of 8%. The detection of C on the surface of a target abraded in vacuum, as well as the consistent detection of C on all films grown, suggests that the BN target was the primary source of C in this work. The film grown at 1000°C exhibited an O/B ratio of 2%, that grown at 400°C had a ratio of 9%, while the O/B ratio of the target was 3%. Thus, the films grown at lower substrate temperatures contained more O than did the target. O_2 and H_2O were listed by the supplier as the

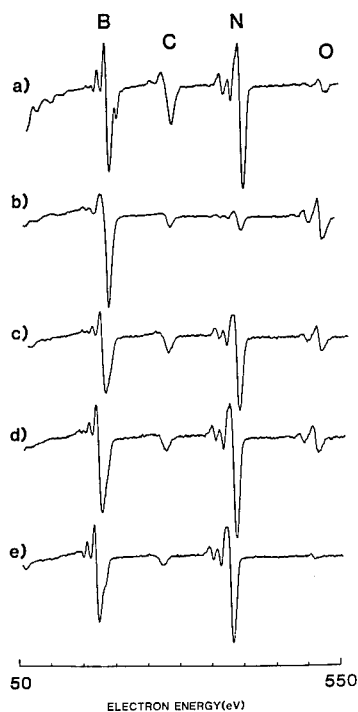


Figure 1.
Auger spectra of (a) BN target,
(b) film grown in high vacuum,
(c) film grown in NH_3 at 400°C ,
(d) film grown in NH_3 at 500°C ,
and (e) film grown in NH_3 at
 1000°C .

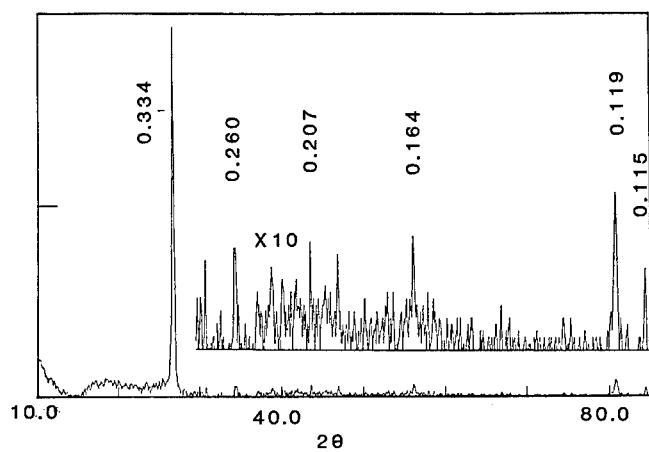


Figure 2. Grazing incidence x-ray diffraction spectrum
of film grown in NH_3 at 500°C .

major contaminants in the NH_3 ; these are the most likely source of O on the lower temperature films.

TABLE I
ATOMIC RATIOS FROM AUGER DATA

Sample	N/B	C/B	O/B
BN target	1.00	0.31	0.03
High vacuum film*	0.19	0.11	0.13
400°C film	1.04	0.19	0.09
500°C film	1.11	0.11	0.07
1000°C film	1.05	0.08	0.02

* Change in B peak shape

Raman spectra were recorded from the BN target and from a film grown at 500°C in NH_3 . Both spectra exhibited a peak at 1366 cm^{-1} , although the peak appearing in the film spectrum was somewhat broader. This peak is a vibration assigned to the B-N stretching mode in hexagonal BN. The similarity of the two spectra suggests the film to also be hexagonal BN.

Presented in Figure 2 is the grazing incidence (incident beam 5° from sample surface) x-ray diffraction spectrum of the film grown at 500°C in NH_3 . A sharp, well defined peak is observed at $26.65^\circ (2\theta)$ corresponding to a lattice parameter of 0.334 nm. Low intensity ($I/I_0 \sim 5\%$) peaks are observed at 2θ values of 43.6° , 50.2° , 56.1° , 80.8° , 82.2° , and 84.4° . Observed data for the PLE film and the BN target are listed in Table II, along with data from the powder diffraction file [10]. As indicated, no (100) diffraction peak is observed in the film. In addition, a low intensity peak is observed with a 0.260 nm d-spacing which is not produced by BN. This peak may be produced by a B_2O_3 phase (see powder file 31-210), but, at present, this cannot be confirmed. No evidence of cubic BN is observed.

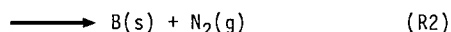
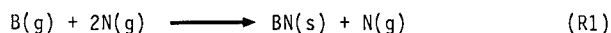
TABLE II
X-RAY DIFFRACTION DATA SUMMARY

Observed PLE Film		Observed BN Target		hkl	Powder File Hexagonal BN	
d (nm)	I/I ₀	d (nm)	I/I ₀		I/I ₀	d (nm)
0.334	100	0.334	100	(002)	100	0.33281
		0.217	9	(100)	15	0.21693
0.207	3	0.206	5	(101)	6	0.20619
0.182	1	0.181	6	(102)	9	0.18176
0.164	2	0.166	4	(004)	6	0.16636
0.117	1	0.117	2	(112)	5	0.11720
0.119	4					
0.260	3	---			--	

These x-ray diffraction data and the Raman spectra clearly identify the film as hexagonal BN. Furthermore, the relative intensity ratios showing an enhanced (002) intensity and no observed (100) peak suggest a preferred orientation of basal plane alignment with the substrate surface.

The nature of the species evaporated from the BN target was investigated, in order to better understand the N-deficient nature of the films grown under UHV conditions. Shown in Figure 3 is a TOF mass spectrum of the positive ions evaporated from BN under the same conditions used to grow the films. There are peaks due to $^{10}\text{B}^+$ and $^{11}\text{B}^+$, as well as a smaller peak due to N^+ . There is also an intense peak due to laser-evaporated H^+ . There were also very small peaks at longer flight times (not shown) due to the cluster ions B_xN_y . Of course, the relative intensities of the species seen in Figure 3 most likely are not representative of the total relative intensities of the (more abundant) neutral species. Differences in ionization efficiency as well as neutralization probability make a direct comparison difficult. Nevertheless, this spectrum does indicate that the most intense ionized species evaporated from the target are B^+ and H^+ . Presented in Figure 4 is a TOF velocity distribution of the positive ions. The dashed lines in Figure 4 are the TOF spectra predicted by a Maxwellian distribution for H^+ and B^+ , with both species at an effective temperature of 2600K. The fit to the experimental TOF data is excellent. It is interesting to note that a value of 2600K has been reported [9] as the decomposition temperature of BN. The close correspondence between the observed plasma temperature and the reported decomposition temperature may be fortuitous, since the evaporation conditions were above threshold.

The TOF results indicate that, under the conditions used in this feasibility study, PLE of BN produces primarily atomic species with an effective translational temperature of 2600K. Thermodynamic calculations [10], carried out on the two reactions,



with the reactants at 2600K and the products at 298K, indicate reaction (2) to be more exothermic by 231 kJ/mole. Thus, the N-deficient nature of the films can be understood by the greater strength of the N-N bond compared to that of B-N. The results of residual gas analysis confirmed this assessment in that molecular N_2 was detected during PLE of the BN target.

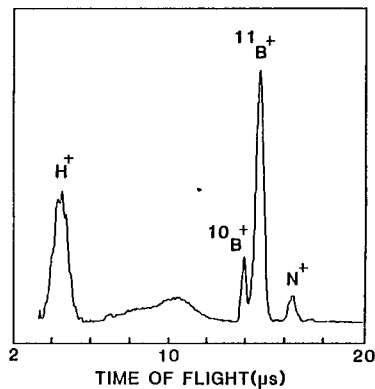


Figure 3. TOF mass spectrum of the positive ions ejected from a BN target by PLE.

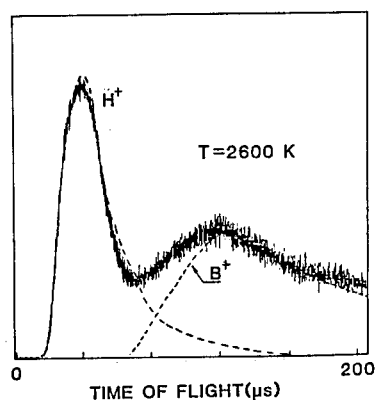


Figure 4. TOF velocity distribution of positive ions ejected from BN by PLE.

SUMMARY

PLE of BN under high vacuum conditions produces films which are N-deficient. This can be understood in terms of the greater bond strength of N_2 versus BN. PLE of BN in an NH_3 atmosphere results in growth of highly oriented, stoichiometric films of BN. This can be accomplished at substrate temperatures as low as $400^\circ C$. These results indicate that PLE is a feasible method of growing stoichiometric films of BN for tribology applications.

REFERENCES

1. M. H. Rand and J. F. Roberts, *J. Electrochem. Soc.* **115**, 423 (1968).
2. M. Hirayama and K. Shohnu, *J. Electrochem. Soc.* **122**, 167 (1975).
3. S. P. Murarka, C. C. Chang, D. N. K. Wang, and T. E. Smith, *J. Electrochem. Soc.* **126**, 1951 (1979).
4. A. C. Adams and C. D. Capio, *J. Electrochem. Soc.* **127**, 399 (1980).
5. E. Yamaguchi and M. Minakata, *J. Appl. Phys.* **55**, 3098 (1984).
6. P. T. Murray, J. D. Wolf, J. A. Mescher, J. T. Grant, and N. T. McDevitt, *Mater. Lett.* **5**, 250 (1987).
7. B. A. Mamyrin, V. I. Krataev, D. V. Shmikk, and V. A. Zagulin, *Zh. Eksp. Teor. Fiz.* **64**, 8 (1973); *Sov. Phys.-JETP* **37**, 45 (1973).
8. G. Hanke and K. Müller, *J. Vac. Sci. Technol.* **A2**, 964 (1984).
9. M. W. Chase, C. A. Davies, J. R. Downey, D. J. Frurip, R. A. McDonald, and A. N. Syverud, *JANAF Thermochemical Tables*, *J. Phys. Chem. Ref. Data* **14**, 1 (1985).
10. Powder Diffraction File: Set 34, International Centre for Diffraction Data, Swarthmore, PA, 1987, No. 34-421.

EFFECTS OF ION BOMBARDMENT ON THE ENVIRONMENTAL DURABILITY
OF SILVER COATINGS

G.A. Al-Jumaily, T.A. Mooney, and A. Smajkiewicz

Barr Associates, Inc.
2 Lyberty Way
Westford, MA 01886

ABSTRACT

Effects of ion bombardment during deposition on the environmental durability of silver coatings have been examined. Films deposited under otherwise identical conditions were bombarded at different levels with 300 eV argon ions. Examination of the environmental durability of coatings revealed that films deposited with ion assisted deposition are more durable than evaporated coatings. Adhesion and scratch resistance of coatings were also improved as a result of ion bombardment.

Introduction

Metal coatings are widely used as wide-band high reflectors in optical systems, and as interconnectors for microelectronic applications. The most widely used of the metal coatings are gold (Au), silver (Ag), and aluminum (Al). Aluminum coatings are durable but have lower overall reflectance in the IR and visible than Ag and Au. Although Au has the highest reflectance in the IR as well as good durability, its poor reflectance in the visible makes it less attractive. Silver has the highest reflectance in the visible, and its IR reflectance is almost as high as that of Au. Silver coatings suffer from very poor stability.

Thin films deposited using conventional techniques are unstable when exposed to the environment. The instability of coatings is caused by the columnar microstructure which is typical of evaporated coatings. The presence of voids between the columns allows moisture to penetrate into the coatings and increase the surface area of the coatings which is in contact with the environment. The columnar growth of thin films should be prevented in order to improve the environmental stability of thin films.

Several novel deposition techniques have been proposed to improve the stability of optical coatings. Many of these techniques, such as ion assisted deposition (IAD), ion beam sputtering, and ion plating, involve ion bombardment.[1] It has been shown that ion bombardment during deposition causes significant improvements in the optical and mechanical properties of dielectric [1,2] and metal [2,3] coatings. Metal coatings deposited using IAD have been shown to have improved optical constants, and less optical scatter.[2,3] In this paper we examine the effects of IAD on the environmental durability of metal coatings.

Sample Preparation

Coatings were deposited in a 60 cm box γ -coater. The system is cryogenically pumped to a base pressure of 3×10^{-7} Torr. Deposition rate and film thickness were monitored using a crystal monitor. Samples were deposited using thermal evaporation from a resistively heated boat. Some of the samples were bombarded during deposition with 300 eV argon ions from an ion source. The ion source is a 3 cm Kaufmann source. Films were approximately

40 nm thick. The deposition rate for all the coatings was 2 nm/sec. Films were deposited on unheated glass substrates. In the case of IAD samples, substrates were pre-cleaned with 300 eV Ar ions prior to coating for two minutes.

The environmental durability of silver coatings was examined by exposing the samples to extreme conditions of temperature and humidity. The humidity chamber is kept at a constant temperature of 65° C and 95% relative humidity. The degradation to coatings as a result of exposure to moisture was monitored by examining the samples after different periods of exposure to humidity using a Nomarski microscope.

Results

Figure 1 includes three Nomarski micrographs illustrating the effects of moisture on evaporated Ag coatings. The three micrographs represent one Ag coating before and after 5 and 15 minutes of exposure to humidity. Note that the damage to the coating occurred in the first few minutes of exposure to humidity.

Three Ag coatings deposited on glass substrates were examined. One coating was deposited with no ion bombardment, the other two were bombarded with 300 eV Ar ions, with beam current densities of 15 and 30 $\mu\text{A cm}^{-2}$. Hence, the relative arrival rates of argon ions to Ag atoms were 1:10 and 2:10, respectively. Micrographs representing the three samples after two hours of exposure to humidity are shown in Fig. 2. Note that the unbombarded sample was totally damaged as a result of exposure to moisture; the second sample (15 $\mu\text{A cm}^{-2}$) was partially damaged after two hours; while the sample bombarded with the highest ion flux (30 $\mu\text{A cm}^{-2}$) showed no damage.

Effects of IAD on the adhesion and abrasion resistance of coatings were examined. Samples were subjected to a tape pull test. Samples deposited with IAD passed the tape test, while samples deposited with no ion bombardment failed. Scratch resistance of coatings was also examined by rubbing the coatings with cheesecloth by a force of 2.5 pounds. Results showed significant improvement in scratch resistance in IAD samples.

Summary

In summary we have examined the effects of ion bombardment on the environmental durability and mechanical properties of silver coatings. Results indicated a significant improvement in the durability of silver coatings deposited using IAD.

References

1. P.J. Martin and R.P. Netterfield, in *Progress in Optics XXIII*, E. Wolf, Ed., Chapter III (Elsevier, Amsterdam, 1986).
2. G.A. Al-Jumaily, S.R. Wilson, L.L. DeHainaut, J.J. McNally, and J.R. McNeil, "Optical Properties of Cu Films Deposited Using Ion Assisted Deposition," *J. Vac. Sci. Technol. A* **5**, 1909 (1987).

3. G.A. Al-Juamly, "Influence of Metal Films on the Optical Scatter and Related Surface Microstructure of Coated Surfaces," Ph.D. Dissertation (University of New Mexico, Albuquerque, NM 1986).

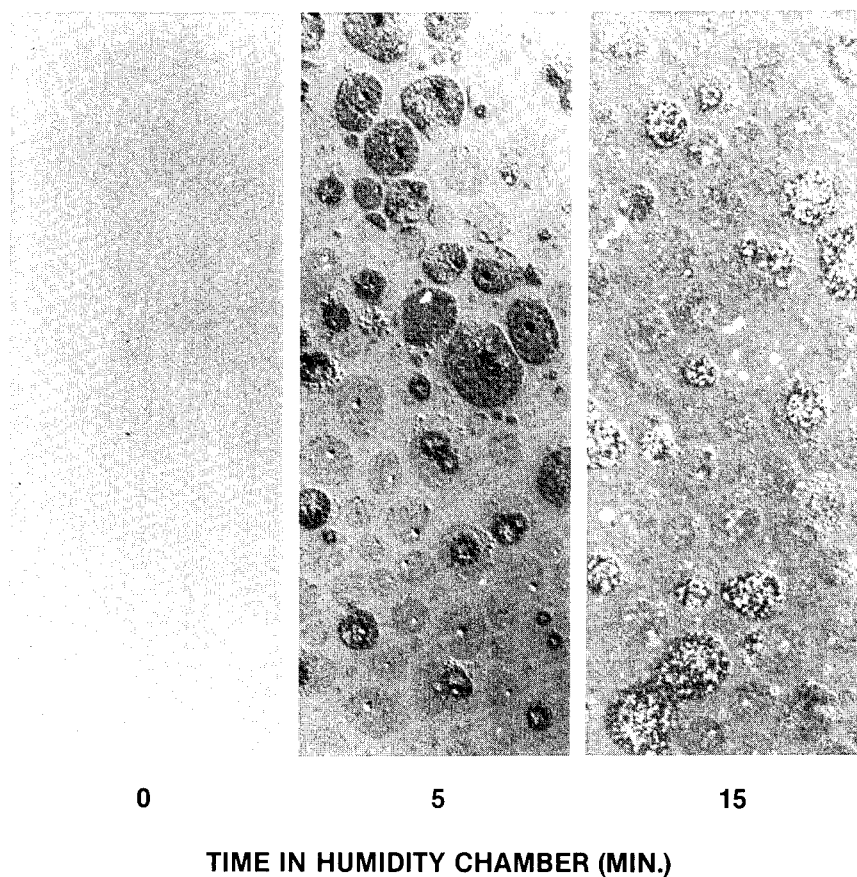


Figure 1. Effects of moisture on evaporated (no ion bombardment) silver coatings. Micrographs represent the sample before and after 5 and 15 minutes of exposure to 95% RH and 65°C.

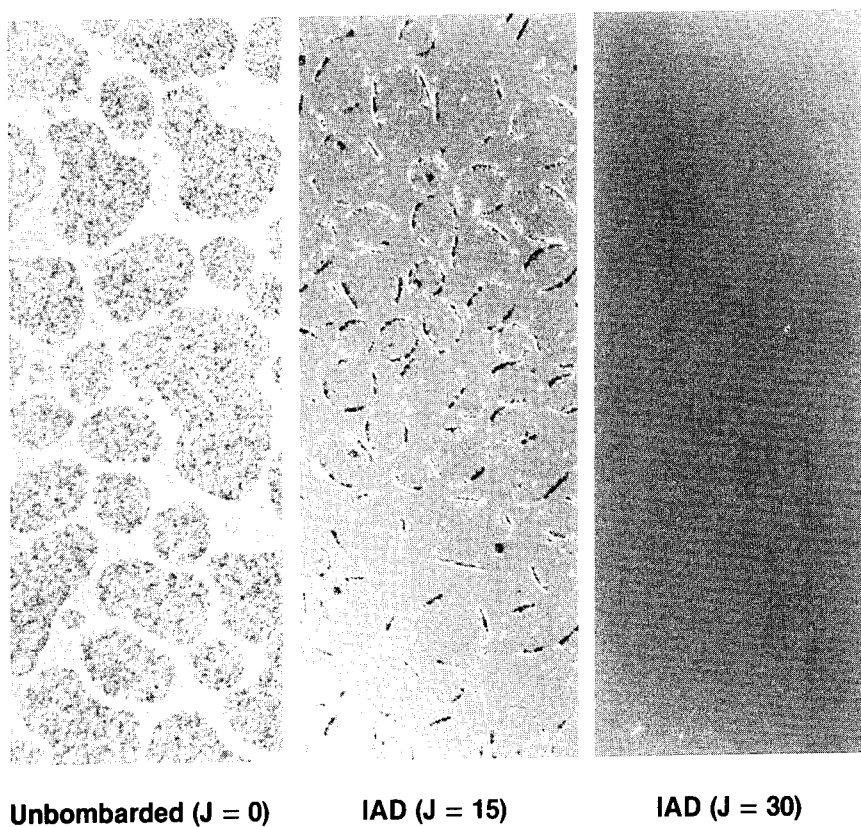


Figure 2. Effects of ion bombardment on the durability of Ag coatings. Coatings were bombarded with 0, 15, and 30 $\mu\text{A}/\text{cm}^2$ of 300 eV. Ar ions were exposed to 95% relative humidity and 65°C for 2 hours.

A STUDY OF THE ANODIC OXIDATION ON ALUMINIUM BY ION-IMPLANTED XE IONS MARKER AND RBS ANALYSIS TECHNIQUES

Heming Chen, Xinde Bai, Wangpei Li, Mingjiang Dai,
Department of Engineering Physics, Tsinghua University,
Beijing, China

ABSTRACT

This paper presents the results on the mechanism of the anodic oxidation on Al by means of ion-implanted marker layer of xenon and RBS analysis techniques. Experimentally, it has been shown that the mechanisms of anodic oxidation on Al are different in the different electrolytes. In the solution of 15%wt sulphuric-acid, the anodic oxide film is formed by the reaction between metal cations at the metal/oxide interface and continuously migrated oxygen anions. While in the solution of 5%wt ammonium citrate, both the migration of the metal cations and that of the oxygen anions contribute to the formation of the anodic film, and the oxidization takes place in internal region of the oxide film or at the interface. The transport numbers for Al in 5% wt ammonium citrate were found to vary with the voltage or current density from 44% to 64%.

INTRODUCTION

Some effective methods have been employed to study the anodic oxidation on metals, e.g. O^{18} tracer technique^{1,2} has been used to study the process of oxygen migration during anodic oxidation and superimposed metallic layers have been employed by S. Rigo and J. Siejka³ to investigate the process of metal transportation. Besides, ion-implanting marker layers of noble gas in fresh metals of pre-oxidized metal oxide films were developed to study the anodization of various metals. F. Brown⁴ studied the behaviors of various ion-implanted atoms during the aluminium anodic oxidation, J.P.S. Pringle⁵ reported the transport numbers of tantalum and oxygen using ion-implanted marker layer of noble gas.

The aim of the present work is to study the mechanism of aluminium anodization in different solutions by the ion-implanted marker layer of xenon and RBS analysis techniques and the effects of temperature, current density and voltage on the transport numbers of aluminium and oxygen.

THE PRINCIPLE AND THE METHOD

A marker layer of xenon is implanted into the aluminium samples which will then be oxidized in given conditions. The xenon positions in the samples after anodization and the thicknesses of the total oxide films are obtained by the RBS analysis technique. That the positions of xenon do not move after anodic oxidation indicate that aluminium cations do not reach the oxide/solution interface through the films to form new oxide there. While if the positions of xenon after anodic oxidation move towards the metal/oxide interface, the aluminium cations must have migrated towards the oxide/solution interface.

The transport numbers for the aluminium can be calculated by

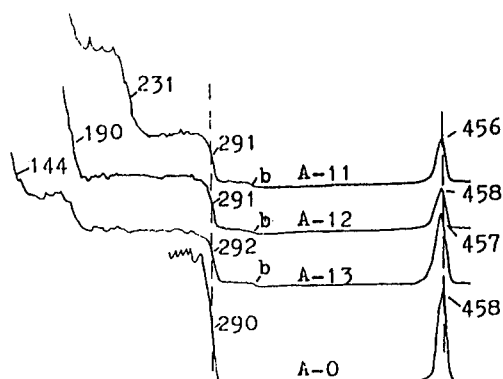


Fig.1. The RBS spectra of Al oxidized in 15%wt sulphuric acid at a constant voltage of 10V for different times.

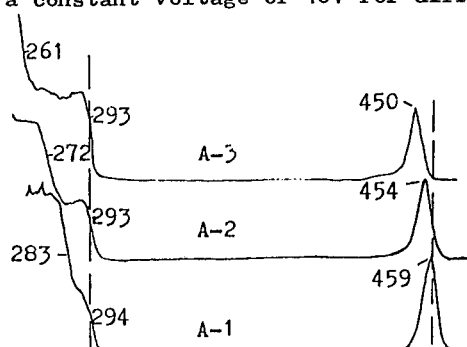


Fig.2. The RBS spectra of Al oxidized in 5%wt ammonium citrate at constant voltages.

the following formula.

$$T_m = \frac{D_{xe}}{D_{tot}} \quad (1)$$

where D_{xe} is the thickness of the oxide above the marker layer and D_{tot} is the total thickness of the formed oxide, and the transport number for oxygen is $T_o = 1 - T_m$.

EXPERIMENTAL DETAILS

Pure aluminium sheets, having dimensions of 20mm×11mm×0.5mm, were used as the samples. The treatments on aluminium sheets before Ion-Implantation involved the following steps.

1. Washing in 10%wt caustic soda solution for 10 minutes.
2. Immersion in a mixture of 15%wt sodium phosphate + 20%wt sodium carbonate for 10 minutes.
3. Chemically polishing in a mixture of 90%wt phosphoric acid + 5%wt nitric acid + 5%wt sulphuric acid at 368K-373K.

4. Rinsing in distilled water and drying in a cold air stream.

Xenon implantation was carried out using the isotope separator working in a high vacuum of 10^{-6} torr at an energy of 40 KeV and a dose of 5×10^{16} atoms/cm². The implanted aluminium sheets were oxidized in 15%wt sulphuric acid or in 3%wt ammonium citrate (The sample A-0 was not oxidized). The constant current power supply and the manostatic power supply with 1.5 grade of precision had a stability of 3%. After that, the specimens were bombarded vertically with He ions at an energy of 2MeV, using a 2.1M cascade accelerator with the surface barrier silicon detector, which was placed at an angle of 15° (the scattering angle equal to 165°) to the beam. The whole system had a resolution of 20 KeV at 2MeV.

EXPERIMENTAL RESULTS AND INTERPRETATION

Fig. 1 is the RBS spectra of aluminium samples oxidized at 295K in 15%wt sulphuric acid at a constant voltage of 10V. The sheets were oxidized for 3 minutes, 5 minutes and 7 minutes respectively. It was found that the positions of xenon did not move, which indicated that the new oxide was formed by oxygen anions migrating towards the metal/oxide interface and that no new oxide was formed at the oxide/solution interface. This result agrees with that reported by C.Charki and J.Siejka⁶. The occurrence of a little bench b was due to the existence of sulfur in the corporation of SO_4^{2-} ions into the films from the solution. The movements of xenon positions in aluminium sheets oxidized at 295K in the 3%wt ammonium citrate at constant voltages are showed in Fig. 2. The sheets were oxidized at 50V, 100V and 150V respectively until the current density dropped to zero. It was evident that the positions of xenon moved towards the inner interface, which confirmed that aluminium cations migrated towards the outer interface to form new oxide during oxidization. The conclusion is consistent with that in Ref[1]. Results from the RBS spectra showed that the positions of xenon did not reach the inner interface, which meant that oxygen anions also migrated, but towards the opposite direction. We conclude that new oxide was formed by the migration of both aluminium cations and oxygen

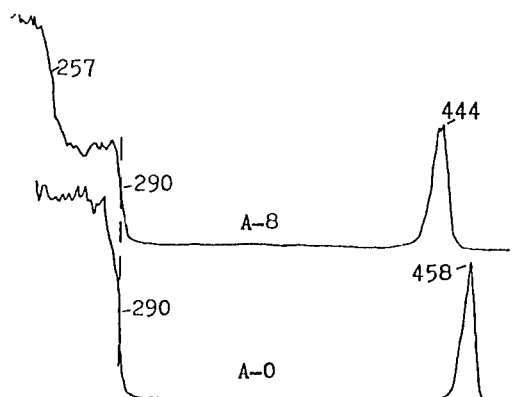


Fig.3. The RBS spectra of Al oxidized in 5%wt ammonium citrate at a constant current.

anions in contrary directions to react at the interface or some region in the film.

Fig.3 is the RBS spectra of aluminium sheets oxidized in the solution of 3%wt ammonium citrate at a constant current of $3\text{mA}/\text{cm}^2$. The result is similar to that of the constant voltage anodization in the same solution.

The transport numbers for aluminium in the solution of 3%wt ammonium citrate were calculated by the formula mentioned above, the absolute errors of these calculations were about 6%. At the constant voltage, the transport numbers for aluminium decrease with the increase of voltage. At the constant current density, the transport numbers for aluminium decrease with the increase of current density. Temperature has some influences on the transport number for aluminium. At low temperature, the transport numbers for aluminium are little larger than that at high temperature. These results are listed in Table I.

CONCLUSIONS

1. Aluminium anodizations in different electrolytes have different mechanisms
2. Temperature, voltage and current density all have influences on transport numbers for aluminium during anodization.

Table I transport numbers for Al in 5%wt ammonium citrate

No.	temp. (K)	voltage or current	Xenon position atoms/ cm^2	thickness atoms/ cm^2	transport number for Al
A-1	295K	50V	5.0×10^{19}	9.0×10^{19}	56%
A-2	295K	100V	8.0×10^{19}	1.6×10^{20}	50%
A-3	295K	150V	1.0×10^{20}	2.1×10^{20}	47%
A-4	273K	50V	5.5×10^{19}	8.5×10^{19}	64%
A-5	273K	100V	8.5×10^{19}	1.5×10^{20}	56%
A-6	273K	150V	1.1×10^{20}	2.2×10^{20}	50%
A-7	273K	$1\text{mA}/\text{cm}^2$	1.2×10^{20}	2.2×10^{20}	55%
A-8	273K	$3\text{mA}/\text{cm}^2$	9.5×10^{19}	2.1×10^{20}	45%
A-9	273K	$5\text{mA}/\text{cm}^2$	1.0×10^{20}	2.3×10^{20}	43%
A-10	273K	$7\text{mA}/\text{cm}^2$	1.0×10^{20}	2.3×10^{20}	43%

REFERENCES

1. G.Amsel, D.Amsel, J.Phys. Chem. Solid 23, 1707 (1962).
2. J.Perroere, J.Siejka, J.Electrochem. Soc., 130 (6), 1267 (1983).
3. S.Rigo, J.Siejka, Solid State Comm., 15, 259 (1974).
4. F.Brown, W.D.Mackintosh, J.Electrochem. Soc., 120 (8), 1096 (1973).
5. J.P.S.Pringle, J.Electrochem. Soc., 120 (3), 398 (1973).
6. C.Cherki, J.Siejka, J.Electrochem. Soc., 120 (6), 784 (1973).

ION BEAM PROCESSING OF OPTICAL MATERIALS

F. L. Williams, L. L. Boyer, D. W. Reicher, J. J. McNally[†],
G. A. Al-Jumaily^{††}, and J. R. McNeil

University of New Mexico
Department of Electrical and Computer Engineering
Center for High Technology Materials
Albuquerque, NM 87131

ABSTRACT

We have deposited thin films of optical materials using ion beam sputtering and ion assisted deposition techniques. It is possible to obtain good quality film material deposited on substrates at temperatures lower than normally required. Ion assisted deposition influences film stoichiometry and packing density, which in turn determine optical and mechanical properties of the film material. We discuss two general indicators which appear helpful in predicting the degree to which these occur.

1.0 Introduction

The technique of processing optical and electronic materials using low energy ion beams ($E_i < 1500\text{eV}$) has been a subject of research for many years. Two techniques that are used in producing high-quality thin films are ion assisted deposition (IAD)¹⁻⁵ and ion beam sputtering (IBS).^{6,7} The former technique involves bombarding a substrate with ions during deposition of thin film material generated from evaporation or sputtering, and the latter method entails the use of ion beams to produce thin films by sputtering. In the case of IAD, additional surface energy is imparted to the adatoms via ion bombardment during deposition. One distinct advantage of IAD over conventional deposition techniques is that it allows the production of coatings at moderate deposition rates ($1\text{\AA s}^{-1} \leq R_{\text{depo}} \leq 10\text{\AA s}^{-1}$) that have improved properties. Both IBS and IAD allow the production of improved coatings at low substrate temperature ($T_{\text{sub}} \approx 100^\circ\text{C}$). Standard deposition techniques typically require heating substrates to high temperatures ($T_{\text{sub}} \approx 300^\circ\text{C}$) in order to achieve thin films of acceptable optical performance.⁸

Present Address:

[†] Department of Physics
USAFA/DFP

United States Air Force Academy, CO 80840

^{††} Barr Associates
Westford, MA 01886

This work supported in part by the Air Force Weapons Laboratory and Los Alamos National Laboratory.

We have investigated the use of both IAD and IBS to produce metal oxide thin films. The first section of this paper will summarize results of IAD applied to thin films of materials typically used in optical coatings, while the second section of this paper describes results of using IBS to deposit an optical nonlinear material, PLZT.

2.0 Ion Assisted Deposition of Optical Coatings at Reduced Substrate Temperature

IAD can increase film packing density and stoichiometry, resulting in improvements in optical properties, environmental stability, abrasion resistance and adhesion.^{1-5,9} Low temperature deposition processes have become increasingly important in practical applications involving certain substrate materials (*e.g.*, plastics¹⁰ and heavy metal fluoride glass^{9,11}), and for increasing throughput for coating large, precision elements. Results presented here will be restricted to substrate temperatures of approximately 100°C.

Thin films were deposited in an apparatus that is described in detail in Reference 12. The thin film starting material was electron beam evaporated at a deposition rate of $\sim 2\text{\AA s}^{-1}$, and the chamber was backfilled with oxygen during deposition to a pressure of $P_{\text{O}_2} \sim 10^{-4}$ Torr. Substrates were heated to $\sim 100^\circ\text{C}$ prior to starting the coating process, with the substrate temperature rising to $\sim 125^\circ\text{C}$ at the end of the coating due to heat from the evaporative sources. A Kaufman ion source¹³ provided either argon or oxygen ions for bombarding the substrates. Substrates were ion precleaned with $75\text{ }\mu\text{A cm}^{-2}$ of 500 eV argon ion bombardment for 4 minutes prior to deposition, and then bombarded with oxygen ions during film deposition. The ion current density was measured with a probe mounted on a shutter near the substrate surface.

Coatings of SiO_2 , Al_2O_3 , Ta_2O_5 and TiO_2 were deposited at different levels of oxygen ion energy and current density, and were analyzed for refractive index and extinction coefficient. A homogeneous envelope technique developed by Manafacier *et al.* (1976) was used to determine optical constants from the spectral transmittance of coated samples.¹⁴

Results

Figure 1 illustrates the variation of the index of refraction of Ta_2O_5 films with respect to ion energy and current density deposited using IAD. The upper horizontal axis of the figure represents the arrival ratio γ , which is the ratio of the flux of oxygen atoms from the ion beam to the flux of film atoms arriving at the substrate. It can be seen that the film refractive index of IAD Ta_2O_5 initially increases for a corresponding increase in ion current density, and the rate of increase is greater for greater ion energy. This increase continues until γ reaches a so-called "critical value." Note that essentially bulk values of refractive index (~ 2.28) are attained for the Ta_2O_5 film material for 300 eV ion

bombardment. Films deposited at bombardment levels greater than the critical value exhibit refractive indices that are less than those obtained at current densities below the critical value. The critical value is never attained for films deposited with 150 eV ion energy. Similar characteristics have been observed in films of Al_2O_3 and TiO_2 deposited using IAD.

Thin films of SiO_2 deposited using IAD do not display any significant increase in refractive index. Unbombarded films of SiO_2 have refractive indices (measured at $\sim 350\text{nm}$), of ~ 1.42 , while SiO_2 films deposited using IAD display values of ~ 1.44 . Transmittance spectra of SiO_2 films recorded around the $2.8\ \mu\text{m}$ water optical absorption band, however, show that use of IAD dramatically reduces film water content. Thus, the lack in variation of IAD SiO_2 film refractive index is most likely attributable to the small difference between the index of refraction of water and bulk SiO_2 , rather than a lack of film densification.

The extinction coefficient of IAD Ta_2O_5 also depends on bombardment conditions. Figure 2 illustrates the effect of oxygen IAD on the extinction coefficients of Ta_2O_5 thin films deposited at reduced substrate temperature. Low temperature deposition of Ta_2O_5 by conventional means typically results in absorbing films,¹⁵ as illustrated in Figure 2 by appreciable extinction coefficient ($\sim 15 \times 10^{-4}$) for $J=0$. The extinction coefficient is reduced to values $< 2 \times 10^{-4}$, however, by low-level oxygen ion bombardment, presumably due to improvements in film stoichiometry caused by oxygen ions. Similar in nature to the effect of IAD on refractive index, the rate of decrease is greater for greater bombardment energy in the region of decreasing extinction coefficient. For current densities near the critical value, the extinction coefficient begins to increase for increasing current density.

This result is *not* obtained for thin films of Al_2O_3 and TiO_2 deposited using IAD. For these materials, the extinction coefficients are typically low ($k < 4 \times 10^{-4}$) for unbombarded films, and the effect of IAD is to further reduce the extinction coefficients of these materials to values that are less than the sensitivity of our measurement technique. No increase in absorption is observed for an increase in current density.

Discussion

For the materials investigated, the presence of suboxide material can dramatically increase the amount of optical absorption measured in thin films. Because of this, the optical extinction coefficient is a sensitive indicator of metal oxide film stoichiometry.¹⁶ We have examined samples of tantalum and titanium oxides using Rutherford backscattering spectrometry (RBS). In the case of large amounts of absorption there is a correlation between film extinction coefficient and sample substoichiometry. However,

for films of low absorption, RBS techniques are not sufficiently accurate to determine film stoichiometry.¹⁷

A qualitative picture of the response of film extinction coefficient to ion bombardment is provided by the fractional sputtering yield (Y_O/Y_M), which gives the ratio of the oxygen atomic sputtering yield to the metal atomic sputtering yield of a compound metal oxide target. A value of (Y_O/Y_M) > 1 implies that oxygen atoms are more readily sputtered from the surface than are metal atoms, so that ion bombardment results in a reduced metal oxide material. This process is known as preferential sputtering,¹⁸ and is most likely responsible for the increase in extinction coefficients observed from thin films of Ta₂O₅.

Malherbe *et al.* (1986) have developed a method for predicting the composition of metal oxides reduced by ion bombardment.¹⁹ Their argument gives the fractional sputtering yield of a compound target as

$$\frac{Y_O}{Y_M} = \left(\frac{A_M}{A_O}\right)^{1/3} \left(\frac{U_M}{U_O}\right)^{2/3},$$

where A_j and U_j are the atomic weight and surface binding energy, respectively, of the metal (M) and oxygen (O). While the expression for (Y_O/Y_M) was derived for bulk target material, the preferential sputtering for thin films is expected to be approximately the same. Values of (Y_O/Y_M) calculated for the metal oxides investigated in this study are listed in Table 1. The values in Table 1 show that the theory of Malherbe *et al.* is reasonably accurate in predicting the experimental result that use of IAD to deposit Ta₂O₅ produces films having significantly greater optical absorption compared to that of films of Al₂O₃, SiO₂ and TiO₂.

Table 1 Fractional Sputtering Yields

Target	A_M/A_O	U_M/U_O	Y_O/Y_M
Al ₂ O ₃	1.69	0.77	1.00
SiO ₂	1.76	0.81	1.00
TiO ₂	2.99	1.09	1.50
Ta ₂ O ₅	11.31	1.23	2.50

The model for preferential sputtering does not include the effects of bombarding with reactive ions. Reactive ions may engage in specific chemical interactions with the target to synthesize compound thin films.²⁰ Also, oxygen IAD of metal oxides occurs in a reactive atmosphere, where ion bombardment may induce chemical reactions between

neutral gas species and the surface. Such chemically reactive mechanisms are probably responsible for the low values of extinction coefficient observed in TiO_2 thin films deposited with oxygen IAD, even though the theory of preferential sputtering predicts that IAD of TiO_2 should result in reduced thin film material.

Much work has been done in recent years to model the effects of ion bombardment during film growth. The most successful model uses binary collisions and molecular dynamics to explain the densification of ion assisted thin films in terms of surface atom recoil implantation.^{21,22} The results of this model indicate that an increase in sputtering yield increases the probability of a recoil implantation event occurring. For the same material, the sputtering yield will be greater for greater ion energy.²³ Since film refractive index strongly depends on film density, a change in index of refraction is assumed to represent a change in density. Therefore, greater bombardment energies result in greater increases in refractive index for the same increase in ion current density (i.e. greater $\partial n/\partial J$). Greater sputtering yields are also expected for smaller values of target mass. This can be characterized by the kinematic factor κ , which is a measure of the fraction of energy imparted to a target by an energetic projectile. For a projectile of mass M_1 and a target of mass M_2 , the kinematic factor is given by

$$\kappa = \frac{4M_1M_2}{(M_1+M_2)^2}$$

Table 2 lists values of κ for the collisions $\text{O} \rightarrow \text{TiO}_2$, $\text{O} \rightarrow \text{Al}_2\text{O}_3$ and $\text{O} \rightarrow \text{Ta}_2\text{O}_5$. From Table 2, it is seen that the kinematic factor is greater for TiO_2 than for Al_2O_3 , and that the value of κ is greater for Al_2O_3 than for Ta_2O_5 . Thus, although the kinematic factors are consistent with the result that IAD of Al_2O_3 exhibits greater rates of increase in refractive index ($\partial n/\partial \gamma$) than is observed for Ta_2O_5 , there is an inconsistency with the results that ($\partial n/\partial \gamma$) for Al_2O_3 is also greater than that for TiO_2 . This may be due to the fact that oxygen IAD results in generation of crystalline material in thin films of TiO_2 , but does not promote the growth of crystallites in thin films of the other materials investigated.^{5,24}

Table 2 Kinematic factors for O on various metal oxides

Collision	κ
$\text{O} \rightarrow \text{SiO}_2$	0.66
$\text{O} \rightarrow \text{TiO}_2$	0.56
$\text{O} \rightarrow \text{Al}_2\text{O}_3$	0.47
$\text{O} \rightarrow \text{Ta}_2\text{O}_5$	0.13

Competing with bombardment-induced film densification is the mechanism of ion incorporation associated with ion bombardment. Three important observations have been made by researchers investigating the effects of ion bombardment on reactor materials: (1) the ion incorporation probability η is greater for greater ion energy, (2) it is possible for the ion incorporation mechanism to become saturated and (3) there is a threshold ion energy E_T below which no ion incorporation occurs (i.e., $\eta = 0$ for $E_i < E_T$). For the low-energy regime, Carter et al. (1980)²⁵ have derived an approximate expression for E_T

$$E_T \approx 100\pi Na^2 (Z_1 Z_2)^{3/4} ,$$

where E_T is in eV, N is the areal atomic density of the target (atoms m^{-2}), Z_1 and Z_2 are the atomic numbers of the ion and target, respectively, and a is the Andersen-Sigmund range ($a = 2.2 \times 10^{-11} m$).²⁶ The expression for E_T shows that, for the same ion species and flux, bombardment of a lighter target material will result in greater values of η compared to values of η for a heavier target material.

The results reported above may be used to develop a picture which is consistent with material-dependent differences in maximum packing density obtained from IAD of thin films. There is evidence indicating that ion incorporation causes a reduction in film density due to the presence of trapped gas in the film. Therefore, there will be a maximum film density obtained using IAD due to the competing mechanisms of recoil implantation and ion incorporation.

Table 3 lists values of E_T for the collisions $O \rightarrow Al_2O_3$, $O \rightarrow TiO_2$ and $O \rightarrow Ta_2O_5$. Mean atomic numbers were used for Z_1 and Z_2 in the calculation for E_T . For example, in the case of $O \rightarrow Al_2O_3$, $Z_1 = 8$, $Z_2 = 10.5$, and $N = 2.40 \times 10^{19}$ atoms m^{-2} , yielding a value of $E_T = 101$ eV. It can be seen that the estimated threshold energies for ion incorporation to occur in Ta_2O_5 is roughly twice that value for Al_2O_3 and TiO_2 . Thus, for a given ion energy and flux, there is a greater probability of ion incorporation occurring for both Al_2O_3 and TiO_2 compared to the ion incorporation probability for Ta_2O_5 . This result is consistent with the fact that IAD of Ta_2O_5 yields a greater value of maximum film packing density than is achieved using IAD to deposit either Al_2O_3 or TiO_2 . The decrease and saturation in packing density of IAD metal oxide thin films at high ion flux levels may be explained in terms of saturation of the gas trapping mechanism.

Table 3 Ion incorporation threshold energy (E_T) for various collisions

Collision	E_T (eV)
O→SiO ₂	72
O→Al ₂ O ₃	101
O→TiO ₂	108
O→Ta ₂ O ₅	212

3.0 PLZT Film Deposition

Lanthanum-modified lead zirconate-titanate, $Pb_{1-x}La_x(Zr_yTi_z)_{1-x/4}O_3$ or PLZT, is a very attractive class of ceramic material because of its pronounced electro-optic characteristics. In addition, the stoichiometry can be varied to produce material with different characteristics. The material has been investigated in bulk form for a number of years, and more recently in thin film form.^{27,28} Thin film PLZT has numerous possible applications in electronic and electro-optic devices such as FET nonvolatile memory, optical switches, optical displays, and image storage. Most recently, thin film PLZT has been used to frequency double light at 1.06 microns wavelength.²⁹

PLZT thin films were prepared by IBS. The experimental apparatus included a 5 cm Kaufman ion source directed at a pressed powder target of composition (x/y/z) of (28/0/100). The substrates were heated to temperatures ranging from 500°C to 650°C prior to deposition. The ion source was operated with Ar at a pressure of 5×10^{-5} Torr. The chamber was backfilled during deposition with O₂ to a pressure of 2×10^{-4} Torr. Substrates used for this investigation include Si <100>, Si <111>, Si <100> with 2 μ m of SiO₂ as a buffer layer, and fused silica. The thickness of the films were approximately 5000Å. Thin film crystallography was determined by x-ray diffraction (Cu K α radiation). The thin film composition was determined by SEM/EDAX measurements.

Results

Highly oriented PLZT thin films have been obtained with ion beam sputtering. Figure 3 illustrates the x-ray diffraction characteristics of three samples of PLZT deposited on Si at substrate temperatures of approximately 500, 550, and 650°C. The sample deposited at a substrate temperatures of 550°C is highly oriented with only the <100> crystalline orientation of the perovskite form of the material detectable. This is very desirable for applications of the material. The sample deposited at 650°C is very polycrystalline, while the sample deposited at 500°C illustrates the x-ray diffraction characteristics of pyrochlore PLZT. Neither of these other forms of PLZT is desirable for electro-optic applications. Good quality PLZT was also deposited on Si wafers having

a buffer layer of SiO_2 approximately 2 microns thick. This is very encouraging because the configuration can be used as a waveguide structure, and also because this illustrates the compatibility of Si and PLZT technologies. Devices of Si (*e. g.* drivers, etc.) can be produced with PLZT on the same wafer. Good quality PLZT has also been deposited on fused silica substrates.

We have observed second harmonic generation in ion beam sputtered PLZT deposited on the buffer layer of SiO_2 on a Si substrate. The second harmonic conversion increases quadratically with applied electric field in the configuration shown in figure 4, indicating this is a third order effect. The incident wavelength was 1.06 microns, and the reflected beams were 0.53 and 1.06 microns. We are presently characterizing this effect more thoroughly, including extending the incident wavelength to 10.6 μm .

In addition we have observed a significant difference in the surface morphology of IBS and magnetron sputtered samples of PLZT. The IBS sample had an rms roughness approximately 60 percent of that of the magnetron sputtered sample. Excessive surface roughness can prohibit use of the material in applications requiring low optical scatter loss, such as waveguiding. A possible explanation for this difference in surface roughness is the lower pressure at which the ion beam sputtered material was deposited. In addition, the magnetron deposited sample was exposed to an unknown level of ion bombardment as a result of being immersed in the discharge of the arrangement; this was not the case for the ion beam sputtered sample.

4.0. Conclusions

Good quality oxide materials have been deposited on substrates at reduced temperature using IAD techniques. For some film materials, values of bulk refractive index are obtained. Preferential sputtering of oxygen from the film material is sometimes an issue. General indicators of these two behavioral characteristics promoted by ion bombardment include threshold energy for ion incorporation and relative sputter yields of film atomic species. Good quality, highly oriented films of PLZT have been deposited on substrates of Si, Si with a buffer layer of SiO_2 , and fused silica using ion beam sputtering. The material has displayed strong second harmonic generation at 1.06 microns incident wavelength. In addition the surface morphology of the ion beam deposited PLZT appears to be of higher quality than that of r.f. magnetron sputtered films of the same composition.

The authors thank A. Mukherjee and S. R. J. Brueck for second harmonic characterization of PLZT. We also thank Feiling Wang for his photolithography work necessary to characterize these films.

REFERENCES

1. W. C. Herrmann, Jr., and J. R. McNeil, "Ion Beam Applications for Optical Coating," *Optical Thin Films*, Proc. SPIE, 325, 101 (1982).
2. J. M. E. Harper, J. J. Cuomo, and H. R. Kaufman, "Technology and Applications of Broad-Beam Ion Sources Used in Sputtering. Part II. Applications," *J. Vac. Sci. Technol.* 21, 737 (1982).
3. E. H. Hirsch, and I. K. Varga, "Thin Film Annealing by Ion Bombardment," *Thin Solid Films*, 69, 99 (1980).
4. P. J. Martin, H. A. MacLeod, R. P. Netterfield, G. C. Pacey, and W. G. Sainty, "Ion Beam-Assisted Deposition of Thin Films," *Appl. Opt.* 22, 178 (1983).
5. F. L. Williams, D. W. Reicher, C.-B. Juang, and J. R. McNeil, "Metal Oxides Deposited Using Ion Assisted Deposition at Low Temperature," *J. Vac. Sci. Technol.* A7, in press (1989).
6. J. R. Sites, P. Gilstrap, and R. Rujkorakarn, "Ion Beam Sputter Deposition of Optical Coatings," *Opt. Eng.* 22, 447, (1983).
7. J. M. E. Harper, J. J. Cuomo, and H. T. G. Hentzell, "Quantitative Ion Beam Process for the Deposition of Compound Thin Films," *Appl. Phys. Lett.*, 43, 547 (1983).
8. S. Ogura, and H. A. Macleod, "Water Sorption Phenomena in Optical Thin Films," *Thin Solid Films*, 34, 371 (1976).
9. J. J. McNally, G. A. Al-Jumaily, J. R. McNeil, and B. Bendow, "Ion Assisted Deposition of Optical and Protective Coatings for Heavy Metal Fluoride Glass," *Appl. Opt.*, 25, 1973 (1986).
10. R. E. Hurley, and E. W. Williams, "Ion Plating on Plastic Substrates," *Thin Solid Films*, 92, 99 (1982).
11. D. C. Tran, G. H. Sigel, Jr., and B. Bendow, "Heavy Metal Fluoride Glasses and Fibers, A Review," *J. Lightwave Technol.*, 2, 566 (1984).
12. J. J. McNally, K. C. Jungling, F. L. Williams, and J. R. McNeil, "Optical Coatings Deposited Using Ion Assisted Deposition," *J. Vac. Sci. Technol.*, A5, 2145 (1987).
13. H. R. Kaufman, J. J. Cuomo, and J. M. E. Harper, "Technology and Applications of Broad-Beam Ion Sources Used in Sputtering. Part I. Ion Source Technology," *J. Vac. Sci. Technol.*, 21, 725 (1982).
14. J. C. Manafacier, J. Gasiot, and J. P. Fillard, "A Simple Method for the Determination of the Optical Constants n , k and the Thickness of a Weakly Absorbing Thin Film," *J. Phys. E. Sci. Instrum.*, 9, 1002 (1976).
15. W. C. Herrmann, Jr., "E-Beam Deposition Characteristics of Reactively Evaporated Ta_2O_5 for Optical Interference Coatings," *J. Vac. Sci. Technol.*, 18, 1303 (1981).
16. H. Demiryont, J. R. Sites and K. Geib, "Effects of Oxygen Content on the Optical Properties of Tantalum Oxide Films Deposited by Ion-Beam Sputtering," *Appl. Opt.* 24, 490 (1985).
17. R. Behrisch, and B. M. U. Scherzer, "Rutherford Backscattering as a Tool to Determine Electronic Stopping Powers in Solids," *Thin Solid Films*, 19, 247 (1973).
18. S. Hofmann, and J. M. Sanz, "Quantitative XPS Analysis of the Surface Layer of Anodic Oxides Obtained During Depth Profiling by Sputtering with 3 keV Ar^+ Ions," *J. Trace Microprobe Tech.*, 1, 213 (1982-1983).
19. J. B. Malherbe, S. Hofmann, and J. M. Sanz, "Preferential Sputtering of Oxides: A Comparison of Model Predictions with Experimental Data," *Appl. Surf. Sci.*, 27, 355 (1986).
20. R. P. Netterfield, K. -H. Mueller, D. R. McKenzie, M. J. Goonan, and P. J. Martin, "Growth Dynamics of Aluminum Nitride and Aluminum Oxide Thin-Films Synthesized by Ion-Assisted Deposition," *J. Appl. Phys.*, 63, 760 (1988).
21. K. -H. Mueller, "Model for Ion Assisted Thin-Film Densification," *J. Appl. Phys.*, 59, 2803 (1986).

22. K. -H. Mueller, "Ion-Beam-Induced Epitaxial Vapor-Phase Growth: A Molecular-Dynamics Study," *Phys. Rev.*, **B35**, 7906 (1987).
23. P. Sigmund, "Theory of Sputtering, I. Sputtering Yield of Amorphous and Polycrystalline Targets," *Phys. Rev.*, **184**, 383 (1969).
24. F. L. Williams, R. D. Jacobson, J. R. McNeil, G. J. Exarhos and J. J. McNally, "Optical Characteristics of Thin Films Deposited at Low Temperature Using Ion Assisted Deposition," *J. Vac. Sci. Technol.*, **A6**, 2020 (1988).
25. G. Carter, D. G. Armour, S. E. Donnelly, and R. P. Webb, "The Injection of Gas Ions into Solids: Their Trapping and Escape," *Rad. Eff.*, **53**, 143 (1980).
26. H. H. Andersen, and P. Sigmund, "Defect Distributions in Channeling Experiments," *Nucl. Instru. Meth.*, **38**, 238 (1965).
27. H. Higashino, T. Kawaguchi, H. Adachi, T. Makino, and O. Yamazaki, "High Speed Optical TIR Switches Using PLZT Thin-Film Waveguides on Sapphire," *Proc. of the 6th Intl. Meeting on Ferroelec.*, Kobe 1985, *Jap. J. Appl. Phys.*, **24**, supplement 24-2, 284 (1985).
28. H. Adachi, T. Mitsuyu, O. Yamazaki, and K. Wasa, "Bragg A-O Deflector Using A Piezoelectric PLZT Thin Film," *Proc. of the 6th Intl. Meeting on Ferroelect.*, Kobe 1985, *Jap. J. Appl. Phys.*, **24**, supplement 24-3, 287 (1985).
29. A. Mukherjee, S. R. J. Brueck, and A. Y. Wu, "Electric Field Induced Second Harmonic Generation in PLZT," to be published, (1989).

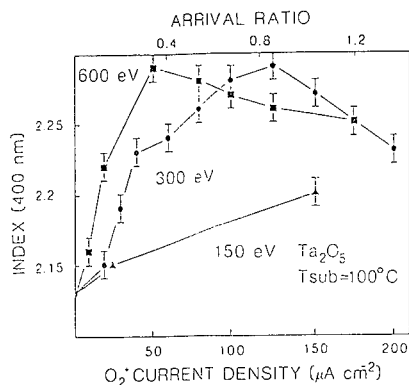


Fig. 1. Variation of film index of refraction with bombarding oxygen ion energy and current density

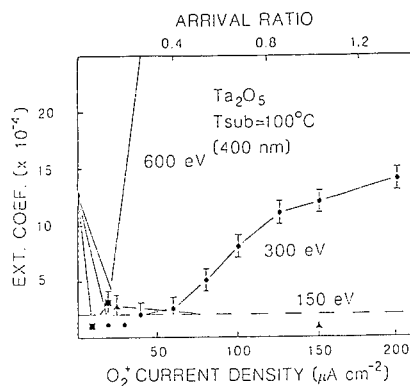


Fig. 2. Variation of film extinction coefficient with bombarding oxygen ion energy and current density.

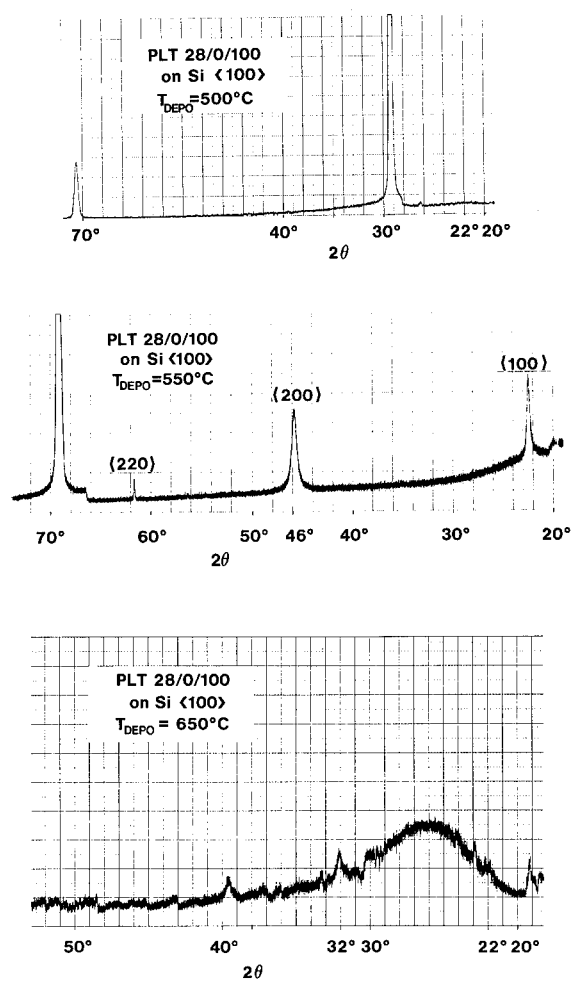


Fig. 3. X-ray diffraction characteristics of PLZT thin film material ion beam sputter deposited on Si substrates at temperature of 500, 550 and 650°C .

ELECTRIC FIELD INDUCED SECOND HARMONIC GENERATION

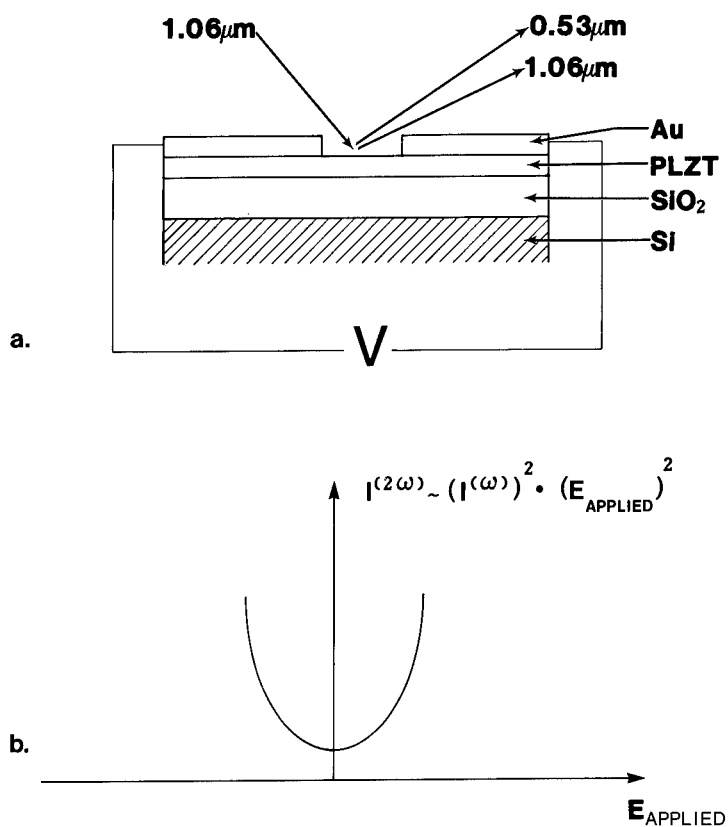


Fig. 4. Field induced second harmonic generation of PLZT thin film material ion beam sputter deposited onto a Si substrate having a buffer layer of SiO₂; (a) schematic illustration of the process; and (b) variation of the intensity of the second harmonic signal with applied field.

ION-ASSISTED DEPOSITION OF PROTECTIVE OVERLAYERS FOR MAGNETO-OPTIC ALLOYS.

Kenneth D. Cornett, Ursula J. Gibson, Anthony Taylor, Optical Sciences Center, University of Arizona, Tucson, AZ 85721.

Abstract

Rare-Earth Transition-Metal alloys such as Tb-Fe-Co are being studied and used as magneto-optic data storage materials. These materials are susceptible to oxidation by either oxygen or water vapor, particularly the rare earth component. Pitting corrosion is also a problem when protective overlayers have pinholes or a porous microstructure. Both degradation mechanisms are significant for application of this material to optical data storage. We have used ion assisted deposition (IAD) to produce protective overlayers of refractory oxides, such as Al_2O_3 and ZrO_2 . These layers were deposited both with and without IAD onto iron films and exposed to environments with controlled temperature and humidity. A scanning micro-reflectometer capable of detecting micrometer-sized pinholes was used to monitor the degradation of the iron layer with exposure time.

Introduction

IAD is known to alter the microstructure of evaporated films[1-3] and affect the corrosion resistance of bilayer structures[4]. We chose Al_2O_3 and ZrO_2 since they have received considerable study with IAD, but have not been as widely studied as protective overlayers for TbFeCo. They also have different preferred microstructures and behave somewhat differently under IAD.

We also chose to use evaporated Fe films as a degradable media rather than TbFeCo. This is both practical and purposeful, since the investment required to deposit TbFeCo is large. TbFeCo samples received from other sources must have some kind of interim protective overlayer which would first have to be removed, and may not be completely effective. Immediately overcoating an iron film with the desired overlayer without breaking vacuum was a preferable first step. Furthermore, pinhole formation studies on Fe/overlayer systems should be a good test of overlayer integrity. Once the parameters to produce the best overlayers on iron were determined, optimized layers could be applied to TbFeCo for further evaluation.

Deposition Procedure

All films were deposited in a vacuum system equipped with a liquid nitrogen trapped diffusion pump, resistive and electron beam evaporation sources, and a sample introduction system on a stainless steel belljar. Base pressures measured by an ion gauge were in the range of $2\text{--}4 \times 10^{-6}$ torr. For most films, a residual gas analyzer (RGA) was available to measure the partial pressures of several gases. A Kaufman-type ion source was used to ion sputter the substrates prior to deposition as well provide ion assistance during the deposition of the protective overlayers. Argon gas was used in the ion mill at all times. No changes in the partial pressures of residual H_2 , H_2O , N_2 , O_2 , or CO_2 were observed when Ar was flowed through the ion source. The total system pressure measured by the ion gauge was approximately 1×10^{-4} torr during operation of the ion source. Iron was resistively evaporated from an aluminum oxide coated basket. The oxides were evaporated from a small electron beam source. Since the small amount of oxide source material had to be replenished every few runs, no additional oxygen was added to the residual background during oxide depositions. The substrates were at ambient temperature at the start of the depositions, but their temperatures were subsequently neither controlled nor monitored.

Glass substrates (approximately $25 \times 19 \times 1$ mm) were cleaned and then loaded into the vacuum chamber from a sample introduction system. Substrate preparation consisted of

scrubbing the substrate with cotton in a detergent solution, then ultrasonically agitating them once in detergent solution, twice in de-ionized water, and finally in anhydrous methanol (with low particulate count). The substrates were rinsed with de-ionized water before each step. After the methanol cycle, the substrates were blown dry with nitrogen and immediately loaded onto the sample introduction stub. A final blast of gas (either N_2 or chlorofluorocarbon) an instant before capping and evacuating the introduction chamber was found to significantly reduce the number of initial pinhole defects in the deposited iron films. Once in the chamber and just prior to deposition of the iron (iron hot but not melted), the substrates were ion sputtered with 150eV Ar^+ ions, at a current density of $20\mu A/cm^2$ for one minute. After turning off the ion source, the argon gas supply was closed and the system pressure allowed to decrease while the iron was melted and a stable deposition rate established. Iron deposition onto the substrate was initiated as soon as possible (within 2-3 minutes) at a rate of 0.4-0.5 nm/s. The iron films were deposited to a nominal thickness of 40nm for the ZrO_2 overlayers, and 25nm for the Al_2O_3 overlayers.

If the overlayer was to be deposited with ion assistance, the Ar gas flow and ion source were set to the desired operating point while cooling the Fe evaporation source below the iron melting point. An electron beam source was used to evaporate the oxides at the deposition rate desired. The time between depositions was again kept as small as possible, typically 2-4 minutes, depending on the time required to stabilize the oxide deposition rate. Overlayers of both ZrO_2 and Al_2O_3 were deposited to nominal thicknesses of 100nm. Upon removal from the deposition chamber, the films were visually inspected in transmission. If there were more than one or two obvious defects visually observable, that sample was not used for further study and the deposition repeated.

When several samples had been deposited, they were taken to a sputter coater used to prepare SEM samples. A small piece of glass with a square corner was placed on the oxide overlayer and a film of Au was deposited. Subsequent removal of the glass cover revealed a window into the sample which was not coated by the gold (figure 1). The square corner of the window provided a reference position for the micro-reflectometer, which could detect the difference in reflectance between masked and unmasked regions.

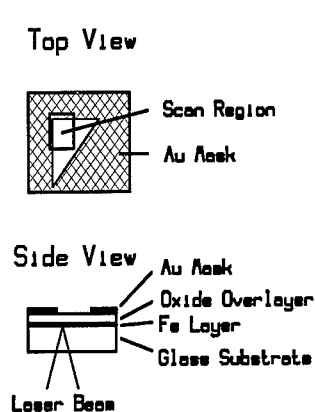


figure 1. Schematic views of sample geometry. The region scanned for pinholes includes the square corner of the Au mask layer. Counts from the masked area are not included in the histogram.

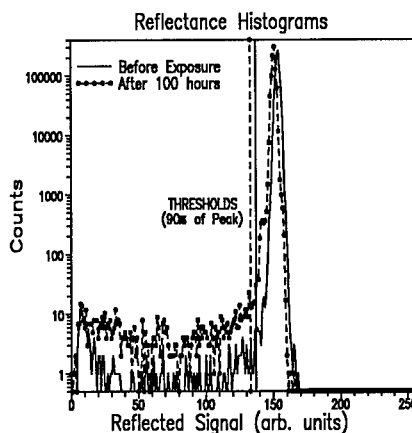


figure 2. Reflectance histograms from a sample before and after exposure to a $50^\circ C$, 90% RH environment. All counts from reflectances lower than the thresholds are considered to be degraded.

Degradation Measurements

The micro-reflectometer has been previously described in detail[5]. A modified compact disk player provided an auto-focused spot, about 1 μm in size, from its laser diode. The disk player's auto-tracking servo was disengaged and independent XY sample translation provided by stepper motor driven stages with a step size of 1 μm . The reflected signal detected by photodiodes in the disk player was sampled by a data acquisition system. Both the data acquisition system and translation stages were under microcomputer (IBM PC) control.

The samples were oriented such that the diode laser beam was incident to the iron layer through the glass substrate, and positioned with the square corner of the gold mask included in the scanned area. This insured that the same region of a sample was scanned every time. The reflected signal was sampled on a 1032x1032 array at 3 μm intervals, and stored as an 8 bit quantity (0-255). This choice reflected a tradeoff between the desire to maximize the total area scanned (so that it is representative of the film as a whole) and limitations imposed by the data storage and processing capabilities available (IBM PC and PC-AT compatible). Each sample was scanned shortly after deposition of the Au mask and after successive exposures to a 50°C, 90% relative humidity (RH) environment.

The degraded area was determined by generating a histogram of reflectance values recorded from the area not covered by the Au mask. The reflectance value with the highest number of counts was determined and a threshold set at 90% of that value. All pixels with a lower reflectance than the threshold were counted as degraded area (figure 2). Since the starting position of each scan varied slightly with respect to the corner of the mask, no two histograms contained exactly the same number of pixels. In order to compare results, it is necessary to use the fraction or percentage of the total number of pixels in a histogram which represent degraded area. We present here only the change in degraded area percent after a time in the humidity chamber from the initial pre-exposure scan. There was no correlation between the initial degraded area percent and the degraded area percent after the last exposure.

Additionally, false-color and black/white reflectance images were generated and examined on a computer screen so that individual defects could be monitored after each exposure. In general, we found that the increase in degraded area was mainly caused by formation of new sites rather than the growth of existing ones.

Results and Discussion

The change in degraded area with exposure time for the Al_2O_3 and ZrO_2 overlayers is presented in figures 3a,3b along with their deposition parameters. Inspection of figure 3a reveals that as the intensity of the ion bombardment on the Al_2O_3 overlayers is increased, the amount of degradation after approximately 100 hours at 50°C, 90%RH is generally reduced. Al_2O_3 films tend to be amorphous both with and without ion bombardment. The principle effect of IAD on this material is to reduce the columnar microstructure and increase packing density[3]. These effects should improve the performance of a protective overlayer. Some investigators have suggested that the densification observed in several types of IAD films can be correlated with the ion momentum bombardment per deposited atom, γ [6,7]. A quantity proportional to this can be calculated using the formula

$$\Gamma = \frac{\sqrt{E} \cdot J}{D}, \quad (1)$$

where E is the ion energy (eV), J is the ion current density ($\mu\text{A}/\text{cm}^2$), and D is the deposition rate (nm/s). Plotting the change in area percent degraded after 100 hours versus Γ shows that this is a reasonable interpretation of the results for our Al_2O_3 overlayers (figure 4a).

Two films, however, do not follow the trend towards lower degradation with increased ion momentum parameter. The first is a conventionally evaporated film ($\Gamma = 0$) for which the ion pre-cleaning step was omitted due to a failure in the ion source. Substrate cleanliness should certainly affect the homogeneity and structure of the iron films. This is especially true if ions from the detergent washing step in the substrate preparation are not adequately removed by the subsequent rinses. Chlorine and fluorine ions in particular are

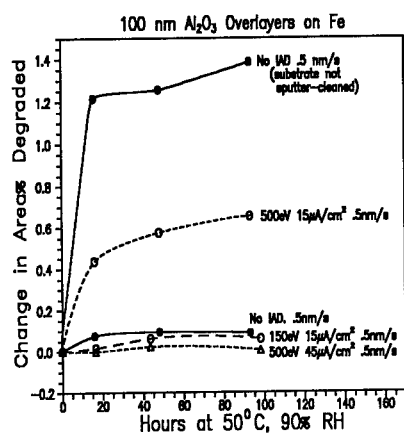


figure 3a
Change in the degraded (pinhole) area under Al_2O_3 and ZrO_2 overlayers is monitored after successive cycles in a humidity chamber. (Data from selected films.)

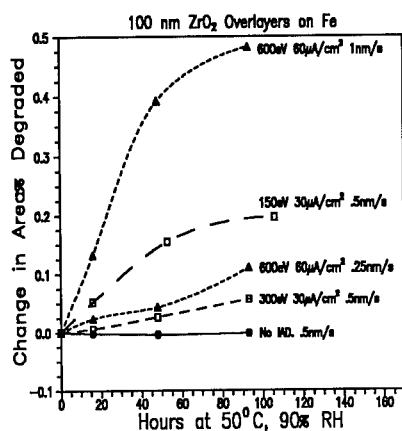


figure 3b.

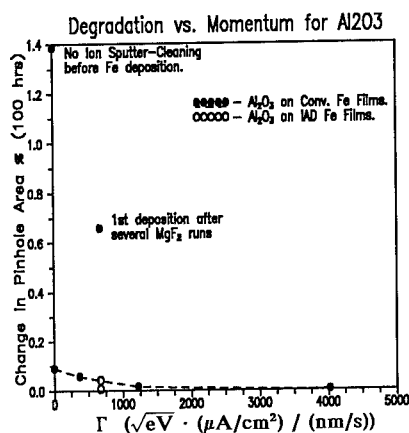


figure 4a
Correlation of degraded area (change after 100 hours at 50°C, 90/RH) with an ion momentum parameter for Al_2O_3 and ZrO_2 overlayers. (All films included.)

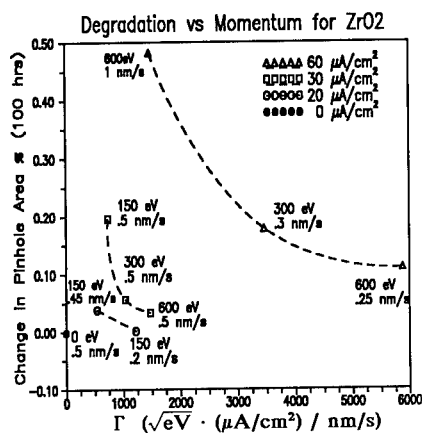


figure 4b

known to greatly enhance pitting corrosion in iron and steels[9]. The second film ($T = 671$) was the first run after several depositions of MgF_2 were made in the system for another project. We hypothesize that residual fluorine contaminated this film and was responsible for the anomalously high degradation. Two additional samples were made with the same deposition parameters as this second "bad" sample except that both the ion pre-cleaning and the iron deposition were performed with the same ion assistance that was used for their Al_2O_3 overlayers (500eV, $15\mu A/cm^2$). These films (indicated by open circles on the plot) fell within the trend of the of the non-IAD iron films for their given overlayers.

The ZrO_2 overlayers presented a much more complicated system. A simple plot of the change in degraded area after 100 hours versus the momentum parameter (disregarding all other parameters) yielded considerable initial disappointment. Closer inspection of the data, however, revealed that the absolute ion flux (as opposed to a flux ratio) appeared to classify the samples into distinct and consistent groupings (figure 4b). Within each grouping, the degradation decreased with increasing momentum bombardment parameter. In two groups ($20\mu A/cm^2$ and $60\mu A/cm^2$), the increase in momentum parameter was mostly due to a decreased deposition rate. In another group ($30\mu A/cm^2$), the increase in momentum parameter was strictly due to increased ion energy. Analysis of the ZrO_2 overlayers is currently underway to determine if these results can be correlated to changes in their microstructure.

All but three of the ZrO_2 overlayers exhibited some minor tensile stress failure at the edges of the substrate after time. Visual inspection (in transmission) of the films which exhibited this stress failure also showed significant amounts of pitting under the gold coated area. The amount of pinholing was greater than in the area which was not covered by gold (from which the pinhole data was derived). This is probably the result of gold atoms migrating into defects in the overlayer or regions of locally high tensile stress, electrically contacting the iron layer, and forming a microscopic galvanic cell. The iron at such contacts would be anodic with respect to the gold and rapidly attacked. The three ZrO_2 sample which had a negligible amount of flaking at the substrate edges did not have observable pinholing under the gold coated area. These three were deposited at ($20\mu A/cm^2$, 150eV, 0.2nm/s), ($60\mu A/cm^2$, 600eV, 0.25nm/s), and ($60\mu A/cm^2$, 600eV, 1.0nm/s) and can be located in figure 4b. None of the Al_2O_3 overlayers had any flaking around the edges or visually observable pinholing under the gold coated area.

At present, we have not yet attempted to repeat the degradation results. Since each of the data points represents only a single film, there is little proof of repeatability. Without definite information regarding possible correlations between the deposition parameters and the microstructure of these overlayers (crystalline or amorphous, grain size and orientation), it would be premature to make definite claims. Rather, a number of avenues for further research are suggested. First and foremost is the need to finish the microstructural characterization work currently underway to determine if ion flux or pinhole degradation can be directly correlated to the microstructure. Repetition of at least some of these samples is also in order. Extending the range and combinations of deposition parameters sampled, if this systematic behavior is confirmed, would also be desirable.

One hypothesis is that the ion flux is competing with some other process which is relatively constant for all of these ZrO_2 films. A likely candidate is the adsorption of a residual gas such as water vapor. Such behavior would not be without precedent. Recently, it has been shown that IAD[9] and residual gas partial pressures[10] can control the preferred orientation and grain size of evaporated films. If the microstructural characterization supports this premise, then perhaps studies relating water partial pressure and ion flux to resulting microstructure are in order.

Conclusions

We have found that argon IAD of Al_2O_3 overlayers reduced pinhole degradation of thin iron films placed in a warm, humid environment. Densification of the amorphous overlayer is thought to be the mechanism responsible for the improved performance. An ion momentum parameter was found to be suitable for correlating the IAD process parameters to the improved performance.

Argon IAD of ZrO_2 overlayers produced mixed and complex results. Ion flux appeared to be an important factor, along with the momentum parameter, in determining performance of the overlayer. More research is needed to confirm and explain these results.

Fluorine (and/or chlorine) contamination was found to be particularly damaging and must be avoided at all costs. Ion sputter-cleaning the substrates prior to deposition was found to markedly reduce pitting corrosion.

Iron films protected by the best of samples of either Al_2O_3 or ZrO_2 did not suffer from any measurable pinhole degradation after approximately 100 hours at 50°C , 90% relative humidity.

Acknowledgements

This work was sponsored by the Optical Data Storage Center at the University of Arizona Optical Sciences Center. We would also like to thank H. Angus Macleod and Shahida Rana of the Optical Sciences Center for use of their humidity chamber.

References

- (1) J.M.E. Harper, J.J. Cuomo, R.J. Gambino, and H.R. Kaufman, Ion Bombardment Modification of Surfaces, edited by O. Auciello, and R. Kelly (Elsevier, Amsterdam 1984).
- (2) P.J. Martin, J. Mat. Sci. **21**, 1 (1986).
- (3) U.J. Gibson, Physics of Thin Films, vol. 13, edited by M.H. Francombe and J.L. Vossen (Academic Press, San Diego, 1987), pp. 109-150.
- (4) W.G. Sainty, R.P. Netterfield, P.J. Martin, Applied Optics **23**, 1116 (1984).
- (5) K.D. Cornett, U.J. Gibson, Rev. Sci. Instrum. **59**, 1341 (1988).
- (6) J.D. Targove, L.J. Lingg, J.P. Lehan, H.A. Macleod, Applied Optics **27**, 1988 (1988).
- (7) C.K. Hwangbo, L.J. Lingg, et al, Applied Optics (accepted for publication).
- (8) Ralls, Courtney, Wulff, An Introduction to Material Science and Engineering, (Wiley, New York, 1976), pp. 288-292.
- (9) L.J. Lingg, C.K. Hwangbo, et al, Technical Digest of the Topical Meeting on Optical Interference Coatings, Tucson, AZ, 1988, ThB10, (Optical Society of America, 1988).
- (10) Himel, M. D., Microstructure effects on light propagation in zinc sulfide thin film waveguides, (Ph.D. Dissertation, University of Arizona 1988), pp. 107-115.

THERMAL ANNEALING INVESTIGATION OF THE OPTICAL PROPERTIES OF $\text{Si}_{1-x}\text{N}_x$ FILMS FABRICATED BY ION BEAM ASSISTED DEPOSITION

E.P. Donovan, C.A. Carosella, D. Van Vechten*
Naval Research Laboratory, Code 4671, Washington, DC 20375-5000
*Sachs-Freeman Associate at NRL

ABSTRACT

The annealing behavior of the optical properties of silicon nitride films ($\text{Si}_{1-x}\text{N}_x$) is described for films fabricated by ion beam assisted deposition. The data are needed for the precise manufacture of optical filters, where the index of refraction must be predicted from deposition parameters and film annealing history.

The reflection of homogeneous, amorphous samples deposited on (100) silicon substrates was measured from 500 to 3120 nm. Fits to the interference spectra were obtained over the range 1000 to 3120 nm to obtain the index of refraction vs wavelength as a function of film nitrogen content. Nitrogen atom fraction was varied from .2 to .58 by variation of the incident relative fluxes of nitrogen ion beam current to evaporant silicon flux. The films were annealed in argon at 450 C, 600 C, 750 C, and 1100 C and the measurements repeated. The systematic shifts in index of refraction with annealing temperature are described.

INTRODUCTION

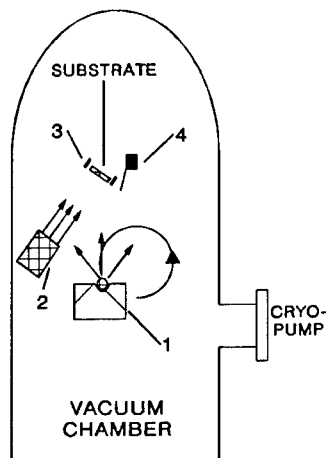
The relaxation of simple covalent amorphous systems fabricated by ion beam techniques has been a subject of great interest in recent years [1-4]. Infrared reflection measurements, for example, have been used to correlate the heat of relaxation of ion implantation amorphized germanium layers with changes in the index of refraction upon temperature ramp annealing [4]. Among ion beam fabrication techniques, ion beam assisted deposition is of increasing importance [5]. Ion beam nitrogen and evaporant silicon deposition is useful for the fabrication of complex inhomogeneous infrared optical filters [6], but the performance changes upon annealing due to refractive index changes have not been well understood. Therefore, the purpose of this work is to measure the index of refraction changes which occur in homogeneous silicon nitride films which span the composition range needed for the filter fabrication, as a function of annealing temperature.

EXPERIMENTAL

A schematic of the ion beam assisted deposition system used to fabricate the films is shown in Figure 1. Base pressure of the chamber is 2×10^{-7} Torr and operating pressure with the nitrogen feed gas in the chamber is 2×10^{-4} Torr. Silicon (100) substrates were polished on one side and roughened on the back with silicon carbide grit, then cleaned with ethanol prior to insertion in the vacuum chamber. The substrates were sputter cleaned in situ prior to deposition. The substrate was mounted directly over the 40 cc hearth electron beam evaporation source, at an angle of 20° to the evaporant stream. The substrate surface normal points directly at the center of the extraction grids of a 3 cm Kaufman ion source, which is normally operated at 500 eV. Three apertures for the voltage suppressed Faraday cups are mounted symmetrically about the substrate to measure the charged fraction of the energetic particle beam, normally 0.0-0.35 mA/cm².

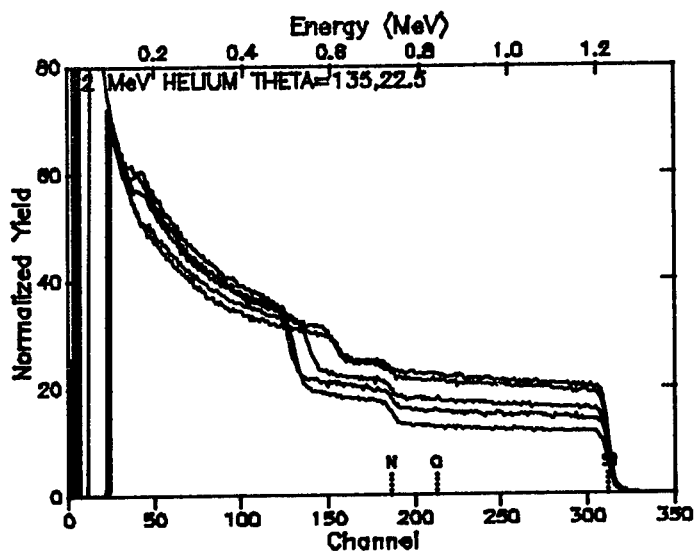
Figure 1. Schematic diagram of ion beam assisted deposition (IBAD) system, with ion beam normal to substrate surface.

- (1) Electron beam evaporator with silicon charge
- (2) Kaufman ion source with nitrogen feed gas, dual collimated extraction grids.
- (3) Faraday cups with secondary electron suppression.
- (4) Quartz crystal evaporation monitor, shielded from the ion beam.



A unique double gimbal arrangement was designed to allow the ion source to be aimed with the rotation axes centered on the extraction grids, using an x-y translator attached by bellows to the chamber. The beam spatial profile can then be aimed and centered on the cups in situ to reduce the

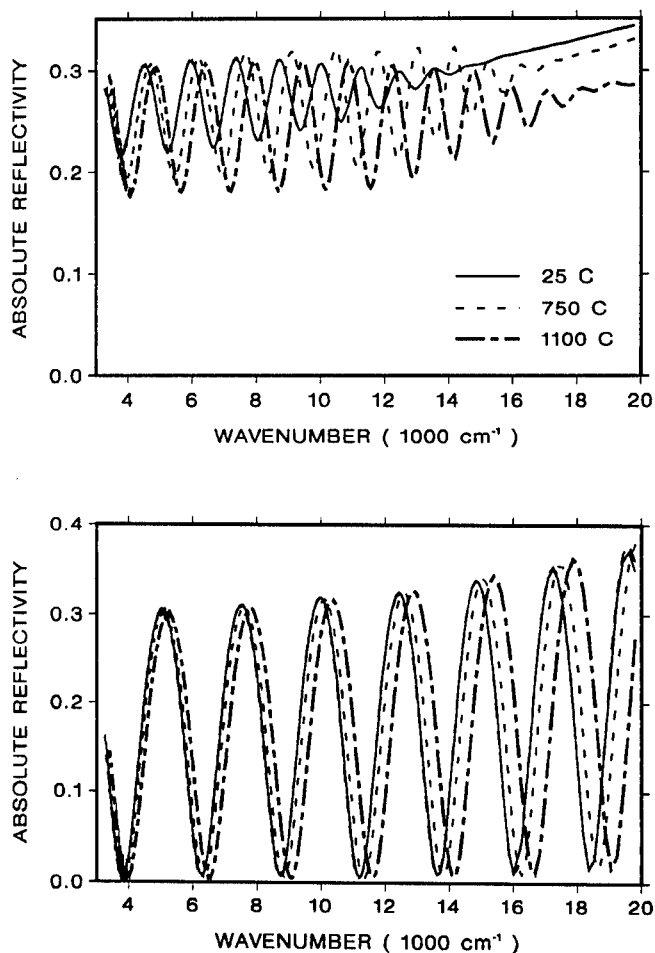
Figure 2. Rutherford backscattering spectroscopy of as-deposited IBAD silicon nitride films.



problem of small shifts in the ion optics due to thermal cycling. This has been found to greatly reduce the variation of composition in films of the same ratio of ion current flux to evaporant flux, which are fabricated on different days [7]. The evaporant flux, normally 0.5-1 nm/s, is measured by a quartz crystal oscillator mounted in the plane of the substrate 4.3 cm from it and shielded from the energetic particle beam.

Rutherford backscattering spectroscopy (RBS) measurements were performed on the films with 2 MeV $^4\text{He}^+$ ions [8] (Figure 2) and the compositions extracted with the help of the Cornell University program [9].

Figure 3. Absolute reflection vs wave number for as-deposited and as-annealed films: a) (above) $\text{Si}_{(73)}\text{N}_{(27)}$; b) (below) $\text{Si}_{(42)}\text{N}_{(58)}$



Infrared reflection spectra were taken over the range 500 nm to 3125 nm relative to the reflection of an aluminum mirror, the spectra were then corrected for the aluminum reflection before analysis. The back-roughening procedure prevented complications to the analysis of the interference fringes caused by reflections from the back interface. The samples were then annealed and the measurements repeated after each anneal. The anneals were performed in a furnace under flowing argon, 1 hr. at 450 C, 2 hr. at 600 C, 1 hr. at 750 C, and 1 hr. at 1100 C. After the latter two anneals, a short etch was performed with hydrofluoric acid to remove any oxide. When annealed at 1200 C, some samples showed crystallization of silicon nitride in the spherulitic morphology [10,11]. As only one anneal was performed at each temperature, it was not determined if the relaxations were complete. Some representative spectra are shown in Figure 3.

The absolute reflection spectra were fit using a multiple interference code [12]. The dispersion relation for the index of refraction of the films was assumed to follow a form of the Sellmeier equation [13]:

$$n^2 = (C_1 * [C_2 + 1. / (1. - v^2 / C_3^2)])$$

where v is the wave number in cm^{-1} . Each spectrum was fit over the range 1000 - 3125 nm ($10000 - 3200 \text{ cm}^{-1}$) using C_1 , C_2 , C_3 , and the film thickness D as fit parameters. Some fits were extended to higher wave numbers using an assumed form of the extinction coefficient k as follows:

$$\ln(k) = C_4 + C_5 * \ln(v)$$

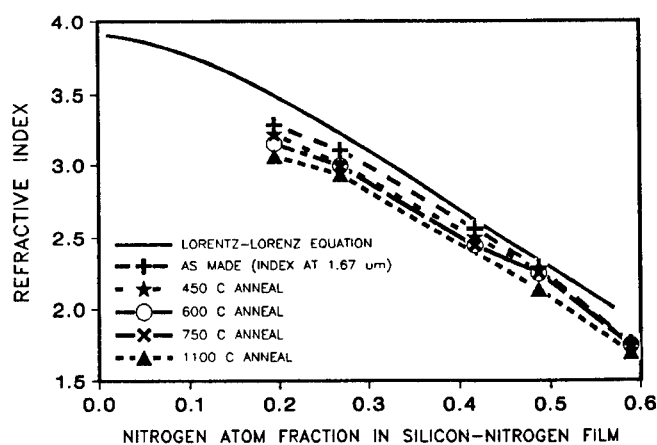
RBS measurements were not repeated after the anneals.

RESULTS

The RBS data are shown in Figure 2. There were charge collection problems, so a correction factor was applied to each spectrum so that the low channel regions overlapped. The energy of backscattering particles from surface silicon, nitrogen, and oxygen are indicated. In all cases the surface oxygen content was below the detection limit of RBS in this geometry. Each spectrum was simulated by a homogeneous layer of silicon and nitrogen on the substrate silicon to obtain the composition. Nitrogen atom fractions obtained from the data are listed in Table I.

The absolute reflectivity for two films is shown in Figure 3. For clarity, only some of the annealed spectra are shown. For the lower nitrogen content film (Figure 3a), the amplitude of the oscillation clearly grows with annealing temperature, as the index of the film decreases farther from the substrate silicon index. The absorption above 10000 cm^{-1} also decreases, as evidenced by the increase of the amplitude of the decaying oscillation. The amplitude decrease in that range for the 1100 C anneal may also show some decrease from interference from another layer, possibly due to crystal growth at the interface or incomplete removal of the surface oxide. The behavior is still under investigation. The behavior of an approximately stoichiometric Si_3N_4 film is illustrated in Figure 3b. There is very little absorption in the film for all the spectra. The index drops only slightly at the highest temperature anneals. The index at 6000 cm^{-1} (1667 nm) was calculated from the Sellmeier fit parameters and the results plotted in Figure 4 and listed in Table I. This wavelength was chosen arbitrarily to compare with previous results. The trend is not quite regular, but clearly the index drops as the annealing temperature increases.

Fig. 4. Refractive index at 6000 cm^{-1} vs. nitrogen atom fraction in as-deposited and annealed films. The line is calculated using the Lorentz-Lorenz equation with literature values for the indices of pure amorphous silicon and of silicon nitride.



DISCUSSION

The solid line of Figure 4 is a calculation based on the Lorentz-Lorenz equation [13],

$$a = (3/4\pi) (M/A_V/\rho) * (n^2 - 1)/(n^2 + 2)$$

where a is the polarizability, A_V is Avagadro's number, M is the molecular weight, and ρ the density in gm/cm^3 , and n is the index. Literature values for the density and index of amorphous silicon [3] and of silicon nitride [14] were used to calculate an average polarizability in the pure materials, linear extrapolations in the density and mass were employed. The polarizability was calculated with the assumption that all nitrogen atoms bond in Si_3N_4 regions and the remaining silicon atoms bond in amorphous silicon regions. The calculation is inconsistent with the measured data, since the film index for the stoichiometric composition is smaller than the literature value. Reasons for this discrepancy are under investigation. Measurements of the hydrogen content and more sensitive measurements of the oxygen content, and of density in the films are planned.

Table I: Index of films at 6000 cm^{-1} vs composition for several anneals

x_N	25 C	450 C	600 C	750 C	1100 C
.2	3.28	3.22	3.15		3.06
.27	3.10	3.00	2.99	2.99	2.93
.42	2.56	2.5	2.44		
.49	2.29	2.26	2.24	2.24	2.13
.58	1.76	1.76	1.75	1.75	1.72

SUMMARY

The near infrared index of refraction of silicon nitride films decreases upon annealing at temperatures up to 1100 C, in the nitrogen atom fraction range 0.2 to 0.58. The change is probably caused by structural relaxation in the amorphous phase [1-4], since no evidence was found for crystallization at these temperatures in similar films [10].

REFERENCES

1. W.C. Sinke, T. Warabisako, M. Miyao, T. Tokuyama, S. Roorda, F.W. Saris, "Transient Structural Relaxation and Melting Temperature of Amorphous Silicon," *Mat. Res. Soc. Symposium Proc.* 100 1988
2. E. P. Donovan, F. Spaepen, D. Turnbull, J. M. Poate, D. C. Jacobson, "Calorimetric Studies of Crystallization and Relaxation of Amorphous Si and Ge Prepared by Ion Implantation," *Journal of Applied Physics*, 57, 1795-1804 (1985)
3. G. K. Hubler, E. P. Donovan, K-W Wang, W. G. Spitzer, "Thermal Annealing Behavior of Hydrogen-Free Amorphous Silicon and Germanium," *S.P.I.E.*, 530 222 (1985)
4. E. P. Donovan, G. K. Hubler, C. N. Waddell, "Correlation of Optical Changes in Amorphous Ge with Enthalpy of Relaxation," *Nuclear Instruments and Methods in Physics Research B* 19/20 983 (1987)
5. S.M. Rossmagel, and J.J. Cuomo "Ion-Beam-Assisted Deposition and Synthesis" *Mat. Res. Soc. Bull.* 12 (1987) 40
6. E.P. Donovan, D. Van Vechten, A.D.F. Kahn, C.A. Carosella, G.K. Hubler, "Si_(1-x)N_x Near Infrared Rugate Filter Fabrication by Ion Beam Assisted Deposition," *Applied Optics*, in press
7. D. Van Vechten, G.K. Hubler, E.P. Donovan, "Summary Abstract: Factors Important to Achieving Compositional Control and Reproducibility in a Reactive Ion Beam Assisted Deposition Process," *J. Vacuum Science and Technology* A6 1934 (1988)
8. W.K. Chu, J.M. Mayer, and M. Nicolet, *Backscattering Spectroscopy*, Academic Press, New York (1978)
9. L.R. Doolittle "Algorithms for the Rapid Simulation of Rutherford Backscattering Spectra" *Nucl. Instr. and Methods* B9 (1985) 344
10. K.S. Grabowski, A.D.F. Kahn, E.P. Donovan, C.A. Carosella. "Thermal Stability of Silicon Nitride Coatings Produced by Ion Assisted Deposition," *Nuclear Instruments and Methods in Physics Research B*, in press
11. H.D. Keith and F.J. Padden "A Phenomenological Theory of Spherulitic Crystallization" *J. Appl. Phys.* 34 (1963) 2409
12. O. Heavens, *Optical Properties of Thin Solid Films* Dover Publications, New York, NY (1965)
13. E. Hecht, and A. Zajak *Optics* Addison Wesley, Reading, MA (1979)
14. J.T. Milek, *Silicon Nitride for Microelectronic Applications, Part 1. Preparation and Properties* Handbook of Electronic Materials, 3 p. 54 (1971) (IFI-Plenum, New York)

PASSIVATION OF GaAs LASER MIRRORS BY ION-BEAM DEPOSITED Al_2O_3

D.J. WEBB, H.-P. DIETRICH, F. GFELLER, A. MOSER, AND P. VETTIGER
IBM Research Division, Zurich Research Laboratory, 8803 Rüschlikon, Switzerland

ABSTRACT

The use of ion-beam sputtered Al_2O_3 to passivate the mirrors of semiconductor injection lasers is described. Dense films, which offer considerable protection against corrosion, can be deposited without damage to the crystal surface. The overall quality of the passivation is demonstrated by long-term stress testing of the lasers.

INTRODUCTION

The mirrors of semiconductor injection lasers [1] are usually made by cleaving the crystal on which the laser structures are fabricated. The cleaved crystal facets have a reflectivity of about 30% and initially have excellent characteristics. Such mirrors however will degrade during operation of the laser unless they are protected. Degradation occurs not only through oxidation [2] but also through non-radiative recombination at surface states [3]. This recombination can deposit a large amount of energy into the crystal. This energy causes heating which at high optical power may destroy the mirror (catastrophic optical mirror damage or COMD). At lower powers this can accelerate degradation through either corrosion or by recombination-enhanced defect reactions [4].

Laser mirrors are usually passivated by coating them with an inert, transparent, electrically insulating material. It is important that this material be compact and that the semiconductor/coating interface have as low a recombination velocity as possible. Various materials and deposition methods have been investigated (see for example [5] for a review) and Al_2O_3 has gained general acceptance. Ion-beam sputter deposition has been shown to be an excellent method of producing optical coatings [6]; however, little has been published on its use for laser passivation. This paper investigates not only the optical quality of Al_2O_3 deposited by this method, but also the electrical quality of the coating/substrate interface.

DEPOSITION SYSTEM, PROCESS AND FILM PROPERTIES

The ion-beam deposition equipment is shown in Figure 1. A Kaufmann-type 3-cm-diameter ion-source emits a beam of Ar ions in the energy range 300-1000 eV. This sputters material from an Al_2O_3 target onto the sample.

Oxygen is bled into the system during deposition, the partial pressure being 2×10^{-5} mbar. Laser bars are clamped into a holder, p-contact to n-contact, and deposition takes place at a slight angle to the facet normal to avoid shadowing. The films are deposited at room temperature without additional ion bombardment.

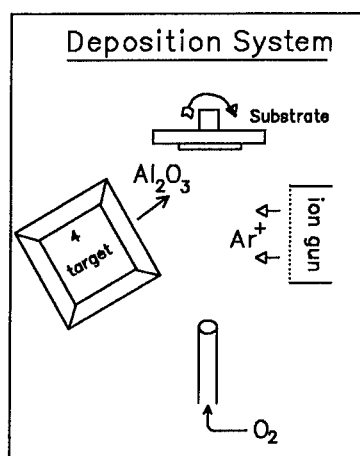
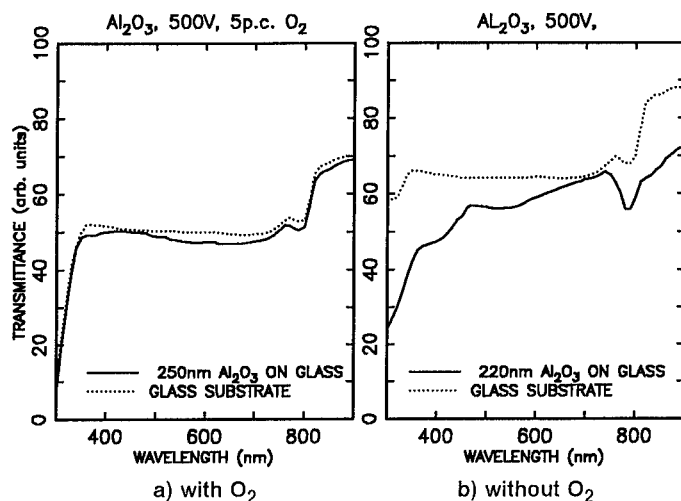


Figure 1. Ion-beam deposition system

The pressure in the system before deposition is about 5×10^{-8} mbar and during deposition it is 4×10^{-4} mbar.

Figure 2 shows the optical transmittance of films of Al_2O_3 deposited on glass substrates, compared with the transmittance of the substrates alone. The transmittance is much lower, i.e., the absorption is much higher, for the film deposited without O_2 . The refractive index of this film is higher (1.92) than for bulk Al_2O_3 , indicating that it is probably metal-rich. After accounting for optical interference, the absorption of the film deposited with O_2 is estimated to be less than 0.5%, which is of the order of our measurement precision.

Figure 2. Optical absorption of Al_2O_3 films

The lasers used in this study are single-quantum-well, graded-index, separate-confinement heterostructure (SQW-GRINSCH). Lateral optical and current confinement is provided by an etched ridge [7].

FILM PROPERTIES AS CORROSION BARRIER

In ion-beam sputter deposition, the sputtered alumina molecules have a relatively high energy so that the growing film is compacted [6]. The compactness of these films as a function of Ar ion energy has been examined. Table I shows some properties of the films as a function of beam voltage. The refractive indices are measured at 633 nm and the stresses are all compressive.

Table I. Properties of Al_2O_3 films

sputter voltage	refractive index	etch rate nm sec^{-1}	stress dynes cm^{-2}	depos. rate nm/mA/min
300	1.70-1.71	1.25 ± 0.02	4 ± 2	0.071
500	1.66-1.70	1.28 ± 0.03	5 ± 2	0.117
1000	1.66-1.69	1.22 ± 0.02	3 ± 2	0.118

The etch is $\text{HF}/\text{HNO}_3/\text{H}_2\text{O}$ (18/15/455). Little change either in stress, refractive index or etch rate is observed as the Ar ion energy is increased from 300 to 1000 eV. In addition to these tests, lasers were coated on both mirrors using beam voltages of 300, 500 and 800 V. The lasers were then soaked (but not operated) in deionised water at 85°C and removed at intervals for measurement of their threshold current (I_{th}) or differential efficiency (η_{D}). Figure 3 shows the change of I_{th} with soak time, where any change is a sign of degradation.

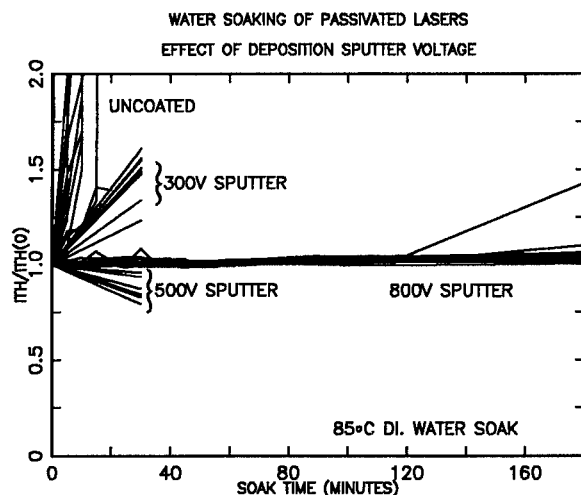


Figure 3. Resistance to hot water of $\lambda/2$ Al_2O_3 films.

It is seen that a strong correlation exists between degradation rate and ion-beam voltage. Uncoated lasers degrade very rapidly through the growth of an oxide film on the surface (about 100 nm in 15 min). This oxide film is rough, and a combination of scattering and interference effects causes deterioration of the laser properties. Degradation is slowed down in films sputtered at 500 V or less. However it is almost entirely eliminated for soaking times of up to 3 hours by Al_2O_3 sputtered at 800 eV. The coating shows only very slight signs of surface roughening and its refractive index decreases by only 4% during the soak. Thus films sputtered at 800 V or more are effective corrosion barriers, and much less permeable compared with films sputtered at lower voltages.

INTERFACE PROPERTIES

In this section the question of sputter damage of the semiconductor surface either by sputter precleaning or by energetic bombardment during the initial stages of the film growth is studied. Preliminary measurements of sub-threshold laser-diode I-V characteristics showed increased leakage currents when 100 eV Ar ion-sputter cleaning was done before deposition. The deposition alone caused very little additional leakage currents. C-V measurements of MOS capacitors using the mirror passivation as the dielectric also showed strong evidence of damage when the 100-V preclean was done. From these initial experiments, it was concluded that the deposition process itself causes very little damage to the semiconductor surface, although the surface quality is far from that obtained with Si/SiO₂. However, injudicious sputter cleaning does cause very obvious damage. Consequently all laser-coating runs have been made without a preclean.

A very useful practical measure of the interface quality can be obtained from a measurement of the COMD power. Kappeler *et al.* [8] have modelled the COMD power as a function of pulse length. They find that the COMD-power limit for a given laser structure is a sensitive function of the surface recombination velocity at the laser mirrors. Figure 4 shows measurements of the COMD-power ratio of coated to uncoated mirrors for the coatings deposited at 300, 500 and 800 eV. It is first of all evident that each coating improves the COMD threshold by up to a factor of two, independent of the sputter voltage used. Qualitatively the results are consistent with a decrease of surface recombination velocity. Some of this improvement may possibly be due to the thermal mass of the coating. It is however evident that these coating processes significantly improve the laser characteristics. This measurement of COMD threshold provides not only information about the quality of the semiconductor surface, but is also a useful operational parameter in its own right.

With pulse lengths of 100 ns, the maximum output power of these lasers is of the order of 0.5 to 0.8 W, exiting from an area of the laser mirror about 4 μm by 1.0 μm . The average power density is therefore of the order of 12.5 to 20 MW cm^{-2} . The peak electric field in the semiconductor at this power is within a factor of 2 of the DC breakdown strength of GaAs. However, the pulsed damage threshold of alumina films on fused silica [9] is about 1600 MW cm^{-2} . Therefore, breakdown of the passivation film should not be a limiting factor in laser power output.

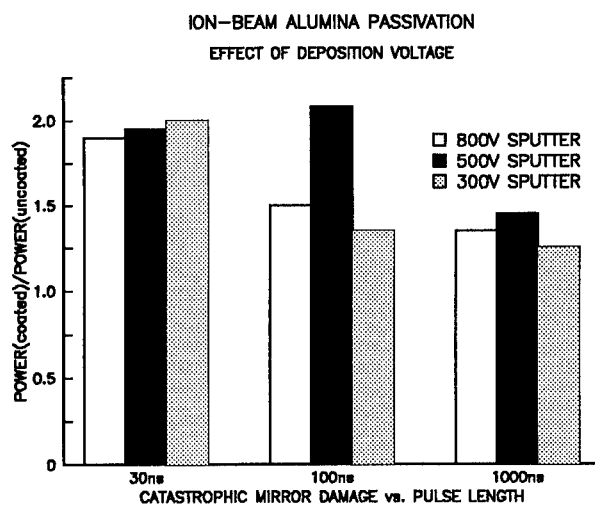


Figure 4. COMD improvement by Al_2O_3 $\lambda/2$ films

LONG-TERM STRESS TESTS

Long-term laser stress testing is necessary to finally determine the efficacy of a mirror passivation process. Accordingly, laser bars were coated on both facets with $\lambda/2$ films of Al_2O_3 , and stressed at constant output power, in an air ambient for up to 2500 hours in some cases. The effect of output power and case temperature on the long-term degradation rate was studied. Uncoated lasers were simultaneously studied for comparison. Some of the results are shown in Figure 5.

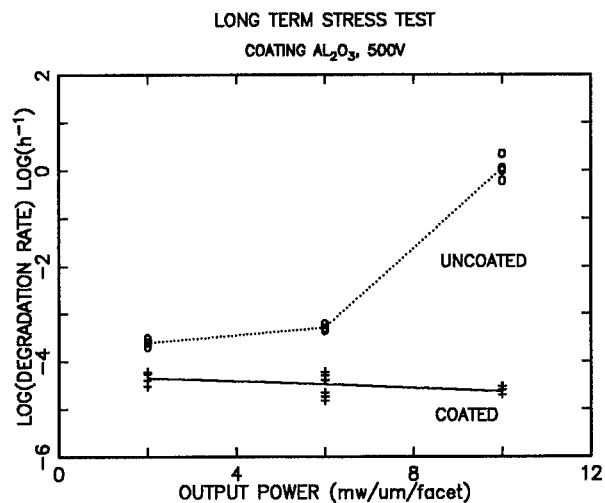


Figure 5. Long-term stress tests of passivated lasers

Here, the degradation rate is the linearized rate of increase of drive current, over stress time, needed to maintain a constant output power. The degradation rate of uncoated lasers is shown to be very power dependent and very rapid at high powers. The degradation rate of the coated lasers is found to be essentially independent of output power and is very much reduced compared to uncoated lasers. This degradation rate is respectable at low powers, but it is a very good value for high-power operation. However the coatings for these life tests were sputtered at 500 eV because problems with the ion-source did not allow the use of higher voltages. Peek [10] has shown a definite correlation between coating porosity and degradation rate, and based on the water-soaking experiments described above it is expected that even better results should be obtained with films sputtered at up to 800 V or more.

CONCLUSION

Ion-beam sputtered Al_2O_3 films have been shown to passivate the mirrors of semiconductor lasers very effectively. When sputtered at 800 V or more, they are excellent corrosion barriers. COMD threshold power is raised indicating a good passivation/semiconductor interface, and degradation rates under long-term stress at high powers are low.

ACKNOWLEDGEMENTS

The authors would like to thank K. Dätwyler, U. Deutsch, H. Richard and G. Sasso for the fabrication of the lasers, H.P. Ott for expert mechanical engineering, H.P. Meier for the epitaxial growth, and C. Harder for very helpful discussions. We would also like to thank the IBM Corporation for facilitating this work and for permission to publish the results.

REFERENCES

1. G.H.B. Thompson, The Physics of Semiconductor Lasers, (John Wiley & Sons, New York, 1980).
2. T. Yuasa, K. Endo, T. Torikai, H. Yonezu, *Appl. Phys. Lett.*, **34** (10), 685 (1979).
3. C.H. Henry, P.M. Petroff, R.A. Logan, F.R. Meritt, *J. Appl. Phys.*, **50** (5), 3721 (1979).
4. L.C. Kimmerling, *Solid-State Electronics*, **21** 1391 (1978).
5. M. Fukuda, *IEEE J. Quantum Electron.*, **QE-19** (11), 1692 (1983).
6. M. Varasi, C. Misiano, L. Lasaponara, *Thin Solid Films*, **117**, 163 (1984).
7. C. Harder, P. Buchmann, H. Meier, *Electron. Lett.* **22** (20), 1081 (1981).
8. F. Kappeler, K. Mettler, K.-H. Zschauer, *IEE Proc.*, **129**, Pt. 1, No. 6, 256 (1982).
9. T.W. Walker, A.H. Guenther, P.E. Nielsen, *IEEE J. Quantum Electron.*, **QE-17** (10) 2041 (1981).
10. J.A.F. Peek, *IEEE J. Quantum Electron.*, **QE-17** (5), 781 (1981).

EVALUATION OF MULTILAYERS FOR SOFT X-RAY FABRICATED BY ION BEAM SPUTTERING.

I.KATAOKA, I.YAMADA, K.ETO and K.ITO

Japan Aviation Electronics Industry, Limited, Akishima Plant, 1-1
Musashino 3-chome, Akishima-shi, Tokyo 196 Japan.

ABSTRACT

Multilayer structures of Li_2O and Ni were deposited onto polished fused quartz by the dual ion beam sputtering method. Optical and physical properties of the multilayer structure were evaluated. Reflectivity of multilayer mirrors at an incident angle of 79.6 deg. was 17% for 44Å (C-K line). There was good agreement with the calculated value considering the interface roughness and residual oxygen contamination in the Ni layer from the background of Li_2O deposition.

INTRODUCTION

It is well known that the protein of the cell can be observed without absorption of water by X-rays of wavelengths from 23.3Å to 44Å; because in the above mentioned wavelength region, the absorption coefficient of carbon for X-rays is bigger by about ten times than that of oxygen[1]. A number of studies on soft X-ray optics for biological use have been made, and we are also investigating these optics and materials for reflective layers. Furthermore we have been paying attention to the characteristic feature of this field, namely, a wide selection of materials for multilayers is available because the problem of X-ray durability is thought to be small in the biological field. Then we can select the materials mainly with a view of getting high reflectivity without considering X-ray durability.

In the previous paper[2], we proposed that the use oxides or hydrides for space layers gives very high reflectivity in this wavelength region. In this paper we prepare multilayer structures of $\text{Li}_2\text{O}/\text{Ni}$ by the dual ion beam sputtering method and evaluate the optical and physical properties.

CALCULATION OF REFLECTIVITY

In order to select a combination of materials, we calculated peak reflectivity of the multilayers with many material combinations in the wavelength region from 10Å to 50Å, which includes the region of interest for biological microscopic studies. In Figure 1 we show the spectral dependence of the calculated reflectivity of multilayer mirrors. Peak reflectivity is obtained for 199 layers with the incident angle $\theta = 70$ deg. when the thickness of each layer is optimized at each wavelength. We determined the thickness by the method of linking the reflectivity line for each material to the point where an overall smooth curve is made on the complex plane[2]. The reflectivity was calculated by solving the asymptotic equation, using Fresnel's coefficient. The index of materials used for the calculation were taken from Henke's f data book[3].

Space layers should be made of a material with index close to unity and an absorption coefficient as small as possible. Figure 1 shows the calculated results using Li, LiH, Li_2O and Be

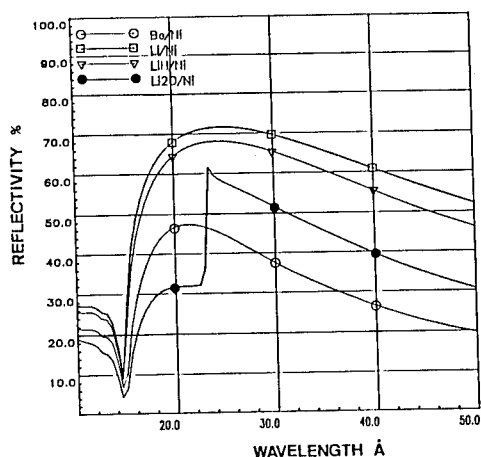


Figure 1. The dependence of calculated reflectivity of multilayer mirrors on wavelength for Be/Ni, Li₂O/Ni, LiH/Ni and Li/Ni at the incident angle $\theta = 70$ deg. The number of layers is 199.

as space layers, and Ni as the heavy layer. Be is the most popular material for space layers in this wavelength region. From figure 1, the reflectivity of Li₂O/Ni is 1.3 times as high as that of Be/Ni, LiH/Ni 1.5 times and Li/Ni 1.6 times, respectively.

FABRICATION OF MULTILAYERS

As mentioned above, multilayers which are constructed with Li or its hydride, or oxide for space layers can be expected to be of high reflectivity. However, the thin films of these materials fabricated by conventional ways are said to be unstable. But, in the case of lithium oxide, we could prepare more stable thin films by the dual ion beam sputtering method with adequate oxygen ion assistance. (Dual ion beam sputtering method is known to be able to produce high density and smooth layers, especially in optical coatings, to make high quality multilayers[4])

Figure 2 shows a schematic diagram of a dual ion beam sputtering system used to fabricate multilayers. It has two Kaufman-type ion sources; one is for the sputtering of the target, and the other is for ion assistance. The targets were cooled by water. The film thickness was controlled by the quartz thickness monitor. The chamber can be pumped out to 1×10^{-6} Pa.

Multilayers evaluated in this paper were fabricated under the conditions below: The growth rate was about $0.7 \text{ \AA}/\text{sec}$ for Ni and $0.05 \text{ \AA}/\text{sec}$ for Li₂O, the arrival rate of oxygen ions was about 2.5 times that of the incident atoms on the substrate during Li₂O growth; and the rate of argon ions was 5% of the rate of incident Ni atoms. The energy of the ions was about 50 eV. Polished fused silica was used for substrates, and they were not heated intentionally.

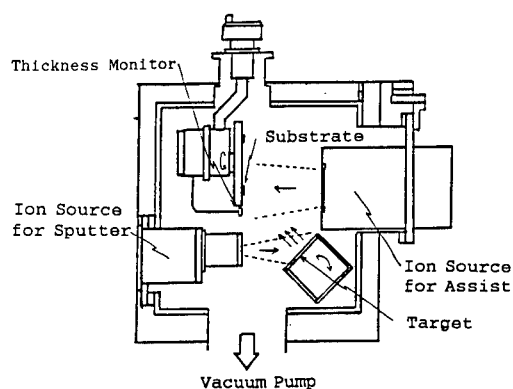


Figure 2. Schematic diagram of the dual ion beam sputtering system.

RESULTS AND DISCUSSION

Figure 3 shows the small angle X-ray (Cu-K α) diffraction curves of Li₂O/Ni multilayers fabricated by dual ion beam sputtering. From these curves, the thickness of layer pairs was calculated to be 150Å. The fact that we could observe out to 8th diffraction peak shows there is little difference in thickness between respective Li₂O and Ni layers and that the interfaces are sharp.

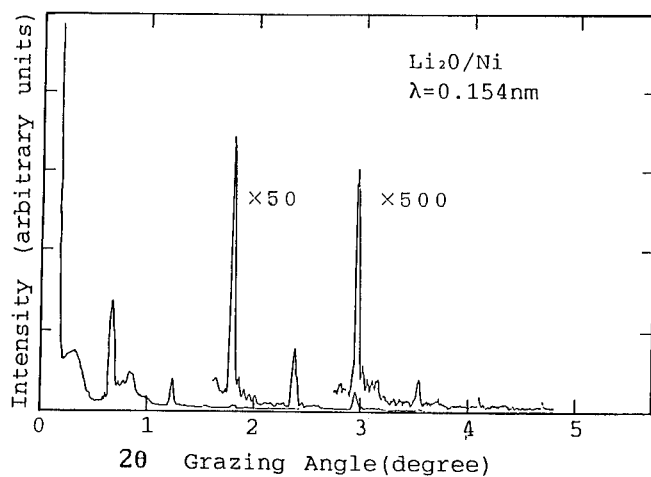


Figure 3. Small angle X-ray(Cu-K α) diffraction curves of Li₂O/Ni multilayer

However, because we used oxides for space layers, the problem of residual oxygen contamination to Ni layers during deposition should be considered. We estimated the oxygen density in the Ni layers with the Auger electron spectroscopy (AES) system. Figure 4 shows the curves of AES for the fabricated Ni layers. We estimated the oxygen content to be about 15% in that Ni layer. We also evaluated the packing density of Ni layers by means of measuring its weight with a micro-balance in an inert gas environment. From this measurement, the packing density of Ni(+NiO) can be estimated about 0.94.

Figure 5 shows the dependence of reflectivity of $\text{Li}_2\text{O}/\text{Ni}$ multilayer on the incident angle, measured by C-K line (44Å) and calculated as a function of surface roughness $\sigma = 0\text{\AA}$, 10\AA and 15\AA . The scattering intensity was estimated by Beckmann's model[5]. Although there were some problems with high incident angles, near the first peak it should be a good approximation. The packing density of each layer is considered in calculating optical constants using Henke's f data simultaneously. It can be seen that the simulation with $\sigma = 15\text{\AA}$ shows a good agreement with the experimental results near the first peak.

Figure 6 shows the calculated reflectivity of multilayer with inter-diffusion length $i = 0\text{\AA}$, 30\AA , 40\AA respectively. From these results, the effect of inter-diffusion on reduction of reflectivity can be estimated at about 2%. So it can be concluded that inter-diffusion is not the dominant cause of the reduction of reflectivity.

Therefore, the main reasons for a decrease reflectivity are thought to be roughness of interface and contamination of residual oxygen in the Ni layers from the background.

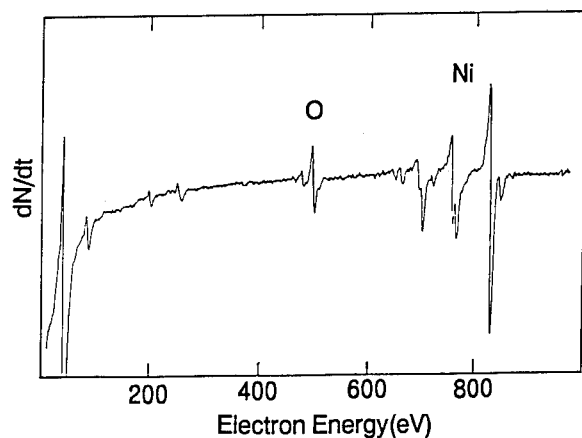


Figure 4. Auger Electron Spectrum for fabricated Ni layer

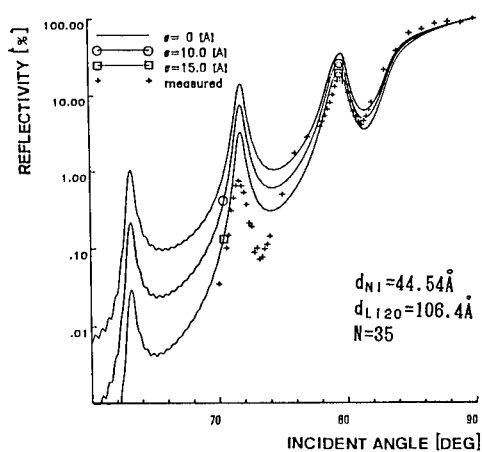


Figure 5. The dependence of reflectivity of $\text{Li}_2\text{O}/\text{Ni}$ multilayer on incident angle as function of surface roughness $\sigma = 0\text{\AA}$, 10\AA , 15\AA

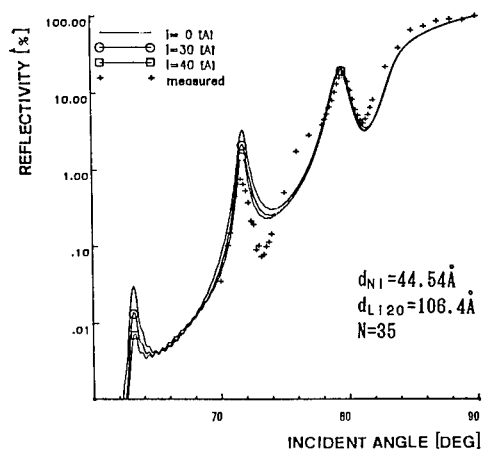


Figure 6. The dependence of reflectivity of $\text{Li}_2\text{O}/\text{Ni}$ multilayer on incident angle as a function of inter-diffusion length $l = 0\text{\AA}$, 30\AA , 40\AA . The surface roughness is 15\AA

CONCLUSION

The $\text{Li}_2\text{O}/\text{Ni}$ multilayer structure, which was expected to have high reflectivity in the wavelength region from 23.3\AA to 44\AA , was fabricated by the dual ion beam sputtering method and its optical and physical properties were evaluated. The dependence on incident angle of reflectivity was measured with X-ray(C-K) beam facilities. The peak reflectivity was 17% at an incident angle of 79.6° but ideal reflectivity of this combination was calculated to be 35.9%. The main reasons for reducing the reflectivity were thought to be interface roughness of multilayer structure and residual oxygen contamination in Ni layers from the background during Li_2O deposition.

ACKNOWLEDGMENTS

We express our thanks to Dr. H. Kunieda and co-researchers of Nagoya University for measuring the samples with the X-ray beam facility and for valuable discussions.

Present research effort is included in the National Research and Development Program on "Advanced Material Processing and Machining System" conducted under a program set by the Agency of Industrial Science and Technology, Ministry of International Trade and Industry.

REFERENCE

1. B.Niemann et al., Nucl. Inst. Meth. A246,675(1986).
2. K.Etoh, I.Kataoka and K.Ito, presented at The International Congress on Optical Science and Engineering, Hamburg, FRG, 1988(to be published)
3. B.L.Henke, AIP Proc. 75,340(1981)
4. S.E.Barnes, D.C.Gridrod, T.W.Jolly and C.J.Shaw, Proceedings of 6th International Conference of Ion & Plasma Assisted Techniques, Brighton, UK, 1987, p. 441
5. P.Beckmann and A.Spizzichino, The Scattering of E.M.Waves from Rough Surfaces, (Pergamon, New York, 1963)

HIGH DOSE IMPLANTATION OF NITROGEN AND PHOSPHOR INTO SILICA GLASS

Takashi Tagami, Keiji Oyoshi and Shuhei Tanaka
Tsukuba Research Laboratory, Nippon Sheet Glass Co., Ltd.,
5-4 Tokodai, Tsukuba City, Ibaraki, 300-26 Japan

ABSTRACT

The surface chemistry of silica glass implanted with N^+ or P^+ ions has been studied. The X-ray photoelectron spectroscopy (XPS) spectra of $N(1s)$ for silica glass implanted with N^+ shows the possibility of the formation of oxynitride glass. For the first time, the effect of the implantation of N^+ and additional Si^+ on the surface chemistry of silica glass has been studied and found to be significant in increasing the nitrogen concentration in the silica glass. The peak concentration of N increases several times, and does not change even if the sample is annealed at 900°C.

The XPS spectra of $P(2p)$ for silica glass implanted with P^+ ions shows two interactions, both P-O and P-P. Therefore, the XPS spectra shows the possibility for the formation of phosphosilicate glass using P^+ implantation into silica glass.

1. INTRODUCTION

The use of ion-implantation in many cases improves the surface properties of glass, such properties as optical quality, wearing strength and diffusion conditions can be controlled. It was reported that glass implanted with nitrogen can be applied to the production of low-loss optical wave guides[1] as well as to increasing the microhardness numbers[2]. The changes of the chemical fraction and physical properties of some glasses were also caused by network damage due to ion bombardment[3-7].

In this work, using N^+ implantation into silica glass, we try to form an oxynitride glass ($SiON$), which has an excellent chemical durability and higher hardness as compared with other glasses. It was already reported that implanted nitrogen combines with the silicon and oxygen in the glass, but experiments for increasing the SiN concentration in the glass have not been reported. So, methods to increase the SiN concentration in the glass are discussed. Using P^+ implantation into silica glass, we also discuss the formation of phosphosilicate glass (PSG).

2. EXPERIMENT

We have examined the surface chemistry of silica glass implanted with 150keV N^+ or P^+ ions to a dosage of 1×10^{17} ions/cm². Some samples were implanted with N^+ and Si^+ ions to a dose of 1×10^{17} ions/cm². These samples were annealed up to 900°C for 60 min in a N_2 atmosphere. The evaluation of the implanted silica glasses was carried out using secondary ion mass spectroscopy (SIMS) and Rutherford Backscattering (RBS) to obtain ion related profiles, and X-ray photoelectron spectroscopy (XPS) to determine the nature of the chemical

bonds. A silica glass of 1 mm thickness was used for the experiment.

3. RESULTS AND DISCUSSION

3.1 The Formation of SiON

A. Implantation with N^+ Ions

Using SIMS analysis, the depth profile of N in the silica glass implanted with 150keV N^+ ions to a dosage of 1×10^{17} ions/cm² is obtained as shown in Fig.1. The concentration of N is maximum at a depth of 330 nm, which is the same as the projection range calculated by the LSS theory. But the depth profile of N shows a trapezoidal shape. This trapezoidal shape appears at dose above 3×10^{16} ions/cm² with 150 keV N^+ ions. In order to examine whether the trapezoidal depth profile represents a real depth profile or not, we used RBS to analyze the depth profile of N.

Figure 2(a) shows RBS spectra for silica glass implanted with N^+ ions. Using Fig.2(a), the depth profiles of N, Si and O are obtained as shown in Fig.2(b). As shown in Figs.2(a) and 2(b), the depth profile of N is a trapezoidal

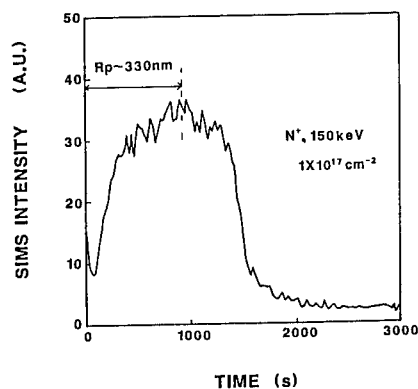


Fig.1 Depth profile of nitrogen in silica glass implanted with 150keV N^+ ions to a dose of 1×10^{17} ions/cm².

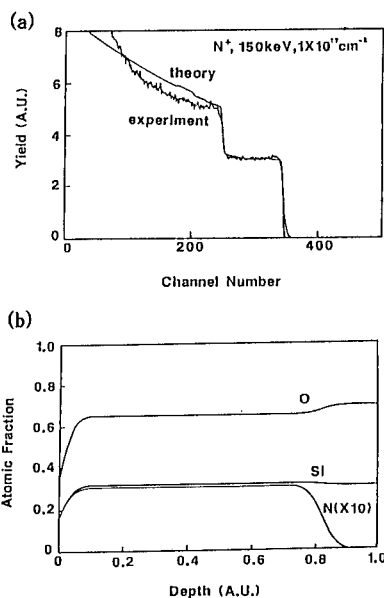


Fig.2 (a) RBS spectra for nitrogen implanted silica glass. (b) Depth profiles of N, Si and O. The Sample is the same as in Fig.1.

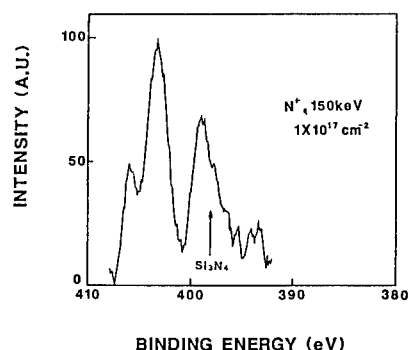


Fig.3 XPS spectra of N(1s) for nitrogen implanted silica glass at a depth of 330nm. The sample is the same as in Fig.1.

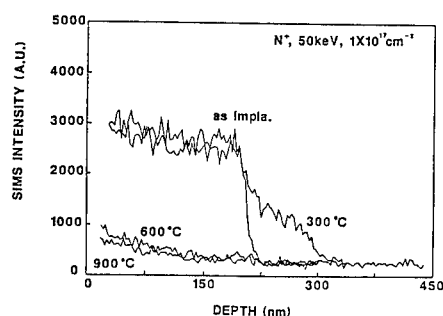


Fig.4 Depth profiles of nitrogen in the silica glass implanted with 50keV N^+ ions to a dose of 1×10^{17} ions/cm². Each sample was annealed at 300°C, 600°C and 900°C for 60 min in a N_2 atmosphere.

shape, which was confirmed by the SIMS analysis. Therefore, the depth profile of N in the silica glass has a trapezoidal shape for high dose conditions. But the peak concentration of N is only a few percent.

The XPS spectra of N(1s) for nitrogen implanted silica glass at a depth of 330 nm, which is the projection range of the N^+ ion, is shown in Fig.3. The XPS spectra of N(1s) can be roughly divided into two peaks, at 398eV and 403eV. The peak at 398eV agrees with the energy of N(1s) for Si_3N_4 . Thus, this peak indicates the interaction between Si and N. The other peak at 403eV probably indicates the interaction between N and N, or N and O. Therefore, the XPS spectra of N(1s) shows the possibility of the formation of SiON using N^+ implantation into silica glass.

Silica glasses implanted with 50keV N^+ ions to a dose of 1×10^{17} ions/cm² were annealed at 300°C, 600°C and 900°C for 60 min in a N_2 atmosphere. The sample annealed at 300°C showed a slight change in the depth profile, but the samples annealed above 600°C show a drastic decrease of nitrogen (see Fig.4). Therefore, the concentration and the stability of implanted N in the silica glass should be considered.

B. Implantation with N⁺ and Si⁺ Ions

In this experiment, 50keV N⁺ ions at a dose of 1×10^{17} ions/cm² were implanted into silica glass, and then Si⁺ ions at a dose of 1×10^{17} ions/cm² were implanted at 100keV, 150keV and 200keV. The depth profiles of N for these samples were obtained by using SIMS analysis. As shown in Fig.5, the depth profiles of N are nearly Gaussian distribution. This distribution might be caused by the mixing of nitrogen during Si⁺ implantation. The nitrogen concentration in these samples increases several times in contrast to the case of nitrogen implantation alone. Moreover, as shown in Fig.5, the nitrogen depth profiles did not change when the samples were annealed at 900°C. Thus, additional Si⁺ implantation has the effect of increasing peak nitrogen concentration and improves the nitrogen stability in the silica glass.

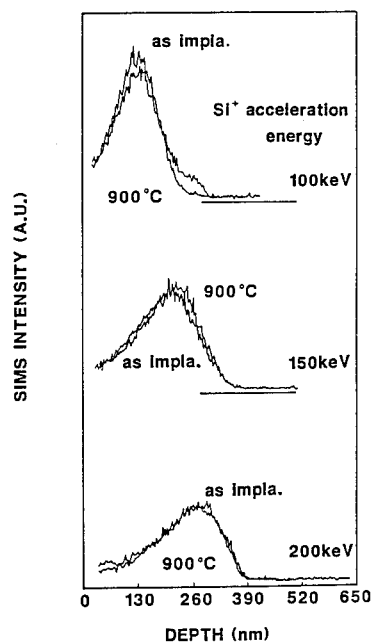


Fig.5 Depth profiles of nitrogen in the silica glass implanted with N⁺ and Si⁺ ions. Implanting conditions are 50keV N⁺ ions at a dose of 1×10^{17} ions/cm² and 100keV, 150keV, 200keV Si⁺ ions at a dose of 1×10^{17} ions/cm².

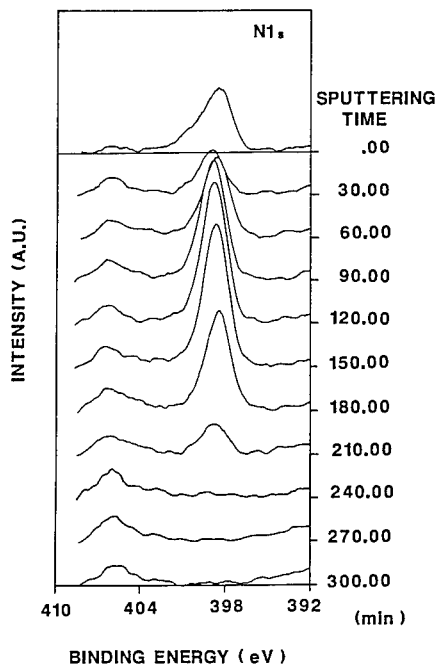


Fig.6 Depth profile of XPS spectra of N(1s) for silica glass implanted with 50keV N⁺ ions and 100keV Si⁺ ions. Each ion was implanted to a dose of 1×10^{17} ions/cm².

The depth profile of the XPS spectra of N(1s) is obtained using Ar⁺ ion sputtering. As shown in Fig.6, the peak at 398eV, which is the same peak as silicon nitride, has a strong intensity. Thus, we can increase the SiN concentration using an additional Si⁺ implantation.

3.2 The formation of PSG

Using SIMS analysis, the depth profile of P in the silica glass implanted with 150keV P⁺ ions to a dose of 1×10^{17} ions/cm² is obtained as shown in Fig.7. The concentration of P is maximum at a depth of 150 nm, which is nearly same as the projection range calculated by the LSS theory. As shown in Fig.7, the depth profile of P has nearly a Gaussian distribution. The same depth profile was also obtained using XPS with Ar⁺ ion sputtering.

The XPS spectra of P(2p) for P⁺ implanted silica glass at a depth of 150 nm, which is the projection range of the P⁺ ion, is shown in Fig.8. The XPS spectra of P(2p) can be roughly divided into two peaks, at 130eV and 135eV. The peak at 135eV agrees with the energy of P(2p) for P₂O₅. Thus, this peak indicates the interaction between P and O. The other peak at 130eV agrees with the energy of P(2p) for solid phosphor. Thus, the peak at 130eV probably indicates the interaction between P and P, which are implanted into the silica glass.

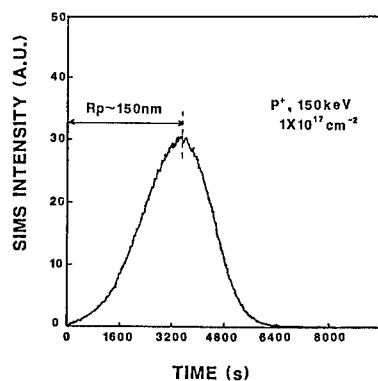


Fig.7 Depth profile of phosphor in the silica glass implanted with 150keV P⁺ ions to a dose of 1×10^{17} ions/cm².

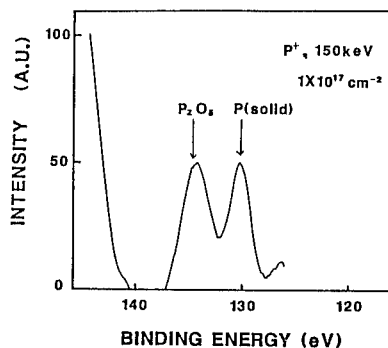


Fig.8 XPS spectra of P(2p) for phosphor implanted silica glass at a depth of 150 nm. The sample is the same as in Fig.7.

According to the network model of PSG[8], P atoms combine with O atoms. Therefore, the XPS spectra shows the possibility for the formation of PSG using P⁺ implantation into silica glass. P and P interactions probably show the depletion of O.

4. CONCLUSION

The surface chemistry of silica glass implanted with N⁺ or P⁺ ions has been studied using SIMS, RBS and XPS. The XPS spectra of N(1s) for silica glass implanted with N⁺ ions shows the possibility of the formation of SiON. The depth profile of nitrogen shows a trapezoidal shape in high dose conditions. The peak concentration of N is a few percent, but decreases when annealed above 600 °C. By using additional implantation with Si⁺ ions, the nitrogen concentration increases several times, and does not change even if the sample is annealed at 900 °C. The XPS spectra of P(2p) for silica glass implanted with P⁺ ions shows the possibility for the formation of PSG. The interaction of P-P, which probably indicates the depletion of oxygen, should be considered.

The present research effort is included in the National Research and Development Program on "Advanced Material Processing and Machining Systems", conducted under a program set by the Agency of Industrial Science and Technology, Ministry of International Trade and Industry.

REFERENCES

- [1] I.K.Naik, Appl.Phys.Lett., 43, 519 (1983).
- [2] C.Wang, Y.Tao and S.Wang, J.Non-Cryst.Solids, 52, 589 (1982).
- [3] P.Mazzoldi, Nucl.Instrum.and Methods, 209/210, 1089 (1983).
- [4] G.W.Arnold, Radiat.Eff., 65, 257 (1982).
- [5] C.Jech and Z.Bastl, Radiat.Eff.Lett., 76, 25 (1983).
- [6] C.Wang and Y.Tao, J.Non-Cryst.Solids, 71, 397 (1985).
- [7] H.Solnick-Legg and K.O.Legg, Met.Pro., 129, 25 (1986).
- [8] P.Balkand and J.M.Eldridge, Proc.IEEE, 57, 1558 (1969).

MICROTOPOGRAPHY OF ION BEAM ETCHED NiP FILMS.

KAZUHIKO NOGUCHI, RYUZI UEDA, YOSHITAKA MAEYAMA,
SHIGEO SASAKI, AND KAZUMICHI MACHIDA
Manufacturing Development Laboratory, Mitsubishi Electric Corp.,
Amagasaki, Hyogo, Japan

ABSTRACT

The microtopography of NiP films (P content, 8.7-12wt.% ; thickness, 40-50 μm) prepared by electroless plating on 18-8 stainless steel plates for molds and etched with a 10 keV Ar^+ ion beam was studied both by SEM observations and Talystep surface profile measurements.

With films containing less than 9.6wt.%P, which is supposed to have a transient structure between the supersaturated solid solution and the amorphous solid, smooth surfaces were obtained down to a few micrometers of etch depth and after that craters were formed. As for the mechanism of crater formation, it is considered that Ni crystallites locally precipitate by ion bombardment and then are etched selectively. With amorphous films containing 10.6wt.%P, microcavities less than 0.02 μm Rmax instead of craters were observed regardless of the etch depth.

The ion beam etching of NiP films has been found to be very promising for the preparation of precision molds of various grades, e.g. for plastic lenses used in opto-electronics, by selecting P content according to the desired surface roughness and etch depth of a particular application.

INTRODUCTION

Ultra precision processing with a high dimensional accuracy has been demanded for the preparation of precision molds for plastic lenses used in opto-electronics. Widely applied ultra precision turning sometimes induces figure errors by edge waviness of diamond tools. Machining of any figures with smaller size than the nose radius of the tool and free curved surfaces is difficult with the turning. Moreover, figure errors of very small size and complex contours can't be corrected by conventional polishing. Therefore we investigated the possibility of precision machining or finishing by ion beam etching which is generally used for microfabrication of semiconductors.

Neither single- nor poly-crystalline materials are suitable for the preparation of precision molds, since the former is expensive and the latter induces the discontinuities at grain boundaries. There is a possibility, however, of obtaining smooth surfaces from amorphous materials which have no order in atomic arrangement and thus no grain boundaries.

In this study, NiP films of various compositions prepared by electroless plating were given heat-treatment to change solid structures. These films were then etched with an Ar^+ ion beam to study etching characteristics as a first step for the development of a new micro-machining technique.

EXPERIMENTAL METHOD

NiP films with 40-50 μm thickness containing 8.7-12wt.% of phosphorus were prepared by electroless plating from various kinds of plating solutions on finely polished surfaces of 18-8 stainless steel plates (10x10x2 mm). They were then heat-treated in a vacuum at temperatures of room temperature(R.T.) to 400°C for one hour. Phosphorus content (wt.%P) in the films were quantitatively measured by Electron Probe Micro Analysis (EPMA:Model JXA-8600 of JEOL). Crystalline structures of the films were

determined by X-ray Diffractometry (XD:Model RAD-RB of RIGAKU).

Ion beam etching of the films was performed with a 10 keV Ar^+ ion beam having a Gaussian profile of current density, peak values of $1.8\text{--}6\text{ mA/cm}^2$ and half width of about $300\text{ }\mu\text{m}$.

Microtopography of the ion beam etched films was investigated with Secondary Electron Microscope (SEM:Model T-220A of JEOL) and a diamond stylus profilometer (Talystep of Taylor-Hobson). The latter was used also to measure the etch depth.

RESULTS AND DISCUSSIONS

The etch rate for Ni-9.6wt.%P films as a function of ion current density is shown in Fig.1. Ni-9.6wt.%P alloy is generally used for the fabrication of precision molds with a diamond turning. The NiP films were heat-treated at 200°C . The obtained etch rate for the films was $0.155(\mu\text{m/min})/(\text{mA/cm}^2)$ and is about one fifth of the rate for monatomic Ni crystal.

The dependence of the etch rate on angle of ion incidence is shown in Fig.2, where rates are normalized with the rate at 0° . The peak etch rate at 60° is about 1.3 times as large as at 0° . This angular effect is similar to the known effect for monatomic crystals but is small. The NiP films were found to have no crystalline structures by XD analysis; therefore the difference of the peak rates may be attributed the difference of the crystalline structures.

Sputtering is caused by cascade phenomenon under ion bombardment and takes place more effectively for crystalline metals than for non-crystalline metals. Effect of heat-treatment temperature on etch rate for Ni-9.6wt.%P films is shown in Fig.3. The etch rates at temperatures below 250°C and at 400°C were $0.155(\mu\text{m/min})/(\text{mA/cm}^2)$ and $0.21(\mu\text{m/min})/(\text{mA/cm}^2)$, respectively. XD analysis shows that the films have no crystalline structures between R.T. at 200°C , Ni crystallites precipitated in the non-crystalline metal at 250°C and eutectic alloy structures of Ni and Ni_3P at 400°C . Therefore sudden increase of the etch rate at 400°C is attributed to the structural change of the films. The structural change of the films also induces the difference of microtopography of etched surfaces. Similar microtopography were obtained for the films heat-treated at R.T. to 250°C , whereas deterioration of surface roughness was observed for the film heat-treated at 400°C . The deterioration is induced by discontinuities at the grain boundaries of Ni and Ni_3P crystals. This phenomenon is generally observed for films consisted of poly-crystalline materials or eutectic alloy materials.

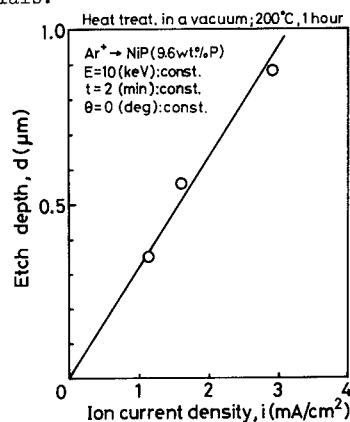


Fig.1. Relationship between the etch depth and ion current density for Ni-9.6wt.%P film.

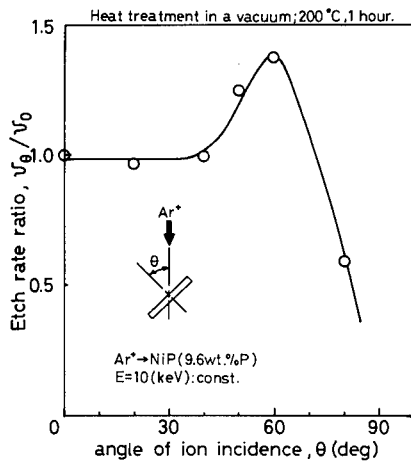


Fig. 2. Dependence of the etch rate on angle of ion incidence.

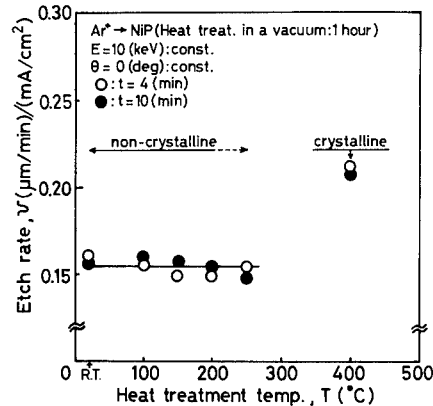


Fig. 3. Effect of heat-treatment temperature on etch rate for Ni-9.6wt.%P films.

The deterioration of surface roughness is also caused by further ion beam etching. Fig. 4 and 5 show micrographs by SEM and surface roughnesses by Talystep of ion etched Ni-9.6wt.%P films. Etch depth increases linearly with the increase of etch time, as shown in Fig. 4. Surface roughness down to a few micrometers of etch depth was as smooth as before etch and 0.01 μmR_{max} (Fig. 5(a)), whereas craters of a few micrometer diameter were formed when etch depth was more than a few micrometers (Fig. 5(b)). The craters increased in number as the etch depth increased (Fig. 5(c)). The surface roughnesses of the films at the etch depth of 4.3 μm and 8.8 μm were 0.026 μmR_{max} and 0.036 μmR_{max} , respectively. The formation of craters deteriorates surface roughness. These data show that smooth surfaces ($<0.01 \mu mR_{max}$) can be obtained by selecting etch depth of the film.

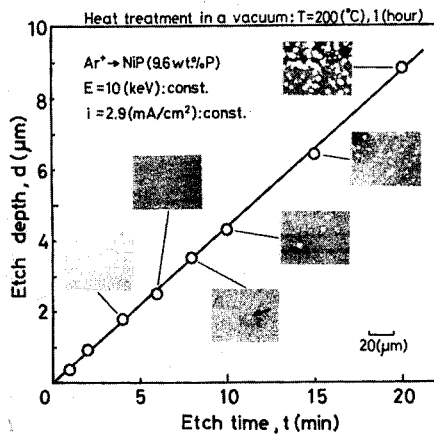


Fig. 4. Relationship between the etch depth and etch time for Ni-9.6wt.%P film.

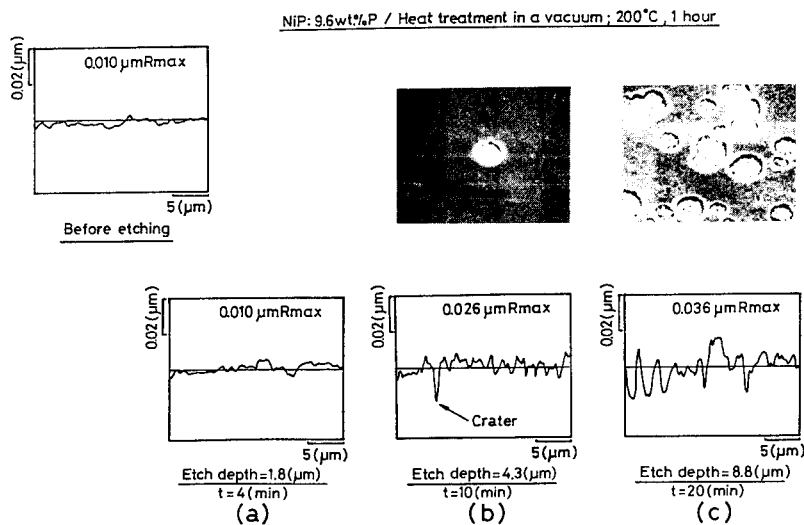


Fig.5. Micrographs by SEM and surface roughnesses by Talystep of the etched Ni-9.6wt.%P films.

Effect of P content on etch rate and microtopography of an ion etched surface was investigated to obtain further information about the crater formation. The effect of P content on solid structures of NiP prepared by electroless plating has been reported by A.H.Graham et al.[1], G.S.Cargill[2], and M.Matsuoka[3]. They describe that NiP film containing less than 7wt.%P, 7-10wt.%P, and more than 10wt.%P has, respectively, a structure of supersaturated solid solution, a transient structure between the supersaturated solid solution and the amorphous solid, and the amorphous structure. Fig.6 shows the relationship between etch rate and phosphorus content. Increase of the etch rate was observed as the P content increased. This figure indicates that the cascade phenomenon occur more effectively in the amorphous structure than in the transient structure.

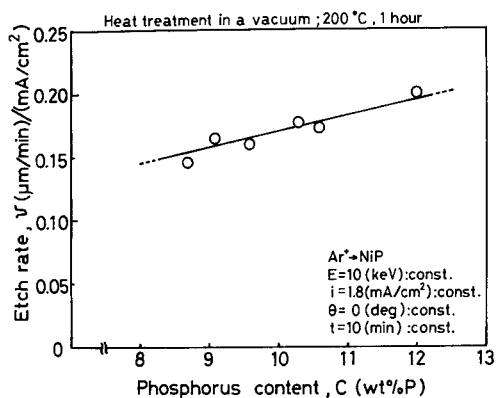


Fig.6. Relationship between etch rate and phosphorus content.

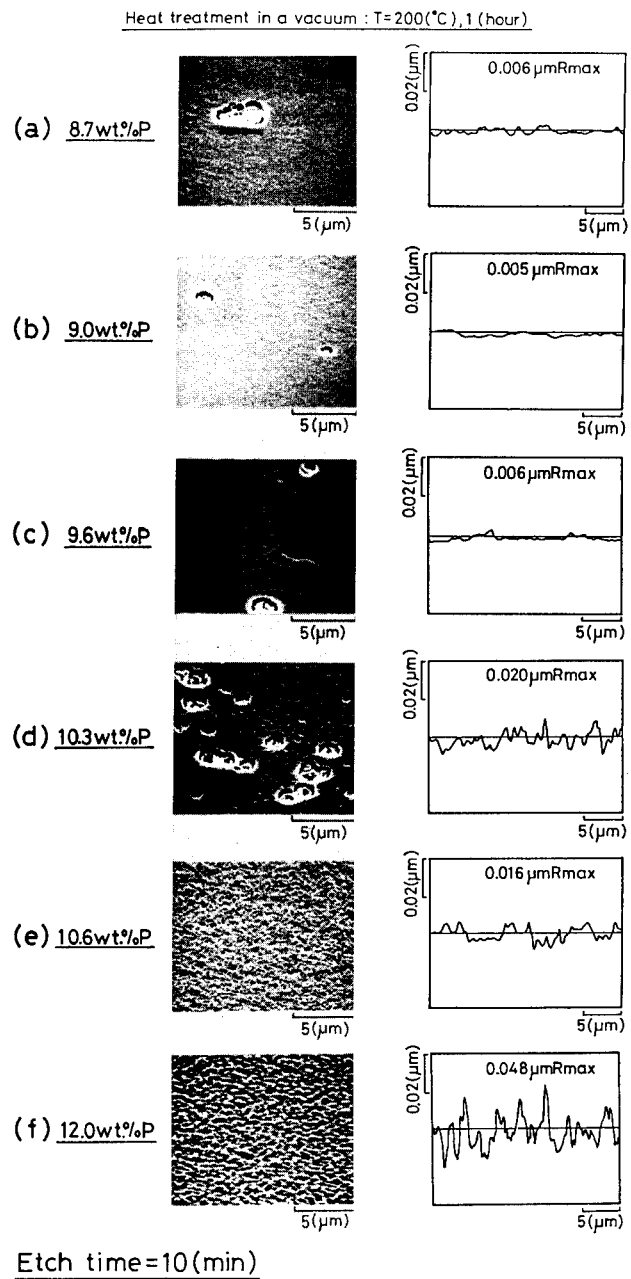


Fig.7. Micrographs by SEM and surface roughnesses by Talystep of etched films containing various P content.

Micrographs and surface roughnesses of ion etched films containing various P content are shown in Fig.7. The etch time was 10 min. With films containing 8.9-9.6wt.%P, craters of 0.02-0.03 μmRmax were formed, as mentioned above (Fig.5), when the etch depth was more than a few micrometers (Fig.7(a)-(c)). Roughnesses (0.005 and 0.006 μmRmax) shown in these figures are obtained from smooth areas beside areas with the craters. However, with films containing 10.6wt.%P (Fig.7(e)) and 12wt.%P (Fig.7(f)), homogeneous microcavities of less than 0.02 μmRmax and 0.05 μmRmax respectively were observed at any etch depth, instead of craters. With film containing 10.3wt.%P, a mixture of craters and microcavities was observed (Fig.7(d)). Because the amorphous structure is more thermostable than the transient structure, thermal phenomenon under ion bombardment is considered to induce the slight movement of P atoms, leading to a uniform formation of microcavities. The mechanism of crater formation is proposed below.

(1) P atoms invaded Ni lattices in the transient structure are locally removed by the thermal and cascade phenomena under ion bombardment.

(2) Ni crystallites precipitate locally near the surface.

(3) Selective etching of the crystallites occurs and then micro pits grow into craters on continued etching.

Fig.3 and 7 show that ion beam etching is capable of micro-machining of NiP films by selecting P content and heat-treatment temperature.

CONCLUSIONS

Etching characteristics of NiP films of various compositions and solid structures were investigated with Ar^+ ion beam. NiP alloys are widely used for the production of precision molds. The capability to control the surface roughness by selecting etch rate, P content and heat-treatment temperature suggest that a micro-machining technique with an Ar^+ ion beam is very promising for the preparation of precision molds.

ACKNOWLEDGMENTS

The authors are very grateful to Mr.N.Ohmori for technical support and to Mr.A.Shuhara and Dr.T.Tomoda for the technical help with manuscript preparation.

REFERENCES

- [1] A.H.Graham et al., J. Electrochem. Soc., 112, 401 (1965).
- [2] G.S.Cargill, J. Appl. Phys., 41, 12 (1970).
- [3] M.Matsuoka, in Physical Properties of Functional Plating Films, edited by Society for Scientific Research of Electro-plating, (Daily Industrial News, JAPAN, 1986), pp.82-87.

PART V

Electronic Materials

ION-BEAM-INDUCED EPITAXY AND SOLUTE SEGREGATION AT THE Si CRYSTAL-AMORPHOUS INTERFACE

J. M. POATE*, D. C. JACOBSON*, F. PRIOLO*^(a), and MICHAEL O. THOMPSON**

*AT&T Bell Laboratories, Murray Hill, NJ 07974

**Department of Materials Science, Cornell University, Ithaca, NY 14853

ABSTRACT

Segregation and diffusion of impurities in amorphous Si during furnace and ion-beam-induced epitaxy will be discussed. The use of ion beams to enhance the crystal growth process has resulted in novel behavior for fast diffusers such as Au. Diffusion is enhanced in the temperature range 300-700 K with activation energies ~0.3 eV. Segregation and trapping are analogous to behavior at liquid-solid interfaces.

INTRODUCTION

The epitaxial crystal growth of Si is a subject of widespread fundamental and technological importance, encompassing crystal growth and dopant segregation phenomena from the liquid, solid and vapor phase. These processes are important in Si technology for both bulk crystal growth and for the formation of thin electrically doped epitaxial layers. In this review we will concentrate on a somewhat novel aspect of Si epitaxy - the use of energetic ion beams to induce solid phase epitaxy^[1]. Three condensed phases of Si are commonly recognized; crystal (c), amorphous (a) and liquid. Amorphous Si is thermodynamically unstable in contact with crystalline Si and furnace heating will cause the amorphous layer to recrystallize^[2]. If the interface between the crystal and amorphous phase is clean, epitaxial growth ensues. Using ion implantation to produce essentially ideal a-Si layers, solid phase epitaxy has been measured^[3] over the temperature range 500-1200°C. This crystal growth process is quite remarkable. The interface motion remains planar and its velocity is characterized by a single activation energy of 2.7 eV over a range of 10^{-10} cm/sec to 10^{-1} cm/sec. Despite this knowledge, the basic mechanisms at the heart of solid phase epitaxy are almost completely unknown at the level of the interfacial defects and bond breaking processes. Much of this problem stems from a lack of knowledge about basic defect creation and diffusion processes in a-Si.

Solid phase epitaxy can be extended to even lower temperatures by means of heavy ion irradiation. Figure 1 shows the a-c interface velocity as a function of temperature for thermal (i.e. furnace) and ion-beam conditions. The a-Si layers on (100)Si are typically several thousand Å thick. For this example, 2.5 MeV Ar ions were used to induce crystal growth at a dose rate of 7×10^{13} ions/cm² sec. The interface motion is characterized by an activation energy of 0.3 eV with enormous velocity enhancement over the simple, thermal epitaxy for temperatures <400°C. The ability to induce interface motions at such low temperatures has allowed us to investigate several unusual crystal growth and segregation phenomena^[4].

(a) Permanent address: Physics Dept., University of Catania, Sicily, Italy

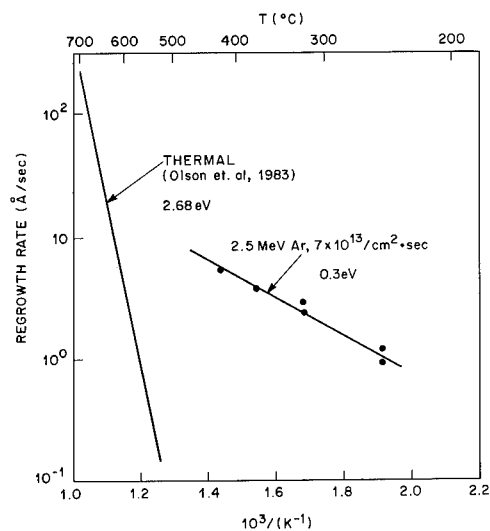


Figure 1. Comparison of Si(100) a-c interface velocities for thermal (i.e. furnace) and ion-beam-enhanced conditions. The 2.5 MeV Ar ion dose rate is 7×10^{13} ions/cm² sec.

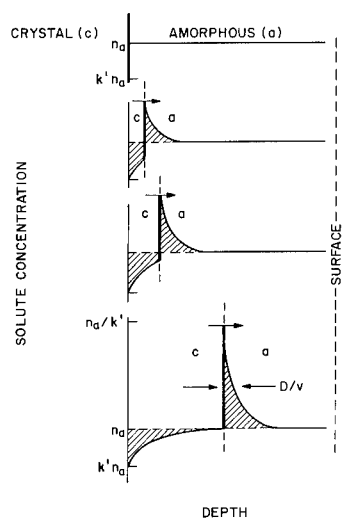


Figure 2. Evolution of the solute spike during segregation.

Solute atoms are segregated at phase boundaries because of differing solubilities in the two phases. Most of our understanding of this process comes from studies of zone-refining during solidification^[5]. Figure 2 shows schematically the segregation of a solute at a phase boundary. In amorphous crystallization we also observe segregation at the a-c interface as the impurity or solute atoms are more soluble in the a-phase than c-phase. The ratio of the solute concentrations in c-Si to that in a-Si at the interface is given by the interfacial segregation coefficient, k' . Assuming a uniform solute concentration, n_a , in the a-Si, the first a-Si layers to crystallize will have a solute composition of $k'n_a$. As crystallization proceeds, solute accumulates in the a-Si in the near interface region until a steady state interface concentration n_a/k' is attained. The width of this segregated spike is given by D/v where D is the solute diffusivity in a-Si and v is the c-a interface velocity. The fact that solute has to be conserved at steady state requires that the shaded areas be equal i.e. the solute removed in the initial transient must equal the solute transported in the segregated spike. The width of the initial transient, X_c , is given by $D/k'v$.

The conditions shown in Figure 2 usually pertain to the case of solidification where diffusion in the liquid phase is much greater than that in the solid. The solute atoms can therefore diffuse ahead of the interface and build up a segregation spike. This classic behavior is not usually observed during solid phase epitaxy^[6]. Figure 3 shows schematically the observed behavior of impurities in the solid phase. The upper figure shows implanted As in a-Si; movement of the c-a interface does not measurably perturb the As depth distribution. Such results imply that $k' \approx 1$ i.e. the interfacial solubilities are identical. Moreover the lack of profile broadening shows that diffusion is negligible in both the c- and a- phases at typical growth conditions of 500°C.

While there is much data on diffusion in c-Si we know little about diffusion in a-Si. We^[7] and Kalbitzer and coworkers^[8,9] have pointed out some experimental and phenomenological correlations concerning diffusion in a-Si and c-Si. Firstly Cu, Ag and Au are relatively fast diffusers in a-Si with well defined activation energies. Species such as As, In or Sb have immeasurably small diffusion lengths in a-Si for temperatures <500°C. (By immeasurably small, we mean diffusion lengths smaller than the depth resolution of Rutherford Backscattering techniques i.e. <100Å. Measurable diffusion can be observed for very high concentrations of In in a-Si but this is probably a localized melting phenomenon). This difference correlates with the behavior of these species in c-Si where Cu, Ag and Au are fast or interstitial diffusers and As, In or Sb are slow or substitutional diffusers. Figure 4 shows diffusion coefficients for Au in a- and c-Si and As in c-Si. The high temperature diffusion of As in c-Si has been well characterized^[10]. If As diffusion in a-Si is characterized by the same activation energy and pre-exponential we would expect diffusion lengths at 500°C for 10^4 sec of approximately 1Å. Figure 4 shows the measured diffusivity of Au in a-Si where the diffusion length for the same temperature and time is 10^3 Å. We also point out the intriguing correlation between the Au a- and c-diffusion coefficients. Recent measurements by Coffa *et al*^[11] are shown for the effective diffusion coefficient of Au in c-Si. A kick-out mechanism is assumed where interstitial Au is produced by ejection of Au from substitutional sites by Si interstitials. The diffusion coefficient is a product of the interstitial diffusivity multiplied by the ratio of the interstitial and substitutional solubilities. The high temperature c-Si measurements correlate well with our low temperature a-Si data. While we do not push these correlations too far it is important to emphasize that the fast diffusers in c-Si are also fast diffusers in a-Si. Similarly the slow diffusers in c-Si appear to have small diffusion coefficients in a-Si.

IMPURITY SEGREGATION DURING SOLID PHASE EPITAXY

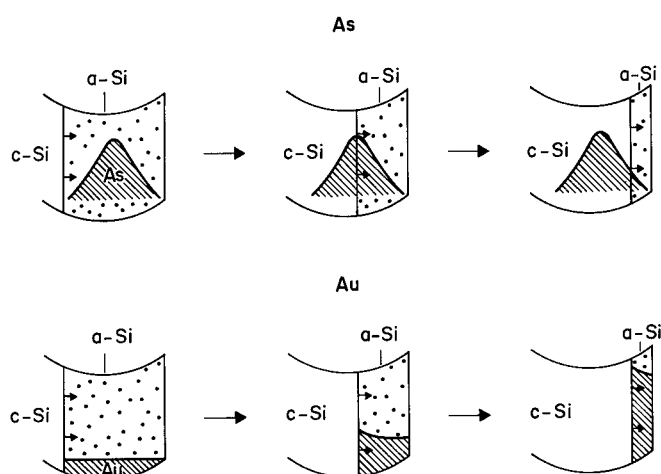


Figure 3. Schematic of c-a Si interface motion and dopant behavior during furnace epitaxy for upper, slow diffusers (As) and lower, fast diffusers (Au).

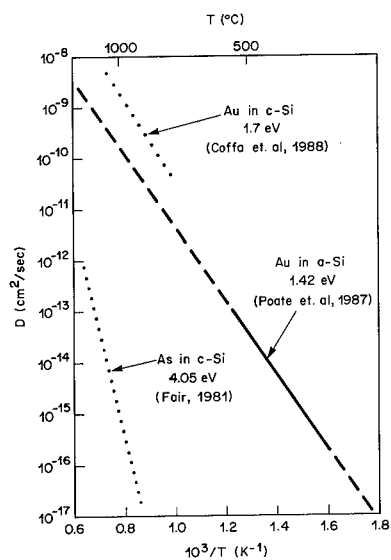


Figure 4. Diffusion coefficients of Au in a- and c-Si and As in c-Si.

The behavior of the rapid diffusers under solid phase epitaxy conditions is shown schematically for Au^[12] in the lower part of Figure 3. Not only does Au have high diffusivity but we estimate Au to be eight orders of magnitude more soluble in a-Si than c-Si at 515°C. The enhanced solubility and diffusivity is nicely demonstrated by the fact that Au can be completely equilibrated within a-Si layers at temperatures ~500°C without penetrating the underlying c-Si substrate. Solid phase epitaxy at temperatures ~500°C results in the Au being retained within the narrowing amorphous layer. The Au diffusivity is so high that the Au outruns the interface motion thus producing essentially flat segregation profiles. The process has not reached steady state but we clearly observe $k' < 10^{-1}$. The segregation and diffusion of Cu and Ag at the a-c interface is discussed by Custer *et al* at this meeting.

NONEQUILIBRIUM SEGREGATION AND TRAPPING

The previous section presented some of the phenomena associated with solute segregation in both the liquid and solid phase. There has been renewed interest in segregation because of the very rapid interface motion and nonequilibrium crystal growth associated with laser melting of surface layers. The crystallizing Si interfaces can approach speeds of 15 m/sec. Under such conditions solute can be segregated with k' values exceeding equilibrium values by several orders of magnitude. This solute trapping is a direct consequence of the undercooling (or chemical potential driving force) produced by the high interface velocities and occurs when the liquid-phase diffusive velocity of the solute is comparable to the interface velocity. In liquid-phase bulk crystal growth, D/v is $\approx 50\mu\text{m}$ whereas in surface laser melting it is $\approx 50\text{\AA}$. As D/v approaches the interatomic spacing, the probability increases for solute atoms to be engulfed or trapped by the advancing interface. For ion-beam-induced crystal growth at 250°C, D/v is less than the interatomic spacing if we use the Au thermal diffusivity presented previously. As we will discuss, however, the diffusivity is also enhanced by the ion-beam irradiation to give D/v escape distances of $\approx 20\text{\AA}$. These values result in another intriguing segregation and trapping regime.

We produced the following structures to study ion-beam-induced crystallization and segregation^[4]. Gold was uniformly diffused through micron thick a-Si layers formed by implantation. Typical diffusion conditions were 485°C for 24 hours at 10^{-7} Torr resulting in a-Si layers 1.1 μm thick with Au concentrations ~0.2at%. Ion-beam-induced crystallization experiments were carried out in the temperature range 250-420°C using 2.5 MeV ion bombardment. Figure 5 shows Rutherford Backscattering depth profiles of the Au as a function of Ar dose at 320°C and dose rate of 7×10^{13} ions/cm² sec. The dose rate was kept constant yielding an interface velocity (v) of $\sim 3\text{\AA}/\text{sec}$. The zone-refined profiles display the characteristic features of the segregation process; build-up of segregated solute at the interface and concomitant removal of material during the initial transient. It should be noted that the initial transient, X_c , extends for 0.2 μm . At steady state the amount of material in the segregation spike remains constant and solute is rejected behind the moving interface at the original concentration. It is remarkable that the Au is trapped in c-Si at concentrations some ten orders of magnitude greater than the equilibrium solubility in c-Si. Transmission electron microscopy shows this c-Si to be defect free without evidence of Au precipitation although Rutherford Backscattering and channeling measurements give no evidence of the Au being substitutional.

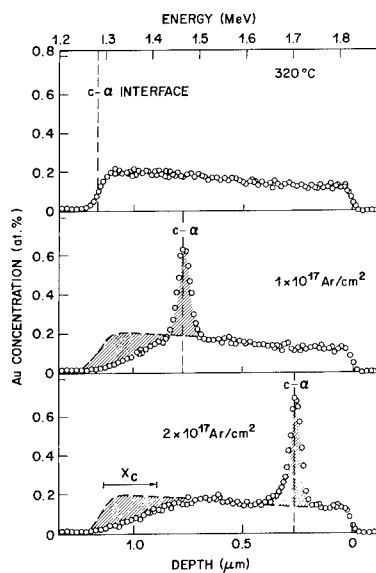


Figure 5. Gold depth profiles in c- and a-Si following 2.5 MeV Ar induced crystallization. The equilibration distance, X_c , is indicated. From Poate *et al*^[4].

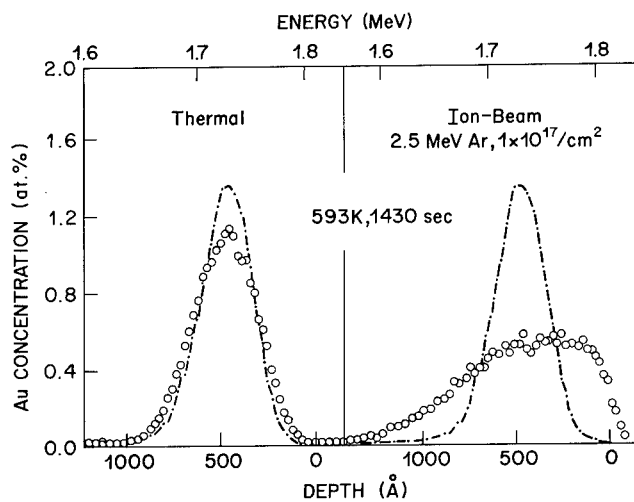


Figure 6. Depth profiles of implanted Au markers in a-Si before and after 1430 sec annealing at 593K with and without 2.5 MeV Ar ion irradiation. The Ar irradiation was for a dose of $1 \times 10^{17}/\text{cm}^2$. From Priolo *et al*^[13].

ION-BEAM-ENHANCED DIFFUSIVITY

It is not possible to model the profiles shown in Figure 5 using the usual thermal diffusion coefficients because the Ar ion irradiation enhances the Au diffusivity at the c-a interface. As little was known about the effects of radiation on diffusive properties in a-Si, we carried out the following experiments^[13]. Si substrates were implanted with Cu, Ag and Au at energies in the range 70-150 keV and doses in the range $5 \times 10^{14} - 5 \times 10^{15}$ ion/cm² at liquid nitrogen temperature. The samples were subsequently amorphized to approximately 2 μ m using a standard^[2] series of MeV Ar implants, producing an a-Si layer with well-defined kinetic and thermodynamic properties. The diffusion measurements were made in the temperature range 77-700 K. The samples were irradiated by a 2.5 MeV Ar beam at doses in the range $2 \times 10^{16} - 2 \times 10^{17}$ ions/cm² and dose rates in the range $3.5 \times 10^{12} - 1.4 \times 10^{14}$ ions/cm²sec. The impurity depth profiles were measured by 2.0 MeV He⁺ Rutherford Backscattering. The profiles were then fitted for Dt , the diffusion length squared, by an analytical solution of the diffusion equation which assumed an initial Gaussian profile and total reflection at the surface. The samples were also analyzed by transmission electron microscopy before and after irradiation. This analysis ensured that neither impurity precipitation nor a-Si recrystallization had occurred during the irradiation process. Figure 6 compares the experimental depth profiles of Au ion irradiation after thermal annealing at 593K and after 2.5 MeV Ar irradiation at the same temperature. After the 1430 sec thermal annealing [Figure 6 (a)], the depth profile broadens slightly. This broadening is considerably enhanced in the ion-beam irradiated samples [Figure 6 (b)], where a profile after 2.5 MeV Ar irradiation at a dose of 1×10^{17} /cm² is reported. The dose rate was 7×10^{13} ions/cm² sec resulting in an irradiation time of 1430 sec. Similar measurements were made with dose rates in the range 3.5×10^{12} and 1.4×10^{14} ions/cm² sec and, within our experimental resolution, no difference was observed between the depth profiles. The ion-beam-enhanced diffusion lengths squared, D^*t , were obtained by subtracting the thermal component, $D_{th}t$, from the total diffusion, Dt . We observed a linear dependence between D^*t and bombarding dose. We also observed a linear dependence between D^*t and nuclear energy loss.

The diffusion coefficients of Cu, Ag and Au in a-Si are reported in Figure 7 versus $1/T$ for irradiations with a 2.5 MeV Ar-beam at a dose rate of 7×10^{13} ions/cm²sec. The pure thermal diffusion for these three impurities is also reported with heavy lines. At the lowest temperatures the diffusion is almost athermal and due to ion-beam mixing. The measured values are 9×10^{-16} , 4.5×10^{-16} and 2×10^{-16} cm²/sec for Cu, Ag and Au respectively. Increasing the temperature results in a transition from the ion beam mixing to a thermally activated regime. In this regime the diffusion is much higher than the purely thermal diffusion. Finally, at higher temperatures, the purely thermal diffusion dominates. Figure 8 shows a plot of the thermally-activated ion-beam-enhanced coefficient, D^* . We obtain D^* by subtracting both the thermal and ion-beam mixing components from the total diffusivity. An Arrhenius behavior is observed with activation energies of $0.27 (\pm .1)$, $0.39 (\pm .1)$ and $0.37 (\pm .1)$ eV for Cu, Ag and Au respectively.

We have also carried out diffusion measurements for As, In, Sb, Fe, Ni and Pt implanted in a-Si for similar time, temperature and irradiation conditions^[13] used in the Cu, Ag and Au measurements. Negligible diffusion, either ion-beam-enhanced or purely thermal, is observed. Those results are consistent with previous measurements^[14] of ion-beam-enhanced crystal growth of As and In doped layers where no perturbation of the dopant profiles were observed.

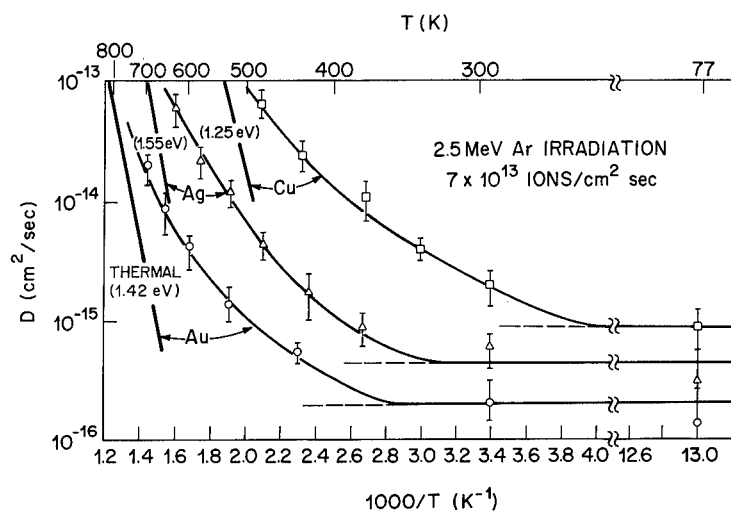


Figure 7. Total diffusion coefficients of Cu, Ag, and Au in a-Si vs. $1000/T$ for 2.5 MeV Ar irradiation at dose rates of 7×10^{13} ions/cm² sec. The pure thermal components are shown as heavy lines. From Priolo *et al.*^[13].

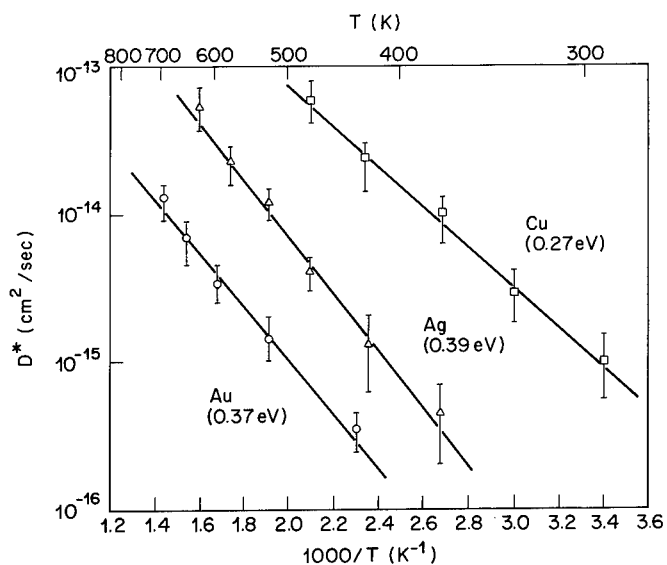


Figure 8. The ion-beam-enhanced, coefficient D^* , for Cu, Ag, and Au in a-Si, obtained from the total diffusion coefficients by subtracting the ion-beam-mixing and the thermal components, vs. $1000/T$ for Cu, Ag, and Au for 2.5 MeV Ar irradiation at dose rates of 7×10^{13} ions/cm² sec. From Priolo *et al.*^[13].

There are several interesting facets to these data in terms of the ion-beam processes and diffusion mechanisms in amorphous systems. The diffusion lengths squared, i.e. D^*t , depend linearly on ion dose but not dose rate. They also depend linearly on the rate of nuclear energy loss of the bombarding species. These facts would indicate^[15] that diffusion is caused by an intracascade phenomenon where the defect creation, diffusion and annihilation processes are localized to an individual cascade. There is no interaction between cascades. However as pointed out by Rehn and Okamoto^[15] these results differ from other measurements of ion-beam-enhanced diffusion in both crystalline^[16] and amorphous^[17] metallic systems where dose rate dependences are observed. We note that Park *et al* at this meeting also show that ion-beam-enhanced interdiffusion in thin a-Si/Ge multilayers is dose rate independent. It will be interesting to establish whether these differences arise because of basic differences in the cascade generation mechanisms or differences in the defects created by the cascades. Whatever the mechanisms, Si and Ge are clearly interesting model systems for studying intracascade effects. Again we note that large ion-enhancement effects are seen for those impurities that are *also* characterized by interstitial components in their diffusion mechanisms in c-Si.

INTERFACIAL SEGREGATION COEFFICIENTS

Combining the measured segregation profiles of Figure 5 with the diffusion coefficients of Figure 7, we can fit the segregation behavior using only one free parameter - that of the interfacial segregation coefficient, k' . Figure 9 shows a fit to the 320°C data using the measured interface velocity of 2.85Å/sec and radiation-enhanced diffusivity of $4.4 \times 10^{-15} \text{ cm}^2/\text{sec}$, giving k' of 0.007 ± 0.004 . To allow for detector resolution, straggling and the waviness of the interface (as measured by TEM), these fits have been convoluted with a Gaussian of $\sigma \approx 300\text{Å}$. The width (D/v) of the segregated spike is expected to be $\approx 20\text{Å}$ with a peak Au concentration at the interface of 20 at.%. This value is clearly in excess of equilibrium solubilities of Au in a-Si which, for example, we measure to be 0.7 at.% at 515°C. The solubility of Au in a-Si in the interface region must therefore be markedly enhanced by the ion irradiation over the 20Å spike width.

The velocity and temperature dependences of k' demonstrate some of the unique characteristics of the ion-beam process. The interface velocity scales with the Ar dose rate. We observe that an order of magnitude change in velocity (i.e. same dose but different dose rates) produces identical segregation profiles. Specifically, the equilibration distance $D/k'v$ remains constant for all interface velocities. Since both the diffusivity and velocity scale linearly with the dose rate, D/v is independent of interface velocity. Hence the segregation coefficient, k' , is also observed to be independent of velocity. This behavior is a consequence of the beam-induced crystallization process and is quite different than that occurring in liquid phase epitaxy where k' scales with v because the chemical driving force for trapping increases with the velocity-dependent undercooling in the liquid.

The segregation coefficient, k' , does however vary strongly with temperature, as shown in Figure 10. These data were taken for the same ion beam conditions described previously with the substrate temperature varied in the range 250-420°C. At high temperatures, k' is tending towards the equilibrium value with essentially no trapping of Au in the crystalline phase. We do not yet have an understanding of these results in terms of the crystal growth processes. The driving force for trapping is related to the chemical potentials of the impurities in the a- and c-Si and hence should depend on temperature but not necessarily on the interface velocity. However, we do

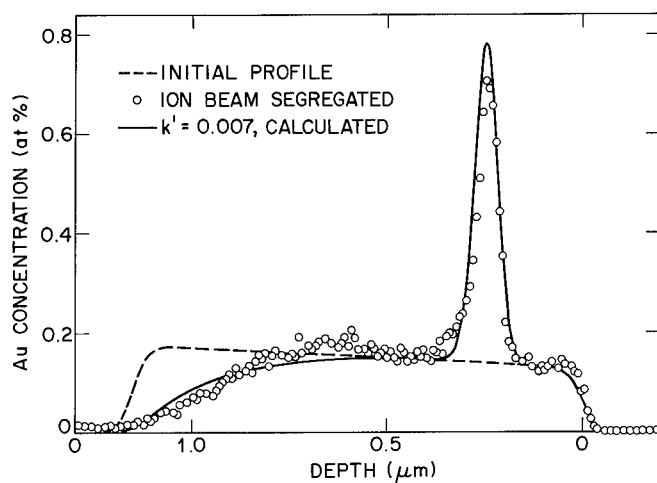


Figure 9. Gold depth profile in c- and a-Si following 2.5 MeV Ar induced crystallization at a temperature of 320°C and dose of $2 \times 10^{17}/\text{cm}^2$. The smooth line is a fit to the experimental profile assuming only one free parameter, k' . From Poate *et al*^[4].

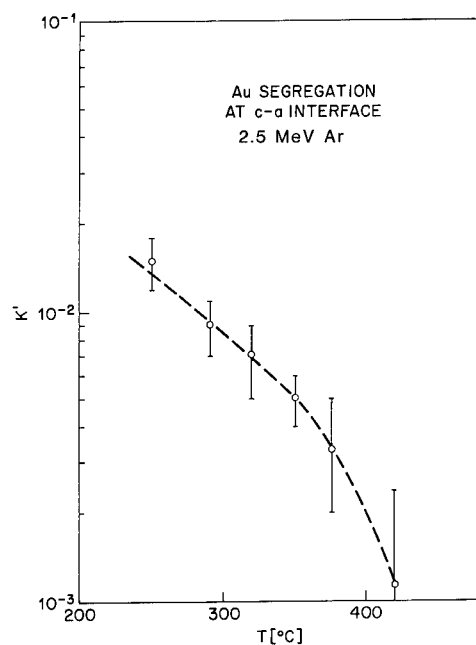


Figure 10. The interfacial segregation coefficients, k' , of Au at the c-a Si interface as a function of temperature, under Ar ion induced crystallization.

not know how significantly the production of defects by the ion beam will change the chemical driving forces. Moreover ion-beam mixing of atoms at the interface may also play a role in the non-equilibrium trapping of Au in the growing crystalline phase.

DISCUSSION

We have presented data on a novel regime of crystal growth and impurity segregation in the solid phase. The novelty lies in the use of ion beams to epitaxially crystallize a-Si at very low temperatures. Rapid diffusers, such as Au, demonstrate classic segregation behavior at the moving c-a interface except that Au is trapped in the lattice at concentrations far in excess of equilibrium values. The segregation profiles can be fitted using measured interfacial velocities and ion-beam-enhanced diffusivities. The slow diffusers such as As are not measurably perturbed by movement of the c-a interface. The picture is consistent in that we phenomenologically understand the role that interface velocity and diffusion play in the segregation process. Moreover a-c Si is a beautiful model system for demonstrating some of the classic features of interface motion and segregation. Ion-beam-enhanced growth extends the a-c Si system into an entirely new regime of crystal growth. This provides opportunities for measuring impurity interactions in the growth process over an extremely wide temperature range and under conditions ranging from pure equilibrium to highly non-equilibrium in the collision cascade. Moreover, since we can go from one regime to the other, the possibility exists for directly testing the microscopic models in both regimes. In addition we can now compare liquid phase growth from laser annealing and the collision cascade induced growth. This should enable us to test the models that depict the collision cascade as a liquid-like phase.

While we have a phenomenological understanding of the ion-beam-enhanced segregation and diffusion processes there are several issues concerning the basic mechanisms:

- *Crystal Growth* - We have not discussed specific mechanisms for the ion-beam-induced epitaxy. Jackson^[18] has recently presented an intracascade model in terms of competition between amorphization and crystallization at the c-a interface. The model fits the data well. It is speculated that amorphization is produced by diffusion and condensation of vacancies and interstitials from c-Si at the interface and that crystallization results from the motion of dangling bonds in the a-Si at the interface.
- *Segregation* - The behavior of impurities at the interface should be sensitive to the presence of the defects postulated in the Jackson model. There is not, however, a consistent picture of the role that defects play in the diffusive process in a-Si. In terms of the basic segregation and trapping processes, it is necessary to establish the relative roles of the equilibrium driving forces (i.e. chemical potential differences between a- and c-Si) and non-equilibrium processes (e.g. defect generation and ion-beam mixing at the interface).
- *Diffusion* - We have established that ion-beam-enhanced diffusion of the fast diffusers (e.g. Cu, Ag and Au) in a-Si are dominated by intracascade effects with well-defined activation energies. It will be useful in terms of cascade behavior to determine the atomistic or thermodynamic relationships of these activation energies. The data demonstrate for both furnace and ion-beam conditions that the fast diffusers in c-Si are fast diffusers in a-Si and that the slow diffusers in c-Si have very small diffusion coefficients in a-Si. These correlations are either

fortuitous or imply intriguing similarities in the a- and c-Si diffusion mechanisms.

ACKNOWLEDGEMENTS

We are indebted to Rob Elliman, Jan Linnros and Jim Williams for collaborating in the early measurements and to Ugo Campisano, Jonathan Custer, George Gilmer, Horst Hahn, Ken Jackson, Sam Myers and Lynn Rehn for discussion.

REFERENCES

1. R. G. Elliman, J. S. Williams, W. L. Brown, A. Leiberich, D. M. Maher, and R. V. Knoell, Nucl. Instr. and Meth. *B19/20*, 435 (1987).
2. E. P. Donovan, F. Spaepen, D. Turnbull, J. M. Poate, and D. C. Jacobson, J. Appl. Phys. *57*, 1795 (1985).
3. G. L. Olson, Materials Research Society Proceedings *35*, 25 (1985).
4. J. M. Poate, J. Linnros, F. Priolo, D. C. Jacobson, J. L. Batstone and M. O. Thompson, Phys. Rev. Lett. *60*, 1322 (1988).
5. B. Chalmers, *Principles of Solidification*, [John Wiley & Sons, New York, 1964].
6. J. S. Williams, Chapter 5 in *Surface Modification and Alloying*, ed. by J. M. Poate, G. Foti, and D. C. Jacobson, [Plenum, New York, 1983].
7. J. M. Poate, D. C. Jacobson, J. S. Williams, R. G. Elliman, and D. O. Boerma, Nucl. Instr. and Meth. *B19/20*, 480 (1987).
8. M. Reinelt and S. Kalbitzer, J. Phys. (Paris) Colloq. *C4-843* (1981).
9. S. Kalbitzer, M. Reinelt and W. Stolz in *Proceedings of the 4th EC Photovoltaic Solar Energy Conference, Stresa, May 1982* edited by W. H. Bloss and G. Grassi [Reidel, Dordrecht, Holland, 1982], p. 163.
10. R. B. Fair, Chapter 7 in *Impurity Doping Processes in Silicon*, ed. by F. F. Y. Wang [North Holland, New York, 1981].
11. S. Coffa, L. Caleagno, S. U. Campisano, G. Calleri and G. Ferla, J. Appl. Phys. (in press).
12. D. C. Jacobson, J. M. Poate, and G. L. Olson, Appl. Phys. Lett. *48*, 118 (1986).
13. F. Priolo, J. M. Poate, D. C. Jacobson, J. Linnros, J. L. Batstone, and S. U. Campisano, Appl. Phys. Lett. *52*, 1213 (1988); IBMM to be published.
14. R. G. Elliman, J. S. Williams, D. M. Maher, and W. L. Brown, Materials Research Society Proceedings *51*, 319 (1986).
15. L. E. Rehn and P. R. Okamoto, Nucl. Instr. and Meth. (in press).
16. A. Müller, V. Naundorf, and M.-P. Macht, J. Appl. Phys. *64*, 3445 (1988).
17. R. S. Averback, H. Hahn, and Fu-Rong Ding, J. Less-Common Metals *140*, 267 (1988).
18. K. A. Jackson, J. Mater. Res. *3*, 1218 (1988).

SEGREGATION OF AG AND CU DURING ION BEAM AND THERMALLY INDUCED RECRYSTALLIZATION OF AMORPHOUS SI

J. S. Custer,[†] Michael O. Thompson,[†] and J. M. Poate[‡]

[†]Dept. of Materials Science and Engineering, Cornell University, Ithaca, NY 14853

[‡]AT&T Bell Laboratories, Murray Hill, NJ 07974

Abstract

The segregation of Ag and Cu impurities in amorphous Si during both thermal and ion beam induced epitaxial crystallization has been studied. During thermal regrowth at 550°C, both Ag and Cu are initially trapped at increasing concentration in the shrinking a-Si layer. At a critical concentration, though, regrowth becomes non-planar and the impurities are no longer entirely trapped in the a-Si. Above 0.08 at% and 0.15 at% respectively, the excess impurity is lost to the crystal region and diffuses rapidly away from the interface. Under low temperature (200 – 400°C) epitaxy induced by a 2.5 MeV Ar⁺ beam, segregation and trapping are initially observed. As regrowth proceeds, however, the segregation no longer follows the simple model.

Introduction

Solid phase epitaxy (SPE) of pure amorphous Si (a-Si) on a crystal Si (c-Si) substrate has been extensively studied.^{1,2} Thermal regrowth is an activated process exhibiting a single activation energy $E_a = 2.7$ eV from 400 to 1200°C. This activation energy is the same for a-Si produced in the very different kinetic regimes of ion implantation,² UHV deposition,² or the rapid quench following pulsed laser melting.³

The SPE rate is, however, affected by impurities in the a-Si.^{2,4,5} Electrically active dopants such as B, P, and As, enhance the SPE rate through an electronic effect.² Other impurities such as N, C, and O generally decrease the SPE rate.⁵ A notable exception to this decrease is Au.⁶ Enhancements up to a factor of 50 in the SPE rate were measured, and the degree of enhancement increased with the Au interfacial concentration until a level of 0.7 at% was reached. Unlike the normal dopants, Au remains confined in the narrowing a-Si during regrowth and the high thermal diffusivity of Au⁷ results in even redistribution throughout the layer.

High energy ion beams can also induce solid phase epitaxy at substantially reduced temperatures (200 – 400°C), a process termed Ion Beam Enhanced Epitaxial Crystallization (IBEEC). Although first identified some 15 years ago, it has only recently been studied in detail.^{8–11} IBEEC displays an apparent activation energy of ~ 0.25 eV, with enhancements over the low temperature thermal SPE rate by many orders of magnitude. Under IBEEC the regrown thickness depends primarily on the total implanted dose and hence the interface velocity can be varied by changing the dose rate.

The comparatively rapid interface velocity achievable during IBEEC, coupled with the high radiation enhanced diffusivity of Au in a-Si¹² allows velocity dependent segregation to be investigated in the solid state. Compared to liquid phase segregation, the solid state has an advantage in that the interface can be halted at any time to obtain the impurity concentration profile. IBEEC of a-Si with Au impurities results in apparently classical segregation and trapping,¹³ except that Au is trapped in the crystal eight orders of magnitude above the solid solubility.¹⁴ As regrowth proceeds, the Au is pushed ahead of the interface resulting in the creation of a segregation spike. As the segregation spike gains material, the trapping in the c-Si also increases until steady state is reached. At this point, the same amount of Au entering the spike on the a-Si side is trapped in the c-Si. The segregation coefficients are independent of the interface velocity but vary with temperature. At very high Au concentrations the interface was observed to break down into twins.¹⁵

We have studied the recrystallization of a-Si with Ag and Cu impurities. These elements are also fast diffusors in a-Si, both thermally⁷ and under irradiation.¹² There are three different regimes to be investigated. First is furnace annealing where both the regrowth and diffusivities are purely thermal for Au, Ag, and Cu. Second is IBEEC of Au and Ag doped a-Si, where the regrowth and diffusivities are determined primarily by radiation effects. The third regime is IBEEC of Cu doped a-Si, where the regrowth is controlled by the radiation, but the thermal component of the diffusivity still dominates. Thus the behavior of the interface can be compared and contrasted in different regrowth regimes in an attempt to determine the microscopic processes leading to the observed segregation and trapping phenomena.

Experiment

Ag and Cu impurities were implanted into pre-amorphized $\langle 100 \rangle$ Si at 150 keV and doses between 8×10^{14} and $2.5 \times 10^{15} \text{ cm}^{-2}$. The a-Si was produced by a $2 \times 10^{15} \text{ cm}^{-2}$ 250 keV ^{28}Si implant at liquid nitrogen temperature. These implants created a continuous amorphous layer extending from the surface to approximately 450 nm, with the impurity in the near surface region. The solute was subsequently evenly redistributed throughout the a-Si layer by low temperature thermal anneals. For Cu, 1 hr at 400°C was sufficient while Ag required 3 hrs at 450°C. No measurable Ag or Cu was observed in the underlying c-Si.

Solid phase epitaxy was induced either thermally in a $<1 \times 10^{-7}$ Torr vacuum furnace at 550°C or by IBEEC using a 2.5 MeV Ar^+ ions. For the IBEEC irradiations, a spatially uniform beam profile was obtained by overfocussing the $\sim 1 \mu\text{A}$ beam onto a small (1-1.5mm diameter) aperture and dithering slightly. The maximum beam current was limited to 100nA to prevent beam heating effects. Samples were intimately mounted on a resistively heated copper stage which was held at a constant temperature ranging from 200 to 400°C during irradiation. At fixed temperature, the epitaxial regrowth velocity was varied by changing the Ar^+ dose rate over the range 5×10^{12} to $7 \times 10^{13} \text{ cm}^{-2}\text{sec}^{-1}$, the upper limit due to beam heating considerations, and the lower limit due to finite available accelerator time. A 2.5 MeV Ar^+ ion has a range of greater than $2 \mu\text{m}$ and hence no Ar was introduced into the recrystallizing region.

Epitaxy was normally halted before the a-Si layer was completely regrown so solute concentration profiles in both the a-Si and c-Si could be observed. These profiles and the a-Si layer thicknesses were obtained before and after epitaxy using Rutherford backscattering spectroscopy (RBS) in combination with the channeling effect. Ag profiles were measured using 2.0 MeV $^4\text{He}^+$, while Cu profiles were measured with 2.5 MeV $^4\text{He}^+$. Pulse pileup in the spectra, an acute problem for the Cu samples, was determined from the background¹⁶ and subtracted from the measured spectra to obtain the impurity profiles.

Results for Ag

Under thermal anneals the Ag samples initially regrew epitaxially with all of the Ag remaining trapped in the narrowing a-Si layer. Because of the high diffusivity⁷ of Ag at 550°C a flat Ag concentration profile was maintained in the a-Si. In Fig. 1, the initial Si channelled RBS spectra (a), and Ag impurity profiles (b) are shown as open circles (o). A 35 minute anneal at 550°C, leading to epitaxy and conservation of material, is shown by triangles (Δ). When the Ag concentration in the a-Si reaches $\sim 0.08 \text{ at\%}$, however, the regrowth characteristics change dramatically. First, the interface becomes non-planar as indicated by a broadening of the back edge of the a-Si in the channelled RBS spectra. This development of a non-planar interface was also observed by time resolved reflectivity (TRR) measurements.⁵ During further regrowth, Ag is lost from the a-Si layer so that the concentration in the a-Si is maintained at 0.08 at%, until p-Si is formed as discussed below. The Ag lost to the crystal phase diffuses away rapidly and is not detected by RBS. A rough lower limit for the diffusion coefficient in c-Si would be $1 \mu\text{m}$ in 1000 sec for $D \geq 10^{-15} \text{ cm}^2/\text{sec}$. The loss of material can be seen in Fig. 1(c), where the integrated amount of Ag observed (in both a-Si and c-Si) is plotted as a function of the interface position. We believe that regrowth in this regime is limited by transport of Ag out of the a-Si and into the bulk crystal.

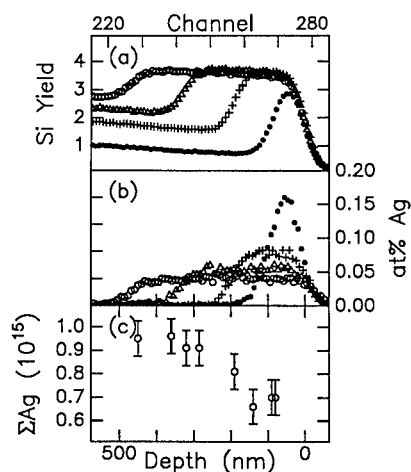


FIG 1. RBS spectra following the thermal anneal of Ag: channeling spectra of the Si (a), Ag concentration vs. depth (b), and total Ag detected vs. interface position (c) for unannealed (○), and 550°C anneals for 35 minute (Δ), 65 minute (+), and 100 minutes (●).

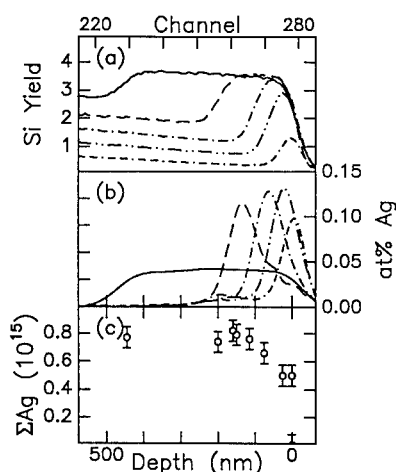


FIG 2. RBS Channeling spectra of the Si (a), smoothed Ag concentration vs. depth (b), and total Ag detected vs. interface position (c) of 325°C IBEEC regrowth for unirradiated (—), 1.0 (---), 1.6 (---), 1.8 (---), and $2.0 \times 10^{17} \text{ Ar}^+/\text{cm}^2$ (---). Detector resolution prevents measuring the actual Ag concentration at the interface.

After further annealing, a non-aligned layer at the surface is formed, shown by filled circles (●) in Fig. 1. Since this layer does not change with further annealing, we interpret it as the formation of polycrystalline Si (p-Si) in the near surface region. No further Ag loss is observed after the p-Si formation, since the remaining Ag can be segregated into the grain boundaries.

Ion beam enhanced regrowth of a-Si with Ag impurities is initially similar to that observed for Au.¹³ The diffusivity of Ag, also radiation dominated, is an order of magnitude higher than for Au.¹² A segregation spike is built up ahead of the moving, planar interface, with a characteristic width $D/v \approx 50 \text{ nm}$. Due to detector resolution, the peak concentration cannot be directly measured with RBS. The segregation spike moves with the interface, building up until steady state is reached where the amount of material segregated behind the spike is equal to the material entering the spike at the front edge. For Au, the steady state corresponds to Au being trapped in the c-Si at the original concentration. In marked contrast, the trapped Ag in the c-Si is only at 0.01 at%, well below the initial concentration of 0.045 at%. The balance of the Ag in the c-Si diffuses rapidly into the bulk. Therefore, only 20% of the Ag is retained in the c-Si near the interface. This behavior is shown in Fig. 2 for regrowth at 325°C, where again (a) is the Si spectra, (b) is the smoothed Ag concentration profiles, and (c) is the integrated Ag vs. interface position. For continued irradiation after regrowth is complete, nearly all of the Ag eventually disappears from the near surface region, including the previously trapped material. Small amounts of Ag remain near the surface and near the original a-Si/c-Si interface, probably associated with end of range damage from the original amorphizing Si implant.

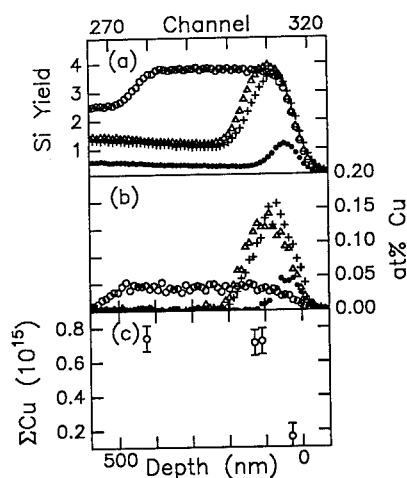


FIG 3. RBS Channeling spectra of the Si (a), Cu concentration vs. depth (b), and total Cu detected vs. interface position (c) of 550°C anneals for unannealed (o), 35 minutes (Δ), 75 minutes (+), and 100 minutes (●).

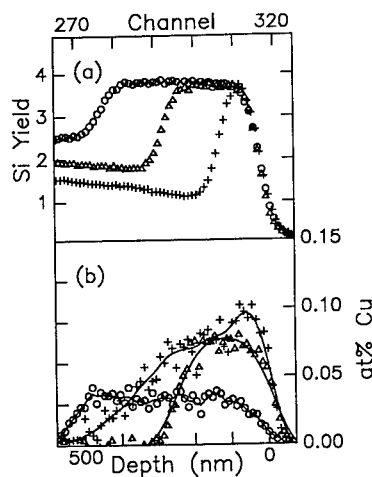


FIG 4. RBS Channeling spectra of the Si (a) and Cu concentration vs. depth (b) for an unirradiated sample (o), a low initial concentration with $8.2 \times 10^{16} \text{ Ar}^+/\text{cm}^2$ (Δ), and a higher concentration sample irradiated with $1.2 \times 10^{17} \text{ Ar}^+/\text{cm}^2$ (+). The drastic change in segregation behavior is readily apparent. The lines are meant only as a guide for the eye.

Results for Cu

Furnace regrowth of Cu doped a-Si at 550°C is also initially epitaxial. Like Ag, the Cu is confined to the narrowing a-Si layer until the concentration reaches $\sim 0.15 \text{ at\%}$. Further annealing from this point leads to a non-planar interface and loss of Cu into the bulk. TRR measurements by Olson on similar sample structures confirms that the interface is non-planar, indicated by a loss of interference contrast.¹⁷ As the interface degrades, regrowth continues as Cu is shed out of the a-Si. We have observed nearly complete regrowth, with concomitant loss of the Cu. Fig. 3. shows this range of behavior for Cu doped a-Si.

IBEEC of Cu samples also initially leads to normal segregation. In this case, however, the diffusivity of Cu is sufficiently large⁷ that no segregation spike is seen in the data; the expected width is on the order of $1 \mu\text{m}$. It should be noted that the Cu diffusivity is dominated by the thermal component even under irradiation, unlike either Au or Ag.

When the Cu concentration exceeds $\sim 0.13 \text{ at\%}$, the segregation characteristics change dramatically. Large amounts of Cu are shed into the c-Si, with the concentration in the a-Si remaining near the 0.13 at\% level. This behavior is similar to the thermal case, except that at 325°C Cu does not diffuse fast enough to disappear into the c-Si. Also, unlike the thermal anneals, the interface appears to remain planar in the RBS spectra. Fig. 4. shows an initial and two final spectra, with the final spectra coming from two different initial concentration samples. These concentrations illustrate the dramatic change in behavior of the segregation characteristics.

Discussion – Thermal Anneals

During thermal anneals, a-Si doped with Au, Ag, or Cu behave qualitatively the same and low levels of these impurities do not affect the quality of epitaxy. The major differences during the epitaxy process is in the SPE rate. Au is observed to enhance the epitaxy rate by

up to a factor of 50, while Cu and Ag have shown at most enhancements of 3.^{5,6,17} In our work, the Cu doped samples regrow faster than Ag. The data presented here indicate that the epitaxy breaks down at a critical interfacial concentration of the impurity, ~ 0.15 at% for Cu and ~ 0.08 at% for Ag at 550°C. TRR data from Olson shows a loss of interference contrast when the a-Si layer with $1 \times 10^{15} \text{ cm}^{-2}$ Cu was about ~ 120 nm thick, leading to an estimated concentration of 0.16 at%, in close agreement with the measurements presented here. Once the interface becomes non-planar, further recrystallization is probably limited by transport of the impurity away from the a-Si layer. In this case, it is not surprising that Cu doped a-Si regrows faster than Ag doped samples since Cu has both a higher solubility and diffusivity in c-Si.^{7,14} It appears that for Ag, the epitaxy is slowed sufficiently that the competing process of p-Si nucleation can be observed.

It should be noted that the peak as-implanted concentration of Ag (≈ 0.25 at%) was higher than that observed in the p-Si. However, this implanted peak subsequently diffused to a uniform concentration in the a-Si layer indicating that it is not *just* the concentration of Ag in the a-Si that leads to p-Si formation, *i.e.*, we have not yet measured the solid solubility limits of Au, Ag or Cu in a-Si.

Discussion – IBEEC

Au in a-Si is segregated and trapped in an apparently classical segregation manner during IBEEC, but with trapping of Au eight orders of magnitude above the solid solubility. The steady state segregation spike is observed, and Au is trapped in c-Si at the initial concentration. In the case of Au, the radiation controls both the regrowth rate and Au diffusivity; thermal components are negligible at these temperature. Since the interfacial concentration of Au during IBEEC far exceeds that observed thermally, a radiation enhanced solubility effect is also indicated.

Ag segregation also occurs in the radiation controlled regime during IBEEC. However, very different segregation behavior is observed. The initial buildup of the segregation spike is similar to the Au case with a wider spike due to the higher diffusivity of Ag. However, the steady state behavior is markedly different. The fact that the steady state trapped level in the c-Si is less than the initial concentration has never, to our knowledge, been observed previously. This effect may be caused by a limited number of defects available to trap Ag in c-Si.

Cu provides the contrasting case. For these samples, only the regrowth is controlled by the ion beam while the diffusivity, in this temperature range, is thermal. The segregation behavior at 325°C undergoes a radical change when the interfacial concentration approaches 0.13 at%, a concentration close to the thermal breakdown value. As in the Ag case, the interface remains planar, even after this point. The Cu shed into the c-Si is slowly diffusing away from the interface. There is an anomaly in the fact that although Cu is considered the faster diffuser, it does not exhibit the same rapid component in the diffusivity observed for Ag.

Conclusions

We have compared and contrasted impurity behavior under two distinctly different recrystallization regimes, thermal and ion beam enhanced. The fast diffusers Cu, Ag, and Au respond similarly to thermal annealing. The epitaxy confines the impurity in the a-Si layer until a critical interfacial concentration is reached. Away from the a-Si/c-Si interface higher concentrations of the impurities are observed to diffuse normally, indicating that the critical concentrations observed here are an interfacial property. Once this critical interface concentration has been reached, further annealing results in breakdown of the interface and loss of solute. This result suggests that regrowth is limited by transport of the impurity out of the a-Si layer and into the bulk, a process dependent on the solid solubility and c-Si diffusivity of the impurity.

Ion beam enhanced epitaxy, however, leads to a range of behaviors. On one extreme is the apparently classical, yet non-equilibrium, segregation and trapping of Au. The intermediate case, Ag, behaves similarly to Au except that steady state segregation loses material due to rapid diffusion of some fraction of the trapped material. The opposite extreme is Cu, which

is similar to the thermal case, except that the interface does not break down at the critical concentration. Although the interface is being driven in a highly non-equilibrium fashion by the ion beam, the Cu appears to behave in an equilibrium fashion. This is not the case for Au and Ag since the diffusivities, and potentially the solubilities, are dictated by radiation effects.

Work at Cornell was supported by NSF-PYIA (J. Hurt). We also acknowledge the National Nanofabrication Facility (NSF) at Cornell for sample fabrication facilities.

References

- ¹ L. Csepregi, J. W. Mayer, and T. W. Sigmon, *Physics Letters* **54A**, 157 (1975).
- ² G. L. Olson, S. A. Kokorowski, J. A. Roth, and L. D. Hess, *Mat. Res. Soc. Symp. Proc.* **13**, 141 (1983).
- ³ J. S. Custer, Michael O. Thompson, and P. H. Bucksbaum, *Appl. Phys. Lett.* **53**, 1402 (1988).
- ⁴ E. F. Kennedy, L. Csepregi, J. W. Mayer, and T. W. Sigmon, *J. Appl. Phys.* **48**, 4241 (1977).
- ⁵ G. L. Olson and J. A. Roth, *Mat. Sci. Reports* **3**, 3 (1988).
- ⁶ D. C. Jacobson, J. M. Poate, and G. L. Olson, *Appl. Phys. Lett.* **48**, 118 (1986).
- ⁷ J. M. Poate, D. C. Jacobson, J. S. Williams, R. G. Elliman, and D. O. Boerma, *Nucl. Instr. and Meth. B* **19/20**, 480 (1987), and references therein.
- ⁸ G. Holmen and P. Hogberg, *Radiat. Eff.* **12**, 77 (1972).
- ⁹ I. Golecki, G. E. Chapman, S. S. Lau, B. Y. Tsaur, and J. W. Mayer, *Physics Letters* **71A**, 267 (1979).
- ¹⁰ J. Nakata, and K. Kajiyama, *Appl. Phys. Lett.* **40**, 686 (1982).
- ¹¹ J. Linnros, G. Holmen, and B. Svensson, *Phys. Rev. B* **32**, 2270 (1985).
- ¹² F. Priolo, J. M. Poate, D. C. Jacobson, J. L. Batstone, and S. U. Campisano, *Ion Beam Modification of Materials*, Tokyo, 1988 (to be published).
- ¹³ J. M. Poate, J. Linnros, F. Priolo, D. C. Jacobson, J. L. Batstone, and Michael O. Thompson, *Phys. Rev. Lett.* **60**, 1322 (1988).
- ¹⁴ F. A. Trumbore, *Bell Syst. Tech. Journal*, **39**, 205 (1960).
- ¹⁵ F. Priolo, J. L. Batstone, J. M. Poate, J. Linnros, D. C. Jacobson, and Michael O. Thompson, *Appl. Phys. Lett.* **52**, 1043 (1988).
- ¹⁶ Lucien Wielopolski and Robin P. Gardner, *Nucl. Instr. and Meth.* **133**, 303 (1976).
- ¹⁷ G. L. Olson, private communication

STUDY OF ENHANCED SOLID PHASE EPITAXY OF AMORPHOUS SILICON WITH LOW CONCENTRATIONS OF IMPLANTED PHOSPHOROUS

YOUNG-JIN JEON¹, WON WOO PARK², M. F. BECKER^{1,2}, and
RODGER. M. WALSER^{1,2,3}

¹Center for Materials Science and Engineering, The University of Texas, Austin, TX 78712, U.S.A., ²Department of Electrical and Computer Engineering, The University of Texas, Austin, TX 78712, U.S.A., ³J. H. Herring Centennial Professor in Engineering

ABSTRACT

In this work we measured the functional dependence of the solid phase epitaxial (SPE) regrowth of amorphous silicon on the implanted phosphorous concentration, N_p . The growth rates of self-ion amorphized layers in silicon wafers with (100) substrate orientation were measured by *in situ*, high precision, isothermal cw laser interferometry for temperatures from 460°C to 590°C, and concentrations in the range $2 \times 10^{17} \text{ cm}^{-3} < N_p < 4 \times 10^{20} \text{ cm}^{-3}$. For low impurity concentrations, the fractional increase in the intrinsic SPE growth velocity $\Delta V/V_i$ depended linearly on N_p as previously established for boron. For a given impurity concentration, the relative change V/V_i decreased with increasing annealing temperature.

INTRODUCTION

Silicon solid phase epitaxy has been widely studied for implanted layers [1], and for amorphous layers deposited on single crystal silicon [2,3]. Currently, SPE is of interest in creating shallow p⁺-n junction [4], three-dimensional silicon on insulator structures [5], and for monolithic hot-electron devices [6], all examples of the continued pressure for higher packing densities for very large scale integration. Important information about the SPE of amorphous silicon has been derived from experimental studies of the electronic impurity effect, the existence of which is unambiguously established by the observation of a compensation effect in SPE [1,7,8]. Recent attempts to model this process have concentrated on determining the functional dependence of the growth velocity, V , of the amorphous-crystalline interface in SPE on the impurity concentration [9,10]. This work established that, for low implanted boron concentrations, the fractional change in the intrinsic SPE growth velocity $\Delta V/V_i$ depended linearly on the implanted boron concentration, N_B . For all annealing temperatures (450, 475, 500, 525 and 550°C), we found that $\Delta V/V_i = N_B/N_i$ where $N_i = N_{i0} \exp(-E_i/kT)$ was a thermally activated factor determined experimentally. The primary objective of the present study was to determine whether a similar relationship would hold for implanted phosphorous impurities.

EXPERIMENTAL

In this work, we utilized a CW laser interferometer technique introduced by Olson and co-workers [11] for in-situ, continuous monitoring of the reflectivity of amorphous layers on silicon wafers during annealing. Annealing was performed in a vacuum of 10^{-6} – 10^{-7} Torr and in the temperature range of 460–590°C at 10°C intervals, i.e. at 14 annealing temperatures. The details of the entire system were described in Ref.[9]. Three different phosphorous concentrations were implanted in three wafers (CZ., 2 inch diameter, $<1-0-0>$, $1-5 \Omega \cdot \text{cm}^{-1}$) after amorphization by self-ion implantation with energies and doses [9] that produced an approximately 3200 Å thick amorphous layer (3500 Å for the P1 sample). Table 1 gives the ³¹P ion implantation schedules used.

The impurity concentration profiles to a depth of 4000 Å were determined by secondary ion mass spectroscopy (SIMS) measurements of as-implanted wafers. The results are shown in Fig.1 for samples with three different doses. Though the same implantation energy was used for all samples, the depth of the peak concentration in the P2 sample was shallower than those of the P1 and P3 samples. The reason for this inconsistency is not known. The growth rates as a

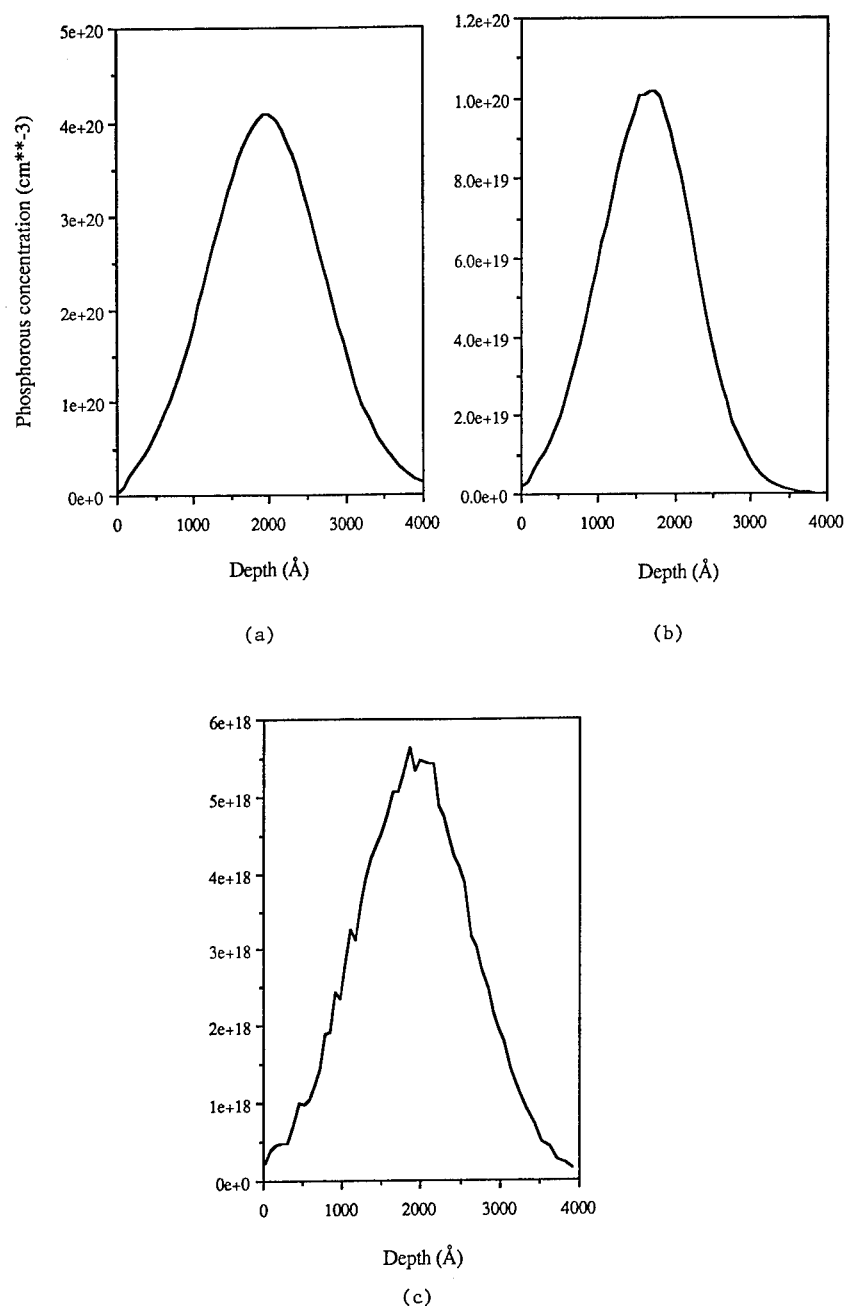


Fig.1. Phosphorous concentration-depth profiles of as-implanted samples by secondary ion mass spectroscopy: (a) P1, (b) P2 and (c) P3.

Table 1. ^{31}P ion implantation parameters employed to produce the distribution of impurity atoms in the amorphous layer.

Sample	Ion	Energy (KeV)	Dose (cm^{-2})
P1	^{31}P	110	3.7×10^{15}
P2	^{31}P	110	9.9×10^{14}
P3	^{31}P	110	6.2×10^{13}

function of the as-implanted impurity concentration were determined by the method discussed in [9] and are plotted in Fig. 3.

RESULTS AND DISCUSSION

The effect of phosphorous on SPE could be measured at all concentrations except in the P3 sample for $N_{\text{P}} < 5.4 \times 10^{18} \text{ cm}^{-3}$. Given the sensitivity of our measuring system, the ΔV at these low concentrations, obtained by linearly extrapolating the results for larger N_{P} shown from Fig.3, should have been detected. The ineffectiveness on SPE, of impurity concentrations below some limit, must ultimately be incorporated in SPE models.

The experimental results for the P2 sample in Fig.2 show that the SPE velocity was different for equal concentrations on either side of the as-implanted phosphorous impurity profile obtained from SIMS. The growth rate on the deep side of the peak concentration (at $\sim 1700 \text{ \AA}$ depth) was smaller than that on the shallow side as shown in Fig.2. This result is opposite to that reported by Olson et al.[12] who used Pearson IV coefficients determined by SIMS measurement to calculate a donor (arsenic) concentration profile. The asymmetry in the velocity and concentration profiles is quite sensitive to small variations in the position of the peak impurity concentration. Our SIMS profiles have a small residual uncertainty that we have not resolved. That uncertainty prevents us from addressing this issue at this time, but this question will be considered in our future work. The other issues raised in the balance of this paper were not significantly influenced by the uncertainty in the SIMS data.

The SPE regrowth rate increased linearly with the implanted phosphorous concentration to $N_{\text{P}} \approx 4.2 \times 10^{19} \text{ cm}^{-3}$ as shown in Fig.3. Data from only 4 representative annealing temperatures are shown in Fig.3 with data at 10 others omitted for clarity. This linear region was also found for boron impurities in low concentrations [10]. Fig.4 shows that, in the linear range, the

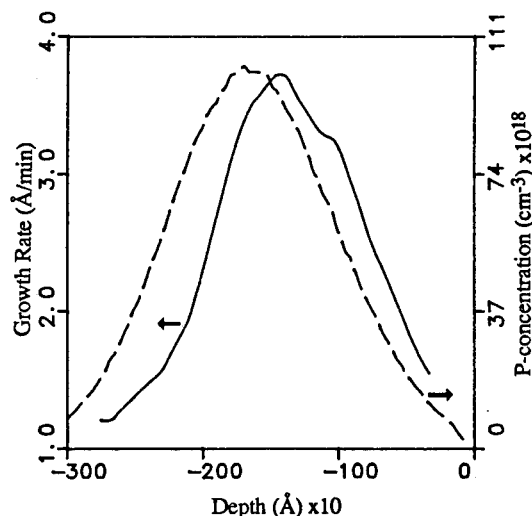


Fig.2. Regrowth rate and implanted concentration profile for sample P2 at 470°C.

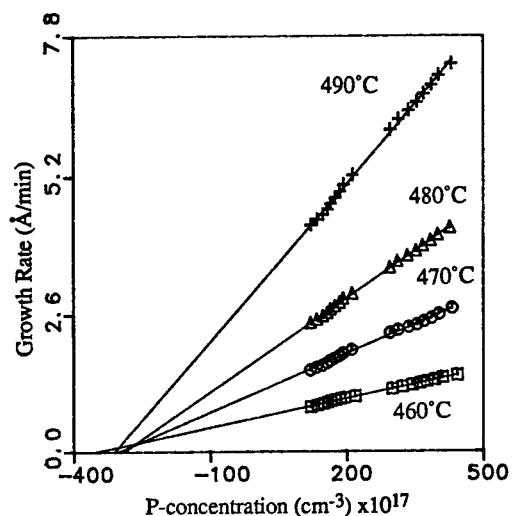


Fig.3. Regrowth rates as a function of phosphorous concentration in linear region (sample ; P2). Solid lines are least square fitting lines.

normalized regrowth data from all 14 annealing temperatures satisfied a general equation of the form: $V/V_i = 1 + N/N_i$, identical to that found for boron [10]. N_i is a temperature dependent quantity obtained from an activation plot of the intersections of the regrowth data (e.g. Fig.3) with the horizontal axis. Similarly, V_i was obtained from an activation plot of the intersections of the data with the vertical axis (nominal zero impurity concentration in Fig.3). The results :

$$\begin{aligned} N_i(T) &= 1.5 \times 10^{21} \times \exp(-0.25/kT) \text{ cm}^{-3} \\ V_i(T) &= 1.5 \times 10^{18} \times \exp(-2.68/kT) \text{ Å/min} \end{aligned} \quad (1)$$

were used to normalize the growth rate vs. concentration curves, at all measurement temperatures, in the form shown in Fig.4. Similar data were obtained for boron [13].

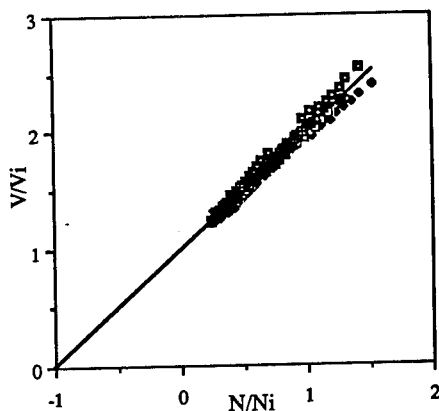


Fig.4. Normalized growth rate vs. normalized impurity concentration for phosphorous implanted sample from all annealing temperature data. Solid line is least square fitting line for all data points.

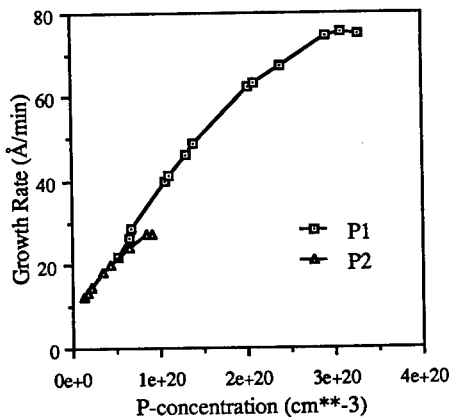


Fig.5. Regrowth rate as a function of implanted phosphorous concentration (annealing temperature ; 510°C).

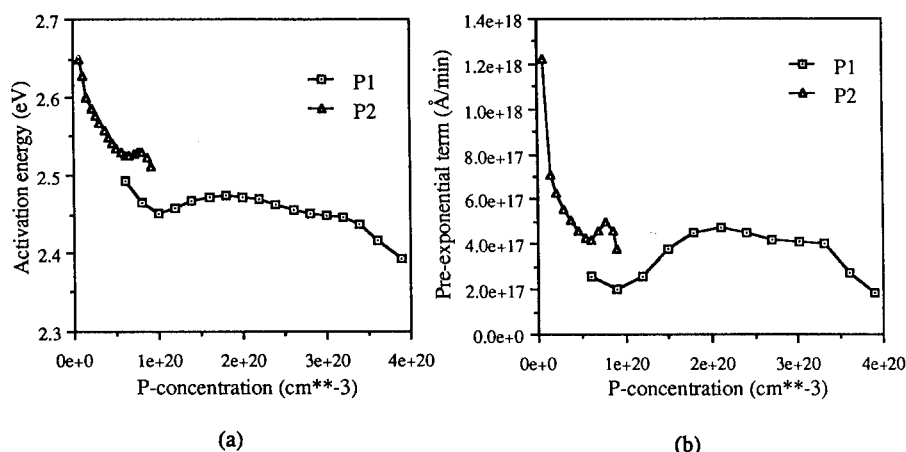


Fig.6. (a) Activation energy and (b) pre-exponential term of (100) silicon SPE as a function of phosphorous concentration.

For larger concentrations, the regrowth velocity varied nonlinearly with the implanted phosphorous concentration as shown in Fig.5, and there were two different growth rates for the P1 and P2 samples over a portion of the concentration range. The different growth rates were measured in samples implanted with different doses as can be seen in Table 1.

The regrowth data for a constant composition could be fit to an Arrhenius equation from which apparent, impurity-modified activation energies and entropies could be determined as noted previously [9]. As shown in Fig.6(a) the result could be interpreted as an impurity-induced change in the intrinsic activation energy of (100) silicon SPE regrowth. Fig. 6 shows that both quantities decreased sharply for small N_p , but changed more gradually for concentrations larger than $\approx 1 \times 10^{20} \text{ cm}^{-3}$.

Alternatively, for a given value of N_p , the normalized velocity V/V_i could be determined as a function of temperature from the data; e.g. Fig.3. The result for $N_p = 3.0 \times 10^{20} \text{ cm}^{-3}$ in Fig. 7 shows that V/V_i decreased with annealing temperature. Similar variations with temperature were obtained for phosphorous concentrations in the range from 5.4×10^{18} to $3.6 \times 10^{20} \text{ cm}^{-3}$.

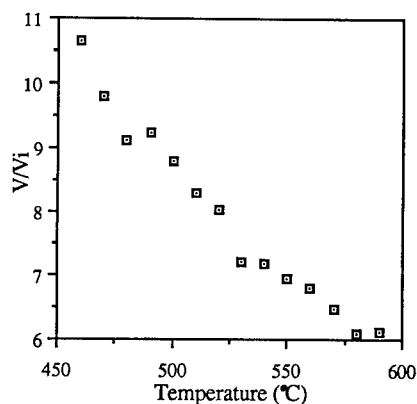


Fig.7. Variation of V/V_i as a function of annealing temperature with implanted phosphorous concentration $3 \times 10^{20} \text{ cm}^{-3}$.

SUMMARY

The results of this study confirmed that the fractional change in the SPE velocity in (100) silicon is linearly dependent on the implanted phosphorous impurity concentrations in the range $5.4 \times 10^{18} \text{ cm}^{-3}$ to $4.3 \times 10^{19} \text{ cm}^{-3}$. The fitting parameters, i.e. the pre-exponential and activation energy terms in N_i and V_i , were determined and were found to be comparable to those determined previously for boron [13]. The experiments also showed that phosphorous concentrations below $\approx 5 \times 10^{18} \text{ cm}^{-3}$ had no measurable effect on SPE. Direct plots of the data showed that, for a given impurity concentration, the ratio of the impurity-modified SPE velocity to the intrinsic velocity, decreased with increasing temperature.

ACKNOWLEDGMENT

This research was supported by funds received from the state of Texas under the Texas Advanced Technology Research Program. We are grateful to D. Goodnight for assistance in ion implantation.

REFERENCES

1. G.L. Olson and J.A. Roth, Materials Science Reports **3**(1), 1-78 (1988).
2. L.S. Hung, S.S. Lau, M. von Allmen, J.W. Mayer, B.M. Ullrich, J.E. Baker, P. Williams, and W.F. Tseng, Appl. Phys. Lett. **37**, 909 (1980).
3. Y. Kunii, M. Tabe, and K. Kajiyama, Jpn. J. Appl. Phys. **21**, 1431 (1982).
4. M.C. Ozturk, J.J. Wortman, and R.B. Fair, Appl. Phys. Lett. **52**(12), 963 (1988).
5. Y. Kunii, M. Tabe, and K. Kajiyama, J. Appl. Phys. **54**, 2847 (1983).
6. J.M. Shannon and B.J. Goldsmith, Thin Solid Films **89**, 21 (1982).
7. A. Lietoila, A. Wakita, T.W. Sigmon, and J.F. Gibbons, J. Appl. Phys. **53**(6), 4399 (1982).
8. I. Suni, G. Goltz, M.G. Grimaldi, and M-A. Nicolet, Appl. Phys. Lett. **40**(3), 269 (1982).
9. W.W. Park, M.F. Becker, and R.M. Walser, J. Mater. Res. **3**(2), 298 (1988).
10. W.W. Park, M.F. Becker, and R.M. Walser, Appl. Phys. Lett. **52**(18), 1517 (1988).
11. G.L. Olson, J.A. Roth, L.D. Hess, and J. Narayan, Appl. Phys. Lett. **37**, 1019 (1980).
12. G.L. Olson, J.A. Roth, L.D. Hess, and J. Narayan, Mat. Res. Soc. Symp. Proc. **23**, 375 (1984).
13. op cit. Ref.10 ; $N_i(T) = 1.2 \times 10^{21} \times \exp(-0.27/kT) \text{ (cm}^{-3}\text{)}$ and $V_i(T) = 4.6 \times 10^{18} \times \exp(-2.75/kT) \text{ (Å/min)}$ were obtained from boron concentration profiles of as-implanted samples obtained by SIMS measurements. This procedure yields slightly different values than those obtained in Ref.10 from calculated profiles by the Pearson IV method.

INFLUENCE OF PHOSPHORUS DOPANT CONCENTRATION ON RECRYSTALLIZATION OF BURIED AMORPHOUS LAYERS IN Si(100) PRODUCED BY CHanneled IMPLANTS

R.J. SCHREUTELKAMP, K.T.F. JANSSEN⁺ AND F.W. SARIS

F.O.M. Institute for Atomic and Molecular Physics, Kruislaan 407, 1098 SJ Amsterdam, The Netherlands

+ Philips Research Laboratories, p.o. box 80.000, 5600 JA Eindhoven, The Netherlands

J.F.M. WESTENDORP AND R.E. KAIM

ASM Ion Implant, 123 Brimbal Avenue, Beverley, MA 01915, USA

Abstract

Buried amorphous layers are produced in Si(100) by implantation of 100 keV P⁺ and Si⁺ ions under channeling condition along the <100>-direction. Rutherford Backscattering Spectrometry in combination with channeling shows that a continuous buried amorphous layer with a thickness of 1300 Å results under a crystalline toplayer with a thickness of 600 Å. After Solid Phase Epitaxy a highly concentrated defect layer remains for all implants at the depth where the two amorphous/crystalline interfaces of the buried amorphous layer meet. Planar channeling along (100)-direction shows that dislocation loops are present after SPE regrowth at the 'interface' of the two crystalline regions for all implants. The size of the dislocation loops becomes smaller in the presence of phosphorus. Moreover, channeling analysis shows that in case of Rapid Thermal Annealing treatment in addition to the SPE regrowth process the defect structures present after full recrystallization can be more easily dissolved in case of the phosphorus implants as compared to the silicon self implant.

1. Introduction

Channeled ion implantation, with the major axis aligned with the incident ion beam, is an attractive alternative to conventional non-zero tilt angle ion implantation. In channeling condition, deep penetration of dopants at modest ion energies can be achieved and damage levels are significantly reduced. Moreover, ion beam shadowing by high aspect ratio features in IC manufacturing is prevented.

For conventional ion implantation into semiconductor materials (energies up to 200 keV) damage annealing has been extensively studied and reviewed over the years [1]. Much insight has been gained on post-implantation processes like Solid Phase Epitaxy (SPE), implantation induced defect formation and annihilation during annealing [2,3,4]. However, for high energy implants where larger ion penetration depths are involved, the mechanisms of defect annihilation appear to be quite different. This is a result of the fact that during high energy implantation a buried defect layer is produced. Because of the buried defect layer formation in case of high energy implants, the surface can not act as an effective sink for defects as it can in case of low energy implants [5]. Furthermore, in case of high dose implants at high energy buried amorphous layers can be produced which implies annealing of damage from two fronts [6]. This is contrary to the annealing behaviour of amorphized layers produced by high dose implants at low energy [7].

We have shown in earlier work [8,9] that doping profiles which are highly uniform across 150mm silicon wafers can be achieved with channeled implantation. Phosphorus ions with an energy of 100 keV were implanted into Si(100) and buried amorphous layers with well defined amorphous/crystalline interfaces were formed. Thus, defect layers produced in channeled implantations, are comparable to those reported with MeV implants [6].

In this paper, preliminary results on the damage annealing of 100 keV P⁺ and Si⁺ channeled implants are reported, using SPE and Rapid Thermal Annealing (RTA). The presence of

residual defects at the depth where the two interfaces meet during SPE has been studied by Rutherford Backscattering Spectrometry (RBS) and channeling. The influence of dopant concentration in the amorphous layer on the resulting crystalline quality after annealing has been investigated.

2. Experimental

Implantations were performed with the ASM 220 medium current ion implanter [10]. All implants were performed under channeling condition along the $\langle 100 \rangle$ -direction of Si(100). Highly uniform doping profiles in silicon wafers of sizes up to 150mm diameter were obtained for different channeled implants [8,9]. All implants were performed at room temperature. Typical beam current on target was 100 μA to avoid beam heating effects during implantation. Dual implants of $^{28}\text{Si}^+$ and $^{31}\text{P}^+$ were performed in 125mm diameter, 1 Ωcm , p-type CZ Si-wafers. For all implants the total dose was kept at $1\text{E}15/\text{cm}^2$. Beam contamination due to N_2^+ was less than 1%. This has been determined by measuring the ratios of the silicon isotopes present in the beam before implantation and comparison with the natural abundances.

Rutherford Backscattering Spectrometry (RBS) with MeV He^+ ions in combination with planar and axial channeling was used to investigate damage in the as-implanted as well as in the annealed samples.

Annealing treatments were performed in a vacuum furnace at a base pressure of 10^{-7} Torr. Rapid Thermal Annealing (RTA) was done with an AG Associates Heatpulse 410 Rapid Thermal Processor under a continuous Ar-flow.

3. Results and Discussion

To investigate the role of phosphorus on the annealing behaviour of defects the phosphorus dose was varied between $5\text{E}13/\text{cm}^2$ and $1\text{E}15/\text{cm}^2$. In addition, implants of silicon were performed to obtain a total dose of $1\text{E}15/\text{cm}^2$. Furthermore, single implants of $1\text{E}15 \text{ Si}^+/\text{cm}^2$ and $1\text{E}15 \text{ P}^+/\text{cm}^2$ were performed. Due to an almost identical mass the total damage produced per incident ion is nearly the same. Therefore the buried amorphous layer resulting from these high dose channeled implants are nearly identical for all implants as can be observed from the RBS and channeling analysis in figure 1a. Completely amorphized buried layers are formed for all implants.

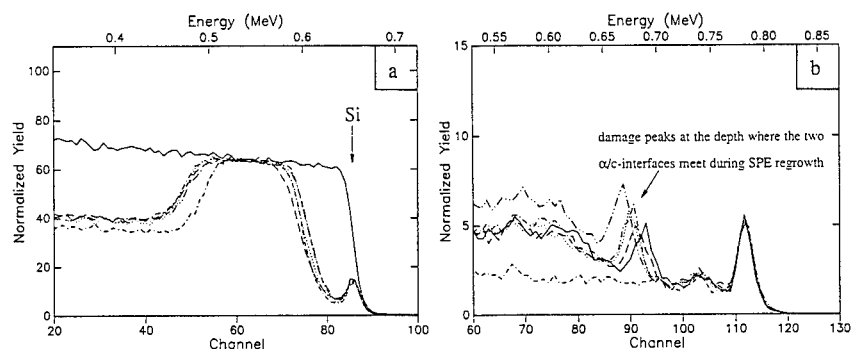


Fig 1 a) Damage profiles in as-implanted Si for 100 keV dual implants of Si^+ and P^+ as determined with RBS in combination with channeling. Total implanted dose was $1\text{E}15/\text{cm}^2$. b) RBS channeling spectra of damage profiles after SPE at 550°C for 1hr. (---) $1\text{E}15 \text{ Si}^+/\text{cm}^2$; (---) $1\text{E}15 \text{ P}^+/\text{cm}^2$.

The resulting structure after implantation consists of a crystalline silicon toplayer with a thickness of approximately 600 Å and a buried amorphous layer with a thickness of approximately 1300 Å.

The resulting damage structure differs from random condition implantation, under further identical implantation conditions, because of the channeling effect. The thickness of the buried amorphous layer, however, is almost identical to the thickness obtained after random condition implantation [13]. This is because only for low dose (i.e. $<5 \times 10^{13} \text{ P}^+/\text{cm}^2$) implants a relatively high fraction of the implanted ions becomes well-channeled, while for higher doses the incoming ions will be channeled only in the near-surface region [9]. For all dual implants the phosphorus was implanted first. Although in case of a subsequent silicon implant distortion of the phosphorus profile will occur mainly because of ion mixing phenomena, this effect is not regarded to be of much importance for the present study.

Figure 1b shows RBS channeling spectra for all implants after annealing for 1 hr at 550°C. This annealing time of 1 hr is much longer than the time needed for full recrystallization of a Si layer amorphized by self implantation with a thickness of 1300 Å [2]. After the SPE regrowth process the buried amorphous layers are fully recrystallized by the movement of two amorphous/crystalline interfaces. Where the α/c -interfaces meet a damage peak remains. The depth of the peak position is dependent on the phosphorus dose. For all implants the peak concentration of the phosphorus profile lies near the backside of the buried amorphous layer [12].

In table 1 the depth d_2 corresponding to the position of the residual damage peak after SPE is given for all implants. The depths d_1 and d_3 correspond to the positions of the frontside and backside α/c -interfaces of the buried amorphous layer, respectively.

Implant	$d_1(\text{\AA})$	$d_2(\text{\AA})$	$d_3(\text{\AA})$	$(d_3-d_2)/(d_2-d_1)$
$1.0 \times 10^{15} \text{ Si}^+/\text{cm}^2$ $0.0 \times 10^{20} \text{ P}^+/\text{cm}^2$	690	1310	1955	1.04(0.05)
$9.5 \times 10^{14} \text{ Si}^+/\text{cm}^2$ $5.0 \times 10^{13} \text{ P}^+/\text{cm}^2$	560	1200	1975	1.22(0.07)
$8.0 \times 10^{14} \text{ Si}^+/\text{cm}^2$ $2.0 \times 10^{14} \text{ P}^+/\text{cm}^2$	635	1210	1960	1.31(0.11)
$5.0 \times 10^{14} \text{ Si}^+/\text{cm}^2$ $5.0 \times 10^{14} \text{ P}^+/\text{cm}^2$	560	1165	1915	1.25(0.10)
$0.0 \times 10^{20} \text{ Si}^+/\text{cm}^2$ $1.0 \times 10^{15} \text{ P}^+/\text{cm}^2$	635	1100	1770	1.45(0.20)

Table 1 Depths of the α/c -interfaces of the buried amorphous layers and depth of the residual damage peak after SPE for all considered implants. d_1 and d_3 represent the positions of the front- and backside α/c -interfaces, respectively, while d_2 represents the position of the residual damage peak. The differences in the ratio $(d_3-d_2)/(d_2-d_1)$ are explained in the text.

During SPE the interface at depth d_1 moves inward and the interface at depth d_3 moves towards the surface. The interfaces meet at the depth d_2 . Phosphorus influences the SPE regrowth rate [14] and for the higher phosphorus concentrations we observe an increase in regrown layer thickness (d_3-d_2) with respect to the regrown layer thickness (d_2-d_1) as pointed out in the last column of table 1.

In figure 1b the spectrum showing the highest amount of dechanneling near the position of the damage peak corresponds to the silicon implant without phosphorus. The amount of dechanneling decreases for a higher concentration of phosphorus.

All spectra in figure 1b show that besides the damage peak an amount of dechanneling can be observed at a depth corresponding to the position of the original α/c -interface at the backside. This amount of dechanneling only disappears after high temperature annealing (as will be discussed later).

A more detailed analysis of the damage remaining after SPE is possible with planar channeling measurements [15,16,17]. Figure 2a gives an example of a planar channeling measurement along (100)-direction in virgin Si and in Si implanted with $1E15 \text{ P}^+/\text{cm}^2$ after SPE at 550°C for 1hr. In case of the implanted silicon a noticeable increase in amount of dechanneling can be observed after SPE. From a depth of 850\AA to 1300\AA the amount of dechanneling strongly increases. This is exactly at the depth where the two α/c -interfaces have met. The cause of the increase in amount of dechanneling can be determined by energy dependent planar channeling measurements [15,17].

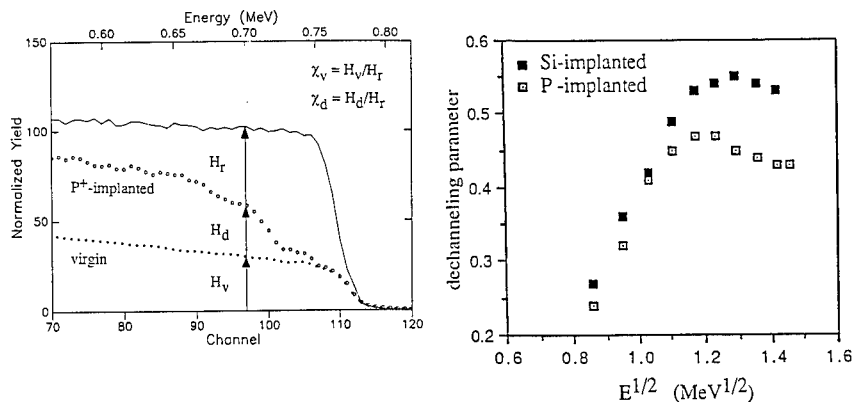


Figure 2 a) Planar channeling measurements for 1.4 MeV He^+ ions along (100)-direction for virgin and $1E15 \text{ P}^+/\text{cm}^2$ implanted Si after SPE at 550°C for 1hr. b) Energy dependence of the dechanneling parameter for (□) $1E15 \text{ P}^+/\text{cm}^2$ and (■) $1E15 \text{ Si}^+/\text{cm}^2$ implanted Si after SPE at 550°C for 1hr.

In figure 2a χ_d represents the channeled yield in the implanted silicon after SPE at 550°C for 1hr at a depth of 1300\AA while χ_v represents the channeled yield for unimplanted Si at the same depth. We have determined the minimum yield χ_d as a function of incident beam energy at the depth as pointed out in figure 2a. This minimum yield for implanted silicon can be compared with the minimum yield χ_v for virgin silicon. In figure 2b the dechanneling parameter $-\ln((1-\chi_d)/(1-\chi_v))$ is given as a function of the square root of the energy of the incident analysing beam. For the P⁺-implanted silicon we observe an $E^{1/2}$ dependence of the dechanneling parameter for low energies. Above $E^{1/2} = 1.3 (\text{MeV})^{1/2}$ the value of the dechanneling parameter decreases. This means that the dechanneling is caused by dislocation loops [17]. In case of the Si⁺-implant without phosphorus the dechanneling parameter increases upto a higher energy of the analysing beam. This is caused by the presence of larger

dislocation loops.

Thus, the residual dechanneling after SPE is caused by dislocation loops at the position where the two α/c -interfaces have met during SPE. A channeling He-beam will at this position penetrate the underlying crystal which is slightly shifted relative to the top crystalline Si. The peak in the axial channeling spectra can therefore be interpreted as an interface peak. This peak will only disappear after annealing at high temperatures as observed from the RTA results of figure 3a and 3b.

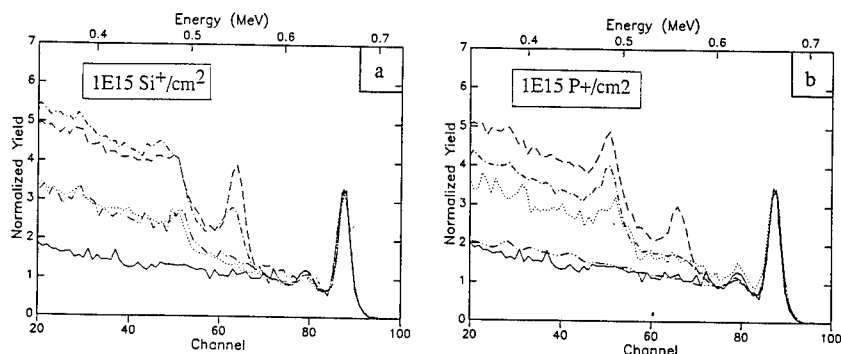


Fig. 3 a) RBS channeling measurements for $1E15 \text{ Si}^+/\text{cm}^2$ implanted Si after RTA treatment at (---) 800°C for 60s, (- - -) 900°C for 60s, (...) 1000°C for 60s and (- . -) 1000°C for 150s. In all cases SPE at 550°C for 1hr was performed as first annealing step.
 b) RBS channeling measurements for $1E15 \text{ P}^+/\text{cm}^2$ implanted Si after RTA treatment at (---) 800°C for 60s, (- - -) 900°C for 60s, (...) 1000°C for 60s and (- . -) 1000°C for 150s. In all cases SPE at 550°C for 1hr was performed as first annealing step

Figure 3a shows that after RTA at 800°C for 60s in addition to SPE no change in damage peak can be observed while at 900°C for 60s the peak starts to shrink. Although the damage peak disappears after 1000°C for 60s even for an annealing time of 150sec dechanneling can still be observed. This in case of the $1E15 \text{ Si}^+/\text{cm}^2$ implant.

In case of the P^+ -implanted silicon annealing of the damage structure can be accomplished more easily as observed from figure 3b. After annealing at 900°C for 60s the interface peak has completely disappeared while at 1000°C for 60s the amount of dechanneling is not higher than in case of virgin Si.

4. Conclusions

High dose channelled implants result in the formation of buried amorphous layers comparable to high dose MeV implants.

In both Si^+ as well as P^+ implanted Si dislocation loops are present after full recrystallization of the buried amorphous layer.

Residual damage present at the 'interface' of the two crystalline regions as well as at the depth of the original α/c -interface at the backside can be more easily annealed in case of the presence of phosphorus compared with Si self implantation.

Acknowledgements

We would like to thank drs. H. Jongste of the department for submicron technology of the Technical University of Delft for assistance with the RTA-annealings.

This work is part of the research program of the Stichting voor Fundamenteel Onderzoek der Materie (Foundation for Fundamental Research on Matter) and was made possible by financial support from the Nederlandse Organisatie voor Zuiver Wetenschappelijk Onderzoek (Netherlands Organization for Advancement of Pure Research).

References

- [1] J. Gyulai in ION IMPLANTATION Science and Technology, 2nd ed., edited by J.F. Ziegler (Academic Press, New York, 1988) pp. 93-163
- [2] G.L. Roth and J.A. Olson, *Mat. Res. Lett.* **2** (1988)
- [3] M. Tamura, *Phil. Mag.* **35**, 663 (1977)
- [4] T. Tokuyama, M. Miyao and N. Yoshihiro, *Jap. Journ. of Appl. Phys.* **17**, 1301 (1978)
- [5] M. Tamura, N. Natsuaki, Y. Wada and E. Mitani, *Nucl. Instr. and Meth.* **B21**, 438 (1987)
- [6] P.F. Byrne, N.W. Cheung, S. Tam, C. Hu, Y.C. Shih, J. Washburn and M. Strathman in Ion Implantation and Ion Beam Processing of Materials, edited by G.K. Hubler, O.W. Holland, C.R. Clayton and C.W. White (Mater. Res. Soc. Proc. **27**, Boston, MA, 1983) pp. 253-258
- [7] L. Csepregi, E.F. Kennedy, T.J. Gallagher, J.W. Mayer and T.W. Sigmon, *Journ. of Appl. Phys.* **48**, 4234 (1977)
- [8] J.F.M. Westendorp, R.E. Kaim, G.B. Odium, K.T.F. Janssen, R.J. Schreutelkamp and F.W. Saris, to be published in *Nucl. Instr. and Meth. B* (1988)
- [9] R.J. Schreutelkamp, F.W. Saris, J.F.M. Westendorp, R.E. Kaim, G.B. Odium and K.T.F. Janssen, to be published in *Nucl. Instr. and Meth. B*
- [10] D.W. Berrian, R.E. Kaim, J.W. Vanderpot and J.F.M. Westendorp, to be published in *Nucl. Instr. and Meth. B* (1988)
- [11] M. Tamura, N. Natsuaki, Y. Wada and E. Mitani, *Nucl. Instr. & Methods* **B21**, 438 (1987)
- [12] R.J. Schreutelkamp, F.W. Saris, K.T.F. Janssen, J.J.M. Ottenheim, J.F.M. Westendorp, R.E. Kaim and G.B. Odium, to be published
- [13] S. Prussin, David I. Margolese, and Richard N. Tauber, *J. Appl. Phys.* **57**, 180 (1985)
- [14] J.A. Roth and G.L. Olson in Beam-Solid Interactions and Transient Processes, edited by M.O. Thompson, S.T. Picraux and J.S. Williams (Mater. Res. Soc. Proc. **74**, Pittsburgh, PA, 1987) pp. 319-325
- [15] S.T. Picraux in Materials Analysis by Ion Channeling (Academic Press, New York, 1982) pp. 88-116
- [16] S.T. Picraux, D.M. Follstaedt, P. Baeri, S.H. Campisano, G. Foti and E. Rimini, *Rad. Eff.* **49**, 75 (1980)
- [17] H. Kudo, *Phys. Rev.* **B18**, 5995 (1978)

ION-ASSISTED REGROWTH OF DEPOSITED Si LAYERS MECHANISMS AND MORPHOLOGY

F. PRIOLO^{a)}, C. SPINELLA^{a)}, A. LA FERLA^{a)}, A. BATTAGLIA^{a)},
E. RIMINI^{a)}, G. FERLA^{b)}, A. CARNERA^{c)} AND A. GASPAROTTO^{c)}

a) Dipartimento di Fisica, Università di Catania, Catania (ITALY)

b) SGS-Thomson, Catania (ITALY)

c) Dipartimento di Fisica, Università di Padova, Padova (ITALY)

ABSTRACT

Ion-assisted regrowth of chemical vapor deposited amorphous Si layers was investigated for different cleaning procedures. The process was directly monitored by transient reflectivity measurements. The c-a interface stops at the deposited layer/substrate interface for doses depending on the effectiveness of the cleaning procedure in removing the native oxide. Small concentrations of twins are found in the regrown layer. Their amount is also correlated to the cleaning procedure. In oxygen implanted bare Si samples the ion-induced growth rate is reduced to 0.3 of the normal value at a peak O concentration of $1 \times 10^{21}/\text{cm}^3$. The results on the ion-induced regrowth of deposited layers are explained in terms of oxygen profile broadening during irradiation and retardation of the growth for the presence of dissolved O.

INTRODUCTION

Several attempts have been made to epitaxially deposit at relatively low temperatures ($\sim 800^\circ\text{C}$) Si layers onto single crystal Si substrates. The problems are related to the presence of an interfacial native oxide layer. Several procedures have been used to clean the substrates before deposition and in some cases [1] reasonable single crystals were obtained.

Alternatively, one can thermally regrow previously deposited amorphous Si (a-Si) layers. Solid Phase Epitaxial Growth (SPEG) by conventional thermal annealing can, however, be inhibited by the contaminants present at the interface. SPEG can be enhanced by ion irradiation[2-4]. In this case the regrowth occurs at temperature as low as 200°C and has an Arrhenius temperature dependence with an apparent activation energy of 0.3 eV. The ion-beam-induced growth rate is less sensitive to the presence of impurities dissolved in the a-layer with respect to pure thermal regrowth[4-5]. Recently[6-7] thin a-Si layers deposited onto single crystal substrates have been epitaxially regrown by a 600 keV Kr irradiation at 450°C . The regrowth occurs by a uniform layer by layer crystallization despite the presence of an interfacial oxide layer thick enough to prevent any regrowth by con-

ventional thermal annealing. In the present work we report a more detailed investigation of this process following the ion-induced regrowth *in situ* by transient reflectivity measurements. The influence of different cleaning procedures on the growth rate and on the defects present in the regrown layers has been investigated.

EXPERIMENTAL

Silicon layers, 50 nm thick, were deposited onto $\langle 100 \rangle$ single crystal substrates by chemical vapor deposition. Prior to deposition a set of substrates was cleaned with the FPN (H_2O : $(NH_4)_2HPO_4$: NH_4F : H_3PO_4) procedure a second set experienced just a dip in HF, and a third set was loaded into the reactor as received from the manufacture, with a 2-3 nm thick native oxide.

After deposition the samples were implanted at room temperature with a 150 keV Ge-beam to a dose of $5 \times 10^{14}/cm^2$. This implant ensures that the structure of the deposited layer is amorphous; moreover it forms an ~ 65 nm thick a-layer below the deposited layer/substrate interface.

The crystallization was induced by a 600 keV Kr beam electrostatically scanned over a 1 inch diameter sample area. During irradiation the samples were mounted on a resistively heated copper block whose temperature was varied in the range 350-500°C. The c-a interface motion was monitored *in situ* by transient reflectivity measurements. This technique has been extensively used in the past to study the pure thermal regrowth[8] and it has been recently applied also to the ion-induced regrowth[4,7]. A σ -polarized He-Ne laser beam was focussed onto the Kr-irradiated sample surface. The reflectivity of the sample will oscillate due to constructive and destructive interferences occurring between the light reflected from the surface and that from the advancing c-a interface. For instance, in the adopted set up, the change in reflectivity from a maximum to a contiguous valley corresponds to a displacement of the c-a interface of 33 nm. In our experiments, because of double reflection at the sample surface, the squared reflectivity is actually measured.

After irradiations the samples were analyzed by 2 MeV He^+ Rutherford backscattering (RBS) in combination with the ion channeling. Some selected samples were also analyzed by Transmission Electron Microscopy (TEM). The broadening of the interfacial oxygen was measured by Secondary Ion Mass Spectrometry (SIMS) using a Cs beam to sputter the surface.

RESULTS AND DISCUSSION

Fig.1a shows the reflectivity trace of a ~ 50 nm deposited a-Si layer amorphized with Ge ions and recrystallized by a 600 keV Kr-irradiation at 450°C. The data refer to a sample on which no cleaning procedure was adopted before the deposition. The reflectivity shows an initial oscillation followed by a plateau. This behavior is associated with the initial regrowth of

the a-layer formed by the Ge-implantation behind the deposited Si/substrate interface and with a subsequent halt at this interface. After an incubation dose, ϕ_p (which corresponds to the plateau between arrows in Fig. 1), the change in reflectivity reappears indicating that crystallization is propagating in the deposited layer. At a total dose of $\sim 6 \times 10^{15}/\text{cm}^2$, a single crystal is finally obtained as also detected by RBS and TEM analyses. Fig.1b shows the reflectivity trace of a sample cleaned in HF before deposition and irradiated under similar conditions. The behavior is also similar but the extent of the plateau is smaller.

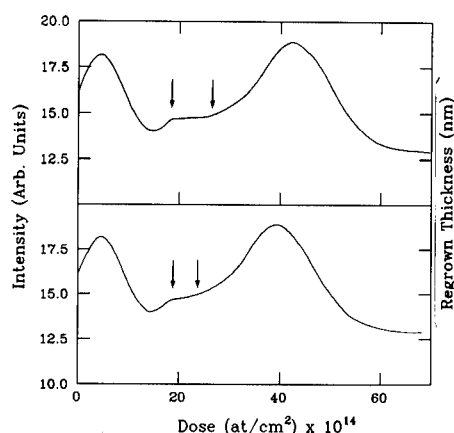


Fig.1 Reflectivity traces of deposited a-Si layers recrystallized with Kr ions at 450°C . Signals for layers deposited without any previous cleaning (a), and after an HF dip (b), are shown.

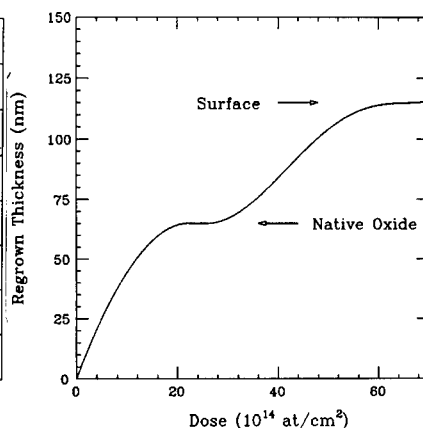


Fig.2 Regrown thickness vs. Kr-dose as obtained by a fit of the reflectivity trace shown in Fig.1a.

A plot of the regrown thickness versus Kr-dose, obtained by a fit of the trace shown in Fig.1a, is reported in Fig.2. The initial regrowth, the halt in the presence of the native oxide and the successive crystallization of the deposited layer are evident. The ion-induced growth rate can be easily obtained by making a derivative of the regrowth vs. dose curve. The results (continuous line) are shown in Fig.3 as a function of depth. For a comparison, the growth rate of an a-layer obtained by Ge-implantation of a $\langle 100 \rangle$ single crystal wafer and then recrystallized under the same conditions (600 keV Kr, 450°C) is also shown (dashed line). The growth rate of the implanted a-layer decreases continuously with decreasing depth, and this behavior is associated with the depth dependence of the energy lost into elastic collisions by the impinging Kr ions [4]. Similar behavior is observed for the growth rate of the deposited a-layer, but the rate falls to zero at depths close to the location of the native oxide.

We made similar experiments, changing the irradiation temperature and the cleaning procedure of the substrates. The results are similar but the delay

dose, ϕ_p , was dependent both on temperature and on substrate cleaning (see Fig.1a and Fig.1b). Fig.4 shows this delay dose as a function of the reciprocal temperature. Data for substrates cleaned with the FPN solution (\bullet), dipped in HF (\blacktriangle) and uncleaned at all before deposition (\blacksquare), are reported. The delay dose is similar for FPN- and HF-cleaned samples, but is somewhat higher in the case of substrates with an interfacial native oxide. The temperature dependence is linear in an Arrhenius plot with an activation energy of $\sim 0.41 \pm 0.1$ eV.

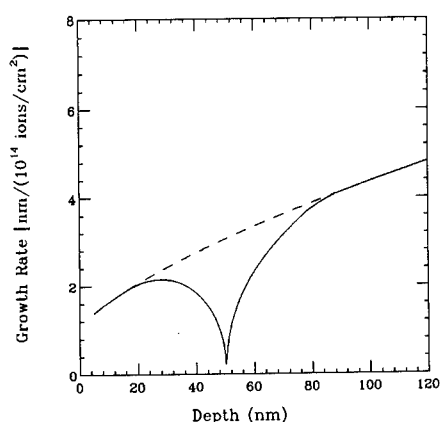


Fig.3 Growth rate vs. depth obtained by making a derivative of data shown in Fig.2 (continuous line). For a comparison the growth rate of a Ge-implanted a-layer is also shown (dashed line).

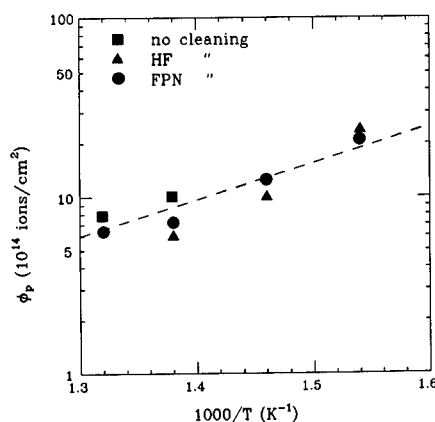


Fig.4 Delay Kr-dose (between arrows in Fig.1) as a function of the reciprocal temperature and for different cleaning procedures.

The decrease of the growth rate in the presence of the interfacial O, and its dependence on the cleaning procedure (i.e. on the O content at the interface), suggest that the ion-induced growth rate is, as in the pure thermal case[9], strongly dependent on O concentration. We have therefore investigated the ion-assisted regrowth of O-implanted a-Si layers. Preamorphized Si samples on $\langle 100 \rangle$ substrates have been implanted with 20 keV O to a dose of $6.2 \times 10^{15}/\text{cm}^2$ in order to obtain an almost Gaussian profile with a peak concentration of $1 \times 10^{21}/\text{cm}^3$. The ion-beam regrowth was induced by a 600 keV Kr irradiation at 450°C . The reflectivity trace was fitted to obtain a growth rate vs. depth plot. In order to eliminate the depth dependence introduced by the energy lost into elastic collisions, the growth rate has been normalized to that of a Ge-implanted sample regrown under the same conditions (Fig.3, dashed line). The normalized growth rate is shown in Fig.5. In the same figure is reported the implanted O profile as calculated from the program *Profile Code*[10]. The growth rate strongly depends on the O concentration. At a concentration of $1 \times 10^{21}/\text{cm}^3$, it is 0.3 of its normal value. It should be noted, however, that the same O concentration would

have decreased the growth rate during pure thermal annealing by more than 4 orders of magnitude (extrapolating data from ref.9). The average velocity in the ~ 2 nm interfacial region between the deposited a-layer and the substrate is instead ~ 0.2 nm/ 10^{14} ions/cm², i.e. 0.07 of its normal value. This value is consistent with a peak O concentration of more than 2×10^{21} /cm³.

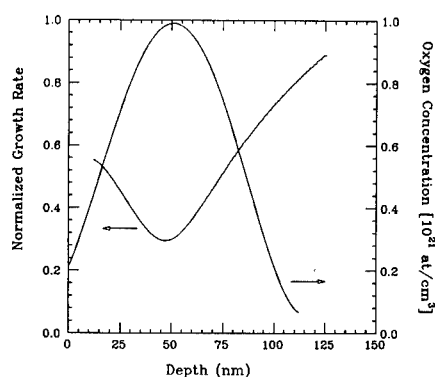


Fig.5 Normalized growth rate vs. depth for an O-implanted a-layer. The rate has been normalized to that of a Ge-implanted a-layer. The O profile is also reported.

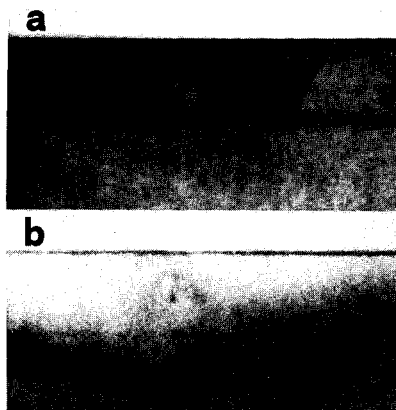


Fig.6 Cross sectional TEM images of a-layers deposited without cleaning (a), and after an HF dip and recrystallized with Kr ions at 450°C (b).

The mechanism responsible for the ion-induced regrowth of deposited layers is not yet completely understood. It has been tentatively proposed[7] that Kr-irradiation produces Si-O bond breaking at the interface and a subsequent enhanced diffusion of the oxygen atoms. As the O concentration at the interface decreases, the c-a front can pass through, and epitaxy occurs. This idea is supported by the observation that the interfacial O profile broadens under Kr irradiation (as observed by SIMS analysis). For instance, at 450°C, and after a Kr dose of 7×10^{15} /cm², the interfacial oxygen is observed to have a FWHM of ~ 6 nm. The incubation dose is then associated to the required spreading of the oxygen distribution caused by a radiation-enhanced like diffusion process. At this high O concentration the ion induced motion of the c-a interface is extremely low. It must be pointed out that the activation energy for the delay dose is similar, within the experimental error, with those reported for radiation-enhanced diffusion in a-Si[11].

The structure of the ion-beam-recrystallized deposited layers has been observed by TEM. Fig.6a is a cross sectional TEM micrograph of a 50 nm deposited layer with a native interfacial oxide recrystallized at 450°C. The presence of twinned crystal is evident. A plan view of the same sample (not shown) demonstrates that the twinned region is $\sim 12\%$ of the total area; the remaining sample being single crystal material. Fig.6b is a cross sectional

analysis of a sample dipped in HF before deposition and regrown under the same conditions. A good quality single crystal is observed. A planar image of the same sample (not shown) demonstrates, however, that a small fraction ($\leq 4\%$) of the total area is still twinned. A more detailed description of the morphology of ion-beam regrown deposited layers will be reported in a further publication[12].

CONCLUSIONS

The ion-induced regrowth of deposited a-Si layers has been directly followed *in situ* by transient reflectivity measurements. The planar c-a front stops at the deposited layer/substrate interface, and epitaxy continues only after a delay dose which depends on both temperature and substrate cleaning. The data have been tentatively explained in terms of a radiation-enhanced diffusion of O atoms coupled with a decrease in the growth rate due to the high interfacial O concentration. TEM analyses show that a small concentration of twinned material is present in the single crystal matrix. This concentration decreases noticeably with an appropriate cleaning of the substrates prior to deposition.

This work was supported in part by *Progetto Finalizzato Materiali e Dispositivi per l'Elettronica a Stato Solido*, Consiglio Nazionale delle Ricerche.

REFERENCES

- (1) G.P. Burns, Appl. Phys. Lett. **53**, 1423 (1988)
- (2) J. Linnros, G. Holmen, and B. Svernnson, Phys. Rev. **B32**, 2270 (1980)
- (3) R.G. Elliman, J.S. Williams, W.L. Brown, A. Leiberich, D.H. Maher and R.V. Knoell, Nucl. Instrum. Meth. **B19/20**, 435 (1987)
- (4) F. Priolo, A. La Ferla, and E. Rimini, J. Mater. Res. **3**, Nov./Dec. (1988)
- (5) M. Harith, A. La Ferla, G. Ferla and E. Rimini, Semicond. Sci. Technol. **3**, 641 (1988)
- (6) A. La Ferla, E. Rimini and G. Ferla, Appl. Phys. Lett. **52**, 712, (1988)
- (7) F. Priolo, A. La Ferla, C. Spinella, E. Rimini, G. Ferla, F. Baroetto, and A. Licciardello, Appl. Phys. Lett. , Dec. 26 (1988)
- (8) G.L. Olson, S.A. Kokoroski, J.A. Roth, and L.D. Hess, Meter. Res. Soc. Symp. Proc. **13**, 141 (1983)
- (9) E.F. Kennedy, L. Csepregi, J.W. Mayer and T. W. Sigmon J. Appl. Phys. Lett. **48**, 4241 (1980)
- (10) Program made by Implant Sciences Co., Danvers, MA
- (11) F. Priolo, J.M. Poate, D.C. Jacobson, J. Linnros, J.L. Batstone, and S.U. Campisano, Appl. Phys. Lett. **52**, 1213 (1988)
- (12) C. Spinella et al., to be published

SELF ANNEALING IMPLANTATION OF As⁺ IN SILICON

M.BERTI*, A.V.DRIGO**, R.LOTTI***, G.LULLI*** and P.G.MERLI***

* Dipartimento di Fisica "G.Galilei", GNSM-CISM, Università di Padova, Via Marzolo 8 - 35131 Padova, Italy

** Dipartimento di Scienza dei Materiali, GNSM-CISM, Università di Lecce, Via Arnesano - 73100 Lecce, Italy

*** CNR - Istituto LAMEL, Via de' Castagnoli 1 - 40126 Bologna, Italy

ABSTRACT

The structure of silicon layers implanted with high current As⁺ beams at different power densities under self-annealing conditions (i.e. with simultaneous damage recovery activated by beam heating) has been investigated with Rutherford Backscattering and Transmission Electron Microscopy techniques. The results have been compared with previous ones obtained with P⁺ implantation. They show that, in both cases, an ion-induced mechanism of recrystallization, characterized by an activation energy of the order of 0.3 eV, is operative at temperatures below the values necessary to activate thermal epitaxy. Chemical impurity profiles in samples self-annealed with As⁺ ions at high beam power density, show the occurrence of two relevant radiation-induced effects: i) diffusion enhancement in the tail region; ii) formation of two impurity peaks, separated by a depletion region centred at the ion projected range. While the deeper peak disappears with increasing irradiation time, the one located at the maximum of nuclear energy loss grows, apparently as a consequence of segregation of As atoms at large clusters of vacancy-type defects.

INTRODUCTION

Dynamic annealing effects occurring in silicon during implantation at elevated temperature, have been investigated in the last years [1-9]. One reason for such interest is the introduction of high-current, high energy implanters in the process of manufacturing electronic devices. In fact, due to the large beam power density, they generally cause a transient increase of wafer temperature, which may lead to partial or total recrystallization of the layer amorphized during the early stage of implantation.

It is known that under irradiation, this process occurs at temperatures below the value necessary to activate Solid Phase Epitaxy (SPE) in a furnace. Experiments performed by irradiating pre-amorphized silicon layers kept at constant temperature, with various ion species [8,9] have pointed out the essential features of ion induced recrystallization which are i) activation energy of the order of 0.3 eV; ii) proportionality of the recrystallization effect to the nuclear energy loss of the implanted ion.

In previous works [4,6,7] we characterized the structural evolution of thermally insulated, virgin Si samples, subjected to implantation with P⁺ ions at elevated beam power densities. In this paper we extend the study to self-annealing with As⁺ ions, by using Rutherford Backscattering (RBS) and Cross Sectional Transmission Electron Microscopy (XTEM) techniques. Recrystallization data are discussed and compared with the results previously obtained with P⁺ ions. The possibility to use RBS for measuring chemical profiles of As in Si, allows the investigation of the effects of anomalous diffusion which occur during self-annealing. The anomalous behaviour is discussed in terms of interaction between impurities and radiation-induced defects.

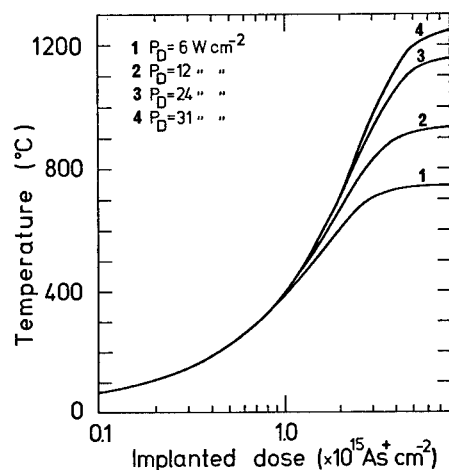


Fig.1 Calculated temperature as a function of the implanted dose in thermally insulated samples irradiated with 150 KeV As^+ ions at power densities of: 1) 6, 2) 12, 3) 24, and 4) 31 W cm^{-2} .

EXPERIMENTAL

The details of the apparatus used for self-annealing experiments have been illustrated elsewhere [6]. (100), p-type, Cz-grown, 1 $\Omega\cdot\text{cm}$, thermally insulated Si samples, were implanted with 150 keV As^+ ions at nominal current densities $J=40, 80, 160$ and $207 \mu\text{A/cm}^2$, corresponding to power densities $P_D=6, 12, 24$ and 31 W/cm^2 . As described in [6], the actual value of P_D , directly monitored during irradiation, allows the calculation of the transient temperature cycle. The reliability of the calculations was checked by testing the peak temperatures with heat labels stuck on the back of the samples. Fig.1 reports the calculated temperature variation as a func

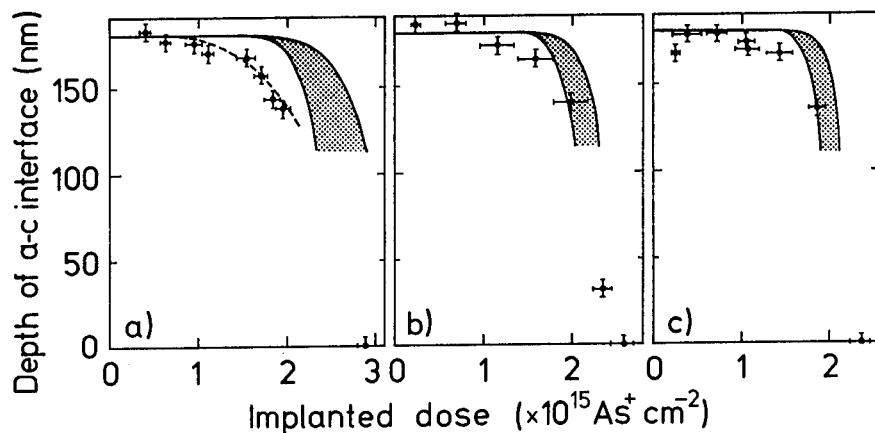


Fig.2 Position of the a-c interface in samples self-annealed with As^+ ions at nominal power densities of: a) 6, b) 12, c) 24 W cm^{-2} . Solid lines bounding the dashed regions simulate the thermal epitaxial growth calculated with bound values for the rate of SPE, relative to intrinsic and heavily doped n-layers [10]. Dashed line in a) simulates the regrowth calculated by assuming the same ion-beam induced mechanism previously observed in self-annealing with P^+ ions [6].

tion of the implanted dose for the different nominal values of P_D used in the experiments. Structural characterization was performed by RBS and XTEM techniques [6].

RESULTS AND DISCUSSION

Fig.2 a), b) and c) report the position of the amorphous-crystalline (a-c) interface measured with RBS, as a function of implanted dose, for irradiation at nominal P_D of 6, 12 and 24 W cm⁻², respectively. The early stage of implantation produces an amorphous layer of about 180 nm width. The solid lines which bound the dashed regions represent the results of two simulations of the regrowth, made under the assumption of purely thermal recrystallization induced by beam heating. Bound values of SPE rate have been used in the simulations, namely the recrystallization rate of an intrinsic amorphous layer and the recrystallization rate of a heavily doped n-layer, larger by a factor of seven [10]. Thus, the dashed area is the region where we should find the experimental points if the regrowth was of purely thermal nature. An effect of ion-induced epitaxial growth, operative at temperatures for which thermal effects are negligible, is detectable for all the values of P_D . The dashed line in Fig.2a) is the position of the a-c interface calculated by assuming a regrowth rate $v = v_0 \exp(-E_a/kT)$ where $E_a = 0.33$ eV and $v_0 = 8 \times 10^3$ nm s⁻¹. This last value is greater than the value measured for self-annealing with 100 keV P⁺ ions at $P_D = 6$ W cm⁻² [6], by a factor of about 3, which takes into account the larger nuclear stopping of As⁺ ions, and the lower beam current density (40 μ A/cm² in comparison with 60 μ A/cm²) used to have the same value of P_D with a higher beam energy. The agreement is satisfactory over a range of doses $10^{15} \leq D \leq 2 \times 10^{15}$ As⁺cm⁻² and points out the similarity of the regrowth mechanisms. For higher doses, temperature increases above 600°C (see Fig.1) and thermal effects become dominant. If we compare the present results with previous ones obtained in self-annealing with P⁺ ions [6], we observe here a larger thermal effect for the same implanted dose. This is due to the higher As⁺ beam energy, chosen in order to have impurity profiles sufficiently broad to be measured with good accuracy. In fact, for the same P_D , the current density is lower and the time necessary to implant the same dose is higher. As a consequence, the temperature is higher too, and thermal SPE becomes appreciable for lower values of the implanted dose.

As clearly visible in Fig.2 b) and c), thermal effects become increasingly important with increasing P_D . In fact the temperature increases faster with time, thus favouring the thermal process, which is characterized by a higher activation energy.

RBS spectra of samples irradiated with the dose necessary to achieve complete recrystallization, show a good crystalline quality of the surface region, with a peak of residual damage remaining at a depth of about 180 nm. Better annealing conditions cannot be achieved: In fact, increasing the irradiation time the damage peak continuously increases.

Another point to be noted is the absence of the surface recrystallization effects which were observed in self-annealing with P⁺ ions at current densities of 60 and 120 μ A/cm² [6,7]. The higher nuclear energy loss of As⁺ ions is probably responsible for the increased amorphization efficiency of the silicon surface. As a consequence no residual surface crystalline material survives the early, amorphizing stage of the process and recrystallization from the surface is not observed.

Fig.3 reports the As chemical profiles, measured with RBS in samples self-annealed at a nominal P_D of 31 W cm⁻² for times of 2, 3, 4, 5 and 6 s. The profile calculated with SUPREM III by assuming a pure mechanism of thermal diffusion in the sample irradiated for 6 s, is reported in the same figure.

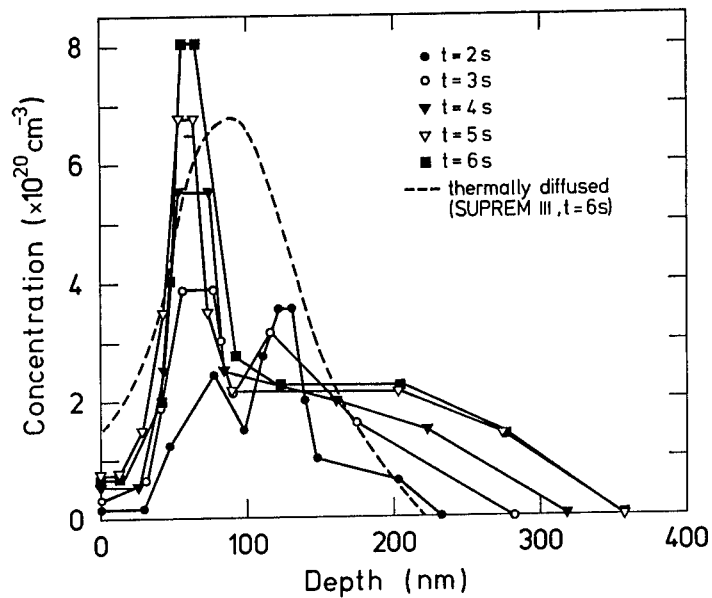


Fig.3 As chemical profiles measured with RBS in samples irradiated at nominal power density of 31 W cm^{-2} for different times. Maximum temperatures reached by the samples at the beam shut-off are $T=850^\circ\text{C}$ for $t=2\text{s}$, $T=1100^\circ\text{C}$ for $t=3\text{s}$, $T=1200^\circ\text{C}$ for $t=4\text{s}$, $T=1250^\circ\text{C}$ for $t=5\text{s}$, $T=1260^\circ\text{C}$ for $t=6\text{s}$. Dashed line represents the theoretical profile of the sample irradiated for $t=6\text{s}$, simulated with SUPREM III by assuming simple thermal diffusion due to beam heating.

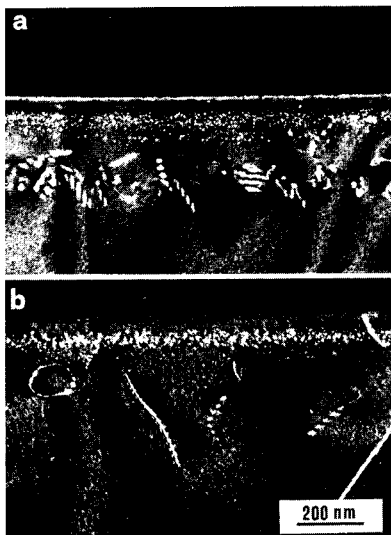


Fig.4 TEM weak-beam images of the samples irradiated at nominal power density of 31 W cm^{-2} , for a) $t=3\text{s}$, b) $t=5\text{s}$.

Although the sensitivity of RBS technique does not allow the detailed description of impurity profile for concentration $C < 10^{20} \text{ cm}^{-3}$, the evolution of the profile in the region where $C \geq 10^{20} \text{ cm}^{-3}$ is sufficient to point out some remarkable features of impurity diffusion during self-annealing process, namely:

- i) impurity depletion at $x \approx R_p$, where R_p is the ion projected range ($R_p \approx 93 \text{ nm}$ for 150 keV As^+ in Si [11]), evident for irradiation times $t=2$ and $t=3 \text{ s}$, which is accompanied by the formation of two peaks, one approximately located at $x \approx 0.7 R_p$, which corresponds to the maximum of nuclear energy deposition, and the other at $x \approx 120 \text{ nm}$;
- ii) the growth of the peak at $x \approx 0.7 R_p$ and contemporary reduction and disappearance (for $t = 4 \text{ s}$) of the peak at $x \approx 120 \text{ nm}$, with increasing irradiation time;
- iii) formation of a fast diffusing impurity tail in the region $x \geq 120 \text{ nm}$.

To investigate the correlation between such features and the microstructure of the recrystallized layer we report in Fig.4 a) and b) XTEM, weak beam images of the samples irradiated for 3 and 5 s, respectively. Essentially two kinds of defects are observed in both samples:

- i) extended defects, located at depths $150 \leq x \leq 300 \text{ nm}$ in the sample irradiated for $t=3 \text{ s}$, and $150 \leq x \leq 500 \text{ nm}$ in the sample irradiated for $t=5 \text{ s}$, which are the result of coalescence of end of range damage produced during the early amorphizing stage of implantation;
- ii) defects, which appear in the photographs as white, small rhomboidal dots. Their approximate maximum size is of $\approx 5 \text{ nm}$ in the sample irradiated for $t=3 \text{ s}$ and of 10 nm in the sample irradiated for $t=5 \text{ s}$. Out of focus observations reveal that these defects are voids [12]. They form a band about 40 nm width, centred at a depth of about 70 nm in both samples. A further, less pronounced, thin band is visible at a depth of about 120 nm , only in the sample irradiated for $t=3 \text{ s}$. The size of the voids in the band located at $x \approx 0.7 R_p$ increases with increasing irradiation time, while the voids in the narrower band at a depth of 120 nm tend to disappear. It can be observed, by comparing Fig.3 and Fig.4, the close correspondence existing between the location of impurity peaks and the position of the vacancy agglomerates.

The double-peak structure of impurity concentration profiles occurring in samples irradiated with particle-beams at elevated temperature, is a well known phenomenon. The hypothesis generally made to explain such effect assumes coupling of impurities with radiation generated defects and diffusion of the complexes in their concentration gradients, with transport properties depending on defect and impurity concentrations [13-15].

In the present situation it looks like vacancy-impurity complexes mainly formed at a depth where most As^+ ions are stopped, diffuse away from this region, producing depletion at $x=R_p$ and accumulation at $x \approx 0.7 R_p$ and $x \approx 120 \text{ nm}$, where the formation of large vacancy-type clusters immobilizes As atoms. With increasing irradiation time and temperature the voids located at $x \approx 120 \text{ nm}$, i.e. in a region of low density of defects formation, tend to dissolve and/or to be annihilated by mobile self interstitials which escape the region of maximum defect production. The contemporary growth of the voids at $x \approx 0.7 R_p$ is probably favoured by the large vacancy supersaturation which is expected here as a consequence of the faster diffusion of self interstitials away from the region. The final effect is that the large voids at $x \approx 0.7 R_p$ trap As atoms, while the mobile point defects escaping from the region of maximum damage production give rise to large enhancement of As diffusivity in the tail of impurity profile.

CONCLUSIONS

RBS and XTEM analysis of Si samples implanted with As^+ ions at high P_p have emphasized the following features of recrystallization and impurity diffusion processes occurring during irradiation:

- i) low-temperature, ion induced recrystallization effects occur, with an activation energy of the order of 0.3 eV and with a mechanism similar to the one observed in previous experiments with P^+ ions. The only appreciable difference is the absence of recrystallization effects at the surface which is due to the higher nuclear stopping power of As^+ ions.
- ii) Anomalous diffusion effects occur, characterized by diffusivity enhancement in the tail of the profile, probably due to mobile point defects escaping from the defect generation region, and segregation of impurity in correspondence of vacancy-type agglomerates, mainly formed at the position of the maximum of nuclear energy loss as a consequence of irradiation at elevated temperature.

ACKNOWLEDGMENTS

Thanks are due to F.Corticelli for TEM specimen preparation. This work was supported by CNR, Progetto Finalizzato Materiali e Dispositivi per l'Elettronica a Stato Solido.

REFERENCES

- [1] M.Tamura, K.Yagi, N.Sakudo, K.Tokiguti and T.Tokuyama in The Proceedings of the International Conference on Ion Beam Modification of Materials, 1978, p.515, (T.Gyulai, T.Lohner, E.Pasztor Eds.).
- [2] G.F.Cembali, P.G.Merli and F.Zignani, Appl.Phys.Lett. **38**, 808 (1981).
- [3] S.Prussin, D.I.Margolese and R.N.Tauber, J.Appl.Phys. **54**, 2316 (1983).
- [4] E.Gabilli, R.Lotti, G.Lulli, P.G.Merli and M.Vittori Antisari, Japan.J.Appl.Phys. **24**, L14 (1985).
- [5] S.Cannavò, M.G.Grimaldi and E.Rimini, Appl.Phys. Lett. **47**, 138 (1985).
- [6] M.Berti, A.V.Drigo, G.Lulli, P.G.Merli and M.Vittori Antisari, phys.stat.sol.(a) **94**, 95 (1986).
- [7] M.Berti, A.V.Drigo, G.Lulli, P.G.Merli and M.Vittori Antisari, phys.stat.sol.(a) **97**, 77 (1986).
- [8] J.Linnros, B.Svensson and G.Holmén, Phys.Rev.B **30**, 3629 (1984).
- [9] R.G.Elliman, S.T.Johnson, A.P.Pogany and J.S.Williams, Nucl.Instr. and Meth. **B7/8**, 310 (1985).
- [10] L.Csepregi, E.F.Kennedy, T.J.Gallagher and J.W.Mayer, J. Appl. Phys. **48**, 4234 (1977).
- [11] J.P. Biersack and J.F. Ziegler in Ion Implantation Techniques, eds. H.Ryssel, H.Glawisching, Springer Series in Electrophysics, vol.10 (1982).
- [12] M.Ruhle and M.Wilkins in Electron Microscopy 1972 (Proceedings of the 5th European Congress on Electron Microscopy - The Institute of Physics, London and Bristol, 1982), p.416.
- [13] W.Akutagawa, H.L.Dunlap, R.Hart and O.J.Marsh, J. Appl. Phys. **50**, 777 (1979).
- [14] S.Loualiche, C.Lucas, P.Baruch, J.P.Gailliard and J.C. Pfister, phys.stat.sol.(a) **69**, 663 (1982).
- [15] K.Holldack, H.Kerkow, W.Frentrup, phys.stat.sol.(a) **94**, 357 (1986).

ION BEAM SELF ANNEALING IN THIN SILICON FILMS

J.D. RUBIO*, R.P. VIJAY*, R.R. HART* AND J.D. PEARCE†

*Dept. of Nuclear Engineering, Texas A&M University, College Station,
Texas 77843†E.I. duPont de Nemours and Company, Atomic Energy Division, Savannah
River Laboratory, Aiken, South Carolina 29801

ABSTRACT

Residual lattice disorder in 1 μ m-thick silicon films as a function of the dose rate of 120 keV Ar⁺ ion implantations has been investigated. At a fluence of 1 \times 10¹⁴ ions/cm², low dose rates produced a highly damaged surface layer as expected; however, at a dose rate sufficient to locally heat the implanted film to a temperature of approximately 700°K, essentially complete annealing of the lattice disorder was observed. This temperature is significantly less than that normally required for post-implant thermal annealing. Measurements of lattice disorder were based on medium energy Rutherford backscattering and channeling analyses.

INTRODUCTION

Early investigations [1-3] which demonstrated the annealing effects of ion beams have led to more recent studies of ion beam self annealing [4-9] and ion beam induced epitaxial crystallization [10-12]. The results of the latter investigations have shown that ion bombardment can lead to the recrystallization of an amorphous layer at temperatures much lower than those required for purely thermal processes. The ion beam induced recrystallization takes place in a planar fashion along the amorphous/crystalline interface and has an activation energy which is an order of magnitude smaller than that for thermal regrowth. However, a major drawback to this method is that the annealing ions leave extensive damage at the depth corresponding to their range.

Ion beam self annealing studies have relied on poor thermal contact between the target and its holder to allow the power input by the ion beam to raise the temperature of the sample. During the initial stages of these high dose rate implantations, the sample temperature is below a threshold value, and damage accumulates to create an amorphous layer. If the fluence is large enough, however, the sample temperature can reach a point (>500°K) where ion beam enhanced epitaxial crystallization occurs and the amorphous layer is regrown. Residual damage at the end of range of the ions has also been observed after this type of self-annealing implant.

In contrast to previous investigations, the present study focused on self-annealing implantations in which amorphous layers were not formed during the early stages of the implantation. In order to perform high fluence implantations without forming amorphous layers, very thin thermally isolated silicon films were used as targets. The temperature of these thin films can be rapidly increased during implantation, to a level where dynamic annealing dominates the damage production process, before significant resultant damage occurs.

EXPERIMENTAL PROCEDURE

The 1 μm -thick, 1cm-diameter, self-supporting $\langle 100 \rangle$ silicon single crystal films were prepared using the method described by Meek [13] on epitaxial wafers obtained from SPIRE Corp. The n-type epitaxial layers were 1 μm -thick and had a dopant concentration of $1.5 \times 10^{15} \text{ As/cm}^3$ while the n^+ substrates were 305 μm thick and had a dopant concentration of $1 \times 10^{19} \text{ As/cm}^3$. After preparation the film thickness was checked by proton transmission measurements. The implantations and RBS/channeling analyses were conducted in a 200 kV Cockroft-Walton accelerator previously described in reference [14]. The final beam collimator was 0.32 cm in diameter and was centered on the film during the Ar^+ implantations. The samples were implanted to fluences of $1 \times 10^{14} \text{ ions/cm}^2$ with dose rates between 13.9-23.7 $\mu\text{A/cm}^2$. Typical implantation times were about 1 sec and all the implantations except one (at 140 keV) were performed at 120 keV. One of the films utilized during the investigation was 0.7 μm thick. The RBS/channeling analyses were performed with a 180 keV H^+ beam collimated to 0.08 cm diameter.

RESULTS AND DISCUSSION

Typical backscattering spectra using 180 keV protons are shown in Fig.1 and Fig.2. In Fig.1 are shown random and $\langle 100 \rangle$ -aligned spectra of an unimplanted 1 μm -thick film and a $\langle 100 \rangle$ -aligned spectrum following implantation with 120 keV Ar^+ at 23.7 $\mu\text{A/cm}^2$ to a fluence of $1 \times 10^{14} \text{ ions/cm}^2$. It can be seen that, within the sensitivity of RBS/channeling analyses, no lattice damage is present after the implantation. In Fig.2 the two aligned spectra from Fig.1 are presented in closer detail to show that they agree to within counting statistics. The small peaks in the aligned spectra located at 129 keV and 140 keV correspond to carbon and oxygen on the sample surface. The oxygen is from the surface oxide layer, and the carbon is presumably from hydrocarbon impurities inside the target chamber. These peaks were also present in the backscatter spectrum of the unimplanted sample.

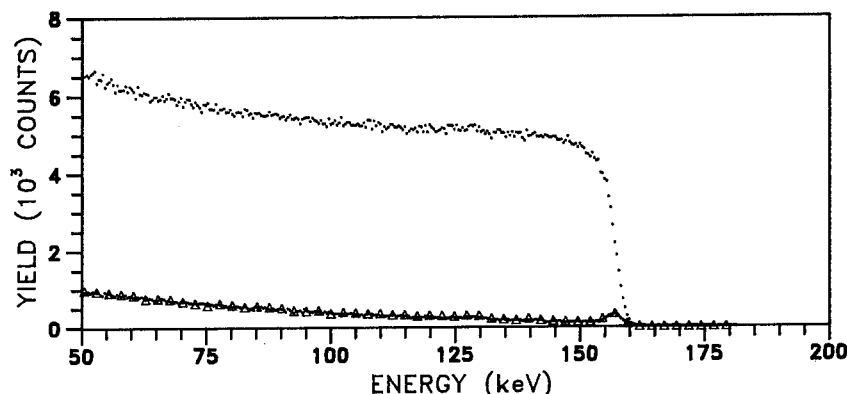


Fig.1 Random and $\langle 100 \rangle$ -aligned backscattering spectra of 1 μm -thick $\langle 100 \rangle$ Si film: unimplanted (\bullet) and after self-annealing implantation with 120 keV Ar^+ at 23.7 $\mu\text{A/cm}^2$ to a fluence of $1 \times 10^{14} \text{ ions/cm}^2$ (Δ).

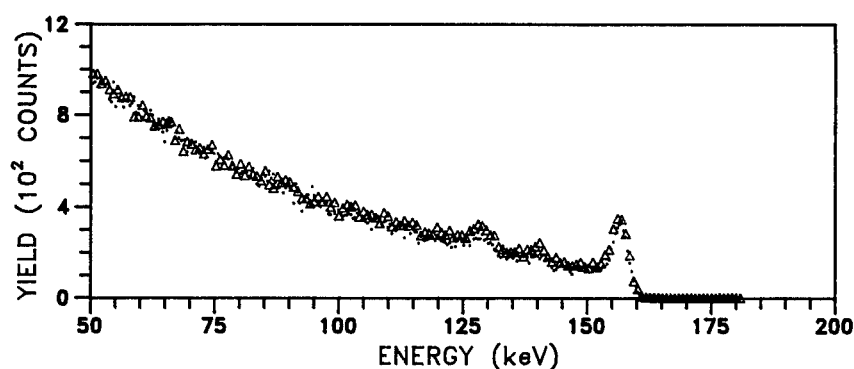


Fig.2 The $\langle 100 \rangle$ -aligned spectra of Fig.1 shown in greater detail: unimplanted (\bullet) and after self-annealing implantation with 120 keV Ar^+ at $23.7 \mu\text{A}/\text{cm}^2$ to a fluence of 1×10^{14} ions/ cm^2 (Δ).

Additional self-annealing implants using 120 keV Ar^+ at dose rates of 13.9, 14.4 and $17.1 \mu\text{A}/\text{cm}^2$ on a $0.7 \mu\text{m}$ -thick film and 140 keV Ar^+ at $22.7 \mu\text{A}/\text{cm}^2$ on a $1 \mu\text{m}$ -thick film yielded aligned spectra before and after implantation that coincided within experimental error. Although not shown, in contrast to the above results, a $\langle 100 \rangle$ -aligned spectrum of a $0.7 \mu\text{m}$ -thick film following 120 keV Ar^+ implantation to a fluence of 1×10^{14} ions/ cm^2 at a low dose rate of $1.6 \mu\text{A}/\text{cm}^2$ revealed a highly damaged (nearly amorphous) surface layer. Thus, the higher dose rate implantations were required to achieve self annealing.

A numeric algorithm, WAFER, was developed to calculate the temperature of the sample during implantation by solving the nonlinear, time dependent heat balance equation including radiative losses. The results from WAFER show that the steady state centerline temperature varied between 670-745°K for the different self-annealing implantations. However, there is uncertainty in these values due to the lack of data for the emittance of thin silicon films. In WAFER, the emittance values used are those recommended for 2 mm thick silicon crystals in reference [15]. WAFER calculations also indicate that a value 95% that of the steady state centerline temperature was achieved 0.1 sec after the implantation began. This would correspond to a fluence $< 1.5 \times 10^{13}$ ions/ cm^2 which is an order of magnitude smaller than that required to create an amorphous layer. For the implantation at $1.6 \mu\text{A}/\text{cm}^2$ the steady state centerline temperature was calculated to be 340°K using WAFER.

CONCLUSIONS

Self annealing, within the sensitivity of RBS/channeling analyses, was observed in a $1 \mu\text{m}$ -thick film following implantation with 120 keV Ar^+ to a fluence of 1×10^{14} ions/ cm^2 at a dose rate of $23.7 \mu\text{A}/\text{cm}^2$ and following 140 keV Ar^+ implantation to the same fluence at $22.7 \mu\text{A}/\text{cm}^2$. Self annealing was also observed in a $0.7 \mu\text{m}$ -thick film following implantations of 120 keV Ar^+ to a fluence of 1×10^{14} ions/ cm^2 at dose rates of 13.9, 14.4 and $17.1 \mu\text{A}/\text{cm}^2$. A highly damaged surface layer was observed in a $0.7 \mu\text{m}$ -thick film following an implant of 120 keV Ar^+ at $1.6 \mu\text{A}/\text{cm}^2$ to the same fluence.

The steady state centerline temperature of the samples as calculated by WAFER varied between 670-745°K for the self-annealing implantations and was 340°K for the low dose rate implant.

In contrast to previous self annealing studies the implantations performed in this investigation did not lead to the production of amorphous layers and their subsequent regrowth. This was confirmed by a WAFER calculation which indicated that the implanted fluence before reaching a temperature 95% of the steady state value was $<1.5 \times 10^{13}$ ions/cm²; this is an order of magnitude smaller than that required to create an amorphous layer. It is believed that the lack of significant disorder produced during the initial heating phase of the implantation led to a reduction in observed residual lattice damage as compared to the results of previous investigators.

ACKNOWLEDGEMENTS

This material is based in part upon work supported by the Texas Advanced Research Program (Advanced Technology Program) under Grant No. 4287.

REFERENCES

1. G. Holmen and P. Hogberg, Radiat. Eff. 12, 77 (1972).
2. G. Holmen, S. Peterstrom, A. Buren and E. Bogh, Radiat. Eff. 24, 45 (1975) .
3. H.E. Roosendaal, W.H. Kool and F.W. Saris, Radiat. Eff. 36, 35 (1978).
4. G. Cembali, M. Finetti, P.G. Merli and F. Zignani, Appl. Phys. Lett. 40, 62 (1982).
5. O.W. Holland and J. Narayan, Nucl. Instr. Meth. B7/8, 243 (1985).
6. S. Cannavo, A. La Ferla, E. Rimini, G. Ferla and L. Gandolfi, J. Appl. Phys. 59, 4038 (1986).
7. F.F. Komarov, E.V. Kotov, A.P. Novikov, S.A. Petrov and V.I. Chit'ko, Radiat. Eff. 105, 79 (1987).
8. M. Berti, A.V. Drigo, E. Gabilli, R. Lotti, G. Lulli, P.G. Merli and M. Antisari, Nucl. Instr. Meth. B19/20, 475 (1987);
9. R. Galloni, R. Rizzoli, A. Larsen and S. Shiryayev, Nucl. Instr. Meth. B19/20, 466 (1987).
10. I. Golecki, G.E. Chapman, S.S. Lau, B.Y. Tsaur and J.W. Mayer, Phys. Lett. 71A, 267 (1979).
11. J. Linnros, B. Svensson and G. Holmen, Phys. Rev. B30, 3629 (1984).
12. J.S. Williams, R.G. Elliman, W.L. Brown and T.E. Seidel, Phys. Rev. Lett. 55, 1482 (1985).

13. R.L. Meek, W.M. Gibson and R.H. Braun, Nucl. Instr. Meth. 94, 435 (1971).
14. S.R. Lee and R.R. Hart, Nucl. Instr. Meth. B28, 470 (1987).
15. Y.S. Touloukian and C.Y. Ho, Thermophysical Properties of Selected Aerospace Materials Part I, (Purdue University, Indiana, 1976), p. 553.

INFLUENCE OF THE IMPLANTED SPECIES ON THE RESIDUAL DAMAGE AFTER HOT IMPLANTS IN SILICON

L.Calcagno*, C.Spinella*, M.Catania*, S.U.Campisano*, G.Foti*,
G.Ferla# and E.Rimini*

*Dipartimento di Fisica, Corso Italia 57 - 95129 Catania (Italy)

#SGS-Thompson, Stradale Primosole 50-95100 Catania (Italy)

ABSTRACT

Damage formation during hot implants of 600 keV As or Ge ions into Si was investigated by changing the target temperature ($>150^\circ\text{C}$) and the ion fluence. The defect distributions, as obtained by channeling analysis, are characterized by a gaussian shape whose maximum coincide with the peak of the energy density deposition and with a width of 200 nm. The amount of damage is a factor of two higher for Ge than for As ion implants, and a similar result was found for the damage created by Ge implants into bare Si or Si doped with a near constant As concentration of $2 \times 10^{20}/\text{cm}^3$. The transition to amorphous formation is quite sharp for As (around 120°C) and quite broad for Ge implants. The different amount and kind of extended defects is probably due to an interaction of the mobile point defects, vacancies and interstitials, with As. The interaction probably increases the defects annihilation rate.

INTRODUCTION

The damage created by ion implantation depends on the ballistic parameters of the colliding ion-atom couple and on the target temperature. During irradiation the generated point defects, Frenkel pairs, migrate, recombine, anneal out at the preexisting sinks, agglomerate into amorphous regions, small dislocation loops, dislocations network. The prevalence of one mechanism over the others is mainly determined by temperature. Silicon amorphous layers are formed at room temperature at a fluence of about $10^{14} \text{ As}/\text{cm}^2$. The fluence for amorphization increases rapidly with temperature and above 200°C the transition to the amorphous phase does not occurs [1,2].

The majority of experiments has been performed at relatively low ion energy, 25-100 keV, with the dopants confined in the near surface region. Infact the predeposition step to dope silicon is the main industrial application of ion implantation. The surface, provided the defects are mobile, may play, in this case, an important role being an active sink for defect annihilation. High energy implants are now being used for several applications in microelectronics devices and ion-assisted processes, as the epitaxial regrowth of amorphous silicon layers [3]. The growth process, under ion irradiation occurs at temperatures as low as 200°C with an apparent

activation energy of about 0.3 eV, one order of magnitude lower than that of the pure thermal process [4]. It induces epitaxial crystallization even in chemical vapor deposited amorphous layer, or in layers heavily contaminated with argon or oxygen [5]. This process has a draw back in the generation of extended defects during the irradiation at high temperature. A suitable annealing step is necessary to remove, at least in part, the residual damage [6,7].

The amorphous-extended defects transition with increasing implantation temperature is of relevance for both basic and technological aspects. In several high current implanters the cooling system is appropriate to maintain the wafer temperature below 100 °C [8]. The range around 100 °C is crucial for the transition amorphous-extended defects at least for high energy implants. Recently it has been found that the damage created by high energy implants of Kr and As into hot silicon substrates is species dependent: it is higher for Kr than for As ions, although their defect generation rate is nearly the same [7].

We report an investigation on the amount and kind of damage left by As and Ge implants in Si at several temperatures. The two species were chosen to ascertain the influence of the chemical specie on the dynamical annealing, being equal for both of them the collisional effects.

EXPERIMENTAL

Silicon wafers <100> oriented p-type, 20 ohm-cm resistivity were implanted with As or Ge ions of 600 keV energy in the temperature range 25-400 °C and with fluences ranging from 10^{15} to $6 \times 10^{15}/\text{cm}^2$. Other wafers were multiple energy As implanted, to obtained a near constant concentration of $2.0 \times 10^{20}/\text{cm}^3$ up to a depth of 450 nm. These samples were annealed at 1100 °C, 4 s to regrow the amorphous layer and to locate substitutionally the implanted dopant. Hot implants of Ge ions were subsequently performed also on these samples. 2.0 MeV He^+ Rutherford backscattering in combination with channeling effect, was used to analyze the damage.

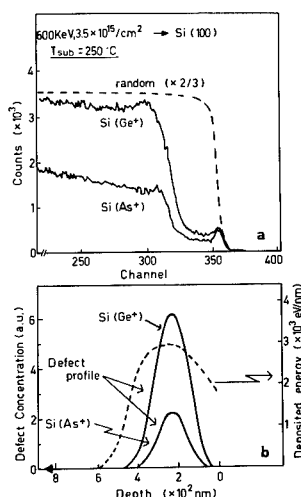
RESULTS AND DISCUSSION

The channeling analysis of <100> Si wafers implanted with $3.5 \times 10^{15}/\text{cm}^2$, 600 keV As or Ge ions at 250 °C is shown in Fig.1a. Common features of these hot implants is the sharp increase of the aligned yield at a depth of about 240 nm and the near constant value beyond 450 nm. The near surface region is practically defect free, at least from the channeling analysis. The yield is low and constant for the first 150-200 nm. At large depths the yield of the Ge implant is about a factor two higher than that of the As implants, in spite of the near equal energy deposition profiles. The projected ranges, R_p , for 600 keV As and Ge are 380 nm and 400 nm, while the stragglings, ΔR_p , are 85 nm and 90 nm respectively.

The energy density profile has been evaluated with the TRIM program assuming 15 eV for the threshold energy displacement of

Si atoms and 2.0 eV for the binding energy. The profile is reported as dashed line in Fig.1b. The energy density is already considerable at the surface and reaches the maximum value, a factor of two than that at the surface, at a depth of 240 nm. The distribution is quite flat up to a depth of 400 nm and then falls down rapidly.

Fig.1. Aligned and random yields of <100> Si samples implanted at 250 °C with 600 keV Ge and As ions at a fluence of $3.5 \times 10^{15}/\text{cm}^2$ (a). Depth dependence of the dechanneling parameter $l_d \lambda_d(z)$, which is related to the defect distribution, for the two analyses shown in the upper part. The dashed line represents the energy deposited into elastic collisions (b).



The comparison of defect distribution with the deposited energy density is not straightforward. The quantitative evaluation of the damage from the channeling analysis is based on several assumptions. The shape of the yields indicates the presence of a large amount of extended defects as dislocation loops. Extended defects can cause distortions of the surrounding crystal and give rise mainly to an high dechanneling rate. In this case, assuming for simplicity the presence of just one kind of extended defect, the dechanneling probability per unit depth is given by the product of the defect dechanneling length, λ_d , and the defect density $l_d(z)$ [9,10]. From the measured normalized yields in unimplanted, X_v , and in the damaged, X_d , sample, one obtains

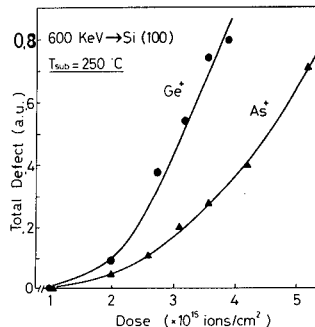
$$l_d \lambda_d(z) = \frac{d}{dz} \ln [(1 - X_v)/(1 - X_d)]$$

The normalized raw yields were smoothed by fitting small portions of the spectrum with third order polynomial function and imposing the continuity of its first and second order derivative. The obtained distributions, shown in Fig.1b, indicate that the peak of the defect density occurs at the maximum of the energy density distribution. Defects migrate, interact among themselves, with impurities and clusters where their density is higher i.e. at the peak of the energy density distribution. The increase of the fluence by a factor of two

does not produce a substantial increase of damage in the near surface region, which remains practically still free of defects. Clearly, migration of defects from this region toward either the surface sink or the defect agglomerates takes place.

The amount and the kind of extended defects is dependent on the target temperature, and on the implanted species through the interaction of mobile point defects with impurities. The damage associated to As implants is about one half of that associated to Ge implants. The dependence has been investigated at different fluences and the results are shown in Fig.2 for a target temperature of 250 °C. At a fluence of $2 \times 10^{15}/\text{cm}^2$, i.e. at a peak concentration of $1 \times 10^{20}/\text{cm}^3$ the total amount of defect $l_d \lambda_d$ for As is already half of that of Ge. With increasing the fluence the difference between the two amount of defects for Ge is a factor of two that for As. This ratio increases with fluence.

Fig.2. Total amount of defect, in arbitrary units, given from the dechanneling parameter $l_d \lambda_d$ measured at a depth of 450 nm as a function of 600 keV As or Ge ions fluences. The target temperature during implants was 250 °C.

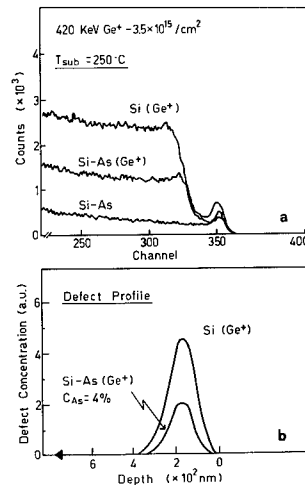


The effect of the As impurities on the formation of extended defects was also investigated by Ge implants in samples previously doped with a near constant As concentration of $2.0 \times 10^{20}/\text{cm}^3$ up to a depth of 450 nm. The channeling analysis of 420 keV - $3.5 \times 10^{15}/\text{cm}^2$ Ge implants into undoped and As doped samples is shown in Fig.3a. The beam energy was decreased to 2/3 of the previous one, 600 keV, so that all the Ge energy deposition profile was located within the As doped layer. The resulting depth profiles are shown in Fig.3b. The data clearly confirm the influence on the damage of the As impurities, either present in the sample or introduced simultaneously with the defects.

The influence of the target temperature on the amount of damage has been investigated in the range 20 °C - 400 °C. Some preliminary results are shown in Fig.4, where the total amount of defect is plotted vs. temperature for 600 keV As and Ge implants at a fluence of $3.5 \times 10^{15}/\text{cm}^2$. The trend of As data indicates an abrupt transition from amorphous buried layer to extended defects at a target temperature of about 120 °C. At a temperature of 100 °C the channeling spectrum indicates the

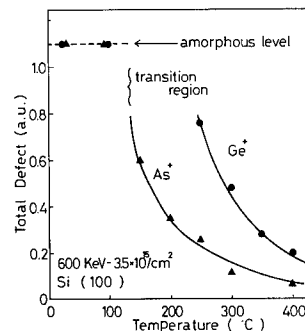
presence of an amorphous layer extending from 90 nm to 440 nm

Fig.3. Aligned yields of $\langle 100 \rangle$ Si samples implanted at 250 °C with $3.5 \times 10^{15}/\text{cm}^2$, 420 keV Ge ion. The Si(As) sample contains substitutional As at a concentration of $2.0 \times 10^{20}/\text{cm}^3$ prior to the Ge implant (a). Defects distribution, in arbitrary units, as given by the dechanneling parameter $1_d \lambda_d$ extracted from the corresponding channeling spectra (b).



from the surface. At a temperature of 150 °C only extended defects are observed. In the case of Ge ions and for implantation temperatures up to 100 °C the results are nearly equal to those of As implants. In the temperature range 100-200 °C the channeling analysis evidences the simultaneous presence of extended defects and isolated amorphous regions. At temperatures above 200 °C only extended defects are revealed. The transition region from amorphous to extended defects configuration requires a more detailed investigation. In both cases above the threshold temperature the total amount of extended defects decreases by increasing the target temperature.

Fig.4. Total amount of defects, in arbitrary units, up to a depth of 450 nm, given by the dechanneling parameter $1_d \lambda_d$, as a function of temperature for 600 keV As or Ge ions at a fluence of $3.5 \times 10^{15}/\text{cm}^2$. (The channeling spectra at 100 °C and below reach the random level at a depth of 90 nm and for a thickness of about 350 nm).



The data clearly indicate the chemical effect of As on the damage produced during hot implants. The presence of As atoms

decreases the total amount of extended defects probably by increasing the rate of annihilations of point defects. The present results indicate a trend different from that found for the threshold dose for the amorphization of undoped and As doped Si at room temperature [11]. In that case in fact to amorphize an As doped crystal a dose of ~40% lower than that required to amorphize pure Si was required. The difference can be ascribed to different kind of point defects responsible for the formation of amorphous layers and extended defects respectively and to the temperature dependence of their mobility and lifetime.

CONCLUSIONS

The extended defects created during hot implants of high energy As or Ge ions are species dependent. The amount of damage, as obtained by channeling analysis, is higher for Ge than for As implants. During irradiation the dynamical annealing is then more effective in the presence of As atoms. They may induce the formation of vacancy or interstitial pairs. There is then an higher probability for mutual recombination, thus decreasing the total amount of damage. Some preliminary TEM analyses indicate the presence of small dislocation loops in the As implanted samples, while an high density of dislocations is seen in the Ge implanted samples. The transition to amorphous damage with decreasing the target temperature occurs sharply in the As implants, but it is broad in the Ge implants. In this last case the channeling analysis indicate the presence of extended defects and random displaced atoms.

REFERENCES

1. F.F.Moheread, B.L.Crowder; *Rad.Eff.* **6**(1970)27
2. J.M.Poate and J.S.Williams; *Ion implantation and beam processing* (Academic Press, New York 1984) cap.2 -pag.13
3. J.S.Williams R.G.Elliman, W.L.Brown and T.E.Seidel; *Phys.Rev.Lett.* **55**(1985)1482
4. G.L.Olson; *Mater.Res.Soc.Symp.Proc.* **35** (Mat.Res.Soc.Pittsburg USA 1985)p.25
5. A.La Ferla, E.Rimini, and G.Ferla; *Appl.Phy.Lett.* **52**(1988)712
6. T.E.Seidel, D.J.Lischner, C.S.Pai, R.V.Knoell, D.H.Meher and D.C.Jacobson; *Nucl.Instr.Meth.* **B7/8**(1985)251
7. S.Coffa, L.Calcagno, C.Spinella, S.U.Campisano, G.Foti and E.Rimini; *Nucl.Instr.Meth.* (In Press)
8. D.G.Beanland, in: *Ion implantation and beam processing* eds.J.S.Williams and J.M.Poate (Academic Press, New York) (1984)p.261
9. L.C.Feldman, J.W.Mayer and S.T.Picraux; *Material Analysis by ion channeling* (Academic Press, New York, 1982) ch.4-5
10. G.Foti, S.T.Picraux, S.U.Campisano and E.Rimini; *Phys.Rev.* **B18**(1978)2078
11. A.V.Dvurechenskii, R.Groetzel and V.P.Popov; *Phys.Lett.* **A116**(1986)399

FURNACE ANNEAL OF a-AXIS SAPPHIRE AMORPHISED BY INDIUM ION IMPLANTATION

D.K. Sood and D.X. Cao*

Microelectronics and Materials Technology Centre, Royal Melbourne Institute of
Technology, GPO Box 2476V, Melbourne 3001, Australia

*Permanent address: Institute of Nuclear Research Academia Sinica, Shanghai, P.O. Box
8204, China

ABSTRACT

Indium implantation at 77°K into a-axis sapphire to peak concentrations of 6–45 mol % In produces amorphous surface layers. Isothermal annealing in Ar at temperatures between 600–900°C shows effects strongly dependent on ion dose. At lower doses $<2 \times 10^{16}$ In/cm², the amorphous layer undergoes epitaxial regrowth as the amorphous to crystalline interface advances out towards the surface. Regrowth velocity is high in about the first half hour of the anneal. Regrowth obeys Arrhenius behaviour with an activation energy of 0.7eV for initial faster growth and 1.28eV for further anneal times. The amorphous phase transforms directly to α -Al₂O₃ without any evidence of an intermediary γ -phase. At higher doses, epitaxial regrowth is substantially retarded and rapid diffusion of In within the amorphous phase dominates.

1. INTRODUCTION

Surface modification of ceramics by ion implantation is being used to create novel optical, chemical, mechanical and electrochemical properties [1]. Many of these properties are influenced by the lattice damage, defect solute interaction and the behaviour of damage and solute atoms during post-implantation annealing. Previous studies on ion implanted Al₂O₃ have shown a) lattice damage accumulates to amorphise Al₂O₃ [2,3] at an optimum damage energy density, b) during annealing, amorphous Al₂O₃ prepared by stoichiometric implantation into c-axis Al₂O₃ crystals, converts first to the γ -phase which then transforms to the α -phase [2] by the outward motion of a well defined planar interface, c) implanted species either undergo a recrystallization – driven migration outwards to the surface or do not diffuse appreciably [3,4], and under certain conditions a rapid isotropic diffusion of In within the amorphous Al₂O₃ layer can proceed at effective diffusion coefficients up to about 8 orders of magnitude larger than those in crystalline Al₂O₃ [5].

In this work we report on a study of annealing of amorphous surface layers produced by indium implantation to high concentrations (up to 45 mol % In) in a-axis Al₂O₃ over a temperature range of 600–900°C. Crystallization, indium diffusion and phase separation are studied in detail. We also provide, to the best of our knowledge for the first time, evidence for truly epitaxial regrowth of amorphous Al₂O₃ to α -Al₂O₃ without any occurrence of an intermediary γ -phase as reported previously [2] for c-axis samples.

2. EXPERIMENTAL

The optically flat, a-axis Al₂O₃ single crystals ($\langle 1\bar{2}10 \rangle$ orientation) were used after preannealing at 1400°C in an oxygen environment for 5 days, so that these sapphire slices were damage free. Indium ion implantation was performed at 100keV energy, about 7° off surface normal of the sample held at 77°K. Current density was less than 2 μ A/cm² and the chamber vacuum was about 5×10^{-7} Torr. Ion doses ranged from 0.8×10^{16} In/cm² to 6×10^{16} In/cm². Isothermal annealing was performed in flowing high purity Ar gas ambient at 600, 700, 800 and 900°C. Anneal time was varied from 10 minutes to 24 hours. Samples were analysed using techniques of Rutherford Back-Scattering and Channeling (RBSC),

Reflection High Energy Electron Diffraction (RHEED), and Scanning Electron Microscopy (SEM).

3. RESULTS AND DISCUSSION

After ion implantation at all doses, an amorphous surface layer was formed (as confirmed by RHEED and RBSC) which had an abrupt interface with the underlying single crystal. Isothermal annealing shows effects which are complex and strongly dependent upon ion dose.

3.1 Lower Dose Regime: ($<2 \times 10^{16}$ In/cm²): Fig. 1 shows typical RBSC spectra from an In implanted sample after isothermal annealing at 900°C, for oxygen sublattice (Fig. 1 a) and Al sublattice (Fig. 1 b). There is a clear evidence of epitaxial regrowth of as implanted amorphous layer of 61 nm up to 1 hour anneal time, as the amorphous to crystal (a-c) interface moves towards the surface. The 2 hours anneal, produces a change in crystallisation mode as dechanneling yield drops below random yield without any appreciable change in thickness of the layer. This trend continues as the anneal time is increased to 3,5,7,10 and 24 hours (data not shown here). The dechanneling yield drops, without any appreciable reduction in the width of the damage peak. This behaviour could result from a non-planar epitaxial crystallization process. Fig. 2 shows a plot of the regrown layer versus anneal time. Three regions can be clearly identified. Region I and II show epitaxial regrowth which is faster in region I. Region III shows non-planar epitaxial transformation of amorphous phase into α -Al₂O₃. There is no evidence of any γ -phase formation from RHEED results. Region III persists up to 24 h anneal as seen in Fig. 5a. Very similar behaviour is observed for annealing at other temperatures 600, 700 and 800°C with the extent of the three regions varying somewhat, e.g. 600°C data shows no region III. Growth velocities (determined e.g. from slope of the curves of Regions I and II in Fig. 2) are plotted in Fig. 3 as a function of inverse of temperature T. They exhibit an Arrhenius behaviour and data points are fitted with activation energies of $Q_I = 0.7$ eV and $Q_{II} = 1.28$ eV for the two regions of epitaxial regrowth. The solid line is based on the Oak Ridge group data [2] on near epitaxial regrowth (via an intermediary γ -phase) of intrinsic amorphous layers produced by stoichiometric implantation of O and Al ions. This solid line represents the variation of γ/α interface velocity corresponding to an activation energy of 3.6 eV.

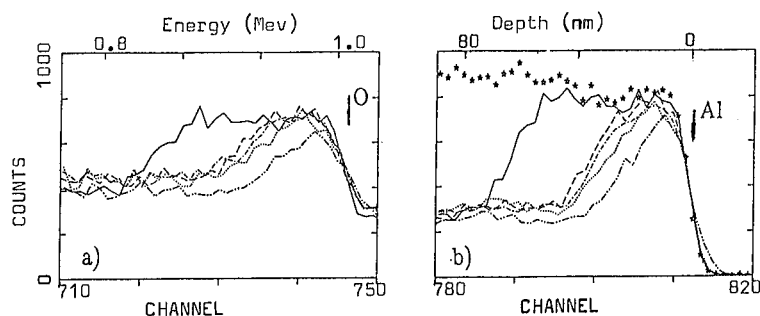


Fig.1 Backscattering spectra from In ($100\text{keV } 0.8 \times 10^{16}/\text{cm}^2$) implanted a-axis Al₂O₃ with isothermal annealing at 900°C in Ar. (a) oxygen sublattice, (b) aluminium sublattice.

* as implanted (random), — as implanted (aligned),
 — 10 min (aligned), - - - 0.5h (aligned),
 1h (aligned), - · - · - 2h (aligned).

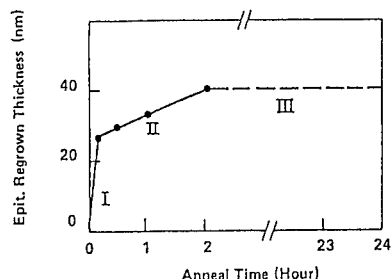


Fig. 2 Implanted Al_2O_3 with a dose of 0.8×10^{16} In/cm² at 100 keV 77°K. Isothermal anneal at 900°C in Ar.

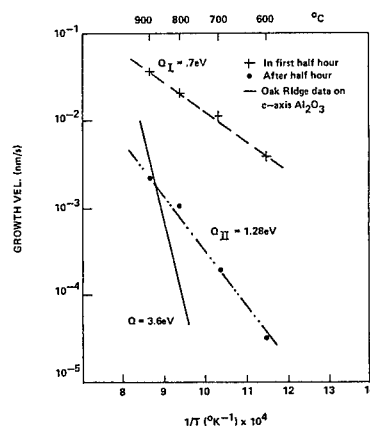


Fig. 3 An Arrhenius plot for a-axis Al_2O_3 samples implanted at 77°K with 0.8 – 1.8×10^{16} In/cm² at 100keV.

Thus the addition of In impurity ions to amorphous Al_2O_3 produces a change in the mode of crystallization — the amorphous phase transforms directly (epitaxially) to α - Al_2O_3 without any trace of the intermediary γ -phase. The growth velocity is now much higher showing a clear reduction of the activation energy (for γ/α transformation) from 3.6eV to 0.7eV for a/ α transformation. From a detailed analysis of data at the four temperatures, we conclude that the effect of In induced enhancement in growth rate is dose dependent. As In dose is increased, the epitaxial growth is retarded. The transition in Fig. 2 from region I to II occurs as the c-a interface arrives at a depth where In concentration is high enough to appreciably slow down the epitaxial growth rate. Region III would commence as still higher In concentration is encountered (at depths closer to In range) wherein the epitaxial mechanism breaks down. For example, the depth at which region III commences in Fig. 2 is 25 nm from the surface, whereas the observed range of In is 24 nm with straggling width of 11 nm. The onset of region III occurs at a specific volume concentration of In and is temperature dependent, e.g. about 0.6×10^{21} In/cm³ at 700°C and about 1.0×10^{21} In/cm³ at 900°C. Similar implanted impurity concentration dependent effects have been reported for epitaxial regrowth of amorphous Si on underlying single crystal substrates [6].

3.2 Higher Dose Regime ($>2 \times 10^{16}$ In/cm²): The effect of annealing a sample implanted with 6×10^{16} In/cm² for half hour at 700°C is shown in Fig. 4. Epitaxial regrowth and rapid diffusion of In within the amorphous layer occur simultaneously. The a-c interface moves out towards the surface (Fig. 4a) and stops after advancing by about 28 nm. The as-implanted profile of In redistributes with two clear components (Fig. 4b) — I (shaded area) corresponding to rapid diffusion within amorphous layer and — II a surface pile up peak of In with a tail. Further annealing up to 24 h, produces no noticeable change in the In distribution and the implanted layer remains amorphous (as indicated by RBSC spectra not shown here). The RHEED data (Fig. 4b) obtained on the sample after 24 h anneal shows a family of well defined rings which all index to In_2O_3 phase. Analysis of RHEED patterns indicates that small (<10 nm diameter) particles of In_2O_3 constitute the surface layer. There is no evidence for any precipitates of In, Al or crystalline Al_2O_3 . The RHEED micrograph in Fig. 4a confirms that the as implanted layer is amorphous.

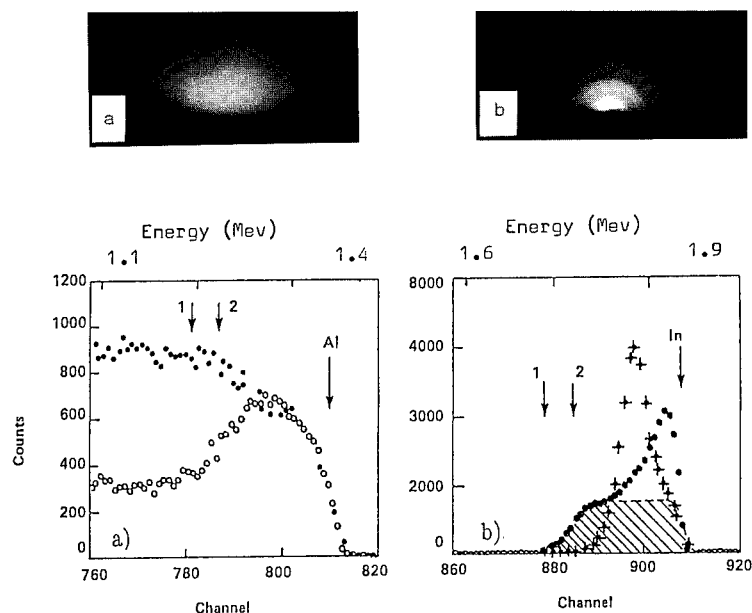


Fig. 4 Backscattering of indium ($100\text{keV } 6 \times 10^{16}/\text{cm}^2$) implanted a-axis Al_2O_3 annealed at 700°C in Ar for half hour. (1) original c-a interface (2) c-a interface after anneal. + as implanted (random), • after annealing (random), o after annealing (aligned)

The observed broadening (shaded region in Fig. 4b) in component-I corresponds to an effective diffusion co-efficient of $1.04 \times 10^{-14} \text{ cm}^2/\text{s}$ for In in amorphous Al_2O_3 , which is just over one order of magnitude higher than our previously reported [5] value of $8.3 \times 10^{-16} \text{ cm}^2/\text{s}$ at 600°C . It may be noted that these values are at least about 8 orders of magnitude larger than those ($\sim 10^{-25} \text{ cm}^2/\text{s}$) obtained by an extrapolation to 600°C of self (Al ion) diffusion coefficients measured by previous workers (7) in crystalline $\alpha\text{-Al}_2\text{O}_3$.

At higher anneal temperatures, similar In redistribution behaviour continues, except that the relative amount of component-I diminishes as more and more In comes out to the surface to form In_2O_3 . The migration of In gets faster, since all the observed migration is found to be completed within the first short anneal of 15 minutes at 800°C and 10 minutes at 900°C . Further annealing up to 24 h produces no more change in the Indium profile. The underlying amorphous layer however, regrows into an imperfect crystal. Some examples of the terminal stages — as implanted and after 24 h anneal, are shown in the following figures, which also compare the dose dependent behaviour.

The data for 800°C anneal are shown in Fig. 5. For the lower dose sample (Fig. 5a), even after 24 h anneal, the crystal is still imperfect compared with virgin. Up to about 76% In is lost but no surface peak of In is observed. The residual In shows about 50% substitutionality. This remarkable behaviour is quite different from 'the push out effect' reported earlier [4] for several species implanted in c-axis Al_2O_3 . RHEED data on this sample (inset Fig. 5a), shows an essentially single crystal surface, with spot broadening,

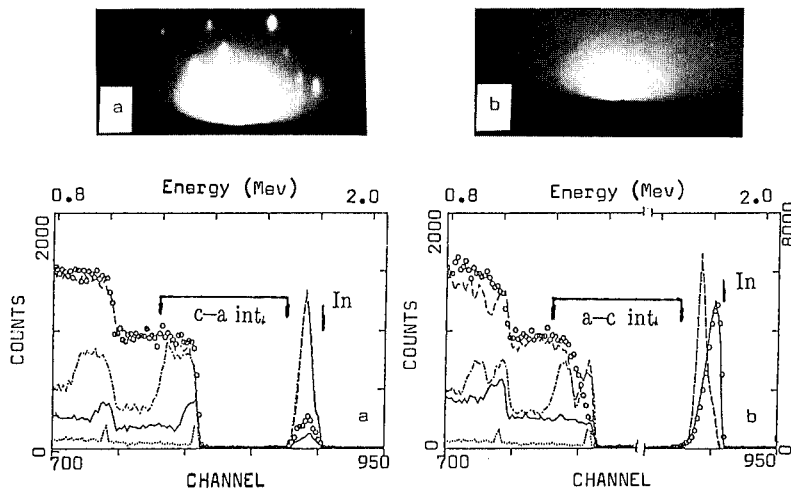


Fig. 5 Backscattering spectra of Al_2O_3 for different doses, annealed at 800°C in Ar (a) 1.1×10^{16} In/cm^2 (b) 6×10^{16} In/cm^2 — as implanted (random), --- as implanted (aligned), o 24h anneal (random), — 24h anneal (aligned), virgin crystal sapphire (aligned).

possibly indicating crystalline disorder such as small misorientation of columns or blocks. Comparison with unimplanted area of the same specimen, however, shows good overall epitaxial alignment. There is no detectable In_2O_3 phase. In contrast, the higher dose sample shows (Fig. 5b), no surface damage peak after 24 h anneal, but a plateau of rather high dechanneling yield indicating quite imperfect crystal (compare with the virgin spectrum in Fig. 5b). However, nearly all the Indium is driven out to the surface and it is non-substitutional. Note the absence of In at the original a-c interface and no indication of inwards migration of In. The RHEED data shows a ring pattern characteristic of In_2O_3 . The surface topography of these samples as measured by SEM is shown in Fig. 6. The surface of the low dose sample (Fig. 6a) is structureless and is similar to the as-implanted surface. However, the higher dose sample shows (Fig 6b) many bright islands (which are rich in In as confirmed by EDX analysis). Combining the information from RBSC, RHEED and SEM techniques leads to an identification of these bright islands as In_2O_3 particles. The surface topography for the high dose sample after 24 h anneal at 700°C is shown in Fig. 6c for comparison. The In_2O_3 particles are much smaller but more

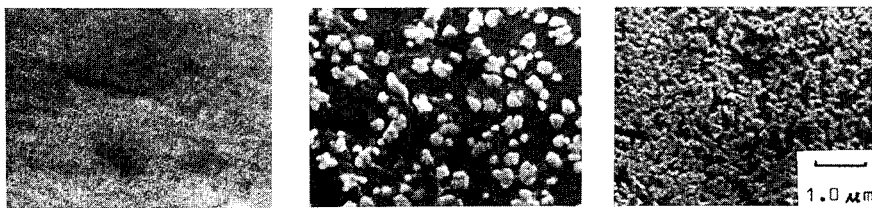


Fig. 6 SEM image of surface topography (a) For lower dose of 1.1×10^{16} In/cm^2 , 24 hour anneal at 800°C , (b) For high dose of 6×10^{16} In/cm^2 24 hour anneal at 800°C , (c) For high dose of 6×10^{16} In/cm^2 . 24 hour anneal at 700°C .

numerous. The source of oxygen is not clear. Oxygen could have come from one or more of the following — traces of moisture or oxygen in Ar gas used, internal reduction reaction with Al_2O_3 or due to brief exposure to air when the sample was still hot. The internal reduction reaction is expected to produce excess Al within the implanted layer. RHEED patterns were carefully examined for any presence of Al particles. No evidence for Al precipitates was found. Further work using TEM is in progress.

4. SUMMARY

In implantation, at liquid nitrogen temperature, to peak concentrations of 6–45 mol.% In produces amorphous surface layers in a-axis Al_2O_3 . Isothermal annealing in Ar ambient between 600–900°C shows effects strongly dependent on ion dose, as follows:

a) Low dose regime ($<2 \times 10^{16}$ In/cm²):

1. Amorphous surface layer undergoes epitaxial regrowth at a well defined planar amorphous to crystalline interface which advances out towards the surface.
2. Regrowth velocity is retarded as the concentration of In increases.
3. Regrowth obeys Arrhenius behaviour with an activation energy of 0.7 eV for initial faster growth and of 1.28 eV for further anneal times.
4. Above a critical In concentration (about 0.6×10^{21} In/cm³ at 700°C and about 1×10^{21} In/cm³ at 900°C) epitaxial regrowth mechanism breaks down.
5. The amorphous phase transforms directly to α - Al_2O_3 without any evidence of an intermediary γ -phase.

b) High dose regime ($>2 \times 10^{16}$ In/cm²):

6. Epitaxial regrowth is substantially retarded or even inhibited and rapid diffusion of In within and out of the amorphous phase dominates.
7. The effective diffusion coefficients for In in amorphous Al_2O_3 are at least 8 orders of magnitude larger than those obtained by an extrapolation of self (Al ion) diffusion coefficients reported in literature in crystalline α - Al_2O_3 .
8. In segregates at the surface to produce islands of In_2O_3 .
9. In migration is completed within the shortest anneal times used (~10 min.). No further redistribution of In is observed up to 24 h anneal times.

5. ACKNOWLEDGEMENTS

This work was performed under an Australian Research Grants Scheme funding. We thank A.P. Pogany for assistance and advice on RHEED analysis and V. Sood for SEM measurements.

6. REFERENCES

1. C.J. McHargue, Nucl. Instrum. Meth. **B19/20**, 797 (1987) and references therein.
2. C.W. White, P.S. Sklad, L.A. Boatner, G.C. Farlow, C.J. McHargue, B.C. Sales and M.J. Aziz, Mat. Res. Soc. Symp. Proc. **60**, 337 (1986).
3. A.P. Mouritz, D.K. Sood, D.H. St. John, M.V. Swain and J.S. Williams, Nucl. Instrum. Meth. **B19/20**, 805 (1987).
4. M. Ohkubo, T. Hioki and J. Kawamoto, J. Appl. Phys. **60**, 1325 (1986).
5. D.X. Cao, D.K. Sood and A.P. Pogany, in 'Fundamentals of Beam Solid Interactions and Transient Thermal Processing' (MRS, Pittsburgh, 1988) eds. M.J. Aziz et al, p. 113.
6. J.S. Williams and J.M. Poate in 'Ion Implantation and Beam Processing' (Acad. Press, New York, 1984) Chapter 2, p.11.
7. A.E. Paladino and W.D. Kingery, J. Chem. Phys. **37**, 957 (1962).

DAMAGE FORMATION IN SEMICONDUCTORS DURING MeV ION IMPLANTATION †

T. P. SJOREEN, O. W. HOLLAND, M. K. EL-GHOR, AND C. W. WHITE
Solid State Division, Oak Ridge National Laboratory, Oak Ridge, TN 37831

ABSTRACT

Damage produced by 1.0–2.5 MeV self-ion and O-ion implantation into Si and Ge single crystals has been characterized by cross-sectional electron microscopy and ion channeling. In Si, it is observed that the damage morphology varies substantially along the ion's track. Near the end-of-range of the ion, damage accumulation is very similar to that which occurs during medium- to low-energy implantation (i.e., damage increases monotonically with dose until the lattice is made completely amorphous). In front of this end-of-range region, however, damage saturates at a very low level for moderate implantation fluences. A model based on homogeneous damage nucleation in Si is discussed. For Ge, damage accumulation is very different; a monotonic increase of damage with dose is observed over the entire range of the ion. Possible mechanisms responsible for the differences between Si and Ge are discussed.

INTRODUCTION

It is of interest to study the mechanisms responsible for the nucleation and growth of damage in semiconductors during ion irradiation. During irradiation, collisions between the ion and the atoms of the solid as the ion penetrates the lattice lead to a transfer of energy to the lattice atoms. These collisions lead to energetic knock-ons (i.e., atoms that are displaced from lattice sites) which can then produce their own sequence of displacement collisions. The collection of the scattering events initiated by the ions, as well as the energetic knock-ons, is referred to as the collision cascade of the ion. The role of the collision cascade in damage nucleation and growth remains controversial.

One concept is that of heterogeneous nucleation in which stable damage is produced directly by a collision cascade. Early on, Brinkman ascribed a special importance to the cascade in damage nucleation.¹ He put forth the idea of a displacement cascade in which dislocations are nucleated near the end-of-range (EOR) of the ion as a result of spatial separation of interstitials and vacancies in the cascade. Another heterogeneous nucleation concept is that of the thermal spike.² In this model, the agitation of the lattice atoms within the volume of the collision cascade is considered to be represented by a local rise in the lattice temperature. In very dense cascades, where the energy deposited per unit path length is high, the temperature rise is thought to exceed the melting point of the solid. Such localized melting and rapid solidification has been used to account for the crystalline-to-amorphous transition observed in Si during heavy-ion irradiation.³

However, there are many aspects of damage nucleation and growth which do not lend themselves to this interpretation of the collision cascade's role. Damage growth in Si during ion irradiation has been shown to increase with dose rate for a constant fluence of self-ions.⁴ Since the collision cascade quenches (thermalizes) on a very short time scale (10^{-11} – 10^{-13} s), the possibility of overlap is nil. Rather, this dose rate effect was shown to be consistent with a model in which damage is nucleated homogeneously as a result

† Research sponsored by the Division of Materials Sciences, U. S. Department of Energy under contract no. DE-AC05-84OR21400 with Martin Marietta Energy Systems, Inc.

of interactions between point defects created by the cascade.⁴ The homogeneous model assumes that the defects are long-lived relative to the life-time of the cascade so that any spatial variation of the various defect populations can be ignored. This relegates the role of the collision cascade in the damage production process to that of a source of point defects. As such, details of the cascade including its dimensions, quench-time, and density become unimportant. Recently, the damage accumulation in Si irradiated with high-energy (MeV) ions was shown to be consistent with such a homogeneous model.⁵

In the present paper, a brief review of some of the results involving high-energy irradiation of Si are given, as well as evidence in support of the homogeneous model. This includes a discussion of the damage morphology and rate of damage growth which is shown to vary significantly along the ion's track. Results for MeV, self-ion irradiation of Ge are presented also and shown to be markedly different than in Si. These differences are detailed and interpreted in terms of cascade effects.

EXPERIMENTAL PROCEDURE

Commercially available Si and Ge (100) single crystal wafers with p- and n-type resistivity, respectively, were used in these experiments. The Si wafers were implanted with 1.25-MeV $^{28}\text{Si}^+$ ions, while for the Ge wafers 1.3-MeV $^{16}\text{O}^+$ and 2.5-MeV $^{74}\text{Ge}^+$ ions were used. These energies were chosen so that the projected range for all ion-target combinations was about 1.3 μm . The current densities were 200–400 nA/cm² for the self-ion irradiations and 800–900 nA/cm² for O^+ . The doses for the Si samples ranged from $0.25\text{--}1.0 \times 10^{16}/\text{cm}^2$ and from $0.05\text{--}20.0 \times 10^{14}/\text{cm}^2$ for Ge. The irradiations were done at room temperature with the samples oriented along a random direction near the $\langle 100 \rangle$ axis. The samples were characterized by Rutherford backscattering ion channeling (RBS) and cross-sectional transmission electron microscopy (XTEM). The RBS analysis used 2.9-MeV He^+ ions incident on the $\langle 110 \rangle$ axis and detected at 160° .

RESULTS AND DISCUSSION

Damage growth in Si is observed to change along the track of the ion. This can be seen in the XTEM micrographs of Fig. 1 which show the self-implantation damage morphology for both low-dose ($0.25 \times 10^{16}/\text{cm}^2$) and high-dose (1.0×10^{16}) irradiations. For the low dose case, a band (denoted by the arrows in Fig. 1a) of defects and dislocation loops near the EOR can be seen, but in the near surface no defects are observed. By increasing the dose by a factor of 4, as shown in Fig. 1b, the region centered near the EOR is amorphized over a depth of about 0.4 μm with extended defects and dislocation loops present on either side of the layer. However, the top 1.0 μm of the sample remains remarkably free of any defects observable by XTEM. RBS analysis⁵ of these samples showed that damage growth essentially saturates in the beginning-of-range region extending over the top 1.0 μm . This damage was determined to have saturated even at the lowest dose studied ($0.25 \times 10^{16}/\text{cm}^2$) and to consist primarily of divacancy defects. This identification was made from the characteristic annealing behavior in this region. However, near the ion's EOR, damage was observed to increase monotonically with the ion fluence until a continuous, buried amorphous layer forms. The amorphous layer was found to expand from the front interface during continued ion irradiation by what appeared to be a layer-by-layer growth. However, in the top layer, damage remained saturated at a low level until consumed by the expansion of the buried amorphous layer.

Many of these aspects of damage growth during high-energy ion irradiation are consistent with homogeneous nucleation. In particular, chemical rate equations which express the relationship of the defect reactions can be used to show that, in the absence

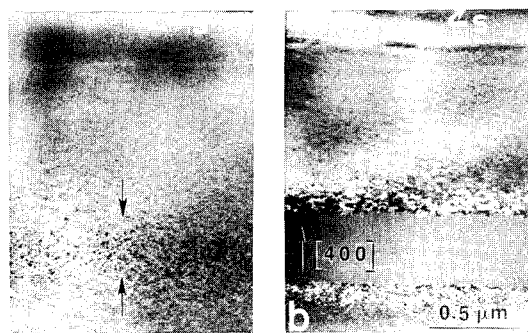


Fig. 1. Cross-sectional transmission electron micrographs of Si single crystal implanted with 1.25 MeV ^{28}Si for doses of (a) $0.25 \times 10^{16}/\text{cm}^2$ and (b) $1.0 \times 10^{16}/\text{cm}^2$.

of unsaturable sinks (such as dislocations), damage will saturate.⁵ This is a result of achieving a steady-state condition where the defect reactions (recombination, annealing) are balanced by the generation rate. Saturation of damage ahead of the EOR region can be explained by such a balancing which occurs in the absence of sinks. With this in mind, additional support for the homogeneous model has been obtained recently from a study⁶ of MeV-ion-beam annealing of Si that had been pre-damaged in the near surface with 100-keV Si^+ ions. It is shown that damage consisting of simple-types of defects is annealed by MeV-ion beams, but more complex damage morphologies, such as a buried amorphous layer, remain stable. The layer-by-layer growth of the buried amorphous layer is explained in terms of the homogeneous model by assuming that the amorphous/crystalline interface acts as a sink for interstitials. The depletion of interstitials in the vicinity of the interface removes the steady-state condition for damage saturation allowing the point defect concentration to increase until the critical damage density for amorphization is achieved.

The results for Ge offer an interesting contrast to Si. Many of the differences can be seen in the RBS/channeling results of Ge samples implanted with different ion fluences (see Fig. 2). It is clear from the aligned scattering yield that damage increases monotonically with dose over the entire range of the implanted Ge^+ or O^+ ions. No saturation of damage ahead of the EOR is observed as in Si. The aligned scattering yield increases with dose until it reaches the random/amorphous level. However, no evidence for the formation of a buried amorphous layer with a distinct front interface is seen. Therefore, unlike Si, the formation of an amorphous layer over the range of the implanted ions appears to occur as a result of random nucleation of growth of amorphous Ge over the entire range rather than proceeding via an interfacial process. Also the channeling spectra indicate a significant amount of dechanneling from the defects rather than direct scattering. This makes determination of the damage profile from the channeling spectra difficult, but does suggest that much of the damage at the lower fluences is dislocation type rather than amorphous.

The differences between Si and Ge were further confirmed by XTEM analysis of the Ge self-implants for doses of $0.5 \times 10^{13}/\text{cm}^2$ and $5.0 \times 10^{13}/\text{cm}^2$ as shown in Fig. 3. These will be referred to as low dose (LD) and medium dose (MD). For the LD sample (Fig. 3a) the micrograph shows a scatter of damage clusters that increase in density with depth reaching a maximum around 0.9–1.0 μm . This distribution of defects agrees with that observed in RBS. Many of these damage clusters were examined by micro-diffraction

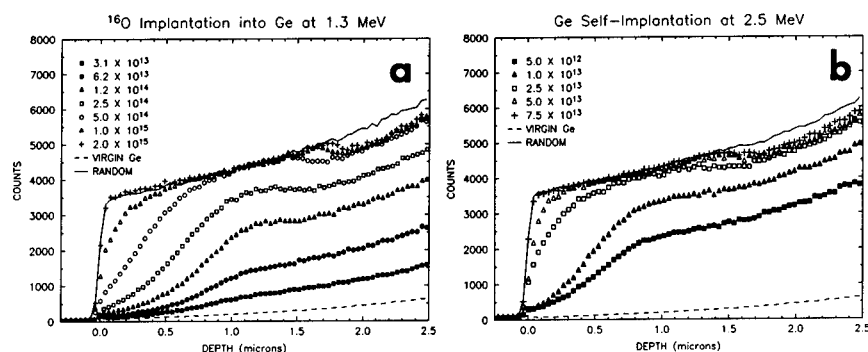


Fig. 2. $\langle 110 \rangle$ aligned RBS spectra obtained from (a) O-implanted and (b) self-implanted Ge single crystal by backscattering 2.9-MeV He^+ ions at 160° .

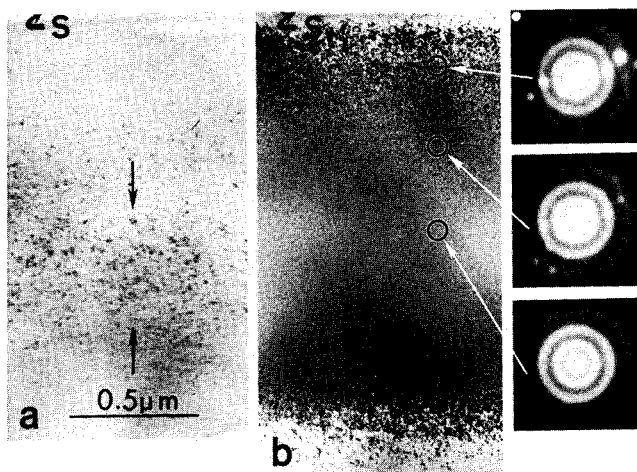


Fig. 3. Cross-sectional transmission electron micrographs of Ge single crystal implanted with 2.5-MeV ^{74}Ge for doses of (a) $0.5 \times 10^{13}/\text{cm}^2$ and (b) $5.0 \times 10^{13}/\text{cm}^2$.

and found to be crystalline in nature rather than isolated amorphous regions. No evidence for formation of amorphous phase Ge was found in this LD sample by electron diffraction. This contrasts with an early TEM study⁷ of damage in Ge by irradiation of 100-keV O^+ ions in which it was shown that individual ion tracks can produce an amorphous cluster. However, a study⁸ of neutron damage in Ge showed that damage clusters were crystalline.

The micrograph of the MD sample (Fig. 3b) shows another case where the damage is very different than that in Si. In this sample a damaged layer extends from about 0.1 to $1.4 \mu\text{m}$ in depth. The RBS spectrum for this sample (the open triangles in Fig. 2b) suggests that the sample is completely amorphous from 0.3 to $1.5 \mu\text{m}$. However, micro-diffraction measurements on cross-sectionally thinned TEM samples show that the layer contains both crystalline and amorphous phases with the amorphous fraction increasing with increasing depth up to $1.0 \mu\text{m}$ (see the micro-diffraction images in Fig. 3b). The micro-diffraction patterns in Fig. 3b show that at the different depths both amorphous

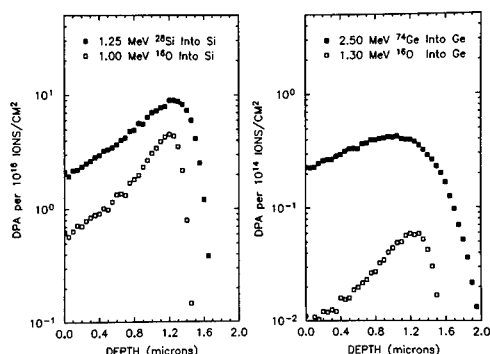


Fig. 4. Results of a TRIM⁹ calculation. Note the difference of the vertical scales to reflect the different damage production rates as discussed in the text.

and crystalline phases exist. Intensity variation of the ring pattern (for the amorphous phase) and spot pattern (for the crystalline phase) can be clearly seen and indicate a significant amorphous fraction at 1.0 μm . It is clear, however, that no continuous amorphous layer forms at this dose, and no distinct interface ahead of the damaged region can be identified.

Some insight into the differences between the ion-target combinations studied can be obtained from the TRIM⁹ calculations of Fig. 4 in which the displacements per atom (dpa) as a function of ion depth are shown. The vertical axes in this figure were normalized to the dose necessary to amorphize the substrate at the peak of the damage profile by self implantation. This corresponds to $\sim 10^{16}$ ions/cm² for Si and $\sim 10^{14}$ ions/cm² for Ge. What is immediately obvious from this figure is that a factor of about 25 more dpa's is needed in Si to produce the same level of damage as in Ge. Also there is almost a one-to-one correspondence in Ge between the damage and the dpa's, while significant in-situ annealing/recombination occurs in Si. Furthermore, the scaling between damage and dpa's in Ge roughly holds, not only for self-ion irradiation, but also for O⁺-ion implantation. While the shape of the dpa curves is seen to vary somewhat for particular ion-target combinations, the data suggest that the differences in damage between Si and Ge are related either to the material or to the nature of the collision cascade.

The mean deposited energy density per atom $\bar{\theta}_v$ in a collision cascade is often used as a parameter to predict the influence of the cascade on damage growth. Dense cascades with $\bar{\theta}_v \simeq 1$ eV/atom are generally thought to play a substantial role in such processes. In Table I, $\bar{\theta}_v$ has been calculated using equation 5 of Ref. 10 for several self-ion energies in both Si and Ge. It is clear that $\bar{\theta}_v$ of the primary cascade for high energy ions is very low in both materials. However, $\bar{\theta}_v$ in the cascades for lower energy self ions is seen to be quite high in Ge. Such dense cascades will occur near the ion's EOR, and also along the primary track in the subcascade regions. Therefore it is reasonable to assume that damage can be nucleated in Ge in these dense cascade regions (associated with energetic knock-ons and the primary ion near EOR). This is consistent with the observation that damage increases monotonically over the entire range of the ion in Ge with a high damage/dpa ratio. Since no amorphous Ge is observed at low implant fluences, overlap of dense cascades must occur to produce a high enough damage density to stimulate this transformation. Such a mechanism would account for the lack of a continuous amorphous layer and a front amorphous/crystalline interfacial region at high damage levels.¹¹

TABLE I. $\bar{\theta}_v$ for Self-Ion Implantation in Si and Ge

Ion Energy (keV)	Si (eV/atom)	Ge (eV/atom)
2500		6.4×10^{-5}
1250	3.8×10^{-5}	
100	9.6×10^{-4}	2.3×10^{-2}
10	0.041	0.41
1	0.44	2.3

CONCLUSIONS

Damage produced in Si and Ge (100) crystals by self-ion and O-ion implantation at MeV energies has been studied and characterized by RBS and XTEM. The most remarkable observed feature is the saturation of damage in the top 1.0 micron in Si. The annealing behavior of this damage indicates that for this saturated region the primary defect produced is the divacancy.⁵ The EOR damage in Si grows monotonically with dose until an amorphous region is formed. The amorphous region then proceeds to grow layer by layer toward the surface with increasing dose. The damage production in Si is interpreted in terms of a model based on damage formation by homogeneous damage nucleation of point defects. For Ge, damage production is observed to be very different than Si. Damage is observed to grow monotonically with dose over the entire range of the ion. No saturation of damage is observed and the amorphization process is substantially different. Comparison of the experimental results with TRIM calculations shows that in Ge there is close to a one-to-one correspondence between damage and dpa, whereas in Si nearly a factor of 25 more dpa's are needed to produce comparable damage levels. Comparison of these results with estimates of the subcascade energy densities for Ge and Si are consistent with the interpretation that in Ge the energy density of the knock-on cascades is sufficiently high to treat the damage processes by a heterogeneous nucleation model.

ACKNOWLEDGEMENTS

We wish to thank M. F. Chisholm for assistance with the micro-diffraction analysis and helpful discussions.

REFERENCES

1. J. A. Brinkman, J. Appl. Phys. **25**, 961 (1954).
2. F. Seitz and J. S. Koehler, Progress in Solid State Physics **2**, 305 (1956).
3. J. A. Davies, in *Ion Implantation and Beam Processing*, edited by J. S. Williams and J. M. Poate (Academic Press, New York, 1984), p. 81.
4. O. W. Holland, D. Fathy, J. Narayan, and O. S. Oen, Radiat. Eff. **90**, 127 (1985).
5. O. W. Holland, M. K. El-Ghor, and C. W. White, Appl. Phys. Lett. **53**, 1282 (1988).
6. O. W. Holland, Appl. Phys. Lett., (in press).
7. J. R. Parsons, Phil. Mag. **12**, 1159 (1965).
8. M. L. Swanson, J. R. Parsons, and C. W. Hoelke, Radiat. Eff. **9**, 249 (1971).
9. J. P. Biersack and L. G. Haggmark, Nucl. Instrum. Methods **174**, 257 (1980).
10. D. A. Thompson, Radiat. Eff. **56**, 105 (1981).
11. John R. Dennis and Edward B. Hale, J. Appl. Phys. **49**, 1119 (1978).

ELECTRICAL ACTIVATION OF HEAVILY DOPED ARSENIC IMPLANTED SILICON

J. SAID*, H. JAOUEN*, G. GHIBAUDO*, I. STOEMENOS**,
P. ZAUMSEIL***

*Laboratoire de Physique des Composants à Semiconducteurs,
ENSERG, 23 Rue des Martyrs, B.P. 257, 38016 Grenoble Cedex,
France

**Department of Physics, University of Thessaloniki,
Thessaloniki, Greece

***Akademie der Wissenschaften der DDR, Institut für
Halbleiterphysik, Frankfurt, Krosingstr 2, 1200-Frankfurt,
GDR

ABSTRACT

The combination of electrical, Transmission Electron Microscopy and Triple Crystal X-ray Diffraction measurements allow us to separate the existence of a local impurity activation process from the amorphous-crystal transformation. The local process occurs in the highly damaged surface layer induced by the arsenic implantation and is efficient well below the Solid Phase Epitaxy transition temperature. It is suggested that point defect migration should play an important role in the electrical impurity activation at low annealing temperatures.

1- INTRODUCTION

The understanding of the annihilation process of implantation induced defects has been the subject of much studies during the last years. However, a certain confusion still remains about the mechanisms by which the impurities are electrically activated and the surface layer reconstructed.

In this work, we investigate separately the role of the impurity activation and the recrystallization processes by combining Spreading Resistance, Triple crystal X-ray diffraction (TCD) and Transmission Electron Microscopy (TEM) measurements. Such a combination of electrical and physical characterizations should yield a better insight in the defect annihilation process in highly doped silicon.

2- EXPERIMENTAL DETAILS

Samples were realized on P type silicon wafers with $\langle 100 \rangle$ crystal orientation and $3.9 \Omega \cdot \text{cm}$ substrate resistivity. Prior to implantation, the wafers were provided with a 40 nm thick SiO_2 thermally grown passivating layer. Arsenic ions of 150-200 keV were then implanted, at room temperature, in the dose range 10^{13} - 10^{15} cm^{-2} . After implantation the silicon samples were subsequently thermally annealed under a dry nitrogen ambient for various temperatures (200°C-1100°C) and various durations.

The Spreading Resistance measurements were carried out using a Solid State Measurements system (ASR-100B). The resistivity profiles of the implanted layers were deduced from the gross Spreading Resistance curves by applying the

Local Slope Approximation of the Dickey model [1]. In addition, the samples were analyzed by TEM and TCD in order to determine the spatial extension of the defected region and the amorphous layer thickness at the surface of the silicon sample both before and after thermal annealing.

3- RESULTS AND DISCUSSION

Fig.1 shows the thermal annealing effect on the resistivity profile for a N^+/P sample implanted at $2 \times 10^{14} \text{ cm}^{-2}$. After annealing, the surface resistivity of a low temperature annealed sample (400°C , 1h) drops by more than 7 decades, though the surface layer is still amorphous as it is clearly shown by the corresponding TEM micrographs of Fig.2.

The above results, correlated with the sheet resistance data of [2], lead us to conclude that this decrease of the surface resistivity occurs at an annealing temperature around $420\text{--}430^\circ\text{C}$ mainly because of the electrical activation of the majority of the impurity atoms within a highly damaged surface region. By contrast, the recrystallization of the amorphous layer, that becomes increasingly efficient at higher annealing temperatures ($T_a = 550\text{--}600^\circ\text{C}$), does not induce a significant reduction of the resistivity even around the amorphous-crystal interface where no resistivity discontinuity appears (see Fig.1).

This last point suggest that a local impurity activation occurs both in the crystalline and the amorphous regions via a local reconstruction process. Therefore, the resistivity, $\rho(x)$, can be described by an exponential kinetics function of the annealing time t as [2,3]:

$$\rho(x, t) = \rho_f(x) + [\rho_i(x) - \rho_f(x)] \exp\left(-\frac{t}{\tau(x)}\right), \quad (1)$$

where $\rho_f(x)$ and $\rho_i(x)$ are respectively the final and initial values of $\rho(x)$ and $\tau(x)$ is the relaxation time constant of the local electrical activation process at depth x . In practice, $\rho_f(x)$ is given by the resistivity profile of a well annealed sample ($T_a \approx 800^\circ\text{C}$, by neglecting the impurity diffusion) and $\rho_i(x)$ by that of a non annealed one. In this context, $\tau(x)$ can be represented by an expression of the form [3]:

$$\tau(x) = \frac{\epsilon k T_a}{4 \pi q^2} \frac{1}{D(x) N(x)} \quad (2)$$

with

$$D(x) = D_0(x) \exp\left(-\frac{E_a(x)}{k T_a}\right), \quad (3)$$

where $D(x)$ and $N(x)$ are respectively the diffusivity and concentration of the point defects ensuring the electrical activation of the impurities, ϵ is the dielectric constant, q is the absolute electron charge and k is the Boltzmann constant.

The activation energy E_a has been determined experimentally by a proper analysis of the Arrhenius plot of the quantity $Q(x) = (\rho_i(x) - \rho_f(x)) / (\rho(x) - \rho_f(x))$ [2]. As a

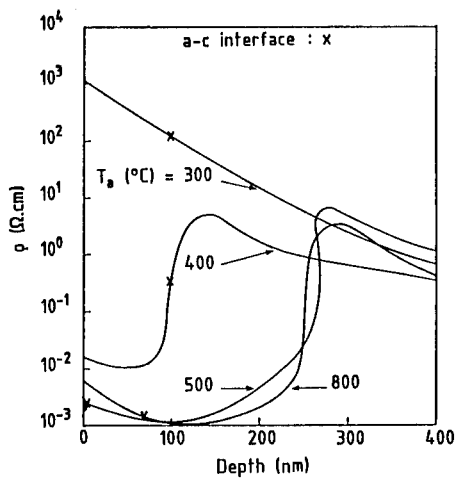


Fig.1 : Resistivity profiles as obtained after various isochronal (1h) anneals for N^+/P type arsenic implanted samples ($2 \times 10^{14} \text{As}/\text{cm}^2$).

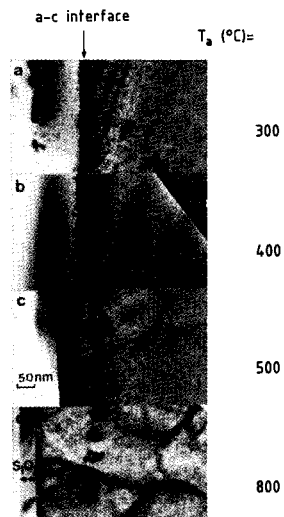


Fig.2 : TEM micrographs obtained on a N^+/P type arsenic implanted samples for various annealing temperatures.
(As $2 \cdot 10^{14} \text{cm}^{-2}$, 200 keV)

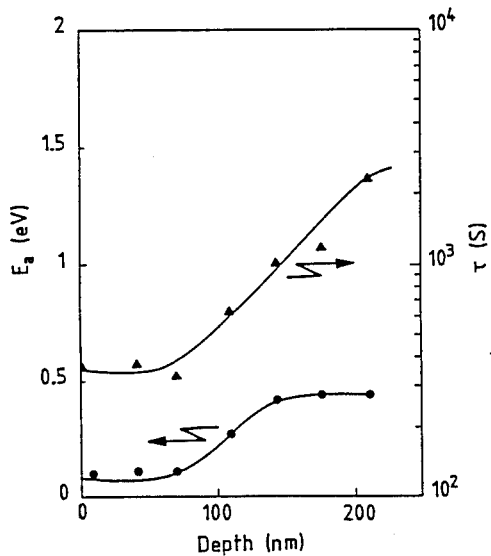


Fig.3 : Variations of activation energy and time constant with depth.
(As $2 \cdot 10^{14} \text{cm}^{-2}$, 200 keV)

result, E_a is found to be weakly depth dependent and is always smaller than 0.5 eV (Fig.3). Furthermore, it has been inferred experimentally that the activation energy found by this analysis is practically independent on the annealing duration, confirming, therefore, the consistency of the kinetics model of equations 1 to 3 with regard to its time dependence.

Likewise, the variation of the relaxation time with depth, $\tau(x)$, has been also deduced (Fig.3). $\tau(x)$ essentially increases when going from the surface towards the substrate. This feature is also consistent with the adopted local relaxation process in which it is shown that the relaxation time is inversely proportional to the diffusivity and the concentration of the point defect species involved in the doping activation.

Besides, Triple crystal diffraction experiments have been conducted on the same samples. As is well known [4], X ray methods are sensitive to a relative change of the lattice constant ϵ and to the static lattice disorder through the Debye-Waller factor $\exp(-L_H)$ [5]. Fig.4 shows the results of TCD analysis for a low temperature annealed sample and a well annealed one. It must be pointed out that, since the tetrahedral radius of arsenic is nearly the same as that of silicon, substitutional arsenic does not change the lattice constant of the doped layer. Therefore, the TCD data are actually indicative of the lattice distortion due to implantation induced defects. In particular, the negative surface strain is likely related to an excess of vacancies while the positive strain is associated with an excess of interstitials.

Moreover, the comparison of the values of the activation energy of Fig.3 with those of usual point defect migrations (0.25eV for a vacancy-interstitial pair, 0.51eV for silicon interstitials, 0.8eV for a vacancy-As⁺ complex and 0.33eV for vacancy [6,7]) suggests that the migrating species involved in the annealing process should be associated with a vacancy and/or an interstitial diffusion. More precisely, in view of the evolution of $E_a(x)$, it can be concluded, in agreement with our TCD data, that vacancy-like defects are presumably the dominant species in the first 100nm, while interstitials seem to prevail above 100nm.

Besides, Fig.5 displays the values of the activation energy both of the relaxation time constant associated with the electrical local activation process and that of the regrowth velocity corresponding to the recrystallization mechanism as obtained from our TEM analysis and from the literature [8]. It is clear from Fig.5 that the activation energies deduced from our resistivity data, $E_a \approx 0.1-0.5$ eV, are in any case much smaller than those for a regrowth process, $E_a \approx 2.5-2.7$ eV. In the former case, the electrical activation of the impurity undergoes via a low energy consuming mechanism whereas, in the latter one, the Solid Phase Epitaxy involves a higher energy consuming process in which the re-ordering at the interface requires the breaking of silicon bonds [9].

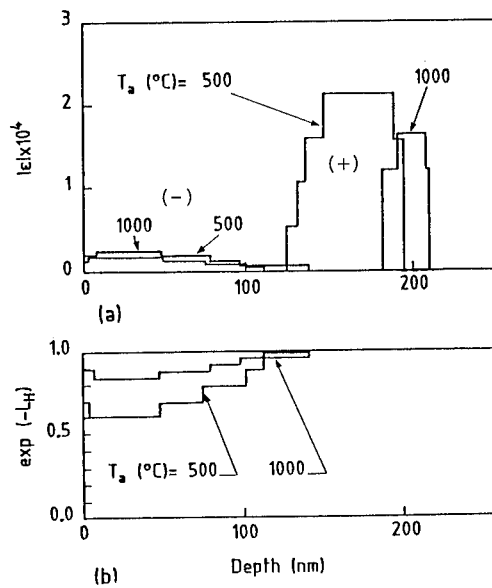


Fig.4 : Mechanical relative strain (a) and Debye-Waller factor (b) variations with depth as obtained by TCD measurements ($10^{15}\text{As}/\text{cm}^2$, 200KeV).

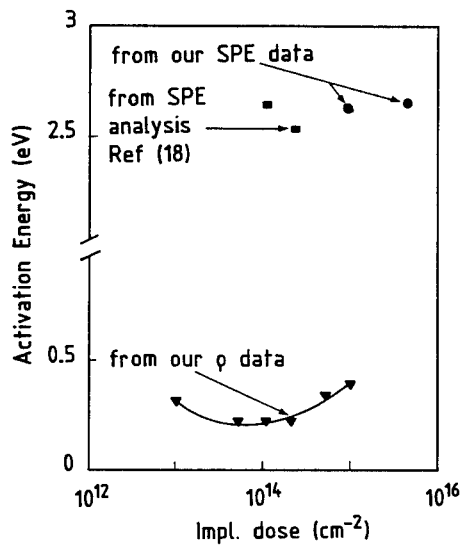


Fig.5 : Activation energy variations with implantation dose as obtained from our resistivity data (depth= 80nm) and from SPE studies.

4- CONCLUSION

It has been shown that the dopant electrical activation in highly doped arsenic implanted silicon is independent of the reconstruction mechanism occurring by Solid Phase Epitaxy. In contrast, the impurity activation process has been shown to be satisfactorily described by a local relaxation model in which the relaxation time is inversely proportional to the diffusivity and the concentration of the point defects leading to the dopant incorporation. Regarding the values of the activation energies found for this process, it is suggested that the migration of vacancies and/or silicon interstitials presumably plays a prevailing role in the impurity activation process.

REFERENCES

1. J.R. Ehrstein, in Nondestructive Evaluation of Semiconductors Materials and Devices, edited by J. N. Zemel (Plenum Press, 1978).
2. C. Christofidès, G. Ghibaudo and H. Jaouen, Rev. Phys. Appl., 22, 407 (1987).
3. C.S. Fuller, in Defects Interactions in Semiconductors, American Chemical Society Monograph Series, No 140, edited by N. B. Hannay (Reinhold Publishing Corporation, New York, 1959) p. 209.
4. P. Zaumseil, Phys. Stat. Sol. (a), 91, K31 (1985).
5. P. Zaumseil, U. Winter, F. Cembali, M. Servidori and Z. Sourek, Phys. Stat. Sol. (a), 100, 95 (1987).
6. B. Boltaks, Diffusion et Défauts Ponctuels dans les Semiconducteurs (Mir, Moscou, 1977).
7. G.D. Watkins and J.W. Corbett, Phys. Rev. A, 134, 1359 (1964).
8. S.A. Kokorowski, G.L. Olson and L.D. Hoss, J. Appl. Phys., 53, 921 (1982).
9. S.T. Picraux, Defects in semiconductors, edited by J. Narayan and T. Y. Tan (North Holland, New York, 1981) p. 135.

RADIATION DAMAGE OF SiO_2/Si BY ENERGETIC NEUTRAL BEAM AND VUV PHOTONS

Tatsumi Mizutani, Shigeru Nishimatsu and Takashi Yunogami

Central Research Laboratory, Hitachi Ltd.
Kokubunji, Tokyo 185, Japan

ABSTRACT

To clarify the generation mechanism of radiation damage induced in SiO_2/Si by plasma processes, effects of three different beams, i.e., ions, neutrals and vacuum ultraviolet (VUV) photons have been evaluated independently. The radiation damage caused by these energetic bombardments has been measured by capacitance-voltage (C-V) measurements. These reveal that bombardments with a 250 eV Ne^0 neutral beam generate far less flat-band voltage shifts (ΔV_{FB}) than those with a Ne^+ ion beam of equal kinetic energy. This can be interpreted in terms of the differences in charge build-up and in hole production upon the incidence of these particles. VUV photons produced in the plasma are also responsible for large ΔV_{FB} .

INTRODUCTION

Plasma processes are now indispensable technologies in the current VLSI fabrication processes. Plasma etching can delineate extremely fine patterns down to deep submicron range by virtue of directional ion-assisted etching mechanism [1,2]. It has been applied successfully to almost every kind of microelectronics fabrication including VLSI's, magnetic bubble devices and surface acoustic wave devices. This technology, however, has a potential disadvantage since it utilizes glow discharge plasma which contains a lot of energetic particles generating radiation damage within solid state devices. These radiation damage will prohibit or at least limit the wide application of plasma processes. It is then needed to improve the current plasma process or to develop low damage surface processes.

Among the many kinds of radiation damage we are particularly interested in charge-associated damage[3] and in vacuum ultraviolet (VUV) induced damage[4] since we believe that these would be fatal to thin insulators such as MOSFET's gate dielectrics and capacitor insulators. In order to understand the generation mechanism of the damage stated above, we constructed a beam-irradiation apparatus which can independently generate ion beams, neutral beams and VUV photons and we measured the corresponding radiation damage. Here we demonstrate that the radiation damage induced in SiO_2 during plasma processes is mainly due to ionic charge and VUV photons.

EXPERIMENTAL

A. Generation of energetic particles from a plasma

Low energy ion beams, neutral beams and VUV photons were produced from a magneto-microwave plasma [5]. The low energy ion beams were extracted through two multiaperture electrodes at desired energies ranging from 100 to 500 eV as shown in Fig. 1. Typical ion current densities were in the range of 0.1-0.3 mA/cm². Neutral beams were produced by charge exchange reactions between extracted ions and background neutrals [6,7,8]. Background gas pressures were 0.09-0.10 Pa. Retarding potentials were applied to the grids set up in front of the specimen as shown in Fig.1 to eliminate residual ions and electrons from the beam. The extracted ion beams were deflected by a magnetic field of about 500 Gauss so that VUV photons generated in the plasma do not impinge on the specimen surface together with ion or neutral beams [9]. This apparatus enabled independent irradiation experiments by ion beams, neutral beams and VUV photons. The ion and neutral beam fluxes were measured by a Faraday cup and by Cu sputtering yield measurements using a quartz crystal oscillator [8].

B. Measurements of radiation damage

SiO₂ surfaces of oxidized Si without metallization were bombarded by an ion beam, a neutral beam or VUV photons. Specimens were not annealed after energetic particle irradiations. Capacitance-voltage (C-V) characteristics were measured using a mercury probe. Flat-band voltage shifts (ΔV_{FB}) from the unbombarded standard specimen were adopted as indexes of radiation damage. Specimens were Si (p-type, (100), 10 Ω cm) wafers oxidized in dry oxygen at 1000°C and subsequently annealed in hydrogen at 400°C for 20 min. The thickness of the SiO₂ layer was 115 nm.

RESULTS

Flat-band voltage shifts (ΔV_{FB}) induced in SiO₂ by Ne⁺ ion beams and by Ne⁰ neutral beams were measured as a function of the particle dose. The results are shown in Fig. 2. Although the kinetic energies of Ne⁺ ions and Ne⁰ neutrals were both 250 eV, the ΔV_{FB} caused by Ne⁰ bombardment

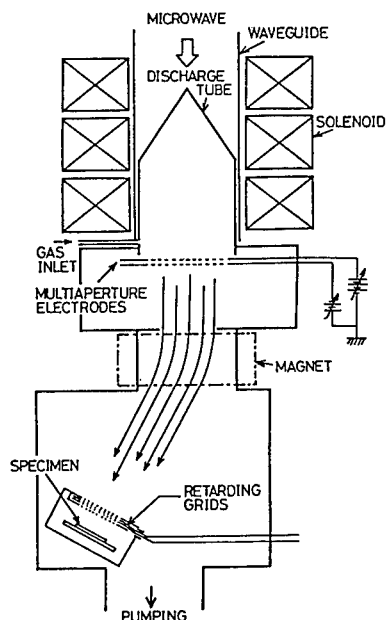


Fig.1. Schematic of ion and/or neutral beam irradiation apparatus. Ion beams are deflected immediately after ion beam extraction. VUV photons generated in the plasma region do not impinge on the specimen surface.

was much smaller than that by Ne^+ . This indicates that most of the ΔV_{FB} by 250 eV Ne^+ should be attributed to its electric charge rather than to its kinetic energy. This will be discussed in detail later.

Also shown in Fig. 2 is the ΔV_{FB} caused by VUV photons generated in the plasma under the same conditions with Ne^+ and Ne^0 beam production. A 100 nm thick Al film was evaporated onto the SiO_2 surface, so that only the strong resonance lines at 73.6 and 74.4 nm of Ne plasma (see Fig. 3(a)) can be transmitted through Al and cause radiation damage in SiO_2 . Any other energetic particles such as ions and fast neutrals are stopped at the Al surface. The transmittance of VUV photons of 74 nm wavelength through a 100 nm Al film is about 50 % [10]. Therefore the obtained ΔV_{FB} by these irradiation experiments were multiplied by a factor of 2. The ΔV_{FB} s due to VUV photons were much larger than those by Ne⁰ neutral bombardments. Thus, it can be concluded that the radiation damage induced in SiO_2 and measured by V_{FB} is mainly due to particle's charge and to VUV photons.

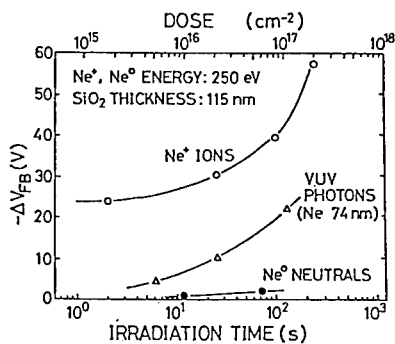


Fig.2. Flat-band voltage shifts (ΔV_{FB}) of SiO_2/Si induced by 250 eV Ne^+ ion and Ne^0 neutral bombardments and by VUV photons.

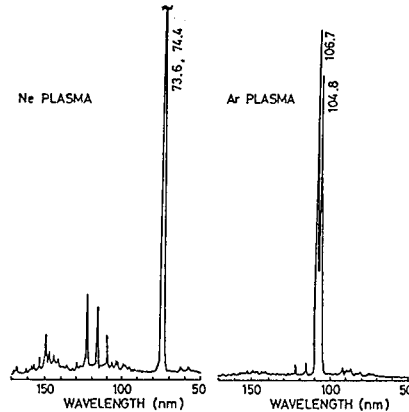


Fig.3. Emission spectra of magneto-microwave plasmas of (a) Ne and (b) Ar in the VUV region.

It has been demonstrated that V_{FB} due to VUV photons appears when photon energy exceeds SiO_2 bandgap energy, i.e., 8.8 eV [11]. VUV emission spectrum of Ar plasma is shown in Fig. 3(b). Strong resonance lines are observed at wavelengths of 104.8 and 106.7 nm whose photon energies are 11.8 and 11.6 eV well above the SiO_2 bandgap energy. The ΔV_{FB} 's caused by these VUV photons are shown in Fig. 4. When the SiO_2 surface is covered with an Al film, these strong resonance lines cannot be transmitted through the Al and henceforth only weak emissions whose wavelengths are below the Al absorption edge (~ 80 nm) can contribute to ΔV_{FB} . Therefore small ΔV_{FB} 's were obtained for Al covered specimens as shown in Fig. 4. Strong VUV emissions are usually observed in glow discharge plasmas of various kinds of gases which are widely used in current plasma processes. Typical VUV emission spectra were measured for the plasmas

produced in the apparatus shown in Fig. 1. The results are shown in Fig. 5 for O_2 and CF_4 . All emissions whose wavelengths are below 140 nm (≈ 8.8 eV) in Fig. 5 are responsible for ΔV_{FB} 's. These VUV photons ought to be eliminated or at least minimized in fluxes to realize low-damage plasma processes.

DISCUSSIONS

Ne^0 neutral bombardments onto SiO_2 induced much less ΔV_{FB} 's than Ne^+ ion bombardments, although kinetic energies were 250 eV in both cases. We believe this is due to less charge build-up on SiO_2 surfaces and to the smaller number of electron-hole pairs created under neutral bombardments than under ion bombardments. In the latter case, an ion becomes neutralized immediately prior to incidence within a few Angstroms distance from the surface by an Auger or resonance neutralization [12]. This process creates one or two holes in the SiO_2 valence band. In addition the neutralized particle impinges upon the surface where a thermal hot spot is generated by the particle's kinetic energy. This high temperature region will also produce some electron-hole pair excitations. In the case of neutral bombardment, however, only the latter mechanism for electron-hole pair creation works. Moreover, less charge build-up on the SiO_2 surface will cause a smaller amount of hole drift toward the SiO_2/Si interface region. In the case of photon incidence, a photon whose energy exceeds the SiO_2 bandgap energy directly induces an electron-hole pair creation and some electrons are emitted from the surface as secondary electrons, which will lead to surface charge build-up to some extent. This in turn will cause hole drift toward the SiO_2/Si interface as in the case of ion bombardment. The above discussions are schematically depicted in Fig. 6.

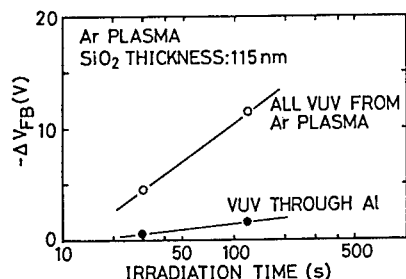


Fig.4. Flat-band voltage shifts (ΔV_{FB}) of SiO_2/Si induced by VUV photons in Ar plasma and by transmitted photons through an Al films deposited on the SiO_2 surface.

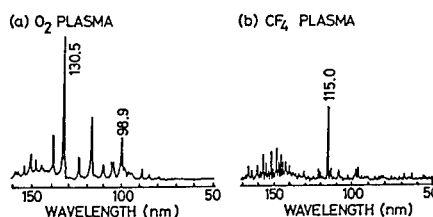


Fig.5. VUV emission spectra of magneto-microwave plasmas of O_2 and CF_4 . Emissions whose wavelengths are less than 140 nm are responsible for ΔV_{FB} formation in SiO_2 .

Figure 7 shows Al electrode voltage dependence of ΔV_{FB} caused by VUV irradiation. ΔV_{FB} decreased gradually as the voltage applied to the thin Al electrode decreased from 20 V down to -30 V. As is well known, a simple mechanism for ΔV_{FB} due to irradiation is as follows. Holes created at the near-surface region of SiO_2 adjacent to the Al film move toward the SiO_2/Si interface whereupon they are trapped to become trapped positive charges or to be converted to interface traps. If the ΔV_{FB} is caused only by this process, the ΔV_{FB} should show a drastic decrease when the Al electrode voltage decreases from positive to negative, since holes should drift toward the Al electrode side. Therefore, the gradual decrease of ΔV_{FB} in Fig. 7 means that mechanisms such as chemical species diffusion other than hole drift may participate in ΔV_{FB} formation. Detailed study including SiO_2 film characterization is necessary to clarify the real mechanism for ΔV_{FB} formation during irradiation.

The results obtained in this study lead us to an expectation that low energy neutral beams are promising energy source for low-damage surface modification processes such as etching technologies and thin film depositions. In addition, VUV photons generated in the plasma must be eliminated from the beam to achieve low-damage surface processes.

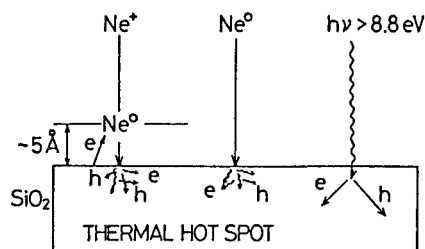


Fig.6. A schematic of electron-hole pair creation in SiO_2 upon the incidence of either ions, neutrals or VUV photons.

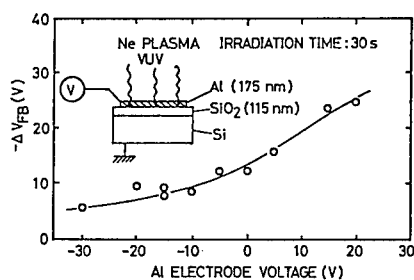


Fig.7. Al electrode voltage dependence of ΔV_{FB} caused by VUV irradiations.

CONCLUSION

Low energy neutral beams (250 eV Ne^0) induce far less radiation damage characterized by ΔV_{FB} in SiO_2 than ion beams having the same kinetic energy. This is due to less charge build-up on the surface and to less amount of electron-hole pair creation in SiO_2 . In addition, VUV photons generated in the plasma induce significant ΔV_{FB} comparable to that produced by ion bombardment. Low energy neutral beams are promising energetic beams to achieve low-damage surface processes for future ULSI fabrication.

ACKNOWLEDGMENTS

The authors would like to express their gratitude to Drs. Keizo Suzuki and Masahiko Ogirima for their discussions and encouragement.

REFERENCES

1. J.W.Coburn and H.F.Winters, J.Appl.Phys.50,3189(1979).
2. T.M.Mayer and R.A.Barker, J.Vac.Sci.Technol.21,757(1982).
3. T.Watanabe, Solid State Technol.1985 (April),263.
4. R.J.DiMaria, L.M.Ephrath, and D.R.Young, J.Appl.Phys.50,4015 (1979).
5. K.Suzuki, S.Okudaira, S.Nishimatsu, K.Usami, and J.Kanomata, J.Electrochem.Soc.129,2764(1982).
6. R.Robinson, J.Vac.Sci.Technol.16,185(1979).
7. D.Rapp and W.E.Francis, J.Chem.Phys.37,2631(1962).
8. T.Mizutani and S.Nishimatsu, J.Vac.Sci.Technol.A6,1417(1988).
9. T.Mizutani and S.Nishimatsu, submitted to J.Vac.Sci.Technol.A.
10. C.Kunz, Synchrotron Radiation -Techniques and Application (Springer-Verlag, 1979) pp.101.
11. R.J.Powell and G.F.Derbenwick, IEEE Trans.Nucl.Sci. NS-18, 99(1971).
12. H.D.Hagstrum, Phys.Rev.104,309(1956).

A COMPARISON OF LOW ENERGY BF_2 IMPLANTATION IN Si AND Ge PREAMORPHIZED SILICON

Gary A. Ruggles*, Shin-Nam Hong*, Jimmie J. Wortman*, Mehmet Ozturk*, Edward R. Myers*, John J. Hren*, and Richard B. Fair**

*North Carolina State University, Raleigh, NC 27695

**Microelectronics Center of North Carolina, Research Triangle Park, NC 27709

ABSTRACT

Low energy (6 keV) BF_2 implantation was carried out using single crystal, Ge-preamorphized, and Si-preamorphized silicon substrates. Implanted substrates were rapid thermal annealed at temperatures from 600°C to 1050°C and boron channeling, diffusion, and activation were studied. Ge and Si preamorphization energies were chosen to produce nearly identical amorphous layer depths as determined by TEM micrographs (approximately 40 nm in both cases).

Boron segregation to the end-of-range damage region was observed for 6 keV BF_2 implantation into crystalline silicon, although none was detected in preamorphized substrates. Junction depths as shallow as 50 nm were obtained. In this ultra-low energy regime for ion implantation, boron diffusion was found to be as important as boron channeling in determining the junction depth, and thus, preamorphization does not result in a significant reduction in junction depth. However, the formation of junctions shallower than 100 nm appears to require RTA temperatures below 1000°C which can lead to incomplete activation unless the substrate has been preamorphized. In the case of preamorphized samples, Hall measurements revealed that nearly complete electrical activation can be obtained for preamorphized samples after a 10 second rapid thermal anneal at temperatures as low as 600°C.

INTRODUCTION

Ion implantation has been the workhorse for establishing and controlling dopant profiles in VLSI technology. The demands on this technology continue to increase as device dimensions shrink. For future 0.25 μm CMOS designs, source and drain junction depths may be as shallow as 70 nm [1]. The extension of ion implantation into the regime of very shallow junctions necessitates a reduction in ion energy. For p⁺n junctions, the reduction in B ion energy may be accomplished in two distinct ways. The incident B⁺ ion energy may be reduced (to less than approximately 5 keV for junctions shallower than about 150 nm [2]) or molecular implant species, such as BF_2 may be employed. The former approach suffers from the practical limitation of a required ion energy below that which is available on most commercial implanters. This limitation can be overcome, and is the subject of study reported elsewhere [3]. The later approach, which is the subject of the current study, works because the BF_2 ions dissociate upon impact with the Si substrate surface, dividing the total energy between B⁺ ions and F⁺ ions in a ratio of (11/49) to (38/49). This technique, however, is clearly more complex, involving the simultaneous implantation of F⁺ ions into Si, as well as the desired B⁺ ions.

Unfortunately, low energy B implantation into crystalline Si results in the creation of a channeling tail, which can lead to deeper junctions. For this reason, heavier ions such as Si⁺ or Ge⁺ are frequently used to preamorphize the silicon prior to B implantation. Although BF_2 implantation can preamorphize the substrate, the preamorphized region is so shallow that no significant reduction in channeling occurs. This paper compares the effects of Ge⁺ vs. Si⁺ preamorphization on B profiles and activation allowing some interesting conclusions to be drawn.

EXPERIMENTAL TECHNIQUES

Wafers used in this study were Cz-grown, n-type, $\langle 100 \rangle$ oriented silicon substrates with resistivities of 8 - 15 Ωcm . Preamorphization was carried out using both 27 keV/ 3×10^{14} Ge^+ ions at room temperature and 22 keV/ 8×10^{14} Si^+ ions at liquid nitrogen temperature. These two preamorphization conditions resulted in the formation of continuous amorphous layers approximately 40 nm deep (determined by cross sectional TEM). Rapid Thermal Annealing (RTA) of the implanted samples was carried out in a HEAT-PULSE 210T at temperatures ranging from 600°C to 1050°C for 10 seconds in pure Ar. The 10 s RTA's were the only anneals that samples from this study were subjected to. For this work, annealing was carried out using a 1 cm^2 piece of each sample. The small piece was centered on a four inch wafer during the RTA. The temperature during annealing was monitored via a thermocouple mounted within a small Si chip adjacent to the annealing sample. Because of the concern over temperature accuracy, the temperatures reported in this work were calibrated using sheet resistance data for 35 keV B^+ implants supplied by AG Associates. There is concern about the use of thermocouples for temperature measurement in RTA systems, and in fact, results reported here differ from those previously reported using the same system [4]. We have found that the sample mounting geometry can be important in determining both the actual sample temperature during the RTA, as well as the heating and cooling rates (this finding will be reported in detail elsewhere). We believe that differences in boron profiles obtained from the present study and those reported previously for similar implantation and annealing conditions [4] are due the differences in sample mounting geometry. In the previous work, quarters of four inch wafers were annealed while being supported on quartz beads. We have observed substantial differences in actual sample temperature (based on sheet resistance data) for the same RTA time/temperature settings due to this difference in mounting geometry alone.

Boron profiles were determined by Secondary Ion Mass Spectroscopy (SIMS) using a Cameca IMS 3F employing a 2.5 keV O_2 primary beam. Calibration of concentrations was done by normalizing the data to the implanted B dose. The activated percentage of boron was determined using Hall measurements coupled with estimates of total dose from SIMS profiles.

RESULTS AND DISCUSSION

As implanted B profiles for 6 keV BF_2 implantation into single crystal and pre-amorphized silicon are compared to a theoretical profile for implantation into an amorphous substrate in Figure 1. As is evident from the figure, the pre-amorphization conditions chosen still result in a significant deviation from

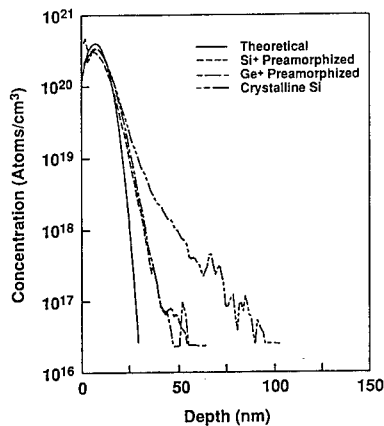


Fig. 1. As implanted boron profiles for 6 keV/ 5×10^{14} BF_2 implanted into crystalline and preamorphized Si.

theoretical behavior, although significant channeling is not evident. This is in contrast to the large channeling tail obtained for implantation into crystalline silicon. The Ge^+ and Si^+ pre-amorphized profiles are nearly identical and appear to be determined primarily by the amorphous layer depth which is 40 nm in both cases.

After annealing, the crystalline and pre-amorphized samples exhibit quite different behavior, as expected. Figure 2 shows boron profiles for implantation into single crystal Si and Ge pre-amorphized Si at various annealing temperatures.

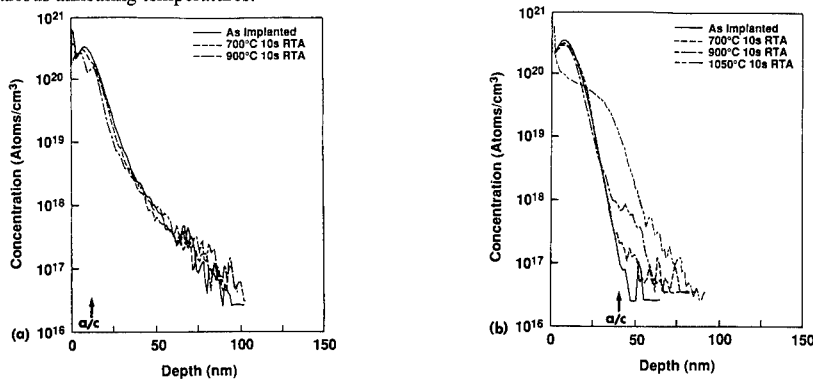


Fig. 2. (a) Boron profiles for 6 keV BF_2 implanted into crystalline silicon. (b) Boron profiles for 6 keV BF_2 implanted into 27 keV Ge pre-amorphized Si.

For the implant into crystalline Si (Figure 2a), the channeling tail determines the junction depth for RTA temperatures up to about 900°C (BF_2 implantation creates an amorphous layer only 10 nm deep). Thereafter, diffusion in the tail region causes a gradual increase in junction depth. This behavior is similar to that reported previously [4]. Boron segregation to the end-of-range damage region (just beyond the amorphous/crystalline (a/c) interface at 10 nm) is evident in Figure 2a. In the case of Ge^+ pre-amorphized Si shown in Figure 2b, there is only a small channeling tail (the amorphous layer depth is about 40 nm), and enhanced boron diffusion in the region beyond the a/c interface results in significant profile broadening after annealing. Here, it is evident that pre-amorphization is effective at reducing junction depth only when the RTA temperature can be maintained below about 900°C. Results from Si^+ pre-amorphization are essentially the same. In Figure 3, B profiles for 6 keV BF_2 implantation into Si^+ and Ge^+ pre-amorphized samples are directly compared for a 900°C RTA.

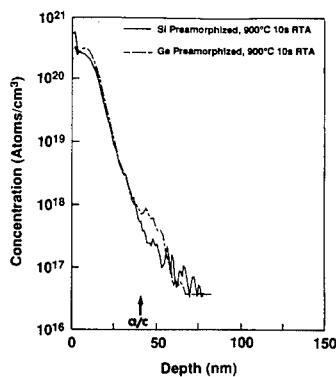


Fig. 3. A comparison of boron profiles for 6 keV/ 5×10^{14} BF_2 implantation into Si^+ and Ge^+ pre-amorphized Si substrates after a single step RTA in Argon.

It appears that, in addition to the similarity in as implanted profiles shown in Figure 1, the profiles after rapid thermal annealing are nearly identical to within the limits of the SIMS measurement. The only significant difference in the profiles is to be found near the peak region where the Si^+ pre-amorphized samples appear to suffer from more outdiffusion of dopant from the sample surface.

The defect annealing behavior can be discerned from cross sectional TEM micrographs of annealed samples. Figures 4a and b are TEM cross sections for 6 keV BF_2 implanted into crystalline Si and annealed at 700°C and 900°C.

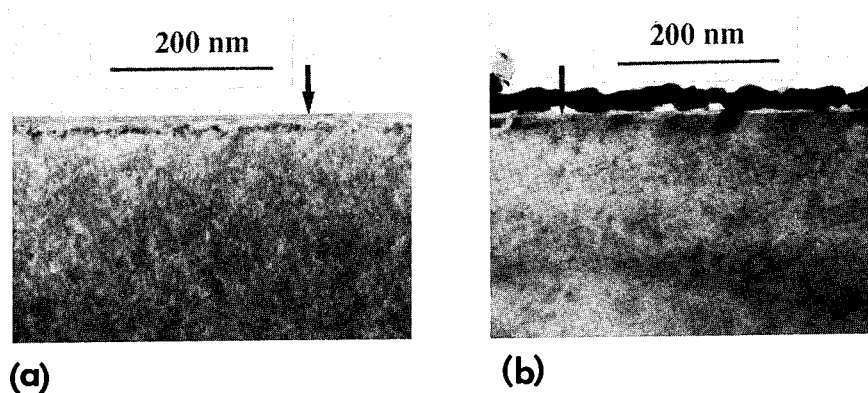


Fig. 4. Cross sectional TEM micrograph of single crystal Si substrate implanted with 6 keV BF_2 after RTA at (a) 700°C, and (b) 900°C.

In Figure 4a, the 700°C RTA can be seen to have resulted in the formation of a region of extended defects located approximately 18 nm from the surface (just beyond the original a/c interface). From Figure 4b, it would appear that a 900°C 10s RTA is sufficient to remove the end-of-range damage. However, based on the boron and fluorine segregation observed in SIMS profiles for the 900°C RTA samples, some damage may likely still exist. Figures 5a and b show similar views for Ge^+ pre-amorphized samples.

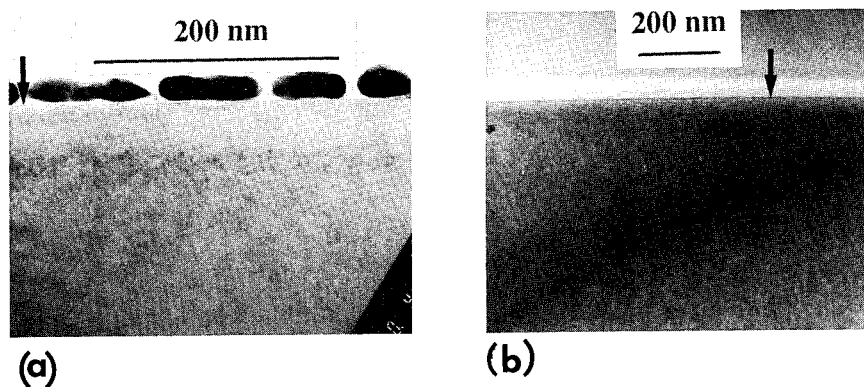


Fig. 5. Cross sectional TEM micrograph of Ge^+ pre-amorphized Si substrate implanted with 6 keV BF_2 after RTA at (a) 700°C, and (b) 900°C.

In this case, some residual dislocation loops are still evident after the 900°C RTA. Defect removal is expected to be more difficult for the pre-amorphized samples because of the deeper end-of-range damage created by the 27 keV Ge⁺ implantation as compared to the 6 keV BF₂ implantation.

Activated boron percentages were calculated based on measured Hall data and the dose determined from the SIMS profile. The percentages in the table therefore reflect the activated percentage of remaining boron after the anneal, after any loss of boron from the surface due to outdiffusion has occurred. The results for crystalline and Ge pre-amorphized Si at two RTA temperatures are summarized in Table I.

Table I. Activated boron percentage for 6 keV BF₂ implantation into crystalline and Ge⁺ pre-amorphized Si substrates for two RTA conditions.

	Crystalline	Ge Preamorphized
600°C/10s	31 %	100 %
1050°C/10s	68 %	98 %

From the data in Table I, it is apparent that nearly complete activation of dopants can be achieved at very low RTA temperatures, as low as 600°C, if the substrate has been pre-amorphized. Pre-amorphization permits dopant atoms to find substitutional lattice sites more readily because they do not need to displace a Si atom to become substitutional. They occupy the correct sites during the solid phase epitaxy that takes place during the low temperature anneal. Without pre-amorphization, high temperatures are required for dopant activation as evident in the table. This data underscores the most significant contribution of pre-amorphization to very low energy B implantation processes - the ability to attain high levels of dopant activation while keeping RTA temperatures very low. Of course, the issue of residual damage present after a 600°C anneal must be addressed. Such defects have been shown to detrimental to device performance, resulting in high junction leakage currents. However, careful control of the location of such residual defects with respect to the junction depletion layer may minimize this effect [5].

CONCLUSIONS

The results of this study indicate that nearly identical B profiles and junction depths may be obtained for low energy BF₂ implantation into Si⁺ and Ge⁺ pre-amorphized substrates. In both cases, junction depths as shallow as 50 nm were obtained for low temperature RTA's. It is apparent that the choice of whether or not to use pre-amorphization in a given process may depend on several factors. The data indicate that implantation into crystalline Si results in the formation of a large channeling tail which is consumed during subsequent annealing. Hence the junction depth tends to be determined by the channeling tail in this case. Without pre-amorphization, annealing temperatures must be high to activate a significant fraction of the implanted boron. Even so, junction depths in the range of 100 nm are obtainable without the use of pre-amorphization. When pre-amorphization is employed, the as-implanted profiles are much shallower than the implants into crystalline Si. But due to enhanced diffusion, particularly beyond the end of range damaged region, the junction depths obtained are not that different from the crystalline case when RTA temperatures are higher than 900°C. The key advantage to preamorphization in this low energy regime appears to be that significant activation can be achieved under low temperature annealing conditions. This can be advantageous both for the formation of ultra shallow junctions (~ 50 nm), and in the case of shallow junction formation which is to be followed by subsequent processing with restrictions on maximum temperature (i.e. silicidation). The advantage of low temperature activation must be kept in balance with the possibility of increased junction leakage currents in devices. A

shallower preamorphization depth should reduce junction leakage by removing defects from the proximity of the depletion region. At the same time, however, the percentage of activated dopant will decrease as less of the implanted boron is within the preamorphized region.

ACKNOWLEDGEMENTS

This work was supported in part by the Semiconductor Research Corporation and the Microelectronics Center of North Carolina.

REFERENCES

- [1] G. Bacarani, M. R. Wordeman, and R. H. Dennard, *IEEE Trans. Electron Devices*, **ED-31**, 452 (1984).
- [2] D. E. Davies, *IEEE Electron Device Lett.*, **EDL-6**, 397 (1985).
- [3] S. N. Hong, G. A. Ruggles, J. J. Paulos, J. J. Wortman, and M. C. Ozturk, *Appl. Phys. Lett.*, **53**, 1741 (1988).
- [4] M. C. Ozturk, J. J. Wortman, and R. B. Fair *Appl. Phys. Lett.*, **52**, 963, (1988).
- [5] Mehmet C. Ozturk, Jimmie J. Wortman, Carlton M. Osburn, Atul Ajmera, George A. Rozgonyi, Eric Frey, Wei-Kan Chu, and Clinton Lee *IEEE Trans. Electron Devices*, **ED-35**, 659 (1988).

ION IMPLANTATION DOPING OF SIMOX WITH ^{31}P AND ^{69}Ga

K. S. Jones, D. Venables, C. R. Horne, Department of Materials Science and Engineering, University of Florida, Gainesville, FL 32611 and G. Davis, DNA/RAEE, 6801 Telegraph Road, Alexandria, VA 22310

ABSTRACT

Implantations of annealed SIMOX and Si wafers have been done using P and Ga to investigate the effect of excess oxygen and oxygen precipitates on amorphous layer regrowth and category II (end-of-range) dislocation loop elimination. Solid phase epitaxial regrowth of the amorphous silicon in both SIMOX and Si control wafers occurred at 550°C without the formation of category III defects and annealing at 900°C 16 hours resulted in complete removal of the category II defects. In an oxidizing ambient, the implanted SIMOX wafer again exhibited complete defect elimination whereas the Si control wafer showed growth and development of extrinsic stacking faults. It is speculated that the buried oxide may act as a sink for the Si. SIMS results indicate the dopant getters to the Si/SiO₂ interfaces and that redistribution can be modelled reasonably well with SUPREME III.

INTRODUCTION

As the lateral and vertical dimensions of integrated circuit devices decrease, the requirements for sensitive control of doping through ion implantation become significantly more stringent. To date, a very large research effort has been focussed on understanding the evolution of defect microstructures and dopant profiles following implantation and annealing in bulk silicon [1,2]. However, relatively little has been published on ion implantation doping in SIMOX silicon-on-insulator structures [3-5]. The unusual thin film geometry of SOI structures in general, and the unique microstructure of SIMOX in particular, could well lead to anomalous dopant distribution and defect evolution effects. It is necessary to understand these effects if the full promise of SIMOX (or other SOI technologies) for radiation hardened and other device applications is to be realized.

The fabrication of shallow, low leakage current p-n junctions by ion implantation requires the removal of category II (end-of-range) damage [2] with a minimal amount of dopant redistribution during post-implantation thermal treatments. In bulk silicon, we have previously demonstrated that category II defects (extrinsic dislocation loops) become unstable during thermal annealing provided the implanted species has exceeded solid solubility and the precipitates thus generated are also unstable and dissolve during the anneal [2,6]. This enhanced elimination of category II dislocation loops has been demonstrated for P, Ga and As implants in bulk Si wafers [6]. Enhanced elimination of defects has also been observed by Ajmera and Rozgonyi [7] with very shallow implants of boron into preamorphized Si substrates. In this case, the proximity of the defects to the surface (a presumed interstitial sink) appears to play an important role in destabilizing the implant damage.

In the preliminary research reported here, the evolution of dopant profiles and implantation related defects in the thin film geometry of SIMOX was investigated and compared to that in bulk silicon.

EXPERIMENTAL PROCEDURE

The SIMOX wafer was a p-type $\langle 100 \rangle$, 10-20 $\Omega\text{-cm}$ silicon wafer implanted with 150 keV O^+ to a dose of $1.7 \times 10^{18} \text{ O}^+/\text{cm}^2$ at 535-550°C. The wafer was subsequently capped with a 6000 Å SiO₂ layer and annealed at 1250°C for 8 hours in a $\text{N}_2 + 1\% \text{ O}_2$ ambient. This anneal yielded a SIMOX structure consisting of a 1500 Å thick surface silicon layer with $\approx 10^{19} \text{ cm}^{-3}$ threading

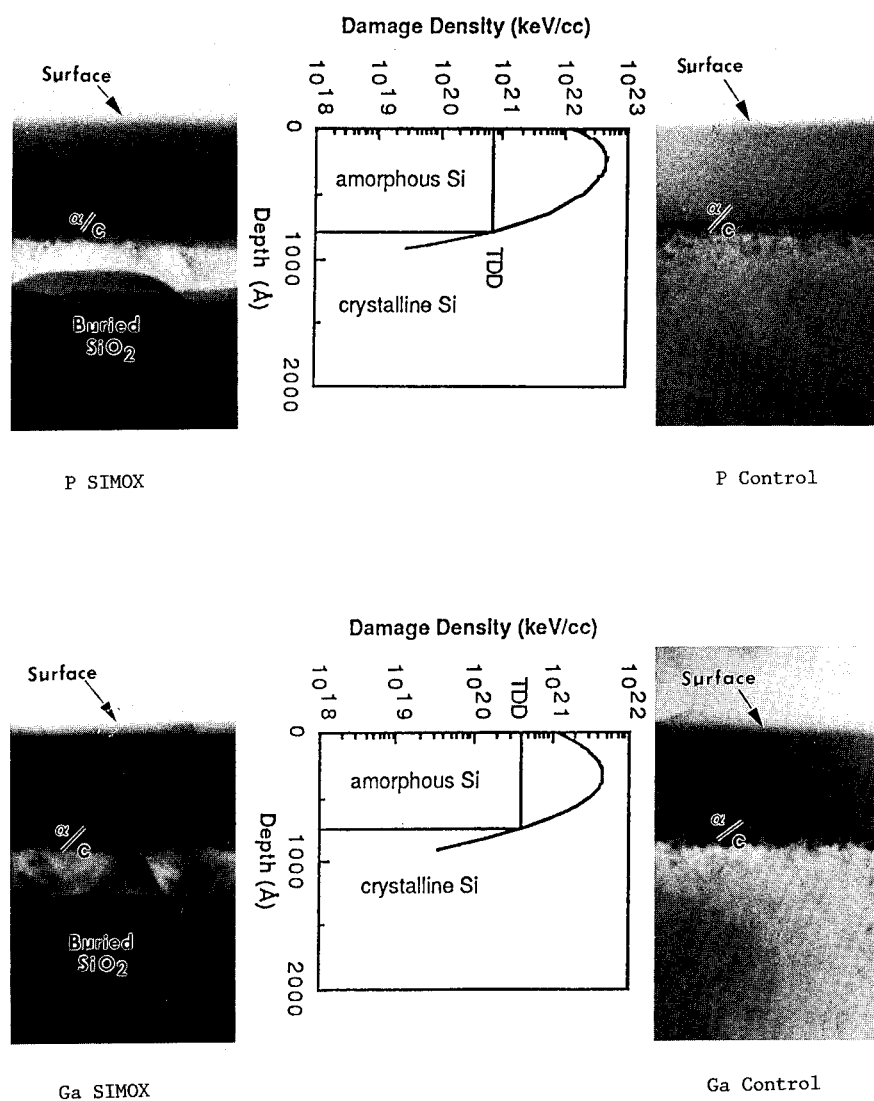


Figure 1. Bright field XTEM micrographs of as-implanted SIMOX and control Si wafers. For comparison, plots of damage density vs. depth are shown (see text).

dislocations and some large SiO_2 precipitates near the surface silicon/buried oxide interface. The buried oxide was ≈ 3600 Å thick. Diced pieces of this annealed SIMOX wafer and of a control, bulk $\langle 100 \rangle$ silicon wafer were etched to remove surface oxides and implanted with either $^{31}\text{P}^+$ or $^{69}\text{Ga}^+$ at doses of $1 \times 10^{16} \text{ P}^+/\text{cm}^2$ or $5 \times 10^{14} \text{ Ga}^+/\text{cm}^2$. These doses and energies produce a continuous (surface) amorphous layer to a depth of ≈ 750 Å and have been reported to result in enhanced elimination of end-of-range damage upon annealing in bulk silicon [8].

Thermal regrowth of the amorphous layers was performed at 550°C for 16 hours in flowing N_2 . The samples were then annealed at 900°C for either 0.5 or 16 hours in N_2/O_2 . The evolution of the microstructure and of the dopant profiles were monitored by cross sectional TEM and SIMS depth profiles. Bright field TEM micrographs were obtained under two beam conditions with the g_{022} reflection operating at the (011) zone. Diffuse dark field images of SiO_2 precipitates were obtained by selecting the broad, diffuse diffraction rings from the amorphous SiO_2 with the objective aperture.

RESULTS AND DISCUSSION

Figure 1 shows the as-implanted microstructure of the SIMOX and control wafers. A continuous amorphous layer was formed to a depth of ≈ 750 Å for all specimens. This depth is in excellent agreement with the amorphous/crystalline interface depth calculated from Brice's damage density curves [9] using Jones' [2] measured values for the threshold damage density in bulk silicon (see Figure 1). Thus, the amorphization process in SIMOX is comparable to that in bulk silicon and the threshold damage density is the same in SIMOX and bulk Si. This is important in future modelling of dopant implants in SIMOX.

The microstructure of SIMOX and control wafers after a 550°C , 16 hour anneal is shown in Figure 2a. Good quality solid phase epitaxial (SPE) regrowth was observed for both SIMOX and control samples, despite the high residual oxygen concentration in the superficial silicon layer of SIMOX. This high oxygen concentration appears in the form of microprecipitates of SiO_2 throughout the superficial silicon layer (Figure 3) and as relatively large SiO_2 precipitates near the surface silicon/buried oxide interface. Apparently, these precipitates did not act as nuclei for category III (SPE regrowth-related) defects since the apparent line defect density is approximately the same ($\approx 10^9/\text{cm}^2$) as in the original (unimplanted) SIMOX wafer. Although no category III defects were apparent after the 550°C anneal, there was a layer of category II defects at the original amorphous/crystalline interface depth. This end-of-range damage was observed for both SIMOX and control silicon wafers.

Annealing at 900°C for 16 hours in a non-oxidizing ambient results in complete elimination of the category II defects in silicon [8]. Annealing at 900°C for 16 hours in an oxidizing ambient resulted in the complete elimination of these category II defects in SIMOX, but not in the control specimens (Figure 2b). In addition, the control specimens showed extensive defect formation (oxidation-induced stacking faults) as a result of surface oxidation during the anneal, whereas the SIMOX did not. Both the enhanced elimination of category II defects and the resistance of SIMOX to near surface defect formation may be related to the proximity of the buried oxide/surface silicon layer interface to the implanted region. This interface may act as a sink for excess Si during the anneal, thus preventing the formation of OSF's and assisting in the dissolution of the end-of-range damage.

SIMS depth profiles as a function of annealing treatment are shown in Figure 4. The high residual oxygen concentration in the superficial silicon layer is shown to average $\approx 10^{22}/\text{cm}^3$. The phosphorus implant profile and diffusion for the control wafer are modelled reasonably well by SUPREME III simulations [10]. No preferential gettering of the phosphorus to the

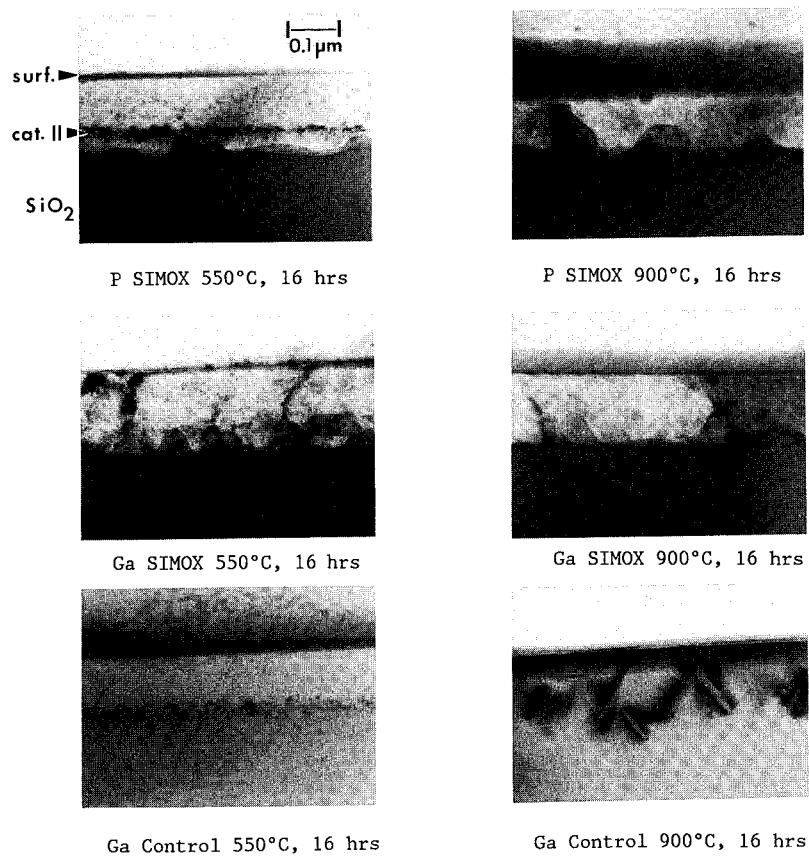


Figure 2. Bright field XTEM micrographs of implanted SIMOX and control Si as a function of annealing treatment.

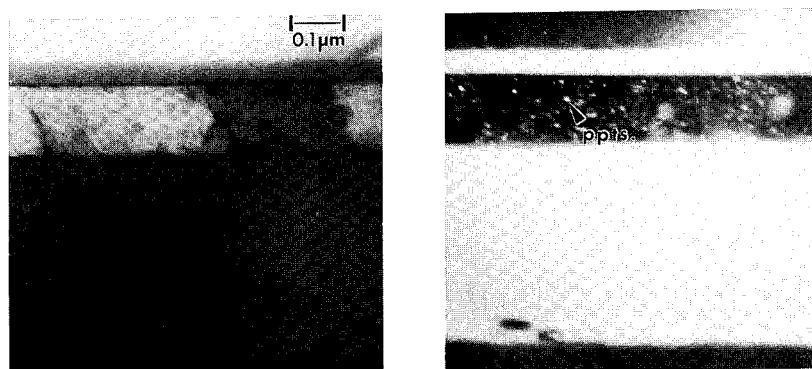


Figure 3. Bright field/diffuse dark field pair showing microprecipitates of SiO₂ throughout surface silicon layer of SIMOX.

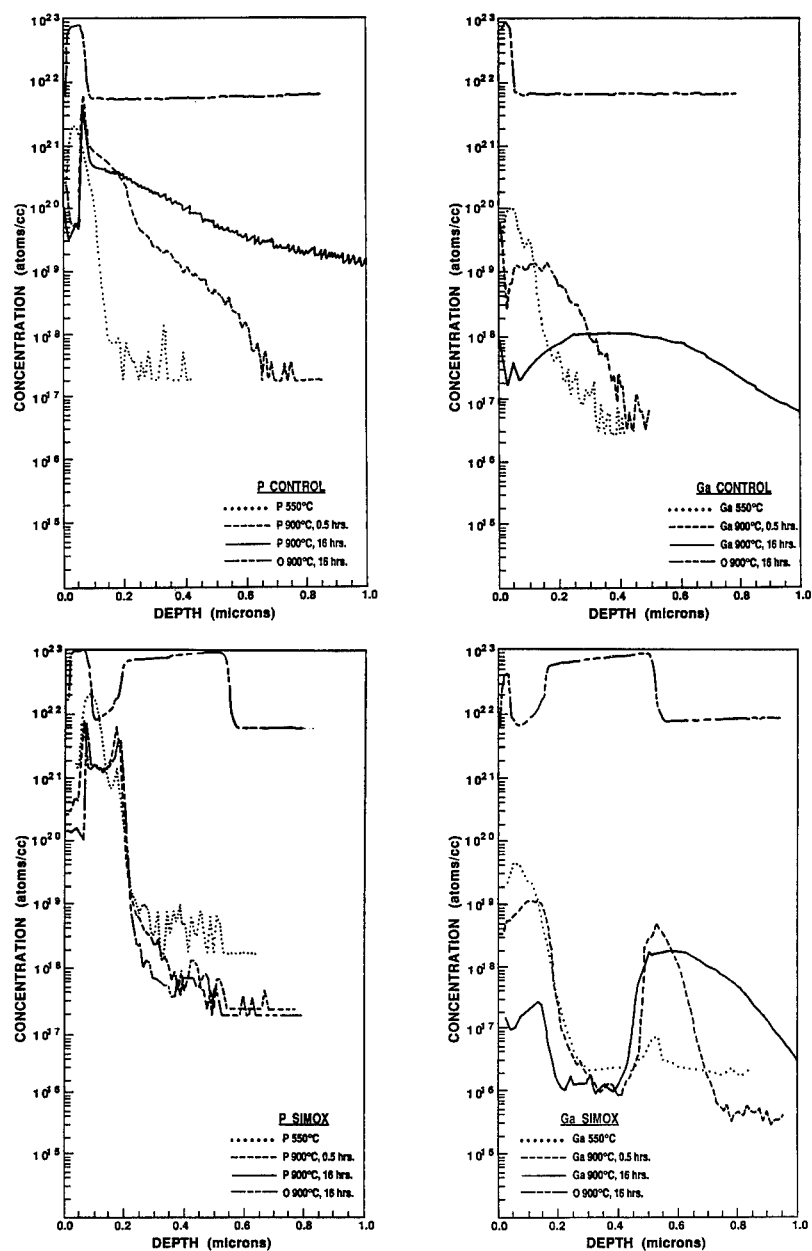


Figure 4. SIMS profiles of ^{31}P and ^{69}Ga implants into annealed SIMOX and control Si wafers as a function of annealing treatment.

category II dislocations was observed. Upon annealing, the $^{31}\text{P}^+$ implant into SIMOX, phosphorus was observed to 'pile-up' strongly at both the surface oxide/silicon interface and the buried oxide/silicon interfaces in SIMOX. The interface peaks may be associated with the formation of a phosphosilicate glass layer. Comparison with the control wafer shows that the decreased diffusivity of the phosphorus in SiO_2 is reflected in the buried oxide acting as diffusion barrier.

In contrast, Ga diffused easily through the buried oxide and into the bulk silicon layer of SIMOX. The solubility of Ga in the SiO_2 was $1 \times 10^{16}/\text{cm}^3$ at 900°C . Again gettering to the interface regions was observed although this is masked to a certain extent by the increased solubility of Ga in Si. In the control Si, Ga unlike P, was observed to getter to the category II defects after 550°C anneal presumably because of its higher diffusivity.

CONCLUSIONS

The residual concentration of oxygen present in our annealed SIMOX wafers, as measured by SIMS to average $1 \times 10^{22}/\text{cm}^3$, well above solid solubility ($10^{18}/\text{cm}^3$ at 1250°C). The form of this oxygen is small microprecipitates as confirmed by cross-sectional diffuse dark-field TEM. This oxygen did not significantly alter the threshold damage density for amorphization of the silicon. The precipitates were not observed to be redistributed by solid phase epitaxy (presumably oxygen diffusion limited) nor did the precipitates appear to induce any high concentrations of category III defects upon solid phase epitaxy. Enhanced elimination of the extrinsic category II (end-of-range) defects was observed for both P and Ga implants into annealed SIMOX wafers. The category II defects appear to be even less stable in SIMOX than in bulk Si under an oxidizing ambient. This may be associated with the close proximity of the Si/ SiO_2 interface or the large number of oxide precipitates either of which might behave as an interstitial sink. The decreased defect stability in SIMOX might also result from enhanced interstitial diffusion to the surface via dislocation in the superficial silicon. The phosphorus redistribution upon 900°C annealing was severely restricted by the buried SiO_2 layer in the SIMOX wafers, in sharp contrast to the gallium redistribution. The solubility of Ga in SiO_2 was observed to be $1 \times 10^{16}/\text{cm}^3$ at 900°C . The diffusivity of Ga and P in the control silicon can be modeled by the SUPREME III program, implying that no additional enhanced diffusion occurs because of the enhanced dissolution of category II defects. This does not eliminate the possible correlation between enhanced defect elimination and the anomalous diffusion nature of the implanted species, i.e. the kink and tail profile of phosphorus diffusion. Future studies including Hall effect results will be published elsewhere [10].

REFERENCES

1. For example, S. Mader, "Ion Implantation: Science and Technology", ed. J.F. Ziegler (Academic Press, New York), 109, 1988.
2. K.S. Jones, S. Prussin and E.R. Weber, Appl. Phys. A, 45, 1-35, 1988.
3. N. Guillemot, J. Stoemenos, P. Normand, D. Tsoulinlas, 1988 IEEE SOS/SOI Technology Workshop, October 3-5, 1988.
4. D.J. Godfrey, R. Chater, A.K. Robinson, P.D. Augustus, J.R. Alderman, J.R. Davis, J. Kilner and P.L.F. Hemment, *ibid*.
5. K. Des, S. McClelland and J.B. Butcher, Elect. Lett., 20, 526, 1984.
6. K.S. Jones, S. Prussin and D. Venables, MRS Symp. Proc., 100, 277, (1988).
7. A.C. Ajmera and G.A. Rozgonyi, Appl. Phys. Lett. 49, 19, (1986).
8. K.S. Jones, S. Prussin and E.R. Weber, J. Appl. Phys. 62, 4114, (1987).
9. D.K. Brice, Ion Implantation Range and Energy Deposition Distribution, (Plenum Press, New York), 1975.
10. K.S. Jones, D. Venables and G.E. Davis, Mat. Sci. and Eng. B to be published.

LOW-DEFECT, HIGH-QUALITY SIMOX PRODUCED BY MULTIPLE OXYGEN
IMPLANTATION WITH SUBSTOICHIOMETRIC TOTAL DOSE*

F. NAMAVAR, E. CORTESI, and P. SIOSHANSI
Spire Corporation, Patriots Park, Bedford, MA 01730

ABSTRACT

This work addresses the formation of Separation by Implantation of Oxygen (SIMOX) structures by multiple oxygen implantation into silicon and high temperature annealing. We observed no threading dislocation defects in the several plane view TEM and XTEM micrographs of each of the samples implanted with a single dose of up to $8 \times 10^{17} \text{ O}^+/\text{cm}^2$. We also demonstrated that with a multiple low-dose (3 to $4 \times 10^{17} \text{ O}^+/\text{cm}^2$) oxygen implantation and high temperature annealing process, we are able to produce continuous and uniform buried SiO_2 layers with a total dose of $1.1 \times 10^{18} \text{ O}^+/\text{cm}^2$ (about 60% of the total dose for standard SIMOX). The density of defects is about $10^5/\text{cm}^2$. There are no silicon islands in the buried layer, no SiO_2 precipitates in the silicon top layer, and the Si-SiO₂ interfaces are sharp and smooth. SIMOX material with a high-quality Si top layer and a continuous buried layer has been produced with a total dose of $7 \times 10^{17} \text{ O}^+/\text{cm}^2$ (40% of the total dose for standard SIMOX) and a two-step process. However, in this case there are a few Si islands present in the buried SiO_2 layer.

INTRODUCTION

The SIMOX process for formation of silicon-on-insulator (SOI) material has been studied extensively in recent years because of the technological importance of the material [1-5]. Standard commercially available SIMOX wafers are produced with a single implantation of 1.6 to $1.8 \times 10^{18} \text{ O}^+/\text{cm}^2$ by means of high current implanters. A post-implant anneal is required to regrow the silicon and redistribute the oxygen [6,7]. Recent results indicate that very high temperature anneals, between 1250°C [8] and 1405°C , [9] are required in order to increase the oxygen mobility sufficiently to completely getter all oxygen to the Si-SiO₂ interfaces. The standard SIMOX wafer typically has a silicon surface layer about 1400 to 1500 \AA thick and a buried layer about 4000 \AA thick. The interfaces are generally smooth and sharp, but there are some silicon islands in the buried oxide layer even when annealed at temperatures as high as 1405°C [9]. In general, for annealing temperatures $>1250^\circ\text{C}$, SiO_2 precipitates in the Si top layer disappear. However, threading dislocation defects in the silicon top layer continue to exist. The density of defects in this material has typically been observed at a level of about 10^8 to $10^{10}/\text{cm}^2$ [2,9,10]. Although in some cases we have observed defect densities as low as $10^6/\text{cm}^2$, a large sampling of our own standard wafers by plane view TEM has shown that the defect density is typically 10^8 to $10^9/\text{cm}^2$. For the most part, these defects do not seem to play an important part from the point of view of CMOS device fabrication. However, they are considered detrimental for bipolar structures.

For some time, we have studied [11] two methods to reduce the defect density in SIMOX wafers: (1) preventing the formation of defects by sequential low-dose oxygen implantation and high-temperature annealing, and (2) eliminating already formed threading dislocations by low-dose implantation of Ge to create a strained layer to deflect or stop dislocations during subsequent solid phase epitaxy regrowth.

* This work was supported in part by the Department of Defense, Rome Air Development Center/ESR, under contract No. F19628-86-C-0069.

In this paper we present preliminary results for fabrication of low-defect, high-quality SIMOX with a multiple low-dose implantation process.

EXPERIMENTAL PROCEDURE

Four-inch silicon wafers with (100) orientation were implanted at 160 keV with dose steps ranging from 2×10^{17} to 8×10^{17} O^+/cm^2 . The beam was generated by an Eaton NV-10-160 implanter which has been joined to a specially designed end station. Oxygen implantation was carried out with a current density of about 10-12 microamperes/ cm^2 and wafer temperature during implantation was about 500-550°C. The wafers were subsequently annealed at 1300°C for six hours in N_2 . In order to reduce impurity contamination that can result from the lengthy high temperature anneals, the wafers were protected by multilayer SiO_2 caps. In addition, annealing was carried out in a Si tube furnace with a SiC liner.

EXPERIMENTAL RESULTS

Dependence of Threading Dislocations on Dose

Homma et al. [12] observed a large increase in the density of defects when implantation dose was higher than a threshold dose of between 4 and 6×10^{17} O^+/cm^2 . We have carried out a large number of implantations to establish the threshold for our implantation conditions. We implanted wafers with doses of 4, 5, 6, 7.5, and 8×10^{17} O^+/cm^2 . Our results, as obtained by XTEM and plane view TEM of the silicon top layer, have shown that threading dislocations are below $10^5/cm^2$ for doses $\leq 8 \times 10^{17}$ O^+/cm^2 .

Typical results are shown in Figure 1a, which shows the formation of a quasi-continuous buried layer about 1600 Å thick with a silicon top layer about 3200 Å thick with a single dose of 7.5×10^{17} O^+/cm^2 at 170 keV. However, the buried layer has silicon islands. Figure 1b is a plane view TEM of the silicon top layer and shows the absence of threading dislocations.

Formation of Low Defect, High Quality SIMOX Wafers by Multiple Low-Dose Oxygen Implantation

Figure 2 is an XTEM of a wafer implanted with a total dose of 1.1×10^{18} O^+/cm^2 in three implantation steps. The wafer was annealed after each step for six hours at 1300°C in N_2 . As is shown, this resulted in the formation of a uniform and continuous buried oxide layer with sharp and smooth interfaces. Both XTEM and plane view TEM have shown the absence of SiO_2 precipitates in the silicon top layer and the absence of silicon islands in the buried layer. No threading dislocations have been observed in the TEM measurements of this sample and thus we assume that threading dislocation density is $< 10^5/cm^2$. In this process, we implanted a fraction of the oxygen at a lower temperature (about 400°C) and then the remainder at higher temperature (about 500°C). Our results have shown that changing the implantation temperature in this way is essential for reducing the total dose as well as for eliminating waviness at the Si-SiO₂ interfaces. Indeed, implantation similar to that reported in references 13 and 14 resulted in a slightly wavy Si(sub)-SiO₂ interface (Figure 3). This and previous work [15] has shown that implantation below the critical temperature of 500-550°C results in a more uniform buried layer because a finer dispersion of SiO_2 precipitates is created. Initial low temperature implantation followed by high temperature implantation results in a good quality buried layer as well as a low-defect silicon top layer.

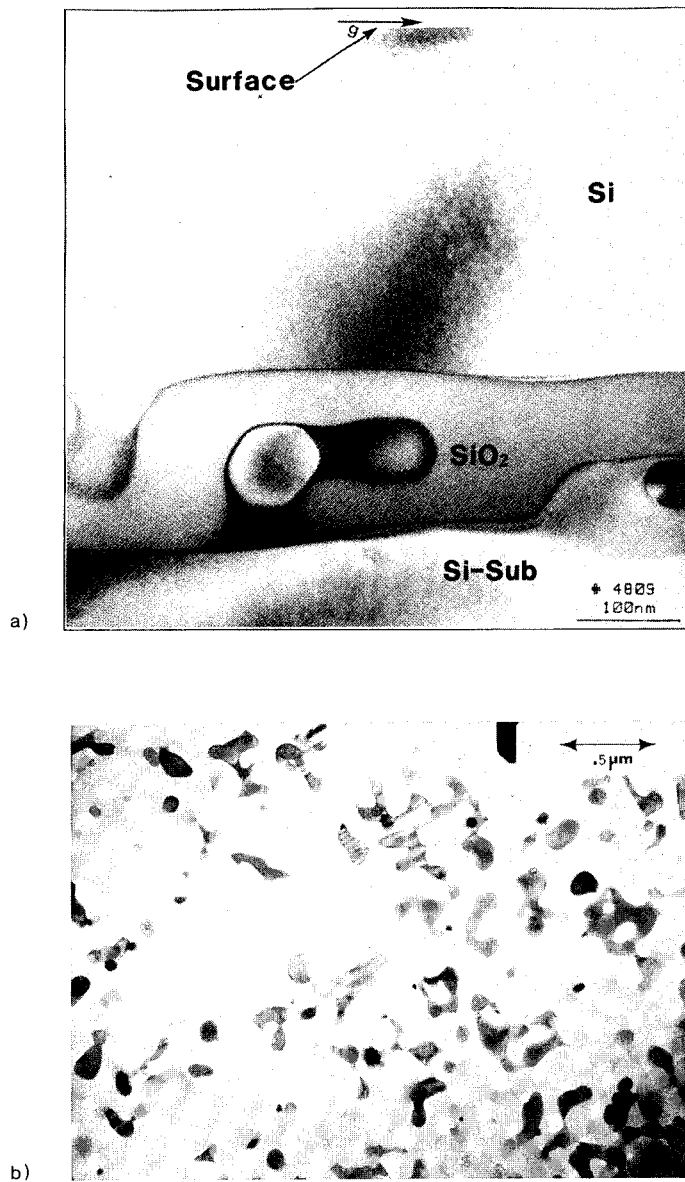


Figure 1. TEMs of wafer implanted with a single dose of $7.5 \times 10^{17} \text{ O}^+/\text{cm}^2$ at 170 keV and annealed at 1300°C for six hours in N_2 . (a) XTEM and (b) Plane View TEM. No defects were observed in any of the TEMs of this sample or any other sample implanted with a total dose of $\leq 8 \times 10^{17} \text{ O}^+/\text{cm}^2$.

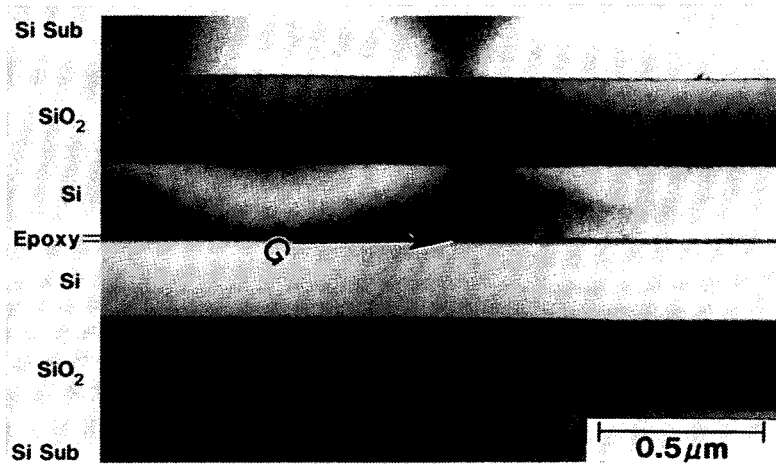


Figure 2. XTEM of a superior quality, low-defect wafer implanted with a total dose of $1.1 \times 10^{18} \text{ O}^+/\text{cm}^2$ at 160 keV by multiple oxygen implantation at two different temperatures.

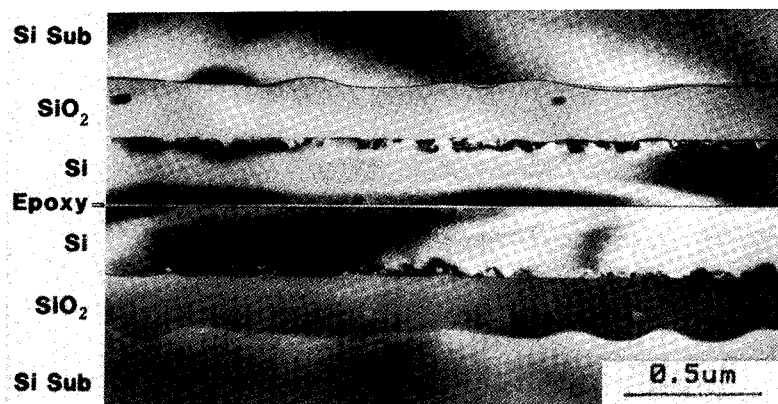


Figure 3. XTEM of a wafer implanted in two steps with a total dose of $7 \times 10^{17} \text{ O}^+/\text{cm}^2$ at 160 keV. No threading dislocations were observed. Twinning defects will be eliminated upon further implantation.

Figure 3 shows a SIMOX wafer produced with a total dose of $7 \times 10^{17} \text{ O}^+/\text{cm}^2$. As can be seen, a continuous buried oxide layer has been produced although there are some silicon islands present. Absolutely no threading dislocations were observed in any of the TEMs of this sample. The sample shown in Figure 3 was produced by a two-step process, namely, implantation with doses of $3 \times 10^{17} \text{ O}^+/\text{cm}^2$ and $4 \times 10^{17} \text{ O}^+/\text{cm}^2$. High temperature annealing was done after each implant. The only defects present in the silicon top layer are twins which disappear upon further implantation [11] (see Figure 4). This sample was produced with implantation at a constant temperature of 500-550°C, as compared with the results shown in Figure 2 in which the first implantation was carried out at lower temperature. It appears that the bulges are due to the presence of Si islands in the buried layer. These islands could not be eliminated by annealing processes alone. Generally, a third implantation eliminates [11] the twins, as well as the silicon islands in the SiO_2 (see Figure 3). Further implantation however, even with very high doses, does not result in the complete elimination of the waviness at the SiO_2 -Si(sub) interface (see Figure 4).

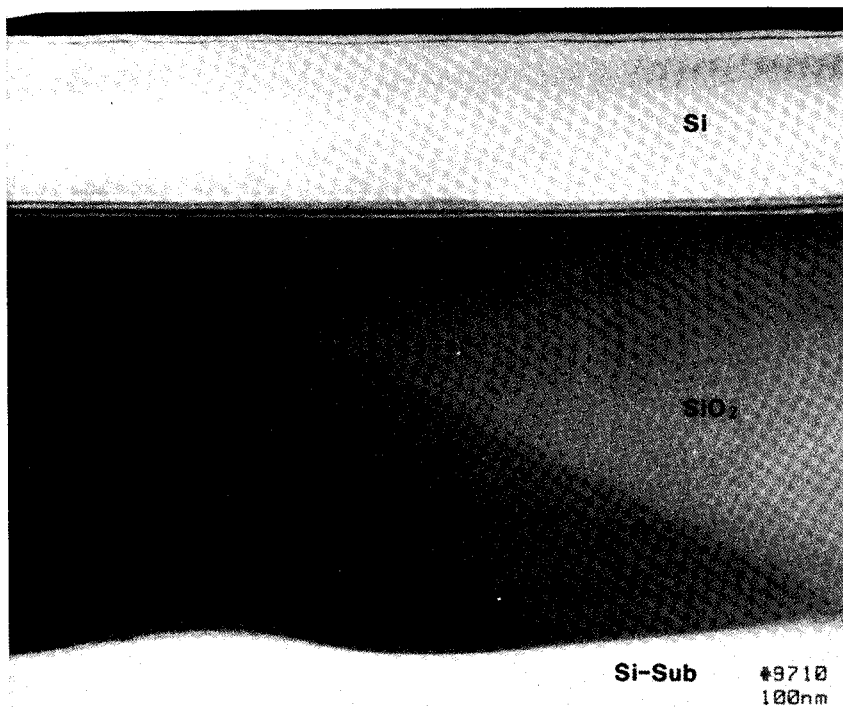


Figure 4. XTEM of wafer implanted with a total dose of $1.8 \times 10^{18} \text{ O}^+/\text{cm}^2$ at 160 keV by a multiple oxygen implantation process.

SUMMARY/CONCLUSION

In this work we have shown that for our experimental conditions no threading dislocations are observed by plane view TEM or XTEM for implantation with a single dose of up to $8 \times 10^{17} \text{ O}^+/\text{cm}^2$. A quasi-continuous buried layer is formed with a single dose of $7.5 \times 10^{17} \text{ O}^+/\text{cm}^2$. However, there are large silicon islands in the buried layer.

In contrast, using a two-step implantation process with a total dose of $7 \times 10^{17} \text{ O}^+/\text{cm}^2$ (40% of the dose for SIMOX produced by the standard process) results in a continuous buried SiO_2 layer with a few small silicon islands at the SiO_2 -Si(sub) interface but no threading dislocations were observed.

Our preliminary results have also shown that superior quality SIMOX can be produced (Figure 2) if oxygen implantation is carried out first at lower temperature and then at the critical temperature. Implantation at a constant temperature (500-550°C) appears to result in a slight waviness at the SiO_2 -Si(sub) interface [14] (see also Figure 4).

Our results have been reproduced several times and they are consistent with those reported by Hill et al. [13] and Cheek et al. [14]. Thus, we believe that the multiple implantation process can play an important role in extending the applications of the SIMOX process because not only can low-defect SIMOX material be produced but the total required dose can be reduced.

ACKNOWLEDGMENTS

We are very grateful to Dr. Walter Shedd at RADC for his direction and support in this work. The authors would also like to acknowledge the assistance of Dr. S.N. Bunker, O. DeSilvestre, R. Bricault, M. Sanfacon, G. Beals, N. Martell, L. Geoffroy, and J. Breen. We would like to extend our gratitude to B. Buchanan, J. Hirvonen, and E. Johnson for fruitful discussion, to Dr. V. Jalan (Electrochem, Inc.) for TEM work, and to Professor Q. Kessel for his help with RBS/Channeling experiments.

REFERENCES

1. R.F. Pinizzotto, Mat. Res. Soc. Symp. Proc. 27, 265 (1984).
2. B.Y. Tsaur, Mat. Res. Soc. Symp. Proc. 35, 641 (1985).
3. P.L.F. Hemment, Mat. Res. Soc. Symp. Proc. 53 (1986).
4. K. Izumi, Nucl. Instr. and Meth. B21, 124 (1987).
5. J.R. Davis, K.J. Reeson, P.L.F. Hemment, and C.D. Marsh, IEEE Electron Dev. Lett. EDL-8 (7), 291 (1987).
6. R.F. Pinizzotto, B.L. Vaandrager, S. Matteson, H.W. Lam, S.D.S. Malhi, A.H. Hamdi, and F.D. McDaniel, IEEE Trans. Nucl. Sci. NS-30 (2), 1718 (1983).
7. C. Jaussaud, J. Margail, J. Stoemenos, and M. Bruel, Mat. Res. Soc. Symp. Proc. 100, 17 (1988).
8. C. Jaussaud, J. Stoemenos, J. Margail, M. DuPuy, B. Blanchard, and M. Bruel, Appl. Phys. Lett. 46 (11), 1064 (1985).
9. G.K. Celler, P.L.F. Hemment, K.W. West, and J.M. Gibson, Appl. Phys. Lett. 48 (8) 532 (1986).
10. B.Y. Mao, P.H. Chang, H.W. Lam, B.W. Shen, and J.A. Keenan, Appl. Phys. Lett. 48 (12), 794 (1986).
11. F. Namavar, unpublished data in several monthly reports to Rome Air Development Center, 1987, and to be published.
12. Y. Homma, et al., Japan, J. Appl. Phys. 21 (6), 890 (1982).
13. D. Hill, P. Fraundorf, and G. Fraundorf, J. Appl. Phys. 63, 4932 (1988).
14. T.F. Cheek, Jr., and D. Chen, Mat. Res. Soc. Symp. Proc. 107, 53 (1988).
15. P. Sioshansi and F. Namavar, Mat. Res. Soc. Symp. Proc. 107, 67 (1988).

INFLUENCE OF ION-IMPLANTATION ON CHARACTERISTICS OF PICOSECOND PHOTOCONDUCTIVE SWITCHES

JOHN F. KNUDSEN, ROBERT C. BOWMAN, JR., DUANE D. SMITH, AND STEVEN C. MOSS.

The Aerospace Corporation, 2350 E. El Segundo Blvd., El Segundo, CA 90245

ABSTRACT

Ion-implantation induced amorphization has been used to modify the linearity of response of ultrafast photoconductive switches fabricated on SOS. The extent of amorphization was determined using various materials characterization techniques. TRIM-86 Monte Carlo calculations were used to model the defect densities produced by ion implantation. Linearity of response is critically dependent upon the nature of the semiconductor region under metallic contacts and the character of the response is opposite to that expected from reports in the literature.

INTRODUCTION

We have characterized the ion-implantation induced amorphization of Silicon-on-Sapphire (SOS) using RBS, Raman spectroscopy, and Electron Beam-modulated ElectroReflectance (EBER) measurements and have related the extent of amorphization to the linearity of response of ultrafast photoconductive switches fabricated upon SOS. The use of RBS in conjunction with Raman spectroscopy and EBER measurements allowed us to investigate the disorder through the bulk as well as near the Si surface and the Si-sapphire interface. While photocarriers will be generated throughout the Si epilayer, the response of these switches will be affected by the nature of the metal-semiconductor contact and by the effects of trapping states near the Si-sapphire interface. Despite extensive recent studies [1] of ultrafast photoconductive switches produced by ion-implantation of SOS, no measurements have been reported which display the photoconductive response as a function of electrical bias. Nonetheless, picosecond optoelectronic sampling techniques based upon ultrafast photoconductive switches have been used both to generate and to sample ultrafast electrical waveforms [2], to measure the pulse-response of high speed electronic devices [3], to measure the frequency dependence of the scattering parameters of high speed microwave devices [4] as well as the transient electrical waveforms generated during optical excitation of high speed photosensitive devices [5]. Reliable extraction of the scattering parameters of microwave devices and determination of the temporal impulse response of photosensitive devices requires that the photoconductive response of these fast switches be linear with electrical bias and signal as well as incident optical power.

It is commonly believed that contacts fabricated on crystalline semiconductors will display rectifying behavior [6] unless special processing such as sintering is used, and that contacts fabricated on semiconductors heavily damaged by ion-implantation will display ohmic response [6] without special processing steps. Our measurements show that ultrafast photoconductive switches fabricated on a Si epilayer heavily damaged by ion-implantation do not have a response which is linear with electrical bias, and that switches fabricated on a c-Si epilayer, which is implanted after metalization, yield an ultrafast photoresponse which is linear with electrical bias.

EXPERIMENTAL DETAILS

SAMPLES: Picosecond (ps) electrical pulses are generated by ps optical pulses focused into a photoconducting gap in a microwave waveguide. The waveguide is a microstrip line fabricated using an SOS wafer. In order to test the linearity of the response of individual switches, a single switch is illuminated with an ultrashort dye laser pulse and the signal produced on the microstrip line is measured as a function of electrical bias. SOS samples were 175 μm thick substrates with a 0.5 μm thick layer of Si. Metalization for microstrip structures consisted of a 200 Å layer of Ti/W alloy beneath a 2 μm overlayer of Au. Microstrip lines were 175 μm wide to produce a nominal distributed

impedance of 50Ω and an effective dielectric constant of 6.65. Photoconductive gaps were $20\mu\text{m}$ wide and $175\mu\text{m}$ long. Three of the samples were implanted before metalization, while two of the samples were implanted after metalization, as shown in Table I. Interchanging these two processing steps allowed us to study how the metal-semiconductor interfacial condition affects linearity of photoconductive response.

IMPLANTATION CONDITIONS: All samples were Si-ion implanted at 300°K as shown in Table I. A 1 cm^2 beam spot was raster scanned over an area of 22.3 cm^2 at frequencies of 2569 Hz vertically and 256 Hz horizontally to provide uniform implantation over the sample area. A 2-inch diameter beam aperture was used to define the implant area. Beam currents were limited to $5\mu\text{A}$. Wafer temperature due to beam heating effects did not exceed 60°C under these implant conditions. One sample (B1) was implanted with a single 375 keV $1\text{E}15\text{ cm}^{-2}$ dose before metalization. Two samples (B2 and A1) were implanted with a triple energy (100/200/400 keV) implant, each energy at a dose of $1\text{E}14\text{ cm}^{-2}$. Two samples (B3 and A2) were implanted with a triple energy (100/200/400 keV) implant, each energy at a dose of $1\text{E}15\text{ cm}^{-2}$. For these triple energy implants one sample was implanted before metalization and one after metalization.

TABLE I. SOS IMPLANTATION CONDITIONS AND PROCESSING ORDER

SAMPLE	ION SPECIE	ION ENERGY (keV)	ION DOSAGE (/sq.cm)	IMPLANT BEFORE/AFTER METALIZATION
B1	$^{28}\text{Si}^+$	375	10^{15}	BEFORE
B2	$^{28}\text{Si}^+$	100/200/400	10^{14}	BEFORE
B3	$^{28}\text{Si}^+$	100/200/400	10^{15}	BEFORE
A1	$^{28}\text{Si}^+$	100/200/400	10^{14}	AFTER
A2	$^{28}\text{Si}^+$	100/200/400	10^{15}	AFTER

RESULTS AND DISCUSSION

RBS CHARACTERIZATION: Aligned RBS data for the unimplanted SOS sample are shown as filled circles in Fig. 1. The unimplanted Si epilayer was quite disordered compared to typical bulk Si. Rotational random RBS data for the unimplanted SOS wafer are shown as the dashed line. Backscatter from the single energy $1\text{E}15\text{ }^{28}\text{Si}^+\text{ cm}^{-2}$ implant is shown as the open circles. Backscattering spectra from the triple-energy $1\text{E}15\text{ }^{28}\text{Si}^+\text{ cm}^{-2}$ implant are shown as the dash-dotted line. The observed backscatter from all depths of the Si layer that had a 100/200/400 keV, $1\text{E}15\text{ }^{28}\text{Si}^+\text{ cm}^{-2}$ implant was indistinguishable from the randomly oriented sample. As far as RBS can determine, the Si layer was completely amorphized by the higher dosage triple energy implant. In contrast, the 375 KeV, $1\text{E}15\text{ }^{28}\text{Si}^+\text{ cm}^{-2}$ implant produces very little increase in the disorder of the Si layer over the disorder present in the as-received wafer. In fact, this single energy 375 keV implant at $1\text{E}15$ actually improved the quality of the near surface region by recrystallization due to solid phase epitaxy (SPE) [7]. Although not shown here, the observed backscatter from all depths of the Si layer that had a 100/200/400 keV, $1\text{E}14\text{ }^{28}\text{Si}^+\text{ cm}^{-2}$ implant was indistinguishable from the as-received sample. The resolution of the RBS measurements was limited to $\approx 100\text{ \AA}$ near the Si surface and to $\approx 300\text{ \AA}$ near the Si-sapphire interface. Consequently, these RBS measurements do not yield information concerning the degree of amorphization in the near surface region immediately under the contacts. Information about the ion-implantation induced disorder in these regions is described in the sections on our Raman and EBER measurements.

TRIM-86 MONTE CARLO VACANCY SIMULATION: TRIM-86 [8] was used to model the implantation-induced amorphization of c-Si epilayers on SOS. We find reasonable agreement between defect density versus depth profiles predicted by TRIM simulations

as shown in Fig. 2, and the disorder measured by RBS for the highest dosage triple implants. The 100/200/400 keV $1\text{E}15\text{ cm}^{-2}$ implant (B3) modeling predicted total amorphization of the 500 nm epilayer, as shown in Fig. 2, and is in reasonable agreement with the RBS results shown in Figure 1. These TRIM results are unphysical in that they show more vacancies produced than there are Si atoms. This merely indicates that most of the Si atoms have been knocked from a "lattice" site more than once at this high dosage. TRIM is meant to be used to model ion-implantation into amorphous materials, not crystalline materials. The reasonable agreement we obtain between TRIM and the heaviest multiple implant (B3) is probably due to the disorder produced by the first implant which subsequently affects the two succeeding implants. Disorder generated by the first implant reduces ion-channeling resulting in defect profiles closer to those simulated in TRIM. However, TRIM suggests that a single 400 keV $1\text{E}15\text{ cm}^{-2}$ implant would achieve amorphization (i.e., 10 % vacancies). This disagrees with measurements by Golecki [9] in which 2-2.5 times this dosage was required. Our RBS measurements of the disorder created by the single 375 keV $1\text{E}15\text{ cm}^{-2}$ implant (B1) do not show the amorphization which would be predicted by TRIM-86 and are consistent with Golecki's results. Furthermore, a single 400 keV $1\text{-}3\text{E}15\text{ }^{28}\text{Si}^+\text{ cm}^{-2}$ implant typically leaves a thin surface layer of single crystal material suitable for seeding SPE. RBS results, shown in Fig. 1, indicate that ion-implantation induced recrystallization resulted in an improvement in χ_{min} from 23% to 15 % for the 375 keV implant due to SPE [7]. Recrystallization effects are not incorporated in the TRIM-86 simulation. The TRIM simulation of the triple energy 100/200/400 keV $1\text{E}14\text{ cm}^{-2}$ implant predicts amorphization of the middle region of the epilayer. This prediction is not supported by the RBS results. Consequently, while TRIM does not adequately predict the results of multiple implants into c-Si for dosages up to $1\text{E}14\text{ cm}^{-2}$, it does a reasonable job at higher dosages.

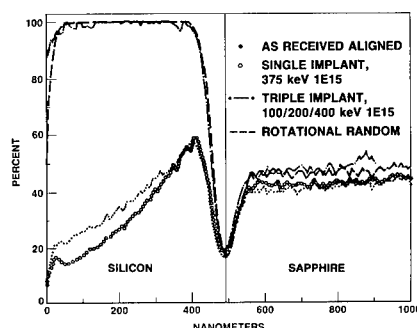


Figure 1. RBS spectra of Si ion implanted SOS wafers; 500 nm Si epilayer.

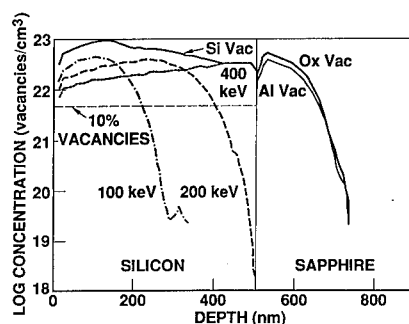


Figure 2. TRIM-86 Monte Carlo simulation of the vacancy concentration profile of a triple energy implant in SOS.

RAMAN SPECTRA: Raman spectroscopy measurements, shown in Fig. 3, were made at 300°K with both the 488 nm line from an Ar^+ laser and the 442 nm line from a HeCd laser. The scattered light was analyzed with a SPEX double monochromator and standard photon-counting techniques. Nominal sampling depths of the Ar^+ and HeCd laser lines are $\approx 600\text{ nm}$ and 100 nm , respectively, for c-Si but only about 50 nm and 10 nm , respectively, for a-Si. Several of the expected Raman peaks of the sapphire substrate were seen (although quite weakly) when the unimplanted Si surfaces were illuminated with the Ar^+ laser line; whereas, these sapphire peaks were not observed after the implants nor with the HeCd line under any conditions. Spectra were obtained from both sides of the SOS wafer, i.e., the Si surface and through the sapphire side to assess the uniformity of the implant damage throughout the epilayer. Unimplanted SOS wafers gave a sharp phonon peak centered at 524 cm^{-1} from the Si epilayer, which is about 3.5 cm^{-1} larger than the value for bulk (100) c-Si due to the well-known compressive stress in the

SOS films [10,11]. Figure 3 compares the Raman spectra for 488 nm illuminations on the Si-sides of the SOS wafers after the three B-type implants given in Table I with the Si phonon peak from an unimplanted SOS sample. The 375 keV $1\text{E}15\text{ cm}^{-2}$ (B1) and 100/200/400 keV $1\text{E}14\text{ cm}^{-2}$ (B2) implants reduced the intensity of this peak by 50-70%; however, only minimal changes in the peak position or linewidth were observed. Hence significant amounts of the c-Si epilayer remain relatively undamaged by these implants. On the other hand, the 100/200/400 keV $1\text{E}15\text{ cm}^{-2}$ (B3) implants completely eliminated the c-Si Raman peak when the top surface was examined by either laser. However, a much weaker signal (i.e., about 5-10% of the intensity for unimplanted SOS) was obtained when the B3-implanted sample was examined through the polished sapphire side. Hence, Raman measurements indicate that larger dose implants made the Si layer almost completely amorphous except for the region at the sapphire interface.

ELECTRON BEAM MODULATED ELECTROREFLECTANCE (EBER): EBER spectra [12] of Si epitaxial layers were obtained. A modulated electron beam was used to vary the optical reflectivity of the Si surface. The reflectivity of the Si surface was measured by imaging light from an arc lamp through a monochromator onto the region of the surface influenced by the electron beam. EBER data for an unimplanted (100) SOS wafer is shown in Fig. 4(a). Although there are qualitative differences in the relative phases of the overlapped, contributing peaks, the energies of the major features of the spectra agree with the Si band structure. For a single-energy, deep implant (B1), the EBER spectrum in Fig. 4(b) shows a broadening of the resonance, indicative of partial erosion of the critical points in the electronic density of states and increased reflectivity-change due to ion-beam induced recrystallization. Data in Fig. 4(c) for the triple-energy low-dosage implant (B2) show only a much reduced E_0 peak, higher energy peaks have vanished. Data in Fig. 4(d) for the triple-energy high-dosage implant (B3) show no discernible peaks. Optical probe depths for the heavy dosage implant are 109 Å at 3.4 eV and 76 Å at 4.5 eV. Absence of any spectral structure at 3.4 and 4.5 eV in Fig. 4(d) is consistent with complete amorphization as predicted by TRIM simulations. Furthermore, the data in Fig. 4(b) and 4(c) show that there are substantial structural changes produced in the surface layer by the single energy, deep implant (B1) as well as the triple energy low-dosage implant (B2).

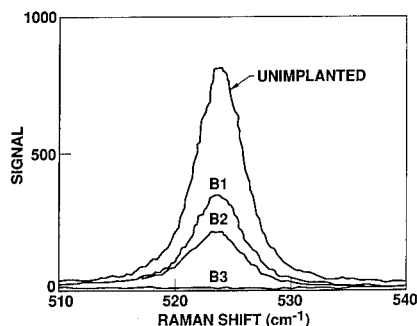


Figure 3. Si surface Raman spectra of SOS with various $^{28}\text{Si}^+$ implant conditions.

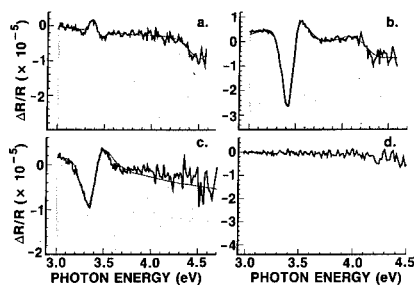


Figure 4. EBER spectra obtained at room temperature from SOS samples with various $^{28}\text{Si}^+$ implant conditions.

PHOTOCURRENT-VOLTAGE CHARACTERISTICS: A rhodamine 6G dye laser synchronously pumped by the frequency-doubled output of an actively modelocked Nd:YAG laser was used to perform photocurrent-voltage measurements. This system produced 6 ps pulses at a repetition rate of 100 MHz with ≈ 200 mW average power. Approximately half of the dye laser output was directed along a beamline and focused onto a photoconductive switch with a spot size of $10\text{ }\mu\text{m}$. This beam train was chopped at 326 Hz with a 50% duty factor. To measure the variation of the ultrafast photoconductive switch response as a function of applied electrical bias, a -15 volt to +15

volt triangle wave was applied to the sidearm of the illuminated switch. The photogenerated signal was fed through a lock-in amplifier to the data acquisition system.

Dependence of the photocurrent on the static electrical potential imposed across the photoconductive gap is shown in Fig. 5. Data shown in Fig. 5 are for wafers implanted prior to metalization. Photoconductive response of each sample is superlinear at low bias levels but gradually becomes linear at higher applied bias. For pre-metalization implants, the difference in linearity between multiple and single-energy implant samples is ostensibly due to differing degrees of amorphization of the surface layer of Si before the metal contact was made. In the case of a single heavy dose, deep implant (B1), the majority of damage is induced near the Si-sapphire interface and very little damage occurs at the Si surface. The switch formed with the single energy implant has a noticeably nonlinear response. Triple-energy implants (B2 and B3) produced a larger density of defects near the surface than the single energy implant and resulted in a more linear photoconductive response. Data in Fig. 6 show that if SOS wafers are implanted after metalization, photocurrent is linear with respect to electrical bias voltage. The observed linearity of the sample that had a low implant dosage ($1\text{E}14\text{ }^{28}\text{Si}^+\text{ cm}^{-2}$) after contact formation indicates that neither amorphization in the gap nor amorphization under the metallic contacts is essential to obtain linearity. Quasi-static, purely electrical, "dark" I-V curves are also nonlinear for the switches before metalization (B1,B2,B3) and are also linear for the switches implanted after metalization (A1,A2). Nonlinearities for the photoconductive I-V curves were typically much more pronounced than the nonlinearities in the dark I-V curves.

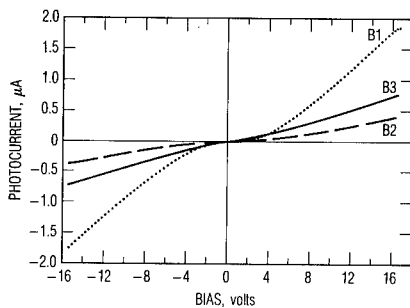


Figure 5. Electrical bias dependence of single switch photocurrent for samples implanted with $^{28}\text{Si}^+$ before metalization.

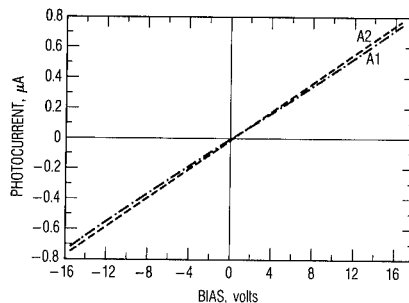


Figure 6. Electrical bias dependence of single switch photocurrent for wafers implanted with $^{28}\text{Si}^+$ after metalization.

CONTACT FORMATION: Fabrication of contacts on polycrystalline Si with Ti/W metalization may produce ohmic contacts because of interdiffusion of Ti/W into grain boundaries. In the unimplanted Si epilayer of these samples there are a large density of defects, mostly dislocations and microtwins which run from the Si-sapphire interface all of the way to the surface of the Si epilayer. Interdiffusion of the Ti/W metalization along these dislocations and microtwins may also produce ohmic contacts. This is consistent with the observed linear dark and photoconductive I-V curves for the samples implanted after metalization. Furthermore, if, during the process of implantation, these surface defects were reduced or eliminated so that there was less interdiffusion of the Ti/W metalization, then contacts would be more Schottky-like. Consequently, contacts to samples with light pre-metalization triple-energy implants and to the single-energy heavy pre-metalization implant would produce non-ohmic response. However, the heavy pre-metalization triple-energy implant would still have the effect of lowering and narrowing the Schottky barrier so that the response would become more ohmic in good agreement with our results [13]. While this explanation is consistent with our observations, it is difficult to understand how significant diffusion of the metal atoms into the

semiconductor can occur at these low processing temperatures ($<150\text{ }^{\circ}\text{C}$) even with a large density of defects in the as-received wafers. Further measurements are underway to elucidate the answer to these perplexing questions.

The effects of surface photoconductance versus bulk photoconductance may also play an important role in the response of these devices. Etching away the surface damage layer to eliminate surface conductance is not effective here since these epilayers must be damaged throughout their thickness to reduce the photocarrier lifetime. Finally, the effects of contamination produced in the near surface region of the Si epilayer during either the implantation or other processing steps may have profound effects upon the current-voltage characteristics [14] of these ultrafast photoconductive switches. Measurements are underway to determine the extent and nature of any possible contaminants produced in the near-surface region of the Si epilayers by any of the processing steps.

SUMMARY AND CONCLUSIONS

We have demonstrated that ultrafast photoconductive switches fabricated under conditions expected to produce Schottky barriers and nonlinear photoresponse may instead produce switches with linear, ohmic photoresponse. These switches are suitable for sampling ultrafast electrical transients and can be reliably used for applications such as measurement of the small-signal scattering parameters of high-speed microwave devices using picosecond optoelectronic techniques. We have also demonstrated that ultrafast photoconductive switches fabricated under conditions expected to produce ohmic photoresponse may instead produce switches with nonlinear photoresponse. While these ultrafast nonlinear switches are suitable for generating ultrafast electrical transients, they are not generally suitable for sampling ultrafast electrical transients.

ACKNOWLEDGEMENTS

This work was supported by the U.S. Air Force-Space Division under contract #F04701-85-C-0086. The authors are grateful to Dr. Jerry A. Gelbwachs and Dr. Roger Newman for their encouragement and support. We thank Dr. M. H. Herman and S. M. Baumann of Charles Evans and Associates for the EBER and RBS measurements.

REFERENCES

1. See, e.g., Picosecond Electronics and Optoelectronics II, Eds. F. J. Leonberger, C.-H. Lee, F. Cappasso, and H. Morkoc, (Springer-Verlag, New York, 1987).
2. D. H. Auston, A. M. Johnson, P. R. Smith, and J. C. Bean, *Appl. Phys. Lett.* **37**, 371-373 (1980).
3. P. R. Smith, D. H. Auston, and W. M. Augustyniak, *Appl. Phys. Lett.* **39**, 739-741 (1981).
4. S. C. Moss, D. D. Smith, and D. E. Cooper, *Proc. SPIE Vol. 795*, 225-246 (1987).
5. D. E. Cooper and S. C. Moss, Ultrafast Phenomena V, Eds. G. R. Fleming and A. E. Siegman, (Springer-Verlag, New York, 1986) pp. 117-119.
6. D. H. Auston, Picosecond Optoelectronic Devices, Ed. C.-H. Lee, (Academic Press, New York, 1984) pp. 73-118.
7. J. F. Knudsen, R. C. Bowman, Jr., P. M. Adams, R. Newman, J. P. Hurrell, R. C. Cole, L. F. Halle, and D. H. Barker, *Proc. Symp. on Advanced Surface Processes for Optoelectronics*, Vol. 126, pp. 177-182, Eds. T. Venkatesan, S. Bernasek, G. Stillman, and H. Temkin (Materials Research Society, Pittsburgh, PA, 1988).
8. J. F. Ziegler, J. P. Biersack, and U. Littmark, The Stopping and Range of Ions in Solids (Pergamon, New York, 1985).
9. R. L. Maddox and I. Golecki, *Electron. Lett.* **21**, 154-155 (1985).
10. I. Golecki, *Mat. Res. Soc. Symp. Proc.* **33**, 3-23 (1984).
11. TH. Englert, G. Abstreiter, and J. Pontcharra, *Sol. St. Electron.* **23**, 31-33 (1980).
12. J. H. McCoy and D. B. Wittry, *J. Appl. Phys.* **42**, 1174-1181 (1971).
13. S. C. Moss, J. F. Knudsen, and D. D. Smith, *J. Mod. Opt.*, Dec. (1988) in press.
14. M. Y. Tsai, B. G. Streetman, R. J. Blattner, and C. A. Evans, Jr., *J. Electrochem. Soc.* **126**, 98-102 (1979).

FORMATION OF SHALLOW BORON P⁺ JUNCTIONS USING Sb AMORPHIZATION

E. Ganin, B. Davari, D. Harame, G. Scilla, and G.A. Sai-Halaszi
IBM T.J. Watson Research Center
Yorktown Heights, NY 10598

Abstract

Shallow P⁺ junctions have been fabricated using reverse-type dopant preamorphization by Sb. The junctions ~100 nm in depth have leakage current below 10 nA/cm², sheet resistance less than 200 Ω/\square and ideality factor in the range 1.01-1.03. This type of amorphization scheme provides electrical activation of B at low temperature, which is very promising for low temperature processing applications. The importance of process optimization was demonstrated. The electrical results were correlated with residual defect structure observed by cross-sectional TEM.

Introduction

Recent studies showed that there are numerous advantages in using preamorphization by heavy ion implantation in order to fabricate shallow boron junctions¹. One of the advantages is in creating sharp crystalline / amorphous (C/A) interface with relatively low dose implant. The residual defects formed after the annealing consist mainly of end-of-range dislocation loops, which can be completely eliminated with reduced thermal budget anneal as compared to self-implantation with Si. This has been demonstrated previously¹ by comparing the effect of In amorphization and self-amorphization by Si on residual defect morphology and annealing kinetics. Low dose indium implantation at 40 keV was successful in forming low reverse bias leakage diodes with reasonably good sheet resistance². However, the indium channeling "tails" were observed in some cases, limiting the minimum achievable junction depth to about 120 nm. The inability to avoid channeling even at a low dose ion implantation can be turned into advantage by using preamorphizing species of an opposite conductivity type than the intended dopant. In this case the implant tail instead of smearing the junction would sharpen it up, leading to a shallow well defined profile. We realized the described scheme using antimony (Sb) as the preamorphizing agent.

Experimental

Diodes were fabricated in N-type (100) substrates by patterning an oxide, ion implanting Sb for amorphization with energies and doses ranging from 40 keV to 60 keV at $5 \times 10^{13} / \text{cm}^2$ to $3 \times 10^{14} / \text{cm}^2$ respectively, ion implanting B at 5 keV with $1 \times 10^{15} / \text{cm}^2$ dose, annealing and metallizing using lift-off. Different rapid thermal annealing (RTA) and furnace annealing schedules were applied with or without low temperature regrowth (LTR) at 580 or 600°C for 30 min. As a control experiment, one wafer was processed using Si self-amorphization with 30 keV Si implant at $1 \times 10^{15} / \text{cm}^2$ dose. This wafer was annealed at 900°C for 15 min to ensure formation of a good quality junction. Sheet resistance, forward bias ideality and reverse bias leakage current measurements were performed. Leakage current measurements were made for the large number (over 100) of diodes ranging from 75 μm^2 to $1 \times 10^6 \mu\text{m}^2$ size. The Sb and B concentration versus depth profiles were measured using SIMS analysis. Cross-sectional TEM (XTEM) was applied to study the residual defect morphology and correlate it with electrical measurements.

Results and Discussion

The experimental conditions and the junctions characteristics are summarized in Table 1. The best junctions with the leakage below 10 nA/cm² and the sheet resistance 160-197 Ω/\square were obtained by using 40 keV/ 1×10^{14} /cm² Sb amorphization and low temperature regrowth followed by 10sec RTA in 900-1000°C range (entries 6-9 in Table 1). The corresponding junction depth varied in the range 95-112 nm. Similarly shallow and low leakage junctions were obtained by furnace annealing at 800°C for 30 min (entries 2-5). However, in this case the sheet resistance increased significantly up to 356-428 Ω/\square . This high sheet resistance value can be reduced by increasing the dose of implanted B to 2×10^{15} /cm², resulting in good quality junctions (entry 10).

TABLE 1
Experimental Conditions and Electrical Results

No.	Ion/Energy/Dose /KeV/atoms/cm ²	Boron Dose atoms/cm ²	LTR	Anneal °C/sec	Xj nm	R Ω/\square	I@(-5.0V) nA/cm ²
1	Sb/40/1 $\times 10^{14}$	1×10^{15}	Y	800/30	102	123	265
2	Sb/40/5 $\times 10^{13}$	1×10^{15}	Y	800/1800	95	428	12
3	Sb/40/5 $\times 10^{13}$	1×10^{15}	N	800/1800	105	374	1000
4	Sb/40/1 $\times 10^{14}$	1×10^{15}	Y	800/1800	105	399	100
5	Sb/40/1 $\times 10^{14}$	1×10^{15}	N	800/1800	115	356	500
6	Sb/40/1 $\times 10^{14}$	1×10^{15}	Y	900/10	95	192	8.0
7	Sb/40/1 $\times 10^{14}$	1×10^{15}	Y	950/10	95	197	7.5
8	Sb/40/1 $\times 10^{14}$	1×10^{15}	Y	1000/10	108	160	2.7
9	Sb/40/1 $\times 10^{14}$	2×10^{15}	Y	950/10	112	170	4.7
10	Sb/40/1 $\times 10^{14}$	2×10^{15}	Y	800/900	118	230	3.6
11	Sb/60/3 $\times 10^{14}$	2×10^{15}	Y	950/10	ND	156	1.3×10^4
12	Si/30/1 $\times 10^{15}$	2×10^{15}	Y	900/900	250	201	150

ND = Not Defined

Reverse bias leakage current was very sensitive to the energy and dose of the amorphizing species (compare entries 9 and 11). SIMS concentration profiles for these compared cases, presented in Fig. 1, illustrate the importance of amorphization energy and dose optimization for a given B implant condition (5 keV). Cross-sectional TEM showed that the amorphous region depth was ~60 and 90 nm for the 40 keV/ 1×10^{14} /cm² and 60 keV/ 3×10^{14} /cm² implants respectively. Although in both cases B was mostly contained within the amorphous region, in the latter case the junction's location was adjacent to the crystalline / amorphous interface at ~90 nm. Therefore, the interstitials created by ion implantation beneath the amorphous region would be expected to contribute to the high leakage and the thermal budget required to annihilate the residual defects would be increased. The leakage current measured in this case was four orders of magnitude higher than for the 40 keV Sb implant (entry 11). Furthermore, the density of interstitials, which is roughly proportional to the dose of Sb, was higher for the 60 keV implant. The optimized condition of Sb-amorphization for the 5 keV B implant corresponds to 40 keV/ 1×10^{14} /cm². In this case the C/A interface located at 60 nm from the surface is spaced away from the junction region and the leakage current is low.

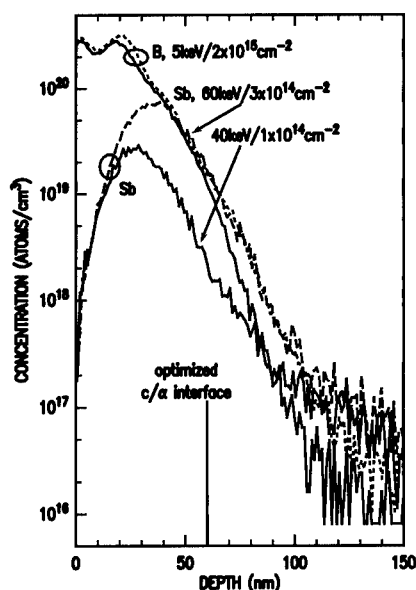


Fig. 1 SIMS B and Sb concentration profiles in Sb-amorphized samples after LTR at 600°C/30 min + RTA at 950°C/10 sec. B is implanted at 5 keV/ $2 \times 10^{15}/\text{cm}^2$; Sb is implanted at 40 keV/ $1 \times 10^{14}/\text{cm}^2$ or 60 keV/ $3 \times 10^{14}/\text{cm}^2$ dose.

The behavior of residual defects formed after the annealing is quite intriguing. None of the furnace annealed samples exhibit any end-of-range dislocation loops, due to the relatively long times of annealing. The dislocation loops behavior was more complex in the RTA samples depending on the total heat cycle received. For thermal budgets not exceeding 800°C/30 sec (Fig. 2A), samples did not contain end-of-range dislocation loops. However, in samples annealed at 900°C/10 sec, end-of-range dislocation loops did appear (Fig. 2B). At an even larger thermal budget of 10 sec at 950°C the dislocation loops disappeared again (Fig. 2C). This behavior is consistent with our understanding of dislocation formation during annealing being a thermally activated process of formation and dissolution. Certain thermal energy is required for the interstitials still remaining after the implantation and the regrowth to form dislocation loops. Therefore, below certain thermal budget (800°C/30 sec) the formation of dislocation loops in their well defined form (like in Fig. 2B), has not occurred yet. At 950°C/10 sec the thermal budget probably exceeded the threshold required for loops annihilation and the junction is free of extended defects. The "annealing window" within which the end-of-range dislocations do exist seems to be quite narrow. Quite surprisingly, the wafer which exhibited end-of-range dislocation loops (Fig. 2B), demonstrated very low leakage current (entry 6). This fact probably means that the loops do not affect the leakage current when located outside of the space charge region.

The junctions obtained by self-amorphization with Si were much deeper than the ones obtained by Sb (entry 12, Table 1). Although some difference in junction depth should be attributed to the different annealing treatments, since generally shallower profiles may be obtained by RTA as compared to furnace anneals. However, for signif-

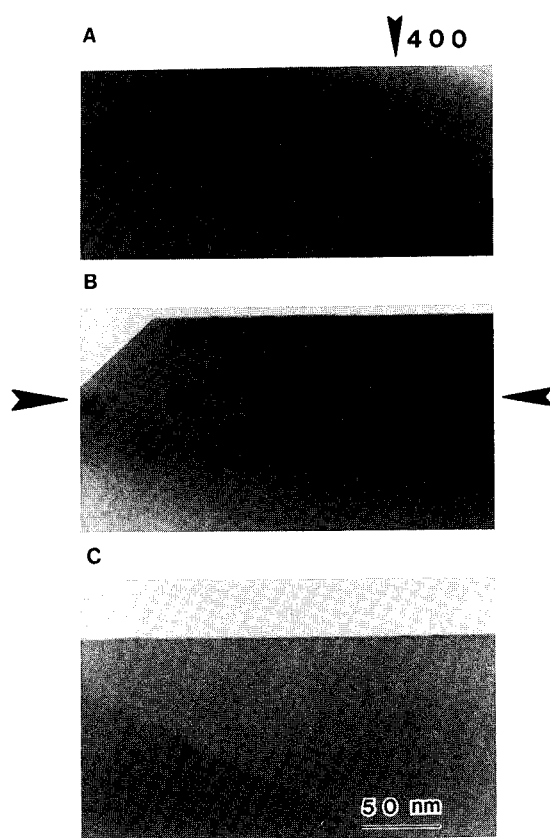


Fig. 2 XTEM of Si sample implanted with Sb at 40 keV/ 1×10^{14} /cm² and B at 5 keV/ 1×10^{15} /cm² after LTR anneal at 600°C/30 min followed by RTA anneal at: (A) 800°C/30 sec; (B) 900°C/10 sec; (C) 950°C/10 sec.

Vertical arrow shows the
[400]

crystal orientation.

Position of end-of-range dislocation loops in (B) is indicated
by horizontal arrows.

icantly deeper junctions one would expect to obtain lower leakage currents. This doesn't seem to be the case. In contrary, the reverse bias leakage current of large area diodes amorphized by Si was about two orders of magnitude higher than for the Sb-amorphized ones. We argue that this difference is due to sharper C/A interface and lower dose needed for amorphization by heavy Sb ions. As one may notice from the SIMS profiles in Fig. 3, for the case of Sb amorphization, the junction depth is defined by the intersection between Sb and B profiles and is generally shallower than it would have been had it been defined by B profile only at the 1×10^{17} / cm² concentration level. The effect of

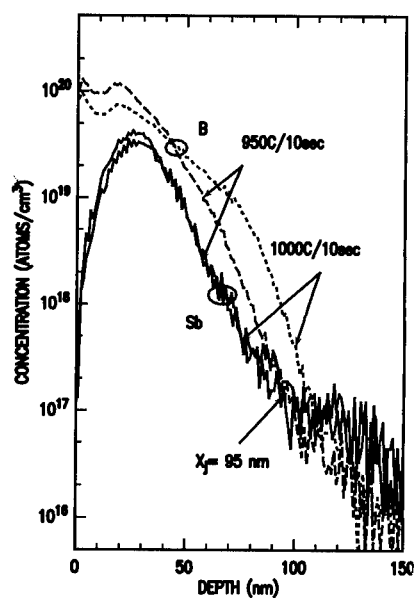


Fig. 3 SIMS B and Sb concentration profiles in Sb-amorphized samples after LTR at 600°C/30 min + RTA at 950°C/10 sec or 1000°C/10 sec. B is implanted at 5 keV/ 1×10^{15} /cm²; Sb is implanted at 40 keV/ 1×10^{14} /cm²

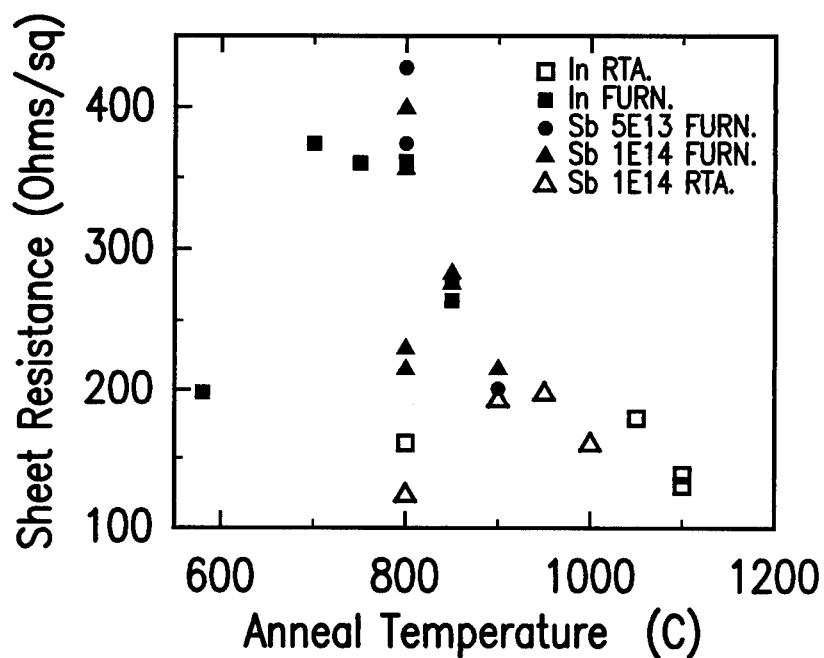


Fig. 4 Sheet resistance of Si samples amorphized with Sb or In prior to B implantation at 5 keV/ 1×10^{15} /cm². Annealing treatments include furnace and RTA.

Sb compensating for the B "tail" is equivalent to sharper junction. The additional capacitance obtained resulting from the sharper junction is not expected to detriment the device behavior. Forward bias characteristics of all diodes were in the range 1.01-1.03.

The sheet resistance measurements data is plotted in Fig. 4. Additionally to the values obtained by Sb amorphization, data for In-amorphized diodes is included. Sheet resistance values vary insignificantly for both types of amorphizing ions. One may note that B is highly active already after 580°C, with no further annealing. This fact is significant and very important for future low temperature processing applications. Junctions formed using LTR and subsequent 30 sec RTA at 800°C (entry 1), were comparable with the ones obtained by Si-amorphization followed by 900°C /30 min anneal (entry 12). (Note the difference in junction depth.) Further reduction in leakage currents to ~ 3 nA/cm² was achieved by applying 10 sec RTA in 900-1000°C range. The wafers exposed to LTR prior to higher temperature furnace anneal exhibited up to about 2 orders of magnitude less leakage than the ones with no regrowth (compare entries 2 with 3 and 4 with 5).

Samples annealed by RTA exhibit significantly lower resistance values than furnace annealed ones. The most dramatic difference is for the 800°C regime. The 30 sec RTA results in 160 Ω/\square and the sheet resistivity value increases up to 428 Ω/\square for 30 min anneal. This behavior can be explained by the following. The solubility limit of B at 800°C is greatly exceeded and given the length of time sufficient to diffuse, B is leaving the substitutional sites. Therefore, the long time annealing results in relatively low electrically active concentration of B. At the temperatures above 900°C the difference between sheet resistance values of RTA and furnace annealed samples was not significant.

Summary

Sb amorphization prior to low energy B implantation combined with reduced thermal budget anneal can be successfully used for shallow junction formation. Diodes, formed by using this approach, exhibited close to ideal characteristic in forward bias, low leakage current in reverse bias mode and low sheet resistance. The sheet resistance in the case of RTA diodes was always lower than 200 Ω/\square . The feasibility of a truly low temperature process when the highest annealing regime (800°C/30 sec) is compatible with "silicidation anneal" is demonstrated. Low temperature regrowth prior to the activation anneal was effective in reducing the leakage current.

TEM observation showed no extended defects presence at the end of the amorphous region even after reduced thermal budget anneals like 800°C/30 min or rapid thermal anneal at 950°C/10 sec. No increase in leakage current was observed in the sample exhibiting end-of-range dislocation loops after 900°C/10 sec anneal, as compared with the case of loops absence. We conclude that these loops are harmless when remote from the space charge region.

Optimizing the energy and dose of amorphizing species, one can control the position of C/A interface and therefore the junction properties.

REFERENCES

1. E. Ganin, G. Scilla, T. O. Sedgwick, and G. A. Sai-Halasz, Materials Research Symposium A, vol.74, p.717 (1987)
2. E. Ganin, D. Hame, G. Scilla, and G. A. Sai-Halasz, Unpublished Results

SILICIDED SHALLOW JUNCTION FORMATION USING ION IMPLANTATION AND THERMAL ANNEALING

LEONARD M. RUBIN*, N. HERBOTS*, D. HOFFMAN**, AND D. MA**

*Department of Materials Science and Engineering, Massachusetts Institute of Technology, 77 Massachusetts Avenue, Cambridge, MA 02139

**Standard Microsystems Corp., 35 Marcus Boulevard, Hauppauge, NY 11788

ABSTRACT

The combination of arsenic and boron implantation with rapid thermal annealing (RTA) has been investigated to form shallow p-n junctions under a titanium silicide (TiSi_2) metallization. The use of TiSi_2 as a connection material can lead to the destruction of the junction if the kinetics of silicidation and doping are not well controlled. The purpose of this study is to better understand and control these kinetics, using far-from equilibrium processing such as ion implantation and RTA. The structures were characterized by Rutherford Backscattering Spectrometry (RBS) for arsenic and silicide profiling, Secondary Ion Mass Spectrometry (SIMS) for boron profiling, Scanning Electron Microscopy (SEM), and electrical sheet resistance measurements. Two procedures were investigated. Both involved the thermal reaction of Ti thin films, sputter-deposited with thicknesses ranging between 40 and 80 nm. In the first experiment, the as-deposited films were implanted with either 115 keV arsenic or 28 keV boron to form the junction, disperse the native oxide, and ion beam mix the Ti and Si. The films were then subjected to an RTA at 750°C for 15 to 60 seconds, which leads to TiSi_2 formation in unimplanted films. Implantation was found to actually prevent TiSi_2 formation. Ion transport calculations indicated that dopant pile-up at the interface might inhibit silicidation while higher energies and larger implant doses can more effectively ion beam mix Ti and Si. A more attractive solution consists of first forming TiSi_2 from the as-deposited Ti by RTA, and then implanting to form the junction. This resulted in better control of the junction thickness. A sharp increase in the TiSi_2 resistivity was found after implantation but the original value could be restored by a second RTA. This RTA also electrically activated the dopants and recrystallized the junction. The material properties of Ti/Si and TiSi_2 /Si under ion bombardment, RTA, doping, and conventional furnace annealing will be discussed.

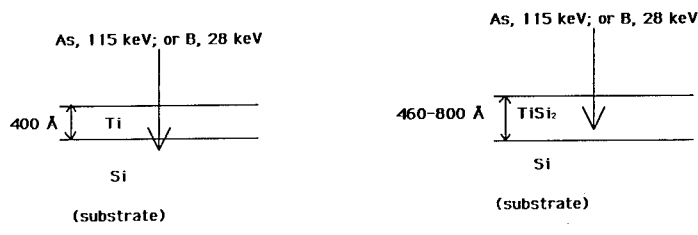
INTRODUCTION

Silicides have come into widespread use in recent years as low resistivity interconnect films for integrated circuits. Titanium silicide is especially suited for this purpose, because of its low resistivity (about $15 \mu\Omega\text{-cm}$) [1,2] and its ease of formation by thermal reaction of Si and a deposited Ti film. This step is often performed in a rapid thermal annealing machine, because of the tight process control afforded by RTA and the rapid rate at which the reaction proceeds in the temperature range 650-850°C [3,4]. Sheet resistivities of 1-2 Ω/square have been achieved over the diffused regions of MOS circuits by forming TiSi_2 , as compared to 50 Ω/square for unsilicided regions [5].

In current silicidation schemes, the heavily doped regions of the junctions are formed by implantation and thermal drive-in prior to the deposition and reaction of the Ti film. This technique has two large drawbacks. First, the amount of silicon consumed by the advancing TiSi_2 /Si interface is almost as great as the thickness of the resulting TiSi_2 film. In order to form a film with sufficiently low resistivity (e.g. 1.5 Ω/square), it is necessary to consume about 1000 Å of heavily doped silicon. As junction depths are scaled down in future devices, there is a risk that the interface will proceed past the depth of the junction, shorting the TiSi_2 to the substrate. Also, the surface concentration of the silicon is reduced by removing the most heavily doped layers. The second drawback is that large variations in TiSi_2 thickness can be caused by small variations in the thickness of the native SiO_2 that is always present between the Ti and the Si. A significant amount of the anneal time is necessary to reduce this oxide, resulting in only partial formation of the TiSi_2 film.

Two alternate techniques for forming silicided shallow junctions have been investigated. These techniques are illustrated in figure 1. In the first, the junction is implanted after the Ti has been deposited but before it has been reacted to form TiSi_2 . If done properly, the junction

implant will cause ion beam mixing of the Ti and Si at the interface and disperse the native oxide. This should result in a more uniform TiSi_2 film in less time upon reacting. The second method entails implanting the junction after the formation of the TiSi_2 film is complete. This eliminates the possibility that the junction will be consumed by the advancing interface during silicide formation. Additionally, most of the implant induced damage will be confined to the silicide instead of the silicon, reducing the heat treatment required to recrystallize the silicon and activate the dopants.



Case I - Implant through Ti film.

Case II - Implant through TiSi_2 film.

Figure 1. Diagram of samples showing different implanting conditions.

Estimates of the projected ranges of arsenic and boron in Ti and TiSi_2 were made with the TRIM (TRansport of Ions in Matter) program. TRIM is a Monte-Carlo simulation program that calculates the trajectories of energetic ions in matter and the number of atoms displaced by these interactions [6]. These estimates indicated that some of the implanted boron and almost all of the implanted arsenic would be stopped before reaching the silicon layer. This implies that the diffusivity of these dopants in TiSi_2 at typical annealing temperatures is of great importance. An attempt was made in this work to determine these diffusivities under rapid thermal annealing conditions.

EXPERIMENTAL PROCEDURE

All experiments were performed on Si (100) substrates. Both N^+ (arsenic) and P^+ (boron) implants were investigated. Arsenic was implanted at energies of 80 and 115 keV and at doses of 3.0 , 6.7 , and $10 \times 10^{15}/\text{cm}^2$. The boron implant doses were 1.0 , 3.0 , and $6.0 \times 10^{15}/\text{cm}^2$ at energies of 28 and 35 keV. Ti was deposited on the wafers by a Varian 3190 sputtering system. The as-deposited films were 400-800 Å thick. Silicide formation was done in an AG Associates model 2101 rapid thermal annealer. Wafers were annealed one at a time, using intense visible radiation. All silicide formation was done at 750°C in a nitrogen ambient. Prior to annealing, the chamber was purged with N_2 so as to minimize oxidation of the Ti film. The length of this anneal was varied between 15 and 60 seconds. An etch bath of H_2O , NH_4OH , and H_2O_2 in the ratios 5:1:1 was used to remove any unreacted Ti from the surface. For case II in figure 1, the implant was done after this etch, with no intervening steps. Following the implant (or etch, if the implant was done prior to silicidation), each wafer was given a second RTA anneal. This anneal was always for 30 seconds at 850°C in an argon ambient. At this point, the thickness of the TiSi_2 film was measured by removing an unmasked section in HF, and measuring the resultant step with a profilometer. The final step was a conventional furnace anneal for 30 minutes in N_2 . Temperatures for this anneal were varied between 850 - 950°C .

The sheet resistivity of each film was measured with a 4 point probe after each processing step that was expected to change it (e. g. implantation, annealing). Some of the wafers had $100 \mu\text{m} \times 100 \mu\text{m}$ diodes fabricated so that reverse leakage current and junction depth measurements could be made and compared to unsilicided diodes.

In order to estimate the diffusivity of arsenic and boron in TiSi_2 , 3000 Å films of this material were prepared by thermal reaction of 1500 Å of Ti on Si substrates. Arsenic was implanted into some of the samples at a dose of $6.7 \times 10^{15}/\text{cm}^2$ and an energy of 115 keV, while boron was implanted into similar films at a level of $3.0 \times 10^{15}/\text{cm}^2$ and 28 keV. The silicide films were then annealed in argon in the RTA for times ranging from 20 to 180 seconds and at

temperatures from 600-900°C. RBS profiles were used to determine the movement of arsenic as a function of annealing conditions, while SIMS data provided similar information about the boron implanted samples.

RESULTS AND DISCUSSION

TiSi₂ Formation from Ti Films Implanted with Arsenic and Boron

In the case of implanting through as-deposited 400 Å Ti films, the enhanced silicide growth due to ion beam mixing did not occur. Instead, silicide growth was diminished by the implants, much more so by the arsenic than the boron. Figure 2 shows the amount of TiSi₂ formed as a function of the silicidation time in the RTA. No TiSi₂ was formed on the arsenic implanted wafers until the anneal time was extended to 45 seconds. Even after 60 seconds, the TiSi₂ thickness was less than half what was measured after 15 seconds on the unimplanted samples. This silicide had bulk resistivities in the range 39-55 μΩ-cm, 2 to 3 times as high as the controls. TiSi₂ was formed on all of the boron implanted samples, but was not as thick as on the control wafers for a 15 second anneal.

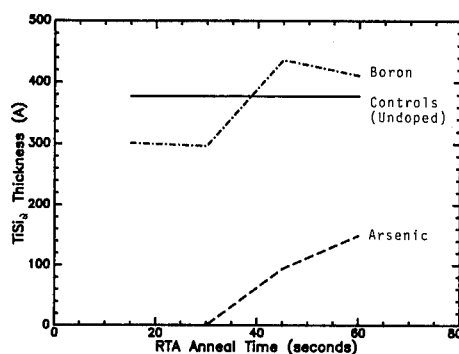


Figure 2. Silicide thickness as a function of silicide growth time for samples implanted through a 400 Å as-deposited Ti film. All control wafers were annealed for 15 seconds only.

Simulations made with the TRIM program to try to understand these results indicated that the boron implant conditions in this case were not sufficient to disperse the native oxide (assumed to be 25 Å thick) and amorphize the silicon. The arsenic dose was clearly sufficient to amorphize the silicon, but the simulations showed that a significant excess of oxygen atoms remained at the interface after the implantation. This implies that the native oxide was not dispersed. In addition, a large pile-up of arsenic was found in the silicon near the Ti/Si interface in the simulated profiles. Silicide growth on silicon heavily doped with arsenic is generally less than that formed over lightly doped Si, whether or not the arsenic was implanted through the Ti film [7]. This may have caused the observed lack of TiSi₂ formation.

Other researchers have found that 170 keV is a sufficient arsenic implant energy to amorphize the interface and allow for good silicide growth [8]. Our simulations have shown that a 170 keV arsenic implant should result in significantly more vacancy and interstitial formation in the interfacial region than a 115 keV implant would produce, and a more even arsenic distribution throughout the silicon, with virtually no pile-up at the Ti/Si interface (Fig. 3). Thus, we conclude that implant energy must be carefully chosen to give the desired results with this technique.

Characteristics of TiSi₂ Films Subject to Arsenic and Boron Implantation

The immediate effect of ion implantation on a TiSi₂ film is to raise its sheet resistivity by an order of magnitude. The observed increase was twice as great for arsenic implants as for boron implants. These results are independent of the initial thickness of the TiSi₂ film. In all

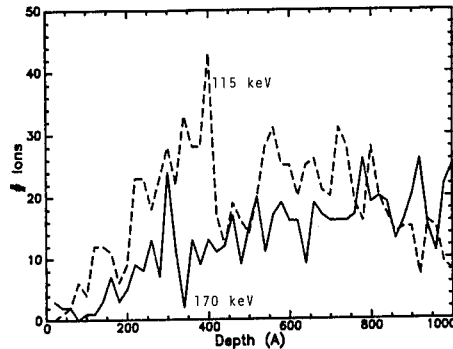


Figure 3. TRIM estimates of the arsenic concentration as a function of depth for 115 and 170 keV implants through a 400 Å Ti film. Note the pile-up of arsenic just below the Ti/Si interface in the 115 keV case.

cases, the TiSi_2 sheet resistivity was returned to its pre-implant value by a 30 second RTA anneal at 850°C. From this we conclude that the implant damage to the silicide is easily repaired and is not a drawback to this fabrication technique. Because much of the implant damage is confined to the silicide layer, it was possible to recrystallize the silicon and activate the dopants in the same RTA anneal that restored the low resistivity of the TiSi_2 . Leakage currents as low as 160 nA/cm² were observed on P+/N and N+/P test diodes fabricated by this technique. The dopant concentrations at the TiSi_2 /Si interface were higher than $5 \times 10^{19}/\text{cm}^3$, as determined by spreading resistance profiling.

When these samples were subjected to a 30 minute furnace anneal in N_2 at 850°C, both arsenic and boron diffused into the silicide film, as indicated by a lower surface concentration of these species (Fig. 4). Arsenic has been reported to have a high solubility in TiSi_2 at elevated temperatures [9], but the results for boron were quite surprising. This, combined with coalescence effects observed in TiSi_2 films [10,11], means that post-implant thermal processing will have to be kept to the absolute minimum to achieve good doping profiles under a low resistivity TiSi_2 film.

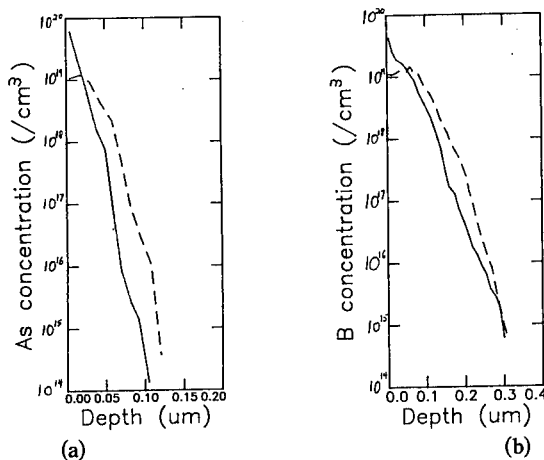


Figure 4. Dopant concentrations in silicon before (solid lines) and after (dashed lines) an 850°C, 30 minute furnace anneal in nitrogen. In both cases the surface concentration of the dopant was reduced by diffusion into the adjacent silicide film. The concentrations were determined by spreading resistance profiling. (a) arsenic (b) boron.

Diffusivity of Arsenic and Boron in TiSi₂

Prior to annealing, the peak of the as-implanted distribution was 540 Å below the TiSi₂ surface, as determined by RBS spectra. The TRIM calculated value of 530 Å for the projected range is in excellent agreement with this. The diffusivity of arsenic in TiSi₂ during RTA annealing was found to be extremely high. Complete redistribution from an as-implanted Gaussian distribution to a uniform concentration across the 3000 Å silicide film was observed after a 20 second anneal at 900°C. This diffusivity is even higher than that reported for arsenic diffusion during furnace annealing [12]. At lower temperatures the diffusivity was greatly reduced, but was still several orders of magnitude higher than diffusion in silicon at corresponding temperatures. After a 30 second anneal at 600°C, the arsenic profile was almost the same as the profile measured prior to annealing.

TRIM simulations estimated the projected range of 28 keV boron in TiSi₂ at 860 Å. This is close to the value of 800 Å obtained from SIMS profiles of as-implanted boron. After the most severe RTA anneal of 180 seconds at 900°C, the resulting boron profile was indistinguishable from the as-implanted profile. This is quite a difference from the case of arsenic. Similar results were observed by Gas et. al., who hypothesized that the boron forms TiB₂, which appears in the silicide film in the form of immobile precipitates. The heat of formation of this compound is -77 kcal/mole, as compared to -32 kcal/mole for TiSi₂, making the formation of TiB₂ quite feasible [12]. However, others have reported a diffusivity of 10⁻¹² cm²/sec, well above what was observed here, for boron diffusion in an RTA at this temperature [13]. Further investigation is required to resolve this discrepancy.

CONCLUSIONS

The formation of 1000 Å N⁺/P junctions and 3000 Å P⁺/N junctions has been achieved by implanting through a previously formed TiSi₂ layer. Low silicide resistivities and low leakage currents are observed after a brief RTA anneal that activates the dopants in the silicon and repairs the implant damage in the TiSi₂. Ion beam mixing was not induced by a 1 x 10¹⁶/cm², 115 keV arsenic implant through a deposited Ti film. It is likely that a higher energy implant will give better results. Arsenic diffusion in TiSi₂ is extremely rapid at normal annealing temperatures, while boron is immobile. However, both dopants dissolved in the silicide during furnace annealing, leaving a region of less heavily doped silicon at the TiSi₂/Si interface. For this reason, it is critical that post-implant thermal processing be kept to a minimum.

REFERENCES

- [1] S. P. Murarka, M. H. Read, C. J. Doherty, and D. B. Fraser, *J. Electrochem. Soc.* **129** 293 (1982).
- [2] S. P. Murarka, *J. Vac. Sci. Tech.* **17** 775 (1980).
- [3] C. K. Lau, Y. C. See, D. B. Scott, J. M. Bridges, S. M. Perna, and R. D. Davis, *IEDM Tech. Dig.*, 714 (1982).
- [4] N. de Lanerolle, D. Hoffman, and D. Ma, *J. Vac. Sci. Tech. (B)* **5** 1689 (1987).
- [5] L. Rubin, unpublished data.
- [6] J. P. Biersak, W. Eckstein, *Appl. Phys. A* **34** 73 (1984).
- [7] H. K. Park, J. Sachitani, M. McPherson, T. Yamaguchi, and G. Lehman, *J. Vac. Sci. Tech. (A)* **2** 264 (1984).
- [8] D. Pramanik, M. Deal, A. N. Saxena, and O. K. Wu, *Advanced Applications of Ion Implantation*, SPIE vol. **530** 159 (1985).
- [9] A. H. van Ommen, H. J. W. van Houtum, and A. M. L. Theunissen, *J. Appl. Phys.* **60** 627 (1986).
- [10] R. K. Shukla and J. S. Multani, *IEEE V-MIC Conf.* 470 (1987).
- [11] C. Y. Ting, F. M. d'Heurle, S. S. Iyer, and P. M. Fryer, *J. Electrochem. Soc.* **133** 2621 (1986).
- [12] P. Gas, V. Deline, F. M. d'Heurle, and G. Scilla, *J. Appl. Phys.* **60** 1634 (1986).
- [13] Y. H. Ku, E. Louis, S. K. Lee, D. K. Shih, D. L. Kwong, C. O. Lee, and J. R. Yeargain, *Advanced Processing of Semiconductor Devices*, SPIE vol. **797** 61 (1987).

ON THE STRUCTURE, COMPOSITION, AND I-V CHARACTERISTICS OF AL/Ti:W/a-Si CONTACTS.

S. BERGER AND Y. KOMEM*

Department of Materials Engineering, Technion, Haifa ISRAEL

* On leave from the Technion, IBM, T.J. Watson Research Center,
Yorktown Heights, NY 10598.

ABSTRACT

The effect of heat treatments on the microstructure, composition and I-V characteristics of Al/TiW/a-Si contacts was studied.

It was found that heat treatments of the amorphized contacts at the temperature range of 450-520°C led to an interdiffusion of Si atoms into the Al film and of Al atoms into the a-Si region through the Ti:W layer and silicides formation. However, no such interdiffusion and silicides formation could be detected in the contacts made of the unamorphized Si substrate under identical heat treatments.

The I-V characteristics of the amorphized contacts are explained by a model of electrical conductivity in amorphous solids.

INTRODUCTION

The development and application of devices based on contacts between an a-Si and thin metal films [1] enhanced research on their microstructure and electrical properties. The interaction between an Al thin film and an a-Si has been studied extensively [2]. It was found that Si dissolved, diffused and recrystallized in the Al film and Al penetrated into the a-Si as a result of heat treatments at temperatures between 450-540°C. These interdiffusion and recrystallization processes are not desirable since they can alter the electrical properties of the contacts and can lead to an electrical short in shallow contacts. One of the methods to eliminate the interdiffusion between the Al and Si is the interposition of a diffusion barrier layer between the Al film and the Si substrate [3]. The pseudo alloy of Ti:W (10:90 wt%) has been investigated as a diffusion barrier between an Al film and a single crystalline Si substrate [4]. The Ti:W layer prevented the diffusion of Si into the Al film and no silicides were formed as a result of heat treatments at temperatures between 450 and 520°C.

This paper presents a study of the effect of heat treatments on the structure, composition and I-V characteristics of Al(2%Cu)/Ti:W/a-Si contacts.

EXPERIMENTAL DETAILS

The samples, composed of n-type (100)Si wafers (15-25 Ω cm), were first implanted with Ar ions with energies between 60-180 Kev and a dose of 1×10^{16} ions/cm² in order to form an amorphous surface layer with a projected range between 60-180nm [5]. Subsequently, an intermediate layer of Ti:W (10:90

wt%, 150nm thick) was sputtered on the implanted surface followed by a sputtering of an Al (2wt% Cu) film (1 μ m thick) on the Ti:W layer. The samples were heat treated in the temperature range of 450-520°C between 0.5-12 hours under a controlled N_2 gas ambient.

The microstructure and composition of the samples were studied by means of Transmission Electron Microscopy (TEM), X-Ray diffraction (XRD) and Auger Electron Spectroscopy (AES). The TEM study was performed with a Jeol 100CX electron microscope with 100Kv accelerating voltage and in situ energy dispersive x-ray spectroscopy (EDS). The microstructure analysis was done both on vertical cross section and flat on specimens. The XRD measurements were carried out with a PW 1050/25 computerized diffractometer by using an X-ray source of Cu-K α . The system was operated at an accelerating voltage of 40Kv and a current of 25mA. The AES measurements were performed using a PHI 590A Scanning Auger Microprobe. The base pressure in the specimen chamber was 10^{-9} - 10^{-10} Torr. A primary electron energy of 5 Kev and a current of 0.5nA were employed for the compositional depth analysis of the Si, Ti, W, Al and oxygen elements with simultaneous sputtering of (2Kev) Ar ions.

The I-V measurements were performed, with an hp 4145A Semiconductor Parameter Analyzer, in forward and reversed bias modes between 0-10 Volts and at room temperature.

EXPERIMENTAL RESULTS

Fig.1 presents a representative AES depth profiles of Al, Si, Ti, W and oxygen in the heat treated contacts. One can see that Si diffused through the Ti:W layer into the Al film and Al diffused through the Ti:W layer into the Si substrate (The Al peak, shown within the time range of 22-27 Min., is located in the a-Si region).

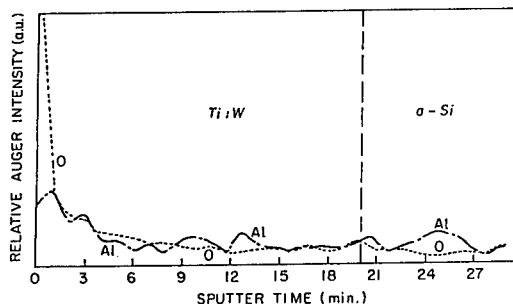


Fig.1: AES depth profiles of Al, Ti, W, Si and oxygen taken from the Al/Ti:W/a-Si contacts. The contacts substrate was Si(100) implanted with Ar ions having an energy of 60Kev and a dose of 1×10^{16} ions/cm². The contacts were heat treated at 450°C for 0.5 hour. The Al film was selectively etched prior to the AES measurements.

The amount of Si and Al that diffused through the Ti:W layer increased with increasing the heat treatment temperature and time. The diffusion of Si and Al through the Ti:W layer was not observed by AES depth profiles in specimens underwent

identical heat treatments and their substrate was single crystalline Si.

Fig.2 presents X-ray diffractions of the heat treated contacts.

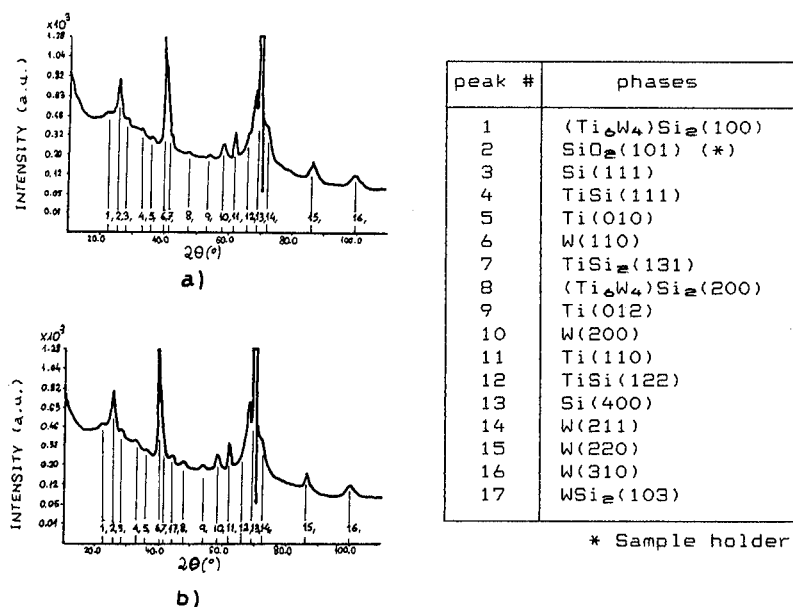


Fig.2: XRD spectrums of the Al/Ti:W/a-Si system where the (100) Si substrate was implanted with Ar ions having an energy of 60Kev and a dose of 1×10^{16} ions/cm² and heat treated: a) At 450°C for 0.5Hr. b) At 500°C for 12Hrs. The Al film was selectively etched after the heat treatments and prior to the XRD measurements.

In Fig.2 one can see that as a result of the heat treatment at 450°C for 0.5 hour the silicides: TiSi , TiSi_2 and $(\text{Ti}_6\text{W}_4)\text{Si}_2$ were formed. The increase of the heat treatment temperature to 500°C led to a formation of an additional silicide, WSi_2 .

Fig.3 is a representative TEM vertical cross section micrograph of the heat treated samples. It was taken from the sample that was heat treated at 520°C for 1 hour. One can see that the interface between the Al film and the Ti:W layer is undulating and EDS analysis at this interface showed Si in addition to W, Ti and Al. This undulating morphology is not continuous along this interface and there are regions, not shown in Fig.3, where the interface is flat and does not contain Si. The undulating regions contain grains that grow both laterally along this interface and vertically into the Al film as a result of increasing the heat treatment temperature. Electron diffraction patterns that were taken from the Al/Ti:W interface showed that they contain TiSi , TiSi_2 , AlTi_3 grains. (For example, Fig.4b shows a TiSi grain at this interface.) The analysis of the TEM vertical cross section samples shows that the morphology of

the Ti:W/a-Si and the a-Si/Si(100) interfaces is relatively uniform (see Fig.3) and no epitaxial growth of Si from the a-Si/Si(100) interface was detected.

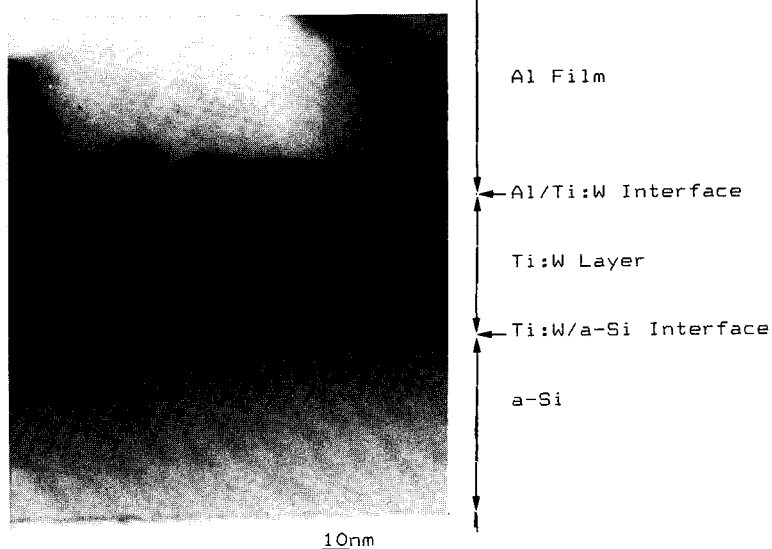


Fig.3: A bright field TEM micrograph of the Al/Ti:W/a-Si vertical cross section sample heat treated at 520°C for 1Hr. The samples substrate was implanted with Ar ions having an energy of 60Kev and a dose of 1×10^{16} ions/cm².

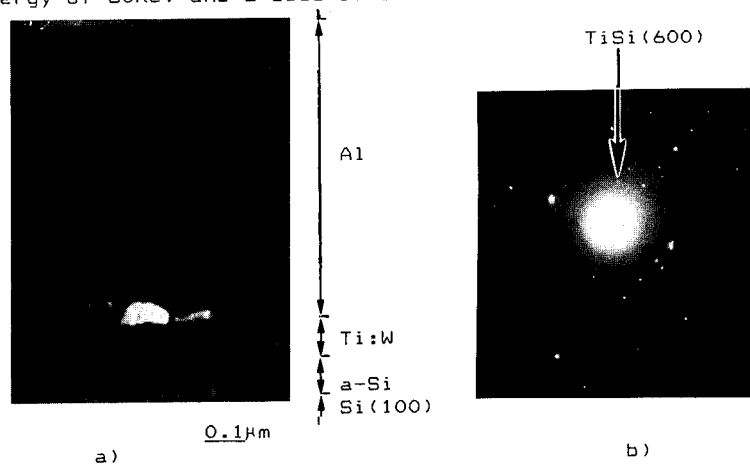


Fig.4: a) An electron diffraction pattern taken from the Al/Ti:W interface in the sample heat treated at 520°C for 1Hr. b) A TEM dark field image taken from reflection (600) of a TiSi grain(indicated in Fig.a) located at the Al/Ti:W interface.

Fig.5 presents the effect of the implantation energy and the heat treatments on the I-V curves of the amorphized contacts.

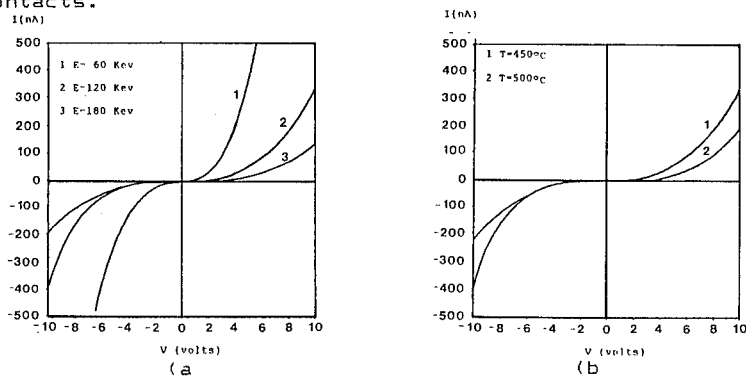


Fig.5: a) I-V curves of four contacts implanted with the energies: 60,120,180 Kev and a dose of 1×10^{14} ions/cm². The contacts were heat treated at 450°C for 0.5 hour. b) I-V curves of the contacts implanted with energy of 120Kev and heat treated at temperatures:450,500°C for 0.5Hr.

In Fig.5 one can see that the I-V curves have the same shape in the forward and reversed bias modes. At low voltages there is an identical symmetry between the forward and reversed bias modes while at higher voltages the current in the forward bias mode is higher compared to the reversed one. The electrical resistance of the contacts (dV/dI) increased with increasing the implantation energy and the heat treatment temperature.

DISCUSSION

The AES compositional depth profiles presented at Fig.1 show that Si diffused from the amorphized region through the Ti:W layer into the Al film while Al diffused through the Ti:W layer into the a-Si region. These AES depth profiles are characteristic of grain boundary diffusion[6]. This kind of diffusion of Al and Si through the Ti:W grain boundaries was not observed for identical heat treatments when the substrate was Si single crystal. Therefore one can conclude that the a-Si at the a-Si/Ti:W interface is directly related to the diffusion of Si through the Ti:W grain boundaries.

It was found that the following silicides: TiSi₂, TiSi₃, (Ti₃W₂)Si₂ and WSi₂ were formed only in the samples where the Si substrate was amorphized and not in the samples where the substrate was single crystalline Si. Therefore one can conclude that the excess free energy of the Si atoms in the amorphous state compared to that of Si atoms in a single crystalline state supplies a sufficient driving force for the diffusion of the Si through the Ti:W layer, nucleation and growth of the silicides. The preferential heterogeneous nucleation of the silicides at the Al/Ti:W interface rather than at the Ti:W/a-Si interface can result from a lower

interfacial and strain free energies at the Al/Ti:W interface compared to the Ti:W/a-Si interface.

The I-V characteristics of the contacts can be explained by a model of electrical conductivity in amorphous solids. The model is based on ionization of local defects by an applied field and charge carriers transportation through adjacent ionized sites[7]. According to this model the current density is equal to:

$$J = 2eN_s(KT)^{-1} \exp[-(E_{\infty} - eFs/2)/KT] \sinh(\alpha) \quad (1)$$

Where, J is the current density, e is the electron charge, N_s is the distribution of density of states with energy, s is the distance between adjacent ionized and ionizable defects, E_{∞} is the ionization energy of the defects, F is the applied field and $\alpha = eFs/2KT$. The J-F curve depicted according to equation (1) has the same shape as the experimental I-V curves of the amorphized contacts. The result that the shape of the I-V curves remained the same through all the range of the heat treatments shows that the mechanism of the electrical conductivity of the contacts remained unchanged as well. Since the electrical conductivity of the contacts is controlled by ionization of defects and transportation of charge carriers between the ionized defects than the increase of the electrical resistance of the contacts as a result of increasing the heat treatment temperature shows that the defects were annealed. The annealing of the defects can occur due to local reordering of Si atoms around defects and/or due to the Al atoms that penetrated into the a-Si region and could share electrons with Si atoms around defects. According to equation (1) the annealing of the defects can cause a decrease in N_s and/or an increase in E_{∞} and consequently a decrease in the conductivity.

SUMMARY

We have studied the effect of heat treatments on the structure, composition and I-V characteristics of Al(2%Cu)/Ti:W/a-Si contacts. As a result of the heat treatments Si and Al diffused through the Ti:W layer, the silicides, $TiSi$, $TiSi_2$, $(Ti_4W_4)Si_3$, WSi_2 , and the $AlTi_3$ compound were formed at the Al/Ti:W interface and the electrical resistance of the contacts increased.

REFERENCES

1. P.B.Lecomber, J. Non-Crystal. Solids, **90**, 219 (1987).
2. R.L. Boatright and J.G. McCaldin, J. Appl. Phys., **47**, 2260 (1976).
3. M.-A. Nicolet, Thin Solid Film, **52**, 415 (1978).
4. P.B. Gate, J.C. Blair, C.R. Fuller and G.E. McGuire, Thin Solid Film, **53**, 117 (1978).
5. B.S. Harwell, Ion Implantation Range Data For Silicon and Germanium Device Technologies, (1977).
6. J.M. Poate, K.N. Tu and J.W. Mayer, Thin Films- Interdiffusion and Reactions, (John Wiley & Sons, 1978).
7. R.M. Hill, Phil. Magazine, **23**, 59 (1971).

SYNTHESIS OF TWO-LAYER TiB_2 - $TiSi_2$ STRUCTURES BY BORON IMPLANTATION INTO TITANIUM FILM AND RAPID THERMAL ANNEALING

V.V. Tokarev*, A.I. Demchenko*, A.I. Ivanov*, V.E. Borisenko**, and D.I. Zarovsky**

*Institute of Solid State and Semiconductor Physics, the BSSR Academy of Sciences, P. Browka 17, 220726 Minsk, USSR

**Minsk Radioengineering Institute, P. Browka 6, 220600 Minsk, USSR

1. INTRODUCTION

Further progress in IC dimension reduction, increase in integration degree and speed require development and use of new current-conducting materials. This is due to the fact that existing current-conducting systems based on aluminium are low temperature, characterized by low electromigration stability and require use of complex barrier layers[1]. Polycide current-conducting materials have quite high resistance, interact with aluminium and are sensitive to the formation conditions. From this point of view, borides and titanium borides in particular are very promising for making current-conducting systems since they are very much characterized by good barrier properties, high conductance, properties and electromigration stability[2].

2. EXPERIMENTAL

This paper presents experimental results on synthesis of two-layer boride-titanium silicide structures by pulse heat treatment of boron-implanted titanium films on single-crystalline silicon.

80-300 nm titanium films were deposited onto chemically cleaned, n-type single-crystalline silicon (100) wafers using electron-beam evaporation at residual pressure of about 10^{-6} Pa. The prepared structures were divided into two groups. The samples of the first group were annealed at 250, 450, 650 and 850°C for 30 min. The second group was not annealed. The samples were then implanted with boron ions with doses of $1E16$ - $1E18$ cm $^{-2}$ and mean projected ranges of 50-100 nm using experimental ion implantation setup with ion beam integrated current of 10 mA. The temperature of the samples during implantation was kept at 50°C. The subsequent rapid thermal annealing (RTA) was performed in dried argon using halogen lamp intensive radiation under transient thermal balance conditions for 10-40 s at induced temperatures of 600-900°C[3].

Diffusion processes occurring in the structures investigated were controlled by Auger electron spectroscopy (AES). Phase composition of the layers formed was analysed using x-ray diffraction analysis.

3. RESULTS AND DISCUSSION

X-ray diffraction analysis and study of AES spectra of the samples after preliminary stationary heat treatment showed that heat treatment below 650°C didn't cause diffusion redistribution of titanium and silicon and silicide formation.

Heat treatment at higher temperatures results in diffusion mixing of silicon and titanium. The resulting silicide layers consist mainly of titanium disilicide (TiSi_2) and metal-rich silicide (Ti_5Si_3) inclusions (Fig. 1a).

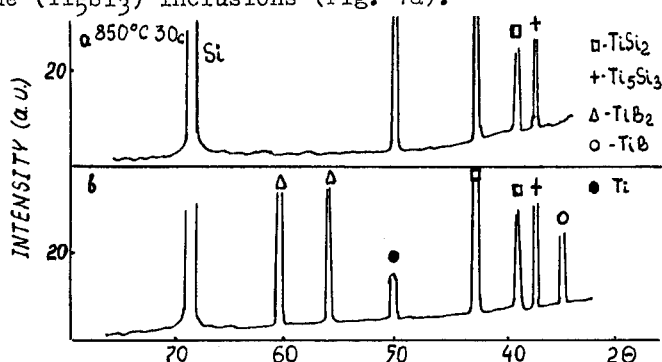


Fig. 1. X-ray diffraction patterns of layers synthesized by heat treatment of systems (a) Ti-Si and (b) Ti(B)-Si.

AES spectra show that when titanium films with thickness more than 100 nm are used, a layer of unreacted titanium remains on the sample surface. For instance, in case of initial film thicknesses of 300 nm and heat treatment at 850°C the unreacted film thickness amounts to 140-200 nm.

Boron implantation and subsequent rapid thermal annealing result in complex diffusion and phase transformations in the investigated samples. In this case initial structure and its phase composition considerably affect kinetics of diffusion processes and phase formation. Fig. 2 shows sequence of diffusion processes and phase formation after RTA as a function of initial titanium layer thickness and temperature of preliminary heating and subsequent pulse heat treatment.

This figure shows that pulse heat treatment of boron-implanted titanium films with a dose less than $1\text{E}16\text{ cm}^{-2}$ leads to diffusion redistribution of boron in the titanium film with a slight segregation at the TiSi_x -Ti interface even at induced temperatures $\sim 650^\circ\text{C}$ (Fig. 3). Implantation with a dose higher than $1\text{E}16\text{ cm}^{-2}$ leads to the formation of boron-rich layers at the interface after heat treatment at 600°C for 10s. The formed layer hampers diffusion mixing of titanium and silicon and silicide formation which occur at higher temperatures. A marked diffusion mixing in such system starts at 850°C and more, resulting in the formation of layers containing inclusions of metal-rich titanium silicides Ti_3Si , Ti_5Si_3 and borides TiB and TiB_2 in the titanium film (Fig. 1b). With longer anneal time intensity of lines corresponding to silicon-rich titanium silicides also increases indicating increase in their concentration.

Boron implantation into fully synthesized layers based on titanium disilicide along with RTA in the whole investigated range of doping and subsequent rapid thermal annealing conditions leads to diffusion redistribution of boron on the whole silicide layer volume, interaction between boron and metal and silicon resulting in the formation of borides inclusions in the silicide layer. Boron starts to diffuse actively into the

local zones containing borides.

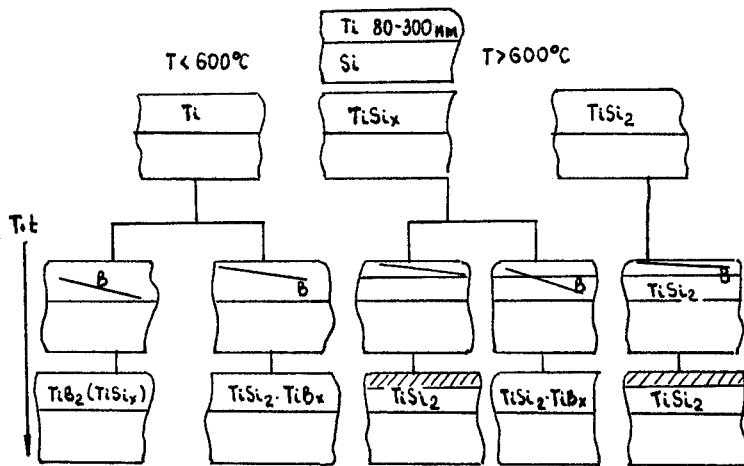


Fig. 2. Temperature-time diagram of processes in Ti-Si and Ti(B)-Si systems.

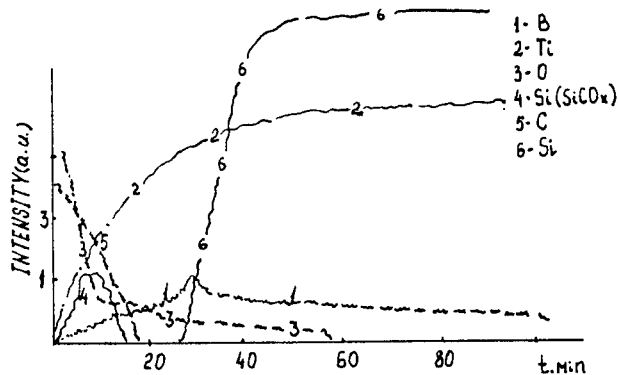


Fig. 3. AES spectrum of impurity distribution profile in Ti(B)-Si system for a dose of $1\text{E}16 \text{ B}^+/\text{cm}^2$.

With increase in temperature and duration of treatment the thickness of the formed boron-rich and boron-poor regions increases too. Furthermore, a partial silicide dissociation takes place in the bulk of the disilicide layer, resulting in the formation of continuous layers of titanium borides. A typical x-ray diffraction pattern of such layers is presented in Fig. 4a. It should also be noted that boron oxides such as B_2O_3 were found to form in thin surface layer of some samples which served as a protective cover against anneal atmosphere effect.

Quite a different picture is observed when boron is im-

planted into Ti-TiSi₂-Si system with energies at which all the implanted boron is found in the metal layer.

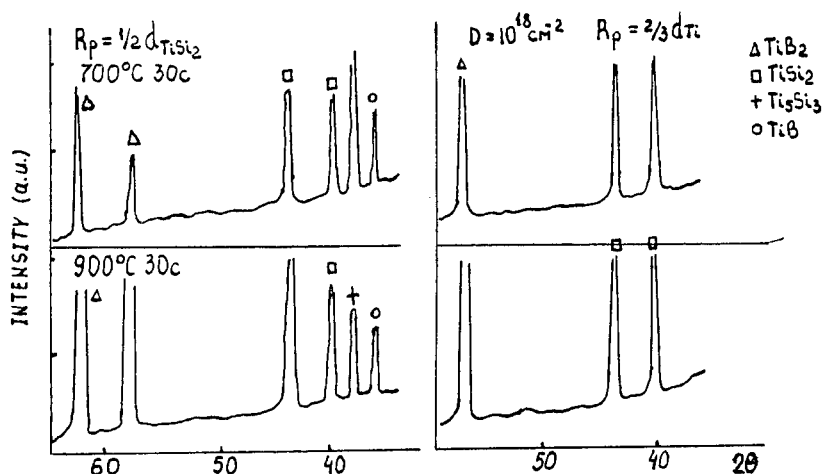


Fig. 4. X-ray diffraction patterns of the layers after heat treatment of boron-implanted (a) TiSi₂-Si and (b) Ti-TiSi₂-Si structures.

Rapid thermal processing of these layers leads to the formation of TiB₂ even at 700°C. Continuous boride layers are formed after implantation with doses of about 5E17 cm⁻² and more. At the same time further diffusion of silicon is observed, resulting in disilicide formation. Fig. 5 shows elemental distribution profiles in such structures and typical x-ray diffraction patterns of the formed layers are presented in Fig. 4b.

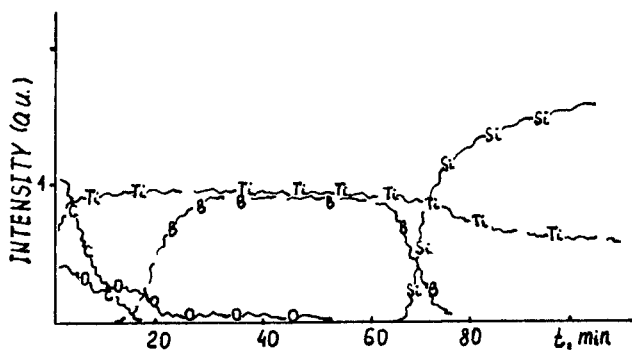


Fig. 5. AES profiles of boron in Ti-TiSi₂-Si system after heat treatment.

The elemental depth distribution profiles show that optimum conditions of implantation, preliminary heating and rapid

thermal processing yield layers with a sharp interface. Nonobservance of optimum formation conditions results in structures with a diffuse interface due to the formation of boride inclusions in the disilicide. It should be noted that if boron actively diffused into the growing silicide, silicon atoms were pushed away by the growing boride.

Boron implantation into the same structure with energy at which boron localization occurs in the silicide layer or at the silicide-titanium interface leads to the formation of titanium boride inclusions in the disilicide layer and the formation of metal-rich titanium silicides with boride inclusions. In this case boron hampers further diffusion mixing of titanium and silicon and further silicide layer formation.

In conclusion, the experimental results show that boron implantation into various structures causes complex phase transformations with one well-established process, that is boride and silicide formation reactions are competing in nature, with silicide formation being inhibited by boride layer formation.

REFERENCES

1. R. Rosenberg, M.J. Sullivan, J.K. Howard, in *Thin Films - Interdiffusion and Reactions* edited by J.M. Poate, K.N. Tu, and J.W. Mayer (Wiley, New York, 1978), p. 39.
2. J. Shappirio, J. Finnegan et al., *J. Vac. Sci. Technol.* A3 (6), 2255 (1985).
3. V.E. Borisenko, V.V. Gribkovsky, V.A. Labunov, and S.G. Yudin, *Phys. Stat. Sol. (a)* 86, 573 (1984).

SYNTHESIS OF TRANSITION METAL EPITAXIAL SILICIDES ON SILICON (100), (111)

V.V. Tokarev*, V.E. Borisenko**, and T.M. Pyatkova***

*Institute of Solid State and Semiconductor Physics, the
BSSR Academy of Sciences, P. Browka 17, 220726 Minsk, USSR

**Minsk Radioengineering Institute, P. Browka 6, 220600
Minsk, USSR

***the Ural Polytechnical Institute, 620002 Sverdlovsk, USSR

1. INTRODUCTION

Epitaxial silicide growth is of great interest to many researchers and process engineers working in the field of microelectronics. The interest towards epitaxial silicides is due, firstly to the fact that these structures are suitable for systematic investigation of physics of a metal-semiconductor interface, and secondly that epitaxial intermetallic structures on silicon allow development of new devices such as three-dimensional ones. At present, however, one can successfully form layers with epitaxial structure with thickness of no more than 150 nm using solid-state reaction in the metal layer-silicon substrate system. Such values satisfy researchers dealing with problems of epitaxial growth because main processes occur in the range of 10-20 Å. From a technological point of view, however, it is desirable to form layers with thickness up to 1 μ m.

2. EXPERIMENTAL

Polished phosphorus-doped, 20 Ohm cm, (100) and (111) silicon wafers were used as original substrates. Thin cobalt and nickel films were deposited using electron-beam evaporation in vacuum at residual pressure of 5×10^{-8} Torr. They had thickness between 60 and 100 nm. The prepared structures were implanted with 50-150 keV argon ions having penetration depth of 0.25, 0.65 and 1.0 of film thickness. Integrated current was 300 μ A and beam size was 1 cm². Implantation doses were in the range of 1×10^{15} - 5×10^{16} cm⁻². The temperature of the samples during implantation was kept at 700°C.

Implanted and unimplanted samples were subjected to rapid thermal annealing (RTA) in vacuum at residual pressure of 6×10^{-6} Torr. The exposure time was 10-40 s and radiation powers from halogen lamps provided induced temperature variation in the range of 450-1050°C and the temperature was determined with accuracy of 5°C.

3. RESULTS AND DISCUSSION

Nickel and silicon layer interactions stimulated by argon implantation and pulse heat treatment were analysed using four-point measurements of sheet resistance, x-ray diffraction, and Rutherford backscattering of 1 MeV H⁺ and He⁺ ions. The structure of silicide layers was determined using channeling and shade effects during interaction of energetic ions with solid atoms and Auger electron spectroscopy.

Electrophysical and phase properties of synthesized sili-

cides are treated below. Fig. 1 and 2 show anneal temperature dependence of sheet resistance and reflection intensities for Ni-Si and Co-Si systems.

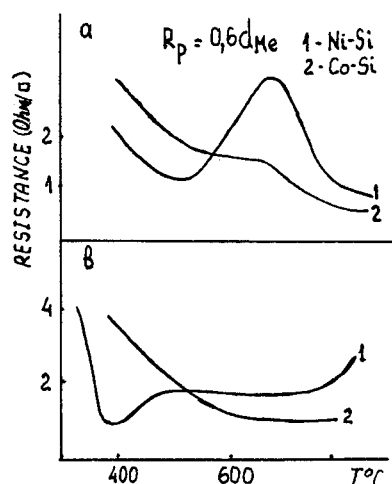


Fig. 1. Temperature dependence of nickel and cobalt disilicide layers (100 nm) resistance for (a) implanted and (b) unimplanted Me-Si systems.

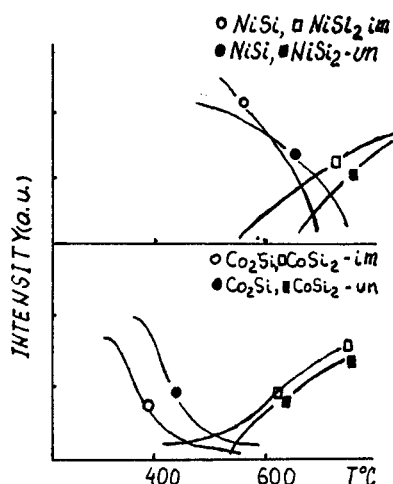


Fig. 2. Anneal temperature dependence of integrated intensity of reflections of phases for Ni-Si and Co-Si systems.

Strong similarity between resistance behaviour and phase formation is observed for nickel and cobalt silicides. In case of silicide synthesis, increase in resistance corresponds to changes in phase composition of the film. Ion implantation stimulates this change and phase transition region on the resistance curve shifts towards lower temperatures, with the temperature range in which metal-rich and silicon-rich silicides exist simultaneously being reduced.

Increase in irradiation energy and dose favours more rapid reaction in Ni-Si and Co-Si systems. However, the films implanted with argon ions with maximum range of 0.65-0.70 of the initial film thickness had better electrophysical characteristics. These films did not contain oxygen inclusions typical for films irradiated at higher energy.

X-ray and backscattering measurements showed that without implantation, nickel and cobalt disilicide phases were formed at 650 and 550°C respectively. Implantation considerably reduces this temperature by 200-250°C. It affects not only silicide formation rate but silicide structure perfection as well. Both implanted and unimplanted structures have no remarkable crystal perfection at disilicide formation temperature which is different for each case. Increase in temperature by 200-300°C results in polycrystalline-to-crystalline transformation in the films. This temperature ranges from 720 to 820°C for implanted samples of nickel disilicide and from 800 to 850°C for implanted samples of cobalt disilicide. For unimplanted

samples, this temperature is in the range of 950-1000°C, with nickel and cobalt disilicides formed at 620 and 550°C respectively. Fig. 3 shows scattered ions yield χ_{\min} as a function of implantation energy and anneal temperature for implanted and unimplanted samples of cobalt and nickel disilicides.

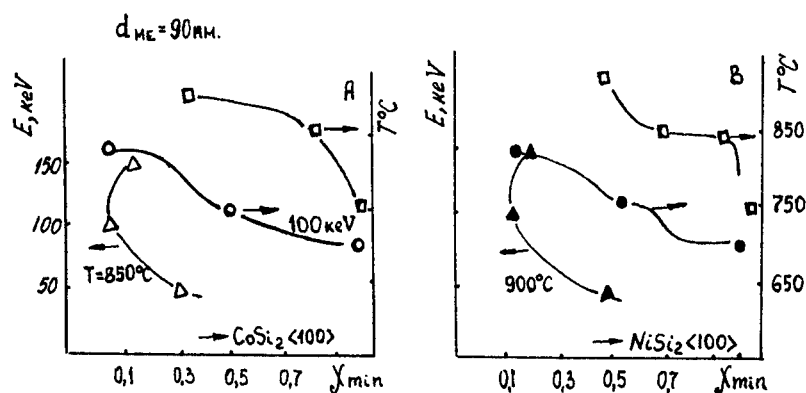


Fig. 3. Dependence of χ_{\min} on implantation energy and anneal temperature of cobalt (A) and nickel (B) disilicides for implanted (○, ●) and unimplanted (□, ■) samples.

On the basis of analysis of AES and backscattering spectra, nickel and cobalt atomic concentrations were determined across the film thickness (Fig. 4).

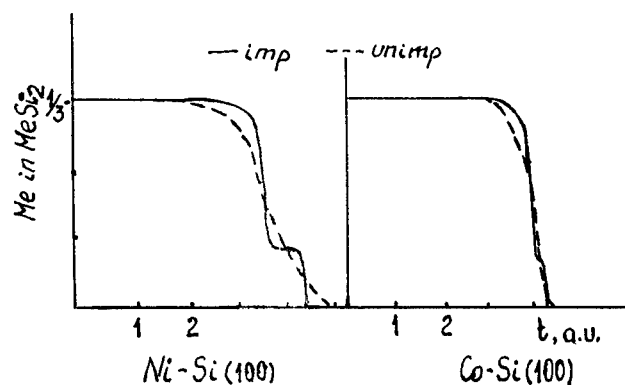


Fig. 4. Nickel and cobalt atomic concentration distributions across the disilicide film thickness.

33.3% nickel atomic content is observed practically through the whole film thickness but near the disilicide-silicon interface there appears a transition region with excess of silicide. This transition region is well controlled for nickel disilicide. Its value was reduced for transition from silicon (100) to silicon (111) and from nickel to cobalt. It should be noted that for Co-Si(111) system, the transition region was not observed and for Co-Si(100) system, one would expect existence of this region though very thorough analysis was required to prove that. More reliable results, however, can be obtained using cross-sectional transmission electron microscopy.

One should mention that this region boundaries were quite different for implanted and unimplanted samples. In case of irradiated Me-Si systems the form of these boundaries depended on ion energy and dose.

While for unimplanted structures cobalt and nickel concentration profiles were slightly sloping (with nickel penetrating deeper), for implanted samples the transition region had sharp boundaries with practically constant concentration and smaller thickness.

This transition region favours growth of epitaxial transition metal silicide films. Channeled proton scattering studies also showed difference in silicide structures between implanted and unimplanted samples. Fig. 5 shows scattered proton patterns of cobalt and nickel disilicides.

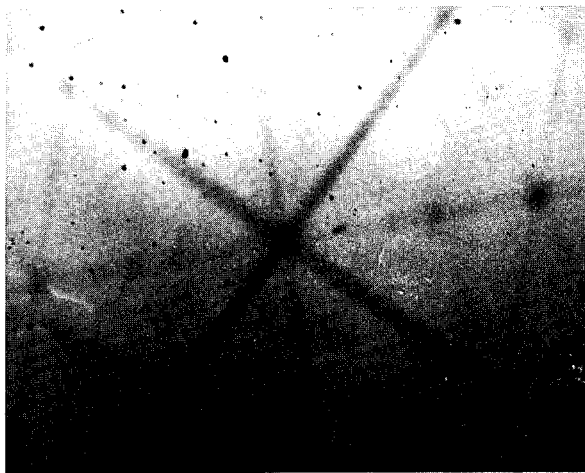


Fig. 5a. Scattered proton pattern of nickel disilicide.

These silicides have similar structure, i.e. fcc lattice as CaF_2 . Silicon has similar lattice. Epitaxial effect of the substrate can be estimated not only with energy spectra of angular dependences of backscattered proton yield (Fig. 6) but also considering the fact that fcc (100) silicide grows on silicon (100) and the silicide of the same orientation grows on Si(111).

Based on the experimental results a model for epitaxial

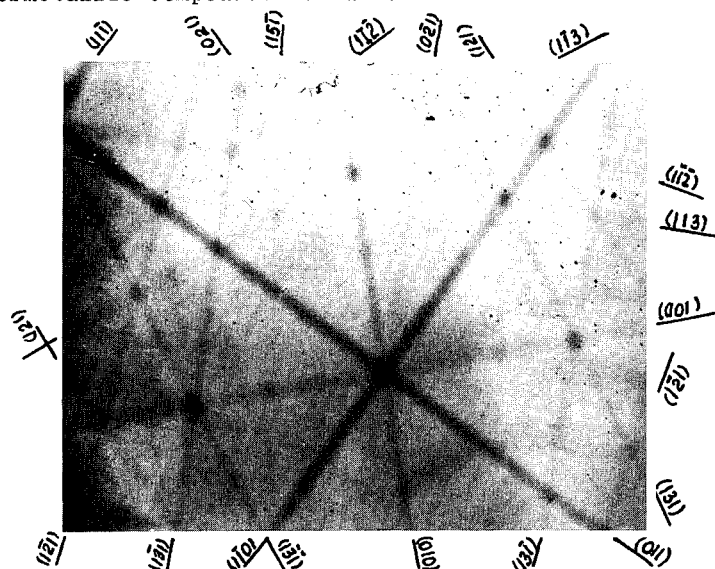


Fig. 5b. Scattered proton pattern of cobalt disilicide.

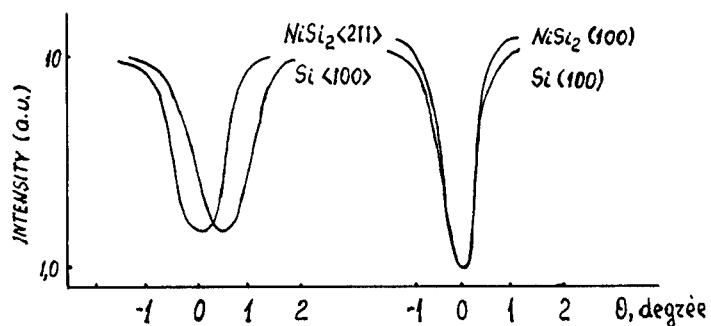


Fig. 6. Angular dependence of backscattered proton yield.

The structures of silicon and nickel and cobalt disilicides have lattice mismatch of less than 5%. If the lattice constant of the silicide is denoted as b and the lattice constant of silicon is denoted as a , then mismatch coefficient may be expressed as

$$g = \frac{a - b}{b} \quad (1)$$

Introducing such a coefficient we can determine epitaxial silicide thickness t along with the transition region d_{trans} using Nabarro-Peierls model. Calculation of free energy of the growing film and introduction of spinodal potential into the equation in linear harmonic approximation give (P)

$$t = C \frac{P}{g^2 (d_{ab} + d_{trans})} \quad (2)$$

which is the thickness of epitaxial silicide with the bulk silicide structure, provided stresses in the structure are absent. The transition region contributes to the increase of χ_{min} in case of MeSi₂-Si system when analysing ideal impurity-free system.

Thus the value of g will determine the thickness of epitaxial layer and the formation of the transition layer. For example, structure analysis using backscattering with channeling and shade effects exhibits the presence of the transition region d_{trans} for NiSi₂-Si(100) system and absence of this region for CoSi₂-Si(111) system.

The correctness of these speculations is confirmed by the fact that quantity d has orientation dependence. Silicides NiSi₂ and CoSi₂ formed on Si(100) have a more defective structure than those on Si(111), that is the transition region incorporates oriented defects which have effect on silicide layer formation.

From the experimental point of view, argon implantation leads to the formation and stabilization of the transition layer along with the simultaneous formation of thin disilicide layer at the interface between transition region and the rest of the metal layer. With the increase of anneal temperature argon implanted into the film together with the formed thin epitaxial layer NiSi₂ control silicon and nickel arrival at the silicide formation region. This allows to prevent disilicide dissociation when there is an excess of metal and epitaxial silicide growth will proceed via seed mechanism when thin NiSi₂ layer serves as the seed for disilicide formation in the whole structure. If there is no stimulated formation of the transition layer in the system, stresses typical for thick metal films hamper substrate epitaxial effect. In this case, disilicide growth is to a greater extent, influenced by film-substrate thickness ratio and by impurity inclusions which lead to the worsening of the silicide crystallinity.

In conclusion, the proposed model for epitaxial disilicide film growth via the reaction of thick metal layers preirradiated with argon ions showed that this growth is controlled by the nucleation mechanism with disilicide phase. The possibility of formation of such nucleation centers which are stable through the whole growth process, results in the formation of silicides with high crystal perfection.

REFERENCES

1. R.T. Tung, A.F.J. Levi, and J.M. Gibson, J. Vac. Sci. Technol. B 4(6), 1435 (1986).

ATOMIC PROFILES AND ELECTRICAL CHARACTERISTICS OF VERY HIGH ENERGY (8-20 MeV) Si IMPLANTS IN GaAs

PHILLIP E. THOMPSON,* HARRY B. DIETRICH,* JAMES M. ERIDON,* AND THOMAS
GRESKO**

*Naval Research Laboratory, Washington DC 20375-5000

**Department of Physics, George Mason University, Fairfax, VA 22030

ABSTRACT

High energy Si implantation into GaAs is of interest for the fabrication of fully implanted, monolithic microwave integrated circuits. Atomic concentration profiles of 8, 12, 16, and 20 MeV Si have been measured using SIMS. The range and shape parameters have been determined for each energy. The theoretical atomic concentration profile for 12 MeV Si calculated using TRIM-88 corresponded to the SIMS experimental profile. No redistribution of the Si was observed for either furnace anneal, 825°C, 15 min, or rapid thermal anneal, 1000°C, 10 s. The activation of the Si improved when co-implanted with S. The co-implanted carrier concentration profiles did not show dopant diffusion. Peak carrier concentration of $2 \times 10^{18}/\text{cm}^3$ was obtained with a Si and S dose of $1.5 \times 10^{14}/\text{cm}^2$, each.

INTRODUCTION

High energy n-type implants into GaAs are of interest for the monolithic integration of microwave devices. Many devices, such as mixer diodes, varactor diodes, and PIN switches require deep (several microns) conductive layers. While these layers can be fabricated using an epitaxial process (MBE, MOCVD, VPE), the resulting structures are not suitable for monolithic integration with devices requiring shallow conductive layers, e. g. FETs. Through the use of selective implantation the deep and shallow conductive layers can be fabricated while maintaining a planar geometry.

We have previously reported electrical and atomic profile parameters for 1 to 6 MeV Si implants in GaAs[1-4]. We have also reported several applications for this technology[5-6]. In this paper the energy interval has been extended using the 3MV tandem accelerator at NRL. GaAs has been implanted with Si having a maximum energy of 20 MeV. Secondary ion mass spectroscopy (SIMS) has been used to determine range and higher distribution moments of the implanted Si in both unannealed samples and samples activated using either furnace anneal (FA) or rapid thermal anneal (RTA). Co-implantation with high energy S has also been investigated. The activation and distribution of the Si and Si and S implants have been measured with electrochemical capacitance-voltage (ECV) profiling and Hall measurements.

EXPERIMENTAL TECHNIQUES

Samples were implanted at a variety of energies using the National Electrostatics 3 MV tandem particle accelerator at the Naval Research Laboratory. A schematic of the accelerator and implantation leg is shown in Fig. 1. Cathodes of either bulk silicon or sulfur were sputtered with cesium ions to form Si⁺ or S⁺. After acceleration up to the terminal potential, the ions were stripped of electrons by nitrogen gas. The appropriate charge state was selected for the final beam energy. For example, for 20 MeV Si, the terminal potential was set at 2.86 MV and the component of the Si beam having charge state 6+ was selected. The beam currents ranged from 5×10^{-7} to 3×10^{-6} ampere. The ion beams were rastered over the target apertures which varied from 6.5 to

58 cm². The selection of the aperture was based on: 1. The aperture should be large enough to allow sufficient time for implant uniformity and 2. The aperture should be small enough to allow a reasonably short implant time. Because the sample platform is thermally insulated, the sample will typically heat up during the implantation. At the dose rates and energies used in this work, the platform temperature was always below 100°C.

All implantation was done on semi-insulating GaAs grown by M/A COMM. For the SIMS study sections of the implanted wafers were annealed either in a furnace at 825°C for 15 min or in a rapid thermal annealer (AG 410 system) at 1000°C for 10 s. In both cases a Si₃N₄ cap, 1000 Å thick, was deposited on the sample prior to anneal using plasma-assisted chemical vapor deposition. The atmosphere during anneal was forming gas (90% N₂ and 10% H₂). The Si depth distributions were measured using Cs primary beam SIMS and negative ion mass spectroscopy at Charles Evans and Associates, Redwood, CA. Carrier concentration profiles were obtained using ECV (Polaron Semiconductor Profile Plotter) which employs repetitive etch and low voltage CV measurements. Electron mobility, sheet carrier concentration, and sheet resistance were determined using Hall measurements.

RESULTS AND DISCUSSION

Atomic Profile Distributions

SIMS atomic depth distributions for 8, 12, 16, and 20 MeV Si in GaAs are shown in Fig. 2. Almost three orders of magnitude of dynamic range have been obtained using an implant dose of $5 \times 10^{14}/\text{cm}^2$. Note that only the 8 MeV profile demonstrates evidence of a slight channeling tail, beginning at $4 \times 10^{16}/\text{cm}^3$. There were no observable differences in the atomic distribution profiles of the unannealed substrates and the substrates annealed by either FA or RTA. Therefore, within the limits of uncertainty of the SIMS measurements, annealing under the conditions used here causes no measurable dopant redistribution.

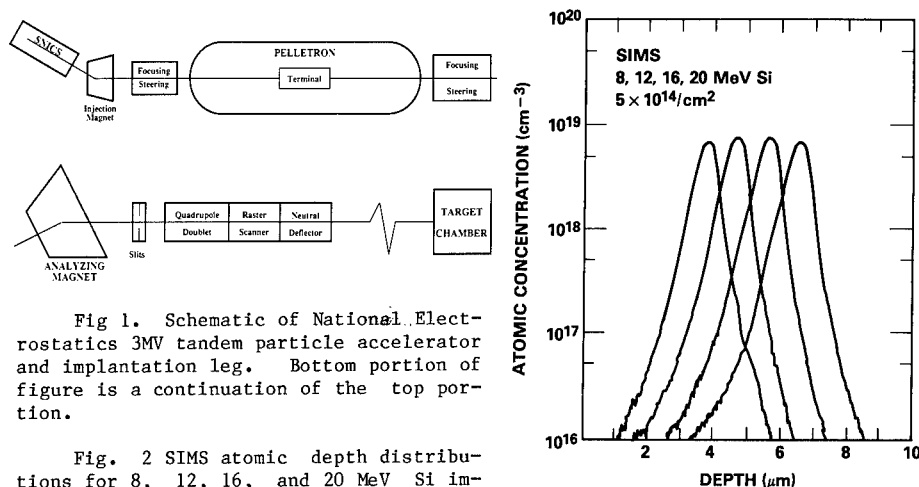


Fig 1. Schematic of National Electrostatics 3MV tandem particle accelerator and implantation leg. Bottom portion of figure is a continuation of the top portion.

Fig. 2 SIMS atomic depth distributions for 8, 12, 16, and 20 MeV Si implanted into GaAs.

The first four statistical moments of these depth distributions have been calculated, Table I. The first two

moments, called the projected range, R_p , and the range straggle, ΔR_p , are used for profile reconstruction, assuming a Gaussian distribution. The third and fourth central moments are reported relative to the range straggle and are unitless. They are called the skewness, γ_1 , and the kurtosis, β_2 . A method of profile reconstruction which uses the first three moments is the joined half-Gaussian distribution[7]. All four moments are used in the Pearson IV distribution reconstruction[8-10]. Combining the results from our earlier work, Fig. 3 presents the range and range straggle for Si in GaAs from 1 to 20 MeV. It is seen that the range straggle does not significantly increase with depth at energies greater than 8 MeV.

Table I. Range and Shape parameters for Si in GaAs obtained from SIMS

Energy	Projected Range	Range Straggle	Skewness γ_1	Kurtosis β_2
MeV	microns	microns		
8	3.67	0.45	-0.86	8.23
12	4.62	0.47	-1.29	10.08
16	5.60	0.44	-1.43	11.52
20	6.48	0.45	-1.42	11.04

A theoretical atomic distribution profile for 12 MeV Si in GaAs was calculated using the computer code TRIM-88. The calculated profile and the equivalent SIMS profile are compared in Fig. 4. R_p and ΔR_p for the SIMS profile and the TRIM profile were 4.62 μm and 0.47 μm and 4.66 μm and 0.42 μm , respectively. Previously it was reported[1,2] that the range calculated using TRIM-86 was less than the experimental SIMS range and that the interior half of the calculated profiles decreased substantially faster than the SIMS profiles. In this case there is no perceptible channeling, which may explain the excellent agreement between the experimental and calculated profiles. Another possible explanation is that the TRIM and SIMS profiles have better agreement at higher energies due to internal parameters in the TRIM computer code.

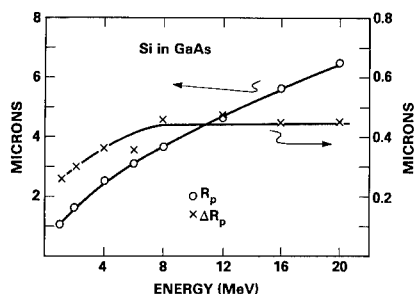


Fig. 3 Range and range straggle for Si implanted into GaAs.

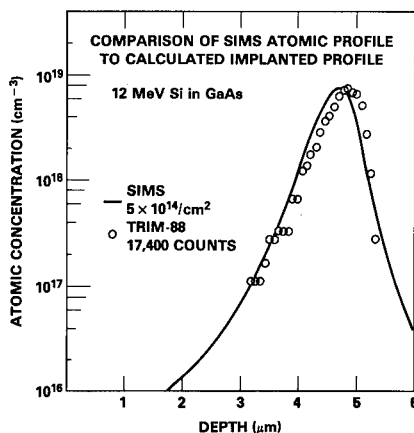


Fig. 4 Comparison of experimental SIMS profile and calculated TRIM-88 profile for 12 MeV Si implanted into GaAs.

Activation of Si Implants and Si and S Co-Implants

The activation of the samples used for the SIMS profiles was measured using the Hall effect. These samples all had an implant dose of $5 \times 10^{14}/\text{cm}^2$. The percentage of activation was the same for samples annealed using the 825°C, 15 min FA or the 1000°C, 10 s RTA, and was 25%. The bulk Hall mobilities differed between the two activation processes. Samples activated with FA had a mobility of $1500 \text{ cm}^2/\text{Vs}$, while those activated with RTA had a mobility of $2000 \text{ cm}^2/\text{Vs}$.

Since Si is an amphoteric dopant in GaAs at high doses, the activation of a lower dose, which is more suitable for an n^+ implant, was studied. GaAs was implanted with 8, 10, 12, 14, or 16 MeV Si, at a dose of $1.5 \times 10^{14}/\text{cm}^2$. Another set of samples was first implanted with S having an energy 10% higher than the associated Si energy, so that the range of the S and the Si would be approximately the same. In these samples the dose of the S and the Si was each $1.5 \times 10^{14}/\text{cm}^2$. All samples were activated with RTA, 1000°C, 10s. The results of the bulk Hall measurements are presented in Table II. It is seen that the percentage of activation increased when S was co-implanted with the Si, even though the total implant concentration had increased to $3 \times 10^{14}/\text{cm}^2$. The increase in the activation is reflected in the decrease in the sheet resistance for the co-implanted samples. The reduction in the mobility for the co-implanted samples is caused by increased ionized impurity scattering. Carrier concentration profiles of two pairs of samples are shown in Figs. 5 and 6. It is seen that, although S has been shown to diffuse upon activation using FA [12,13], the redistribution has been controlled by employing RTA. It is also seen that the increased activation is not just the arithmetic addition of the S, but an improved activation of the Si. While Si is amphoteric at high doses, that is it can occupy a Ga site and be a donor or occupy an As site and be an acceptor, S can only occupy an As site and be a donor [14]. Since the S occupies the As sites, the Si is forced to occupy the Ga sites and the n-type activation is improved. Using the co-implantation, peak carrier concentrations of $2 \times 10^{18}/\text{cm}^3$ have been achieved. The sheet resistances, which are of concern for device performance, can easily be lowered by using multiple energy implants, producing a thicker active layer.

Table II. Activation of Si and Si-S co-implants. Dose for each ion is $1.5 \times 10^{14}/\text{cm}^2$

Energy (MeV)		Sheet Resistance (ohms/)	Mobility (cm^2/Vs)	Carrier Concentration (cm^{-2})	Activation %
Si	S				
8	-	28.3	2860	7.72×10^{13}	51.5
10	-	27.4	2850	8.02×10^{13}	53.5
12	-	36.5	2860	5.99×10^{13}	39.9
14	-	27.7	2730	8.24×10^{13}	54.9
16	-	24.5	3000	8.53×10^{13}	56.9
8	8.8	11.1	2430	2.31×10^{14}	77.0
10	11.0	11.7	2360	2.26×10^{14}	75.3
12	13.2	12.2	2410	2.12×10^{14}	70.7
14	15.4	12.0	2330	2.23×10^{14}	74.3
16	17.6	11.2	2180	2.56×10^{14}	85.3

CONCLUSIONS

Range and shape parameters have been obtained for 8, 12, 16, and 20 MeV Si in GaAs from SIMS data. Excellent agreement was found between the calculated TRIM profile and the SIMS profile for 12 MeV Si. Co-implantation of S

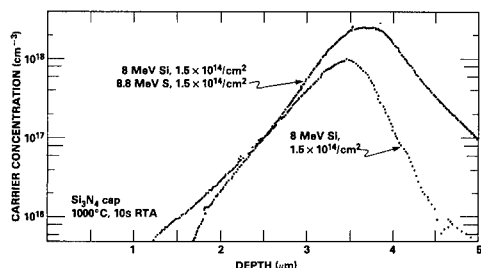


Fig. 5 Carrier profiles of a. 8 MeV Si, $1.5 \times 10^{14}/\text{cm}^2$, implanted into GaAs and b. 8 MeV Si, $1.5 \times 10^{14}/\text{cm}^2$, and 8.8 MeV S, $1.5 \times 10^{14}/\text{cm}^2$, co-implanted into GaAs.

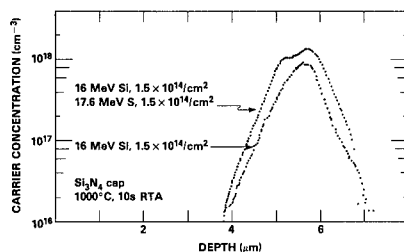


Fig. 6 Carrier profiles of a. 16 MeV Si, $1.5 \times 10^{14}/\text{cm}^2$, implanted into GaAs and b. 16 MeV Si, $1.5 \times 10^{14}/\text{cm}^2$, and 17.6 MeV S, $1.5 \times 10^{14}/\text{cm}^2$, co-implanted into GaAs.

with Si increased the net activation percentage and significantly reduced the sheet resistance. Co-implantation of S and Si, each having a dose of $1.5 \times 10^{14}/\text{cm}^2$, activated using RTA, produced peak carrier concentrations of $2 \times 10^{18}/\text{cm}^3$.

References

1. P. E. Thompson, R. G. Wilson, D. C. Ingram, and P. P. Pronko in Materials Modification and Growth Using Ion Beams, edited by U. Gibson, P. P. Pronko, and A. E. White (Mater. Res. Soc. Proc. **93** Pittsburgh, PA 1987) pp. 73-77.
2. P. E. Thompson, R. G. Wilson, D. C. Ingram, and P. P. Pronko, accepted for publication in the J. Appl. Phys.
3. P. E. Thompson, H. B. Dietrich, and D. C. Ingram, Nucl. Instr. and Meth. **B6**, 287 (1985).
4. P. E. Thompson, H. B. Dietrich, M. Spencer, and D. C. Ingram, SPIE **530**, 35 (1985).
5. C. M. Krowne and P. E. Thompson, Solid State-Electron. **30**, 497 (1987).
6. P. E. Thompson, H. B. Dietrich, Y. Anand, V. Higgins, and J. Hillson, Electronics Letters **23**, 725 (1987).
7. J. F. Gibbons and S. Mylroie, Appl. Phys. Lett. **22**, 568 (1973).
8. W. K. Hofker, Phillips Research Reports Supplements, **8**, 41 (1975).
9. W. K. Hofker, D. P. Oosthoek, N. J. Koeman, and H. A. M. De Grefte, Rad. Effects **24**, 223 (1975).
10. R. G. Wilson, Rad. Effects **46**, 141 (1980).
11. J. F. Ziegler, J. P. Biersack, and U. Littmark, The Stopping Power and Range of Ions in Solids (Pergamon Press Inc., New York, 1985).
12. S. J. Pearton and K. D. Cummings, J. Appl. Phys. **58**(14), 1500 (1985).
13. R. G. Wilson and D. M. Jamba, Appl. Phys. Lett. **39**, 715 (1981).
14. R. S. Bhattacharya, P. P. Pronko, and S. C. Ling, Appl. Phys. Lett. **42**(10), 880 (1983).

INTERBAND OPTICAL PROPERTIES OF THE MICROCRYSTALLINE COMPONENT
WITHIN THE DAMAGE LAYER OF Be⁺-IMPLANTED GaAs

G.F. FENG AND R. ZALLEN

Department of Physics, Virginia Tech, Blacksburg, VA 24061 USA

ABSTRACT

The damage layer in unannealed Be⁺-implanted GaAs samples (45-keV Be⁺ ions, 10^{13} to 5×10^{14} ions/cm²) consists of a fine-grain mixture of amorphous GaAs and GaAs microcrystals, with the characteristic microcrystal size L of the microcrystalline component decreasing with increasing fluence. We have carried out reflectivity measurements on these samples for photon energies from 2.0 to 5.6 eV, in the electronic interband regime. Using Lorentz oscillator analysis and the effective medium approximation, we have extracted the dielectric function of the microcrystalline component (μ -GaAs) within the damage layer. The optical properties of μ -GaAs deviate appreciably from those of the bulk crystal near the interband absorption peaks. The linewidths of these peaks are found to increase over the bulk-crystal value by an amount proportional to $(1/L)$, the increase being about 0.2 eV when $L = 100$ Å. These finite-size effects can be understood in terms of a lifetime reduction caused by the short time it takes for electrons to reach the microcrystal boundaries.

INTRODUCTION

In a recent study of near-surface damage in unannealed Be⁺-implanted GaAs, Holtz et al. [1] used a combination of Raman scattering and chemical etch to obtain microstructural information for samples subjected to various fluences. Information derived included the microcrystalline volume fraction f_{μ} , the characteristic microcrystal size L , and their depth dependence. Here we report the results of visible and ultraviolet reflectivity experiments on the same Raman-characterized samples. One purpose of this work is to determine the effect of microcrystal size in the 100-Å range on the optical properties and interband excitations in microcrystalline GaAs (μ -GaAs). While microcrystalline Si has recently been extensively investigated [2], little is known about μ -GaAs.

EXPERIMENT

The samples were (100)-oriented wafers which had been implanted with 45-keV Be^+ ions incident at 9° from the normal. No post-implant anneal was done. Further details of sample preparation are given in Ref. 1. Reflectivity measurements were performed with a prism-grating spectrometer, using chopped radiation and lock-in detection. Details of the reflectivity calibration, as well as of the analysis techniques mentioned in the following sections, will be given in a more complete article in preparation on this work [3].

Figure 1 shows our results for the reflectivity spectra $R(E)$ of four beryllium-implanted GaAs samples. Panels (a), (b), (c), and (d) show the spectra observed after implantation with fluences of 1×10^{13} , 5×10^{13} , 1×10^{14} , and 5×10^{14} ions/cm², respectively. Along with the data on the ion-implanted samples, indicated by the points, each panel also contains two curves which correspond to the spectra of crystalline GaAs [4], labelled c, and of amorphous GaAs, labelled a. These two curves are repeated in each panel in order to provide visual benchmarks for the

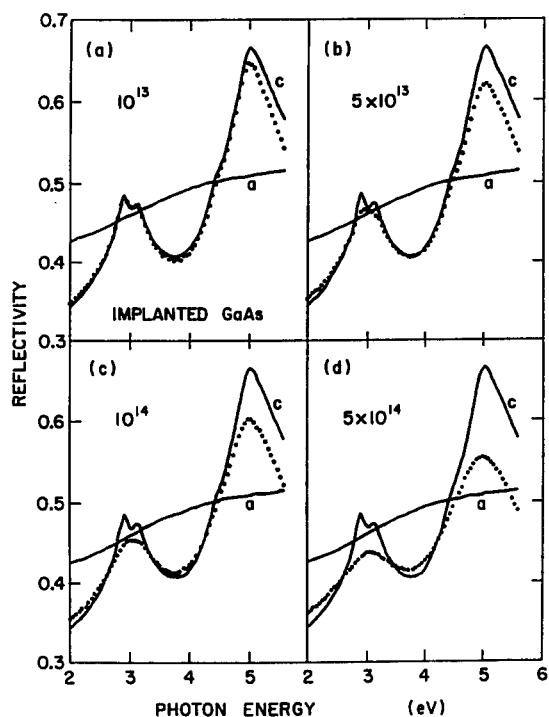


Fig. 1 Reflectivity of the implanted samples.

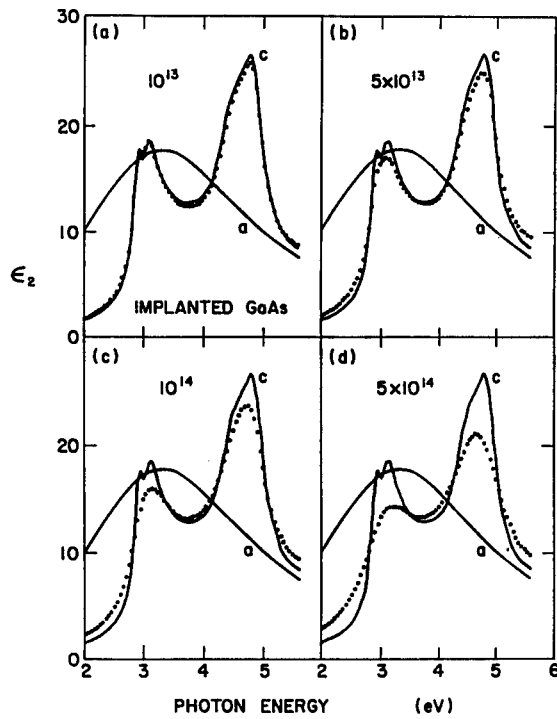


Fig. 2 Dielectric function of the implanted samples.

evolution of the GaAs spectrum with increasing implantation dose. Systematic change is evident in Fig.1; the higher the ion fluence, the greater the deviation from the spectrum of bulk, crystalline GaAs (c-GaAs).

DIELECTRIC FUNCTION OF THE IMPLANTED MATERIAL

To obtain the complex dielectric function $\epsilon = \epsilon_1 + i\epsilon_2$ and other optical properties from each measured reflectivity spectrum, a Lorentz oscillator expression [5] was fitted to the observed reflectivity. Here $\epsilon(\omega)$ is composed of terms of the form $s_i[\omega_i^2 - \omega^2 - i\Gamma_i\omega]^{-1}$, where s_i , ω_i , and Γ_i are the strength, position, and linewidth parameters of the i^{th} oscillator. Seven oscillators were used to obtain an excellent fit, as in the ellipsometry studies of Erman et al. [5]. The fitting technique was checked by applying it to c-GaAs, for which the reflectivity and the dielectric function are accurately known [4].

We limit our discussion here to $\epsilon_2(E)$, the imaginary (absorptive) part of the dielectric function. E is the photon energy $\hbar\omega$. Figure 2 shows $\epsilon_2(E)$ for the four implanted samples.

DIELECTRIC FUNCTION OF μ -GaAs, THE MICROCRYSTALLINE COMPONENT

Chemical-etch depth-profile Raman studies of these samples support a structural model of the implantation-induced damage layer as a fine-scale mixture of amorphous GaAs and GaAs microcrystals [1]. There is a high-damage plateau extending from the surface to a depth of about 1500 Å, followed by a graded transition region. For the above-bandgap reflectivity work reported here, the optical penetration depth is smaller than the plateau depth, so that a macroscopically uniform region is being probed. This region is characterized by a microcrystalline fraction f_μ ($f_\mu + f_a = 1$, where f_a is the amorphous fraction) and a characteristic microcrystal dimension L . For the $5 \times 10^{14} \text{ cm}^{-2}$ implant, f_μ is 0.75 and L is about 55 Å.

We used the effective medium approximation (EMA) to analyze the optical properties of our two-phase system [6]. Details will be presented elsewhere [3]; here we can give only the main strategy. Although the usual use of the EMA is to calculate the dielectric function of a two-component mixture in terms of the dielectric functions of the constituent phases, that cannot be done here because the dielectric function of μ -GaAs is not known; it is different from the dielectric function of c-GaAs, and it changes with L.

In our analysis, the dielectric function of the two-component medium is known, determined by experiment (e.g., the experimental results of Fig. 2 for the four different damage layers). The composition of each sample (f_μ, f_c) is also known, from the Raman work. The dielectric function of the amorphous component is assumed to be the same as that of pure a-GaAs. Since $\epsilon(E)$ of a-GaAs is bland and featureless in this spectral region so that the observed peaks of Fig. 2 arise from μ -GaAs, this assumption is reasonable. We then use the EMA to extract from these data the dielectric function of μ -GaAs, the microcrystalline component of each damage layer.

The results for $\epsilon_2(E)$ of μ -GaAs are shown in Fig. 3. These results represent the spectra of pure microcrystalline material in the absence of an amorphous component. Included in each panel is the ϵ_2 of c-GaAs, for comparison. With increasing fluence, the characteristic microcrystallite size L decreases and the spectrum deviates more significantly from that of the bulk crystal.

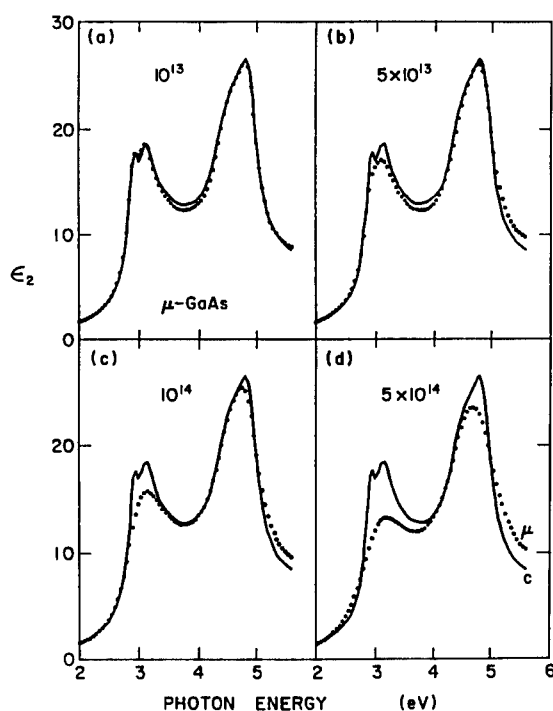


Fig. 3 Dielectric function of microcrystalline GaAs.

FINITE-SIZE EFFECTS IN GaAs MICROCRYSTALS

The essential point to be made about the family of curves in Fig. 3 can be expressed in terms of the effect of microcrystal size on the spectral linewidth of the three prominent interband peaks at 2.9, 3.1 and 4.9 eV (for which the corresponding direct transitions are conventionally labelled E_1 , $E_1 + \Delta_1$, and E_2 , respectively). Figure 4 presents a plot of Γ versus $(1/L)$ for each of the three peaks. Γ is the observed linewidth parameter for the peak, while L is the Raman-derived microcrystal size for the μ -GaAs sample. In analyzing the spectra of Fig. 3, we find that the spectral changes are concentrated in the Γ values.

While a fuller discussion will be given in Ref. 3 for the linear increase in linewidth with inverse microcrystal size, a simple interpretation can be briefly stated. Small microcrystal size implies a short time for an excited carrier to reach, and be scattered by, the microcrystal boundary. This size-induced limitation on the excited-state lifetime broadens the excited-state energy.

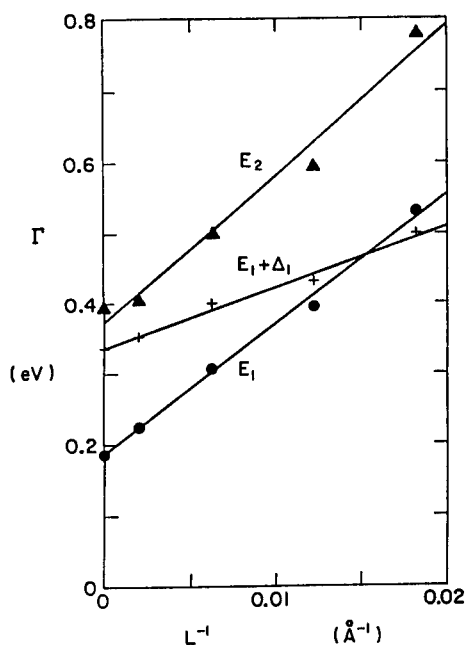


Fig. 4 Correlation of linewidth with microcrystal size.

ACKNOWLEDGEMENTS

The authors are grateful for the support of Texas Instruments and the Virginia Center for Innovative Technology.

REFERENCES

1. M. Holtz, R. Zallen, O. Brafman, and S. Matteson, Phys. Rev. B 37, 4609 (1988).
2. H. Richter and L. Ley, J. Appl. Phys. 52, 7281 (1981); Z. Iqbal and S. Veprek, J. Phys. C 15, 377 (1982); H.N. Liu, D. Pfof, and J. Tauc, Solid State Commun. 50, 987 (1984); S. Kumar, B. Drevillon, and C. Godet, J. Appl. Phys. 60, 1542 (1986); S. Veprek, F.A. Sarott, and Z. Iqbal, Phys. Rev. B 36, 3344 (1987).
3. G.F. Feng and R. Zallen, to be published.
4. D.E. Aspnes and A.A. Studna, Phys. Rev. B 27, 985 (1983).
5. M. Erman, J.B. Theeten, P. Chambon, S.M. Kelso, and D.E. Aspnes, J. Appl. Phys. 56, 2664 (1984).
6. A.G. Bruggeman, Ann. Phys. (Leipzig) 24, 636 (1935); D.E. Aspnes, Thin Solid Films 89, 249 (1982).

CHARACTERISTICS OF SI-IMPLANTED (211) VERSUS (100) GaAs

J. EPP, J. G. DILLARD, A. SIOCHI, R. ZALLEN, E. D. COLE, S. SEN, A. VASEASHTA, AND L. C. BURTON
Virginia Polytechnic Institute & State University, Blacksburg, VA 24061, USA

ABSTRACT

Transport, Raman and XPS measurements were made on Si-implanted ($1.7 \times 10^{13} \text{cm}^{-2}$, 50keV) and rapid-thermal annealed (100) and (211) GaAs substrates in an effort to distinguish differences between the two orientations. With these techniques, no significant differences were found. The implant-damage depth was about 1200Å for both orientations, with slightly higher near-surface damage (and lower mobility) apparent for (211). No unusual features in the (211) carrier concentration profile, as was previously reported, were evident.

INTRODUCTION

For Si-implanted GaAs MESFETs, (100) is the traditional substrate orientation. It has recently been reported, however, that using the (211) orientation results in better devices [1]. Unusual non-Gaussian carrier concentration profiles, with a natural n^+ surface region, were obtained. Higher transconductances and lower noise figures resulted for devices made on (211) substrates.

In this paper we report measurements aimed at discerning differences between certain materials related properties for Si-implanted (100) and (211) GaAs substrates.

EXPERIMENTS

(100) and (211)-oriented GaAs substrates were implanted with $1.7 \times 10^{13} \text{cm}^{-2}$ of Si ions at 50 keV energy. Rapid thermal anneals were performed with silicon nitride caps which were subsequently removed. Annealing conditions were: none; 750°C, 850°C and 950°C for 30 sec. Specific annealing conditions will be noted below where appropriate.

For electrical measurements, ohmic contacts in the van der Pauw configuration were prepared by depositing 88:12 Au:Ge, plus a Ni cap, and annealing at 440°C in forming gas. A four-stripe conductor arrangement was used for the photoconductivity measurements. Electrical and optical profiles were made by measuring after sequential etches using a 1:1:100 $\text{H}_2\text{SO}_4:\text{H}_2\text{O}_2:\text{H}_2\text{O}$ etch, which removes GaAs at a rate of approximately 600Å min^{-1} [2,3]. Raman measurements were made in the backscatter configuration with a laser wavelength of 4579Å. XPS measurements were made on a Perkin Elmer Model 5300 instrument.

RESULTS AND DISCUSSION

Carrier concentration and mobility profiles for the implanted and annealed (100) and (211) orientations are very similar. Such profiles are shown in Figures 1 and 2, for the 850°C anneal. The only discernible difference is slightly lower mobility values for (211) near the surface. With respect to carrier concentration profiles, the very flat profile for (211) between 200Å and 1000Å, with a sharp increase in carrier concentration within 200Å of the surface, as reported by Banerjee et al. [1], was not found. Carrier concentration and mobility profiles for the three annealing temperatures were almost identical.

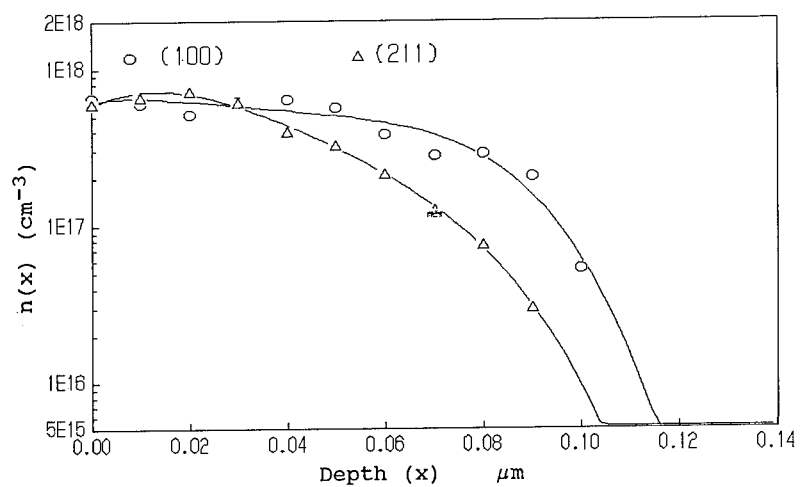


Figure 1. Carrier concentration profiles for Si-implanted (100) and (211) GaAs.

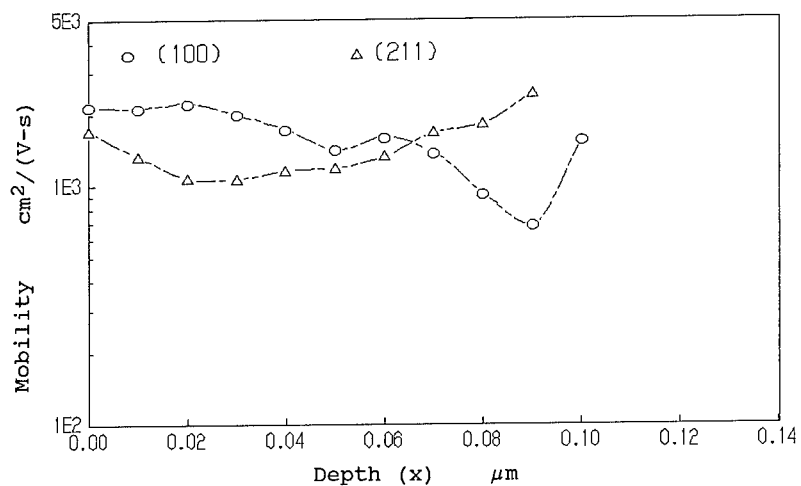


Figure 2. Mobility profiles for Si-implanted (100) and (211) GaAs.

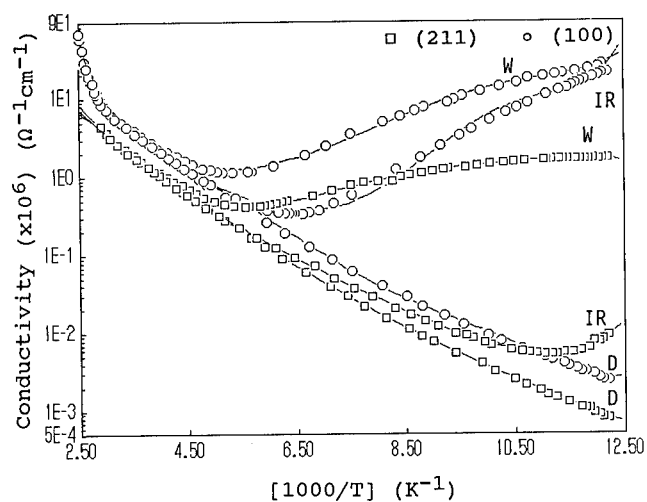


Figure 3. Photoconductivity versus inverse temperature for un-annealed (100) and (211) GaAs. (D = dark, W = white light, IR = $0.9\mu\text{m}$).

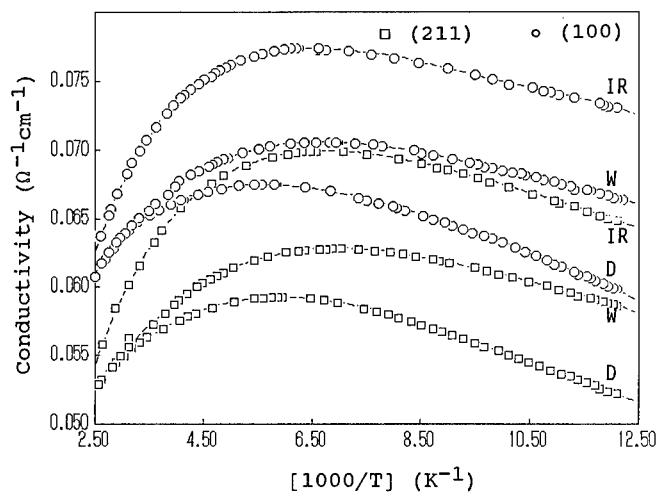


Figure 4. Photoconductivity versus inverse temperature for 850°C annealed (100) and (211) GaAs. (D = dark, W = white light, IR = $0.9\mu\text{m}$).

Photoconductivity measurements were performed on similar samples in an effort to distinguish differences in thermal or photo-activation for the (100) and (211). Results are shown in Figures 3 and 4 for un-annealed and 850°C annealed cases respectively. (The designations D, W and IR stand for dark, white light, and infra red centered at 0.9 μ m, the latter two at the same incident photon flux level of 10¹⁵cm⁻²).

For the un-annealed case (Fig. 3), the dark and white light illuminated results are somewhat similar, with the (211) orientation having a slightly higher resistance. There is a striking difference between the (100) and (211) curves, however, for IR illumination at 0.9 μ m. The minor change in the (211) curve from its dark value may be due to the fact that the photoconductance changes for this orientation are due predominantly to photoexcitation near the surface; the 0.9 μ m photons are absorbed deeper. It is not clear why the (100) and (211) cases are so different under 0.9 μ m illumination, since the Raman measurements (discussed below) indicate similar damage profiles. However, the trap distributions that provide the carriers for photoconductivity may be significantly different throughout the damaged, un-annealed layers for the two orientations.

The large difference in IR photoconductivity for the two orientations was almost totally removed by annealing (Fig. 4). The (100) orientation again shows higher conductivity than (211) for all illumination and temperature conditions investigated.

Raman spectra at different etch depths are shown in Figure 5, and Full Width Half Maximum (FWHM) versus depth in Figure 6, for the (100) and (211) orientations (un-annealed). A comparison of the depth profiles shows no substantial difference. The FWHM vs. depth curves do show slightly greater near-surface damage for (211), a constant damage plateau for (100) of about 400Å, and within experimental error, demonstrate that both (211) and (100) have a damage layer of 1200Å thickness. Intensity and peak shift versus depth data were also taken and show slight differences which can be accounted for by experimental error.

XPS spectra for the (100) and (211) substrates were not significantly different. The Ga to As ratio increased with annealing temperature, as did the amount of oxide on the surface. These phenomena were essentially the same for both orientations.

CONCLUSIONS

The major conclusion drawn from these studies is that, for the measuring techniques used, there are no apparent significant differences between Si-implanted and annealed (100) and (211) substrates that could impact device performance. Differences that we did see -- slightly greater near-surface damage for (211) from Raman spectra, accompanied by lower mobility -- lean toward the (100) orientation being the better of the two, which is opposite to what was reported. Of course, other differences not visible in our measurement methods could exist in surface or near-surface parameters, which could affect MESFET characteristics. More extensive measurements would be required to delineate such differences, if any, and determine their impact on device behavior.

ACKNOWLEDGEMENTS

We would like to thank Texas Instruments and Virginia's Center for Innovative Technology for supporting this work.

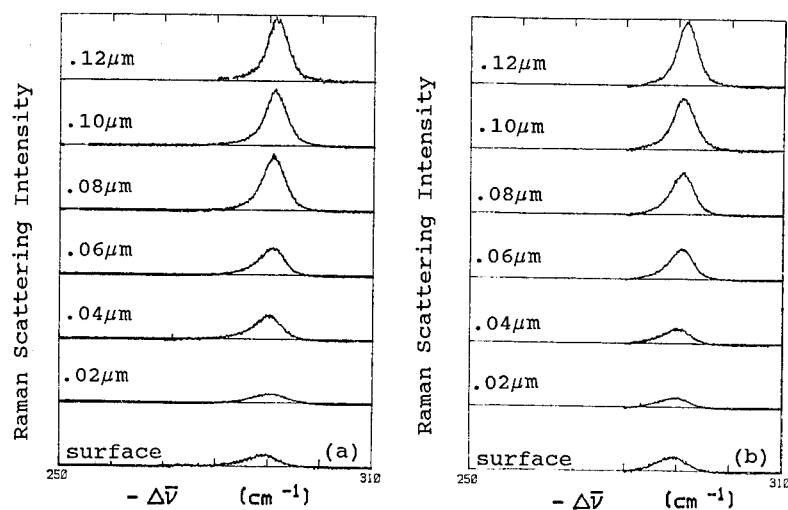


Figure 5. Raman spectra taken at different depths for un-annealed GaAs; a) (211), b) (100) (Etch depths indicated on spectra).

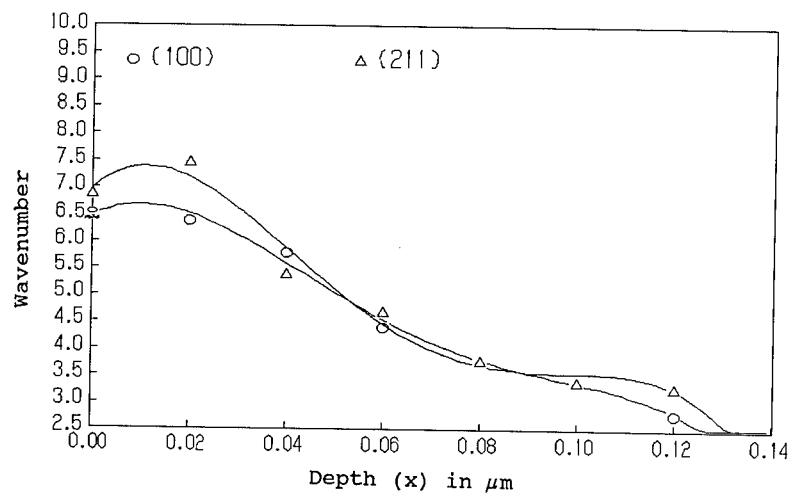


Figure 6. Raman spectra Full Width Half Maximum (FWHM) versus etch depth for un-annealed (100) and (211) GaAs.

REFERENCES

1. I. Banerjee, P. W. Chye, and P. E. Gregory, IEEE Elect. Dev. Lett. **9**, 10 (1988).
2. H. Ryssel et al., *Ion Implantation*, Wiley, p. 193 (1986).
3. Holtz, et al., Phys. Rev. B **37**, 4610 (1988).

ABOUT SOME PECULIARITIES IN DEFECT APPEARANCE IN ELEMENTAL AND
III-V COMPOUND SEMICONDUCTING MATERIALS

MARIA G. KALITZOVA*, N.K. PASHOV*, G. VITALI** AND M. ROSSI**

*Institute of Solid State Physics, Bulgarian Academy of Sciences, 72 Lenin Blvd,
Sofia 1784, Bulgaria

**Energetics Department, University of Rome "La Sapienza", via Scarpa 14, 00161
Roma, Italy

ABSTRACT

High Resolution Transmission Electron Microscopy (HRTEM) has been used to obtain direct information on the structure of damage clusters and in-depth radiation damage distribution in ion-implanted Ge and GaAs with Te^+ and Si^+ respectively, at doses far below the amorphization threshold. The observed changes in damage contrast in Te^+ implanted Ge emphasize the existence of well defined separation between vacancies and interstitials in the lattice damage clusters. For GaAs an integrated "grey zone" was found as a typical effect of Si^+ implantation.

INTRODUCTION

Transmission Electron Microscopy (TEM) has been extensively used in the past to obtain direct information about defect cluster structures produced by individual displacement cascades. Also in-depth radiation damage distributions as observed by TEM provide knowledge about damage processes in ion bombarded semiconductors.

It was recognized that HRTEM provides the most valuable insight into the atomic structure of the damage created by isolated collision cascades in solids during energetic particle irradiation. Following the early HRTEM examination of the structure of damaged regions in neutron irradiated Ge made by Parsons, Rainville and Hoelke /1/ there has been considerable recent activity in the use of HRTEM-contrast analysis to improve understanding of cascade damage processes in semiconductors /2-10/. In the present communication results from plan-view HRTEM and Cross-Sectional High Resolution TEM (XHRTEM) are presented. They are used for direct imaging of isolated radiation damage clusters and in-depth disorder in implanted Ge and GaAs far below their amorphization thresholds. The features of in-depth radiation damage in Ge are compared with those of GaAs as representative of elemental and III-V compound semiconductors with diamond type lattices. On the basis of HRTEM phase contrast analysis of individual damage clusters and the computed separation of interstitials from vacancies for implanted Ge, arguments for interpreting the changes in XHRTEM contrast of implanted GaAs as resulting from radiation enhanced diffusion are given.

EXPERIMENTAL

$\langle 111 \rangle$ and $\langle 110 \rangle$ Ge single crystals were implanted, at room temperature, with 46 keV Te^+ , at ion fluences of 1.3×10^{12} ions/cm² and 5×10^{13} ions/cm² respectively. In both implantations the ion beam was oriented about 6-7° to the specimen normal. $\langle 100 \rangle$ GaAs wafers were implanted with 140 keV Si^+ at room temperature to a dose of 1×10^{13} ions/cm² in a random direction. Plan-view specimens for HRTEM investigations of Ge were prepared by chemical polishing of $\langle 110 \rangle$ Ge plates. The $\langle 110 \rangle$ cross-sections from $\langle 111 \rangle$ implanted Ge and $\langle 100 \rangle$ implanted GaAs slices were obtained by a technique similar to that used in /11/. Final thinning was accomplished by Ar^+ mil-

ling of both specimen sides simultaneously at $E=7$ keV and with a current density of 6 mA/cm^2 (per gun) at glancing incidence of 20° to the surface of the specimen. It was verified /8/ that the effect of a thin amorphous layer obtained on the two surfaces of the cross-sectional specimens in the process of Ar^+ thinning was not essential to the HRTEM imaging of thinned parts of the crystals. The samples were analyzed in a JEM 100C Electron Microscope equipped with an ultrahigh resolution pole piece and 10° double tilt goniometer, operating at 100 keV. The HRTEM images of plan-view and cross-sectional Ge specimens were formed by three beams in a dark field lattice plane imaging mode /5/. The crystal lattice imaging of cross-sectional GaAs specimens was performed in bright field by means of 9-beam mode (as better detailed on /9/).

Calculations based on the MARLOWE computer code were used /5/ to simulate the evolution of atomic collision cascades induced by 40 keV Te^+ in crystalline Ge. The TRIM Monte Carlo computer code was also applied /9/ to estimate the depth profile of energy deposited in GaAs by nuclear stopping of Si^+ in our experimental conditions.

RESULTS AND DISCUSSION

Lateral and longitudinal characteristics of individual damage clusters in Ge

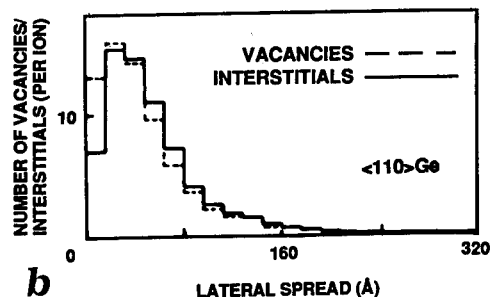
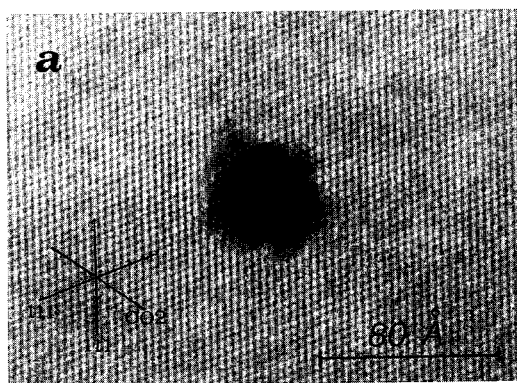


fig.1 a) HRTEM of a damage cluster in $\langle 110 \rangle$ Ge ($5 \times 10^{13} \text{ Te}^+ \text{ cm}^{-2}$, 46 keV)

b) calculated lateral spread distribution of point defects (Te^+ , 40 keV)

It is known that when the deposited energy density, \bar{Q}_v , in an individual cascade is high enough, visible damage clusters may be created. In our previous study /5/ it was found that the efficiency for obtaining a visibly damaged region in $\langle 110 \rangle$ Ge (46 keV Te^+) was ≈ 0.006 for $\bar{Q}_v \approx 0.05 \text{ eV/atom}$.

In the lattice plane imaging mode damage clusters are seen, in all the cases, to have markedly darker contrast in comparison with that of the undisturbed matrix, fig.1a. As seen by the micrograph, two components of the damaged lattice could be distinguished: a damage core of the cluster and an interface "grey zone" with lighter contrast than the cluster core. This interface has a thickness between 10 and 20 Å. In fig.1b is reported the computed lateral spread distribution of point defects generated in $\langle 110 \rangle$ Ge. The histogram indicates that the probability of finding vacancies near the ion impact is much higher than for interstitials. This

behaviour was also derived by the phase contrast analysis of HRTEM micrographs /5/. The value of doubled most probable lateral spread for interstitials is estimated to be about 16 Å larger than that for vacancies (as reported on /5/, Tab. 2), which is in good agreement with the HRTEM measured thickness of the "grey zone". Thus, the spatial separation of interstitials from vacancies is clearly demonstrated resulting in a cascade center rich in vacancies and a periphery with more interstitial atoms.

In summary we relate the darker contrast of detected damage clusters in HRTEM micrographs with accumulation of vacancies and the lighter contrast of the periphery "grey zones" with an accumulation of interstitials. It is worth noting that, for defect clusters produced by individual displacement cascades in implanted metals, a similar interpretation of spatial distribution of vacancies and interstitials was derived mainly by TEM observations /12/. The obtained XHRTEM images of the longitudinal spread distribution of isolated damage clusters in Te^+ implanted Ge demonstrate an analogy with observed contrasts in plan-view HRTEM /10/.

In the literature /13, 14/ another idea about the "grey zone" contrast interpretation was proposed. On the basis of diffraction contrast some authors suggest that "grey zones" appear as a result of overlapped individual cascades, that increase the damage level in the peripheral regions, so producing a diffraction contrast in more extensive regions of the cascades.

Our results support the idea that the observed "grey zones" are essentially elements of individual cascades, arising during their evolution.

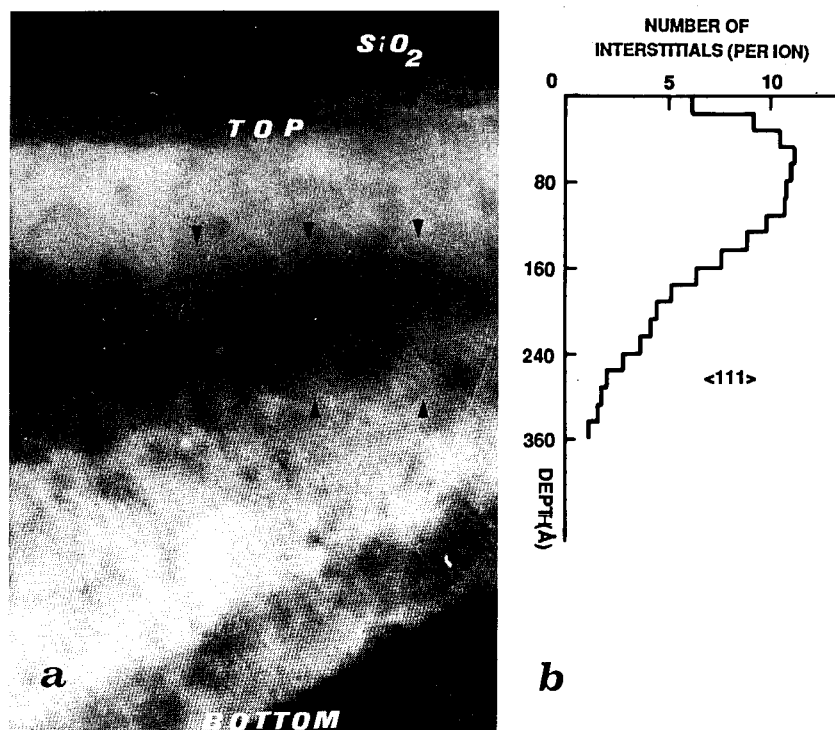


fig.2 a) XHRTEM along $\langle 110 \rangle$ Ge ($1.3 \times 10^{12} \text{Te}^+ \text{cm}^{-2}$);
b) computer simulated damage profile (same depth scale for a) and b)).

Depth distribution of radiation damage in Ge and GaAs

Fig.2 shows a comparison of experimental results on damage-depth distribution with the computer simulated disorder for Te^+ bombarded $\langle 111 \rangle$ Ge. The micrograph shows a three-beams dark-field lattice-plane image of a $\langle 110 \rangle$ projection of $\langle 111 \rangle$ Ge. It gives a direct image of the depth distribution of damage clusters. The triangular marks indicate the band of maximal cluster concentration. It begins at a depth of $\approx 140 \text{ \AA}$ from the implanted surface (marked with "top") and has a width $\approx 170 \text{ \AA}$. Isolated clusters developed in the crystal at depths below the region of maximum damage can be identified as well. On the bottom side corresponding to the most thin part of the specimen a narrow well defined dark band along the crystalline edge is seen. This band is correlated to a local deformation of the specimen, and is not a result of Te^+ implantation.

The calculated peak position appears at about 80 \AA from the surface (see fig. 2b). An analogous result has been obtained by Jager and Merkle /15/ from a comparison of an experimentally (TEM contrast analysis technique) determined cluster-depth distribution with the vacancy distribution calculated by MARLOWE, for Bi^+ bombarded Au. These authors explain the observed shift to greater depth with a higher probability for cascades with quasi-channeling trajectories to produce a stable visible clusters.

The depth distribution of radiation damage clusters in $\langle 100 \rangle$ GaAs created by Si ions can be seen in the high resolution $\langle 110 \rangle$ cross-section micrograph in fig.3a, where we have distinguished four main zones (A,B,C,D), described in greater detail on /9/, fig. 2 and 4. The location of maximum damage cluster density at a depth of about 1000 \AA , observed from the TEM results, agrees well with the expected depth from the calculated (without including any diffusion effects) energy deposition by

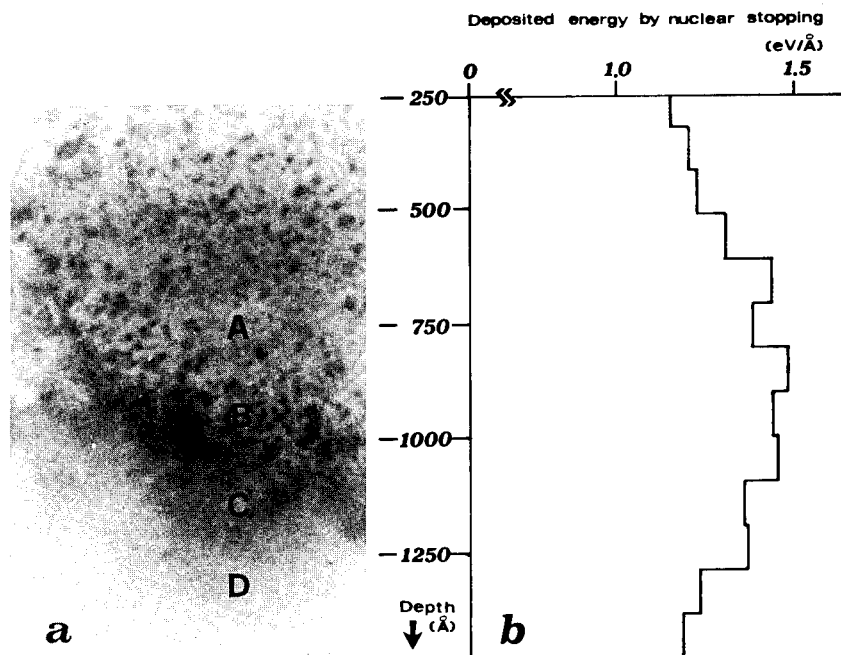


fig.3 a) $\langle 110 \rangle$ XHRTEM of Si^+ GaAs, b) calculated energy deposited by nuclear stopping

nuclear stopping, fig.3b.

A specific characteristic of Si^+ implanted GaAs (which was not found in implanted Ge) is the existence of integrated "grey zone C" beyond the depth of maximum damage cluster density (for comparison see the micrograph of fig.2a and 3a). The characteristics of the diffusion zone "C" and its interface with the maximum damaged region and undisturbed GaAs lattice are illustrated in fig. 4. The width of this zone is estimated on the order of 200-300 Å. One interesting feature of zone "C" is that $\{002\}$ planes are more strongly expressed here than in the lattice imaging of the undisturbed crystal matrix. In such a way, a visual criterium for the position of the interface between diffusion zone and undisturbed GaAs lattice could be the boundary of vanishing $\{002\}$ planes contrast. It has been shown by Petroff et al./16/ that $\{002\}$ -diffracted beam intensities which are proportional to $(f_{\text{Ga}} - f_{\text{As}})^2$ (f_{Ga} and f_{As} being the atomic scattering factors for Ga and As), are quite sensitive to composition. On the basis of this conclusion we suppose that the evidently strong contrast of $\{002\}$ planes is related to disturbed stoichiometry of GaAs, due to an enhanced diffusion of As interstitials. The reasons supporting such an interpretation are given as follows:

1. As it was discussed in connection with fig. 1a, a clear spatial separation of interstitials from vacancies was observed by structure-like HRTEM imaging of damage clusters and shown by MARLOWE computer simulation.
2. Hirayama et al. /17/, investigating the radiation enhanced interdiffusion of host atoms in GaAs-AlAs superlattices (by photoluminescence measurements), found the

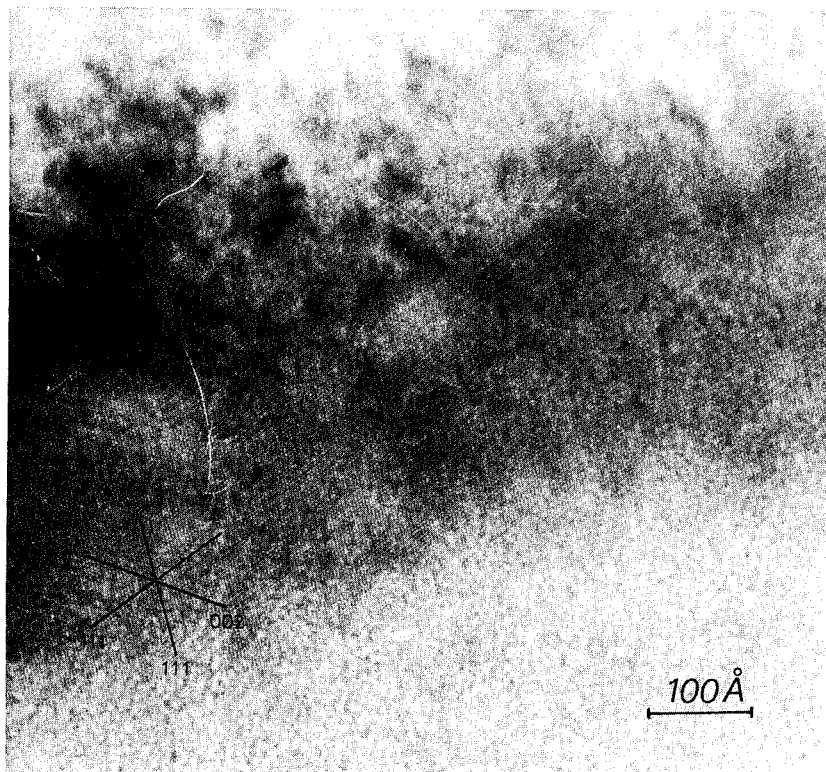


fig. 4 $\langle 110 \rangle$ XHRTEM of Si^+ implanted GaAs, detailed imaging of diffusion zone "C".

largest interdiffusion coefficient of host atoms at GaAs-AlAs heterointerfaces for implantation of Si ions in comparison to other ion species (F^+ , As^+ , B^+ , Ar^+ , Be^+).

3. The latest conclusion of Newman and Woodhead /18/, proved by their experiments on high-resolution infrared-absorption, identify the mobile interstitials produced by room-temperature irradiation of GaAs as As atoms.

We connect the contrast of integrated "grey zone" in GaAs with host atoms and not with diffusion of Si atoms, since in our case the volume concentration of Si in GaAs at the depth of zone "C" is quite low (10^{18} atoms/cm³).

SUMMARY AND CONCLUSIONS

The use of HRTEM and XHRTEM analysis, supported by computer simulation studies, gives complementary results for a comprehensive understanding of the nature of damage created in ion bombarded elementary and compound semiconductors. On the basis of the general tendency of space separation of vacancies from interstitials (clearly observed in Ge), an explanation on the nature of the diffusion zone beyond the damage peak in Si^+ implanted GaAs is proposed, as being connected with a high interstitial concentration.

The obtained data about this "grey zone" in implanted GaAs could stimulate further calculations of defect probability distributions by computer simulation programs tackling radiation enhanced diffusion.

References

1. J.R. Parsons, M. Rainville and C.W.Hoelke, *Phil. Mag.* **21**, 1105 (1970).
2. P. Werner and M. Pasemann, *Ultramicroscopy* **7**, 267 (1982).
3. T. Gessner, M. Pasemann and B. Schmidt, *Phys. Stat. Sol. a* **77**, 133 (1983).
4. M.O. Ruault, J. Chaumont, J.M. Penisson and A. Bourret, *Phil. Mag.* **50**, 667 (1985).
5. M.G. Kalitzova, D.S. Karpuzov and N.K. Pashov, *Phil. Mag.* **A51**, 373 (1985).
6. J. Narayan, O.S. Oen, D. Fathy and O.W. Holland, *Mater. Lett.* **3**, 67 (1985).
7. D.K. Sadana, *Nucl. Instr. Meth.* **B7/8**, 375 (1985).
8. G. Vitali, M. Rossi, M. Kalitzova, N. Pashov, P. Werner and H. Bartsch, *Il Nuovo Cimento D* **10**, 271 (1988).
9. G. Vitali, M. Kalitzova, N. Pashov, P. Werner, H. Bartsch and D. Karpuzov, *Appl. Phys.* **A46**, 185 (1988).
10. M.G. Kalitzova, D.S. Karpuzov and N.K. Pashov, in *Solid State Phenomena* vol.1&2, edited by D. Stievenard and J.C. Bourgoin (TTP Ltd., Switzerland, 1988), p. 465.
11. T.T. Sheng and R.B. Markus, *J. Electrochem. Soc.* **127**, (1980).
12. W. Jager, *J. Microsc. Spectrosc. Electron.* **6**, 437 (1981).
13. M.O. Ruault, J. Chaumont and H. Bernas, *Nucl. Instr. Meth.* **209/210**, 351 (1983).
14. L.M. Howe and M.H. Rainville, *Nucl. Instr. Meth.* **B19/20**, 61 (1987).
15. W. Jager and K.L. Merkle, *Phil. Mag.* **A57**, 479 (1988).
16. P.M. Petroff, A.C. Gossard, W. Wiegmann and A. Savage, *J. Cryst. Growth* **44**, 5 (1978).
17. Y. Hirayama, Y. Suzuki and H. Okamoto, *Jpn. J. Appl. Phys.* **24**, 1498 (1985).
18. R.C. Newman and J. Woodhead, *J. Phys. C* **17**, 1405 (1984).

ION ENERGY AND DOSE EFFECTS DURING ION-ASSISTED EPITAXIAL GROWTH OF InAs ON Si(100)

C.-H. CHOI AND S.A. BARNETT

Department of Materials Science and Engineering and the Materials Research Center, Northwestern University, Evanston IL 60208

ABSTRACT

Epitaxial InAs films have been grown on Si(100) substrates using triode ion-assisted deposition (TRIAD). The ratio r of the impinging Ar ion flux J to the deposited InAs flux was varied from 2.5 to 8.5 for Ar ion energies E from 5 to 55 eV. The growth temperature T was 350°C while the growth rate R was fixed at 0.6 $\mu\text{m/h}$. Two types of experiments were carried out. First, in order to investigate ion damage effects, X-ray diffraction rocking curve full-widths at half-maximum (FWHM) were measured as a function of E and r . In these experiments, the first 50 nm of InAs was always grown under the same conditions, $r = 5$ and $E = 25$ eV, in order to eliminate possible complicating effects caused by ion irradiation during InAs nucleation on Si, followed by 550 nm of growth at different E and r values. FWHM values increased with increasing E and r from 2800 arcsec, a value limited by defects arising from the 11% mismatch between InAs and Si, to 8900 arcsec as a result of ion damage. The FWHM value was found to be dependent on the total number of atomic displacements due to ion irradiation, estimated using a modified Kinchin-Pease expression. In the second set of experiments, E during the first 50 nm of growth was varied while ion irradiation damage in the remaining 550 nm was minimized. Increasing E from 15 to 40 eV resulted in a decrease in the FWHM from 5500 to 2600 arcsec, followed by a gradual increase when E was increased above 40 eV. Ion irradiation at the onset of film growth thus reduced the propagation of defects from the InAs/Si interface into the film.

INTRODUCTION

The use of low energy ion bombardment during epitaxial growth has attracted considerable interest due to beneficial effects of ion-surface interactions. For example, low-energy irradiation (where low can be roughly defined as < 200 eV) has been used to decrease epitaxial temperatures,[1-4] decrease defect densities,[5,6] increase dopant incorporation probabilities,[7-10] decrease dopant segregation,[10] increase P and As incorporation probabilities during growth of III-V alloys,[11,12] and allow the growth of a range of metastable alloys [13,14]. In addition, ion sputtering is an important technique for cleaning surfaces prior to epitaxial growth [15,16].

The successful application of ion-assisted semiconductor growth requires that ion damage be avoided or minimized. However, the understanding of the complex, depth-dependent collisional and thermal processes at the surface of a growing film - point defect production, defect diffusion, defect annihilation, and agglomeration of point defects into stable extended defects such as dislocation loops - is incomplete. In the results described above, ion damage was usually negligible for ion energies $E < 200$ eV. Increasing E above a critical value, which may depend on other parameters such as the growth rate R , the ion flux J , and the growth temperature T , resulted in the coalescence of point defects into dislocation loops [5,6]. There are also indications that defect production is sensitive to the ion flux. During sputter cleaning of Si at 750°C with 100 eV ions, surface damage resulted when the ion flux was increased above a critical level [15,16].

In order to obtain a more detailed understanding of defect production during ion-assisted deposition, we have carried out X-ray diffraction rocking curve analyses of epitaxial InAs films grown on Si(100) substrates as a function of ion energy and flux. Very low ion energies (5 - 55 eV) were used

in order to examine the limit where damage is produced only at the surface while very high r values (2.5 to 8.5) gave enough displacements that damage was readily resolved. The value $T = 350^\circ\text{C}$ used in these experiments was $> 50\%$ of the melting point of InAs, such that improvements in film quality due to ion-enhanced adatom mobilities [5,6] were probably not a factor. The initial results presented in this paper indicate that ion damage production is a function of both E and r , and is proportional to the point defect creation rate as given by a modified Kinchin-Pease relation. On the other hand, the quality of 600 nm thick InAs films was improved when they were grown on a 50 nm thick intentionally-ion-damaged buffer layer.

EXPERIMENTAL PROCEDURES

InAs films were grown using a triode ion-assisted deposition (TRIAD) system described in detail elsewhere [17]. The growth chamber is fully bakeable, has a sample-insertion load lock, and is evacuated using a turbomolecular pump to a base pressure of $\sim 10^{-9}$ Torr. During InAs film growth, the As_4 flux was evaporated from a high-purity graphite effusion cell filled with 99.9999% pure As. The effusion cell temperature was 340°C , slightly higher than the value required to obtain As-stabilized growth. The In flux was sputtered from a water-cooled, 99.999% pure In target. The Si substrates used in this study were polished (100)-oriented 20 - 40 Ohm cm n-type wafers. They were cleaned using organic solvents and sputter cleaned prior to beginning deposition as described below.

Ion bombardment of the In target, Si substrate, and growing InAs film was provided by a triode discharge that was confined between liquid-nitrogen-cooled shrouds. The discharge was maintained in 5×10^{-3} Torr of 99.999% pure Ar, which was further purified by first passing it through a 900°C Ti getter, by applying 40 V between an incandescent W filament cathode and the anode. Independent control over the fluxes and energies of Ar ions bombarding these surfaces was achieved [17].

In these experiments the ratio r of the impinging Ar flux to the flux of accumulating film atoms was varied from 2.5 to 8.5 by adjusting the intensity of the discharge. However, since the discharge also supplied ions for sputtering the In target, the negative target voltage V_t with respect to the anode was varied in order to maintain a constant net growth rate R of 0.6 $\mu\text{m/h}$. The negative substrate voltage V_s with respect to the anode was varied from 10 to 60 V. While exact ion energies are not known, previous plasma potential V_p measurements on a triode discharge operated under similar conditions gave a V_p value $\sim 5\text{V}$ negative with respect to the anode [18]. Ion energies $E \sim e(V_s - 5)$ in the present experiments thus varied from ~ 5 to 55 eV. Reductions in the growth rate due to sputtering of the growing film [17] were compensated for by adjusting V_t .

Prior to initiating deposition, the Si substrate was sputter cleaned at an ion current density $J = 0.56 \text{ mA/cm}^2$, $E = 100 \text{ eV}$, and temperature $T = 350^\circ\text{C}$ for 15 mins. The In target was simultaneously sputter cleaned. V_s , V_t , and J were then adjusted to the values to be used during growth, and the shutter removed to expose the substrate to the In and As_4 fluxes. All films were grown using a two-layer technique with $T = 350^\circ\text{C}$ and $R = 0.6 \mu\text{m/h}$. In one series of experiments, films were grown with $V_s = 30 \text{ V}$ and $r = 5$ ($J = 0.56 \text{ mA/cm}^2$) for the first 50 nm, after which the irradiation conditions were adjusted to values in the ranges $V_s = 10 - 60 \text{ V}$ and $r = 2.5 - 8.5$ for the remainder of the deposition. In a second series of experiments, the V_s value used during the first 50 nm was varied with $r = 5$ while $V_s = 15 \text{ V}$ and $r = 5$ were used during the growth of the remaining film.

The crystalline perfection of the InAs films was measured qualitatively in-situ using reflection high-energy electron diffraction (RHEED). Quantitative assessment of film perfection was made using X-ray diffraction rocking curve peak widths for the InAs (400) reflection. Rocking curve widths were used since they are much more sensitive to defects than θ - 2θ peak widths [19].

RESULTS AND DISCUSSION

Ion Damage Effects

In this section, the ion damage induced in InAs films as a function of ion energy E and ion-to-deposited-atom ratio r is described. As discussed above, the ion irradiation conditions were maintained constant during the first 50 nm of growth in order that ion-induced changes in the film perfection occurring at the nucleation stage were eliminated. The first-layer values were chosen so as to obtain good crystalline perfection, as discussed in the following section.

Films grown under the conditions given above were epitaxial as indicated by RHEED. The only exceptions were in cases of high V_s and high r values where patterns with additional rings suggesting polycrystalline growth were observed. Figure 1 is a plot of the X-ray rocking curve full-width at half maximum (FWHM), measured for the (400) InAs reflection, as a function of V_s and r . For $V_s < 25$ V, the FWHM was ~ 3000 arcsec. The peak broadening in this case was due mainly to threading dislocations propagating from the film-substrate interface as a result of the 11% lattice mismatch between InAs and Si. Evidence that the FWHM values were limited by threading dislocations was obtained by growing thicker films with $V_s = 15$ V, resulting in a monotonic decrease in the FWHM to 1800 arcsec for a thickness of 1.9 μm . This trend is in good agreement with previous results for lattice-mismatched growth which show a decrease in threading dislocation density with increasing film thickness t [20]. Dislocation densities deduced from the FWHM values were $< 10^9 \text{ cm}^{-2}$, in good agreement with results for InAs/InP and InAs/GaAs films of comparable t [20]. InAs was recently grown on Si for the first time by molecular beam epitaxy [21], but threading dislocation densities were not reported.

For $V_s > 25$ eV, the FWHM was due mainly to ion damage. This was shown by comparing films grown with $V_s = 30$ V and $r = 3.5$ of different t . The FWHM was independent of t indicating that threading dislocations did not play a major role in determining the FWHM. The FWHM shown in Fig. 1 increased with both V_s and r . For the highest r value, appreciable ion damage was already present (FWHM = 5400 arcsec) for $V_s = 26$ V. On the other hand, for an r value four times lower, little damage was present (FWHM = 3200 arcsec) for V_s up to 33 eV. These results indicate that the threshold energy for damage production was very low, near to the threshold energy for displacement, and that the amount of damage produced was related to the total ion energy per deposited atom.

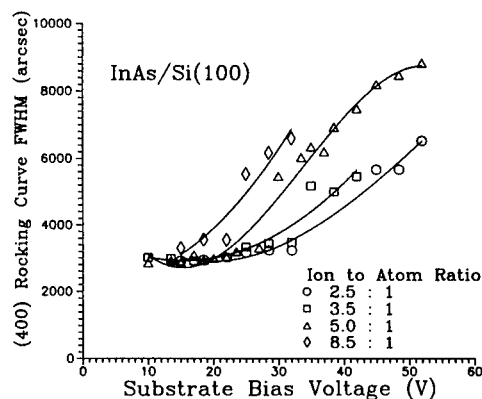


Figure 1. The InAs (400) rocking curve FWHM for 0.6 μm thick films plotted vs. the substrate bias voltage V_s for four different ion to deposited atom ratios r .

We propose the following model to explain these results. Since T was greater than half the InAs melting point in these experiments, the point defect concentration away from the growth interface is expected to rapidly reach equilibrium values. The residual damage measured by the FWHM was thus due to the aggregation of a supersaturation of point defects into more stable extended defects, probably dislocation loops [5,6]. The total dislocation loop line length produced, and hence the measured FWHM, is expected to be a function of the steady state point defect density produced at the growing film surface by ion irradiation.

This steady state density depends on the point defect production and annihilation rates. Point defects are produced at the growing film surface (due to the low penetration depth of the low energy ions) at a rate given by the ion flux J times the number of displacements N produced per ion. N can be estimated for an ion with energy E using a modified Kinchin-Pease expression [22]

$$N = (E - E_{th})/2E_{th}, \quad (1)$$

where the modification is to subtract the threshold energy for displacement E_{th} from E in order to make N zero at $E = E_{th}$. Annihilation of point defects occurs by recombination of interstitials and vacancies, diffusion to the growing film surface, and by aggregation into extended defects.

Since R and T were maintained constant in all experiments, for a given damage production rate JN the annihilation rate, the steady state point defect density, and the rate of formation of dislocation loops should be the same. Any ion irradiation conditions giving the same JN value should thus result in the same FWHM. Fig. 2 is a re-plot of the FWHM values shown in Fig. 1 as a function of the damage production rate normalized to the deposited atom flux $n = rN$, i.e. the number of displacements per deposited atom. E_{th} was used as a fitting parameter and a best fit was obtained for $E_{th} = 10$ eV as shown in Fig. 2. While the threshold energy for displacement in InAs is not known, the value $E_{th} = 10$ eV is reasonable considering that $E_{th} = 9$ and 9.4 eV have been measured for GaAs [23], a similar material. The fact that the data fit on the same curve within experimental accuracy indicates that the parameter n determines damage production for a given T and R and for low energy ions.

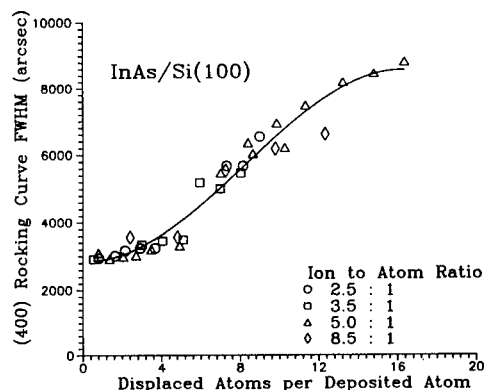


Figure 2. The InAs (400) rocking curve FWHM for 0.6 μ m thick films plotted vs. the number of displaced atoms per deposited atoms as calculated using eqn. 1.

It should be noted that n can be used to predict the ion damage only in the limit of very low E values, for the following reasons. First, increasing E increases the damage depth, which should significantly alter defect annihilation and loop formation rates. Second, E values large enough to give a large number of defects localized in a collision cascade may result in the localized nucleation of dislocation loops even for low average rN values.

The present results can be compared with those of Hultman et al. [5,6] who found using TEM that dislocation loops were produced when epitaxial TiN films were bombarded with > 400 eV N_2 ions at $r \sim 1$. The ion energy per deposited atom, 400 eV/atom, was considerably greater than the value causing damage in InAs. This difference is due to the much larger threshold energy expected [23] for a refractory material such as TiN.

Ion-Induced Improvements in InAs/Si Film Quality

Initial experiments using different V_s values and $r = 5$ during the growth of the first 50 nm were also carried out. In this case, the remaining 550 nm was grown with $V_s = 15$ V and $r = 3.5$ in order to minimize ion damage. Figure 3 shows the FWHM measured for first layer V_s values from 15 to 60 V. The FWHM decreased rapidly for an increase in V_s from 15 to 40 V, before increasing slightly for further increases to 60 V. That is, depositing a highly ion damaged initial layer (see Fig. 1) improved the crystalline perfection of the subsequently deposited film. This is possible since dislocation loops are closed-end defects that do not propagate from the damaged layer into the remainder of the film [6].

Two explanations of the improved FWHM can be made. First, the ion irradiation may significantly alter the nucleation of InAs on Si yielding a change in film perfection. Second, the ion-induced damage may itself play a role. Reductions in threading dislocation densities with increasing film thickness are a result of dislocation-dislocation interactions to form networks and closed loops [24]. Intentionally introducing a high density of defects such as dislocation loops may more rapidly decrease threading dislocation densities yielding the observed decrease in FWHM.

Acknowledgements

The authors gratefully acknowledge the financial support of the Office of Naval Research under contract number N00014-86-K-0629 and the use of facilities supported by the National Science Foundation through Northwestern University Materials Research Center, Grant No. DMR 85-20280.

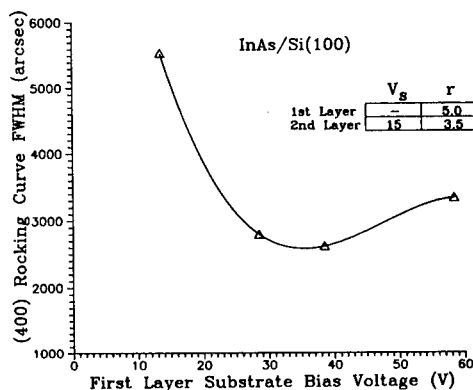


Figure 3. The InAs (400) rocking curve FWHM for 0.6 μ m thick films plotted vs. the substrate bias voltage V_s used during the first 50 nm of growth. $V_s = 15$ V and $r = 3.5$ was used during the remaining film growth.

References

1. H. Yamada and Y. Torii, *J. Appl. Phys.* **64**, 702 (1988).
2. T. Narusawa, S. Shimizu, S. Komiya, *J. Vac. Sci. Technol.* **16**, 366 (1979).
3. G.E. Thomas, L.J. Beckers, J.J. Vrakking, and B.R. de Koning, *J. Cryst. Growth* **56**, 257 (1982).
4. N. Herbots, T.S. Noggle, B.R. Appleton, and R.A. Zhur, *J. Vac. Sci. Technol.*, in press.
5. L. Hultman, U. Helmersson, S.A. Barnett, J.-E. Sundgren, and J.E. Greene, *J. Appl. Phys.* **61**, 552 (1987).
6. L. Hultman, S.A. Barnett, J.-E. Sundgren, J.E. Greene, *J. Cryst. Growth*, in press.
7. Y. Ota, *J. Appl. Phys.* **51**, 1102 (1980).
8. H. Sugiura, *J. Appl. Phys.* **51**, 2630 (1980).
9. See J.E. Greene, S.A. Barnett, A. Rockett, and G. Bajor, *Appl. Surf. Sci.* **22/23**, 520 (1985), and references contained therein.
10. M.A. Hasan, J. Knall, S.A. Barnett, J.-E. Sundgren, L.C. Markert, A. Rockett, and J.E. Greene, *J. Appl. Phys.*, in press.
11. S. Shimizu, T. Tsukakoshi, S. Komiya, and Y. Makita, in *GaAs and Related Compounds (1985)*, Ed. by M. Fujimoto, *Inst. Phys. Conf. Ser. No. 79*, p. 91.
12. S. Maruno, Y. Morishita, T. Isu, Y. Nomura, and H. Ogata, *J. Electronic Mater.* **17**, 21 (1988).
13. S.A. Barnett, B. Kramer, L.T. Romano, S.I. Shah, M.A. Ray, S. Fang, and J.E. Greene, in *Layered Structures, Epitaxy, and Interfaces*, Ed. by J.M. Gibson and L.R. Dawson, (*Mater. Res. Soc., Pittsburgh, 1985*), p. 285.
14. J.E. Greene, *J. Vac. Sci. Technol. A* **5**, 1947 (1987).
15. J.H. Comfort, L.M. Garverick, and R. Reif, *J. Appl. Phys.* **62**, 3388 (1987).
16. L.M. Garverick, J.H. Comfort, T.R. Uyeh, R. Reif, R.A. Baiocchi, and H.S. Luftman, *J. Appl. Phys.* **62**, 3398 (1987).
17. S. Rohde, S.A. Barnett, and C.-H. Choi, *J. Vac. Sci. Technol. A*, in press.
18. P. Ziemann, K. Koehler, J.W. Coburn, and E. Kay, *J. Vac. Sci. Technol. B* **1**, 31 (1983).
19. A.T. Macrander, R.D. Dupuis, J.C. Bean, and J.M. Brown, in *Semiconductor-Based Heterostructures*, Ed. by M.L. Green, J.E.E. Baglin, G.Y. Chin, H.W. Deckman, W. Mayo, and D. Narasinhham, (*Metall. Soc., 1986*), p. 75.
20. P. Sheldon, K.M. Jones, M.M. Al-Jassim, and B.G. Yacobi, *J. Appl. Phys.* **63**, 5609 (1988).
21. S. Kalem, J. Chyi, C.W. Litton, H. Morkoc, S.C. Kan, and A. Yariv, *Appl. Phys. Lett.* **53**, 562 (1988).
22. G.H. Kinchin and R.S. Pease, *Rep. Prog. Phys.* **18**, 1 (1955).
23. L.W. Hobbs, in *Introduction to Analytical Electron Microscopy*, Ed. by J.J. Hren, J.I. Goldstein, and D.C. Joy (Plenum, New York, 1979), p. 446.
24. G.W. Turner, in *Semiconductor-Based Heterostructures*, Ed. by M.L. Green, J.E.E. Baglin, G.Y. Chin, H.W. Deckman, W. Mayo, and D. Narasinhham, (*Metall. Soc., 1986*), p. 235.

ION BOMBARDMENT EFFECTS ON GaAs USING 100eV NITROGEN IONS

W.M. LAU

Surface Science Western, University of Western Ontario, London,
Ontario, Canada N6A 5B7

ABSTRACT

The ion bombardment effects of low energy molecular nitrogen ions (100eV) on GaAs have been investigated using in-situ polar angle dependent X-ray photoelectron spectroscopy. It was found that arsenic and gallium nitrides were formed as a result of the nitrogen ion bombardment. The ion bombardment also caused a depletion of arsenic in the near surface region. For example, with a dose of $6 \times 10^{15} \text{ cm}^{-2}$ of nitrogen molecular ions at 100eV, the surface structure can be described approximately as 1.5 nm of $\text{Ga}_{0.67}\text{As}_{0.33}\text{N}$ on GaAs. The ion bombardment moves the Fermi levels of both n-type and p-type GaAs to mid-gap. Heating the ion bombarded samples in a vacuum chamber to 500°C desorbs all arsenic nitrides but most of the gallium nitrides remain on the surface. The Fermi levels of both n-type and p-type are then stabilized at about 0.4 eV from the valence band maximum. A surface type-inversion of the n-type substrate is therefore induced by the nitrogen-ion-bombardment/annealing treatment.

1. Introduction

The ability to control Schottky barrier height is technologically important. However, in the past, it was generally believed that Fermi level pinning near mid-gap is inevitable upon metal deposition on GaAs, and that the control of Schottky barrier height on GaAs is difficult [1]. However, several techniques for preparing GaAs surfaces prior to metal deposition have been recently reported which promise the possibility of controlling Schottky barrier height on GaAs. The approach taken by Brillson et al. [2] is to prepare a high quality GaAs film by molecular beam epitaxy and to cap it in the same chamber with a thin overlayer of arsenic. The protective arsenic cap is then thermally desorbed in the metal deposition chamber in order to regenerate a clean and stoichiometric surface with a low defect density prior to Schottky contact formation. Another approach is to use an ultrathin sandwich-layer between the GaAs substrate and the Schottky metal in order to achieve the control of Schottky barrier height. For example, $1.5\text{-}3 \text{ nm}$ of Si [3], surface oxide [4], and adsorbed inorganic sulfide [5] have been used as the sandwich-layer for this purpose. An alternative approach similar to this sandwich-layer technique is to type invert the near surface region of the GaAs substrate before metal deposition. For example, Zhang et al. [6] reported that high temperature annealing of refractory metal nitrides on n-GaAs led to the formation of metal/p⁺/n structures and, thereby, to an increase of Schottky barrier height. This group has also reported that nitrogen bombardment ($<400 \text{ eV}$) of the GaAs substrate prior to the metal nitride deposition further increased the barrier height by about 0.1 eV [7]. Details on the role of nitrogen at the metal-semiconductor interface are, to our understanding, not yet available.

This paper reports on a study of the effects of low energy (100eV) nitrogen ion bombardment of GaAs. In-situ angle dependent X-ray photoelectron spectroscopy (XPS) was used to characterize the changes in surface composition and surface band-bending on both n-type and p-type substrates.

II. Experimental

The samples used in this study were HF-etched n-GaAs (100) wafers, and flat-band n-type and p-type GaAs (110) surfaces prepared by cleaving GaAs wafers (n-type: Si doped to $3 \times 10^{18} \text{ cm}^{-3}$; p-type: Zn doped to $3 \times 10^{17} \text{ cm}^{-3}$) in an ultra-high vacuum (UHV) chamber of the XPS system. The details of the configuration of the XPS system have been reported elsewhere [8]. The nitrogen ion bombardment experiments were carried out using a small preparation chamber directly linked to the XPS system. The base pressure of the ion chamber was $2 \times 10^{-6} \text{ Pa}$ which increased to $5 \times 10^{-3} \text{ Pa}$ when the ion source was in operation. The ion source was a Colutron ion source. In this study, an extraction voltage of 100V was used. Although it is possible to adjust the separation between the ion source and the sample by a transfer device, a separation of 8cm was consistently used in this study. The current density was measured to be about $0.3 \mu\text{A}/\text{cm}^2$. Hu et al. have shown that under similar operating conditions, the nitrogen ion beam is composed of about 96% molecular nitrogen ions and 4% atomic nitrogen ions [9]. Since the kinetic energy of the molecular ions (100eV in this study) is much larger than the dissociation limit of the free molecule (9.5eV), the molecular ions will dissociate before interacting with the substrate [9]. In addition, the nitrogen ions will be neutralized efficiently above the surface by resonance or Auger neutralization [10]. Therefore, the reactants in this study are actually nitrogen atoms with an average energy of 50eV.

The characterizations of surface composition and surface band-bending were carried out with in-situ polar angle dependent XPS. The details of the analysis technique and the XPS system can be found elsewhere [8]. The binding energy calibration was done using the $\text{Au } 4f_{7/2}$ peak at 83.93eV as a reference. Surface compositions were estimated using the Scofield factors [11]. However, it should be noted that the As/Ga ratios on cleaved GaAs samples that we measured using the intensity ratios of As 3d to Ga 3d have been consistently less than unity. For example, 20 recent measurements on 10 different cleaved surfaces showed an average As/Ga ratio of 0.80 with a standard deviation of 0.03. With an assumption that the calibration factor of gallium is correct, the arsenic sensitivity factor for the As 3d level has been adjusted accordingly to compensate this deviation in the estimation of surface compositions in this study.

III. Results and discussion

A. Nitrogen ion bombardment effects

It was found in this study that while molecular nitrogen does not react with GaAs, nitrogen ions have a rather strong chemical reaction with GaAs. For example, the incorporation of nitrogen into GaAs as a result of nitrogen ion bombardment is

illustrated in Fig. 1. The sample has received an ion dose of about $1 \times 10^{16} \text{ cm}^{-2}$ of molecular nitrogen ions. A comparison of the spectral signals in the binding energy region of 385-405 eV of the GaAs surface before and after ion bombardment shows an intense N 1s peak at 398 eV as a result of the ion bombardment. The As 3d (Fig. 2 (a)) and Ga 3d (Fig. 2 (b)) of the bombarded surface, when compared to the results before bombardment, further indicate that arsenic nitrides and gallium nitrides have been induced by the incorporation of nitrogen. Further studies are necessary, however, for the interpretation of the bombardment induced spectral components and for the understanding of the chemical nature of these nitrides.

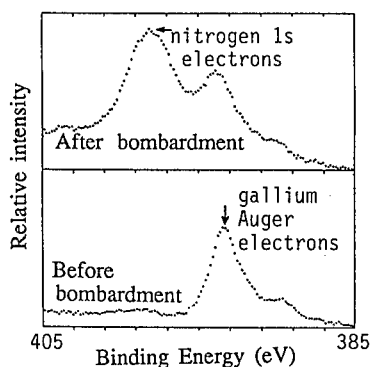


Fig. 1 The incorporation of nitrogen into GaAs by 100 eV nitrogen ion bombardment

The incorporation of nitrogen as a function of ion bombardment time (with a current density of about $0.3 \mu\text{A}/\text{cm}^2$) is shown in Fig. 3. The nonlinear behavior suggests that the chemical interaction between the incoming nitrogen and the substrate plays an important role in the retaining of the arrived nitrogen. Once a sufficient amount of nitrides has been formed, some of the incoming nitrogen may not be trapped by the substrate but re-enter the vacuum. The As/Ga ratios have also been measured as a function of ion bombardment time, and are now plotted in Fig. 3. The data show that the ion bombardment has induced a loss of arsenic. The mechanism of the arsenic loss is, however, still not clear. It is possible that the ion bombardment causes a preferential desorption of arsenic nitride.

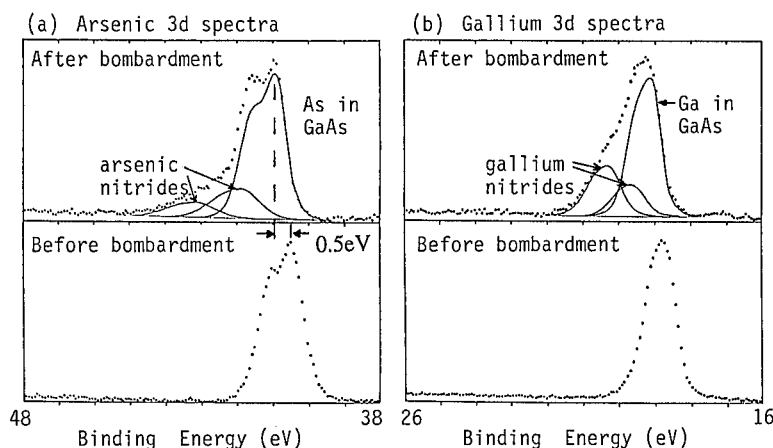


Fig. 2 XPS spectra of (a) As 3d and (b) Ga 3d indicating the formation of nitrides in p-GaAs by 100 eV nitrogen ion bombardment

The angle dependent XPS results on an n-GaAs with a dose of $6 \times 10^{15} \text{ cm}^{-2}$ of molecular nitrogen ions at 100eV give some additional information on the changes of the surface chemical structure induced by the low energy nitrogen ion bombardment. Using the general analysis technique for nondestructive depth profiling with angle dependent XPS data [11], the thickness of the nitride overlayer is estimated to be 1.5nm. The estimation assumes that the composition of the overlayer is uniform and that the inelastic mean free paths of the N 1s, As 3d, and Ga 3d photoelectrons in GaAs and in the nitride overlayer are 2.5nm. The experimental angle dependent XPS data of the ion bombarded sample and the simulated data from a structure of 1.5nm $\text{Ga}_{0.67}\text{As}_{0.33}\text{N}$ on GaAs are compared in a triangular phase diagram of atomic concentrations of nitrogen, arsenic, and gallium in Fig. 4. Each vertex represents the pure form of the chemical element. The data points closer to the nitrogen vertex were collected with a larger polar angle and are, therefore, more surface sensitive. The fact that all data points are on the right half of the triangle indicates that the XPS probed volume is arsenic deficient. It is apparent that the depletion of arsenic is more serious towards the top surface. In fact, the simulated data for 1.5nm of $\text{Ga}_{0.67}\text{As}_{0.33}\text{N}$ on GaAs fits the experimental data points quite well except near the top surface. Therefore, the ion bombarded sample has an approximate structure as 1.5nm of $\text{Ga}_{0.67}\text{As}_{0.33}\text{N}$ on GaAs with an arsenic depletion near the top surface.

The nitrogen ion bombardment also changed the surface band-bending significantly. Surface band-bending was estimated by measuring the shift of As $3d_{5/2}$ peak of the arsenic in GaAs. It was found that the peak position for the n-GaAs (110) and p-GaAs (110) surfaces prepared in the UHV spectrometer chamber were 41.75 and 40.45eV respectively. The separation is very

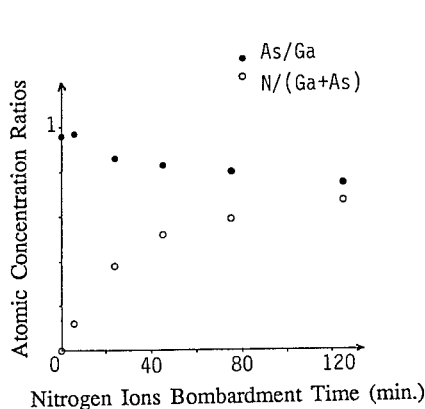


Fig. 3 Surface composition changes induced by 100eV nitrogen ion bombardment

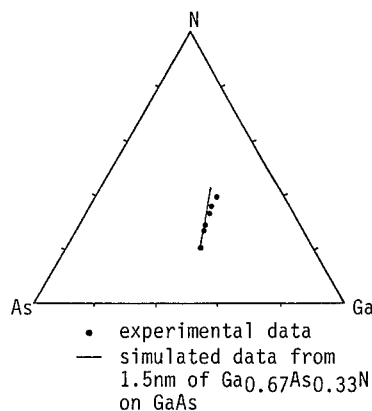


Fig. 4 Angle dependent XPS data of nitrides on GaAs

close to the bandgap of GaAs; therefore, both the n-type and p-type surfaces were flat band surfaces. The nitrogen ion bombardment, even with a dose of less than $5 \times 10^{14} \text{ cm}^{-2}$, stabilized the Fermi levels of the n-type and p-type substrates at 0.7eV and 0.6eV respectively from the valence band maximum (with an estimated error of 0.1eV). Therefore, high densities of donor and acceptor defects must have been induced near mid-gap by the nitrogen ion bombardment.

B. Annealing effects

In order to study the thermal stability of the bombarded surfaces, in-situ annealing of the ion bombarded samples was carried out at a pressure of 1×10^{-6} Pa. After a heat treatment at 500°C , significant changes in both surface composition and surface band-bending occurred. For example, after the treatment, the p-substrate with an ion

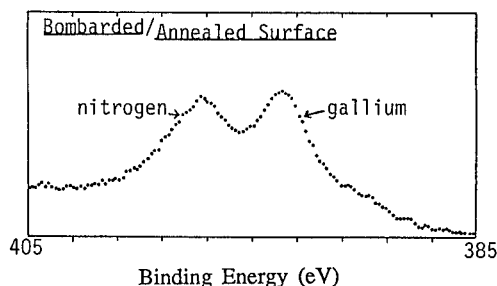


Fig. 5 Annealing effects on nitrogen

dose of $1 \times 10^{16} \text{ cm}^{-2}$ showed a decrease of nitrogen (Fig. 5 vs. Fig. 1) and a complete loss of arsenic nitrides (Fig. 6 (a) vs. Fig. 2 (a)). But the amounts of gallium nitrides did not change significantly (Fig. 6 (b) vs. Fig. 2 (b)). The heat treatment also moved the Fermi level of the p-type substrate back to 0.3eV from the valence band maximum. The most interesting result is that the Fermi level of the n-type substrate was stabilized at 0.4eV from the valence band maximum. The band-bending results indicate that the donor states induced by the nitrogen ion bombardment have been largely removed by the heat treatment. However, a large number of acceptor states were still present and caused a surface type-inversion of the n-substrate. The results agree with the previous reports [6,8] which described the formation of a surface type-inversion by annealing metal nitride on n-GaAs or by annealing nitrogen ion bombarded n-GaAs.

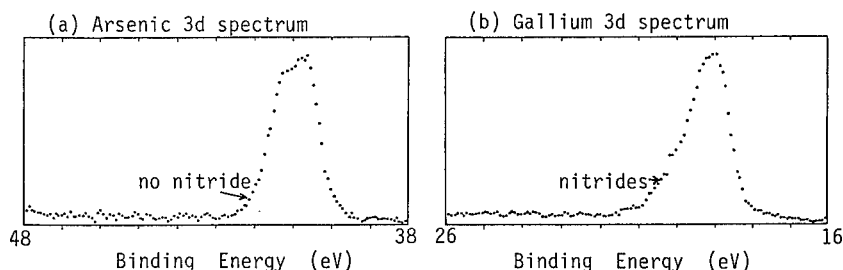


Fig. 6 Annealing effects on arsenic and gallium nitrides

The present technique for controlling Schottky barrier height, to our understanding, seems to be very similar to the method of partial desorption of surface oxide [4]. However, control of Schottky barrier height in the latter technique was proposed to be the removal of interface states. This is in contrast to the mechanism observed in this study. More work is required for a better understanding of these mechanisms.

IV. Conclusion

Nitride formation occurs when GaAs is bombarded with low energy nitrogen ions. With a dose of $6 \times 10^{15} \text{ cm}^{-2}$ of nitrogen molecular ions, the surface structure can be approximately described as $1.5 \text{ nm Ga}_{0.67}\text{As}_{0.33}\text{N}$ on GaAs with a depletion of arsenic near the top surface. The Fermi levels of both n-type and p-type substrates were pinned at mid-gap even with a dose of less than $5 \times 10^{14} \text{ cm}^{-2}$. Annealing the bombarded samples at 500°C in a vacuum chamber removed all arsenic nitrides but most of the gallium nitrides remained on the heated surface. The final band-bendings were 0.3 eV for the p-type substrate and 1.0 eV for the n-type substrate.

References:

1. S.M. Sze, Physics of Semiconductor Devices, 2nd ed. (Wiley-Interscience, New York, 1981), pp.274-297.
2. L.J. Brillson, R.E. Viturro, C. Mailhot, J.L. Shaw, N. Tache, J. McKinley, G. Margaritondo, J.M. Woodall, P.D. Kirchner, G.D. Pettit, and S.L. Wright, *J. Vac. Sci. Technol. B*, 1263(1988).
3. J.R. Waldrop and R.W. Grant, *Appl. Phys. Lett.* 52, 1794(1988).
4. M.T. Schmidt, D.V. Podlesnik, C.F. Yu, X. Wu, R.M. Osgood, Jr., and E.S. Yang, *J. Vac. Sci. Technol. B*, 1436(1988).
5. B.J. Skromme, C.J. Sandroff, E. Yablonovitch, and T. Gmitter, *Appl. Phys. Lett.* 51, 2022(1987).
6. L.C. Zhang, S.K. Cheung, C.L. Liang, and N.W. Cheung, *Appl. Phys. Lett.* 50, 445(1987).
7. L.C. Zhang, S.K. Cheung, C.L. Liang, and N.W. Cheung, presented at the 45th Device Research Conf., Santa Barbara, CA, 1987.
8. W.M. Lau, R.N.S. Sodhi, and S.I.J. Ingre, *J. Vac. Sci. Technol. A*, 1371(1988).
9. H-K. Hu, Y. Fukuda, R.A. Baldwin, P.T. Murray, and J.W. Rabalais, *J. Chem. Phys.* 72, 6158(1980).
10. G. Carter and J.S. Colligon, Ion Bombardment of Solids (Elsevier, New York, 1968).
11. J.H. Scofield, *J. Electron Spectrosc. Relat. Phenom.* 8, 129(1976).
12. S. Hofmann, in Practical Surface Analysis by Auger and X-ray photoelectron Spectroscopy, edited by D. Briggs and M.P. Seah (John Wiley & Sons, Chichester, 1983), pp. 141-179.

THIN FILMS OF p-TYPE CdTe GROWN WITH ION-BEAM-ASSISTED DOPING

Paul Sharps, Alan L. Fahrenbruch, Adolfo Lopez-Otero, and Richard H. Bube
Dept. of Materials Science and Engineering, Stanford University, Stanford, CA 94305

The purpose of the present work is to investigate p-CdTe thin films grown by ion-assisted doping (IAD). Controlled doping in homo-epitaxial films resulting in carrier densities up to $2 \times 10^{17} \text{ cm}^{-3}$ was obtained using P ions as the dopant. About 1.5% of the impinging P ions became electrically active in the films. Solar cells of n-CdS/p-CdTe were prepared and used as a diagnostic tool in understanding the p-CdTe films.

INTRODUCTION

Many of the common dopants in semiconductors do not perform satisfactorily when used to dope films grown from the vapor phase. Control over doping has been difficult if not impossible due to low incorporation probabilities, surface segregation, and/or reevaporation. Many of the dopants evaporate in the form of molecular species (P_4 , As_4 , Sb_2 , etc.) that require high dissociation energies to produce atomic species that can be readily incorporated into a growing film. However, by use of ionized and accelerated dopant beams, the dopant incorporation is increased, surface segregation is decreased, and reevaporation is reduced [1]. Dopant incorporation is increased due to trapping (low energy implantation) and to increased chemisorption of the ions on the growing surface. Surface segregation is decreased due to collisional mixing and increased diffusion through point defects created by ion bombardment [2]. Reevaporation is reduced due to increased chemisorption of the ions on the surface [2]. Some defects are annihilated at the surface, providing an annealing effect [2]. Sputtering of the growing film may also occur [2] (Fig. 1). Ion assisted doping has been used by several investigators to improve the dopant incorporation in epitaxially grown Si and GaAs [3-6]. Bajor and Greene have developed a model that describes the incorporation of an ionized dopant during film growth [7].

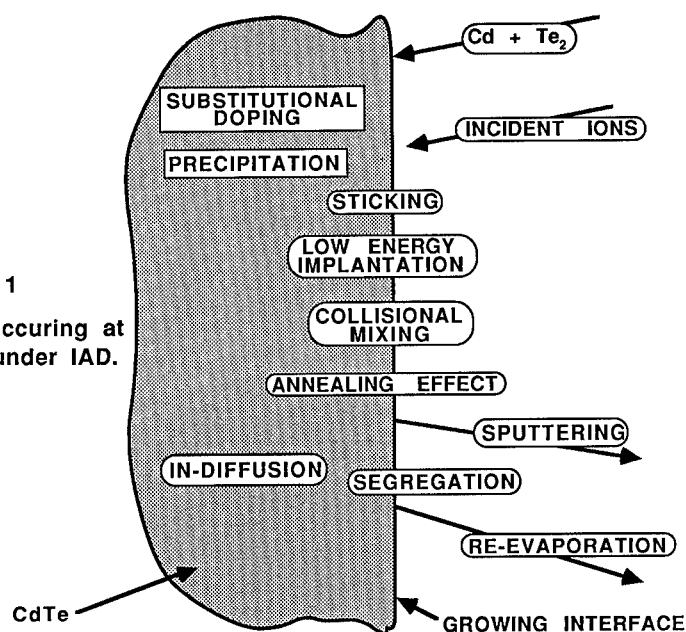
The motivation for this work is to improve the electrical properties of p-CdTe for use as a solar cell collector material. CdTe has an ideal bandgap (1.45 eV) for matching the solar spectrum. Although polycrystalline CdTe solar cells have demonstrated a high efficiency, e.g. [8], a major difficulty has been in obtaining a high enough p-type carrier density in order to lower high bulk and contact resistances. A second advantage in controlling the carrier density in p-CdTe is in the potential optimization of the open-circuit voltage, V_{oc} [9].

Group V elements P, As, or Sb are readily incorporated into single crystals of CdTe grown from the liquid [10], with the carrier density reaching a maximum of $\approx 2 \times 10^{17} \text{ cm}^{-3}$ using P [11]. On the other hand, preparation of p-CdTe from the vapor by conventional film growth techniques has been difficult. In our lab we have used close spaced vapor transport (CSVT) and hot-wall vacuum evaporation (HWVE) with additional sources for the dopant in order to grow and simultaneously dope films from the vapor. The lack of clear results after using a variety of dopants and growth conditions led us to the likely conclusion that the dopants were not being incorporated into the growing films.

Recently, new techniques have been developed that have successfully shown that epitaxial p-CdTe thin films can be doped to carrier densities to 10^{16} and 10^{17} cm^{-3} . Bicknell et. al. have demonstrated p-type doping of CdTe epilayers to $5 \times 10^{16} \text{ cm}^{-3}$ with Sb by a photoassisted molecular beam epitaxy [12,13]. Ghandi et. al. have shown p-type doping of CdTe layers up to $2 \times 10^{17} \text{ cm}^{-3}$ with As by organometallic vapor phase epitaxy [14]. Work in our own lab had already demonstrated doping of CdTe by As and P to $6 \times 10^{16} \text{ cm}^{-3}$ using IAD [15].

FIG. 1

Phenomena occurring at an interface under IAD.



For polycrystalline films, however, the incorporation of the dopant is not so straightforward [16,17]. Oppositely charged grain boundary states may effectively compensate p-type dopants such that the free carrier density is much lower than the doping density. The grain boundaries may also act as a sink for the dopant, leading to segregation and possibly compound formation. The grains are depleted, and the grain boundary barriers reduce the carrier mobility. Increasing the dopant level to greater than 10^{17} cm^{-3} would not only overcome the grain boundary compensation, but also would decrease the grain boundary barrier height. The difficulty, then, in doping polycrystalline CdTe films is twofold: 1) getting the dopant into the film in electrically active form, and 2) getting the carrier density in the film at such levels that it overcomes the effects of the grain boundaries.

In the present work we investigate the IAD of epitaxial p-CdTe films with P ions. In particular, we examine the reduction in carrier density with increased ion current which occurs after a maximum in the carrier density has been reached. The ability to make carrier density profiles and to grade junctions is demonstrated. Solar cells prepared using the epitaxial p-CdTe films as the collector material and n-CdS as the window are used as a diagnostic tool in understanding the p-CdTe films grown by IAD.

EXPERIMENTAL TECHNIQUE

Our experimental equipment has been described elsewhere [15]. One modification included equipping the system with a shutter so that film growth can be started or stopped instantaneously. This also helps in the preparation of samples with a stepped carrier density, by allowing us to interrupt the growth in order to adjust the ion current to a new value before proceeding again with the deposition of the film. Although As and P had been previously used as the dopant [15], in this work we have concentrated on P doping since work with single crystals grown from the melt has indicated that a higher dopant level can be achieved with P and since P is less toxic than As.

In order to show clearly that ionized p-type dopants could be incorporated into the crystalline structure we decided at first to avoid problems associated with the grain

boundaries mentioned above and grow on single crystal CdTe [18]. Substrates of size $4 \times 12 \times 2 \text{ mm}^3$ were cut from the boules that contained several large grains. The substrates were oriented with the help of Laue patterns with most of the substrates 20° off (100), toward (111). Previous work in our lab indicated that this direction gave good epitaxial films. Some of the substrates had twins and smaller grains of other orientations. The substrates were lapped on 600 grit SiC wheels using water as a lubricant, then chem-mechanically polished in a 1.5% bromine-polyethylene glycol solution. Immediately prior to film growth a substrate was ultrasonically cleaned in trichloroethane, blown dry with dry nitrogen, etched 5 minutes in a 3% bromine-methanol solution, rinsed with methanol, blown dry with dry nitrogen, and then loaded into the substrate holder. A thermocouple was pressed onto the back of the substrate holder to monitor the temperature. Once the conditions for each growth were achieved the shutter was opened to commence film growth.

Solar cells were prepared by evaporating a two-layer CdS film onto the epitaxial CdTe film to prevent creation of a buried homojunction [19]. Following the cooling of the p-CdTe films to room temperature, the samples were removed and immediately placed on a substrate holder and loaded into a vacuum evaporator. A substrate of microscope glass was also loaded onto the substrate holder with the CdTe film, in order to provide a check of the CdS quality and resistivity. The substrates were heated to 200°C , and CdS was evaporated from a Knudsen effusion source in a background pressure of $\approx 3 \times 10^{-7}$ torr. An undoped layer of CdS $\approx 0.3 \mu\text{m}$ was deposited, followed by an In doped layer that was $\approx 1 \mu\text{m}$ thick. The resistivity of the In doped CdS, as determined from 4 point measurements made on the films grown on the glass, was $\approx 0.04 \Omega\text{-cm}$. An In grid was evaporated on the CdS for a front contact. After a 5 minute etch of the back surface with dichromate/sulfuric acid/deionized water etch, a Au contact was evaporated onto the back. A Schottky barrier of In was also evaporated onto the CdTe films on an area that was not covered with CdS. Dark and light (AM 1.5, 100 mW/cm^2) current density-voltage plots were made on the solar cells and open-circuit voltage (V_{oc}) and short circuit current density (J_{sc}) were determined. Spectral response data were measured, current-voltage (I-V), and capacitance-voltage (C-V) data were obtained from the Schottky barriers, and carrier density profiles were determined from $1/C^2$ vs. V data taken at 1 MHz.

RESULTS AND DISCUSSION

The films grown on the single crystal substrates were epitaxial, mirror like and smooth. If a substrate contained a grain with another orientation, the film followed the orientation of the grain beneath it.

One advantage to ion-assisted doping is the ability to profile the carrier density in the films. By changing the ion current flux, the carrier density can be changed at will. Profiles can be made abruptly, with little surface segregation or diffusion occurring to flatten out the dopant profile (Fig. 2). Graded junctions can also be prepared by slowly varying the ion current. The ability to grade junctions is useful in preparing various kinds of devices with built in carrier density profiles.

Carrier density profiles, as determined from $1/C^2$ vs. V measurements on In Schottky barriers, were measured to see how the carrier density varied as a function of standard ion current flux (J_{ion}), for two different ion energies and growth temperatures (Figs. 3,4). For films grown at temperatures of 475°C and above, the carrier density was much lower ($\approx \text{mid } 10^{15} \text{ cm}^{-3}$) for any ion energy between 40 eV and 80 eV. The best results were obtained with an ion energy of 80 eV and a growth temperature of 450°C . The carrier density increased with (J_{ion}) to a maximum of $\approx 2 \times 10^{17} \text{ cm}^{-3}$, corresponding to a J_{ion} of $\approx 6.5 \times 10^{-2} \mu\text{A/cm}^2\text{-}\mu\text{m}$ at the substrate. Because of a variability in film thickness, the ion current flux at the substrate was divided by the film thickness, to standardize the ion currents. Increasing J_{ion} further led to a decrease in the carrier density. At the

FIG. 2

Carrier density as a function of film depth, giving an idea of the grading that is possible.

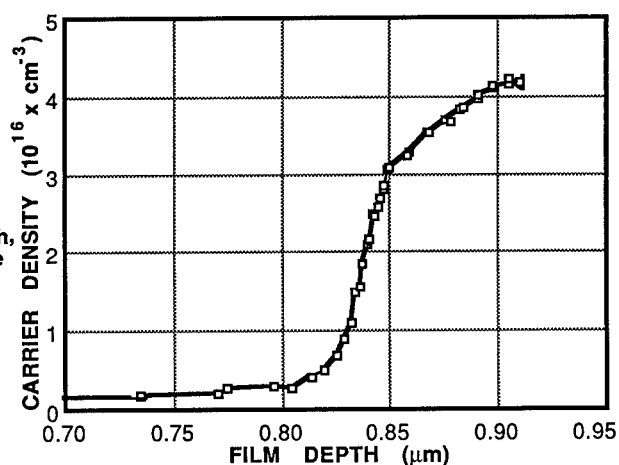


FIG. 3

Carrier density as a function of standard ion current for an ion energy of 60 eV and a growth temperature of 400 °C.

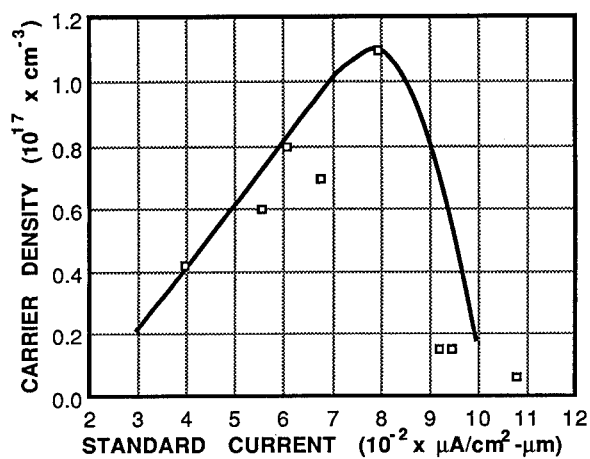
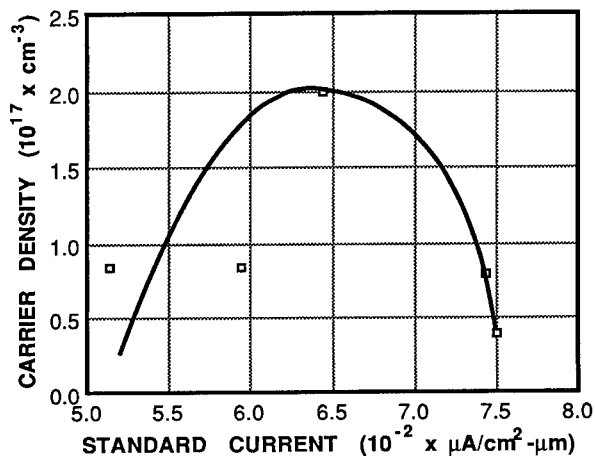


FIG. 4

Carrier density as a function of standard ion current for an ion energy of 80 eV and a growth temperature of 450 °C.



maximum, approximately 1.5% of the impinging ions were becoming electrically active in the film. At higher energies, corresponding to a greater likelihood for dopant incorporation, the maximum shifted toward lower J_{ion} . The C-V measurements on the films grown at 400 °C and at 450 °C showed two general trends. For films with J_{ion} smaller than the maximum the (C-V) measurements were on the whole were linear. The films with greater J_{ion} than the maximum, on the other hand, indicated a curvature in the (C-V) measurements. The corresponding carrier density profiles on the films with J_{ion} greater than the maximum showed a gradient in the carrier density with film depth. If the In Schottky barrier was removed with hydrofluoric acid, about 0.2 mm of the film etched off in a 0.1% bromine-methanol solution, and another In Schottky barrier reevaporated onto the etched surface, the same gradient was seen in the film. This same gradient remained after repeated etchings. Such gradients were generally not seen for the films with smaller J_{ion} than the maximum.

One possible explanation to account for the maximum in carrier density observed in Figs. 3 and 4 concerns the incorporation of the P. If P at first goes onto vacant Te sites, then substitutional doping occurs, and the carrier density increases with increased J_{ion} . When the Te vacancies are completely saturated with P, the P may then go onto Cd sites. P on Cd sites would be a donor, compensating the P on the Te sites and decreasing the carrier density. If the P on Cd sites acted as a deep donor, it would influence the C-V measurements and lead to the gradients that were observed in the carrier density profiles [20,21]. The carrier density in the films cannot be increased indefinitely. A maximum occurs, depending on the conditions of the film growth. For ion energies and growth temperatures of 80 eV and 450 °C, the maximum in carrier density was $2 \times 10^{17} \text{ cm}^{-3}$, the same maximum seen in single crystals using P as a dopant [11].

All the solar cells were prepared using the same two layer n-CdS window configuration. The p-CdTe film configuration varied, being of two types: 1) a single layer, with a constant carrier density, and 2) two layers, one with a constant carrier density, and the other, next to the CdS, without any doping. The best results to date were obtained with the CdTe films with the two layer configuration. J_{sc} 's, V_{oc} 's, and overall efficiencies were higher for the cells prepared with the two layer CdTe configuration (Table I). Preliminary deep level transient spectroscopy (DLTS) results have indicated the presence of deep levels near the middle of the gap in the ion-assisted doped films, levels that are not seen in either undoped films or in P doped single crystals grown from the melt. It should be mentioned that these DLTS measurements can only see deep levels in the lower portion of the gap, and hence any deep level in the upper half of the gap would not be seen. The deep levels could lead

TABLE I
Results for solar cells prepared from IAD p-CdTe.

Cell No.	CdTe Configuration	Ion Energy (eV)	Standard Ion Current ($\mu\text{A}/\text{cm}^2\text{-}\mu\text{m}$)	Growth Temp (°C)	Carrier Density ($10^{17} \text{ x cm}^{-3}$)	V_{oc} (volts)	J_{sc} (mA/cm^2)	Fill Factor	Efficiency % ^c
19	S ^a	60	0.072	400	0.7	0.36	5.5	0.51	1.0
35	S	80	0.069	425	2	0.31	7.0	0.55	1.2
37	T ^b	80	0.060	450	0.5	0.60	16.7	0.64	6.2
42	T	60	0.035	450	0.6	0.63	15.4	0.35	3.4

^a Single Layer

^b Two Layer

^c AM 1.5, 100 mW/cm²

to recombination, reducing the J_{sc} and hence the cell efficiency. The undoped CdTe layer in the solar cell not only had no deleterious deep levels, but also gave a larger depletion region, leading to a greater likelihood that photogenerated carriers would be collected.

CONCLUSIONS

Carrier density levels in p-CdTe epitaxial films up to $2 \times 10^{17} \text{ cm}^{-3}$ using ion assisted doping with P as the dopant have been achieved. The growth temperature and growth rate were 450°C and $0.15 \text{ } \mu\text{m}/\text{min}$ respectively, the ion energy was 80 eV and the standard ion current flux at the substrate was $6.5 \times 10^{-2} \text{ } \mu\text{A}/\text{cm}^2\text{-}\mu\text{m}$. Increasing J_{ion} further led to a decrease in the carrier density. About 1.5% of the impinging P ions became electrically active in the films near the maximum in the carrier density. For solar cells prepared from the p-CdTe films, the best results were obtained when a two layer CdTe film configuration was used. Deep levels in the doped p-CdTe films may lead to recombination and a decrease in cell properties.

ACKNOWLEDGEMENTS

We are grateful for the continued support of the Solar Energy Research Institute, and in particular the University Participation Program. Paul Sharps is supported by an AT&T Bell Labs fellowship.

REFERENCES

1. J. E. Greene, T. Matooka, J.-E. Sundgren, A. Rockett, S. Gorbalkin, D. Lubben, and S.A. Barnett, *J. Crystal Growth* **79**, 19 (1986).
2. J. E. Greene and S. A. Barnett, *Proc. Intl. Ion Engineering Congress-ISIAT '83 & IPAT '83, Kyoto* **1983**, 1049.
3. J. C. Bean and R. Dingle, *Appl. Phys. Lett.* **35**, 925 (1979).
4. Y. Ota, *J. Appl. Phys.* **51**, 1102 (1980).
5. H. Sugiura, *J. Appl. Phys.* **51**, 2630 (1980).
6. S. Shimizu and S. Komiya, *J. Vac. Sci. Technol.* **18**(3), 765 (1981).
7. G. Bajor and J. E. Greene, *J. Appl. Phys.* **54**, 1579 (1983).
8. Y. S. Tyan, F. Vazan, and T. S. Barge, *Proc. 17th IEEE Photovoltaic Spec. Conf.* **1984**, 835.
9. C. M. Fortmann, A. L. Fahrenbruch, and R. H. Bube, *J. Appl. Phys.* **61**, 2038 (1987).
10. A. J. Strauss, *Rev. Phys. Appl.* **12**, 167 (1977).
11. R. H. Bube, *Progress Report #2, SERI Subcontract XW-1-9330-1*, April 30, 1981.
12. R. N. Bicknell, N. C. Giles, and J. F. Schetzina, *Appl. Phys. Lett.* **49**, 1735 (1986).
13. J. F. Schetzina (private communication).
14. S. K. Ghani, N. R. Tasker, and I. B. Bhat, *Appl. Phys. Lett.* **50**, 900 (1987).
15. A. L. Fahrenbruch, A. Lopez-Otero, K. F. Chien, P. Sharps, and R. H. Bube, *Proc. 19th IEEE Photovoltaic Spec. Conf.* **1987**, 1309.
16. T. P. Thorpe, Jr., A. L. Fahrenbruch, and R. H. Bube, *J. Appl. Phys.* **60**, 3622 (1986).
17. W. Huber, A. L. Fahrenbruch, C. Fortmann, and R. H. Bube, *J. Appl. Phys.* **54**, 4038 (1983).
18. CdTe single crystals grown at the Stanford University Center for Material Research Crystal Synthesis Lab by R. Raymakers and R. Route.
19. T. Anthony, C. Fortmann, W. Huber, R. H. Bube, and A. Fahrenbruch, *Proc. 17th IEEE Photovoltaic Spec. Conf.* **1984**, 827.
20. L. C. Kimmerling, *J. Appl. Phys.* **45**, 1839 (1974).
21. J. J. Shiao, A. L. Fahrenbruch, and R. H. Bube, *J. Appl. Phys.* **59**, 2879 (1986).

ION IMPLANTATION OF BORON IN DIAMOND

G.S. SANDHU, M.L. SWANSON and W.K. CHU
 University of North Carolina, Department of Physics and Astronomy,
 Chapel Hill, NC 27599-3255, USA

ABSTRACT

It has been a challenge to inject dopant atoms onto diamond lattice sites by ion implantation, because of the complications of ion damage and defect clustering during annealing. We re-investigated this topic by implanting boron ions into an insulating natural diamond (type II-A) which was pre-damaged by carbon ion implantation. Both of the implantations were performed at liquid nitrogen temperature. The amount of pre-damage was adjusted to produce enough vacancies and interstitials in diamond to promote boron substitutionality during subsequent annealing. Samples were characterized by optical absorption and electrical measurements. It was found that optical absorption of the implanted samples strongly depends on the post implant annealing sequence. The activation energies obtained from electrical measurements match very closely to those due to boron atoms in natural p-type diamonds. Photoconductivity measurements showed that the fraction of remaining electrically active radiation defects in the implanted and annealed samples depends on the relative fluences of boron and carbon.

INTRODUCTION

Diamond based semiconductor devices may turn out to be of significant importance thanks to the unique physical and electronic properties of diamond. Few such devices have been realized till now because of difficulties in doping. Standard doping techniques such as diffusion or introduction of impurities during crystal growth are not applicable because of the high temperatures required for the former and the absence of any reliable technique for the latter. Therefore, the most promising way to dope diamond in a controlled manner is by means of ion implantation. So far, this method has yielded only limited success [1,2] because it requires finding annealing conditions which will drive the implants into electrically active sites and restore the diamond crystal structure, a task which is complicated by the tendency of the damaged diamond to turn into graphite [3,4]. When the ion dose is low enough to prevent graphitization, very few of the dopant atoms end up in electrically active sites [1,4].

It has been shown [5,6] that boron is responsible for the semiconducting properties of p-type natural diamond (type II-B). Consequently, it is very desirable to use boron as a test case for achievement of implantation doping of insulating natural diamonds (type II-A). A number of groups have attempted to achieve p-type doping in natural diamonds by ion implantation of boron at room temperature [1,2] as well as at high temperatures [2] (1200 °C), followed by annealing up to 1400 °C. It was observed that although high temperature implantation allowed higher doses of boron to be implanted with relatively less damage to the diamond lattice, it did not lead to higher fractions of dopant atoms in electrically active sites. This could result from the compensation by vacancy clusters in the lattice left in the aftermath of the implantation and annealing cycle. Once formed, these vacancy clusters are very difficult to eliminate.

Studies on carbon ion implantation into diamond have indicated that the radiation damage introduced during implantation shows characteristics which are strongly dependent on the sample temperature during the implantation [7,8]. It was suggested that this is caused by the non-diffusability of point defects created in the collision cascades at low temperatures (for example liquid nitrogen temperature), whereas at room and higher temperatures, at least some of the interstitial atoms diffuse out of the implanted layer leaving behind an excess of vacancies. This suggests the possibility of using low temperature implantation to enhance the probability of interstitial dopants occupying vacant lattice sites during the annealing subsequent to implantation, as suggested by Prins [9]. In addition to this, some of the 'frozen in' boron projectiles resulting from the previous boron cascades spontaneously combine with vacancies in the later collision cascades. In the present experiment, through the use of carbon implantation at 77 K we have injected vacancies at a range which overlaps subsequent boron implantation at 77 K, thereby enhancing the boron substitutionality.

EXPERIMENTAL

We have implanted insulating natural diamonds (type II-A) with carbon atoms with and without subsequent boron implantation at liquid nitrogen temperature. Type II-A diamonds of dimensions 3x3x0.25 mm were cleaned in hot chromic acid prior to implantation. After implantation some of the diamonds were subjected to isochronal annealing in vacuum (5×10^{-6} Torr) in the temperature range of 300 to 900 °C and others were subjected to rapid thermal anneal at 1100 °C for 2 minutes. The implantation energies were selected so as to match the range of boron ions to that of the vacancy distribution produced by the previous carbon implantation. This was achieved with the help of computer simulations using the TRIM-88 program [10]. The probability of boron atoms occupying vacant sites in the lattice is expected to be enhanced during irradiation and post implant annealing if most of the boron atoms are in the vacancy-rich region. This argument is not applicable in the case when only boron is implanted. The various implantations into type II-A diamonds are summarized in table I.

TABLE I

SAMPLE	IMPLANTED ION	ENERGY (keV)	DOSE (atoms/cm ²)
1	C	200	2×10^{15}
2	C	200	2×10^{15}
followed by	B	120	1×10^{14}
3	C	200	3×10^{15}
followed by	B	120	1×10^{15}
4	C	200	2×10^{15}
followed by	B	120	3×10^{14}
5	C	200	3×10^{14}
followed by	B	120	1×10^{15}

All the implantations were done at liquid nitrogen temperature, and the samples 3 and 5 were then brought to room temperature gradually. The samples 1, 2 and 4 were rapidly brought to 1100 °C from liquid nitrogen temperature.

All the optical measurements were performed at room temperature in the transmission mode. Photoconductivity measurements were done on samples 3 and 5 at room temperature using a Xenon lamp and a monochromator to scan the wavelength region between 350 nm to 700 nm.

RESULTS AND DISCUSSION

The optical absorption spectra of all the diamonds were measured before and after ion implantation followed by room temperature annealing, and after higher temperature annealing in some cases. The results of these measurements are shown in figures 1 and 2. Figure 1 compares the absorption spectrum of samples 1 and 2 in the UV-VIS region after RTA and furnace annealing. It shows the radiation damage induced absorption band (GR1) [5,11] after implantation. The gradual annealing of the radiation damage has been observed to appear as a decrease in absorption of the GR1 band and a more dramatic upward movement of the absorption edge at 220 nm [12]. The samples implanted with boron have higher transmission near the absorption edge which could result from compensation of GR1 defect centers by acceptor levels induced by substitutional boron. This behaviour has been observed in natural p-type diamonds containing substitutional boron atoms [13].

The absorption spectra for sample 4 at different stages of annealing in the far infrared region is shown in figure 2. The large absorption band around 2200 cm^{-1} is due to two phonon absorption by carbon atoms in the diamond lattice [14] and is present in all diamonds. The most intriguing feature of the spectra appeared at 1064 cm^{-1} after implantation and RTA. This absorption band was absent before implantation and is seen only when implantation was followed by RTA at 1100°C . It disappeared after 980°C annealing for 45 minutes in all the samples. This absorption was not observed when samples were gradually brought to room temperature after implantation and then annealed. We tentatively believe that the absorption band around 1064 cm^{-1} is related to nitrogen similar to the bands observed in the case of type IA natural diamonds containing large amounts of nitrogen [15]. The trace amounts of nitrogen clusters present in our samples presumably dissociated during RTA.

The results of the resistance versus temperature measurements done on samples 3 and 5 are shown in figure 3. The three orders of magnitude difference in resistance between samples 3 and 5 is significant in the light of the fact that they received the same boron fluence. The higher carbon fluence in the case of sample 3 produced larger numbers of vacancies which enhanced the probability of a boron atom to go into a substitutional site during the annealing cycle. Both of the samples demonstrated low activation energies at room temperature which are thought to be caused by conduction through the variable range hopping mechanism. However, a larger activation energy (0.37 eV) characteristic of p-type conduction by boron doped natural diamonds was observed at higher temperatures. The 0.86 eV activation in the case of sample 3 is due to interplay between substitutional boron atoms and residual defects in diamond [16].

Figure 4 shows the photo-resistance of sample 5 as a function of wavelength of the incident light. The decrease in the resistance in the presence of blue to u.v. light is caused by creation of holes by ionization of GR1 defect centers in diamond [17]. The most striking feature of the measurement was the increase in the resistance of the sample to values higher than dark resistance in the presence of yellow to red light with a peak at 600 nm. This could happen due to the light induced enhancement in the hole capture cross-section of GR1 defects in diamond. After the photoconductivity measurements, the dark resistance of the sample did not go to the same value as before the experiment. The resistance did however decrease to the normal value after the sample was annealed at room temperature for a few days. Further studies to determine the mechanism causing this phenomenon are in progress. However, the absence of any measurable photoconductivity for blue

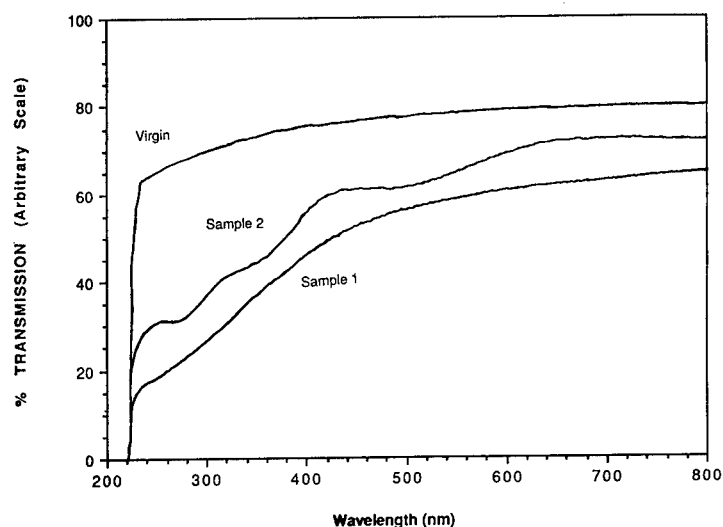


FIG. 1. U.V.-visible absorption spectra of samples 1 and 2 (see Table I) after implantations at 77K, RTA at 1100 °C and furnace annealing at 980 °C for 45 minutes. Sample 2 (implanted with boron) showed different absorption characteristics compared to sample 1 implanted with carbon only. For comparison, an absorption spectrum for an unimplanted sample is also shown.

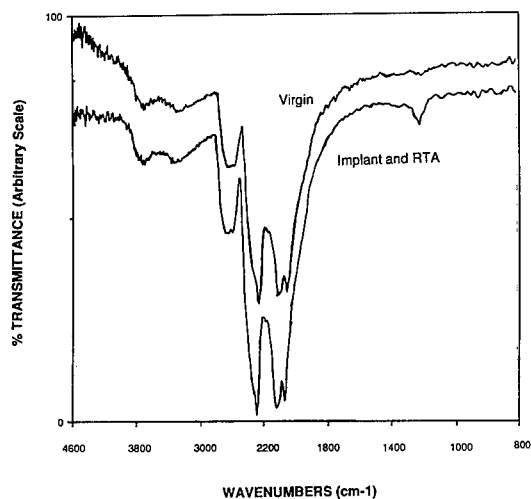


FIG. 2. I.R. absorption spectra of diamond implanted with 200 keV carbon ions and 120 keV boron ions. The sample was held at 77K during implantation and then rapidly brought to 1100 °C. The absorption peak at 1064 cm⁻¹ disappeared after 980 °C annealing for 45 minutes.

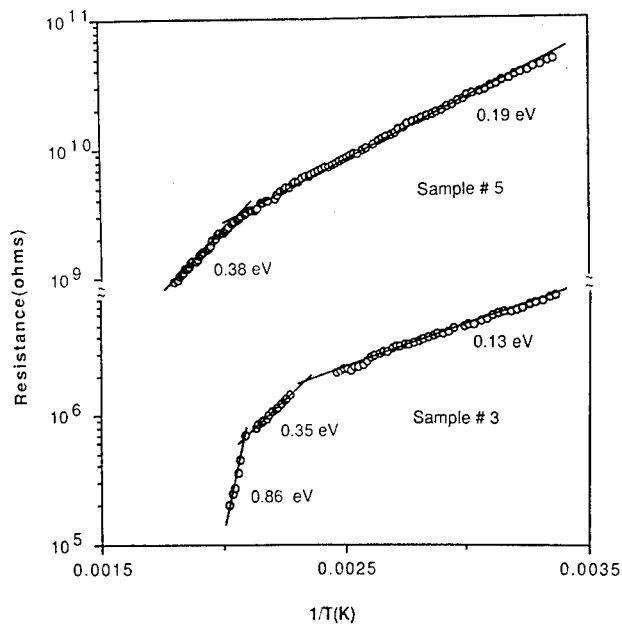


FIG. 3 Electrical resistance versus reciprocal temperature for samples 3 and 5 (see Table I) after furnace annealing and 1100°C RTA.

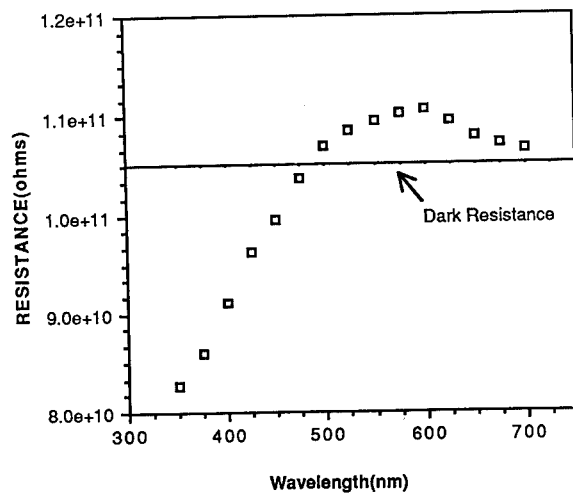


FIG. 4 Electrical resistance versus wavelength of incident light at room temperature for sample 5 after furnace annealing and 1100°C RTA.

to u.v. light in sample 3 indicates that the majority of the carriers are produced by substitutional boron acceptors and that most of the residual damage is compensated by boron acceptor centers.

CONCLUSIONS

We have shown that substitutional boron is produced by low temperature implantation followed by high temperature annealing. The optical absorption of implanted samples was found to strongly depend on the post implant annealing sequence as well as the relative dose of boron to carbon ions. Electrical measurements indicated the presence of substitutional boron in implanted samples. Photo-conductivity measurements indicated that the ratio of substitutional boron to residual vacancies is large and dependent on relative fluences. The number of residual vacancies in the lattice after annealing would tend to compensate p-type boron atoms and therefore would play a major role in determining the degree of success in doping of diamond. Further work to understand the results of IR absorption and photo-conductivity measurements are in progress.

ACKNOWLEDGEMENT

This work is supported by the Office of Naval Research contract N00014-87-K-0243. We have greatly benefited from constant communication with J. F. Prins at University of the Witwatersrand, South Africa during the course of this work. Ion implantation was done in the microelectronics laboratory at North Carolina State university and optical measurements were performed at Research Triangle Institute (RTI) of North Carolina.

REFERENCES

1. G. Braunstein and R. Kalish, J. Appl. Phys, **54**, 2106 (1983).
2. V.S. Vavilov, M.S. Gukasyan, M.I. Guseva, and E.A. Konorova, Sov. Phys. Semicond., **6**, 742 (1972).
3. R. Kalish, T. Bernstein, B. Shapiro and A. Talmi, Rad. Effects, **52**, 153 (1980).
4. G. Braunstein, A. Talmi, R. Kalish., T. Bernstein and R. Beserman, Rad. Effects, **48**, 139 (1980).
5. E.C. Lightowers and A.T. Collins, Diamond Research (Suppl. Ind. Diam. Rev.), p 14, J. Phys. D.: Appl. Phys. (1976).
6. A.T. Collins, A.W.S. Williams, J. Phys. C: Solid St. Phys. **4**, 1789 (1971)
7. J.F. Prins, Rad. Eff. Lett., **76**, 79 (1983).
8. J.F. Prins, T.E. Derry, and J.P.F. Sellschop, Phys. Rev. B, **34**, 8870 (1986).
9. J.F. Prins, Phys. Rev. **B38**. (to be published in 1988)
10. J.F. Ziegler, J.P. Biersak and U. Littmark, The Stopping Range of Ions in Solids, Pergamon, New York, 1985.
11. H.B. Dyer and L. du Preez, J. Chem. Phys., **42**, 1898 (1965).
12. G.S. Sandhu, M.L. Swanson, and W.K. Chu, IBMM '88, June 12-17, 1988, Tokyo, Japan.
13. J.F.H. Custers, Physica **20** 183-184(1954).
14. S.D. Smith and W. Taylor, Proc. Phys. Soc., **79**, 1142 (1962).
15. E.C. Lightowers and P.J. Dean, Diamond Research (Suppl. Ind. Diam. Rev.) p 14-21 (1964).
16. G.S. Sandhu, W.K. Chu, M.L. Swanson, and J.F. Prins, SPIE's 32'nd Annual International Technical Sym. on Optical and Optoelec. Appl. Sci. & Engg., 14-19 August 1988.(To be published in the proceedings)
17. R.G. Farrer and L.A. Vermeulen, J.Phys. C:Solid St. Phys. **5**, 2762-2767 (1972).

ION IMPLANTATION AND ION BEAM ANALYSIS OF LITHIUM NIOBATE

G. W. ARNOLD

Sandia National Laboratories, Ion-Solid Interactions Division 1111, Albuquerque, NM 87185-5800

ABSTRACT

Implantations of He and Ti were made into LiNbO_3 and the H and Li profiles determined by elastic recoil detection (ERD) techniques. The loss of Li and gain of H depends upon the supply of surface H (surface contaminants or ambient atmosphere). For 50 keV He implants into LiNbO_3 through a 200 Å Al film, the small Li loss is governed by the interface H. This is also the case for He implants into uncoated LiNbO_3 in a beam line with low hydrocarbon surface contamination; similar implants under conditions of greater hydrocarbon deposition result in proportionally larger Li loss and H gain in the implant damage region. The exchange is possible only for those He energies, i.e., 50 keV, where the damage profile intersects the surface. For Ti implants Li is lost with little H gain. For this case the Li loss is believed to result from radiation-enhanced diffusion. Where He implantation is used to establish waveguiding in LiNbO_3 , the presence or absence of H in the implanted region is crucial with regard to refractive index stability, due to the replacement of H by Li from the bulk.

INTRODUCTION

One of the means of establishing waveguiding in LiNbO_3 is ion implantation [1-4]. It has the advantage over proton-exchange (PE) and Ti-diffusion in that it is a low-temperature (< 100°C), relatively fast (depending on beam current) procedure, and lends itself to standard planar technology techniques. There are, however, some questions concerning the composition of the material after implantation and the index stability. These concerns are also common to the PE method [5] and have been addressed in previous work [6]. Elastic recoil detection (ERD) techniques were used in that work [6] to measure H and Li profiles after PE and their changes with time, temperature, and crystallographic orientation. H was found to replace Li in a 1:1 ratio and index instabilities were clearly due to the exchange, with time, of H in the exchange region with Li from the bulk. Previous work on He implantation [4] has shown that 50 keV He implants into LiNbO_3 can result in Li loss from the damage region due to interchange with incumbent surface H. This effect was noted only for 50 keV implants, where the damage profile intersects the surface, but not for 800 keV He implants where this is not the case. The near-surface extraordinary index, for implantations with 50 keV He, decreased at low fluences (< 1×10^{16} He/cm²) due to damage-induced positive lattice dilatation and increased at higher fluences due to the increasingly dominant effect of the simultaneously occurring Li loss. At higher He energies, where Li loss is not observed, most of the lattice damage is located at the end of the ion track. This lowered index region allows light to be trapped in the higher index region between the end of the track and the surface. The electronic energy deposition along the ion track has not been observed to result in Li loss. However, the extraordinary index in this region has been observed [7,8] to increase for 1-2 MeV He implants, consonant with a Li loss. It has been suggested [7,8] that this effect may be due to the movement of Li to a metastable lattice position with subsequent lattice relaxation. As a result of the success of the Ti-indiffusion process [9] for making waveguides in LiNbO_3 , Ti-implantation [2,3] has also been employed as a processing technique.

In the present paper, we have further examined the role of surface H in 50 keV He implantations and have investigated the changes in stoichiometry brought about by Ti-implantation. The results indicate that Li-loss as a consequence of Ti-implantation is due to radiation enhanced diffusion while extraordinary index changes which can occur with 50 keV He implantation are critically dependent on the presence of surface H.

EXPERIMENTAL

Most of the results obtained in the present study were obtained on LiNbO_3 from Crystal Technology. Implantations of He were made with a High Voltage Europa 400 keV ion implanter. Ti implants were performed using an 80 keV Lintott implanter. All implants were made at 5-7° off-axis and with beam currents such that the sample temperature did not exceed 100°C. In some cases a 200 Å Al film was deposited on the sample surface by electron-beam evaporation. The ERD measurements were carried out with a 24 MeV ²⁸Si beam generated by the Sandia EN tandem Van de Graaff accelerator. The Si beam was incident on the sample at

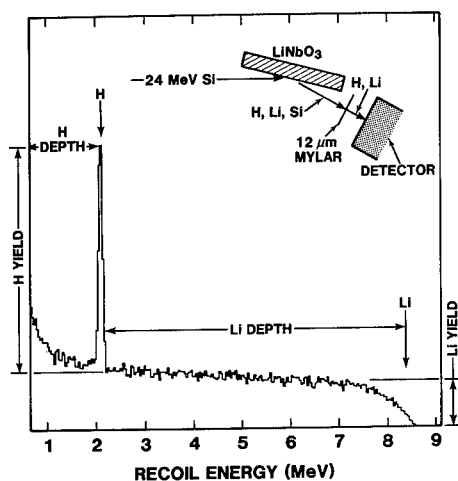


Fig. 1. Typical ERD spectrum showing the H and Li yields as a function of recoil energy for 24 MeV Si incident on unimplanted LiNbO₃. Inset shows the ERD geometry.

an angle of 15° with respect to the surface normal. The recoiled H and Li was detected at a forward scattering angle of 30° by a Si surface-barrier detector which was protected by a 12 μm Mylar range foil. This geometry is shown in Fig. 1 which also shows the raw H and Li ERD data for a LiNbO₃ sample. The depth resolution was on the order of 200 Å. Surface energies were established with suitable standards. The system yield was referred to a calibrated hydrated Si₃N₄ layer on Si.

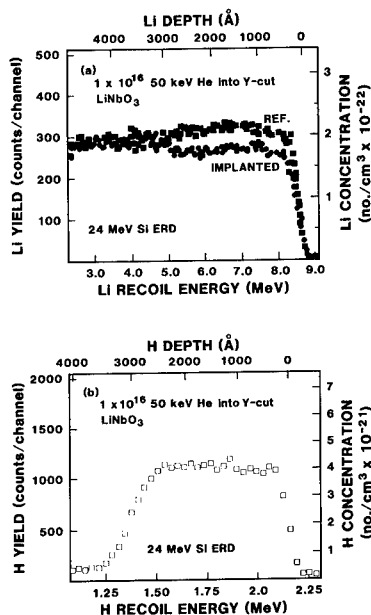


Fig. 2. (a) Li yield versus Li recoil energy/depth for unimplanted material and for a 1×10^{16} 50 keV He-implanted sample. (b) H yield versus H recoil energy/depth for the same implanted sample. The H in the reference sample was neglected.

RESULTS AND DISCUSSION

Figure 2 shows the Li and H profiles typical of those obtained in an earlier investigation [4] where the 50 keV He implants were made using a different implanter than that used in the present investigation. The H (gain)/Li(loss) ratio is near unity. The compositional changes occur to a depth of about 2000–2500 Å which is the expected damage depth. The surface of the sample was not coated. In contrast, for the same energy and fluence He implant, using the implanter described in the Experimental section, very little Li loss is observed and the incumbent H, after implantation, is about a monolayer coverage (spectrum not shown). The results for He implantation through a 200 Å Al layer are shown in Fig. 3. In this case more H is present at the Al/LiNbO₃ interface after film deposition and before implantation. After implantation, the interface H profile has the same areal density but is seen to extend further into the bulk. The Li profile shows a loss of Li over the same depth. The Li loss is about 3 times as large as the H gain. Measurements have also been made for Y- and Z-cut material and there appears to be some slight differences in compositional changes which may be attributable to the space available in the direction of the surface normal for Li/H interchange as illustrated in Fig. 4. The arrangement of the LiNbO₃ constituent atoms is such that the space available along the different crystallographic directions increases in the order Y > X > Z and the amount of Li lost by diffusion to the surface is found to vary in the same order with implantation. This crystallographic orientation effect was quite marked in the study of PE material [6].

Figure 5 shows the results for a 1×10^{16} Ti/cm² implant. No Al coating was deposited. The Li loss extends to a depth greater than expected from the ion range ($R_p + \Delta R_p \approx 1500$ Å) and the center of the damage depth (~800 Å) although the tail of the TRIM-86 [10] damage profile extends to ~2500 Å. The Li loss is clearly not balanced by a H gain; the H profile is

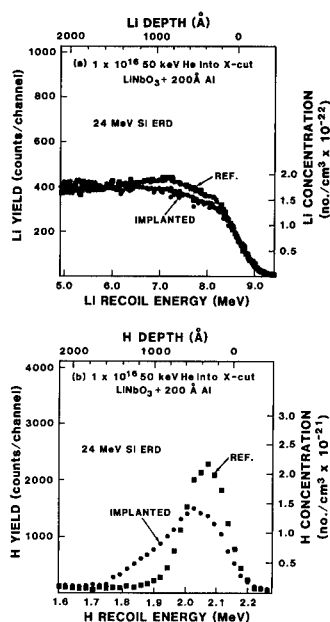
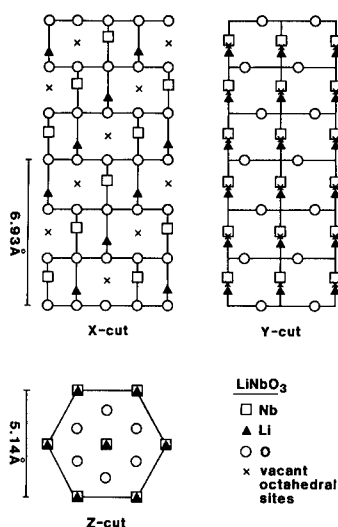
LATTICE SITE ARRANGEMENT IN LiNbO_3 

Fig. 3. (left) (a) Li yield versus Li recoil energy/depth for unimplanted material and for a 1×10^{16} 50 keV He-implanted sample. Both samples were coated with a 200 Å Al surface film. (b) H yield versus H recoil energy/depth for the same samples. Note the appreciable interface H on the reference sample.

Fig. 4. (right) Lattice site arrangements for X-, Y-, and Z-cut LiNbO_3 . (After Ref. 12).

about that expected for monolayer coverage. Figure 6 is for a multiple-energy Ti implant ($1 \times 10^{15}/\text{cm}^2$ at 35 keV, $3.3 \times 10^{15}/\text{cm}^2$ at 100 keV, 1×10^{16} at 200 keV). Although the loss of Li is greater, the H profile remains at surface-coverage concentrations.

These results for He and Ti implantation suggest that Li loss is governed by two separate mechanisms. In the case of 50 keV He, the loss of Li seems clearly dependent on the presence of H on the surface and a damage profile which intersects the surface. Under these circumstances H and Li can interchange throughout the damaged region thereby increasing the extraordinary index in that region. For higher He energies, where the damage profile is effectively buried, it is observed [7,8] that the index increases along the ion track but without observable Li loss. It has been suggested [7,8] that this might be explained if it is assumed that the lattice undergoes a new configuration brought about by the displacement of Li by electronic processes to a different lattice position with a subsequent relaxation. Whether this is a correct explanation or not, it seems clear that the index changes which can be brought about by implantation without the loss of Li (and gain of H) will be inherently more stable than those in which H incursion occurs due to loss of Li. This greater stability is predicated on the experience gained with PE LiNbO_3 [6] where instabilities occurred due to the interchange of bulk Li with H in the PE region after exchange. Low energy He implants, e.g., 50 keV, should, on this basis, be made under conditions where surface contamination during implantation is minimized.

The data show that Ti implants are accompanied by Li loss but without the replacement with surface H. The Li loss for this implantation condition can be understood as one which takes place due to a damage-induced increase in diffusion coefficient throughout the damaged region. A sink is established at the surface by preferential sputtering of Li from the first few atomic layers. This mechanism [11] has been used successfully to explain and model alkali-loss in alkali-silicate glasses as a consequence of heavy-ion ($Z > 1$) bombardment. The Li profiles produced by Ti-implantation (Figs. 5, 6) do not indicate a build-up of Li at the surface. Other Ti-implantation studies [2,3] have shown that a Li compound was formed at the surface after implantation and exposure to the atmosphere. These observations presumably indicate the interchange of H from the atmosphere with Li from the bulk after implantation and the

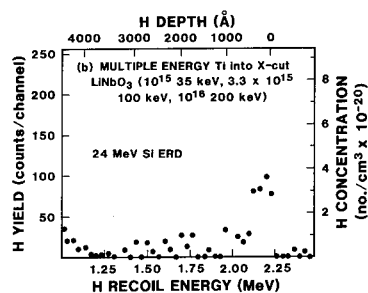
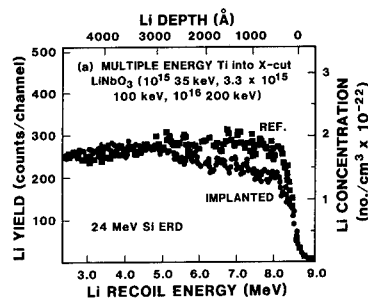
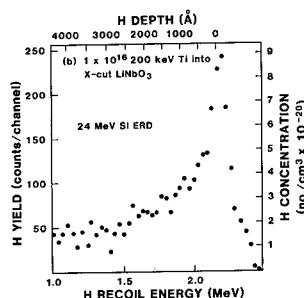
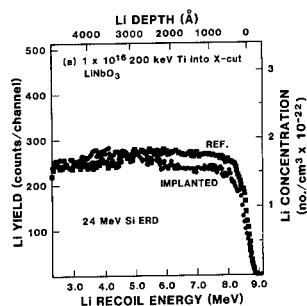


Fig. 5. (left) (a) Li yield versus Li recoil energy/depth for unimplanted material and for a 1×10^{16} 200 keV Ti-implanted sample. (b) H yield versus H recoil energy/depth for the same implanted sample. The surface H on the reference sample was negligible.

Fig. 6. (right) (a) Li yield versus Li recoil energy/depth for unimplanted material and for a multiple-energy Ti-implanted sample (1×10^{15} 35 keV, 3.3×10^{15} 100 keV, 1×10^{16} 200 keV). (b) H yield versus H recoil energy for the same implanted sample. The surface H on the reference sample was negligible.

subsequent chemical reactions with atmospheric constituents. We have observed that H or D implantations result in an accumulation of Li at the surface, presumably due to the chemical combination of the H/D with surface Li. The processing of Ti-implanted LiNbO_3 [2,3] involves a low-temperature implant followed by epitaxial regrowth of the damaged region by annealing at 1000°C so the complications of long-term interchange of Li and H are not expected.

CONCLUSIONS

These studies of He- and Ti-implanted LiNbO_3 have led to the following conclusions:

- (1) Li is lost from LiNbO_3 , when implanted with 50 keV He ions, if H is present as a surface contaminant. This loss, which is dependent on the surface H concentration, occurs due to the interchange of H and Li throughout the damaged region which extends to the surface. For higher He energies where the damaged region is buried beneath the surface, this interchange cannot occur. Instabilities can result from the further interchange of bulk Li with H in the exchanged region. Index changes along the ion track which occur even without the loss of Li may be due to a lattice rearrangement due to the displacement and relocation of Li by electronic processes.
- (2) Ti implantation results in Li loss but without the incursion of surface H. The movement of Li to the surface is probably brought about by an enhanced diffusion coefficient in the damage region and a sputter-induced sink at the surface. The virtual absence of H in the material should result in a more stable composition and index after implantation except for interactions with H and O from the atmosphere. However, these interactions should not be of great importance if the material is processed for epitaxial growth at high temperatures.

ACKNOWLEDGEMENTS

The expert assistance of D. P. Wrobel and C. A. Herr with respect to the ion implantations, and of N. D. Wing in the operation of the tandem Van de Graaff accelerator, is gratefully acknowledged. This work was supported by the U.S. Department of Energy under contract number DE-AC04-76P00789.

REFERENCES

1. G. L. Destefanis, J.-P. Gaillard, E. G. Ligeon, S. Vallette, B. W. Farmery, P. D. Townsend, and A. Perez, *J. Appl. Phys.* **50**, 7898 (1979).
2. B. R. Appleton, G. M. Beardsley, G. C. Farlow, W. H. Christie, and P. R. Ashley, *J. Mater. Res.* **1**, 104 (1986).
3. Ch. Buchal, P. R. Ashley, and B. R. Appleton, *J. Mater. Res.* **2**, 222 (1987).
4. S. A. M. Al-Chalabi, B. L. Weiss, K. M. Barfoot, and G. W. Arnold, *J. Appl. Phys.* **63**, 1032 (1988).
5. J. L. Jackel and C. E. Rice, *Proceedings of SPIE* **460**, 43 (1984).
6. G. W. Arnold, A. Carnera, G. Mazzi, and P. Mazzoldi, *Mat. Res. Soc. Proc. Vol. 101*, 453 (1988).
7. P. J. Chandler and P. D. Townsend, *Nucl. Instr. and Meth.* **B19/20**, 921 (1987).
8. E. Glavas, L. Zhang, P. J. Chandler, and P. D. Townsend, *Nucl. Instr. and Meth.* **B32**, 45 (1988).
9. M. N. Armenise, C. Canali, M. DeSario, A. Carnera, P. Mazzoldi, and G. Celotti, *J. Appl. Phys.* **54**, 62 (1983).
10. J. F. Ziegler, J. P. Biersack, and U. Littmark, *The Stopping and Range of Ions in Solids* (Pergamon, New York, 1985).
11. A. Miotello and P. Mazzoldi, *J. Phys. C* **16**, 221 (1983).
12. G. Götz and H. Karge, *Nucl. Instr. and Meth.* **209/210**, 1079 (1983).

ION IMPLANTATION OF KNbO_3 AND LiNbO_3 AT ELEVATED TEMPERATURES

CH. BUCHAL*, R. IRMSCHER* and P. GÜNTER**

* KFA-ISI, D-5170 Jülich, W. Germany

** ETH Hönggerberg, CH-8093 Zürich, Switzerland

ABSTRACT

Ion implantation, annealing and channeling of single crystalline samples of KNbO_3 and LiNbO_3 have been studied. Raising the substrate temperature above 600 K, greatly increases the tolerance of the crystals for high-dose implantation. In LiNbO_3 dynamic recrystallization has been observed for the first time.

INTRODUCTION

Oxide ceramic single crystals are very important for optical applications. They are needed for the fabrication of modulators, switches and other integrated optics devices. Their range of applications for linear and nonlinear optics is wide and rapidly growing. A recent review is found in Ref. 1.

A general prerequisite for device fabrication is the formation of an optical waveguide within the material. This is a region of enhanced optical index, which acts as a "light guide". Typically, microfabrication processes, as in use for microelectronics are transferred to oxide substrates for waveguide patterning. At this point, each material develops a surprisingly different response and this paper is concerned with the ion implantation properties of KNbO_3 , a strongly nonlinear material and LiNbO_3 , which now has become the workhorse for linear electrooptic and acoustooptic devices. LiNbO_3 is available commercially in large high quality wafers and it permits the application of in-diffusion or ion exchange techniques for local alterations of its optical indices (see Ref. 2 for a review). Also implantation of light ions has been studied extensively [3,4] and direct implantation of high doses of Ti for optical index enhancement has been used for optical device fabrication [5,6,7]. This tolerance for diffusion or high dose implantation together with its high Curie temperature of approx. 1400 K make LiNbO_3 a unique electrooptical material.

THE STRUCTURE OF KNbO_3 AND LiNbO_3

KNbO_3 crystallizes in the Perovskite structure with an almost cubic cell with K^+ ions at the corners, O^{2-} ions on the six faces and one Nb^{5+} ion near the center. Using Pauling's ionic radii, the lattice may be constructed from close-packed (111) planes, containing a uniform pattern of large K^+ -ions, surrounded by six O^{2-} ions of equal size (i.e.: 3 O^{2-} for each K^+). Between the hcp planes, small Nb^{5+} ions are inserted into octahedral positions between 6 O^{2-} ions [1,5]. Any diffusion of K^+ ions requires O^{2-} vacancies and vice versa, O^{2-} diffusion is hampered by K^+ ions within this hcp sublattice.

The LiNbO_3 structure is somewhat related, since it also consists of close-packed planes of large O^{2-} -ions. The small Nb^{5+} ions and the small Li^+ ions move into the numerous available octahedral positions, which really are interstitials within the oxygen sublattice [5,8]. Therefore the lattice of the large ions (O^{2-}) is uninterrupted by cations. If vacancies in the O^{2-} sublattice are available, the oxygen diffusion in LiNbO_3 is relatively easy. Due to their small size, Li^+ ions start diffusing via interstitials at 200°C. The high mobility of the Li ions and the undisturbed hcp oxygen sublattice with oxygen diffusion probably are responsible for the processing flexibility of LiNbO_3 .

On the other hand, the dense packing of anions and cations and their mutual interaction reduce diffusion in KNbO_3 . Thermal generation of vacancies is very limited if the structural phase transition at 703 K or even the low Curie temperature of 496 K are set as upper processing temperatures. This leaves KNbO_3 fairly unsuited for diffusion or ion exchange processing. As of now, only one successful experiment of permanent waveguide fabrication in KNbO_3 by He ion implantation has been performed [9]. Besides this, electrical field induced waveguiding has been used for integrated optics using KNbO_3 [10].

IMPLANTATION AT AMBIENT TEMPERATURE

Numerous electrooptical devices have been fabricated by Ti implantation into LiNbO_3 , while cooling the substrates to 80 K in order to retard diffusion before further processing [6,7]. For improved ease of fabrication, we have recently performed these high dose Ti implantations at room temperature and

fabricated very good waveguides by annealing immediately after implantation.

An analogous treatment of KNbO_3 substrates failed due to embrittlement and cracking. Fig. 1 shows a Ti depth profile in KNbO_3 after implanting $7.5 \times 10^{16} \text{Ti/cm}^2$ at 400 keV. This was the highest dose which could be administered without breaking the crystal. The observed profile agrees with TRIM 84 - calculations [11]. Channeling measurements show an amorphization depth of 4000 Å. Samples implanted with doses of 10^{15} , 10^{16} and $7.5 \times 10^{16} \text{Ti/cm}^2$ have been annealed at 693 K for 27 h in air in order to regrow the lattice but all samples showed unchanged disorder, when analyzed by channeling. Their optical appearance was colored and opaque. Fig. 1 also shows a small redistribution of Ti within the amorphized volume during the heat treatment. A striking difference is observed, if the same treatment is applied to LiNbO_3 , see Fig. 2. This crystal regrows very well from the completely amorphized state, even if the annealing temperatures are kept low [12]. On the other hand KNbO_3 does not show any lattice restoration, even at tenfold lower implant dose.

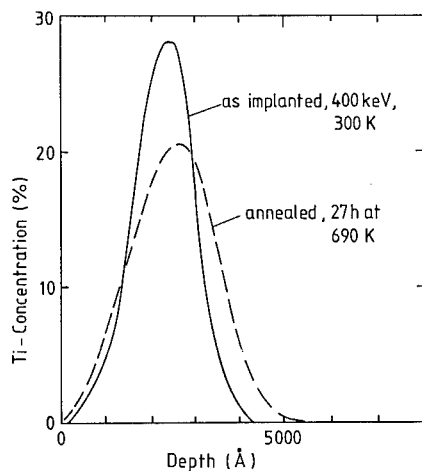


Fig. 1 SIMS measurements of implanted Ti profiles in KNbO_3 before and after annealing

IMPLANTATION AT ELEVATED TEMPERATURE AND DYNAMIC RECRYSTALLIZATION

In order to improve the tolerance of the KNbO_3 crystals against ion implantation, the substrate temperature was raised to 620 K. This was successful, as we could implant up to $2 \cdot 10^{17} \text{ Ti/cm}^2$ at 200 keV without breaking the samples. After implantation the sample appearance ranged from slightly darkened (10^{15} cm^{-2}) to metallic ($2 \cdot 10^{17} \text{ cm}^{-2}$) in the implanted areas, with shiny and undamaged surfaces. Ion channeling revealed total amorphization over the implanted depth even at the lowest dose of 10^{15} Ti/cm^2 . Search for regrowth in these samples by performing extended annealing programs is in progress.

Analogous experiments with LiNbO_3 displayed its superior processing flexibility and revealed for the first time dynamic annealing of an electrooptic ceramic. Dynamic defect annealing has been studied in Si [13] and is employed for the formation of buried epitaxial silicides [14,15]. It is observed that at temperatures exceeding 30 percent of the melting temperature, Si substrates retain a noticeable amount of crystallinity during implantation, and only if the substrate temperature is lowered, total amorphization will be achieved. A similar but less pronounced effect has been discovered by C.W. White during Cr implantation into Al_2O_3 , which had to be cooled to 80 K in order to achieve complete amorphization [16].

Fig. 3 demonstrates dynamical annealing at 620 K of Ti-implanted LiNbO_3 . A sample implanted with a dose of 10^{15} Ti/cm^2 displays a channeling yield completely identical to that of a virgin sample except at the surface, where inevitable oxygen losses during implantation form a few monolayers of disturbed structure. Raising the dose to 10^{16} Ti/cm^2 (200 keV) shows

- i) a further increased disturbed surface layer
- ii) point defects between 1000 and 1500 Å depth in the Nb sublattice (see peak around channel 700 in Fig. 3b)
- iii) a stronger dechanneling over the entire depth of the material, as is typical for beam spreading by extended defects (dislocations) in the implanted volume

Implants with doses up to $4 \cdot 10^{17} \text{ Ti/cm}^2$ (200 keV) have been performed and showed dynamical annealing of decreasing strength. At high doses the implanted Ti profiles start deviating from the standard form (Fig. 1) due to radiation enhanced diffusion during implantation. These samples have been

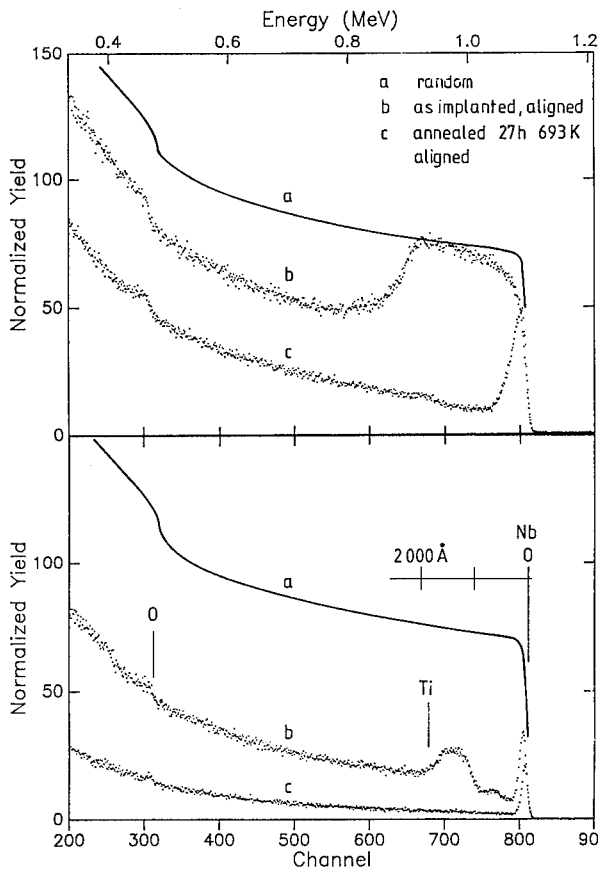


Fig. 2

Fig. 3

Fig. 2 He backscattering spectrum ($E_0 = 1.3$ MeV, normal incidence) of epitaxial regrowth of a LiNbO_3 sample, implanted with 10^{16} Ti/cm^2 (200 keV) at 80 K and annealed for 27 h at 693 K in air. The as-implanted spectrum shows total amorphization over a depth of 2500 Å. After annealing, regrowth is observed, except in the first 500 Å near the surface.

Fig. 3 Dynamical recrystallization of LiNbO_3 during implantation of Ti at 620 K

- a) Random for reference
- b) 10^{16} Ti/cm^2 , as implanted, aligned
- c) 10^{15} Ti/cm^2 , as implanted, aligned

subjected to subsequent annealing (90 min at 1273 K in wet oxygen ambient) and displayed good waveguiding [17].

SUMMARY

"Hot implantation" into LiNbO_3 and KNbO_3 shows promising processing potential especially for high-dose applications. During this process LiNbO_3 shows strong dynamic recrystallization comparable to that observed in silicon.

ACKNOWLEDGEMENT

We gratefully acknowledge the SIMS-measurements by H. Beske and H. Holzbrecher, stimulating discussions with K. Kohlhof, technical support by M. Gebauer, and optical measurements by T. Bremer.

REFERENCES

1. P. Günter (Edt.), Electrooptic and Photorefractive Materials, Springer Proc. in Phys. 18 (Berlin 1987).
2. R.B. Hunsperger, Integrated Optics: Theory and Technology (Springer, Berlin-New York, 1985).
3. G. Götz, Radiation Eff. 98, 189 (1986).
4. P.D. Townsend, Rep. Progr. Phys. 50, 501 (1987).
5. Ch. Buchal in: Structure-Property Relations in Ion-Beam Surface Modified Ceramics ed. C.J. McHargue (Kluwer 1989).
6. Ch. Buchal, P.R. Ashley, D.K. Thomas, B.R. Appleton, Mat. Res. Soc. Symp. Proc. 88, 93 (1987).
7. P.R. Ashley, W.S.C. Chang, Ch. Buchal, D.K. Thomas to be publ. in IEEE Lightwave Techn. (1989).
8. R.S. Weis, T.K. Gaylord, Appl. Phys. A37, 191 (1985).
9. T. Bremer et al., Ferroelectr. Lett. 9, 11 (1988).
10. J. Baumert, C. Walther, P. Buchmann, H. Melchior, P. Günter in "Integrated Optics" ed. H. Nolting, R. Ulrich (Springer, Berlin 1985) p.44
11. J. Biersack, L. Haggmark, Nucl. Instr. Meth. 174, 257 (1980) and recent updates of computer codes
12. D.B. Poker, D.K. Thomas, Mat. Res. Soc. Symp. Proc. 100, 311 (1988).
13. R.G. Ellimann et al., Nucl. Instr. Meth. B19/20, 435 (1987).
14. A.E. White et al., Appl. Phys. Lett. 50, 95 (1987).
15. K. Kohlhof, S. Mantl, B. Stritzker, W. Jäger, Nucl. Instr. Meth. B in print (1988/89).
16. C.J. McHargue et al., Nucl. Instr. Meth. B10/11, 569 (1985).
17. Ch. Buchal and T. Bremer, to be published.

EFFECT OF MICROSTRUCTURE ON THE SHEET RESISTANCE OF ION-BEAM DEPOSITED ZnO THIN FILM

SALIMAN A. ISA, P.K. GHOSH AND P. G. KORNREICH
Department of Electrical and Computer Engineering,
Syracuse University, Syracuse, New York 13244

ABSTRACT

ZnO thin films were deposited by ion-beam sputtering technique. Preliminary results show that the films are stoichiometric and crystalline in nature. The microstructure of ZnO films obtained depends very much on the process parameters. Among these parameters is the substrate temperature whose effect has been carefully examined.

ZnO films were deposited with substrate temperatures ranging from 200°C to 350°C. We observed that the sheet resistance of the films varies with their microstructure. In this investigation, a sheet resistance of 6.6 Mega-ohms per square is measured on a dense film deposited at a substrate temperature of 325°C.

We present in this paper a correlation between the film's microstructure and stoichiometry with some of its electrical properties.

Introduction

Zinc Oxide material has long been recognized as having the strongest piezoelectric effect of any non-ferroelectric material. As a vacuum deposited thin film, it finds considerable application especially in piezoelectric transducers for the generation and detection of bulk and surface acoustic waves at microwave frequencies [1][2]. For this type of application, the piezoelectric quality film must meet the basic characteristic of high electrical resistivity and an oriented crystalline structure that yields a very strong piezoelectric effect. These properties in turn depend on the film's microstructure. The microstructural properties of the film are also dictated by the deposition parameters.

The Zinc Oxide (ZnO) thin films discussed here have been deposited by an ion-beam bombardment sputtering technique. The adjustable parameters considered in this investigation are the sputtering gas composition (Argon + Oxygen), sputtering pressure, and substrate temperature. The effect of these parameters on the microstructure and the sheet resistance of the films have been investigated. The scanning Electron Microscopy (SEM) has been used to examine the microstructure, and a four point probe also has been used to measure the sheet resistance of the films.

Experimental Procedures

ZnO thin films have been deposited by sputtering from a high grade (99.99) ZnO ceramic target. The sputtering system used is the Veeco 3-inch micro-etch system utilizing the Kaufman type of ion source. The ion source is located on a Vesco 7700 series high vacuum pumping station.

The ions needed for sputtering are provided by the ion source where an arc discharge between the cathode and the anode takes place. The positive ions of the plasma are extracted and accelerated by a special multi-grid system with the resulting homogenous, collimated and monoenergetic ion beam bombarding the surface of the ZnO target located below the grid assembly in the vacuum chamber. Sputtering then takes place and the sputtered atoms are deposited on the substrate which is located close to the target. The film growth rate which is a function of the number of sputtered atoms arriving at the substrate is directly related to the energy and current density of the ion beam. We can control these parameters via the arc discharge, magnetic field strength, and the accelerating potential.

The system is prepared for sputtering by sputter-etching the target for about 1/2 hour before the substrates are placed in the system. After mounting clean substrates, the system is then pumped down to an initial background pressure of 5×10^{-6} torr. In hot deposition scheme (i.e., increased substrate temperature), this process is followed by heating the substrates to a temperature of about 300°C so that the substrates can degas sufficiently prior to film deposition. The substrate temperature is then set to the desired temperature for that deposition run. The system chamber pressure is also stabilized at 2×10^{-4} torr by the introduction of sputtering gas into the system. Sputtering is then initiated using the typical parameter values in table i below.

Table i

Parameter	Current	Voltage
Cathode	20A	7.5V
Arc discharge	1.0A	38V
Magnet	0.8A	28V
Suppressor	6mA	-200V
Acceleration	30mA	1Kv
Neutralizer	4A	16V

Experimental Results and Discussions

In general, processes of a film deposition involve phase transformations. The formation of a thin film can be understood by a study of the thermodynamics and kinetics of these phase transformations.

However, the resulting film properties are dictated by the processes which occur during film growth. In particular, the properties of sputtered Zinc Oxide thin films are highly dependent on the process parameters. Some of the parameters we have considered in this investigation are the substrate temperature, sputtering pressure, and sputtering gas composition. The variation in the microstructure of the film with these parameters, and the resulting variation in the sheet resistance of the film were investigated.

A mixture of Argon and Oxygen is used as the sputtering gas. The oxygen content is mainly to help maintain the stoichiometry of the growing film. Our experimental results of the deposited ZnO films indicate that the stoichiometry of the films increases with increasing Oxygen content in the

sputtering gas. The same results also show that the more stoichiometric the film is the higher the sheet resistance. But increase in the Oxygen content of the sputtering gas results in decrease in the growth rate. This can be understood since Oxygen is a poor sputterer (less atomic weight). The effect of Oxygen content on the film quality was first investigated with no substrate heating. Films were deposited with Oxygen contents of 0, 25, 40, and 60%. Sheet resistance in the range 290 Ohm per square and 3.2 kilo-Ohm per square were measured. However, these films exhibit poor structural quality.

The sputtering pressure is normally a system dependent function. It does however, control the fiber grain size and structural density of the film. A set of depositions were carried out to determine the sputtering pressure for the system. The acceleration voltage of 1KV, gas composition of 75% Ar.+25% O_2 and 5 hrs. deposition time were maintained. The pressure was varied between 4×10^{-5} torr and 5×10^{-5} torr. We chose these limits from the standpoint of view of system stability and film quality. During this investigation, we discovered that a sputtering pressure of 2×10^{-4} torr is not only suitable for the smooth operation of the system, it also results in good quality films as evident from films deposited at higher substrate temperatures. Fig. 1 shows the SEM photograph of film deposited at a pressure of 2×10^{-4} torr and no substrate heating. This

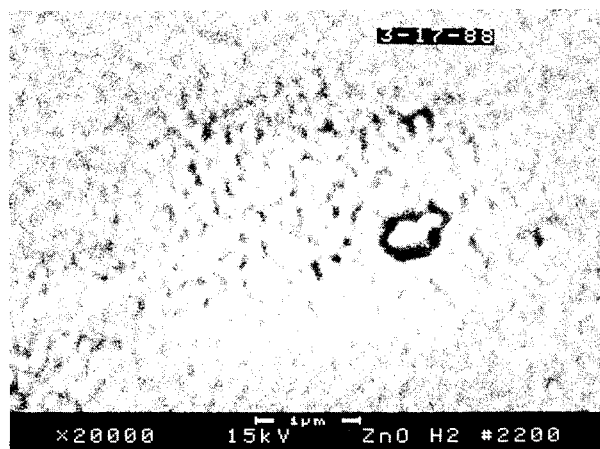


Fig.1

film appears cloudy and demonstrated poor structural quality. One of the main reasons for this is the lack of adatom mobility of the arriving species on the substrate surface. Fig.2 is the graph showing the sheet resistance of films deposited under various pressures and no substrate heating. There is not much change noticed in the sheet resistances of the films (2.3 to 2.9 kilo-Ohm per square).

It has long been established, by earlier workers [3], [4], that the quality of ZnO films produced are highly dependent on the substrate temperature. Many workers have also reported that substrate temperatures in the range 200°C to 400°C, depending on the system, produce good quality ZnO films. We have used this as a guide in the hot depositions scheme. The hot depositions

were carried out under constant pressure (2×10^{-4} torr), constant acceleration voltage (1KV), and constant deposition time (8 hrs.). The substrate temperature was varied (at increments of 25°C) between 200°C and 350°C . The results of the SEM photographs indicate that films produced at higher substrate temperatures have good microstructural qualities (fine grain sizes, dense structure) and good physical properties (clear and smooth upper surfaces). Our data on the sheet resistance

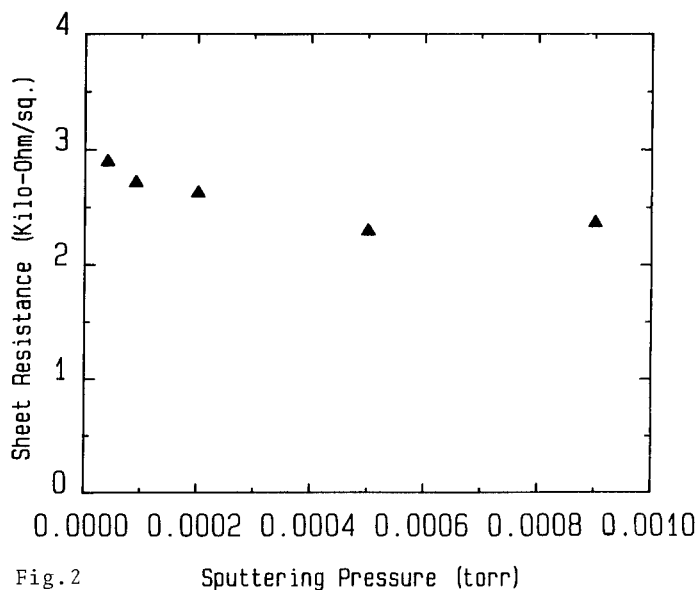


Fig.2

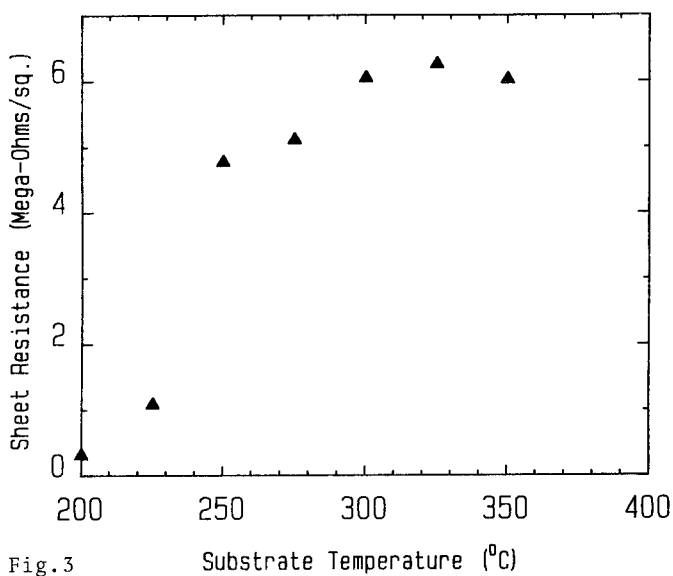


Fig.3

measurement (fig.3) also show a trend of increasing sheet resistance with increasing substrate temperature. In particular, a substrate temperature of 325°C produced the best film. The SEM photograph of such film is as in fig.4. Notice the clear and smooth upper surface of this film as compared to that of fig.1.



Fig.4

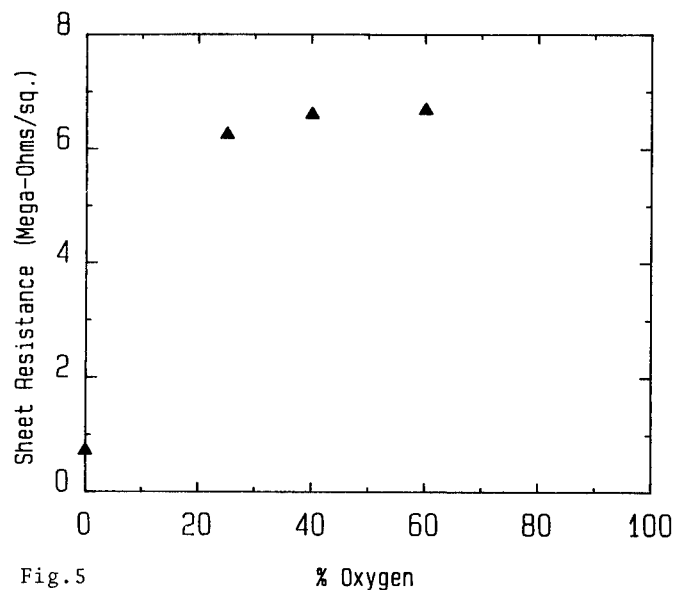


Fig.5

The variation in the sheet resistance of the film deposited at substrate temperature of 325°C and at varying Oxygen content is also shown in fig.5. As shown, the highest sheet resistance of 6.6 Mega-Ohm per square was measured from the film deposited with Oxygen content of 40%. The Auger analysis performed on

the same film also revealed its stoichiometric nature.

Conclusion

The dependence of the sheet resistance of Zinc Oxide thin films on their microstructures has been examined. These films were deposited with the Ion-Beam sputtering technique. The effect of various deposition parameters like the pressure, gas composition, and substrate temperature were investigated. Our results show that lower pressures favor good quality films and in particular, a pressure of 2×10^{-4} torr was found quite suitable from the standpoint of system stability and film quality. Increase in Oxygen content of the sputtering gas demonstrated an increase in the stoichiometry, better microstructural quality, and increase in the sheet resistance of the film. Although too much Oxygen content results in decreased growth rate. The effect of the substrate temperature was also quite noticeable. The quality of the structural properties of the films increases with increasing substrate temperature (within the limits used in this investigation). The best film obtained during this investigation (in terms of the sheet resistance) was deposited at a substrate temperature of 325°C and a gas composition of 60% Argon + 40% Oxygen. In particular, a sheet resistance of 6.6 Mega-Ohm per square was measured.

Acknowledgement

The authors would like to thank Don Calabrese of RADC/RBRE Griffis AFB, Rome, New York who has provided the SEM photographs for the examination of the microstructure, and to Lois Walsh of the same address, for performing the Auger analysis of the films.

References

1. E. Dieulesaint, and D. Royer, Elastic Waves in Solids, (John Wiley & Sons Publishers, New York 1980), p. 427.
2. O. Yamazaki, T. Mitsuyu and K. Wasa, IEEE Transonics. Ultrason. 27(6), 369-379, (1980).
3. F. S. Hickernell, IEEE. Proc. 64(5), 631-635, (1976).
4. B. T. Khuri-Yakub, G. S. Kino, and P. Galle, J. Appl. Phys. 46(8), 3266-3272, (1975).

EFFECT OF ION BOMBARDMENT ON THE DOPANT DIFFUSION DURING
REACTIVE ION ETCHING (RIE) OF DIELECTRIC FILMS DEPOSITED ON SILICON

K. SHENAI, N. LEWIS, G. A. SMITH, and B. J. BALIGA*

General Electric Corporate Research and Development Center, River Road,
Schenectady, NY 12301

ABSTRACT

We report on the results obtained from a study conducted to understand the effect of reactive ion etching (RIE) of oxide films on the dopant diffusion in ion-implanted silicon. Thermally grown oxide films on silicon were plasma etched in a CHF_3/CO_2 plasma. The residual silicon surface damage created during plasma etching was removed by employing a low ion-bombardment, two-step surface plasma cleaning process. The samples with oxide films etched in a wet chemical etchant provided the control for evaluating the effect of the RIE process. The samples were implanted with boron and boron was activated under various conditions to form p-n junctions to obtain a range of boron doping profiles and junction depths. Some boron doped samples were implanted with arsenic to form a heavily doped n^+ region at the silicon surface. The resulting doping profiles were analysed using spreading resistance profiling (SRP), four-point probe measurements, and secondary ion-mass spectrometry (SIMS) to understand the activation, diffusion, and precipitation of various dopants. Detailed transmission electron microscopy (TEM) analysis was used to study the microstructural effects. It was observed that plasma etching of the oxide films prior to the formation of boron diffused surface regions in silicon resulted in significant changes in boron diffusion. For low boron implant doses, plasma etched silicon surfaces resulted in retarded boron diffusion. For high boron implant doses, plasma etched silicon surfaces lead to enhanced boron diffusion.

INTRODUCTION

Submicron VLSI technologies demand low thermal budgets (product of dopant diffusivity and diffusion time) to facilitate the formation of shallow junctions [1-3]. Various techniques to form heavily doped shallow source/drain junctions have been proposed in the literature [4-6]. It has been pointed out that the characteristics of the surface damage and surface point defects play an important role in determining the properties of shallow junctions in silicon [7]. There is, however, limited experimental data and understanding pertaining to the formation of deep-diffused junctions in silicon [8]. The diffusion of dopants at extremely high temperatures in excess of 1100°C is usually required to form phosphorus and boron doped deep junctions used in silicon VLSI and smart power applications [9-12]. Predeposition as well as ion-implantation of impurities have been used to form deep diffused junctions in silicon. The microstructural properties of surface damage and defects generated during the incorporation of dopants by these two techniques may not be similar.

* Present Address: Department of Electrical and Computer Engineering, North Carolina State University, Raleigh, NC 27695-7911

The incorporation of dopants in silicon is generally performed using a self-aligned mask etched in polysilicon and/or in dielectric films. Reactive ion etching (RIE) of polysilicon and dielectric films in a gaseous plasma is becoming a premiere approach for fabricating densely-packed device and interconnect features [13-15]. The near surface silicon damage created by ion-bombardment during plasma etching may lead to poor wafer yield, degrade contact resistance [16], and cause adhesion problems because of the polymeric residues left at the silicon surface. The incorporation of extraneous elements into silicon resulting from the decomposition of gas species in the plasma may cause severe reliability problems, especially in MOS-gated devices [17,18]. Silicon surface damage removal using isotropic, low ion-bombardment dry etching is becoming an attractive alternative to wet etching of damaged silicon surface [19,20].

In many applications, the silicon surface condition may not favor a surface plasma cleaning process to remove the residual silicon surface damage caused by high ion-bombardment plasma processing. Ion-implantation or predeposition and diffusion of dopants will create additional silicon surface damage and will generate point defects. The interaction of damage created during plasma processing and that generated during the incorporation of dopants into silicon may have important bearing on the dopant diffusion and final doping profiles in silicon.

In this paper, we demonstrate for the first time that plasma etching of oxide films in a CHF_3/CO_2 plasma to perform selective boron implantation results in significant changes in boron diffusion. The samples with wet etched oxide films provided the process control required to isolate the effects of plasma etching on boron diffusion. The boron implantation dose and activation were varied to obtain a range of boron doping profiles. Detailed electrical, chemical, and microstructural analyses were performed to understand the surface morphological changes occurring from plasma processing and the resulting boron depth profiles.

EXPERIMENTAL PROCEDURE AND RESULTS

The silicon substrates used in this study were $\langle 100 \rangle$ oriented and $\approx 1 \times 10^{16} \text{ cm}^{-3}$ phosphorus doped on top of which 500 Å of gate SiO_2 was thermally grown at 1000°C under TCA oxidation conditions. The gate oxide on some samples was plasma etched in a 80 % $\text{CHF}_3/20$ % CO_2 plasma (total flow of 25 sccm, 35 mTorr, 0.22 W/cm^2) using silicon as the etch stop. This etch chemistry provided a 10:1 etch rate selectivity of oxide to silicon [16]. The wafers were cleaned in an oxygen plasma for 30 min. to remove any polymeric surface residue on silicon. Following a standard RCA clean for 30 sec. in 1 % HF, the silicon surface was dry cleaned using a two-step plasma cleaning sequence [16,21]. First, the native oxide grown on the silicon surface was removed using a 80 % $\text{CHF}_3/20$ % CO_2 plasma for 30 sec. following which approximately 300 Å of silicon was dry-etched in a 50 % $\text{SF}_6/50$ % Cl_2 plasma for 30 sec (total flow of 30 sccm, 65 mTorr, 0.08 W/cm^2). The gate oxide on some samples was wet etched in 5 % HF. Wet etched wafers served as controls to monitor the surface damage induced by the plasma process.

Following standard RCA clean in 1 % HF for 30 sec., all samples were implanted with 140 keV boron. Boron implant dosage was varied from $6 \times 10^{13} \text{ cm}^{-2}$ to $1 \times 10^{14} \text{ cm}^{-2}$. The boron implant was activated at 1100°C in nitrogen ambient for various durations. Prior to boron diffusion in nitrogen, the samples were thermally oxidized in a dry oxygen ambient by ramping the furnace temperature from 700°C to 1050°C . The oxide film thickness was measured to be in the range of 220 Å - 250 Å. The oxide film on the silicon surface was wet etched and the silicon sheet resistance was measured after the 1100°C anneal. Tables 1 and 2 list the average sheet resistance R_{SH} of boron diffused silicon as a function of process variants. The sheet resistance was measured using the four-point probes and corresponds to an average value of twenty measurements across 4 in. diameter silicon wafers. The sheet resistances of dry and wet etched samples

are within the accuracy of four-point probe measurements. These results suggest that two different boron activations and silicon etching had negligible effect on the final silicon sheet resistance.

Table 1. Sheet resistance of boron implanted silicon
diffused at 1100°C for 180 min.

Sample #	Etch Type	Boron Dose (cm^{-2})	R_{SH} (Ω/\square)
1	dry	6×10^{13}	543
4	dry	7×10^{13}	480
7	dry	8×10^{13}	423
10	dry	1×10^{14}	391
13	wet	6×10^{13}	564
16	wet	7×10^{13}	477
19	wet	8×10^{13}	435
22	wet	1×10^{14}	386

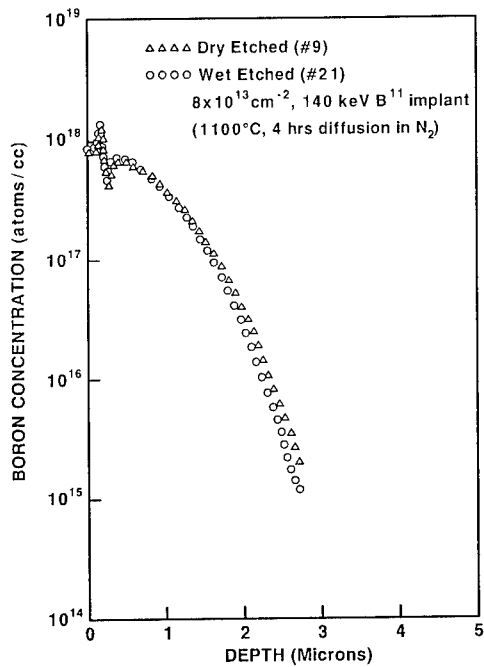


Fig. 1 SIMS depth profiles of boron for dry (# 9) and wet (# 21) etched samples. The boron implant dose was $8 \times 10^{13} \text{ cm}^{-2}$, and the implant activation was 1100°C for 4 hrs. in nitrogen

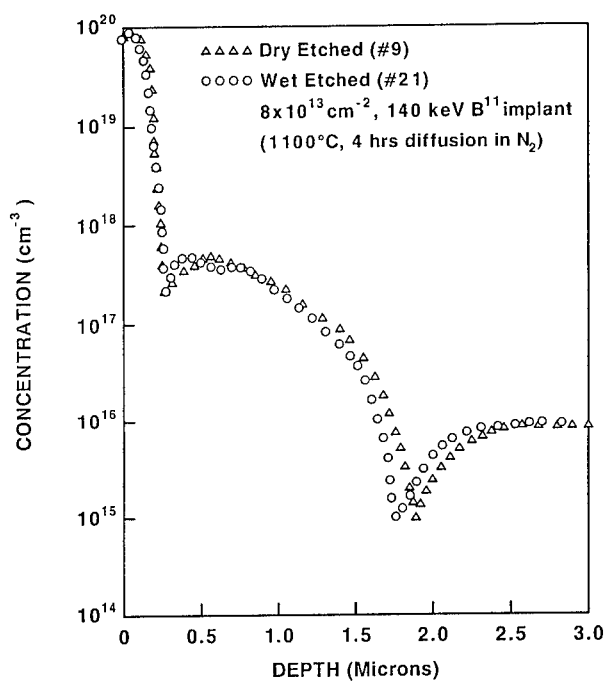


Fig. 2 Spreading resistance profiles of arsenic implanted, dry (# 9) and wet (# 21) etched samples. The boron implant dose was $8 \times 10^{13} \text{ cm}^{-2}$ and the boron activation was 1100°C for 4 hrs. in nitrogen.

Table 2. Sheet resistance of boron implanted silicon
diffused at 1100°C for 240 min.

Sample #	Etch Type	Boron Dose (cm^{-2})	R_{SH} (Ω/\square)
3	dry	6×10^{13}	542
6	dry	7×10^{13}	471
9	dry	8×10^{13}	432
12	dry	1×10^{14}	368
15	wet	6×10^{13}	524
18	wet	7×10^{13}	470
21	wet	8×10^{13}	431
24	wet	1×10^{14}	367

Following the p-base diffusion, some samples were standard RCA cleaned in 1 % HF for 5 sec. and implanted with $5 \times 10^{13} \text{ cm}^{-2}$, 180 keV arsenic and diffused at 900°C in nitrogen for 60 min. Prior to diffusion in nitrogen ambient, the samples were oxidized in a 700°C - 900°C ramp in dry oxygen. The resulting thermally grown oxide thickness was $\approx 60 \text{ \AA}$. The oxide grown on the samples was wet etched and the sheet resistance of arsenic diffused silicon was measured to be equal to $38 \Omega/\square$ using the four-point probes.

Detailed spreading resistance profiling (SRP) and secondary ion-mass spectrometry (SIMS) analyses were performed on all samples. Typical SIMS depth profiles of boron for wet and dry etched samples are shown in Fig. 1 for samples 9 and 21, boron implanted with $8 \times 10^{13} \text{ cm}^{-2}$, respectively. The spike at the silicon surface corresponds to arsenic diffused region. The boron implant was activated at 1100°C for 4 hrs. in nitrogen. The SIMS profiles show that the chemically active boron extends deeper into silicon for the dry etched sample. The spreading resistance profiles of the same samples are shown in Fig. 2 which suggest a substantial enhancement of boron diffusion for the plasma etched sample. Similar results were obtained for samples implanted with higher boron dosages. A comparison of SRP and SIMS depth profiles suggests nearly a 70 % activation of boron. For samples implanted with lower boron doses, plasma etched silicon surface lead to retarded boron diffusion. Detailed transmission electron microscopy (TEM) analysis was performed on various specimens. The TEM analysis reveals no residual damage left at the silicon surface after boron diffusion.

SUMMARY

It is shown that near surface silicon damage caused by ion bombardment during plasma processing leads to changes in boron diffusion. Most of the damage at the silicon surface was removed using a low-dose ion-bombardment, isotropic, two-step plasma process. In this work, only the effect of plasma etching thermally grown oxide films in a CHF_3/CO_2 plasma was studied. Plasma etching in other gas species needs to be investigated to understand in more detail the role of defect chemistry on dopant diffusion.

REFERENCES

- [1] M. Y. Tsai and B. G. Streetman, *J. Appl. Phys.*, 50, 183 (1979).
- [2] J. F. Gibbons, *Proc. IEEE*, 66, 9 (1972).
- [3] W. K. Hofker, *Phillips Res. Rep.*, no. 8, 1 (1975).
- [4] A. E. Michel, in *Rapid Thermal Processing*, vol. 52, T. O. Sedgwick, T. E. Seidel, and B. Y. Tsaur, Eds., *Mater. Res. Soc. Symp. Proc.* (Pittsburgh, PA), 3 (1986).
- [5] R. T. Hodgson, J. E. E. Baglin, A. E. Michel, S. M. Mader, and J. C. Gelpey, in *Energy Beam-Solid Interactions and Transient Thermal Processing*, vol. 23, J. C. C. Fan, and N. M. Johnson, Eds., *Mater. Res. Soc. Symp. Proc.*, 253 (1984).
- [6] J. F. Marchiando, P. Roitman, and J. Albers, *IEEE Trans. Electron Devices*, ED-32, 2322 (1985).
- [7] R. B. Fair, in *Proc. First Int. Symp. Advanced Materials for ULSI*, vol. 88-19, M. Scott, Y. Akasaka, and R. Reif, Eds., *The Electrochemical Soc. Symp. Proc.*, 123 (1988).
- [8] S. Al-Marayati, K. Shenai, N. Lewis, and B. J. Baliga, in *Extended Abstracts of the ECS Fall Meeting*, Abstract No. 317, vol. 88-2, 461 (1988).

- [9] See, for instance, *VLSI Technology*, S. M. Sze, Ed., McGraw Hill: New York (1983).
- [10] B. J. Baliga, *Modern Power Devices*, Wiley: New York (1987).
- [11] K. Shenai, C. S. Korman, B. J. Baliga, and P. A. Piacente, General Electric TIS Rep. No. 87CRD207 (1987).
- [12] V. Rumennik, *IEEE Spectrum*, 22, 42 (1985).
- [13] J. W. Coburn, *Plasma Etching and Reactive Ion Etching*, American Vacuum Soc. Monograph Series, New York (1982).
- [14] R. A. Gottscho, *Phys. Rev. A.*, 36, 2233 (1987).
- [15] R. J. Saia, B. Gorowitz, D. Woodruff, and D. M. Brown, in *Proc. Sixth Symp. Plasma Processing*, G. S. Mathad, G. C. Schwartz, and R. A. Gottscho, Eds., *The Electrochemical Soc. Symp. Proc.*, 173 (1987).
- [16] K. Shenai, S. Al-Marayati, R. Saia, N. Lewis, G. A. Smith, and B. J. Baliga, in *Proc. Seventh Symp. Plasma Processing*, G. S. Mathad, G. C. Schwartz, and D. W. Hess, Eds., *The Electrochemical Soc. Symp. Proc.*, vol. 88-22, 179 (1988).
- [17] G. S. Oehrlein, S. W. Robey, J. L. Lindstrom, K. K. Chan, M. A. Jaso, and G. J. Scilla, in *Proc. Seventh Symp. Plasma Processing*, G. S. Mathad, G. C. Schwartz, and D. W. Hess, Eds., *The Electrochemical Soc. Symp. Proc.*, vol. 88-22, 151 (1988).
- [18] K. Shenai, P. A. Piacente, R. Saia, W. Hennessy, C. S. Korman, and B. J. Baliga, to appear in *IEDM Technical Digest*, (1988).
- [19] M. J. Kim, S. S. Cohen, D. M. Brown, P. A. Piacente, and B. Gorowitz, in *IEDM Technical Digest*, 134 (1984).
- [20] J. L. Mauer, J. S. Logan, L. B. Zielinski, G. S. Schwartz, *J. Vac. Sci. Technol.*, 15, 1734 (1978).
- [21] B. Gorowitz, R. J. Saia, and E. W. Balch, in *VLSI Electronics: Microstructure Science*, N. G. Einspruch, S. S. Cohen, and G. Gildenblatt, Eds., Academic Press: New York, vol. 15, ch. 4, 159 (1987).

ELECTRICALLY CONDUCTING THIN FILMS BY ION IMPLANTATION OF PYROLYZED POLYACRYLONITRILE

R. A. BASHEER
General Motors Research Laboratories
Warren, MI 48090-9055

ABSTRACT

Heat treatment of polyacrylonitrile leads to products with semiconductor to metal like conductivities. The electrical properties of these materials are further modified by ion implantation. It is noted that the conductivity ($\sim 10^{-7} (\Omega \text{ cm})^{-1}$) of heat treated Polyacrylonitrile at 435°C (PAN435) increases upon ion implantation with As^+ , Kr^+ , Cl^+ or F^+ reaching a maximum value of $8.9 \times 10^{-1} (\Omega \text{ cm})^{-1}$ at a dose of $5 \times 10^{16} \text{ ion/cm}^2$ and an energy of 200 KeV for the case of F^+ implantation. On the other hand, ion implantation of the more conducting heat treated PAN at 750°C (PAN750) leads to a decrease in the electrical conductivity of the material. It is proposed that the conductivity modifications are primarily due to structural rearrangements induced by the energetic ions. Specific chemical doping contribution to conductivity is noted for halogen implantation in PAN435. The temperature dependence of conductivity of PAN heat treated at 750°C suggests a two path conduction, namely, a three dimensional variable range hopping conduction and a metallic conduction. After ion implantation, the conductivity-temperature dependence is interpreted in terms of a variable range hopping conduction mechanism.

INTRODUCTION

Interest in organic conducting polymers has been growing steadily ever since the discovery of high electrical conductivity in doped polyacetylene. A large number of experimental and theoretical investigations have been devoted to the elucidation of the electronic properties of doped polyacetylene [1]. However, the chemical instability of this material under ambient conditions has prompted interest in air stable conductive polymers as an alternative to polyacetylene. In this regard, I have been investigating thin film materials obtained by pyrolysis of polyacrylonitrile. The products of pyrolysis are stable in air and show a wide range of conductivity depending on the degree of carbonization or "graphitization" which is controlled by the applied pyrolytic temperature. Furthermore, it has been shown that such materials may be chemically doped by electron acceptors or donors to produce higher conductivities [2]. In this study, ion implantation is employed as an alternative method in the modification of the electrical conductivity of pyrolyzed Polyacrylonitrile products. This was motivated by recent studies showing dramatic increases in the electrical conductivity of certain insulating and semiconducting polymers [3]. Experiments involving implantation with ions of varied chemical reactivities and ionic masses were conducted in order to ascertain the nature of ion implantation induced conductivity modifications in these materials.

Experimental

Polyacrylonitrile thin films (0.3 - 1 μ) were deposited from dimethylformamide solution onto a thermally grown silicon dioxide on a silicon wafer. After complete removal of the solvent at 200°C under vacuum in a tube furnace, the samples were pyrolyzed at the desired temperature (435 - 750°C) for a period of ten hours. The ion implantation experiments were conducted at room temperature at an energy of 200 KeV and doses ranging

between 5×10^{14} - 5×10^{16} ion/cm². The implanted ions were Kr, As, Cl and F. Chemical doping was performed by exposure to iodine vapor in an evacuated tube at room temperature for several hours. The electrical contacts to the films were made from a silver-epoxy compound which provided ohmic behavior. For convenience, the samples were labeled with PAN (for polyacrylonitrile) followed by the pyrolysis temperature and then by the chemical symbol of the implanted ion.

RESULTS AND DISCUSSION

Pyrolysis of PAN under vacuum leads to large conductivity increases as shown in Table I. These values are in good agreement with those reported in

TABLE I
Conductivities of Pyrolyzed, Ion Implanted,
and Iodine Doped PAN Films

Sample	Dose (ion/cm ²)	Conductivity (Ω cm) ⁻¹	Sample	Dose (ion/cm ²)	Conductivity (Ω cm) ⁻¹
PAN435	--	1.4×10^{-7}	PAN550	--	9.5×10^{-3}
PAN435I ₂ *	--	2.1×10^{-3}	PAN550I ₂ *	--	4.7×10^{-2}
PAN435Kr	5 E 16	1.1×10^{-1}	PAN550As	1 E 16	3.2×10^{-1}
PAN435As	5 E 16	1.4×10^{-1}	PAN750	--	9.1
PAN435Cl	5 E 16	6.3×10^{-1}	PAN750I ₂ *	--	16.7
PAN435F	5 E 16	8.9×10^{-1}	PAN750As	1 E 16	3.7×10^{-1}

* Chemical doping

the literature [2]. The rise in conductivity is associated with the thermal conversion (cyclization) of PAN chains first to a singly conjugated polyimine structure and eventually to a doubly conjugated ladder structure at temperatures between 200 - 500°C [2]. Thermal treatment at higher temperatures leads to carbonization or "graphitization" of the material (Fig. 1). The conductivity of these pyrolyzed products may be further

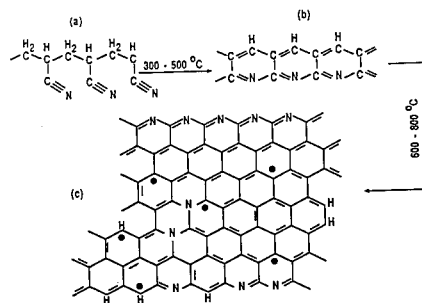


Fig. 1 Pyrolytic structural evolution of PAN.

modified by chemical doping with oxidizing or reducing species. This is shown in Table I for doping with iodine vapor at room temperature. The product of pyrolysis at 435°C (PAN435) exhibited the largest rise in conductivity upon iodine doping, whereas, the product of pyrolysis at 750°C (PAN750) was the least affected with this treatment. The increase in conductivity is associated with a complex formation [4] between the iodine and the heteroaromatic structure given in Fig. 1b. The small conductivity increase in the case of PAN750 is also due to iodine complex formation with

the heteroaromatic structure, remnants of which exist after pyrolysis at 750°C. After several hours in an air environment, the conductivity of the iodine doped products decreased by about an order of magnitude as a consequence of iodine desorption.

In comparison, ion implantation of PAN435 provided larger conductivity increases than those obtained by iodine doping. The measured average conductivities of ion implanted PAN435 are given in Table I for the implantation of krypton, arsenic, chlorine, and fluorine ions. The choice of Kr and As was motivated by their differing chemical reactivities and their similar ionic masses. It is clear that while all ions raised the conductivity of PAN435, krypton, which is chemically inert, produced a conductivity similar to that obtained by the somewhat more reactive arsenic ion. Since the ionic masses of arsenic and krypton are similar, this observation suggests that the increase in conduction is due to structural transformations. The energy density in the track of the ion determines the degree of molecular rearrangements. The greater the mass of the ion (at constant energy, dose rate, and dose) the higher is the energy density and the greater is the number of reactive intermediates produced. Thus, for ions of comparable masses, as in the case of arsenic and krypton, equivalent levels of structural rearrangements are produced in the material giving rise to the observed similar conductivity values.

Implantation of chlorine and fluorine ions, which are more chemically active, yet which possess smaller ionic masses than krypton, were somewhat more effective in raising the conductivity of PAN435. Unless there are some offsetting effects in the cases of krypton and arsenic implantations, the higher conductivity noticed for halogen implantations is at least partly due to chemical doping effects by these elements. The dose-conductivity dependence of ion implanted PAN435 is typical of those observed in ion irradiated polymers [3], Fig. 2. The conductivity of PAN435 increases sharply in the dose range between 1×10^{15} - 5×10^{15} ion/cm². This is followed by more modest increases at higher doses, indicating the onset of saturation. The behavior of the more conducting PAN750 towards ion implantation was entirely different from that noted for PAN435. The electrical conductivity actually decreased upon ion irradiation. A typical

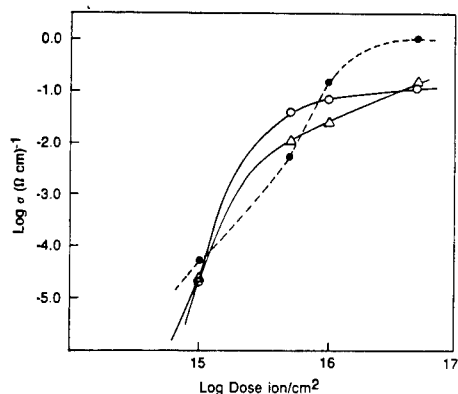


Fig. 2 Conductivity-dose dependence for PAN435 implanted with (●) F, (○) Kr, and (Δ) As.

example is given in Fig. 3 showing a comparison of the conductivity-dose dependence for the case of arsenic ion implantation at 200 KeV. The conductivity is given in terms of the ratio of the conductivity after implantation (σ_I) to the conductivity before implantation (σ_0). Also shown in Fig. 3 is the effect of implantation on the intermediately conducting PAN550. In this case, the material exhibited an initial decrease ($\log \sigma_I/\sigma_0$ is negative) in conductivity at an irradiation dose of 1×10^{15} ion/cm².

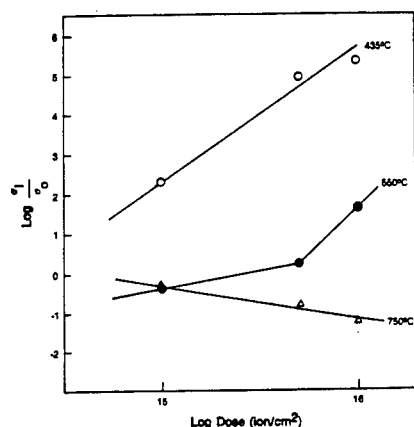


Fig. 3 The Ratio of conductivity (σ_I/σ_0) as a function of dose in arsenic implanted - pyrolyzed PAN.

followed by an increase at higher doses. In fact, the actual plot of the conductivity-dose relationship (not given in text) shows a convergence of the conductivity values of the three materials at higher doses. These results suggest some similarity in the structures of the final implantation products of PAN435, PAN550 and PAN750.

The increase in the electrical conductivity of PAN435 may be primarily due to increased carrier density. Wasserman et al. [3] have recently reported that the magnitude of the thermopower in arsenic implanted (1×10^{16} ion/cm²) PAN is very small (3 mV/K) which is consistent with a large concentration of low mobility carriers ($\mu \leq 10^{-3}$ cm²/V sec). Increases in carrier density have also been noted for ion irradiation of carbon films [5]. However, increased carrier mobility due to radiation induced structural transformations may also be a contributing factor to the enhanced conductivity of PAN435. The low conductivity value ($\sim 10^{-7}$ (Ω cm)⁻¹) and the large energy band gap (3 eV) [6] associated with the heteroaromatic structure of PAN435 (Fig. 1b) are due to the presence of a nitrogen atom in the aromatic ring. Reynaud et al. [7], in their study of the electronic structure of pyrolyzed PAN, established a correlation between the departure of nitrogen atom and the formation of graphite-like orbitals. They also showed that the nitrogen atom in such structures inhibit the formation of extended delocalized electronic states. In other words, the nitrogen atom does not favor a strong π -orbital overlap, and thus provides some degree of electronic localization.

Elemental analyses using ESCA have shown that ion irradiation causes a significant reduction in the nitrogen content of PAN435 [8]. This eventually results in a material the structure of which can be envisaged as composed of a randomly crosslinked network of polynuclear aromatic units similar to amorphous carbon. In this regard, the infrared spectrum of ion implanted PAN435 exhibited broad overlapping absorptions in the 1300-1600 cm⁻¹ range, similar to the spectrum of PAN pyrolyzed at 750°C [8]. The broad absorption features in this region are consistent with a fused aromatic structure. It should be noted, however, that the size or the average effective unit length of the polynuclear aromatic conjugation in the irradiated material is limited by the presence of defect sites (implanted ion, bond saturation, dangling bonds, etc.) in the material. The carrier mobility in this carbon-like product can be greater than that provided by the heteroaromatic structure proposed for the unirradiated material. The decrease in conductivity of PAN750 (Fig. 3) may be explained in terms of the conversion of the extended polyconjugated graphite-like structure (Fig. 1c) into a new structure for which the effective unit length

of polyconjugation is small compared to that of the parent unirradiated material. Thus, although the carrier density increases upon implantation (3), the mobility of these carriers is significantly reduced by virtue of increasing charge localization. A similar explanation may be provided for the behavior of PAN550 towards ion implantation. The structure of PAN550 before implantation consists of an extended polyconjugated graphite-like configuration and of a significant proportion of the much less conducting heteroaromatic fused ring structure [2]. The initial decrease in the conductivity of PAN550 upon implantation at a dose of 1×10^{15} ion/cm² can then be explained in terms of radiation induced conversion of the conducting polyconjugated pattern into a disordered or a more defective and slightly less conducting system. In other words, this low ion implantation dose is sufficient to distort the π -electron configuration of the polyconjugated system but not high enough to transform the remaining heteroaromatic part of the structure into that state (polyconjugated state with defects). However, as the applied dose increases, the total structure is gradually converted into the more conducting disordered polyconjugated network structure.

The behavior of conductivity as a function of temperature provided additional information regarding the structures of the pyrolyzed material before and after ion implantation. The conductivity of PAN750 and arsenic implanted PAN750, plotted as a function of $T^{-1/4}$ is given in Fig. 4. The

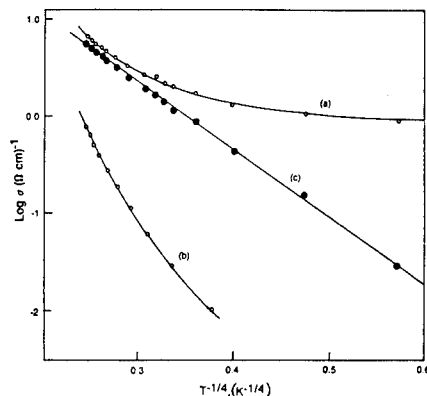


Fig. 4 The temperature-dependence of conductivity of PAN750 (a and c) and arsenic implanted PAN750 at a dose of 1×10^{16} ion/cm² (b).

conductivity of PAN750 shows a temperature independent characteristic at low temperatures. The estimated value of the temperature independent conductivity ($0.89 (\Omega \text{ cm})^{-1}$) is subtracted from the data of Fig. 4a, and the results are plotted as a function of $T^{-1/4}$ in Fig. 4c. Thus, the total conductivity of PAN750 can be described by an equation of the form

$$\sigma = \sigma_m + \sigma_T = \sigma_m + \sigma_1 \exp[-(T_0/T)^{1/4}]$$

where σ_m is the temperature-independent conductivity and $\sigma_1 \exp[-(T_0/T)^{1/4}]$ is the temperature-dependent conductivity derived for a variable range hopping conduction mechanism [9]. In other words, pyrolysis of PAN at 750°C produces a material with structural inhomogeneities providing two conducting paths; one is metallic with extended electronic states (graphite-like) for which the conductivity has no temperature dependence, and the other is a disordered system where the conduction is by a variable range hopping mechanism.

A different conductivity-temperature behavior is displayed by the arsenic implanted PAN750, indicating an implantation induced structural transformation. Of particular importance is the absence of temperature

independent conductivity which clearly suggests a significant reduction in the volume fraction of the extended electronic states (the metal like regions) in the material. This observation together with the noted decrease in the room temperature conductivity by two orders of magnitude demonstrate that ion implantation of pyrolyzed PAN results in a breakup of the polyconjugated graphite-like structure. In this case, the conduction may be through a variable range hopping mechanism [9]. The fact that the relationship in Fig. 4b is not exactly linear may indicate some metallic conduction contribution, presumably, due to the presence of small fraction of unaffected graphite-like polyconjugated structure. It should be noted that the data of Fig. 4b did not follow a simple thermal excitation dependence, nor did it follow the functional form of a thermally activated one-dimensional hopping conduction mechanism, $\log \sigma \propto T^{-1/2}$ [10]. This is unlike the recent finding of Wasserman et al. [3] that the conductivity of arsenic implanted pristine PAN exhibited a temperature dependence of the form $\log \sigma \propto T^{-1/2}$. This may be due to structural differences in the resulting implanted products of pristine and pyrolyzed PAN.

REFERENCES

1. J. C. W. Chien, Polyacetylene, Academic Press, Orlando, FL (1984).
2. S. Kazama, T. Hashimoto and A. Takaku, Synth. Met., 14, 153 (1986).
3. B. Wasserman, G. Braunstein, M. S. Dresselhaus, and G. E. Wnek, Mat. Res. Soc. Symp. Proc., 27, 423 (1984).
4. N. R. Lerner, Polym., 24, 800 (1982).
5. T. Venkatesan, R. C. Dynes, B. Wilkens, A. E. White, J. M. Gibson and R. Hamm, Nucl. Inst. Meth. B1, 599 (1984).
6. J. L. Bredas, B. Themans, and J. M. André, J. Chem. Phys., 78, 10, 6137 (1983).
7. C. Reynaud, C. Boiziau, C. Juret, S. Leroy, and Perreau, Synth. Met., 11, 159 (1985).
8. R. A. Basheer and S. Simko, unpublished data.
9. F. N. Mott, Phil. Mag., 19, 835 (1969).
10. V. Ambegaokar, B. I. Halperin, and S. J. Langer, Phys. Rev. Lett., 30, 699 (1973).

MICRO-RBS ANALYSIS OF MASKLESSLY FABRICATED STRUCTURES

A. Kinomura, M. Takai, T. Matsuo, M. Satou*, M. Kiuchi*, K. Fujii*
and S. Namba

Faculty of Engineering Science and Research Center for Extreme Materials,
Osaka University, Toyonaka, Osaka 560, Japan

*Government Industrial Research Institute Osaka, Ikeda, Osaka 563, Japan

ABSTRACT

Rutherford backscattering (RBS) analysis of small-sized structures, fabricated by laser chemical vapor deposition (LCVD) with a focused laser beam and ion implantation with a focused ion beam (FIB), has been performed by a microprobe with focused 1.5 MeV helium ions. Micro-RBS spectra and RBS-mapping images revealed a local distribution of masklessly deposited Mo layers on GaAs and local doses of masklessly implanted Au atoms in Si.

INTRODUCTION

Maskless fabrication processes of semiconductor integrated circuits have recently attracted considerable attention due to increasing requirements for repairing and customizing circuits [1]. A focused ion beam (FIB) system has made it possible to masklessly implant ions in semiconductors with minimum spot sizes close to ion ranges [2]. Local chemical-reactions induced by focused laser or ion beams have also realized maskless etching or deposition in micro areas from several microns down to submicron [3,4].

Such local interactions or reactions have unique characteristics which cannot be observed in processes for large areas [1]. Therefore, a microprobe technique suitable for characterization of the local structures is needed. An RBS analysis can provide information on elemental distribution in depth without etching a substrate. Although a spot size of conventional RBS systems ranges about 0.5 - 1 mm, recent developments of MeV ion microprobe have realized a minimum spot size of several microns down to submicron [5-7]. The MeV ion microprobe has made it possible to perform not only RBS analysis of micro areas but also three-dimensional elemental mapping which cannot be obtained by electron microprobes [6-9].

In this study, RBS analyses of Mo lines, delineated by a maskless LCVD process, and gold lines, masklessly implanted by a focused ion beam system, were made by the microprobe with focused 1.5 MeV helium ions. Micro-RBS spectra of the delineated line and elemental mapping image by an RBS-mapping method were obtained. Distributions of the deposited Mo and local dose of implanted Au atoms were discussed.

EXPERIMENTAL PROCEDURE

Figure 1 shows the schematic diagram of the analytical system. The microprobe was realized with piezo-driven objective collimators and a magnetic quadrupole doublet. 1.5 MeV helium ions or protons supplied by a Van de Graaff accelerator can be focused down to a spot sizes of $0.9 \mu\text{m} \times 1.2 \mu\text{m}$ and $1.2 \mu\text{m} \times 1.4 \mu\text{m}$, respectively. A spot size used in this study was $3 \mu\text{m} \times 3 \mu\text{m}$ to increase a beam current for obtaining good statistics in the RBS analysis. The beam current was 100 pA for this spot size. The detailed parameters of the ion optics used in this study has been published elsewhere [6,7,10].

A target position to be analyzed is roughly aligned, with manually controllable micrometers by monitoring an optical microscope with a

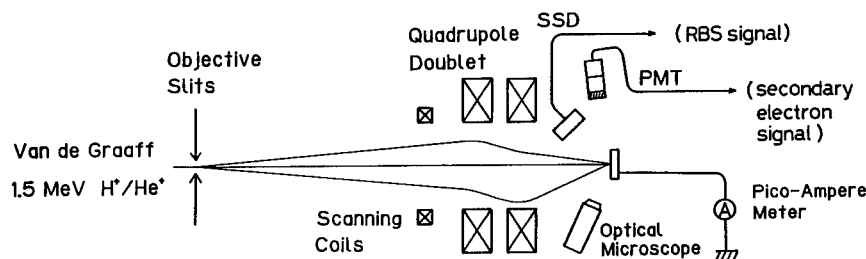


Fig. 1 Schematic diagram of the microprobe system.

magnifying factor of 5, and precisely positioned by secondary electron images with a maximum scanning area of $140\ \mu\text{m} \times 50\ \mu\text{m}$ for helium ions. Time for data acquisition of a secondary electron image is 2 sec. A surface-barrier silicon solid-state detector (SSD) for the RBS analysis is located at an angle of 45° to a beam axis with a solid angle of 28 mstr. An energy resolution of the SSD is 15 KeV. The RBS spectrum is displayed in a 256 channel MCA with a resolution of 4.4 keV per channel.

An elemental mapping image of specific atoms in a specific depth can be obtained by the RBS-mapping method [6-9]. Data acquisition time greatly depends on the beam current and the scattering-cross-section of a target atom. In general, it takes 30 - 60 min to obtain one image. However, longer acquisition time increases the quality of the mapping image. The mapping images are shown on a CRT display with 8 colors or dot patterns corresponding to signal intensities.

RESULTS AND DISCUSSION

LCVD Mo line

RBS analysis of Mo lines masklessly delineated on GaAs by a LCVD method was made by the microprobe. The Mo lines are deposited by a thermochemical dissociation process of atmospheric metal-organic gas: Mo(CO)_6 [11]. A tightly focused Ar^+ laser with a spot size of $18.2\ \mu\text{m}$ ($1/e^2$ intensity) was used to locally heat the substrate. A line pattern can be formed by scanning the laser beam. The width of the Mo line depends on a temperature profile in the vicinity of the beam spot, so that the line width in a low laser power region is smaller than the spot size.

Figure 2a shows the secondary electron image of the Mo line with a laser power of 0.6 W and a scan speed of $6\ \mu\text{m}/\text{sec}$. A line pattern is indistinct in this image. This is due to the nonuniformity of the surface of the Mo line. Besides the main pattern with a width of about $3\ \mu\text{m}$, scattered patterns on the left-hand side is observed in the vicinity with a maximum spread of about $10\ \mu\text{m}$. The temperature rise at the point of $10\ \mu\text{m}$ from the laser spot center was calculated to be $210\ ^\circ\text{C}$, while Mo(CO)_6 dissociates at the temperature of more than $150\ ^\circ\text{C}$ under atmospheric pressure. Therefore, the scattered pattern is considered to show the deposited Mo.

Figure 2b shows the micro-RBS spectra of the Mo line shown in Fig 2a. The open circle shows the spectrum at the center of the Mo line, where the probe-position was aligned by monitoring the secondary electron image. The closed circle shows the reference spectrum obtained outside the line. The yield for Mo observed in the spectrum are much lower than that for a bulk Mo layer. It suggests that the deposited Mo is not uniform.

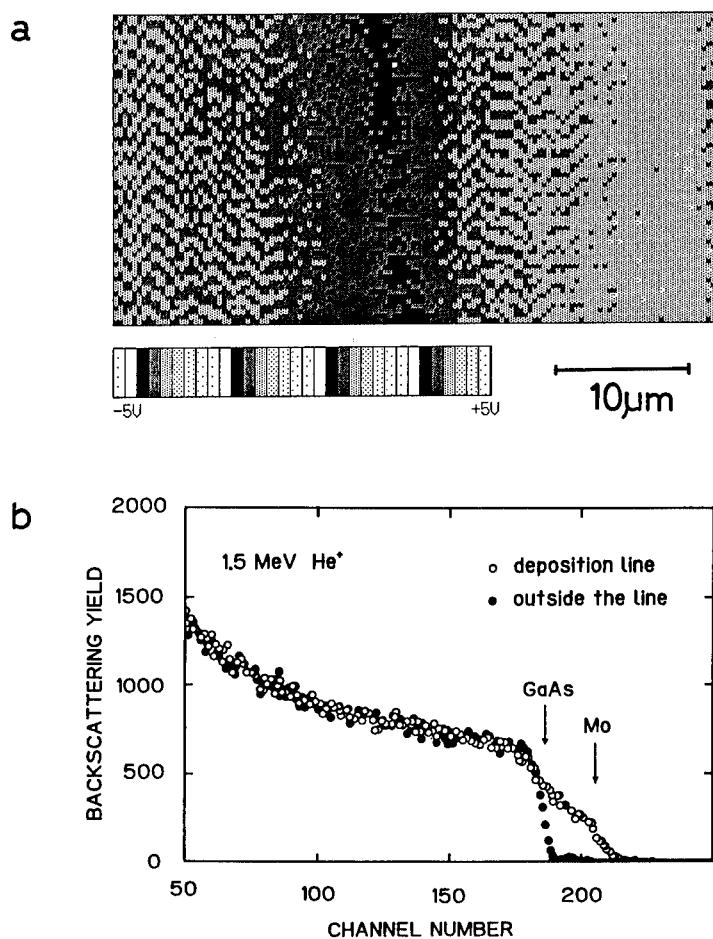


Fig. 2 (a) secondary electron image of the Mo line deposited by LCDV using an Ar^+ laser, (b) micro-RBS spectrum of the Mo line.

Figure 3a shows the RBS-mapping image of the Mo line, which is not the identical part with that shown in Fig. 2. Dot patterns show backscattering yields at each probe-position. An energy window for the mapping was adjusted to all of the Mo signals except the overlapping region with GaAs signals. The total dose for this RBS-mapping was $4.3 \times 10^{16} \text{ cm}^{-2}$. Although the maximum yield is four counts, the position of the line can be clearly imaged in this case.

Figure 3b shows the lateral profile across the deposited line which is accumulation of all the horizontal profiles extracted from the RBS-mapping image shown in Fig. 3a. This profile provides an integrated distribution of Mo across the line. The open circle shows the integrated data and the solid line shows the result of least square fitting of a gaussian profile.

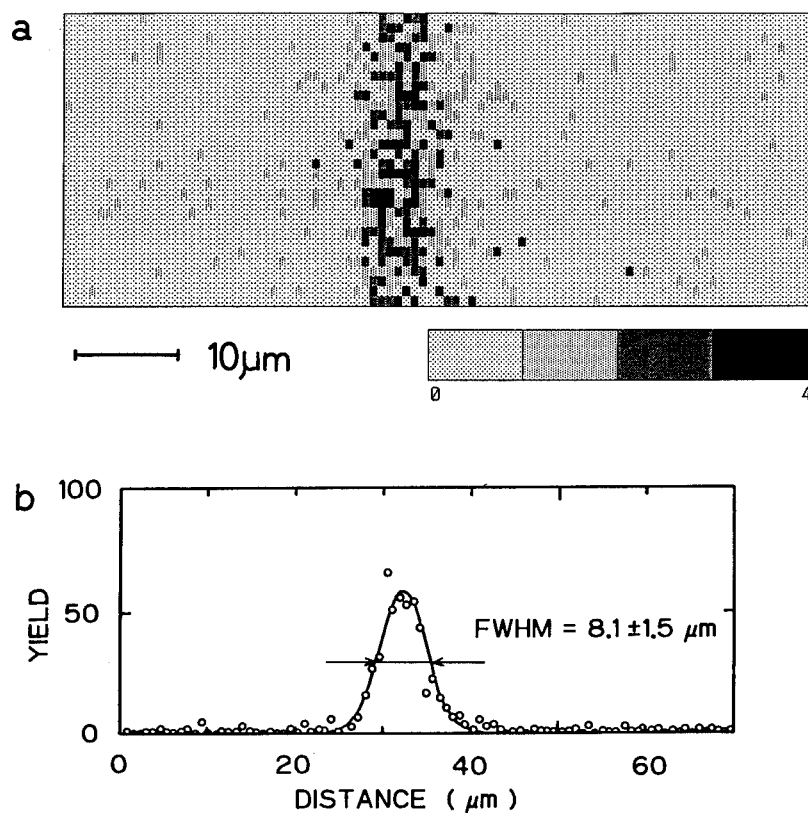


Fig. 3 (a) RBS-mapping image of the Mo line deposited by LCVD, (b) cross-sectional distribution of the line obtained from the RBS-mapping image.

The FWHM of the profile was calculated to be $8.1 \pm 1.5 \mu\text{m}$. The width of the Mo line was estimated to be $7.5 \pm 1.6 \mu\text{m}$. The width of the line was also measured to be about $6 \mu\text{m}$ by an optical microscope. The measured value is in agreement with the estimated value from Fig. 3b.

Implanted Au line

The RBS analysis of Au lines, masklessly implanted in Si at an energy of 100 keV to a local dose of $6 \times 10^{16} \text{ cm}^{-2}$ with a line width of $1 \mu\text{m}$, was made by the microprobe. The sample was prepared by the 200 keV FIB system having an Au-Si-Be liquid metal ion source and E x B mass filter [2]. Single charged Au ions were implanted in a line mode with a flux density of $2.4 \times 10^{16} \text{ cm}^{-2}$.

The microprobe was aligned to the implanted region by searching electrode patterns used as marker patterns for Au implantation. Fig. 4a and 4b show the secondary electron and the RBS-mapping images of the implanted line. The total He ion dose for the RBS-mapping was 2.3×10^{16}

cm^{-2} . The square pattern shows in the right-hand side is the electrode patterns. The implanted line should start at the edge of the electrode and proceed to the left-hand side. Although the implanted line cannot be detected in the secondary electron image, a line pattern similar to Fig. 4b is observed in Fig. 4a. This is due to the surface roughness caused by sputtering effects of the Au ion bombardment with a high dose rate. On the other hand, Au distribution in Si is clearly observed in the RBS-mapping image.

The implanted dose of the line can be estimated by the micro-RBS spectrum (not shown) at the implanted line. The estimated value was $3.9 \times 10^{16} \text{ cm}^{-2}$ with a statistical error of 4.6 %. Difference observed between the implanted dose and the measured dose probably arises from the loss of Au by sputtering effects shown in the secondary electron image.

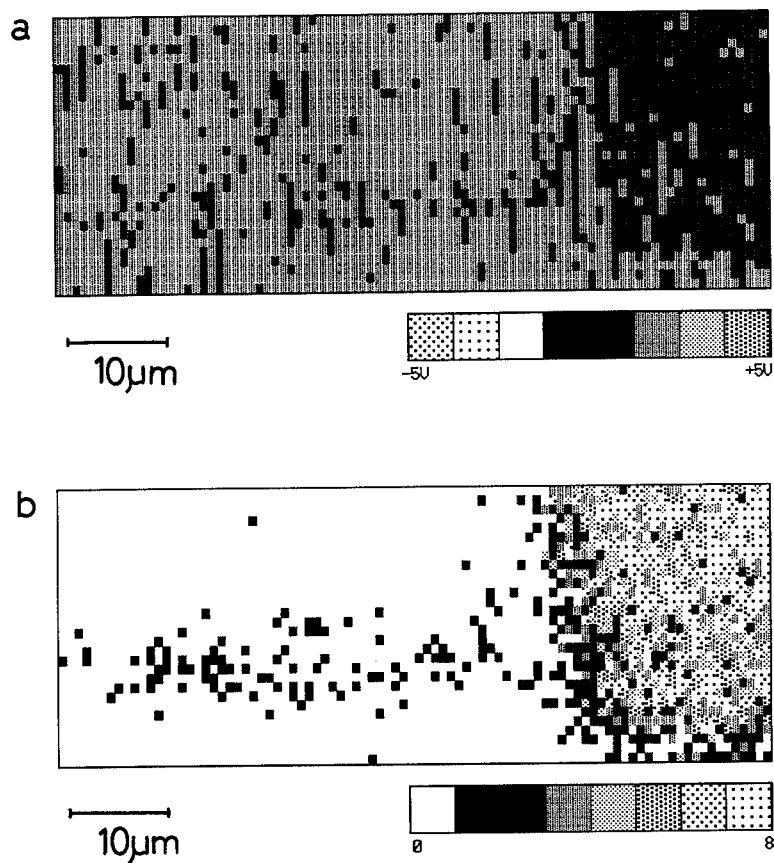


Fig. 4 (a) secondary electron image of the Au line implanted by 100 keV FIB system, (b) RBS-mapping image of the implanted Au line.

SUMMARY

Masklessly fabricated lines of deposited Mo on GaAs and implanted Au in Si was analyzed using a micro-RBS analysis with 1.5 MeV helium ions. An RBS-mapping method of the Mo line provided the elemental distribution of Mo atoms on GaAs and the width of a delineated Mo line. A micro-RBS spectrum of the Mo line showed the nonuniformity of the Mo layer. Comparison between a secondary electron image and an RBS-mapping image of the implanted Au lines revealed the usefulness of the microprobe application for characterization of FIB implantation.

ACKNOWLEDGEMENT

The authors wish to thank K. Inoue, S. Ujiie and K. Matsunaga for their cooperation.

REFERENCES

1. D. J. Ehrlich and J. Y. Tsao, *J. Vac. Sci. Tech.* **B1** 969, (1983)
2. T. Shiokawa, P. H. Kim, K. Toyoda, S. Namba, K. Gamo, R. Aihara and N. Anazawa, *Jpn. J. Appl. Phys.* **24**, L566 (1985)
3. M. Takai, J. Tsuchimoto, H. Nakai, K. Gamo and S. Namba, *Jpn. J. Appl. Phys.* **23**, L852 (1984)
4. K. Gamo, N. Takakura, N. Samoto, R. Shimizu and S. Namba, *Jpn. J. Appl. Phys.* **23**, L293 (1987)
5. Principles and Applications of High-Energy Ion Microbeams, edited by F. Watt and G. W. Grime (Adam Hilger, Bristol, 1987)
6. M. Takai, K. Matsunaga, K. Inoue, M. Izumi, K. Gamo, M. Sato and S. Namba, *Jpn. J. Appl. Phys.* **26**, L550 (1987)
7. K. Inoue, M. Takai, K. Matsunaga, M. Izumi, K. Gamo, S. Namba and M. Satou, *Nucl. Instrum. and Methods* **B30**, 580 (1988)
8. A. Kinomura, M. Takai, K. Inoue, K. Matsunaga, M. Izumi, T. Matsuo, K. Gamo, S. Namba and M. Satou, *Nucl. Instrum. and Methods* **B33**, 862 (1988)
9. A. Kinomura, M. Takai, T. Matsuo, S. Ujiie, S. Namba, M. Satou, M. Kiuchi, K. Fujii and T. Shiokawa, in Proc. of the 6th Intern. Conf. on Ion Beam Modification of Materials, edited by S. Namba (to be published in *Nucl. Instrum. and Methods* 1989)
10. A. Kinomura, M. Takai, T. Matsuo, M. Kiuchi, K. Fujii, M. Satou and S. Namba, *Jpn. J. Appl. Phys.* **27**, L1346 (1988)
11. M. Takai, H. Inoue, Y. Hashizume and S. Namba (in preparation)

DEPTH PROFILING OF ION BEAM INDUCED DAMAGE IN SEMICONDUCTOR HETEROSTRUCTURES

R. GERMANN*, A. FORCHEL*, G. HÖRCHER* AND G. WEIMANN**

*4. Physikalisches Institut, Universität Stuttgart, Pfaffenwaldring 57, D-7000 Stuttgart 80, Federal Republic of Germany

**FTZ der Deutschen Bundespost, Am Kavalleriesand 3, D-6100 Darmstadt, Federal Republic of Germany. Present adress: TU München, Walter Schottky Institut, Am Coulombwall, D-8046 Garching, Federal Republic of Germany

ABSTRACT

We have produced beveled cross-sections of GaAs/GaAlAs multiple quantum well structures with inclination angles of 0.55 minutes of arc with a special ion beam etching technique. The extension of the damage which is induced during the dry etching process can be evaluated directly by a comparison of spatially resolved secondary ion mass spectroscopy and photoluminescence measurements. We observe a thickness of the damaged surface layer between 36 nm for 250 eV Argon ions and 160 nm for 1000 eV Argon ions in a GaAs/GaAlAs multiple quantum well structure.

INTRODUCTION

Ion assisted dry etching techniques are commonly used for the fabrication of semiconductor microstructures with lateral dimensions below 1 micron. The advantages of these techniques are the anisotropic etching characteristic and the good reproducibility [1]. The most significant drawback of these methods is the induced etching damage, which is caused by the ions used with typical energies of a few hundred electron volts. The damage can be described by an amorphous surface-near region and an implantation of ions in deeper regions of the samples.

The range and the depth distribution of the created damage is of fundamental interest, because it is the limiting factor for device fabrication by dry etching. Surface damage plays a more and more critical role if the dimensions of microstructures are reduced, because of the increasing ratio between surface and volume. The electrical and optical properties of dry etched devices depend strongly on the induced damage.

Some results have been reported recently for GaAs. Scherer et al. [2] determined the damage depth from the I-V characteristic of Schottky contacts on a GaAs surface etched by ion beam etching. The fabrication of the Schottky contacts is generally a critical step and the determination of the damage depth is indirect. Yuba et al. [3] made DLTS measurements on dry etched GaAs samples. The depth distribution of different defects could be revealed after a low temperature annealing. In this case a Schottky contact is also necessary. Both authors report damage depths far beyond the ion range calculated with standard LSS theory [4].

We present a method which shows directly the extension of the damage in ion beam etched samples without any treatment (as evaporation or annealing) of the samples after the etching process. The method is based on the fabrication of a bevel with an inclination angle below one minute of arc by an ion beam etching process with a special etching geometry and subsequent spatially resolved measurements with secondary ion mass spectroscopy (SIMS) and photoluminescence (PL) on the bevel surface.

In the following sections we first describe the bevel fabrication and then the measuring method with SIMS and PL. The depth of the damage created by Argon ion beam etching with ion energies between 250 eV and 1000 eV is discussed for a GaAs/GaAlAs multiple quantum well (mqw) structure.

BEVEL FABRICATION

We use an ion-milling system (Technics RIB-ETCH 160) with a 5 inch Kaufman-type ion source for the preparation of the beveled cross-sections. A special geometry of sample and mask is necessary for the fabrication of the bevels. The geometry is shown schematically in Fig. 1, left side. A metal mask (in our case Tantalum) with a knife edge is mounted at a distance h above the sample surface. The angle of incidence of the argon beam with respect to the normal direction is non-zero. For the situation shown the boundary between the unetched and the etched area is located at point A. When the sample and the mask are rotating together, the shadow travels periodically between point A and point B. The right-hand side of Fig. 1 shows this effect more clearly. Here we consider sample and mask as fixed and the ion beam rotates under the angle of incidence α to the normal direction. The sample is never etched on the left-hand side of point A. On the right-hand side of point B the sample is etched the whole time. Between point A and B we obtain a locally varying etch time and therefore a locally varying etch depth for each point x .

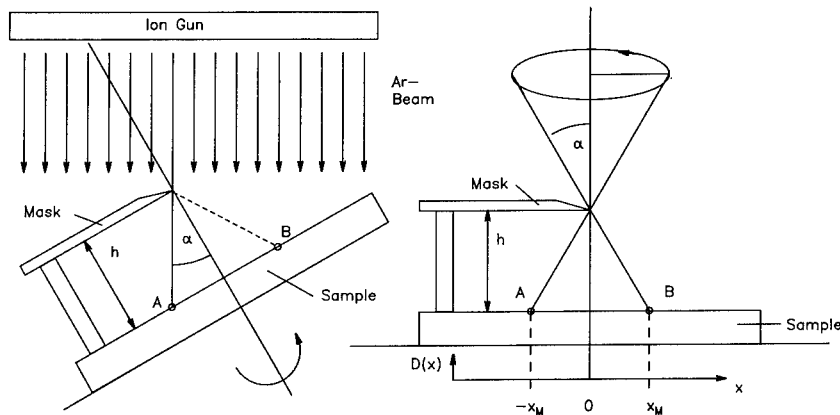


Fig. 1. Geometry of the ion milling process. Sample and mask rotate together at a given inclination angle α (left). The equivalent geometry of a fixed sample and a rotating beam is shown on the right side.

The profile shape $D(x)$ of the bevel-etched area can be described by a simple model:

$$D(x) = D_0 - D \cdot [1 - (1/\pi) \cdot \arccos(x/x_M)],$$

$$D = n \cdot T \cdot R, \quad x_M = h \cdot \tan \alpha \quad (1)$$

With: D_0 - position of the original surface, D - maximum etch depth, α - angle of incidence of the argon beam, R - etch rate at the angle α , T - time for one rotation of the sample, n - number of rotations, h - distance between sample and mask, $2 \cdot x_M$ - width of the bevel. Note that the equation is only valid for full terms of rotations n .

The profile $D(x)$ is shown schematically in Fig. 2. It depends in its central part linearly on x with a deviation of 4% at $\pm 0.8 \cdot x_M$. The slope of the linear approximation yields the inclination angle β :

$$\tan \beta = D/(\pi \cdot x_M) \quad (2)$$

Equation (2) shows that any small inclination angle β can be achieved if the etch depth D is decreased by adjusting the etching parameters (R, n, T) or if the value of x_M is increased by choosing an appropriate geometry. The bevel fabrication by this method and the possibilities of its application is discussed in more detail in two other publications [5,6].

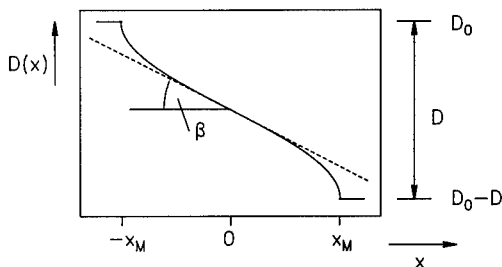


Fig. 2. Calculated profile shape of a bevel-etched sample according to equation (1). The dashed line is a linear approximation of the central part of the profile.

We have fabricated bevels on a GaAs/GaAlAs mqw structure for our investigations. The structure of the sample is shown on the left side in Fig. 3. The sample was grown by MBE and consists of two mqw structures. The mqw structure at the top includes 10 GaAs quantum well layers with $L_z = 3.6$ nm and 11 $\text{Ga}_{0.63}\text{Al}_{0.37}$ barrier layers with $L_B = 21.3$ nm. The mqw structure at the bottom consists of 10 GaAs quantum wells with $L_z = 9.0$ nm and 11 $\text{Ga}_{0.5}\text{Al}_{0.5}\text{As}$ barriers with $L_B = 20.3$ nm. A bevel with an inclination angle of 0.552 minutes of arc was fabricated on the sample. Ion beam etching was done with 500 eV argon ions and a current density of 0.4 mA/cm^2 at a pressure of $1 \cdot 10^{-4}$ mbar. The angle of incidence α was 25 degree, the distance between sample and mask was $h = 3.4$ mm. The etch rate was 36.4 nm/min for GaAs, 31.5 nm/min for $\text{Ga}_{0.63}\text{Al}_{0.37}\text{As}$ and 29.7 nm/min for $\text{Ga}_{0.5}\text{Al}_{0.5}\text{As}$. Fig. 3 depicts in the right part the profile of the bevel-etched cross-section of the sample. The profile was obtained by scanning the surface of the sample with a stylus profiler (Dektak IIa). The profile shape shows an approximately linear relation between the position on the x-axis and the depth over a wide range of the sample.

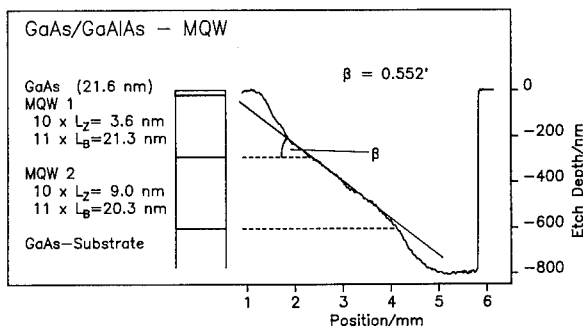


Fig. 3. Schematic structure of the bevel-etched GaAs/GaAlAs mqw sample (left). The right side shows the measured profile of the beveled section of the sample.

The bevel transforms the vertical structure of the sample into a lateral series of single quantum well layers at the surface of the beveled area. With the angle of 0.552 minutes of arc a layer with a thickness of 10 nm is expanded to a length of $62.3 \mu\text{m}$ in lateral direction. The depth variation of a sample can be now investigated by spatially resolved measurements at the surface of the bevel-etched sample.

SIMS- AND PHOTOLUMINESCENCE MEASUREMENTS

Fig. 4 shows schematically a cross-section of a bevel-etched mqw structure. The argon ions which are used for the ion beam etching process induce a damaged layer of constant thickness over the whole range of the beveled area. Spatially resolved SIMS- and PL-measurements are used for the determination of the damage depth.

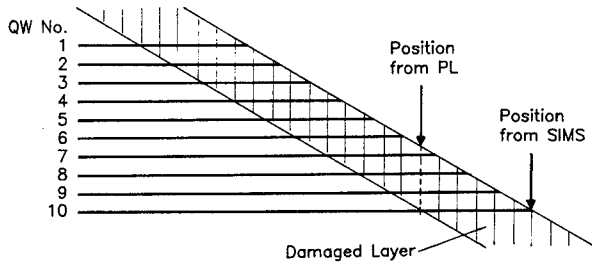


Fig. 4. Schematic side view of a bevel-etched mqw sample indicating the damaged surface layer.

The SIMS-measurements were performed with an Atomika A-DIDA primary ion gun (O_2^+ ions) and a quadrupole mass spectrometer. The energy of the primary ions was 5 keV at a beam current of 1 nA. The diameter of the primary ion spot was $30\text{ }\mu\text{m}$ under these conditions. In the line scan mode, the sample is moved relative to the fixed primary ion beam with a velocity of $8.33\text{ }\mu\text{m/s}$. The primary ions remove less than one atomic layer from the sample surface. The sputtered secondary ions are analyzed and yield information about the position of the quantum well layers at the sample surface. For example, qw no. 10 in Fig. 4 will appear in the SIMS-measurement at the position indicated by the arrow at the right-hand side.

For the PL-measurements the samples were excited with an Argon ion laser at a wavelength of 457.9 nm and at a temperature of 2K. The luminescence was dispersed with a 0.32 m monochromator and detected with single photon counting and a GaAs multiplier. For spatially resolved measurements the sample could be moved with a stepping motor relative to the laser beam. High lateral resolution could be achieved with a laser spot of approximately $10\text{ }\mu\text{m}$ and a minimal step width of $5\text{ }\mu\text{m}$. Different to SIMS the spatially resolved PL-measurements are sensitive to a damage of the quantum well layers. Only the parts of the quantum wells which are not located inside the damaged layer will contribute to the PL-signal. This means that for example the emission from qw no. 10 will disappear at the position indicated by the arrow on the left-hand side of Fig. 4. The shift of the position of qw no. 10 measured with PL and SIMS yields therefore directly the thickness of the damaged surface layer.

Experimental results of SIMS- and PL-measurements for our beveled GaAs/GaAlAs mqw sample are shown in Fig. 5. The upper curve shows the Ga-signal from a SIMS line scan. The center positions of the 10 GaAs quantum well layers with $L_z = 9.0\text{ nm}$ are clearly revealed. The position of the quantum well layer closest to the substrate is indicated by the vertical line 1. The dashed curve shows a PL line scan. The quantum wells with $L_z = 9.0\text{ nm}$ show an excitonic transition with a peak energy of 1.555 eV and a full half width of 2 meV. During the PL line scan the intensity of the quantum well emission at 1.555 eV was monitored. The luminescence of the quantum well layer disappears at position 2 as indicated in Fig. 5. The difference between the location of the last quantum well detected with SIMS (position 1) and PL (position 2) corresponds to a depth of 2.7 periods of the mqw structure. This means that the thickness of the damaged layer which is induced by the 500 eV Argon ions is 79 nm.

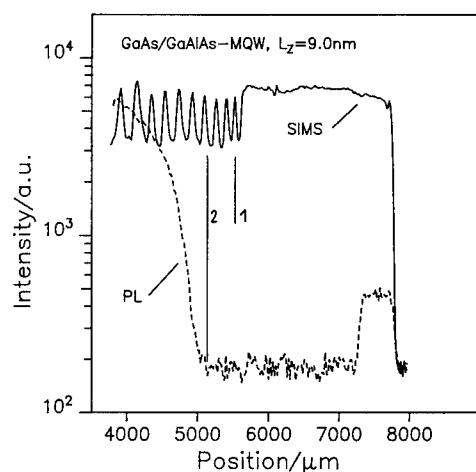


Fig. 5. Comparison of spatially resolved SIMS- and PL-measurements for a GaAs/GaAlAs mqw structure.

ENERGY DEPENDENCE OF THE DAMAGED LAYER THICKNESS

We fabricated three bevels of the same sample with identical inclination angles by ion beam etching with an ion energy of 250 eV, 500 eV and 1000 eV. The thickness of the damaged layer was evaluated as demonstrated in the last section. The results are shown in Fig. 6 for the mqw structure with $L_z = 9.0$ nm (squares) and $L_z = 3.6$ nm (circles). In the case of the 3.6 nm quantum wells the damaged layer thickness varies from 36 nm for an ion energy of 250 eV to 107 nm for 1000 eV ions. In the case of the 9.0 nm quantum wells the damaged layer thickness ranges from 41 nm to 160 nm for 250 eV and 1000 eV argon ions. The different behaviour may be due to the different Aluminium content of the barrier layers, which is 37% for the 3.6 nm mqw structure and 50% for the 9 nm quantum wells. A lower Aluminium content means a higher stopping power and therefore a smaller thickness of the damaged layer.

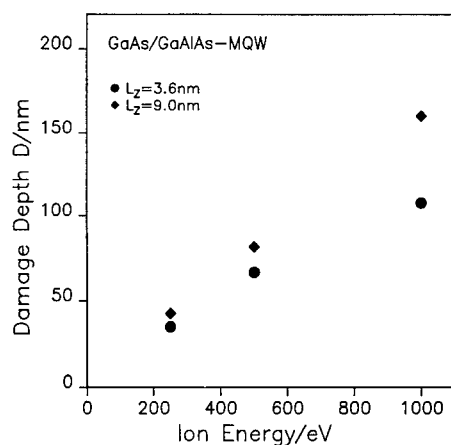


Fig. 6. Thickness of the damaged layer as a function of the energy of the Argon ions used in the ion beam etching process.

Our values for the damaged layer thickness are much higher than the ion range calculated from the standard LSS theory. We obtain an ion range of 1.20 nm with a standard deviation of 0.72 nm for 250 eV Argon ions in GaAlAs with an Aluminium content of 50%, compared to an experimentally derived damage depth of 41 nm. This discrepancy is mainly due to the fact that the average effective Ar concentration at the surface can be estimated to 10^{22} cm^{-3} whereas the luminescence may be quenched by effective nonradiative centers for concentrations of 10^{16} cm^{-3} already. In terms of the LSS model this would correspond to an effective standard deviation of about 8 nm. The remaining discrepancy may be due to channeling or diffusion, which are known to lead to strong deviations of ion profiles for depths much larger than the predicted ion range.

CONCLUSION

We have developed a new method for the direct monitoring of the thickness of a damaged surface layer which is caused by ion beam etching. In the case of a GaAs/GaAlAs mqw structure etched with low energy Argon ions we obtain a damaged layer thickness ranging from 36 nm for 250 eV ions to 160 nm for 1000 eV ions.

ACKNOWLEDGEMENTS

We acknowledge stimulating discussions with M.H. Pilkuhn. The financial support of this work by the Deutsche Forschungsgemeinschaft is gratefully appreciated.

REFERENCES

- [1] A.R. Reinberg, in VLSI Electronics Microstructure Science, edited by N.G. Einspruch, (Academic Press, New York, 1981), pp. 2-35
- [2] A. Scherer, H.G. Craighead, M.L. Roukes, and J.B. Harbison, *J. Vac. Sci. Techn. B* **6**(1), 277 (1988)
- [3] Y. Yuba, T. Ishida, K. Gamo, and S. Namba, *J. Vac. Sci. Techn. B* **6**(1), 253 (1988)
- [4] J.F. Ziegler, J.P. Biersack, and U. Littmark, in The Stopping and Range of Ions in Solids, edited by J.F. Ziegler (Pergamon Press, New York, 1985)
- [5] R. Germann, and A. Forchel in Growth, Characterization, Processing, of III-V Materials with Correlations to Device Performances, edited by Y.I. Nissim, and P.A. Glasow, (European Mat. Res. Soc. Proc., Vol. XVI, Les Ulis Cedex, 1987), pp. 311-316
- [6] R. Germann, A. Forchel, and G. Weimann, *Appl. Phys. A* **47**, (1988) in press

Author Index

- Al-Jumaily, G.A., 61, 475, 483
 Allen, Charles W., 297
 Amaral, L., 315
 Anderson, Alfredo C., 67
 Andreadis, T.D., 151, 175, 201
 Arnold, G.W., 713

 Baca, A.G., 249
 Bai, Xinde, 479
 Balanzat, E., 357
 Baldo, Pete, 213
 Baliga, B.J., 731
 Barnett, S.A., 689
 Basheer, R.A., 737
 Bassel, R.H., 151
 Battaglia, A., 563
 Baxi, H., 231
 Becker, M.F., 551
 Behar, M., 315
 Berger, S., 647
 Berti, M., 569
 Birtcher, R.C., 303
 Børghesen, P., 207, 219, 261
 Borisenko, V.E., 653, 659
 Bouffard, S., 357
 Boulding, A., 17
 Bowman, Jr., Robert C., 629
 Boyer, L.L., 483
 Bradley, R.M., 269
 Bube, Richard H., 701
 Buchal, Ch., 719
 Burke, R., 291
 Burton, L.C., 677

 Calcagno, L., 581
 Campisano, S.U., 581
 Cao, D.X., 587
 Carnera, A., 563
 Carosella, C.A., 79, 501
 Catania, M., 581
 Cerofolini, G.F., 181
 Chang, Albert L., 433
 Chason, Eric, 35
 Chen, G-S., 195
 Chen, Heming, 479
 Chen, Q.M., 225
 Cheng, C.C., 445
 Cheng, Y.-T., 189
 Choi, C.-H., 689
 Chu, W.K., 375, 707
 Cirlin, E.-H., 189
 Clayton, Clive, 463
 Clemens, B.M., 189
 Cole, E.D., 677
 Cornett, Kenneth D., 495

 Cortesi, E., 623
 Culbertson, R.J., 321
 Cuomo, Jerome J., 23
 Custer, J.S., 545

 Dai, Mingjiang, 479
 Daly, James, 463
 Dauplaise, H.M., 61
 Davari, B., 635
 Davis, G., 617
 de Beurs, H., 403
 De Hosson, J. Th. M., 403
 Delafond, J., 91
 Demchenko, A.I., 653
 Dieleman, Jan, 3
 Dietrich, H.-P., 507
 Dietrich, Harry B., 665
 Dillard, J.G., 677
 Dillich, S.A., 427
 Dodson, Brian W., 137
 Donley, M.S., 469
 Donovan, E.P., 55, 79, 501
 Dow, A.A., 189
 Drigo, A.V., 569

 Echeverria, A., 231
 El-Ghor, M.K., 593
 Epp, J., 677
 Erck, R.A., 445
 Eridon, James M., 175, 201, 665
 Eto, K., 513

 Fahrenbruch, Alan L., 701
 Fair, Richard B., 611
 Fan, Y.D., 225
 Farkas, D., 195
 Feng, G.F., 671
 Fenske, G.R., 445
 Ferla, G., 563, 581
 Follstaedt, D.M., 309, 389
 Forchel, A., 749
 Foti, G., 581
 Franzen, W., 321
 Fujihana, Takanobu, 415
 Fujii, K., 743

 Ganin, E., 635
 Gasparotto, A., 563
 Germann, R., 749
 Gfeller, F., 507
 Ghibaud, G., 599
 Ghosh, P.K., 725
 Gibson, Ursula J., 495
 Gilmore, C.M., 163

Grabowski, K.S., 279
 Greenwald, Anton C., 109, 463
 Gresko, Thomas, 665
 Guillermet, M., 291
 Günter, P., 719

Haeri, A., 163
 Harame, D., 635
 Harper, J.M.E., 269
 Hart, R.R., 575
 Haynes, T.E., 47
 Heim, D.J., 285
 Herbots, N., 641
 Hirvonen, J-P., 85, 439, 451, 457
 Hirvonen, James K., 85, 109, 439
 Hoffman, D., 641
 Holesinger, T.G., 285
 Holland, O.W., 47, 593
 Hong, Shin-Nam, 611
 Hörcher, G., 749
 Horn, K.M., 35
 Horne, C.R., 617
 Hörnström, S.E., 269
 Hren, John J., 611
 Huang, J.S., 327
 Huang, L.J., 225
 Hubler, G.K., 55, 79, 151

Inoue, K., 381
 Irmscher, R., 719
 Isa, Saliman A., 725
 Ishibashi, K., 381
 Iskanderova, Z.A., 169
 Ito, K., 513
 Ivanov, A.I., 653
 Iwaki, Masaya, 415, 421

Jacobson, D.C., 243, 533
 Jaggi, Narendra K., 109
 Janssen, K.T.F., 557
 Jaouen, H., 599
 Jaulin, M., 91
 Jeon, Young-Jin, 551
 Jervis, T.R., 451, 457
 Jiankun, Zhou, 73
 Johnson, H.H., 207, 219
 Jones, K.S., 249, 617
 Jousset, J.C., 357
 Jun, Li, 237

Kaim, R.E., 557
 Kalitzova, Maria G., 683
 Kant, R.A., 55, 279, 427, 433
 Karasinski, J., 17
 Kasi, S.R., 101
 Kataoka, I., 513
 Kawata, Y., 381
 Kenik, E.A., 333

Kinomura, A., 743
 Kiuchi, M., 743
 Knapp, J.A., 389
 Knudsen, John F., 629
 Koike, J., 339, 345
 Komem, Y., 647
 Kornreich, P.G., 725

La Ferla, A., 563
 Lakin, K.M., 125, 285
 LaPlanche, G., 91
 Lau, W.M., 695
 Leiderman, R. Yu., 169
 Levenson, Leonard L., 131
 Lewis, N., 731
 Li, H-D., 225
 Li, Jian, 255, 297
 Li, Wangpei, 479
 Lichtenwalner, D.J., 67
 Lifshitz, Y., 101
 Lilienfeld, D.A., 207, 219, 261
 Liu, A.S., 303
 Liu, B.X., 225
 Liu, Joyce C., 297
 Lopez-Otero, Adolfo, 701
 Lotti, R., 569
 Lowder, L.J., 321
 Lulli, G., 569

Ma, D., 641
 Machida, Kazumichi, 525
 Maeyama, Yoshitaka, 525
 Martin, J.A., 457
 Massalski, T.B., 231
 Matsuo, T., 743
 Mayer, J.W., 255, 297
 Mazzone, A.M., 157
 McDevitt, N.T., 469
 McNally, J.J., 483
 McNeil, J.R., 483
 Meda, L., 181
 Meng, W.J., 345
 Merli, P.G., 569
 Meroth, John, 463
 Meshii, M., 339
 Mizutani, Tatsumi, 605
 Mooney, T.A., 61, 475
 Moser, A., 507
 Moss, Steven C., 629
 Mueller, G.P., 151
 Murray, P.T., 469
 Musket, R.G., 327
 Myers, Edward R., 611
 Myers, S.M., 309

Nagakubo, M., 29
 Namavar, F., 623
 Namba, S., 381, 743
 Naoe, M., 29

Nastasi, Michael, 333, 351,
451, 457
Nishimatsu, Shigeru, 605
Noguchi, Kazuhiko, 525

Ohwaki, Takeshi, 41
Okabe, Yoshio, 415
Okamoto, P.R., 339, 345
Oliver, Richard, 463
Oliver, W.C., 457
Oyoshi, Keiji, 519
Ozturk, Mehmet, 611

Parikh, N.R., 375
Park, B., 243
Park, Won Woo, 551
Parker, G., 439
Parkin, Don M., 351
Pashov, N.K., 683
Pearce, J.D., 575
Pearson, S.J., 249
Pennycook, S.J., 47
Petkie, R., 17
Pharr, G.M., 457
Picraux, S.T., 35
Pimbert-Michaux, S., 91
Ping, Cai Wei, 237
Poate, J.M., 243, 533, 545
Pope, L.E., 389
Priolo, F., 243, 533, 563
Pyatkova, T.M., 659

Qadri, S.B., 279
Qu, Yi, 409

Rabalais, J.W., 101
Radjabov, T.D., 169
Ramos, Stella M.M., 315
Rangaswamy, M., 195
Rehn, Lynn E., 213, 297, 339,
345
Reicher, D.W., 483
Rimini, E., 563, 581
Rizzo, H.F., 231
Rosen, D.J., 175
Rosen, M., 151, 175, 201
Rossi, M., 683
Roy, Ronnen A., 17, 23
Rubin, Leonard M., 641
Rubio, J.D., 575
Rudeck, P.J., 269
Rudman, D.A., 67
Ruggles, Gary A., 611
Run, Wu, 237

Sai-Halasz, G.A., 635
Said, J., 599
Sampath, W.S., 409
Sandhu, G.S., 707
Saris, F.W., 557

Sartwell, B.D., 427
Sasaki, Jun, 421
Sasaki, Shigeo, 525
Satou, M., 743
Scheuer, Udo, 213
Schreutelkamp, R.J., 557
Scilla, G., 635
Sen, S., 677
Shanks, H.R., 125, 285
Sharps, Paul, 701
Shenai, K., 731
Shichang, Zou, 73
Short, K.T., 249
Siochi, A., 677
Sioshansi, Piran, 463, 623
Sjoreen, T.P., 593
Smajkiewicz, A., 475
Smith, Duane D., 629
Smith, G.A., 731
Sood, D.K., 587
Spaepen, F., 243
Spinella, C., 563, 581
Sprague, J.A., 163, 427
Spurgeon, W.A., 61
Stoemenos, I., 599
Suzuki, N., 381
Swansiger, W.A., 309
Swanson, M.L., 375, 707
Swartzlander, Amy B., 131

Taga, Yasunori, 41
Tagami, Takashi, 519
Takagi, Toshinori, 131
Takai, M., 381, 743
Tanaka, Shuhei, 519
Taylor, Anthony, 495
Tesmer, J.R., 451
Tetreault, Thomas G., 439
Thompson, Michael O., 533,
545
Thompson, Phillip E., 665
Tokarev, V.V., 653, 659
Toulemonde, M., 357
Tsao, J.Y., 35
Tukfatullin, F.K., 169
Turner, D.E., 125

Ueda, Ryuzi, 525
Usui, Hiroaki, 131

Vallier, L., 291
Van Vechten, D., 55, 79, 501
Vardiman, R.G., 369
Vaseashta, A., 677
Vasquez, A., 315
Venables, D., 617
Vettiger, P., 507
Vijay, R.P., 575
Vitali, G., 683
Voisin, E., 291

Volpones, C., 181

Wall, M.A., 327
Walser, Rodger M., 551
Wang, S.Q., 255
Webb, D.J., 507
Wei, Huang, 73
Wei, Ronghua, 409
Wei, Tian, 237
Weimann, G., 749
Westendorp, J.F.M., 557
White, C.W., 593
Wilbur, P.J., 409
Williams, F.L., 483
Williamson, D.L., 409
Wistrom, R.E., 207, 219
Wortman, Jimmie J., 611
Wu, C.S., 249

Xianghuai, Liu, 73

Yamada, I., 513
Yamada, Isao, 113, 131
Yamamoto, T., 29
Yee, Dennis S., 17, 23
Youshan, Chen, 73
Yu, N., 375
Yunogami, Takashi, 605

Zallen, R., 671, 677
Zarovsky, D.I., 653
Zaumseil, P., 599
Zawislak, F.C., 315
Zhang, Z.H., 375
Zhihong, Zheng, 73
Zinkle, S.J., 363
Zocco, T.G., 451, 457
Zuhr, R.A., 47
Zuyao, Zhou, 73

Subject Index

- adhesion, 439, 445, 475
- alloy
 - AgCu, 231
 - AgFe, 231
 - AgZn, 175
 - Al-Cu, 269
 - Co-Ti, 219
 - Cr-Ni, 237
 - Cr-Ni-Cr, 237
 - CuTi, 339
 - CuW, 231
 - Fe-Cr, 421
 - Fe-Cu, 225
 - Fe-Mo, 225
 - Fe-Ti, 207, 213, 219
 - Fe-Ti-C, 451
 - MoCu, 231
 - NiAl, 333
 - Ni₂Al₃, 333
 - Ni-Ti, 207, 219
 - PdTi, 219
 - PuTa, 231
 - PuV, 231
 - Ti-Al, 219
 - Ti6Al4V, 463
 - Ti-Cu, 219
 - Ti-W, 647
 - Zr₃Al, 345
- aluminum oxynitride, 61
- amorphization, 181, 333, 339, 345, 351, 629, 635
- amorphous, 79, 213, 231, 237, 243, 327, 351, 389, 501, 533, 545, 557, 563, 587, 599, 647
- angle of incidence, 269, 321
- annealing, 501, 587, 677
- anodic oxidation, 237, 479
- Auger electron spectroscopy, 73, 327, 427, 653, 659
- bonding, 463
- carbide
 - SiC, 91, 369
 - TiC, 91, 369
- carbonitrides, 315
- cascade, 151, 157, 189, 195
- cavity, 363, 525
- cluster beam, 113, 125, 131, 285
- coating, 169
- colloids, 363
- columnar structure, 29
- composition, 269, 427
- compressive state, 403
- computer simulation, 137, 151, 157, 163, 175
- contacts, 647
- corrosion, 463, 507
- crystallization, 369, 545, 557, 563, 569, 719
- damage, 181, 581, 593, 605, 671, 677, 689, 707, 749
- damage depth, 749
- defects, 175, 201, 357, 689
- densification, 151
- deposition, 17, 41, 85, 91, 101, 109, 131, 169, 475, 513, 563, 725, 743
- deuterium, 309
- diamond, 101, 707
- diamond-like, 109
- diffusion, 131, 163, 189, 201, 213, 243, 533, 587, 653, 731
- dilatational strain, 345
- dislocations, 363, 557
- disorder, 333, 575
- dissolution, 315
- dopant, 617, 701, 707, 731, 737
- dose rate, 243
- electrical activation, 599, 611, 635, 665, 701, 707
- electrical conductivity, 737
- electroless plating, 525
- electrolytes, 479
- electron irradiation, 333, 339, 345, 351
- electron microscopy
 - analytical, 333
 - cross-sectional TEM, 445, 593, 635
 - high resolution, 683
 - Nomarski, 285
 - RHEED, 35, 285
 - SEM, 285, 433, 641
 - TEM, 47, 73, 91, 231, 237, 309, 333, 363, 369, 427, 433, 445, 569, 599, 623, 683, 731
- electronic excitation, 357
- element
 - a-Si, 551, 647

- Ag, 125, 131, 175, 255, 475, 545
 Al, 61, 131, 479, 647
 Ar, 409, 575
 As, 569, 581, 599
 Au, 297, 309, 533, 743
 B, 109, 375, 421, 653, 707
 Ba, 261
 Be, 671
 Bi, 261
 C, 85, 109, 327, 389
 Co, 47
 Cr, 237, 255, 421, 445
 Cu, 3, 261, 309, 545
 Fe, 29, 47, 237, 315, 321, 415
 Ga, 617
 Ge, 35, 125, 151, 285, 581, 593, 611, 683
 H, 85, 219, 345, 439, 713
 He, 363
 Li, 713
 Mo, 743
 N, 61, 315, 375, 409, 415, 421, 463, 519, 695
 N₂, 55
 Nb, 269, 327
 Ni, 47, 279, 303, 513
 O, 85, 309, 363, 375, 463, 563, 593, 623
 P, 519, 551, 557, 617
 S, 665
 Si, 3, 41, 61, 113, 157, 243, 279, 291, 533, 545, 551, 557, 563, 569, 575, 581, 593, 611, 617, 623, 659, 665, 677, 689, 731, 743
 Ta, 269
 Ti, 47, 237, 255, 369, 389, 457
 W, 17
 Y, 261
 Zn, 175
 Zr, 255
 ellipsometry, 285
 embedded atom method, 175
 energy loss
 electronic, 357
 nuclear, 569
 enhanced diffusion, 213, 243
 epitaxial, 101, 279, 291, 545, 569, 587, 659, 689, 701
 etching
 ion-beam, 525, 749
 reactive ion, 731
 evaporation, 23
 Fermi level, 695
 film, 17, 29, 41, 55, 79, 445, 575
 focused ion beam, 743
 fractal, 189
 friction, 389, 421, 439, 451, 457, 463
 GeV ions, 357
 Gibbs phase rule, 327
 grain boundary, 261, 297
 grain growth, 297
 growth, 35, 163, 291, 533, 659
 hard film, 85, 439
 hardness, 79, 421, 439, 457, 463
 heat of mixing, 207, 231
 high-energy, 445, 665
 hopping conduction, 737
 hot implants, 581
 I-V characteristics, 647
 icosahedral, 225
 impingement ratio, 55, 79, 433
 implantation depth, 421
 impurity, 545, 551, 599
 index of refraction, 79, 501
 inert gas, 303
 interface structure, 445
 intermetallic, 231, 345
 ion-assisted deposition, 445, 483, 495
 ion-beam analysis
 channeling, 279, 375, 557, 575, 581, 593, 659
 elastic recoil detection, 713
 forward recoil spectroscopy, 85
 light element detection, 375
 microprobe, 381, 743
 nuclear reaction, 85, 309
 PIXE, 381
 quantitative, 375
 Rutherford backscattering, 47, 73, 255, 375, 381, 415, 479, 519, 557, 569, 575, 629, 641, 659, 743
 ion beam annealing, 575
 ion beam mixing, 195, 207, 213, 219, 225, 243, 249, 261, 451
 ion bombardment, 29, 55, 213, 269, 297, 409, 427
 ionization, 285
 junction, 611

- Knoop hardness, 415
- laser
 - evaporation, 469
 - interferometry, 551
 - melting, 457
 - mixing, 451
 - processing, 403
- lattice defects, 357
- lattice parameter, 303
- liquid-solid interface, 533
- low-energy, 137, 157, 189, 291, 445, 483, 611, 695
- magnetic, 29, 225, 357
- magneto-optic, 495
- maskless, 743
- mass spectrometer, 3, 125
- melting, 303
- metal film, 23, 113
- metal-semiconductor, 659
- metallization, 249, 641
- metastable solid solution, 327
- microhardness, 23
- microstructure, 23, 131, 269, 363, 369, 409, 427, 445
- microtopography, 525
- migration energy, 175, 201
- modeling, 137, 151, 157, 163, 169, 175, 181, 195
- molecular beam epitaxy, 35
- molecular dynamics, 137, 157
- molecular ions, 181, 695
- morphology, 237, 433
- Mossbauer, 315, 409
- multilayers, 219, 225, 243
- neutral beam, 605
- nitride
 - BN, 79, 85, 439, 469
 - FeN, 321
 - Fe₄N, 415
 - NbN, 67
 - SiN, 439, 501
 - Si₃N₄, 369
 - TiN, 55, 73, 427, 433, 439
- nucleation, 163
- optical
 - coatings, 507
 - materials, 483
 - properties, 61, 79, 501, 671, 707
 - waveguide, 719
- orientation, 269, 321
- oxide, 61, 731
 - Al₂O₃, 363, 495, 507, 587
 - CuO, 255
 - Fe₂O₃, 415
 - KNbO₃, 719
 - LiNbO₃, 713, 719
 - Li₂O, 513
 - SiO₂, 41, 513, 605, 623, 731
 - Y₃Fe₅O₁₂, 357
 - ZnO, 725
 - ZrO₂, 495
- oxygen precipitates, 617
- oxynitride, 519
- p-n junctions, 731
- passivation, 507
- permeability, 309
- phase stability, 333, 357
- phosphosilicate glass, 519
- photoconductive switches, 629
- photoconductivity, 707
- photoluminescence, 749
- pin-on-disk, 451, 463
- pitting corrosion, 495
- plasma
 - assisted epitaxy, 291
 - etching, 67, 731
- plastic lenses, 525
- point defect, 195, 345, 581, 599
- pole figure, 279
- polyacrylonitrile, 737
- porosity, 445
- precipitate, 303, 315, 333, 369
- precision molds, 525
- prostheses, 463
- protective overlayers, 495
- proton, 375
- quadrupole, 381
- quantum, 749
- quartz, 513
- radiation damage, 351, 683
- radiation-enhanced diffusion, 213
- radiation-induced
 - segregation, 333
- Raman, 629, 677
- range, 665
- rapid thermal annealing, 557, 641, 659, 677
- reactive
 - ion etching, 731
 - physical vapor deposition, 427
 - sputtering, 67
- refractive index, 713
- regrowth, 545, 551, 563, 617
- resistivity, 23, 47, 285
- roughening, 35

- scanning micro-reflectometer, 495
- Schottky barrier, 249, 695
- scratch, 475
- secondary ion, 41
- secondary ion mass spectrometry, 519, 665, 749
- segregation, 201, 333, 533, 545
- self annealing implantation, 569
- semiconductor
- Al₂O₃, 363, 495, 507, 587
 - CdTe, 701
 - GaAlAs, 749
 - GaAs, 249, 665, 671, 677, 683, 695, 749
 - Ge, 35, 125, 151, 285, 581, 593, 611, 683
 - InAs, 689
 - KNbO₃, 719
 - LiNbO₃, 713, 719
 - NiP, 525
 - Si, 3, 41, 61, 113, 157, 243, 279, 291, 533, 545, 551, 557, 563, 569, 575, 581, 593, 611, 617, 623, 659, 665, 677, 689, 731, 743
 - SiO₂, 41, 513, 605, 623, 731
 - TiB₂, 653
 - TiSi₂, 641
 - WSi, 249
 - ZnO, 725
- semiconductor injection lasers, 507
- shallow junction, 635, 641
- sheet resistance, 635, 641, 659, 725
- silica glass, 519
- silicide, 47, 249, 647, 653, 659
- silicon-on-insulator, 623
- silicon-on-sapphire, 629
- silicon oxynitride, 61
- SIMOX, 617, 623
- smoothing, 35
- solar cells, 701
- solid phase epitaxy, 551, 557, 563, 599
- solid-state reaction, 255
- sputtering, 29, 41, 67, 91, 109, 231, 269, 333, 483, 507, 513, 725
- steel, 91, 315, 389, 439, 451, 457
- sticking coefficient, 55
- stress, 17, 23, 507
- subplantation model, 101
- superadditivity, 181
- superconductor, 261, 351
- surface
- morphology, 35, 131, 285, 695
 - processes, 3, 163
 - ripple, 269
 - structure, 457
- Talystep, 525
- tensile stress, 403
- texture, 17
- thermal spike, 157, 163, 189, 195, 261
- thin film, 41, 47, 61, 109, 131, 163, 269, 469, 575
- time-of-flight, 3, 125, 469
- topography, 269
- transient reflectivity, 563
- tribology, 91, 389, 403, 409, 415, 421, 427, 433, 439, 451, 463
- ultraviolet reflectivity, 671
- vacancy, 175, 219, 569, 581
- vacuum ultraviolet photons, 605
- Vickers hardness, 421
- void, 151
- waveguiding, 713
- wear, 389, 403, 409, 439, 457, 463
- x-ray
- diffraction, 17, 73, 231, 243, 255, 279, 321, 415, 469, 599, 653, 659, 689
 - optics, 513
 - photoelectron spectroscopy, 415, 519, 677, 695